frontiers | Research Topics

Bioactive bone regenerative materials and bionic prosthesis interfaces

Edited by
He Liu, Jianxun Ding and Chao Zhao

Published in
Frontiers in Bioengineering and Biotechnology
Frontiers in Materials

ISSN 1664-8714
ISBN 978-2-83251-166-4
DOI 10.3389/978-2-83251-166-4

About Frontiers

Frontiers is more than just an open access publisher of scholarly articles: it is a pioneering approach to the world of academia, radically improving the way scholarly research is managed. The grand vision of Frontiers is a world where all people have an equal opportunity to seek, share and generate knowledge. Frontiers provides immediate and permanent online open access to all its publications, but this alone is not enough to realize our grand goals.

Frontiers journal series

The Frontiers journal series is a multi-tier and interdisciplinary set of open-access, online journals, promising a paradigm shift from the current review, selection and dissemination processes in academic publishing. All Frontiers journals are driven by researchers for researchers; therefore, they constitute a service to the scholarly community. At the same time, the *Frontiers journal series* operates on a revolutionary invention, the tiered publishing system, initially addressing specific communities of scholars, and gradually climbing up to broader public understanding, thus serving the interests of the lay society, too.

Dedication to quality

Each Frontiers article is a landmark of the highest quality, thanks to genuinely collaborative interactions between authors and review editors, who include some of the world's best academicians. Research must be certified by peers before entering a stream of knowledge that may eventually reach the public - and shape society; therefore, Frontiers only applies the most rigorous and unbiased reviews. Frontiers revolutionizes research publishing by freely delivering the most outstanding research, evaluated with no bias from both the academic and social point of view. By applying the most advanced information technologies, Frontiers is catapulting scholarly publishing into a new generation.

What are Frontiers Research Topics?

Frontiers Research Topics are very popular trademarks of the *Frontiers journals series*: they are collections of at least ten articles, all centered on a particular subject. With their unique mix of varied contributions from Original Research to Review Articles, Frontiers Research Topics unify the most influential researchers, the latest key findings and historical advances in a hot research area.

Find out more on how to host your own Frontiers Research Topic or contribute to one as an author by contacting the Frontiers editorial office: frontiersin.org/about/contact

Bioactive bone regenerative materials and bionic prosthesis interfaces

Topic editors

He Liu — Jilin University, China

Jianxun Ding — Changchun Institute of Applied Chemistry, Chinese Academy of Sciences (CAS), China

Chao Zhao — University of Alabama, United States

Citation

Liu, H., Ding, J., Zhao, C., eds. (2023). *Bioactive bone regenerative materials and bionic prosthesis interfaces*. Lausanne: Frontiers Media SA.

doi: 10.3389/978-2-83251-166-4

Table of contents

05 Editorial: Bioactive bone regenerative materials and bionic prosthesis interfaces
He Liu, Yuhang Tian, Chao Zhao and Jianxun Ding

08 The Development of a Magnesium-Releasing and Long-Term Mechanically Stable Calcium Phosphate Bone Cement Possessing Osteogenic and Immunomodulation Effects for Promoting Bone Fracture Regeneration
Jun Wu, Feihong Liu, Zejin Wang, Yuan Liu, Xiaoli Zhao, Christian Fang, Frankie Leung, Kelvin W. K. Yeung and Tak Man Wong

23 Advanced Surface Modification for 3D-Printed Titanium Alloy Implant Interface Functionalization
Xiao Sheng, Ao Wang, Zhonghan Wang, He Liu, Jincheng Wang and Chen Li

48 D-arginine Enhances the Effect of Alpha-Amylase on Disassembling *Actinomyces viscosus* Biofilm
Baosheng Li, Qing Cai, Zixuan Wang, Shuwei Qiao, Yanzhen Ou, Rui Ma, Chuanfu Luo and Weiyan Meng

62 Chitosan-Based Biomaterial Scaffolds for the Repair of Infected Bone Defects
Yuhang Tian, Danhua Wu, Dankai Wu, Yutao Cui, Guangkai Ren, Yanbing Wang, Jincheng Wang and Chuangang Peng

83 Engineering Multifunctional Hydrogel With Osteogenic Capacity for Critical-Size Segmental Bone Defect Repair
Shaowei Zheng, Haobo Zhong, Hao Cheng, Xu Li, Guowei Zeng, Tianyu Chen, Yucong Zou, Weile Liu and Chunhan Sun

94 Fabrication and Effect of Strontium-Substituted Calcium Silicate/Silk Fibroin on Bone Regeneration *In Vitro* and *In Vivo*
Yuning Zhou, Yue Hu, Mamoru Uemura, Lunguo Xia, Xingge Yu and Yuanjin Xu

105 Biomaterials for Interbody Fusion in Bone Tissue Engineering
Han Zhang, Zhonghan Wang, Yang Wang, Zuhao Li, Bo Chao, Shixian Liu, Wangwang Luo, Jianhang Jiao and Minfei Wu

126 Total Talar Replacement With Custom-Made Vitallium Prosthesis for Talar Avascular Necrosis
Wenbin Luo, Hanyang Zhang, Qing Han, Zhaoyan Li, Zhuan Zhong, Guoliang Jia, Yuxuan Liu, Fei Chang and Jincheng Wang

135 Advances and Prospects in Antibacterial-Osteogenic Multifunctional Dental Implant Surface
Zixuan Wang, Baosheng Li, Qing Cai, Xiaoyu Li, Zhaoyi Yin, Birong Li, Zhen Li and Weiyan Meng

145 Improving the Stability of a Hemipelvic Prosthesis Based on Bone Mineral Density Screw Channel and Prosthesis Optimization Design
Rongqi Zhou, Haowen Xue, Jincheng Wang, Xiaonan Wang, Yanbing Wang, Aobo Zhang, Jiaxin Zhang, Qing Han and Xin Zhao

156 Mechanical Distribution and New Bone Regeneration After Implanting 3D Printed Prostheses for Repairing Metaphyseal Bone Defects: A Finite Element Analysis and Prospective Clinical Study
Bingchuan Liu, Xingcai Li, Weipeng Qiu, Zhongjun Liu, Fang Zhou, Yufeng Zheng, Peng Wen and Yun Tian

166 Combined Application of Er:YAG and Nd:YAG Lasers Enhances Osseointegration at Dental Bone-Implant Interface
Tianyuan Zhao and Meihua Li

176 Bone Engineering Scaffolds With Exosomes: A Promising Strategy for Bone Defects Repair
Mingming Zhang, Yi Li, Taojin Feng, Ran Li, Zhongqi Wang, Licheng Zhang, Pengbin Yin and Peifu Tang

188 Progress of Platelet Derivatives for Cartilage Tissue Engineering
Siyu Wu, Wenlai Guo, Rui Li, Xi Zhang and Wenrui Qu

209 Novel Design of the Compound Sleeve and Stem Prosthesis for Treatment of Proximal Femur Bone Defects Based on Topology Optimization
Haowen Xue, Haotian Bai, Rongqi Zhou, Jincheng Wang, Bin Zhou, Xiaonan Wang, Wenbin Luo and Xin Zhao

219 Improved repair of rabbit calvarial defects with hydroxyapatite/chitosan/polycaprolactone composite scaffold-engrafted EPCs and BMSCs
Hedong Yu, Lingyun Xia, Xieyuan Leng, Yongji Chen, Li Zhang, Xiaobing Ni, Jie Luo and Weidong Leng

230 Nanocarriers for intracellular co-delivery of proteins and small-molecule drugs for cancer therapy
Zhihong Cheng, Yongshuang Li, Duoyi Zhao, Wei Zhao, Meng Wu, Weilin Zhang, Yan Cui, Peng Zhang and Zhiyu Zhang

250 Advanced materials for enamel remineralization
Jiarong Xu, Hui Shi, Jun Luo, Haiyan Yao, Pei Wang, Zhihua Li and Junchao Wei

268 Natural biopolymer scaffold for meniscus tissue engineering
Yachen Peng, Meng Lu, Zhongsheng Zhou, Chenyu Wang, Enbo Liu, Yanbo Zhang, Tong Liu and Jianlin Zuo

287 Alginate-modified mesoporous bioactive glass and its drug delivery, bioactivity, and osteogenic properties
Haiyan Yao, Jun Luo, Yunyun Deng, Zhihua Li and Junchao Wei

297 Bone regeneration materials and their application over 20 years: A bibliometric study and systematic review
Xudong Zhang, Qianming Li, Zhengxi Wang, Wei Zhou, Linlin Zhang, Yingsheng Liu, Ze Xu, Zheng Li, Chen Zhu and Xianzuo Zhang

frontiers | Frontiers in Bioengineering and Biotechnology

TYPE Editorial
PUBLISHED 13 December 2022
DOI 10.3389/fbioe.2022.1111743

OPEN ACCESS

EDITED AND REVIEWED BY
Hasan Uludag,
University of Alberta, Canada

*CORRESPONDENCE
He Liu,
heliu@jlu.edu.cn
Chao Zhao,
czhao15@eng.ua.edu
Jianxun Ding,
jxding@ciac.ac.cn

SPECIALTY SECTION
This article was submitted to Biomaterials, a section of the journal Frontiers in Bioengineering and Biotechnology

RECEIVED 30 November 2022
ACCEPTED 07 December 2022
PUBLISHED 13 December 2022

CITATION
Liu H, Tian Y, Zhao C and Ding J (2022), Editorial: Bioactive bone regenerative materials and bionic prosthesis interfaces. *Front. Bioeng. Biotechnol.* 10:1111743. doi: 10.3389/fbioe.2022.1111743

Editorial: Bioactive bone regenerative materials and bionic prosthesis interfaces

He Liu[1]*, Yuhang Tian[1], Chao Zhao[2]* and Jianxun Ding[3]*

[1]Department of Orthopedics, The Second Hospital of Jilin University, Changchun, China, [2]Department of Chemical and Biological Engineering, The University of Alabama, Tuscaloosa, AL, United States, [3]Key Laboratory of Polymer Ecomaterials, Changchun Institute of Applied Chemistry, Chinese Academy of Sciences, Changchun, China

KEYWORDS

bioactive materials, bone regenerative materials, bionic prosthesis interfaces, controlled drug delivery, regenerative medicine

Editorial on the Research Topic
Bioactive bone regenerative materials and bionic prosthesis interfaces

Bone defects caused by high-energy trauma, infection, and tumor reconstruction have been a severe clinical challenge and placed a significant burden on patients. Although autografting has been recognized as the gold standard for the treatment of bone defects, it still has many unavoidable disadvantages. The development of bioactive bone regeneration materials has brought innovations to the reconstruction of skeletal functions.

The bone regeneration biomaterials should have the appropriate biocompatibility and enhanced mechanical, antibacterial, and osteogenic properties. When bioactive bone regeneration materials are implanted into the defect site, they should promote integration of the prosthetic interface with the surrounding bone tissue and maintain long-term stability, which is essential for bone repair.

Herein, this Research Topic covered 21 publications submitted by 151 researchers, comprising 11 original research articles and 10 review articles (total views: 26196 views as of 10 December 2022). These studies included antibacterial materials for dental implant surgery, bone tissue engineering, drug release system, and finite element analysis. The papers included in this topic are briefly discussed below.

In dental implant surgery, ideal osteointegration of the implant with the surrounding bone tissue provides the basis for bone regeneration (Wang et al.) However, the biofilm formed on the prosthesis interface after infection destroys the bone integration ability and severely affects the progress of bone repair. Therefore, it is necessary to develop antibacterial biomaterials to prevent and treat peri-implantitis. α-Amylase (α-Amy) effectively destroyed the biofilm of *Actinomyces viscosus* by decomposing the complex polysaccharide. However, 0.1%–0.5% of α-Amy showed significant toxicity to MC3T3-E1 cells. D-arginine was investigated to enhance the biofilm-decomposing ability of 0.01% α-Amy without any cytotoxicity by augmenting the catalytic triad and stabilizing the

calcium binding region (Li et al.) Moreover, biomaterials with remineralization property are also essential in the dental implant surgery, especially in dental caries. These advanced materials, including inorganic, organic, and polymer materials, have the ability of reconstructing re-mineralized tissue on damaged surfaces while enhancing mechanical strength at the same time. The detailed classification and functions of these materials were reviewed (Xu et al.) Apart from the single anti-infection or osteogenic property, the dual functional modification of dental implant surface with both antibacterial and osteogenic properties, such as bio-macromolecule, polymer, titanium dioxide (TiO_2) nanotube, and metal ion/nanoparticle coatings, and their effect on soft tissue integration, bone regeneration, and immune response were also summarized (Wang et al.). In addition to biomaterials, the laser-assisted implant for bone repair has a good development prospect. Er:YAG laser is a kind of dental hard tissue laser approved by the American Food and Drug Administration (FDA). Ti alloy scaffold improved surface wettability, accelerate osteoblast adhesion, and generate new bone after Er:YAG laser therapy. Combining Er:YAG laser with Nd:YAG, another low-intensity laser promoting the osteoblast differentiation at early edge, achieved the best results in bone regeneration and implant tissue construction (Zhao and Li).

Bone tissue engineering integrates the traditional methods and ideas from materials engineering and biological science to produce the desired bone substitution. The scaffolds, cells, and regulatory factors are essential elements in bone tissue engineering. The tetraethyl orthosilicate-based supramolecular hydrogel was used as an ideal osteo-inductive factor to promote the osseointegration at the bone defect site and combined with poly(vinyl alcohol) and sodium tetraborate to accelerate osteogenic performance *in vitro* and *in vivo* (Zheng et al.) In the process of bone regeneration, neovascularization is also an essential element. Blood vessels served as a communication network between the new bone and surrounding tissues, maintaining the stability of new bone. The strontium-substituted calcium silicate (SrCS) has significant osteogenic and angiogenesis properties. The SrCS and silk fibroin composite scaffold was prepared, and its osteogenesis and angiogenesis were well evaluated for calvarial defect reconstruction (Zhou et al.) Besides, the platelet derivatives, including platelet-rich plasma (PRP), platelet-rich fibrin (PRF), and platelet lysates (PL), which are rich in growth factors and adhesion proteins were combined with biomaterial scaffolds for application in cartilage tissue engineering to address the limited self-renewal capacity of articular cartilage due to the lack of blood vessels and nerves (Wu et al.) Typically, natural biopolymers, such as collagen, silk, hyaluronic acid, chitosan, and extracellular matrix, for the repair of meniscal injury have also been well-reviewed (Peng et al.)

Interbody fusion surgery is a promising approach to the treatment of disc protrusion and spondylolisthesis. The three-dimensional (3D) printed biomaterial scaffolds realized the customized interbody fusion cage to achieve biological stability (Zhang et al.) In general, 3D printed implants, especially 3D printed Ti alloy, have been widely applied in orthopedics. However, the Ti alloy implant surfaces always need to be modified to achieve ideal osseointegration. Common modification methods include chemical surface modification, physical surface modification, and biological surface modification through which the prosthetic interface obtained the antibacterial property, enhanced osseointegration, and improved mechanical properties (Sheng et al.)

The sustained-release system for delivery of bioactive agents through a variety of biomaterials is an indispensable method for promoting bone regeneration. Mesoporous bioactive glass (MBG) was known as an excellent drug carrier due to its porosity and osteogenic property. Herein, the alginate-modified MBG was prepared to improve the loading efficiency and prolong the sustained release period (Yao et al.) Metal magnesium ion (Mg^{2+}) promoted bone regeneration by regulating the behaviors of bone marrow mesenchymal stem cells. The magnesium-contained calcium phosphate cement was prepared for the sustained release of Mg^{2+} to achieve long-term mechanical stability and osteogenic property (Wu et al.) Moreover, co-delivery could be preferred for tumor therapy, and the intracellular co-delivery of proteins and small molecular antitumor drugs from nanocarriers was presented (Cheng et al.)

Chitosan, an emerging biomaterial, has been extensively used in bone regeneration due to its outstanding properties. The characteristics of chitosan and its derivatives, as well as the specific application forms in infected bone defects, were specifically summarized (Tian et al.) Yu et al. investigated the chitosan/hydroxyapatite/polycaprolactone composite scaffold to inoculate endothelial progenitor cells and bone marrow mesenchymal stem cells to evaluate the bone repair ability by detecting osteogenesis-related genes (Yu et al.) The results demonstrated that this dual-cell treatment was better than single-cell or cell-free treatments. Moreover, the application of exosomes to cure bone defects has some advantages compared to cell therapy, such as a wide range of sources and not limited to stem cells. The mechanisms of exosomes regulating osteogenesis, angiogenesis, and inflammation modulation were summarized (Zhang et al.)

In addition to the ability to integrate the prosthesis interface with the surrounding bone tissue, the biomechanical properties of designed prosthesis were important factors in promoting bone regeneration and functional reconstruction. In this Research Topic, several studies used finite element analysis to analyze the biomechanical distribution of 3D printed prostheses. After finite element verification, the different fixation methods of 3D printed prosthesis for the repair of metaphyseal bone defects resulted in different mechanical behaviors (Liu et al.) A unique bone mineral density screw was designed and compared with the traditional screw by finite element analysis method for mechanical properties and then improved by topology optimization (Zhou et al.)

Furthermore, based on topology optimization, an optimized prosthesis with enhanced biomechanical properties was designed to repair the bone defect of proximal femur (Xue et al.) Vitallium Prosthesis, a customized 3D printed prosthesis was also designed and applied to the patients with ischemic necrosis of the talus and gained the expected results (Luo et al.)

Finally, the research hotspots of bone regeneration materials at each stage in the past 20 years, the latest progress of existing research, and the exploration direction for the future are comprehensively evaluated (Zhang et al.)

In summary, this invited Research Topic covered several fundamental and clinical studies with various bone regeneration biomaterials and bionic prosthesis interfaces. This interdisciplinary research has created an excellent theoretical and practical basis for the innovation of biomaterials and the transformation of clinical medicine, and also helps readers to better understand this field.

Author contributions

All authors listed have made a substantial, direct and intellectual contribution to the work, and approved it for publication.

Acknowledgments

The editors appreciate the contributions of all authors to this Research Topic, the constructive comments of all the reviewers, and the editorial support from Frontiers throughout the publication process.

Conflict of interest

The authors declare that the research was conducted in the absence of any commercial or financial relationships that could be construed as a potential conflict of interest.

Publisher's note

frontiers in Bioengineering and Biotechnology

ORIGINAL RESEARCH
published: 11 January 2022
doi: 10.3389/fbioe.2021.803723

The Development of a Magnesium-Releasing and Long-Term Mechanically Stable Calcium Phosphate Bone Cement Possessing Osteogenic and Immunomodulation Effects for Promoting Bone Fracture Regeneration

Jun Wu[1,2†], Feihong Liu[1†], Zejin Wang[1], Yuan Liu[3], Xiaoli Zhao[3], Christian Fang[1,2], Frankie Leung[1,2], Kelvin W. K. Yeung[1,2] and Tak Man Wong[1,2*]*

[1]Shenzhen Key Laboratory for Innovative Technology in Orthopaedic Trauma, The University of Hong Kong-Shenzhen Hospital, Shenzhen, China, [2]Department of Orthopaedics and Traumatology, The University of Hong Kong, Pokfulam, Hong Kong SAR, China, [3]Research Center for Human Tissues and Organs Degeneration, Institute of Biomedicine and Biotechnology, Shenzhen Institutes of Advanced Technology, Chinese Academy of Sciences, Shenzhen, China

OPEN ACCESS

Edited by:
He Liu,
Jilin University, China

Reviewed by:
Kaili Lin,
Shanghai Jiao Tong University, China
Ahmed El-Fiqi,
Dankook University, South Korea

***Correspondence:**
Kelvin W. K. Yeung
wkkyeung@hku.hk
Tak Man Wong
wongtm@hku.hk

[†]These authors have contributed equally to this work and share first authorship

Specialty section:
This article was submitted to Biomaterials, a section of the journal Frontiers in Bioengineering and Biotechnology

Received: 28 October 2021
Accepted: 20 December 2021
Published: 11 January 2022

Citation:
Wu J, Liu F, Wang Z, Liu Y, Zhao X, Fang C, Leung F, Yeung KWK and Wong TM (2022) The Development of a Magnesium-Releasing and Long-Term Mechanically Stable Calcium Phosphate Bone Cement Possessing Osteogenic and Immunomodulation Effects for Promoting Bone Fracture Regeneration. Front. Bioeng. Biotechnol. 9:803723. doi: 10.3389/fbioe.2021.803723

Bone grafts are commonly used for the treatment of critical sized bone defects. Since the supply of autologous bone is insufficient, allogeneic bone grafts have been used most of the time. However, the poor osteogenic property of allogeneic bone grafts after pretreatment results in delayed union, non-union, or even occasional deformity. Calcium phosphate cement (CPC) is one of the most promising bone filling materials due to its good biocompatibility and similar chemical components as natural bone. However, clinical applications of CPC were hampered by limited osteogenic effects, undesired immune response which results in resorption, and poor mechanical stability *in vivo*. Magnesium (Mg) has been proven to trigger bone regeneration through modulating cell behaviors of mesenchymal stem cells and macrophages significantly. Unfortunately, the degradation raters of pure Mg and Mg oxide are extremely fast, resulting in early collapse of Mg contained CPC. In this study, we developed a novel magnesium contained calcium phosphate bone cement (Mg-CPC), possessing long-term mechanical stability and osteogenic effects through sustained release of Mg. Furthermore, *in vitro* studies showed that Mg-CPC had no cytotoxic effects on hBMMSCs and macrophage RAW 264.7, and could enhance the osteogenic differentiation as determined by alkaline phosphate (ALP) activity and calcium nodule staining, as well as suppress the inflammatory as determined by expression of anti-inflammatory cytokine IL-1RA. We also found that Mg-CPC promoted new bone formation and bone maturation *in vivo*. These results suggest that Mg-CPC should be a good substitute material for bone grafts in clinical use.

Keywords: calcium phosphate cement (CPC), immunomodulation, osteogenic, bone regeneration, anti-collapsibility

1 INTRODUCTION

Each year, a large number of people suffer from critical sized bone defects caused by high-energy trauma or diseases (Wiese and Pape, 2010). The repair of critical bone defect has always been a clinical challenge (Zhao et al., 2009). Autologous bone grafting is the preferred treatment option in many cases of orthopedic surgeries (Bauer and Muschler, 2000; Jung et al., 2020). But for critical sized bone defects, the donor sites for autologous bone harvest are always insufficient, and a second operation is sometimes needed, leading to additional pain and increased complication risks (Arrington et al., 1996). Allogeneic bone graft is another choice (De Long et al., 2007). However, to eliminate immune rejection and infection, pretreatment inactivation is needed before implantation, which decreases the osteogenic activity as well (Zimmermann and Moghaddam, 2011), resulting in delayed healing, non-union, or even occasional deformities (Orchard et al., 2014). Therefore, scientists have long attempted to develop novel implants with good biocompatibility and osteogenic effects (Reichert et al., 2009).

Calcium phosphate bone cement (CPC) is a biological material with good biocompatibility, bone conductivity, and similar mechanical strength to cancellous bone. The final product formed after curing is hydroxyapatite (HA), which is similar to the main inorganic component of natural bone (Nair et al., 2013) and is considered one of the most promising potential bone graft substitutes (Scheer and Adolfsson, 2009). CPC was invented by Brown and Chow in the 1980s (Brown and Chow, 1983) and was approved for clinical use by the FDA in 1996 (Friedman et al., 1998). However, CPC has limited osteogenic effects, and implant failures due to delayed healing or non-union have been observed. Many researchers have tried to add osteogenic substances, such as growth factors, stem cells and so on, into bone cement to improve the osteogenesis of bone cement (Meraw et al., 2000; Zhao et al., 2011), but few have explored the effect of immune response, which plays important roles in modulating bone regeneration after a fracture. Moreover, prolonged inflammation is one of the major causes of implant failure (Han et al., 2014; Kovach et al., 2015).

Biomaterial implants inevitably cause immune response to the host and have a profound impact on the process of bone healing (Franz et al., 2011). Macrophages have long been considered to be important immune-benefit cells, and their polarization can be divided into two types: classical activation into inflammatory macrophages M1-type and selective activation into therapeutic macrophages M2-type (Stein et al., 1992). M1-type macrophages can produce pro-inflammatory cytokines, which promote inflammation and affect wound healing. M2-type macrophages can produce anti-inflammatory cytokines, which stimulate arginase activity and promote wound healing. They can be converted into each other under certain conditions (Mosser and Edwards, 2008).

Recent studies have reported the application of magnesium implants in fracture healing. Chen et al. (2014) prepared a kind of β-TCP scaffold containing an Mg coating that could effectively induce the differentiation of macrophages into M2 compared with uncoated β-TCP, indicating that magnesium has the potential of immune regulation of the bone. Wang et al. (2016) prepared a magnesium-containing CPC by mixing the cement derived from magnesium oxide (MgO) in a fixed ratio on the basis of ordinary CPC. *In vitro* experiments showed that this bone cement could not only promote osteogenesis but also effectively reduce pro-inflammatory cytokines. However, the underlining mechanisms of modulating bone immunology by magnesium-containing CPC are still to be revealed.

Therefore, it is of great interest to incorporate magnesium into orthopedic implants to increase osteogenic effects and to modulate immune responses for bone regeneration. However, magnesium-based implants usually degrade too fast under certain physiological conditions, which causes the early collapse of CPC and hampers their clinical applications. In the previous study, our research group synthesized a strontium-containing CPC possessing bone regeneration-promoting effects that could rapidly self-solidify at room temperature. In this study, a novel magnesium-containing calcium phosphate bone cement (Mg-CPC) was developed by incorporating a magnesium compound with a compatible degradation rate, combined with an organic cross-linking agent to achieve collapse resistance, sustained magnesium release, and long-term mechanical stability. To reveal the mechanism of enhanced bone healing by Mg, the osteogenic and anti-inflammatory properties of the Mg-CPC and CPC were tested *in vitro* and *in vivo*. The results showed that the Mg-CPC could enhance osteogenic differentiation and suppress prolonged inflammation. Furthermore, the sustained release of magnesium contributed to the in-growth of new bone tissue, which facilitated the union of Mg-CPC and bone tissue, while the mechanical strength of Mg-CPC was not deteriorated. The presented Mg-CPC might be used in promising applications in healing critical sized bone defects.

2 MATERIALS AND METHODS

2.1 Fabrication of the Magnesium-Releasing Calcium Phosphate Bone Cement

The calcium phosphate cement was synthesized by thoroughly stirring the liquid phase and the powder phase (**Table 1**). The liquid phase consists of 20% (wt%) citric acid (sigma) and 12% (wt%) polyvinylpyrrolidone K-30 (PVP, sigma) in ultrapure water. The powder phase consists of tetracalcium phosphate (TTCP, Wako) and dicalcium phosphate anhydrous (DCPA, sigma). We used magnesium phosphate dibasic trihydrate (DMPA, sigma) to make Mg-CPC. The cement paste was prepared by mixing the liquid and powder phases at a ratio of 0.7 ml/g. In this study, the power and liquid phases of cement with different magnesium contents (0, 5, 10, and 20%) were fully mixed and injected into the customized mold to form cylindrical

TABLE 1 | The powder composition of calcium phosphate bone cement.

Group	Mg/(Mg + Ca) (mole ratio)	TTCP [$Ca_4(PO_4)_2O$] (mole ratio)	DCPA [$CaHPO_4$] (mole ratio)	DMPA [$MgHPO_4$] (mole ratio)
CPC	0	1	1	0
5% Mg-CPC	5%	1	0.75	0.25
10% Mg-CPC	10%	1	0.5	0.5
20% Mg-CPC	20%	1	0	1

samples with a bottom diameter of 6 mm and a height of 12 mm and then removed after curing and ethylene oxide sterilization. The curing reaction of classical calcium phosphate cement can be divided into two stages: hydration and precipitation. The phosphate compound of calcium firstly produces a large number of calcium ions and phosphate ions through hydration, which then react slowly to form HA (**Eqs 1, 2, 6**; Liu et al., 2003).

The chemical reaction equation is as follows

(a) Dissolution

$$Ca_4(PO_4) + H_2O \rightarrow 4Ca^{2+} + 2PO_4^{3-} + 2OH^- \quad (1)$$

$$CaH(PO_4) \rightarrow Ca^{2+} + 2HPO_4^{2-} \quad (2)$$

$$MgH(PO_4) \rightarrow Mg^{2+} + 2HPO_4^{2-} \quad (3)$$

(b) Chelation

$$3Mg^{2+} + 2H_3Cit \rightarrow Mg_3Cit_2 \quad (4)$$

$$3Ca^{2+} + 2H_3Cit \rightarrow Ca_3Cit_2 \quad (5)$$

(c) HA formation

$$10Ca^{2+} + 6PO_4^{3-} + 2OH^- \rightarrow Ca_{10}(PO_4)_6(OH)_2 \quad (6)$$

2.2 Material Characterizations

2.2.1 Surface Morphology and Chemical Composition

The cement samples were immersed in simulated body fluid (SBF) solution and placed in a 37°C incubator. After immersion for 0, 14, and 28 days, quenching with liquid nitrogen for 30 min to stop the setting reaction of cements. Then the cements were dried using a freeze-drying machine (Alp2-4LD, Christ, Germany) for 15 h. The surface structure of the bone cement was observed using a scanning electron microscope (SEM) (ZEISS SUPRA *R* 55, Zeiss, Germany), and the surface distribution of calcium and magnesium was determined by energy dispersive spectrometer (EDS) after being gold plated. Each cement was ground into a powder using an amber mortar and analyzed by X-ray diffraction (XRD) (D8 Advance, Bruker, Germany) using Cu Kα (k = 1.5406 Å) radiation in step-scan mode (2y = 0.02 per step). Three samples were tested in each group.

2.2.2 Compressive Strength and Setting Time

The CPC and Mg-CPCs were made into a cylinder with a diameter of 6 mm and a height of 12 mm by using a mold. After setting and incubate at 37°C for 24 h. The cement samples were immersed in SBF for 0 and 28 days at 37°C. The volume (ml) of SBF was determined according to the equation of V = S/10, in which the S is the surface area of the cements (mm^2). The SBF was changed every 3 days. The material test machine (Instron E10000, United States) was taken out under a load of 1KN, and the speed was 0.1 mm/min, until the cement breaks. Three samples were tested in each group.

The setting time of cements were tested using the Gillmore apparatus according to the ASTM: C266-89 standard. Which have two kinds of needles, the light and thick needle with a 113.4 g weight and 2.13 mm diameter needle tip, the heavy and thin needle with 453.6 g weight and 1.06 mm diameter needle tip. After fully mixed the liquid and powder phases, moved into the customized mold with a bottom diameter of 6 mm and a height of 12 mm, two needles with different diameters and weights were gently placed on the cement surface. The initial setting time was measured by a light and thick needle. When the cement surface has no visual marks of the needle tip, record the time. Each test was repeated three times.

2.2.3 *In Vitro* Ion Release

The CPC and Mg-CPCs were made into a cylinder with a diameter of 4.5 mm and a height of 6 mm by using a mold. After setting and incubate at 37°C for 24 h, the cement samples were immersed in an 8 ml phosphate buffer saline (PBS) solution (without calcium and magnesium ions, PH = 7.35) and placed in a 37°C incubator. At days 1, 3, 7, 14 and 28 after immersion, all the extracts were collected and replaced with fresh PBS. An inductively coupled plasma emission spectrometer (Perkin Elmer, Optima 7000, United States) was used to detect the concentration of Mg and Ca ions in the extracted samples. The process was repeated three times for each group of samples.

2.3. *In Vitro* Characterizations

2.3.1. Cell Culture

The murine-derived macrophage cell line RAW 264.7 cells (RAW cells, Cell Bank, purchased from the Chinese Academy of Sciences) and human bone marrow mesenchymal stem cells (hBMMSCs) were purchased from Cyagen Biosciences Inc. (Guangzhou, China). The RAW 264.7 cells were cultured using the Dulbecco's modified Eagle's medium (DMEM, Gibco) supplemented with 10% (v/v) fetal bovine serum (FBS, Gibco) and antibiotics (100 U/ml of penicillin and 100 mg/ml of streptomycin) (Thermo Fisher Scientific, United States). The hBMMSCs were cultured using Minimal Essential

Medium Alpha (α-MEM, Gibco) supplemented with 10% (v/v) FBS and antibiotics (100 U/ml of penicillin and 100 mg/ml of streptomycin).

2.3.2 Cell Viability of Human Bone Marrow Mesenchymal Stem Cells and RAW264.7

The hBMMSCs were seeded on the 96-well plate with a density of 0.5×10^4 in each well at 37°C with 5% CO_2 for 24 h; then the medium was removed, and the extract was added to each well. At days 1 and 3, cell viability was tested using Cell Counting Kit-8 (Dojindo, Japan). The RAW264.7 macrophages at a density of 10,000 cells per well in the 96-well plate were incubated at 37°C and supplemented with 5% CO_2 for 1 d and then cultured with the extraction solution. The optical density (OD) was tested by a microplate reader (Epoch, BioTek, United States) at an absorbance of 450 nm. The extract solution was prepared according to ISO 10993-5, and the cements were immersed in the culture medium for 24 h at a ratio of 0.2 g/ml.

2.3.3 Alkaline Phosphatase Activity and ECM Mineralization of Human Bone Marrow Mesenchymal Stem Cells

The hBMMSCs were seeded on a 48-well plate (with a density of 2×10^4 for each well), incubated at 37°C, and supplemented with 5% CO_2. The cells were cultured using α-MEM supplemented with 10% (v/v) FBS and antibiotics. After 24 h, the culture mediums were replaced with extracts of CPC or Mg-CPC; for the Alkaline phosphatase activity (ALP) activity test, osteogenic differentiation materials [10 mM β-glycerophosphate (sigma), 50 μM ascorbic acid (sigma), and 10 nM dexamethasone (sigma)] were added to the mediums. After incubation for 3, 7, and 14 days, the cells were washed three times using PBS and then lysed by 0.1% Triton X-100 at 4°C for 30 min. The ALP activity was determined using an alkaline phosphatase assay kit (Nanjingjianchen, China). After incubation for 21 days, the cells were washed three times using PBS, fixed on ice with paraformaldehyde for 30 min, and washed again three times with PBS.

2.3.4 Immune Modulation Effects of Magnesium Contained Calcium Phosphate Bone Cement

2.3.4.1 Immunofluorescence

For the primary antibodies and antibodies, iNOS (Abcam, United States) and arginase (Abcam, United States) were chosen as markers for M1 and M2, respectively. RAW 264.7 cells were inoculated on the cement samples and cultured for 24 h. The supernatant was abandoned, and the cells on CPCs were fixed by 4% paraformaldehyde for 30 min. After fixation, the samples were washed three times using PBS and permeabilized with 0.25% Triton X-100 (PBST) for 10 min. They were then washed three times again using PBS and blocked for 30 min at room temperature using 5% FBS. The cells were then incubated with primary antibodies at 4°C overnight, washed again three times with PBS, and incubated with secondary antibodies (Abcam, United States) for 1 h at room temperature in the dark. The cells were washed again three times with PBS, stained with 4′,6-diamidino-2-phenylindole (DAPI, Abcam, United States), and observed using a fluorescence microscope (LEICA, Germany).

2.3.4.2 The Expression of Inflammatory Genes

RAW264.7 was seeded on bone cement at a cell density of 300,000 cells per well in 24-well plates. The cells were cultured for 1 days. Total RNA was extracted using an RNAprep Pure Cell/Bacteria Kit (TIANGEN, China), and reverse transcription was performed using a RevertAid First Strand cDNA Synthesis Kit (Thermo Fisher Scientific, United States). Then, a qRT-PCR test was performed using the real-time PCR system (Light Cycler 480, Roche, United States) with QuantiNova^{TM} SYBR Green PCR Master MIX (Qiagen, Germany). The target gene sequence primers, as shown in **Supplementary Table S1**, used GPDH as the house-keeping gene. The relative gene expression was calculated by Ct ($2^{-\Delta\Delta Ct}$). All the test procedures followed the manufacturer's instructions. Three samples were tested in each group.

2.3.4.3 Enzyme-Linked Immunosorbent Assay

The RAW264.7 cells were incubated on the bone cements for 1 and 3 days. The cell supernatant was used to the measure cytokine concentration using an ELISA assay kit (R&D Systems, United States). The operation was done according to the manufacturer's instructions and calibrated by standard curves. Three samples were tested in each group.

2.4 *In Vivo* Studies

2.4.1 Bone Defect in Rats

Animal experiments were approved by the Ethics Committee of the University of Hong Kong-Shenzhen Hospital. A total of 24 3-month-old Sprague–Dawley rats were used and randomly divided into four groups: a CPC group, a 10% Mg-CPC group, and a 20% Mg-CPC group. Using 4% chloral hydrate anesthesia, the right leg was selected as the surgical site. After surgical site shaving and disinfection, a scalpel was used to expose the distal femoral, and a 2.5 mm-diameter, 4 mm-long hole was created by drilling the bone at the lateral epicondyle on the femur. The area was saline washed three times, and the CPC, 10% Mg-CPC, and 20% Mg-CPC samples were implanted in the defect areas of the rats in each group, respectively. The areas were then sutured layer by layer and disinfected, followed by routine feeding.

2.4.2 Micro-CT Analysis

A CT scan was performed on the rats in each group at 4 and 8 weeks after the operations using a Micro-CT machine (Skyscan 1176, Bruker). The animals were then put into a respiratory anesthesia apparatus. After anesthesia, they were put into the slot of the micro-CT scanner, and a respiratory anesthesia mask was put on them. Then, each rat was placed on its side to fully expose the bone defect, the hatch was closed, and the scanning was started. After the scan, the animal was removed and the data were saved. Skyscan 1176 was used to select the scanning parameters: energy/intensity of 65 kVP, 385 A, a scanning time of 283 s, scanning accuracy of

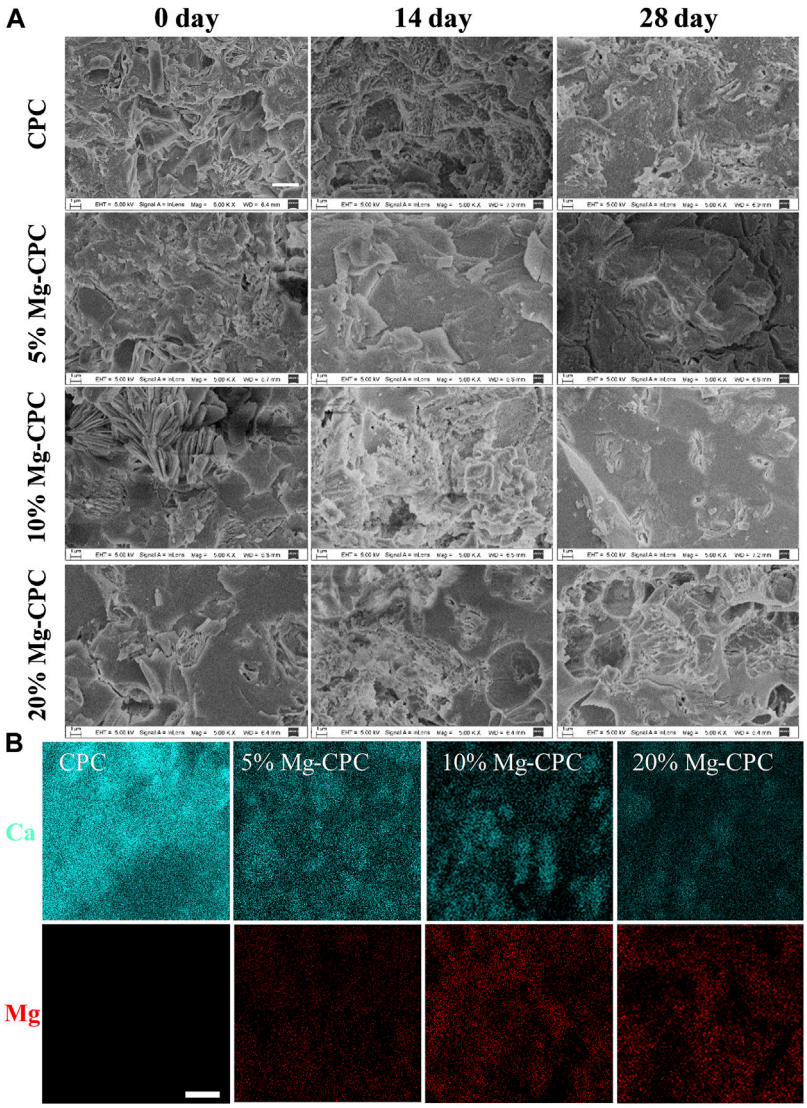

FIGURE 1 | Surface morphology of CPC and Mg-CPCs samples by SEM. **(A)** The SEM images of CPC and Mg-CPCs samples after immersion in SBF (Scale bar = 3 μm). **(B)** EDS mapping of Ca (blue dots), Mg (red dots); EDS analysis elements' composition on cement surfaces after immersion in SBF (Scale bar = 10 μm).

18.04 μm, the bx2 mode, and a scanning angle of 0.5°, scanning 360° at once. NRecon software was used for 3D reconstruction, DataViewer was used for analysis, and CTan was used to draw VOI. We take ROI as a circle with a radius of 90 pixels and analyze a thickness of 0.722 mm. On this basis, the circle with a radius of 75 pixels was removed, and the remaining part is the range of our analysis. The analysis included the tissue volume (TV), the bone volume (BV), the relative bone volume or the bone volume fraction (BV/TV) and Bone mineral density (BMD).

2.4.3 Histology

The rats were sacrificed, and their femurs were taken and fixed in 4% paraformaldehyde for 24 h at 4 and 8 weeks. The samples were decalcified using 10% EDTA, embedded in paraffin by an embedding machine (EG11504, Leica), and cut to 4 μm thick by a slicing machine (RM2235, Leica). The sections were stained with H&E (Solarbio) and Masson trichrome stain (Solarbio) and analyzed and photographed with a microscope panoramic scan.

2.5 Statistical Analysis

All the experiments had at least three independent replicates. The experimental chart was made using GraphPad Prism 7. All the results of each time point were presented as the mean ± standard deviation from three or more replicates. The statistical analysis was performed by Student's *t*-test and one-way analysis of variance use SPSS 17. The p value <0.05 was considered statistically significant.

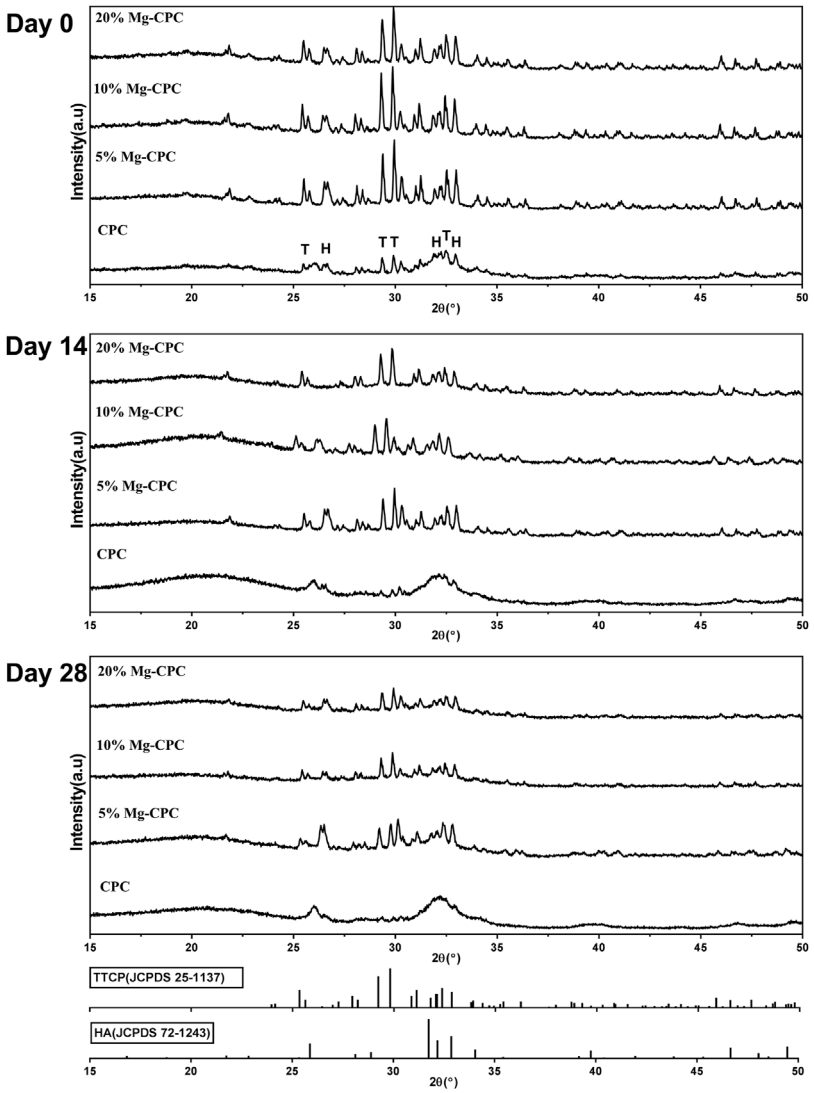

FIGURE 2 | XRD patterns of cement types. After immersion in SBF 0, 14, and 28 days, all the cement groups were freeze-dried to remove moisture and then ground into a powder for tested. The results were compared with the standard card of HA (JCPDS 72-1243) and TTCP (JCPDS 25-1137) (H: HA, T: TTCP).

3 RESULTS

3.1 The Material Characterization of Magnesium-Releasing Calcium Phosphate Bone Cement

3.1.1 Surface Morphology and Magnesium Distribution

The SEM images of the CPC and Mg-CPC groups showed that after setting, similar irregular crystals could be observed (**Figure 1A**). As the immersion time increased, the irregular crystals gradually disappeared. After immersion in SBF for 28 days, the irregular crystals were almost disappeared. Porous structures could be observed in the Mg-CPC group, which was due to the release of magnesium (**Figure 1A**). The EDS showed that the calcium and the magnesium were uniformly distributed throughout the cement samples, and the content of Mg was increased by incorporating a higher ratio of magnesium phosphate dibasic trihydrate (**Figure 1B**).

3.1.2 Crystal Structure

XRD patterns of CPC and Mg-CPC immersed in SBF were shown in **Figure 2**. Diffraction peaks of all raw materials could be observed at day 0, as well as diffraction peaks of HA, indicating that hydration reaction of TTCP is incomplete during cement solidification. As the immersion time increased, the intensities of diffraction peaks attributed to HA increased, while that of TTCP decreased, indicating that TTCP was hydrated to form HA gradually. At the day 28, the diffraction peak of TTCP disappeared and the broad diffraction peaks of HA was observed,

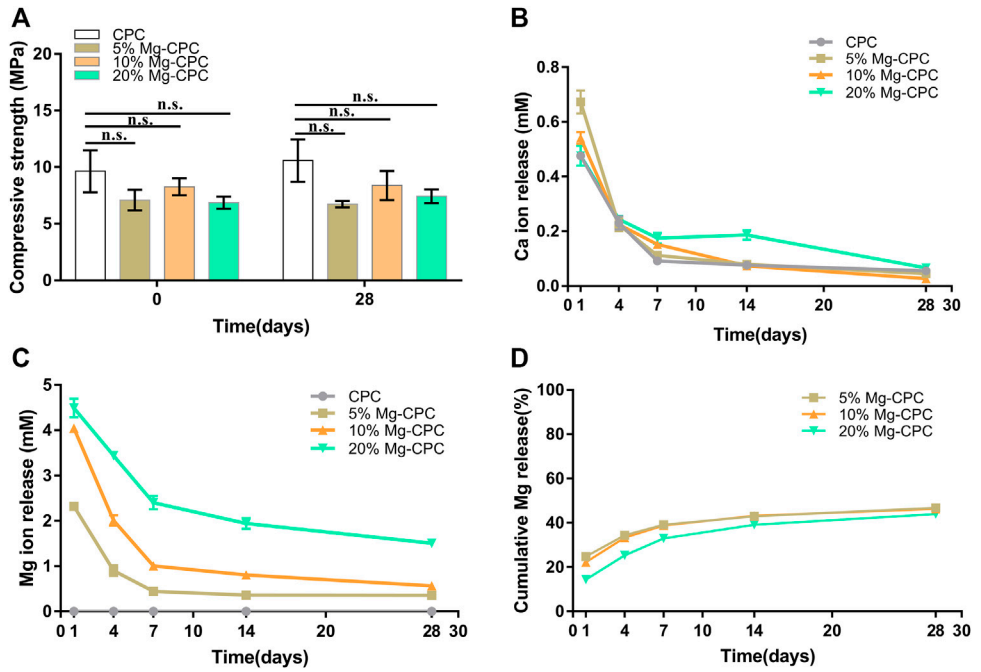

FIGURE 3 | Material characterization of bone cement *in vitro*. **(A)** Compressive strength of CPC and Mg-CPCs samples after immersion in SBF at day 0 and 28 (n.s., no significant difference). **(B)** Ca released into PBS determined by ICP-MS. **(C)** Mg released into PBS determined by ICP-MS. **(D)** Cumulative release of Mg.

TABLE 2 | Compressive strength and setting time of cements.

Group	CPC	5% Mg-CPC	10% Mg-CPC	20% Mg-CPC
Compressive strength (MPa)				
Day 0	9.64 ± 3.21	7.08 ± 1.58	8.26 ± 1.31	6.85 ± 0.945
Day 28[a]	10.57 ± 3.25	6.73 ± 0.50	8.37 ± 2.22	7.42 ± 1.05
Setting time (min)				
Initial	10.86 ± 0.34	9.55 ± 0.34	9.89 ± 0.26	11.05 ± 0.25
Final	21.39 ± 0.51	15.5 ± 0.5	17.77 ± 0.25	19.38 ± 0.53

[a]*The time of immersion in SBF.*

indicating that TTCP in CPC group was completely hydrated and amorphous HA were formed. Diffraction peaks of TTCP and HA were detected in the Mg-CPC groups at day 28, indicating that the hydration rate of TTCP was slower in Mg-CPC groups.

3.1.3 Mechanical Strength, Setting Time and *In Vitro* Ion Release

The compressive strength of the cement samples (**Figure 3A**) showed that, although the incorporation of Mg decreased the compressive modulus of CPC, their mechanical strengths were still close to cancellous bone. Furthermore, after immersion for 0 and 28 days, the compressive strengths of Mg-CPCs were almost unchanged, confirming the long-term mechanical stability of Mg-CPC. For comparison, MgO was also incorporated into CPC (MgO-CPC) as a substitution of magnesium phosphate dibasic trihydrate. After immersion in SBF, MgO-CPC quickly collapsed due to the fast degradation rate of MgO (**Supplementary Figure S1**).

The setting time of CPC and Mg-CPCs are shown in **Table 2**. The initial setting time of CPC and Mg-CPCs were about 10 min. The final setting time of Mg-CPCs decreased with the addition of DMPA compare with CPC. However, with the addition of DMPA increased, the setting time also increased.

The Ca ion concentration in the extract was shown in **Figure 3B**. An initial burst release was observed on day 1. After that, the release rate rapidly decreased. The ratio of Mg showed no effect on the release profiles of calcium.

The release profiles of Mg ion are shown in **Figure 3C**. Similar to Ca, initial burst releases on day 1 were observed in all the groups. After that, the release rates of Mg rapidly decreased until day 7, when near zero-order releases were achieved.

3.1.4 Effects of Magnesium-Releasing Calcium Phosphate Bone Cement on Human Bone Marrow Mesenchymal Stem Cells

To verify the effect of Mg-CPC on hBMMSCs, we used bone cement extract to test cytotoxicity, ALP activity, and *in vitro* mineralization. As shown in the figure, we tested the cell activity on day 1 and day 3 under the extract culture conditions and found

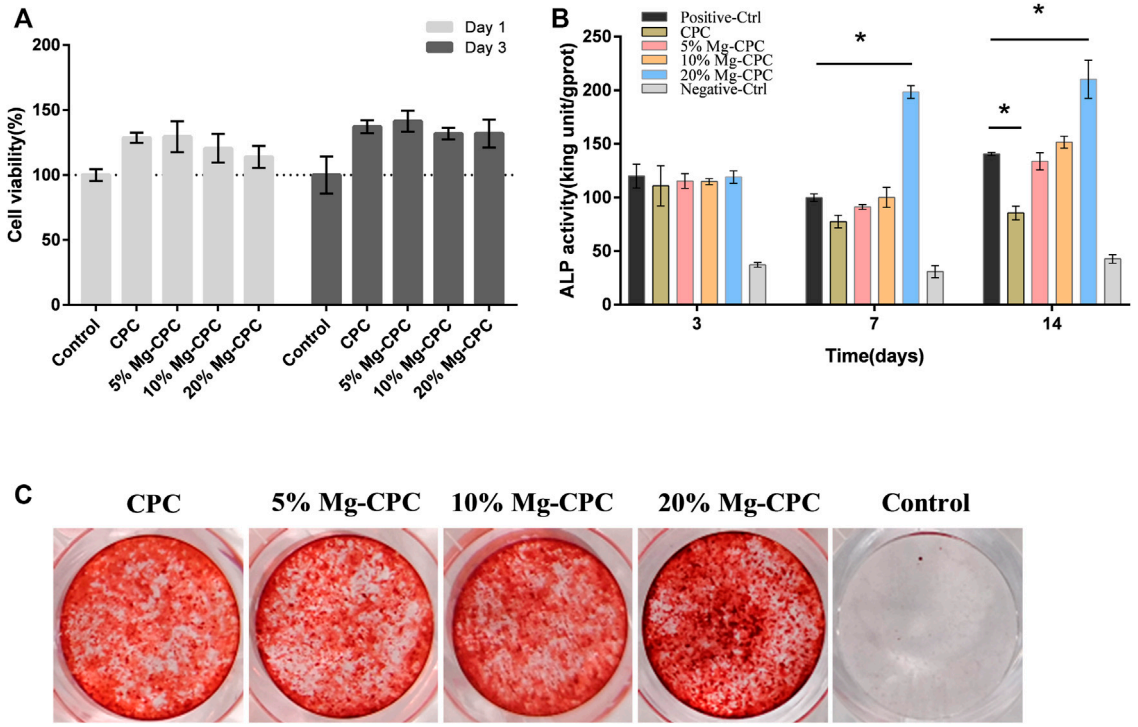

FIGURE 4 | Effect of cement on hBMMSCs. **(A)** Cell viability assay of CPC and Mg-CPCs. **(B)** ALP activity assay of CPC and Mg-CPC. **(C)** Alizarin red staining of CPC and Mg-CPCs (*$p < 0.05$).

that the cell viabilities of all the cement groups were higher than that of the blank control group, and none of the cement groups showed any toxicity to hBMMSCs. Indicating that all the cement samples had good biocompatibility (**Figure 4A**).

In the ALP activity test, we detected ALP activity on day 3, day 7, and day 14 and found that on day 3, no difference was observed between the cement group and the control group. The ALP activity of the 20% Mg-CPC group significantly increased on day 7 and day 14 (**Figure 4B**).

The mineralization effects of the Mg-CPCs were evaluated using alizarin red staining, which stained the calcium nodules in ECM into a red color. The results showed that the 20% Mg-CPC group exhibited more calcium nodules compared with the control group and the other Mg-CPC groups. The ALP test and alizarin red staining demonstrated that 20% Mg-CPC had the best osteogenic effects.

3.1.5 Animal Study

To investigate the osteogenic effect of magnesium release cement *in vivo*, we used a rat model of a critical bone defect of the femur (**Figure 5A**). Histological staining was performed at 4 and 8 weeks after bone cement implantation. Decalcification was performed without the implant being removed. The H&E staining results showed that a small amount of bone tissue could be observed in 20% Mg-CPC at week 4, but not in the control group. Interestingly, a large amount of bone tissue was observed in the 20% Mg-CPC at week 8 (**Figure 5A**), suggesting new bone had thoroughly grown into the 20% Mg-CPC. To observe bone maturation, mason trichrome stain was used. Mature bone (red color) could be observed in the 20% Mg-CPC at week 4, which was not observed in the CPC group. More red color appeared in the 20% Mg-CPC group at week 8, suggesting more mature bone in the 20% Mg-CPC group (**Figure 5B**).

Micro-CT evaluations were performed at 4 and 8 weeks after surgery. To visually observe the new bone formation, we performed a three-dimensional reconstruction of the bone defect site (**Figure 6A**). No significant difference was found in the bone volume of the new bone formation between the CPC and the Mg-CPCs at week 4. The bone volume of newly formed bone was significantly different in the 20% Mg-CPC group compared to the CPC and 10% Mg-CPC group at week 8 (**Figure 6B**). By calculating the BMD, we found that there was a significant difference between 20% Mg-CPC and CPC at week 4. However, at the week 8, the BMD was significantly different in Mg-CPC groups compared to the CPC group, with 20% Mg-CPC groups having the highest BMD (**Figure 6C**).

3.1.6 Effects of Magnesium-Releasing Calcium Phosphate Bone Cement on RAW 264.7

Immunofluorescence staining analysis of the polarization of the macrophages (**Figure 7A**) in the negative-control group did not show signs of iNOS and arginase. In all the cement groups, iNOS and arginase obtained different degrees of signal expression; the iNOS signal was weaker compared with the arginase signal, indicating that CPC could simultaneously promote the

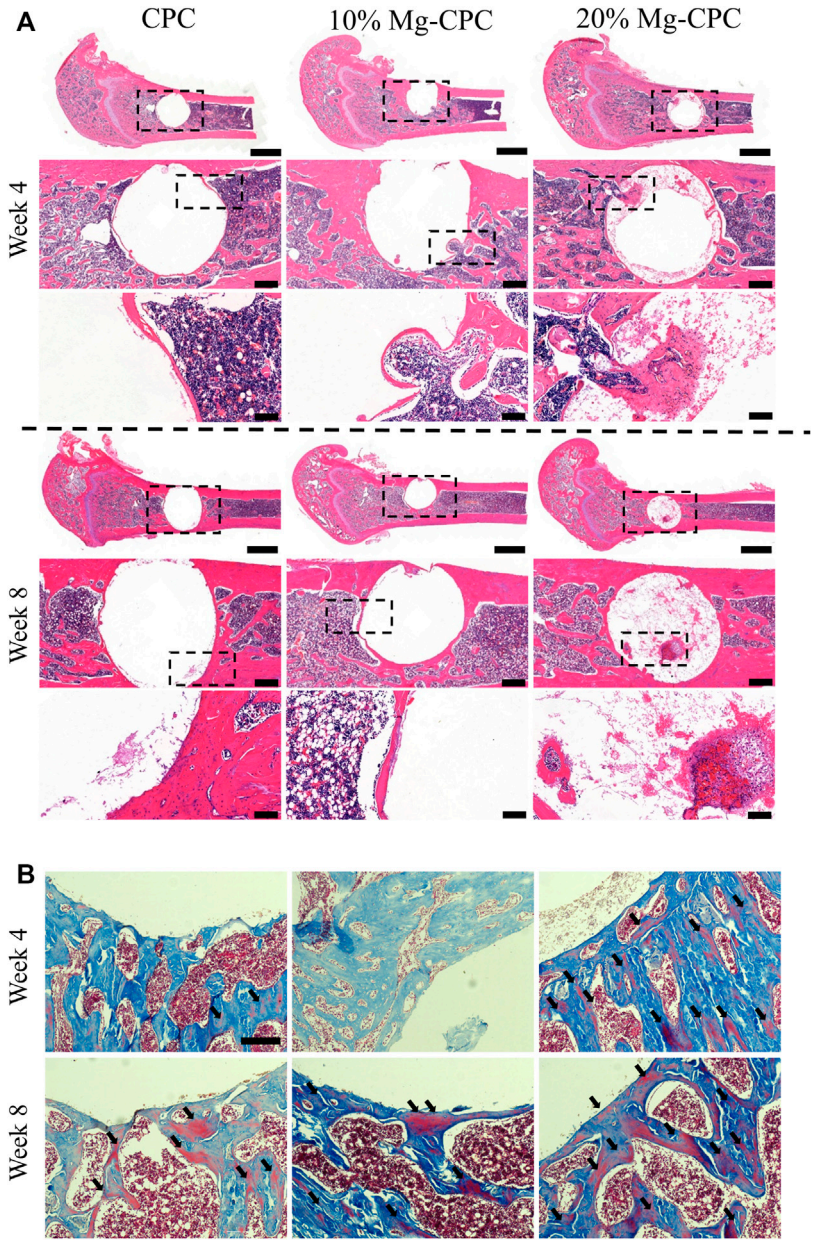

FIGURE 5 | Histological staining after surgery. **(A)** H&E staining (scale bar = 2,000, 500, 100 μm); **(B)** Masson trichrome stain, red color represents mature bone (back arrow). Scale bar: 200 μm.

polarization of RAW 264.7 toward the M1 and M2 types, while the effect of promoting the polarization of the M2 type was stronger.

By comparing the mean fluorescence intensity of the two kinds of cements, we found no significant difference in the M2 markers between them, but CPC expressed more M1 markers (**Figure 7B**).

To verify magnesium-releasing CPC of macrophage RAW264.7 cell toxicity in mice, we used the bone cement extract for the cytotoxicity test (**Figure 8F**). Under the condition of extract culture, we tested the cytotoxicity at 1 and 2 days. On the first day all the cement groups showed no toxicity compare with the control group, however, CPC cell activity was lower than 80% in the control group, indicating cell toxicity at day 2.

To measure the gene expression of pro-inflammatory cytokines and anti-inflammatory cytokines, a q-PCR test was used. The expression of TNF-α (**Figure 8E**), IL-6 (**Figure 8A**), and Il-1β (**Figure 8B**) of the pro-inflammatory cytokine were all lower in MG-CPC than in the blank control group. The 20% Mg-CPC inhibited the gene expression of pro-inflammatory cytokine. In terms of the expression of anti-inflammatory cytokine genes, both CPC and Mg-CPC promoted the expression of IL-1RA

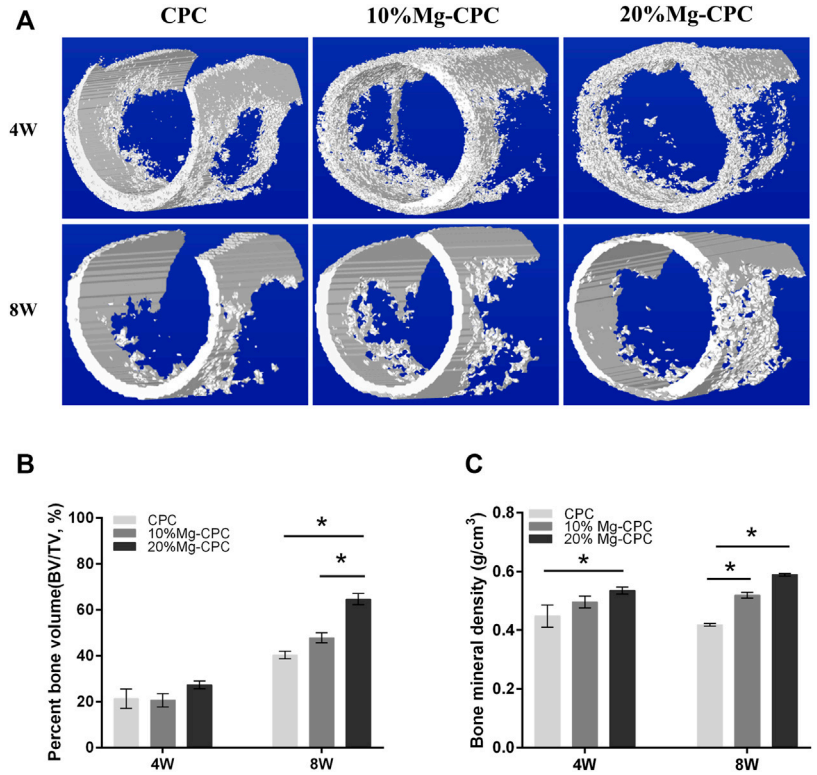

FIGURE 6 | Micro-CT evaluation after surgery. **(A)** 3D reconstruction models of new bone formation at the defect sites at different time points; **(B)** The Percent bone volume (BV/TV) of newly formed bone tissue at 4 and 8 weeks after surgery; **(C)** The bone mineral density values of different cement groups at 4 and 8 weeks after surgery (*$p < 0.05$).

(**Figure 8C**), but showed no effect on the expression of the IL-10 (**Figure 8D**) gene. A further ELISA assay showed that the concentration of IL-1RA in the 20% Mg-CPC had significantly increased at day 3 (**Figure 8G**) compared to the CPC group.

4 DISCUSSION

Evaluations of bioactive materials are suitable for clinical inquiry and are important in determining biological characteristics. CPC has good biological characteristics. For example it is similar to the composition of bone in terms of its hydration properties. Moreover, its absorption rate is consistent with the speed of new bone formation, it does not affect the bone healing process, it is easy to shape, and it has no obvious side effects. Its potential clinical applications is strong compared to other bioactive materials (Won et al., 2010). Unfortunately, the effect of CPC alone on osteogenesis is limited, which may cause bone healing delay or even implant failure. Many researchers have improved CPC; however, few studies have been done on the mechanisms of its limited osteogenic effects. Immune regulation plays an important role in osteogenesis, and the limited osteogenic qualities of CPC may be related to immune regulation. Magnesium has excellent bone-promoting and immune regulation abilities (Hu et al., 2018; Nabiyouni et al., 2018). Therefore, magnesium was introduced into CPC in this study to examine the causes and mechanisms of its limited bone-promoting ability.

CPC is highly biocompatible with almost no toxicity, while magnesium, as one of the elements of human body, has no cytotoxicity in the appropriate concentration range and has demonstrated good biological safety (Feyerabend et al., 2010). This study also found no cytotoxicity in the treatment of hBMMSCs (**Figure 4A**). Many articles have reported the beneficial effect of magnesium ions on bone formation, and they can regulate the osteogenic differentiation of hBMMSCs in various ways to promote bone healing. Studies have found that magnesium ions can significantly improve the activity of alkaline phosphatase and the expression of osteogenic-related genes, promote the osteogenic differentiation of mouse MC3T3-e1 pre-osteoblasts, and promote the mineralization of the extracellular matrix (Wong et al., 2013). Magnesium ions can enter the periosteum and induce neurons to produce a calcitonin gene-related polypeptid-α (CGRP) and stimulate periosteum-derived stem cells (PDSCs) to undergo osteogenic differentiation to promote bone healing (Zhang et al., 2016). The 20% Mg-CPC synthesized in this study could significantly improve the activity of ALP and promote the mineralization of ECM (**Figure 4C**), while the ALP activity of CPC significantly decreased on day 14 (**Figure 4B**), indicating that CPC had an inhibitory effect on the osteogenic differentiation of hBMMSCs. In addition to the decreased ALP activity, other mechanisms of

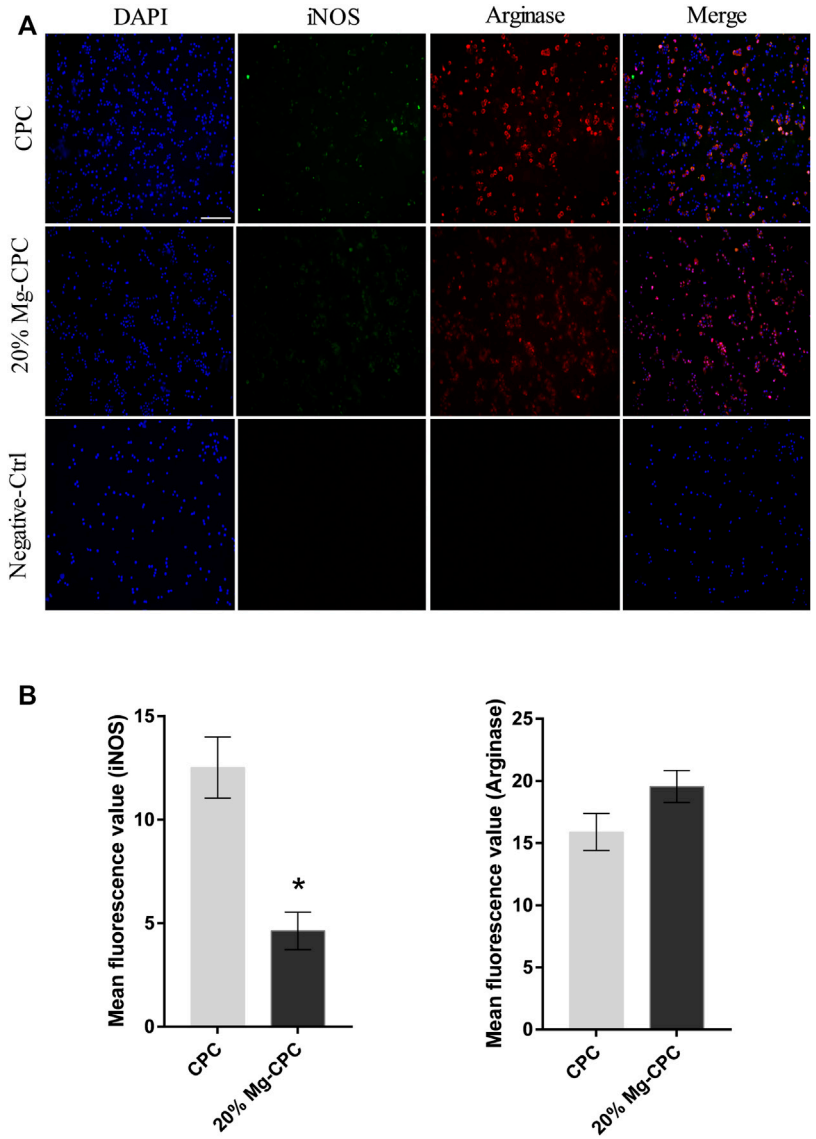

FIGURE 7 | Immunofluorescence staining of iNOS and Arginase in RAW 264.7. **(A)** Fluorescence images of RAW 264.7 cultured on cement for 24 h; blue dot: DAPI; green dot: iNOS; red dot: arginase (scale bar = 200 μm); **(B)** mean fluorescence intensity calculation by software ImageJ (*$p < 0.05$).

inhibiting hBMMSCs osteogenic differentiation need to be demonstrated in further studies. The animal study showed consistent results the *in vitro* study, and the 20% Mg-CPC showed better osteoconduction (**Figure 5**) and osteogenesis (**Figure 6**).

Immunomodulatory function is believed to play a key role in the process of bone healing (Takayanagi, 2007). The bone healing delay caused by CPC is also related to the effect of CPC on immune regulation. When the macrophage RAW264.7 was treated with extracts of CPC and Mg-CPC, the Mg-CPC group had no cytotoxicity, but the CPC group showed cytotoxicity (**Figure 8F**), indicating that CPC has a negative effect on immune cells that was ameliorated by magnesium ions. Macrophage polarization is one of the manifestations of immune regulation. M1-type macrophages promote inflammation, and M2-type macrophages promote wound healing. The immunofluorescence staining in this study showed that the two phenotypes of M1-type and M2-type macrophages coexisted, but there were more M1-type macrophages in CPC group than in Mg-CPC group (**Figure 7**). The NF-κB signaling pathway is closely related to inflammatory and immune responses, and the activation of the NF-κB signaling pathway promotes the expression of pro-inflammatory cytokines, which further activates the NF-κB signaling pathway. Sustained activation of the NF-κB signaling pathway leads to long-term inflammatory responses that lead to cellular damage and inhibit osteogenic differentiation (Lin et al., 2017). In this study, the anti-inflammatory cytokine IL-1RA gene

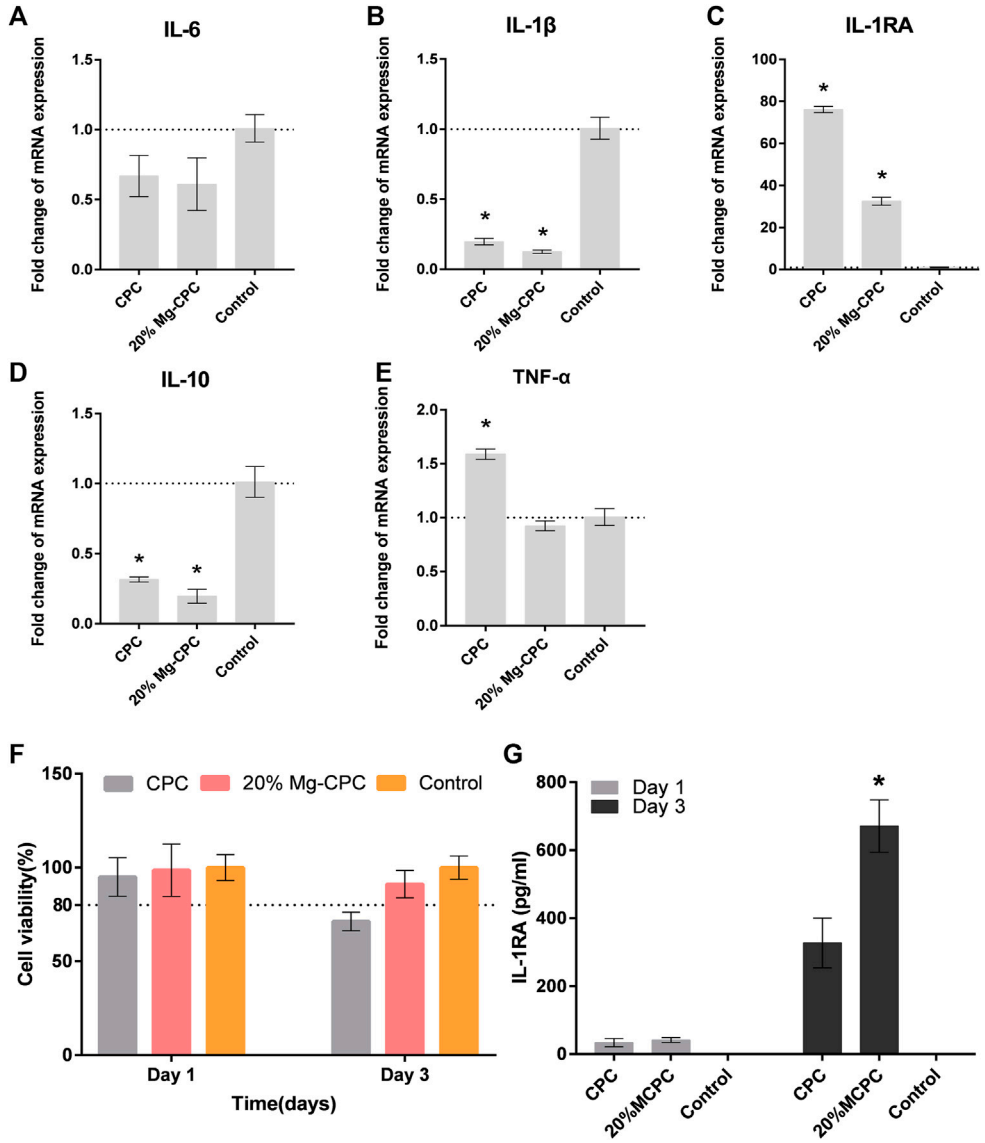

FIGURE 8 | The effect of CPC and Mg-CPC on RAW264.7. **(A–E)** Gene expression of IL-6, IL-1β, IL-1Ra, IL-10, and TNF-α after culture on cement, detected by real-time PCR assay. **(F)** Cell viability assays. **(G)** The concentration of IL-1RA in the supernatant of RAW264.7 using ELISA (*$p < 0.05$).

was significantly up-regulated in Mg-CPC-treated macrophages; a further ELISA assay showed that the concentration of IL-1RA had significantly increased. The anti-inflammatory cytokine IL-1RA effectively blocked the binding of IL-1 to its membrane-bound receptor IL-1RI (Gabay et al., 2010), thereby inhibiting the NF-κB pathway activation. In macrophages treated with CPC, inhibiting inflammatory cytokines IL-1RA have also been raised, but the pro-inflammatory cytokines TNF-α gene increases, and the TNF-α, IL-6, and IL-1β genes in macrophages treated with Mg-CPC groups were down-regulated (**Figures 7A–E**). TNF-α can continuously activate the NF-κB pathway (Wang et al., 2017), produce inflammatory cytokines, and inhibit bone formation by blocking the Wnt signaling pathway (Vincent et al., 2009). The release concentrations of calcium ion were similar between the CPC group and the Mg-CPC groups. In summary, CPC is cytotoxic to macrophage RAW264.7 *in vitro* and promotes the secretion of TNF-α by macrophage RAW264.7 to activate the NF-κB pathway, promote an inflammatory response, and inhibit osteogenic differentiation that leads to a bone healing delay (Ye et al., 2016; Yu et al., 2020). The introduction of magnesium can ameliorate these adverse effects and inhibit TNF-α production, thereby reducing the release of pro-inflammatory cytokines (Weglicki et al., 1992).

Magnesium is one of indispensable elements in the human body's life activities. A large number of studies have found that the mechanical properties of magnesium alloys can promote bone growth *in vivo* along with biological activity to accelerate fracture healing. However, magnesium alloys will gradually and

eventually degrade (Witte, 2010), and the corrosion rate of magnesium alloys is too fast; it cannot provide mechanical support for a long time, and its corrosive byproducts are harmful to the local microenvironment (Wong et al., 2010), limiting its clinical application. Therefore, this study introduced magnesium into calcium phosphate cement to explore the potential of this combined material.

The water-resistance and collapsibility of bone cement is an important factor for its clinical application. If rapid collapse occurs after bone cement is implanted, it cannot provide a support role, and it also produces a large number of vesicles containing inflammatory exudates. Moreover, it increases the infiltration of inflammatory cells, aggravates the inflammatory response, and may result in embolism formation in the blood vessels, which are serious consequences (Miyamoto et al., 1999). In our previous studies, we have accelerated the solidification of CPC by optimizing concentration of citric acid in liquid phase, which functioned as a chelation agent for calcium ions (Kuang et al., 2012). In this study, citric acid in the liquid phase can chelate calcium ions and magnesium ions to form complex, accelerate cement solidification, and resist water and collapse. PVP in the liquid phase were increase the viscosity of water agent, and stability of the system. PVP could also improve the thixotropy after mixing, which would improve the injectability and facilitate to shaping of bone cement in the clinical requirements. The water resistance experiment results show that the MgO group quickly collapsed in a PBS solution, but the magnesium and hydrogen phosphate groups still maintained complete form after immersion in PBS for 3 months (**Supplementary Figure S1**). It showed that the addition of MgO had a great influence on the bone cement system, and its water-resistant ability was directly lost. It suggested that hydration products of MgO disrupt the crosslinking network of the CPC system. However, magnesium hydrogen phosphate can be well integrated into a CPC system so that it can maintain good water resistance and collapse-resistant ability.

Mg-CPC offers long-term stable magnesium release and mechanical strength. Even as a non-weight-bearing bone repair material, bone cement can maintain a certain mechanical strength for a long time, which is very important for clinical applications (Yetkinler et al., 2001). In this study, the mechanical strength of the Mg-CPC decreased compared with bone cement (**Figure 3A**), indicating that the introduction of magnesium had an adverse effect on the original mechanical strength. This adverse effect occurs after the Mg-CPC has solidified. After immersion in SBF and using SEM to observe the surfaces of the bone cement groups (**Figure 1A**), the crystals gradually disappeared as the hydration reaction progressed, and the HA in the cement gradually increased, as determined by XRD (**Figure 2**). With an increase of HA, the mechanical strength should be enhanced (Lacout et al., 1996). However, no increase in mechanical strength was observed in our results, which may be due to the release of the magnesium ions. In the Mg-CPC groups, a large number of magnesium ions appeared to be releases in the first 3 days, and the subsequent release became stable (**Figure 3C**). The release of magnesium accounted for more than 40% of the added weight at day 28 according to theoretical calculations, while the release of calcium in all the groups was negligible. Magnesium release reduces mechanical properties, while HA formation increases mechanical properties. To sum up, our results showed that, the sustained release of magnesium and long-term mechanically stable can be achieved at the same time by synergistic effects of DMPA and citric acid. Based on the chemical properties of magnesium hydrogen phosphate dissolved in dilute acid, DMPA dissolves in citric acid and the released magnesium ions are chelated by citric acid and citric acid also can chelate the calcium ions of TTCP in the early hydration reaction (Yu et al., 2019). As the chelation reaction progresses, chelate complex and the hydration products to form the cross-linking network, slow down the TTCP hydrolysis (Shi et al., 2019; Zhong et al., 2020), that's why we can still observe the diffraction peak of TTCP in the XRD pattern on day 28 (**Figure 2**). Although will slow down the formation of HA, but the cross-linking network can improve the water resistance ability of Mg-CPC, so that it is not to collapse in water (**Supplementary Figure S1**), and maintain long-term mechanical stability (**Figure 3A**). After setting, the PH value increases, the solubility of DMPA decreases and slowly hydrolyzes in water, therefore, the magnesium ions sustained release have achieved.

In conclusion, the poor ability of CPC to promote bone healing is mainly manifest in two aspects: stem cell osteogenesis and immune osteogenesis. *In vitro* study, CPC had no cytotoxic effects on hBMMSCs, but inhibited ALP activity at day 14, was cytotoxic to macrophages, and promoted the secretion of the pro-inflammatory cytokine TNF-α by macrophage RAW 264.7. Mg-CPC can enhance the activity of ALP, the mineralization ability on hBMMSCs, suppress the M1 polarization of macrophage and the expression of anti-inflammatory cytokine IL-1RA on macrophage RAW 264.7. In the animal study, magnesium ions were shown to improve the osteoconduction ability of CPC. In addition, the Mg-CPC synthesized in this study had anti-collapsibility, long-term stable mechanical properties and showed no significant difference in compressive strength from CPC; it also showed a magnesium sustained-release capability. These factors suggest that Mg-CPC should be a good substitute material for bone grafts in clinical use.

DATA AVAILABILITY STATEMENT

The raw data supporting the conclusion of this article will be made available by the authors, without undue reservation.

ETHICS STATEMENT

The animal study was reviewed and approved by The Ethics Committee of the University of Hong Kong-Shenzhen Hospital.

AUTHOR CONTRIBUTIONS

JW: Conceptualization, Methodology, Formal analysis, Investigation, Writing—original draft, FL: Conceptualization,

Methodology, Formal analysis, Investigation, Writing—original draft. ZW: Conceptualization, Supervision. YL: Conceptualization, Methodology. CF: Supervision, Funding acquisition. KY: Conceptualization, Methodology, Data curation, Validation, Writing—review & editing. TW: Conceptualization, Methodology, Data curation, Validation, Writing-review & editing.

FUNDING

This work was supported by National Key R&D Program of China (2018YFC1105100), National Natural Science Foundation of China (81802959), Guangdong Basic and Applied Basic Research Foundation (2018A030313888 & 2021A1515010191), the Shenzhen Science and Technology Innovation Program (JSGG20180507183242702 & JCYJ20200109150420892), High Level-Hospital Program, Health Commission of Guangdong Province, China (HKUSZH201901021), HKU-SZH Fund for Shenzhen Key Medical Discipline (SZXK2020084) and Sanming Project of Medicine in Shenzhen "Team of Excellence in Spinal Deformities and Spinal Degeneration" (SZSM201612055).

SUPPLEMENTARY MATERIAL

The Supplementary Material for this article can be found online at: https://www.frontiersin.org/articles/10.3389/fbioe.2021.803723/full#supplementary-material

REFERENCES

Arrington, E. D., Smith, W. J., Chambers, H. G., Bucknell, A. L., and Davino, N. A. (1996). Complications of Iliac Crest Bone Graft Harvesting. *Clin. Orthop. Relat. Res.* 329, 300–309. doi:10.1097/00003086-199608000-00037

Bauer, T. W., and Muschler, G. F. (2000). Bone Graft Materials. An Overview of the Basic Science. *Clin. Orthop. Relat. Res.* (371), 10–27. doi:10.1097/00003086-200002000-00003

Brown, W. E., and Chow, L. C. (1983). A New Calcium Phosphate Setting Cement. *J. Dental Res.* 62, 672–679.

Chen, Z., Mao, X., Tan, L., Friis, T., Wu, C., Crawford, R., et al. (2014). Osteoimmunomodulatory Properties of Magnesium Scaffolds Coated with β-tricalcium Phosphate. *Biomaterials* 35 (30), 8553–8565. doi:10.1016/j.biomaterials.2014.06.038

De Long, W. G., Jr., Einhorn, T. A., Koval, K., McKee, M., Smith, W., Sanders, R., et al. (2007). Bone Grafts and Bone Graft Substitutes in Orthopaedic Trauma Surgery. *J. Bone Jt. Surg.* 89 (3), 649–658. doi:10.2106/jbjs.F.00465

Feyerabend, F., Fischer, J., Holtz, J., Witte, F., Willumeit, R., Drücker, H., et al. (2010). Evaluation of Short-Term Effects of Rare Earth and Other Elements Used in Magnesium Alloys on Primary Cells and Cell Lines. *Acta Biomater.* 6 (5), 1834–1842. doi:10.1016/j.actbio.2009.09.024

Franz, S., Rammelt, S., Scharnweber, D., and Simon, J. C. (2011). Immune Responses to Implants - A Review of the Implications for the Design of Immunomodulatory Biomaterials. *Biomaterials* 32 (28), 6692–6709. doi:10.1016/j.biomaterials.2011.05.078

Friedman, C. D., Costantino, P. D., Takagi, S., and Chow, L. C. (1998). BoneSource? Hydroxyapatite Cement: A Novel Biomaterial for Craniofacial Skeletal Tissue Engineering and Reconstruction. *J. Biomed. Mater. Res.* 43 (4), 428–432. doi:10.1002/(sici)1097-4636(199824)43:4<428:aid-jbm10>3.0.co;2-0

Gabay, C., Lamacchia, C., and Palmer, G. (2010). IL-1 Pathways in Inflammation and Human Diseases. *Nat. Rev. Rheumatol.* 6 (4), 232–241. doi:10.1038/nrrheum.2010.4

Han, H.-J., Kim, S., and Han, D.-H. (2014). Multifactorial Evaluation of Implant Failure: A 19-Year Retrospective Study. *Int. J. Oral Maxillofac. Implants* 29 (2), 303–310. doi:10.11607/jomi.2869

Hu, T., Xu, H., Wang, C., Qin, H., and An, Z. (2018). Magnesium Enhances the Chondrogenic Differentiation of Mesenchymal Stem Cells by Inhibiting Activated Macrophage-Induced Inflammation. *Sci. Rep.* 8 (1), 3406. doi:10.1038/s41598-018-21783-2

Jung, W.-H., Takeuchi, R., Kim, D.-H., and Nag, R. (2020). Faster Union Rate and Better Clinical Outcomes Using Autologous Bone Graft after Medial Opening Wedge High Tibial Osteotomy. *Knee Surg. Sports Traumatol. Arthrosc.* 28 (5), 1380–1387. doi:10.1007/s00167-019-05463-w

Kovach, T. K., Dighe, A. S., Lobo, P. I., and Cui, Q. (2015). Interactions Between MSCs and Immune Cells: Implications for Bone Healing. *J. Immunol. Res.* 2015, 1–17. doi:10.1155/2015/752510

Kuang, G.-M., Yau, W. P., Lam, W. M., Wu, J., Chiu, K. Y., Lu, W. W., et al. (2012). An Effective Approach by a Chelate Reaction in Optimizing the Setting Process of Strontium-Incorporated Calcium Phosphate Bone Cement. *J. Biomed. Mater. Res.* 100B (3), 778–787. doi:10.1002/jbm.b.32511

Lacout, J. L., Mejdoubi, E., and Hamad, M. (1996). Crystallization Mechanisms of Calcium Phosphate Cement for Biological Uses. *J. Mater. Sci. Mater. Med.* 7 (6), 371–374. doi:10.1007/bf00154552

Lin, T.-h., Gibon, E., Loi, F., Pajarinen, J., Córdova, L. A., Nabeshima, A., et al. (2017). Decreased Osteogenesis in Mesenchymal Stem Cells Derived from the Aged Mouse is Associated with Enhanced NF-κB Activity. *J. Orthop. Res.* 35 (2), 281–288. doi:10.1002/jor.23270

Liu, C., Shao, H., Chen, F., and Zheng, H. (2003). Effects of the Granularity of Raw Materials on the Hydration and Hardening Process of Calcium Phosphate Cement. *Biomaterials* 24 (23), 4103–4113. doi:10.1016/s0142-9612(03)00238-2

Meraw, S. J., Reeve, C. M., Lohse, C. M., and Sioussat, T. M. (2000). Treatment of Peri-Implant Defects with Combination Growth Factor Cement. *J. Periodontol.* 71 (1), 8–13. doi:10.1902/jop.2000.71.1.8

Miyamoto, Y., Ishikawa, K., Takechi, M., Toh, T., Yuasa, T., Nagayama, M., et al. (1999). Histological and Compositional Evaluations of Three Types of Calcium Phosphate Cements when Implanted in Subcutaneous Tissue Immediately After Mixing. *J. Biomed. Mater. Res.* 48 (1), 36–42. doi:10.1002/(sici)1097-4636(1999)48:1<36:aid-jbm8>3.0.co;2-i

Mosser, D. M., and Edwards, J. P. (2008). Exploring the Full Spectrum of Macrophage Activation. *Nat. Rev. Immunol.* 8 (12), 958–969. doi:10.1038/nri2448

Nabiyouni, M., Brückner, T., Zhou, H., Gbureck, U., and Bhaduri, S. B. (2018). Magnesium-Based Bioceramics in Orthopedic Applications. *Acta Biomater.* 66, 23–43. doi:10.1016/j.actbio.2017.11.033

Nair, A. K., Gautieri, A., Chang, S.-W., and Buehler, M. J. (2013). Molecular Mechanics of Mineralized Collagen Fibrils in Bone. *Nat. Commun.* 4, 1724. doi:10.1038/ncomms2720

Orchard, T. S., Larson, J. C., Alghothani, N., Bout-Tabaku, S., Cauley, J. A., Chen, Z., et al. (2014). Magnesium Intake, Bone Mineral Density, and Fractures: Results from the Women's Health Initiative Observational Study. *Am. J. Clin. Nutr.* 99 (4), 926–933. doi:10.3945/ajcn.113.067488

Reichert, J. C., Saifzadeh, S., Wullschleger, M. E., Epari, D. R., Schütz, M. A., Duda, G. N., et al. (2009). The challenge of Establishing Preclinical Models for Segmental Bone Defect Research. *Biomaterials* 30 (12), 2149–2163. doi:10.1016/j.biomaterials.2008.12.050

Scheer, J. H., and Adolfsson, L. E. (2009). Tricalcium Phosphate Bone Substitute in Corrective Osteotomy of the Distal Radius. *Injury* 40 (3), 262–267. doi:10.1016/j.injury.2008.08.013

Shi, H., Zhang, W., Liu, X., Zeng, S., Yu, T., and Zhou, C. (2019). Synergistic Effects of Citric Acid - Sodium Alginate on Physicochemical Properties of α-tricalcium Phosphate Bone Cement. *Ceram. Int.* 45 (2), 2146–2152. doi:10.1016/j.ceramint.2018.10.124

Stein, M., Keshav, S., Harris, N., and Gordon, S. (1992). Interleukin 4 Potently Enhances Murine Macrophage Mannose Receptor Activity: A Marker of Alternative Immunologic Macrophage Activation. *J. Exp. Med.* 176 (1), 287–292. doi:10.1084/jem.176.1.287

Takayanagi, H. (2007). Osteoimmunology: Shared Mechanisms and Crosstalk between the Immune and Bone Systems. *Nat. Rev. Immunol.* 7 (4), 292–304. doi:10.1038/nri2062

Vincent, C., Findlay, D. M., Welldon, K. J., Wijenayaka, A. R., Zheng, T. S., Haynes, D. R., et al. (2009). Pro-Inflammatory Cytokines TNF-Related Weak Inducer of Apoptosis (TWEAK) and TNFα Induce the Mitogen-Activated Protein Kinase (MAPK)-Dependent Expression of Sclerostin in Human Osteoblasts. *J. Bone Mineral Res.* 24 (8), 1434–1449. doi:10.1359/jbmr.090305

Wang, K. S., Lv, Y., Wang, Z., Ma, J., Mi, C., Li, X., et al. (2017). Imperatorin Efficiently Blocks TNF-α-Mediated Activation of ROS/PI3K/Akt/NF-κB Pathway. *Oncol. Rep.* 37 (6), 3397–3404. doi:10.3892/or.2017.5581

Wang, M., Yu, Y., Dai, K., Ma, Z., Liu, Y., Wang, J., et al. (2016). Improved Osteogenesis and Angiogenesis of Magnesium-Doped Calcium Phosphate Cement via Macrophage Immunomodulation. *Biomater. Sci.* 4 (11), 1574–1583. doi:10.1039/c6bm00290k

Weglicki, W. B., Phillips, T. M., Freedman, A. M., Cassidy, M. M., and Dickens, B. F. (1992). Magnesium-Deficiency Elevates Circulating Levels of Inflammatory Cytokines and Endothelin. *Mol. Cell Biochem.* 110 (2), 169–173. doi:10.1007/bf02454195

Wiese, A., and Pape, H. C. (2010). Bone Defects Caused by High-Energy Injuries, Bone Loss, Infected Nonunions, and Nonunions. *Orthop. Clin. North Am.* 41 (1), 1–4. doi:10.1016/j.ocl.2009.07.003

Witte, F. (2010). The History of Biodegradable Magnesium Implants: A Review. *Acta Biomater.* 6 (5), 1680–1692. doi:10.1016/j.actbio.2010.02.028

Won, T. Y., Lee, K. J., Cho, C. B., Oh, J. Y., Park, H. K., Chough, C. K., et al. (2010). Clinical Application of the Calcium Phosphate Cement (PolyBone) for the Skull Bone Defects After Microvascular Decompression. *J. Korean Neurotraumatol Soc.* 6 (1), 53. doi:10.13004/jknts.2010.6.1.53

Wong, H. M., Wu, S., Chu, P. K., Cheng, S. H., Luk, K. D. K., Cheung, K. M. C., et al. (2013). Low-Modulus Mg/PCL Hybrid Bone Substitute for Osteoporotic Fracture Fixation. *Biomaterials* 34 (29), 7016–7032. doi:10.1016/j.biomaterials.2013.05.062

Wong, H. M., Yeung, K. W. K., Lam, K. O., Tam, V., Chu, P. K., Luk, K. D. K., et al. (2010). A Biodegradable Polymer-Based Coating to Control the Performance of Magnesium alloy Orthopaedic Implants. *Biomaterials* 31 (8), 2084–2096. doi:10.1016/j.biomaterials.2009.11.111

Ye, X., Huang, H., Zhao, N., Zhang, J., and Yang, P. (2016). Inhibition of Runx2 Signaling by TNF-α in ST2 Murine Bone Marrow Stromal Cells Undergoing Osteogenic Differentiation. In Vitro *Cell Dev. Biol. Animal* 52 (10), 1026–1033. doi:10.1007/s11626-016-0068-3

Yetkinler, D. N., McClellan, R. T., Reindel, E. S., Carter, D., and Poser, R. D. (2001). Biomechanical Comparison of Conventional Open Reduction and Internal Fixation versus Calcium Phosphate Cement Fixation of a Central Depressed Tibial Plateau Fracture. *J. Orthop. Trauma* 15 (3), 197–206. doi:10.1097/00005131-200103000-00009

Yu, J., Shen, L., Liu, Y., Ming, H., Zhu, X., Chu, M., et al. (2020). The m6A Methyltransferase METTL3 Cooperates with Demethylase ALKBH5 to Regulate Osteogenic Differentiation through NF-κB Signaling. *Mol. Cell Biochem.* 463 (1–2), 203–210. doi:10.1007/s11010-019-03641-5

Yu, S., Liu, L., Xu, C., and Dai, H. (2019). Magnesium Phosphate Based Cement with Improved Setting, Strength and Cytocompatibility Properties by Adding Ca(H2PO4)2·H2O and Citric Acid. *J. Mech. Behav. Biomed. Mater.* 91, 229–236. doi:10.1016/j.jmbbm.2018.12.004

Zhang, Y., Xu, J., Ruan, Y. C., Yu, M. K., O'Laughlin, M., Wise, H., et al. (2016). Implant-Derived Magnesium Induces Local Neuronal Production of CGRP to Improve Bone-Fracture Healing in Rats. *Nat. Med.* 22 (10), 1160–1169. doi:10.1038/nm.4162

Zhao, L., Tang, M., Weir, M. D., Detamore, M. S., and Xu, H. H. (2011). Osteogenic Media and rhBMP-2-Induced Differentiation of Umbilical Cord Mesenchymal Stem Cells Encapsulated in Alginate Microbeads and Integrated in an Injectable Calcium Phosphate-Chitosan Fibrous Scaffold. *Tissue Eng. Part A* 17 (7–8), 969–979. doi:10.1089/ten.TEA.2010.0521

Zhao, Z., Yang, D., Ma, X., Zhao, H., Nie, C., and Si, Z. (2009). Successful Repair of a Critical-Sized Bone Defect in the Rat Femur with a Newly Developed External Fixator. *Tohoku J. Exp. Med.* 219 (2), 115–120. doi:10.1620/tjem.219.115

Zhong, W., Sun, L., Yu, T., and Zhou, C. (2021). Preparation and Characterization of Calcium Phosphate Cement with Enhanced Tissue Adhesion for Bone Defect Repair. *Ceram. Int.* 47, 1712–1720. doi:10.1016/j.ceramint.2020.08.288

Zimmermann, G., and Moghaddam, A. (2011). Allograft Bone Matrix versus Synthetic Bone Graft Substitutes. *Injury* 42 (Suppl. 2), S16–S21. doi:10.1016/j.injury.2011.06.199

Conflict of Interest: The authors declare that the research was conducted in the absence of any commercial or financial relationships that could be construed as a potential conflict of interest.

Publisher's Note: All claims expressed in this article are solely those of the authors and do not necessarily represent those of their affiliated organizations, or those of the publisher, the editors and the reviewers. Any product that may be evaluated in this article, or claim that may be made by its manufacturer, is not guaranteed or endorsed by the publisher.

frontiers in Bioengineering and Biotechnology

REVIEW
published: 01 March 2022
doi: 10.3389/fbioe.2022.850110

Advanced Surface Modification for 3D-Printed Titanium Alloy Implant Interface Functionalization

*Xiao Sheng[1], Ao Wang[1], Zhonghan Wang[1,2], He Liu[1,2], Jincheng Wang[1,2] and Chen Li[1,2]**

[1]*Department of Orthopedics, The Second Hospital of Jilin University, Changchun, China,* [2]*Orthopaedic Research Institute of Jilin Province, Changchun, China*

With the development of three-dimensional (3D) printed technology, 3D printed alloy implants, especially titanium alloy, play a critical role in biomedical fields such as orthopedics and dentistry. However, untreated titanium alloy implants always possess a bioinert surface that prevents the interface osseointegration, which is necessary to perform surface modification to enhance its biological functions. In this article, we discuss the principles and processes of chemical, physical, and biological surface modification technologies on 3D printed titanium alloy implants in detail. Furthermore, the challenges on antibacterial, osteogenesis, and mechanical properties of 3D-printed titanium alloy implants by surface modification are summarized. Future research studies, including the combination of multiple modification technologies or the coordination of the structure and composition of the composite coating are also present. This review provides leading-edge functionalization strategies of the 3D printed titanium alloy implants.

Keywords: 3D-printed, titanium alloy, implant interface, surface modication, surface functionalization

OPEN ACCESS

Edited by:
Masoud Mozafari,
University of Toronto, Canada

Reviewed by:
Nan Jiang,
Sichuan University, China
Tuli Dey,
Savitribai Phule Pune University, India
Qihui Zhou,
Qingdao University, China

****Correspondence:***
Chen Li
chenliortho@jlu.edu.cn

Specialty section:
This article was submitted to Biomaterials, a section of the journal Frontiers in Bioengineering and Biotechnology

Received: *07 January 2022*
Accepted: *28 January 2022*
Published: *01 March 2022*

Citation:
Sheng X, Wang A, Wang Z, Liu H, Wang J and Li C (2022) Advanced Surface Modification for 3D-Printed Titanium Alloy Implant Interface Functionalization. Front. Bioeng. Biotechnol. 10:850110. doi: 10.3389/fbioe.2022.850110

INTRODUCTION

Titanium alloy has been extensively used in the medical fields of orthopedics, dentistry, and vascular surgery owing to its high strength, low density, high corrosion resistance, and excellent biocompatibility (Domínguez-Trujillo et al., 2018). Traditional titanium alloy implants have been manufactured by iso-material mold casting or subtractive technologies such as machining, multipoint forming and NC machining (Minto et al., 2020; Khorasani et al., 2016; Herzog and Tille 2021; Markopoulos et al., 2018). Hence, they are difficult to simulate the structure of cortical bone and cancellous bone in real bone tissue (Bozkurt and Karayel, 2021). With the advent of 3D-printed technology, these issues may be solved. The use of 3D-printed medical devices in the direct treatment of patients has increased considerably since 2015. And the most prevalent is in surgery, especially in orthopedics (36%) and orthopedic oncology (32%), followed by maxillofacial surgery (6%), neurosurgery (4%), and plastic surgery (1%) (Kermavnar et al., 2021). 3D-printed technology is divided into powder bed method and power deposit method. The energy source is controlled by a computer system to scan and treat discrete materials distributed layer by layer, in order to directly form parts with a 3D structure (**Figure 1**) (Wang et al., 2017). Various types of 3D-printed technologies such as fused deposit modelling (FDM), stereolithography, and laser sintering have been used in the manufacture of orthopedic implant (Liaw and Guvendiren, 2017). Compared to traditional implant manufacturing methods, 3D-printed technology has two advantages. In terms of microstructure, 3D-printed technology can precisely control the Young's modulus of the prosthesis to match natural bone by predesigned pores that can effectively reduce the stress shielding effect of

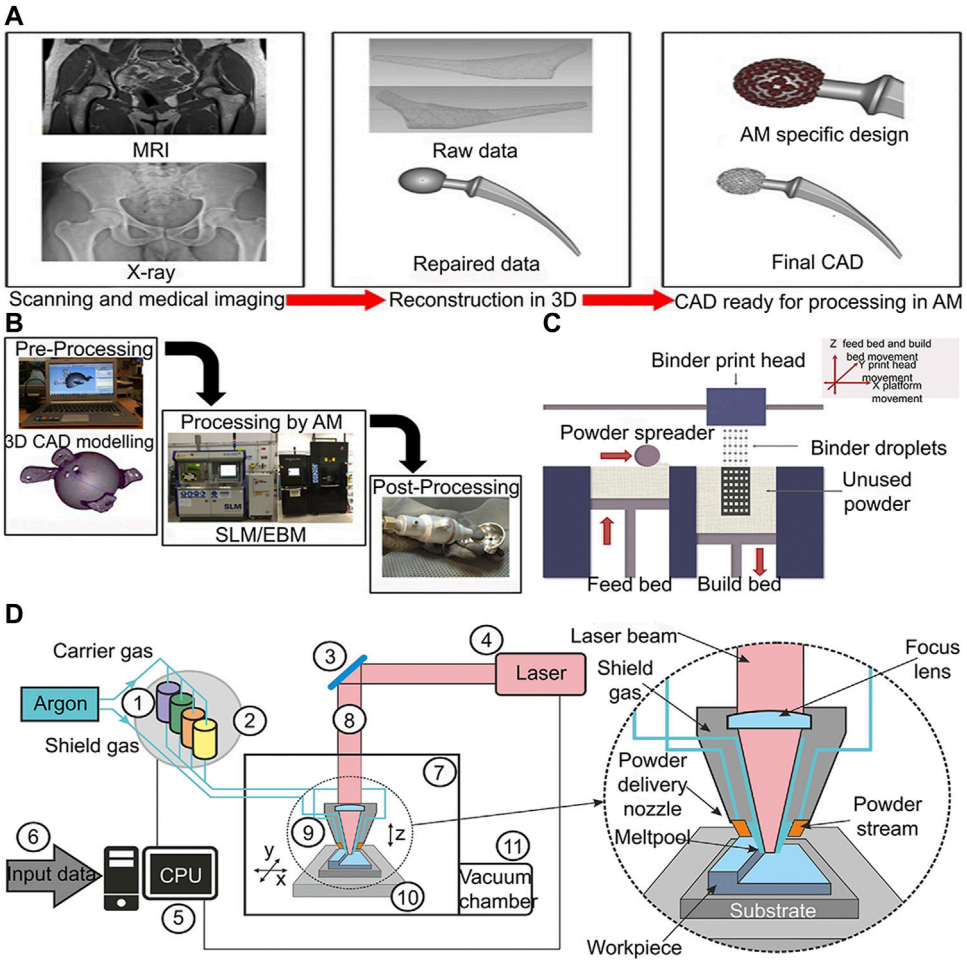

FIGURE 1 | 3D-printing of titanium alloy process diagram **(A)** 3D-printed customized implant data acquisition process (Sing et al., 2016). **(B)** Process chain for preparing orthopedic implants by 3D-printed technology (Sing et al., 2016). **(C)** Schematic diagram of powder bed process (Wang et al., 2017). **(D)** Lens process schematic diagram (Antolak-Dudka et al., 2019).

the implant and reduce the incidence of peri implant osteolysis (Minto et al., 2020). In terms of macro structure, implant shape can be designed with 3D-printed technology, accurately matching the complex bone defect through computed tomography (CT) images, so as to achieve the dual adaptation of the mechanical properties and shapes of the implant to the natural bone tissue (Wong, 2016). The different between traditional titanium alloy implant manufacturing method and 3D printing technology have been summarized in **Table 1**.

With the rising number of orthopedic implant surgeries, patients face the risk of bacterial infection, poor osseointegration, and aseptic inflammation (Bauer and Schils 1999; Ding et al., 2020; Zardi and Franceschi, 2020). Although titanium alloy has the advantages of excellent biocompatibility and corrosion resistance, titanium alloy has three obvious disadvantages (Domínguez-Trujillo et al., 2018). First, untreated titanium alloy implants always possess a bioinert surface that prevents reactions between the organism and implant. Second, a titanium alloy implant is unable to prevent bacterial infection by itself. Third, although titanium alloy materials have good biocompatibility, once the oxidation film on the surface has been damaged, harmful metal ions may enter the blood circulation, resulting in serious consequences (Wang C et al., 2018). In recent years, the development of surface modification technologies has provided new ideas for resolving the aforementioned problems. Researchers change the surface morphology or add certain substances to implant surface to achieve the effects of anti-infection, osteogenesis, wear resistance, corrosion resistance, and oxidation resistance (Zhang S et al., 2015; Li B et al., 2019; Maimaiti et al., 2020; Tang et al., 2020). Basically, 3D-printed titanium alloy surface modification technologies can be divided into three categories: chemical modification technologies, physical modification technologies, and biological modification technologies. Within chemical modification technologies, implants are usually exposed to a chemical solution or gas that bond to bioactive substances by chemical links (Zhang S et al., 2018; Llopis-Grimalt et al., 2020). Different from chemical methods, physical surface modification

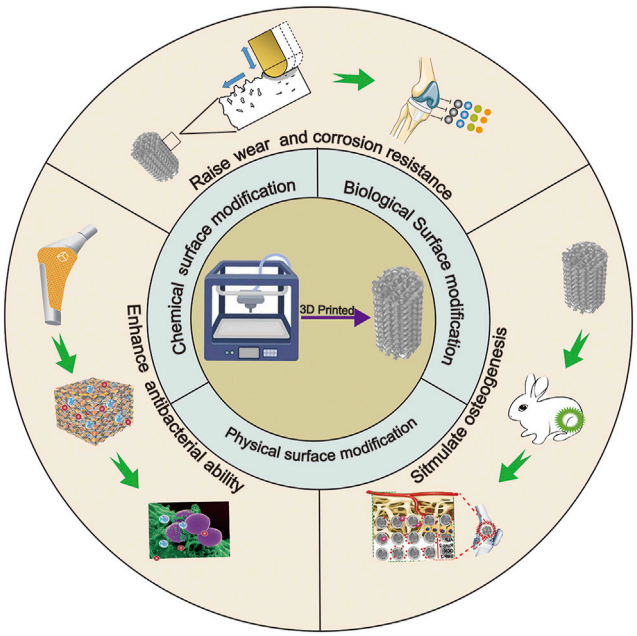

SCHEME 1 | Surface modification technologies and biological functionalization of 3D-printed titanium alloy implants.

technologies do not change the chemical properties of substrate materials, but depend on lasers, high-energy particles, ultrasonics, and magnetic fields to modify the surface appearance and microscopic morphology of titanium alloy materials (Ma et al., 2017; Shin et al., 2017; Guo et al., 2020). Biological surface modification technologies may also form chemical bonds between implant surface and coating, but they mainly combine bioactive materials on the implant surface by using Van der Waals force, electrostatic interaction, and hydrogen bonds (Amin Yavari et al., 2020). The different surface modification technologies advantages and disadvantages have been summarized in **Table 2**. Some technologies often use multiple physical, chemical, and biological processes to establish various surface topographies on the implant surface.

Surface modification technologies are key factors that enhance the bionic properties of implants. This review focuses on chemical, physical, and biological surface modification technologies in the application of 3D-printed implants. In addition, the article also summarizes the performance of implants after surface modification with respect to antibacterial, osteogenesis, and mechanical properties, and provides further details to improve the surface modification technologies and manufacture biomimetic implants with excellent performance in the future (**Scheme 1**).

SURFACE MODIFICATION TECHNOLOGY

Surface modification refers to the method of improving the biological properties by preparing coatings or changing the surface morphology of implants (**Figure 2**). The different surface modification technologies, coating materials and functions have been summarized in **Table 3**.

Chemical Surface Modification

Chemical surface modification technologies include anodic oxidation, micro-arc oxidation, electrophoretic deposition, chemical vapor deposition, alkali heating and atomic layer deposition. These technologies facilitate the formation of chemical bonds to connect new substances with strong binding force. In addition, the chemical surface modification technologies have been adapted by the implants with complex shapes and have great prospects of application in the modification of 3D-printed implants (Xiu et al., 2016; Su 2021).

Anodizing

Anodizing belongs to electrochemical technology, which has been widely used in sewage treatment, battery energy, and bionanotechnology (Mandal et al., 2017; Davoodi et al., 2020; Janaina and Santos, 2021). In recent years, anodizing has been extensively used in implant surface for modifications owing to its simplicity, economy, and universality (Tang et al., 2016). In anodizing, titanium alloy is used as the anode, and lead or platinum plate is used as the cathode. The positive and negative ions in the electrolyte diffuse to the anode through the action of an electric field, and then the oxidation-reduction reaction occurs, forming a micro-nano structure on the titanium

TABLE 1 | Summary of different implant manufacturing technologies, manufacturing principle, cost and personalization.

Implant manufacturing technology	Manufacturing principle	Cost	Personalization	References
Machining	Using turning, milling and grinding ect. to form base material with specific shape	High	Poor	Khorasani et al. (2016)
Multipoint forming	Creating a mould that can be adapted to the part to be produced and thus it is not necessary to produce a mould for each individual part	Low	Poor	Herzog and Tille (2021)
NC machining	Using the control system sends out instructions to make the cutting tool make various movements that meet the requirements, and represent the shape and size of the workpiece in the form of numbers and letters for machining	High	Great	Markopoulos et al. (2018)
3D-printed technology	Firstly, the 3D image is obtained by CT scanning, then the raw material powder is deposited layer by layer by computer-controlled 3D printer, and finally the molten material is cast into a pre-designed 3D shape	Low	Great	Wang et al. (2017)

TABLE 2 | Summary of surface modification technology, advantages and disadvantages.

Surface modification technology	Advantages	Disadvantages	References
MAO	Low cost, simple equipment, easy operation, high coating efficiency, strong adhesion with base material, adapt to complex structures, high biological activity, high wear resistance	Reducing the fatigue strength of the base material	Fan et al. (2012), Wang et al. (2011), Yang Y. W et al. (2020), Myakinin et al. (2021), Nagarajan et al. (2018)
Anodizing	Low cost, simple equipment, easy operation, high biological activity, form TiO_2 nanotube structures, reduce bacterial adhesion	Reducing the fatigue strength of the base material, the coating quality is poor than MAO	Tang et al. (2016), Minagar et al. (2013), Peng et al. (2013), Sarraf et al. (2021), Krzakala et al. (2013)
EPD	High-quality coatings, adapt to complex structures, precise controllable coating thickness	High temperature sintering is required when depositing specific materials	Pishbin et al. (2014), Seuss et al. (2014), Boccaccini et al. (2010), Narayanan et al. (2008)
CVD	High-quality coatings, adapt to complex structures	High cost, high equipment demand, high temperature environment required	Choy (2003), Zhao et al. (2019)
ALD	Precise thickness control, nano-precision coating, exceptional large-area uniformity, strong bonding strength, low growth temperature, excellent reproducibility	High cost, low working voltage, and slower coating production speed	Liu et al. (2017b), Bishal et al. (2015)
Alkali heating	Low cost, simple equipment, easy operation, high biological activity	The coating state cannot be accurately controlled	Tamilselvi et al. (2009), Kokubo and Yamaguchi (2010)
LSE	Accurately control the 3D shape of the coating	High temperature environment required	Fathi-Hafshejani et al. (2020), Shin et al. (2017)
AIP	Strong adhesion with base material, low deposition temperature	High equipment demand	Chung et al. (2011)
Shot peening	Increase fatigue resistance and wear resistance of implant	May have certain cytotoxicity	Liu et al. (2019)
UNSM	Improving the yield strength and wear resistance	High equipment demand	Karimbaev et al. (2020), Amanov et al. (2012)
LBL	Low cost, simple equipment, easy operation, precise coating control	Poor adhesion with base material	Zhang T et al. (2018), Ma et al. (2015)
Hydrogel	Low cost, simple equipment, easy operation adapt to complex structures, excellent drug carrier	Poor adhesion with base material	Yue et al. (2020)

surface (Park et al., 2008). Anodizing is usually performed under galvanostatic conditions, up to a determined cell voltage or the passage of a determined charge, or by potential sweep. The process parameters which most frequently determine the properties of the growing oxide are the electrochemical parameters (current density, cell voltage, possible stabilization time) as well as the electrolyte specifications (com-position, pH, and temperature) and of course, the composition of the metal itself and its surface conditions (Diamanti, et al., 2011). With the increase in voltage, the size of the micropores of the oxide film increase, the anatase and rutile phases co-exist in the porous layer of titanium dioxide (TiO_2) (Park et al., 2008). The TiO_2 film with micro-nano structure exhibits lower contact angle (higher hydrophilicity) and higher surface energy (Minagar et al., 2013). That is conducive to the faster proliferation of osteoblasts on the implant surface. In addition, anodic oxidation also forms TiO_2 nanotube structures on the titanium alloy. This nanotube structures can improve osseointegration by promoting the adhesion of the bone apatite layer. Furthermore, it also reduces bacterial adhesion to inhibit bacterial growth (Peng et al., 2013; Sarraf et al., 2021). Moreover, TiO_2 nanotubes are often used as carriers to transform drugs or cells. On the one hand, researchers enhance bone growth by integrating CaP, BMP-2, metformin, and other osteogenic active substances into nanotubes (Li J. L et al., 2019; Hashemi et al., 2020; Yao et al., 2020). In addition nanotubes are used to incorporate antibacterial agents such as Ag^+, Cu^{2+}, vancomycin, and gentamicin to improve the antibacterial properties of implants (Caliskan et al., 2014; Li M et al., 2015; Wang et al., 2016; Zong et al., 2017). The diameter and length of TiO_2 nanotubes are dependent on electrochemical oxidation conditions such as electrolyte type, concentration, pH, applied potential, and oxidation time (Minagar et al., 2012). However, there is no explicit data to determine the optimal nanotechnology that is conducive to cell response, and further research is needed to find the optimal size of nanotube length and diameter.

Microarc Oxidation Technology

Microarc oxidation (MAO), also known as plasma electrolytic oxidation (PEO), is a common metal surface modification technology (Shimabukuro, 2020). As an upgrade of anodic oxidation technology, MAO can prepare higher quality coatings. Compared with anodic oxidation, MAO coating has higher wear resistance and corrosion resistance (Chen et al., 2007). MAO is the method of using arc discharge to enhance and activate the reaction on the anode on the basis of ordinary anodic oxidation, to form a high-quality reinforced ceramic film on the metals (Li et al., 2004). In the electrolytic oxidation process, various parameters affect the quality of the coating, such as voltage, type of current, electrolyte composition, substrate material, and process duration (Sikdar et al., 2021). Similar to anodizing, MAO also forms porous micro-nano structure on the implant surface. The structure not only enables the implant to form contact bone formation with the surrounding bone tissue rather than distance bone formation,

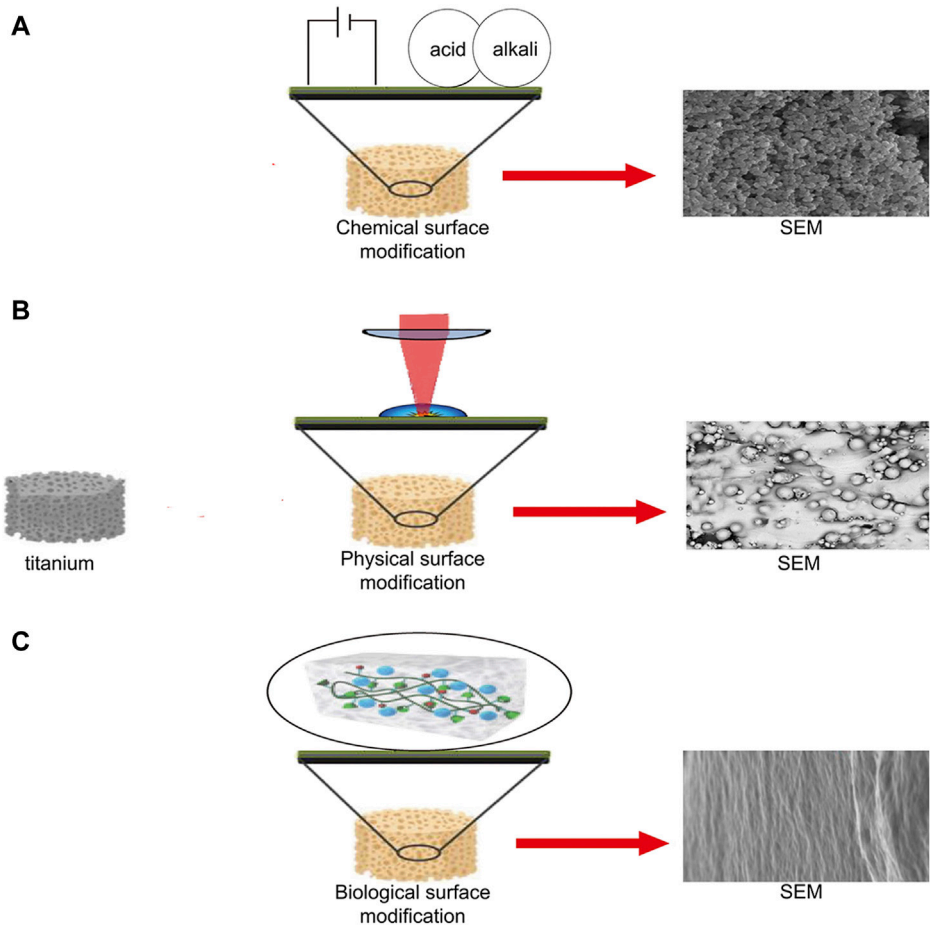

FIGURE 2 | Schematic diagram of chemical, physical, and biological surface modification technologies. **(A)** Implant surface microstructure produced by electrophoretic deposition (Surmeneva et al., 2019). **(B)** Microstructure of implant surface produced by laser peening (Soyama and Takeo, 2020). **(C)** Surface microstructures of implants produced by hydrogel packaging (Mieszkowska et al., 2020).

which greatly increases the binding force and stability of the implant, but also enhances the wear resistance of implant (Xiu et al., 2016). Moreover, the implant surface treated by MAO has high osteogenic activity. This may be because the micro-nano porous surface has a high degree of roughness and hydrophilia (Ribeiro et al., 2015). This is more conducive to the adhesion and proliferation of osteoblasts. Furthermore, MAO can also firmly binds to the materials on the surface of the implant by electrolysis of a specific electrolyte solution to prepare coatings (Komarova et al., 2020). Common coatings include CaP, Sr^{2+}, BMP-2, chitosan, and vancomycin (Yao et al., 2010; Kim S.-Y. et al., 2019; Li N et al., 2019; Shimabukuro 2020; Zhang T et al., 2020; Zhao B et al., 2020). In addition, researchers are combining MAO with other surface modification technologies to produce multifunctional coatings. For instance, ultrasonic MAO (UMAO) was achieved by combining ultrasonic technology with MAO. A study showed that antibacterial properties and cell adhesion of Ti-Cu alloy can be enhanced by UMAO treatment (Hu et al., 2020). The microwave-assisted hydrothermal method is used to treat the nano-surface formed by MAO to form discrete nano-morphologies and retain the original micro pores, sub-micron pores, surface calcium, and phosphorus content. Lin et al. (2019) reported that MAO coating treated by MWDD has strong hydrophilicity and cell adhesion. Finally, the coating prepared by MAO may reduce the fatigue strength of implants and the fatigue limits of the MAO samples decreases as the coating thickness increasing (Kong et al., 2015). Therefore, in the future work, it is crucial to find out the best process parameters to control the thickness of MAO coating.

Electrophoretic Deposition Technology

Electrophoretic deposition (EPD) is used to prepare high-quality coatings on materials (Pishbin et al., 2014). Over the past few years, EPD has accelerated its application in the field of implant surface modification because of lower cost, simple process, and superior coating quality (Maciag et al., 2021). Unlike anodizing, anodizing is the anodic electrochemical technique while electrophoretic and cathodic depositions are the cathodic electrochemical techniques (Kim and Ramaswamy 2009). EPD is a colloidal treatment generally performed in a two-electrode electrolyte cell. Under the action of an electric field, the charged particles suspended in the solution move and are deposited on the

TABLE 3 | Summary of surface modification technology, coating constructing methods, and functions.

Implantmaterial	3D-printed method	Surface modificationtechnology	Coating materials	Function	References
Ti_6Al_4V	SLM	MAO	Ag^+, Sr, CaP, BMP-2, Vancomycin	MAO can produce micro-nano structures that promote osteogenesis on the implant surface, and different substances can be deposited by changing the electrolyte	Zhang W et al. (2020), Rodríguez-Contreras et al. (2020), Chen et al. (2019), Wei et al. (2020), Teng et al. (2019)
Ti_6Al_4V	SLM	Anodizing	Ag^+, HA, MBG, MTANi	Anodic oxidation can form TiO_2 nanotube structure on the surface of implants, which can be used as a carrier for a variety of drugs.	Shivaram et al. (2017), Qin et al. (2018), Zhao P et al. (2020), Li X et al. (2020)
Ti_6Al_4V	EBM	EPD	CaP, AgNPs, Vancomycin	Electrophoretic deposition can deposit solid particles suspended in solution on the implant surface to form a uniform coating	Bakhshandeh et al. (2017), Chudinova et al. (2019)
Ti_6Al_4V	EBM	CVD	Quercitrin	CVD deposited gaseous substances on the implant surface to form uniform coatings, and prepared coatings with different functions by depositing different substances	Llopis-Grimalt., et al. (2020)
Ti_6Al_4V	EBM	ALD	AlN	ALD can deposit materials on the implant surface in the form of monatomic films, and there is a correlation between each layer of atomic films.	Moll et al. (2021)
Ti_6Al_4V	SLM	Alkali heating	Sr, HA, Ga	Alkali heating can form micro-nano surfaces with osteogenic induction ability on the implant surface.	Shimizu et al. (2020), Rodríguez-Contreras et al. (2020), Li M et al. (2019)
Pure Ti, Ti_6Al_4V	SLA, LES, SLM Laser cladding	LSE	Si_3N_4, CaP, TiN-TiB, SiC	LSE can form a coating with 3D shape on the substrate by controlling the movement of high-energy laser source.	Das et al. (2014), Zanocco et al. (2020), Sahasrabudhe and Bandyopadhyay (2018), LiY et al. (2019)
Ti_6Al_4V	SLM	AIP	Mg, Ti-Cu/Ti-Cu-N	AIP forms a coating with strong adhesion on the implant surface by plasma bombarding gas substances.	Guo et al. (2020), Du et al. (2019)
Ti_6Al_4V	DMLS	Shot peening	No	Shot peening can produce a strengthening layer with high residual stress on the implant surface to improve the fatigue strength of the implant.	Soyama and Takeo (2020)
NiTi	SLM	UNSM	No	UNSM produces plastic deformation by impacting the implant surface with ultrasonic and shot peening to improve the wear resistance and tensile strength of the implant.	Ma et al. (2017)
Pure Ti	SLM	LBL	Gelatin, Chitosan, BMP-2, Vancomycin Rifampicin	LBL can alternatively deposit different substances on the implant surface by means of molecular interaction to form a coating with complete structure, stable performance, and specific function.	Amin Yavari et al. (2020), Jahanmard et al. (2020)
Ti_6Al_4V	EBM	Hydrogel	HA, Phloroglucinol, Simvastatin	Hydrogels can encapsulate different drugs in hydrogels and control the release of drugs through the degradation of hydrogels.	Zhang W et al. (2020), Kumar et al. (2018), Mieszkowska et al. (2020)

substrate in an orderly manner, thus forming films and coatings (Boccaccini et al., 2010). The electric field and colloidal solution determine the properties of EPD coating. Among the most important parameters related to the EPD suspension, particle size is worth mentioning, as it directly affects the stability of the electrolyte. No general law has been defined regarding this criterion, although concerns with respect to the settlement due to gravity of larger particles have been reported (Bakhshandeh and Amin Yavari 2018). The advantage of EPD is prepares uniform coatings and achieves a precise controllable coating thickness (Seuss et al., 2014). Furthermore, owing to the electrolytic process being carried out in solution, EPD is capable of covering the substrate materials with a complex shape. EPD is widely used in preparing inorganic coatings on the surface of orthopedic implants, such as hydroxyapatite (HA), graphite oxide (GO), and Ag^+ in coatings (Boccaccini et al., 2010; Shalom et al., 2018; Dulski et al., 2020; Srimaneepong et al., 2020). Moreover, the depositing environment of EPD is milder than the technologies requiring high temperature environment, such as plasma spraying and chemical vapor deposition. Accordingly, EPD is suitable for the preparation of organic bioactive coatings. For the past few years, EPD has been used to deposit various organic bioactive coatings such as bovine serum albumin (BSA) coating and double-layer silk fibroin (SF) coating layers (Hohn et al., 2017; Cheng et al., 2021). These biomimetic coatings show more powerful osteoinduction than traditional inorganic coatings.

Chemical Vapor Deposition Technology

Chemical vapor deposition (CVD) is used for solvent-free preparation of thin films and coatings (Khlyustova et al., 2020). The CVD system comprises three parts: a chemical gas precursor supply system, a chemical vapor repository reactor, and an exhaust gas treatment system. The CVD process begins with the generation of reactive gas reactants in the chemical gas pre-supply system; then, the reactants are pushed into the reactor with inert gas for reaction, and finally the reactants are adsorbed on the heated substrate to form a thin film. CVD coats the base materials with intricate shapes and deposits thin films with excellent coverage (Choy, 2003). CVD is often used to prepare diamond coatings (Pandey et al., 2021). For instance, Aaqil Rifai et al. (2018) prepared diamond coating on the surface SLM-Ti by CVD. The experimental results showed that the coating can promote cell proliferation and inhibit the growth of bacteria. However, complex equipment and high cost limit the application of CVD. In addition, traditional CVD may damage temperature-sensitive materials (base materials or coating materials). Moreover, the inefficiency of the precursor gas heating process leads to a major waste of energy (Zhao et al., 2019). Recently, researchers have transformed the energy supply mode of CVD by using different energy sources, so that CVD can be carried out at lower temperature, such as plasma enhanced chemical vapor deposition (PCVD) and initiation chemical vapor deposition (iCVD). In the PCVD process, high-energy plasma is used to provide the energy necessary for the reaction and render the preparation of coatings with a high temperature environment unnecessary (Okada, 2016). Moreover, iCVD is a new type of green polymer film preparation method. Its principle is to utilize an initiator to crack at a lower heating temperature to polymerize the monomer into a polymer film and deposit on the surface of the substrate (Su et al., 2020). The reaction conditions of iCVD are milder and more controllable than PCVD, and it is able to perfectly retain the required functional groups. In this regard, iCVD has the advantage of depositing organic coating materials. In a study, iCVD was used to secure rhBMP2 to the surface of titanium implants. Compared to the untreated implant, iCVD-treated implant significantly increases osteoinduction and calcium deposition (Youn et al., 2019).

Alkali Heating

Alkali heating is a simple and economical surface modification technology. It is often used to increase the surface of titanium alloys osteoconductivity as well as osteoinductivity (Kokubo and Yamaguchi 2015). In the process, the titanium alloy material is immersed in an NaOH aqueous solution at 60°C for 24 h, and then the sample is maintained at 600–800°C to obtain a porous oxide surface (Kim et al., 1996). The surface treated by the alkali heating can generate rutile and a feather-like sodium titanate structure, and induce a strong apatite formation ability in SBF (Tamilselvi et al., 2009; Kokubo and Yamaguchi 2010). That is because the sodium titanate on the surface of the Ti metal releases Na^+ via exchange with the H_3O^+ in SBF so as to produce a local alkaline environment on the Ti metal. Consequently, the surface of the Ti metal heat-treated after exposure to the alkali solution is negatively charged. Its surface combine with the positively charged Ca^{2+}, forming an amorphous calcium phosphate (Kokubo and Yamaguchi 2015). Furthermore, the surface treated by alkali heating presents a characteristic of a nano-double crystal state. The rough surface plays a pivotal role in increasing the contact between the bone and implant (Tsukimura et al., 2011). Alkali heating can be used as a pretreatment for other surface modification technologies and ensures the biological activity of the implant surface when preparing the implant surface with additional functions.

Atomic Layer Deposition

Atomic layer deposition (ALD) is an approach in which substances are deposited layer by layer on the substrate in the form of monolayer atom, and is used to prepare ultra-thin surface coatings (Listewnik et al., 2019). During ALD, the reactive gas is successively introduced into the reactor for reaction, and only one layer of atoms is deposited in each reaction; hence, each layer of atomic film is associated. This sequential process is a key difference between CVD and ALD, which consequently makes ALD a self-limiting reaction without gas phase reactions and gives unique characteristics to this method (Hashemi Astaneh et al., 2021). ALD has several obvious advantages such as precise thickness control, nano-precision coating, exceptional large-area uniformity, strong bonding strength, low growth temperature, excellent reproducibility, and resistance to sensitive substrates' applicability (Liu H. et al., 2017). For 3D printing implants with complex porous structure, ALD can perfectly form a uniform film on its surface (Hashemi Astaneh et al., 2021). However, higher cost, lower working voltage, and slower coating production speed

limit the application of ALD in the implant coating field (Bishal et al., 2015). To solve these problems, plasma-enhanced ALD (PEALD) and free radical-enhanced ALD (REALD) were proposed and established. PEALD can operate at lower temperatures than traditional thermal ALD, which is conducive to depositing unstable polymers at a high temperature. However, PEALD needs to provide the energy required for the reaction through plasma dissociation, which leads to damage of the substrate surface exposed to the environment of plasma discharge and high-energy electron bombardment (Li P et al., 2019). REALD is similar to PEALD in that, it exposes the cultured substrate and film to free radicals and eliminates substrate exposure to high-energy ions and electron bombardment. These free radicals, as reactants, are formed by gas dissociation using a hot wire feeder. Owing to the reactive free radicals, the process can be carried out at a lower temperature (closer to room temperature) (Bishal et al., 2015).

Physical Surface Modification

Physical surface modification mainly changes the ultrastructure of the implant surface, including laser surface engineering, arc ion plating, shot peening, and ultrasonic nanotechnology. Physical modification is often used to enhance the wear resistance, corrosion resistance, and oxidation resistance. Compared to chemical modification, the bonding force of the coating is weak.

Laser Surface Engineering

Laser surface engineering (LSE) is a material processing method that can be utilized to manufacture implants and also to modify the surface of implants. When LSE modifies the implant surface, it only changes the texturing of the surface, and maintains the chemical state of the substrate materials (Kurella and Dahotre, 2005). During LSE, the deposited substances need to be first coated on the implant surface, and then melted by high-energy laser irradiation and combined with the implant surface (Fathi-Hafshejani et al., 2020). The advantage of LSE is that it can precisely control the texture of the coating, including the formation of the size and morphology of the pre-determined pores (Shin et al., 2017; Fathi-Hafshejani et al., 2020). Implant surface texture is a key for biomedical devices/surfaces because the materials-cells interaction is largely affected by surface morphology and their mechanical properties (Dong et al., 2021). One study reported that the laser micro/nanotexturing process modified the surface properties related to osseointegration, include biocompatibility, protein adsorption and cell/surface interactions (Shivakoti et al., 2021). Therefore, the design of the micro morphology of the implant surface may be able to promote the osteogenesis of the implant surface, inhibit the growth of bacteria and improve the wear resistance of the implant. In addition, LSE is well suitable for high temperature-resistant inorganic coating of materials (e.g., CaP, Si_3N_4, TiN-TiB, SiC) (Das et al., 2014; Sahasrabudhe and Bandyopadhyay 2018; Li P et al., 2019; Zanocco et al., 2020). Niobium (Nb) is a costly refractory material with greater wear resistance and biocompatibility (Zhang Y et al., 2015). A study reported that porous Nb coating can be effectively prepared on the surface of titanium alloy by SLM, demonstrating that SLM can prepare coatings with individually customized shapes and/or porosity from IVB and VB biomedical metals and their alloys (Zhang Y et al., 2015).

Other Physical Modification

Arc ion plating (AIP) is an excellent physical vapor deposition technology that can produce strong adhesion coatings at low temperature (<170°C) (Tsou et al., 2012; Liu L. et al., 2017). The AIP device is mainly composed of a deposition chamber, an arc power supply, a pumping system, and a gas flow control system. During the deposition process, the gas enters the deposition chamber and is bombarded by the metal ions emitted by the highly ionized arc onto the surface of the substrate, which then condenses on the substrate surface in the form of a solid film to form a coating (Chung et al., 2008). AIP has advantages over other technologies in the preparation of TiO_2 coatings, such as high growth rate, strong film adhesion, and low deposition temperature (Chung et al., 2011). Finally, AIP is suitable for the preparation of inorganic metal coatings including MgCu, CaP, and TiCu/Ti-Cu-N coatings (Yu et al., 2018; Zhao et al., 2019; Guo et al., 2020).

Shot peening is an effective method to increase fatigue resistance and wear resistance of an implant (Liu et al., 2019). Shot peening can be divided into traditional mechanical shot peening and laser shock peening. In the mechanical shot peening process, a high-speed projectile stream is injected onto the surface of the material to cause plastic deformation. Then, residual stresses that are useful to improve the fatigue performance are introduced to the surface of the part (Nie et al., 2020). Laser shock peening compared to the mechanical shot peening is a non-contact process. This type of surface treatment can only be carried out using an intense laser pulse directed at a material surface in very short intervals rather than a continuous wave laser beam. The facilitated compressive residual stress is as much as four times larger than that of the mechanical shot peening technique (Shukla et al., 2013). The ability of shot peening to improve fatigue strength is suitable for the application of 3D-printed titanium alloy implants with weak fatigue strength. However, biocompatibility, osseointegration, and cytotoxicity of the shot-peened implants need to be further investigated.

Ultrasonic nano-crystal surface modification (UNSM) is a severe plastic surface deformation technology that can enhance the overall performance of metallic materials, in particular, the yield strength (Karimbaev et al., 2020). UNSM introduces plastic deformation, which leads to refinement of the grain size and high residual compressive stress on the surface and subsurface layers, while improving the mechanical properties of metal materials (Karimbaev et al., 2020). UNSM used the superposition of ultrasonic low frequency vibration on the static load to generated severe plastic deformation on the material surface, which further causes to surface nanocrystallization. The plastic deformation produced on the material surface during the UNSM process was induced by mechanical impacts. The high-frequency impact of the ball causes severe plastic deformation on the material surface, which leads to the introduction of high-density dislocation and grain boundaries. Thus, the nanostructured layer with a certain gradient is received (Amanov et al., 2012). The UNSM technique is a cold-forging process in which the ball made of silicon nitride and

tungsten carbide mechanically impact on the material surface at a constant vibration frequency of 20 kHz and a certain region is processed within a certain period of time. Researchers can control the nanostructure surface layer thickness, mechanical properties, tribological properties and fatigue properties by changing the impact parameters (Liu et al., 2021). UNSM before the use of 3D printed implants can effectively prolong their service life, which is of great significance to patients who need joint replacement surgery.

Biological Surface Modification

Biological surface modification is a primary technology that combines organic bioactive materials such as proteins on the surface of implants through electrostatic interaction, hydrogen bonds, and other forms. Different from chemical modification, it does not involve complex chemical reactions. Biological surface modification can deposit most organic biological coating materials. Therefore, biological modification has gradually evolved into an extensively researched topic for implant surface modification.

Layer-By-Layer Self-Assembly

Layer-by-layer (LBL) self-assembly is a film preparation method that has been widely used in various biomedical applications (Zhang T et al., 2018). The principle of LBL is to develop a laminated coating by alternating deposition of opposite-load polyelectrolytes on the surface of a laden substrate (Escobar et al., 2020). In the LBL process, multilayer films are deposited on the substrate surface through alternating adsorption of interactive materials, including polyelectrolytes, micelles, GO, antiparticles, and proteins (Park et al., 2018; Alkekhia et al., 2020). Hydrophobicity, Van der Waals forces, hydrogen bonds, covalent bonds, and bio-specific interactions promote film growth and are the main driving force of assembly (Park et al., 2018; Alkekhia et al., 2020). In addition, LBL can fabricate controllable coatings on almost all materials (Ma et al., 2015). For instance, fine control of composition, thickness, and topography can be achieved by adjusting the assembly parameters involving solution properties, like concentration, ionic strength, and pH, and process parameters, such as temperature, time, and drying conditions. Compared to other methods for fabricating nanofilms, there are three prominent advantages of the LBL, these include precise control of the composition and structure of nanofilms, large-scale fabrication capacity on various types of substrates regardless of size and shape, and mild and confined formation environments (Zhang T et al., 2018). Furthermore, LBL is good at manufacturing thin films for drug delivery, because it has no restriction on the size or shape of the substrate and can avoid the inactivation of some active substances caused by exposing the coating material to high temperature or high pressure (Park et al., 2018). Owing to the multivalent interaction between multilayer film and film components, it can carry high drug loads. Changing the number of layers can adjust the dose of the loaded drug (Alkekhia et al., 2020). In general, LBL is capable of achieving the loading and release of various types of drugs on the implant, thereby achieving the goal of biofunctionalization of the implant (**Figure 3**).

Hydrogel Combination

Hydrogel is a highly hydrated 3D network of interconnected polymer chains (Gibbs et al., 2016). Because of the different compositions of hydrogels, the physical and chemical properties of hydrogels vary widely. Hydrogel can be formed from natural (e.g., collagen and hypertonic acid), synthetic (e.g., polyethylene glycol), and semi-synthetic (e.g., combination of polyethylene glycol and cholesterol-containing polysaccharides) polymers (Gibbs et al., 2016). While natural polymers are typically characterized by a high degree of biocompatibility, they lack reliability and consistency due to their natural origin leading to troublesome batch-to-batch variations. By contrast, synthetic polymers are highly reproducible materials with precisely controlled chemical and physical characteristics. Unfortunately, they are classically less biocompatible than natural biopolymers either due to the material properties themselves or due to harmful residues arising from the manufacturing process which often involves cytotoxic or non-biocompatible organic solvents, starting monomers, or by-products (Utech and Boccaccini 2015). Hydrogels can absorb and retain large amounts of water (several times their dry weight) and swell, while maintaining its 3D structure, mechanical strength, and elasticity (Sosnik and Seremeta, 2017). As well being an excellent drug and cell carrier, hydrogels can be made into any shape and size according to application. Therefore, hydrogels can be completely covered in the microporous structure of 3D-printed implants (Yue et al., 2020). Hydrogels have been widely applied in the surface modification of 3D-printed titanium alloy implants. When hydrogel is used as a drug carrier, it disseminates drug molecules into surrounding tissues or cells through interconnected pores (Chyzy and Plonska-Brzezinska, 2020). For instance, Zhang W et al. (2020) developed a poloxamer 407 hydrogel loaded with simvastatin for filling porous 3D-printed titanium alloy intervertebral cages that achieved stable drug release and significantly promoted bone growth. Furthermore, the strategy of promoting bone regeneration through stem cell transplantation has become an important research topic to repair bone defects and promote bone integration. Kumar et al. (2018) developed a sodium alginate hydrogel containing preosteoblast for surface modification of 3D-printed titanium alloy. *In vitro* tests have revealed that the bioactivity of the titanium alloy implant can be significantly enhanced by adopting a hybrid system and a bioactive hydrogel. In addition, some hydrogel materials such as gelatin methacrylate (GelMA) can promote bone and angiogenesis by itself. It has a significant influence on the expression of genes associated with osteogenesis and angiogenesis across the Pi3K/Akt/mTOR pathway (**Figure 4**) (Ma et al., 2021).

FUNCTIONALIZATION OF THE IMPLANT SURFACE

Antibacterial Modification

Artificial joint infection is a serious complication of knee and hip replacement surgery, causing catastrophic clinical consequences

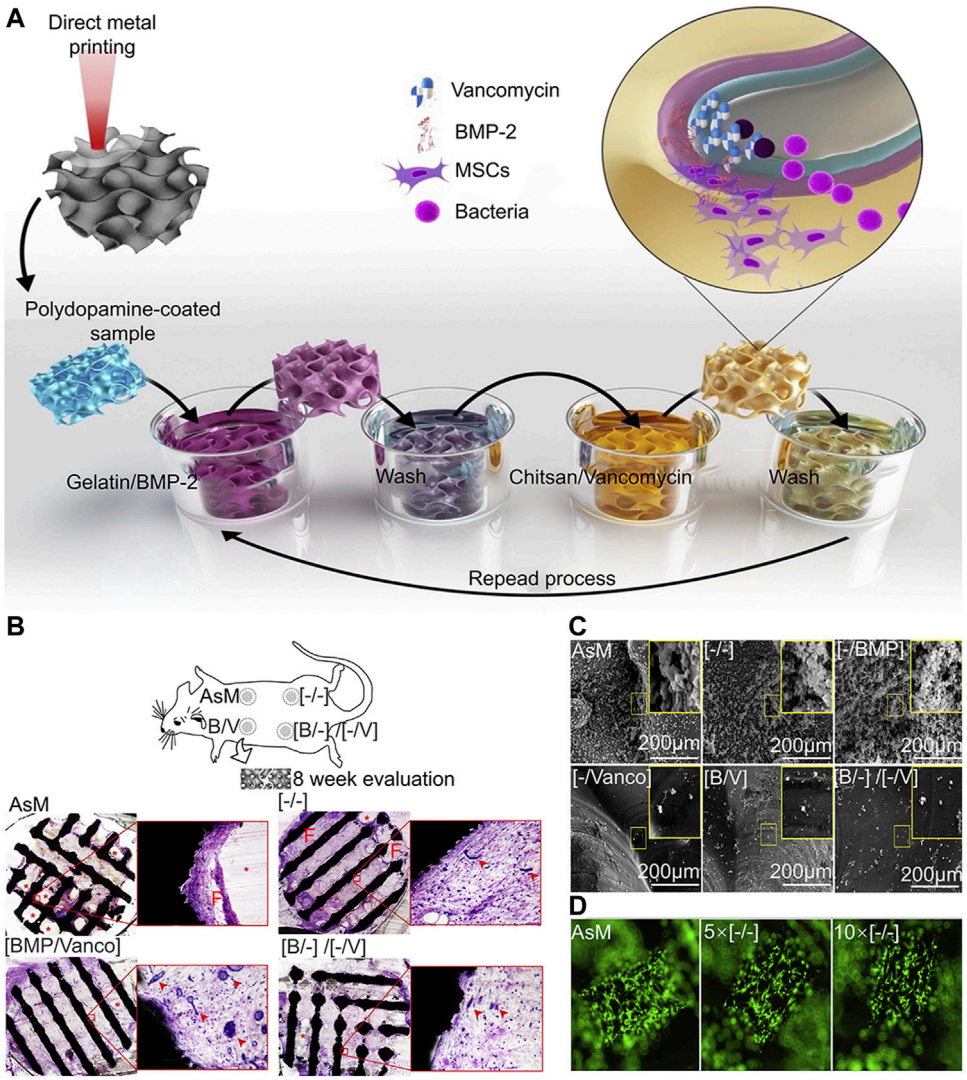

FIGURE 3 | LBL vancomycin and BMP-2-coated implants (Amin Yavari et al., 2020). **(A)** Schematic illustration of the layer-by-layer coating process. **(B)** The biocompatibility of the scaffold was analyzed 8 weeks after implantation, the porous Ti structures did not induce an adverse tissue response in any of the groups, shown by the absence of acute inflammation or fibrous encapsulation at the material-tissue interface. In the case of any LBL remnants, no acute inflammatory response was seen around the polymer. At the same time, we observed a high density of blood vessel formation. **(C)** Representative images of planktonic and adherent bacteria on the surfaces of different experimental groups. In the experimental group containing vancomycin, the number of bacteria was significantly less. **(D)** In the live death staining experiment, the surface of the implant was completely covered by living cells, and the surface coating had no inhibitory effect on cell adhesion and proliferation.

(Zardi and Franceschi, 2020). With the development of implant surface modification technologies, researchers have reduced the adhesion of bacteria by loading antibacterial drugs on the implant surface and changing the surface morphology of the implant, which can effectively protect against artificial joint infection. Common antibacterial coatings include silver agents, antibiotics, polysaccharides, antimicrobial peptides (AMP), and antiparticles (Gonzalez-Henriquez et al., 2019). 3D-printed implants have a larger surface area than traditional implants, which means it has more antibacterial agents per unit volume. Accordingly, it is able to release large doses of antibacterial agents locally to obtain effective preventive and therapeutic effects (Croes et al., 2018). In view of this, 3D-printed implants with antibacterial coatings may become an effective method to prevent and treat implant infection in the future.

Silver Ion (Ag^+) and Silver Nanoparticles (AgNPs) Coating

Ag is a highly effective antibacterial agent, specifically for drug-resistant bacteria. Ag-plated medical devices must produce an Ag^+ concentration that is high enough to achieve the desired antibacterial effect. However, because of the cytotoxic effect of Ag^+, it is necessary to avoid undesirable effects on cells surrounding the implant (Chernousova and Epple, 2013). When Ag is used as an antibacterial agent, it is usually made in two dosage forms: Ag^+ and AgNPs. The antibacterial

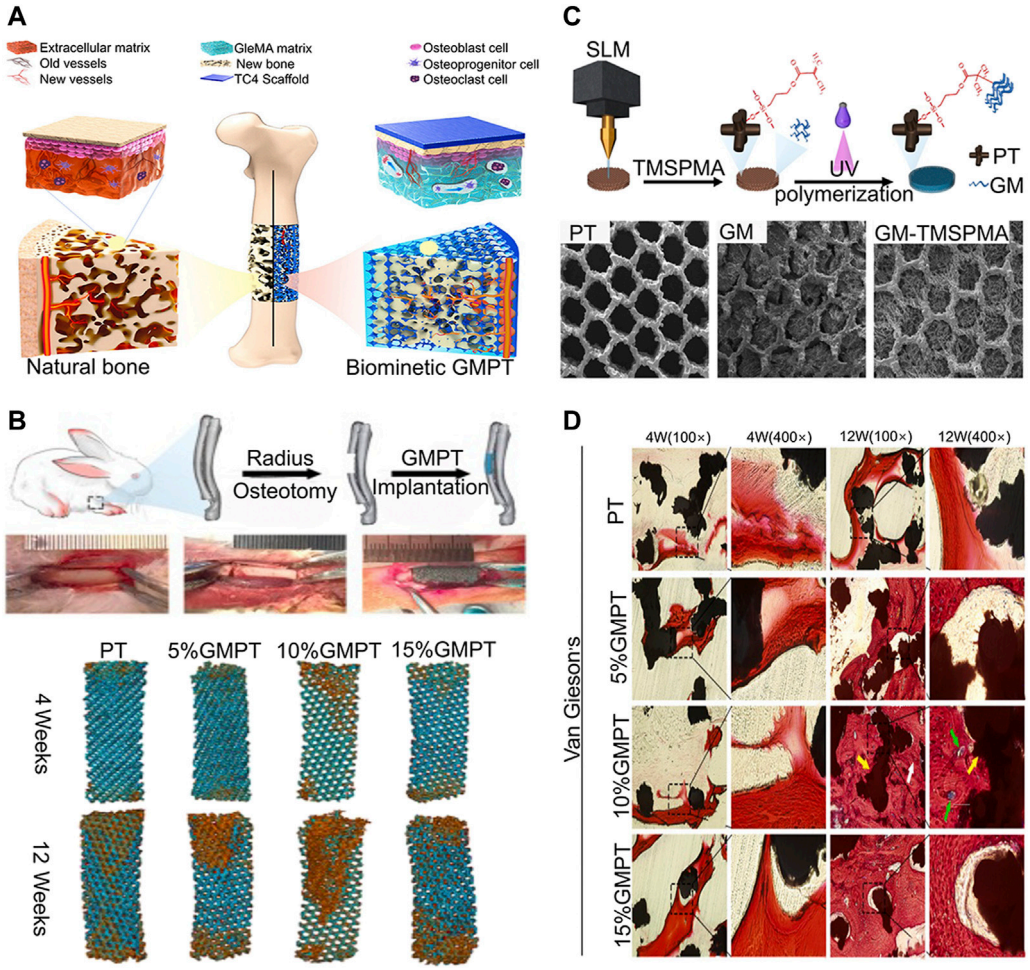

FIGURE 4 | Ti6Al4V alloy/GelMA hybrid implant with dual bionic features (GMPT) for bone defect repair (Ma et al., 2021). **(A)** Schematic illustrations of the biomimetic GMPT with dual-bionic features. **(B)** *In situ* implantation of PT and GMPT implants, micro-CT 3D reconstruction of PT and GMPT in critical radius defects of rabbits. The implants in GMPT group had higher osteogenic activity than uncoated implants, and the osteogenic ability of the 10% GMPT group was the strongest. **(C)** The fabrication process and characterization of GMPT. **(D)** Histological analysis of implant samples after 4 and 12 weeks in rabbit radius defect sites. The GMPT group showed thicker and higher number of trabeculae than the PT group at both weeks 4 and 12 (yellow arrows indicate the PT implant, white arrows indicate new bone, and green arrows reveal new vessels). The 10% GMPT group showed the best osteogenesis and angiogenesis ability.

mechanisms of Ag^+ can be divided into three categories: (1) interacting with the bacterial cell envelope, (2) interacting with molecules inside the cell (e.g., nucleic acids and enzymes), and (3) producing reactive oxygen species (ROS) (Kedziora et al., 2018). The antibacterial mechanism of AgNPs is not explicit, but the existing studies showed that AgNPs can continually release Ag^+ to resist bacteria. In addition, AgNPs interact with bacterial cell membrane and organelles, resulting in bacterial death (Yin et al., 2020). 3D-printed implants can carry high doses of Ag agents; therefore, researchers adopted different methods to carry Ag^+ on the surface of 3D-printed titanium alloy implants (Razzi et al., 2020). Amin Yavari et al. (2016) loaded Ag^+ in nanotubes produced by anodic oxidation to prepare an antibacterial coating. Although large numbers of Ag^+ show high antibacterial capability, they also cause high cytotoxicity (**Figure 5**). Conversely, Anish Shivaram et al. (2017) fixed Ag^+ in nanotubes and electrolyzing Ag^+ solution again. The Ag^+ coating prepared by this method has a high antibacterial capacity and no evident cytotoxicity. Loaded AgNPs in carriers may further enhance the binding force between AgNPs and the implant surface, which significantly reduces the cytotoxicity of AgNPs. For instance, Jia et al. (2016) fixed AgNPs with PDA and on the micro-nano titanium alloy surface which is modified by MAO to construct an AgNPs/PDA/TiO_2 coating. Compared with the previous modification method, this composite coating showed excellent antibacterial effect and low cytotoxicity of AgNPs. In addition, in the treatment of patients with infectious bone defect, implants are required to not only have strong antibacterial effect but also release more osteogenic substances to promote bone regeneration. Sumeneva et al. (2019) developed an AgNPs/CaP coating on 3D-printed titanium alloy implants to repair infectious bone defects. The multifunctional coating significantly inhibited *Staphylococcus aureus* and promoted bone ingrowth. Another study showed that AgNPs

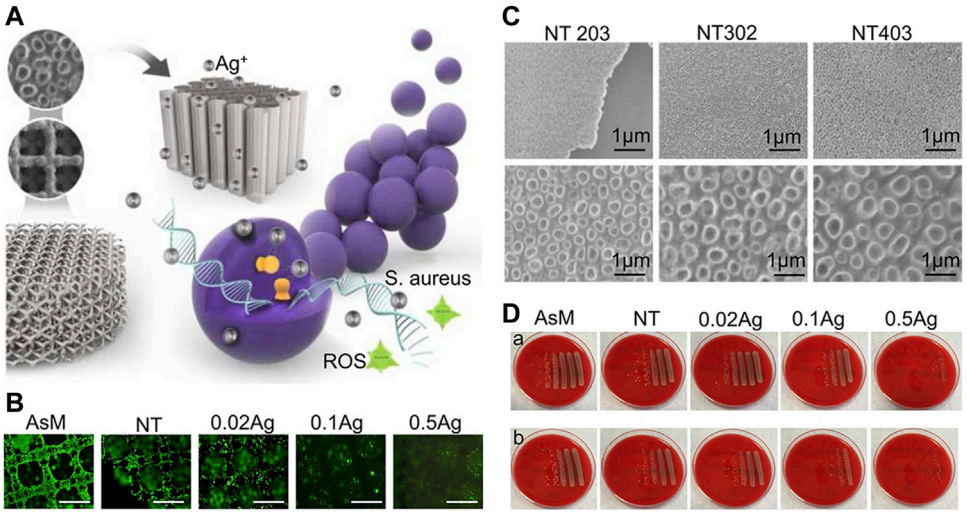

FIGURE 5 | Ag^+ coating of nanotubes prepared by anodic oxidation (Amin Yavari et al., 2016). **(A)** Schematic diagram of 3D-printed titanium alloy surface covered with nanotubes and carrying Ag^+ to inhibit bacterial growth. **(B)** The inhibitory effect of different concentrations of Ag^+ loaded on the implant surface on cell proliferation and adhesion. **(C)** SEM images of anodized porous titanium with the following parameters: 20 V, 3 h; 30 V, 2 h; 40 V, 3 h. **(D)** Antibacterial performance of AsM, NT, NT-0.02 Ag^+, NT-0.1 Ag^+, and NT-0.5 Ag^+ against *Staphylococcus aureus* after 7 days. The first row corresponds to planktonic bacteria and the second row to adherent bacteria; the group with higher Ag^+concentration had obvious antibacterial ability than the group with lower Ag^+ concentration.

and SF fixed on 3D-printed titanium implants could effectively inhibit the proliferation of *S. aureus* and induce bone regeneration (Jia et al., 2019).

Antibiotic Coating

Antibiotics are the most widely used antibacterial medications, particularly in the prevention and treatment of infections after joint replacement (Miller et al., 2020; Ricciardi et al., 2020). In the post-operative stage, systemic prophylactic antibiotics are often used to preventing infection. However, the dose of systemic antibiotics is quite limited and may easily lead to bacterial drug resistance (Myers et al., 2020). Compared to systemic administration, local application of antibiotics can provide large doses of antibiotics at the surgical site, reducing the risk of bacterial drug resistance (Tan et al., 2012). In addition to the application of antibiotic containing bone cement, the antibiotic coating is a local drug delivery strategy. The antibiotic coating and 3D-printed microporous implant can further improve the local antibiotic concentration. For instance, Li X et al. (2020) developed a 3D-printed intervertebral cage covered with polyvinyl alcohol coating loaded with vancomycin that could effectively inhibit the reproduction of *Escherichia coli*, *S. epidermidis,* and *S. aureus* (**Figure 6**). Moreover, the combination of antibiotics and Ag^+ may produce synergistic effects, reducing bacterial drug resistance and playing a stronger antibacterial function. Bakhshandeh et al. (2017) developed a chitosan-gelatin coating containing vancomycin and Ag^+, which could be continuously released on the surface of the titanium alloy and was manufactured by 3D printing with high area. This chitosan-gelatin coating had better antibacterial properties than simple Ag^+ or vancomycin coating. Aside from the simple antibacterial coating, combination of antibacterial coating and osteogenic coating may be an effective way to treat infectious bone defects. Amin Yavari et al. (2020) developed a vancomycin-hydrogel BMP-2 coating and applied it onto a porous titanium alloy surface. Results showed that the biomimetic implant efficiently inhibits bacteria within 2–3 weeks and increases the activity and mineralization of ALP on the implant surface.

Osteointegration Modification

The intrinsic biological inertia of titanium alloy implants is a significant reason for the failure of implant surgery. Biological inertia refers to materials that can remain stable in the biological environment (Xia et al., 2020). When a biologically inert material exists in the body for a long time, it may have an exudation tissue reaction with the biological body, which can cause implant loosening and subsequent implantation failure (Han et al., 2018). In addition, bioinert materials lack osteoinduction, which may lead to the instability of bone implant binding (Wang S et al., 2018). Therefore, it has become important to increase the biological activity of titanium alloy implants, which is the focus of several ongoing research studies. Changing the surface morphology of implants (such as the surface of micro-nano structures produced by MAO) or preparing implant coatings (such as HA coatings) are two effective methods to solve this problem (Su et al., 2020; Myakinin et al., 2021). In the process of implant surface modification, these methods enhance the biological activity of the implant and promote osseointegration.

Calcium Phosphate Coating

CaP is a general term for a class of minerals, in which the cation is Ca^{2+} and the anions can be orthophosphate, metaphosphate, pyrophosphate, hydrogen, or hydroxide ions (Eliaz and Metoki,

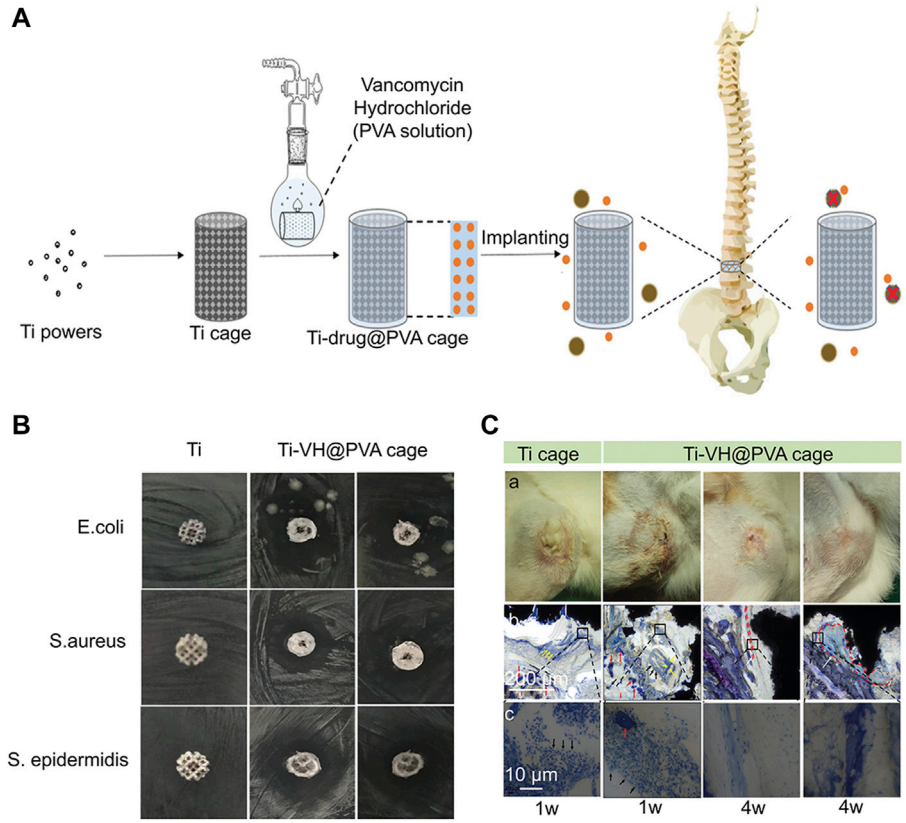

FIGURE 6 | A 3D-printed titanium cage combined with a drug-releasing system for *in situ* drug release and bactericidal action (Li Y et al., 2020). **(A)** The schematic illustration of a 3D-printed titanium cage coated with PVA-vancomycin for preventing surgical site infections (Berbel, Banczek et al.) after spine surgery. **(B)** Antibacterial evaluation of Ti-VH@PVA cages *in vitro*. The obvious bacteriostatic circle was observed with regard to *Staphylococcus aureus* and *Staphylococcus epidermidis*. **(C)** Evaluation of Ti-VH@PVA cages for preventing SSIs *in vivo*. With the extension of time, the infiltration of inflammatory cells decreased significantly in Ti-VH@PVA cage. Furthermore, the thickness of the discontinuous fibrous capsule between the trabecular bone and the Ti-VH@PVA cage increased. This indicates that Ti-VH@PVA cage has a significant inhibitory effect on *Staphylococcus aureus*.

2017a). When the CaP is immersed in SBF (with ion concentrations that are nearly equal to those of human blood plasma), the deposition of $Ca^{2+}$and formation of a phosphate layer are hypothesized to be crucial steps for the initiation of the growth of bone-like apatite on biocompatible implants. The relationship between the bioactivity and solubility of the implant surface and the formation of the apatite layer in SBF is often interpreted as a first indication of its potential bioactivity *in vivo* (Surmenev et al., 2014). In general, CaP can promote the formation of new bone by inducing HA deposition on the implant surface (Eliaz and Metoki, 2017). In addition, studies found that CaP nanoparticles (CaPNPs) may have stronger ability to promote bone integration than ordinary CaP, which may be due to the increase of hydrophilicity of the implant surface caused by CaPNPs coating (Wennerberg and Albrektsson, 2009; Chudinova et al., 2019).

HA ($Ca_{10}(PO_4)_6(OH)_2$) is a form of CaP, which accounts for 70% of the bone composition (Ramesh et al., 2018). HA has superior biological activity, biocompatibility, and osteoconductivity both *in vitro* and *in vivo* (Ramesh et al., 2018). The test showed that HA coating of direct bonding strength with metal materials is weak, and it is difficult to completely cover the implant with complex shape (Huynh et al., 2019). Accordingly, HA coating is often firmly bonded to the implant surface through some modification techniques to make it play an osteogenic role by electrochemical deposition. For instance, Qin et al. (2018) prepared an HA coating on the surface of 3D-printed titanium alloy implant by anodic oxidation technology and Kodama's alternative immersion method (AIM) that exhibited a strong bone integration ability.

Bioactive Glass

BAG is a type of bioactive material, involved in a variety of clinical applications in orthopedic and other hard tissue regeneration (Skallevold et al., 2019). When BAG makes contact with body fluids (BF) or simulated body fluids (SBF), it can undergo ion dissolution and glass degradation through the exchange of H^+ in the solution and Na^+ and Ca^{2+} from the glass network. These ions play a crucial role in osteoinduction (Rahaman et al., 2011). The most important property of BAG is induction of HA formation on the implant surface to stimulate bone growth (Skallevold et al., 2019). The composition of mesoporous BAG (MBG) is similar to

that of BAG, but has a larger surface area and controllable mesoporous structure, and MBG has a stronger apatite-inducing ability (Kong C. H. et al., 2018; Lalzawmliana et al., 2020; Zhang et al., 2021). Bioactive ions such as Si^{2+} released from MBG can significantly stimulate osteogenic differentiation of osteoblasts and hBMSCs through activation of specific signaling pathways (Zhu et al., 2019). The formation of BAG coating on 3D-printed titanium alloy is a strategy to enhance osteoinduction. However, MBG coating is quickly consumed in Tris HCl buffer solution, resulting in a short time for the release of bioactive ions, so it lacks a long-term promoting effect on osteogenesis (Cerruti et al., 2005). Researchers have found that the deposition of MBG on the implant surface by anode oxidation can effectively slow down its degradation and play a biologically stimulating role (Zhao B et al., 2020). Accordingly, MBG can also be mounted on porous titanium alloy by spin coating (Ye et al., 2017). This simple method not only retains the unique mechanical structure and chemical composition of MBG but also establishes an excellent interface link with the matrix.

Metal Coating

Strontium (Sr) is an important osteogenic trace element which is widely used as an oral drug for the treatment of osteoporosis (Wang et al., 2020). The comparison of Sr^{2+} and other divalent ions (Mg^{2+}, Ca^{2+}, Ba^{2+}) shows that Sr^{2+} has a more significant effect on promoting bone formation, inhibitory effect on osteoclastogenesis, immunogenicity, and fibrosis (Xu et al., 2020). The exact mechanism of Sr^{2+} in osseointegration remains unclear, but it has been proposed that Sr^{2+} acts on similar cellular targets as Ca^{2+} by activating the calcium-sensing receptor (CaSR), thus interacting with Ca-driven signaling pathways related to bone metabolism regulation (Wan et al., 2020). In addition, Sr^{2+} has high security. First, the binding ability of Sr to human plasma protein is low (~25%), but it shows high affinity to bone tissue. Second, Sr^{2+} is adsorbed on the surface of bone minerals instead of replacing Ca^{2+} which is conducive to its rapid elimination (Martin-Del-Campo et al., 2019). Recently, it has been reported that releasing Sr^{2+} from the surface of functional implants can increase the dose of local medication, reducing side effects, and improving bone integration (Wei et al., 2020). As a result, 3D-printed titanium alloy implants with Sr^{2+} coating are well suited for osteoporosis patients requiring joint replacement surgery. Shimizu et al. and Wei et al. (2020, 2020) adopted a strategy of fixing Sr^{2+} on the implant surface with micro-nano structure to enhance the early bone binding ability by continuously releasing Sr^{2+}. Moreover, to achieve long-term release of Sr^{2+} on the implant surface and obtain long-term bone induction ability, Wang S et al. (2018) developed a coating combining Sr^{2+} with zeolite to reduce the release rate of Sr^{2+} due to the zeolite cation exchange function.

Gallium ions (Ga^{3+}) play an important role in orthopedic biological materials owing to its excellent antibacterial properties, inhibits osteolysis, prevents bone calcium release, and increases bone mass (Yu et al., 2020). A study showed that Ga^{3+} interacts with cellular particles and HA of bone. That means Ga^{3+} can resist bone resorption when used in patients with osteoporosis (Tharani Kumar et al., 2020). Moreover, it should be noted that Ga^{3+} also has the function of treating cancer-induced hypercalcemia and inhibiting the growth of tumor cells (Farrell et al., 2018). Therefore, 3D-printed implants with Ga^{3+} coating may be an effective means of treating bone defects caused by tumor resection in the future.

The concentration of Mg ranks fourth among all cations in the human body (Yang H et al., 2020). More than half of the Mg in the human body is stored in bone tissue in the form of biological Mg (Matsuzaki, 2006). Mg^{2+} is the most abundant cation in cells and regulates a variety of cellular functions such as cellular signal, cell growth, metabolism, and proliferation. A high concentration of Mg^{2+} can activate the calcium channels on the cell membrane (Li J et al., 2020). Furthermore, Mg is necessary for bone growth because it can inhibit osteoclast differentiation and bone resorption. A severe Mg^{2+} deficiency will lead to osteoporosis, which is characterized by reduced bone formation and increased bone resorption (Du et al., 2019). Studies showed that a small amount of dissolved Mg^{2+} is harmless in the body. Excess Mg can be metabolized by the kidneys and eventually excreted in the urine (Julmi et al., 2019). Therefore, it is important to prepare Mg^{2+} coating on 3D-printed titanium alloy implant to improve bone integration in patients with osteoporosis. Du et al. (2019) proved that the preparation of Mg^{2+} coating on the surface of 3D-printed titanium alloy implant can effectively solve the problem of poor bone integration in the osteoporosis model. Accordingly, Mg^{2+} can modify the coating with trace elements. Mg^{2+} could improve the chemical stability and mechanical resistance of $CaSiO_3$ with a high degradation rate and low mechanical resistance. Tsai et al. (2019) developed a mixed coating of $CaSiO_3$/Mg^{2+} and chitosan. The high bioactivity of $CaSiO_3$ and Mg^{2+} significantly increased the bone induction capability of titanium alloy implants.

High Molecular Polymer Coating

Polycaprolactone (PCL) is a semi-crystalline aliphatic polymer commonly used to manufacture implants, drug carriers, and biodegradable packaging materials (Kiran et al., 2018). PCL has high biocompatibility, mechanical properties, processability (melting point: 60°C), and degradation absorption (Ghosal et al., 2017; Makkar et al., 2018). Moreover, PCL can maintain the porous structure of 3D-printed implants and frequently be used as a degradable carrier material for surface modification (Grau et al., 2017). For instance, Roland et al. (2015, 2016) loaded the PCL coating with vascular endothelial growth factor (VEGF), high-mobility group protein 1 (HMGB1), and other pro-angiogenic factors to stimulate the angiogenesis of porous titanium alloy implants.

Polylactide glycolic acid (PLGA) is one of the most widely used degradable materials for medical applications. PLGA has excellent mechanical properties, low immunogenicity, low toxicity, and adjustable degradation rate (Kong J. et al., 2018; Zhang H et al., 2019). Diabetes is a high-risk factor leading to implant failure. PLGA coating can alleviate diabetic condition (DC)-induced endothelial cell dysfunction and increase vascular ingrowth under DC conditions, because lactic acid (LA), the degradation product of PLGA, can stimulate angiogenesis and indirectly improve the bone formation of bone implant interface

(BII) (Hu et al., 2018). Furthermore, PLGA can improve the bone integration in diabetic environment by inhibiting advanced glycation end products (AGEs) (Hu et al., 2018). In addition, as a drug carrier, PLGA materials can carry most kinds of drugs and control the release rate of drugs (Shokrolahi et al., 2019). Kwon et al. (2018) prepared PLGA coating on the 3D-printed titanium alloy implant and loaded it with ethyl 2,5-dihydroxybenzoate (E-2,5-DHB) (a drug that promotes bone formation and inhibits bone resorption). The results showed that PLGA can effectively immobilize E-2,5-DBH and ensure its steady release. Bionic implants in osteoporotic patients can effectively inhibit bone resorption around the implant and promote bone scarring.

Dopamine (DA) is used as the sole adhesive protein of mussel foot-5 (MEFP-5) and can be associated with various metal ions through its dispersed alcohol groups (Li et al., 2016). Inspired by the natural mussel adhesion phenomenon, DA could self-polymerize to form PDA coating under mild conditions through a simple experimental process (Huang et al., 2016). PDA is used in implant coating for different purposes, such as antibacterial treatment, protein binding, cell culture, and medication administration (Perikamana et al., 2015). The catecholamine-rich PDA coating was found to contribute to the formation of HA on various implanting systems (Kaushik et al., 2020). As is known, PDA is an excellent drug carrier, which can fix AgNPs, HA, vancomycin, magnetic Fe_3O_4 oxide, and other drugs on the surface of the implant to achieve its biological functions (Li Y et al., 2015; Jia et al., 2016; Zhang T et al., 2018; Lingpeng Kong et al., 2020).

Organic and Bioactive Coating

Protein coatings have been key for resolving the poor osseointegration of implants over the past few years. Proteins as implant coating materials can significantly increase the binding force of bone and implant integration, because the surface of the implant covered by the protein is highly recognized as a "host type" tissue and the addition of specific biological clues can change the response of the bone tissue around the implant. Consequently, osteoblasts can be attached to the implant surface more quickly to stimulate bone regeneration (Jurczak et al., 2020). Common protein coatings include growth factors (BMP-2, BMP-7, VEGF), type I collagen (COL I), and albumin.

BMP-2 is an obstetric cytokine in the transforming growth factor-β (TGF-β) family and is currently the most commonly used protein-based bone transplant substitute (Nguyen et al., 2017). BMP-2 plays a major role in embryonic development, bone remodeling, and homeostasis in adulthood. BMP-2 can activate osteogenic genes such as Run-Related transcription factor 2 (*RUNX2*) to promote bone growth (Halloran et al., 2020). Preclinical and clinical studies showed that BMP-2 can be applied for the treatment of a variety of orthopedic diseases such as bone defects, nonunion, spinal fusion, osteoporosis, and root canal surgery (Chen et al., 2004). The incorporation of BMP-2 on implant surfaces appeared as a new strategy aimed at improving osteogenic activity and osseointegration of implant surfaces. A test revealed that BMP-2 can be released steadily on the 3D-printed titanium alloy surface which treated by MAO and the osteoinduction of implants is significantly enhanced (Teng et al., 2019). In addition, it is worth mentioning that BMP-2 can be covalently coated by 3D-printed titanium alloy by ion-assisted plasma polymerization technology to play its osteogenic role (Croes et al., 2020).

Parathyroid hormone (PTH) has the potential to enhance bone regeneration of bone abnormalities (Wojda and Donahue, 2018). Osteostatine is the C-terminal N-terminal 107–111 sequence of PTH. The short length and amino acid composition of this pentapeptide provides stability, and osteostatine has stimulated osteoblast activity and inhibited osteoclast activity. Studies have shown that osteostatine coating on the 3D-printed implants can be effective for bone regeneration (van der Stok et al., 2015).

Introducing organic molecules with functional fragments in the lining is a new strategy to promote osteogenesis. RGD is an artificial peptide that has a specific bio-active sequence. It exists in most ECM proteins including fibronectin, vascular junction protein, and laminin (Hersel et al., 2003). RGD stimulates bone integration by increasing the proliferation and adhesion of osteoblasts on the implant surface (Elmengaard et al., 2005). One study reported that the hybrid molecular coating obtained by chemical crosslinking of amino acid bisphosphonate and linear tripeptide RGD combines, which has a strong ability to stimulate bone integration (Parfenova et al., 2020). Furthermore, another study showed that identifying the exons of hMSC osteogenic differentiation and binding them to the implant surface can achieve acellular bone regeneration and the bone tissue regeneration efficiency of acellular coated implants was equivalent to hMSCs-implanted acellular implants (**Figure 7**) (Zhai et al., 2020).

COL I is the most abundant bone protein (representing 85% of organic constituents) (Sartori et al., 2015). The interaction between cells and collagen plays an important role in regulating the differentiation of bone marrow in the osteogenic pathway (Sartori et al., 2015). Studies have shown that COL I has the capacity to recruit osteoblasts and accelerate mineralization, and enhance bone regeneration (Naomi et al., 2021). COL I of calf skin or mouse tail has been extensively used as a biological coating material for titanium alloy implants. Veronesi et al. (2021) were successful in increasing the bioactivity of implants by binding type I collagen on the surface of a 3D-printed titanium alloy.

Decellularized extracellular matrix (dECM) is a tissue ECM isolated from primitive cells (Yao et al., 2019). With proper detection methods dECM can be easily obtained from tissues/organs of different species (Kim Y. S. et al., 2019). dECM can simulate the structure and components of the natural ECM and offer a good growing environment for cells (Yao et al., 2019). One study showed that dECM coating on the 3D-printed titanium alloy implants can increase cellular proliferation and adhesion to promote bone ingrowth (Kumar et al., 2016).

Quercetin is a class of natural flavonoids, widely found in flowers, leaves, and fruits of various plants, and has anti-cancer, anti-fibrotic, anti-inflammatory, and antioxidant effects (Tang et al., 2019). Llopis-Grimalt et al., (2020) prepared a quercetin coating on the porous 3D-printed titanium alloy. *In vivo* test

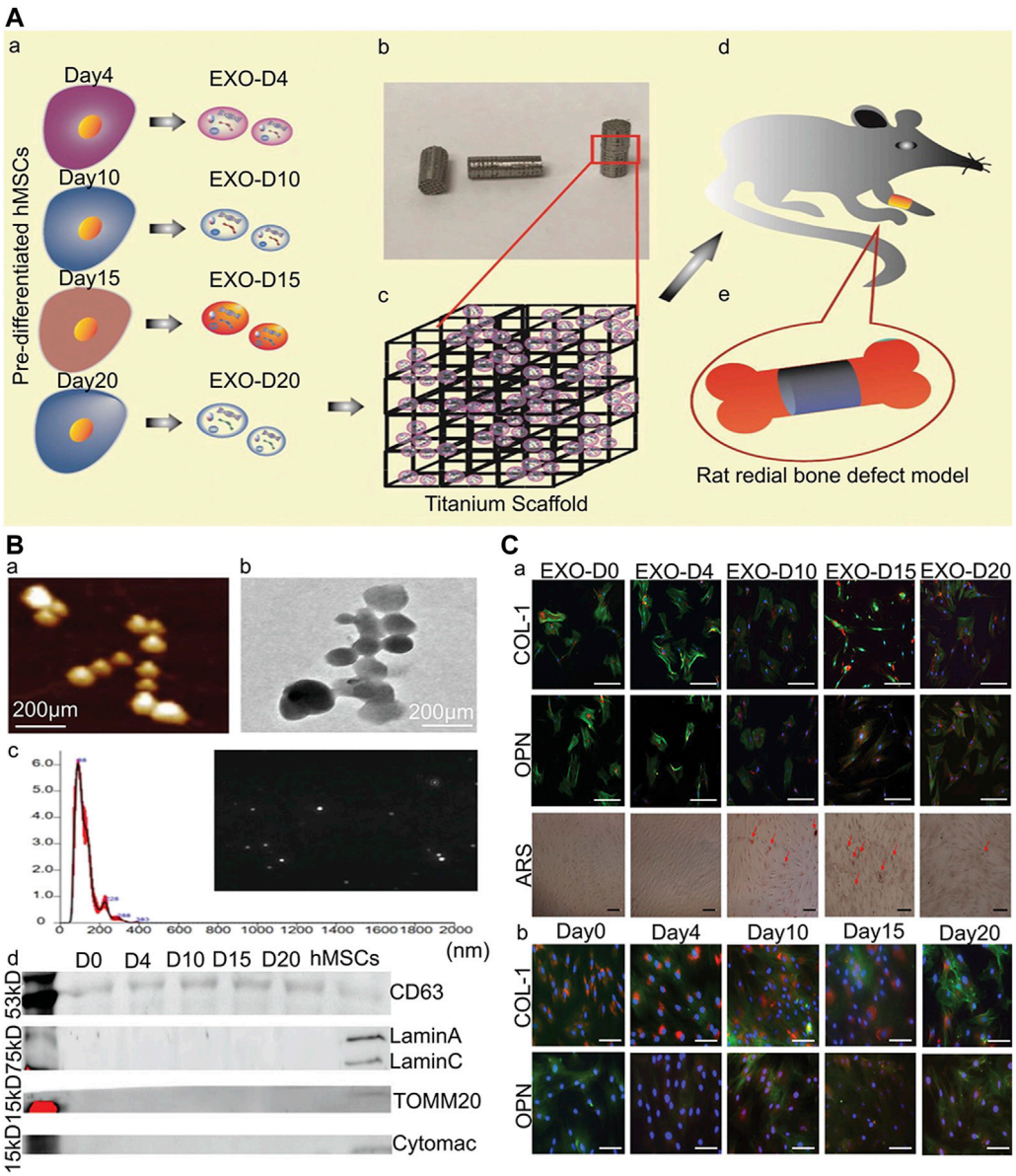

FIGURE 7 | Osteogenic exosomes induce osteogenic differentiation (Zhai et al., 2020). **(A)** The schematic illustration of cell-free bone tissue regeneration by the stem cell-derived exosomes. **(B)** The characterization of the stem cell-derived exosomes. a) AFM and b) TEM showing the size and morphology of the exosomes derived from hMSCs. Scale bar: 200 nm. c) The size and concentration of the hMSCs-derived exosomes by the NanosightNS300. The inset is an image showing the snapshot of video tracking. d) The western blot analysis of the exosome derived from the pre-differentiated hMSCs and hMSCs. **(C)** Osteogenic differentiation of hMSCs by the osteogenic exosomes a) Immunofluorescence staining of osteogenic markers (COL-1, OPN) in hMSCs induced by osteogenic exosomes. b) Immunofluorescence staining of osteogenic markers (COL-1, OPN) in hMSCs induced by osteogenic medium. There was no significant difference between osteogenic exosomes treatment and osteogenic medium treatment, which proved the osteogenic induction function of osteogenic exosomes.

results showed that the quercetin coating had excellent antibacterial capacity and osteogenic induction capacity.

Mechanical Properties Modification

Wear Resistance Modification

Aseptic loosening of the implant is a crucial cause of implantation failure (Apostu et al., 2018). The wear and adhesion of polyethylene, metal, and bone cement in the body may produce debris particles, which cause aseptic inflammatory reactions in the tissues surrounding the operation, leading to bone resorption and implant loosening (Bauer and Schils 1999). Therefore, enhancing the wear resistance of the implant and reducing the generation of wear particles can diminish the incidence rate of implant operation failure. Lately, discontinuous fiber-reinforced titanium-based composite coatings synthesized *in situ* by high-energy lasers have been extensively used. In comparison to monolithic coatings, these coatings have excellent mechanical properties, such as high

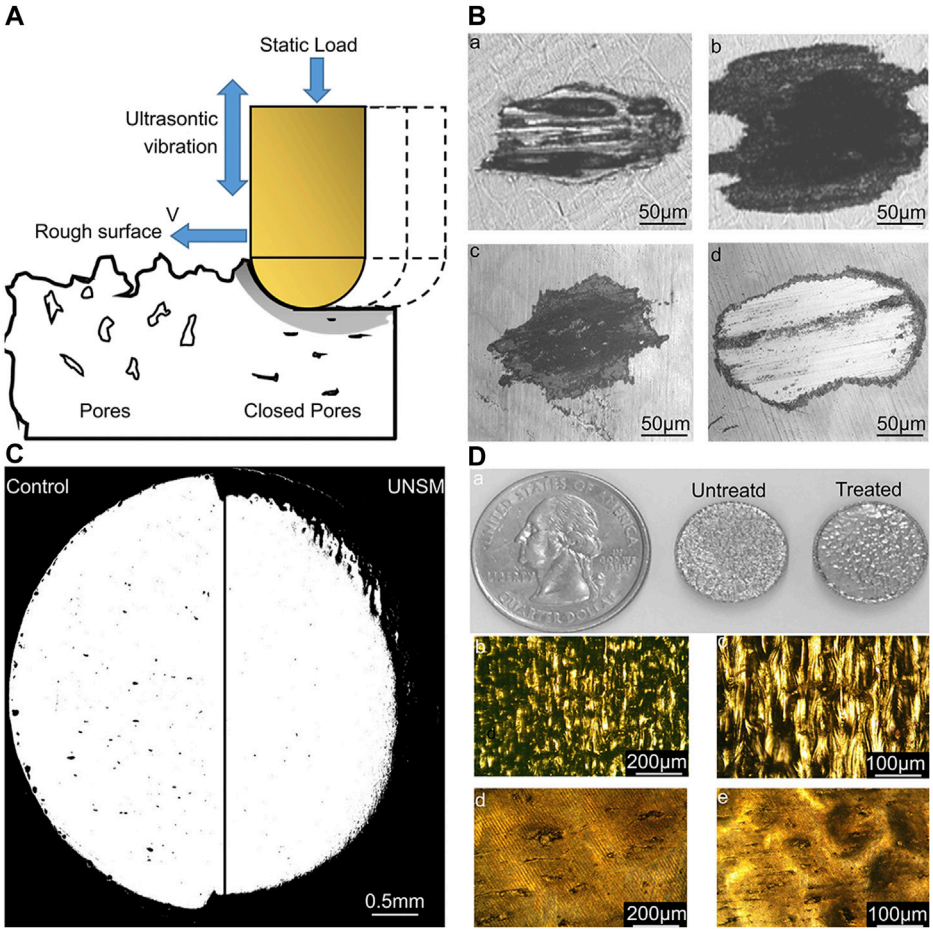

FIGURE 8 | Effect of UNSM treatment on 3D-printed NiTi alloy surface (Ma et al., 2017). **(A)** Schematic of the UNSM processing showing its effect on surface finish, subsurface porosity, and surface hardening. **(B)** Wear scars of untreated (a and b) samples and UNSM-treated (c and d) samples at 6,000 (a and c) and 24,000 (b and d) cycles. **(C)** Porosity distribution on the untreated surface and UNSM-treated surface. **(D)** a) Appearance of the AM NiTi samples before and after UNSM treatment; b) and c) show the optical images of the non-treated sample. d) and e) show the optical images of the UNSM-treated sample. The treated samples have better wear resistance and lower porosity than untreated samples.

toughness and excellent mechanical strength (Das et al., 2014). In addition, changing the surface morphology of an implant is also a way to improve its wear resistance. A study reported that the surface modification of NiTi alloy by UNSM, significantly enhanced the wear as well as corrosion resistance of the implant without changing the chemical properties of the implant surface (**Figure 8**) (Ma et al., 2017).

Fatigue Strength Modification

Although 3D printed titanium alloy stents have many advantages such as personalized customization and matching the elastic modulus of human bones, the fatigue strength of 3D printed titanium alloys is considerably weaker than traditional titanium implants (Soyama and Takeo, 2020). In addition, surface modification technologies (MAO, anodizing, plasma spraying, sand blasting) on the surface of titanium alloy will reduce the fatigue strength of implants (Yang Y. W et al., 2020). To enhance the service life of the implant, it is necessary to increase the fatigue strength of the implant. The fatigue strength is closely related to the porosity and surface morphology of implants (Kelly et al., 2019). In addition to using high-strength implant materials, surface modification may be a strategy to enhance their fatigue strength. Studies have proven that shot peening on the surface of 3D-printed titanium alloys can effectively improve the fatigue strength of implants (Remigiusz Zebrowski et al., 2019; Soyama and Takeo, 2020). In addition, the TiO_2 nanotube coating on the surface of titanium alloys by hydrothermal treatment can also effectively improve the fatigue strength of the titanium alloy (Yang Y. W et al., 2020). At present, there are few studies on surface modification to improve the fatigue strength of 3D-printed titanium alloy. Further improving the fatigue strength of 3D-printed implants may depend on the design of the implant materials and shapes.

Corrosion and Oxidation Resistance Modification

The corrosion resistance of the implant is an important property of the implant, and the level of corrosion resistance determines the biocompatibility of the materials. The lower the corrosion

resistance of the implant, the higher the toxicity of the ions released into the body (Asri et al., 2017). The reason why titanium alloy has a great corrosion resistance is that the passive oxide film will be formed on the surface of the titanium alloy after contact with oxygen (Berbel et al., 2019). When the artificial joint is implanted *in vivo*, the TiO_2 on the surface of the implant may be corroded by the body fluid environment, resulting in the reduction of the corrosion ability of the implant (Rodrigues et al., 2009). In order to increase the service life of the implant and decrease the risk of postoperative adverse reactions, it is necessary to prepare a corrosion-resistant coating. A study showed that chemical polishing of 3D-printed titanium alloy materials can significantly enhance the thickness of the TiO_2 layer of its surface, thus increasing the corrosion resistance of titanium alloys (Zhang Y et al., 2019). Furthermore, the corrosion resistance of titanium alloy can also be improved by MAO treatment (Rafieerad et al., 2015). This may be attributed to the fact that MAO can improve the bonding strength between the coating and titanium alloy and enhance the strength of crystal structure in the coating.

EXPECTATION

3D-printed titanium alloy implants have attracted much attention in orthopedics due to excellent biocompatibility, elastic modulus similar to natural bone, and 3D shape to fit complex bone defects. Implant surface modification technique is an important force that promotes the first generation of implants (biologically inert with good mechanical properties) towards implants with excellent osteoconductivity, osteoinduction, bone healing, and remarkable anti-inflammatory infection capability. This article reviewed various surface modification techniques in the 3D-printed titanium alloy and its improvement in the function of implants. However, further research is essential before these techniques can be clinically applied. Therefore, we provide some future views on the development of 3D-printed titanium alloy surface modifications, which can be used as the basis for further improvement.

Implant Surface Modification to Regulate Pathological Conditions

Most current implant surface modification techniques are aimed at the functionalization of implants under normal physiological conditions. However, many patients who need joint replacement are elderly. Senior patients who suffer from underlying diseases (hypertension, diabetes, coronary heart disease, osteoporosis, tumors) probability is relatively high. Although there are some studies on diabetes and 3D-printed titanium alloy implants with respect to osteoporosis, these studies are only preliminary investigations. In future, the mechanism of bone integration under pathological conditions needs to be extensively studied according to various diseases. In addition, further research on 3D-printed implant coating related to cancers and rheumatic immune diseases needs to be designed. Moreover, it also remains to be seen whether the implant coating for the above pathological conditions, which has been applied on the surface of ordinary implants, can play a role in 3D-printed implants. The combination of degradable 3D implants (PCL, PLGA) with hydrogels can provide an answer to these problems. Dual degradable materials can increase the amount and type of drug loading and determine the time sequence of drug release. The order of drug release can be determined according to the substances required by the new bone tissue.

Preparing Bioactive Material Coatings With Strong Adhesion

The application of bioactive substances as coating materials has recently become a research hotspot. However, because proteins cannot withstand extreme environments such as high temperature and high pressure, researchers often use dip coating to prepare coatings. This leads to weak adhesion between the coating and the implant. Although improved vapor deposition methods such as PCVD and ICVD can greatly reduce the temperature required for deposition, the preparation of biological coatings has not been attempted. Of course, these coating preparation methods have great potential in the preparation of strong-binding biomaterial coatings. In addition, changing the surface roughness of the implant is another way to enhance adhesion between coatings and implants materials. Studies have reported that the micro-nano surface prepared by MAO or anodic oxidation can enhance the adhesion between implant surface and coating, but optimum electrolytic parameters need to be explored further.

CONCLUSION

In this review, various types of 3D implant surface modification techniques including their principles, processes, advantages, disadvantages, and applications are discussed. In addition, this article summarizes the various types of functional modifications, as well as improvements in osteogenesis, antibacterial, wear resistance, corrosion resistance, and oxidation resistance caused by different coating materials and modification methods. Based on these findings, future research should determine the best parameters suited for surface modification techniques and the most suitable coating materials, as these are significant factors for optimizing orthopedic implants.

AUTHOR CONTRIBUTIONS

XS: Writing-original draft, Funding acquisition. AW: Supervision. ZW: Supervision. HL: Conceptualization. JW: Investigation. CL: Investigation, Methodology.

FUNDING

This study was supported by the Science and Technology Development Program of Jilin Province (20210101319JC).

REFERENCES

Alkekhia, D., Hammond, P. T., and Shukla, A. (2020). Layer-by-Layer Biomaterials for Drug Delivery. *Annu. Rev. Biomed. Eng.* 22, 1–24. doi:10.1146/annurev-bioeng-060418-052350

Amanov, A., Cho, I. S., Pyoun, Y. S., Lee, C. S., and Park, I. G. (2012). Micro-dimpled Surface by Ultrasonic Nanocrystal Surface Modification and its Tribological Effects. *Wear* 286-287, 136–144. doi:10.1016/j.wear.2011.06.001

Amin Yavari, S., Croes, M., Akhavan, B., Jahanmard, F., Eigenhuis, C. C., Dadbakhsh, S., et al. (2020). Layer by Layer Coating for Bio-Functionalization of Additively Manufactured Meta-Biomaterials. *Additive Manufacturing* 32. doi:10.1016/j.addma.2019.100991

Amin Yavari, S., Loozen, L., Paganelli, F. L., Bakhshandeh, S., Lietaert, K., Groot, J. A., et al. (2016). Antibacterial Behavior of Additively Manufactured Porous Titanium with Nanotubular Surfaces Releasing Silver Ions. *ACS Appl. Mater. Inter.* 8 (27), 17080–17089. doi:10.1021/acsami.6b03152

Antolak-Dudka, A., Płatek, P., Durejko, T., Baranowski, P., Małachowski, J., Sarzyński, M. T., et al. (2019). Static and Dynamic Loading Behavior of Ti6Al4V Honeycomb Structures Manufactured by Laser Engineered Net Shaping (LENSTM) Technology. *Materials (Basel)* 12 (8). doi:10.3390/ma12081225

Apostu, D., Lucaciu, O., Berce, C., Lucaciu, D., and Cosma, D. (2018). Current Methods of Preventing Aseptic Loosening and Improving Osseointegration of Titanium Implants in Cementless Total Hip Arthroplasty: a Review. *J. Int. Med. Res.* 46 (6), 2104–2119. doi:10.1177/0300060517732697

Asri, R. I. M., Harun, W. S. W., Samykano, M., Lah, N. A. C., Ghani, S. A. C., Tarlochan, F., et al. (2017). Corrosion and Surface Modification on Biocompatible Metals: A Review. *Mater. Sci. Eng. C* 77, 1261–1274. doi:10.1016/j.msec.2017.04.102

Bakhshandeh, S., and Amin Yavari, S. (2018). Electrophoretic Deposition: a Versatile Tool against Biomaterial Associated Infections. *J. Mater. Chem. B* 6 (8), 1128–1148. doi:10.1039/c7tb02445b

Bakhshandeh, S., Gorgin Karaji, Z., Lietaert, K., Fluit, A. C., Boel, C. H. E., Vogely, H. C., et al. (2017). Simultaneous Delivery of Multiple Antibacterial Agents from Additively Manufactured Porous Biomaterials to Fully Eradicate Planktonic and Adherent *Staphylococcus aureus*. *ACS Appl. Mater. Inter.* 9 (31), 25691–25699. doi:10.1021/acsami.7b04950

Bauer, T. W., and Schils, J. (1999). The Pathology of Total Joint Arthroplasty. *Skeletal Radiol.* 28 (9), 483–497. doi:10.1007/s002560050552

Berbel, L. O., Banczek, E. D. P., Karousis, I. K., Kotsakis, G. A., and Costa, I. (2019). Determinants of Corrosion Resistance of Ti-6Al-4V alloy Dental Implants in an *In Vitro* Model of Peri-Implant Inflammation. *PLoS One* 14 (1), e0210530. doi:10.1371/journal.pone.0210530

Bishal, A. K., Butt, A., Selvaraj, S. K., Joshi, B., Patel, S. B., Huang, S., et al. (2015). Atomic Layer Deposition in Bio-Nanotechnology: A Brief Overview. *Crit. Rev. Biomed. Eng.* 43 (4), 255–276. doi:10.1615/critrevbiomedeng.2016016456

Boccaccini, A. R., Keim, S., Ma, R., Li, Y., and Zhitomirsky, I. (2010). Electrophoretic Deposition of Biomaterials. *J. R. Soc. Interf.* 7 Suppl 5 (Suppl. 5), S581–S613. doi:10.1098/rsif.2010.0156.focus

Bozkurt, Y., and Karayel, E. (2021). 3D Printing Technology; Methods, Biomedical Applications, Future Opportunities and Trends. *J. Mater. Res. Tech.* 14, 1430–1450. doi:10.1016/j.jmrt.2021.07.050

Caliskan, N., Bayram, C., Erdal, E., Karahaliloglu, Z., and Denkbas, E. B. (2014). Titania Nanotubes with Adjustable Dimensions for Drug Reservoir Sites and Enhanced Cell Adhesion. *Mater. Sci. Eng. C Mater. Biol. Appl.* 35, 100–105.

Cerruti, M., Perardi, A., Cerrato, G., and Morterra, C. (2005). Formation of a Nanostructured Layer on Bioglass Particles of Different Sizes Immersed in Tris-Buffered Solution. N2 Adsorption and HR-TEM/EDS Analysis. *Langmuir* 21 (20), 9327–9333. doi:10.1021/la051221r

Chen, D., Zhao, M., and Mundy, G. R. (2004). Bone Morphogenetic Proteins. *Growth Factors* 22 (4), 233–241. doi:10.1080/08977190412331279890

Chen, F., Zhou, H., Chen, Q., Ge, Y. J., and Lv, F. X. (2007). Tribological Behaviour of the Ceramic Coating Formed on Magnesium alloy. *Plasma Sci. Tech.* 9 (5), 587–590.

Chen, Z., Yan, X., Chang, Y., Xie, S., Ma, W., Zhao, G., et al. (2019). Effect of Polarization Voltage on the Surface Componentization and Biocompatibility of Micro-arc Oxidation Modified Selective Laser Melted Ti6Al4V. *Mater. Res. Express* 6 (8). doi:10.1088/2053-1591/ab1abc

Cheng, X., Long, D., Chen, L., Jansen, J. A., Leeuwenburgh, S. C. G., and Yang, F. (2021). Electrophoretic Deposition of Silk Fibroin Coatings with Pre-defined Architecture to Facilitate Precise Control over Drug Delivery. *Bioactive Mater.* 6 (11), 4243–4254. doi:10.1016/j.bioactmat.2021.03.046

Chernousova, S., and Epple, M. (2013). Silver as Antibacterial Agent: Ion, Nanoparticle, and Metal. *Angew. Chem. Int. Ed.* 52 (6), 1636–1653. doi:10.1002/anie.201205923

Choy, K. (2003). Chemical Vapour Deposition of Coatings. *Prog. Mater. Sci.* 48 (2), 57–170. doi:10.1016/s0079-6425(01)00009-3

Chudinova, E. A., Surmeneva, M. A., Timin, A. S., Karpov, T. E., Wittmar, A., Ulbricht, M., et al. (2019). Adhesion, Proliferation, and Osteogenic Differentiation of Human Mesenchymal Stem Cells on Additively Manufactured Ti6Al4V alloy Scaffolds Modified with Calcium Phosphate Nanoparticles. *Colloids Surf. B: Biointerfaces* 176, 130–139. doi:10.1016/j.colsurfb.2018.12.047

Chung, C.-J., Lin, H.-I., Tsou, H.-K., Shi, Z.-Y., and He, J.-L. (2008). An Antimicrobial TiO2 Coating for Reducing Hospital-Acquired Infection. *J. Biomed. Mater. Res.* 85B (1), 220–224. doi:10.1002/jbm.b.30939

Chung, C. J., Lin, H. I., and He, J. L. (2011). Microstructural Effect on the Antimicrobial Efficacy of Arc Ion Plated TiO2. *J. Mater. Res.* 22 (11), 3137–3143. doi:10.1557/jmr.2007.0388

Chyzy, A., and Plonska-Brzezinska, M. E. (2020). Hydrogel Properties and Their Impact on Regenerative Medicine and Tissue Engineering. *Molecules* 25 (24). doi:10.3390/molecules25245795

Croes, M., Akhavan, B., Sharifahmadian, O., Fan, H., Mertens, R., Tan, R. P., et al. (2020). A Multifaceted Biomimetic Interface to Improve the Longevity of Orthopedic Implants. *Acta Biomater.* 110, 266–279. doi:10.1016/j.actbio.2020.04.020

Croes, M., Bakhshandeh, S., van Hengel, I. A. J., Lietaert, K., van Kessel, K. P. M., Pouran, B., et al. (2018). Antibacterial and Immunogenic Behavior of Silver Coatings on Additively Manufactured Porous Titanium. *Acta Biomater.* 81, 315–327. doi:10.1016/j.actbio.2018.09.051

Das, M., Bhattacharya, K., Dittrick, S. A., Mandal, C., Balla, V. K., Sampath Kumar, T. S., et al. (2014). *In Situ* synthesized TiB-TiN Reinforced Ti6Al4V alloy Composite Coatings: Microstructure, Tribological and *In-Vitro* Biocompatibility. *J. Mech. Behav. Biomed. Mater.* 29, 259–271. doi:10.1016/j.jmbbm.2013.09.006

Davoodi, E., Zhianmanesh, M., Montazerian, H., Milani, A. S., and Hoorfar, M. (2020). Nano-porous Anodic Alumina: Fundamentals and Applications in Tissue Engineering. *J. Mater. Sci. Mater. Med.* 31 (7), 60. doi:10.1007/s10856-020-06398-2

Diamanti, M. V., Del Curto, B., and Pedeferri, M. (2011). Anodic Oxidation of Titanium: from Technical Aspects to Biomedical Applications. *Jabb* 9 (1), 55–69. doi:10.5301/jabb.2011.7429

Ding, Y., Yuan, Z., Liu, P., Cai, K., and Liu, R. (2020). Fabrication of Strontium-Incorporated Protein Supramolecular Nanofilm on Titanium Substrates for Promoting Osteogenesis. *Mater. Sci. Eng. C* 111, 110851. doi:10.1016/j.msec.2020.110851

Domínguez-Trujillo, C., Peón, E., Chicardi, E., Pérez, H., Rodríguez-Ortiz, J. A., Pavón, J. J., et al. (2018). Sol-gel Deposition of Hydroxyapatite Coatings on Porous Titanium for Biomedical Applications. *Surf. Coat. Tech.* 333, 158–162.

Dong, J., Pacella, M., Liu, Y., and Zhao, L. (2022). Surface Engineering and the Application of Laser-Based Processes to Stents - A Review of the Latest Development. *Bioact Mater.* 10, 159–184. doi:10.1016/j.bioactmat.2021.08.023

Du, Z., Yu, X., Nie, B., Zhu, Z., Ibrahim, M., Yang, K., et al. (2019). Effects of Magnesium Coating on Bone-implant Interfaces with and without Polyether-ether-ketone Particle Interference: A Rabbit Model Based on Porous Ti6Al4V Implants. *J. Biomed. Mater. Res. B* 107 (7), 2388–2396. doi:10.1002/jbm.b.34332

Dulski, M., Balcerzak, J., Simka, W., and Dudek, K. (2020). Innovative Bioactive Ag-SiO2/TiO2 Coating on a NiTi-Shape Memory Alloy: Structure and Mechanism of its Formation. *Materials (Basel)* 14 (1). doi:10.3390/ma14010099

Eliaz, N., and Metoki, N. (2017a). Calcium Phosphate Bioceramics: A Review of Their History, Structure, Properties, Coating Technologies and Biomedical Applications. *Materials (Basel)* 10 (4). doi:10.3390/ma10040334

Eliaz, N., and Metoki, N. (2017b). Calcium Phosphate Bioceramics: A Review of Their History, Structure, Properties, Coating Technologies and Biomedical Applications. *Materials (Basel)* 10 (4). doi:10.3390/ma10040334

Elmengaard, B., Bechtold, J. E., and Søballe, K. (2005). *In Vivo* study of the Effect of RGD Treatment on Bone Ongrowth on Press-Fit Titanium alloy Implants. *Biomaterials* 26 (17), 3521–3526. doi:10.1016/j.biomaterials.2004.09.039

Escobar, A., Muzzio, N., and Moya, S. E. (2020). Antibacterial Layer-By-Layer Coatings for Medical Implants. *Pharmaceutics* 13 (1). doi:10.3390/pharmaceutics13010016

Fan, X., Feng, B., Di, Y., Lu, X., Duan, K., Wang, J., et al. (2012). Preparation of Bioactive TiO Film on Porous Titanium by Micro-arc Oxidation. *Appl. Surf. Sci.* 258 (19), 7584–7588. doi:10.1016/j.apsusc.2012.04.093

Farrell, N. P., Gorle, A. K., Peterson, E. J., and Berners-Price, S. J. (2018). Metalloglycomics. *Met. Ions Life Sci.* 18.

Fathi-Hafshejani, P., Johnson, H., Ahmadi, Z., Roach, M., Shamsaei, N., and Mahjouri-Samani, M. (2020). Phase-Selective and Localized TiO2 Coating on Additive and Wrought Titanium by a Direct Laser Surface Modification Approach. *ACS Omega* 5 (27), 16744–16751. doi:10.1021/acsomega.0c01671

Ghosal, K., Manakhov, A., Zajíčková, L., and Thomas, S. (2017). Structural and Surface Compatibility Study of Modified Electrospun Poly(ε-Caprolactone) (PCL) Composites for Skin Tissue Engineering. *AAPS PharmSciTech* 18 (1), 72–81. doi:10.1208/s12249-016-0500-8

Gibbs, D. M. R., Black, C. R. M., Dawson, J. I., and Oreffo, R. O. C. (2016). A Review of Hydrogel Use in Fracture Healing and Bone Regeneration. *J. Tissue Eng. Regen. Med.* 10 (3), 187–198. doi:10.1002/term.1968

González-Henríquez, C. M., Sarabia-Vallejos, M. A., and Rodríguez Hernandez, J. (2019). Antimicrobial Polymers for Additive Manufacturing. *Int. J. Mol. Sci.* 20 (5). doi:10.3390/ijms20051210

Grau, M., Matena, J., Teske, M., Petersen, S., Aliuos, P., Roland, L., et al. (2017). *In Vitro* Evaluation of PCL and P(3HB) as Coating Materials for Selective Laser Melted Porous Titanium Implants. *Materials (Basel)* 10 (12). doi:10.3390/ma10121344

Guo, Y., Ren, L., Xie, K., Wang, L., Yu, B., Jiang, W., et al. (2020). Functionalized TiCu/Ti-Cu-N-Coated 3D-Printed Porous Ti6Al4V Scaffold Promotes Bone Regeneration through BMSC Recruitment. *Adv. Mater. Inter.* 7 (6). doi:10.1002/admi.201901632

Halloran, D., Durbano, H. W., and Nohe, A. (2020). Bone Morphogenetic Protein-2 in Development and Bone Homeostasis. *J. Dev. Biol.* 8 (3). doi:10.3390/jdb8030019

Han, L., Sun, H., Tang, P., Li, P., Xie, C., Wang, M., et al. (2018). Mussel-inspired Graphene Oxide Nanosheet-Enwrapped Ti Scaffolds with Drug-Encapsulated Gelatin Microspheres for Bone Regeneration. *Biomater. Sci.* 6 (3), 538–549. doi:10.1039/c7bm01060e

Hashemi, A., Ezati, M., Mohammadnejad, J., Houshmand, B., and Faghihi, S. (2020). Chitosan Coating of TiO2 Nanotube Arrays for Improved Metformin Release and Osteoblast Differentiation. *Ijn* 15, 4471–4481. doi:10.2147/ijn.s248927

Hashemi Astaneh, S., Faverani, L. P., Sukotjo, C., and Takoudis, C. G. (2021). Atomic Layer Deposition on Dental Materials: Processing Conditions and Surface Functionalization to Improve Physical, Chemical, and Clinical Properties - A Review. *Acta Biomater.* 121, 103–118. doi:10.1016/j.actbio.2020.11.024

Hersel, U., Dahmen, C., and Kessler, H. (2003). RGD Modified Polymers: Biomaterials for Stimulated Cell Adhesion and beyond. *Biomaterials* 24 (24), 4385–4415. doi:10.1016/s0142-9612(03)00343-0

Herzog, T., and Tille, C. (2021). Review and New Aspects in Combining Multipoint Moulding and Additive Manufacturing. *Appl. Sciences-Basel* 11 (3). doi:10.3390/app11031201

Höhn, S., Braem, A., Neirinck, B., and Virtanen, S. (2017). Albumin Coatings by Alternating Current Electrophoretic Deposition for Improving Corrosion Resistance and Bioactivity of Titanium Implants. *Mater. Sci. Eng. C* 73, 798–807. doi:10.1016/j.msec.2016.12.129

Hong, Z. (2011). "Formation of Porous (Ca, P)-doped TiO2/Dense Ti Double Coatings on NiTi Alloy," in 7th International Forum on Advanced Material Science and Technology, Dalian, PEOPLES R CHINA.

Hu, J., Li, H., Wang, X., Yang, L., Chen, M., Wang, R., et al. (2020). Effect of Ultrasonic Micro-arc Oxidation on the Antibacterial Properties and Cell Biocompatibility of Ti-Cu alloy for Biomedical Application. *Mater. Sci. Eng. C* 115, 110921. doi:10.1016/j.msec.2020.110921

Hu, X.-F., Feng, Y.-F., Xiang, G., Lei, W., and Wang, L. (2018). Lactic Acid of PLGA Coating Promotes Angiogenesis on the Interface between Porous Titanium and Diabetic Bone. *J. Mater. Chem. B* 6 (15), 2274–2288. doi:10.1039/c7tb03247a

Huang, S. S., Liang, N. Y., Hu, Y., Zhou, X., and Abidi, N. (20162016). Polydopamine-Assisted Surface Modification for Bone Biosubstitutes. *Biomed. Res. Int.*

Huynh, V., Ngo, N. K., and Golden, T. D. (20192019). Surface Activation and Pretreatments for Biocompatible Metals and Alloys Used in Biomedical Applications. *Int. J. Biomater.* 2019, 3806504. doi:10.1155/2019/3806504

Jahanmard, F., Croes, M., Castilho, M., Majed, A., Steenbergen, M. J., Lietaert, K., et al. (2020). Bactericidal Coating to Prevent Early and Delayed Implant-Related Infections. *J. Controlled Release* 326, 38–52. doi:10.1016/j.jconrel.2020.06.014

Janaina, Soares., and Santos, P. D. S. A. (2021). "Yasmin Bastos Pissolitto 1, Paula Prenholatto Lopes 1, Anna Paulla Simon 2 3, Mariana de Souza Sikora 2 3, Francisco Trivinho-Strixino 1," in *The Use of Anodic Oxides in Practical and Sustainable Devices for Energy Conversion and Storage*. Materials. doi:10.3390/ma14020383

Jia, Z., Xiu, P., Li, M., Xu, X., Shi, Y., Cheng, Y., et al. (2016). Bioinspired Anchoring AgNPs onto Micro-nanoporous TiO2 Orthopedic Coatings: Trap-Killing of Bacteria, Surface-Regulated Osteoblast Functions and Host Responses. *Biomaterials* 75, 203–222. doi:10.1016/j.biomaterials.2015.10.035

Jia, Z., Zhou, W., Yan, J., Xiong, P., Guo, H., Cheng, Y., et al. (2019). Constructing Multilayer Silk Protein/Nanosilver Biofunctionalized Hierarchically Structured 3D Printed Ti6Al4 V Scaffold for Repair of Infective Bone Defects. *ACS Biomater. Sci. Eng.* 5 (1), 244–261. doi:10.1021/acsbiomaterials.8b00857

Julmi, S., Krüger, A.-K., Waselau, A.-C., Meyer-Lindenberg, A., Wriggers, P., Klose, C., et al. (2019). Processing and Coating of Open-Pored Absorbable Magnesium-Based Bone Implants. *Mater. Sci. Eng. C* 98, 1073–1086. doi:10.1016/j.msec.2018.12.125

Jurczak, P., Witkowska, J., Rodziewicz-Motowidło, S., and Lach, S. (2020). Proteins, Peptides and Peptidomimetics as Active Agents in Implant Surface Functionalization. *Adv. Colloid Interf. Sci.* 276, 102083. doi:10.1016/j.cis.2019.102083

Karimbaev, R., Choi, S., Pyun, Y. S., and Amanov, A. (2020). Mechanical and Tribological Characteristics of Cladded AISI 1045 Carbon Steel. *Materials (Basel)* 13 (4). doi:10.3390/ma13040859

Kaushik, N., Nhat Nguyen, L., Kim, J. H., Choi, E. H., and Kumar Kaushik, N. (2020). Strategies for Using Polydopamine to Induce Biomineralization of Hydroxyapatite on Implant Materials for Bone Tissue Engineering. *Int. J. Mol. Sci.* 21 (18). doi:10.3390/ijms21186544

Kedziora, A., Speruda, M., Krzyzewska, E., Rybka, J., Lukowiak, A., and Bugla-Ploskonska, G. (2018). Similarities and Differences between Silver Ions and Silver in Nanoforms as Antibacterial Agents. *Int. J. Mol. Sci.* 19 (2).

Kelly, C. N., Evans, N. T., Irvin, C. W., Chapman, S. C., Gall, K., and Safranski, D. L. (2019). The Effect of Surface Topography and Porosity on the Tensile Fatigue of 3D Printed Ti-6Al-4V Fabricated by Selective Laser Melting. *Mater. Sci. Eng. C* 98, 726–736. doi:10.1016/j.msec.2019.01.024

Kermavnar, T., Shannon, A., O'Sullivan, K. J., McCarthy, C., Dunne, C. P., and O'Sullivan, L. W. (2021). Three-Dimensional Printing of Medical Devices Used Directly to Treat Patients: A Systematic Review. *3d Printing and Additive Manufacturing* 8 (6), 366–408. doi:10.1089/3dp.2020.0324

Khlyustova, A., Cheng, Y., and Yang, R. (2020). Vapor-deposited Functional Polymer Thin Films in Biological Applications. *J. Mater. Chem. B* 8 (31), 6588–6609. doi:10.1039/d0tb00681e

Khorasani, A. M., Gibson, I., Goldberg, M., Nomani, J., and Littlefair, G. (2016). Machinability of Metallic and Ceramic Biomaterials: A Review. *Sci. Adv. Mater.* 8 (8), 1491–1511. doi:10.1166/sam.2016.2783

Kim, H.-M., Miyaji, F., Kokubo, T., and Nakamura, T. (1996). Preparation of Bioactive Ti and its Alloys via Simple Chemical Surface Treatment. *J. Biomed. Mater. Res.* 32 (3), 409–417. doi:10.1002/(sici)1097-4636(199611)32:3<409:aid-jbm14>3.0.co;2-b

Kim, K.-H., and Ramaswamy, N. (2009). Electrochemical Surface Modification of Titanium in Dentistry. *Dent. Mater. J.* 28 (1), 20–36. doi:10.4012/dmj.28.20

Kim, S.-Y., Kim, Y.-K., Kim, K.-S., Lee, K.-B., and Lee, M.-H. (2019a). Enhancement of Bone Formation on LBL-Coated Mg alloy Depending on

the Different Concentration of BMP-2. *Colloids Surf. B: Biointerfaces* 173, 437–446. doi:10.1016/j.colsurfb.2018.09.061

Kim, Y. S., Majid, M., Melchiorri, A. J., and Mikos, A. G. (2019b). Applications of Decellularized Extracellular Matrix in Bone and Cartilage Tissue Engineering. *Bioeng. Translational Med.* 4 (1), 83–95. doi:10.1002/btm2.10110

Kiran, A. S. K., Kumar, T. S. S., Sanghavi, R., Doble, M., and Ramakrishna, S. (2018). Antibacterial and Bioactive Surface Modifications of Titanium Implants by PCL/TiO_2 Nanocomposite Coatings. *Nanomaterials (Basel)* 8 (10). doi:10.3390/nano8100860

Kokubo, T., and Yamaguchi, S. (2010). Bioactive Ti Metal and its Alloys Prepared by Chemical Treatments: State-Of-The-Art and Future Trends. *Adv. Eng. Mater.* 12 (11), B579–B591. doi:10.1002/adem.201080087

Kokubo, T., and Yamaguchi, S. (2015). Growth of Novel Ceramic Layers on Metals via Chemical and Heat Treatments for Inducing Various Biological Functions. *Front. Bioeng. Biotechnol.* 3, 176. doi:10.3389/fbioe.2015.00176

Komarova, E. G., Sharkeev, Y. P., Sedelnikova, M. B., Prosolov, K. A., Khlusov, I. A., Prymak, O., et al. (2020). Zn- or Cu-Containing CaP-Based Coatings Formed by Micro-arc Oxidation on Titanium and Ti-40Nb Alloy: Part I-Microstructure, Composition and Properties. *Materials (Basel)* 13 (18). doi:10.3390/ma13184116

Kong, C. H., Steffi, C., Shi, Z., and Wang, W. (2018a). Development of Mesoporous Bioactive Glass Nanoparticles and its Use in Bone Tissue Engineering. *J. Biomed. Mater. Res.* 106 (8), 2878–2887. doi:10.1002/jbm.b.34143

Kong, D. J., Liu, H., and Wang, J. C. (2015). Effects of Micro Arc Oxidation on Fatigue Limits and Fracture Morphologies of 7475 High Strength Aluminum alloy. *J. Alloys Comp.* 650, 393–398.

Kong, J., Wei, B., Groth, T., Chen, Z., Li, L., He, D., et al. (2018b). Biomineralization Improves Mechanical and Osteogenic Properties of Multilayer-modified PLGA Porous Scaffolds. *J. Biomed. Mater. Res.* 106 (10), 2714–2725. doi:10.1002/jbm.a.36487

Krzakala, A., Kazek-Kesik, A., and Simka, W. (2013). Application of Plasma Electrolytic Oxidation to Bioactive Surface Formation on Titanium and its Alloys. *Rsc Adv.* 3 (43), 19725–19743.

Kumar, A., Nune, K. C., and Misra, R. D. K. (2016). Biological Functionality and Mechanistic Contribution of Extracellular Matrix-Ornamented Three Dimensional Ti-6Al-4V Mesh Scaffolds. *J. Biomed. Mater. Res.* 104 (11), 2751–2763. doi:10.1002/jbm.a.35809

Kumar, A., Nune, K. C., and Misra, R. D. K. (2018). Design and Biological Functionality of a Novel Hybrid Ti-6 A L-4 V/hydrogel System for Reconstruction of Bone Defects. *J. Tissue Eng. Regen. Med.* 12 (4), 1133–1144. doi:10.1002/term.2614

Kurella, A., and Dahotre, N. B. (2005). Review Paper: Surface Modification for Bioimplants: the Role of Laser Surface Engineering. *J. Biomater. Appl.* 20 (1), 5–50. doi:10.1177/0885328205052974

Kwon, B.-J., Seon, G. M., Seon, G., Lee, M., Koo, M.-A., Kim, M., et al. (2018). Locally Delivered Ethyl-2,5-Dihydroxybenzoate Using 3D Printed Bone Implant for Promotion of Bone Regeneration in a Osteoporotic Animal Model. *eCM* 35, 1–12. doi:10.22203/ecm.v035a01

Lalzawmliana, V., Anand, A., Roy, M., Kundu, B., and Nandi, S. K. (2020). Mesoporous Bioactive Glasses for Bone Healing and Biomolecules Delivery. *Mater. Sci. Eng. C* 106, 110180. doi:10.1016/j.msec.2019.110180

Li, B., Xia, X., Guo, M., Jiang, Y., Li, Y., Zhang, Z., et al. (2019). Biological and Antibacterial Properties of the Micro-nanostructured Hydroxyapatite/chitosan Coating on Titanium. *Sci. Rep.* 9 (1), 14052. doi:10.1038/s41598-019-49941-0

Li, J.-L., Wang, S., Cao, F., Lin, X., Wei, X.-W., Zhao, Z.-H., et al. (2019). Fabrication and Characterization of Nanopillar-like HA Coating on Porous Ti6Al4V Scaffold by a Combination of Alkali-Acid-Heat and Hydrothermal Treatments. *Acta Metall. Sin. (Engl. Lett.* 32 (9), 1075–1088. doi:10.1007/s40195-019-00920-4

Li, J., Mutreja, I., Hooper, G. J., Clinch, K., Lim, K., Evans, G., et al. (2020). Combined Infection Control and Enhanced Osteogenic Differentiation Capacity on Additive Manufactured Ti-6Al-4V Are Mediated via Titania Nanotube Delivery of Novel Biofilm Inhibitors. *Adv. Mater. Inter.* 7 (7). doi:10.1002/admi.201901963

Li, L.-H., Kong, Y.-M., Kim, H.-W., Kim, Y.-W., Kim, H.-E., Heo, S.-J., et al. (2004). Improved Biological Performance of Ti Implants Due to Surface Modification by Micro-arc Oxidation. *Biomaterials* 25 (14), 2867–2875. doi:10.1016/j.biomaterials.2003.09.048

Li, M., Jin, Z.-X., Zhang, W., Bai, Y.-H., Cao, Y.-Q., Li, W.-M., et al. (2019). Comparison of Chemical Stability and Corrosion Resistance of Group IV Metal Oxide Films Formed by thermal and Plasma-Enhanced Atomic Layer Deposition. *Sci. Rep.* 9 (1), 10438. doi:10.1038/s41598-019-47049-z

Li, M., Liu, Q., Jia, Z., Xu, X., Shi, Y., Cheng, Y., et al. (2015). Polydopamine-induced Nanocomposite Ag/CaP Coatings on the Surface of Titania Nanotubes for Antibacterial and Osteointegration Functions. *J. Mater. Chem. B* 3 (45), 8796–8805. doi:10.1039/c5tb01597a

Li, M., Liu, X., Xu, Z., Yeung, K. W. K., and Wu, S. (2016). Dopamine Modified Organic-Inorganic Hybrid Coating for Antimicrobial and Osteogenesis. *ACS Appl. Mater. Inter.* 8 (49), 33972–33981. doi:10.1021/acsami.6b09457

Li, N., Xiong, Y., Xiong, H., Shi, G., Blackburn, J., Liu, W., et al. (2019). Microstructure, Formation Mechanism and Property Characterization of Ti + SiC Laser Cladded Coatings on Ti6Al4V alloy. *Mater. Characterization* 148, 43–51. doi:10.1016/j.matchar.2018.11.032

Li, P., Li, Y., Chen, H., Liu, H., and Cheng, X. (2019). Optimization of Process Parameters for a Chemi-Absorbed Graphene Coating and its Nano Tribological Investigation. *Nanomaterials (Basel)* 10 (1). doi:10.3390/nano10010055

Li, X., Wang, M., Zhang, W., Bai, Y., Liu, Y., Meng, J., et al. (2020). A Magnesium-Incorporated Nanoporous Titanium Coating for Rapid Osseointegration. *Ijn* 15, 6593–6603. doi:10.2147/ijn.s255486

Li, Y., Li, L., Ma, Y., Zhang, K., Li, G., Lu, B., et al. (2020). 3D-Printed Titanium Cage with PVA-Vancomycin Coating Prevents Surgical Site Infections (SSIs). *Macromol Biosci.* 20 (3), e1900394. doi:10.1002/mabi.201900394

Li, Y., Song, Y., Ma, A., and Li, C. (20192019). Surface Immobilization of TiO2 Nanotubes with Bone Morphogenetic Protein-2 Synergistically Enhances Initial Preosteoblast Adhesion and Osseointegration. *Biomed. Res. Int.* 2019, 5697250. doi:10.1155/2019/5697250

Li, Y., Yang, W., Li, X., Zhang, X., Wang, C., Meng, X., et al. (2015). Improving Osteointegration and Osteogenesis of Three-Dimensional Porous Ti6Al4V Scaffolds by Polydopamine-Assisted Biomimetic Hydroxyapatite Coating. *ACS Appl. Mater. Inter.* 7 (10), 5715–5724. doi:10.1021/acsami.5b00331

Liaw, C.-Y., and Guvendiren, M. (2017). Current and Emerging Applications of 3D Printing in Medicine. *Biofabrication* 9 (2), 024102. doi:10.1088/1758-5090/aa7279

Lin, D.-J., Fuh, L.-J., Chen, C.-Y., Chen, W.-C., Lin, J.-H. C., and Chen, C.-C. (2019). Rapid Nano-Scale Surface Modification on Micro-arc Oxidation Coated Titanium by Microwave-Assisted Hydrothermal Process. *Mater. Sci. Eng. C* 95, 236–247. doi:10.1016/j.msec.2018.10.085

Lingpeng Kong, Y. H., Lu, Qingsen., Zhou, Dongsheng., Wang, Bomin., Wang, Dawei., Zhang, Wupeng., et al. (2020). Polydopamine Coating with Static Magnetic Field Promotes the Osteogenic Differentiation of Human Bone-Derived Mesenchymal Stem Cells on Three-Dimensional Printed Porous Titanium Scaffolds by Upregulation of the BMP-Smads Signaling Pathway. *Am. J. Transl Res.*

Listewnik, P., Hirsch, M., Struk, P., Weber, M., Bechelany, M., and Jędrzejewska-Szczerska, M. (2019). Preparation and Characterization of Microsphere ZnO ALD Coating Dedicated for the Fiber-Optic Refractive Index Sensor. *Nanomaterials (Basel)* 9 (2). doi:10.3390/nano9020306

Liu, H., Ran, F., Wang, X., He, N., and Guo, Y. (2017a). A Chromium(III) Oxide-Coated Steel Wire Prepared by Arc Ion Plating for Use in Solid-phase Microextraction of Aromatic Hydrocarbons. *Microchim Acta* 185 (1), 82. doi:10.1007/s00604-017-2535-2

Liu, L., Bhatia, R., and Webster, T. (2017b). Atomic Layer Deposition of Nano-TiO2 thin Films with Enhanced Biocompatibility and Antimicrobial Activity for Orthopedic Implants. *Ijn* 12, 8711–8723. doi:10.2147/ijn.s148065

Liu, R., Yuan, S., Lin, N., Zeng, Q., Wang, Z., and Wu, Y. (2021). Application of Ultrasonic Nanocrystal Surface Modification (UNSM) Technique for Surface Strengthening of Titanium and Titanium Alloys: a Mini Review. *J. Mater. Res. Tech.* 11, 351–377. doi:10.1016/j.jmrt.2021.01.013

Liu, X., Liu, J., Zuo, Z., and Zhang, H. (2019). Effects of Shot Peening on Fretting Fatigue Crack Initiation Behavior. *Materials (Basel)* 12 (5). doi:10.3390/ma12050743

Llopis-Grimalt, M. A., Arbós, A., Gil-Mir, M., Mosur, A., Kulkarni, P., Salito, A., et al. (2020). Multifunctional Properties of Quercitrin-Coated Porous Ti-6Al-4V Implants for Orthopaedic Applications Assessed *In Vitro*. *J. Clin. Med.* 9 (3). doi:10.3390/jcm9030855

Ma, C., Andani, M. T., Qin, H., Moghaddam, N. S., Ibrahim, H., Jahadakbar, A., et al. (2017). Improving Surface Finish and Wear Resistance of Additive Manufactured Nickel-Titanium by Ultrasonic Nano-crystal Surface Modification. *J. Mater. Process. Tech.* 249, 433–440. doi:10.1016/j.jmatprotec.2017.06.038

Ma, L., Cheng, C., He, C., Nie, C., Deng, J., Sun, S., et al. (2015). Substrate-Independent Robust and Heparin-Mimetic Hydrogel Thin Film Coating via Combined LbL Self-Assembly and Mussel-Inspired Post-Cross-linking. *ACS Appl. Mater. Inter.* 7 (47), 26050–26062. doi:10.1021/acsami.5b09634

Ma, L., Wang, X., Zhou, Y., Ji, X., Cheng, S., Bian, D., et al. (2021). Biomimetic Ti-6Al-4V alloy/gelatin Methacrylate Hybrid Scaffold with Enhanced Osteogenic and Angiogenic Capabilities for Large Bone Defect Restoration. *Bioactive Mater.* 6 (10), 3437–3448. doi:10.1016/j.bioactmat.2021.03.010

Maciag, F., Moskalewicz, T., Kowalski, K., Lukaszczyk, A., Hadzhieva, Z., and Boccaccini, A. R. (2021). The Effect of Electrophoretic Deposition Parameters on the Microstructure and Adhesion of Zein Coatings to Titanium Substrates. *Materials (Basel)* 14 (2).

Madhurakkat Perikamana, S. K., Lee, J., Lee, Y. B., Shin, Y. M., Lee, E. J., Mikos, A. G., et al. (2015). Materials from Mussel-Inspired Chemistry for Cell and Tissue Engineering Applications. *Biomacromolecules* 16 (9), 2541–2555. doi:10.1021/acs.biomac.5b00852

Maimaiti, B., Zhang, N., Yan, L., Luo, J., Xie, C., Wang, Y., et al. (2020). Stable ZnO-Doped Hydroxyapatite Nanocoating for Anti-infection and Osteogenic on Titanium. *Colloids Surf. B: Biointerfaces* 186, 110731. doi:10.1016/j.colsurfb.2019.110731

Makkar, P., Kang, H. J., Padalhin, A. R., Park, I., Moon, B.-G., and Lee, B. T. (2018). Development and Properties of Duplex MgF2/PCL Coatings on Biodegradable Magnesium alloy for Biomedical Applications. *PLoS One* 13 (4), e0193927. doi:10.1371/journal.pone.0193927

Mandal, P., Dubey, B. K., and Gupta, A. K. (2017). Review on Landfill Leachate Treatment by Electrochemical Oxidation: Drawbacks, Challenges and Future Scope. *Waste Manage.* 69, 250–273. doi:10.1016/j.wasman.2017.08.034

Markopoulos, A. P., Galanis, N. I., Karkalos, N. E., and Manolakos, D. E. (2018). Precision CNC Machining of Femoral Component of Knee Implant: A Case Study. *Machines* 6 (1). doi:10.3390/machines6010010

Martín-Del-Campo, M., Sampedro, J. G., Flores-Cedillo, M. L., Rosales-Ibañez, R., and Rojo, L. (2019). Bone Regeneration Induced by Strontium Folate Loaded Biohybrid Scaffolds. *Molecules* 24 (9). doi:10.3390/molecules24091660

Matsuzaki, H. (2006). Prevention of Osteoporosis by Foods and Dietary Supplements. Magnesium and Bone Metabolism. *Clin. Calcium* 16 (10), 1655–1660. CliCa061016551660.

Mieszkowska, A., Beaumont, H., Martocq, L., Koptyug, A., Surmeneva, M. A., Surmenev, R. A., et al. (2020). Phenolic-Enriched Collagen Fibrillar Coatings on Titanium Alloy to Promote Osteogenic Differentiation and Reduce Inflammation. *Int. J. Mol. Sci.* 21 (17). doi:10.3390/ijms21176406

Miller, R., Higuera, C. A., Wu, J., Klika, A., Babic, M., and Piuzzi, N. S. (2020). Periprosthetic Joint Infection: A Review of Antibiotic Treatment. *JBJS Rev.* 8 (7), e1900224. doi:10.2106/JBJS.RVW.19.00224

Minagar, S., Berndt, C. C., Wang, J., Ivanova, E., and Wen, C. (2012). A Review of the Application of Anodization for the Fabrication of Nanotubes on Metal Implant Surfaces. *Acta Biomater.* 8 (8), 2875–2888. doi:10.1016/j.actbio.2012.04.005

Minagar, S., Wang, J., Berndt, C. C., Ivanova, E. P., and Wen, C. (2013). Cell Response of Anodized Nanotubes on Titanium and Titanium Alloys. *J. Biomed. Mater. Res.* 101A (9), 2726–2739. doi:10.1002/jbm.a.34575

Minto, J., Zhou, X., Osborn, J., Zhang, L. G., Sarkar, K., and Rao, R. D. (2020). Three-Dimensional Printing: A Catalyst for a Changing Orthopaedic Landscape. *JBJS Rev.* 8 (2)–e0076. doi:10.2106/jbjs.rvw.19.00076

Moll, A., Blandin, J. J., Dendievel, R., Gicquel, E., Pons, M., Jimenez, C., et al. (2021). Coupling Powder Bed Additive Manufacturing and Vapor Phase Deposition Methods for Elaboration of Coated 3D Ti-6Al-4V Architectures with Enhanced Surface Properties. *Surf. Coat. Tech.* 415. doi:10.1016/j.surfcoat.2021.127130

Myakinin, A., Turlybekuly, A., Pogrebnjak, A., Mirek, A., Bechelany, M., Liubchak, I., et al. (2021). *In Vitro* evaluation of Electrochemically Bioactivated Ti6Al4V 3D Porous Scaffolds. *Mater. Sci. Eng. C* 121, 111870. doi:10.1016/j.msec.2021.111870

Myers, T. G., Lipof, J. S., Chen, A. F., and Ricciardi, B. F. (2020). Antibiotic Stewardship for Total Joint Arthroplasty in 2020. *J. Am. Acad. Orthop. Surg.* 28 (18), e793–e802. doi:10.5435/jaaos-d-19-00850

Naomi, R., Ridzuan, P. M., and Bahari, H. (2021). Current Insights into Collagen Type I. *Polymers (Basel)* 13 (16). doi:10.3390/polym13162642

Nagarajan, N., Dupret-Bories, A., Karabulut, E., Zorlutuna, P., and Vrana, N. E., (2018). Enabling Personalized Implant and Controllable Biosystem Development Through 3D Printing. *Biotechnol. Adv.* 36 (2), 521–533. doi:10.1016/j.biotechadv.2018.02.004

Narayanan, R., Seshadri, S. K., Kwon, T. Y., and Kim, K. H. (2008). Calcium Phosphate-Based Coatings on Titanium and its Alloys. *J. Biomed. Mater. Res.* 85B (1), 279–299. doi:10.1002/jbm.b.30932

Nguyen, V., Meyers, C. A., Yan, N., Agarwal, S., Levi, B., and James, A. W. (2017). BMP-2-induced Bone Formation and Neural Inflammation. *J. Orthopaedics* 14 (2), 252–256. doi:10.1016/j.jor.2017.03.003

Nie, L., Wu, Y., Gong, H., Chen, D., and Guo, X. (2020). Effect of Shot Peening on Redistribution of Residual Stress Field in Friction Stir Welding of 2219 Aluminum Alloy. *Materials (Basel)* 13 (14). doi:10.3390/ma13143169

Okada, K. (2016). Plasma-enhanced Chemical Vapor Deposition of Nanocrystalline diamond. *Sci. Tech. Adv. Mater.* 8 (7-8), 624–634. doi:10.1016/j.stam.2007.08.008

Pandey, P. C., Shukla, S., Pandey, G., and Narayan, R. J. (2021). Nanostructured diamond for Biomedical Applications. *Nanotechnology* 32 (13), 132001. doi:10.1088/1361-6528/abd2e7

Parfenova, L. V., Lukina, E. S., Galimshina, Z. R., Gil'fanova, G. U., Mukaeva, V. R., Farrakhov, R. G., et al. (2020). Biocompatible Organic Coatings Based on Bisphosphonic Acid RGD-Derivatives for PEO-Modified Titanium Implants. *Molecules* 25 (1). doi:10.3390/molecules25010229

Park, I. S., Lee, M. H., Bae, T. S., and Seol, K. W. (2008). Effects of Anodic Oxidation Parameters on a Modified Titanium Surface. *J. Biomed. Mater. Res.* 84B (2), 422–429. doi:10.1002/jbm.b.30887

Park, S., Han, U., Choi, D., and Hong, J. (2018). Layer-by-layer Assembled Polymeric Thin Films as Prospective Drug Delivery Carriers: Design and Applications. *Biomater. Res.* 22, 29. doi:10.1186/s40824-018-0139-5

Peng, Z., Ni, J., Zheng, K., Shen, Y., Wang, X., He, G., et al. (2013). Dual Effects and Mechanism of TiO2 Nanotube Arrays in Reducing Bacterial Colonization and Enhancing C3H10T1/2 Cell Adhesion. *Int. J. Nanomedicine* 8, 3093–3105. doi:10.2147/IJN.S48084

Pishbin, F., Mouriño, V., Flor, S., Kreppel, S., Salih, V., Ryan, M. P., et al. (2014). Electrophoretic Deposition of Gentamicin-Loaded Bioactive Glass/chitosan Composite Coatings for Orthopaedic Implants. *ACS Appl. Mater. Inter.* 6 (11), 8796–8806. doi:10.1021/am5014166

Qin, J., Yang, D., Maher, S., Lima-Marques, L., Zhou, Y., Chen, Y., et al. (2018). Micro- and Nano-Structured 3D Printed Titanium Implants with a Hydroxyapatite Coating for Improved Osseointegration. *J. Mater. Chem. B* 6 (19), 3136–3144. doi:10.1039/c7tb03251j

Rafieerad, A. R., Ashra, M. R., Mahmoodian, R., and Bushroa, A. R. (2015). Surface Characterization and Corrosion Behavior of Calcium Phosphate-Base Composite Layer on Titanium and its Alloys via Plasma Electrolytic Oxidation: A Review Paper. *Mater. Sci. Eng. C* 57, 397–413. doi:10.1016/j.msec.2015.07.058

Rahaman, M. N., Day, D. E., Sonny Bal, B., Fu, Q., Jung, S. B., Bonewald, L. F., et al. (2011). Bioactive Glass in Tissue Engineering. *Acta Biomater.* 7 (6), 2355–2373. doi:10.1016/j.actbio.2011.03.016

Ramesh, N., Moratti, S. C., and Dias, G. J. (2018). Hydroxyapatite-polymer Biocomposites for Bone Regeneration: A Review of Current Trends. *J. Biomed. Mater. Res.* 106 (5), 2046–2057. doi:10.1002/jbm.b.33950

Razzi, F., Fratila-Apachitei, L. E., Fahy, N., Bastiaansen-Jenniskens, Y. M., Apachitei, I., Farrell, E., et al. (2020). Immunomodulation of Surface Biofunctionalized 3D Printed Porous Titanium Implants. *Biomed. Mater.* 15 (3), 035017. doi:10.1088/1748-605x/ab7763

Remigiusz Zebrowski, M. W., Korga, Agnieszka., Iwan, 3Magdalena., and Mirosław, Szala. (2019). Effect of Shot Peening on the Mechanical Properties andCytotoxicity Behaviour of Titanium Implants Produced by 3DPrinted Technology. *J. Healthc. Eng.*

Ribeiro, A. R., Oliveira, F., Boldrini, L. C., Leite, P. E., Falagan-Lotsch, P., Linhares, A. B. R., et al. (2015). Micro-arc Oxidation as a Tool to Develop Multifunctional

Calcium-Rich Surfaces for Dental Implant Applications. *Mater. Sci. Eng. C* 54, 196–206. doi:10.1016/j.msec.2015.05.012

Ricciardi, B. F., Muthukrishnan, G., Masters, E. A., Kaplan, N., Daiss, J. L., and Schwarz, E. M. (2020). New Developments and Future Challenges in Prevention, Diagnosis, and Treatment of Prosthetic Joint Infection. *J. Orthop. Res.* 38 (7), 1423–1435. doi:10.1002/jor.24595

Rifai, A., Tran, N., Lau, D. W., Elbourne, A., Zhan, H., Stacey, A. D., et al. (2018). Polycrystalline Diamond Coating of Additively Manufactured Titanium for Biomedical Applications. *ACS Appl. Mater. Inter.* 10 (10), 8474–8484. doi:10.1021/acsami.7b18596

Rodrigues, D. C., Urban, R. M., Jacobs, J. J., and Gilbert, J. L. (2009). In Vivosevere Corrosion and Hydrogen Embrittlement of Retrieved Modular Body Titanium alloy Hip-Implants. *J. Biomed. Mater. Res.* 88B (1), 206–219. doi:10.1002/jbm.b.31171

Rodríguez-Contreras, A., Torres, D., Guillem-Marti, J., Sereno, P., Ginebra, M. P., Calero, J. A., et al. (2020). Development of Novel Dual-Action Coatings with Osteoinductive and Antibacterial Properties for 3D-Printed Titanium Implants. *Surf. Coat. Tech.* 403.

Roland, L., Backhaus, S., Grau, M., Matena, J., Teske, M., Beyerbach, M., et al. (2016). Evaluation of Functionalized Porous Titanium Implants for Enhancing Angiogenesis *In Vitro*. *Materials (Basel)* 9 (4). doi:10.3390/ma9040304

Roland, L., Grau, M., Matena, J., Teske, M., Gieseke, M., Kampmann, A., et al. (2015). Poly-ε-caprolactone Coated and Functionalized Porous Titanium and Magnesium Implants for Enhancing Angiogenesis in Critically Sized Bone Defects. *Int. J. Mol. Sci.* 17 (1). doi:10.3390/ijms17010001

Sahasrabudhe, H., and Bandyopadhyay, A. (2018). *In Situ* reactive Multi-Material Ti6Al4V-Calcium Phosphate-Nitride Coatings for Bio-Tribological Applications. *J. Mech. Behav. Biomed. Mater.* 85, 1–11. doi:10.1016/j.jmbbm.2018.05.020

Sarraf, M., Nasiri-Tabrizi, B., Yeong, C. H., Madaah Hosseini, H. R., Saber-Samandari, S., Basirun, W. J., et al. (2021). Mixed Oxide Nanotubes in Nanomedicine: A Dead-End or a Bridge to the Future. *Ceramics Int.* 47 (3), 2917–2948. doi:10.1016/j.ceramint.2020.09.177

Sartori, M., Giavaresi, G., Parrilli, A., Ferrari, A., Aldini, N. N., Morra, M., et al. (2015). Collagen Type I Coating Stimulates Bone Regeneration and Osteointegration of Titanium Implants in the Osteopenic Rat. *Int. Orthopaedics (Sicot)* 39 (10), 2041–2052. doi:10.1007/s00264-015-2926-0

Seuss, S., Lehmann, M., and Boccaccini, A. (2014). Alternating Current Electrophoretic Deposition of Antibacterial Bioactive Glass-Chitosan Composite Coatings. *Ijms* 15 (7), 12231–12242. doi:10.3390/ijms150712231

Shalom, H., Feldman, Y., Rosentsveig, R., Pinkas, I., Kaplan-Ashiri, I., Moshkovich, A., et al. (2018). Electrophoretic Deposition of Hydroxyapatite Film Containing Re-doped MoS_2 Nanoparticles. *Int. J. Mol. Sci.* 19 (3). doi:10.3390/ijms19030657

Shimabukuro, M. (2020). Antibacterial Property and Biocompatibility of Silver, Copper, and Zinc in Titanium Dioxide Layers Incorporated by One-step Micro-arc Oxidation: A Review. *Antibiotics (Basel)* 9 (10). doi:10.3390/antibiotics9100716

Shimizu, Y., Fujibayashi, S., Yamaguchi, S., Mori, S., Kitagaki, H., Shimizu, T., et al. (2020). Bioactive Effects of Strontium Loading on Micro/nano Surface Ti6Al4V Components Fabricated by Selective Laser Melting. *Mater. Sci. Eng. C* 109, 110519. doi:10.1016/j.msec.2019.110519

Shin, T., Park, S.-J., Kang, K. S., Kim, J. S., Kim, Y., Lim, Y., et al. (2017). A Laser-Aided Direct Metal Tooling Technology for Artificial Joint Surface Coating. *Int. J. Precis. Eng. Manuf.* 18 (2), 233–238. doi:10.1007/s12541-017-0030-7

Shivakoti, I., Kibria, G., Cep, R., Pradhan, B. B., and Sharma, A. (2021). Laser Surface Texturing for Biomedical Applications: A Review. *Coatings* 11 (2). doi:10.3390/coatings11020124

Shivaram, A., Bose, S., and Bandyopadhyay, A. (2017). Understanding Long-Term Silver Release from Surface Modified Porous Titanium Implants. *Acta Biomater.* 58, 550–560. doi:10.1016/j.actbio.2017.05.048

Shokrolahi, F., Khodabakhshi, K., Shokrollahi, P., Badiani, R., and Moghadam, Z. M. (2019). Atorvastatin Loaded PLGA Microspheres: Preparation, HAp Coating, Drug Release and Effect on Osteogenic Differentiation of ADMSCs. *Int. J. Pharmaceutics* 565, 95–107. doi:10.1016/j.ijpharm.2019.05.005

Shukla, P. P., Swanson, P. T., and Page, C. J. (2013). Laser Shock Peening and Mechanical Shot Peening Processes Applicable for the Surface Treatment of Technical Grade Ceramics: A Review. *Proc. Inst. Mech. Eng. B: J. Eng. Manufacture* 228 (5), 639–652. doi:10.1177/0954405413507250

Sikdar, S., Menezes, P. V., Maccione, R., Jacob, T., and Menezes, P. L. (2021). Plasma Electrolytic Oxidation (PEO) Process-Processing, Properties, and Applications. *Nanomaterials (Basel)* 11 (6). doi:10.3390/nano11061375

Sing, S. L., An, J., Yeong, W. Y., and Wiria, F. E. (2016). Laser and Electron-Beam Powder-Bed Additive Manufacturing of Metallic Implants: A Review on Processes, Materials and Designs. *J. Orthop. Res.* 34 (3), 369–385. doi:10.1002/jor.23075

Skallevold, H. E., Rokaya, D., Khurshid, Z., and Zafar, M. S. (2019). Bioactive Glass Applications in Dentistry. *Int. J. Mol. Sci.* 20 (23). doi:10.3390/ijms20235960

Sosnik, A., and Seremeta, K. P. (2017). Polymeric Hydrogels as Technology Platform for Drug Delivery Applications. *Gels* 3 (3). doi:10.3390/gels3030025

Soyama, H., and Takeo, F. (2020). Effect of Various Peening Methods on the Fatigue Properties of Titanium Alloy Ti6Al4V Manufactured by Direct Metal Laser Sintering and Electron Beam Melting. *Materials (Basel)* 13 (10). doi:10.3390/ma13102216

Srimaneepong, V., Rokaya, D., Thunyakitpisal, P., Qin, J., and Saengkiettiyut, K. (2020). Corrosion Resistance of Graphene oxide/Silver Coatings on Ni-Ti alloy and Expression of IL-6 and IL-8 in Human Oral Fibroblasts. *Sci. Rep.* 10 (1), 3247. doi:10.1038/s41598-020-60070-x

Su, C., Hu, Y., Song, Q., Ye, Y., Gao, L., Li, P., et al. (2020). Initiated Chemical Vapor Deposition of Graded Polymer Coatings Enabling Antibacterial, Antifouling, and Biocompatible Surfaces. *ACS Appl. Mater. Inter.* 12 (16), 18978–18986. doi:10.1021/acsami.9b22611

Su, C. K. (2021). Review of 3D-Printed Functionalized Devices for Chemical and. Biochemical Analysis. *Analytica Chim. Acta* 1158. doi:10.1016/j.aca.2021.338348

Surmenev, R. A., Surmeneva, M. A., and Ivanova, A. A. (2014). Significance of Calcium Phosphate Coatings for the Enhancement of New Bone Osteogenesis - A Review. *Acta Biomater.* 10 (2), 557–579. doi:10.1016/j.actbio.2013.10.036

Surmeneva, M., Lapanje, A., Chudinova, E., Ivanova, A., Koptyug, A., Loza, K., et al. (2019). Decreased Bacterial Colonization of Additively Manufactured Ti6Al4V Metallic Scaffolds with Immobilized Silver and Calcium Phosphate Nanoparticles. *Appl. Surf. Sci.* 480, 822–829. doi:10.1016/j.apsusc.2019.03.003

Tan, H. L., Lin, W. T., and Tang, T. T. (2012). The Use of Antimicrobial-Impregnated PMMA to Manage Periprosthetic Infections: Controversial Issues and the Latest Developments. *Int. J. Artif. Organs* 35 (10), 832–839. doi:10.5301/ijao.5000163

Tang, H., Li, Y., Ma, J., Zhang, X., Li, B., Liu, S., et al. (2016). Improvement of Biological and Mechanical Properties of Titanium Surface by Anodic Oxidation. *Bme* 27 (5), 485–494. doi:10.3233/bme-161602

Tang, J., Diao, P., Shu, X., Li, L., and Xiong, L. (20192019). Quercetin and Quercitrin Attenuates the Inflammatory Response and Oxidative Stress in LPS-Induced RAW264.7 Cells: *In Vitro* Assessment and a Theoretical Model. *Biomed. Res. Int.* 2019, 7039802. doi:10.1155/2019/7039802

Tang, J., Chen, L., Yan, D., Shen, Z., Wang, B., Weng, S., et al. (2020). Surface Functionalization with Proanthocyanidins Provides an Anti-oxidant Defense Mechanism that Improves the Long-Term Stability and Osteogenesis of Titanium Implants. *Ijn* 15, 1643–1659. doi:10.2147/ijn.s231339

Tamilselvi, S., Raghavendran, H. B., Srinivasan, P., and Rajendran, N., (2009). *In Vitro* and *In Vivo* Studies of Alkali- and Heat-Treated Ti-6Al-7Nb and Ti-5Al-2Nb-1Ta Alloys for Orthopedic Implants. *J. Biomed. Mater. Res. A.* 90 (2), 380–386.

Teng, F.-Y., Tai, I.-C., Ho, M.-L., Wang, J.-W., Weng, L. W., Wang, Y. J., et al. (2019). Controlled Release of BMP-2 from Titanium with Electrodeposition Modification Enhancing Critical Size Bone Formation. *Mater. Sci. Eng. C* 105, 109879. doi:10.1016/j.msec.2019.109879

Tharani Kumar, S., Prasanna Devi, S., Krithika, C., and Raghavan, R. N. (2020). Review of Metallic Biomaterials in Dental Applications. *J. Pharm. Bioallied Sci.* 12 (Suppl. 1), S14–S19. doi:10.4103/jpbs.JPBS_88_20

Tsai, C. H., Hung, C. H., Kuo, C. N., Chen, C. Y., Peng, Y. N., and Shie, M. Y. (2019). Improved Bioactivity of 3D Printed Porous Titanium Alloy Scaffold with Chitosan/Magnesium-Calcium Silicate Composite for Orthopaedic Applications. *Materials (Basel)* 12 (2). doi:10.3390/ma12020203

Tsou, H.-K., Hsieh, P.-Y., Chi, M.-H., Chung, C.-J., and He, J.-L. (2012). Improved Osteoblast Compatibility of Medical-Grade Polyetheretherketone Using Arc

Ionplated Rutile/anatase Titanium Dioxide Films for Spinal Implants. *J. Biomed. Mater. Res.* 100A (10), 2787–2792. doi:10.1002/jbm.a.34215

Tsukimura, N., Ueno, T., Iwasa, F., Minamikawa, H., Sugita, Y., Ishizaki, K., et al. (2011). Bone Integration Capability of Alkali- and Heat-Treated Nanobimorphic Ti-15Mo-5Zr-3Al. *Acta Biomater.* 7 (12), 4267–4277. doi:10.1016/j.actbio.2011.08.016

Utech, S., and Boccaccini, A. R. (2015). A Review of Hydrogel-Based Composites for Biomedical Applications: Enhancement of Hydrogel Properties by Addition of Rigid Inorganic Fillers. *J. Mater. Sci.* 51 (1), 271–310. doi:10.1007/s10853-015-9382-5

van der Stok, J., Lozano, D., Chai, Y. C., Amin Yavari, S., Bastidas Coral, A. P., Verhaar, J. A., et al. (2015). Osteostatin-coated Porous Titanium Can Improve Early Bone Regeneration of Cortical Bone Defects in Rats. *Tissue Eng. Part. A.* 21 (9-10), 1495–1506. doi:10.1089/ten.TEA.2014.0476

Veronesi, F., Torricelli, P., Martini, L., Tschon, M., Giavaresi, G., Bellini, D., et al. (2021). An Alternative *Ex Vivo* Method to Evaluate the Osseointegration of Ti-6Al-4V alloy Also Combined with Collagen. *Biomed. Mater.* 16 (2), 025007. doi:10.1088/1748-605x/abdbda

Wan, B., Wang, R., Sun, Y., Cao, J., Wang, H., Guo, J., et al. (2020). Building Osteogenic Microenvironments with Strontium-Substituted Calcium Phosphate Ceramics. *Front. Bioeng. Biotechnol.* 8, 591467. doi:10.3389/fbioe.2020.591467

Wang, C., Wang, S., Yang, Y., Jiang, Z., Deng, Y., Song, S., et al. (2018). Bioinspired, Biocompatible and Peptide-Decorated Silk Fibroin Coatings for Enhanced Osteogenesis of Bioinert Implant. *J. Biomater. Sci. Polym. Edition* 29 (13), 1595–1611. doi:10.1080/09205063.2018.1477316

Wang, H., Xu, Q., Hu, H., Shi, C., Lin, Z., Jiang, H., et al. (2020). The Fabrication and Function of Strontium-Modified Hierarchical Micro/Nano Titanium Implant. *Ijn* 15, 8983–8998. doi:10.2147/ijn.s268657

Wang, J., Li, J., Qian, S., Guo, G., Wang, Q., Tang, J., et al. (2016). Antibacterial Surface Design of Titanium-Based Biomaterials for Enhanced Bacteria-Killing and Cell-Assisting Functions against Periprosthetic Joint Infection. *ACS Appl. Mater. Inter.* 8 (17), 11162–11178. doi:10.1021/acsami.6b02803

Wang, S., Li, R., Li, D., Zhang, Z.-Y., Liu, G., Liang, H., et al. (2018). Fabrication of Bioactive 3D Printed Porous Titanium Implants with Sr Ion-Incorporated Zeolite Coatings for Bone Ingrowth. *J. Mater. Chem. B* 6 (20), 3254–3261. doi:10.1039/c8tb00328a

Wang, Y. Q., Wang, Y., Chen, P. M., Shao, Y. W., and Wang, F. H. (2011). Microstructure, Corrosion and Wear Resistances of Microarc Oxidation Coating on Al Alloy 7075. *Acta Metallurgica Sinica* 47 (4), 455–461.

Wang, Z., Wang, C., Li, C., Qin, Y., Zhong, L., Chen, B., et al. (2017). Analysis of Factors Influencing Bone Ingrowth into Three-Dimensional Printed Porous Metal Scaffolds: A Review. *J. Alloys Comp.* 717, 271–285. doi:10.1016/j.jallcom.2017.05.079

Wei, Y., Hu, Y., Li, M., and Li, D. (2020). Fabrication of Sr-Functionalized Micro/nano-Hierarchical Structure Ceramic Coatings on 3D Printing Titanium. *Surf. Eng.* 37 (3), 373–380. doi:10.1080/02670844.2020.1748349

Wennerberg, A., and Albrektsson, T. (2009). Structural Influence from Calcium Phosphate Coatings and its Possible Effect on Enhanced Bone Integration. *Acta Odontologica Scand.* 67 (6), 333–340. doi:10.1080/00016350903188325

Wojda, S. J., and Donahue, S. W. (2018). Parathyroid Hormone for Bone Regeneration. *J. Orthop. Res.* 36 (10), 2586–2594. doi:10.1002/jor.24075

Wong, K. C. (2016). 3D-printed Patient-specific Applications in Orthopedics. *Orr* 8, 57–66. doi:10.2147/orr.s99614

Xia, C., Ma, X., Zhang, X., Li, K., Tan, J., Qiao, Y., et al. (2020). Enhanced Physicochemical and Biological Properties of C/Cu Dual Ions Implanted Medical Titanium. *Bioactive Mater.* 5 (2), 377–386. doi:10.1016/j.bioactmat.2020.02.017

Xiu, P., Jia, Z., Lv, J., Yin, C., Cheng, Y., Zhang, K., et al. (2016). Tailored Surface Treatment of 3D Printed Porous Ti6Al4V by Microarc Oxidation for Enhanced Osseointegration via Optimized Bone In-Growth Patterns and Interlocked Bone/Implant Interface. *ACS Appl. Mater. Inter.* 8 (28), 17964–17975. doi:10.1021/acsami.6b05893

Xu, N., Fu, J., Zhao, L., Chu, P. K., and Huo, K. (2020). Biofunctional Elements Incorporated Nano/Microstructured Coatings on Titanium Implants with Enhanced Osteogenic and Antibacterial Performance. *Adv. Healthc. Mater.*, e2000681. doi:10.1002/adhm.202000681

Yang, H., Yu, M., Wang, R., Li, B., Zhao, X., Hao, Y., et al. (2020). Hydrothermally Grown TiO2-Nanorods on Surface Mechanical Attrition Treated Ti: Improved Corrosion Fatigue and Osteogenesis. *Acta Biomater.* 116, 400–414. doi:10.1016/j.actbio.2020.09.005

Yang, Y. W., He, C. X., Yang, W. J., Qi, F. W., Xie, D. Q., Shen, L. D., et al. (2020). Mg Bone Implant: Features, Developments and Perspectives. *Mater. Des.* 185. doi:10.1016/j.matdes.2019.108259

Yao, Q., Jiang, Y., Tan, S., Fu, X., Li, B., and Liu, L. (2020). Composition and Bioactivity of Calcium Phosphate Coatings on Anodic Oxide Nanotubes Formed on Pure Ti and Ti-6Al-4V alloy Substrates. *Mater. Sci. Eng. C* 110, 110687. doi:10.1016/j.msec.2020.110687

Yao, Q., Zheng, Y.-W., Lan, Q.-H., Kou, L., Xu, H.-L., and Zhao, Y.-Z. (2019). Recent Development and Biomedical Applications of Decellularized Extracellular Matrix Biomaterials. *Mater. Sci. Eng. C* 104, 109942. doi:10.1016/j.msec.2019.109942

Yao, Z. Q., Ivanisenko, Y., Diemant, T., Caron, A., Chuvilin, A., Jiang, J. Z., et al. (2010). Synthesis and Properties of Hydroxyapatite-Containing Porous Titania Coating on Ultrafine-Grained Titanium by Micro-arc Oxidation. *Acta Biomater.* 6 (7), 2816–2825. doi:10.1016/j.actbio.2009.12.053

Ye, X., Leeflang, S., Wu, C., Chang, J., Zhou, J., and Huan, Z. (2017). Mesoporous Bioactive Glass Functionalized 3D Ti-6Al-4V Scaffolds with Improved Surface Bioactivity. *Materials (Basel)* 10 (11). doi:10.3390/ma10111244

Yin, I. X., Zhang, J., Zhao, I. S., Mei, M. L., Li, Q., and Chu, C. H. (2020). The Antibacterial Mechanism of Silver Nanoparticles and its Application in Dentistry. *Ijn* 15, 2555–2562. doi:10.2147/ijn.s246764

Youn, Y. H., Lee, S. J., Choi, G. R., Lee, H. R., Lee, D., Heo, D. N., et al. (2019). Simple and Facile Preparation of Recombinant Human Bone Morphogenetic Protein-2 Immobilized Titanium Implant via Initiated Chemical Vapor Deposition Technique to Promote Osteogenesis for Bone Tissue Engineering Application. *Mater. Sci. Eng. C* 100, 949–958. doi:10.1016/j.msec.2019.03.048

Yu, M., Wang, Y., Zhang, Y., Cui, D., Gu, G., and Zhao, D. (2020). Gallium Ions Promote Osteoinduction of Human and Mouse Osteoblasts via the TRPM7/Akt Signaling Pathway. *Mol. Med. Rep.* 22 (4), 2741–2752. doi:10.3892/mmr.2020.11346

Yu, X., Ibrahim, M., Lu, S., Yang, H., Tan, L., and Yang, K. (2018). MgCu Coating on Ti6Al4V alloy for Orthopedic Application. *Mater. Lett.* 233, 35–38. doi:10.1016/j.matlet.2018.08.063

Yue, S., He, H., Li, B., and Hou, T. (2020). Hydrogel as a Biomaterial for Bone Tissue Engineering: A Review. *Nanomaterials (Basel)* 10 (8). doi:10.3390/nano10081511

Zanocco, M., Boschetto, F., Zhu, W., Marin, E., McEntire, B. J., Bal, B. S., et al. (2020). 3D-additive Deposition of an Antibacterial and Osteogenic Silicon Nitride Coating on Orthopaedic Titanium Substrate. *J. Mech. Behav. Biomed. Mater.* 103, 103557. doi:10.1016/j.jmbbm.2019.103557

Zardi, E. M., and Franceschi, F. (2020). Prosthetic Joint Infection. A Relevant Public Health Issue. *J. Infect. Public Health* 13 (12), 1888–1891. doi:10.1016/j.jiph.2020.09.006

Zhai, M., Zhu, Y., Yang, M., and Mao, C. (2020). Human Mesenchymal Stem Cell Derived Exosomes Enhance Cell-Free Bone Regeneration by Altering Their miRNAs Profiles. *Adv. Sci.* 7 (19), 2001334. doi:10.1002/advs.202001334

Zhang, G., Zhao, P., Lin, L., Qin, L., Huan, Z., Leeflang, S., et al. (2021). Surface-treated 3D Printed Ti-6Al-4V Scaffolds with Enhanced Bone Regeneration Performance: an *In Vivo* Study. *Ann. Transl Med.* 9 (1), 39. doi:10.21037/atm-20-3829

Zhang, H., Jiao, J., and Jin, H. (2019). Degradable Poly-L-Lysine-Modified PLGA Cell Microcarriers with Excellent Antibacterial and Osteogenic Activity. *Artif. Cell Nanomedicine, Biotechnol.* 47 (1), 2391–2404. doi:10.1080/21691401.2019.1623230

Zhang, S., Xing, M., and Li, B. (2018). Biomimetic Layer-By-Layer Self-Assembly of Nanofilms, Nanocoatings, and 3D Scaffolds for Tissue Engineering. *Int. J. Mol. Sci.* 19 (6). doi:10.3390/ijms19061641

Zhang, S., Cheng, X., Yao, Y., Wei, Y., Han, C., Shi, Y., et al. (2015). Porous Niobium Coatings Fabricated with Selective Laser Melting on Titanium Substrates: Preparation, Characterization, and Cell Behavior. *Mater. Sci. Eng. C* 53, 50–59. doi:10.1016/j.msec.2015.04.005

Zhang, T., Wei, Q., Zhou, H., Zhou, W., Fan, D., Lin, X., et al. (2020). Sustainable Release of Vancomycin from Micro-arc Oxidised 3D-Printed Porous Ti6Al4V for Treating Methicillin-Resistant *Staphylococcus aureus* Bone Infection and Enhancing Osteogenesis in a Rabbit Tibia Osteomyelitis Model. *Biomater. Sci.* 8 (11), 3106–3115. doi:10.1039/c9bm01968e

Zhang, T., Zhou, W., Jia, Z., Wei, Q., Fan, D., Yan, J., et al. (2018). Polydopamine-assisted Functionalization of Heparin and Vancomycin onto Microarc-Oxidized 3D Printed Porous Ti6Al4V for Improved Hemocompatibility, Osteogenic and Anti-infection Potencies. *Sci. China Mater.* 61 (4), 579–592. doi:10.1007/s40843-017-9208-x

Zhang, W., Sun, C., Zhu, J., Zhang, W., Leng, H., and Song, C. (2020). 3D Printed Porous Titanium Cages Filled with Simvastatin Hydrogel Promotes Bone Ingrowth and Spinal Fusion in Rhesus Macaques. *Biomater. Sci.* 8 (15), 4147–4156. doi:10.1039/d0bm00361a

Zhang, Y., Li, J., Che, S., Yang, Z., and Tian, Y. (2019). Chemical Leveling Mechanism and Oxide Film Properties of Additively Manufactured Ti-6Al-4V alloy. *J. Mater. Sci.* 54 (21), 13753–13766. doi:10.1007/s10853-019-03855-4

Zhang, Y., Zheng, Y., Li, Y., Wang, L., Bai, Y., Zhao, Q., et al. (2015). Tantalum Nitride-Decorated Titanium with Enhanced Resistance to Microbiologically Induced Corrosion and Mechanical Property for Dental Application. *PLoS One* 10 (6), e0130774. doi:10.1371/journal.pone.0130774

Zhao, B., Li, X., Xu, H., Jiang, Y., Wang, D., and Liu, R. (2020). Influence of Simvastatin-Strontium-Hydroxyapatite Coated Implant Formed by Micro-arc Oxidation and Immersion Method on Osteointegration in Osteoporotic Rabbits. *Ijn* 15, 1797–1807. doi:10.2147/ijn.s244815

Zhao, P., Liu, Y., Li, T., Zhou, Y., Leeflang, S., Chen, L., et al. (2020). 3D Printed Titanium Scaffolds with Ordered TiO_2 Nanotubular Surface and Mesoporous Bioactive Glass for Bone Repair. *Prog. Nat. Sci. Mater. Int.* 30 (4), 502–509.

Zhao, X., Wei, C., Gai, Z., Yu, S., and Ren, X. (2019). Chemical Vapor Deposition and its Application in Surface Modification of Nanoparticles. *Chem. Pap.* 74 (3), 767–778. doi:10.1007/s11696-019-00963-y

Zhu, D.-Y., Lu, B., Yin, J.-H., Ke, Q.-F., Xu, H., Zhang, C.-Q., et al. (2019). Gadolinium-doped Bioglass Scaffolds Promote Osteogenic Differentiation of hBMSC via the Akt/GSK3β Pathway and Facilitate Bone Repair *In Vivo*. *Ijn* 14, 1085–1100. doi:10.2147/ijn.s193576

Zhu, J., Sun, H.-H., Wo, J., Xu, F.-H., Lu, W.-Q., Deng, B., et al. (2020). Duration of Electrochemical Deposition Affects the Morphology of Hydroxyapatite Coatings on 3D-Printed Titanium Scaffold as Well as the Functions of Adhered MC3T3-E1 Cells. *J. Orthopaedic Sci.* 25 (4), 708–714. doi:10.1016/j.jos.2019.09.008

Zong, M., Bai, L., Liu, Y., Wang, X., Zhang, X., Huang, X., et al. (2017). Antibacterial Ability and Angiogenic Activity of Cu-Ti-O Nanotube Arrays. *Mater. Sci. Eng. C* 71, 93–99. doi:10.1016/j.msec.2016.09.077

Conflict of Interest: The authors declare that the research was conducted in the absence of any commercial or financial relationships that could be construed as a potential conflict of interest.

Publisher's Note: All claims expressed in this article are solely those of the authors and do not necessarily represent those of their affiliated organizations, or those of the publisher, the editors and the reviewers. Any product that may be evaluated in this article, or claim that may be made by its manufacturer, is not guaranteed or endorsed by the publisher.

frontiers in Bioengineering and Biotechnology

ORIGINAL RESEARCH
published: 03 March 2022
doi: 10.3389/fbioe.2022.864012

D-arginine Enhances the Effect of Alpha-Amylase on Disassembling *Actinomyces viscosus* Biofilm

Baosheng Li[1,2], *Qing Cai*[1], *Zixuan Wang*[1,2], *Shuwei Qiao*[1,2], *Yanzhen Ou*[1,2], *Rui Ma*[3], *Chuanfu Luo*[4] *and Weiyan Meng*[1]*

[1]Department of Dental Implantology, Hospital of Stomatology, Jilin University, Changchun, China, [2]Jilin Provincial Key Laboratory of Oral Biomedical Engineering, Changchun, China, [3]Xinjiang Laboratory of Phase Transitions and Microstructures in Condensed Matters, College of Physical Science and Technology, Yili Normal University, Yining, China, [4]School of Applied Chemistry and Engineering, University of Science and Technology of China, Hefei, China

Peri-implantitis is the leading cause of dental implant failure, initially raised by biofilm accumulation on the implant surface. During the development of biofilm, *Actinomyces viscosus* (*A. viscosus*) plays a pivotal role in initial attachment as well as the bacterial coaggregation of multispecies pathogens. Hence, eliminating the *A. viscosus*-associated biofilm is fundamental for the regeneration of the lost bone around implants. Whereas clinical evidence indicated that antimicrobials and debridement did not show significant effects on the decontamination of biofilm on the implant surface. In this study, alpha-amylase was investigated for its effects on disassembling *A. viscosus* biofilm. Then, in order to substantially disperse biofilm under biosafety concentration, D-arginine was employed to appraise its enhancing effects on alpha-amylase. In addition, molecular dynamics simulations and molecular docking were conducted to elucidate the mechanism of D-arginine enhancing alpha-amylase. 0.1–0.5% alpha-amylase showed significant effects on disassembling *A. viscosus* biofilm, with definite cytotoxicity toward MC3T3-E1 cells meanwhile. Intriguingly, 8 mM D-arginine drastically enhanced the eradication of *A. viscosus* biofilm biomass by 0.01% alpha-amylase with biosafety in 30 min. The exopolysaccharides of biofilm were also thoroughly hydrolyzed by 0.01% alpha-amylase with 8 mM D-arginine. The biofilm thickness and integrity were disrupted, and the exopolysaccharides among the extracellular matrix were elusive. Molecular dynamics simulations showed that with the hydrogen bonding of D-arginine to the catalytic triad and calcium-binding regions of alpha-amylase, the atom fluctuation of the structure was attenuated. The distances between catalytic triad were shortened, and the calcium-binding regions became more stable. Molecular docking scores revealed that D-arginine facilitated the maltotetraose binding process of alpha-amylase. In conclusion, these results demonstrate that D-arginine enhances the disassembly effects of alpha-amylase on *A. viscosus* biofilm through potentiating the catalytic triad and stabilizing the calcium-binding regions, thus providing a novel strategy for the decontamination of biofilm contaminated implant surface.

Keywords: D-arginine, alpha-amylase, *Actinomyces viscosus*, biofilm, exopolysaccharides, molecular dynamics, molecular docking

OPEN ACCESS

Edited by:
Jianxun Ding,
Changchun Institute of Applied Chemistry (CAS), China

Reviewed by:
Chengcheng Yin,
China Medical University, China
Xiaosong Yi,
Peking University Hospital of Stomatology, China
Mengmeng Lu,
Nanjing Medical University, China

***Correspondence:**
Weiyan Meng
mengwy@jlu.edu.cn

Specialty section:
This article was submitted to Biomaterials, a section of the journal Frontiers in Bioengineering and Biotechnology

Received: *28 January 2022*
Accepted: *17 February 2022*
Published: *03 March 2022*

Citation:
Li B, Cai Q, Wang Z, Qiao S, Ou Y, Ma R, Luo C and Meng W (2022) D-arginine Enhances the Effect of Alpha-Amylase on Disassembling Actinomyces viscosus Biofilm. Front. Bioeng. Biotechnol. 10:864012. doi: 10.3389/fbioe.2022.864012

INTRODUCTION

Dental implants have become the primary protocol for the treatment of dentition defects and edentulous patients nowadays. Despite its high success rates, complications could reduce the long-term cumulative implant survival (Fu and Wang, 2020). Peri-implantitis (PiM), as the primary cause leading to implant failure, could arise about 22% in 10 years after implantation (Derks and Tomasi, 2015). During PiM pathogenesis, the inflammation at the implant-bone interface is evoked to successively cause bone resorption, gingival tissue retraction, and implant surface exposure. To date, plaque biofilm is a putative and pivotal factor that induces the initial inflammation of PiM (Berglundh et al., 2018). Hence, eliminating biofilm is essential for the prevention and treatment of PiM.

In clinical practice, methods for decontaminating the implant surface could be divided into physical and chemical approaches. Physical approaches, such as mechanical scaling, sandblasting, magnetic nanoparticles, and laser therapy, could damage the biological surface, cause material residue, or be difficult to eliminate the massive biofilm matrix enmeshed in the micropores due to the rough character of the implant surface (Elbourne et al., 2020; Lasserre et al., 2020; Vyas et al., 2020). Correspondingly, chemical approaches, including antimicrobial agents, antimicrobial peptides, and photodynamic therapy (PDT), et al., mainly focus on eradicating bacteria or disturbing biofilm's integrity (Chen and Lee, 2018; Liu et al., 2019; Pinto et al., 2020). Whereas the biofilm extracellular matrix, mainly composed of exopolysaccharides (EPS), lipids, proteins, and extracellular DNA (eDNA), represents around 90% of the total biofilm biomass (Fulaz et al., 2019). Consequently, even if the bacteria were thoroughly damaged, the massive biofilm matrix remains attached to the implant surface. Nevertheless, the extracellular matrix protects bacteria from agents penetration and shear stress, making a low bioavailability of agents' germicidal effects (Flemming and Wingender, 2010). Previous *in vivo* studies have demonstrated that there was fibrous connective tissue between regenerated bone and exposed implant surface with PiM after grafting autogenous bone grafts (You et al., 2007), indicating that biofilm-associated contaminants obstructed the re-osseointegration of the implant surface. Till now, the methods for treating PiM are unpredictable yet. Thus, strategies for eradicating the whole biofilm should be prospective.

The biofilm extracellular matrix constitutes the main component of biofilm, while EPS are one of the most constituents of the extracellular matrix (Pinto et al., 2020). Hence, EPS is indispensable to biofilm formation and constitutes the protective barrier of encapsulated bacteria (Flemming and Wingender, 2010). Besides, EPS occupies the main adhesion force binding to the biological surface as well as bacteria and proteins through Van der Waals force, electrostatic attraction, hydrogen bonds (Arciola et al., 2018), thus facilitating the cohesion of the biofilm structure. In addition, EPS is responsible for water retention within the biofilm, and provides nutrient sources and ions for the inner bacteria (Pinto et al., 2020). Therefore, EPS could be a potential target for eradicating the biofilm on implant surface.

Similar to plaque biofilm on teeth, the biofilm formation on implant surface possesses typical stages, namely initial, early, secondary, and late colonizations (Vilarrasa et al., 2018; Bermejo et al., 2019). *Streptococcus oralis* and *Actinomyces viscosus* (*A. viscosus*) are the representative strains in the initial stage, then *Veillonella parvula* in the early stage, *Fusobacterium nucleatum* in the secondary stage, and *Porphyromonas gingivalis* in the late stage. In fact, *Fusobacterium nucleatum* and *Porphyromonas gingivalis* could only produce capsular polysaccharides but not EPS (Davey and Duncan, 2006), while *Veillonella* species utilize EPS secreted by *Streptococci* to adhere to biofilm (Liu et al., 2020). In addition, in the study of multispecies biofilms growing on the implant surface, *Actinomyces* showed about two-fold amount of biomass than *Streptococcus* (Bermejo et al., 2019). Moreover, *Actinomyces* plays an essential role as physical bridges to mediate coaggregation and coadhesion between coaggregating partners, which occurs 5- to 10-fold more often than coadhesion between noncoaggregating cells (Kolenbrander, 2000). Thus, disintegrating the *Actinomyces* EPS and the *Actinomyces*-associated biofilm is critical for the decontamination of the implant surface.

EPS could be composed of glucose, mannose, galactose, N-acetyl-glucosamine, and other monosaccharides (Rabin et al., 2015), which could link as α-1,4 bond, β-1,4 bond, or β-1,3 bond. Glycoside hydrolases are enzymes that hydrolyze the glycosidic linkages between carbohydrates within polysaccharides or oligosaccharides (Naumoff, 2011). α-amylase (Amy) and cellulase effectively disrupted *Staphylococcus aureus* and *Pseudomonas aeruginosa* coculture biofilms by breaking down complex polysaccharides. However, whether glycoside hydrolases could disrupt *A. viscosus* biofilm remains unknown.

Our previous studies demonstrated that D-arginine (R) could disperse *Porphyromonas gingivalis* mature biofilm in 72 h (Li et al., 2020; Zhang et al., 2021). Whereas the treatment time takes too long for feasible clinical practice. The capability of R to disrupt *A. viscosus* biofilm and higher treatment efficiency should be further tested.

Therefore, the aim of this study was to investigate the effects of Amy on disassembling *A. viscosus* biofilm and the enhancing effects of R on Amy. Molecular dynamics (MD) simulations and molecular docking were furtherly exploited to explore the intrinsic mechanisms.

MATERIALS AND METHODS

Disassembly Effects of Multiple Glycoside Hydrolases on *A. viscosus* Biofilm

A. viscosus ATCC 27044 was used in this study. Briefly, *A. viscosus* was subcultured on sterilized brain heart infusion (BHI) (HopeBio, Qingdao, China) supplemented with yeast extract (LP0021, Oxoid), menadione (0.5 μg/ml), hemin (5 μg/ml), and sucrose (0.5 μg/ml), then incubated aerobically at 37°C (80% N_2, 10% H_2, and 10% CO_2). Subsequently, single *A. viscosus* colonies were inoculated into BHI bacterium liquid medium, then

adjusted to 10^8 colony-forming unit counts/ml (CFU/ml) for inoculation to 24-well plates, then incubated for 48 h at 37°C under anaerobic conditions to form mature biofilm. Subsequently, the bacterial supernatant was removed and the culture plate was rinsed with phosphate-buffered saline (PBS) for 3 times. Afterward, 500 μl of the following different glycoside hydrolases were added to each well, respectively: 0.5% (w/v) Amy (Yuanye, Shanghai, China), 0.5% (w/v) cellulase (Yuanye, Shanghai, China), 0.5% (w/v) dextranase (Yuanye, Shanghai, China), 1% (v/v) α-galactosidase (Yuanye, Shanghai, China), 1% (v/v) β-galactosidase (Yuanye, Shanghai, China), and 1% (v/v) Dispersin B (Sigma-Aldrich, St Louis, MO, United States). All glycoside hydrolases were prepared by dissolving lyophilized powder or stock solution in double-distilled water (ddH_2O). 500 μl PBS was used as the control group. After 30 min of treatment at 37°C, crystal violet (CV) assay was carried out as referred to the previous study (Zhang et al., 2021). Finally, the biofilm biomass was evaluated at 595 nm using a microplate reader (Synergy HT, BioTek, Winooski, VT, United States).

Disassembly Effects of Gradient Concentrations of Amy on *A. viscosus* Biofilm

A. viscosus mature biofilm was cultured same to 2.1. Then, gradient concentrations of Amy (0.01, 0.05, 0.1, 0.25, and 0.5%) were employed to investigate their effects on disassembling *A. viscosus* mature biofilm. In order to stabilize Amy, 60 ppm of $CaCl_2$ was added to each group (The following experiments were the same). PBS was used as the control group.

Cytotoxicity Assay

Murine pre-osteoblast MC3T3-E1 cells were resuscitated and then cultured in DMEM solution, placed in an incubator of 5% CO_2 at 37°C. Subsequently, the logarithmic growth phase cells were inoculated in 96-well plates with 0.01% Amy, 0.05% Amy, 0.1% Amy, 0.25% Amy, 0.5% Amy, 2 mM R, 4 mM R, 8 mM R, 16 mM R, and 0.01% Amy + 8 mM R, respectively. Isochoric DMEM was used as the control group. After 1 and 3 days of culture at 37°C, 10 μl CCK-8 (Beyotime, Shanghai, China) was added to each well and sequentially cultured for 2 h at 37°C. The absorbance value was measured at 450 nm.

Effects of R on Interfering Amy Disassembling *A. viscosus* Biofilm

In order to substantially disperse *A. viscosus* biofilm under biosafety concentration, R was employed. Briefly, R was mixed with Amy to form the following concentration ratios: 0.01% Amy + 1/2/4/8 mM R. In addition, mono 1/2/4/8/16 mM R and 0.01% Amy were also determined. The PH of the groups containing R was adjusted to 7.0 by HCl. PBS was used as the control group. 500 μl of the groups mentioned above was added to each well to disrupt *A. viscosus* mature biofilm. Subsequently, in order to verify the component orchestrating the catalytic role, 0.01% Amy or 8 mM R was respectively heat-inactivated by heating the solutions at 95°C for 5 min. PBS was used as the control group. Furtherly, in order to determine an optimal treatment time, 0.01% Amy + 8 mM R was tested for 10, 20, 30, and 60 min.

Effects of R on Enhancing Amy Hydrolyzing Exopolysaccharides

After treatment with 0.01% Amy or 8 mM R or 0.01% Amy + 8 mM R for 30 min, each well was rinsed with 1 ml PBS, the suspension containing dispersed biofilm and agents was collected to the EP tube, centrifuged at ×12,000 g (Centrifuge 5810 R, Eppendorf, Framingham, MA, United States) for 5 min (4°C) to collect the hydrolyzed exopolysaccharides (HEPS) in the supernatant. Thereafter, the residual biofilm was scraped carefully with a cell scraper (Nunc, Thermo Fisher Scientific, Waltham, MA, United States), rinsed with 1 ml PBS, and then centrifuged at ×12,000 g for 5 min (4°C). After removing the supernatant, 200 μl NaOH was added to dissolve the sediment, then centrifuged again. The supernatant was collected as the unhydrolyzed exopolysaccharides (UEPS) of biofilm. Furtherly, in order to compare the enhancing effects between R and Ca^{2+} on Amy, a soluble starch (Sigma-Aldrich, St. Louis, MI, United States) was employed. Briefly, the starch was dissolved in boiling ddH_2O by 2% (w/v). The experimental groups were: 0.01% Amy, 0.01% Amy + 60 ppm $CaCl_2$, 0.01% Amy + 8 mM R, 0.01% Amy + 60 ppm $CaCl_2$ + 8 mM R. Isochoric ddH_2O was used as the control group. 10 μl of each group was added to 1 ml starch solution. After treatment for 3 min at 37°C, the reaction was terminated by heating the solutions at 95°C for 5 min. All above specimens were determined by the DNS method at 540 nm with glucose as standard (Wu et al., 2018).

Confocal Laser Scanning Microscopy Assay

The effects of 0.01% Amy and 0.01% Amy + 8 mM R on *A. viscosus* biofilm as well as EPS were assessed by Confocal Laser Scanning Microscopy (CLSM). SYTO9 (Invitrogen, Waltham, MA, United States), SYPRO Ruby (Invitrogen, Waltham, MA, United States), and Calcofluor (Sigma-Aldrich, St. Louis, MI, United States) were employed for bacteria labeling, protein labeling, and EPS labeling, respectively. In general, biofilm was cultured for 48 h on confocal dishes (WHB, Shanghai, China). Followed by the treatment of the above agents for 30 min and subsequent rinsing with PBS. 200 μl SYTO9, 200 μl SYPRO Ruby, and 15 μl Calcofluor was added to each well simultaneously, then incubated for 30 min at 20°C in a dark area. Afterward, the specimens were detected by a confocal laser scanning microscope (FV3000, Olympus, Japan), with a green channel (480/500 nm) for SYTO9, a red channel (450/610 nm) for SYPRO Ruby, and a blue channel (365/450 nm) for Calcofluor. Images were captured by Imaris software (Zeiss, Germany). The thicknesses and biomass of the biofilm and EPS and the surface to biovolume ratio were calculated using ImageJ COMSTAT2 software (Heydorn et al., 2000).

Scanning Electron Microscopy Analysis

The biofilms in 24-well plates were treated with 0.01% Amy + 0/1/2/4/8 mM R for 30 min. After rinsing with PBS, the specimens

were fixed overnight in 2.5% (v/v) glutaraldehyde at 4°C and dehydrated by gradient ethanol solutions (30/50/70/80/90/95/100%). The biofilm without any treatment was used as the control group. Finally, the biofilms were observed under Scanning Electron Microscopy (SEM) (Merlin, Zeiss, Germany) after oven drying and gold sputter coating.

Transmission Electron Microscopy (TEM) Analysis

The biofilms in 24-well plates were treated with 0.01% Amy + 8 mM R for 30 min. After rinsing with 1 ml PBS, the suspension was collected as the dispersed biofilm. While the residual biofilm on the plate was scraped and then rinsed with 1 ml PBS, the suspension was collected as the undispersed biofilm. The biofilm without any treatment was used as the control group. The specimens were centrifuged at 4,000 rpm (Centrifuge 5810R, Eppendorf, Framingham, MA, United States) for 10 min (4°C). The following preparation process of samples was performed according to previous studies (Lukic et al., 2020; Zhang et al., 2021). Finally, the ultrathin sections were observed under a transmission electron microscope (JEM 1400 PLUS, JEOL, Akishima, Japan, United States).

Molecular Dynamics Simulations

In order to elucidate the mechanisms of R enhancing the effects of Amy hydrolyzing polysaccharides, Molecular Dynamics (MD) simulations and molecular docking were furtherly conducted. In general, the investigated Amy crystal structure from *Bacillus Subtilis* was retrieved from the protein data bank (PDB) under the code 1UA7 (Kagawa et al., 2003). MD simulations were executed using the GROMACS package version 2019.5 (Abraham et al., 2015) under constant temperature/pressure and periodic boundary conditions. Amber99sb and SPC were selected as the all-atomic force field and the water model, respectively. During the MD simulation, all covalent bonds involving hydrogen atoms were constrained by LINCS algorithm, and the integration time step was 2 fs. The electrostatic interaction was calculated using the particle-mesh Ewald (PME) method with the cutoff value set to 1.0 nm. The cutoff value of non-bond interaction was set to 10 Å, updated every 10 steps. The V-rescale temperature coupling method was used to control the simulation temperature to 300 K, while the Parrinello-Rahman method was employed to control the pressure to 1 bar. Firstly, an energy minimization step was conducted using the Steepest Descent algorithm. Then, canonical ensemble (or substance-volume-temperature, NVT) balance and isothermal-isobaric ensemble (or substance-pressure-temperature, NPT) balance simulation were carried out for 100 ps at 300 K. Afterward, 10 molecules of R were added to the system, followed by adding Na^+ and Cl^- ions proportionally to neutralize the system. Finally, MD was carried out with conformations saved per 10 ps, totally simulation for 500 ns. The results were visualized and analyzed using PyMOL version 2.5.2.

Molecular Docking

The three-dimensional structure of maltotetraose was retrieved and then dissociated from PDB under the code 1QPK(Hasegawa et al., 1999). Then, maltotetraose was selected as the ligand, while Amy and Amy + 10 R were selected as receptors, respectively. The structures of ligand and protein were imported into AutoDockTools-1.5.7 software for adding hydrogens and calculating the total charge. After defining a box center at the central point of the catalytic triad, molecular docking was carried out *via* AutoDock. Afterward, the conformations were visualized using PyMOL, and the docking scores were finally analyzed.

Statistical Analysis

Data were expressed as mean ± standard deviation. One-way analysis of variance (ANOVA) with appropriate post-tests was employed using SPSS 24.0 software (SPSS Inc., Chicago, IL, United States). Values of $p < 0.05$ were considered statistically significant.

RESULTS

Effects of Glycoside Hydrolases on Disassembling *A. viscosus* Biofilm

The availabilities of multiple glycoside hydrolases were investigated firstly. As shown in **Figure 1A**, 0.5% Amy showed a sharp effect on disassembling *A. viscosus* biofilm, whereas, other glycoside hydrolases had no significant effects. Subsequently, gradient concentrations of Amy were assessed. 0.1, 0.25, and 0.5% Amy showed statistical differences compared with the control group, while 0.01 and 0.05% Amy could not disperse the *A. viscosus* mature biofilm effectively (**Figure 1B**).

Cytocompatibility

As shown in **Figure 2**, 0.1, 0.25, 0.5% Amy, and 16 mM R had evident cytotoxic effects towards MC3T3-E1 cells both at 1d and 3d. Correspondingly, 0.01%, 0.05% Amy, 1/2/4/8 mM R, and 0.01% Amy + 8 mM R had good biocompatibility with MC3T3-E1 cells. Hence, the groups without cytotoxicity were investigated in the following experiments.

R Enhanced the Effects of Amy on Disassembling *A. viscosus* Biofilm

Since 0.01% is the saturation concentration of Amy, the higher concentrations were excluded in the following experiments. Intriguingly, 0.01% Amy obtained the feasibility of disassembling *A. viscosus* biofilm with the addition of 1/2/4/8 mM R, being a concentration-dependent behavior (**Figure 3A**). Particularly, 0.01% Amy + 8 mM R showed the most striking result. Meanwhile, 1/2/4/8 mM R failed to disperse *A. viscosus* biofilm solely, even at the cytotoxic concentration of 16 mM. **Supplementary Video S1** recorded the dispersing efficiency of the control, 0.01% Amy, and 0.01% Amy + 8 mM R groups after treatment for 30 min. **Supplementary Figure S1** showed that 1/2/4/8 mM R also presented a similar concentration-dependent behavior on enhancing 0.005% Amy, whereas there remained a considerable amount of biofilm in the 0.005% Amy + 8 mM R group. **Figure 3B** shows that the heat-inactivated 0.01% Amy lost its activity in spite of the addition of 8 mM R. While the same

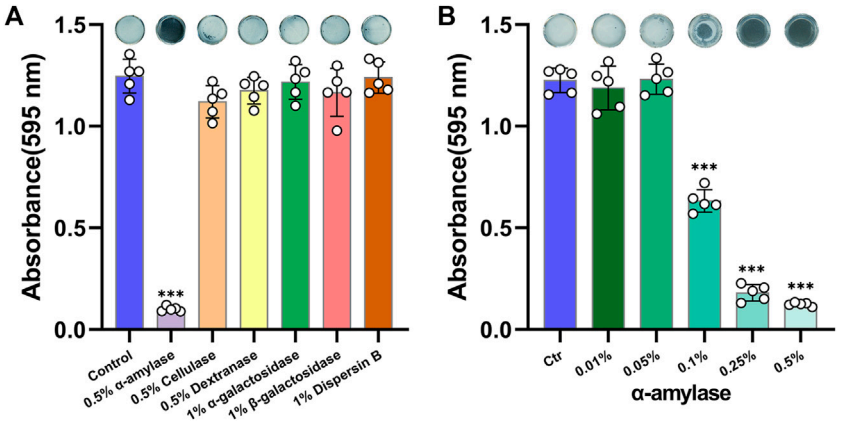

FIGURE 1 | Effects of glycoside hydrolases on disassembling *A. viscosus* biofilm. **(A)** The efficiency of six different glycoside hydrolases on dispersing *A. viscosus* biofilm. **(B)** Disassembly effects of gradient concentrations of Amy on *A. viscosus* biofilm. Data represented as means ± S.D. ($n = 5$). ***$p < 0.001$, vs. control group. Ctr, control.

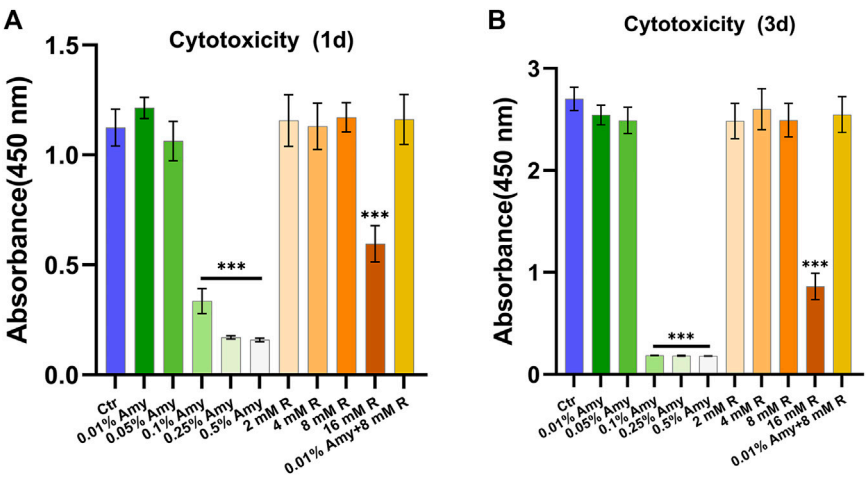

FIGURE 2 | Cytotoxicity of gradient concentrations of Amy, R, and the compounds to murine pre-osteoblast MC3T3-E1 cells. **(A)** Cell viability at day 1. **(B)** Cell viability at day 3. Data represented as means ± S.D. ($n = 5$). ***$p < 0.001$, vs. control group. Ctr, control. Amy, α-amylase. R, D-arginine.

heat-inactivation method did not impede the enhancing effect of 8 mM R on Amy, which showed equivalent behavior compared with none-heated 0.01% Amy + 8 mM R. Moreover, 30 and 60 min of treatment showed better results than 10 and 20 min, respectively. Whereas 60 min did not show a significant difference compared with 30 min (**Figure 3C**).

R Enhanced Amy Hydrolyzing Exopolysaccharides

The standard curve of glucose was generated to define the contents of EPS (**Figure 4A**). As shown in **Figure 4B**, the HEPS of 0.01% Amy + 8 mM R and 0.01% Amy were significantly higher than the control group as well as the 8 mM R group. In addition, 0.01% Amy + 8 mM R showed a better effect compared with 0.01% Amy. The value of UEPS in **Figure 4C** was calculated from the EPS weight within the biofilm divided by the biofilm weight. The results indicated that the remained EPS on the plate of 0.01% Amy + 8 mM R group and 0.01% Amy group was less than the control group and the 8 mM R group, but there was not a statistics difference between the 0.01% Amy + 8 mM R and the 0.01% Amy group.

In order to compare the stabilizing and promoting effects of R and Ca^{2+}on Amy, R or Ca^{2+} was added respectively or simultaneously. As shown in **Figure 4D**, there was no significant increase of Amy hydrolyzing starch with the addition of Ca^{2+}. While 8 mM R showed a definite increase compared with 0.01% Amy solely or 0.01% Amy + Ca^{2+}. Furthermore, 0.01% Amy + Ca^{2+} + 8 mM R showed the most notable effects compared with the above groups.

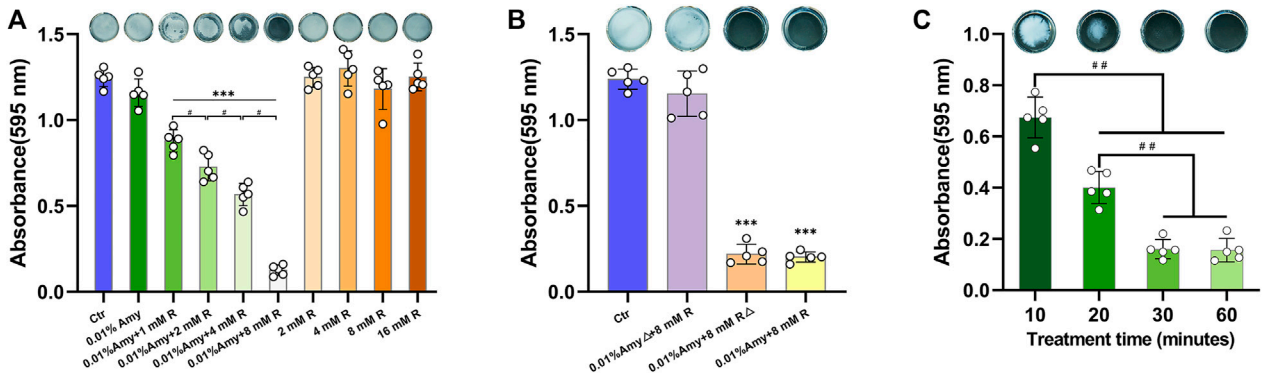

FIGURE 3 | Effects of R on interfering Amy disassembling *A. viscosus* biofilm. **(A)** Effects of different compounds on disassembling *A. viscosus* biofilm. **(B)** Catalytic component determination by heat-inactivation. **(C)** Disassembly efficiency of different treatment time of 0.01% Amy + 8 mM R on *A. viscosus* biofilm. Data represented as means ± S.D. ($n = 5$). ***$p < 0.001$, vs. control group. #, $p < 0.05$. ##, $p < 0.01$. Δ, heat-inactivation at 95°C for 5 min. Ctr, control. Amy, α-amylase. R, D-arginine.

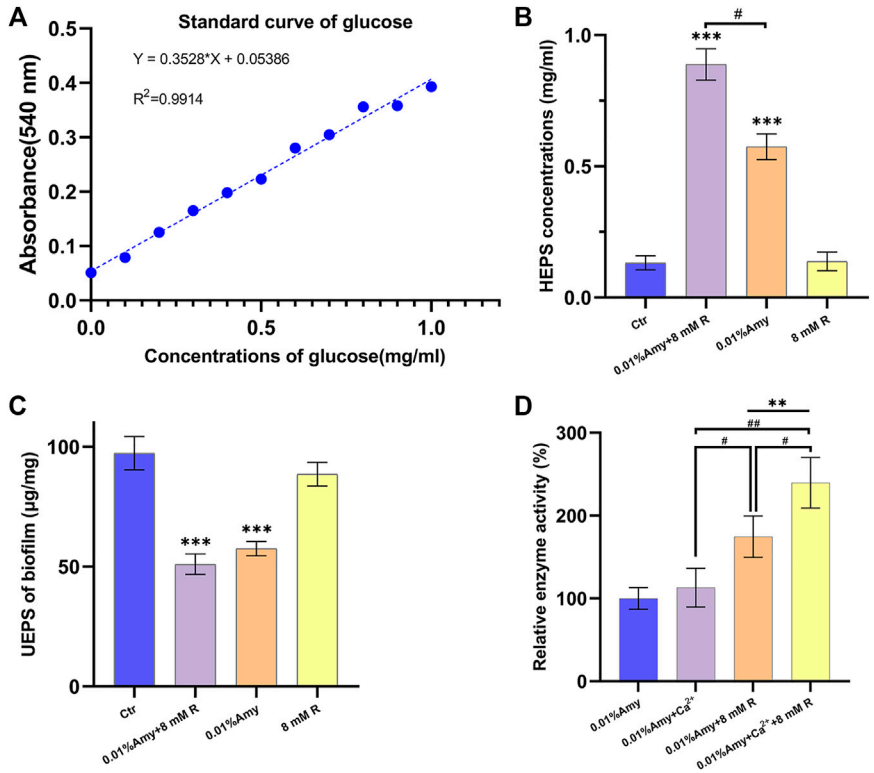

FIGURE 4 | Effects of R on enhancing Amy hydrolyzing *A. viscosus* biofilm EPS and starch. **(A)** Standard curve of glucose. **(B)** The concentrations of HEPS in the dispersed biofilm after treatment for 30 min. **(C)** The contents of UEPS remained on the plate after treatment for 30 min. **(D)** Comparison of 60 ppm Ca^{2+} and 8 mM R on enhancing 0.01% Amy hydrolyzing starch. Data represented as means ± S.D. ($n = 5$). **$p < 0.01$, *vs.* control group. ***$p < 0.001$, vs. control group. #, $p < 0.05$. ##, $p < 0.01$. Ctr, control. Amy, α-amylase. R, D-arginine. HEPS, hydrolyzed exopolysaccharides. UEPS, unhydrolyzed exopolysaccharides.

Thickness and Biomass of *A. viscosus* Biofilm and EPS

The CLSM determined the three-dimensional structure of *A. viscosus* biofilm and EPS distribution. As shown in **Figure 5A**, the bacteria amount, protein content, and EPS biomass were evenly massive in the control group. While the compactness of biofilm in the 0.01% Amy group seemed attenuated, discrete voids could be observed in the mid-slice image. Interestingly, the bacteria, protein, and EPS were drastically sparse in the 0.01% Amy + 8 mM R group. The EPS surface was discontinuous with extensive voids.

Figure 5B indicates that the volume of biofilm and EPS in the control group was consistently thick. With the treatment of 0.01%

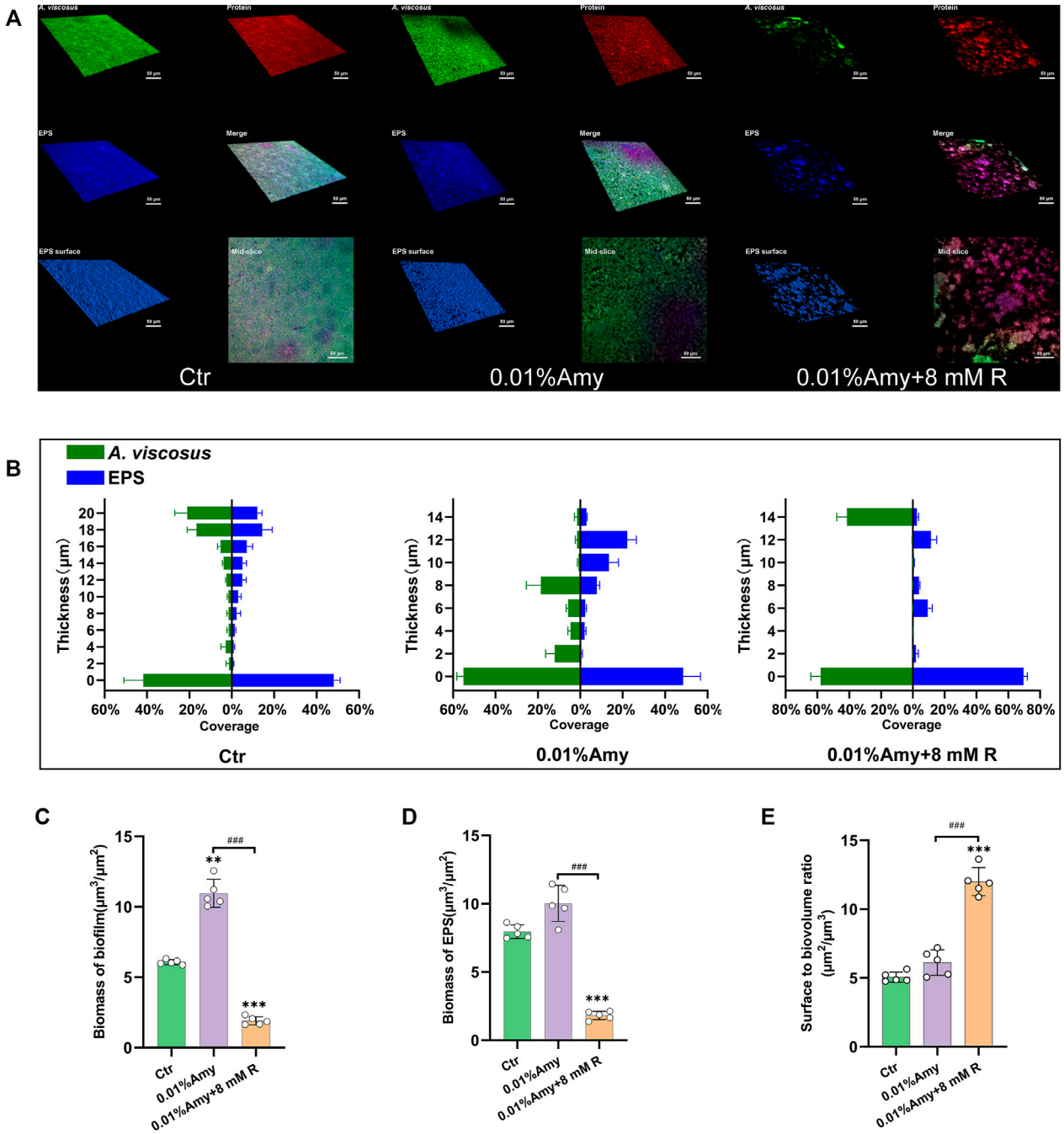

FIGURE 5 | Quantification of biofilm and EPS of *A. viscosus via* CLSM analysis. **(A)** Three-dimensional visualization of *A. viscosus* biofilm cultured on confocal dishes. Live bacteria, protein, and EPS were green-labeled, red-labeled, and blue-labeled, respectively. The fourth, fifth, and sixth image of each group represent the merged labeled image, the EPS surface, and the mid-slice along the thickness-axis of biofilm, respectively. **(B)** Quantification of the thickness of biofilm and EPS of *A. viscosus*. **(C)** The biomass of biofilm of each group. **(D)** The biomass of EPS of each group. **(E)** The surface to biovolume ratio of each group. Data represented as means ± S.D. (n = 5). $^{**}p < 0.01$, vs. control group. $^{***}p < 0.001$, vs. control group. ###, $p < 0.001$. Scale bars: 50 μm. Ctr, control. Amy, α-amylase. R, D-arginine.

Amy, the biofilm became dispersed, presented as the reduction of thickness. 0.01% Amy + 8 mM R thoroughly attenuated the thickness and distribution of biofilm as well as EPS. Only 14 μm of biofilm could be measured. Whereas the thickness of EPS was not strictly consistent with biofilm.

Figures 5C,D show that the biomass of biofilm and EPS in the 0.01% Amy + 8 mM R group were significantly less than the control group and the 0.01% Amy group. Unexpectedly, the biofilm biomass in the 0.01% Amy group was more than the control group.

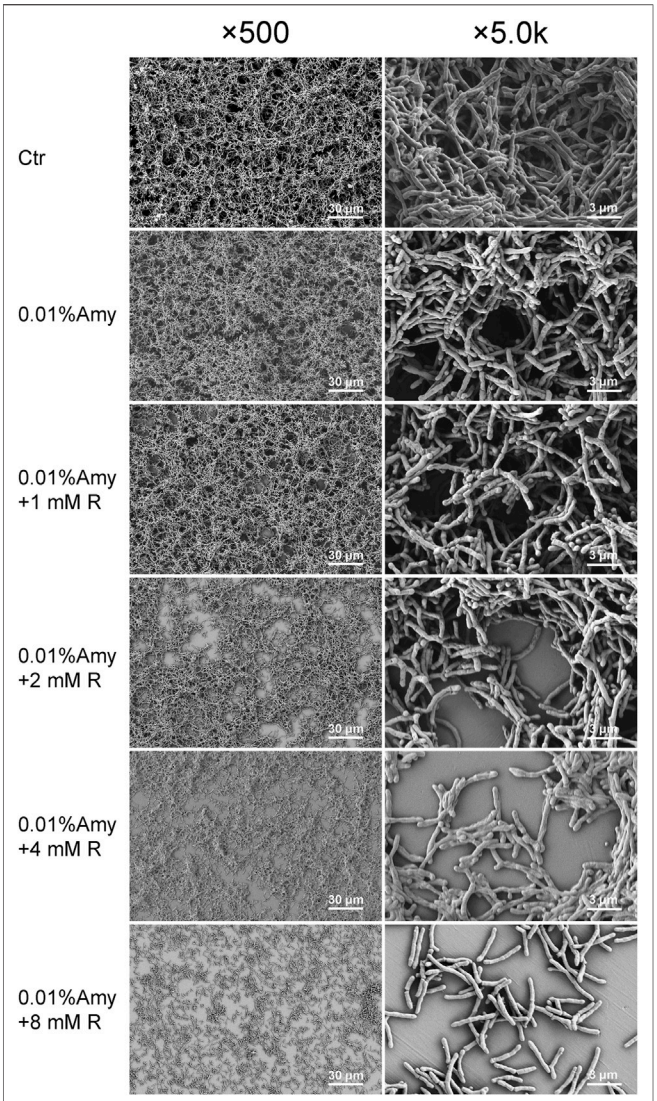

FIGURE 6 | Effects of Amy and R on *A. viscosus* biofilm morphology under SEM. The left column represents ×500 magnification, the right column represents ×5.0 k magnification. Scale bars: 30 μm in the left column, 3 μm in the right column. Ctr, control. Amy, α-amylase. R, D-arginine.

The surface to biovolume ratio of the 0.01% Amy + 8 mM R group was much higher than the control group and the 0.01% Amy group (**Figure 5E**).

A. viscosus Biofilm Morphology

As shown in **Figure 6**, the biofilm in the control group was compact and multi-layered. While 0.01% Amy seemed to loosen the biofilm. With the addition of R by gradient increase of concentrations, the integrity of biofilm was gradually disrupted and the thickness was also diminished. Particularly, the cells in 0.01% Amy + 8 mM R group tended to be sparse, and the extracellular matrix was elusive. The results were consistent with the analysis of CLSM (**Figure 5**).

Structure of *A. viscosus* Biofilm Extracellular Matrix

Figures 7A,D represent the biofilm in the control group, which shows that the extracellular matrix was relatively massive compared with the other groups. The black arrows show the extracellular matrix, and the black triangles indicate the EPS or extracellular matrix binding to the cell surface. **Figures 7B,E** represent the detached substances from the biofilm treated by 0.01% Amy + 8 mM R. The black arrows indicate the sparse detached substances, the volume of which was also much less than the control group. **Figures 7C,F** represent the biofilm remained on the plate after the treatment of 0.01% Amy + 8 mM R. Contrary to the first two groups, the extracellular matrix almost vanished. Few EPS that attached to cell surface were observed (black triangle). There were no profound differences in cell structure among the groups.

Analysis of Molecular Dynamics Simulations and Molecular Docking

MD simulations: **Figure 8A** represents each domain of Amy 1UA7, the calcium ion, and the maltotetraose. **Figure 8B** illustrates the Root-Mean-Square Deviation (RMSD) values of Amy and Amy + 10 R. During the MD simulation, the overall RMSD values of Amy + 10 R were lower than the Amy group, indicating that 10 R might play a pivotal role in stabilizing the structure of Amy. **Figure 8C** depicts the differences of Root-Mean-Square Fluctuation (RMSF) between Amy and Amy + 10 R. Higher fluctuations at residue GLN50 and GLY309-SER320 in Amy + 10 R implied that these flexibilities were affected by the binding to R. While the RMSF values of residue PHE105-ASN151 were decreased, which is the calcium-binding region in Domain B. Moreover, a subtle change in the active site ASP212 could be recognized. **Figure 8D** illustrates the distance changes between catalytic triad (ASP176, GLU208 and ASP269). After the addition of R, the distance between ASP176 and ASP269 was shortened from 11.5 Å to 10.0 Å, while the distance between GLU208 and ASP269 was shortened from 11.0 Å to 10.3 Å. **Figure 8E** shows the contacts between chains within 4.0 Å in the catalytic region of Amy + 10 R. R contacted with multiple residues, including catalytic sites ASP176 and ASP269. **Figure 8F** shows the contacts between chains within 4.0 Å in the two calcium-binding regions of Amy + 10 R. The putative defined calcium-binding sites were tightly in contact with R. The three-dimensional adjacent residues were also closely in contact with R. **Figure 8G** depicts the drastically altered conformation of flexibility at domain A, from GLY309 to SER320, indicating that the flexibility of Amy might be affected by R. **Supplementary Video S2** recorded the three-dimensional comparison of the structures from GLY309 to SER320 between Amy and Amy + 10 R. This conformational change was in line with the results of RMSF in **Figure 8C**.

Molecular docking: **Supplementary Figure S2** and **Supplementary Video S3** represent the position of maltotetraose in the binding pocket. **Figure 8H** illustrates the

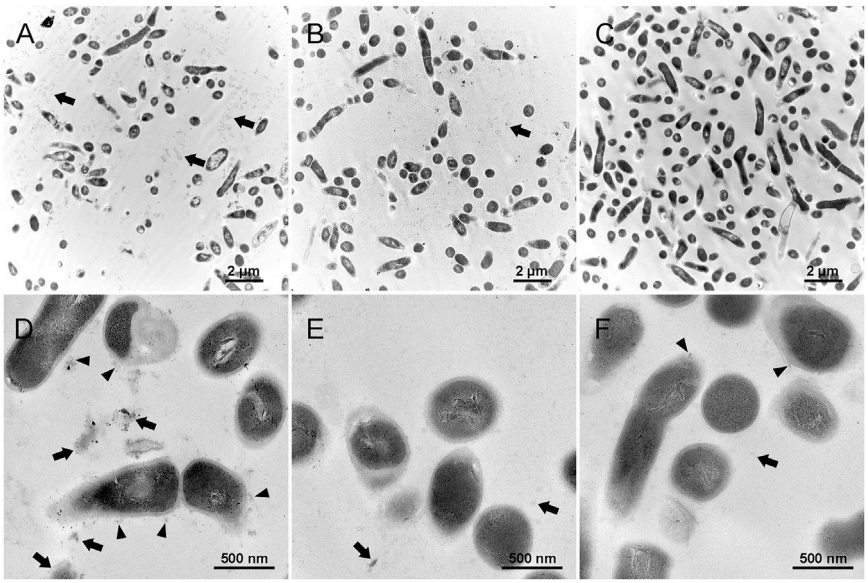

FIGURE 7 | Effects of 0.01% Amy + 8 mM R on the structure of *A. viscosus* biofilm extracellular matrix under TEM. **(A,D)** The extracellular matrix was relatively massive in the biofilm of the control group. The black arrows show the extracellular matrix, and the black triangles indicate the EPS or extracellular matrix binding to the cell surface. **(B,E)** The detached substances from the biofilm that treated by 0.01% Amy + 8 mM R. The black arrows indicate the sparse detached substances, which were much less than the control group. **(C,F)** The biofilm remained on the plate after the treatment of 0.01% Amy + 8 mM R. The extracellular matrix almost vanished, few EPS that attached to cell surface could be observed (black triangles). The black arrows indicate the few extracellular matrix. No profound difference in the cell structure exists among the groups. Scale bars: 2 μm in **(A–C)**, 500 nm in **(D–F)**.

superposition of the best pose of maltotetraose in complex with Amy as well as Amy + 10 R after molecular docking. The maltotetraose kept closer to the catalytic sites in Amy + 10 R than Amy, which might accommodate the maltotetraose in the binding pocket with more efficacy. The docking score of each conformation was drawn in **Figure 8I**. The highest absolute value of Amy and Amy + 10 R was 4.02 kcal/mol and 7.07 kcal/mol, respectively. While the lowest absolute value of Amy and Amy + 10 R was 0.25 kcal/mol and 5.16 kcal/mol, respectively.

DISCUSSION

This study investigated the effects of R on enhancing Amy disassembling *A. viscosus* biofilm, and elucidated the theoretical molecular mechanisms. 8 mM R could prominently enable 0.01% Amy to disassemble *A. viscosus* biofilm in 30 min without cytotoxicity, and 8 mM R performed better effects on enhancing Amy hydrolyzing starch than 60 ppm Ca^{2+}. Furtherly, the mechanisms for R enhancing Amy include R increased the overall stability of Amy and the activity of the catalytic triad, and R also increased the stability of calcium-binding sites.

Implants have been widely used in oral rehabilitation, artificial joints, bone fixators, and other bone-related fields (Hanawa, 2019). An untainted titanium surface is the guarantee of osseointegration (Buser et al., 2017). Nevertheless, biofilm-associated infections are the main cause of the early failure after implantation or for the PiM during the long-term period. Unlike other application fields, dental implants are threatened by bacterial infection for their whole period due to their contact with the multimicrobial oral environment. Plaque biofilm will accumulate around implant attributed to bad oral hygiene habits, food impaction, smoking, et al. Subsequently, the immune response is evoked, leading to soft tissue inflammation, bone resorption, and implant surface exposure (Fu and Wang, 2020). Hence, it is essential to eliminate biofilm to terminate the process of PiM and promote the regeneration of bone around the implants.

Eradicating bacterial biofilms has been a huge concern nowadays. However, the administration of conventional antimicrobial agents lacks efficiency since they fail to approach the massive bacteria encapsulated by the extracellular matrix (Koo et al., 2017). Thus, many studies reported effective antibiofilm agents capable of disrupting the extracellular matrix. Nanocarriers, designed positively charged, could be more likely to interact with the extracellular matrix (Fulaz et al., 2019). For instance, chitosan oligosaccharide-capped gold nanoparticles could eradicate mature *Pseudomonas aeruginosa* (*P. aeruginosa*) biofilm by electrostatic interactions (Khan et al., 2019). On the contrary, tobramycin, being positively charged, was blocked by the *P. aeruginosa* biofilm, while the neutrally charged ciprofloxacin could easily penetrate the biofilm (Tseng et al., 2013). These contradictory results indicate that nanocarriers could not penetrate biofilms with the pure electrostatic theory. Moreover, recent strategies of nanocarriers mainly focus on disrupting eDNA or proteins, not the more quantities of polysaccharides. PDT involves the use of photosensitizers, leading to the production of reactive oxygen

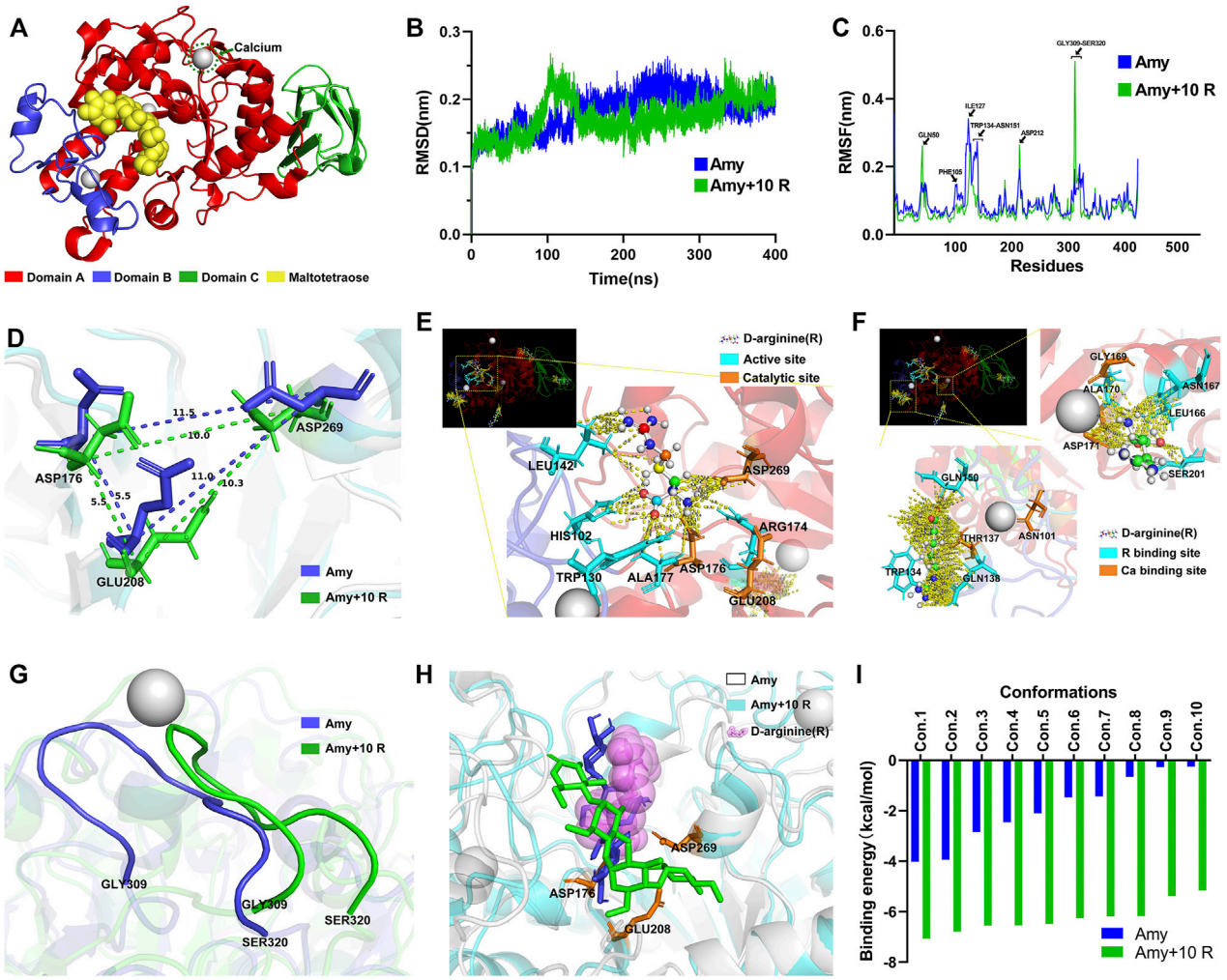

FIGURE 8 | Molecular dynamics simulations and molecular docking. **(A)** Full Amy 1UA7 structure. Domain A, Domain B, Domain C, calcium ions, and maltotetraose is represented in red, blue, green, gray, and yellow, respectively. **(B)** The RMSD values of Amy and Amy + 10 R during 400 ns of simulations. Amy in blue, Amy + 10 R in green. **(C)** The RMSF values of Amy and Amy + 10 R. The residues of GLN50, ASP212, and GLY309-SER320 showed greater fluctuations in Amy + 10 R, while the fluctuations of PHE105-ASN151 residues were drastically attenuated in Amy + 10 R. Amy in blue, Amy + 10 R in green. **(D)** The distances between catalytic triad in Amy and Amy + 10 R. **(E)** The contacts between chains within 4.0 Å in the catalytic region of Amy + 10 R, represented in yellow dotted lines. The R was preset as ball and stick. Active sites were labeled in cyan, catalytic triad was labeled in orange. **(F)** The contacts between chains within 4.0 Å in the calcium-binding regions of Amy + 10 R. The calcium-binding sites as well as adjacent residues were tightly in contact with R. The R was preset as ball and stick. R binding sites were labeled in cyan, calcium-binding sites were labeled in orange. **(G)** The drastically altered conformation of flexibility in domain A, from GLY309 to SER320. Amy in blue, Amy + 10 R in green. **(H)** The superposition of the best pose of maltotetraose in complex with Amy as well as Amy + 10 R after molecular docking. Amy in white, Amy + 10 R in cyan, maltotetraose docking with Amy in blue, maltotetraose docking with Amy + 10 R in green, R was represented as translucent magenta spheres. **(I)** The docking score of each conformation in Amy and Amy + 10 R. Amy in blue, Amy + 10 R in green. Amy, α-amylase. R, D-arginine. RMSD, Root-Mean-Square Deviation. RMSF, Root-Mean-Square Fluctuation.

species (ROS). ROS is considered to oxidize the cellular components, like lipids and DNA. In fact, ROS could also have the capability of attacking extracellular matrix molecules by disrupting the cell-to-cell and cell-to-matrix interactions, which causes the degradation of matrix structure (Li et al., 2013). Nonetheless, PDT also possesses the difficulty to penetrate the biofilm matrix easily and could not degrade the complex matrix rapidly (Pinto et al., 2020). Enzymes that possess the capability of degrading EPS, protein or eDNA could be employed as potential biofilm disruptive agents. Dispersin B is a well-known glycosyl hydrolase that could disrupt the major EPS of *Staphylococcus epidermidis* biofilms by specifically hydrolyzing poly-N-acetylglucosamine (Chen and Lee, 2018; Piarali et al., 2020). Deoxyribonuclease I (DNase I) is highlighted for antibiofilm purposes due to its effects on disrupting eDNA. For instance, DNase I efficiently increased vancomycin activity against the biofilm of *Enterococcus faecalis*, which could decrease the dosage of vancomycin by 8-fold (Torelli et al., 2017). In the present study, Amy showed significant effects on dispersing *A. viscosus* biofilm and hydrolyzing starch with the addition of R,

implying that the Amy + R might be an optimal compound for decontaminating the biofilm-contaminated implant surface.

The PiM-associated biofilm is a cluster of definite bacterium complex. Several studies have assessed bacterial adhesion and colonization on implant surfaces through simple biofilm models or multispecies biofilm models (Schmidt et al., 2017; Vilarrasa et al., 2018; Bermejo et al., 2019). Despite the diversity of bacterial strains, *Actinomyces* is the widely used species for its initial adherence on titanium surfaces as early as 15–20 min after incubation (Guggenheim et al., 2001; Schmidlin et al., 2013). Similarly, *Actinomyces* was selected in the present study to represent the most critical species in forming the biofilm of PiM. After 48 h of incubation, the biofilm expressed compact and multi-layered (**Figure 6**), consistent with the study of Yamane et al. (2013). Especially, there were porous micropores among the biofilm, which might facilitate the exchange of nutrients and gas. A previous study demonstrated that the major components of the EPS of *A. viscosus* were: N-acetylglucosamine (62%), galactose (7%), glucose (4%), uronic acid (3%) (Rosan and Hammond, 1974). Whereas another study revealed that 39% galactose, 37% N-acetylglucosamine, 19% glucose, and 5% mannose were the main components of EPS produced by *A. viscosus* (Imai and Kuramitsu, 1983). Theoretically, N-acetylglucosamines compose poly-N-acetylglucosamine by forming β-1,6 glycosidic bond, galactoses compose lactose by forming α/β-D-galactose residues, and glucan, starch, as well as cellulose could be composed of glucose either by α-1,4 glycosidic bond, or α-1,6 glycosidic bond or β-1,4 glycosidic bond. Therefore, in order to find the feasible glycoside hydrolases for hydrolyzing the above-mentioned glucosidic linkages, Dispersin B, α-galactosidase, β-galactosidase, dextranase, cellulase, and Amy were employed. Unexpectedly, merely Amy at supersaturated concentrations showed assumed results. Amy specifically endohydrolyzes the α-1,4-D-glucosidic linkages in polysaccharides containing three or more α-1,4-linked D-glucose units. Hence, we presume that the EPS of *A. viscosus* biofilm are mainly composed of polysaccharides containing α-1,4 glycosidic bond, which is inconsistent with previous studies (Rosan and Hammond, 1974; Imai and Kuramitsu, 1983). Fleming et al. showed that 0.25% Amy reduced the biomass of *Staphylococcus aureus* and *Pseudomonas aeruginosa* polymicrobial biofilms (Fleming et al., 2017). However, the saturation concentration of Amy is merely 0.01%, higher concentrations could lead to apparent cytotoxicity (**Figure 2**). As a consequence, 0.01% Amy was furtherly investigated.

Most thermostable amylases require the additional Ca^{2+} for their thermostability. For instance, 5 mM Ca^{2+} enhanced the relative activity (%) of α-Amy from 100 to 115% (Lin et al., 1998). 1, 5 and 10 mM Ca^{2+} enhanced the relative activity of α-Amy from 100 to 105, 109, and 116%, respectively (El-Banna et al., 2007). The mechanism might be that the binding of Ca^{2+} ions to the α-helical structure of α-Amy increases the overall stability of α-Amy. **Figure 4D** showed that the mean relative activity of 0.01% Amy was raised from 100 to 113.0% with the addition of 60 ppm Ca^{2+}, but the statistical difference was scant. Strikingly, 8 mM R dramatically increased the efficiency of Amy to 175%. Moreover, 60 ppm Ca^{2+} and 8 mM R showed a synergistic effect on enhancing the relative activity of Amy from 100 to 240%. These results indicate that R expresses a better effect than Ca^{2+} on enhancing Amy, and there is a synergistic mechanism between them. **Figure 8F** depicts the three-dimensional structure at the calcium-binding regions after MD simulations. There were massive hydrogen bonds between the residues of Amy and R. The formally defined calcium-binding sites also showed strong affinity with R. Additionally, the values of RMSF from PHE105 to ASN151 showed a sharp reduction with the addition of R (**Figure 8C**), which could be attributed to the firmly bonding interactions between R and Amy.

The results of CLSM are in line with SEM, both of them indicated that there remained few individual bacteria and sparse EPS after the treatment of 0.01% Amy + 8 mM R. Magdalena et al. reported that glycoside hydrolase ($PelA_h$) reduced the *Pseudomonas. aeruginosa* cells and polysaccharide elements, remained visible bacterial cells on the membrane (Szymanska et al., 2020). Similarly, minor *A. viscosus* could be observed on the plate in this study, whereas the remaining cells were bare without the enmeshing of extracellular matrix. Bacterium could adhere to biomaterials through capsular polysaccharides, fibronectin-binding proteins, collagen-binding adhesin, lipoteichoic acid, or other surface components (Arciola et al., 2018). Likewise, TEM showed the sparse extracellular matrix on the surface of the remaining cells (**Figure 7**). Hence, although the EPS of *A. viscosus* biofilm were entirely eliminated by Amy + R, the initial cells adhering to the surface could not be removed easily by Amy + R for their irreversible attachment *via* active adhesion (Carniello et al., 2018). It is worth noting that 0.01% Amy seemed to increase biofilm biomass (**Figure 5C**), which could be interpreted by the morphology of SEM (**Figure 6**). Briefly, after the treatment of 0.01% Amy, there was no notable reduction of biofilm, nevertheless, several cracks and huge cavities were created to form meshwork-like structures. As a consequence, the biofilm became looser and the volume increased accordingly. With the addition of 8 mM R, the EPS were hydrolyzed more evenly. **Figure 5E** demonstrated that the surface to biovolume ratio of 0.01% Amy + 8 mM R was much higher than the control group as well as 0.01% Amy group, facilitating the accessibility of antimicrobial agents contacting with the cell surface. Brendan revealed that glycoside hydrolase ($Sph3_h$) could potentiate the treating effects of posaconazole on *Aspergillus fumigatus via* disrupting the biofilm (Snarr et al., 2017), revealing the analogous mechanism with **Figure 5E**.

MD simulations predict how each atom in a protein or other molecular substance will move over time, based on experimental structural biology data (Karplus and McCammon, 2002). These simulations can capture a wide variety of important biomolecular processes, including protein folding, ligand binding, conformational changes, and revealing the positions of all the atoms at femtosecond temporal resolution (Hollingsworth and Dror, 2018). Hence, MD simulations could be exploited to determine how a biomolecular system will respond to some perturbation. A number of MD packages, such as CHARMM,

AMBER, GROMACS, and LAMMPS could be used to perform biological macromolecular simulations (Lee et al., 2016). Among them, however, GROMACS might be the fastest MD package for its huge codes constantly written by the developers. In addition, the GROMACS analysis facilities for post-processing trajectories are quite extensive, and many other tools could increase a researcher's productivity, regardless of the simulation package used. Thus, the total time to solution can be minimized by incorporating GROMACS in simulation and analysis (Vermaas et al., 2016). In this study, the molar concentration of R in parts 2.2–2.8 was 8 mM, while the molar concentration of Amy was about 6.4×10^{-5} mM. Therefore, the molecular amount of R was much higher than Amy. In order to optimize the MD simulation process for energy minimization, R was set decuple than Amy in part 2.9. The MD results showed that 6 R molecules interacted directly with Amy, the other four molecules were dissociated in the force field. PDB 1UA7 is a compound of Amy, containing 422 amino acids, from *Bacillus Subtilis* complexed with acarbose. The crystal structure of the Amy is divided into three distinct domains (**Figure 8A**), namely Domain A, Domain B, and Domain C. Domain A (PRO4-ILE100, THR152-LEU352) comprises the typical (α/β)8-Barrels, which is the catalytic domain. Domain B (ASN101-ASN151) is a short loop ring structure extending from Domain A, characterized to hold tightly to a calcium ion, thus being pivotal to the stability of protein. Domain C (SER353-ASP425) comprises a typical antiparallel β-sheet structure. McCorvy et al. (2018) showed that the modified indole-aripiprazole hybrid compounds uncovered the ligand egress of G protein-coupled receptors, indicating the positive response of the receptor to ligand. Dexamethasone privileged only a few poses for the glucocorticoid receptor, providing high rigidity to receptor-ligand complex, thus suitable for recognizing substrates (Alves et al., 2020). Likewise, the RMSD values were reduced and the absolute values of docking scores were significantly improved with the addition of 10 R, implying the potential functional changes of Amy affected by R. Metal-organic frameworks (MOFs) with the shortest inter active site distance (15.6 Å) showed the highest record apparent quantum efficiency in good accordance to biological systems, indicating that a smaller distance leads to higher activity (Gong et al., 2020). In the same vein, greater distances between the catalytic triad in mutant *Solanum tuberosum* resulted in the prevention of hydrogen bonding which is critical for catalytic activity (Hussain and Chong, 2017). In the present study, similarly, the distances between the catalytic triad were shortened by the binding of the catalytic region to R (**Figures 8D,E**), which consequently potentiated the catalytic activity of Amy. Flexibility is a key feature of proteins to maintain local changes in conformation (Hollingsworth and Dror, 2018). **Figure 8G** illustrates the most notable conformational change of Amy with the addition of R, corresponding with the highest peak in RMSF, implying that this random coil from GLY309 to SER320 might reflect the overall stability of Amy.

Comprehensively, based on the results of biofilm biomass, EPS hydrolysis, biofilm morphology, extracellular matrix structure, MD simulations, and molecular docking, 8 mM R could optimally enhance the disassembly effects of 0.01% Amy on *A. viscosus* biofilm. Still, there exist some limitations. For instance, the effects of Amy + R on the biofilms cultured on the titanium surface should be further investigated. In addition, the feasibility of Amy + R on treating multispecies biofilms should be verified in the next phase of development.

CONCLUSION

In summary, this study demonstrates that D-arginine may enhance the disassembly effects of alpha-amylase on *Actinomyces viscosus* biofilm through potentiating the catalytic triad as well as stabilizing the calcium-binding regions, thus providing a novel strategy for the decontamination of biofilm contaminated implant surface.

DATA AVAILABILITY STATEMENT

The raw data supporting the conclusion of this article will be made available by the authors, without undue reservation.

AUTHOR CONTRIBUTIONS

WM contributed to the conception and design of the study. BL performed the experiments and wrote the manuscript. QC and ZW performed the bacterial experiments. SQ and YO tested the cytotoxicity and analyzed the data. RM and CL performed the molecular dynamics simulations.

FUNDING

This research was financially supported by the Department of Science and Technology of Jilin Province, China (Grant No. 20200404108YY), and the Department of Finance of Jilin Province, China (Grant Nos. JCSZ2019378-3 and JCSZ2020304-15).

SUPPLEMENTARY MATERIAL

The Supplementary Material for this article can be found online at: https://www.frontiersin.org/articles/10.3389/fbioe.2022.864012/full#supplementary-material

REFERENCES

Abraham, M. J., Murtola, T., Schulz, R., Páll, S., Smith, J. C., Hess, B., et al. (2015). GROMACS: High Performance Molecular Simulations through Multi-Level Parallelism from Laptops to Supercomputers. *SoftwareX* 1-2, 19–25. doi:10.1016/j.softx.2015.06.001

Alves, N. R. C., Pecci, A., and Alvarez, L. D. (2020). Structural Insights into the Ligand Binding Domain of the Glucocorticoid Receptor: A Molecular Dynamics Study. *J. Chem. Inf. Model.* 60, 794–804. doi:10.1021/acs.jcim.9b00776

Arciola, C. R., Campoccia, D., and Montanaro, L. (2018). Implant Infections: Adhesion, Biofilm Formation and Immune Evasion. *Nat. Rev. Microbiol.* 16, 397–409. doi:10.1038/s41579-018-0019-y

Berglundh, T., Armitage, G., Araujo, M. G., Avila-Ortiz, G., Blanco, J., Camargo, P. M., et al. (2018). Peri-implant Diseases and Conditions: Consensus Report of Workgroup 4 of the 2017 World Workshop on the Classification of Periodontal and Peri-Implant Diseases and Conditions. *J. Periodontol.* 89, S313–S318. doi:10.1002/jper.17-0739

Bermejo, P., Sánchez, M. C., Llama-Palacios, A., Figuero, E., Herrera, D., and Sanz, M. (2019). Topographic Characterization of Multispecies Biofilms Growing on Dental Implant Surfaces: An *In Vitro* Model. *Clin. Oral Impl Res.* 30, 229–241. doi:10.1111/clr.13409

Buser, D., Sennerby, L., and De Bruyn, H. (2017). Modern Implant Dentistry Based on Osseointegration: 50 Years of Progress, Current Trends and Open Questions. *Periodontol. 2000* 73 (73), 7–21. doi:10.1111/prd.12185

Carniello, V., Peterson, B. W., Van Der Mei, H. C., and Busscher, H. J. (2018). Physico-chemistry from Initial Bacterial Adhesion to Surface-Programmed Biofilm Growth. *Adv. Colloid Interf. Sci.* 261, 1–14. doi:10.1016/j.cis.2018.10.005

Chen, K.-J., and Lee, C.-K. (2018). Twofold Enhanced Dispersin B Activity by N-Terminal Fusion to Silver-Binding Peptide for Biofilm Eradication. *Int. J. Biol. Macromolecules* 118, 419–426. doi:10.1016/j.ijbiomac.2018.06.066

Davey, M. E., and Duncan, M. J. (2006). Enhanced Biofilm Formation and Loss of Capsule Synthesis: Deletion of a Putative Glycosyltransferase in Porphyromonas Gingivalis. *J. Bacteriol.* 188, 5510–5523. doi:10.1128/jb.01685-05

Derks, J., and Tomasi, C. (2015). Peri-implant Health and Disease. A Systematic Review of Current Epidemiology. *J. Clin. Periodontol.* 42 (42 Suppl. l), S158–S171. doi:10.1111/jcpe.12334

El-Banna, T. E., Abd-Aziz, A. A., Abou-Dobara, M. I., and Ibrahim, R. I. (2007). Production and Immobilization of Alpha-Amylase from Bacillus Subtilis. *Pak J. Biol. Sci.* 10, 2039–2047. doi:10.3923/pjbs.2007.2039.2047

Elbourne, A., Cheeseman, S., Atkin, P., Truong, N. P., Syed, N., Zavabeti, A., et al. (2020). Antibacterial Liquid Metals: Biofilm Treatment via Magnetic Activation. *ACS Nano* 14, 802–817. doi:10.1021/acsnano.9b07861

Fleming, D., Chahin, L., and Rumbaugh, K. (2017). Glycoside Hydrolases Degrade Polymicrobial Bacterial Biofilms in Wounds. *Antimicrob. Agents Chemother.* 61, e01998. doi:10.1128/aac.01998-16

Flemming, H.-C., and Wingender, J. (2010). The Biofilm Matrix. *Nat. Rev. Microbiol.* 8, 623–633. doi:10.1038/nrmicro2415

Fu, J. H., and Wang, H. L. (2020). Breaking the Wave of Peri-Implantitis. *Periodontol. 2000* 84 (84), 145–160. doi:10.1111/prd.12335

Fulaz, S., Vitale, S., Quinn, L., and Casey, E. (2019). Nanoparticle-Biofilm Interactions: The Role of the EPS Matrix. *Trends Microbiol.* 27, 915–926. doi:10.1016/j.tim.2019.07.004

Gong, X., Shu, Y., Jiang, Z., Lu, L., Xu, X., Wang, C., et al. (2020). Metal-Organic Frameworks for the Exploitation of Distance between Active Sites in Efficient Photocatalysis. *Angew. Chem. Int. Ed.* 59, 5326–5331. doi:10.1002/anie.201915537

Guggenheim, B., Giertsen, E., Schüpbach, P., and Shapiro, S. (2001). Validation of an *In Vitro* Biofilm Model of Supragingival Plaque. *J. Dent Res.* 80, 363–370. doi:10.1177/00220345010800011201

Hanawa, T. (2019). Titanium-Tissue Interface Reaction and its Control with Surface Treatment. *Front. Bioeng. Biotechnol.* 7, 170. doi:10.3389/fbioe.2019.00170

Hasegawa, K., Kubota, M., and Matsuura, Y. (1999). Roles of Catalytic Residues in α-amylases as Evidenced by the Structures of the Product-Complexed Mutants of a Maltotetraose-Forming Amylase. *Protein Eng.* 12, 819–824. doi:10.1093/protein/12.10.819

Heydorn, A., Nielsen, A. T., Hentzer, M., Sternberg, C., Givskov, M., Ersbøll, B. K., et al. (2000). Quantification of Biofilm Structures by the Novel Computer Program COMSTAT. *Microbiology (Reading)* 146 (Pt 10) (Pt 10), 2395–2407. doi:10.1099/00221287-146-10-2395

Hollingsworth, S. A., and Dror, R. O. (2018). Molecular Dynamics Simulation for All. *Neuron* 99, 1129–1143. doi:10.1016/j.neuron.2018.08.011

Hussain, H., and Chong, N. F. M. (2017). Implications of Stisa2 Catalytic Residue Restoration through Site Directed Mutagenesis. *Turkish J. Biochemistry-Turk Biyokimya Dergisi* 42, 149–160. doi:10.1515/tjb-2016-0169

Imai, S., and Kuramitsu, H. (1983). Chemical Characterization of Extracellular Polysaccharides Produced by Actinomyces Viscosus T14V and T14Av. *Infect. Immun.* 39, 1059–1066. doi:10.1128/iai.39.3.1059-1066.1983

Kagawa, M., Fujimoto, Z., Momma, M., Takase, K., and Mizuno, H. (2003). Crystal Structure of Bacillus Subtilis α-Amylase in Complex with Acarbose. *J. Bacteriol.* 185, 6981–6984. doi:10.1128/jb.185.23.6981-6984.2003

Karplus, M., and Mccammon, J. A. (2002). Molecular Dynamics Simulations of Biomolecules. *Nat. Struct. Biol.* 9, 646–652. doi:10.1038/nsb0902-646

Khan, F., Lee, J.-W., Manivasagan, P., Pham, D. T. N., Oh, J., and Kim, Y.-M. (2019). Synthesis and Characterization of Chitosan Oligosaccharide-Capped Gold Nanoparticles as an Effective Antibiofilm Drug against the *Pseudomonas aeruginosa* PAO1. *Microb. Pathogenesis* 135, 103623. doi:10.1016/j.micpath.2019.103623

Kolenbrander, P. E. (2000). Oral Microbial Communities: Biofilms, Interactions, and Genetic Systems. *Annu. Rev. Microbiol.* 54, 413–437. doi:10.1146/annurev.micro.54.1.413

Koo, H., Allan, R. N., Howlin, R. P., Stoodley, P., and Hall-Stoodley, L. (2017). Targeting Microbial Biofilms: Targeting Microbial Biofilms: Current and Prospective Therapeutic Strategies. *Nat. Rev. Microbiol.* 15, 740–755. doi:10.1038/nrmicro.2017.99

Lasserre, J., Brecx, M., and Toma, S. (2020). Implantoplasty versus Glycine Air Abrasion for the Surgical Treatment of Peri-Implantitis: A Randomized Clinical Trial. *Int. J. Oral Maxillofac. Implants* 35, 197–206. doi:10.11607/jomi.6677

Lee, J., Cheng, X., Swails, J. M., Yeom, M. S., Eastman, P. K., Lemkul, J. A., et al. (2016). Charmm-Gui Input Generator for Namd, Gromacs, Amber, Openmm, and Charmm/Openmm Simulations Using the Charmm36 Additive Force Field. *J. Chem. Theor. Comput.* 12, 405–413. doi:10.1021/acs.jctc.5b00935

Li, X., Guo, H., Tian, Q., Zheng, G., Hu, Y., Fu, Y., et al. (2013). Effects of 5-aminolevulinic Acid-Mediated Photodynamic Therapy on Antibiotic-Resistant Staphylococcal Biofilm: an *In Vitro* Study. *J. Surg. Res.* 184, 1013–1021. doi:10.1016/j.jss.2013.03.094

Li, Y.-Y., Li, B.-S., Liu, W.-W., Cai, Q., Wang, H.-Y., Liu, Y.-Q., et al. (2020). Effects of D-Arginine on Porphyromonas Gingivalis Biofilm. *J. Oral Sci.* 62, 57–61. doi:10.2334/josnusd.19-0075

Lin, L. L., Chyau, C. C., and Hsu, W. H. (1998). Production and Properties of a Raw-Starch-Degrading Amylase from the Thermophilic and Alkaliphilic Bacillus Sp. TS-23. *Biotechnol. Appl. Biochem.* 28, 61–68.

Liu, S., Chen, M., Wang, Y., Zhou, X., Peng, X., Ren, B., et al. (2020). Effect of Veillonella Parvula on the Physiological Activity of Streptococcus Mutans. *Arch. Oral Biol.* 109, 104578. doi:10.1016/j.archoralbio.2019.104578

Liu, Y., Shi, L., Su, L., Van Der Mei, H. C., Jutte, P. C., Ren, Y., et al. (2019). Nanotechnology-based Antimicrobials and Delivery Systems for Biofilm-Infection Control. *Chem. Soc. Rev.* 48, 428–446. doi:10.1039/c7cs00807d

Lukic, D., Karygianni, L., Flury, M., Attin, T., and Thurnheer, T. (2020). Endodontic-Like Oral Biofilms as Models for Multispecies Interactions in Endodontic Diseases. *Microorganisms* 8, 674. doi:10.3390/microorganisms8050674

Mccorvy, J. D., Butler, K. V., Kelly, B., Rechsteiner, K., Karpiak, J., Betz, R. M., et al. (2018). Structure-inspired Design of β-arrestin-biased Ligands for Aminergic GPCRs. *Nat. Chem. Biol.* 14, 126–134. doi:10.1038/nchembio.2527

Naumoff, D. G. (2011). Hierarchical Classification of Glycoside Hydrolases. *Biochem. Mosc.* 76, 622–635. doi:10.1134/s0006297911060022

Piarali, S., Marlinghaus, L., Viebahn, R., Lewis, H., Ryadnov, M. G., Groll, J., et al. (2020). Activated Polyhydroxyalkanoate Meshes Prevent Bacterial Adhesion and Biofilm Development in Regenerative Medicine Applications. *Front. Bioeng. Biotechnol.* 8, 442. doi:10.3389/fbioe.2020.00442

Pinto, R. M., Soares, F. A., Reis, S., Nunes, C., and Van Dijck, P. (2020). Innovative Strategies toward the Disassembly of the EPS Matrix in Bacterial Biofilms. *Front. Microbiol.* 11, 952. doi:10.3389/fmicb.2020.00952

Rabin, N., Zheng, Y., Opoku-Temeng, C., Du, Y., Bonsu, E., and Sintim, H. O. (2015). Biofilm Formation Mechanisms and Targets for Developing Antibiofilm Agents. *Future Med. Chem.* 7, 493–512. doi:10.4155/fmc.15.6

Rosan, B., and Hammond, B. F. (1974). Extracellular Polysaccharides of Actinomyces Viscosus. *Infect. Immun.* 10, 304–308. doi:10.1128/iai.10.2.304-308.1974

Schmidlin, P. R., Müller, P., Attin, T., Wieland, M., Hofer, D., and Guggenheim, B. (2013). Polyspecies Biofilm Formation on Implant Surfaces with Different Surface Characteristics. *J. Appl. Oral Sci.* 21, 48–55. doi:10.1590/1678-7757201302312

Schmidt, K. E., Auschill, T. M., Heumann, C., Frankenberger, R., Eick, S., Sculean, A., et al. (2017). Influence of Different Instrumentation Modalities on the Surface Characteristics and Biofilm Formation on Dental Implant Neck,*In Vitro*. *Clin. Oral Impl. Res.* 28, 483–490. doi:10.1111/clr.12823

Snarr, B. D., Baker, P., Bamford, N. C., Sato, Y., Liu, H., Lehoux, M., et al. (2017). Microbial Glycoside Hydrolases as Antibiofilm Agents with Cross-Kingdom Activity. *Proc. Natl. Acad. Sci. USA* 114, 7124–7129. doi:10.1073/pnas.1702798114

Szymańska, M., Karakulska, J., Sobolewski, P., Kowalska, U., Grygorcewicz, B., Böttcher, D., et al. (2020). Glycoside Hydrolase ($PelA_h$) Immobilization Prevents *Pseudomonas aeruginosa* Biofilm Formation on Cellulose-Based Wound Dressing. *Carbohydr. Polym.* 246, 116625. doi:10.1016/j.carbpol.2020.116625

Torelli, R., Cacaci, M., Papi, M., Paroni Sterbini, F., Martini, C., Posteraro, B., et al. (2017). Different Effects of Matrix Degrading Enzymes towards Biofilms Formed by E. faecalis and E. Faecium Clinical Isolates. *Colloids Surf. B: Biointerfaces* 158, 349–355. doi:10.1016/j.colsurfb.2017.07.010

Tseng, B. S., Zhang, W., Harrison, J. J, Quach, TP, Song, JL, Penterman, J, et al. (2013). The extracellular matrix protects Pseudomonas aeruginosa biofilms by limiting the penetration of tobramycin. *Environ Microbiol* 15, 2865–78. doi:10.1111/1462-2920.12155

Vermaas, J. V., Hardy, D. J., Stone, J. E., Tajkhorshid, E., and Kohlmeyer, A. (2016). TopoGromacs: Automated Topology Conversion from CHARMM to GROMACS within VMD. *J. Chem. Inf. Model.* 56, 1112–1116. doi:10.1021/acs.jcim.6b00103

Vilarrasa, J., Delgado, L. M., Galofré, M., Àlvarez, G., Violant, D., Manero, J. M., et al. (2018). *In vitro* evaluation of a multispecies oral biofilm over antibacterial coated titanium surfaces. *J Mater Sci: Mater Med* 29, 164. doi:10.1007/s10856-018-6168-8

Vyas, N., Grewal, M., Kuehne, S. A., Sammons, R. L., and Walmsley, A. D. (2020). High speed imaging of biofilm removal from a dental implant model using ultrasonic cavitation. *Dental Materials* 36, 733–743. doi:10.1016/j.dental.2020.03.003

Wu, Y., Xu, L., Yin, Z., Feng, H., and Huang, L. (2018). Transcription factor VmSeb1 is required for the growth, development, and virulence in Valsa mali. *Microbial Pathogenesis* 123, 132–138. doi:10.1016/j.micpath.2018.06.043

Yamane, K., Nambu, T., Yamanaka, T., Ishihara, K., Tatami, T., Mashimo, C., et al. (2013). Pathogenicity of exopolysaccharide-producingActinomyces orisisolated from an apical abscess lesion. *Int Endod J* 46, 145–154. doi:10.1111/j.1365-2591.2012.02099.x

You, T.-M., Choi, B.-H., Zhu, S.-J., Jung, J.-H., Lee, S.-H., Huh, J.-Y., et al. (2007). Treatment of Experimental Peri-Implantitis Using Autogenous Bone Grafts and Platelet-Enriched Fibrin Glue in Dogs. *Oral Surg. Oral Med. Oral Pathol. Oral Radiol. Endodontology* 103, 34–37. doi:10.1016/j.tripleo.2006.01.005

Zhang, Z., Li, B., Cai, Q., Qiao, S., Wang, D., Wang, H., et al. (2021). Synergistic Effects of D-Arginine, D-Methionine and D-Histidine against Porphyromonas Gingivalis Biofilms. *Biofouling* 37, 222–234. doi:10.1080/08927014.2021.1893309

Conflict of Interest: The authors declare that the research was conducted in the absence of any commercial or financial relationships that could be construed as a potential conflict of interest.

Publisher's Note: All claims expressed in this article are solely those of the authors and do not necessarily represent those of their affiliated organizations, or those of the publisher, the editors and the reviewers. Any product that may be evaluated in this article, or claim that may be made by its manufacturer, is not guaranteed or endorsed by the publisher.

frontiers | Frontiers in Bioengineering and Biotechnology

REVIEW
published: 04 May 2022
doi: 10.3389/fbioe.2022.899760

Chitosan-Based Biomaterial Scaffolds for the Repair of Infected Bone Defects

*Yuhang Tian[1], Danhua Wu[2], Dankai Wu[1], Yutao Cui[1], Guangkai Ren[1], Yanbing Wang[1], Jincheng Wang[1] and Chuangang Peng[1]**

[1]Orthopedic Medical Center, The Second Hospital of Jilin University, Changchun, China, [2]The People's Hospital of Chaoyang District, Changchun, China

OPEN ACCESS

Edited by:
Jianxun Ding,
Changchun Institute of Applied Chemistry (CAS), China

Reviewed by:
Ahmed El-Fiqi,
Dankook University, South Korea
Gu Hailun,
China Medical University, China
Thomas Webster,
Interstellar Therapeutics, United States
Monica Mattioli-Belmonte,
Marche Polytechnic University, Italy
Hua Chen,
Fourth Medical Center of PLA General Hospital, China
Atakan Tevlek,
Middle East Technical University, Turkey

***Correspondence:**
Chuangang Peng
pengcg@jlu.edu.cn

Specialty section:
This article was submitted to Biomaterials, a section of the journal Frontiers in Bioengineering and Biotechnology

Received: 19 March 2022
Accepted: 20 April 2022
Published: 04 May 2022

Citation:
Tian Y, Wu D, Wu D, Cui Y, Ren G, Wang Y, Wang J and Peng C (2022) Chitosan-Based Biomaterial Scaffolds for the Repair of Infected Bone Defects. Front. Bioeng. Biotechnol. 10:899760. doi: 10.3389/fbioe.2022.899760

The treatment of infected bone defects includes infection control and repair of the bone defect. The development of biomaterials with anti-infection and osteogenic ability provides a promising strategy for the repair of infected bone defects. Owing to its antibacterial properties, chitosan (an emerging natural polymer) has been widely studied in bone tissue engineering. Moreover, it has been shown that chitosan promotes the adhesion and proliferation of osteoblast-related cells, and can serve as an ideal carrier for bone-promoting substances. In this review, the specific molecular mechanisms underlying the antibacterial effects of chitosan and its ability to promote bone repair are discussed. Furthermore, the properties of several kinds of functionalized chitosan are analyzed and compared with those of pure chitosan. The latest research on the combination of chitosan with different types of functionalized materials and biomolecules for the treatment of infected bone defects is also summarized. Finally, the current shortcomings of chitosan-based biomaterials for the treatment of infected bone defects and future research directions are discussed. This review provides a theoretical basis and advanced design strategies for the use of chitosan-based biomaterials in the treatment of infected bone defects.

Keywords: chitosan, bone defect, hydrogel, antibacterial, scaffold

1 INTRODUCTION

Bone defects caused by infection pose a great challenge to orthopedic surgeons (Cui et al., 2017). Although bone tissue exhibits self-healing ability, infection with a pathogen may seriously impair the regeneration process (Dreifke et al., 2013). The current clinical treatment of infected bone defects includes infection control and local reconstruction of the defect. Infection control requires surgical debridement of necrotic and infected tissue, followed by extensive treatment with systemic antibiotics. Nevertheless, long-term systemic antibiotic therapy may lead to the development of resistance and side effects affecting organs. Moreover, antibiotics cannot reach the osteomyelitis site at a sufficient concentration, resulting in limited efficacy and poor patient compliance (Orhan et al., 2006). For the reconstruction of local bone defects, autografts, allografts, masquelet membrane induction technology, and bone transfer technology are currently the most effective methods (Cui et al., 2017; Ye et al., 2018a; Shao et al., 2018). However, they are also associated with problems, such as the need for extra surgery, increased hospitalization time, donor site morbidity, and the

occurrence of stress fractures (Keller et al., 2017; Radwan et al., 2020). Therefore, the development of new biomaterials to replace traditional therapeutic methods has become a research hotspot in recent years (Topsakal et al., 2018).

The design and development of a variety of bioactive materials with antimicrobial functions, such as chitosan (CS), silver nanoparticles, magnesium oxide and bioactive glass, have provided a new and promising direction for the treatment of infected bone defects (Galarraga-Vinueza et al., 2017; Shuai et al., 2017). Currently, synthetic and natural materials are commonly used in this setting. These materials offer the advantages of biocompatibility and biodegradability, high porosity, as well as the ability to effectively induce new bone formation (Abueva et al., 2017). Among natural materials, CS (an emerging biological material) has been increasingly used in bone tissue engineering due to its biological and structural similarities with natural tissues (Mostafa et al., 2017).

CS is a biodegradable and biocompatible natural polymer mainly produced by acetylation of chitin, one of the most abundant polysaccharides in nature obtained from the exoskeleton of crustaceans (Kjalarsdóttir et al., 2019; Saravanan et al., 2019). It has a natural polysaccharide structure similar to that of glycosaminoglycan sulfate, which is one of the main components of collagen fibers in the extracellular matrix (ECM). This feature enables CS to provide a microenvironment for cell proliferation and ECM, and has the potential to promote bone formation (Yu et al., 20132013; Zang et al., 2017). Owing to the positive charge on its amino group, CS can bind to the cell membrane, thereby providing the appropriate conditions for cell adhesion (Deepthi et al., 2016; Tang et al., 2020). Moreover, following the depolymerization of CS, chitooligosaccharides with biological activity and improved antibacterial properties are produced. Its monomer product (glucosamine) can be metabolized or excreted from the body (Aam et al., 2010); it also promotes wound healing and hemostasis and reduces inflammation (Shi et al., 2010). In addition, CS can be modified by quaternization, carboxylation, sulfation, and phosphorylation to improve its solubility, antibacterial properties, and chelating ability. It can also be combined with organic materials to improve its biocompatibility and biodegradability, as well as inorganic materials to improve its antibacterial properties. This flexibility renders CS a promising new material for the treatment of infected bone defects (Shin et al., 2005; Venkatesan et al., 2014; Zhou et al., 2017). Given the above properties, numerous studies have investigated the application of CS-based biomaterials for the treatment of infection and promotion of osteogenesis. These studies have demonstrated the ability of CS to induce the repair of infected bone defects (Shi et al., 2010; Covarrubias et al., 2018).

In this review, we discuss the specific mechanisms underlying the antibacterial properties and osteoconductivity of CS. Also, the advanced strategy for improving these functions of CS, which is essential for the application of CS-based biomaterials, is analyzed. Furthermore, considering the different material forms, we summarize the various existing CS-based biomaterial scaffolds utilized in the treatment of infected bone defects (**Scheme 1**). Finally, the shortcomings of CS in bone tissue engineering and the prospects of its derivatives and composite materials in medical applications are discussed. This review provides an advanced strategy and theoretical basis for the treatment of infected bone defects with CS-based biomaterials.

2 FUNCTIONALITY OF CS FOR INFECTED BONE DEFECTS

2.1 Chemical Structure

CS is derived from chitin and is a linear, semi-crystalline polysaccharide composed of (1→4)-2-acetamido -2-deoxy-b-D-glucan (N-acetyl D-glucosamine) and (1→4)-2-amino-2-deoxy-β-D-glucan (D-glucosamine) units (Deepthi et al., 2016; Islam et al., 2016). CS can be prepared by deacetylation of NaOH and borohydride, or it can be deacetylated by sophisticated grinding of chitin powder. After deacetylation into CS, the viscosity of CS was increased. In addition, the reaction conditions are mild, and the methods are environment-friendly and low cost (Muzzarelli et al., 2014). Through deacetylation, the acetamide group in chitin is converted to the primary amine group to produce CS. The structure of CS is similar to that of cellulose. However, different from cellulose, the hydroxyl group of cellulose C-2 is replaced by the acetamide group in the structure of CS. Due to the effect of the $-NH_2$ group at the C2 position, the polymer can be dissolved in acidic solutions; however, the solubility in water is poor. This hydrophobicity is determined by the main polysaccharide chain and the N-acetyl group at the C2 position (Tao et al., 2020a).

The deacetylation degree (DD) is often used to express the number of amino groups in CS; only a DD >60% denotes the production of CS from chitin (Croisier and Jérôme, 2013). CS is the only positively charged polysaccharide in nature, and its charge density depends on the DD and pH values. The DD also has an impact on the biocompatibility of CS. For instance, a higher DD increases the number of positive charges and the interaction between CS and cells, resulting in improved biocompatibility (Kadouche et al., 2016; Aguilar et al., 2019).

2.2 Antibacterial Property

As mentioned above, two cationic units constitute the main part of CS. The different proportions of these units affect the molecular weight (MW), DD, and acetylation mode of CS, and determine the strength of its antibacterial properties (Tan et al., 2014). As an antibacterial material, CS has inherent activity and high effectiveness against a variety of bacteria, such as *Escherichia coli* (*E. coli*) and *Staphylococcus aureus* (*S. aureus*), as well as filamentous fungi and yeast (Li and Zhuang, 2020). The antibacterial properties of CS mainly include three aspects. Firstly, the positively charged CS molecule reacts with the negatively charged bacterial molecule on the cell surface. This reaction changes the permeability of the cell, prevents the entry of the substance into the cell or leakage of the substance from the cell, and inhibits its metabolism. This process results in bacterial death (Raafat et al., 2008). Secondly, CS can bind to bacterial DNA and inhibit the synthesis of proteins expressed by bacterial genes. It can also adsorb electronegative substrates in microbial protein cells to disrupt the physiological activities of microorganisms and lead to cell death (Fei Liu et al., 2001). Thirdly, through the metal chelation mechanism, CS inhibits the absorption of basic elements required for the growth of microorganisms and combines the metal ions required by microorganisms to achieve the purpose of antibiosis (Chung et al., 2011).

The antibacterial properties of CS are dose-dependent and influenced by pH. This is because CS can be dissolved only in

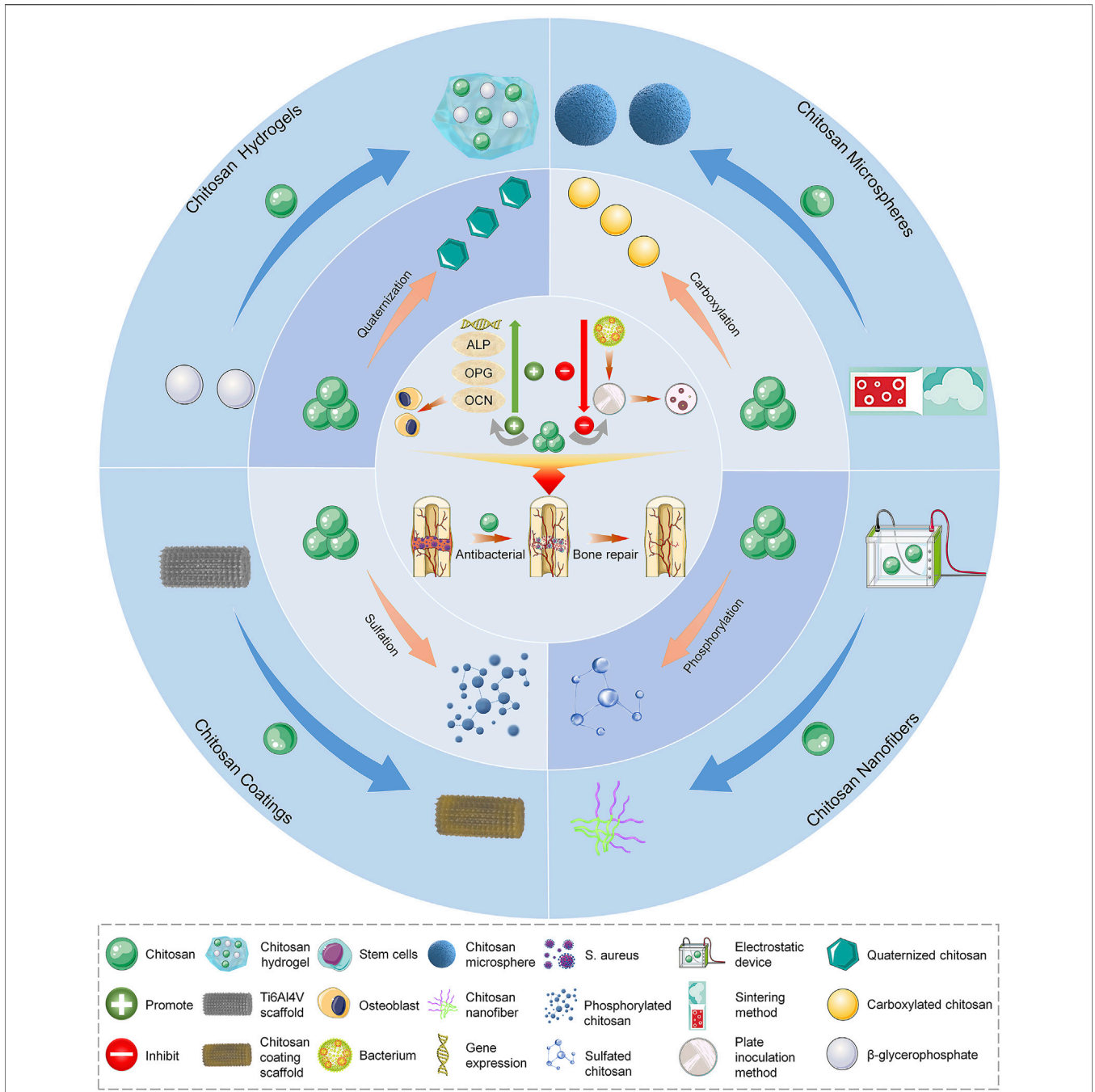

SCHEME 1 | Repair of infected bone defects with different forms and modification methods of chitosan. ALP, alkaline phosphatase; OCN, osteocalcin; OPG, osteoprotegerin; *S. aureus*, *Staphylococcus aureus*.

acidic solutions and becomes polycationic when the pH is < 6.5 (Lim and Hudson, 2004). Ultra-high-MW CS (MW > 10^6) with different DD (range: 51.04–100%) have been used to test the antibacterial performance against *E. coli* and *S. aureus*. The results showed that CS had stronger antibacterial activity under acidic conditions versus neutral and alkaline conditions. Importantly, it demonstrated its best antibacterial activity when the pH was 6, due to the formation of cation NH^{3+} by the amino groups in CS through protonation under acidic conditions. Under the condition of pH 6.0, the antibacterial activity of CS was gradually increased in parallel with the increase in the DD (Li et al., 2016). Moreover, CS exhibits varied antibacterial activity against different strains. The negative charge on the surface of Gram-negative bacteria is higher than that of Gram-positive bacteria, thereby increasing the adsorption of CS on the surface. Peptidoglycan and phosphoric acid are also present in

the cell membrane of Gram-positive bacteria. Therefore, the inhibitory effect of CS on Gram-negative bacteria is stronger than that observed against Gram-positive bacteria (Chung et al., 2004; Rashki et al., 2021). Temperature can also affect the antibacterial property of CS. In the range of 4–37°C, the inhibitory effect of chitosan on *E. coli* will augment with the increase of temperature. This is due to the influence of low temperature on the binding sites of chitosan and cells (Tsai and Su, 1999). Moreover, the temperature also affects the MW of CS, and the antibacterial activity of CS with different MW is also different (Li and Zhuang, 2020). When the MW is below 300 kDa, with the increase of MW, the inhibitory effect of CS on *S. aureus* is enhanced, but the phenomenon of *E. coli* is just the opposite. The inhibition mechanism of CS with high MW and low MW is different. CS with high MW forms a film on the surface of *S. aureus*, which hinders its nutrient absorption, while low MW of CS directly enters the cells of *E. coli* and disturbs cell metabolism (Zhang and Zhu, 2003).

2.3 Bone Repair Promotion

The repair of bone defects depends on many factors, such as the proliferation of bone progenitor cells and bone growth factors (Wang et al., 2018a; Munhoz et al., 2018). In bone tissue engineering, bone substitutes play an important role in supporting cell adhesion, growth, and proliferation at the injury site. As mentioned above, CS is similar to the natural ECM component glycosaminoglycan, which creates a local microenvironment for cell growth and supports the proliferation, differentiation, and mineralization of osteoblasts (Pattnaik et al., 2011). Cell adhesion to CS depends on the DD; higher DD values are linked to greater cell adhesion to the surface (Mao et al., 2004). *In vitro* studies have shown that CS can promote the adhesion and proliferation of osteoblasts and mesenchymal stem cells (MSC). Electrical stimulation and electroactivity improve the proliferation and differentiation of electrically signal-sensitive cells, such as osteoblasts (Zhao et al., 2015). Through its osteoconductivity property, CS can effectively respond to this electrical stimulation effect, thus promoting the proliferation of osteoblasts. Co-culture of adipose mesenchymal stem cells (AD-MSC) and human umbilical vein endothelial cells (HUVEC) in a CS scaffold promoted the expression of CD31 in HUVEC and osteogenic differentiation of AD-MSC following electrical stimulation (Zhang et al., 2018). In addition, the osteogenic ability can be further enhanced by combining CS with hydroxyapatite (HA). This approach interferes with the mineralization process and osteogenesis signal pathway in response to electrical stimulation (Oftadeh et al., 2018). Moreover, CS can also enhance the growth of human bone marrow mesenchymal stem cells (BMSC) by promoting the expression of genes related to osteogenesis and calcium-binding proteins, such as type I collagen, integrin-binding saliva protein, osteopontin (OPN), osteonectin (ON), and osteocalcin (OCN) (Mathews et al., 2011). In addition to the influence of MSC, the scaffolds prepared by mixing CS and bioactive glass in different proportions do not have negative influence on the cell activity of stem cells derived from periosteum, but also promote the osteogenic activity. Moreover, due to the existence of bioactive glass, the mechanical properties of the composite scaffold have been improved (Gentile et al., 2012). It also has been found that CS nanofibrous scaffolds increase the proliferation and DNA replication of human osteoblasts and induce the expression of alkaline phosphatase (ALP) mRNA (Ho et al., 2014). In addition, studies have shown that N-acetylglucosamine (the degradation product of CS) can promote osteoblast activity and fibrous callus formation, and significantly shorten the healing time of bone defects. It may also be related to the increase in the expression of bone morphogenetic protein (BMP) induced by N-acetylglucosamine (Nagel et al., 2013). CS molecules contain a large number of amino groups. Hence, protonation can occur under acidic conditions. This process leads to interaction with various negatively charged proteins and glycolipids on the surface of red blood cells, increased blood viscosity, and activation of platelet adhesion (Fan et al., 2015). Aggregation enhances the transport of platelets to the blood vessel wall to achieve physiological hemostasis and promote angiogenesis (Kyzas and Bikiaris, 2015). In addition, by freeze-drying method, platelet-rich plasma (PRP) can be added to the CS gel scaffold, this scaffold can be used as a carrier to deliver PRP, realizing the controlled release of growth factors in it. Moreover, PRP contributes to the formation of hydrogel, promotes cell adhesion, proliferation and differentiation, and further enhances osteogenesis and angiogenesis (Busilacchi et al., 2013). Therefore, CS can promote blood vessel formation, thereby enhancing bone repair (Saran et al., 2014).

Moreover, the CS scaffold has both osteoconductivity and biodegradability at the bone defect site, which are the advantages associated with its application in the treatment of local bone defects (Mathews et al., 2011). Therefore, in bone tissue engineering, CS is typically used as an osteoconductive material in combination with other materials to further promote bone regeneration. These biological materials include metal ions, nano-hydroxyapatite (nano-HA), graphene oxide, bioglasses, and biologically active substances, such as growth factors, BMP2, as well as other combinations (Gentile et al., 2012; Jayash et al., 2017a; López Tenorio et al., 2019; Koski et al., 2020). Mixing CS/gelatin scaffold with graphene oxide promotes osteoblast differentiation, augments protein adsorption, mineralization and degradability, and promotes the healing of tibial bone defects (Saravanan et al., 2017). Bioactive glass is non-toxic and has no inflammatory reaction when implanted *in vivo*, and its degradation products can promote cell proliferation and activate osteoblast gene expression. The addition of HA and nano-bioactive glass to the CS/gelatin significantly improved the adhesion and proliferation of MG-63 osteoblast-like cells (Peter et al., 2010). Therefore, CS by itself or in combination with other materials to further improve bone repair performance also promotes bone healing to a certain extent.

3 MODIFICATION OF CS FOR IMPROVEMENT OF PROPERTIES

Although CS has good biocompatibility, its solubility in most solvents is poor (i.e., in neutral or high pH solutions), which markedly limits its application (Zang et al., 2017). Moreover, CS is rapidly degraded *in vivo* (Tan et al., 2013). The above characteristics compromise the ability of CS to fully exert its

TABLE 1 | Summary of chemical structure, advantages, disadvantages, and main findings of chitosan and its derivatives.

Chitosan and Derivatives	Chemical Structures	Advantages	Disadvantages	Main Findings	References
CS	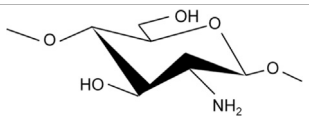	Antibacterial, osteoconductivity, low cost, biocompatibility, biodegradability	Poor water solubility, minimal osteoinductive ability under neutral and alkaline conditions	Promote the proliferation of human osteoblasts by promoting the expression of OPN, OCN and ALP genes	Ho et al. (Ho et al., 2014), Ye et al. (Ye et al., 2018b)
TMC	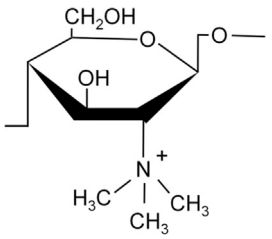	Better water solubility than CS in a wide pH range, enhanced antibacterial and absorption properties	Cytotoxicity at high molecular weight and high degree of substitution	Delivery of osteoprogenitor cells as one of the components of periosteum-mimetic scaffolds	Wu et al. (Wu et al., 2016), Romero et al. (Romero et al., 2015)
HACC	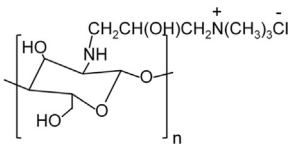	Better antibacterial and water solubility than CS in a wide pH range	Cytotoxicity at medium degree of substitution	Combining with 3D printed scaffolds showed dual functions of antibacterial and osteogenesis both *in vitro* and *in vivo*	Yang et al. (Yang et al., 2016), Yang et al. (Yang et al., 2018)
CMC	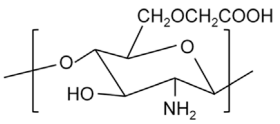	Higher antibacterial activity compared to CS, good water solubility	Mechanical properties may be insufficient	Combining with copper-containing scaffolds to promote bone repair and remove bacteria	Lu et al. (Lu et al., 2018), Shi et al. (Shi et al., 2009)
SCS	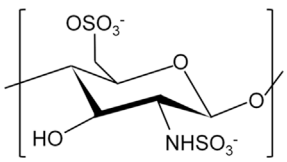	Low cytotoxicity, structure similar to heparin, which enhanced the bioactivity of BMP2	Osteogenic properties may be insufficient when used alone	As a carrier to enhance BMP2 activity, promoting osteoblast proliferation *in vitro* and new bone formation *in vivo*	Zhou et al. (Zhou et al., 2009), Cao et al. (Cao et al., 2014)
PCS	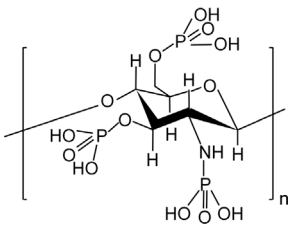	Water solubility with a high degree of substitution, improving mineralization ability by chelating Ca^{2+}	Poor antibacterial property	Repair of rabbit ulna defect as a composite scaffold for promoting osteogenesis and inhibiting bone resorption	Tang et al. (Tang et al., 2011), Chen et al. (Chen et al., 2017)

effect. Therefore, an increasing number of studies have focused on introducing groups into the side chain of CS or modifying it by copolymerization with polymers to comprehensively improve its activity. The currently used chemical modification methods for CS mainly include quaternization, carboxylation, sulfation, and phosphorylation (Wu et al., 2016). Here, we summarize the advantages of modified CS and its application in the treatment of infected bone defects (**Table 1**).

3.1 Quaternized CS (QCS)

QCS is prepared by introducing quaternary ammonium groups into the dissociated hydroxyl or amino groups of CS (Ji et al., 2009). Compared with CS, QCS has increased water solubility and a permanent positive charge. There are two common types of QCS, namely N-(2-hydroxyl)propyl-3-trimethylammonium chitosan chloride (HACC) and N,N,N-trimethyl chitosan (TMC) (LogithKumar et al., 2016; Wang et al., 2018b). HACC is composed of CS and glycidyl trimethylammonium chloride dissolved in distilled water at 80°C and subsequently concentrated and lyophilized. TMC is formed by CS and methyl iodine under the catalysis of sodium hydroxide at 60°C (Yang et al., 2015). Other types of QCS include N-(2-hydroxyl) propyl-3-triethylammonium CS chloride and N-(2-hydroxyl-phenyl)-N,N-dimethyl CS (Yang et al., 2015).

3.1.1 HACC

HACC is a commonly used biomaterial for the treatment of infected bone defects. It has exhibited strong antibacterial activity against *E. coli* and *S. aureus* (Tan et al., 2013). Different proportions of CS and glycidyl trimethylammonium chloride

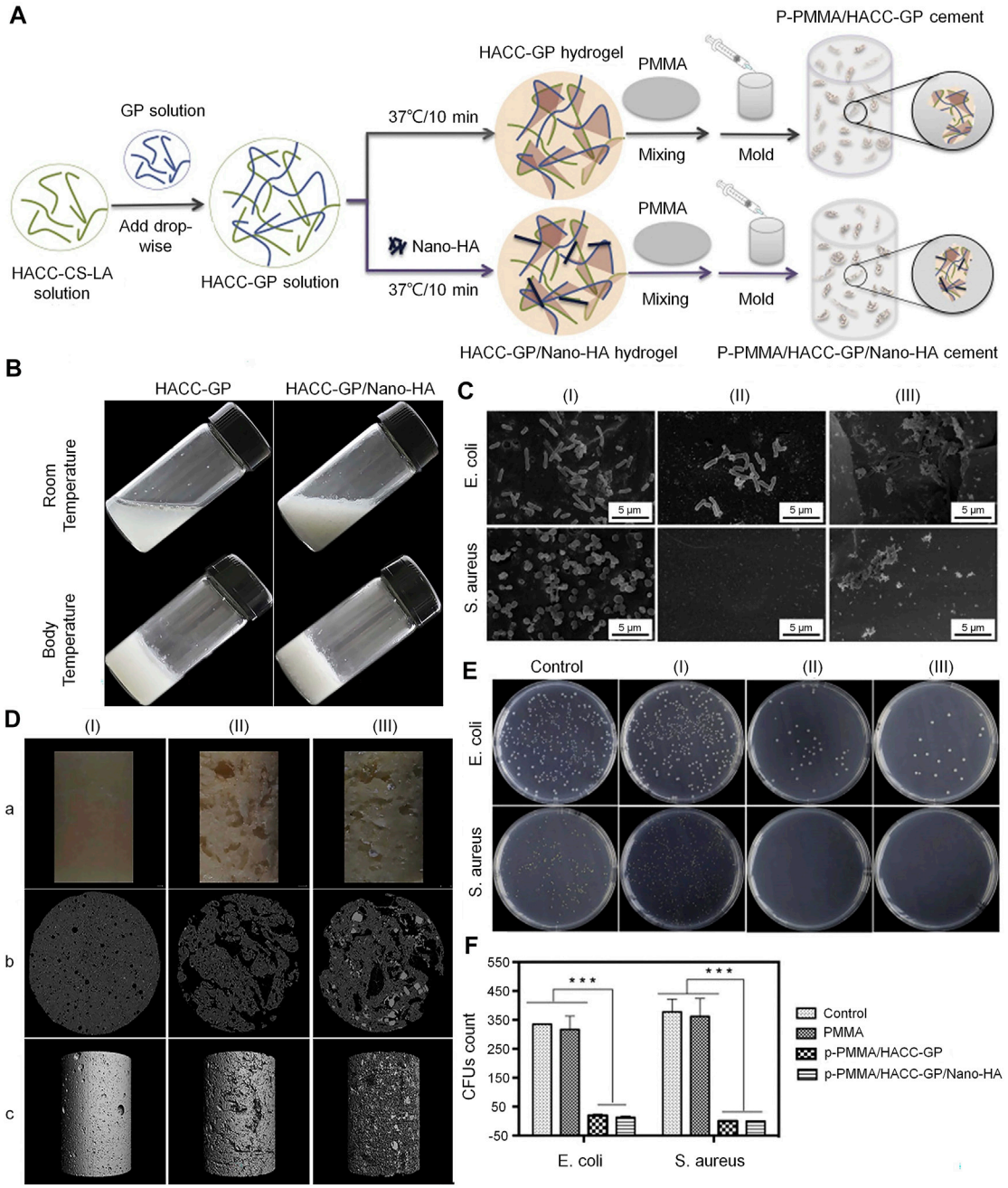

FIGURE 1 | Incorporation of PMMA cement into a HACC-based hydrogel to form a new composite system with dual function for the treatment of infected bone defects (Wang et al., 2018b). **(A)** Synthesis of PMMA-based cement. **(B)** Morphological external phase of HACC-GP and HACC-GP/Nano-HA hydrogel at room temperature and body temperature. **(C)** Bacteriostatic results based on scanning electron microscopy (SEM). **(D)** Surface morphologies (a) and μ-CT observations (b, c) of PMMA-based cements. **(E,F)** Agar plate diffusion and colony count results of PMMA-based cements against *E. coli* and *S. aureus*. CFU, colony forming unit; CS, chitosan; *E. coli*, *Escherichia coli*; GP, glycerophosphate; HA, hydroxyapatite; HACC, N-(2-hydroxyl)propyl-3-trimethylammonium chitosan chloride; LA, lactic acid; μ-CT, micro-computed tomography; PMMA, polymethylmethacrylate; *S. aureus*, *Staphylococcus aureus*.

determine the degree of substitution of HACC. As mentioned above, an increase in the DD in the CS structure increases positive charge density, allowing it to have a higher electrostatic interaction force (Chou et al., 2015). A higher permanent positive charge density on the main chain of HACC strengthens its binding force with the negative charge on the surface of bacteria (Sajomsang et al., 2009). HACC can be electrostatically combined with the bacterial membrane, resulting in a significant reduction in the risk of bacterial resistance. In addition, the physical state and MW also affect the antibacterial activity of HACC. Low-MW HACC easily penetrates the bacterial cell wall to inhibit mRNA synthesis and DNA transcription (Lu et al., 2016; Crismaru et al., 2011). Also, it

has been demonstrated that the water solubility of HACC was increased in parallel with the increase in the degree of substitution. This effect may be due to the quaternary ammonium group with steric hindrance and excellent hydration ability, which greatly reduced the intermolecular and intramolecular hydrogen bonds of CS. The enhancement of water solubility can improve the antibacterial effect. Tan et al. (Tan et al., 2012) successfully prepared the HACC-β-glycerophosphate (β-GP)/nano-HA hydrogel through the addition of polymethylmethacrylate (PMMA) to HACC. This construct demonstrated antibacterial properties against methicillin-resistant *S. aureus*. Furthermore, the existence of the hydrogel endows the system with porosity and mineralization ability. It was also found that HACC-loaded PMMA can prevent the formation of biofilm by staphylococci and downregulate the expression of virulence genes in antibiotic-resistant staphylococci (**Figure 1**) (Wang et al., 2018b). Grafting HACC onto a three-dimensional (3D) printed scaffold composed of poly (lactic-co-glycolic acid) (PLGA) and HA led to both antimicrobial and osteogenic properties *in vitro* (Yang et al., 2016). In subsequent experiments, researchers established models of infected femoral shaft and femoral condyle defects in rats and rabbits, respectively. HACC-grafted PLGA/HA scaffolds exhibited significantly enhanced anti-infection and bone regeneration capabilities in both models of infected bone defects (Yang et al., 2018). However, the increase in the degree of substitution may have a toxic effect on the cells. Additionally, the toxic effect of HACC concentration on cells should be also considered.

Higher degrees of substitution in HACC increase cytotoxicity. The toxic effect of HACC on cells may be related to mitochondrial damage. HACC may cause acute damage to cells by binding to the mitochondrial membrane at a high concentration. Interaction of HACC with negatively charged cellular components and proteins may also be one of the mechanisms underlying this toxicity (Fischer et al., 2003). Xia et al. (2019) found that low-concentration HACC (0–0.2 mg/ml) stimulated the growth and metabolism of mitochondria. However, when the concentration of HACC was increased to 0.4 mg/ml, it inhibited mitochondrial metabolism; this effect is linked to the decoupling phenomenon.

The optimal drug concentration range of HACC also varies under different degrees of substitution. HACC with a substitution degree of 18% was soluble at pH 12–13. The minimum inhibitory concentrations (MIC) against *Staphylococcus epidermidis* (*S. epidermidis*) and *S. aureus* were 32 and 64 μg/ml, respectively. However, it was not toxic to L-929 cells even at a concentration markedly exceeding its MIC (i.e., 2.5 mg/ml) (Peng et al., 2010; Peng et al., 2011). Another study found that when the degree of substitution of HACC was 40%, the MIC of HACC for *E. coli* and *S. aureus* was 40 μg/ml; the half lethal concentration of AD-MSC was 2.67 mg/ml (Zhao et al., 2015). When the degree of substitution of HACC was increased to 44%, its MIC against *S. epidermidis* and *S. aureus* were 16 and 32 μg/ml, respectively, which was similar to 40% HACC. However, slight toxicity to L-929 cells was noted at the concentration of 2.5 mg/ml (Peng et al., 2010; Peng et al., 2011). At the degree of substitution of 66%, HACC at a concentration of 720 μg/ml can kill half of AD-MSC (Zhao et al., 2015). Although Wang et al. showed that HACC with the degree of substitution ranging 95–98% can play an antibacterial role at a micro concentration of 40, 200, and 1,000 μg/ml against *S. aureus* and *E. coli*, HACC at 200 and 1,000 μg/ml simultaneously showed significant cytotoxicity (Wang et al., 2019).

According to the above evidence, compared with simple low-MW CS, the MIC of HACC was significantly decreased with the increase in the substitution degree from 18 to 98%. However, the minimum bactericidal concentration did not change significantly, indicating that the degree of substitution did not affect it (Shagdarova et al., 2019). When the degree of substitution exceeds 44%, the antibacterial activity may be very strong. This indicates that HACC with a high degree of substitution only requires a low dose to exert its antibacterial effect without inducing toxic effects on cells. However, when the substitution is excessively low (<18%), a very high concentration is needed to produce a satisfactory antibacterial effect. Therefore, the optimal concentration of HACC needs to be analyzed under different degrees of substitution. In an optimal range of the degree of substitution, there is no need to consider the toxic effect of excessive concentrations on cells or the insufficient antibacterial effect of low concentrations. According to the above research results, we conclude that the most suitable range for the degree of substitution in HACC is 18–20%. In this range, HACC has optimal biocompatibility that does not cause toxic effects on cells at the concentration of 2–2.5 mg/ml and also has a sufficient antibacterial effect. The MIC of HACC with a 44% degree of substitution is markedly lower than the concentration at which toxicity to cells was initiated. Nevertheless, the results of alizarin red staining and ALP activity test showed that HACC does not have osteogenic properties and cannot be used as the optimal degree of substitution (**Figure 2**). Moreover, the critical degree of substitution for HACC is approximately 90%; when the degree of substitution is >90%, toxicity to cells has been initiated before the occurrence of bacteriostasis.

3.1.2 TMC

TMC, one of the most easily synthesized and common forms of QCS, can be synthesized by two methods, namely direct quaternary ammonium substitution, and N-alkylation (Xu et al., 2010). Compared with HACC, TMC has higher antibacterial activity against *E. coli* and *S. aureus*; it has also exhibited some antibacterial effect on *Candida albicans*. The reported MIC against *E. coli* and *S. aureus* were 0.04 and 0.16 mg/ml, respectively, which are markedly lower than that of HACC. The antibacterial activity of TMC increases in parallel with an increase in the length of the alkyl substituent chain. When TMC was further quaternized to N,N,N-trimethyl O-(2-hydroxy-3-trimethylammonium propyl) CS, it showed higher antibacterial activity than TMC (Jia et al., 2001; Huang et al., 2013). A study showed that novel electrospun silver nanoparticles loaded with nanofiber mats containing TMC, polyacrylic acid, or poly (2-acrylamide-2-methylpropanesulfonic acid) have better antibacterial activity against *E. coli* and *S. aureus* than the film without TMC and silver nanoparticles (Kalinov et al., 2015). The antibacterial and polycation properties of TMC can

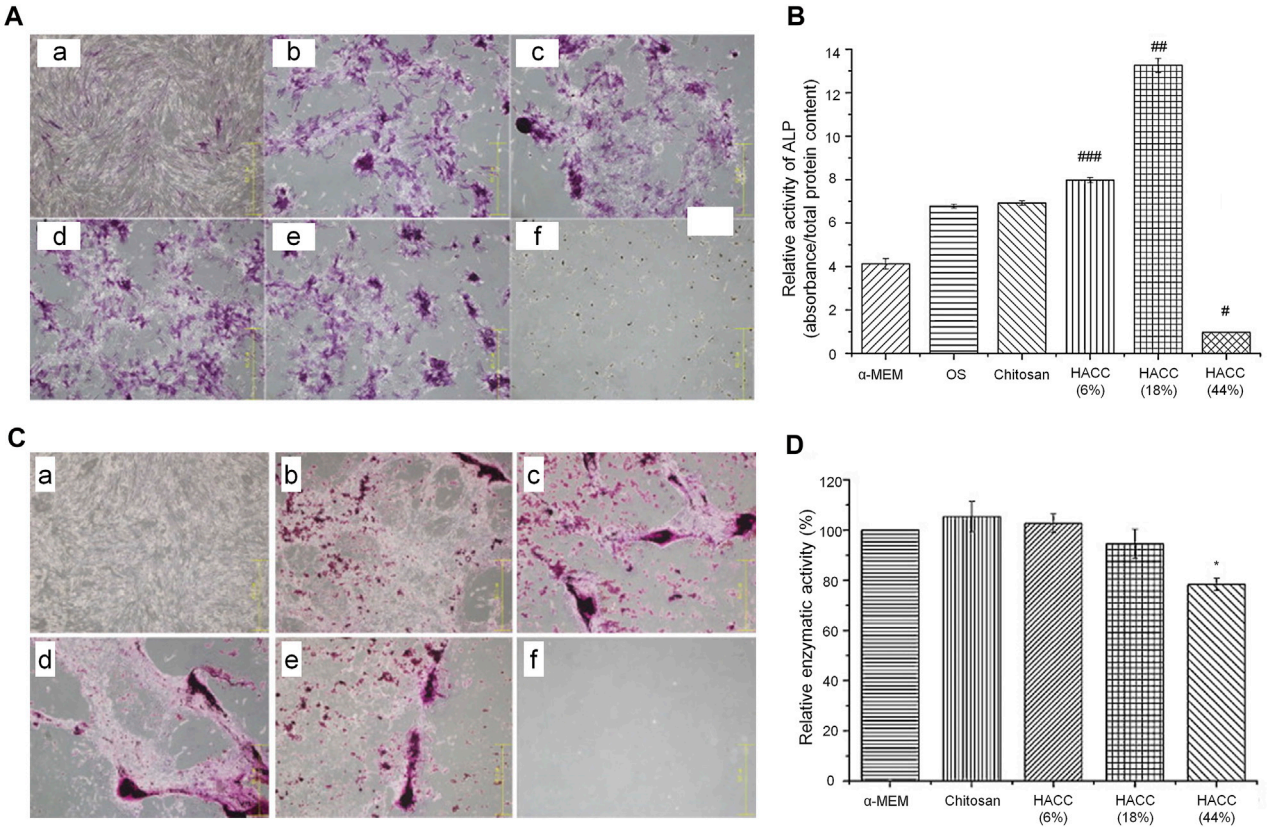

FIGURE 2 | Effects of HACC with different degrees of substitution on cell proliferation and differentiation (Peng et al., 2010). **(A)** ALP staining. (a) α-MEM; (b) osteogenic induction medium (OS) only; (c) chitosan; (d) HACC 6%; (e) HACC 18%; and (f) HACC 44% treated hMSC after 14 days. **(B)** Relative ALP activity in each group after 14 days of culture ($^{###}p < 0.05$, $^{##}p < 0.01$). **(C)** Alizarin red staining results after 28 days of culture. (a) α-MEM medium only; (b) OS; (c) chitosan; (d) HACC 6%; (e) HACC 18%; and (f) HACC 44%. **(D)** MTT test results for L-929 cells after 48 h of exposure ($^{*}p < 0.05$). ALP, alkaline phosphatase; α-MEM, α-Minimum Essential Medium; HACC, N-(2-hydroxyl)propyl-3-trimethylammonium chitosan chloride; hMSC, human mesenchymal stem cells; MTT, 3-(4,5-dimethylthiazol-2-yl)-2,5-diphenyltetrazolium bromide.

be used to develop polyelectrolyte complexes and improve the modification strategy; hence, more application prospects should be explored. Romero et al. showed that a 71% degree of substitution of TMC can be used with heparin as a periosteal mimic to form a multilayer membrane coating to cover the cortical bone for the promotion of bone healing; in this coating, heparin and TMC acted as polyanion and apolipoprotein, respectively. TMC did not have a toxic effect on AD-MSC and exerted a strong antibacterial effect. This experiment confirmed the potential usefulness of TMC for the development of polyelectrolyte complexes (Romero et al., 2015). While the antibacterial capabilities of TMC have been extensively studied, further work is needed to investigate its polycationic nature. Such research would expand its applicability as a growth factor delivery vehicle in the treatment of infected bone defects.

3.2 Carboxylated CS

Most studies on carboxylated CS have focused on carboxymethylation reactions. CS and monohalocarboxylic acid can produce different types of carboxymethyl chitosan (CMC) under different reaction conditions. Common carboxymethyl derivatives are O-CMC, N,O-CMC, N-CMC, and N-succinyl CS (Shi et al., 2006). Similar to QCS, the water solubility of CMC in various pH environments is also controlled by the degree of carboxymethylation (Chen et al., 2004). CMC also has antibacterial properties. However, the degree of substitution of CMC has a minimal impact on its antibacterial activity, which mainly depends on the number of NH^{3+} groups in the structure (Sun et al., 2006). Although carboxylated CS obtained enhanced antibacterial properties, the effects of different types of CMC on Gram-positive or Gram-negative bacteria differed. For example, O-CMC and N,O-CMC exhibited strong antibacterial activity against *E. coli* and *S. aureus*, respectively (Fei Liu et al., 2001). With the gradual increase in the concentration gradient (i.e., 5, 8, and 10 mg/ml), the antibacterial activity of O-CMC and N,O-CMC was also gradually increased in a dose-dependent manner. Moreover, at the concentration of 0.4, 0.8, and 1 mg/ml, O-CMC and N,O-CMC did not show cytotoxicity to the cells (Anitha et al., 2009). Owing to the existence of the $-NH_2-CH_2-COOH$ functional group, CMC has good metal chelating ability. Wahid et al.

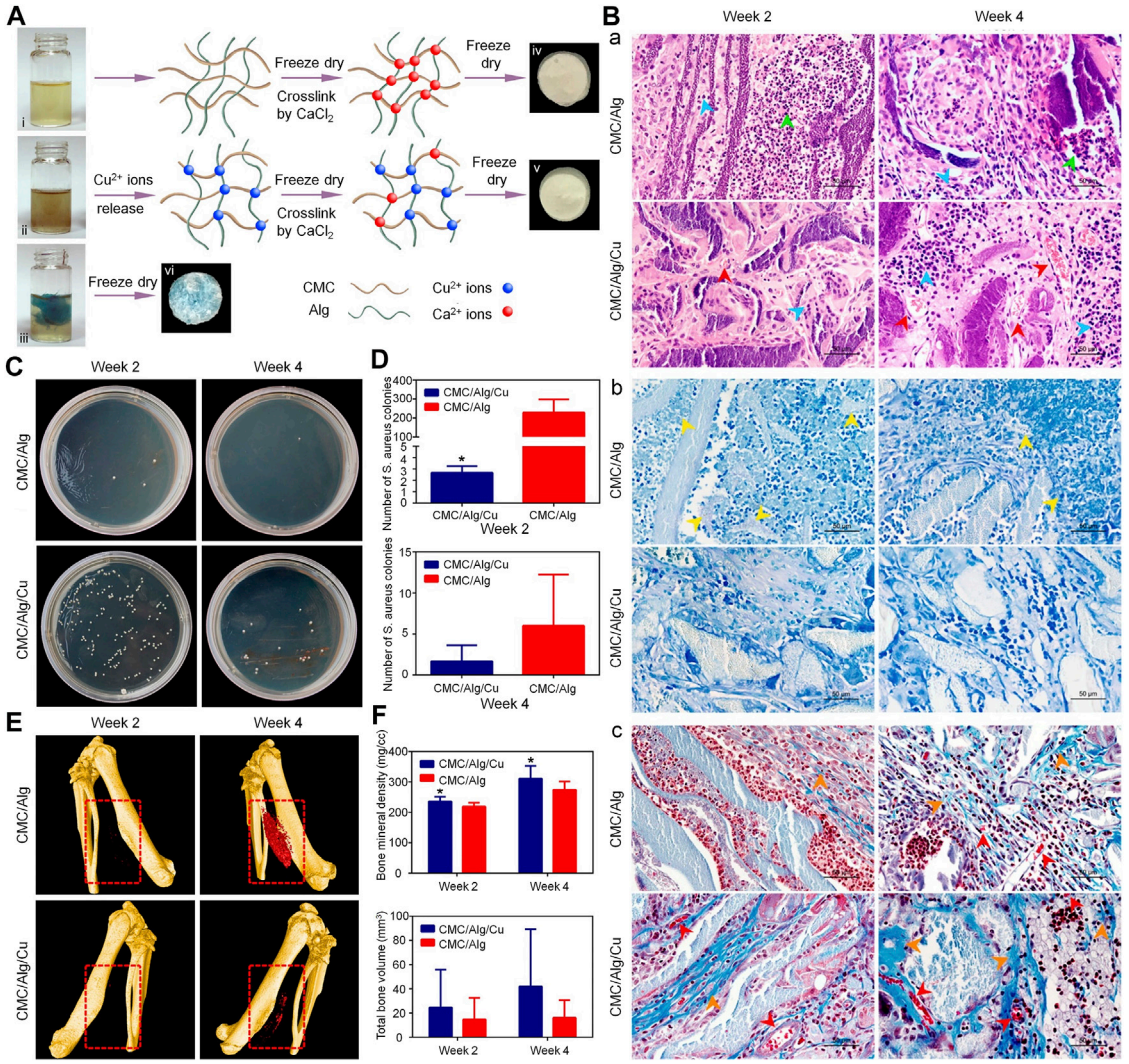

FIGURE 3 | Treatment of infected bone defect with a copper-containing CMC/sodium alginate scaffold (Lu et al., 2018). **(A)** Schematic of the scaffold preparation. i, ii, and iii denote CMC/Alg solution, CMC/Alg solution with Cu nanoparticles, and Cu^{2+} solution with CMC/Alg, respectively. **(B)** H&E (a), Giemsa (b), and Masson's trichrome (c) staining results at 2 and 4 weeks after implantation. **(C,D)** The antibacterial properties of the scaffolds *in vivo*. $^*p < 0.05$. **(E)** The μ-CT results at 2 and 4 weeks after implantation. **(F)** Quantitative analysis of bone regeneration. Alg, alginate; CMC, carboxymethyl chitosan; μ-CT, micro-computed tomography; H&E, hematoxylin and eosin.

(2017). I t has been demonstrated that CMC could be used to prepare supramolecular hydrogels with metal ions, such as Ag^+, Cu^{2+}, and Zn^{2+}. The gelation process of the hydrogel occurs rapidly and can result in good mechanical properties, particularly after combination with metal ions. Moreover, excellent antibacterial properties against *S. aureus* and *E. coli* were also revealed compared with those of pure CMC. Direct crosslinking of CMC with metal ions may lead to uncontrolled release. This problem can be solved through the addition of other polymers to form a mixture. Adding Cu nanoparticles to the CMC and alginate polymer mixture can enable the controllable release of Cu ions to form scaffolds. *In vivo* and *in vitro* experiments showed that the combination of Cu nanoparticles with a CMC/alginate scaffold could produce excellent antibacterial and osteogenic properties, and did not have a toxic effect on MC3t3-E1 cells (**Figure 3**) (Lu et al., 2018). Apart from chelating Cu^{2+} and Zn^{2+} to augment the antibacterial properties, CMC can chelate Ca^{2+} to induce apatite deposition and improve osteogenic activity. This effect may be related to the fact that carboxymethyl groups provide more nucleation sites. N,O-CMC and polyphosphate are crosslinked by a Ca^{2+} bridge; this process yielded a scaffold which has exhibited a strong regeneration-inducing activity in rat skull defects (Müller et al., 2015). BMP and other proteins promote the proliferation of bacteria to some extent; nevertheless, the existence of CMC inhibits or even reverses this effect. CMC can also help overcome the problem of biofilm formation by bacteria on the implant surface. Functionalizing the surface of the titanium alloy material with

CMC and BMP2 by covalent grafting can significantly inhibit *S. aureus* and *S. epidermidis* adhesion. In addition, CMC does not affect the differentiation and proliferation of osteoblasts (Shi et al., 2009). CMC can also be synthesized with other biomaterials to improve its osteogenic performance in bone tissue engineering. The combination of CMC and gelatin with laponite at the concentration of 10% (weight/weight) can significantly enhance the osteogenic differentiation ability of rat BMSC and has a strong compatibility *in vitro*. Notably, it can promote the healing of rat skull defects *in vivo* (Li et al., 2017).

3.3 Sulfated CS (SCS)

CS can be sulfated using sulfuric acid or sulfonic acid salts (Zhang et al., 2015). Unlike the aforementioned two modified CS, SCS is designed to cooperate with BMP2 for the promotion of healing in bone defects. The sulfate group in SCS is similar to natural anticoagulant heparin, which contains BMP2-binding sites. Compared with natural heparin, SCS has stronger activity on BMP2. However, the antibacterial properties of SCS have rarely been reported (Green et al., 2009). Adding SCS to the BMP2-loaded calcium-deficient HA scaffold can increase the cumulative release of BMP2 compared with the scaffold without SCS. This composite scaffold promoted the repair of skull defect in a rat model (Zhao et al., 2012). In another study, 2-N-SCS, 6-O-SCS, and 2-N, 6-O-sulfated chitosan (26SCS) were successfully synthesized. Among them, 26SCS is the most suitable enhancer for BMP2 with a sulfur content of 12.89 ± 14.86%. Low-dose 26SCS (0.625–2.5 μg/ml) stimulates the differentiation of osteoblasts induced by BMP2 *in vitro* and stimulates ectopic bone formation *in vivo*. These effects may be related to the fact that 26SCS can increase the expression levels of noggin (NOG) mRNA. Nevertheless, SCS alone does not promote the osteogenic differentiation of C2C12 myoblast cells. This finding indicated that SCS should work together with BMP2 to indirectly affect osteogenic differentiation (Zhou et al., 2009). The preparation of a photopolymerisable hydrogel incorporating recombinant human BMP2 (rhBMP2)-loaded 26SCS-based nanoparticles can promote the attachment and osteogenic differentiation of human MSC *in vitro*. New bone formation was found in a rabbit model of the radial defect (Cao et al., 2014). Therefore, we conclude that SCS alone cannot be used as a bone-forming material. To achieve this purpose, it needs to be combined with osteogenic biomaterials, such as BMP2. Additionally, the combination of SCS with metal ions or antibacterial substances can be explored to improve the antibacterial properties and serve as a synergistic factor in the regeneration of local infected bone defects.

3.4 Phosphorylated CS (PCS)

Compared with CS, ionic conductivity, and swelling index are both improved in PCS. Although the crystallinity was reduced, the tensile strength remained similar to that of CS. Unlike CS, PCS has a significantly rough surface (Jayakumar et al., 2008). PCS is mainly produced through two approaches. The first approach involves the reaction between the CS hydroxyl group and phosphorus pentoxide group in the presence of methanesulfonic acid, which can be used as a protective agent for the CS amino group (Jayakumar et al., 2007). The second approach involves the reaction of CS hydroxyl functional groups with phosphoric acid in the presence of urea (Jayakumar et al., 2008). Owing to the presence of the phosphate group, PCS has metal chelating ability. It can be combined with calcium phosphate crystal particles, thus improving the mechanical properties of PCS and promoting bone properties. By combining PCS and HA at a weight ratio of 30/40, the maximum mechanical property of approximately 70.25 MPa can be obtained; also, most of its original compressive strength can be maintained for 20 days. (Li et al., 2011). Studies on the osteogenic effect of PCS have shown that it modulates the expression levels of osteoclastogenic factors, nuclear factor κB ligand-receptor activator (RANKL), and osteoprotegerin (OPG) protein. Moreover, it may inhibit osteoclast differentiation by upregulating the expression ratio of OPG and RANKL in human primary osteoblasts (Tang et al., 2011). By mixing PCS and disodium (1→4)-2-deoxy-2-sulphoamino-β-$_D$-glucopyranuronan (SCS) into PLGA/tricalcium phosphate scaffolds, we can obtain scaffolds with dual functions, namely osteogenesis and inhibition of bone resorption. These scaffolds promoted bone healing in an ulna defect model *in vivo* (Chen et al., 2017). Collectively, these properties ensure that PCS can be used as a potential biomaterial in the treatment of infected bone defects.

3.5 Others

This part describes the rarely modified CS; many functions have not been confirmed thus far, and the osteogenesis and antibacterial properties require further investigation. Thiolated chitosan (TCS) can be obtained by adding the thiol group to the primary amino group of CS, which can improve some properties of CS (e.g., good solubility at neutral pH and formation of disulfide bonds with other thiol groups in proteins) (Wang et al., 2020). Compared with the traditional CS/β-GP hydrogel, the TCS/HA/β-GP hydrogel has a higher storage modulus (G') and loss modulus (G"), as well as a more appropriate degradation rate and low cytotoxicity (Liu et al., 2014).

Succinylation of CS can effectively augment water solubility and biocompatibility and yield new functional groups. The succinylated CS hydrogel can controllably release drugs under the influence of pH. Through combination with bone graft material, this hydrogel can increase the rates of cell growth and bone differentiation. Its mechanical properties, such as compressive strength and Young's modulus, decrease with the increase in the rate of succinylation (Lee et al., 2020; Lee et al., 2021). Hydroxypropyl CS and hydroxybutyl CS are two forms of hydroxyalkyl CS. Hydroxyalkyl CS was obtained by the substitution reaction of CS and epoxide on amino or hydroxyl groups; however, it is rarely used in the treatment of bone defects (LogithKumar et al., 2016). By grafting maleic acid, hydroxypropyl CS can effectively inhibit >90% of *E. coli* and *S. aureus* within only 30 min. In addition, hydroxybutyl CS can rapidly form a gel, stably exist *in vivo*, and is injectable (Peng et al., 2005; Dang et al., 2006). The ethylene glycol CS has better mechanical properties and a slower degradation rate than pure CS (Huang et al., 2016). The above modified CS is rarely reported.

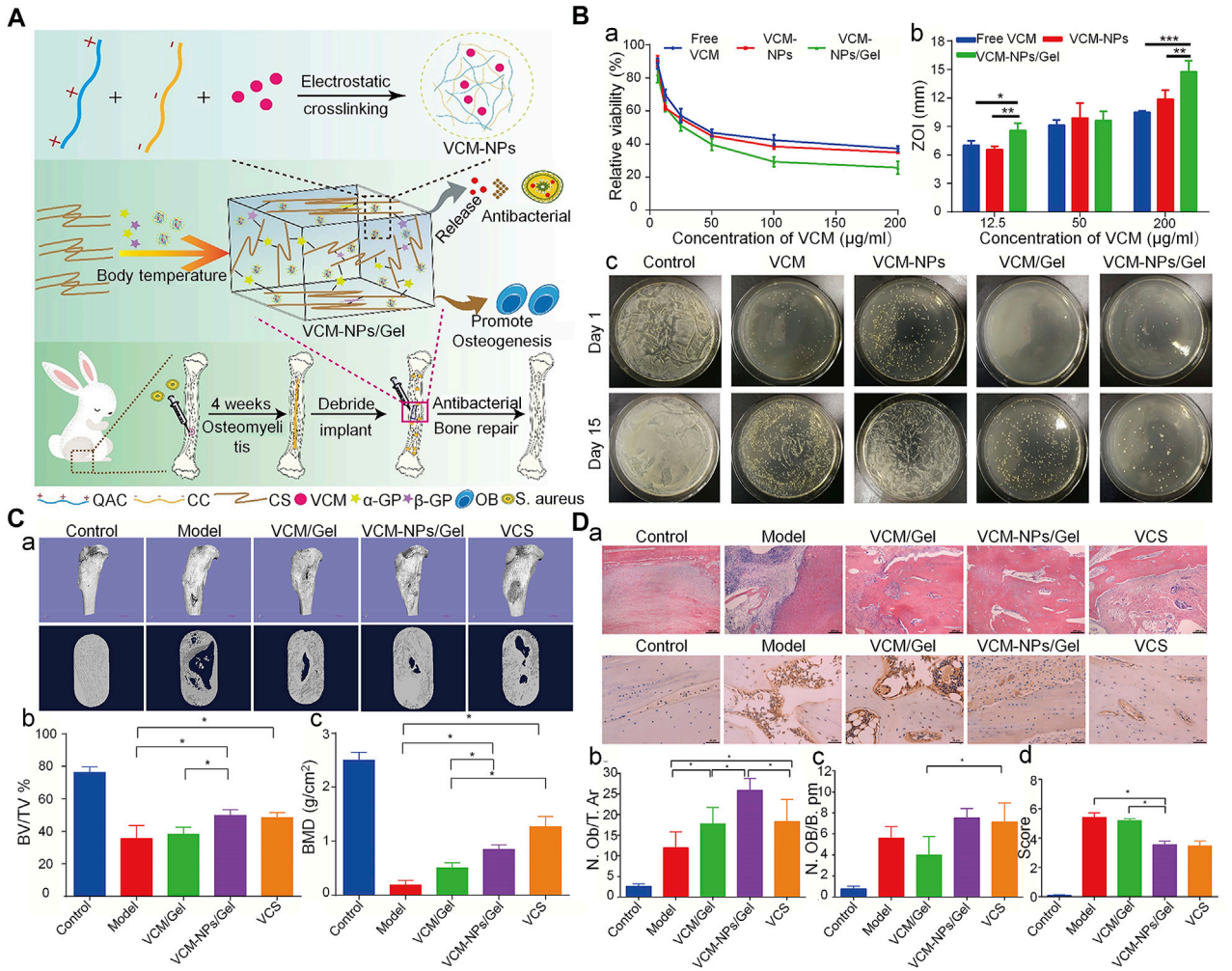

FIGURE 4 | Injectable thermosensitive hydrogel system for the delivery of VCM in the treatment of osteomyelitis (Tao et al., 2020b). **(A)** Schematic diagram of the synthesis of antibacterial and osteogenic hydrogels. **(B)** (a), (b) VCM, VCM-NPs, and VCM-NPs/Gel against *S. aureus* with different concentrations of VCM; (c) Agar plate diffusion of different groups at 1 and 15 days. **(C)** (a) The results of μ-CT bone morphology after treatment with VCM/Gel, VCM-NPs/Gel, and vancomycin-calcium sulfate (VCS); (b), (c) Quantitative analysis of μ-CT in each group. **(D)** (a) Histopathology and IL6 immunohistochemical analysis of the rabbit tibia; (b), (c) Quantitative analysis of new bone formation and (d) Quantitative analysis of IL-6 immunohistochemical staining. (*$p < 0.05$; **$p < 0.01$, and ***$p < 0.001$). BMD, bone mineral density; BV/TV, bone volume/total volume; IL6, interleukin 6; μ-CT, micro-computed tomography; N. Ob/T. Ar, osteoblast number/trabecular bone area; N. OB/B. pm, osteoblast number/bone perimeter; NPs, nanoparticles; *S. aureus*, *Staphylococcus aureus*; VCM, vancomycin; ZOI, zone of inhibition.

Although its performance has been improved, its synthesis may be more complicated. Further investigation is warranted to improve its performance and render it suitable for the treatment of infected bone defects.

4 APPLICATION IN THE TREATMENT OF INFECTED BONE DEFECTS

In addition to the chemical modification of CS, mixing CS with other materials (e.g., antibacterial and osteogenesis-promoting substances) is an excellent strategy for improving its properties. CS can be used as a carrier for the delivery of antibacterial drugs and osteogenic molecules (e.g., vancomycin, parathyroid hormone, and BMP2), thereby increasing its effectiveness in the treatment of infected bone defects (Wang et al., 2018a; Nancy and Rajendran, 2018). This part summarizes the application of CS-based biomaterials in the treatment of infected bone defects.

4.1 Injectable Hydrogels

The CS hydrogel scaffold has a 3D porous structure, which can simulate the microenvironment of the ECM, promote cell adhesion and proliferation, and allow nutrient and metabolite exchange and cell migration. Moreover, it can encapsulate osteoblasts or growth factors to promote the regeneration of bone tissue (Sultankulov et al., 2019). The CS-based thermosensitive hydrogel has recently attracted attention in bone tissue engineering. CS itself is not a thermosensitive polymer, however, through modification, thermosensitivity

can be realized. For example its thermal gelation can achieved by adding GP to the CS solution (Ji et al., 2009). GP is a natural organic compound that exists in the body and one of the components of the osteogenic medium. It can promote the differentiation of MSC into osteoblasts by extracellular related kinases (Wang et al., 2018b). This type of hydrogel can exist in a fluid state at room temperature. Following injection into the body, it forms an *in-situ* stable hydrogel under body temperature conditions (Zhou et al., 2015). This property of the CS hydrogel allows it to be injected directly into the bone defect cavity, regardless of the shape and size. Moreover, changing from the original liquid state to the gel state can make it act as a favorable drug carrier. Therefore, the CS/β-GP injectable hydrogel is considered an outstanding biomaterial for bone reconstruction. Nevertheless, it is also characterized by certain shortcomings, such as mechanical stability, and insufficient osteoconductivity. Some modification methods have been developed to solve this problem. For instance, the CS/GP hydrogel can be used as a carrier of cells, growth factors, and drugs. Using the CS/GP hydrogel, Huang et al. (Huang et al., 2011) added collagen and nano-HA to prepare a stable gel for the delivery of rat BMSC. The gel showed good stability, which may be related to the hydrogen bond formed between collagen and CS. This hydrogel system showed enhanced mechanical properties and ability to induce osteogenesis. To further improve the osteogenic properties of the CS hydrogel, Jayash et al. produced an OPG-CS gel for the treatment of critical-sized skull defects in rabbits. Rabbits in the OPG-CS gel group exhibited more obvious new bone formation at 6 and 12 weeks after treatment compared with those in the CS gel group (Jayash et al., 2017b). Moreover, using the CS/GP hydrogel as a carrier for the delivery of antibiotics can realize an appropriate antibacterial effect. A CS/GP hydrogel containing nanoparticles loaded with vancomycin released the drug continuously for >26 days, inhibiting *S. aureus* both *in vitro* and *in vivo* (**Figure 4**) (Tao et al., 2020b).

In addition, CS can be modified and mixed with other materials to improve its performance. Single-component polymer hydrogels may have poor mechanical properties and insufficient cell adhesion. Sun et al. (Sun et al., 2021) used polyethylene glycol diacrylate/TCS to form a double-network hydrogel. This dual-network hydrogel has excellent mechanical properties, high crosslinking density, and low swelling degree. In an *in vivo* rat model of skull bone defects, it was demonstrated that addition of BMP2 to this hydrogel can significantly augment new bone formation and biocompatibility. In addition, modification of this hydrogel with thiolated halloysites improves adhesion to MC3T3-E1 cells and further promotes proliferation. This is related to the participation of thiol on the outer surface in the disulfide exchange during the process of cell adhesion, which is mediated by fibronectin and collagen (Rosenberg et al., 2019).

Traditional methods (e.g., crosslinking agents and chemical reactions) for the synthesis of gels may have adverse effects on living cells and biologically active factors. Guanidinylated CS supramolecular hydrogels, which are driven by reversible non-covalent bonds, include ionic interaction and hydrophobic interaction hydrogen bonds, and have been associated with self-healing and injectable properties (Zhang et al., 2020). Laponite acts as a physical crosslinker with osteoinductive properties; the hydrogel enhances cell adhesion and promotes osteogenic differentiation of MSC by activating the Wnt/β-catenin signaling pathway.

4.2 Coatings

A major goal in the field of orthopedic implant materials is to provide a bio-interactive surface that can prevent bacterial adhesion and enhance biological activity (Leedy et al., 2011). The osteoconductivity, biodegradability, antibacterial, drug delivery properties, and flexibility of processing and modification of CS render it a potential coating material for orthopedic implants. The conventional preparation processes for CS coating include electrophoretic deposition (EPD), spin coating, electrostatic spinning, and sol-gel methods (Kumari et al., 2021). EPD has become one of the most commonly used methods for the preparation of coatings due to its ability to control the coating composition and complex shape, high efficiency, simplicity, and the absence of a need for a crosslinking agent (Obregón et al., 2019). CS is also highly positively charged; thus, it is easy to prepare a coating using the cathodic EPD method. The use of CS as a coating material has two main functions. Firstly, it can induce calcium deposition on the surface of the coating, thus improving the mineralization ability and promoting osteogenesis. Li et al. (2021) coated the CS/gelatin hydrogel on the poly (aryl ether nitrile ketone)-containing phthalazinone moiety substrate (PPENK) through the spin coating method. Due to the presence of CS, this composite coating can chelate Ca^{2+} to promote the deposition of calcium phosphate at the mineral phase on the surface of the PPENK matrix and enhance the biomineralization potential of the coating, which has exhibited biocompatibility and osteogenic properties for MCET3-E1.

Secondly, as a carrier for the delivery of antibiotics, biomaterials, and growth factors, the CS coating has many advantages, such as a controllable drug release rate and a slow degradation rate (Frank et al., 2020). Coating CS on titanium alloy scaffold to delivery ciprofloxacin can strongly inhibit *S. aureus*, and does not affect the osteogenic activity of MG63 osteoblast-like cells *in vitro*. In addition, about 77% of total ciprofloxacin was released in 7 days (Mattioli-Belmonte et al., 2014). Beenken et al. (Beenken et al., 2014) demonstrated that CS-coated calcium sulfate containing daptomycin can effectively delay the release of daptomycin and maintain the activity of the released drug for 10 days *in vitro*. In the absence of CS coating, the concentration of daptomycin eluted from the calcium phosphate particles was rapidly decreased. In a rabbit model, calcium sulfate pellets with CS coating exerted a better effect on osteomyelitis than those without CS coating. Nancy et al. (Nancy and Rajendran, 2018) produced a double-layer coating through the EPD method, using the TiO_2-strontium-incorporated HA as the first layer and vancomycin-added CS/gelatin as the second layer. This

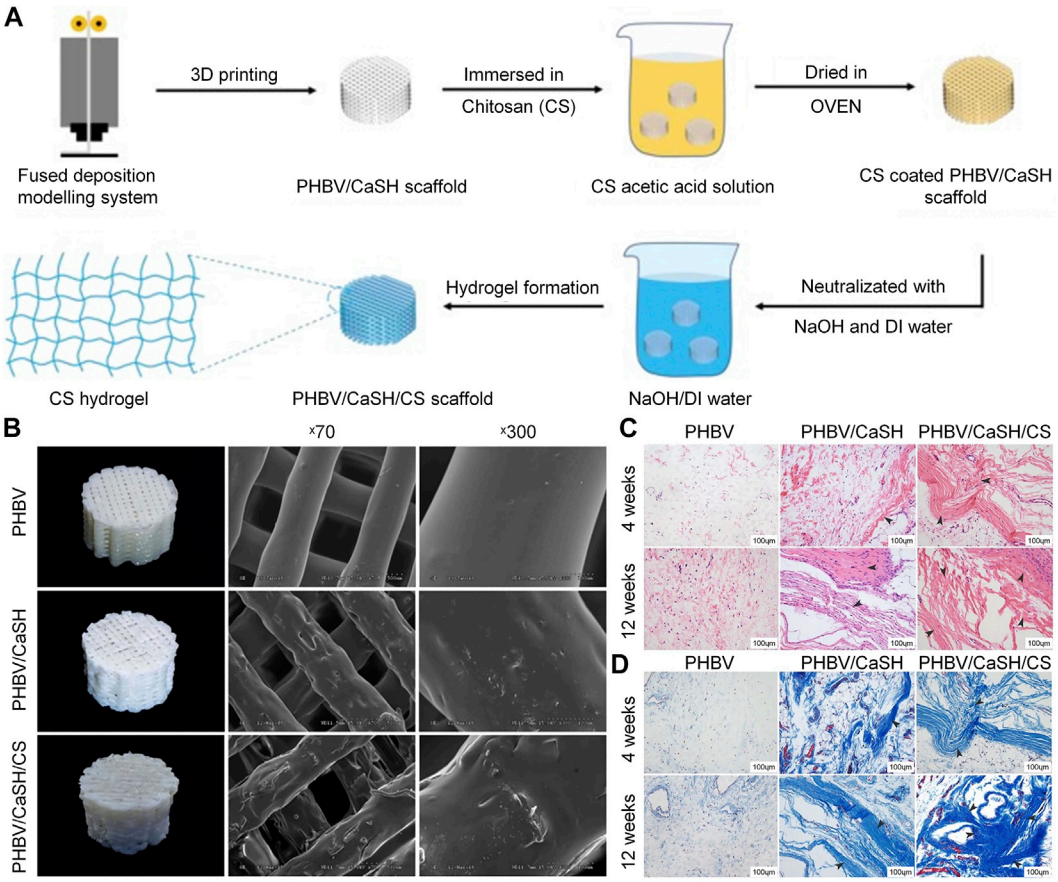

FIGURE 5 | Chitosan-coated PHBV/CaSH scaffold was used to improve the bone repair (Ye et al., 2018b). **(A)** Preparation process for the PHBV/CaSH/CS scaffold. **(B)** Surface morphology and mechanical properties of the PHBV, PHBV/CaSH and PHBV/CaSH/CS scaffolds. **(C)** H&E staining results at 4 and 12 weeks. **(D)** Masson's trichrome staining performed at 4 and 12 weeks. 3D, three-dimensional; CS, chitosan; DI, deionized; H&E, hematoxylin and eosin; PHBV/CaSH, poly (3-hydroxybutyrate-co-3-hydroxyvalerate)/calcium sulfate hemihydrate.

double-layer coating has both antibacterial and osteogenic properties, and can sustain the release of vancomycin over 48 h. In bone tissue engineering, porous bioglass is also commonly used as a carrier of osteogenic or antibacterial drugs. However, it is often characterized by burst release of drugs, which shortens the duration of its effectiveness (Soundrapandian et al., 2010). This shortcoming can be overcome by combining CS with bioactive glass, which can effectively prolong the release cycle to prevent the occurrence of osteomyelitis. Patel et al. (2012) synthesized a composite coating with CS and bioactive glass nanoparticles via the EPD method. Ampicillin was eluted continuously from the CS-bioactive glass nanoparticles coating for 10–11 weeks, confirming its ability for long-term drug delivery. Besides CS molecules, calcium and silicon ion products eluted from bioactive glass nanoparticles can promote the osteogenic ability of MC3T3-E1 cells. Furthermore, bioactive glass nanoparticles and CS can jointly promote the formation of apatite on the coating surface and enhance the mineralization ability. Because of their hydrophobicity, most synthetic polymeric materials do not support cell adhesion, proliferation and differentiation. The surface coating formed with CS can enhance the surface hydrophilicity of the polymer material, thereby increasing the cell adhesion (Tong et al., 2011). Coating CS on a 3D-printed poly (3-hydroxybutyrate-co-3-hydroxyvalerate)/calcium sulfate hemihydrate scaffold through a fused deposition modeling approach can improve the osteogenic performance of the scaffold both *in vivo* and *in vitro* (**Figure 5**). Due to the presence of CS, the scaffold can promote the adhesion and proliferation of rat BMSC, and upregulate the expression of osteogenesis-related genes (e.g., OCN, OPN, and BMP2) to enhance the osteogenic ability (Ye et al., 2018b).

4.3 Microspheres

Microspheres are flowing particles typically composed of inorganic or polymer materials. Generally, microspheres are thought to be excellent cell or drug transport vehicles. Cell or drug/microsphere complexes may be implanted directly into the body, which can simplify procedures and improve cell survival (Grellier et al., 2009). Notably, microspheres have a large specific surface area; therefore, modification of their surfaces may promote cell–or drug–substrate contact (Park et al., 2010).

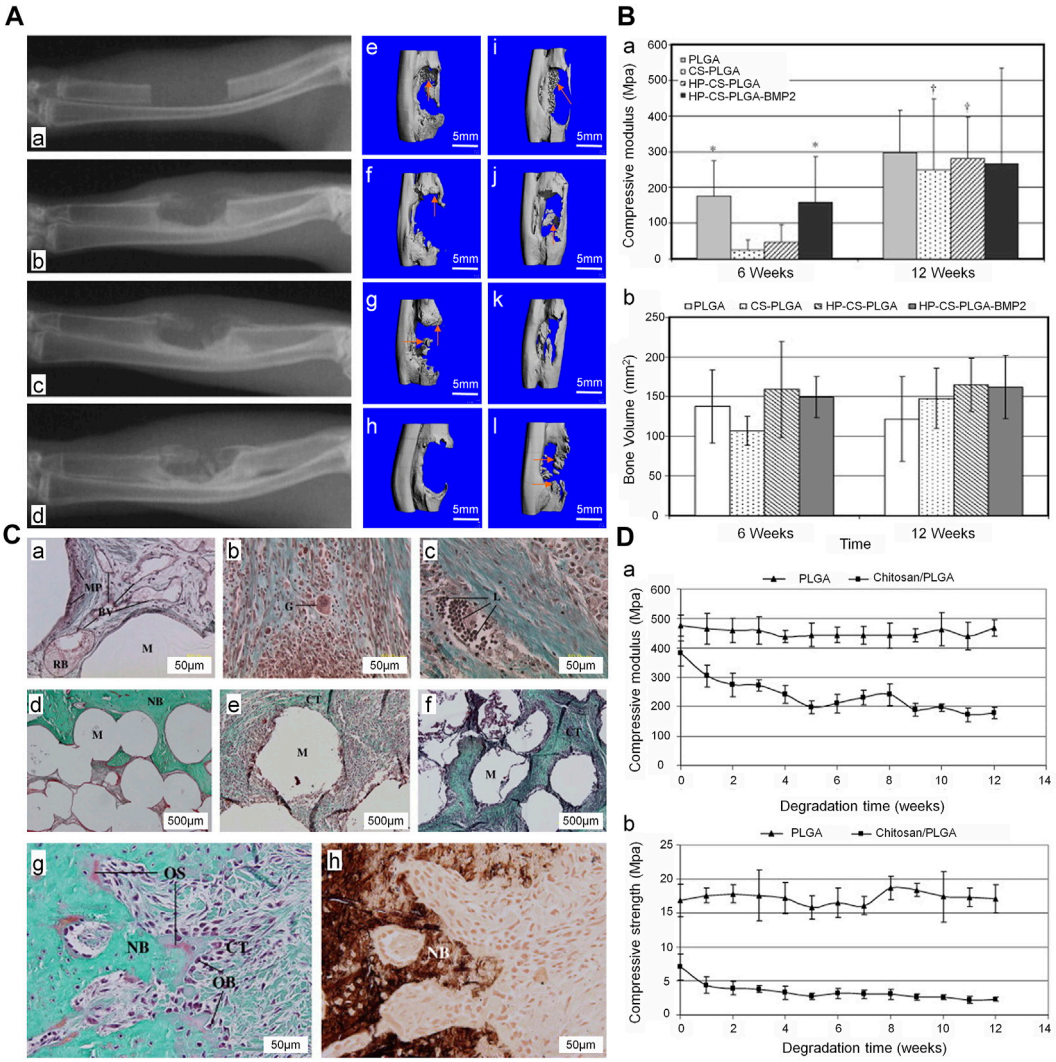

FIGURE 6 | Treatment of ulna defect with CS/PLGA sintered microspheres (Jiang et al., 2010). **(A)** The X-ray images of the ulna defect (a), X-ray (b, c, d) at 4, 8, and 12 weeks after implantation in the HP-CS-PLGA-BMP2 group. Three-dimensional CT, (e–h) and (i–l) at 6 and 12 weeks after implantation in the PLGA, CS-PLGA, HP-CS-PLGA, and HP-CS-PLGA-BMP2 groups, respectively. **(B)** (a) Compressive modulus (b) and bone volume at 6 and 12 weeks after implantation (*$p < 0.1$). **(C)** Masson's trichrome staining performed (a) at 6 weeks after implantation in the PLGA group and (b, c) at 6 and 12 weeks after implantation in the HP-CS-PLGA group. Masson's trichrome staining (d–f) performed at 12 weeks after implantation in the PLGA, HP-CS-PLGA, and HP-CS-PLGA-BMP2 groups. Masson's trichrome (g) and von Kossa staining of HP-CS-PLGA performed at 12 weeks after implantation at 50 μm. **(D)** Compressive modulus (a) and compressive strength (b) analysis ($p < 0.05$). BMP2, bone morphogenetic protein 2; CS, chitosan; CT, computed tomography; HP, heparin; PLGA, and poly (lactic-co-glycolic acid).

CS has good biocompatibility and biodegradability. Sintering, coagulation precipitation, and emulsion crosslinking methods are the most widely utilized processes for producing microspheres from CS (Huang et al., 2014). Using the sintering microsphere technique, Jiang et al. (2010) produced a CS and PLGA sintered microsphere scaffold. The mechanical properties of the scaffold were within the range of the human trabecular bone, and the degradation rate was slower than that recorded for the pure PLGA scaffold. Addition of heparin and BMP2 to the scaffold promoted bone formation at the bone defect in the early stage (**Figure 6**). The acidic products of some polymers (e.g., polylactic acid) may cause inflammatory reactions and metabolic disorders at the local implantation site. In contrast, the metabolites of CS are neutral or slightly alkaline, which is beneficial to the adhesion, proliferation, and differentiation of cells (Dias et al., 2011). By adjusting the proportions of CS microspheres and calcium phosphate cements, the absorbability can be improved without affecting the overall compressive strength. This composite containing 10% (weight/weight) CS microsphere had a compressive strength of 14.78 ± 0.67 MPa, which is similar to that measured for cancellous bone. In rabbit model of femoral defects, at 24 weeks after implantation, the CS microsphere scaffold had been mostly absorbed and a large number of new bones was observed in the transplantation area (Meng et al., 2015). This is attributed to the fact that CS in the form of microspheres can promote the degradation of calcium phosphate cements and the

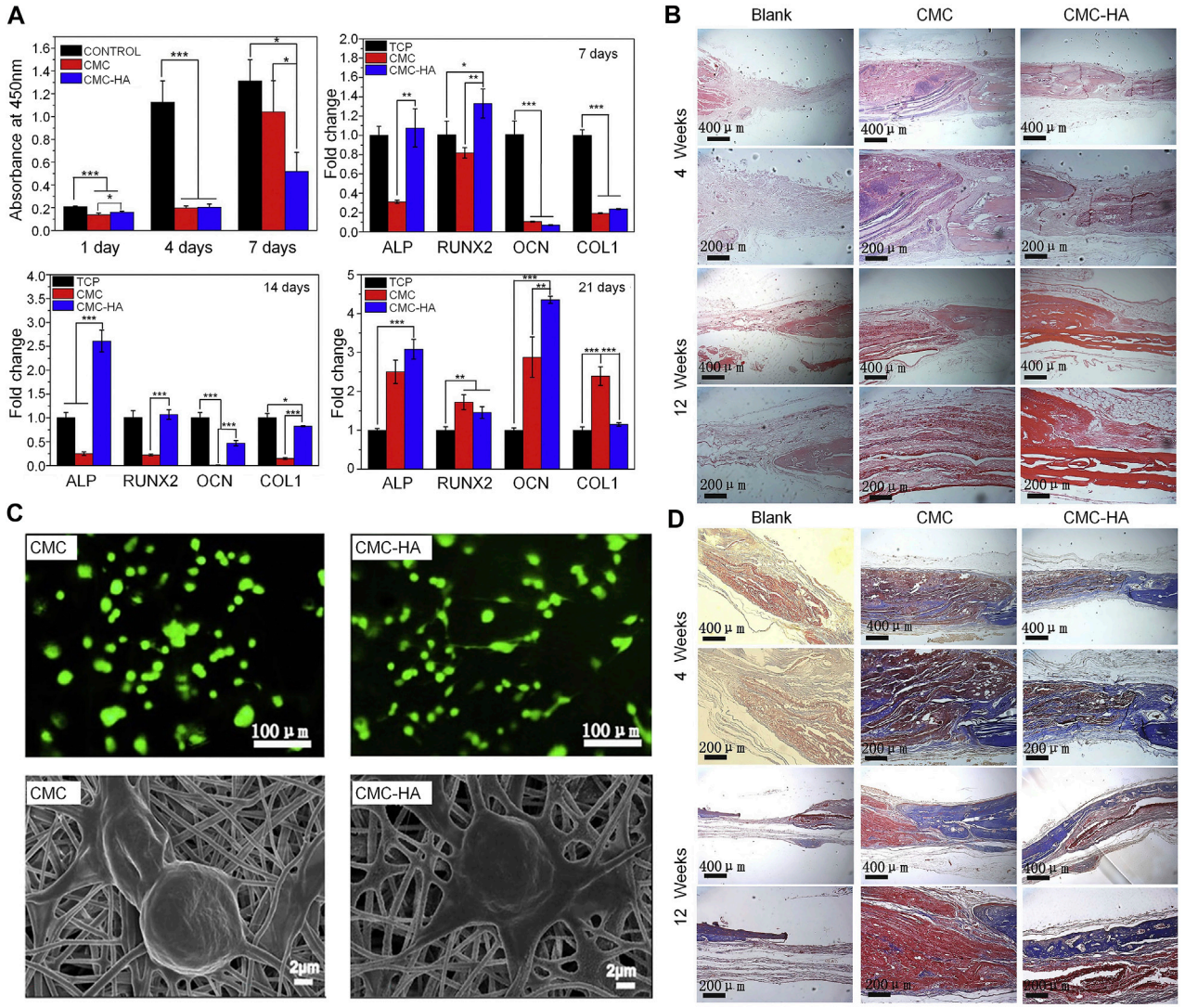

FIGURE 7 | CMC nanofibers have a biomimetic mineralization function *in vitro* and *in vivo* (Zhao et al., 2018). **(A)** CCK-8 test results after 1, 4, and 7 days of culture, and osteogenic gene expression levels analyzed by RT-PCR after 7, 14, and 21 days of culture (*$p < 0.05$, **$p < 0.01$, and ***$p < 0.001$). **(B)** H&E staining results at 4 and 12 weeks. **(C)** Results of LIVE/DEAD staining after 12 h of culture and cell morphology after 6 h of culture using SEM. **(D)** Masson's trichrome staining results at 4 and 12 weeks. ALP, alkaline phosphatase; CCK-8, Cell Counting Kit-8; CMC, carboxymethyl chitosan; COL1, collagen type 1; HA, hydroxyapatite; H&E, hematoxylin and eosin; OCN, osteocalcin; RT-PCR, reverse transcription-polymerase chain reaction; RUNX2, runt-related transcription factor 2; SEM, scanning electron microscopy.

formation of new bones. In addition, CS microspheres prepared by the emulsion crosslinking method showed better compatibility and osteogenesis with BMSC. Moreover, the degree of bone regeneration *in vivo* was greater than that obtained via the coagulation precipitation method (Xu et al., 2014). Therefore, differences in the preparation of CS microspheres will affect cell expression and bone regeneration. In the treatment of infected defects, appropriate preparation methods should be selected to maximize the utilization of CS microspheres.

4.4 Nanofibers

As a nanofiber scaffold material, its unique characteristics (i.e., large surface area, high porosity, and sufficient mechanical strength) endow CS with extraordinary biological properties (Rasouli et al., 2019). Nanofiber scaffolds can mimic the nanoscale characteristics of the ECM, promote cell adhesion and migration, and enhance metabolism and the transport of nutrients (Sofi et al., 2018). As special biomaterials with nanometer size, CS nanofibers scaffolds can be fabricated by electrospinning, self-assembly, thermal separation, ultrasonic treatment, and chemical synthesis (Ding et al., 2014). Among them, electrospinning is the most commonly used technology for preparing CS nanofibers. By altering the parameters of electrospinning (e.g., voltage, flow rate, viscosity, and solution concentration), the structure and diameter of CS nanofibers can be adjusted to enhance the behavior, function and mechanical properties of cells (Beachley and Wen, 2009). Compared

with CS films, CS nanofibers prepared through electrospinning can better promote the adhesion and proliferation of mouse osteoblasts. Moreover, CS nanofibers can stimulate the proliferation and maturation of osteoblasts by inducing the runt-related transcription factor 2 (RUNX2)-mediated regulation of OPN, OCN, and ALP gene expression in osteoblasts through the BMP signaling pathway (Ho et al., 2014). In a model of femoral defects, implantation of the CS nanofiber scaffold promoted bone healing by stimulating and improving the quantity and quality of trabecular bone formation (Ho et al., 2015). CS nanofibers can also improve the mechanical properties of composite biomaterial scaffolds. The fabrication of high-strength nanofiber scaffolds is a major focus in the field of bone defect therapy. The excellent mechanical properties of such scaffolds contribute to maintaining the structural stability of biomaterials *in vivo*. CS lacks sufficient mechanical properties; hence, the mechanical strength of nanofibers can be optimized by combining CS with other materials. CS and HA nanofiber scaffolds crosslinked using genipin can simulate the Young's modulus of the periosteum, reaching a strength of 142 ± 13 MPa; this strength increases in parallel with the increase in the concentration of HA. By simulating the modulus of bone, this composite scaffold can also enhance the differentiation ability of osteoblast precursor cells and ECM deposition. Therefore, this type of scaffold can be used as a biological template for the formation of new bone (Frohbergh et al., 2012). A novel type of PRP-incorporated electrospun polyvinyl-alcohol-CS-HA nanofibers exhibited remarkable biological and mechanical properties, similar to those of human tissue. Furthermore, this composite scaffold improved the ability of osteoblasts for adhesion and proliferation (Abazari et al., 2019). In addition to physical properties, such as mechanical properties and porosity, composite nanofibers containing CS may offer antibacterial activity. The use of the copper (I)—catalyzed azide-alkyne cycloaddition (CuAAC) reaction to graft polycaprolactone (PCL) to the CS by the electrospinning method has been reported. Subsequently, magnesium-doped hydroxyapatite (Mg-HA) was added to the blend composite to prepare a CS-g-PCL/Mg-HA nanofiber scaffold. The triazole group produced by the CuAAC reaction can interact with lipids on the microbial cell membrane to produce antibacterial properties and enhance the osteoblast activity of MG-63 cells (Sedghi et al., 2020). Although electrospinning is one of the most commonly used methods in bone tissue engineering, it is associated with some challenges. For example, the selection of solvents will affect the cytotoxicity of CS nanofibers, and the process of electrospinning is relatively complicated (Chahal et al., 2019). The preparation of polycationic CS and polyanionic ulvan nanofibers by the molecular self-assembly method can also promote the proliferation of osteoblasts and maintain the morphology of osteoblasts. The manufacturing method is simpler than that of the electrospinning method (Toskas et al., 2012). The side chain groups of CS can also be modified to prepare nanofibers. Compared with the solvent used for electrospinning CS nanofibers, CMC nanofibers are water-soluble, non-toxic, and do not require the removal of acid salts generated during electrospinning (Su et al., 2016). The CMC nanofibers with HA can be prepared by the electrospinning method through simple biomimetic mineralization. CMC nanofibers have more mineral deposits than CS nanofibers at 16 h after mineralization. This observation is mainly attributed to the fact that carboxymethyl groups provide more nucleation sites, which is consistent with the findings described above. CMC nanofibers can effectively promote the differentiation of mouse BMSC *in vitro* and augment osteogenesis in rat calvarial bone defects *in vivo* (**Figure 7**) (Zhao et al., 2018).

5 CONCLUSION AND PROSPECTS

Infected bone defects continue to pose a challenge in the field of orthopedics. CS is a bioactive material commonly used in bone tissue engineering. CS kills bacteria through the combination of positive and negative charge. Moreover, CS promotes the proliferation of osteoblasts by increasing the expression of genes related to calcium binding and mineralization, such as ALP, OPN, and OCN. Also, combination with inorganic and organic molecules (e.g., metal ions, graphene oxide, and nano-HA) improves the osteogenic performance of CS. In addition, these properties of CS can be enhanced by side chain modification, yielding QCS, CMC, SCS, and PCS. Among them, QCS is the most common form; it is characterized by enhanced antibacterial activity, an optimal degree of substitution of 20%, and a critical degree of substitution of 90%. In addition, carboxylation, sulfation, and phosphorylation also promote the antibacterial and osteogenic properties of CS. At present, CS can be applied to the treatment of infected defects in many forms, including hydrogels, coatings, microspheres, and nanofibers, all of which have achieved good therapeutic effects.

Although there have been significant advances in the research on the treatment of infectious bone defects with CS, there are still some deficiencies that need to be implemented to promote its extensive clinical application. First of all, the hydrophobicity of CS greatly limits its application, and the antibacterial property of pure CS is not as effective as that of antibiotics. Although some modification of CS can solve this problem, the modified CS will inevitably produce some toxicity. Furthermore, the synthesis of modified CS is complicated, and it is not easy to control the quantification. Therefore, future research should focus on the development of cell-compatible solvents and modification methods to enhance the antibacterial activity and bone-promoting ability of CS while maintaining good biocompatibility. In addition, the insufficient mechanical properties of CS limit its wide application. The combination of CS with other materials such as inorganic materials can make up for the deficiencies. Therefore, these mixed materials deserve further study. Moreover, there is limited research on the relationship between the degradation rate and MW of CS *in vivo*. Many studies on CS are still in the laboratory stage, and further research is needed to be used as bone graft biomaterial for treating infection in clinical treatment. In summary, future research should focus on the efficiency of CS to maximize its antibacterial and osteogenic properties under physiological conditions and more natural bioactive materials mixed with CS need to be developed to further improve biological performance. Such evidence would help overcome the existing difficulties and provide a new perspective for the treatment of infected bone defects.

AUTHOR CONTRIBUTIONS

YT: Writing original draft, Funding acquisition. DHW: Supervision. DKW: Supervision. YC: Conceptualization. GR: Conceptualization. YW: Funding acquisition. JW: Investigation. CP: Investigation, Methodology.

FUNDING

This study was supported by the Program of Jilin Provincial Health Department (2019SCZT014); Scientific Development Program of Jilin Province (20200404140YY, 20200404190YY).

REFERENCES

Aam, B. B., Heggset, E. B., Norberg, A. L., Sørlie, M., Vårum, K. M., and Eijsink, V. G. H. (2010). Production of Chitooligosaccharides and Their Potential Applications in Medicine. *Mar. Drugs* 8 (5), 1482–1517. doi:10.3390/md8051482

Abazari, M. F., Nejati, F., Nasiri, N., Khazeni, Z. A. S., Nazari, B., Enderami, S. E., et al. (2019). Platelet-rich Plasma Incorporated Electrospun PVA-Chitosan-HA Nanofibers Accelerates Osteogenic Differentiation and Bone Reconstruction. *Gene* 720, 144096. doi:10.1016/j.gene.2019.144096

Abueva, C. D. G., Jang, D.-W., Padalhin, A., and Lee, B.-T. (2017). Phosphonate-Chitosan Functionalization of a Multi-Channel Hydroxyapatite Scaffold for Interfacial Implant-Bone Tissue Integration. *J. Mat. Chem. B* 5 (6), 1293–1301. doi:10.1039/c6tb03228a

Aguilar, A., Zein, N., Harmouch, E., Hafdi, B., Bornert, F., Offner, D., et al. (2019). Application of Chitosan in Bone and Dental Engineering. *Molecules* 24 (16), 3009. doi:10.3390/molecules24163009

Anitha, A., Divya Rani, V. V., Krishna, R., Sreeja, V., Selvamurugan, N., Nair, S. V., et al. (2009). Synthesis, Characterization, Cytotoxicity and Antibacterial Studies of Chitosan, O-Carboxymethyl and N,O-carboxymethyl Chitosan Nanoparticles. *Carbohydr. Polym.* 78 (4), 672–677. doi:10.1016/j.carbpol.2009.05.028

Beachley, V., and Wen, X. (2009). Effect of Electrospinning Parameters on the Nanofiber Diameter and Length. *Mater. Sci. Eng. C* 29 (3), 663–668. doi:10.1016/j.msec.2008.10.037

Beenken, K. E., Smith, J. K., Skinner, R. A., McLaren, S. G., Bellamy, W., Gruenwald, M. J., et al. (2014). Chitosan Coating to Enhance the Therapeutic Efficacy of Calcium Sulfate-Based Antibiotic Therapy in the Treatment of Chronic Osteomyelitis. *J. Biomater. Appl.* 29 (4), 514–523. doi:10.1177/0885328214535452

Busilacchi, A., Gigante, A., Mattioli-Belmonte, M., Manzotti, S., and Muzzarelli, R. A. A. (2013). Chitosan Stabilizes Platelet Growth Factors and Modulates Stem Cell Differentiation toward Tissue Regeneration. *Carbohydr. Polym.* 98 (1), 665–676. doi:10.1016/j.carbpol.2013.06.044

Cao, L., Werkmeister, J. A., Wang, J., Glattauer, V., McLean, K. M., and Liu, C. (2014). Bone Regeneration Using Photocrosslinked Hydrogel Incorporating rhBMP-2 Loaded 2-N, 6-O-Sulfated Chitosan Nanoparticles. *Biomaterials* 35 (9), 2730–2742. doi:10.1016/j.biomaterials.2013.12.028

Chahal, S., Kumar, A., and Hussian, F. S. J. (2019). Development of Biomimetic Electrospun Polymeric Biomaterials for Bone Tissue Engineering. A Review. *J. Biomaterials Sci. Polym. Ed.* 30 (14), 1308–1355. doi:10.1080/09205063.2019.1630699

Chen, L., Tian, Z., and Du, Y. (2004). Synthesis and Ph Sensitivity of Carboxymethyl Chitosan-Based Polyampholyte Hydrogels for Protein Carrier Matrices. *Biomaterials* 25 (17), 3725–3732. doi:10.1016/j.biomaterials.2003.09.100

Chen, S., Lau, P., Lei, M., Peng, J., Tang, T., Wang, X., et al. (2017). Segmental Composite Porous Scaffolds with Either Osteogenesis or Anti-bone Resorption Properties Tested in a Rabbit Ulna Defect Model. *J. Tissue Eng. Regen. Med.* 11 (1), 34–43. doi:10.1002/term.1828

Chou, C.-K., Chen, S.-M., Li, Y.-C., Huang, T.-C., and Lee, J.-A. (2015). Low-molecular-weight Chitosan Scavenges Methylglyoxal and N ε-(carboxyethyl) lysine, the Major Factors Contributing to the Pathogenesis of Nephropathy. *Springerplus* 4, 312. doi:10.1186/s40064-015-1106-4

Chung, Y.-C., Yeh, J.-Y., and Tsai, C.-F. (2011). Antibacterial Characteristics and Activity of Water-Soluble Chitosan Derivatives Prepared by the Maillard Reaction. *Molecules* 16 (10), 8504–8514. doi:10.3390/molecules16108504

Chung, Y. C., Su, Y. P., Chen, C. C., Jia, G., Wang, H. L., Wu, J. C., et al. (2004). Relationship between Antibacterial Activity of Chitosan and Surface Characteristics of Cell Wall. *Acta Pharmacol. Sin.* 25 (7), 932–936.

Covarrubias, C., Cádiz, M., Maureira, M., Celhay, I., Cuadra, F., and von Marttens, A. (2018). Bionanocomposite Scaffolds Based on Chitosan-Gelatin and Nanodimensional Bioactive Glass Particles: *In Vitro* Properties and *In Vivo* Bone Regeneration. *J. Biomater. Appl.* 32 (9), 1155–1163. doi:10.1177/0885328218759042

Crismaru, M., Asri, L. A. T. W., Loontjens, T. J. A., Krom, B. P., de Vries, J., van der Mei, H. C., et al. (2011). Survival of Adhering Staphylococci during Exposure to a Quaternary Ammonium Compound Evaluated by Using Atomic Force Microscopy Imaging. *Antimicrob. Agents Chemother.* 55 (11), 5010–5017. doi:10.1128/aac.05062-11

Croisier, F., and Jérôme, C. (2013). Chitosan-based Biomaterials for Tissue Engineering. *Eur. Polym. J.* 49 (4), 780–792. doi:10.1016/j.eurpolymj.2012.12.009

Cui, X., Huang, W., Zhang, Y., Huang, C., Yu, Z., Wang, L., et al. (2017). Evaluation of an Injectable Bioactive Borate Glass Cement to Heal Bone Defects in a Rabbit Femoral Condyle Model. *Mater. Sci. Eng. C* 73, 585–595. doi:10.1016/j.msec.2016.12.101

Dang, J. M., Sun, D. D. N., Shin-Ya, Y., Sieber, A. N., Kostuik, J. P., and Leong, K. W. (2006). Temperature-responsive Hydroxybutyl Chitosan for the Culture of Mesenchymal Stem Cells and Intervertebral Disk Cells. *Biomaterials* 27 (3), 406–418. doi:10.1016/j.biomaterials.2005.07.033

Deepthi, S., Venkatesan, J., Kim, S.-K., Bumgardner, J. D., and Jayakumar, R. (2016). An Overview of Chitin or Chitosan/Nano Ceramic Composite Scaffolds for Bone Tissue Engineering. *Int. J. Biol. Macromol.* 93 (Pt B), 1338–1353. doi:10.1016/j.ijbiomac.2016.03.041

Dias, L. L. S., Mansur, H. S., Donnici, C. L., and Pereira, M. M. (2011). Synthesis and Characterization of Chitosan-Polyvinyl Alcohol-Bioactive Glass Hybrid Membranes. *Biomatter* 1 (1), 114–119. doi:10.4161/biom.1.1.17449

Ding, F., Deng, H., Du, Y., Shi, X., and Wang, Q. (2014). Emerging Chitin and Chitosan Nanofibrous Materials for Biomedical Applications. *Nanoscale* 6 (16), 9477–9493. doi:10.1039/c4nr02814g

Dreifke, M. B., Ebraheim, N. A., and Jayasuriya, A. C. (2013). Investigation of Potential Injectable Polymeric Biomaterials for Bone Regeneration. *J. Biomed. Mat. Res.* 101A (8), 2436–2447. doi:10.1002/jbm.a.34521

Fan, L., Yang, J., Wu, H., Hu, Z., Yi, J., Tong, J., et al. (2015). Preparation and Characterization of Quaternary Ammonium Chitosan Hydrogel with Significant Antibacterial Activity. *Int. J. Biol. Macromol.* 79, 830–836. doi:10.1016/j.ijbiomac.2015.04.013

Fei Liu, X., Lin Guan, Y., Zhi Yang, D., Li, Z., and De Yao, K. (2001). Antibacterial Action of Chitosan and Carboxymethylated Chitosan. *J. Appl. Polym. Sci.* 79 (7), 1324–1335. doi:10.1002/1097-4628(20010214)79:7<1324::aid-app210>3.0.co;2-l

Fischer, D., Li, Y., Ahlemeyer, B., Krieglstein, J., and Kissel, T. (2003). *In Vitro* Cytotoxicity Testing of Polycations: Influence of Polymer Structure on Cell Viability and Hemolysis. *Biomaterials* 24 (7), 1121–1131. doi:10.1016/s0142-9612(02)00445-3

Frank, L. A., Onzi, G. R., Morawski, A. S., Pohlmann, A. R., Guterres, S. S., and Contri, R. V. (2020). Chitosan as a Coating Material for Nanoparticles Intended for Biomedical Applications. *React. Funct. Polym.* 147, 104459. doi:10.1016/j.reactfunctpolym.2019.104459

Frohbergh, M. E., Katsman, A., Botta, G. P., Lazarovici, P., Schauer, C. L., Wegst, U. G. K., et al. (2012). Electrospun Hydroxyapatite-Containing Chitosan Nanofibers Crosslinked with Genipin for Bone Tissue Engineering. *Biomaterials* 33 (36), 9167–9178. doi:10.1016/j.biomaterials.2012.09.009

Galarraga-Vinueza, M. E., Mesquita-Guimarães, J., Magini, R. S., Souza, J. C. M., Fredel, M. C., and Boccaccini, A. R. (2017). Anti-biofilm Properties of Bioactive

Glasses Embedding Organic Active Compounds. *J. Biomed. Mat. Res.* 105 (2), 672–679. doi:10.1002/jbm.a.35934

Gentile, P., Mattioli-Belmonte, M., Chiono, V., Ferretti, C., Baino, F., Tonda-Turo, C., et al. (2012). Bioactive Glass/Polymer Composite Scaffolds Mimicking Bone Tissue. *J. Biomed. Mat. Res.* 100A (10), 2654–2667. doi:10.1002/jbm.a.34205

Green, S., Roldo, M., Douroumis, D., Bouropoulos, N., Lamprou, D., and Fatouros, D. G. (2009). Chitosan Derivatives Alter Release Profiles of Model Compounds from Calcium Phosphate Implants. *Carbohydr. Res.* 344 (7), 901–907. doi:10.1016/j.carres.2009.02.022

Grellier, M., Granja, P. L., Fricain, J.-C., Bidarra, S. J., Renard, M., Bareille, R., et al. (2009). The Effect of the Co-immobilization of Human Osteoprogenitors and Endothelial Cells within Alginate Microspheres on Mineralization in a Bone Defect. *Biomaterials* 30 (19), 3271–3278. doi:10.1016/j.biomaterials.2009.02.033

Ho, M. H., Liao, M. H., Lin, Y. L., Lai, C. H., Lin, P. I., and Chen, R. M. (2014). Improving Effects of Chitosan Nanofiber Scaffolds on Osteoblast Proliferation and Maturation. *Int. J. Nanomedicine* 9, 4293–4304. doi:10.2147/IJN.S68012

Ho, M. H., Yao, C. J., Liao, M. H., Lin, P. I., Liu, S. H., and Chen, R. M. (2015). Chitosan Nanofiber Scaffold Improves Bone Healing via Stimulating Trabecular Bone Production Due to Upregulation of the Runx2/Osteocalcin/Alkaline Phosphatase Signaling Pathway. *Int. J. Nanomedicine* 10, 5941–5954. doi:10.2147/IJN.S90669

Huang, J., Jiang, H., Qiu, M., Geng, X., Yang, R., Li, J., et al. (2013). Antibacterial Activity Evaluation of Quaternary Chitin against Escherichia Coli and Staphylococcus Aureus. *Int. J. Biol. Macromol.* 52, 85–91. doi:10.1016/j.ijbiomac.2012.10.017

Huang, W., Li, X., Shi, X., and Lai, C. (2014). Microsphere Based Scaffolds for Bone Regenerative Applications. *Biomater. Sci.* 2 (9), 1145–1153. doi:10.1039/c4bm00161c

Huang, Y., Zhang, X., Wu, A., and Xu, H. (2016). An Injectable Nano-Hydroxyapatite (N-HA)/Glycol Chitosan (G-CS)/Hyaluronic Acid (HyA) Composite Hydrogel for Bone Tissue Engineering. *RSC Adv.* 6 (40), 33529–33536. doi:10.1039/c5ra26160k

Huang, Z., Yu, B., Feng, Q., Li, S., Chen, Y., and Luo, L. (2011). In Situ-forming Chitosan/Nano-hydroxyapatite/Collagen Gel for the Delivery of Bone Marrow Mesenchymal Stem Cells. *Carbohydr. Polym.* 85 (1), 261–267. doi:10.1016/j.carbpol.2011.02.029

Islam, S., Bhuiyan, M. A. R., and Islam, M. N. (2016). Chitin and Chitosan: Structure, Properties and Applications in Biomedical Engineering. *J. Polym. Environ.* 25 (3), 854–866. doi:10.1007/s10924-016-0865-5

Jayakumar, R., Nagahama, H., Furuike, T., and Tamura, H. (2008). Synthesis of Phosphorylated Chitosan by Novel Method and its Characterization. *Int. J. Biol. Macromol.* 42 (4), 335–339. doi:10.1016/j.ijbiomac.2007.12.011

Jayakumar, R., Reis, R. L., and Mano, J. F. (2007). Synthesis and Characterization of pH-Sensitive Thiol-Containing Chitosan Beads for Controlled Drug Delivery Applications. *Drug Deliv.* 14 (1), 9–17. doi:10.1080/10717540600739872

Jayash, S. N., Hashim, N. M., Misran, M., and Baharuddin, N. (2017). Formulation Andin Vitroandin Vivoevaluation of a New Osteoprotegerin-Chitosan Gel for Bone Tissue Regeneration. *J. Biomed. Mat. Res.* 105 (2), 398–407. doi:10.1002/jbm.a.35919

Jayash, S. N., Hashim, N. M., Misran, M., and Baharuddin, N. (2017). Local Application of Osteoprotegerin-Chitosan Gel in Critical-Sized Defects in a Rabbit Model. *PeerJ* 5, e3513. doi:10.7717/peerj.3513

Ji, Q. X., Chen, X. G., Zhao, Q. S., Liu, C. S., Cheng, X. J., and Wang, L. C. (2009). Injectable Thermosensitive Hydrogel Based on Chitosan and Quaternized Chitosan and the Biomedical Properties. *J. Mater Sci. Mater Med.* 20 (8), 1603–1610. doi:10.1007/s10856-009-3729-x

Jia, Z., Shen, D., and Xu, W. (2001). Synthesis and Antibacterial Activities of Quaternary Ammonium Salt of Chitosan. *Carbohydr. Res.* 333 (1), 1–6. doi:10.1016/s0008-6215(01)00112-4

Jiang, T., Nukavarapu, S. P., Deng, M., Jabbarzadeh, E., Kofron, M. D., Doty, S. B., et al. (2010). Chitosan-poly(lactide-co-glycolide) Microsphere-Based Scaffolds for Bone Tissue Engineering: *In Vitro* Degradation and *In Vivo* Bone Regeneration Studies. *Acta Biomater.* 6 (9), 3457–3470. doi:10.1016/j.actbio.2010.03.023

Kadouche, S., Farhat, M., Lounici, H., Fiallo, M., Sharrock, P., Mecherri, M., et al. (2016). Low Cost Chitosan Biopolymer for Environmental Use Made from Abundant Shrimp Wastes. *Waste Biomass Valor* 8 (2), 401–406. doi:10.1007/s12649-016-9593-2

Kalinov, K. N., Ignatova, M. G., Manolova, N. E., Markova, N. D., Karashanova, D. B., and Rashkov, I. B. (2015). Novel Antibacterial Electrospun Materials Based on Polyelectrolyte Complexes of a Quaternized Chitosan Derivative. *RSC Adv.* 5 (67), 54517–54526. doi:10.1039/c5ra08484a

Keller, L., Regiel-Futyra, A., Gimeno, M., Eap, S., Mendoza, G., Andreu, V., et al. (2017). Chitosan-based Nanocomposites for the Repair of Bone Defects. *Nanomedicine Nanotechnol. Biol. Med.* 13 (7), 2231–2240. doi:10.1016/j.nano.2017.06.007

Kjalarsdóttir, L., Dýrfjörd, A., Dagbjartsson, A., Laxdal, E. H., Örlygsson, G., Gíslason, J., et al. (2019). Bone Remodeling Effect of a Chitosan and Calcium Phosphate-Based Composite. *Regen. Biomater.* 6 (4), 241–247. doi:10.1093/rb/rbz009

Koski, C., Vu, A. A., and Bose, S. (2020). Effects of Chitosan-Loaded Hydroxyapatite on Osteoblasts and Osteosarcoma for Chemopreventative Applications. *Mater. Sci. Eng. C* 115, 111041. doi:10.1016/j.msec.2020.111041

Kumari, S., Tiyyagura, H. R., Pottathara, Y. B., Sadasivuni, K. K., PonnammaDouglas, D. T. E. L., Douglas, T. E. L., et al. (2021). Surface Functionalization of Chitosan as a Coating Material for Orthopaedic Applications: A Comprehensive Review. *Carbohydr. Polym.* 255, 117487. doi:10.1016/j.carbpol.2020.117487

Kyzas, G., and Bikiaris, D. (2015). Recent Modifications of Chitosan for Adsorption Applications: a Critical and Systematic Review. *Mar. Drugs* 13 (1), 312–337. doi:10.3390/md13010312

Lee, J. S., Kim, H.-S., Nah, H., Lee, S. J., Moon, H.-J., Bang, J. B., et al. (2021). The Effectiveness of Compartmentalized Bone Graft Sponges Made Using Complementary Bone Graft Materials and Succinylated Chitosan Hydrogels. *Biomedicines* 9 (12), 1765. doi:10.3390/biomedicines9121765

Lee, J. S., Nah, H., Moon, H.-J., Lee, S. J., Heo, D. N., and Kwon, I. K. (2020). Controllable Delivery System: A Temperature and pH-Responsive Injectable Hydrogel from Succinylated Chitosan. *Appl. Surf. Sci.* 528, 146812. doi:10.1016/j.apsusc.2020.146812

Leedy, M. R., Martin, H. J., Norowski, P. A., Jennings, J. A., Haggard, W. O., and Bumgardner, J. D. (2011). "Use of Chitosan as a Bioactive Implant Coating for Bone-Implant Applications," in *Use of Chitosan as a Bioactive Implant Coating for Bone-Implant Applications" in Chitosan for Biomaterials II*. Editors R. Jayakumar, M. Prabaharan, and R. Muzzarelli (Berlin, Heidelberg: Springer), 129–165. doi:10.1007/12_2011_115

Li, B., Huang, L., Wang, X., Ma, J., and Xie, F. (2011). Biodegradation and Compressive Strength of Phosphorylated Chitosan/Chitosan/Hydroxyapatite Bio-Composites. *Mat. Des.* 32 (8–9), 4543–4547. doi:10.1016/j.matdes.2011.04.039

Li, J., Wu, Y., and Zhao, L. (2016). Antibacterial Activity and Mechanism of Chitosan with Ultra High Molecular Weight. *Carbohydr. Polym.* 148, 200–205. doi:10.1016/j.carbpol.2016.04.025

Li, J., and Zhuang, S. (2020). Antibacterial Activity of Chitosan and its Derivatives and Their Interaction Mechanism with Bacteria: Current State and Perspectives. *Eur. Polym. J.* 138, 109984. doi:10.1016/j.eurpolymj.2020.109984

Li, T., Liu, Z., Xiao, M., Yang, Z., Liu, Z., Zhou, X., et al. (2017). *In Vitro* and *In Vivo* Studies of a Gelatin/Carboxymethyl Chitosan/LAPONITE® Composite Scaffold for Bone Tissue Engineering. *RSC Adv.* 7 (85), 54100–54110. doi:10.1039/c7ra07588j

Li, Y., Liu, C., Liu, W., Cheng, X., Zhang, A., Zhang, S., et al. (2021). Apatite Formation Induced by Chitosan/Gelatin Hydrogel Coating Anchored on Poly(aryl Ether Nitrile Ketone) Substrates to Promote Osteoblastic Differentiation. *Macromol. Biosci.* 21 (11), e2100262. doi:10.1002/mabi.202100262

Lim, S.-H., and Hudson, S. M. (2004). Synthesis and Antimicrobial Activity of a Water-Soluble Chitosan Derivative with a Fiber-Reactive Group. *Carbohydr. Res.* 339 (2), 313–319. doi:10.1016/j.carres.2003.10.024

Liu, X., Chen, Y., Huang, Q., He, W., Feng, Q., and Yu, B. (2014). A Novel Thermo-Sensitive Hydrogel Based on Thiolated Chitosan/Hydroxyapatite/Beta-Glycerophosphate. *Carbohydr. Polym.* 110, 62–69. doi:10.1016/j.carbpol.2014.03.065

LogithKumar, R., KeshavNarayan, A., Dhivya, S., Chawla, A., Saravanan, S., and Selvamurugan, N. (2016). A Review of Chitosan and its Derivatives in Bone Tissue Engineering. *Carbohydr. Polym.* 151, 172–188. doi:10.1016/j.carbpol.2016.05.049

López Tenorio, D., Valencia, C., Valencia, C., Zuluaga, F., Valencia, M., Mina, J., et al. (2019). Evaluation of the Biocompatibility of CS-Graphene Oxide Compounds *In Vivo*. *Ijms* 20 (7), 1572. doi:10.3390/ijms20071572

Lu, H., Liu, Y., Guo, J., Wu, H., Wang, J., and Wu, G. (2016). Biomaterials with Antibacterial and Osteoinductive Properties to Repair Infected Bone Defects. *Ijms* 17 (3), 334. doi:10.3390/ijms17030334

Lu, Y., Li, L., Zhu, Y., Wang, X., Li, M., Lin, Z., et al. (2018). Multifunctional Copper-Containing Carboxymethyl Chitosan/Alginate Scaffolds for Eradicating Clinical Bacterial Infection and Promoting Bone Formation. *ACS Appl. Mat. Interfaces* 10 (1), 127–138. doi:10.1021/acsami.7b13750

Mao, J. S., Cui, Y. L., Wang, X. H., Sun, Y., Yin, Y. J., Zhao, H. M., et al. (2004). A Preliminary Study on Chitosan and Gelatin Polyelectrolyte Complex Cytocompatibility by Cell Cycle and Apoptosis Analysis. *Biomaterials* 25 (18), 3973–3981. doi:10.1016/j.biomaterials.2003.10.080

Mathews, S., Gupta, P. K., Bhonde, R., and Totey, S. (2011). Chitosan Enhances Mineralization during Osteoblast Differentiation of Human Bone Marrow-Derived Mesenchymal Stem Cells, by Upregulating the Associated Genes. *Cell Prolif.* 44 (6), 537–549. doi:10.1111/j.1365-2184.2011.00788.x

Mattioli-Belmonte, M., Cometa, S., Ferretti, C., Iatta, R., Trapani, A., Ceci, E., et al. (2014). Characterization and Cytocompatibility of an Antibiotic/chitosan/cyclodextrins Nanocoating on Titanium Implants. *Carbohydr. Polym.* 110, 173–182. doi:10.1016/j.carbpol.2014.03.097

Meng, D., Dong, L., Wen, Y., and Xie, Q. (2015). Effects of Adding Resorbable Chitosan Microspheres to Calcium Phosphate Cements for Bone Regeneration. *Mater. Sci. Eng. C* 47, 266–272. doi:10.1016/j.msec.2014.11.049

Mostafa, A. A., El-Sayed, M. M. H., Mahmoud, A. A., and Gamal-Eldeen, A. M. (2017). Bioactive/Natural Polymeric Scaffolds Loaded with Ciprofloxacin for Treatment of Osteomyelitis. *AAPS PharmSciTech* 18 (4), 1056–1069. doi:10.1208/s12249-016-0605-0

Müller, W. E. G., Tolba, E., Schröder, H. C., Neufurth, M., Wang, S., Link, T., et al. (2015). A New Printable and Durable N,O-carboxymethyl Chitosan-Ca2+-Polyphosphate Complex with Morphogenetic Activity. *J. Mat. Chem. B* 3 (8), 1722–1730. doi:10.1039/c4tb01586j

Munhoz, M. A. S., Hirata, H. H., Plepis, A. M. G., Martins, V. C. A., and Cunha, M. R. (2018). Use of Collagen/Chitosan Sponges Mineralized with Hydroxyapatite for the Repair of Cranial Defects in Rats. *Injury* 49 (12), 2154–2160. doi:10.1016/j.injury.2018.09.018

Muzzarelli, R., Mehtedi, M., and Mattioli-Belmonte, M. (2014). Emerging Biomedical Applications of Nano-Chitins and Nano-Chitosans Obtained via Advanced Eco-Friendly Technologies from Marine Resources. *Mar. Drugs* 12 (11), 5468–5502. doi:10.3390/md12115468

Nagel, A. K., Schilling, M., Comte-Walters, S., Berkaw, M. N., and Ball, L. E. (2013). Identification of O-Linked N-Acetylglucosamine (O-GlcNAc)-Modified Osteoblast Proteins by Electron Transfer Dissociation Tandem Mass Spectrometry Reveals Proteins Critical for Bone Formation. *Mol. Cell. Proteomics* 12 (4), 945–955. doi:10.1074/mcp.m112.026633

Nancy, D., and Rajendran, N. (2018). Vancomycin Incorporated Chitosan/gelatin Coatings Coupled with TiO2-SrHAP Surface Modified Cp-Titanium for Osteomyelitis Treatment. *Int. J. Biol. Macromol.* 110, 197–205. doi:10.1016/j.ijbiomac.2018.01.004

Obregón, S., Amor, G., and Vázquez, A. (2019). Electrophoretic Deposition of Photocatalytic Materials. *Adv. Colloid Interface Sci.* 269, 236–255. doi:10.1016/j.cis.2019.05.003

Oftadeh, M. O., Bakhshandeh, B., Dehghan, M. M., and Khojasteh, A. (2018). Sequential Application of Mineralized Electroconductive Scaffold and Electrical Stimulation for Efficient Osteogenesis. *J. Biomed. Mat. Res.* 106 (5), 1200–1210. doi:10.1002/jbm.a.36316

Orhan, Z., Cevher, E., Mülazimoglu, L., Gürcan, D., AlperAraman, M. A., Araman, A., et al. (2006). The Preparation of Ciprofloxacin Hydrochloride-Loaded Chitosan and Pectin Microspheres. *J. Bone Jt. Surg. Br. volume* 88-B (2), 270–275. doi:10.1302/0301-620x.88b2.16328

Park, J. S., Yang, H. N., Jeon, S. Y., Woo, D. G., Na, K., and Park, K.-H. (2010). Osteogenic Differentiation of Human Mesenchymal Stem Cells Using RGD-Modified BMP-2 Coated Microspheres. *Biomaterials* 31 (24), 6239–6248. doi:10.1016/j.biomaterials.2010.05.002

Patel, K. D., El-Fiqi, A., Lee, H.-Y., Singh, R. K., Kim, D.-A., Lee, H.-H., et al. (2012). Chitosan-nanobioactive Glass Electrophoretic Coatings with Bone Regenerative and Drug Delivering Potential. *J. Mat. Chem.* 22 (47), 24945–24956. doi:10.1039/c2jm33830k

Pattnaik, S., Nethala, S., Tripathi, A., Saravanan, S., Moorthi, A., and Selvamurugan, N. (2011). Chitosan Scaffolds Containing Silicon Dioxide and Zirconia Nano Particles for Bone Tissue Engineering. *Int. J. Biol. Macromol.* 49 (5), 1167–1172. doi:10.1016/j.ijbiomac.2011.09.016

Peng, Y., Han, B., Liu, W., and Xu, X. (2005). Preparation and Antimicrobial Activity of Hydroxypropyl Chitosan. *Carbohydr. Res.* 340 (11), 1846–1851. doi:10.1016/j.carres.2005.05.009

Peng, Z.-X., Tu, B., Shen, Y., Du, L., Wang, L., Guo, S.-R., et al. (2011). Quaternized Chitosan Inhibits IcaA Transcription and Biofilm Formation by Staphylococcus on a Titanium Surface. *Antimicrob. Agents Chemother.* 55 (2), 860–866. doi:10.1128/aac.01005-10

Peng, Z.-X., Wang, L., Du, L., Guo, S.-R., Wang, X.-Q., and Tang, T.-T. (2010). Adjustment of the Antibacterial Activity and Biocompatibility of Hydroxypropyltrimethyl Ammonium Chloride Chitosan by Varying the Degree of Substitution of Quaternary Ammonium. *Carbohydr. Polym.* 81 (2), 275–283. doi:10.1016/j.carbpol.2010.02.008

Peter, M., Binulal, N. S., Nair, S. V., Selvamurugan, N., Tamura, H., and Jayakumar, R. (2010). Novel Biodegradable Chitosan-Gelatin/nano-Bioactive Glass Ceramic Composite Scaffolds for Alveolar Bone Tissue Engineering. *Chem. Eng. J.* 158 (2), 353–361. doi:10.1016/j.cej.2010.02.003

Raafat, D., von Bargen, K., Haas, A., and Sahl, H.-G. (2008). Insights into the Mode of Action of Chitosan as an Antibacterial Compound. *Appl. Environ. Microbiol.* 74 (12), 3764–3773. doi:10.1128/aem.00453-08

Radwan, N. H., Nasr, M., Ishak, R. A. H., Abdeltawab, N. F., and Awad, G. A. S. (2020). Chitosan-calcium Phosphate Composite Scaffolds for Control of Post-operative Osteomyelitis: Fabrication, Characterization, and In Vitro-In Vivo Evaluation. *Carbohydr. Polym.* 244, 116482. doi:10.1016/j.carbpol.2020.116482

Rashki, S., Asgarpour, K., Tarrahimofrad, H., Hashemipour, M., Ebrahimi, M. S., Fathizadeh, H., et al. (2021). Chitosan-based Nanoparticles against Bacterial Infections. *Carbohydr. Polym.* 251, 117108. doi:10.1016/j.carbpol.2020.117108

Rasouli, R., Barhoum, A., Bechelany, M., and Dufresne, A. (2019). Nanofibers for Biomedical and Healthcare Applications. *Macromol. Biosci.* 19 (2), e1800256. doi:10.1002/mabi.201800256

Romero, R., Chubb, L., Travers, J. K., Gonzales, T. R., Ehrhart, N. P., and Kipper, M. J. (2015). Coating Cortical Bone Allografts with Periosteum-Mimetic Scaffolds Made of Chitosan, Trimethyl Chitosan, and Heparin. *Carbohydr. Polym.* 122, 144–151. doi:10.1016/j.carbpol.2015.01.015

Rosenberg, N., Mor-Cohen, R., Sheptovitsky, V. H., Romanenco, O., Hess, O., and Lahav, J. (2019). Integrin-mediated Cell Adhesion Requires Extracellular Disulfide Exchange Regulated by Protein Disulfide Isomerase. *Exp. Cell Res.* 381 (1), 77–85. doi:10.1016/j.yexcr.2019.04.017

Sajomsang, W., Gonil, P., and Tantayanon, S. (2009). Antibacterial Activity of Quaternary Ammonium Chitosan Containing Mono or Disaccharide Moieties: Preparation and Characterization. *Int. J. Biol. Macromol.* 44 (5), 419–427. doi:10.1016/j.ijbiomac.2009.03.003

Saran, U., Gemini Piperni, S., and Chatterjee, S. (2014). Role of Angiogenesis in Bone Repair. *Archives Biochem. Biophysics* 561, 109–117. doi:10.1016/j.abb.2014.07.006

Saravanan, S., Chawla, A., Vairamani, M., Sastry, T. P., Subramanian, K. S., and Selvamurugan, N. (2017). Scaffolds Containing Chitosan, Gelatin and Graphene Oxide for Bone Tissue Regeneration *In Vitro* and *In Vivo*. *Int. J. Biol. Macromol.* 104 (Pt B), 1975–1985. doi:10.1016/j.ijbiomac.2017.01.034

Saravanan, S., Vimalraj, S., Thanikaivelan, P., Banudevi, S., and Manivasagam, G. (2019). A Review on Injectable Chitosan/Beta Glycerophosphate Hydrogels for Bone Tissue Regeneration. *Int. J. Biol. Macromol.* 121, 38–54. doi:10.1016/j.ijbiomac.2018.10.014

Sedghi, R., Shaabani, A., and Sayyari, N. (2020). Electrospun Triazole-Based Chitosan Nanofibers as a Novel Scaffolds for Bone Tissue Repair and Regeneration. *Carbohydr. Polym.* 230, 115707. doi:10.1016/j.carbpol.2019.115707

Shagdarova, B., Lunkov, A., Il'ina, A., and Varlamov, V. (2019). Investigation of the Properties of N-[(2-hydroxy-3-trimethylammonium) Propyl] Chloride Chitosan Derivatives. *Int. J. Biol. Macromol.* 124, 994–1001. doi:10.1016/j.ijbiomac.2018.11.209

Shao, R. X., Quan, R. F., Wang, T., Du, W. B., Jia, G. Y., Wang, D., et al. (2018). Effects of a Bone Graft Substitute Consisting of Porous Gradient HA/ZrO2 and Gelatin/chitosan Slow-Release Hydrogel Containing BMP-2 and BMSCs on Lumbar Vertebral Defect Repair in Rhesus Monkey. *J. Tissue Eng. Regen. Med.* 12 (3), e1813–e1825. doi:10.1002/term.2601

Shi, P., Zuo, Y., Li, X., Zou, Q., Liu, H., Zhang, L., et al. (2010). Gentamicin-impregnated Chitosan/Nanohydroxyapatite/Ethyl Cellulose Microspheres Granules for Chronic Osteomyelitis Therapy. *J. Biomed. Mat. Res. A* 93 (3), 1020–1031. doi:10.1002/jbm.a.32598

Shi, X., Du, Y., Yang, J., Zhang, B., and Sun, L. (2006). Effect of Degree of Substitution and Molecular Weight of Carboxymethyl Chitosan Nanoparticles on Doxorubicin Delivery. *J. Appl. Polym. Sci.* 100 (6), 4689–4696. doi:10.1002/app.23040

Shi, Z., Neoh, K. G., Kang, E. T., Poh, C. K., and Wang, W. (2009). Surface Functionalization of Titanium with Carboxymethyl Chitosan and Immobilized Bone Morphogenetic Protein-2 for Enhanced Osseointegration. *Biomacromolecules* 10 (6), 1603–1611. doi:10.1021/bm900203w

Shin, S.-Y., Park, H.-N., Kim, K.-H., Lee, M.-H., Choi, Y. S., Park, Y.-J., et al. (2005). Biological Evaluation of Chitosan Nanofiber Membrane for Guided Bone Regeneration. *J. Periodontology* 76 (10), 1778–1784. doi:10.1902/jop.2005.76.10.1778

Shuai, C., Guo, W., Gao, C., Yang, Y., Wu, P., and Feng, P. (2017). An nMgO Containing Scaffold: Antibacterial Activity, Degradation Properties and Cell Responses. *Int. J. Bioprint* 4 (1), 120. doi:10.18063/IJB.v4i1.120

Sofi, H. S., Ashraf, R., Beigh, M. A., and Sheikh, F. A. (2018). Scaffolds Fabricated from Natural Polymers/Composites by Electrospinning for Bone Tissue Regeneration. *Adv. Exp. Med. Biol.* 1078, 49–78. doi:10.1007/978-981-13-0950-2_4

Soundrapandian, C., Datta, S., Kundu, B., Basu, D., and Sa, B. (2010). Porous Bioactive Glass Scaffolds for Local Drug Delivery in Osteomyelitis: Development and *In Vitro* Characterization. *AAPS PharmSciTech* 11 (4), 1675–1683. doi:10.1208/s12249-010-9550-5

Su, H., Liu, K.-Y., Karydis, A., Abebe, D. G., Wu, C., Anderson, K. M., et al. (2016). *In Vitro* and *In Vivo* Evaluations of a Novel Post-electrospinning Treatment to Improve the Fibrous Structure of Chitosan Membranes for Guided Bone Regeneration. *Biomed. Mat.* 12 (1), 015003. doi:10.1088/1748-605x/12/1/015003

Sultankulov, B., Berillo, D., Sultankulova, K., Tokay, T., and Saparov, A. (2019). Progress in the Development of Chitosan-Based Biomaterials for Tissue Engineering and Regenerative Medicine. *Biomolecules* 9 (9), 470. doi:10.3390/biom9090470

Sun, L., Du, Y., Fan, L., Chen, X., and Yang, J. (2006). Preparation, Characterization and Antimicrobial Activity of Quaternized Carboxymethyl Chitosan and Application as Pulp-Cap. *Polymer* 47 (6), 1796–1804. doi:10.1016/j.polymer.2006.01.073

Sun, Q.-B., Xu, C.-P., Li, W.-Q., Meng, Q.-J., and Qu, H.-Z. (2021). Halloysites Modified Polyethylene Glycol Diacrylate/Thiolated Chitosan Double Network Hydrogel Combined with BMP-2 for Rat Skull Regeneration. *Artif. Cells, Nanomedicine, Biotechnol.* 49 (1), 71–82. doi:10.1080/21691401.2020.1858845

Tan, H.-l., Ao, H.-y., Ma, R., Lin, W.-t., and Tang, T.-t. (2014). *In Vivo* Effect of Quaternized Chitosan-Loaded Polymethylmethacrylate Bone Cement on Methicillin-Resistant Staphylococcus Epidermidis Infection of the Tibial Metaphysis in a Rabbit ModelTibial Metaphysis in a Rabbit Model. *Antimicrob. Agents Chemother.* 58 (10), 6016–6023. doi:10.1128/aac.03489-14

Tan, H., Ma, R., Lin, C., Liu, Z., and Tang, T. (2013). Quaternized Chitosan as an Antimicrobial Agent: Antimicrobial Activity, Mechanism of Action and Biomedical Applications in Orthopedics. *Ijms* 14 (1), 1854–1869. doi:10.3390/ijms14011854

Tan, H., Peng, Z., Li, Q., Xu, X., Guo, S., and Tang, T. (2012). The Use of Quaternised Chitosan-Loaded PMMA to Inhibit Biofilm Formation and Downregulate the Virulence-Associated Gene Expression of Antibiotic-Resistant Staphylococcus. *Biomaterials* 33 (2), 365–377. doi:10.1016/j.biomaterials.2011.09.084

Tang, T., Zhang, G., Py Lau, C., Zheng, L. Z., Xie, X. H., Wang, X. L., et al. (2011). Effect of Water-Soluble P-Chitosan and S-Chitosan on Human Primary Osteoblasts and Giant Cell Tumor of Bone Stromal Cells. *Biomed. Mat.* 6 (1), 015004. doi:10.1088/1748-6041/6/1/015004

Tang, Y.-Q., Wang, Q.-Y., Ke, Q.-F., Zhang, C.-Q., Guan, J.-J., and Guo, Y.-P. (2020). Mineralization of Ytterbium-Doped Hydroxyapatite Nanorod Arrays in Magnetic Chitosan Scaffolds Improves Osteogenic and Angiogenic Abilities for Bone Defect Healing. *Chem. Eng. J.* 387, 124166. doi:10.1016/j.cej.2020.124166

Tao, F., Cheng, Y., Shi, X., Zheng, H., Du, Y., Xiang, W., et al. (2020). Applications of Chitin and Chitosan Nanofibers in Bone Regenerative Engineering. *Carbohydr. Polym.* 230, 115658. doi:10.1016/j.carbpol.2019.115658

Tao, J., Zhang, Y., Shen, A., Yang, Y., Diao, L., Wang, L., et al. (2020). Injectable Chitosan-Based Thermosensitive Hydrogel/Nanoparticle-Loaded System for Local Delivery of Vancomycin in the Treatment of Osteomyelitis. *Ijn* Vol. 15, 5855–5871. doi:10.2147/ijn.s247088

Tong, H.-W., Wang, M., and Lu, W. W. (2011). Electrospun Poly(hydroxybutyrate-Co-Hydroxyvalerate) Fibrous Membranes Consisting of Parallel-Aligned Fibers or Cross-Aligned Fibers: Characterization and Biological Evaluation. *J. Biomaterials Sci. Polym. Ed.* 22 (18), 2475–2497. doi:10.1163/092050610x540675

Topsakal, A., Uzun, M., Ugar, G., Ozcan, A., Altun, E., Oktar, F. N., et al. (2018). Development of Amoxicillin-Loaded Electrospun Polyurethane/Chitosan/β -Tricalcium Phosphate Scaffold for Bone Tissue Regeneration. *IEEE Trans.on Nanobioscience* 17 (3), 321–328. doi:10.1109/tnb.2018.2844870

Toskas, G., Heinemann, S., Heinemann, C., Cherif, C., Hund, R.-D., Roussis, V., et al. (2012). Ulvan and Ulvan/Chitosan Polyelectrolyte Nanofibrous Membranes as a Potential Substrate Material for the Cultivation of Osteoblasts. *Carbohydr. Polym.* 89 (3), 997–1002. doi:10.1016/j.carbpol.2012.04.045

Tsai, G.-J., and Su, W.-H. (1999). Antibacterial Activity of Shrimp Chitosan against *Escherichia coli*. *J. Food Prot.* 62 (3), 239–243. doi:10.4315/0362-028x-62.3.239

Venkatesan, J., Bhatnagar, I., and Kim, S.-K. (2014). Chitosan-Alginate Biocomposite Containing Fucoidan for Bone Tissue Engineering. *Mar. Drugs* 12 (1), 300–316. doi:10.3390/md12010300

Wahid, F., Wang, H.-S., Zhong, C., and Chu, L.-Q. (2017). Facile Fabrication of Moldable Antibacterial Carboxymethyl Chitosan Supramolecular Hydrogels Cross-Linked by Metal Ions Complexation. *Carbohydr. Polym.* 165, 455–461. doi:10.1016/j.carbpol.2017.02.085

Wang, B., Guo, Y., Chen, X., Zeng, C., Hu, Q., Yin, W., et al. (2018). Nanoparticle-modified Chitosan-Agarose-Gelatin Scaffold for Sustained Release of SDF-1 and BMP-2. *Ijn* Vol. 13, 7395–7408. doi:10.2147/ijn.s180859

Wang, D., Liu, Y., Liu, Y., Yan, L., Zaat, S. A. J., Wismeijer, D., et al. (2019). A Dual Functional Bone-defect-filling Material with Sequential Antibacterial and Osteoinductive Properties for Infected Bone Defect Repair. *J. Biomed. Mater Res.* 107 (10), 2360–2370. doi:10.1002/jbm.a.36744

Wang, M., Sa, Y., Li, P., Guo, Y., Du, Y., Deng, H., et al. (2018). A Versatile and Injectable Poly(methyl Methacrylate) Cement Functionalized with Quaternized Chitosan-Glycerophosphate/Nanosized Hydroxyapatite Hydrogels. *Mater. Sci. Eng. C* 90, 264–272. doi:10.1016/j.msec.2018.04.075

Wang, Z., Liu, X., Martin, V. T., Abdi, M. A., Chen, L., Gong, Y., et al. (2020). Sequential Delivery of BMP2-Derived Peptide P24 by Thiolated Chitosan/Calcium Carbonate Composite Microspheres Scaffolds for Bone Regeneration. *J. Nanomater.* 2020, 1–10. doi:10.1155/2020/4929151

Wu, M., Long, Z., Xiao, H., and Dong, C. (2016). Recent Research Progress on Preparation and Application of N, N, N-Trimethyl Chitosan. *Carbohydr. Res.* 434, 27–32. doi:10.1016/j.carres.2016.08.002

Xia, C., Li, W., Fu, B., and Qin, C. (2019). Microcalorimetric and Microscopic Studies of the Effect of Chitosan Quaternary Ammonium Salt on Mitochondria. *Int. J. Biol. Macromol.* 126, 828–833. doi:10.1016/j.ijbiomac.2018.12.272

Xu, F., Ding, H., Song, F., and Wang, J. (2014). Effects of Preparation Methods on the Bone Formation Potential of Apatite-Coated Chitosan Microspheres. *J. Biomaterials Sci. Polym. Ed.* 25 (18), 2080–2093. doi:10.1080/09205063.2014.970604

Xu, T., Xin, M., Li, M., Huang, H., and Zhou, S. (2010). Synthesis, Characteristic and Antibacterial Activity of N,N,N-trimethyl Chitosan and its Carboxymethyl Derivatives. *Carbohydr. Polym.* 81 (4), 931–936. doi:10.1016/j.carbpol.2010.04.008

Yang, X., Zhang, C., Qiao, C., Mu, X., Li, T., Xu, J., et al. (2015). A Simple and Convenient Method to Synthesize N-[(2-hydroxyl)-propyl-3-trimethylammonium] Chitosan Chloride in an Ionic Liquid. *Carbohydr. Polym.* 130, 325–332. doi:10.1016/j.carbpol.2015.05.014

Yang, Y., Chu, L., Yang, S., Zhang, H., Qin, L., Guillaume, O., et al. (2018). Dual-functional 3D-Printed Composite Scaffold for Inhibiting Bacterial Infection and Promoting Bone Regeneration in Infected Bone Defect Models. *Acta Biomater.* 79, 265–275. doi:10.1016/j.actbio.2018.08.015

Yang, Y., Yang, S., Wang, Y., Yu, Z., Ao, H., Zhang, H., et al. (2016). Anti-infective Efficacy, Cytocompatibility and Biocompatibility of a 3D-Printed Osteoconductive Composite Scaffold Functionalized with Quaternized Chitosan. *Acta Biomater.* 46, 112–128. doi:10.1016/j.actbio.2016.09.035

Ye, X., Li, L., Lin, Z., Yang, W., Duan, M., Chen, L., et al. (2018). Integrating 3D-Printed PHBV/Calcium Sulfate Hemihydrate Scaffold and Chitosan Hydrogel for Enhanced Osteogenic Property. *Carbohydr. Polym.* 202, 106–114. doi:10.1016/j.carbpol.2018.08.117

Ye, Y., Pang, Y., Zhang, Z., Wu, C., Jin, J., Su, M., et al. (2018). Decellularized Periosteum-Covered Chitosan Globule Composite for Bone Regeneration in Rabbit Femur Condyle Bone Defects. *Macromol. Biosci.* 18 (9), e1700424. doi:10.1002/mabi.201700424

Yu, B., Zhang, Y., Li, X., Wang, Q., Ouyang, Y., Xia, Y., et al. (20132013). The Use of Injectable Chitosan/Nanohydroxyapatite/Collagen Composites with Bone Marrow Mesenchymal Stem Cells to Promote Ectopic Bone Formation *In Vivo*. *J. Nanomater.* 1–8. doi:10.1155/2013/506593

Zang, S., Zhu, L., Luo, K., Mu, R., Chen, F., Wei, X., et al. (2017). Chitosan Composite Scaffold Combined with Bone Marrow-Derived Mesenchymal Stem Cells for Bone Regeneration: *In Vitro* and *In Vivo* Evaluation. *Oncotarget* 8 (67), 110890–110903. doi:10.18632/oncotarget.22917

Zhang, J., Neoh, K. G., and Kang, E. T. (2018). Electrical Stimulation of Adipose-derived Mesenchymal Stem Cells and Endothelial Cells Co-cultured in a Conductive Scaffold for Potential Orthopaedic Applications. *J. Tissue Eng. Regen. Med.* 12 (4), 878–889. doi:10.1002/term.2441

Zhang, L. Y., and Zhu, J. F. (2003). Study on Antimicrobial Activity of Chitosan with Different Molecular Weights. *Carbohydr. Polym.* 54 (4), 527–530. doi:10.1016/j.carbpol.2003.07.009

Zhang, X., Fan, J., Lee, C.-S., Kim, S., Chen, C., and Lee, M. (2020). Supramolecular Hydrogels Based on Nanoclay and Guanidine-Rich Chitosan: Injectable and Moldable Osteoinductive Carriers. *ACS Appl. Mat. Interfaces* 12 (14), 16088–16096. doi:10.1021/acsami.0c01241

Zhang, X., Zhang, Y., Ma, G., Yang, D., and Nie, J. (2015). The Effect of the Prefrozen Process on Properties of a Chitosan/Hydroxyapatite/Poly(methyl Methacrylate) Composite Prepared by Freeze Drying Method Used for Bone Tissue Engineering. *RSC Adv.* 5 (97), 79679–79686. doi:10.1039/c5ra14549j

Zhao, J., Shen, G., Liu, C., Wang, S., Zhang, W., Zhang, X., et al. (2012). Enhanced Healing of Rat Calvarial Defects with Sulfated Chitosan-Coated Calcium-Deficient Hydroxyapatite/Bone Morphogenetic Protein 2 Scaffolds. *Tissue Eng. Part A* 18 (1–2), 185–197. doi:10.1089/ten.TEA.2011.0297

Zhao, X., Li, P., Guo, B., and Ma, P. X. (2015). Antibacterial and Conductive Injectable Hydrogels Based on Quaternized Chitosan-Graft-Polyaniline/Oxidized Dextran for Tissue Engineering. *Acta Biomater.* 26, 236–248. doi:10.1016/j.actbio.2015.08.006

Zhao, X., Zhou, L., Li, Q., Zou, Q., and Du, C. (2018). Biomimetic Mineralization of Carboxymethyl Chitosan Nanofibers with Improved Osteogenic Activity *In Vitro* and *In Vivo*. *Carbohydr. Polym.* 195, 225–234. doi:10.1016/j.carbpol.2018.04.090

Zhou, D., Qi, C., Chen, Y.-X., Zhu, Y.-J., Sun, T.-W., Chen, F., et al. (2017). Comparative Study of Porous Hydroxyapatite/Chitosan and Whitlockite/Chitosan Scaffolds for Bone Regeneration in Calvarial Defects. *Ijn* Vol. 12, 2673–2687. doi:10.2147/ijn.s131251

Zhou, H., Qian, J., Wang, J., Yao, W., Liu, C., Chen, J., et al. (2009). Enhanced Bioactivity of Bone Morphogenetic Protein-2 with Low Dose of 2-N, 6-O-Sulfated Chitosan *In Vitro* and *In Vivo*. *Biomaterials* 30 (9), 1715–1724. doi:10.1016/j.biomaterials.2008.12.016

Zhou, H. Y., Jiang, L. J., Cao, P. P., Li, J. B., and Chen, X. G. (2015). Glycerophosphate-based Chitosan Thermosensitive Hydrogels and Their Biomedical Applications. *Carbohydr. Polym.* 117, 524–536. doi:10.1016/j.carbpol.2014.09.094

Conflict of Interest: The authors declare that the research was conducted in the absence of any commercial or financial relationships that could be construed as a potential conflict of interest.

Publisher's Note: All claims expressed in this article are solely those of the authors and do not necessarily represent those of their affiliated organizations, or those of the publisher, the editors and the reviewers. Any product that may be evaluated in this article, or claim that may be made by its manufacturer, is not guaranteed or endorsed by the publisher.

frontiers | Frontiers in Bioengineering and Biotechnology

ORIGINAL RESEARCH
published: 09 May 2022
doi: 10.3389/fbioe.2022.899457

Engineering Multifunctional Hydrogel With Osteogenic Capacity for Critical-Size Segmental Bone Defect Repair

Shaowei Zheng[1,2†], Haobo Zhong[1†], Hao Cheng[2†], Xu Li[1], Guowei Zeng[3], Tianyu Chen[4], Yucong Zou[4], Weile Liu[1] and Chunhan Sun[1]**

[1]Department of Orthopaedic, Huizhou First Hospital, Guangdong Medical University, Huizhou, China, [2]Department of Orthopaedic Surgery, Nanfang Hospital, Southern Medical University, Guangzhou, China, [3]Graduate School, Guangdong Medical University, Zhanjiang, China, [4]Department of Orthopedics, The Third Affiliated Hospital of Southern Medical University, Guangzhou, China

OPEN ACCESS

Edited by:
He Liu,
Jilin University, China

Reviewed by:
Yilong Cheng,
Xi'an Jiaotong University, China
Zuhao Li,
Shanghai Jiao Tong University, China

***Correspondence:**
Weile Liu
liuweile2006@126.com
Chunhan Sun
sunchunhan@126.com

†These authors have contributed equally to this work

Specialty section:
This article was submitted to Biomaterials, a section of the journal Frontiers in Bioengineering and Biotechnology

Received: *18 March 2022*
Accepted: *01 April 2022*
Published: *09 May 2022*

Citation:
Zheng S, Zhong H, Cheng H, Li X, Zeng G, Chen T, Zou Y, Liu W and Sun C (2022) Engineering Multifunctional Hydrogel With Osteogenic Capacity for Critical-Size Segmental Bone Defect Repair. Front. Bioeng. Biotechnol. 10:899457. doi: 10.3389/fbioe.2022.899457

Treating critical-size segmental bone defects is an arduous challenge in clinical work. Preparation of bone graft substitutes with notable osteoinductive properties is a feasible strategy for critical-size bone defects. Herein, a biocompatible hydrogel was designed by dynamic supramolecular assembly of polyvinyl alcohol (PVA), sodium tetraborate ($Na_2B_4O_7$), and tetraethyl orthosilicate (TEOS). The characteristics of the supramolecular hydrogel were evaluated by rheological analysis, swelling ratio, degradation experiments, and scanning electron microscopy (SEM). In *in vitro* experiments, this TEOS-hydrogel had self-healing property, low swelling rate, degradability, good biocompatibility, and induced osteogenic differentiation of bone marrow mesenchymal stem cells (BMSCs) by upregulating the expression of Runx-2, Col-1, OCN, and osteopontin (OPN). In segmental bone defect rabbit models, the TEOS-containing hydrogel accelerated bone regeneration, thus restoring the continuity of bone and recanalization of the medullary cavity. The abovementioned results demonstrated that this TEOS-hydrogel has the potential to realize bone healing in critical-size segmental bone defects.

Keywords: critical bone defect, hydrogel, BMSCs, osteogenic differentiation, bone regeneration

INTRODUCTION

The treatment of critical-size segmental bone defects caused by high-energy trauma, infection, revision arthroplasty, and after resection of bone tumor is one of the most challenging clinical issues, especially for patients with poor osteogenic capability (Zhang et al., 2021; Li et al., 2022). Although autologous bone tissue possesses a certain self-healing capacity, it may still be insufficient under some special states such as critical-size segmental bone defects (Russow et al., 2019). Once critical-size defects occur, poorly healed bone tissues are easily found in some serious complications, for example, non-union, bone atrophy, bone deformities, and so on (Brandi, 2013; Bottai et al., 2015). Currently, conventional treatments like bone autografts and allografts and bone cement reconstruction have been used to repair bone defects with primary stability and long-term regeneration; however, these strategies also show some drawbacks (Bai et al., 2020b; Butscheidt et al., 2021; Chen et al., 2021). Among them, bone autografts are considered the gold standard for treatment of bone defects owing

to the excellent osteoconduction, osteoinduction, and osteogenesis in bone regeneration (Hindiskere et al., 2020). However, some disadvantages, such as donor-site morbidity, high cost, and long rehabilitation time, limit the application of bone autografts (Boriani et al., 2017; Fahmy-Garcia et al., 2018; Lim et al., 2019; Han et al., 2020). Bone allografts maintain osteoconductivity, but the risks of immune rejection and infection result in inferior healing and high costs increase the economic burden, limiting its popularization (Cao et al., 2016; Santos et al., 2019). As a synthetic alternative material for bone tissue, bone cements have the opportunity to cause serious complications after implantation, for instance, non-biodegradation, exothermic reaction, the release of cytotoxic monomers, and pulmonary embolism (Lewis et al., 2010; Lai et al., 2013; Hwa et al., 2021; Nonoyama et al., 2021). Therefore, the treatment strategy which can promote critical-size bone defects healing efficiently and safely is of high clinical significance to address these problems.

Alternative bioactive materials with notable osteogenic induction effects have attracted extensive interest in bone regeneration. Recently, TEOS, a silicon-based organic compound, was used as a bone induction factor to induce osteogenesis and osseointegration at the prosthesis interface (Qiao S. et al., 2020). A series of studies have demonstrated that silicon supplementation has a significant connection with bone mineral density (Jugdaohsingh, 2007; Casarrubios et al., 2020). The silicon-incorporated polymers or cements have been explored to a great extent as materials applied in bone implants owing to their biocompatibility and osteoinductive ability (Deng et al., 2018; Yu et al., 2020). This inorganic biomaterial has superior bone induction capacities but is limited to the short-term release of the incorporated particles, and it is thus difficult to use it to exert a long-term osteogenic effect (Zhang et al., 2016). Hydrogels could achieve drug encapsulation and sustained release by either chemical adaptability or a hybrid of different polymers (Kluin et al., 2013; Li et al., 2021). Therefore, designing combined organic–inorganic hydrogels, comprising organic polymers and osteoconductive mineralized components, is a potential strategy for the treatment of critical-size segmental bone defects.

In this study, we developed a novel multifunctional hydrogel to improve the healing efficiency of segmental bone defects (**Scheme 1**). The hydrogel was prepared by dynamic supramolecular assembly of polyvinyl alcohol (PVA), sodium tetraborate ($Na_2B_4O_7$), and tetraethyl orthosilicate (TEOS). In addition to encapsulated osteogenic active ingredients (TEOS), the reversible networks between $Na_2B_4O_7$ and PVA form the backbone networks of hydrogels. The hydrogels are generated from mainly dynamic supramolecular assembly of $Na_2B_4O_7$ and PVA that is attributed to the dynamic reactions of PVA–borax–PVA. Self-healing hydrogels maintain affluent adaptable linkages which can be decomposed and are automatically re-combined in a dynamic convertible way, minimizing the adverse influence on the nearby tissue and sustaining their long-term integrality (Zhang and Khademhosseini, 2017). At the same time, self-healing hydrogels supply a permissive microenvironment for the delivery of the substance. The abovementioned advantages cause this self-healing hydrogel to be favorable for multifunctional ingredient-loading in bone defect treatment. The goal of this research is to evaluate the function of this composite hydrogel in inducing osteogenesis in the critical-size radius bone defect rabbit models. Thus, the study will provide a novel strategy for developing bone substitutes in segmental bone defects.

MATERIALS AND METHODS

Materials

Sodium tetraborate ($Na_2B_4O_7.10H_2O$) was purchased from Beijing Chemical Works (Beijing, China). PVA (≈99% hydrolyzed, Mw ≈130,000) and TEOS were obtained from Sigma-Aldrich. The rabbit BMSCs were supplied by American Type Culture Collection (ATCC, MD, United States). Low-glucose Dulbecco's modified Eagle's medium (LG-DMEM), fetal bovine serum (FBS), and streptomycin–penicillin were obtained from Gibco® Life Technologies (CA, United States). The Cell Counting Kit-8 (CCK-8) kit and Calcein-AM/PI staining kit were supplied by Beyotime Biotechnology (Shanghai, China). The mediums for osteogenic differentiation of BMSCs and Alizarin Red stain were obtained from Cyagen Biosciences (CA, United States). Phosphate buffer (PBS) and 4% paraformaldehyde were provided by Solarbio (Beijing, China). The Eastep Super Total RNA Extraction Kit was purchased from Promega (Shanghai, China), and the Perfect Real-Time RT reagent kit was supplied by Takara Bio (Dalian, China). Hematoxylin–eosin stain was obtained from Thermo Fisher Scientific, MA, United States. Primary antibodies, runt-related transcription factor-2 (Runx-2), type I collagen (Col-1), osteocalcin (OCN), and osteopontin (OPN) were purchased from Abcam (Cambridge, United Kingdom), and secondary antibodies were obtained from Jackson ImmunoResearch Laboratories (West Grove, PA, United States).

Preparation of Hydrogels

The multifunctional hydrogel was manufactured by the listed protocols. Different concentration of PVA was dissolved in 10 ml of deionized water with magnetic stirring at 90°C. Subsequently, 0.4 mmol TEOS was supplemented into the abovementioned solution. The mixture was strongly stirred. After the components are completely dissolved, 10 ml $Na_2B_4O_7$ solution was added to the mixture under continuous stirring at 90°C for 10 min until the hybrid hydrogel was constructed. The hydrogel consisting of PVA, $Na_2B_4O_7$, and TEOS was recognized as TEOS@Gel, while the hydrogel consisting of PVA and $Na_2B_4O_7$ was abbreviated as Gel as a control.

Characterization of Hydrogels

The rheology of the hydrogels was investigated by a rheometer (Malvern, United Kingdom). The fixture utilized a circular parallel plate, the diameter of that was 10 mm, and the gap was set as 1,000 μm. During the progression of the experiment, to protect the gel from draining out, the hydrogel

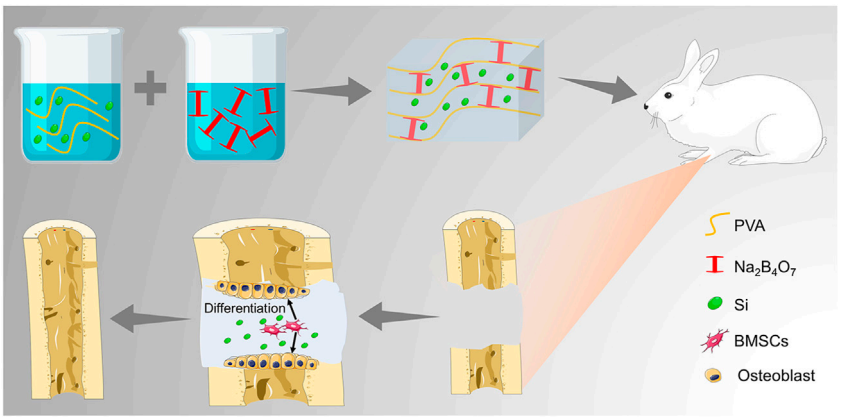

SCHEME 1 | Illustration of the TEOS-hydrogel enhancing critical-size segmental bone defect healing by inducing BMSC osteogenic differentiation.

was covered with a hood to prevent water evaporation. When the hydrogel was tested in the time sweep mode, the frequency of the rheometer was 10 rad/s, and the strain was 0.1%. While in the strain sweep mode, the frequency and the temperature were set as mentioned above, and the strain was set from 1% to 100%. The morphology of the TEOS hydrogel was observed by field emission scanning electron microscopy (FE-SEM) (JSM-7000F, JEOL, Tokyo, Japan) at 3 kV after freeze-drying, and the obtained images were further analyzed by Image J software (NIH, MD, United States).

The equilibrium cumulative ratio was evaluated by measuring the variation in wet weight by incubating the hydrogels in PBS. In brief, a certain amount of hydrogel (1 g) was weighed and added to PBS, and the quantity of the initial wet hydrogel was noted as W_0. At predetermined intervals, the hydrogels were collected from the PBS, and the weight was regarded as Wt. The swelling rate = $W_t/W_0 \times 100\%$. The degradation of hydrogels was conducted by studying the variation of the hydrogel in the dry mass mode. Briefly, the lyophilized hydrogel (100 mg) was placed in PBS at 37°C. At predetermined points, the residual hydrogels were gathered, and the mass loss was recorded after lyophilization.

Biocompatibility of Hydrogels

To investigate the biocompatibility of the prepared hydrogels, the CCK-8 assay and dead/live staining were conducted. BMSCs were seeded at a density of 2×10^4/well in 24-well plates for different treatment processes. The plates coated with Gel and TEOS/Gel were set as the experimental groups and those without the hydrogel were observed as the control group (abbreviated as Ctrl). At the scheduled time points, cell proliferation was detected by a CCK-8 assay. Briefly, 10% CCK-8 solution was added to the samples and then incubated for 2 h at 37 C. The absorbance was measured by a microplate reader (Multiskan EX, Thermo Fisher Scientific, MA, United States) at 450 nm.

The cell viability was investigated by a Calcein-AM/PI kit after 3 days of incubation according to the manufacturer's instructions. In brief, Calcein-AM and PI were added to the samples and incubated in the dark for 15 min at 4°C. The fluorescent images were observed and photographed by a confocal laser scanning microscope (CLSM, FV1000, Olympus, Japan), and the cell survival rates were analyzed by ImageJ software according to the proportion of live cells.

TABLE 1 | Primer sequences of genes.

Gene	Oligonucleotide primers (5′-3′)
Runx-2	F: 5′-ACTACCAGCCACCGAGACCA-3′
	R: 5′-ACTGCTTGCAGCCTTAAATGACTCT-3′
Col-1	F: 5′-TCCGGCTCCTGCTCCTCTTA-3′
	R: 5′-GGCCAGTGTCTCCCTTG-3′
OCN	F: 5′-AGCCACCGAGACACCATGAGA-3′
	R: 5′-AGCCACCGAGACACCATGAGA-3′
OPN	F: 5′-GCTAAACCCTGACCCATCT-3′
	F: 5′-CGTCGGATTCATTGGAGT-3′
GAPDH	F: 5′-CAATGACCCCTTCATTGACC-3′
	R: 5′-TGGACTCCACGACGTACTCA-3′

In Vitro Osteogenic Induction of Hydrogels

To evaluate the osteogenic differentiation ability of the TEOS-hydrogel, BMSCs were seeded into the 24-well plates at a density of 5×10^4 cells/well. After incubation for 24 h, the medium was changed by the osteogenic induction medium, including LG-DMEM along with β-glycerol-phosphate (10 mM), ascorbate-2-phosphate (50 μM), and dexamethasone (0.1 μM). After 14 and 21 days of osteogenic induction culture, Alizarin Red staining was performed to evaluate the cell mineralization by observing the calcium nodule deposition. Subsequently, 10% cetylpyridinium chloride was added to the samples to dissolve the mineralized nodules for further semi-quantitative analysis by a microplate reader at 562 nm.

Real Time-qPCR

The expression of genes involved in osteogenic differentiation was determined by real-time quantitative PCR (RT-qPCR), including *Runx-2*, *Col-1*, *OCN*, and *OPN*, in the BMSCs at 14

and 21 days after osteogenic induction and bone tissues. The primers sequences are listed in **Table 1**. Total RNA was collected by TRIzol reagent. Synthesis of cDNA was performed using an Eastep Super Total RNA Extraction Kit according to the manufacturer's instructions. An A260/A280 value of approximate 2.0 was generally accepted for further analysis. The amplification and performance of RT-qPCR were carried out by adopting 2× Fast SYBR Green Master Mix (Roche Diagnostics, Basel, Switzerland) and detected by a LightCycler 480 (Roche Diagnostics). The relative mRNA expression was normalized by GAPDH and calculated according to the formula of the $2^{-\Delta\Delta CT}$ method. For RT-qPCR of the bone, tissues were collected and quickly placed in a mortar precooled with liquid nitrogen and repeatedly ground to powder in liquid nitrogen for RT-qPCR as previously described.

Immunofluorescence

After 21 days of osteogenic induction culture, immunofluorescence was conducted to investigate the Runx-2, Col-1, OCN, and OPN expression. Briefly, the cell samples were fixed with 4% paraformaldehyde for 20 min and then permeabilized with 0.1% Triton X-100 solution for 5 min. After that, nonspecific binding was blocked with 3% BSA for 30 min. The samples were incubated with primary antibodies, including anti-Runx-2 (1:100), anti-Col-1 (1:250), anti-OCN (1: 200), and anti-OPN (1:250) overnight at 4°C. The samples were then washed with PBS three times and treated with the secondary antibody for 5 h. Goat anti-rabbit IgG and goat anti-mouse IgG conjugated to fluorescein isothiocyanate were added at a dilution of 1:200 and incubated. The negative control samples were not subjected to primary antibody incubation. After being washed with PBS three times, the nucleus was stained with DAPI. Finally, the fluorescence intensity of the cells was observed with a CLSM.

Establishment of Critical-Size Bone Defect Models

A total of 36 New Zealand white rabbits (female, six months old) were selected to prepare the infected radius fracture models. The critical-size segmental radial bone defect models were prepared under general anesthesia with 3% (w/ v) pentobarbital at the dose of 50 mg/kg. After preoperative preparation, the left lateral radial incision was selected to expose the tissue layer by layer. When the bony surface of the left radius was exposed, a 15- mm segmental bone defect was prepared by a bone drill. The periosteum around the ends of the defect was excised to prevent ossification. Then, the defects were rinsed, and the animals were divided into three groups, namely, the control group without hydrogel implantation, the Gel group with 500 μl hydrogel, and the TEOS/Gel group with 500 μl TEOS-hydrogel. Finally, the incisions were sutured layer by layer, and the animals were injected intramuscularly with penicillin (1.5 mg/kg) for 3 consecutive days to prevent infection.

At 6 and 12 weeks after surgery, the rabbits were euthanized by intravenous injection of pentobarbital sodium (120 mg/kg). The left radius samples were collected for sequential studies.

Micro-CT

To evaluate the bone regenerative efficiency, the bone tissues were scanned by Micro-CT (SkyScan 1076 scanner, Bruker, Belgium) in a high-resolution scanning mode with a pixel size of 18 μm. Subsequently, quantitative morphometric analysis of bone volume/tissue volume ratio (BV/TV, %) of the original defect region, regarded as the region of interest, was analyzed by micro-CT auxiliary software (NRecon version 1.6.6).

Histological Evaluation

All collected radius samples were fixed with 4% paraformaldehyde for 1 week and then decalcified in Morse's solution for another 5 weeks. The samples were dehydrated in graded ethanol series, paraffin-embedded, and sectioned to 5-μm thickness slices. Hematoxylin and eosin (H&E) staining was conducted to observe new bone formation.

In addition, immunofluorescence staining was performed to detect the expression of Runx-2, Col-1, OCN, and OPN in the regenerative tissues. Briefly, the slices were washed with PBS and blocked with 3% BSA in PBS containing 0.2% Triton X-100 for 60 min. Subsequently, the slices were incubated with primary antibodies, 1:200 Runx-2 anti-mouse polyclonal antibody along with 1:250 Col-1 anti-rabbit monoclonal antibody and 1:150 OCN anti-mouse polyclonal antibody along with 1:200 OPN anti-rabbit polyclonal antibody overnight at 4°C. After washing with PBS three times, the slices were then incubated with 1: 600 Cy3-conjugated goat anti-rabbit or 1:800 goat anti-mouse IgG DyLight 488-conjugated secondary antibodies for 1 h at 37°C. The nuclei were stained with DAPI (1:600) and observed by CLSM.

Statistical Analysis

All results were calculated as mean ± standard deviation (SD). Comparisons among groups were analyzed with one-way ANOVA followed by Tukey's post hoc test using SPSS 19.0 (SPSS Inc., Chicago, IL, United States). $P < 0.05$ was considered statistically significant.

RESULTS AND DISCUSSION

Preparation and Characterization of Hydrogels

The preparation strategy of the hydrogels is shown in **Figure 1A**. Completely dissolved PVA and TEOS were added into the $Na_2B_4O_7$ solution at 90°C. Subsequently, the temperature was decreased to 25°C to complete the sol–gel transition rapidly. The hydrogels were designed by dynamic supramolecular assembly of $Na_2B_4O_7$, PVA, and TEOS. The microstructures of the prepared hydrogels were observed by SEM, and the images showed that the lyophilized hydrogels had an interconnected porous structure (**Figure 1B**). These interconnected nanochannels benefit oxygen and nutrient transport, thus promoting cell communication and improving cell survival, which is valuable for biological applications (Kumar et al., 2018).

The mechanical properties of hydrogels can be adjusted by changing the proportion of crosslinking components. The gel

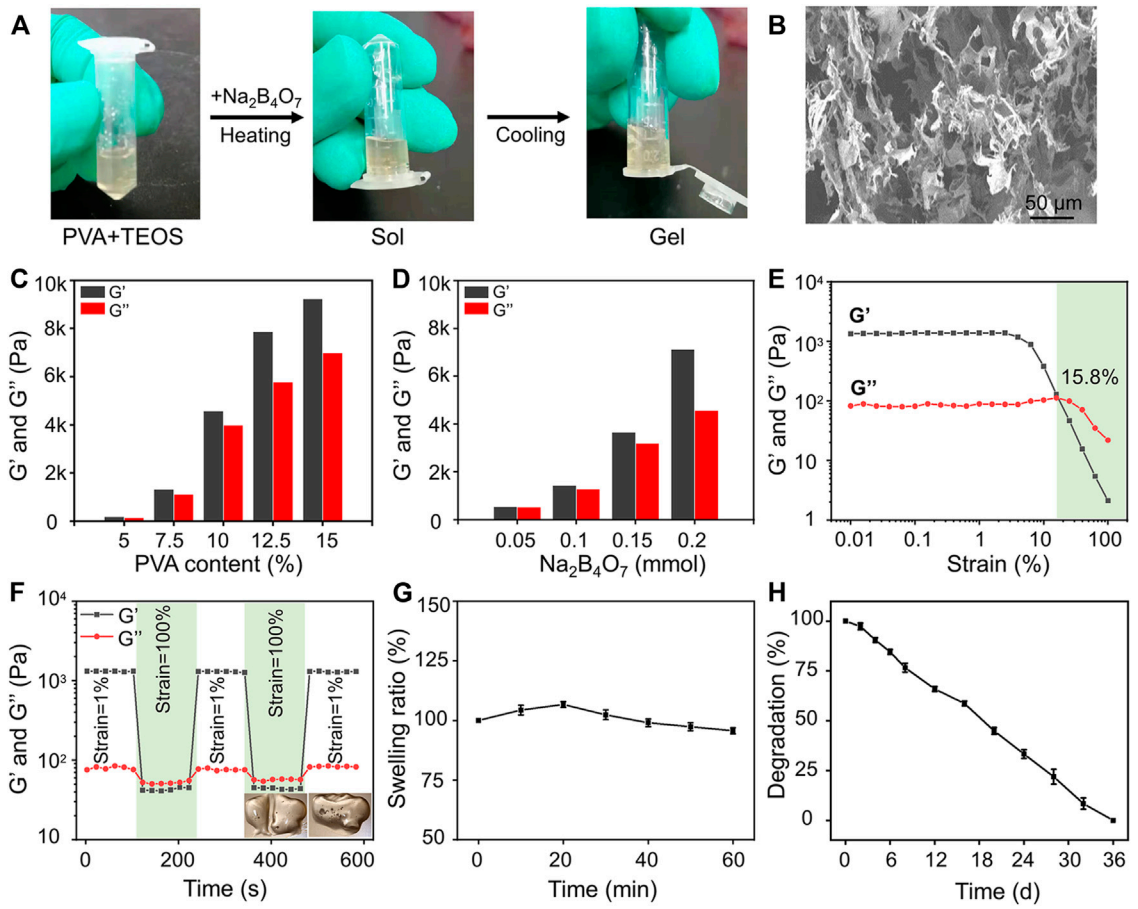

FIGURE 1 | Preparation and characterization of hydrogels. **(A)** Photographs of the gelation progress. The mixture of the prepared PVA and TEOS solution was presented in the sol state, and it experienced sol–gel transition after adding $Na_2B_4O_7$ solution. **(B)** SEM observation of prepared hydrogels. **(C)** Storage modulus and loss modulus of prepared hydrogels as the concentration of PVA increased from 5 to 15 wt%. **(D)** Storage modulus and loss modulus of prepared hydrogels as the concentration of $Na_2B_4O_7$ increased from 0.05 to 0.20 mmol. **(E)** Strain amplitude sweep of the hydrogel. **(F)** Step strain measurements of the hydrogel with a fixed frequency of 1 rad/s, and the macroscopic observation of self-healing property. **(G)** Equilibrium swelling ratio. **(H)** *In vitro* degradation (the tested hydrogel formula is 10 wt% PVA, 0.20 mmol $Na_2B_4O_7$, 0.4 mmol TEOS).

dynamics of hydrogels with different concentrations were monitored by recording the storage modulus (G′) and loss modulus (G″) in the time scan mode. According to the rheological analysis, the results indicated that along with the PVA and $Na_2B_4O_7$ content increase, the G′ and G″ of the hydrogels increased correspondingly (**Figures 1C,D**). On the contrary, the concentration of TEOS had little effect on the dynamic properties of the hydrogels. As shown in **Figure 1E**, rheological performances of the prepared hydrogels were detected under the strain scan mode (0.01%–100%). In the low-strain area, both G′ and G″ are maintained at a constant value. Along with the strain increase, the G′ and G″ curves intersected at a strain of 15.8%, which was the required critical strain value to destruct the hydrogel network. In addition, based on the strain amplitude scanning results, the self-healing property of hydrogels was observed by continuous variation of shear strains (1% and 100%). As exhibited in **Figure 1F**, G″ was higher than G′ at higher shear strains (100%) indicating that the hydrogels were destroyed. Soon afterward, when the shear strain dropped to 1%, G′ and G″ almost completely recovered to the initial value, showing that the hydrogel network structure was restored. This repeatable process proved that this hydrogel has a durable self-healing property. For macroscopic observation, the hydrogels were physically cut into two halves, and two separate hydrogels can be reassembled into one whole in 30 min, displayed in the lower right of **Figure 1F**. This excellent self-healing feature is attributed to the dynamic characteristics of boronate formation between the $Na_2B_4O_7$ and PVA. Self-healing hydrogels have affluent adaptable linkages that can be broken and reconnect automatically in the form of dynamic reversibility to minimize adverse effects on the surrounding tissue and maintain their long-term integrity.

Then, the swelling performance of the hydrogels was investigated in PBS and shown in **Figure 1G**. The hydrogels reached swelling equilibrium at about 20 min, and the maximum swelling rate of the hydrogels was about 7%. Moreover, in the process of the swelling test, the hydrogels maintained its initial shape without destruction.

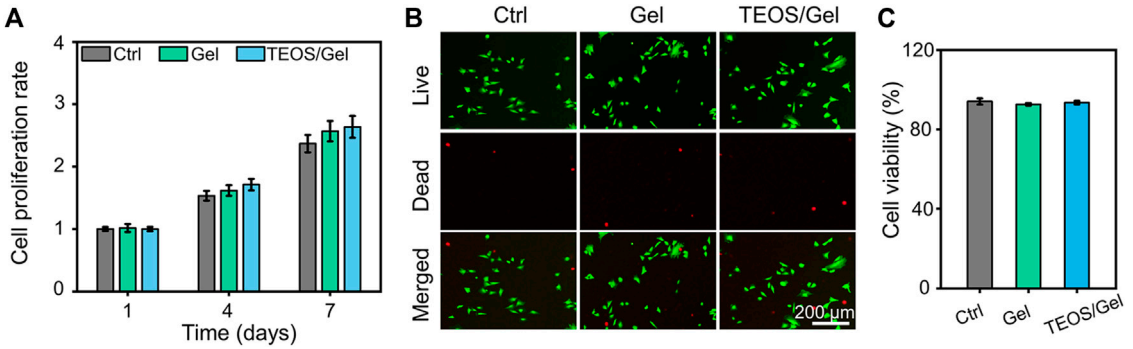

FIGURE 2 | Biocompatibility of the prepared hydrogels. **(A)** Cell proliferation rate at days 1, 4, and 7. **(B)** Calcein AM/PI staining of BMSCs at day 3. **(C)** Quantitative analysis of the cell survival rate by Calcein AM/PI staining.

This physical and chemical stability made the hydrogels an ideal implant for *in vivo* application. The degradation property of materials is also another critical factor for transplantation. According to the measurement of the change of dry weight of the hydrogels, we found that the hydrogels could degrade completely within 36 days (**Figure 1H**).

Biocompatibility of Hydrogels

The biocompatibility of hydrogels is the prerequisite for their biomedical applications. The cell proliferation and viability of BMSCs cultured in the hydrogels were revealed by CCK-8 detection and Calcein-AM/PI staining. The results indicated that BMSCs in the control, Gel, and TEOS/Gel groups proliferated gradually without statistical difference among the groups on days 4 and 7 (**Figure 2A**), indicating that the TEOS hydrogel did not have any negative effect on the proliferation of BMSCs. The pictures of Calcein AM/PI staining demonstrated that the BMSCs maintained good cell viability in all groups on day 3 (**Figure 2B**). Furthermore, the cell survival rate of BMSCs in the control, Gel, and TEOS/Gel groups was 94.1 ± 1.6%, 92.6 ± 0.7%, and 93.5 ± 0.9%, respectively, and there was no significant difference among the groups (**Figure 2C**). The abovementioned results demonstrated that our hydrogels had good biocompatibility for BMSCs and had wide application prospects in tissue engineering.

Tetraethyl Orthosilicate Hydrogel Induced Bone Marrow Mesenchymal Stem Cell Osteogenic Differentiation

In addition to the biocompatibility of the materials, the capacity of inducing BMSC osteogenic differentiation is a crucial factor for the initiation of bone formation. The deposition of calcium nodules is a hallmark event of osteogenic differentiation of BMSCs, which can be observed by Alizarin Red dye (Bai et al., 2020a). As indicated in **Figure 3A**, gross images showed that more calcium nodules were observed in the TEOS/Gel group than in the control group and Gel group on the 14th and 21st days. More precisely, semi-quantitative analysis was used to further demonstrate that the absorbance in the TEOS/Gel group was significantly higher than that in the control group and Gel group ($p < 0.05$, **Figure 3B**). These results indicated that the TEOS hydrogel enhanced the deposition of mineralized nodules. In addition, to investigate the influence of the TEOS hydrogel on osteogenic differentiation at the gene level, the expression of some crucial osteogenic-related genes, including *Runx-2*, *Col-1*, *OCN*, and *OPN*, was analyzed by RT-qPCR. The upregulation of *Runx-2* expression is a key event in the early osteogenic differentiation process, which can activate the expression of *OCN* and *OPN* (Sivashanmugam et al., 2017). As displayed in **Figure 3C**, the expression of *Runx-2* in the TEOS/Gel group was 1.9-fold and 1.8-fold on the 14th day and 1.6-fold and 1.4-fold on the 21st day, higher than that in the control group and Gel group, respectively ($p < 0.05$). Similarly, the expression of *Col-1*, *OCN*, and *OPN* in the TEOS/Gel group was significantly upregulated than that in the control group and Gel group (**Figures 3D–F**).

In addition, to investigate the function of the TEOS hydrogel on the expression of osteogenic differentiation at the protein level, protein markers (Runx-2, Col-1, OCN, and OPN) were stained by double immunofluorescence after 21 days of osteogenic induction culture (**Figure 4A**). As shown in**Figures 4B–E**, quantitative analysis of the fluorescence of osteogenic-related markers revealed that the intensity in the TEOS/Gel group was significantly enhanced than that of the control group ($p < 0.05$) and Gel group ($p < 0.05$).

Owing to the positive role of silicon in inducing bone regeneration, various silicon-based bone substitutes (such as nano silicates, silicon dioxide, etc.) have been widely studied and developed as potential orthopedic implants (Carlisle, 1970). It is of importance that a series of studies have demonstrated that the bioactive Si ions can enhance cell proliferation and promote stem cell osteogenic differentiation (Wang et al., 2013). Incorporating Si ions into bone tissue engineering biomaterials significantly upregulated angiogenic factor expression and induced osteogenic differentiation of BMSCs (Sun et al., 2018). Herein, the TEOS hydrogel was prepared, and the osteogenic induction capacity was investigated. The results demonstrated that our TEOS hydrogel could significantly enhance calcium nodule deposition and upregulate osteogenesis-related marker expression, thus inducing BMSC osteogenic differentiation.

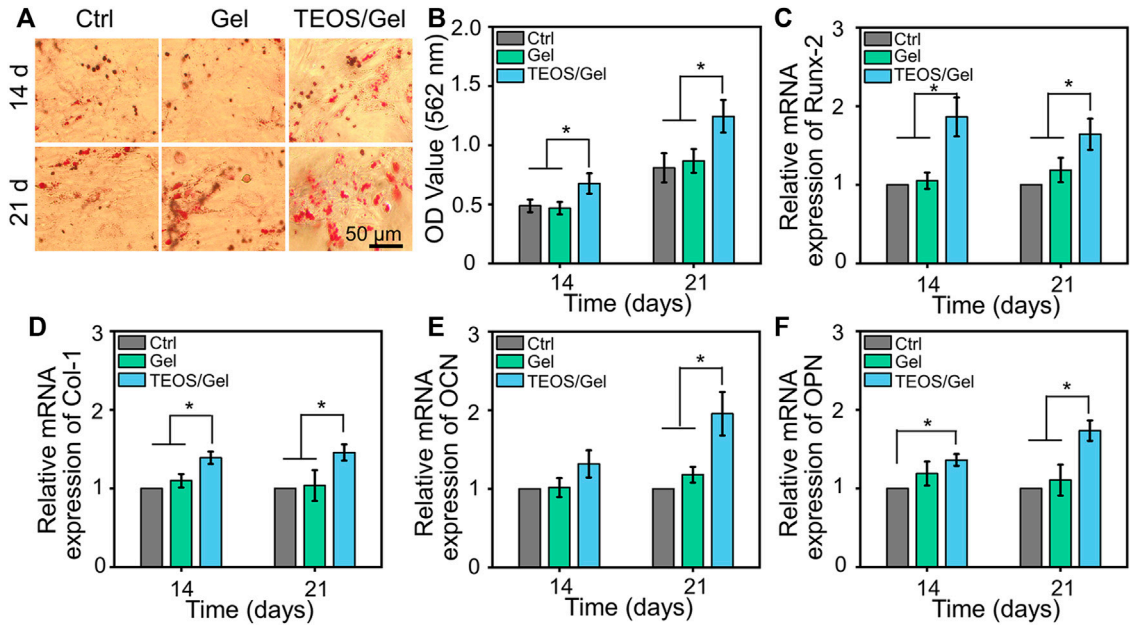

FIGURE 3 | TEOS hydrogel induces BMSC osteogenic differentiation. **(A)** Gross images of Alizarin Red staining. **(B)** Semi-quantitative analysis of Alizarin Red staining. **(C–F)** mRNA expression levels of osteogenic-related genes, including *Runx-2*, *Col-1*, *OCN*, and *OPN*, in BMSCs after osteogenic induction for 14 and 21 days (*$p < 0.05$).

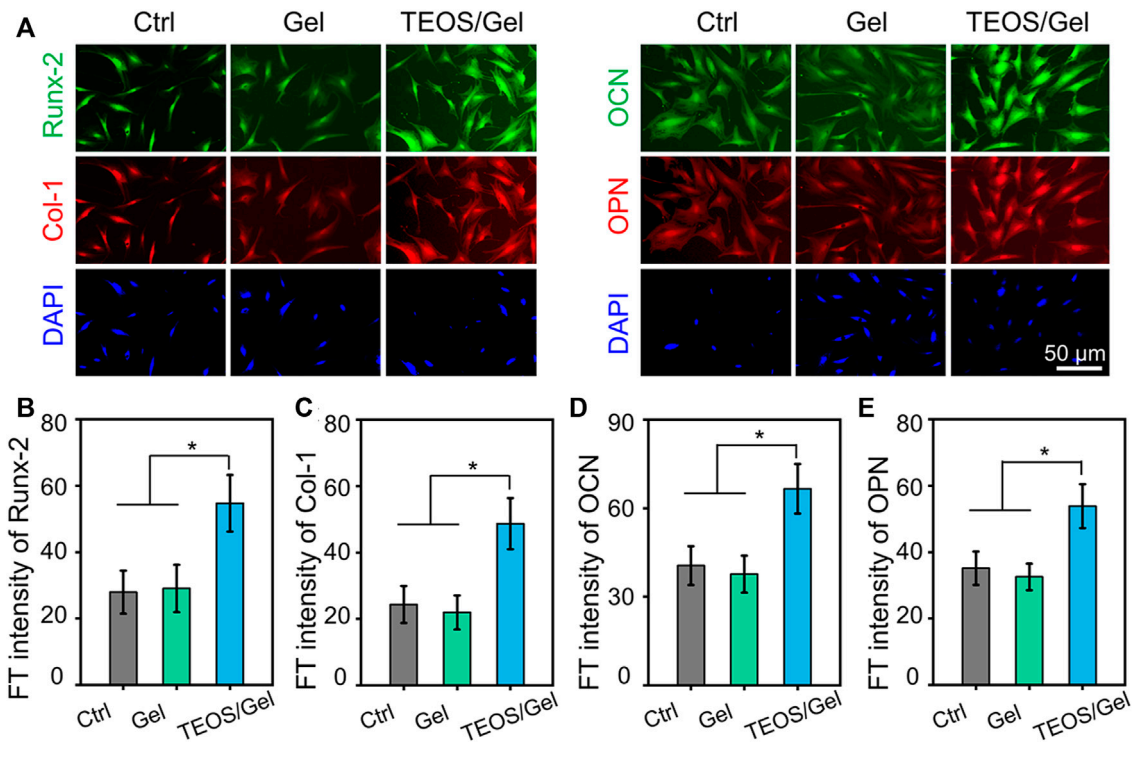

FIGURE 4 | TEOS hydrogel induces BMSC osteogenic differentiation at the protein level. **(A)** Double immunofluorescent staining of cartilage-specific markers Runx-2, Col-1, OCN, and OPN in BMSCs after osteogenic induction for 21 days. **(B–E)** Quantitative analysis of the immunofluorescence intensity of Runx-2, Col-1, OCN, and OPN (*$p < 0.05$).

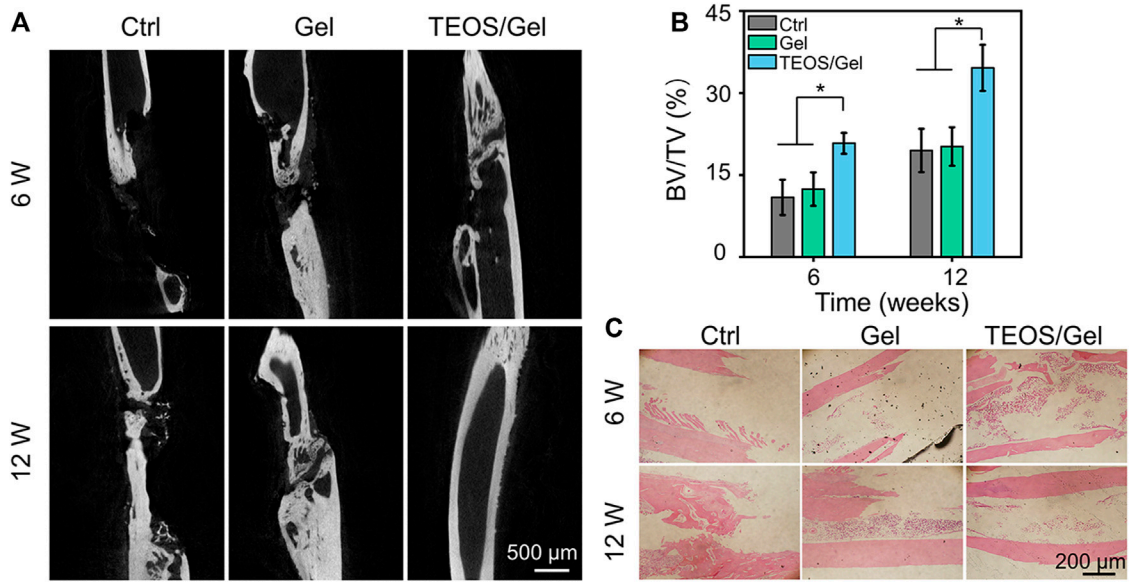

FIGURE 5 | TEOS hydrogel promoted critical-size segmental bone defect repair. **(A)** Micro-CT images of regenerated bone tissue at the 6th and 12th week after transplantation. **(B)** Quantitative analysis of BV/TV of the regenerated bone in the defects according to micro-CT. **(C)** H&E staining for histological observation of radius critical-size defects (*$p < 0.05$).

Tetraethyl Orthosilicate Hydrogel Promoted Critical-Size Segmental Bone Defect Repair

Severe trauma, bone tumors, congenital malformation, or extensive infection of bone tissue can be the causes of critical-size bone defects. A critical-size bone defect is defined as an orthotropic intraosseous wound that does not self-heal without additional surgical intervention (Van Houdt et al., 2021). The repair of critical-size segmental bone defects is still a great challenge in clinic. Over the past decades, different types of synthetic bone grafts have been developed, of which particularly calcium phosphate (CaP) and hydroxyapatite-based bone substitutes have shown great potential (Zhao R. et al., 2020; Zhao Y. et al., 2020; Chae et al., 2021; Liu et al., 2021; He et al., 2022). In view of increased demands for synthetic bone grafts with advantageous properties, we designed a self-healing hydrogel consisting of PVA, $Na_2B_4O_7$, and TEOS. In this study, micro-CT was conducted during the 6th and 12th weeks after surgery to investigate the efficacy of the TEOS hydrogel on bone healing in critical-size bone defects. As displayed in **Figure 5A**, the TEOS hydrogel induced bone healing and restored the defects in a time-dependent manner. Obvious bone regeneration was observed at the 6th week, and the defects almost healed at the 12th week after transplantation in the TEOS/Gel group. However, in the control group and Gel group, limited bone regeneration, bone discontinuity, and non-union can be observed at the defects. To further quantify bone repair in the defects, the area of critical-size segmental bone defects was regarded as the region of interest to analyze the regenerated bone mass by Micro-CT software. The bone volume/total volume (BV/TV) values of the control, Gel, and TEOS/Gel groups were 10.9 ± 3.2%, 12.4 ± 3.0%, and 20.8 ± 1.9% during the 6th week and 19.5 ± 3.9%, 20.2 ± 3.5%, and 34.6 ± 4.2% during the 12th week, respectively (**Figure 5B**). Furthermore, H&E staining was performed to further observe the regenerated bone. As exhibited in **Figure 5C**, the histological observation was consistent with that of Micro-CT analysis, which indicated that the absence of bony bridge formation was in the area of the defects in the control group and Gel group. Moreover, the TEOS/Gel transplantation achieved satisfactory bone repair effect and recanalization of the medullary cavity. The abovementioned radiological evaluation and histological observation indicated that the critical-size segmental bone defects were difficult to self-regenerate effectively without additional treatment intervention, but our TEOS hydrogel with fascinating osteogenic induction function can significantly promote bone repair.

Tetraethyl Orthosilicate Hydrogel Enhanced Osteogenic-Related Marker Expression *In Vivo*

To investigate the *in vivo* mechanism of the TEOS hydrogel promoting bone healing, we collected bone tissue for RT-qPCR detection and immunofluorescence of osteogenesis-related markers. Runx-2 is a member of the Runx family of transcription factors and is also one of the earliest indications of osteoblastic differentiation. Runx-2 can induce the expression of key osteogenic genes such as OCN and OPN (Bai et al., 2020b). Col-1 is another critical osteogenic differentiation gene. The reticular structure formed by Col-1 is not only the premise of realizing the mineralization function of osteoblasts but also an important index reflecting the bone formation ability (Zhao Y. et al., 2020). OCN and OPN are bone-specific proteins

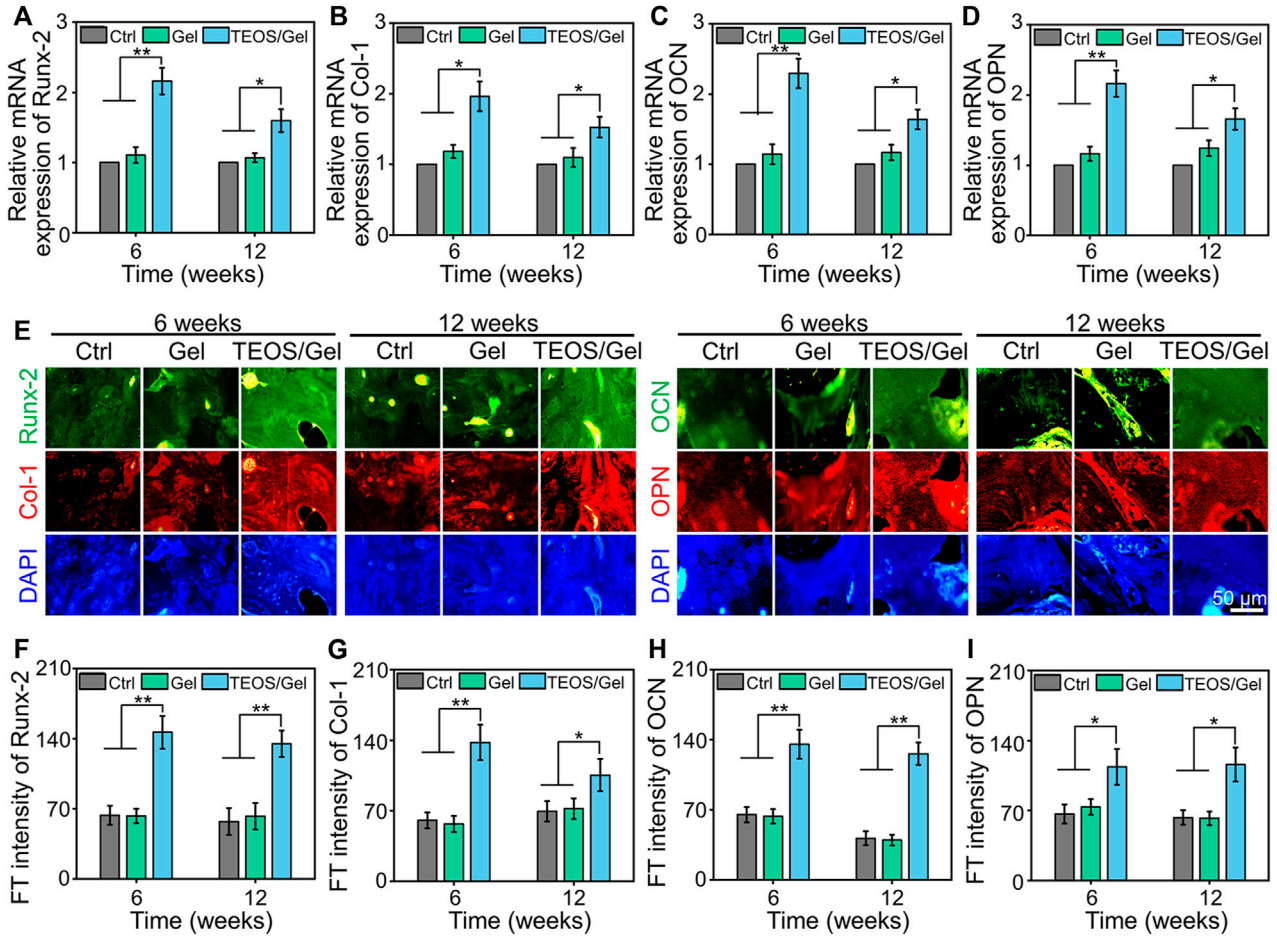

FIGURE 6 | TEOS hydrogel enhanced osteogenic-related marker expression. **(A–D)** RT-qPCR analysis of *Runx-2*, *Col-1*, *OCN*, and *OPN* in the regenerated bone tissues. **(E)** Representative immunofluorescence images. **(F–I)** Quantitative analysis of fluorescence intensity of Runx-2, Col-1, OCN, and OPN in the regenerated bone tissues (*$p < 0.05$; **$p < 0.01$).

synthesized by osteoblasts and recognized as a marker to assess osteogenic maturation and bone formation, and it shows the highest level during the late stage of osteogenesis (Qiao Y. et al., 2020; Kim et al., 2021). The expression of *Runx-2*, *Col-1*, *OCN*, and *OPN* at the transcriptional level in the TEOS/Gel group was significantly upregulated compared with that of the control group and Gel group in the regenerated bone tissues (**Figures 6A–D**). Moreover, immunofluorescence was performed to further reveal the expression of osteogenic differentiation markers in the regenerated bone tissues at the translation level (**Figure 6E**). Quantitative analysis of the immunofluorescence images indicated that the fluorescence intensity of Runx-2, Col-1, OCN, and OPN in each group had the same trend as the expression at the gene level **(Figures 6F–I)**. These abovementioned results demonstrated that transplantation of the TEOS hydrogel to the critical-size segmental bone defects can promote the upregulation of osteogenic markers.

In general, materials with osteogenic induction capacity are considered potential complementary components in implants to obtain better bone regeneration outcomes (Huang et al., 2016). Silicon is one of the essential trace elements in the human body, which shows a critical role in bone development and repair. Si is widely distributed in organelles such as mitochondria and acts as a cross-linking agent for collagen and proteoglycans, thus inducing Col-1 secretion and enhancing mineralization in the early stage of bone regeneration (He et al., 2018). In addition, Si ions can regulate the interaction between cells and induce stem cell migration and differentiation to promote osteogenesis and angiogenesis (Wang et al., 2018). Taking into account the critical function of Si in bone regeneration, the application of Si in hydrogel design is highly valued. In our study, the silicon-containing TEOS hydrogel can induce osteogenic differentiation of BMSCs and promote critical-size segmental bone defect repair *in vivo* by upregulating osteogenic-related markers, including Runx-2, Col-1, OCN, and OPN.

CONCLUSION

We prepared a functional hydrogel with satisfactory osteogenic effects through the dynamic supramolecular assembly of PVA, $Na_2B_4O_7$, and TEOS, as bone substitutes. This TEOS hydrogel has

adjustable mechanical properties, self-healing capacity, degradability, and biocompatibility, and it promotes BMSC osteogenic differentiation. Above all, the TEOS hydrogel significantly promotes bone healing in critical-size segmental bone defects. Therefore, it is anticipated that the TEOS hydrogel may have potential applications in the management of critical-size segmental bone defects.

DATA AVAILABILITY STATEMENT

The original contributions presented in the study are included in the article/Supplementary Material; further inquiries can be directed to the corresponding authors.

ETHICS STATEMENT

The animal study was reviewed and approved by the Animal Care and Use Ethics Committee of Guangdong Medical University.

AUTHOR CONTRIBUTIONS

SZ, HZ, and HC: Conceptualization, Investigation, Writing original draft, and Manuscript revision. XL: Data curation, Visualization, and Writing original draft. GZ and TC: Conceptualization, Methodology. YZ: Data curation, Investigation. WL and CS: Supervision, Writing—review & editing.

FUNDING

This work was supported by the Foundation of Huizhou Priority Clinical Speciality Cultivation Project ([2018]885), the Foundation of Huizhou Priority Clinical Speciality Cultivation Project ([2019]462), the Scientific Research Projects of Guangdong Provincial Bureau of Traditional Chinese Medicine (20221400 and 20222241), and the Research and Innovation Fund of Huizhou First Hospital (2021JC001).

REFERENCES

Bai, H., Cui, Y., Wang, C., Wang, Z., Luo, W., Liu, Y., et al. (2020a). 3D Printed Porous Biomimetic Composition Sustained Release Zoledronate to Promote Osteointegration of Osteoporotic Defects. *Mater. Des.* 189, 108513. doi:10.1016/j.matdes.2020.108513

Bai, H., Zhao, Y., Wang, C., Wang, Z., Wang, J., Liu, H., et al. (2020b). Enhanced Osseointegration of Three-Dimensional Supramolecular Bioactive Interface through Osteoporotic Microenvironment Regulation. *Theranostics* 10, 4779–4794. doi:10.7150/thno.43736

Boriani, F., Fazio, N., Fotia, C., Savarino, L., Nicoli Aldini, N., Martini, L., et al. (2017). A Novel Technique for Decellularization of Allogenic Nerves and *In Vivo* Study of Their Use for Peripheral Nerve Reconstruction. *J. Biomed. Mater. Res.* 105, 2228–2240. doi:10.1002/jbm.a.36090

Bottai, V., Dell'osso, G., Celli, F., Bugelli, G., Cazzella, N., Cei, E., et al. (2015). Total Hip Replacement in Osteoarthritis: the Role of Bone Metabolism and its Complications. *ccmbm* 12, 247–250. doi:10.11138/ccmbm/2015.12.3.247

Brandi, M. L. (2013). Healing of the Bone with Anti-fracture Drugs. *Expert Opin. Pharmacother.* 14, 1441–1447. doi:10.1517/14656566.2013.801959

Butscheidt, S., Von Kroge, S., Sturznickel, J., Beil, F. T., Gehrke, T., Puschel, K., et al. (2021). Allograft Chip Incorporation in Acetabular Reconstruction: Multiscale Characterization Revealing Osteoconductive Capacity. *J. Bone Joint. Surg. Am.* 103, 1996–2005. doi:10.2106/JBJS.20.01943

Cao, H., Guan, H., Lai, Y., Qin, L., and Wang, X. (2016). Review of Various Treatment Options and Potential Therapies for Osteonecrosis of the Femoral Head. *J. Orthopaedic Translation* 4, 57–70. doi:10.1016/j.jot.2015.09.005

Carlisle, E. M. (1970). Silicon: a Possible Factor in Bone Calcification. *Science* 167, 279–280. doi:10.1126/science.167.3916.279

Casarrubios, L., Gómez-Cerezo, N., Sánchez-Salcedo, S., Feito, M. J., Serrano, M. C., Saiz-Pardo, M., et al. (2020). Silicon Substituted Hydroxyapatite/VEGF Scaffolds Stimulate Bone Regeneration in Osteoporotic Sheep. *Acta Biomater.* 101, 544–553. doi:10.1016/j.actbio.2019.10.033

Chae, S., Hong, J., Hwangbo, H., and Kim, G. (2021). The Utility of Biomedical Scaffolds Laden with Spheroids in Various Tissue Engineering Applications. *Theranostics* 11, 6818–6832. doi:10.7150/thno.58421

Chen, Q., Zou, B., Lai, Q., Wang, Y., Zhu, K., Deng, Y., et al. (2021). 3D Printing and Osteogenesis of Loofah-like Hydroxyapatite Bone Scaffolds. *Ceramics Int.* 47, 20352–20361. doi:10.1016/j.ceramint.2021.04.043

Deng, C., Zhu, H., Li, J., Feng, C., Yao, Q., Wang, L., et al. (2018). Bioactive Scaffolds for Regeneration of Cartilage and Subchondral Bone Interface. *Theranostics* 8, 1940–1955. doi:10.7150/thno.23674

Fahmy-Garcia, S., Van Driel, M., Witte-Buoma, J., Walles, H., Van Leeuwen, J. P. T. M., Van Osch, G. J. V. M., et al. (2018). NELL-1, HMGB1, and CCN2 Enhance Migration and Vasculogenesis, but Not Osteogenic Differentiation Compared to BMP2. *Tissue Eng. A* 24, 207–218. doi:10.1089/ten.tea.2016.0537

Han, S., Park, B., Lim, J.-W., Youm, J.-Y., Choi, S.-W., Kim, D. H., et al. (2020). Comparison of Fusion Rate between Demineralized Bone Matrix versus Autograft in Lumbar Fusion : Meta-Analysis. *J. Korean Neurosurg. Soc.* 63, 673–680. doi:10.3340/jkns.2019.0185

He, X., Zhang, X., Li, J., Hang, R., Huang, X., Yao, X., et al. (2018). Titanium-based Implant Comprising a Porous Microstructure Assembled with Nanoleaves and Controllable Silicon-Ion Release for Enhanced Osseointegration. *J. Mater. Chem. B* 6, 5100–5114. doi:10.1039/c8tb00713f

He, Y., Tian, M., Li, X., Hou, J., Chen, S., Yang, G., et al. (2022). A Hierarchical-Structured Mineralized Nanofiber Scaffold with Osteoimmunomodulatory and Osteoinductive Functions for Enhanced Alveolar Bone Regeneration. *Adv. Healthc. Mater.* 11 3, 2102236. doi:10.1002/adhm.202102236

Hindiskere, S., Doddarangappa, S., and Chinder, P. S. (2020). What Are the Challenges and Complications of Sterilizing Autografts with Liquid Nitrogen for Malignant Bone Tumors? A Preliminary Report. *Clin. Orthop. Relat. Res.* 478, 2505–2519. doi:10.1097/corr.0000000000001347

Huang, Q., Elkhooly, T. A., Liu, X., Zhang, R., Yang, X., Shen, Z., et al. (2016). Effects of Hierarchical Micro/nano-Topographies on the Morphology, Proliferation and Differentiation of Osteoblast-like Cells. *Colloids Surf. B: Biointerfaces* 145, 37–45. doi:10.1016/j.colsurfb.2016.04.031

Hwa, T. P., Luu, N., Henry, L. E., Naples, J. G., Kaufman, A. C., Brant, J. A., et al. (2021). Impact of Reconstruction with Hydroxyapatite Bone Cement on CSF Leak Rate in Retrosigmoid Approach to Vestibular Schwannoma Resection: A Review of 196 Cases. *Otology & Neurotology* 42, 918–922. doi:10.1097/mao.0000000000003072

Jugdaohsingh, R. (2007). Silicon and Bone Health. *J. Nutr. Health Aging* 11, 99–110. doi:10.1016/j.jneb.2006.09.001

Kim, H. D., Hong, X., An, Y. H., Park, M. J., Kim, D. G., Greene, A. K., et al. (2021). A Biphasic Osteovascular Biomimetic Scaffold for Rapid and Self-Sustained Endochondral Ossification. *Adv. Healthc. Mater.* 10, e2100070. doi:10.1002/adhm.202100070

Kluin, O. S., Van Der Mei, H. C., Busscher, H. J., and Neut, D. (2013). Biodegradable vs Non-biodegradable Antibiotic Delivery Devices in the Treatment of Osteomyelitis. *Expert Opin. Drug Deliv.* 10, 341–351. doi:10.1517/17425247.2013.751371

Kumar, A., Nune, K. C., and Misra, R. D. K. (2018). Design and Biological Functionality of a Novel Hybrid Ti-6 A L-4 V/hydrogel System for

Reconstruction of Bone Defects. *J. Tissue Eng. Regen. Med.* 12, 1133–1144. doi:10.1002/term.2614

Lai, P.-L., Chu, I.-M., Chen, L.-H., and Chen, W.-J. (2013). Chemical and Physical Properties of Bone Cement for Vertebroplasty. *Biomed. J.* 36, 162–167. doi:10.4103/2319-4170.112750

Lewis, G., Towler, M. R., Boyd, D., German, M. J., Wren, A. W., Clarkin, O. M., et al. (2010). Evaluation of Two Novel Aluminum-free, Zinc-Based Glass Polyalkenoate Cements as Alternatives to PMMA Bone Cement for Use in Vertebroplasty and Balloon Kyphoplasty. *J. Mater. Sci. Mater. Med.* 21, 59–66. doi:10.1007/s10856-009-3845-7

Li, Z., Zhao, Y., Liu, H., Ren, M., Wang, Z., Wang, X., et al. (2021). pH-Responsive Hydrogel Loaded with Insulin as a Bioactive Dressing for Enhancing Diabetic Wound Healing. *Mater. Des.* 210. doi:10.1016/j.matdes.2021.110104

Li, Z., Zhao, Y., Wang, Z., Ren, M., Wang, X., Liu, H., et al. (2022). Engineering Multifunctional Hydrogel-Integrated 3D Printed Bioactive Prosthetic Interfaces for Osteoporotic Osseointegration. *Adv Healthc Mater.* 11, e2102535. doi:10.1002/adhm.202102535

Lim, Z. X. H., Rai, B., Tan, T. C., Ramruttun, A. K., Hui, J. H., Nurcombe, V., et al. (2019). Autologous Bone Marrow Clot as an Alternative to Autograft for Bone Defect Healing. *Bone Jt. Res.* 8, 107–117. doi:10.1302/2046-3758.83.bjr-2018-0096.r1

Liu, L., Shang, Y., Li, C., Jiao, Y., Qiu, Y., Wang, C., et al. (2021). Hierarchical Nanostructured Electrospun Membrane with Periosteum-Mimic Microenvironment for Enhanced Bone Regeneration. *Adv. Healthc. Mater.* 10 21, 2101195. doi:10.1002/adhm.202101195

Nonoyama, T., Wang, L., Tsuda, M., Suzuki, Y., Kiyama, R., Yasuda, K., et al. (2021). Isotope Microscopic Observation of Osteogenesis Process Forming Robust Bonding of Double Network Hydrogel to Bone. *Adv. Healthc. Mater.* 10, e2001731. doi:10.1002/adhm.202001731

Qiao, S., Wu, D., Li, Z., Zhu, Y., Zhan, F., Lai, H., et al. (2020). The Combination of Multi-Functional Ingredients-Loaded Hydrogels and Three-Dimensional Printed Porous Titanium Alloys for Infective Bone Defect Treatment. *J. Tissue Eng.* 11, 2041731420965797. doi:10.1177/2041731420965797

Qiao, Y., Liu, X., Zhou, X., Zhang, H., Zhang, W., Xiao, W., et al. (2020). Gelatin Templated Polypeptide Co-cross-linked Hydrogel for Bone Regeneration. *Adv. Healthc. Mater.* 9, e1901239. doi:10.1002/adhm.201901239

Russow, G., Jahn, D., Appelt, J., Märdian, S., Tsitsilonis, S., and Keller, J. (2019). Anabolic Therapies in Osteoporosis and Bone Regeneration. *Int. J. Mol. Sci.* 20, 010083. doi:10.3390/ijms20010083

Santos, I. G. B. P., Santana, C. M. M., Alves, A. T. N. N., Uzeda, M. J. P. G., Calasans-Maia, M. D., and Santana, R. B. (2019). Effects of Methods of Hydration of a Biphasic Ceramic Graft on Bone Regeneration of Extraction Socket Defects. *J. Periodontol.* 90, 425–432. doi:10.1002/jper.18-0209

Sivashanmugam, A., Charoenlarp, P., Deepthi, S., Rajendran, A., Nair, S. V., Iseki, S., et al. (2017). Injectable Shear-Thinning CaSO(4)/FGF-18-Incorporated Chitin-PLGA Hydrogel Enhances Bone Regeneration in Mice Cranial Bone Defect Model. *ACS Appl. Mater. Inter.* 9, 42639–42652. doi:10.1021/acsami.7b15845

Sun, W., Zhou, Y., Zhang, X., Xia, W., Xu, Y., and Lin, K. (2018). Injectable Nano-Structured Silicon-Containing Hydroxyapatite Microspheres with Enhanced Osteogenic Differentiation and Angiogenic Factor Expression. *Ceramics Int.* 44, 20457–20464. doi:10.1016/j.ceramint.2018.08.040

Van Houdt, C. I. A., Koolen, M. K. E., Lopez-Perez, P. M., Ulrich, D. J. O., Jansen, J. A., Leeuwenburgh, S. C. G., et al. (2021). Regenerating Critical Size Rat Segmental Bone Defects with a Self-Healing Hybrid Nanocomposite Hydrogel: Effect of Bone Condition and BMP-2 Incorporation. *Macromol Biosci.* 21, e2100088. doi:10.1002/mabi.202100088

Wang, C., Lin, K., Chang, J., and Sun, J. (2013). Osteogenesis and Angiogenesis Induced by Porous β-CaSiO(3)/PDLGA Composite Scaffold via Activation of AMPK/ERK1/2 and PI3K/Akt Pathways. *Biomaterials* 34, 64–77. doi:10.1016/j.biomaterials.2012.09.021

Wang, X., Gao, L., Han, Y., Xing, M., Zhao, C., Peng, J., et al. (2018). Silicon-Enhanced Adipogenesis and Angiogenesis for Vascularized Adipose Tissue Engineering. *Adv. Sci. (Weinh)* 5, 1800776. doi:10.1002/advs.201800776

Yu, M., Du, Y., Han, Y., and Lei, B. (2020). Biomimetic Elastomeric Bioactive Siloxane-Based Hybrid Nanofibrous Scaffolds with miRNA Activation: A Joint Physico-Chemical-Biological Strategy for Promoting Bone Regeneration. *Adv. Funct. Mater.* 30, 1906013. doi:10.1002/adfm.201906013

Zhang, C., Zhang, T., Geng, T., Wang, X., Lin, K., and Wang, P. (2021). Dental Implants Loaded with Bioactive Agents Promote Osseointegration in Osteoporosis: A Review. *Front. Bioeng. Biotechnol.* 9, 591796. doi:10.3389/fbioe.2021.591796

Zhang, S., Guo, Y., Dong, Y., Wu, Y., Cheng, L., Wang, Y., et al. (2016). A Novel Nanosilver/Nanosilica Hydrogel for Bone Regeneration in Infected Bone Defects. *ACS Appl. Mater. Inter.* 8, 13242–13250. doi:10.1021/acsami.6b01432

Zhang, Y. S., and Khademhosseini, A. (2017). Advances in Engineering Hydrogels. *Science* 356, eaaf3627. doi:10.1126/science.aaf3627

Zhao R, R., Chen, S., Zhao, W., Yang, L., Yuan, B., Ioan, V. S., et al. (2020). A Bioceramic Scaffold Composed of Strontium-Doped Three-Dimensional Hydroxyapatite Whiskers for Enhanced Bone Regeneration in Osteoporotic Defects. *Theranostics* 10, 1572–1589. doi:10.7150/thno.40103

Zhao Y, Y., Li, Z., Jiang, Y., Liu, H., Feng, Y., Wang, Z., et al. (2020). Bioinspired mineral Hydrogels as Nanocomposite Scaffolds for the Promotion of Osteogenic Marker Expression and the Induction of Bone Regeneration in Osteoporosis. *Acta Biomater.* 113, 614–626. doi:10.1016/j.actbio.2020.06.024

Conflict of Interest: The authors declare that the research was conducted in the absence of any commercial or financial relationships that could be construed as a potential conflict of interest.

Publisher's Note: All claims expressed in this article are solely those of the authors and do not necessarily represent those of their affiliated organizations, or those of the publisher, the editors, and the reviewers. Any product that may be evaluated in this article, or claim that may be made by its manufacturer, is not guaranteed or endorsed by the publisher.

frontiers | Frontiers in Bioengineering and Biotechnology

ORIGINAL RESEARCH
published: 13 May 2022
doi: 10.3389/fbioe.2022.842530

Fabrication and Effect of Strontium-Substituted Calcium Silicate/Silk Fibroin on Bone Regeneration *In Vitro* and *In Vivo*

Yuning Zhou[1,2†], *Yue Hu*[1,2†], *Mamoru Uemura*[3], *Lunguo Xia*[2,4*], *Xingge Yu*[2,5*] and *Yuanjin Xu*[1,2*]

[1]Department of Oral Surgery, Shanghai Ninth People's Hospital, Shanghai Jiao Tong University School of Medicine, College of Stomatology, Shanghai Jiao Tong University, Shanghai, China, [2]National Center for Stomatology, National Clinical Research Center for Oral Diseases, Shanghai Key Laboratory of Stomatology, Shanghai, China, [3]Department of Anatomy, Osaka Dental University, Hirakata, Japan, [4]Department of Orthodontics, Shanghai Ninth People's Hospital, Shanghai Jiao Tong University School of Medicine, College of Stomatology, Shanghai Jiao Tong University, Shanghai, China, [5]Department of Oral and Cranio-Maxillofacial Science, Shanghai Ninth People's Hospital, Shanghai Jiao Tong University School of Medicine, College of Stomatology, Shanghai Jiao Tong University, Shanghai, China

OPEN ACCESS

Edited by:
He Liu,
Jilin University, China

Reviewed by:
Yoke Chin Chai,
KU Leuven, Belgium
Yunan Qing,
Second Affiliated Hospital of Jilin University, China

***Correspondence:**
Lunguo Xia
xialunguo@hotmail.com
Xingge Yu
yuxingge1991@163.com
Yuanjin Xu
drxuyuanjin@126.com

[†]These authors have contributed equally to this work.

Specialty section:
This article was submitted to Biomaterials, a section of the journal Frontiers in Bioengineering and Biotechnology

Received: 23 December 2021
Accepted: 11 April 2022
Published: 13 May 2022

Citation:
Zhou Y, Hu Y, Uemura M, Xia L, Yu X and Xu Y (2022) Fabrication and Effect of Strontium-Substituted Calcium Silicate/Silk Fibroin on Bone Regeneration In Vitro and In Vivo. Front. Bioeng. Biotechnol. 10:842530. doi: 10.3389/fbioe.2022.842530

Achieving rapid osteogenesis and angiogenesis was the key factor for bone regeneration. In the present study, the strontium-substituted calcium silicate (SrCS)/silk fibroin (SF) composite materials have been constructed by combining the different functional component ratios of SrCS (12.5 wt%, 25 wt%) and SF. Then, the effects of SrCS/SF materials on proliferation, osteogenic differentiation, and angiogenic factor secretion of rat bone marrow-derived mesenchymal stromal cells (rBMSCs) were first evaluated *in vitro*. Moreover, the *in vivo* effect of osteogenesis was evaluated in a critical-sized rat calvarial defect model. *In vitro* studies showed that SrCS/SF significantly enhanced the cell proliferation, alkaline phosphatase (ALP) activity, and the expression of osteogenic and angiogenic factors of rBMSCs as compared with the SF and CS/SF, and the optimum proportion ratio was 25 wt%. Besides, the results also showed that CS/SF achieved enhanced effects on rBMSCs as compared with SF. The *in vivo* results showed that 25 wt % SrCS/SF could obviously promote new bone formation more than SF and CS/SF. The present study revealed that SrCS could significantly promote the osteogenic and angiogenic activities of SF, and SrCS/SF might be a good scaffold material for bone regeneration.

Keywords: strontium-substituted calcium silicate/silk fibroin, bone marrow-derived mesenchymal stem cells, osteogenesis, angiogenesis, bone regeneration

1 INTRODUCTION

In clinical practice, autologous bone transplantation, allogeneic bone transplantation, xenogeneic bone transplantation, and allogeneic material transplantation are the main methods applied for bone defect repair. However, each treatment method possesses its own advantages and disadvantages, which are unable to satisfy the needs of bone defect morphology and functional reconstruction at the same time (Wu V. et al., 2019). Therefore, bone scaffold materials have been continuously researched and developed. After implantation, bone scaffold materials can provide a three-dimensional scaffold

environment, which is conducive to cell adhesion, proliferation, differentiation, and growth (Bose et al., 2017). More importantly, in addition to promoting cell colonization and osteogenic activity, it is also crucial to maintain cell viability, which depends on adequate blood supply. Previous studies discovered that after implanting *in vivo*, the survival of cells mainly depended on the degree of vascularization in the bone scaffold materials (Yan et al., 2019; Yin et al., 2019). The growth of the vascular bed around the defect could only reach the edge of the scaffold materials, while cell death could be discovered in the center, which limited the formation of new bone (Ziebart et al., 2013). In addition, the ingrowth vascular also acted as a communication network between the new bone and adjacent tissues, thus ensuring the stability of the new bone (Chim et al., 2013). Therefore, the ideal scaffold materials for bone regeneration should possess the inductive activities of osteogenesis and angiogenesis.

As a new kind of natural polymer material, silk fibroin (SF) has good biocompatibility, mechanical strength, and toughness, which attracted wide attention in the field of bone repairing biomaterials (Omenetto and Kaplan 2010; Bhattacharjee et al., 2017). However, SF is still lacking in osteoinductive activity (Zhu et al., 2011). Previous studies have shown that the compounded organic and inorganic materials could effectively enhance the biological properties of materials (Ye et al., 2011; Wang et al., 2020). Our previous research revealed that, under the osteoporotic condition, Sr-doped CS bioceramics (SrCS) could promote the osteogenic differentiation and angiogenic factor expression of rBMSCs, which could also stimulate the angiogenic activity of HUVECs (Lin et al., 2013). Moreover, it has been reported that SrCS with different concentrations could promote osteogenesis and inhibit osteoclastogenesis at the same time (Ben et al., 2020). Based on previous studies, it is expected to enhance the osteogenic and angiogenic properties of SF materials by a combination of SrCS bioceramics. However, it is still questioned whether the SrCS compound with SF materials could improve the physicochemical and biological properties of the materials simultaneously, as well as its optimum proportion ratio.

In the present study, our hypothesis is that by combining SrCS bioceramics and SF materials, novel materials (SrCS/SF) with bi-directional osteogenic/angiogenic activity could be designed. To test our hypothesis, rBMSCs were cultured on the composite materials with different concentrations of SrCS, and the effects on the proliferation, osteogenic differentiation, and secretion of angiogenic factors of rBMSCs were scientifically detected. Furthermore, the effects of the composite materials on bone regeneration were investigated in a rat critical-sized calvarial defect model *in vivo*.

2 MATERIALS AND METHODS

2.1 Fabrication and Characterization of the Silk Fibroin, CS/SF, and Strontium-Substituted Calcium Silicate/SF Scaffold Materials

The CS and SrCS bioceramic ultrafine powders with 10 mol% of Ca replaced by Sr were prepared by chemical precipitation, sol–gel method, and hydrothermal reaction technology, while the SF solution was obtained by dialysis, as previously described (Ye et al., 2011; Lin et al., 2013). Then the CS or SrCS nanofibers and SF solution were mixed by ultrasonic wave. A proper amount of 400–600 μm granular NaCl particles was added (Byrne et al., 2008; Kasten et al., 2008; Lee et al., 2019), which were mixed evenly and put into the 6-well plates to a height of 8 mm. And then frozen in − 20oC refrigerator and placed in a freeze dryer. After freeze-drying, the CS/SF and SrCS/SF scaffold materials with a large pore size of 400–600 μm were obtained. By adjusting the concentration of silk protein solution and the ratio of NaCl particles, the porosity and mechanical properties of the composite scaffolds were controlled, and finally, the composite scaffolds with 80–88% porosity were obtained. Moreover, by controlling the quality of CS or SrCS, the 12.5 wt% CS/SF, 25 wt% CS/SF, 12.5 wt% SrCS/SF, and 25 wt% SrCS/SF materials were fabricated separately. In addition, X-ray diffraction (XRD: D/max 2550V, Rigaku, Japan) and scanning electron microscopy (SEM: JSM-6700F, JEOL, Japan) have been performed to detect the characteristics, morphology, and surface topography of the materials, respectively. On the other hand, the macropore sizes of the materials were measured under electron microscopy using the direct observation from cross section method (Engin and Tas 1999). While the porosity of the materials was determined by the Archimedean method using distilled water as the determination medium (Lin et al., 2013).

The compressive mechanical properties of all scaffolds were detected using a universal mechanical testing machine (Instron, United States). The materials were stressed under the loading rate of 1 mm/min. When the compression variable reaches 60%, the stress–strain curve of the material was obtained. Then, the compression modulus at 10% deformation was calculated.

The effect of CS or SrCS addition on the degradation behavior of SF was determined by measuring their weight loss percentage in Tris-HCL buffered solution (0.1 mol/L), which is prepared as per described in the previous study (Xia et al., 2019). Then the samples were soaked in Tris-HCL buffered solution and refreshed every day. On days 1, 3, 5, 7, and 14, the samples were taken out, rinsed with deionized water, and then freeze-dried to measure the weight loss.

The 12.5 wt% and 25 wt% SrCS/SF scaffold materials were soaked in 1 ml medium without FBS and incubated for 4, 7, and 10 days. The medium was collected at each time point, and concentrations of strontium in the medium were measured by inductively coupled plasma atomic emission spectroscopy (ICP-AES; Varian, United States).

2.2 Isolation and Culture of Rat Bone Marrow-Derived Mesenchymal Stromal Cells

The rBMSCs were isolated and cultured following the protocols as described in the previously study (Zhou et al., 2015). Briefly, the 4-week-old male SD rats weighing 50 ± 5 g were sacrificed by overdose of pentobarbital. Then both ends of the femurs were cut off at the metaphyses, and the marrow was flushed out with 10 ml modified Eagle's medium (MEM; Gibco, United States)

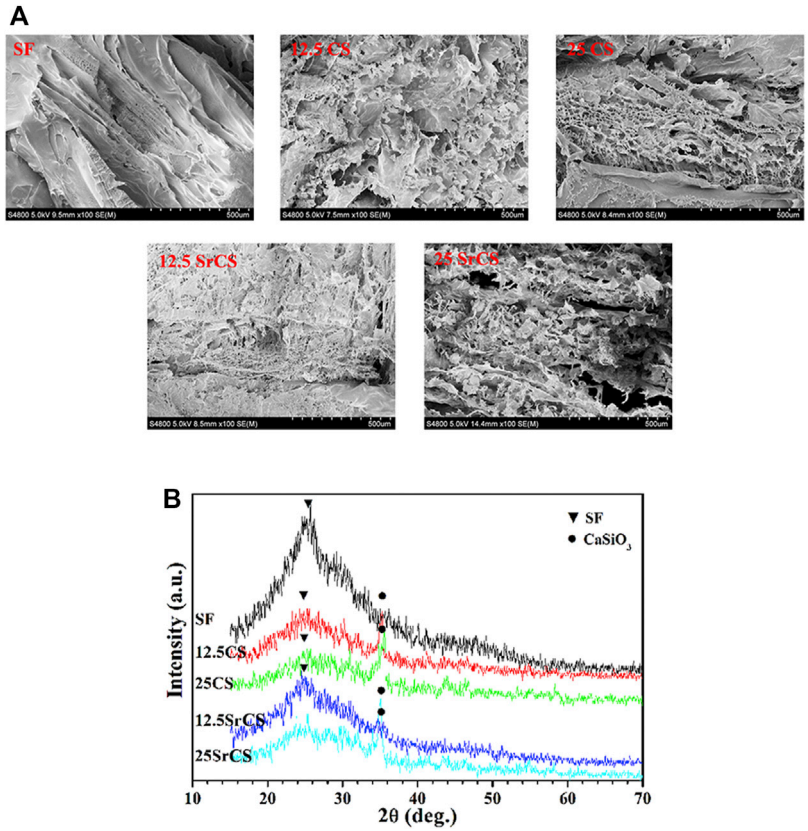

FIGURE 1 | Characteristics of materials. **(A)** SEM micrographs of materials (SF: SF, 12.5 CS: 12.5 wt% CS/SF, 25 CS: 25 wt% CS/SF, 12.5 SrCS: 12.5 wt% SrCS/SF, 25 SrCS: 25 wt% SrCS/SF). **(B)** XRD patterns of materials. **(A)** Scale bar = 500 μm.

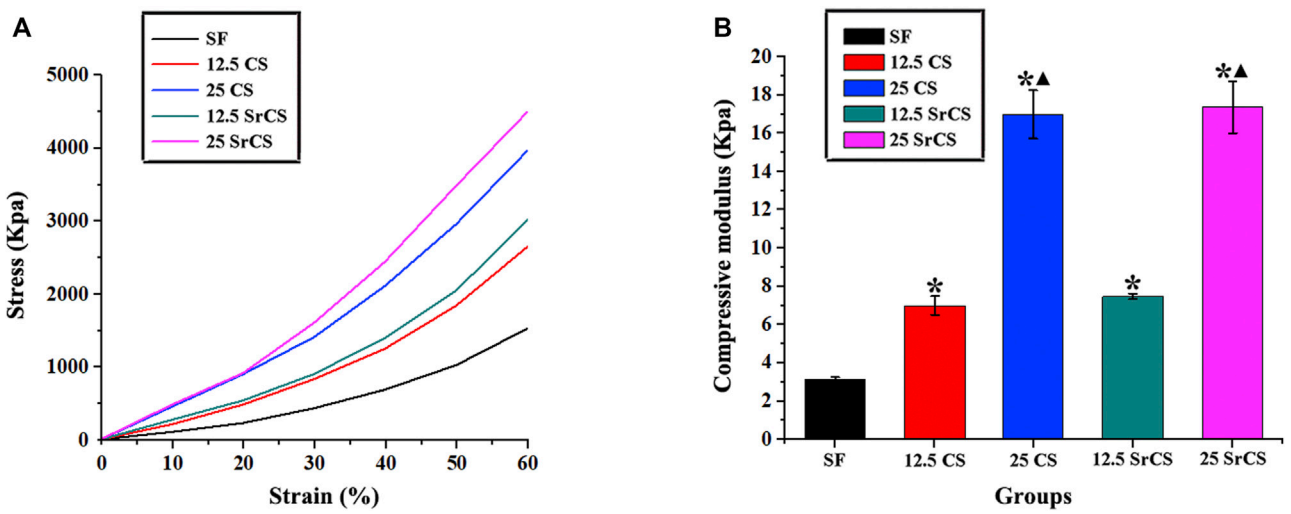

FIGURE 2 | Compressive mechanical properties of materials. **(A)** Stress–strain curve of materials. **(B)** Compressive modulus of materials at 10% strain. (SF: SF, 12.5 CS: 12.5 wt% CS/SF, 25 CS: 25 wt% CS/SF, 12.5 SrCS: 12.5 wt% SrCS/SF, 25 SrCS: 25 wt% SrCS/SF). The SF group was treated as the control group. *p < 0.05 indicates the other groups vs. the SF group. ▲p < 0.05 indicates the 25 CS group or 25 SrCS group vs. the 12.5 CS group or 12.5 SrCS group.

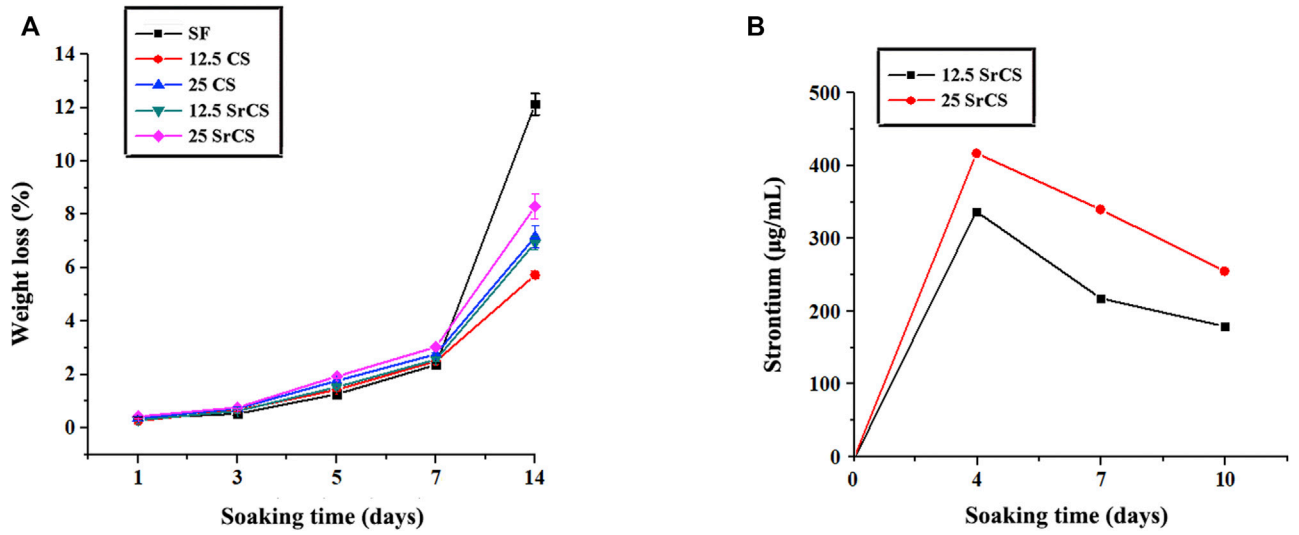

FIGURE 3 | Degradation and ion release properties of materials. **(A)** Degradation behavior of materials. **(B)** Strontium release curve of 12.5 wt% and 25 wt% SrCS/SF scaffold materials. (SF: SF, 12.5 CS: 12.5 wt% CS/SF, 25 CS: 25 wt% CS/SF, 12.5 SrCS: 12.5 wt% SrCS/SF, 25 SrCS: 25 wt% SrCS/SF).

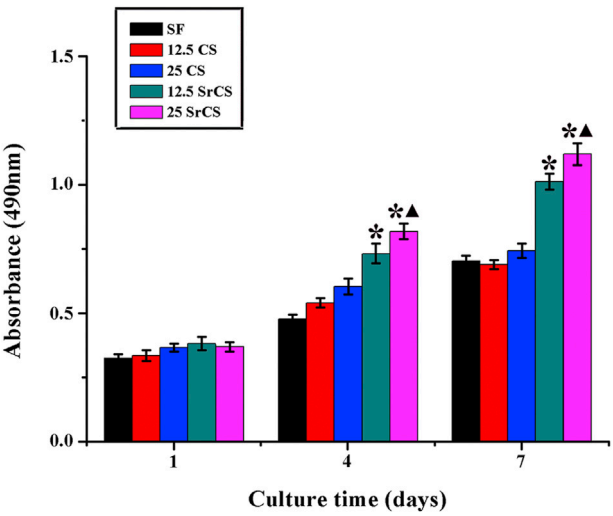

FIGURE 4 | MTT assay. The effect of different materials (SF: SF, 12.5 CS: 12.5 wt% CS/SF, 25 CS: 25 wt% CS/SF, 12.5 SrCS: 12.5 wt% SrCS/SF, 25 SrCS: 25 wt% SrCS/SF) on the proliferation of rBMSCs. The SF group was treated as the control group. *$p < 0.05$ indicates the other groups vs. the SF group, and ▲$p < 0.05$ indicates the 25 SrCS group vs. the other groups.

supplemented with 10% fetal bovine serum (FBS; Gibco, United States) and antibiotics (penicillin 100 U/mL, streptomycin 100 U/mL). After culturing in an incubator at 37°C with 5% CO_2 for 4 days, the medium was first changed and then renewed every 2 days. At a confluence of approximately 90%, the rBMSCs were washed with phosphate-buffered saline (PBS) and passaged using 0.25% trypsin/ethylenediaminetetraacetic acid (trypsin/EDTA). The cells from passages 1 to 3 were used for subsequent experiments.

2.3 MTT Assay

To investigate the effects of different scaffold materials on cell proliferation of rBMSCs, the MTT assay was performed. First, the cells were plated on the different scaffold materials (SF, 12.5 wt% CS/SF, 25 wt% CS/SF, 12.5 wt% SrCS/SF, and 25 wt% SrCS/SF) into 96-well plates at a density of 5×10^3 cells per piece of material, then cultured in the medium for 1, 4, and 7 days. At each time point, the materials with cells seeded were removed into other blank wells to exclude the influence from the rBMSCs adherented on the wells, and then incubated in MEM containing 10% MTT (Amresco, United States) solution at 37 °C for 4 h. Finally, DMSO was used and the absorbance of the solution was measured at 490 nm using an ELx Ultra Microplate Reader (BioTek, United States). All experiments were performed in triplicate.

2.4 Real-Time Quantitative PCR (RT-PCR) Analysis

To measure the expression of osteogenic and angiogenic genes of rBMSCs seeded on different materials as previously described, the RT-PCR analysis was performed at 4, 7, and 10 days. At each time point, after collecting the cells, the RNA was extracted using TRIzol reagent (Invitrogen, Carlsbad, CA, United States), and complementary DNA (cDNA) was then synthesized using a Prime-Script RT reagent kit (Takara Bio, Japan) following the manufacturer's recommendations. Quantification for ALP, bone morphogenetic protein 2 (BMP-2), osteopontin (OPN), vascular endothelial growth factor (VEGF), and angiogenin-1 (ANG-1) were analyzed with a Bio-Rad MyiQ single-color real-time PCR system, while glyceraldehyde-3-phosphate dehydrogenase (GAPDH) was used as an internal control for normalization. All experiments were performed in triplicate.

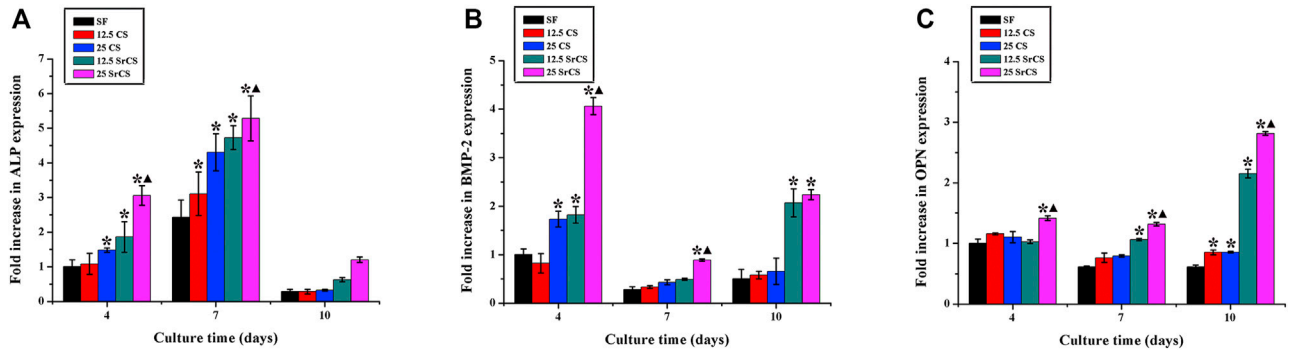

FIGURE 5 | Osteogenic gene expression analysis. The osteogenic gene expression of rBMSCs seeded on different materials (SF: SF, 12.5 CS: 12.5 wt% CS/SF, 25 CS: 25 wt% CS/SF, 12.5 SrCS: 12.5 wt% SrCS/SF, 25 SrCS: 25 wt% SrCS/SF) for 4, 7, and 10 days. **(A)** ALP; **(B)** BMP-2; **(C)** OPN. The SF group was treated as the control group. $^*p < 0.05$ indicates the other groups vs. the SF group, and $\blacktriangle p < 0.05$ indicates the 25 SrCS group vs. the other groups.

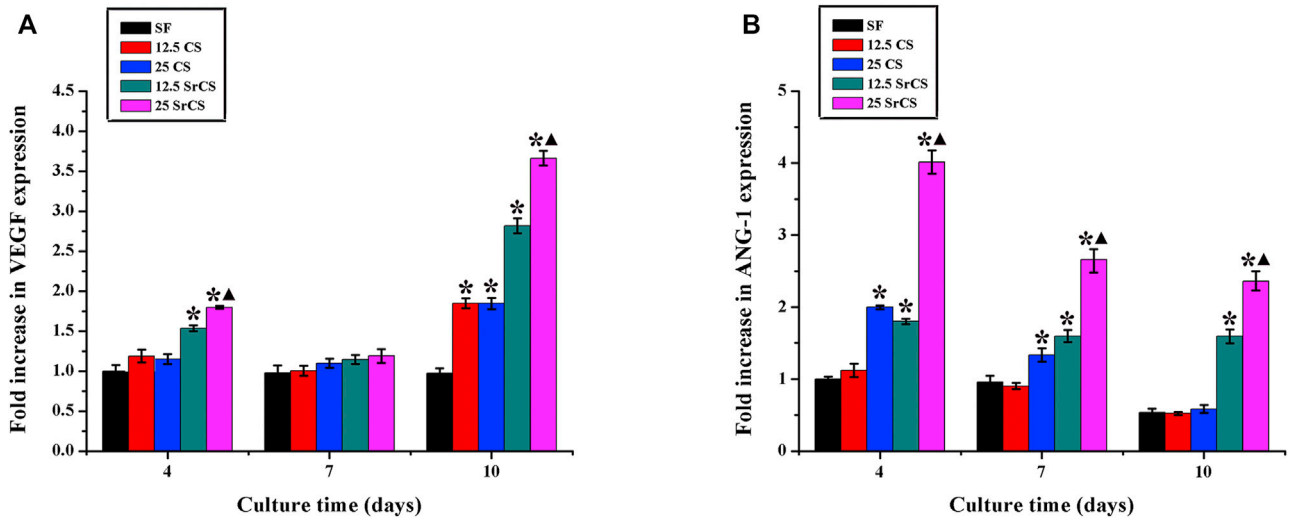

FIGURE 6 | Angiogenic gene expression analysis. The angiogenic gene expression of rBMSCs seeded on different materials (SF: SF, 12.5 CS: 12.5 wt% CS/SF, 25 CS: 25 wt% CS/SF, 12.5 SrCS: 12.5 wt% SrCS/SF, 25 SrCS: 25 wt% SrCS/SF) for 4, 7, and 10 days. **(A)** VEGF; **(B)** ANG-1. The SF group was treated as the control group. $^*p < 0.05$ indicates the other groups vs. the SF group, and $\blacktriangle p < 0.05$ indicates the 25 SrCS group vs. the other groups.

2.5 Alkaline Phosphatase Activity Analysis

After the rBMSCs were seeded on the different scaffolds as described earlier, at 7 days, ALP staining was analyzed. Briefly, the cells were incubated in BCIP/NBT solution (Beyotime, Shanghai, China) in the dark at 37oC, and the areas stained purple were regarded as positive, as the previous study described (Zhou et al., 2015). In addition, after the above experiments, SF, 25 wt% CS/SF and 25 wt% SrCS/SF groups were selected. On days 4, 7, and 10, ALP quantity analysis of BMSCs cultured on these materials was performed following the manufacturer's instructions (Beyotime, China). First, the BMSCs were incubated with 400 μL lysis buffer at 37oC for 4 h, and the samples were vibrated for 30 min. Then the ALP activity was quantified by absorbance at 405 nm (BioTek, United States) using p-nitrophenyl phosphate disodium (p-NPP) as the substrate and calculated according to a reference standard product. Furthermore, the total cellular protein content was measured by detecting the absorbance at 630 nm and calculating with reference to a series of BSA (Sigma, United States) standards, using the Bio-Rad protein assay kit (Bio-Rad, United States). Finally, the ALP quantitative result was accessed as pNP (mM) per milligram of total cellular proteins. All experiments were performed in triplicate.

2.6 Enzyme-Linked Immunosorbent Assay

To analyze the angiogenic protein expression of cells cultured on SF, 25 wt% CS/SF, and 25 wt% SrCS/SF scaffold materials, the VEGF content was measured by using a VEGF ELISA kit (Bender, United States) on days 4, 7, and 10. According to the manufacturer's instructions, the VEGF concentration was specifically measured using a standard curve and was further normalized to the total cellular protein content, as described above. All experiments were performed in triplicate.

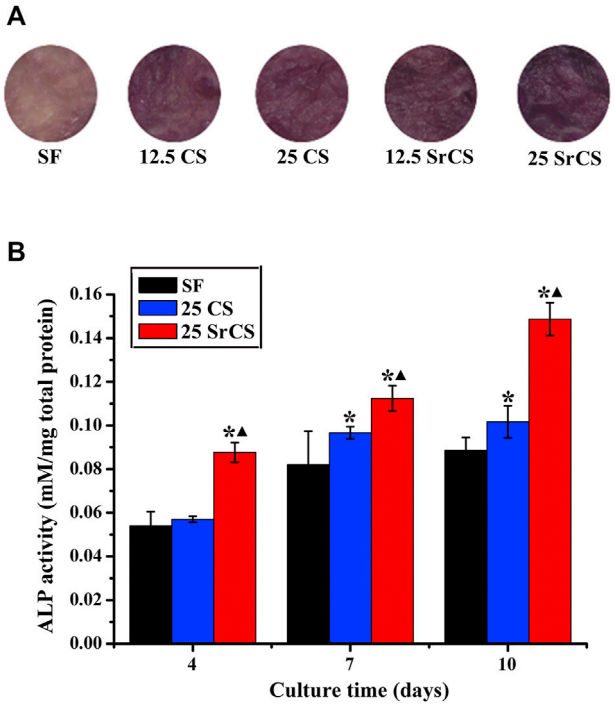

FIGURE 7 | ALP activity analysis. **(A)** ALP staining of rBMSCs seeded on different materials (SF: SF, 12.5 CS: 12.5 wt% CS/SF, 25 CS: 25 wt% CS/SF, 12.5 SrCS: 12.5 wt% SrCS/SF, 25 SrCS: 25 wt% SrCS/SF) for 7 days. **(B)** ALP staining of rBMSCs seeded on different materials (SF: SF, CS/SF: 25 wt% CS/SF, SrCS/SF: 25 wt% SrCS/SF) for 4, 7, and 10 days. *$p < 0.05$ indicates the other groups vs. the SF group, and ▲$p < 0.05$ indicates the 25 SrCS group vs. the other groups.

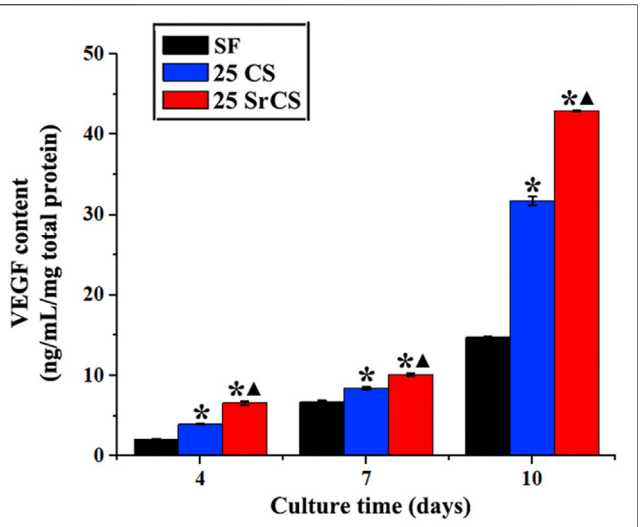

FIGURE 8 | VEGF protein content test by ELISA assay. The protein level of VEGF of rBMSCs seeded on different materials (SF: SF, CS/SF: 25 wt% CS/SF, SrCS/SF: 25 wt% SrCS/SF) for 4, 7, and 10 days. *$p < 0.05$ indicates the other groups vs. the SF group, and ▲$p < 0.05$ indicates the 25 SrCS group vs. the other groups.

2.7 Animal Experiments

First, 9 SD rats of 8-week-old were randomly allocated into three groups: SF group, 25 wt% CS/SF group, and 25 wt% SrCS/SF group. The animals were anesthetized by intraperitoneal injection of pentobarbital (Nembutal 3.5 mg/100 g). On the scalp, a 1.0- to 1.5-cm sagittal incision was made, and the calvarium was exposed by blunt dissection. Two bilateral critical-sized defects were created by using a 5-mm diameter trephine bur (Fine Science Tools, United States). Finally, 18 critical-sized calvarial defects in 9 rats were generated and randomly filled with the scaffolds as previously described (n = 6), respectively. All the rats were sacrificed, and the calvarias were removed after 8 weeks.

2.8 Sequential Fluorescent Labeling

To investigate the new mineralized tissue at different stages, polychrome sequential fluorescent labeling was performed over a period of 8 weeks according to the method as described in the previous study (Ye et al., 2011). Briefly, the animals were intraperitoneally injected with 25 mg/kg tetracycline hydrochloride (TE, Sigma, United States), 30 mg/kg alizarin red (AL, Sigma, United States), and 20 mg/kg calcein (CA, Sigma, United States) at 2, 4, and 6 weeks after the operation, respectively.

2.9 Microcomputed Tomography Examination

At 8 weeks after the operation, the rats in each group were sacrificed using an overdose of pentobarbital. The calvarias were fixed in a 4% phosphate-buffered formalin solution and then detected by a microcomputed tomography (micro-CT) system (μCT-80, Scanco Medical AG, Switzerland) as described in the previous study (Zhou et al., 2017). The segmentation of bone tissue from the CS/SF and SrCS/SF was carried out by the threshold segmentation method, while the selected bone grey threshold range was 120–255. Moreover, the bone mineral density (BMD) and the trabecular thickness (Tb. Th) of the bone defects were calculated by auxiliary histomorphometric software (Scanco Medical AG, Switzerland). All experiments were performed in triplicate.

2.10 Histological and Histomorphometric Observation

By ascending in concentrations of alcohol ranging from 75 to 100% and embedding in polymethylmethacrylate (PMMA), the samples were dehydrated. Three longitudinal sections for each specimen were prepared as the previous study described (Zhou et al., 2017). First, the samples were observed for fluorescent labeling using CLSM (Leica TCS, Germany), and the images inside the calvarial defects were partially magnified. Then, using a personal computer-based image analysis system (Image Pro 5.0, Media Cybernetic, United States), the fluorochrome staining for new bone formation and mineralization was quantified by calculating the percentage of fluorescence area in the defect images, while the image margin was treated as the calculation range. Data pertaining to the colors yellow (TE), red (AL), and green (CA) represent bone regeneration and mineralization at weeks 2, 4, and 6

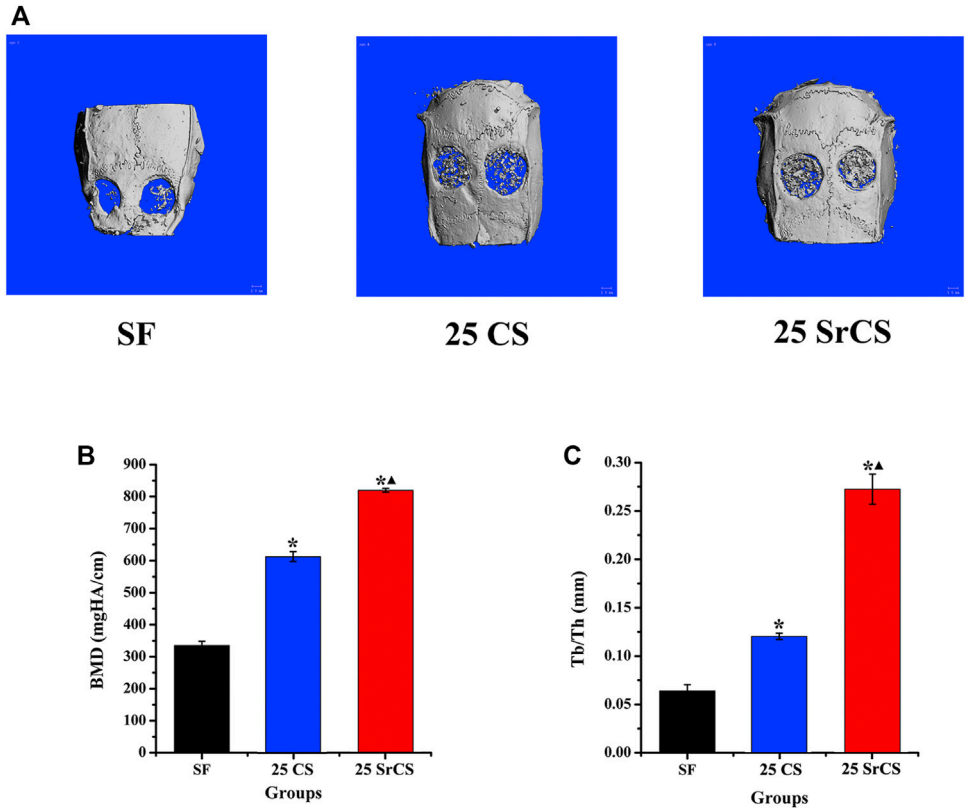

FIGURE 9 | Micro-CT evaluation and morphometric analysis of calvarial bone repairing. **(A)** Representative 3D superficial image of femur bone defects (bone grey threshold range: 120-255). Morphometric analysis of bone mineral density (BMD) **(B)** and trabecular thickness (Tb. Th) **(C)** by micro-CT for each group at 8 weeks post-operation. *$p < 0.05$ indicates the other groups vs. the SF group, and ▲$p < 0.05$ indicates the 25 SrCS group vs. the other groups.

after the operation, respectively. Finally, the samples were stained with van Gieson's (VG) picro-fuchsin for histological observation. Using Image Pro 5.0, the area of new bone formation was quantified along three randomly selected sections from the serial sections collected from each sample and reported as a percentage of the whole bone defect area. All experiments were performed in triplicate.

2.11 Statistical Analysis

The means and standard deviations of all data were calculated. Differences between groups were analyzed by ANOVA and the SNK post hoc or Kruskal–Wallis nonparametric procedure followed by the Mann–Whitney *U* test for multiple comparisons based on the results of the normal distribution and equal variance assumption test (Zhou et al., 2017) using SAS 8.0 software (SAS Inc., United States). A difference was considered statistically significant at a *p*-value < 0.05 (*▲ $p < 0.05$).

3 RESULTS

3.1 Characterization of SF, CS/SF, and SrCS/SF Materials

The CS/SF and SrCS/SF scaffold materials with a large pore size of 400–600 μm and 80–88% porosity were fabricated (**Supplementary Table S2**). As shown in SEM micrographs (**Figure 1A**), compared with the SF and CS/SF materials, the porosity of the SrCS/SF materials increased to a certain degree, including distributed and interconnected porosity. While the macropore sizes and porosity of SrCS/SF were in the range of 400–600 μm and 80–88%, respectively. Meanwhile, the XRD patterns (**Figure 1B**) showed the diffraction peaks (indicated as ▼ and ●), which suggested that both CS and SrCS could be identified as CaSiO3 phase; and confirmed that the obtained materials were compounded by CS or SrCS and SF materials, and the proportion concentration of CS or SrCS did not alter the phase composition.

The result of compressive mechanical properties of the materials showed that the structure of all materials is relatively uniform without large holes or collapses inside (**Figure 2A**). It can be seen that the compressive modulus of the CS/SF and SrCS/SF scaffolds was higher than that of SF, especially in the 25 wt% groups (**Figure 2B**). However, there was no significant difference between 25 wt% SrCS/SF scaffolds and 25 wt% CS/SF scaffolds, indicating that 25 wt % CS/SF and 25 wt% SrCS/SF scaffolds both have better mechanical properties than the other scaffolds.

As shown in **Figure 3A**, the addition of CS or SrCS could reduce the degradation rate of SF, which is better

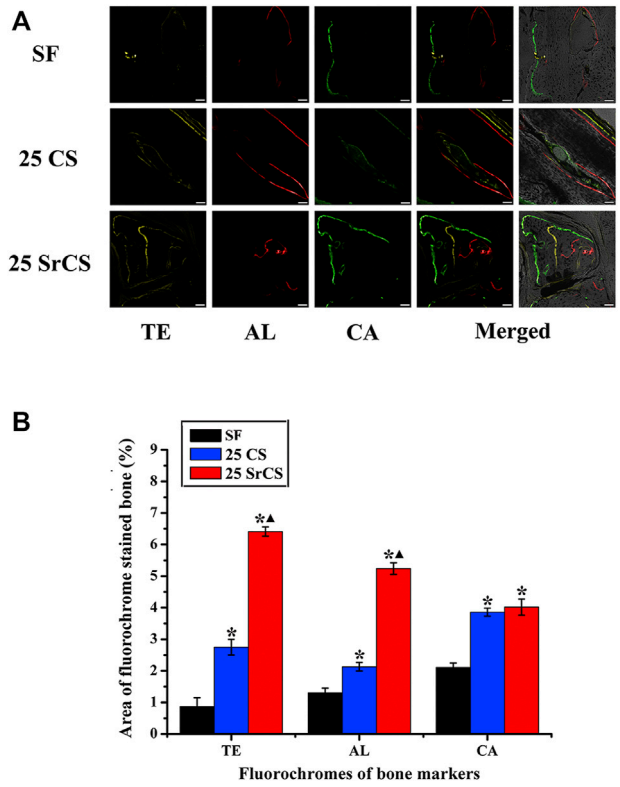

FIGURE 10 | Sequential fluorescent labeling of TE, AL, and CA. **(A)** The images in yellow (TE), red (AL), and green (CA) indicate bone regeneration and mineralization at 2, 4, and 6 weeks after the operation. Merged images of the three fluorochromes or with a brightfield confocal laser microscopy image for the same group. **(B)** Percentages of TE, AL, and CA staining by histomorphometric analysis. *$p < 0.05$ indicates the other groups vs. the SF group, and ▲$p < 0.05$ indicates the 25 SrCS group vs. the other groups. Scale bar = 100 μm.

cooperating with the bone regeneration rate *in vivo*. While the release curve of strontium showed that 12.5 wt% and 25 wt% SrCS/SF scaffold materials could release strontium steadily throughout the whole observation time, the concentration of released strontium became lower with time (**Figure 3B**).

3.2 MTT Analysis

To measure the proliferation of rBMSCs cultured on different materials described previously, the MTT analysis was performed on days 1, 4, and 7. In **Figure 4**, significantly increased cell proliferation was observed in the SrCS/SF groups than in the respective other groups on days 4 and 7. In addition, a significant difference was detected between the 25 wt% SrCS/SF group and the other groups at 4 and 7 days ($p < 0.05$).

3.3 RT-PCR Analysis

To determine the expression of the osteogenic genes, i.e., ALP, BMP-2, and OPN; and the angiogenic genes, i.e., VEGF and ANG-1 of rBMSCs seeded on different materials described above, the RT-PCR analysis was performed (**Figures 5**, **6**). The results for osteogenic genes showed that the expression of ALP in the CS/SF and SrCS/SF groups increased significantly compared with that in the SF group, which peaked at 7 days. However, the expression of BMP-2 in the CS/SF and SrCS/SF groups was higher than that in the SF group, which peaked at 1 day and then slowed down. Additionally, the expression of OPN in the CS/SF and SrCS/SF groups increased significantly compared with that in the SF group at each time point and peaked at 10 days. On the other hand, with respect to the angiogenic genes, the expression of VEGF in the CS/SF and SrCS/SF groups was significantly higher than that in the SF group at 4 and 10 days. In addition, the expression of ANG-1 in the CS/SF and SrCS/SF groups peaked at 4 days compared with that in the SF group. More importantly, the 25 wt% was the optimum ratio.

3.4 Alkaline Phosphatase Activity Analysis

To determine the early osteogenesis of rBMSCs after culturing on the different materials described previously, the ALP staining was examined. It was shown that more intense ALP staining was observed in the CS/SF and SrCS/SF groups than the SF group, especially the 25 wt% SrCS/SF group, on day 7 ($p < 0.05$, **Figure 7A**). As the SF, 25 wt% CS/SF, and 25 wt% SrCS/SF groups were selected, the ALP quantity analysis was detected. In **Figure 7B**, the result revealed that the ALP activity increased with the culture time, while the highest ALP activity was detected in the 25 wt% SrCS/SF group.

3.5 Vascular Endothelial Growth Factor Protein Content

The amount of VEGF protein released from rBMSCs cultured on SF, 25 wt% CS/SF, and 25 wt% SrCS/SF scaffold materials was measured by ELISA on days 4, 7, and 10. The results showed that the VEGF protein level of 25 wt% CS/SF and 25 wt% SrCS/SF increased significantly than SF, especially in the SrCS/SF group (**Figure 8**).

3.6 Microcomputed Tomography Measurement

In **Figure 9**, it showed that obviously promoted new bone formation was observed in the CS/SF and SrCS/SF groups than those in the SF group, while the SrCS/SF was the most osteogenic at 8 weeks after the operation (**Figure 9A**). Furthermore, the similar results of BMD and Tb. Th were detected in the morphometrical analysis ($p < 0.05$) (**Figures 9B**,C).

3.7 Histological Analysis of Bone Regeneration

The different fluorescent labels in **Figure 10** represent new bone regeneration and mineralization at weeks 2, 4, and 6 after the operation. It revealed that, at each time, the percentages of TE labeling (yellow), AL labeling (red), and CA labeling (green) in the SrCS/SF group were significantly higher than those in the SF and CS/SF groups, while the percentages in the CS/SF group were

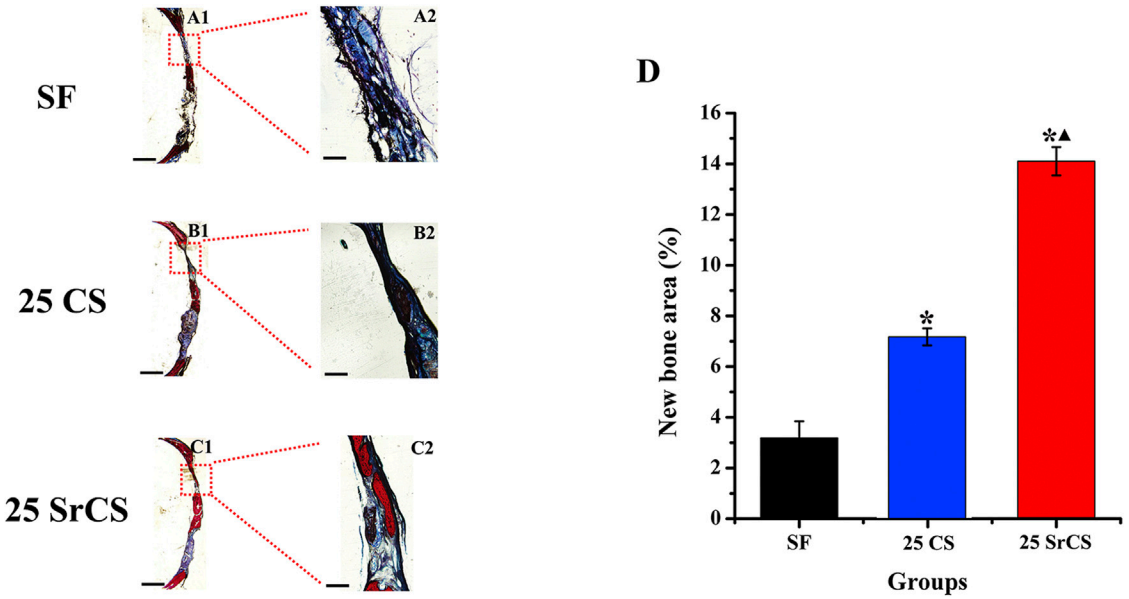

FIGURE 11 | Histological images of newly formed bone in calvarial defects. **(A–C)** Histological images of newly formed bone in calvarial defects. **(D)** Percentage of the new bone area assessed by histomorphometric analysis. *$p < 0.05$ indicates the other groups vs. the SF group, and ▲$p < 0.05$ indicates the 25 SrCS group vs. the other groups, A1–C1: scale bar = 1 mm; A2–C2: scale bar = 100 μm.

higher than those in the SF group ($p < 0.05$). Furthermore, the results of histological analysis showed a similar conclusion The analysis of VG staining showed that more newly formed bone tissue penetrated into the defect center of the SrCS/SF group, and few new bone formations on the defect center were observed in the CS/SF group, whereas only limited new bone formation was observed on the defect bottom of the SF group (**Figure 11**).

4 DISCUSSION

As a kind of natural high molecular fibrin, SF is an important structural protein like collagen in bone tissue. It has been confirmed that SF has many advantages, such as strong mechanical properties, long surgical application history, easy to obtain and modify, good degradability, and so on (Midha et al., 2018; Wu J. et al., 2019; Guo et al., 2021); meanwhile, the degradation products of SF have certain nutritional effects (Setzen and Williams 1997). However, it lacks sufficient osteogenic induction activity. Our previous research revealed that SrCS could promote osteogenesis and angiogenesis of osteoblasts (Lin et al., 2013). Another study also showed that SrCS could regulate the proliferation and osteogenesis of human osteoblasts (Zeng et al., 2020). Therefore, in the present study, to obtain a kind of material with good physiochemical properties and bi-directional osteogenic/angiogenic activity, it was designed by compounding SrCS and SF. As it has been found that material deposition occurs when CS or SrCS is higher than 25 wt% in the fabrication process and particle agglomeration appears in the fabricated scaffold materials, the component ratio of CS or SrCS greater than 25 wt% was not carried out in the present study.

It has been reported that the pore structure of materials could control the development of cells, which is called “contact guidance” (Kuboki et al., 1998). The pore structure of materials includes pore diameter and porosity. It has been reported that the biocompatibility of materials was mainly affected when the microstructure of materials is at the nanometer level. While the cell behavior is mainly influenced, including adhere and direction of arrangement of the cells, when the microstructure of the material is at the micron level (Cben et al., 1997). A previous study revealed that cell differentiation and proliferation could be influenced by the pore diameter of materials (Mygind et al., 2007). It has also been confirmed that high porosity could enhance the osteogenic activity of materials (Karageorgiou and Kaplan, 2005; Ardeshirylajimi et al., 2018; Lai et al., 2019). In the present study, compared with SF and CS/SF materials, the SrCS/SF materials with a large pore size of 400–600 μm and 80–88% porosity have a better pore structure. And the follow-up results showed that the SrCS/SF could promote the rBMSCs’ proliferation, osteogenesis, and secretion of angiogenic factors, as well as enhance the bone regeneration *in vivo*, which revealed that the obtained SrCS/SF materials with the appropriate pore structure have good biological activities.

As a type of widely used stem cell, BMSCs have multipotency and active proliferation, which can also be induced to secrete angiogenic factors under appropriate methods (Jiang et al., 2018). In the present study, the proliferation, osteogenesis, and secretion of angiogenic factors of rBMSCs cultured on different scaffold materials have been analyzed. It has been investigated that SrCS could promote the proliferation of osteoblast-like cells (Zeng et al., 2020; Hu et al., 2017; Chiu et al., 2019). And our previous study also showed that SrCS could promote the proliferation of

rBMSCs-OVX (Lin et al., 2013). In the present study, SF and SrCS materials have been compounded with different proportion ratios. The results of the MTT assay showed that SrCS/SF could enhance the proliferation of rBMSCs rather than SF and CS/SF, which revealed that compounds with SrCS could enhance the biological properties of the proliferation of SF materials. More importantly, the results of ALP staining and RT-PCR analysis showed that, compared with SF and CS/SF materials, SrCS/SF could significantly promote the osteogenesis of rBMSCs. And the *in vivo* results also showed that the bone formation in the SrCS/SF was obviously increased than that in the SF and CS/SF. All the data revealed that rather than CS, SrCS could stimulate the osteogenic activities of SF materials. In addition, previous studies showed that the biological properties of the composite material could be affected by the proportion ratio of materials (Talal et al., 2013; Elkholy et al., 2018; Ma et al., 2018). In the present study, the materials with 12.5 wt% and 25 wt% have been fabricated, while the ratio of 25 wt% was the optimum proportion ratio both in CS/SF groups and SrCS/SF groups.

As simultaneous vascularization is a necessary condition in the process of bone regeneration, it is essential to enhance the angiogenic activity of BMSCs. It has been reported that, without modification, SF has no obvious angiogenic properties neither *in vitro* nor *in vivo* (Bai et al., 2011; Sun et al., 2016). Otherwise, our previous studies investigated that CS and SrCS could induce angiogenesis of BMSCs and HUVECs to some extent (Lin et al., 2013; Wang et al., 2020). In the present study, the results of RT-PCR analysis revealed that SrCS/SF could significantly promote the expression of angiogenic factors of rBMSCs more than SF and CS/SF. And the 25 wt% also was the optimum proportion ratio. All the data revealed that rather than CS, SrCS could upregulate the osteogenic but also angiogenic activities of SF materials, especially for the ratio of 25 wt%.

5 CONCLUSION

In conclusion, compared with SF and CS/SF, SrCS/SF could obviously enhance the cell proliferation, osteogenic differentiation, and angiogenic factor expression of rBMSCs, and the optimum ratio was 25 wt%. Furthermore, the 25 wt% SrCS/SF could promote osteogenesis *in vivo* more than SF and 25 wt% CS/SF. It is suggested that SrCS/SF with bi-directional osteogenic/angiogenic activity may be a good scaffold material for bone regeneration.

DATA AVAILABILITY STATEMENT

The original contributions presented in the study are included in the article/**Supplementary Material**, further inquiries can be directed to the corresponding authors.

ETHICS STATEMENT

The animal study was reviewed and approved by the Animal Ethics Committee, Shanghai Ninth People's Hospital, Shanghai Jiao Tong University School of Medicine.

AUTHOR CONTRIBUTIONS

YZ: conceptualization, methodology, data curation, and writing-original draft. YH: data curation, formal analysis, and investigation. Mamoru UEMURA: software and visualization. LX: supervision. XY: writing-review and editing. YX: writing-review; editing, and project administration.

FUNDING

The authors gratefully acknowledge the fund of the National Natural Science Foundation of China (82071082, 81771038 and 81871490), the Science and Technology Commission of Shanghai Municipality (19142202200), and the Young Doctor Collaborative Innovation Team and the Excellent Youth Program of Ninth People's Hospital Affiliated to Shanghai Jiao Tong University, School of Medicine (QC 2018-02 and jyyq08201621).

SUPPLEMENTARY MATERIAL

The Supplementary Material for this article can be found online at: https://www.frontiersin.org/articles/10.3389/fbioe.2022.842530/full#supplementary-material

REFERENCES

Ardeshirylajimi, A., Delgoshaie, M., Mirzaei, S., and Khojasteh, A. (2018). Different Porosities of Chitosan Can Influence the Osteogenic Differentiation Potential of Stem Cells. *J. Cel. Biochem.* 119, 625–633. doi:10.1002/jcb.26223

Bai, L., Wu, D., Xu, J., Liu, H., Xie, M., Guan, G., et al. (2011). On Model of Angiogenesis and the Mechanism in Porous Silk Fibroin Films. *J. Mater. Sci. Mater. Med.* 22, 927–933. doi:10.1007/s10856-011-4258-y

Ben, Wan., Renxian, Wang., Yuyang, Sun., Jingjing, Cao., Honggang, Wang., Jianxun, Guo., et al. (2020). Building Osteogenic Microenvironments with Strontium-Substituted Calcium Phosphate Ceramics. *Front. Bioeng. Biotechnol.* 8, 591467. doi:10.3389/fbioe.2020.591467

Bhattacharjee, P., Kundu, B., Naskar, D., Kim, H. W., Maiti, T. K., Bhattacharya, D., et al. (2017). Silk Scaffolds in Bone Tissue Engineering: An Overview. *Acta Biomater.* 63, 1–17. doi:10.1016/j.actbio.2017.09.027

Bose, S., Tarafder, S., and Bandyopadhyay, A. (2017). Effect of Chemistry on Osteogenesis and Angiogenesis towards Bone Tissue Engineering Using 3D Printed Scaffolds. *Ann. Biomed. Eng.* 45, 261–272. doi:10.1007/s10439-016-1646-y

Byrne, E. M., Farrell, E., McMahon, L. A., Haugh, M. G., O'Brien, F. J., Campbell, V. A., et al. (2008). Gene Expression by Marrow Stromal Cells in a Porous Collagen-Glycosaminoglycan Scaffold Is Affected by Pore Size and Mechanical Stimulation. *J. Mater. Sci. Mater. Med.* 19, 3455–3463. doi:10.1007/s10856-008-3506-2

Cben, c. S., Mrksieh, M., Huang, S., Whitesides, G. M., and Ingber, D. E. (1997). Ceometric Control of Cell Life and Death. *Science* 276, 1425–1428.

Chim, S. M., Tickner, J., Chow, S. T., Kuek, V., Guo, B., Zhang, G., et al. (2013). Angiogenic Factors in Bone Local Environment. *Cytokine Growth Factor. Rev.* 24, 297–310. doi:10.1016/j.cytogfr.2013.03.008

Chiu, Y. C., Shie, M. Y., Lin, Y. H., Lee, A. K., and Chen, Y. W. (2019). Effect of Strontium Substitution on the Physicochemical Properties and Bone Regeneration Potential of 3D Printed Calcium Silicate Scaffolds. *Int. J. Mol. Sci.* 20, 2729. doi:10.3390/ijms20112729

Elkholy, S., Yahia, S., Awad, M., and Elmessiery, M. (2018). *In Vivo* evaluation of β-CS/n-HA with Different Physical Properties as a New Bone Graft Material. *Clin. Implant Dent. Relat. Res.* 20, 416–423. doi:10.1111/cid.12599

Engin, N. O., and Tas, A. C. (1999). Manufacture of Macroporous Calcium Hydroxyapatite Bio-Ceramics. *J. Eur. Ceram. Soc.* 19, 2568–2572. doi:10.1016/s0955-2219(99)00131-4

Guo, C., Ling, S., Li, C., Motta, A., and Oliveira, J. M. (2021). Editorial: Silk-Based Functional Biomaterials. *Front. Bioeng. Biotechnol.* 9, 721761. doi:10.3389/fbioe.2021.721761

Hu, D., Li, K., Xie, Y., Pan, H., Zhao, J., Huang, L., et al. (2017). The Combined Effects of Nanotopography and Sr Ion for Enhanced Osteogenic Activity of Bone Marrow Mesenchymal Stem Cells (BMSCs). *J. Biomater. Appl.* 31, 1135–1147. doi:10.1177/0885328217692140

Jiang, L., Zhang, W., Wei, L., Zhou, Q., Yang, G., Qian, N., et al. (2018). Early Effects of Parathyroid Hormone on Vascularized Bone Regeneration and Implant Osseointegration in Aged Rats. *Biomater.* 179, 15–28. doi:10.1016/j.biomaterials.2018.06.035

Karageorgiou, V., and Kaplan, D. (2005). Porosity of 3D Biomaterial Scaffolds and Osteogenesis. *Biomater.* 26, 5474–5491. doi:10.1016/j.biomaterials.2005.02.002

Kasten, P., Beyen, I., Niemeyer, P., Luginbühl, R., Bohner, M., and Richter, W. (2008). Porosity and Pore Size of Beta-Tricalcium Phosphate Scaffold Can Influence Protein Production and Osteogenic Differentiation of Human Mesenchymal Stem Cells: An *In Vitro* and *In Vivo* Study. *Acta Biomater.* 4, 1904–1915. doi:10.1016/j.actbio.2008.05.017

Kuboki, Y., Takita, H., Kobayashi, D., Tsuruga, E., Inoue, M., Murata, M., et al. (1998). Ohgushi H. BMP-Induced Osteogenesis on the Surface of Hydroxyapatite with Geometrically Feasible and Nonfcosible Structures: Topology of Osteogenesis. *J. Biomnd. Mater. Res.* 39, 190–199. doi:10.1002/(sici)1097-4636(199802)39:2<190::aid-jbm4>3.0.co;2-k

Lai, Y., Li, Y., Cao, H., Long, J., Wang, X., Li, L., et al. (2019). Osteogenic Magnesium Incorporated into PLGA/TCP Porous Scaffold by 3D Printing for Repairing Challenging Bone Defect. *Biomater.* 197, 207–219. doi:10.1016/j.biomaterials.2019.01.013

Lee, D. J., Kwon, J., Kim, Y. I., Wang, X., Wu, T. J., Lee, Y. T., et al. (2019). Effect of Pore Size in Bone Regeneration Using Polydopamine-Laced Hydroxyapatite Collagen Calcium Silicate Scaffolds Fabricated by 3D Mould Printing Technology. *Orthod. Craniofac. Res.* 22 (Suppl. 1), 127–133. doi:10.1111/ocr.12261

Lin, K., Xia, L., Li, H., Jiang, X., Pan, H., Xu, Y., et al. (2013). Enhanced Osteoporotic Bone Regeneration by Strontium-Substituted Calcium Silicate Bioactive Ceramics. *Biomater.* 34, 10028–10042. doi:10.1016/j.biomaterials.2013.09.056

Ma, L., Wang, X., Zhao, N., Zhu, Y., Qiu, Z., Li, Q., et al. (2018). Integrating 3D Printing and Biomimetic Mineralization for Personalized Enhanced Osteogenesis. Angiogenesis. And Osteointegration. *ACS Appl. Mater. Inter.* 10, 42146–42154. doi:10.1021/acsami.8b17495

Midha, S., Chawla, S., Chakraborty, J., Chameettachal, S., and Ghosh, S. (2018). Differential Regulation of Hedgehog and Parathyroid Signaling in Mulberry and Nonmulberry Silk Fibroin Textile Braids. *ACS. Biomter. Sci. Eng.* 4, 1–13. doi:10.1021/acsbiomaterials.7b00874

Mygind, T., Stiehler, M., Baatmp, A., Li, H., Zou, X., Flyvbjerg, A., et al. (2007). Mesenehymal Stem Cell Ingrowth and Diferentiation on Coralline Hydroxyapatite Scaffolds. *Biomater.* 28, 1036–1047. doi:10.1016/j.biomaterials.2006.10.003

Omenetto, F. G., and Kaplan, D. L. (2010). New Opportunities for an Ancient Material. *Science* 329, 528–531. doi:10.1126/science.1188936

Setzen, G., and Williams, E. F., 3rd. (1997). Tissue Response to Suture Materials Implanted Subcutaneously in a Rabbit Model. *Plast. Reconstr. Surg.* 100, 1788–1795. doi:10.1097/00006534-199712000-00023

Sun, W., Motta, A., Shi, Y., Seekamp, A., Schmidt, H., Gorb, S. N., et al. (2016). Co-Culture of Outgrowth Endothelial Cells with Human Mesenchymal Stem Cells in Silk Fibroin Hydrogels Promotes Angiogenesis. *Biomed. Mater.* 11, 035009. doi:10.1088/1748-6041/11/3/035009

Talal, A., McKay, I. J., Tanner, K. E., and Hughes, F. J. (2013). Effects of Hydroxyapatite and PDGF Concentrations on Osteoblast Growth in a Nanohydroxyapatite-Polylactic Acid Composite for Guided Tissue Regeneration. *J. Mater. Sci. Mater. Med.* 24, 2211–2221. doi:10.1007/s10856-013-4963-9

Wang, L., Wang, J., Zhou, X., Sun, J., Zhu, B., Duan, C., et al. (2020). A New Self-Healing Hydrogel Containing hucMSC-Derived Exosomes Promotes Bone Regeneration. *Front. Bioeng. Biotechnol.* 8, 564731. doi:10.3389/fbioe.2020.564731

Wu, V., Helder, M. N., Bravenboer, N., Ten Bruggenkate, C. M., Jin, J., and Klein-Nulend, J. (2019a). Bone Tissue Regeneration in the Oral and Maxillofacial Region: A Review on the Application of Stem Cells and New Strategies to Improve Vascularization. *Stem Cell Int.* 2019, 6279721. doi:10.1155/2019/6279721

Wu, J., Zheng, K., Huang, X., Liu, J., Liu, H., Boccaccini, A. R., et al. (2019b). Thermally Triggered Injectable Chitosan/Silk Fibroin/Bioactive Glass Nanoparticle Hydrogels for *In-Situ* Bone Formation in Rat Calvarial Bone Defects. *Acta Biomater.* 91, 60–71. doi:10.1016/j.actbio.2019.04.023

Xia, L., Ma, W., Zhou, Y., Gui, Z., Yao, A., Wang, D., et al. (2019). Stimulatory Effects of Boron Containing Bioactive Glass on Osteogenesis and Angiogenesis of Polycaprolactone: *In Vitro* Study. *Biomed. Res. Int.* 2019, 8961409. doi:10.1155/2019/8961409

Yan, Y., Chen, H., Zhang, H., Guo, C., Yang, K., Chen, K., et al. (2019). Vascularized 3D Printed Scaffolds for Promoting Bone Regeneration. *Biomater.* 190-191, 97–110. doi:10.1016/j.biomaterials.2018.10.033

Ye, J. H., Xu, Y. J., Gao, J., Yan, S. G., Zhao, J., Tu, Q., et al. (2011). Critical-Size Calvarial Bone Defects Healing in a Mouse Model with Silk Scaffolds and SATB2-Modified iPSCs. *Biomater.* 32, 5065–5076. doi:10.1016/j.biomaterials.2011.03.053

Yin, S., Zhang, W., Zhang, Z., and Jiang, X. (2019). Recent Advances in Scaffold Design and Material for Vascularized Tissue-Engineered Bone Regeneration. *Adv. Healthc. Mater.* 8, e1801433. doi:10.1002/adhm.201801433

Zeng, J. K., Guo, J. S., Sun, Z. Y., Deng, F. Y., Ning, C. Q., and Xie, Y. Z. (2020). Osteoblastic and Anti-Osteoclastic Activities of Strontium-Substituted Silicocarnotite Ceramics: *In Vitro* and *In Vivo* Studies. *Bioact. Mater.* 5, 435–446. doi:10.1016/j.bioactmat.2020.03.008

Zhou, Y., Wu, Y., Jiang, X., Zhang, X., Xia, L., Lin, K., et al. (2015). The Effect of Quercetin on the Osteogenesic Differentiation and Angiogenic Factor Expression of Bone Marrow-Derived Mesenchymal Stem Cells. *PLOS ONE* 10, e0129605. doi:10.1371/journal.pone.0129605

Zhou, Y., Wu, Y., Ma, W., Jiang, X., Takemra, A., Uemura, M., et al. (2017). The Effect of Quercetin Delivery System on Osteogenesis and Angiogenesis Under Osteoporotic Conditions. *J. Mater. Chem. B.* 5, 612–625. doi:10.1039/c6tb02312f

Zhu, H., Wu, B., Feng, X., Kim, D. H., Kim, S. E., Hyun, Y. T., et al. (2011). Preparation and Characterization of Bioactive Mesoporous Calcium Silicate-Silk Fibroin Composite Films. *J. Biomed. Mater. Res. B Appl. Biomater.* 98B, 330–341. doi:10.1002/jbm.b.31856

Ziebart, T., Schnell, A., Walter, C., Kämmerer, P. W., Pabst, A., Lehmann, K. M., et al. (2013). Interactions Between Endothelial Progenitor Cells (EPC) and Titanium Implant Surfaces. *Clin. Oral Investig.* 17, 301–309. doi:10.1007/s00784-012-0691-7

Conflict of Interest: The authors declare that the research was conducted in the absence of any commercial or financial relationships that could be construed as a potential conflict of interest.

Publisher's Note: All claims expressed in this article are solely those of the authors and do not necessarily represent those of their affiliated organizations, or those of the publisher, the editors, and the reviewers. Any product that may be evaluated in this article, or claim that may be made by its manufacturer, is not guaranteed or endorsed by the publisher.

frontiers | Frontiers in Bioengineering and Biotechnology

REVIEW
published: 17 May 2022
doi: 10.3389/fbioe.2022.900992

Biomaterials for Interbody Fusion in Bone Tissue Engineering

*Han Zhang[1], Zhonghan Wang[1,2], Yang Wang[1], Zuhao Li[1,2], Bo Chao[1], Shixian Liu[1], Wangwang Luo[1], Jianhang Jiao[1] and Minfei Wu[1]**

[1]Department of Orthopedics, The Second Hospital of Jilin University, Changchun, China, [2]Orthopaedic Research Institute of Jilin Province, Changchun, China*

In recent years, interbody fusion cages have played an important role in interbody fusion surgery for treating diseases like disc protrusion and spondylolisthesis. However, traditional cages cannot achieve satisfactory results due to their unreasonable design, poor material biocompatibility, and induced osteogenesis ability, limiting their application. There are currently 3 ways to improve the fusion effect, as follows. First, the interbody fusion cage is designed to facilitate bone ingrowth through the preliminary design. Second, choose interbody fusion cages made of different materials to meet the variable needs of interbody fusion. Finally, complete post-processing steps, such as coating the designed cage, to achieve a suitable osseointegration microstructure, and add other bioactive materials to achieve the most suitable biological microenvironment of bone tissue and improve the fusion effect. The focus of this review is on the design methods of interbody fusion cages, a comparison of the advantages and disadvantages of various materials, the influence of post-processing techniques and additional materials on interbody fusion, and the prospects for the future development of interbody fusion cages.

Keywords: 3D printing, interbody fusion cage, titanium, PEEK, absorbable material, growth factors, ceramic material, coating

OPEN ACCESS

Edited by:
Jianxun Ding,
Changchun Institute of Applied Chemistry (CAS), China

Reviewed by:
Weishi Li,
Peking University Third Hospital, China
Haifeng Wei,
Shanghai Changzheng Hospital, China

****Correspondence:***
Minfei Wu
wumf@jlu.edu.cn

Specialty section:
This article was submitted to Biomaterials, a section of the journal Frontiers in Bioengineering and Biotechnology

Received: *21 March 2022*
Accepted: *21 April 2022*
Published: *17 May 2022*

Citation:
Zhang H, Wang Z, Wang Y, Li Z, Chao B, Liu S, Luo W, Jiao J and Wu M (2022) Biomaterials for Interbody Fusion in Bone Tissue Engineering. Front. Bioeng. Biotechnol. 10:900992. doi: 10.3389/fbioe.2022.900992

1 INTRODUCTION

With population aging, spinal degenerative diseases have become a health problem that cannot be ignored, with a lifetime incidence of >50% (Chong et al., 2016; Lim et al., 2019; May et al., 2019; Warren et al., 2020). In the spinal orthopedics clinic, when nerve compression persists for a long time and conservative treatment fails, decompression surgery has remained the first choice for the treatment of intervertebral disc degeneration, but interbody fusion is crucial for the treatment of impaired vertebral stability, failure of intervertebral disc surgery, spinal deformity and spinal stenosis. (Jain et al., 2016; Mena et al., 2016; Phan and Mobbs 2016; Assem et al., 2017; Iunes et al., 2020). The purpose of this operation is to decompress the nerve root, maintain the height of the intervertebral disc, and achieve bony fusion (Folman et al., 2003; Hoy et al., 2013; Hoy et al., 2019; Fan and Guo 2020). It means we need to convert fibrocartilage joints into hard and continuous bone segments (Smoljanovic et al., 2010). The autogenous iliac bone graft is the gold-standard method for spinal fusion (Vanek et al., 2012; Farrokhi et al., 2017). Harvested autologous bone slices have better osteoinductive properties compared to allogeneic bone grafts (Huang et al., 2014; Grgurevic et al., 2020). However, autologous bone grafts are limited by additional surgical trauma, donor site complications, and the inadequate autogenous bone supply (Sekerci et al., 2013; Fomekong et al., 2017). Fusion failure is often caused by cage loosening and related complications (5–35%), so

TABLE 1 | Experimental studies published recently.

Study	Additive	Scaffold	Technique	Animal Model	Results
(Zhang et al.)	SIM/poloxamer 407 Hydrogel	Ti	3D-printing	Rhesus Macaque	Promoted bone ingrowth and spinal fusion
Liang et al. (2020)	—	HA/PA66	Infiltrating	Goat	Effectively improved intervertebral bony fusion
Rodríguez-Vázquez and Ramos-Zúiga (2020)	—	Ch/HAp	Freeze-drying	Rat	Bone regeneration in a solid and well-structured fusion was induced
Chu et al. (2019)	Iliac crest bone graft	CS/PEEK (4:6)	Fabricated by compounding and injection-molding	Goat	Induced highly effective bone fusion
Gunzburg et al. (2019)	Autologous bone	PEEK	Ti coating	Ovine	Nano-surfaced cages resulted in greater spinal stiffness changes
Lu et al. (2019)	—	Tantalum	3D-knitted	Rabbit	Showed good biocompatibility and osteocompatibility
Walsh et al. (2018)	—	PEEK	Coating	Sheep	Newly formed bone tracked along the thin Ti-coated surface
McGilvray et al. (2018)	—	Titanium	3D-printing	Ovine	Reduced range of motion and increased bone ingrowth and construct stiffness
(Kirk et al., 2017)	Iliac crest bone graft	PEEK titanium composite (PTC)	Hybrid additive manufacturing approaches	Ovine	PTC constructs demonstrated significant reductions in range of motion and a significant increase in stiffness compared to PEEK and PSP
Ren et al. (2017)	—	MAACP/HA/CS	—	Goat	Provided a good fusion effect, enough biomechanical stability, and close integration with the surrounding bone
Bae et al. (2016)	RhBMP-2	PEEK	—	Sheep	RhBMP-2 dose-dependent osteoclastic resorption is a transient phenomenon
Wheeler et al. (2016)	mesenchymal precursor cells (MPCs)	PEEK	—	Ovine	MPCs are an alternative to autologous for lumbar interbody fusion procedures

choosing an appropriate interbody cage or not directly affects the success rate of surgery (Virk et al., 2017).

The ideal bone-substitute material should be characterized by favorable bone induction, good biocompatibility, suitable mechanical strength, and a high performance-to-price ratio (Warburton et al., 2019; Verma et al., 2020). At present, the commonly used materials for interbody fusion cages can be divided into metallic and non-metallic options (Park and Lehman, 2020; Verma et al., 2020). The most commonly used interbody cages are made of non-absorbent materials, such as titanium (Ti) and poly-ether-ether-ketone (PEEK). Ti alloy may cause implant subsidence and segmental instability due to its high elastic modulus, and the use of PEEK is limited due to its poor biocompatibility leading to chronic inflammatory responses (Guo et al., 2020). Absorbable materials include magnesium (Mg) and other polymer materials. With the mechanical strength weakens due to degradation, the materials may not be able to provide sufficient support and lead to the interbody fusion failure. Therefore, it is necessary to explore new materials that promote interbody fusion.

Three-dimensional (3D) printing is a new and widely popular technology (Egan et al., 2018; Burnard et al., 2020). Most importantly, 3D-printed cages can be customized for individual patients to achieve a high degree of implant-to-anatomy match. An appropriate interbody cage is designed to maintain the height of the intervertebral body and keep the upper and lower vertebral bodies stable. In addition, the internal porous structure made by 3D-printing technology can induce new bone ingrowth, which realizes the fusion of the upper and lower vertebral bodies to achieve biological stability (Zhang et al., 2020a). Osseointegration can be further improved by making surface modifications and the addition of drugs and growth factors (Park and Lehman, 2020). Coating is a commonly used surface-modification technology, and better biological activity and osteogenic ability can be obtained with coating materials such as Ti and hyaluronic acid (HA). Commonly used drugs include simvastatin (SIM) and strontium ranelate (SRR), which can improve the local microenvironment and promote osteogenesis in patients with osteoporosis. Growth factors, such as bone morphogenetic protein (BMP) and epidermal growth factor, can promote interbody fusion by regulating the expression of osteogenic genes. And we list all Experimental studies and Clinical studies in **Table 1** and **Table 2** respectively.

Accordingly, we wrote this review to address above issues. Review was retrieved in PubMed databases and Web of Science by the keywords: “interbody fusion”, “cage”. A total of 658 papers were picked, we excluded some earlier published research and clinical articles, and 171 articles were finally selected for this review according to the criteria of inclusion and exclusion. This review introduces the application of interbody fusion cages in bone tissue engineering in detail and focuses on the design methods of interbody cages, including 3D printing, porosity design. The advantages and disadvantages of interbody cages made of different materials, such as Ti, tantalum, Mg, PEEK, and ceramics, are compared and improved methods are proposed. The effects of material post-processing techniques on interbody fusion are summarized, including coating techniques, and the effects of the internal addition of SIM, BMP, and SRR on

TABLE 2 | Clinical studies published recently.

Study	Additive	Scaffold	Technique	Case Number	Results
Mobbs et al. (2019)	Allograft	TI	3D-printing	1	Rapid recovery with significant fusion effects
Zippelius et al. (2018)	—	TI	3D-printing	50	Implant is safe and led to a very high fusion rate
Mokawem et al. (2019)	—	SiCaP-packed TI	3D-printing	93	Provided excellent rates of solid fusion in TLIF and LLIF surgeries
Ohanisian and Dorsi (2019)	—	TI	3D-printing	1	Stimulates osteogenesis and enhances fusion with a remarkable improvement of symptoms
Arts et al. (2020)	—	TI	3D-printing	50	The fusion rates of porous titanium and PEEK with autograft were similar
Siu et al. (2018)	—	TI	3D-printing	30	The subsidence rate was lower compared to that of the PEEK implant
Krafft et al. (2019)	—	TI	3D-printing	1	The difficulties in deformity correction secondary to osteoporotic fractures were overcome

interbody fusion are discussed. In addition, the application challenges of different interbody cages and directions for further exploration are summarized.

STRATEGIES FOR DESIGNING INTERBODY FUSION CAGES

Traditional Interbody Fusion Cages

Before an interbody fusion cage design is chosen, the anatomical location, surgical approach, and implant size need to be considered. The anatomical model may be obtained through a computed tomography (CT) examination, and the matching interbody fusion cage can then be designed accordingly (Duan et al., 2016; Rieger et al., 2017; Sen et al., 2019; Gkt et al., 2020). Combined with the CT data of the intervertebral disc, the computer-aided design software (CAD) with computer-aided manufacturing (CAM) technology was used to design the 3D model of the interbody cage, and then the fused deposition modeling (FDM) and selective laser melting (SLM) technology were used to print interbody cage (Chen et al., 2019; Bassous et al., 2019). The anatomical data of the target implant area include the left–right diameter, anteroposterior diameter, intervertebral height, and the angle between the upper and lower surfaces. In addition, the increase in intervertebral height caused by the destruction of the upper and lower endplates during surgery should also be considered. Undersized implants may cause subsidence, while oversized implants can cause damage to neural structures due to excessive compression (Feng et al., 2014; Girod et al., 2017; Zhang et al., 2020b). The angle between the upper and lower surfaces mentioned above suggests the postoperative physiological curvature of the spine. A proper angle in this context will keep the posterior longitudinal ligament relatively tight after implantation, preventing the posterior longitudinal ligament from going slack and compressing the nerve. Moreover, an optimal angle can also avoid overstretching of the anterior longitudinal ligament, which may cause vertebral instability. Due to the different stages of fusion and the individual differences of the target, the designed interbody cages have various shapes, such as a kidney shape (Madan and Boeree 2003). Joffe *et al.* obtained previous data through CT imaging and designed a corresponding cervical fusion cage, then carried out 3D printing and implantation in a canine cervical interbody fusion model. The implants were not ground or polished in this context because the rough surface structure increased the area of bone contact to facilitate bone growth (Joffe et al., 2019). A customized intervertebral device restores the intervertebral space and achieves a certain degree of interbody fusion (Joffe et al., 2019). In addition, by designing hollow cages, the implantation of autologous bone and other implants can be ensured to promote osseointegration. Walsh *et al.* designed an interbody fusion cage (measuring 4.5 mm high, 10 mm wide, and 20 mm long) with a central hole for transplant material injection, which was printed to fit the L4–L5 intervertebral space of sheep, providing support for clinical implantation (Walsh et al., 2018). The design of the fixed device cannot be ignored, and the nailboard system is the most commonly used method applied to fixation (Hah et al., 2020). Fixed device is generally used to maintain the stability of the intervertebral space for a better fusion effect (Caplan et al., 2020).

Porous Structures

The interconnected micropore structure of an interbody fusion cage can improve the bone-conduction ability, which also benefits cell proliferation and differentiation and bone regeneration. The pore size of human cancellous bone is 500–600 μm (Lim et al., 2019). Considering porous scaffolds applied in bone tissue engineering, the porosity should be >50%, especially in the range of 65–80%, where the structure and elasticity modulus are similar to those of human trabeculae (Zhang F et al., 2018; Bai H. T. et al., 2020). The stress between the cage and the endplates decreases with increasing porosity, while the range of motion of the vertebral bodies decreases with increasing fusion rates of the upper and lower vertebral bodies. Previous experiments have shown that a pore size of 50–500 μm is beneficial for the adhesion, proliferation, and differentiation of osteoblasts (Zhang Z et al., 2018; Bai H. et al., 2020). In a comparison of goat interbody fusion models, McGilvray *et al.* found that the range of motion between the vertebral bodies of the animals using porous Ti interbody cages was significantly reduced and the stability of the interbody fusion was increased, indicating that it obtained a better fusion effect. The reason for this is that bone growth occurs in the cage's microporous structure, resulting in a greater overall mechanical structural stability and more effective fusion (McGilvray et al., 2018). The holes, in addition to providing space for new bone to grow in, can be used for the

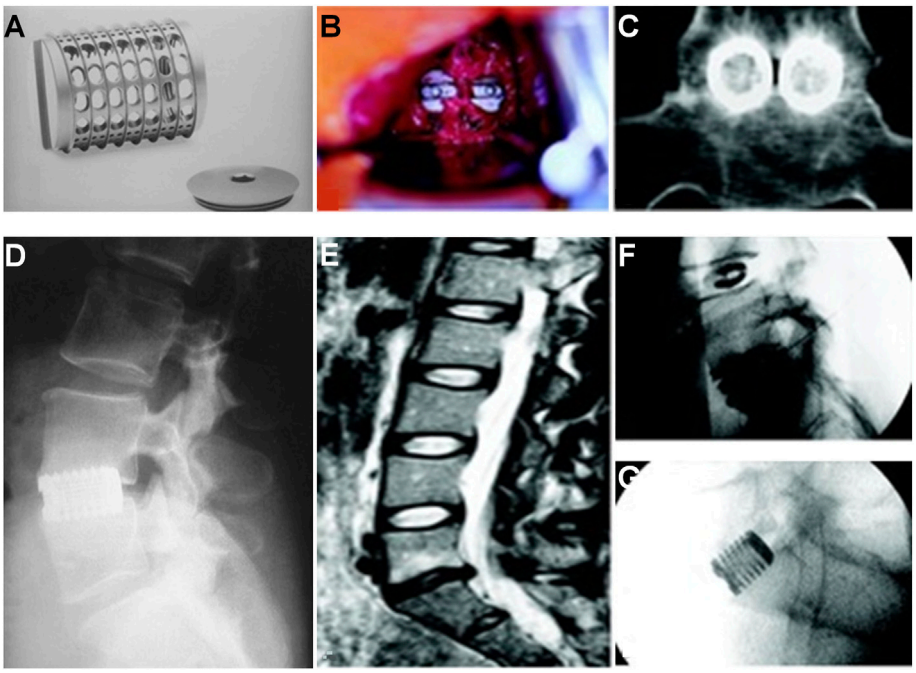

FIGURE 1 | (A) INTER FIX threaded fusion device. **(B)** Intraoperative picture of the two cages implanted at the L5–S1 interspace. **(C)** Coronal CT scan 1 year postoperative. Bone has grown through and around the cages. **(D)** Lateral radiograph of INTER FIX. **(E)** Preoperative sagittal T2-weighted MRI with degeneration of the L5–S1 disc and a normal L4–L5 disc. **(F)** Discogram with morphologic abnormality of the L5–S1 disc and a large posterior anular tear. The L4–L5 disc is anatomically normal. Exact concordant 10/10 pain was reproduced at L5–S1. The L4–L5 injection caused no pain. **(G)** Postoperative lateral radiograph with INTER FIX cages in good position (Sasso et al., 2004).

injection of bioactive structures, such as BMPs, antibiotics, and bioceramics, as well as for post-processing for better fusion results (Schnitzer et al., 2020).

Other Special Structures

In designing the interbody fusion cage, there are some special options available to facilitate certain tasks, such as reducing the difficulty of surgery or promoting the fixation of adjacent vertebral bodies by integrating the cage and the fixator. Sasso *et al.* designed a hollow threaded cylinder with a removable end cover that provides strength while reducing the weight and increasing the space available for the bone autograft. Each cylinder component has multiple holes for implanting the head and tail as well as small transverse holes to enhance the vascularization of the graft in the device. The matching internal fixation device is then designed correspondingly. A good fusion rate was obtained in patients implanted with this device (Sasso et al., 2004) (**Figure 1**). In addition, the threaded structure on the surface of the fusion cage can enhance interbody fusion and reduce the occurrence of postoperative complications, causing autogenous bone transplantation to rarely be needed (Hacker et al., 2000; Burkus et al., 2002). The screw trajectory design, planned screw length, and device matching the patient's unique endplate anatomy should be considered when 3D-printing the threaded hole design to ensure uniform force on the endplate and device and to aid in fixation (Park et al., 2009; Caffrey et al., 2018; Easley et al., 2018). Mobbs *et al.* reported custom features with pre-angled threaded holes designed to enhance post-implantation fixation and endplate interfaces that match patient anatomy to ensure even loading on the endplates and device. Their patient recovered quickly after surgery, and their clinical symptoms were significantly improved (Mobbs et al., 2019). Bionic structures can also be considered. Zippelius *et al.* designed a "banana-shaped" cage made of Ti with curved rails on the surface that can help embed the endplates of the vertebrae, securing the cage to the desired location on the ventral edge strip (such as on the rails) while extending the surface and facilitating better skeletal integration, and they obtained a good fusion rate in 60 patients by using this approach (Zippelius et al., 2018). In addition, Kim *et al.* designed a scalable interbody device (inserted in the form of contraction and expanded *in situ* after being correctly located in the intervertebral space), which is suitable for minimally invasive interbody fusion. Clinical validation found that this device resulted in improved patient-reported clinical outcomes, recovery of disc height, and better fusion rates together with reduced risks of implant displacement, subsidence, rupture, and collapse compared to static devices (Kim et al., 2016) (**Figure 2**).

3 INTERBODY FUSION CAGE MATERIALS

Ti and Its Alloy Material (Ti_6Al_4V)

Ti_6Al_4V is typically selected as the raw material for the manufacture of interbody cages because of its strength,

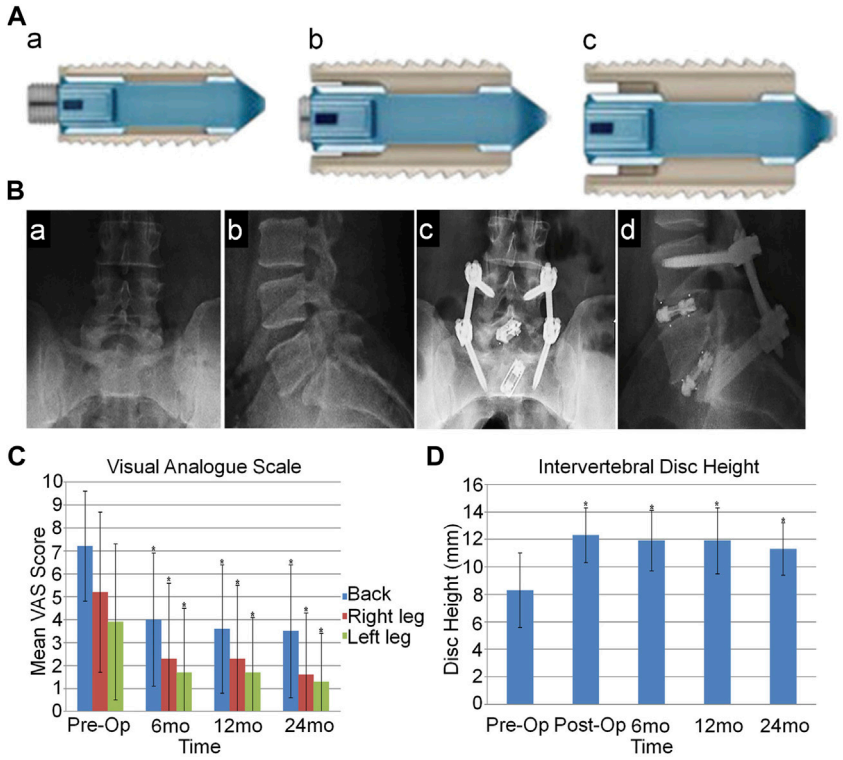

FIGURE 2 | (A) Lateral view of the expandable interbody cage. The implant is shown in contracted **(A)**, expanding **(B)**, and fully expanded **(C)** conditions. **(B)** Preoperative anteroposterior **(A)** and lateral **(B)** plain-film radiographic images of the lumbosacral spine. Postoperative anteroposterior **(C)** and lateral **(D)** radiographic images of the lumbosacral spine demonstrating 2-level interbody reconstruction and transpedicular screw and rod instrumentation at L4eS1. **(C)** The bar graph shows visual analog scale scores for patients from the preoperative assessment through 24 months of follow-up. **(D)** The graph shows intervertebral disc heights of patients from the preoperative assessment through 24 months of follow-up (mean ± standard deviation values) (Kim et al., 2016).

excellent corrosion resistance, low density, biocompatibility, relatively low cost, and compatibility with magnetic resonance imaging (Dai and Jiang 2008; Knutsen et al., 2015; Burkus et al., 2017). The artifacts of Ti alloy generated on CT images are fewer than those associated with other metals, so the condition of the implant can be monitored after surgery (Joffe et al., 2019). 3D-printed porous Ti_6Al_4V, which can be prepared by selective laser melting or electron beam melting, has a low elastic modulus similar to that of cortical bone, so it is a promising orthopedic scaffold material (Liu et al., 2016; Walsh et al., 2019). Advances in 3D-printing technology have enabled the manufacture of Ti cages with complex internal geometries. Postoperative follow-up of 93 patients who received transforaminal lumbar interbody fusion (TLIF) and lateral lumbar interbody fusion (LLIF) using silicate-substituted calcium phosphate (SiCaP)-packaged 3D printing lamellar Ti cages was performed by Mokawem *et al.*, and their results demonstrated that the 3D-printed lamellar Ti cages packaged with SiCaP ensured excellent solid fusion rates during TLIF and LLIF surgeries (Mokawem et al., 2019). 3D printing of Ti makes prostheses rougher. Modifying the surface of an implant, such as its surface roughness and morphology, promotes bone consolidation and prevents the implant from falling off of the vertebral body (Mobbs et al., 2019). Ti implants are beneficial for bone growth because of their metal properties (i.e., valence charge), which attract neighboring proteins, cells, and body fluids (Cheng et al., 2020). In a previous study, however, Hauerberg *et al.* found that, for cervical radiculopathy caused by intervertebral disc herniation, there is no difference between simple discectomy and Ti cage fusion after discectomy (Hauerberg et al., 2008).

Ti has a high elastic modulus such that the porous Ti layer hardly deforms under compression during implantation or under physiological loading (Gunzburg et al., 2019). Arts *et al.* found that the fusion rate of porous Ti was similar to that of autologous bone–filled PEEK at 12 months during a prospective study of single-segment anterior cervical discectomy and fusion (ACDF) patients using 3D-printed porous Ti neck implants (Arts et al., 2020). Through a clinical comparison, Krafft *et al.* found that the sinking rate of 3D-printed porous Ti interbody fusion cages was significantly lower than that of PEEK interbody fusion cages (Krafft et al., 2020). 3D-printed lamellar Ti cages filled with SiCaP bone grafts can also achieve promising fusion rates in adult degenerative diseases by providing more consistent bone growth and biological fixation (McGilvray et al., 2018; Mokawem et al., 2019). However, the Ti_6Al_4V material has a high elastic modulus. Due to the different elastic moduli of cortical bone, the spinal fusion cage easily sinks, resulting in a decrease in intervertebral height, pedicle stenosis, and so on

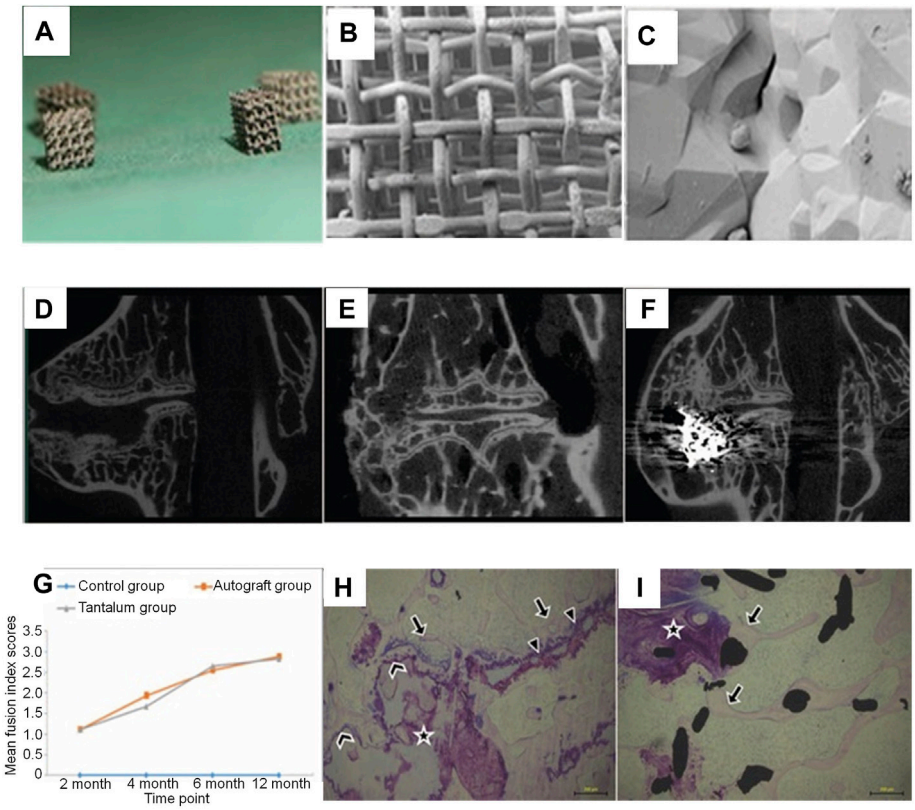

FIGURE 3 | (A–C) The outlook of cubic porous tantalum implants (whose length, width, and height are 2.5–3.0 mm). Scanning electron microscopic images of porous tantalum taken at a lower magnification (B; 85×) and a higher magnification (C; 5,000×). **(D–F)** Micro-CT images of operative lumbar intervertebral spaces in the 3 different procedures at 12 months postoperatively: **(D)** discectomy-only space (control group), **(E)** discectomy with autologous bone implanted space (autograft group), and **(F)** discectomy with porous tantalum implanted space (tantalum group). Both the autograft and tantalum groups developed solid fusion with a continuous bony bridge from the cranial to the caudal vertebra, while non-fusion was observed in the control group. **(G)** The imaging fusion index scores at different postoperative time points. Stained non-decalcified sections showing new bone formation associated with osteonecrosis in the autograft **(H)** and porous tantalum interface **(I)** groups (Lu et al., 2019).

(Seaman et al., 2017). At present, through the use of 3D-printing technology, Ti_6Al_4V materials have been successfully used in artificial hip replacements, semi-pelvic replacements, and artificial vertebral replacements in patients with spinal tumors. The advantages of 3D-printing technology in creating medical Ti alloys are gradually being highlighted due to the abundant processing methods in play (Niu et al., 2019).

Tantalum

Tantalum has been increasingly used in the field of orthopedics because of its good histocompatibility, strong corrosion resistance, and so on (Zardiackas et al., 2001; Veillette et al., 2006). Lu *et al.* demonstrated through *in vitro* and *in vivo* experiments that porous tantalum implants can achieve good fusion, and tantalum is expected to be an effective biomaterial for interbody fusion cages. Porous tantalum has a structure and mechanical properties to similar to those of human bone, allowing trabecular bone to grow into the pores of a cage implant to achieve better osseointegration. In addition, tantalum stimulates cell proliferation and enhances the osteogenic capacity of human osteoblasts, improving vertebral fusion efficiency (Lu et al., 2019) (**Figure 3**). Above all, compared to autogenous iliac bone graft, the adverse events in donor site can be avoided. On the other hand, tantalum has been reported in the treatment of infectious bone defects and bone tumors, which can be used in interbody fusion and spinal metastases after vertebrectomy (Hua et al., 2020; Wang J et al., 2020). At present, there are few reports about tantalum interbody fusion cages in the clinic and experiments, and its effect and characteristics need to be further verified (Iv, Beutler et al., 2010).

PEEK

PEEK is a kind of high-molecular-weight semi-crystal polyaromatic linear polymer and thermoplastic material characterized by biological inertia, radiation transmission, low density, strong corrosion resistance, and a bone-like hardness (Basgul et al., 2019). Compared to alloy, PEEK can minimize stress shielding and bone resorption around the implant to avoid implant loosening (McGilvray et al., 2018; Chu et al., 2019). However, the formation of a biofilm on the surface of PEEK inhibits its binding to the host bone, preventing solid fusion (McGilvray et al., 2017; Gunzburg et al., 2019). In addition, PEEK

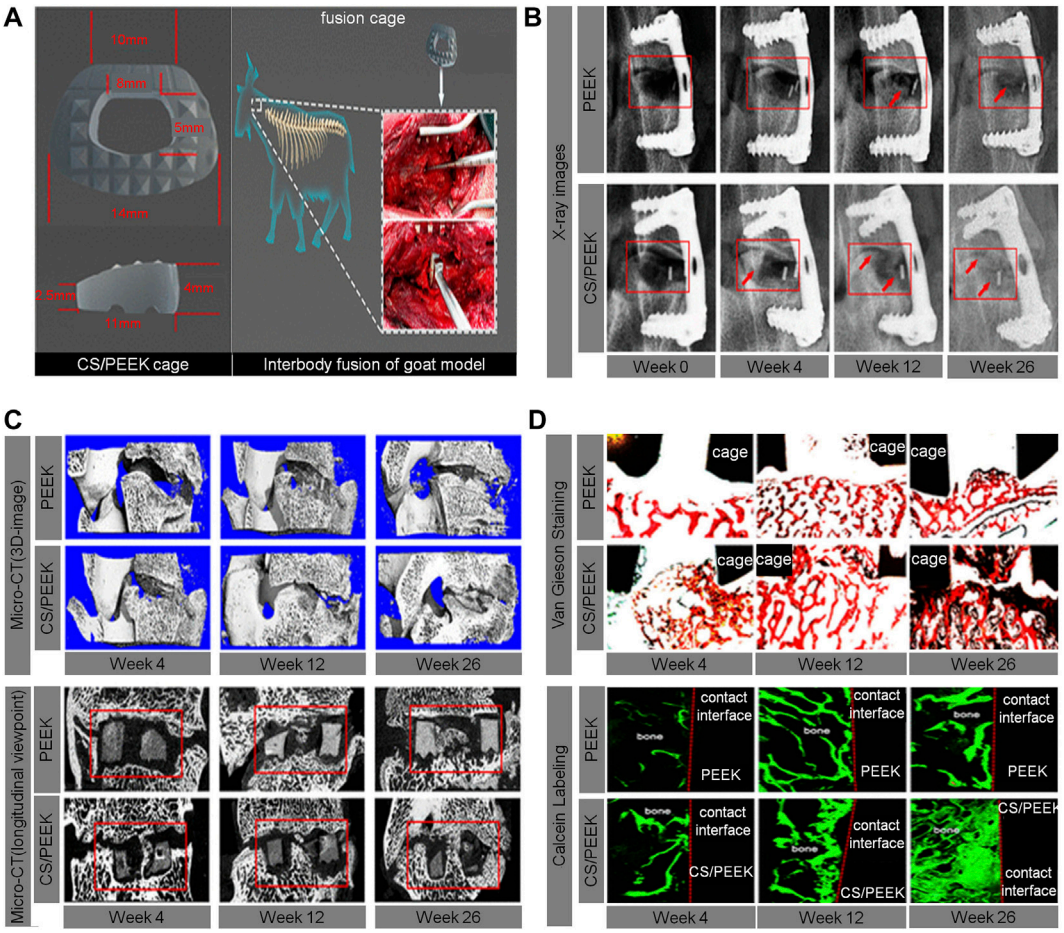

FIGURE 4 | (A) The size and implantation of the CS/PEEK cage in a goat interbody fusion model. **(B)** Interbody fusion at 0, 4, 12, and 26 weeks based on the X-ray observation; representative X-ray images with red arrows indicate the bone ingrowth. **(C)** 3D and longitudinal images of the interbody fusion of bone formation in the interbody fusion at 4, 12, and 26 weeks based on the micro-CT scans. **(D)** Analysis of osseointegration at 4, 12, and 26 weeks based on histological assessment, including Van Gieson staining and fluorescence labeling by calcein (Chu et al., 2019).

cages can cause local inflammation, which may lead to bone non-union and osteolysis (Mokawem et al., 2019; Cheng et al., 2020). In recent years, the technology for 3D-printing PEEK interbody cages has matured, and there have been reports of its successful clinical application. Because of PEEK high melting point, laser sintering is commonly used, and the mechanical properties, biocompatibility, and heat resistance of PEEK can be effectively improved by adding in other inorganic materials and polymers (Tan et al., 2005). It is reported that the fusion rate of PEEK interbody devices is similar to that of allogeneic bone grafts (Jain et al., 2020).

The calcium silicate (CS)/PEEK composite used by Chu *et al.* was prepared by infusing CS into PEEK through compounding and injection-molding techniques. According to the mechanical property test results, the best ratio of CS is 40% (wt%). Through the analysis of the results from a goat interbody fusion model, it was found that the CS/PEEK composite had good biomechanical stability, osteogenic effects, and osseointegration ability. This bioactive material has great potential to facilitate the development of clinical interbody fusion cages (Chu et al., 2019) (**Figure 4**).

McGilvray *et al.* found that, compared to the standard PEEK stent, the range of motion of a PEEK–Ti composite stent made using a mixture of PEEK and Ti was significantly reduced, the hardness was significantly increased, and the fusion effect was better (McGilvray et al., 2017). Dai *et al.* confirmed in their study that a PEEK interbody fusion cage containing β-tricalcium phosphate was efficient for the treatment of cervical spondylosis (Dai and Jiang 2008). The elastic modulus of the PEEK interbody fusion cage is similar to that of vertebral cortical bone, which is beneficial for the dispersion of load and stress and greatly reduces the probability of the cage sinking (Lim et al., 2019). William *et al.* found that the introduction of HA into a scaffold made of PEEK matrix allowed for direct bone-attachment growth and exhibited better fusion in a goat cervical fusion model. Although PEEK cages with HA can improve interbody fusion, there are no clinical studies to support their use (Walsh et al., 2016) (**Figure 5**). Also,

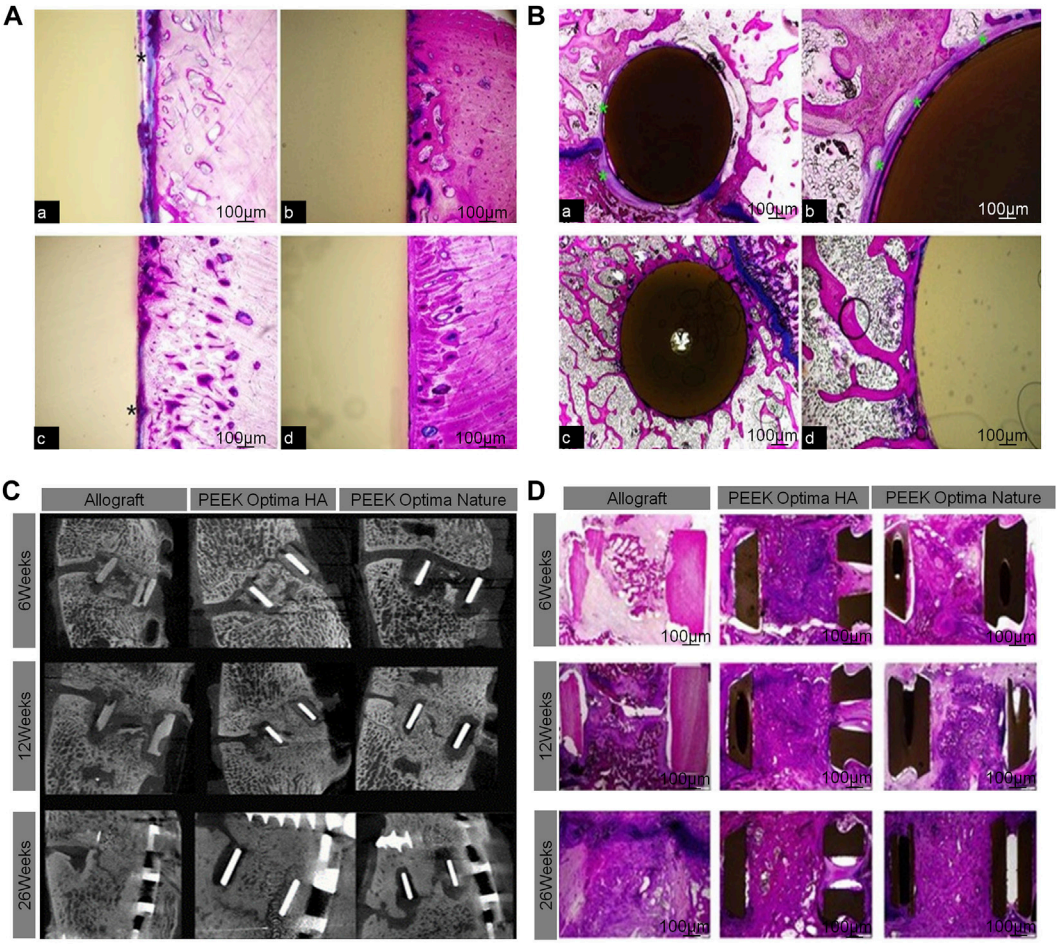

FIGURE 5 | (A) Bone ingrowth in cortical sites for PEEK cage **(A,C)** and PEEK-HA cage **(B,D)** at 4 and 12 weeks demonstrated the presence of a fibrous tissue interface for PEEK (*), whereas a direct bone-to-implant interface was observed for PEEK-HA at the magnification used. **(B)** Bone ingrowth in cancellous sites for PEEK **(A,C)** and PEEK-HA **(B,D)** at 12 weeks demonstrated the presence of a fibrous tissue interface for PEEK (*), whereas a direct bone-to-implant interface was observed for PEEK-HA at the magnification used. **(C)** Micro-CT at 6, 12, and 26 weeks for allograft, PEEKHA, and PEEK demonstrated progression in fusion versus time for all groups. **(D)** Macroscopic overview of PMMA histology (Walsh et al., 2016).

although PEEK interbody fusion cages are relatively mature structures, their composite materials need to be further explored.

Absorbable Materials

Absorbable materials have relatively good biocompatibility and can be hydrolyzed or enzymatically hydrolyzed into non-toxic small molecules that can be absorbed by organisms, with some even participating in biological metabolism (Hojo et al., 2005). Polylactide (PLA), alkyl polyglycoside, and polydioxane are considered safe and sufficiently stable absorbable materials, while iron, Mg, and zinc are the main absorbable metal elements. Although the inconvenience of a second surgery can be avoided by harvesting biomaterials, the possible complications, such as soft-tissue reactions, unwanted osteolysis, and low primary mechanical loading capacity, also limit the use of absorbable interbody fusion cages (Ulum et al., 2019; Pisecky et al., 2021). The hardness of the bioabsorbable fusion cage is similar to that of bone, which may accelerate interbody fusion. Meanwhile, as the fusion cage degrades, the load is gradually transferred to the healed bone to aid with bone remodeling. At present, PLA is the most commonly used bioabsorbable scaffold material, but rapid degradation and osteolysis around the scaffold have been reported (Ren et al., 2017). In a previous study, Lu *et al.* compared a novel PLA/nanoscale β-tricalcium phosphate bioabsorbable self-retaining cervical cage (BCFC) with an autologous bone graft and PEEK cage for anterior cervical discectomy and interbody fusion and found that the BCFC device had better fusion than the autologous bone graft or PEEK cage. This device may be a potential alternative to current PEEK cages (Lu et al., 2017). Knutsen *et al.* designed a bioabsorbable polycaprolactone (PCL) cervical cage and tested its compression, compression-shear, and torsion, concluding that PCL bioabsorbable cages may require additional fixation to achieve the effect of fused vertebral bodies (Knutsen et al., 2015). Through a clinical comparison, Jiya *et al.* found that absorbable poly-L-lactide-co-D,L-lactide (PLDLLA) implants

are less effective in assisting with spinal fusion than PEEK implants, have a lower fusion rate, and are more prone to subsidence and osteolysis, so their benefits need to be further proven. The sterilization of PLDLLA cages by electron beam irradiation may lead to preliminary cage rupture, which is the main cause of mechanical failure (Jiya et al., 2009; Jiya et al., 2011). Ren *et al.* evaluated the fusion effect, biomechanical stability, and histological characteristics of a novel absorbable poly–amino acid copolymer/nano-hydroxyapatite/calcium sulfate (MAACP/HA/CS) interbody fusion cage in a goat cervical fusion model. Compared to a Ti cage and autogenous bone graft, the MAACP/HA/CS cage had a better fusion effect, combined closely with the surrounding bone, and maintained an appropriate intervertebral disc height (Ren et al., 2017). Although the absorbable material interbody fusion cage attained a good fusion rate because of its excellent biocompatibility and easy absorption, given its high failure rate, its clinical application needs to be further explored and studied.

Mg has a similar mechanical behavior to natural bone, good bone conduction activity, and radiation transparency, so it is widely regarded as a potential ideal absorbable orthopedic material superior to traditional metal and other biodegradable implants (Wang Y et al., 2020). The density of Mg and its alloy is close to that of human bone mineral, and its elastic modulus is about 45 GPa, which is lower than that of Ti_6Al_4V, tantalum, and other implantable metals (Staiger et al., 2006). Furthermore, it has been shown that implant-derived Mg induces local neuronal production of calcitonin gene–related polypeptide-α to improve bone-fracture healing (Zhang et al., 2016). The Mg^{2+} released from the degradation of Mg-based implants is considered an effective material to promote osteogenesis, but there are few studies on Mg-based implant fusion. Through degradation, interbody fusion, and biocompatibility testing of a goat cervical vertebra model, Guo *et al.* found that Mg-based interbody fusion cage had better histological fusion, but the total fusion area needed to be improved. This is the first report of successful histological fusion of a Mg-based interbody fusion cage (Guo et al., 2020). The main obstacle to limiting the clinical application of Mg-based cages is the adverse reactions caused by the rapid degradation of Mg. The degradation rate is faster in the first 3 weeks after implantation, then slows down gradually thereafter. However, excessive Mg accumulation caused by rapid implant corrosion will lead to a severe foreign body reaction, tissue stimulation, decreased mechanical strength of new bone, and abnormal precipitation of calcium, which will eventually hinder osteogenesis. Moreover, Mg generates a large amount of hydrogen during the corrosion process, resulting in tissue loosening or excessive pressure, which is not conducive to bone formation (Wessels et al., 2012). This may be because Mg scaffolds corrode faster than new bone formation, leading to local scaffold collapse, resulting in differences in intervertebral pressure and ultimately leading to fusion failure (Staiger et al., 2006). In an experiment of a silicon-coated Mg alloy (AZ31) fusion cage in a goat cervical vertebra model, Zhang *et al.* found that excessive Mg accumulation could inhibit the formation of new bone, the intervertebral Mg ion concentration increased significantly after implantation, and the intervertebral Ca/P ratio decreased under the condition of high Mg accumulation, which may be the main reason for the failure of interbody fusion (Zhang F et al., 2018). However, there is only a single case of successful fusion in the literature; moreover, even after modification to balance the degradation rate, the fusion region is still too small to meet clinical needs, so more research is needed to improve it. It is a feasible method to slow down the degradation rate of Mg by reducing the purity of Mg (Chang et al., 2020). At present, Mg as an intraspinal plant is still in an exploratory stage, and its clinical application requires more experimental support.

Ceramic Materials

Bioceramics have inorganic components similar to natural bone which are widely used for bone tissue scaffolds fabricating. Due to its similar composition to natural bone, bioceramics present a significant osteogenic differentiating capability (Dxa et al., 2020). Bioceramic materials consist of calcium phosphate ceramics (CaP) such as hydroxyapatite (HA), tricalcium phosphate (TCP), and bioglass (Zhao et al., 2021). It is known that the biologically active $CaO\text{-}SiO_2\text{-}P_2O_5\text{-}B_2O_3$ glass–ceramic can chemically combine with bone to form a carboxyapatite layer to promote the differentiation of human bone marrow mesenchymal stem cells into osteoblasts. Li *et al.* found that the fusion rate and improvement of clinical symptoms of $CaO\text{-}SiO_2\text{-}P_2O_5\text{-}B_2O_3$ glass–ceramic spacers were similar to those of Ti cages. In an *in vivo* model, cylindrical implants showed better osseointegration with adjacent bones than HA, and the surface coating was found to improve the osseointegration of the implant, while its compressive and flexural strength were ≥2 times that of HA alone. The compressive strength of $CaO\text{-}SiO_2\text{-}P_2O_5\text{-}B_2O_3$ glass–ceramics is 4 times that of PEEK and 1.3 times that of Ti, respectively. However, this increased mechanical strength correlates with a greater risk of sinking in patients with osteoporosis (Lee et al., 2016). Ceramic implants made of silicon nitride show better biocompatibility and bone conductivity and are expected to reduce complications like subsidence and displacement. Kersten *et al.* compared a silicon nitride interbody fusion cage and PEEK interbody fusion cage in patients with symptomatic degenerative lumbar disc disease for the first time, but their results have not yet been published (Kersten et al., 2014). HA is a widely used ceramic biomaterial because it is the basis of bone tissue. In addition, it also provides enough matrix for the endogenesis of tissue in the process of bone regeneration. It generally needs to be used in combination with other materials. When the scaffold is made of chitosan and HA in a ratio of 20–80, scaffold has both elasticity and an osteogenic ability. In a mouse spinal fusion model, a chitosan/HAp composite scaffold showed good biocompatibility and sufficient spinal stability and induced solid and well-structured bone regeneration (Rodriguez-Vazquez and Ramos-Zuniga, 2020). In addition, a hollow HA/polyamide 66 stent (HA/PA66) has been used in anterior cervical reconstruction. Liang *et al.* verified in a goat cervical fusion model that porous HA/PA66 with a 300-μm pore size is more conducive to bone growth and can more effectively promote interbody fusion, providing a

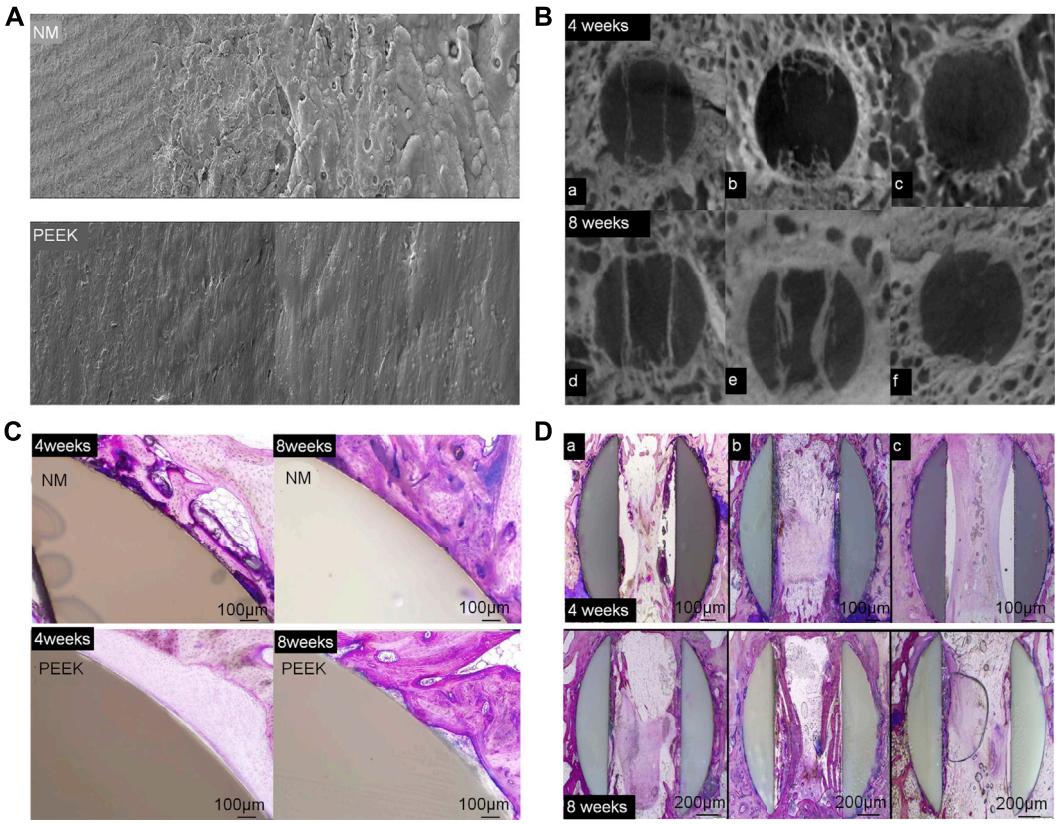

FIGURE 6 | (A) Scanning electron microscopy was used to examine the surface topography of NanoMetalene (NM) and PEEK at magnifications of ×500, 5,000×, 20,000×, and 50,000×. **(B)** Micro-CT image reconstructions in the middle of an aperture at 4 and 8 weeks in the sagittal plane for each group. Group 1 was coated with NM on all surfaces, Group 2 had a NM coating inside the apertures with a PEEK outside, and Group 3 had PEEK with no coating. **(C)** A typical higher-magnification visual of the outside of the NM-coated surface and PEEK implants at 4 and 8 weeks. Direct bone contact with the Ti coating with NM occurred at 4 weeks, which improved over time to 8 weeks. PEEK surfaces presented a typical non-reactive fibrous tissue interface at 4 weeks, with some focal bone contact at 8 weeks. **(D)** PMMA histology in the middle of the apertures at 4 and 8 weeks in the sagittal plane (Walsh et al., 2018).

potential application prospect for intervertebral reconstruction after vertebrae resection (Liang et al., 2020).

4 POST-PROCESSING TECHNIQUES

Coating

Coating technology is also widely used in orthopedic implant modification. The coating of the cage can modify the surface of the material to amend and increase its surface roughness without changing its biomechanical properties. Coating an interbody cage reduces the vertebral body subsidence and pseudoarthrosis (Rao et al., 2014; MacBarb et al., 2017). Coating techniques, including plasma spraying, chemical vapor deposition, metal–organic chemical vapor deposition, electrochemical vapor deposition, molten coating, physical vapor deposition, thermal or diffusion conversion, and sol-gel, have been used to deposit micron and nanometer coatings on various substrates, including Ti and its alloys. Nano-coating technology refers to thin films with thicknesses of 1–1,000 nm or those less than micro-coatings (<1 μm) (Choi et al., 2020). Here, we will introduce the coating techniques commonly used in interbody fusion.

Gunzburg *et al.* verified that a PEEK material coated with nano-Ti can achieve greater spinal stiffness than a pure PEEK material in spinal fusion using a goat model (Gunzburg et al., 2019). The Ti coating on PEEK retains the physical properties of the PEEK substrate and contains a surface that reacts better with the host. Ti-surfaced PEEK implants allow for earlier and better fusion of new bone formation and remodeling by increasing the anchorage of osteoblasts in the endplates and wells. The Ti coating aids in bone formation and remodeling. This is accomplished by stimulating the production of osteoprotegerin, transforming growth factor (TGF)-β1, vascular endothelial growth factor (VEGF) A, fibroblast growth factor (FGF), and angiopoietin 1. Local levels of these factors were higher in Ti-coated implants than smooth Ti_6Al_4V or PEEK alloys (Bassous et al., 2019; Ohanisian and Dorsi 2019). In a prospective evaluation of 45 patients undergoing ACDF, Krayenbuhl *et al.* achieved good interbody fusion with a low complication rate by placing an empty plasma hole–covered Ti cage after anterior cervical microsurgery. Disc height and lordosis can be preserved with a low incidence of subsidence and good fusion rates (Krayenbühl et al., 2008). Walsh et al. (2018) found that newly formed bone grew along the surface of a nano-

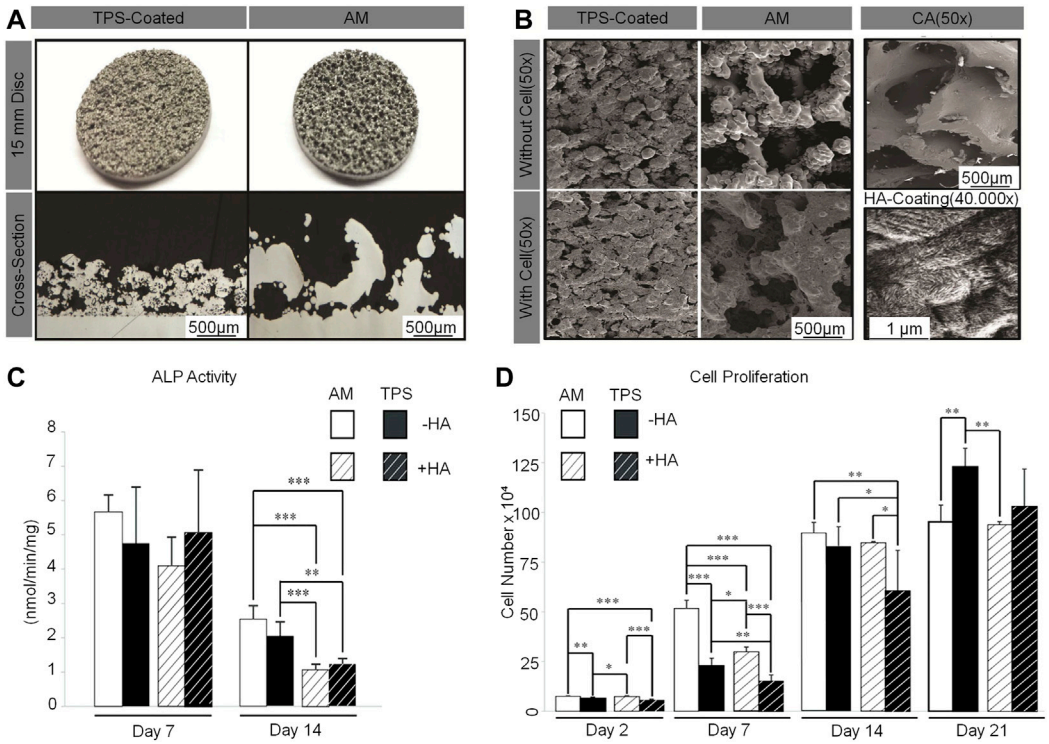

FIGURE 7 | (A) Gross images of TPS-coated and additive-manufactured (AM) discs (top). Cross-section images taken from stereological analysis (bottom). **(B)** Representative scanning electron microscopy images of unseeded TPS-coated and AM discs (top left). Discs after 3 weeks of culture with human 1.19 fetal osteoblast-like (hFOB) cells (bottom left) and of human cancellous bone allograft to show the target surface topography (top right). Representative scanning electron microscopy images of nano-crystalline HA coating on an AM disc (bottom right). **(C)** Two-way analysis of variance of AM compared to TPS-coated discs with and without a nano-crystalline HA coating for alkaline phosphatase activity. **(D)** Two-way analysis of variance of AM compared to TPS-coated discs with and without a nano-crystalline HA coating for cell proliferation (MacBarb et al., 2017).

Ti–coated PEEK fusion cage in a sheep model. On the other hand, the surface of PEEK cage shows non-reactive fiber tissue at the interface (**Figure 6**). The coated PEEK fusion cage had good adhesion and proliferation of bone marrow stromal cells (BMSCs) and can induce a higher cell growth rate and alkaline phosphatase level, which can promote bone growth (Liu et al., 2017).

The common method to enhance osteoblasts' response to a material is to apply HA to the surface of cage (MacBarb et al., 2017; Walsh et al., 2018). Sierra *et al.* 3D-printed a lumbar cage with HA coating and found that it had good biocompatibility through *in vitro* analysis, characterization, and testing (Serra et al., 2016). McBarb *et al.* designed and compared Ti plasma spray (TPS) coatings with and without nano-crystalline HA coatings. Their *in vitro* experiments showed that the HA coating achieved better cell proliferation and osteogenic capacity compared to the uncoated TPS, but the difference was not statistically significant (MacBarb et al., 2017) (**Figure 7**).

The natural extracellular matrix protein is considered a candidate material for the development of biomaterials that can induce specific cell behaviors. As a surface coating of biomaterials, the purified protein can change the proliferation and differentiation of stem cells and the retention of growth factors, which provides a new idea for the coating technology of printing materials. This could be explored in future experiments (Xing et al., 2020).

Internal Fillings

Obtaining good biocompatibility of fillers through internal filling of stents, promoting local proliferation, and obtaining a good osteogenic ability to promote interbody fusion are commonly used methods in basic experiments and clinical practice of spine surgery. Additives such as drugs, growth factors, and platelet-rich plasma (PRP) are added to the pre-designed porous interbody fusion cage by means of negative pressure suction, direct filling, and immersion (Bai H. T. et al., 2020; Leng et al., 2020).

4.2.1 Drugs

4.2.1.1 Simvastatin

Over the years, statins have been widely used to lower cholesterol and reduce the risk of heart attack (Song et al., 2003). SIM, an inhibitor of 3-hydroxy-3-methylglutaryl coenzyme A reductase (HMG-CoA), which has the advantages of a low price, good safety, and ability to promote bone growth in a prosthesis (Jin et al., 2021). SIM overcomes the shortcomings of the high cost and short half-life of biological factors like BMP-2 and VEGF used in previous studies (Zhang et al., 2020a). Topical application of SIM has a good effect on bone formation. Moreover, local

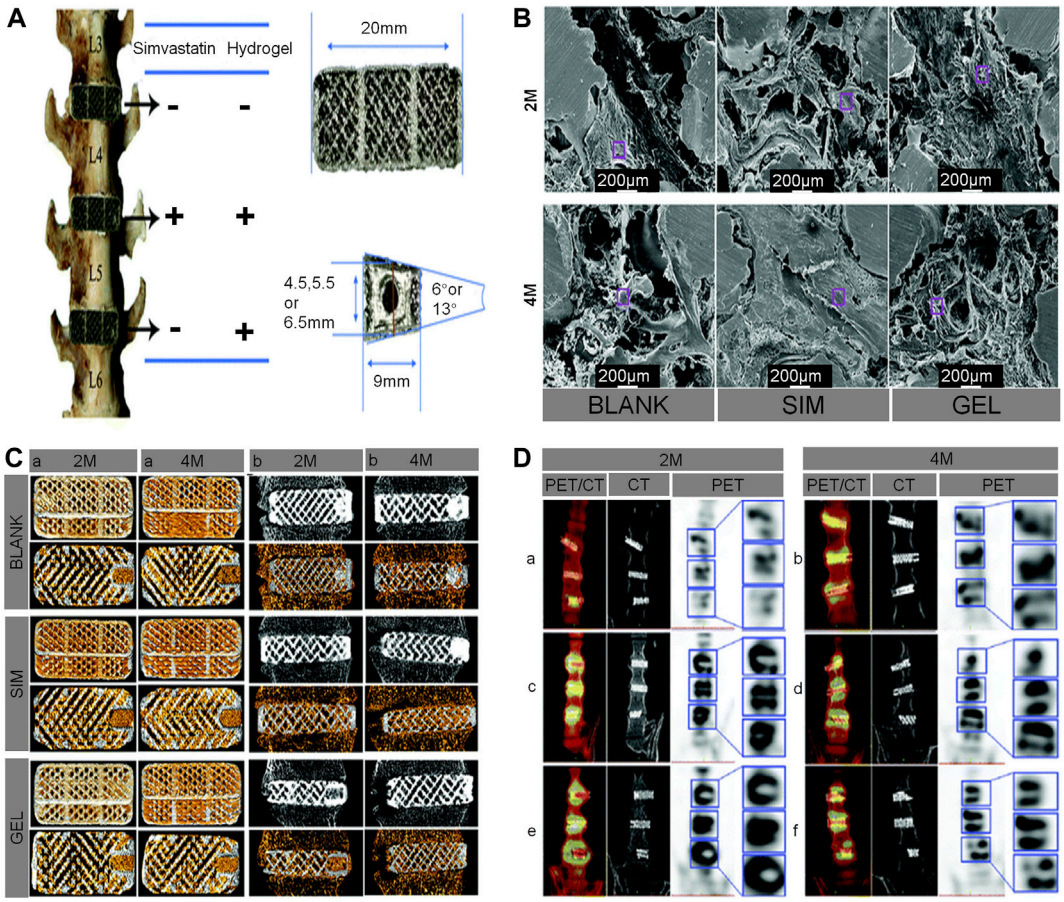

FIGURE 8 | (A) The distribution of the cages in the lumbar interbody spaces, the geometrical parameters of the cages, and a screw hole included on one end of the cage. **(B)** Characterization of the intra-porous morphology in cages using scanning electron microscopy, which showed that the bone formation in the cages of the SIM group was very dense. **(C)** Bone ingrowth in the cages (yellow represents new bone) at 2 and 4 months. For each cage in the different fused segments, the upper panel shows 3D-reconstructed images of the cages, and the lower panel shows axial 2-dimensional images of the cages **(A)**. Osseointegration around the cages (gray in the upper panel and yellow in the lower panel both represent new bone in cages) **(B)**. **(D)** Coronal fused positron emission tomography/CT, CT, and positron emission tomography and a locally enlarged image of the macaques at 2 and 4 months, respectively (Zhang et al., 2020a).

application of PLA has achieved good results in experiments of bone formation promotion and bone defect healing (Zhao et al., 2014; Tan et al., 2015). Using porous Ti cage filled with SIM/poloxamer 407 hydrogel in a rhesus monkey interbody fusion model, Zhang *et al.* found that 3D-printed porous scaffolds containing SIM hydrogel promoted bone growth and spinal fusion. They also speculated that, in the early stage of osteogenesis, the continuous release of SIM from the hydrogel promotes the production of endogenous biological factors, such as BMP-2 and VEGF, which are key regulators of bone formation and angiogenesis during bone regeneration. However, with the passage of time, due to the body's metabolism, the osteogenic effect of SIM gradually decreases (Zhang et al., 2020b) (**Figure 8**).

4.2.1.2 Strontium Ranelate

SRR is an oral drug used for the prevention and treatment of osteoporosis. Different from other anti-osteoporotic drugs, SRR has unique dual effects on bone formation and bone resorption. At the same time, it reduces bone decomposition, stimulates bone reconstruction, prevents bone loss, improves bone strength, and reduces the risk of fracture (Rodrigues et al., 2018; Demirel and Kaya 2020). However, oral SSR may have no synthetic metabolic effect on human bone formation et al., 2018, Marx et al., 2020). Tai *et al.* found that SRR treatment had a relatively mild effect on bone strength and bone remodeling and confirmed its better interbody fusion through histological and mechanical tests in a mouse interbody fusion model, suggesting that SRR treatment can be used as a replenish for human interbody fusion, although an interbody fusion cage was not used in this mouse model. This experiment provides a new idea for interbody fusion under the umbrella of osteoporosis (Tsai et al., 2017).

4.2.2 Platelet-Rich Plasma

PRP obtained by centrifugation is a plasma product containing high concentrations of various growth factors, including platelet-derived growth factor, insulin-like growth factor (IGF), and TGF-β. PRP is known to play an important role in fracture healing. A large number of studies have shown that PRP-modified scaffolds

have a positive effect on bone regeneration and can significantly promote the repair of bone defects (Lowery et al., 1999; Carreon et al., 2005; Leng et al., 2020; Sochacki et al., 2020; Andrade et al., 2021). The application of PRP in a rat spinal fusion model significantly accelerated the speed of interbody fusion without any complications (Shiga et al., 2016). In addition, lyophilized PRP is also widely used due to its advantage of easy storage. Compared to traditional PRP, lyophilized PRP–coated Ti more strongly promoted the cell viability and osteogenic differentiation of BMSCs and triggered better bone formation. Interbody fusion provides a new idea (Qiao et al., 2020). It can be seen from previous literature that there are no animal experiments of interbody fusion cages combined with PRP, but PRP's role in promoting interbody fusion has been tested alone, which provides a direction for future experiments and research.

4.2.3 Growth Factors

Soluble growth factors obtained by protein separation and molecular cloning techniques include TGFs, BMPs, IGFs, FGFs, and epidermal growth factor. However, only some of these growth factors showed a significant bone-induction ability (Kandziora et al., 2003).

4.2.3.1 Bone Morphogenetic Protein

BMP has attracted wide attention because of its inherent potential to improve the process of ossification and induce pluripotent progenitor cells to differentiate along the direction of osteogenesis. RhBMP-2 is an osteoinductive protein that has been used to promote spinal fusion and can induce fusion when used as an implant with a suitable carrier, such as an absorbable sponge (Boden et al., 2000; Burkus et al., 2017). BMP acts as a signal to stimulate BMSCs to migrate to the implantation site and induces marrow stromal cells (MSCs) to proliferate and differentiate into osteoblasts (Grgurevic et al., Bae et al., 2016). Previous studies on BMP-2 engraftment have shown that it has many effects, including angiogenesis, cell recruitment, and even promotion of mesenchymal and hematopoietic progenitor cell proliferation. However, new research suggests that BMP behaves differently at different doses (Burkus et al., 2002; Meisel et al., 2008). By adding RhBMP-2 to the fusion cage, Pan *et al.* found that, although BMP accelerated the speed of interbody fusion, it also produced a significant inflammatory response. In clinical applications, BMP may lead to local adverse structural changes and eclectic bone biomechanical changes, osteolysis, and trabecular thinning (Pan et al., 2017). Sethi *et al.* found that the use of RhBMP-2 can increase the fusion rate, but the incidence of pre-vertebral soft tissue swelling also increases (Sethi et al., 2011). The most common adverse reactions include accidental swelling and inflammation as well as inflammatory cyst formation. Although there is no difference in clinical effect between interbody fusion and autograft placement, BMP can also lead to endplate absorption, sinking, increased incidence of cage migration, osteolysis, and ectopic bone formation (Sethi et al., 2011; Michielsen et al., 2013; Burkus et al., 2017). Use of RhBMP-2 is strictly limited in clinical applications. It is relatively effective in achieving bone fusion, and the fusion rate is similar to that of patients receiving autografts. The incidence of complications was similar between autografts and BMP, but the rates of radiculitis and serum tumor were slightly higher in the BMP group (Khan et al., 2018). There was no significant difference in fusion rate between low and high doses (low: 33.3% and high: 46.7%), but a high dose could easily lead to an increased incidence of osteolysis, adverse events, and swelling (Okada et al., 2020). During a postoperative evaluation of 17 patients with lumbar degenerative disease after implantation of a PEEK interbody cage with 212 mg of a RhBMP collagen gel sponge, Meisel *et al.* found that there was no significant difference between the fusion rate and autologous bone graft, but there was temporary bone resorption around the fusion cage at 3 months without subsidence, pain, or complications (Meisel et al., 2008). In a sheep interbody fusion model, Bae *et al.* used an absorbable sponge with different doses of RhBMP-2 in a customized PEEK interbody fusion cage and found that the osteoclast activity and the corresponding peri-implant bone resorption rate were dose-dependent and reached a peak 4 weeks after operation (Bae et al., 2016). Grgurevic *et al.* induced complete spinal fusion with recombinant human RhBMP-6 based on an autologous blood coagulant (ABC) in sheep model. The best dose was 100 μg of RhBMP-6/mLABC (Grgurevic et al.) (**Figure 9**). An absorbable collagen sponge soaked in recombinant BMP-2 and recombinant BMP-7 combined with bovine collagen have been approved as substitutes for biological bone grafts to close gaps and repair delayed and non-union fractures. Among them, the incidence of complications in different positions is varied. Anterior cervical approach always causes the most serious side effects including anterior cervical edema, osteolysis, graft sedimentation and wound infection. Followed by posterior cervical approach which can cause posterior neck pain. The side effects in anterior and posterior lumbar approaches are relatively mild. Moreover, the tumorigenic effect of BMP should also be noted (Joseph and Rampersaud, 2007). In summary, BMP can significantly promote spinal fusion in the short term, but its side effects and dose sensitivity limit its wide application. Currently, BMP-2 has been proved by Food and Drug Administration (FDA) and used as an INFUSE Bone Graft (Medtronic Sofamor Danek) clinically. The recommended dosage varied between studies, and we draw a comprehensive conclusion among references that 1.5 mg/cm3 is deemed as an ideal effective concentration of BMP-2 (Sethi et al., 2011). Moreover, the following researches should continuously focus on the appropriate BMP dosage weighing the biosafety and effectiveness.

4.2.3.2 Combination of IGF and TGF-β

When the combination of IGF and TGF-β is used for spinal fusion, it can achieve mutual promotion. By adding IGF and TGF-β to HA-coated cages in a goat cervical fusion model, Gu *et al.* found the cage with IGF and TGF-β had significantly higher tensile strengths in extension and scoliosis compared to the other groups, indicating that they achieved better spinal fusion (Gu et al., 2013). Kim *et al.* used a fusion cage with IGF combined with TGF-β in a cervical fusion sheep model and found through quantitative CT that the fusion cage group with IGF combined with TGF-β showed significantly higher values for bone mineral

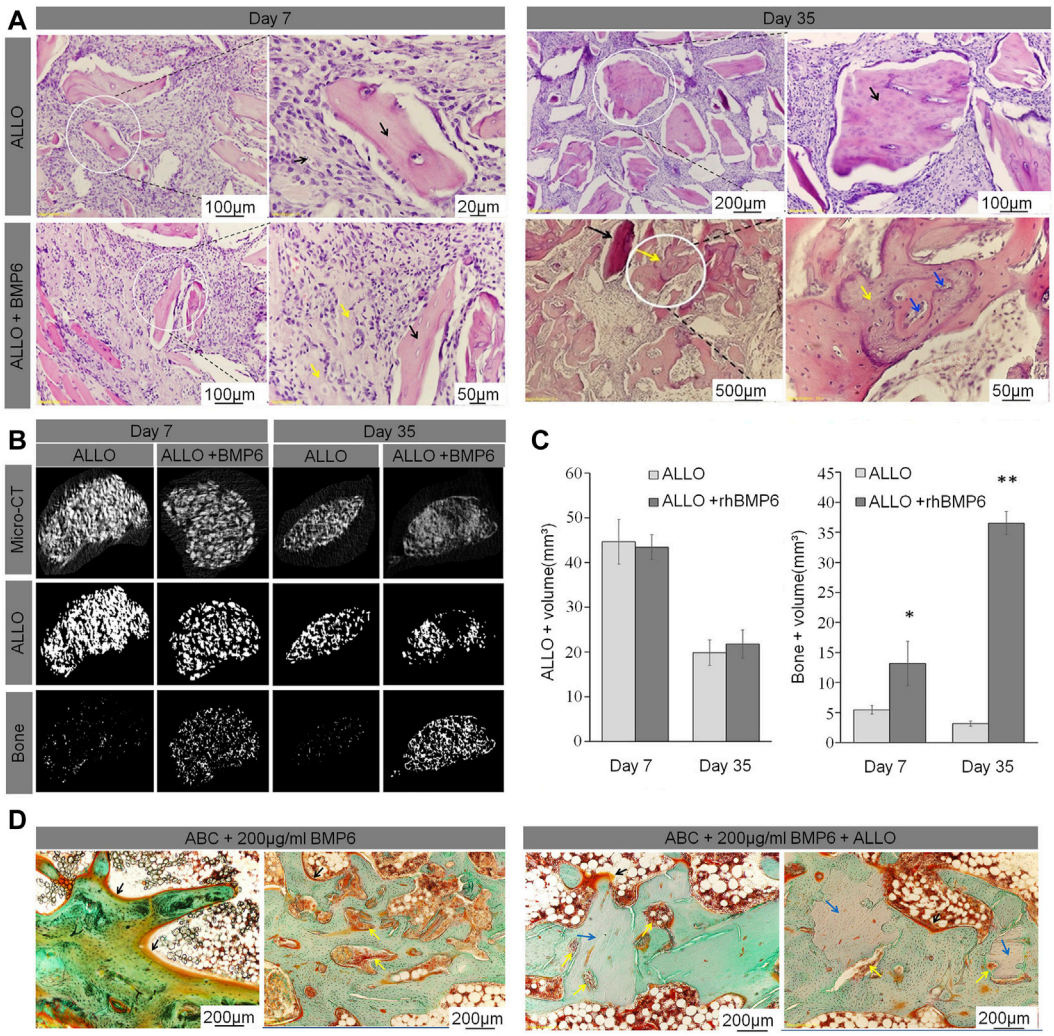

FIGURE 9 | (A) ABC/allograft devitalized bone particles (ALLO) (black arrows) without RhBMP-6 induced formation of fibrotic tissue at days 7 and 35 without any sign of new bone formation. ABC/ALLO with RhBMP-6 had induced new bone formation by day 7 (yellow arrows), and advanced creeping substitution of ALLO with new bone was observed on day 35 (blue arrowhead). **(B)** Overall micro-CT analyses of ABC/ALLO implants without and with RhBMP-6 are shown in the top row, only ALLO particles are visualized in the middle row, and the bottom row shows the newly formed bone (images obtained upon subtracting the ALLO particles from overall micro-CT images), respectively. Note the formation of new bone by day 7, with significant formation by day 35 in ABC/ALLO implants that contained RhBMP-6. ABC/ALLO alone did not induce bone either at 7 or 35 days after implantation. **(C)** Morphometric analysis of ALLO volume in implants on days 7 and 35, indicating a significant decrease in ALLO volume and increased amount of bone in the presence of RhBMP-6. **(D)** Histology of ABC implants without and with ALLO harvested at 14 weeks after surgery in a rabbit model. Note the newly formed bone with a dense trabecular structure with laid-down osteoids at the surface (black arrows), pronounced bone remodeling with numerous blood vessels (yellow arrows), and the newly formed trabeculae assimilated with ALLO (blue arrows) (Grgurevic et al.).

density, bone mineral content, and bony callus volume at 12 weeks after implantation. This shows that these growth factors can improve the formation of the intervertebral bone matrix, but their long-term effects need to be further explored (Kim et al., 2015). By adding BMP and IGF/TGF-β into a Ti cage in a sheep cervical fusion model, Kandziora *et al.* found that the early fusion effects of BMP and IGF/TGF-β were similar. The callus in the BMP group and IGF/TGF-β group had higher bone mineral density and biomechanical stability during extension, rotation, and bending (Kandziora et al., 2002). This fully illustrates the strong potential of the combined use of IGF/TGF-β in spinal fusion and provides a strong basis for future clinical use.

4.2.4 Allogeneic Material

Allogeneic cancellous bone, tricalcium phosphate, decalcified bone matrix (DBM), mineralized collagen, biphasic calcium phosphate, and other alternative materials have been successfully applied to the additives of interbody fusion cage, and good results have been obtained (Cho et al., 2005; Dai and Jiang 2008; Liao et al., 2008; Topuz et al., 2009; Scholz et al., 2010). Among them, CS is a kind of bone-substitute material. CS

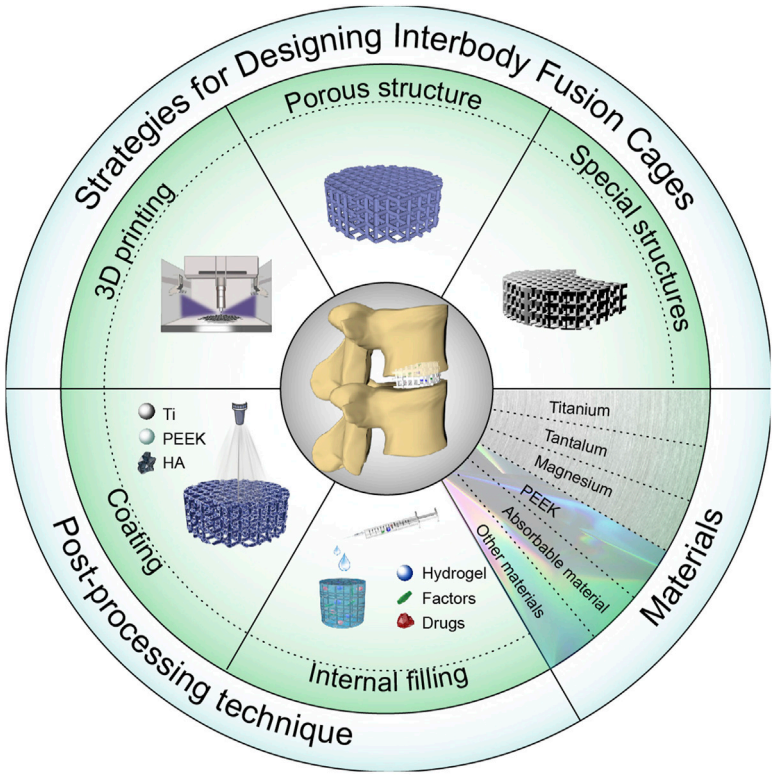

SCHEME 1 | Schematic diagram of an interbody fusion cage. Design and application of the interbody cage.

particles have been successfully used as implantable fillers in the treatment of periodontal bone defects and long bone defects (Thomas and Puleo 2010; Baranes and Kurtzman 2019). DBM has been proven to have the potential for bone conduction and bone induction because of the proteins and various growth factors present in the extracellular matrix. DBM alone can induce good bone bridging in lumbar interbody fusion, but the effect is still not as good as that of autogenous bone graft, so it is recommended that DBM be combined with other materials. Xie *et al.* found that, although the curative effect and fusion rate of a PEEK interbody fusion cage filled with CS/DBM and autogenous bone filler were similar, CS/DBM instead of autogenous bone had the advantages of less intraoperative blood loss and fewer complications at the donor site, so it is a good substitute for autotransplantation (Xie et al., 2015). Biomineralized collagen has a good osteogenic ability, and the osteogenic ability of adjacent bone surfaces has a profound clinical application value, showing a potential application prospect. In clinical cases, Barlocher *et al.* found that, compared to an autologous bone graft and threaded Ti cage, polymethyl methacrylate (PMMA) appears to be a good alternative to cage-assisted fusion. Although many complications caused by autologous transplantation are avoided, the inability to achieve bony fusion still limits its use (Bärlocher et al., 2002). Kong *et al.* created a new biomaterial mineralized collagen–PMMA bone cement by injecting mineralized collagen into PMMA. It was found that PMMA bone cement showed a good osteogenic ability in a sheep model, but this finding needs to be verified in further clinical transformational experiments. Minimally invasive injectable lumbar interbody fusion with mineralized collagen–PMMA bone cement has far-reaching clinical value and shows potential application prospects (Kong et al., 2020). However, not all allogeneic fillers are conducive to fusion. Cho *et al.* found that the fusion effect of a fusion cage containing biphasic calcium phosphate ceramic was lower than that of autogenous iliac bone graft and delayed the fusion period (Cho et al., 2005).

5 INTERBODY FUSION CAGE PROSPECTS

At present, there are many kinds of cages used in clinical and basic experiments that need to be chosen according to their respective advantages and needs. In this review, we list the advantages of different cage materials, internal implants, design methods, and post-processing to inform our use and selection.

In orthopedics clinics, the design of microporous fusion cages is particularly suitable for bone ingrowth and osseointegration, and the research on microporous structures is relatively mature. There are many studies on bone ingrowth with different porosities and pore sizes. Generally, the porosity is 65–80%, and its structure and mechanical properties are similar to those of trabecular bone. A pore size of 50–500 μm is

conducive to the adhesion, proliferation, and differentiation of bone cells. With the innovation of additive manufacturing technology, production now offers unprecedented means of structuring and customization, and the complex anatomy of the spine is very suitable for patient-specific equipment. Improving implant designs through the 3D-printing process may improve osseointegration and reduce the sinking rate. Combined with the current, relatively popular approach of finite element analysis, the preliminary design can be established to analyze whether the elastic modulus under different porosities and pore sizes is similar to that of human bone so that better spinal fusion can be obtained. In addition, topoisomerism technology can render the contact area between the implant and bone larger, which will make bone ingrowth easier. At present, there is no interbody cage with a fixation device available in the implant itself, which is also a direction that can be explored. Combined with these technologies mentioned above, a relatively suitable interbody cage can be obtained before implantation, and then basic and clinical experiments are performed to verify the performance.

Nowadays, the 2 most commonly used materials of interbody fusion cages are Ti alloy and PEEK. While Ti alloy materials have good biocompatibility, their excessive strength is likely to cause fusion. Conversely, the strength of PEEK is similar to that of human bone, and it is often used because of the easy detection of transmitted rays, but its biological inertness limits its further use. However, by modifying the PEEK material or adding other compounds to print the cage, its biocompatibility has been improved. At present, the CS/PEEK cage has been proven to promote interbody fusion, but mixtures with other ceramic-like materials have not appeared, which provides a direction for future research. Tantalum, Mg, and their alloys and absorbable materials have relatively few applications, and their respective deficiencies limit their usefulness. In the future, a new Mg alloy will not fail due to rapid absorption and local collapse; instead, it will achieve a balance between the new bone and the Mg alloy scaffold to perfectly support the pressure between the vertebral bodies before eventually being perfectly replaced by the new bone. Other absorbable materials, such as PLA, can be modified to achieve a degree of compressive strength that can support intervertebral pressure, rendering this issue no longer a problem. In addition, copper alloys, cobalt alloys, and memory metals with antibacterial properties will provide new options for vertebral body fusion under different physiological conditions.

Transplantation of autologous bone and allogeneic bone is the most common method for interbody fusion, offering biocompatibility and no obverse adverse reactions. In addition to the above 2 materials, there are other internal plants and drugs that are conducive to osseointegration. Materials such as SIM, BMP, biomineralized collagen, and PRP all show good bone ingrowth induction function, but there are no precise data to guide their dosage, and further exploration and experiments are necessary. In the future, through research, there will be guidelines developed to standardize their use and dosage. In addition, it is known that, in the process of bone formation, different growth factors are required in different stages. In the future, different drug-release systems will be constructed, and different doses of drugs will be released at corresponding times to regulate intervertebral bone formation.

To sum up, interbody fusion is a process of bony fusion. The selection of materials and additives for general interbody cages serves to enhance their osteogenic properties, but, when designing an interbody cage, the developer must consider that the device needs to withstand the pressure from upper and lower vertebrae; otherwise, the collapse of the implant will lead to fusion failure.

6 CONCLUSION

Good selection and use of the interbody cage are essential in the prognosis of clinical spinal interbody fusion. However, there is still a shortage of systematic discussion of its usage to date. This review focused on the design, materials, and post-processing technologies of the interbody cage. 3D printing is commonly used in the design work, and the design of porous structures is conducive to the ingrowth of new bone, which is more effective in improving the fusion rate. Other special types of interbody cages have been designed to reduce the difficulty of surgery or to facilitate fixation. Ti alloy and PEEK are the more commonly used materials for interbody cages. Other materials are less frequently used; among them, Mg alloy is an absorbable material, and its rapid absorption limits its use. In addition, post-processing technology is also important, including coating technology and internal additives. Ti and HA coatings are more commonly used, and studies so far have found that coating technology can improve spinal fusion to a certain extent. Internal additives, including SIM, BMP, and PRP, can promote bone formation through their own metabolism; however, there are few related studies at present, which provides a direction for future research.

AUTHOR CONTRIBUTIONS

HZ: Writing-original draft, Funding acquisition. ZW: Supervision. YW: Conceptualization. ZL: Supervision. BC: Conceptualization. SL: Conceptualization. WL: Conceptualization. JJ: Conceptualization. MW: Investigation, Methodology.

FUNDING

This study was supported by the Department of Science and Technology of Jilin Province (20210204104YY, 20200201448JC); and the Department of Finance in Jilin Province (2019SCZT031).

REFERENCES

Andrade, A. L. L. D., Sardeli, A. V., Garcia, T. A., Livani, B., and Belangero, W. D. (2021). PRP Does Not Improve the Objective Outcomes of Anterior Cruciate Ligament Reconstruction: a Systematic Review and Meta-Analysis. *Knee Surg. Sports Traumatol. Arthrosc.* 29 (9), 3049–3058. doi:10.1007/s00167-020-06348-z

Arts, M., Torensma, B., and Wolfs, J. (2020). Porous Titanium Cervical Interbody Fusion Device in the Treatment of Degenerative Cervical Radiculopathy; 1-year Results of a Prospective Controlled Trial. *Spine J.* 20 (7), 1065–1072. doi:10.1016/j.spinee.2020.03.008

Assem, Y., Mobbs, R. J., Pelletier, M. H., Phan, K., and Walsh, W. R. (2017). Radiological and Clinical Outcomes of Novel Ti/PEEK Combined Spinal Fusion Cages: a Systematic Review and Preclinical Evaluation. *Eur. Spine J.* 26 (3), 593–605. doi:10.1007/s00586-015-4353-8

Bae, H. W., Patel, V. V., Sardar, Z. M., Badura, J. M., Pradhan, B. B., Seim, H. B., et al. (2016). Transient Local Bone Remodeling Effects of rhBMP-2 in an Ovine Interbody Spine Fusion Model. *J. Bone Jt. Surg.* 98 (24), 2061–2070. doi:10.2106/jbjs.16.00345

Bai, H. T., Cui, Y. T., Wang, C. Y., Wang, Z. H., Luo, W. B., Liu, Y. Z., et al. (2020a). 3D Printed Porous Biomimetic Composition Sustained Release Zoledronate to Promote Osteointegration of Osteoporotic Defects. *Mater. Des.* 189, 108513. doi:10.1016/j.matdes.2020.108513

Bai, H., Zhao, Y., Wang, C., Wang, Z., Wang, J., Liu, H., et al. (2020b). Enhanced Osseointegration of Three-Dimensional Supramolecular Bioactive Interface through Osteoporotic Microenvironment Regulation. *Theranostics* 10 (11), 4779–4794. doi:10.7150/thno.43736

Baranes, D., and Kurtzman, G. M. (2019). Biphasic Calcium Sulfate as an Alternative Grafting Material in Various Dental Applications. *J. Oral Implantol.* 45 (3), 247–255. doi:10.1563/aaid-joi-D-18-00306

Bärlocher, C. B., Barth, A., Krauss, J. K., Binggeli, R., and Seiler, R. W. (2002). Comparative Evaluation of Microdiscectomy Only, Autograft Fusion, Polymethylmethacrylate Interposition, and Threaded Titanium Cage Fusion for Treatment of Single-Level Cervical Disc Disease: a Prospective Randomized Study in 125 Patients. *Neurosurg. Focus* 12 (1), E4. doi:10.3171/foc.2002.12.1.5

Basgul, C., Yu, T., Macdonald, D. W., Siskey, R., and Kurtz, M. S. M. (2019). Does Annealing Improve the Interlayer Adhesion and Structural Integrity of FFF 3D Printed PEEK Lumbar Spinal Cages? *J. Mech. Behav. Biomed. Mater* 102, 103455. doi:10.1016/j.jmbbm.2019.103455

Bassous, N. J., Jones, C. L., and Webster, T. J. (2019). 3-D Printed Ti-6Al-4V Scaffolds for Supporting Osteoblast and Restricting Bacterial Functions without Using Drugs: Predictive Equations and Experiments. *Acta Biomater.* 96, 662–673. doi:10.1016/j.actbio.2019.06.055

Boden, S. D., Zdeblick, T. A., Sandhu, H. S., and Heim, S. E. (2000). The Use of rhBMP-2 in Interbody Fusion Cages. *Spine* 25 (3), 376–381. doi:10.1097/00007632-200002010-00020

Burkus, J. K., Dryer, R. F., Arnold, P. M., and Foley, K. T. (2017). Clinical and Radiographic Outcomes in Patients Undergoing Single-Level Anterior Cervical Arthrodesis. *Clin. Spine Surg.* 30 (9), E1321–E1332. doi:10.1097/bsd.0000000000000409

Burkus, J. K., Transfeldt, E. E., Kitchel, S. H., Watkins, R. G., and Balderston, R. A. (2002). Clinical and Radiographic Outcomes of Anterior Lumbar Interbody Fusion Using Recombinant Human Bone Morphogenetic Protein-2. *Spine* 27 (21), 2396–2408. doi:10.1097/00007632-200211010-00015

Burnard, J. L., Parr, W. C. H., Choy, W. J., Walsh, W. R., and Mobbs, R. J. (2020). 3D-printed Spine Surgery Implants: a Systematic Review of the Efficacy and Clinical Safety Profile of Patient-specific and Off-The-Shelf Devices. *Eur. Spine J.* 29 (6), 1248–1260. doi:10.1007/s00586-019-06236-2

Caffrey, J. P., Alonso, E., Masuda, K., Hunt, J. P., Carmody, C. N., Ganey, T. M., et al. (2018). Strains in Trussed Spine Interbody Fusion Implants Are Modulated by Load and Design. *J. Mech. Behav. Biomed. Mater.* 80, 203–208. doi:10.1016/j.jmbbm.2018.02.004

Caplan, I. F., Sinha, S., Osiemo, B., Mcclintock, S. D., Schuster, J. M., Smith, H., et al. (2020). The Utility of Cervical Spine Bracing as a Postoperative Adjunct to Multilevel Anterior Cervical Spine Surgery. *Int. J. Spine Surg.* 14 (2), 151–157. doi:10.14444/7022

Carreon, L. Y., Glassman, S. D., Anekstein, Y., and Puno, R. M. (2005). Platelet Gel (AGF) Fails to Increase Fusion Rates in Instrumented Posterolateral Fusions. *Spine* 30 (9), E243–E246. doi:10.1097/01.brs.0000160846.85397.44

Chang, C.-W., Chung, Y.-H., Chang, C.-J., Chen, Y.-N., Li, C.-T., Chang, C.-H., et al. (2020). Computational Comparison of Bone Cement and Poly Aryl-Ether-Ether-Ketone Spacer in Single-Segment Posterior Lumbar Interbody Fusion: a Pilot Study. *Phys. Eng. Sci. Med.* 43 (1), 163–173. doi:10.1007/s13246-019-00832-8

Chen, C., Hao, Y., Bai, X., Ni, J. J., Chung, S. M., Liu, F., et al. (2019). 3D Printed Porous Ti6Al4V Cage: Effects of Additive Angle on Surface Properties and Biocompatibility; Bone Ingrowth in Beagle Tibia Model. *Mater Des.* 2019, 175. doi:10.1016/j.matdes.2019.107824

Cheng, B. C., Jaffee, S., Averick, S., Swink, I., Horvath, S., and Zhukauskas, R. (2020). A Comparative Study of Three Biomaterials in an Ovine Bone Defect Model. *Spine J.* 20 (3), 457–464. doi:10.1016/j.spinee.2019.10.003

Cho, D.-Y., Lee, W.-Y., Sheu, P.-C., and Chen, C.-C. (2005). Cage Containing a Biphasic Calcium Phosphate Ceramic (Triosite) for the Treatment of Cervical Spondylosis. *Surg. Neurol.* 63 (6), 497–503. doi:10.1016/j.surneu.2004.10.016

Choi, A. H., Karacan, I., and Ben-Nissan, B. (2020). Surface Modifications of Titanium Alloy Using Nanobioceramic-Based Coatings to Improve Osseointegration: a Review. *Mater. Technol.* 35 (11-12), 742–751. doi:10.1080/10667857.2018.1490848

Chong, E., Mobbs, R. J., Pelletier, M. H., and Walsh, W. R. (2016). Titanium/Polyetheretherketone Cages for Cervical Arthrodesis with Degenerative and Traumatic Pathologies: Early Clinical Outcomes and Fusion Rates. *Orthop. Surg.* 8 (1), 19–26. doi:10.1111/os.12221

Chu, L., Li, R., Liao, Z., Yang, Y., Dai, J., Zhang, K., et al. (2019). Highly Effective Bone Fusion Induced by the Interbody Cage Made of Calcium Silicate/PEEK in a Goat Model. *Acs Biomaterials Sci. Eng.* 5 (5), 2409–2416. doi:10.1021/acsbiomaterials.8b01193

Dai, L.-Y., and Jiang, L.-S. (2008). Anterior Cervical Fusion with Interbody Cage Containing β-tricalcium Phosphate Augmented with Plate Fixation: a Prospective Randomized Study with 2-year Follow-Up. *Eur. Spine J.* 17 (5), 698–705. doi:10.1007/s00586-008-0643-8

Demirel, M., and Kaya, A. I. (2020). Effect of Strontium-Containing Compounds on Bone Grafts. *J. Mater. ence* 55 (3). doi:10.1007/s10853-020-04451-7

Duan, Y., Yang, Y., Wang, Y., Liu, H., Hong, Y., Gong, Q., et al. (2016). Comparison of Anterior Cervical Discectomy and Fusion with the Zero-Profile Device versus Plate and Cage in Treating Cervical Degenerative Disc Disease: A Meta-Analysis. *J. Clin. Neurosci.* 33, 11–18. doi:10.1016/j.jocn.2016.01.046

Dxa, B., Jz, B., Cz, A., Db, C., Hy, B., Lm, B., et al. (2020). The Role of Calcium Phosphate Surface Structure in Osteogenesis and the Mechanisms Involved. *Acta Biomater.* 106, 22–33.

Easley, J., Puttlitz, C. M., Seim, H., Ramo, N., Abjornson, C., Cammisa, F. P., et al. (2018). Biomechanical and Histologic Assessment of a Novel Screw Retention Technology in an Ovine Lumbar Fusion Model. *Spine J.* 18 (12), 2302–2315. doi:10.1016/j.spinee.2018.07.021

Egan, P. F., Bauer, I., Shea, K., and Ferguson, S. J. (2018). Mechanics of 3D Printed Lattices for Biomedical Devices. *J. Mech. Des.* 141 (3).

Fan, W., and Guo, L. X. (2020). The Effect of Non-fusion Dynamic Stabilization on Biomechanical Responses of the Implanted Lumbar Spine during Whole-Body Vibration. *Comput. Methods Programs Biomed.* 192, 105441. doi:10.1016/j.cmpb.2020.105441

Farrokhi, M. R., Nikoo, Z., Gholami, M., and Hosseini, K. (2017). Comparison between Acrylic Cage and Polyetheretherketone (PEEK) Cage in Single-Level Anterior Cervical Discectomy and Fusion. *Clin. Spine Surg.* 30 (1), 38–46. doi:10.1097/bsd.0000000000000251

Feng, Y., Chen, L., Gu, Y., Zhang, Z.-M., Yang, H.-L., and Tang, T.-S. (2014). Influence of the Posterior Lumbar Interbody Fusion on the Sagittal Spino-Pelvic Parameters in Isthmic L5-S1 Spondylolisthesis. *J. Spinal Disord. Tech.* 27 (1), E20–E25. doi:10.1097/bsd.0b013e31828af6f0

Folman, Y., Lee, S.-H., Silvera, J. R., and Gepstein, R. (2003). Posterior Lumbar Interbody Fusion for Degenerative Disc Disease Using a Minimally Invasive B-Twin Expandable Spinal Spacer. *J. Spinal Disord. Tech.* 16 (5), 455–460. doi:10.1097/00024720-200310000-00004

Fomekong, E., Dufrane, D., Berg, B. V., André, W., Aouassar, N., Veriter, S., et al. (2017). Application of a Three-Dimensional Graft of Autologous Osteodifferentiated Adipose Stem Cells in Patients Undergoing Minimally

Invasive Transforaminal Lumbar Interbody Fusion: Clinical Proof of Concept. *Acta Neurochir.* 159 (3), 527–536. doi:10.1007/s00701-016-3051-6

Girod, P.-P., Hartmann, S., Kavakebi, P., Obernauer, J., Verius, M., and Thomé, C. (2017). Asymmetric Pedicle Subtractionosteotomy (aPSO) Guided by a 3D-Printed Model to Correct a Combined Fixed Sagittal and Coronal Imbalance. *Neurosurg. Rev.* 40 (4), 689–693. doi:10.1007/s10143-017-0882-4

Gkt, A., Mgo, B., Ml, B., Rgt, B., and Pmlb, C. (2020). Measuring the Performance of Patient-specific Solutions for Minimally Invasive Transforaminal Lumbar Interbody Fusion Surgery. *J. Clin. Neurosci.* 71, 43–50.

Grgurevic, L., Erjavec, I., Gupta, M., Pecin, M., Bordukalo-Niksic, T., Stokovic, N., et al. (2020). Autologous Blood Coagulum Containing rhBMP6 Induces New Bone Formation to Promote Anterior Lumbar Interbody Fusion (ALIF) and Posterolateral Lumbar Fusion (PLF) of Spine in Sheep. *Bone* 138, 115448. doi:10.1016/j.bone.2020.115448

Gu, Y., Zhang, F., Lineaweaver, W. C., Zhang, J., Qi, L. J., Wang, J., et al. (2013). *In Vivo* Study of Hydroxyapatite-Coated Hat Type Cervical Intervertebral Fusion Cage Combined with IGF-I and TGF-B1 in the Goat Model. *Clin. Spine Surg.* 29 (5), E267–E275. doi:10.1097/BSD.0b013e3182781d52

Gunzburg, R., Colloca, C. J., Jones, C. F., Hall, D. J., Callary, J. S., Hegazy, M. A., et al. (2019). Does Nanoscale Porous Titanium Coating Increase Lumbar Spinal Stiffness of an Interbody Fusion Cage? an *In Vivo* Biomechanical Analysis in an Ovine Model. *Clin. Biomech. (Bristol, Avon)* 67, 187–196. doi:10.1016/j.clinbiomech.2019.04.024

Guo, X., Xu, H., Zhang, F., and Lu, F. (2020). Bioabsorbable High-Purity Magnesium Interbody Cage: Degradation, Interbody Fusion, and Biocompatibility from a Goat Cervical Spine Model. *Ann. Transl. Med.* 8 (17), 1054. doi:10.21037/atm-20-225

Hacker, R. J., Cauthen, J. C., Gilbert, T. J., and Griffith, S. L. (2000). A Prospective Randomized Multicenter Clinical Evaluation of an Anterior Cervical Fusion Cage. *Spine* 25 (20), 2646–2655. doi:10.1097/00007632-200010150-00017

Hah, R. J., Alluri, R., and Anderson, P. A. (2020). Biomechanical Analysis of an Anterior Cervical Discectomy and Fusion Pseudarthrosis Model Revised with Machined Interfacet Allograft Spacers. *Glob. Spine J.* 10 (8), 973–981. doi:10.1177/2192568219884265

Hauerberg, J., Kosteljanetz, M., Bøge-Rasmussen, T., Dons, K., Springborg, P. J. B., and Wagner, A. (2008). Anterior Cervical Discectomy with or without Fusion with Ray Titanium Cage. *Spine* 33 (5), 458–464. doi:10.1097/brs.0b013e3181657dac

Hojo, Y., Kotani, Y., Ito, M., Abumi, K., Kadosawa, T., Shikinami, Y., et al. (2005). A Biomechanical and Histological Evaluation of a Bioresorbable Lumbar Interbody Fusion Cage. *Biomaterials* 26 (15), 2643–2651. doi:10.1016/j.biomaterials.2004.07.020

Høy, K., Bünger, C., Niederman, B., Helmig, P., Hansen, E. S., Li, H., et al. (2013). Transforaminal Lumbar Interbody Fusion (TLIF) versus Posterolateral Instrumented Fusion (PLF) in Degenerative Lumbar Disorders: a Randomized Clinical Trial with 2-year Follow-Up. *Eur. Spine J.* 22 (9), 2022–2029. doi:10.1007/s00586-013-2760-2

Høy, K., Grycel, B., Andersen, T., and Bünger, C. (2019). Does Transforaminal Lumbar Interbody Fusion Produce Leg Pain?-Results from a RCT. *J. Orthop. Surg. Hong. Kong)* 27 (3), 2309499019869469. doi:10.1177/2309499019869469

Hua, L., Lei, T., Qian, H., Zhang, Y., and Lei, Y. P. (2020). 3D-printed Porous Tantalum: Recent Application in Various Drug Delivery Systems to Repair Hard Tissue Defects. *Expert Opin. Drug Deliv.* 18 (122), 625–634. doi:10.1080/17425247.2021.1860015

Huang, H., Jiang, C., Feng, Z., and Jiang, X. (2014). Comparing the Process of Creeping Substitution between Allograft Bone and Local Bone Grafting in Lumbar Interbody Fusion. *Eur. Spine J.* 23 (10), 2068–2074. doi:10.1007/s00586-014-3388-6

Iunes, E. A., Barletta, E. A., Barba Belsuzarri, T. A., Onishi, F. J., Cavalheiro, S., and Joaquim, A. F. (2020). Correlation between Different Interbody Grafts and Pseudarthrosis after Anterior Cervical Discectomy and Fusion Compared with Control Group: Systematic Review. *World Neurosurg.* 134, 272–279. doi:10.1016/j.wneu.2019.10.100

Iv, J. P. M., Beutler, W., Peppelman, W., Harris, R., Slotkin, E., and Gillette, J. (2010). Clinical Outcomes with Porous Tantalum in Lumbar Interbody Fusion. *Spine J.* 10 (9-supp-S), S147–S148.

Jain, A., Marrache, M., Harris, A., Puvanesarajah, V., Neuman, B. J., Buser, Z., et al. (2020). Structural Allograft versus PEEK Implants in Anterior Cervical Discectomy and Fusion: A Systematic Review. *Glob. Spine J.* 10 (6), 775–783. doi:10.1177/2192568219883256

Jain, S., Eltorai, A. E. M., Ruttiman, R., and Daniels, A. H. (2016). Advances in Spinal Interbody Cages. *Orthop. Surg.* 8 (3), 278–284. doi:10.1111/os.12264

Jin, H., Ji, Y., Cui, Y., Xu, L., and Wang, H. J. (2021). Simvastatin-Incorporated Drug Delivery Systems for Bone Regeneration. *ACS Biomater. Sci. Eng.* 7 (6), 2177–2191. doi:10.1021/acsbiomaterials.1c00462

Jiya, T., Smit, T., Deddens, J., and Mullender, M. (2009). Posterior Lumbar Interbody Fusion Using Nonresorbable Poly-Ether-Ether-Ketone versus Resorb Able Poly-L-Lactide-Co-D,l-Lactide Fusion Devices A Prospective, Randomized Study to Assess Fusion and Clinical Outcome. *Spine* 34 (3), 233–237. doi:10.1097/BRS.0b013e318194ed00

Jiya, T. U., Smit, T., van Royen, B. J., and Mullender, M. (2011). Posterior Lumbar Interbody Fusion Using Non Resorbable Poly-Ether-Ether-Ketone versus Resorbable Poly-L-Lactide-Co-D,l-Lactide Fusion Devices. Clinical Outcome at a Minimum of 2-year Follow-Up. *Eur. Spine J.* 20 (4), 618–622. doi:10.1007/s00586-010-1568-6

Joffe, M. R., Parr, W. C. H., Tan, C., Walsh, W. R., and Brunel, L. (2019). Development of a Customized Interbody Fusion Device for Treatment of Canine Disc-Associated Cervical Spondylomyelopathy. *Vet. Comp. Orthop. Traumatol.* 32 (1), 79–86. doi:10.1055/s-0038-1676075

Joseph, V., and Rampersaud, Y. R. (2007). Heterotopic Bone Formation with the Use of rhBMP2 in Posterior Minimal Access Interbody Fusion. *Spine* 32, 2885–2890. doi:10.1097/brs.0b013e31815b7596

Kandziora, F., Pflugmacher, R., Scholz, M., Knispel, C., Hiller, T., Schollmeier, G., et al. (2002). Comparison of BMP-2 and Combined IGF-I/TGF-ss1 Application in a Sheep Cervical Spine Fusion Model. *Eur. Spine J.* 11 (5), 482–493. doi:10.1007/s00586-001-0384-4

Kandziora, F., Pflugmacher, R., Scholz, M., Schafer, J., Schollmeier, G., Schmidmaier, G., et al. (2003). Dose-dependent Effects of Combined IGF-I and TGF-?1 Application in a Sheep Cervical Spine Fusion Model. *Eur. spine J.* 12 (5), 464–473. doi:10.1007/s00586-002-0483-x

Kerolus, M., Turel, M. K., Tan, L., and Deutsch, H. (2016). Stand-Alone Anterior Lumbar Interbody Fusion: Indications, Techniques, Surgical Outcomes and Complications: Expert Review of Medical Devices: Vol 0, No Ja. *Expert Rev. Med. Devices* 13 (12), 1127–1136. doi:10.1080/17434440.2016.1254039

Kersten, R. F., van Gaalen, S. M., Arts, M. P., Roes, K. C., de Gast, A., Corbin, T. P., et al. (2014). The SNAP Trial: a Double Blind Multi-Center Randomized Controlled Trial of a Silicon Nitride versus a PEEK Cage in Transforaminal Lumbar Interbody Fusion in Patients with Symptomatic Degenerative Lumbar Disc Disorders: Study Protocol. *BMC Musculoskelet. Disord.* 15, 57. doi:10.1186/1471-2474-15-57

Khan, T. R., Pearce, K. R., McAnany, S. J., Peters, C. M., Gupta, M. C., and Zebala, L. P. (2018). Comparison of Transforaminal Lumbar Interbody Fusion Outcomes in Patients Receiving rhBMP-2 versus Autograft. *Spine J.* 18 (3), 439–446. doi:10.1016/j.spinee.2017.08.230

Kim, C. W., Doerr, T. M., Luna, I. Y., Joshua, G., Shen, S. R., Fu, X., et al. (2016). Minimally Invasive Transforaminal Lumbar Interbody Fusion Using Expandable Technology: A Clinical and Radiographic Analysis of 50 Patients. *World Neurosurg.* 90, 228–235. doi:10.1016/j.wneu.2016.02.075

Kim, J., Lin, B., Kim, S., Choi, B., Evseenko, D., and Lee, M. (2015). TGF-β1 Conjugated Chitosan Collagen Hydrogels Induce Chondrogenic Differentiation of Human Synovium-Derived Stem Cells. *J. Biol. Eng.* 9 (1), 1. doi:10.1186/1754-1611-9-1

Knutsen, A. R., Borkowski, S. L., Ebramzadeh, E., Flanagan, C. L., Hollister, S. J., and Sangiorgio, S. N. (2015). Static and Dynamic Fatigue Behavior of Topology Designed and Conventional 3D Printed Bioresorbable PCL Cervical Interbody Fusion Devices. *J. Mech. Behav. Biomed. Mater.* 49, 332–342. doi:10.1016/j.jmbbm.2015.05.015

Kong, J., Ma, J., Wu, Z., Wang, H., Peng, X., Wang, S., et al. (2020). Minimally Invasive Injectable Lumbar Interbody Fusion with Mineralized Collagen-Modified PMMA Bone Cement: A New Animal Model. *J. Appl. Biomater. Funct. Mater* 18, 2280800020903630. doi:10.1177/2280800020903630

Krafft, P. R., Osburn, B., Vivas, A. C., Rao, G., and Alikhani, P. (2019). Novel Titanium Cages for Minimally Invasive Lateral Lumbar Interbody Fusion: First Assessment of Subsidence. *Spine Surg. Relat. Res.* 4 (2), 171–177. doi:10.22603/ssrr.2019-0089

Krafft, P. R., Osburn, B., Vivas, A. C., Rao, G., and Alikhani, P. (2020). Novel Titanium Cages for Minimally Invasive Lateral Lumbar Interbody Fusion: First Assessment of Subsidence. *Spine Surg. Relat. Res.* 4 (2), 171–177. doi:10.22603/ssrr.2019-0089

Krayenbühl, N., Schneider, C., Landolt, H., and Fandino, J. (2008). Use of an Empty, Plasmapore-Covered Titanium Cage for Interbody Fusion after Anterior Cervical Microdiscectomy. *J. Clin. Neurosci.* 15 (1), 11–17. doi:10.1016/j.jocn.2006.12.011

Lee, J. H., Kong, C.-B., Yang, J. J., Shim, H.-J., Koo, K.-H., Kim, J., et al. (2016). Comparison of Fusion Rate and Clinical Results between CaO-SiO2-P2o5-B2o3 Bioactive Glass Ceramics Spacer with Titanium Cages in Posterior Lumbar Interbody Fusion. *Spine J.* 16 (11), 1367–1376. doi:10.1016/j.spinee.2016.07.531

Leng, Y., Ren, G., Cui, Y., Peng, C., Wang, J., Wu, D., et al. (2020). Platelet-rich Plasma-Enhanced Osseointegration of Decellularized Bone Matrix in Critical-Size Radial Defects in Rabbits. *Ann. Transl. Med.* 8 (5), 198. doi:10.21037/atm.2020.01.53

Liang, X., Li, F., Gong, X., Li, J., Li, S. Q., Liu, Z., et al. (2020). *In Vivo* evaluation of Porous Nanohydroxyapatite/polyamide 66 Struts in a Goat Cervical Fusion Model. *Sci. Rep.* 10 (1), 10495. doi:10.1038/s41598-020-65341-1

Liao, J. C., Niu, C. C., Chen, W. J., and Chen, L. H. (2008). Polyetheretherketone (PEEK) Cage Filled with Cancellous Allograft in Anterior Cervical Discectomy and Fusion. *Int. Orthop.* 32 (5), 643–648. doi:10.1007/s00264-007-0378-x

Lim, K.-M., Park, T.-H., Lee, S.-J., and Park, S.-J. (2019). Design and Biomechanical Verification of Additive Manufactured Composite Spinal Cage Composed of Porous Titanium Cover and PEEK Body. *Appl. Sci.* 9 (20), 4258. doi:10.3390/app9204258

Liu, H., Li, W., Liu, C., Tan, J., Wang, H., Hai, B., et al. (2016). Incorporating Simvastatin/poloxamer 407 Hydrogel into 3D-Printed Porous Ti6Al4V Scaffolds for the Promotion of Angiogenesis, Osseointegration and Bone Ingrowth. *Biofabrication* 8 (4), 045012. doi:10.1088/1758-5090/8/4/045012

Liu, X., Han, F., Zhao, P., Lin, C., Wen, X., and Ye, X. (2017). Layer-by-layer Self-Assembled Multilayers on PEEK Implants Improve Osseointegration in an Osteoporosis Rabbit Model. *Nanomedicine Nanotechnol. Biol. Med.* 13 (4), 1423–1433. doi:10.1016/j.nano.2017.01.011

Lowery, G. L., Kulkarni, S., and Pennisi, A. E. (1999). Use of Autologous Growth Factors in Lumbar Spinal Fusion. *Bone* 25 (2), 47s–50s. doi:10.1016/s8756-3282(99)00132-5

Lu, C., Qian, C., Li-Bo, J., Xiao-Fan, Y., Chong, B., Hui-Ren, W., et al. (2017). Bioabsorbable Self-Retaining PLA/nano-sized β-TCP Cervical Spine Interbody Fusion Cage in Goat Models: An *In Vivo* Study. *Int. J. Nanomedicine* 12, 7197–7205.

Lu, M., Xu, S., Lei, Z.-X., Lu, D., Cao, W., Huttula, M., et al. (2019). Application of a Novel Porous Tantalum Implant in Rabbit Anterior Lumbar Spine Fusion Model. *Chin. Med. J.* 132 (1), 51–62. doi:10.1097/cm9.0000000000000030

MacBarb, R. F., Lindsey, D. P., Bahney, C. S., Woods, S. A., Wolfe, M. L., and Yerby, S. A. (2017). Fortifying the Bone-Implant Interface Part 1: An *In Vitro* Evaluation of 3D-Printed and TPS Porous Surfaces. *Int. J. Spine Surg.* 11, 15. doi:10.14444/4015

Madan, S., and Boeree, N. R. (2003). Outcome of the Graf Ligamentoplasty Procedure Compared with Anterior Lumbar Interbody Fusion with the Hartshill Horseshoe Cage. *Eur. Spine J.* 12 (4), 361–368. doi:10.1007/s00586-002-0488-5

Marx, D., Rahimnejad Yazdi, A., Papini, M., and Towler, M. (2020). A Review of the Latest Insights into the Mechanism of Action of Strontium in Bone. *Bone Rep.* 12, 100273. doi:10.1016/j.bonr.2020.100273

May, R. D., Frauchiger, D. A., Albers, C. E., Tekari, A., Benneker, L. M., Klenke, F. M., et al. (2019). Application of Cytokines of the Bone Morphogenetic Protein (BMP) Family in Spinal Fusion - Effects on the Bone, Intervertebral Disc and Mesenchymal Stromal Cells. *Cscr* 14 (8), 618–643. doi:10.2174/1574888x14666190628103528

McGilvray, K. C., Easley, J., Seim, H. B., Regan, D., Berven, S. H., Hsu, W. K., et al. (2018). Bony Ingrowth Potential of 3D-Printed Porous Titanium Alloy: a Direct Comparison of Interbody Cage Materials in an *In Vivo* Ovine Lumbar Fusion Model. *Spine J.* 18 (7), 1250–1260. doi:10.1016/j.spinee.2018.02.018

McGilvray, K. C., Waldorff, E. I., Easley, J., Seim, H. B., Zhang, N., Linovitz, R. J., et al. (2017). Evaluation of a Polyetheretherketone (PEEK) Titanium Composite Interbody Spacer in an Ovine Lumbar Interbody Fusion Model: Biomechanical, Microcomputed Tomographic, and Histologic Analyses. *Spine J.* 17 (12), 1907–1916. doi:10.1016/j.spinee.2017.06.034

Meisel, H. J., Schnöring, M., Hohaus, C., Minkus, Y., Beier, A., Ganey, T., et al. (2008). Posterior Lumbar Interbody Fusion Using rhBMP-2. *Eur. Spine J.* 17 (12), 1735–1744. doi:10.1007/s00586-008-0799-2

Michielsen, J., Sys, J., Rigaux, A., and Bertrand, C. (2013). The Effect of Recombinant Human Bone Morphogenetic Protein-2 in Single-Level Posterior Lumbar Interbody Arthrodesis. *J. Bone Jt. Surgery-American* 95 (10), 873–880. doi:10.2106/jbjs.l.00137

Mobbs, R. J., Parr, W. C. H., Choy, W. J., McEvoy, A., Walsh, W. R., and Phan, K. (2019). Anterior Lumbar Interbody Fusion Using a Personalized Approach: Is Custom the Future of Implants for Anterior Lumbar Interbody Fusion Surgery? *World Neurosurg.* 124, 452–458. doi:10.1016/j.wneu.2018.12.144

Mokawem, M., Katzouraki, G., Harman, C. L., and Lee, R. (2019). Lumbar Interbody Fusion Rates with 3D-Printed Lamellar Titanium Cages Using a Silicate-Substituted Calcium Phosphate Bone Graft. *J. Clin. Neurosci.* 68, 134–139. doi:10.1016/j.jocn.2019.07.011

Niu, J., Sun, Z., Chang, H., and Zhou, L. (2019). Review on 3D Printing of Biomedical Titanium Alloy. *Rare Metal Materials and Engineering* 48 (5), 1697–1706.

Ohanisian, L., and Dorsi, M. J. (2019). A Novel 3D Printed Titanium Implant for Anterior Cervical Discectomy and Fusion. *Cureus* 11 (1), e3952. doi:10.7759/cureus.3952

Okada, R., Kaito, T., Ishiguro, H., Kushioka, J., Otsuru, S., Kanayama, S., et al. (2020). Assessment of Effects of rhBMP-2 on Interbody Fusion with a Novel Rat Model. *Spine J.* 20 (5), 821–829. doi:10.1016/j.spinee.2019.12.014

Pan, H. C., Lee, S., Ting, K., Shen, J., Wang, C., Nguyen, A., et al. (2017). Cyst-Like Osteolytic Formations in Recombinant Human Bone Morphogenetic Protein-2 (rhBMP-2) Augmented Sheep Spinal Fusion. *Am. J. Pathology* 187 (7), 1485–1495. doi:10.1016/j.ajpath.2017.03.010

Park, H.-W., Lee, J.-K., Moon, S.-J., Seo, S.-K., Lee, J.-H., and Kim, S.-H. (2009). The Efficacy of the Synthetic Interbody Cage and Grafton for Anterior Cervical Fusion. *Spine* 34 (17), E591–E595. doi:10.1097/brs.0b013e3181ab8b9a

Park, P. J., and Lehman, R. A. (2020). Optimizing the Spinal Interbody Implant: Current Advances in Material Modification and Surface Treatment Technologies. *Curr. Rev. Musculoskelet. Med.* 13 (6), 688–695. doi:10.1007/s12178-020-09673-5

Phan, K., and Mobbs, R. J. (2016). Evolution of Design of Interbody Cages for Anterior Lumbar Interbody Fusion. *Orthop. Surg.* 8 (3), 270–277. doi:10.1111/os.12259

Pisecky, L., Luger, M., Klasan, A., Gotterbarm, T., Klotz, M. C., and Hochgatterer, R. (2021). Bioabsorbable Implants in Forefoot Surgery: a Review of Materials, Possibilities and Disadvantages. *Efort Open Rev.* 6 (12), 1132–1139. doi:10.1302/2058-5241.6.200157

Qiao, S. C., Sheng, Q. B., Li, Z. H., Wu, D. L., Zhu, Y., Lai, H. C., et al. (2020). 3D-printed Ti6Al4V Scaffolds Coated with Freeze-Dried Platelet-Rich Plasma as Bioactive Interface for Enhancing Osseointegration in Osteoporosis. *Mater. Des.* 194. doi:10.1016/j.matdes.2020.108825

Rao, P. J., Pelletier, M. H., Walsh, W. R., and Mobbs, R. J. (2014). Spine Interbody Implants: Material Selection and Modification, Functionalization and Bioactivation of Surfaces to Improve Osseointegration. *Orthop. Surg.* 6 (2), 81–89. doi:10.1111/os.12098

Ren, C., Song, Y., Xue, Y., Yang, X., and Zhou, C. (2017). Evaluation of Bioabsorbable Multiamino Acid Copolymer/Nanohydroxyapatite/Calcium Sulfate Cage in a Goat Spine Model. *World Neurosurg.* 103, 341–347. doi:10.1016/j.wneu.2017.04.005

Rieger, B., Jiang, H., Reinshagen, C., Molcanyi, M., Zivcak, J., Grönemeyer, D., et al. (2017). Effects of Preoperative Simulation on Minimally Invasive Hybrid Lumbar Interbody Fusion. *World Neurosurg.* 106, 578–588. doi:10.1016/j.wneu.2017.06.184

Rodrigues, T. A., Freire, A. O., Bonfim, B. F., Cartágenes, M. S. S. S., and Garcia, J. B. S. (2018). Strontium Ranelate as a Possible Disease-Modifying Osteoarthritis Drug: a Systematic Review. *Braz J. Med. Biol. Res.* 51 (8), e7440. doi:10.1590/1414-431x20187440

Rodríguez-Vázquez, M., and Ramos-Zúñiga, R. (2020). Chitosan-Hydroxyapatite Scaffold for Tissue Engineering in Experimental Lumbar Laminectomy and Posterolateral Spinal Fusion in Wistar Rats. *Asian Spine J.* 14 (2), 139–147. doi:10.31616/asj.2019.0091

Sasso, R. C., Kitchel, S. H., and Dawson, E. G. (2004). A Prospective, Randomized Controlled Clinical Trial of Anterior Lumbar Interbody Fusion Using a Titanium Cylindrical Threaded Fusion Device. *Spine* 29 (2), 113–121. doi:10.1097/01.brs.0000107007.31714.77

Scardueli, C. R., Bizelli-Silveira, C., Marcantonio, R. A. C., Marcantonio, E., Stavropoulos, A., and Spin-Neto, R. (2018). Systemic Administration of Strontium Ranelate to Enhance the Osseointegration of Implants: Systematic Review of Animal Studies. *Int. J. Implant Dent.* 4 (1), 21. doi:10.1186/s40729-018-0132-8

Schnitzer, M., Hudák, R., Sedlačko, P., Rajťúková, V., Findrik Balogová, A., Živčák, J., et al. (2020). A Comparison of Experimental Compressive Axial Loading Testing with a Numerical Simulation of Topologically Optimized Cervical Implants Made by Selective Laser Melting. *J. Biotechnol.* 322, 33–42. doi:10.1016/j.jbiotec.2020.07.010

Scholz, M., Schleicher, P., Eindorf, T., Friedersdorff, F., Gelinsky, M., König, U., et al. (2010). Cages Augmented with Mineralized Collagen and Platelet-Rich Plasma as an Osteoconductive/inductive Combination for Interbody Fusion. *Spine* 35 (7), 740–746. doi:10.1097/brs.0b013e3181bdc6cc

Seaman, S., Kerezoudis, P., Bydon, M., Torner, J. C., and Hitchon, P. W. (2017). Titanium vs. Polyetheretherketone (PEEK) Interbody Fusion: Meta-Analysis and Review of the Literature. *J. Clin. Neurosci.* 44, 23–29. doi:10.1016/j.jocn.2017.06.062

Sekerci, Z., Uğur, A., Ergün, R., and Sanli, M. (2013). Early Changes in the Cervical Foraminal Area after Anterior Interbody Fusion with Polyetheretherketone (PEEK) Cage Containing Synthetic Bone Particulate: a Prospective Study of 20 Cases. *Neurol. Res.* 28 (5), 568–571. doi:10.1179/016164106X110382

Serra, T., Capelli, C., Toumpaniari, R., Orriss, I. R., Leong, J. J., Dalgarno, K., et al. (2016). Design and Fabrication of 3D-Printed Anatomically Shaped Lumbar Cage for Intervertebral Disc (IVD) Degeneration Treatment. *Biofabrication* 8 (3), 035001. doi:10.1088/1758-5090/8/3/035001

Sethi, A., Craig, J., Bartol, S., Chen, W., Jacobson, M., Coe, C., et al. (2011). Radiographic and CT Evaluation of Recombinant Human Bone Morphogenetic Protein-2-Assisted Spinal Interbody Fusion. *Am. J. Roentgenol.* 197 (1), W128–W133. doi:10.2214/ajr.10.5484

Shiga, Y., Orita, S., Kubota, G., Kamoda, H., Yamashita, M., Matsuura, Y., et al. (2016). Freeze-Dried Platelet-Rich Plasma Accelerates Bone Union with Adequate Rigidity in Posterolateral Lumbar Fusion Surgery Model in Rats. *Sci. Rep.* 6, 36715. doi:10.1038/srep36715

Siu, T. L., Rogers, J. M., Lin, K., Thompson, R., and Owbridge, M. (2018). Custom-Made Titanium 3-Dimensional Printed Interbody Cages for Treatment of Osteoporotic Fracture-Related Spinal Deformity. *World Neurosurg.* 111, 1–5. doi:10.1016/j.wneu.2017.11.160

Smoljanovic, T., Bojanic, I., and Vlahovic, Z. (2010). Safety of Posterior Interbody Fusions of the Lumbar Spine Using rhBMP-2. *J. Spinal Disord. Tech.* 23 (1), 78. doi:10.1097/bsd.0b013e3181c1474d

Sochacki, K. R., Safran, M. R., Abrams, G. D., Donahue, J., Chu, C., and Sherman, S. L. (2020). Platelet-Rich Plasma Augmentation for Isolated Arthroscopic Meniscal Repairs Leads to Significantly Lower Failure Rates: A Systematic Review of Comparative Studies. *Orthop. J. Sports Med.* 8 (11), 2325967120964534. doi:10.1177/2325967120964534

Song, C., Guo, Z., Ma, Q., Chen, Z., Liu, Z., Jia, H., et al. (2003). Simvastatin Induces Osteoblastic Differentiation and Inhibits Adipocytic Differentiation in Mouse Bone Marrow Stromal Cells. *Biochem. Biophysical Res. Commun.* 308 (3), 458–462. doi:10.1016/s0006-291x(03)01408-6

Staiger, M. P., Pietak, A. M., Huadmai, J., and Dias, G. (2006). Magnesium and its Alloys as Orthopedic Biomaterials: A Review. *Biomaterials* 27 (9), 1728–1734. doi:10.1016/j.biomaterials.2005.10.003

Tan, J., Yang, N., Fu, X., Cui, Y., and Song, C. (2015). Single-Dose Local Simvastatin Injection Improves Implant Fixation via Increased Angiogenesis and Bone Formation in an Ovariectomized Rat Model. *Med. Sci. Monit.* 21, 1428–1439. doi:10.12659/MSM.892247

Tan, K. H., Chua, C. K., Leong, K. F., Naing, M. W., and Cheah, C. M. (2005). Fabrication and Characterization of Three-Dimensional Poly(ether-Ether-Ketone)/-Hydroxyapatite Biocomposite Scaffolds Using Laser Sintering. *Proc. Inst. Mech. Eng. H.* 219 (3), 183–194. doi:10.1243/095441105x9345

Thomas, M. V., and Puleo, D. A. (2010). Calcium Sulfate: Properties and Clinical Applications. *J. Biomed. Mater Res. B Appl. Biomater.* 88 (2), 597–610. doi:10.1002/jbm.b.31269

Topuz, K., Çolak, A., Kaya, S., Şimşek, H., Kutlay, M., Demircan, M. N., et al. (2009). Two-level Contiguous Cervical Disc Disease Treated with Peek Cages Packed with Demineralized Bone Matrix: Results of 3-year Follow-Up. *Eur. Spine J.* 18 (2), 238–243. doi:10.1007/s00586-008-0869-5

Tsai, T. T., Tai, C. L., Ho, N. Y., Lai, P. L., Fu, T. S., Niu, C. C., et al. (2017). Effects of Strontium Ranelate on Spinal Interbody Fusion Surgery in an Osteoporotic Rat Model. *Plos One* 12 (1), e0167296. doi:10.1371/journal.pone.0167296

Ulum, M. F., Caesarendra, W., Alavi, R., and Hermawan, H. (2019). *In-Vivo* Corrosion Characterization and Assessment of Absorbable Metal Implants. *Coatings* 9 (5), 282. doi:10.3390/coatings9050282

Vanek, P., Bradac, O., Delacy, P., Saur, K., Belsan, T., and Benes, V. (2012). Comparison of 3 Fusion Techniques in the Treatment of the Degenerative Cervical Spine Disease. Is Stand-Alone Autograft Really the "Gold Standard?". *Spine* 37 (19), 1645–1651. doi:10.1097/brs.0b013e31825413fe

Veillette, C. J. H., Mehdian, H., Schemitsch, E. H., and McKee, M. D. (2006). Survivorship Analysis and Radiographic Outcome Following Tantalum Rod Insertion for Osteonecrosis of the Femoral Head. *J. Bone Jt. Surgery-American Volume* 88, 48–55. doi:10.2106/00004623-200611001-00008

Verma, R., Virk, S., and Qureshi, S. (2020). Interbody Fusions in the Lumbar Spine: A Review. *HSS Jrnl* 16 (2), 162–167. doi:10.1007/s11420-019-09737-4

Virk, S. S., Coble, D., Bertone, A. L., Hussein, H. H., and Khan, S. N. (2017). Experimental Design and Surgical Approach to Create a Spinal Fusion Model in a New Zealand White Rabbit (*Oryctolagus cuniculus*). *J. Invest. Surg.* 30 (4), 226–234. doi:10.1080/08941939.2016.1235748

Walsh, W. R., Pelletier, M. H., Bertollo, N., Christou, C., and Tan, C. (2016). Does PEEK/HA Enhance Bone Formation Compared with PEEK in a Sheep Cervical Fusion Model? *Clin. Orthop. Relat. Res.* 474 (11), 2364–2372. doi:10.1007/s11999-016-4994-x

Walsh, W. R., Pelletier, M. H., Christou, C., He, J., Vizesi, F., and Boden, S. D. (2018). The *In Vivo* Response to a Novel Ti Coating Compared with Polyether Ether Ketone: Evaluation of the Periphery and Inner Surfaces of an Implant. *Spine J.* 18 (7), 1231–1240. doi:10.1016/j.spinee.2018.02.017

Walsh, W. R., Pelletier, M. H., Wang, T., Lovric, V., Morberg, P., and Mobbs, R. J. (2019). Does Implantation Site Influence Bone Ingrowth into 3D-Printed Porous Implants? *Spine J.* 19 (11), 1885–1898. doi:10.1016/j.spinee.2019.06.020

Wang, J. L., Xu, J. K., Hopkins, C., Chow, D. H., and Qin, L. (2020). Biodegradable Magnesium-Based Implants in Orthopedics-A General Review and Perspectives. *Adv. Sci. (Weinh)* 7 (8), 1902443. doi:10.1002/advs.201902443

Wang, Y., Wei, R., Subedi, D., Jiang, H., Yan, J., and Li, J. (2020). Tantalum Fusion Device in Anterior Cervical Discectomy and Fusion for Treatment of Cervical Degeneration Disease. *Clin. Spine Surg.* 33 (3), 111–119. doi:10.1097/bsd.0000000000000875

Warburton, A., Girdler, S. J., Mikhail, C. M., Ahn, A., and Cho, S. K. (2019). Biomaterials in Spinal Implants: A Review. *Neurospine* 17 (1), 101–110. doi:10.14245/ns.1938296.148

Warren, J. M., Mazzoleni, A. P., and Hey, L. A. (2020). Development and Validation of a Computationally Efficient Finite Element Model of the Human Lumbar Spine: Application to Disc Degeneration. *Int. J. Spine Surg.* 14 (4), 502–510. doi:10.14444/7066

Wessels, V., Mené, G. L., Fischerauer, S. F., Kraus, T., Weinberg, A. M., Uggowitzer, P. J., et al. (2012). *In Vivo* Performance and Structural Relaxation of Biodegradable Bone Implants Made from Mg Zn Ca Bulk Metallic Glasses. *Adv. Eng. Mater.* 14 (6), B357–B364. doi:10.1002/adem.201180200

Wheeler, D. L., Fredericks, D. C., Dryer, R. F., and Bae, H. W. (2016). Allogeneic Mesenchymal Precursor Cells (MPCs) Combined with an Osteoconductive Scaffold to Promote Lumbar Interbody Spine Fusion in an Ovine Model. *Spine J.* 16 (3), 389–399. doi:10.1016/j.spinee.2015.08.019

Xie, Y., Li, H., Yuan, J., Fu, L., Yang, J., and Zhang, P. (2015). A Prospective Randomized Comparison of PEEK Cage Containing Calcium Sulphate or Demineralized Bone Matrix with Autograft in Anterior Cervical Interbody Fusion. *Int. Orthop. (SICOT)* 39 (6), 1129–1136. doi:10.1007/s00264-014-2610-9

Xing, H., Lee, H., Luo, L., and Kyriakides, T. R. (2020). Extracellular Matrix-Derived Biomaterials in Engineering Cell Function. *Biotechnol. Adv.* 42, 107421. doi:10.1016/j.biotechadv.2019.107421

Yang, S., Yu, Y., Liu, X., Hou, Z. T., Xu, J., Wu, W., et al. (2019). Clinical and Radiological Results Comparison of Allograft and Polyetheretherketone Cage for One to Two-Level Anterior Cervical Discectomy and Fusion: A CONSORT-Compliant Article. *Med. Baltim.* 98 (45), e17935. doi:10.1097/MD.0000000000017935

Zardiackas, L. D., Parsell, D. E., Dillon, L. D., Mitchell, D. W., Nunnery, L. A., and Poggie, R. (2001). Structure, Metallurgy, and Mechanical Properties of a Porous Tantalum Foam. *J. Biomed. Mat. Res.* 58 (2), 180–187. doi:10.1002/1097-4636(2001)58:2<180::aid-jbm1005>3.0.co;2-5

Zhang, F., Xu, H., Wang, H., Geng, F., Ma, X., Shao, M., et al. (2018). Quantitative Analysis of Near-Implant Magnesium Accumulation for a Si-Containing Coated AZ31 Cage from a Goat Cervical Spine Fusion Model. *BMC Musculoskelet. Disord.* 19, 105. doi:10.1186/s12891-018-2027-5

Zhang, W., Sun, C., Zhu, J., Zhang, W., Leng, H., and Song, C. (2020a). 3D Printed Porous Titanium Cages Filled with Simvastatin Hydrogel Promotes Bone Ingrowth and Spinal Fusion in Rhesus Macaques. *Biomater. Sci.* 8 (15), 4147–4156. doi:10.1039/d0bm00361a

Zhang, W., Sun, C., Zhu, J., Zhang, W., Leng, H., and Song, C. (2020b). 3D Printed Porous Titanium Cages Filled with Simvastatin Hydrogel Promotes Bone Ingrowth and Spinal Fusion in Rhesus Macaques. *Biomaterials Sci.* 8 (15), 4147–4156. doi:10.1039/d0bm00361a

Zhang, Y., Xu, J., Ruan, Y. C., Yu, M. K., O'Laughlin, M., Wise, H., et al. (2016). Implant-derived Magnesium Induces Local Neuronal Production of CGRP to Improve Bone-Fracture Healing in Rats. *Nat. Med.* 22 (10), 1160–1169. doi:10.1038/nm.4162

Zhang, Z., Li, H., Fogel, G. R., Xiang, D., Liao, Z., and Liu, W. (2018). Finite Element Model Predicts the Biomechanical Performance of Transforaminal Lumbar Interbody Fusion with Various Porous Additive Manufactured Cages. *Comput. Biol. Med.* 95, 167–174. doi:10.1016/j.compbiomed.2018.02.016

Zhao, R., Yang, R., Cooper, P. R., Khurshid, Z., Shavandi, A., and Ratnayake, J. (2021). Bone Grafts and Substitutes in Dentistry: A Review of Current Trends and Developments. *Molecules* 26 (10), 3007. doi:10.3390/molecules26103007

Zhao, S., Wen, F., He, F., Liu, L., and Yang, G. (2014). *In Vitro* and *In Vivo* Evaluation of the Osteogenic Ability of Implant Surfaces with a Local Delivery of Simvastatin. *Int. J. Oral Maxillofac. Implants* 29 (1), 211–220. doi:10.11607/jomi.3147

Zippelius, T., Strube, P., Suleymanov, F., Putzier, M., and Hölzl, A. (2018). *Sicherheit und Effektivität eines in Electron-Beam-Melting-Technik hergestellten Titan-Mesh-Cages zur intersomatischen lumbalen Fusion; Safety and efficacy of an electron beam melting technique-manufactured titanium mesh cage for lumbar interbody fusion*. Der Orthopäde.

Conflict of Interest: The authors declare that the research was conducted in the absence of any commercial or financial relationships that could be construed as a potential conflict of interest.

Publisher's Note: All claims expressed in this article are solely those of the authors and do not necessarily represent those of their affiliated organizations, or those of the publisher, the editors and the reviewers. Any product that may be evaluated in this article, or claim that may be made by its manufacturer, is not guaranteed or endorsed by the publisher.

frontiers | Frontiers in Bioengineering and Biotechnology

ORIGINAL RESEARCH
published: 20 May 2022
doi: 10.3389/fbioe.2022.916334

Total Talar Replacement With Custom-Made Vitallium Prosthesis for Talar Avascular Necrosis

Wenbin Luo†, Hanyang Zhang†, Qing Han, Zhaoyan Li, Zhuan Zhong, Guoliang Jia, Yuxuan Liu, Fei Chang and Jincheng Wang**

Department of Orthopedics, The Second Hospital of Jilin University, Changchun, China

Background: The current study investigated the application of three-dimensional (3D) printing technology in the treatment of talar avascular necrosis (TAN). Custom-made Vitallium talar prostheses were designed and generated *via* 3D printing. We hypothesized that these talar prostheses would facilitate more stable positioning, better ergonomically fit the ankle joint surfaces, and promote favorable long-term prognoses.

Material and Methods: Computed tomography scans of both ankle joints were acquired from three patients diagnosed with TAN. The talar on the unaffected side was used as the design blueprint. Hence, with the aid of 3D printing technology a customized talar prosthesis made from a novel Vitallium alloy could be manufactured for each individual patient.

Results: In all three cases there were no signs of prosthesis loosening or substantial degenerative change in the surrounding area of the joint, but small osteophytes were observed on the tibial side and navicular side. No chronic infection or other prosthesis-related complications were observed in any of the patients. All three were able to walk without pain at the most recent follow-up.

Conclusion: With the aid of 3D printing and a novel Vitallium alloy, total talar replacement achieved encouraging results in 3/3 patients. All patients were satisfied with their joint function, and were able to return to their daily activities without limitations. Although more cases and longer-term follow-up periods are required, the success rate reported herein is encouraging.

Keywords: total talar replacement, 3D printing, talar avascular necrosis, Interface structure design, bionic prosthesis Interface

OPEN ACCESS

Edited by:
Jianxun Ding,
Changchun Institute of Applied Chemistry (CAS), China

Reviewed by:
Yong Hu,
The Second Hospital of Shandong University, China
Maowei Yang,
The First Affiliated Hospital of China Medical University, China

****Correspondence:***
Fei Chang
ccfei_cn@hotmail.com
Jincheng Wang
jinchengwang2015@gmail.com

†These authors have contributed equally to this work

Specialty section:
This article was submitted to Biomaterials, a section of the journal Frontiers in Bioengineering and Biotechnology

Received: *09 April 2022*
Accepted: *02 May 2022*
Published: *20 May 2022*

Citation:
Luo W, Zhang H, Han Q, Li Z, Zhong Z, Jia G, Liu Y, Chang F and Wang J (2022) Total Talar Replacement With Custom-Made Vitallium Prosthesis for Talar Avascular Necrosis. Front. Bioeng. Biotechnol. 10:916334. doi: 10.3389/fbioe.2022.916334

BACKGROUND

The talus is a bone with five articulating surfaces, and nearly 60% of its surface is covered with articular cartilage. It plays a vital role in the daily functioning of the ankle joint. (Lee et al., 2020) Because the majority of the talus' surfaces are in seamless contact with surrounding bones, the blood supply provided by its remaining bone surface is very fragile and extremely sensitive to injury and other systemic processes that impede blood flow. (Gelberman and Mortensen, 1983) Therefore, talar avascular necrosis (TAN) has been a great challenge for foot and ankle specialists. Treatments for end-stage diseases causing TAN such as advanced ankle arthritis and ankle osteomyelitis remain

limited. Treatment options include talus resection, total ankle arthrodesis, total ankle arthroplasty, and below-knee amputation. (Parekh and Kadakia, 2021) Generally ankle joint fusion surgery can provide a stable joint for daily activities, with acceptable follow-up results. In patients with bilaterally affected ankle joints however, ankle arthrodesis in both joints often leads to deterioration of joint function in association with activities such as climbing stairs, getting out of a chair, walking on uneven surfaces, and running wherein flexion and extension of the ankle joints are needed, resulting in poor long-term follow-up results. (Hintermann et al., 2009; Bussewitz et al., 2014; Schuberth et al., 2020) Fusion surgery is also associated with long recovery times, and a proportion of patients exhibit compromised bone healing. (Fragomen et al., 2012) Total ankle replacement (TAR) is another viable treatment option for such ankle diseases, but unfortunately complications of TAR such as component loosening, subsidence, and collapse limit long-term prognoses. Hence, more optimized options should be considered.

Total talar replacement (TTR) has recently received increased attention from foot and ankle specialists as an alternative treatment method in select cases. Since the first reported case in 2010, (Tsukamoto et al., 2010) TTR has achieved satisfactory outcomes in the treatment of talus necrosis and severe crush fracture. (Angthong, 2014; Taniguchi and Tanaka, 2019) Due to the unique anatomic form of the talus, the vital element for a successful prosthetic TTR is the congruency of the custom-made implant with the adjacent joints. (Mu et al., 2021) Despite the rapid development of TTR prostheses however, full reconstruction of the anatomic features of a native talus—which would optimally stabilize and maintain normal ankle function—remains a challenge. (Ando et al., 2016) Three-dimensional (3D) printing technology integrated with computed tomography (CT) imaging and computer-aided design has now been widely used in surgical planning and custom-made implant design, to achieve anatomic accuracy in talar prosthetic design and production. (Akoh et al., 2020; Mu et al., 2021) 3D printing has shown tremendous potential for the design and production of refined structures with irregular shapes and free surfaces such as the talar body. Thus, the utilization of 3D printing technology in conjunction with TTR may be a promising way for surgeons to provide more personalized, anatomically accurate, and above all more durable surgical solutions with better long-term prognoses.

The current study investigated a prosthetic design and production process incorporating a combination of computer-aided design and 3D printing technology. Using the process, three patients with idiopathic talar necrosis were treated *via* TTR with a Vitallium prosthesis. We hypothesized that these 3D-printed prostheses would facilitate more stable positioning, better ergonomically fit the ankle joint surfaces, and promote favorable long-term prognoses.

MATERIAL AND METHODS

Ethics Approval and Consent to Participate

This study was conducted in accordance with the principles outlined in the Declaration of Helsinki, and was approved by the Ethics Committee of the Second Hospital of Jilin University, China. Written informed consent to participate was obtained from all patients involved in the study. Patient data were kept anonymous to ensure confidentiality and privacy.

Patient Characteristics

Between 2015 and 2019 three women aged 45–58 years with idiopathic talar necrosis underwent TTR with custom-made Vitallium prostheses designed by our team. Physical examinations, visual analogue scale (VAS) pain scores, and American Orthopedic Foot and Ankle Society (AOFAS) scores were recorded. Weight-bearing, anteroposterior, and lateral-view x-rays and magnetic resonance imaging were performed to confirm each diagnosis (**Figure 1**). CT scans of affected and unaffected sides were performed to facilitate the design and production of the prostheses. Patient characteristics are listed in **Table 1**.

Data Acquisition and Image Processing

Bilateral ankle joint imaging data were acquired using a 64-slice spiral CT scanner (Philips Corporation, Japan; x-ray tube current 232 mA and KVP 120 kV, slice thickness 1 mm, reconstruction interval 1 mm).

Prosthesis Design and 3D Printing Process

DICOM files obtained *via* CT scanning were acquired from all patients. Both the normal and the lesion sides of the talus were reconstructed using Mimics 17.0 software (Materialise Inc., Belgium). The normal side's morphological features were considered the standard for the reconstruction of the talus prosthesis (**Figure 2**). For the patient with a bilaterally affected talus (case 3), according to previous research, the prosthesis design was based on the imaging data from the less distorted side to restore the initial shape of the talar. The 3D reconstructed model of the less affected talar was trimmed in CAD software, compared with the mirror images of both sides to recover the damaged lesion to the talar. (Taniguchi et al., 2012) The dimension parameters were readjustment according to the patient's height and weight condition collected by our team. (Han et al., 2019) The reconstructed 3D model was then smoothed and wrapped using Mimics. The standard template library model was exported into Geomagic Studio 12.0 (Geomagic Inc., United States). The talus was smoothed repeatedly during this process *via* automatic and manual methods, until the overall and local details were satisfactory. The standard template library model was mirrored and compared with the talus of the lesion side. The size was rescaled several times until the implant model was consistent with the affected side (**Figure 3**). The prosthesis model was then exported to Magics 13.0 software (Materialise) to be sliced for printing. Vitallium alloy was used for 3D printing, which was conducted with the aid of Arcam EBM Q10plus. The printed prosthesis' surfaces were then polished to reduce abrasion. Lastly the prosthesis was post-processed *via* ultrasonic cleaning, fine cleaning, and drying (**Figure 4A–4C**).

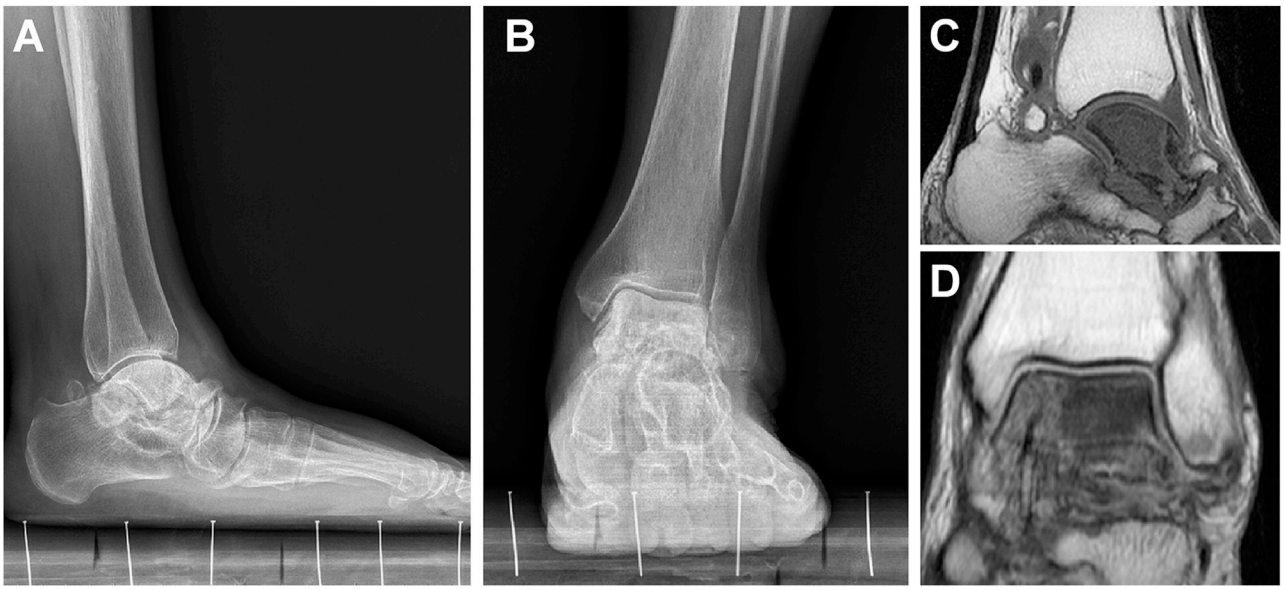

FIGURE 1 | Preoperative weight-bearing anteroposterior and lateral views of patient 1 **(A,B)**. TAN was confirmed by magnetic resonance imaging **(C,D)**.

TABLE 1 | Patient details.

Patient no.	1	2	3
Age/gender	58/F	45/F	46/F
Involved side	L	L	bilateral
Duration of symptoms (months)	24	18	12
Diagnosis	talar necrosis	talar necrosis	talar necrosis
Hospital stays (days)	6	7	6
Duration of follow-up (months)	78	52	29
	Preoperative		
AOFAS score	35	59	37 (L), 61 (R)
VAS score	7	6	9 (L), 6 (R)
	Last follow-up		
AOFAS score	89	98	82 (L), 85 (R)
VAS score	3	0	6 (L), 1 (R)

Surgical Procedure

TTR was performed in accordance with previous studies. (Ando et al., 2016) An anteromedial incision was made between the tibialis anterior and extensor hallucis longus tendons. The articular capsule and ligament attachment of the talus were dissected, and the talus was extracted. After the talus was removed the calcaneus was retracted by hand, and the prosthesis was fixed inside. The implant stabilized between the tibia, calcaneus, and navicular, and exhibited no instability when the ankle joint was moved. The wound was sutured using absorbable sutures (#2-0). Ligament reconstruction was not performed (**Figure 4D**). Postoperative radiography confirmed the position of the 3D printed talar prosthesis (**Figure 5**). Each patient was allowed to walk and bear weight with the help of a walking boot after 1 week. To enable the surrounding soft tissues to heal, ankle joint exercise was not permitted until 4 weeks after surgery. All three patients could walk without an orthosis 4 weeks after surgery.

Follow-Up

The patients were followed up at 6 months, 1 year, 3 years, and every 2 years after surgery. Weight-bearing, anteroposterior, and lateral view x-rays were taken to identify any signs of prosthesis loosening or degenerative change in the surrounding area of the joint. AOFAS and VAS scores, imaging, and videos of the patients in motion were recorded.

RESULTS

Effects of Surgery

In all patients, the TTR operation was completed without any intraoperative complications. The 3D printed prostheses fit the original talar positions precisely and were enveloped steadily by ligaments and soft tissues (**Table 1**). There were no signs of wound infection, skin necrosis, or other surgical complications. Motion ranges and ankle joint stability determinations are shown in **Table 1**.

Follow-Up Results

The patients were followed up for 29–78 months. The most recent follow-up scores are shown in **Table 1**. In all patients there were no signs of prosthesis loosening or serious degenerative change in the surrounding area of the joint, but small osteophytes were observed on the tibial side and navicular side. No chronic infection or other prosthesis-related complications were observed in any of the patients after a mean follow-up of 53 months (**Figure 6**). The mean functional follow-up scores (AOFAS) increased from 48.0 to 88.5. The sagittal motion scores increased to normal or mild restriction in two patients, as did inversion and extension functions. In all three patients, pain scores had decreased markedly at the most recent follow-up. All

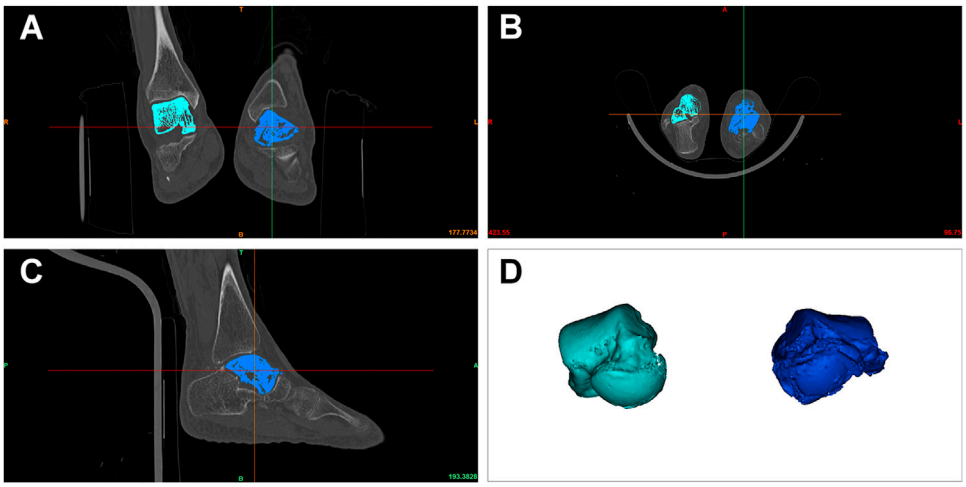

FIGURE 2 | DICOM files obtained *via* CT were processed using Mimics software. Bilateral talars were located based on CT data **(A–C)**, and three-dimensionally reconstructed **(D)**.

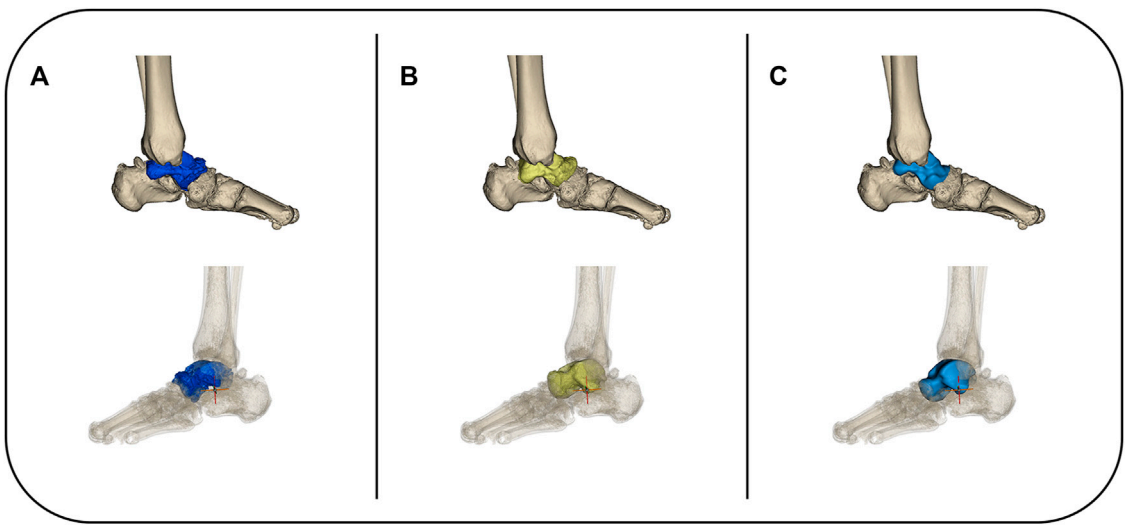

FIGURE 3 | The affected talar was three-dimensionally reconstructed **(A)** and replaced using a mirror of the unaffected side *in situ* **(B)**. The reconstructed 3D model was then smoothed and wrapped until the overall and local details were satisfactory **(C)**.

patients were able to return to their daily lives without any walking aids. Patient 1 was a 58 year-old female patient who presented with a complaint of pain and swelling of the left ankle for 2 years. The patient was unable to walk without the help of crutches. Before the surgery, the patient exhibited limited left ankle movement, dorsiflexion was recorded to be 0°, while plantar flexion was 15°. The AOFAS and VAS scores were 35 and 7, respectively. In the last follow-up, the dorsiflexion was recorded to be 30° and plantar flexion was 20°. The patient reported moderate pain that occasionally occurred in the affected planta pedis, leading to comparatively poor follow-up scores. That patient was later diagnosed with plantar fasciitis and treated *via* physical therapy, and her most recent VAS score indicates slight improvement. Patient 2 was a 45 year-old female patient with swelling and pain in the left ankle with limited movement for 18 months. Before the surgery, the dorsiflexion and plantar flexion of the left ankle was recorded to be about 20°. The AOFAS and VAS scores were 59 and 6, respectively. In the last follow-up, the joint movement had shown noticeable improvement. The pain in the left ankle was also completely relieved. Patient 3 was a 46 year-old female who complained of bilateral ankle pain with movement limitation for more than 1 year. The left AOFAS and VAS scores were 37 and 9, and the right AOFAS and VAS scores were 61 and 6 before the operation. The dorsiflexion was about 15° on both sides and the plantar flexion was about 25° on both sides. Patient 3 complained of

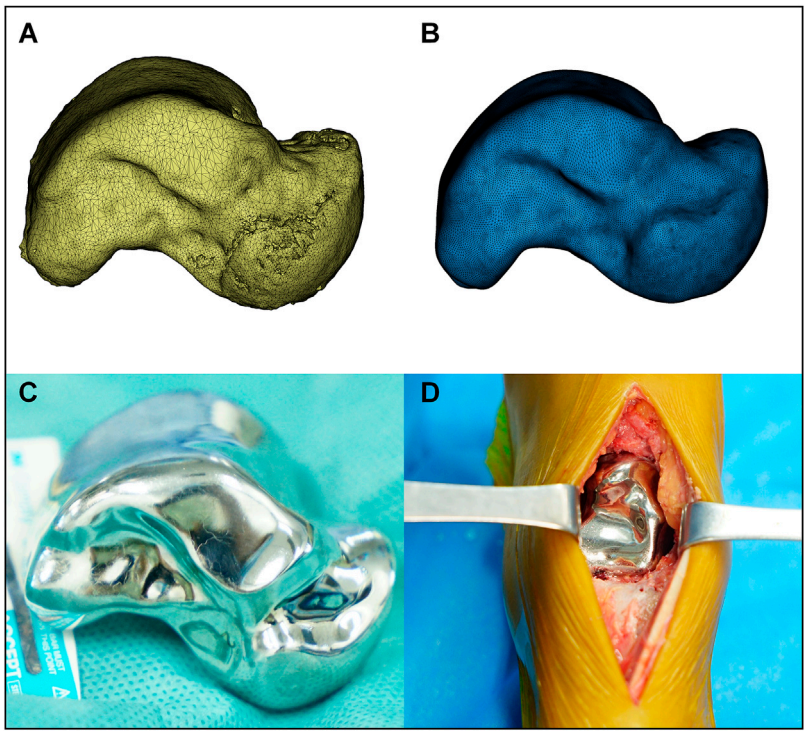

FIGURE 4 | The mirrored model of the unaffected talar was finely trimmed **(A,B)** then 3D printed *via* electron beam melting technology. The prosthesis' surfaces were then polished to reduce abrasion, and sterilized for clinical application **(C)**. TTR was performed in accordance with previously described studies **(D)**.

occasional pain in the left ankle while working. Physical examination revealed tingling and numbness occurred on the skin of the left ankle, which has led to an unsatisfied improvement in follow-up score. Indicating a potential injury of the cutaneous nerve. The patient refused our suggestion of neural block therapy. Meanwhile, the pain score in the most recent follow-up has slightly improved. Changes in this symptom remain to be observed.

DISCUSSION

Conservative treatment is not a viable option for terminal-stage TAN due to serious talar collapse and necrosis. Generally, small osteochondral lesions of the talus can be treated with core depression and bone grafting. All three patients in the current series had suffered severe damage to the whole articular surface and deformation of the talus however, therefore core depression and bone grafting were no longer suitable. Joint arthrodesis was also taken into consideration. The main drawbacks of ankle arthrodesis are stiffness and the effects of foot kinematics and ground reaction force progression of the foot, which can lead to degenerative osteoarthritis of the midtarsal joint due to pressure overload during walking. (Beyaert et al., 2004) Nonunion has been reported in approximately 10% of arthrodesis cases. (Haddad et al., 2007) Patient 1 would have had to receive tibio-talo-calcaneal arthrodesis, and the risk of nonunion would have been even greater. TAR was also an option to restore ankle function. Unfortunately, residual bone quality was relatively poor in all three patients, particularly with respect to potential progression of TAN, therefore there was a high associated risk of prosthesis loosening. In the present patients, TAR was only considered to be a salvage therapy at the present stage for patients with serious cartilage damage in the contralateral joint surface. While for patients with minor cartilage damage on the tibial plafond or calcaneal joint surface, reports of TTR did not consider this condition as a contraindication. (Taniguchi et al., 2015; Taniguchi and Tanaka, 2019; Yamamoto et al., 2021) This strategy was also seen in the studies of hemiarthroplasty of first metatarsophalangeal, in these cases, minor cartilage damages were commonly seen in the contralateral joint surface while the follow-up results noted excellent pain relief, high patient satisfaction, low reoperation rate, and no serious complications. (Butterworth and Ugrinich, 2019) Therefore, to avoid these limitations we opted for a custom-designed talar prosthesis, which provides multiple advantages such as negating specialized surgical techniques, reducing surgical trauma and postoperative complications, a relatively short recovery period, and preservation of joint function. At the most recent follow-ups, there were prominent improvements in joint function and quality of living, with no sign of prosthesis loosening or subsidence.

As a bony structure of the ankle joint, the talus is unique because it is devoid of any tendon or muscular attachments. The stability of the talus is maintained mainly by osseous and ligamentous structures. A thin cartilage profile measuring

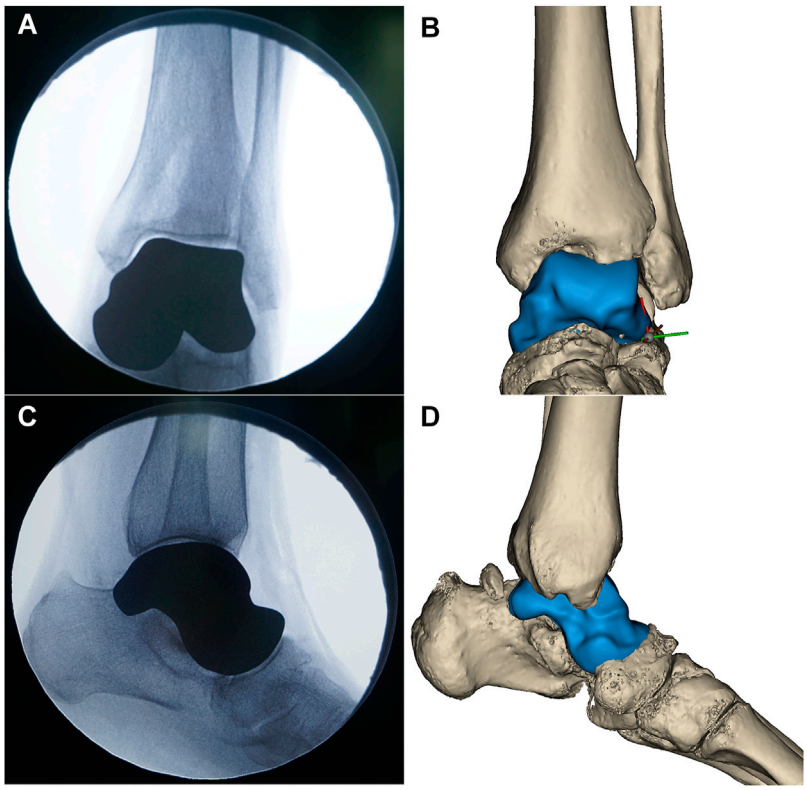

FIGURE 5 | The position of the 3D printed talar prosthesis was confirmed by postoperative radiography **(A,C)**, and matched with the preoperative 3D reconstructed results **(B,D)**.

1.0–1.7 mm covered 70% of the surface of the talus with extremely high compressive modulus and less elasticity, and was more prone to subchondral changes. (Gelberman and Mortensen, 1983; Burston et al., 2011) The cartilaginous interface of the talus between the tibial plafond, medial and lateral malleoli, calcaneus, and navicular aids in even distribution of weight-bearing forces on the ankle joint. (Rodgers, 1988) Together the cartilaginous interfaces withstand five times the weight of the body when walking, and up to 13 times the weight of the body when running, making the talus vital in the locomotive system but also rendering it vulnerable to trauma and subchondral changes. (Shnol and LaPorta, 2018) In a previous study talar prosthetic replacement exhibited a high long-term failure rate due to poor matching to patients' individual talar anatomic and biological features. (Harnroongroj and Vanadurongwan, 1997) The talar prosthesis should have enough strength to brace the dynamic mechanical changes in the ankle joint, and be precisely matched to the complex morphological features of the cartilaginous interface. Studies indicate that a proper fit of the talus prosthesis correlates directly with long-term follow-up results. (Harnroongroj and Harnroongroj, 2014; Ando et al., 2016) Based on these principles, in the patients in the current series CT scanning of the unaffected side was used in conjunction with 3D printing methods to reconstruct the original characteristics of the talus. *Via* the 3D printing approach, the prosthesis could be conveniently rescaled and manufactured. Three sizes of talar prosthesis were prepared for our first patient—original size, plus 1 mm, and minus 1 mm—to simulate the thickness of the cartilage. The original sized prosthesis fitted the calcaneus best, without any signs of instability. With the aid of a 3D printed talus all patients achieved substantial increases in AOFAS and VAS scores. The prosthesis precisely replaced the necrotic talus, and stability was ensured by the surrounding tissues.

Given the complex biological environment and unique surficial features of the talus it is essential to make a talar prosthesis from a material with appropriate biological and biomechanical properties. The choice of prosthetic materials for TTR has evolved from bone cement (Tsukamoto et al., 2010) to alumina ceramic. (Taniguchi et al., 2012; Taniguchi et al., 2015; Taniguchi and Tanaka, 2019; Yamamoto et al., 2021) The primary aims during material selection are to improve the durability of the talar prosthesis and to reduce prosthetic wear. In the present cases, a metal material that has not been previously reported in the construction of talar prostheses was used, Vitallium alloy, and it exhibited satisfactory biocompatibility and minimal effects on corresponding bone and cartilage (Kyomoto et al., 2010; Dobruchowska et al., 2017) as well as low friction and high wear degradation resistance, which maximizes the durability of the service life of the prosthesis. (MacDonald and Wicker,

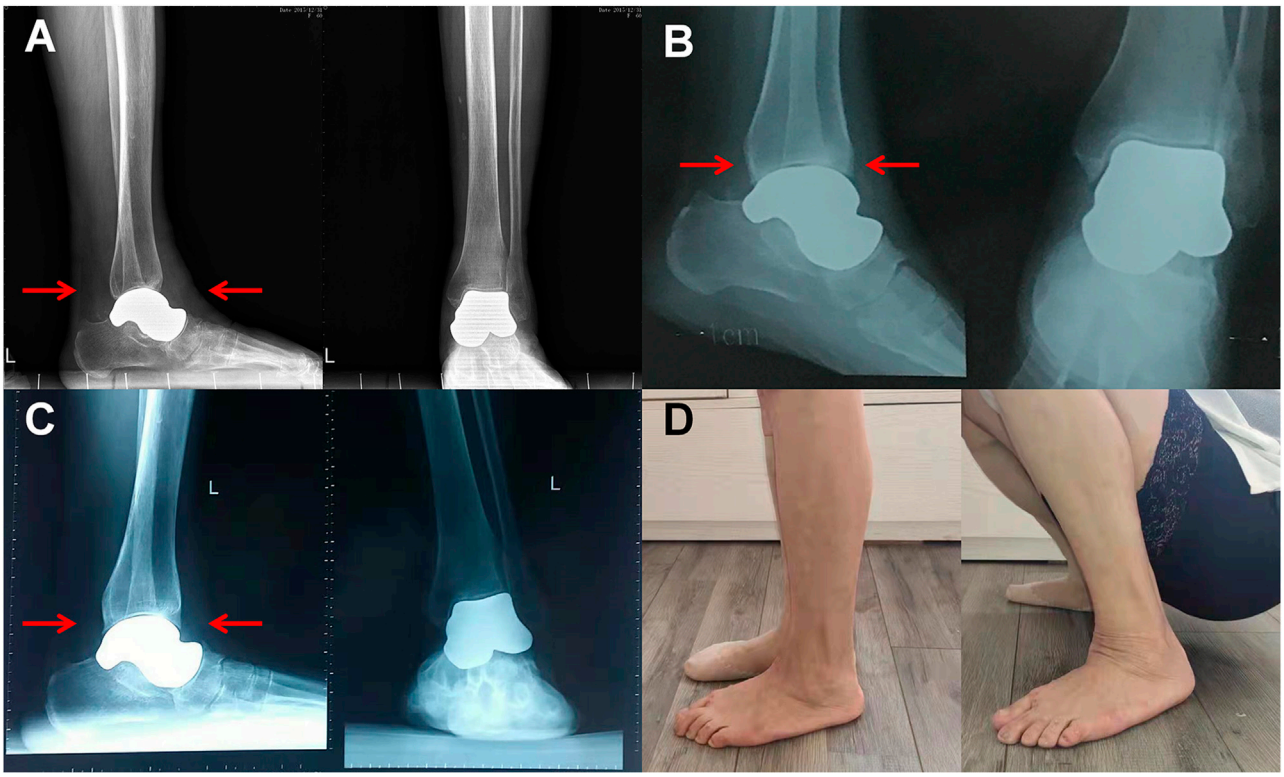

FIGURE 6 | A 58 year-old woman (patient 1) suffered from pain and swelling of the left ankle for 2 years and was unable to walk without crutches. TTR with a 3D printed Vitallium talar prosthesis was performed in 2015. Anteroposterior and lateral radiographs taken postoperatively 1, 3, and 5 years after discharge did not depict any signs of prosthesis-related complications **(A–C)**. The formation of small osteophytes on the tibial side and navicular side was detected **(D)**, but the patient did not report any discomfort and had returned to daily activities.

2016) The use of 3D printed Vitallium alloy has been reported in several previous studies.Chang et al. (2019) compared the marginal adaptation of 3D printed dental implants with that of traditionally fabricated implants. In that study, the 3D printed Vitallium alloy prosthesis met clinical requirements. Zheng et al. (2019) developed an innovative customized 3D printed total temporomandibular joint prosthesis constructed with Vitallium alloy that was safe and efficient in clinical use. When using this new material for TTR prosthetic design, we hoped the resulting custom-made prostheses would adjust the ankle joint, maintain stability, prevent degenerative changes in surrounding cartilaginous structures, and disperse complex dynamic pressure changes.

TTR has multiple advantages, including the preservation of a range of motion, limb length, and joint function, as well as the ease of the surgical technique and the short post-operative recovery period. Since it was first reported in 2010, (Tsukamoto et al., 2010) the fixation method in TTR has always been controversial. Theoretically there is a risk of instability if the talar prosthesis is dissociative in the ankle joint, because ligament reconstruction is not performed routinely in such surgery. (Ando et al., 2016) Hence, some surgeons preferred to fix the talar prosthesis to the calcaneus with screws to enhance stability. (Mu et al., 2021; West and Rush, 2021) Porous coating surfaces and other auxiliary devices have also been used to enhance prosthesis fixation in some studies. (Stevens et al., 2007; Regauer et al., 2017) Notably however, reported cases of prosthesis failure such as loosening and subsidence have mainly occurred at the bone-prosthesis interface. (Yamamoto et al., 2021) To eliminate interaction between the prosthesis and surrounding bone structure in the present cases, no screws or other bony fixation methods were used. The position of the talar prosthesis was restricted by the surrounding tissues. Benefiting from the advantages of 3D printing technology which offers a more precise and personalized way to fabricate talar prostheses. The surface of the prostheses would fit the surrounding joints' facets more accurately to improve the joint's stability. Moreover, to reduce the risk of instability, patients in this study were not allowed for weight-bearing exercise immediately after surgery. The patients were allowed to walk and bear weight with the help of a walking boot after 1 week. To ensure the surrounding soft tissue's healing, ankle joint exercise was not permitted until 4 weeks after surgery. We believed that surrounding bones and residual ligaments and capsules could encapsulate the talar prosthesis and provide enough stability for daily activities. Radiography at the final follow-up 6.5 years postoperatively revealed small osteophytes on the tibial and navicular sides. It appeared to have been caused by the instability of the talar

prosthesis. Nevertheless, the patient did not report any discomfort. Moreover, the osteophytes at the edges of the surrounding bones seemed to have improved the stability of the talar prosthesis, as the formation of the osteophytes had become diminished by the last follow-up. Radiographic follow-up focused on dynamic changes of the ankle joints is still needed. However, reconstructing ligament attachments on the prostheses has not yet been achieved, which is also a key point of our future research.

In terms of the advantages of manufacturing methods and material, the clinical application of the customized 3D printed Vitallium talar prosthesis described herein still has limitations. The number of patients is limited, and long-term follow-up with more detailed assessments is still required. Meanwhile, for now, we are only benefiting from the freedom and convenience of realizing our design provided by 3D printing methods. Further research by our team will focus on the mechanical analysis and structure characteristics of the 3D printed talar prosthesis, especially on the how 3D printing process affects the mechanical features of the material.

CONCLUSION

In the current study, with the aid of 3D printing and a novel Vitallium alloy material, TTR achieved encouraging results in 3/3 patients. The patients were satisfied with their joint function, and were able to return to daily activities without limitation. Although more cases and longer-term follow-up still need to be studied, the success rate in the current series is encouraging.

DATA AVAILABILITY STATEMENT

The original contributions presented in the study are included in the article/Supplementary Material, further inquiries can be directed to the corresponding authors.

ETHICS STATEMENT

The studies involving human participants were reviewed and approved by Ethics Committee of the Second Hospital of Jilin University. The patients/participants provided their written informed consent to participate in this study. Written informed consent was obtained from the individual(s) for the publication of any potentially identifiable images or data included in this article.

AUTHOR CONTRIBUTIONS

WL and HZ contributed equally. FC and JW participated in the design of the study and drafted the manuscript. WL, HZ participated in drafted the manuscript, QH, and ZL participated in collecting data and follow-up visits. ZZ, GJ, and YL participated in the literature review. All authors read and approved the final manuscript.

FUNDING

This work was supported by Industrial Technology Research and Development Project of the Development and Reform Commission of Jilin Province (Grant No. 2021C042-3); Scientific Research Planning Project of the Education Department of Jilin Province (Grant No. JJKH20201075KJ); The Finance Department of Jilin Province (Grant No. 2020SC2T001); The Science and Technology Department of Jilin Province (Grant No. 20190304121YY); The Development and Reform Commission of Jilin Province (Grant No. 2018C502-4); The Health Commission of Jilin Province (Grant No. 602959).

ACKNOWLEDGMENTS

Written consent was obtained from the patient for publication of the study.

REFERENCES

Akoh, C. C., Chen, J., and Adams, S. B. (2020). Total Ankle Total Talus Replacement Using a 3D Printed Talus Component: A Case Report. *J. Foot Ankle Surg.* 59, 1306–1312. doi:10.1053/j.jfas.2020.08.013

Ando, Y., Yasui, T., Isawa, K., Tanaka, S., Tanaka, Y., and Takakura, Y. (2016). Total Talar Replacement for Idiopathic Necrosis of the Talus: A Case Report. *J. Foot Ankle Surg.* 55, 1292–1296. doi:10.1053/j.jfas.2015.07.015

Angthong, C. (2014). Anatomic Total Talar Prosthesis Replacement Surgery and Ankle Arthroplasty: an Early Case Series in Thailand. *Orthop. Rev. (Pavia)* 6, 5486. doi:10.4081/or.2014.5486

Beyaert, C., Sirveaux, F., Paysant, J., Mole, D., and Andre, J. (2004). The Effect of Tibio-Talar Arthrodesis on Foot Kinematics and Ground Reaction Force Progression during Walking. *Gait Posture* 20, 84–91. doi:10.1016/j.gaitpost.2003.07.00610.1016/s0966-6362(03)00147-4

Burston, J. L., Brankov, B., and Zellweger, R. (2011). Reimplantation of a Completely Extruded Talus 8 Days Following Injury: a Case Report. *J. Foot Ankle Surg.* 50, 104–107. doi:10.1053/j.jfas.2010.10.009

Bussewitz, B., DeVries, J. G., Dujela, M., McAlister, J. E., Hyer, C. F., and Berlet, G. C. (2014). Retrograde Intramedullary Nail with Femoral Head Allograft for Large Deficit Tibiotalocalcaneal Arthrodesis. *Foot Ankle Int.* 35, 706–711. doi:10.1177/1071100714531231

Butterworth, M. L., and Ugrinich, M. (2019). First Metatarsophalangeal Joint Implant Options. *Clin. Podiatric Med. Surg.* 36, 577–596. doi:10.1016/j.cpm.2019.07.003

Chang, H.-S., Peng, Y.-T., Hung, W.-L., and Hsu, M.-L. (2019). Evaluation of Marginal Adaptation of Co Cr Mo Metal Crowns Fabricated by Traditional Method and Computer-Aided Technologies. *J. Dent. Sci.* 14, 288–294. doi:10.1016/j.jds.2018.11.006

Dobruchowska, E., Paziewska, M., Przybyl, K., and Reszka, K. (2017). Structure and Corrosion Resistance of Co-cr-mo Alloy Used in Birmingham Hip Resurfacing System. *Acta Bioeng. Biomech.* 19, 31–39.

Fragomen, A. T., Borst, E., Schachter, L., Lyman, S., and Rozbruch, R. S. (2012). Complex Ankle Arthrodesis Using the Ilizarov Method Yields High Rate of Fusion. *Clin. Orthop. Relat. Res.* 470, 2864–2873. doi:10.1007/s11999-012-2470-9

Gelberman, R. H., and Mortensen, W. W. (1983). The Arterial Anatomy of the Talus. *Foot Ankle* 4, 64–72. doi:10.1177/107110078300400204

Haddad, S. L., Coetzee, J. C., Estok, R., Fahrbach, K., Banel, D., and Nalysnyk, L. (2007). Intermediate and Long-Term Outcomes of Total Ankle Arthroplasty and Ankle Arthrodesis. *J. Bone & Jt. Surg.* 89, 1899–1905. doi:10.2106/JBJS.F.01149

Han, Q., Liu, Y., Chang, F., Chen, B., Zhong, L., and Wang, J. (2019). Measurement of Talar Morphology in Northeast Chinese Population Based on Three-Dimensional Computed Tomography. *Med. Baltim.* 98, e17142. doi:10.1097/MD.0000000000017142

Harnroongroj, T., and Harnroongroj, T. (2014). The Talar Body Prosthesis: Results at Ten to Thirty-Six Years of Follow-Up. *J. Bone Jt. Surg.* 96, 1211–1218. doi:10.2106/JBJS.M.00377

Harnroongroj, T., and Vanadurongwan, V. (1997). The Talar Body Prosthesis*. *J. Bone Jt. Surg. Am. Volume)* 79, 1313–1322. doi:10.2106/00004623-199709000-00005

Hintermann, B., Barg, A., Knupp, M., and Valderrabano, V. (2009). Conversion of Painful Ankle Arthrodesis to Total Ankle Arthroplasty. *J. Bone Jt. Surgery-American Volume* 91, 850–858. doi:10.2106/JBJS.H.00229

Kyomoto, M., Moro, T., Saiga, K.-i., Miyaji, F., Kawaguchi, H., Takatori, Y., et al. (2010). Lubricity and Stability of Poly(2-Methacryloyloxyethyl Phosphorylcholine) Polymer Layer on Co-cr-mo Surface for Hemi-Arthroplasty to Prevent Degeneration of Articular Cartilage. *Biomaterials* 31, 658–668. doi:10.1016/j.biomaterials.2009.09.083

Lee, C., Brodke, D., Perdue, P. W., Jr, and Patel, T. (2020). Talus Fractures: Evaluation and Treatment. *J. Am. Acad. Orthop. Surg.* 28, e878–e887. doi:10.5435/JAAOS-D-20-00116

MacDonald, E., and Wicker, R. (2016). Multiprocess 3D Printing for Increasing Component Functionality. *Science* 353, 353. doi:10.1126/science.aaf2093

Mu, M. d., Yang, Q. d., Chen, W., Tao, X., Zhang, C. k., Zhang, X., et al. (2021). Three Dimension Printing Talar Prostheses for Total Replacement in Talar Necrosis and Collapse. *Int. Orthop. (SICOT)* 45, 2313–2321. doi:10.1007/s00264-021-04992-9

Parekh, S. G., and Kadakia, R. J. (2021). Avascular Necrosis of the Talus. *J. Am. Acad. Orthop. Surg.* 29, e267–e278. doi:10.5435/JAAOS-D-20-00418

Regauer, M., Lange, M., Soldan, K., Peyerl, S., Baumbach, S., Böcker, W., et al. (2017). Development of an Internally Braced Prosthesis for Total Talus Replacement. *Wjo* 8, 221–228. doi:10.5312/wjo.v8.i3.221

Rodgers, M. M. (1988). Dynamic Biomechanics of the Normal Foot and Ankle during Walking and Running. *Phys. Ther.* 68, 1822–1830. doi:10.1093/ptj/68.12.1822

Schuberth, J. M., King, C. M., Jiang, S.-f., Ross, J. S., Christensen, J. C., and Steck, J. K. (2020). Takedown of Painful Ankle Arthrodesis to Total Ankle Arthroplasty: A Case Series of 77 Patients. *J. Foot Ankle Surg.* 59, 535–540. doi:10.1053/j.jfas.2020.01.002

Shnol, H., and LaPorta, G. A. (2018). 3D Printed Total Talar Replacement. *Clin. Podiatric Med. Surg.* 35, 403–422. doi:10.1016/j.cpm.2018.06.002

Stevens, B. W., Dolan, C. M., Anderson, J. G., and Bukrey, C. D. (2007). Custom Talar Prosthesis after Open Talar Extrusion in a Pediatric Patient. *Foot Ankle Int.* 28, 933–938. doi:10.3113/FAI.2007.0933

Taniguchi, A., Takakura, Y., Sugimoto, K., Hayashi, K., Ouchi, K., Kumai, T., et al. (2012). The Use of a Ceramic Talar Body Prosthesis in Patients with Aseptic Necrosis of the Talus. *J. Bone Jt. Surg. Br. volume* 94-B, 1529–1533. doi:10.1302/0301-620X.94B11.29543

Taniguchi, A., Takakura, Y., Tanaka, Y., Kurokawa, H., Tomiwa, K., Matsuda, T., et al. (2015). An Alumina Ceramic Total Talar Prosthesis for Osteonecrosis of the Talus. *J. Bone Jt. Surg.* 97, 1348–1353. doi:10.2106/JBJS.N.01272

Taniguchi, A., and Tanaka, Y. (2019). An Alumina Ceramic Total Talar Prosthesis for Avascular Necrosis of the Talus. *Foot Ankle Clin.* 24, 163–171. doi:10.1016/j.fcl.2018.10.004

Tsukamoto, S., Tanaka, Y., Maegawa, N., Shinohara, Y., Taniguchi, A., Kumai, T., et al. (2010). Total Talar Replacement Following Collapse of the Talar Body as a Complication of Total Ankle Arthroplasty. *J. Bone Jt. Surg. Am.* 92, 2115–2120. doi:10.2106/JBJS.I.01005

West, T. A., and Rush, S. M. (2021). Total Talus Replacement: Case Series and Literature Review. *J. Foot Ankle Surg.* 60, 187–193. doi:10.1053/j.jfas.2020.08.018

Yamamoto, T., Nagai, K., Kanzaki, N., Kataoka, K., Nukuto, K., Hoshino, Y., et al. (2021). Comparison of Clinical Outcomes between Ceramic-Based Total Ankle Arthroplasty with Ceramic Total Talar Prosthesis and Ceramic-Based Total Ankle Arthroplasty. *Foot Ankle Int.* 43, 529–539. doi:10.1177/10711007211051353

Zheng, J., Chen, X., Jiang, W., Zhang, S., Chen, M., and Yang, C. (2019). An Innovative Total Temporomandibular Joint Prosthesis with Customized Design and 3D Printing Additive Fabrication: a Prospective Clinical Study. *J. Transl. Med.* 17, 4. doi:10.1186/s12967-018-1759-1

Conflict of Interest: The authors declare that the research was conducted in the absence of any commercial or financial relationships that could be construed as a potential conflict of interest.

frontiers | Frontiers in Bioengineering and Biotechnology

MINI REVIEW
published: 24 May 2022
doi: 10.3389/fbioe.2022.921338

Advances and Prospects in Antibacterial-Osteogenic Multifunctional Dental Implant Surface

*Zixuan Wang[1,2†], Baosheng Li[1†], Qing Cai[1], Xiaoyu Li[1], Zhaoyi Yin[1], Birong Li[1], Zhen Li[1] and Weiyan Meng[1]**

[1]Department of Dental Implantology, Hospital of Stomatology, Jilin University, Changchun, China, [2]Jilin Provincial Key Laboratory of Oral Biomedical Engineering, Changchun, China*

In recent years, dental implantation has become the preferred protocol for restoring dentition defects. Being the direct contact between implant and bone interface, osseointegration is the basis for implant exerting physiological functions. Nevertheless, biological complications such as insufficient bone volume, poor osseointegration, and postoperative infection can lead to implant failure. Emerging antibacterial-osteogenic multifunctional implant surfaces were designed to make up for these shortcomings both during the stage of forming osseointegration and in the long term of supporting the superstructure. In this mini-review, we summarized the recent antibacterial-osteogenic modifications of the dental implant surface. The effects of these modifications on biological performance like soft tissue integration, bone osteogenesis, and immune response were discussed. In addition, the clinical findings and prospects of emerging antibacterial-osteogenic implant materials were also discussed.

Keywords: dental implant, surface modification, antibacterial, osteogenesis, osseointegration, soft tissue integration, immunity

OPEN ACCESS

Edited by:
Jianxun Ding,
Changchun Institute of Applied Chemistry (CAS), China

Reviewed by:
Baixiang Wang,
Zhejiang University, China
Varvara Gribova,
Université de Strasbourg, France

****Correspondence:***
Weiyan Meng
mengwy@jlu.edu.cn

†These authors have contributed equally to this work

Specialty section:
This article was submitted to Biomaterials, a section of the journal Frontiers in Bioengineering and Biotechnology

Received: *15 April 2022*
Accepted: *06 May 2022*
Published: *24 May 2022*

Citation:
Wang Z, Li B, Cai Q, Li X, Yin Z, Li B, Li Z and Meng W (2022) Advances and Prospects in Antibacterial-Osteogenic Multifunctional Dental Implant Surface. Front. Bioeng. Biotechnol. 10:921338. doi: 10.3389/fbioe.2022.921338

INTRODUCTION

With the continuous advancement of implant technology in recent years, dental implantation has become the preferred protocol for treating dentition defects. Professor Brånemark firstly proposed the osseointegration theory in 1966: the implant is in direct and close contact with the surrounding bone tissue under a light microscope, with no non-bone tissue intervention such as fibrous tissue in the middle (Guglielmotti et al., 2019). The osseointegration interface is a criterion of dental implant success, as well as the foundation for implant physiological performance. While intrinsic factors, surgical factors, local and systemic circumstances of the host, biomechanics of implant loading, implant design along with its upper support structure, and peri-implant hygiene conditions all affect osseointegration (Rupp et al., 2018). Moreover, the negative capability of surface forming osseointegration and post-operative infection have become critical factors that will be deleterious to osseointegration and influence the success of implantation, resulting in implant failure.

A wide range of methods has been proposed in basic experiments and clinical studies to improve the osseointegration of implants. Currently, methods to improve implant osseointegration include: changing local factors (such as radiation, oxide layer thickness, electric field, corrosion, etc.), physical therapy (vibration stimulation, etc.), drug therapy, implant surface modification, changing implant and abutment materials, but these methods also have the disadvantages of limited application and unsatisfactory results (Coelho et al., 2015) (Ota et al., 2016) (Guglielmotti et al., 2019) (Guglielmotti et al., 2019) (European Association for Osseointegration, 2019). For instance, the ultrasonic

treatment also causes damage to the implant surface, which seriously affects the attachment of human osteoblast-like cells(Schwarz et al., 2003). Air-polished implant surfaces also did not exhibit a proliferation-promoting effect on osteoblasts (Matthes et al., 2017). The polished and plasma sprayed implant surfaces showed low alkaline phosphatase activity (Guizzardi et al., 2004), which affects the growth and metabolic activity of osteoblasts. Clinically applied coatings that promote osteogenesis, such as calcium phosphate coating, are less stable, have weaker adhesive strength with the substrate material, are prone to coating peeling and degradation, and are not conducive to forming long-term osseointegration (Schunemann et al., 2019).

Emerging antibacterial-osteogenic multifunctional implant surfaces were designed to make up for these shortcomings both during the stage of forming osseointegration and in the long term of supporting the superstructure. In this mini-review, we summarized the recent antibacterial-osteogenic modifications of the dental implant surface, and the effects of these modifications on the biological performance like soft tissue integration, bone osteogenesis, and immune response were discussed. In addition, this article discusses the clinical findings and prospects of emerging antimicrobial-osteogenic implant materials, providing a theoretical basis for improving implant osseointegration and promoting the long-term stability of implants.

ANTIBACTERIAL-OSTEOGENIC MODIFICATIONS OF DENTAL IMPLANT SURFACE

Mechanical Treatment

The micro-nano multi-level microstructure on the implant surface refers to the implant surface topography formed by sandblasting, acid etching, polishing, and other processing technologies (Zhang et al., 2021), which determines the ability of early peri-implant bone formation and the level of bacterial adhesion (Souza et al., 2019). Nano-grooves, nano-pores, and other structures formed on the implant surface can promote the formation and mineralization of the extracellular matrix and accelerate the level of osseointegration (Mendonca et al., 2008; Souza et al., 2019). The implant surface's nanomorphology also has a bactericidal function. The sharp edges of the nanostructure can stretch and rupture the bacterial cell wall, causing bacteria to lyse and reducing their viability (Jager et al., 2017). Zhu et al. used magnetron sputtering to create a tantalum-containing micro/nanocoating on titanium implants (Zhu et al., 2017). The coating not only improved the adhesion and spreading ability of rat bone marrow mesenchymal stem cells (rBMSCs), but also demonstrated antibacterial activity against *Streptococcus mutans* and *Porphyromonas gingivalis*. It has been revealed that the nanotextured surface has a more potent antimicrobial effect and can effectively induce osteogenic differentiation and calcium deposition (Kunrath et al., 2020). Wang et al. created a layered micro/nanomorphic polyetheretherketone implant with specific functional groups (amino and COOH/COOR) that displayed a good antibacterial activity. The micron/nanocoating and specific functional groups aided in the adhesion, proliferation, and osteogenic differentiation of MG-63 osteoblast-like cells (Wang et al., 2018) (**Table 1**).

UV photofunctionalization is the modification of titanium surfaces after UV treatment, which includes changes in physicochemical properties and enhanced biological capabilities (Ogawa, 2014). As a biologically inert material, titanium does not interact directly with cells and biomolecules. UV treatment can change the surface activity of titanium implants and transform the surface of titanium implants from hydrophobic to super hydrophilic. After UV irradiation, the electrostatic state of the titanium surface is changed, allowing direct adsorption of the desired cells. For example, one study found that UV treatment increased osteoblasts' attachment, diffusion, proliferation, and mineralization on the titanium surface (Tsukimura et al., 2011). Compared to untreated implant surfaces, the bone morphology around UV-treated titanium implants changed significantly, allowing for rapid and stable osseointegration and promoting new bone formation with a near 100% bone-to-implant contact rate (Aita et al., 2009b; Kim et al., 2016). The UV-treated implant surface did not affect bacterial viability but significantly reduced bacterial adhesion and biofilm formation (De Avila et al., 2015). In addition, UV treatment effectively optimized the nanostructure of the titanium surface and promoted the adhesion and proliferation of osteoblasts (Tsukimura et al., 2011). In addition to promoting the proliferation of macrophages on the titanium surface and reducing the occurrence of inflammatory reactions (Lyu et al., 2019), UV treatment also increased the bioactivity of titanium dioxide nanotubes in human mesenchymal stem cells (Aita et al., 2009a). Thus, it is clear that UV treatment has positive implications for antimicrobial osteogenic modification of implant surfaces.

Bionanostructures have piqued the interest of researchers in recent years due to their excellent properties such as superhydrophobicity, self-cleaning, and antibacterial osteogenic dual-efficacy. Shahali et al. studied the nanostructures and properties of three cicadas and bionanostatically fabricated them using titanium nanopillars (Shahali et al., 2019). The bionanostructures were found to disrupt the morphology of *Pseudomonas aeruginosa* and *Staphylococcus aureus* (*S. aureus*), reduce bacterial adhesion, and promote osteoblast and actin adhesion and diffusion. In addition to cicada wings, surface nanostructures of dragonfly and butterfly wings, shark skin, gecko feet, taro and lotus leaves, and taro and lotus leaves have similar self-cleaning, bactericidal, and biocompatibility properties, making them more promising for implant surface modification (Jaggessar et al., 2017).

Multifunctional Coating Biomacromolecular Coating

Biomacromolecular coating is the loading of biomacromolecules onto the implant surface through covalent bonding or layer-by-layer self-assembly, which has antibacterial properties and facilitates implant osseointegration (Cloutier et al., 2015). The

TABLE 1 | Antibacterial-osteogenic strategies of dental implant surface based on coating elements.

Coating classification	Material composition	Bacterial Strains	Osteogenesis	References
Biomacromolecular Coating	Vitamin E Phosphate	*S. aureus*	*In vivo*; promoting bone deposition and osseointegration	Lovati et al. (2018)
	TA/8DSS/PEG	*S. aureus* *E. coli*	BMSCs; promoting biomineralization and osseointegration	Han et al. (2021)
	TA/HA/lysozyme	*S. aureus* *E. coli*	MC3T3-E1; promoting osteoblast mineralization and gene expression and ALP activity	Wang G. et al. (2021)
	HA/HBD-3/BMP-2	*S. aureus* *E. coli*	hBMSC; promoting adhesion, proliferation, and osteogenic differentiation	Liu et al. (2018)
	PDA/nZnO/CS/nHA	*S. aureus* *E. coli*	MC3T3-E1; promoting osteogenic differentiation and ALP expression	Wang Z. et al. (2021)
Polymer Coating	Ti-RP/PCP/RSNO	*MRSA*	MC3T3-E1; upregulating the expression of ALP, Opn and Ocn	Li et al. (2020)
	SP@MX-TOB/GelMA	*S. aureus* *E. coli*	MC3T3-E1; improving the proliferation and diffusion of osteoblasts and the mineralization of calcium matrix	Yin et al. (2020)
	SPEEK@ SA(CGA)@BFP	*S. aureus* *E. coli*	MC3T3; improving cell adhesion and proliferation and osteogenic differentiation	He et al. (2019)
	Ti-Br/PEG/RGD	*S. mutans, A. naeslundii*	MC3T3; promoting adhesion and proliferation of osteoblasts	Liu et al. (2016)
TiO2 Nanotube Coating	TNT/GelMA/PMAA-Cl/ BMP-2	*S. aureus* *E. coli*	Osteoblasts; promoting cell adhesion, proliferation and differentiation	Jiao et al. (2020)
	TNT/BMP2/(Chi/SL/ Chi/Gel) $_4$	*S. aureus* *E. coli*	Osteoblasts; improving cell viability, ALP activity, mineralization capacity and osteogenic gene expression	Sutrisno et al. (2018)
	TNT/BMP2/LBLg	*S. aureus* *E. coli*	Osteoblasts; promoting differentiation of osteoblasts	Tao et al. (2019)
	TNT/Au NPs/Pt NPs	*S. aureus*	hMSCs; enhancing osteogenic function	Moon et al. (2020)
Metal Ion/Nanoparticle Coating	Cu/Hier/Ti	*S. aureus*	Macrophages; creating a favorable inflammatory micro-environment for SaOS-2 cells, promoting osseointegration	Huang et al. (2019)
	AH-Sr-AgNPs	*S. aureus*	Macrophages; promoting macrophage polarization and differentiation of pro-osteoblasts	Li et al. (2019)
	PLGA/Ag/Fe_3O_4	*S.mutans*	Osteoblasts; promoting osteoblast proliferation	Yang et al. (2018)
	nAg/μCuO/PDA/SF	*S. aureus* *E. coli*	Ad-MSC; enhancing osteogenic differentiation	Yan et al. (2020)

ADA-Gen, alginate dialdehyde-gentamicin; A.naeslundii, Actinomyces naeslundii; *BFP, grafted peptide; BMP-2, Bone morphogenetic protein-2; CGA, chlorogenic acid; CS/Chi, chitosan; Cu-Hier-Ti, Cu-containing micro/nano-topographical bio-ceramic;* E.coli, Escherichia coli; *GelMA, gelatin methacrylate; HA, hydroxyapatite; HBD-3, human β-defensin 3;* LBLg, LBL/ADA-Gen; MRSA, Methicillin resistant Staphylococcus aureus; *MX, MXene; nAg, silver nanoparticles; nHA, nanocrystal hydroxyapatite; nZnO, ZnO nanoparticles; PCP, PVA/CS/PDA; PDA, polydopamine; PEG, polyethylene glycol; PLGA, poly(lactic-co-glycolic acid; PMAA-Cl, N-Cl modification poly (*N,N′*-methylene bis(acrylamide)); PVA, polyvinyl alcohol; RGD, arginine-glycine-aspartic; RSNO, a NO, donor of S-nitrosuccinic acid; SA, sodium alginate;* S.aureus, Staphylococcus aureus; *SL, sodium hyaluronate-lauric acid;* S.mutans, Streptococcus mutans; *SPEEK/SP, sulfonated polyetheretherketone; TA, tannic acid; TNT, TiO_2 nanotubes; TOB, tobramycin; μCuO, copper oxide microspheres; 8DSS, 8 repeating units of aspartate-serine-serine.*

various extracellular matrix proteins covering the implant surface, which affect cellular activity and trigger signaling pathways, play a crucial role in the interaction between the host and the implant (Liu et al., 2021).

Vitamin E phosphate implant coating reduced bacterial colonization of the implant surface. It increased bone deposition and osseointegration levels in an animal model of implant-associated infection by decreasing bacterial extracellular polysaccharide activity and immunomodulation (Lovati et al., 2018). Using the layer-by-layer self-assembly approach, implant surface was coated with tannic acid (TA), the biomineralization inducer 8DSS (8 repeat units of aspartate-serine-serine), and polyethylene glycol (PEG). PEG contributed to inhibiting bacterial adherence, 8DSS contributed to promoting biomineralization and osseointegration (Han et al., 2021). Wang et al. immobilized TA, hydroxyapatite (HA), and lysozyme on the implant surface, exhibiting a good antibacterial activity against *Escherichia coli* (*E. coli*) and *S. aureus*, meanwhile, the surface also promoted rapid adhesion and proliferation of mouse embryonic osteoblast precursor cells (Wang G. et al., 2021). In addition, Liu et al. developed a titanium implant coating containing nanohydroxyapatite, the natural antimicrobial peptide human *β*-defensin 3, and bone morphogenetic protein-2, which not only inhibited the growth of *S. aureus* and *E. coli*, but also promoted the adhesion, proliferation, and osteogenic differentiation of hBMSCs (Liu et al., 2018). Hence, the implant surface's biomacromolecular coating had a substantial antibacterial and osteogenesis effect.

Chitosan (CS) comprises randomly arranged N-acetyl-glucosamine residues and glucosamine residues. By binding to negatively charged bacteria, CS can increase the permeability of bacterial cell membranes, thus acting as an antibacterial agent. Another antibacterial mechanism of CS is the interaction between its hydrophobic aryl substituents and the hydrophobic structure

inside the bacterial cell wall. It has been found that the antimicrobial effect of CS is also influenced by its physical state and molecular weight, with longer alkyl substituents exhibiting stronger antimicrobial activity (Lu et al., 2016). CS coating can be deposited on the implant surface by electrophoretic deposition, sol-gel, dip-coating, spin-coating, and electrostatic spinning, along with osteogenesis-related factors, exercising dual antibacterial and osteogenic effects (Kumari et al., 2021). Ding et al. synthesized alkynyl-functionalized CS by reacting CS with 3-bromopropyne, showing better antibacterial activity against *E. coli* and *S. aureus* (Ding et al., 2013). Wang et al. created a composite coating (PDA/nZnO/CS/nHA) including polydopamine (PDA), zinc oxide nanoparticles (nZnO), and CS and nanocrystalline HA (nHA) (Wang Z. et al., 2021). Specifically, PDA doping reduced the porous titanium substrate's surface roughness, wettability, and provided high adhesion to the deposited nZnO. While nZnO inhibited the growth of *S. aureus* and *E. coli*. Furtherly, the CS/nHA coating improved the osteogenic differentiation of MC3T3-E1 cells by up-regulating the expression of alkaline phosphatase. Hence, this multi-functional coating demonstrated a superior antibacterial osteogenic capacity.

Polymer Coating

Grafting polymers on the implant surface, such as polyethylene glycol modifications, can inhibit bacteria's ability to form biofilms and cause them to maintain a planktonic phenotype. Owing to the fact that most polymers lack antibacterial action, grafted polymers can only prevent bacterial colonization by preventing bacterial adhesion passively (Nejadnik et al., 2008). Hydrophilic polymer chains are usually physically adsorbed or covalently immobilized to the implant surface to prevent bacterial adhesion to the surface of the implant polymer coating, leaving the polymer layer well-hydrated, which is necessary for the development of antibacterial adhesion properties. A cross-linker can be generated between the polymer chains to make a hydrogel, allowing the polymer coating structure to retain more water without collapsing, improving the surface's antibacterial adhesion capabilities (Swartjes et al., 2015).

Antimicrobial-osteogenic surfaces for hydrophilic implants have been studied using a variety of polymers such as polyethylene glycol, dextran, and hyaluronic acid (Liu et al., 2021). In order to achieve dual antimicrobial-osteogenic effects on the implant surface, it is possible to combine the antibacterial adhesion properties of the polymer with the bactericidal properties of the antimicrobial agent to improve the overall antimicrobial effect, in addition to grafting osteogenic-related factors on the surface of the implant polymer coating (Nejadnik et al., 2008). On the implant surface, block copolymers PF127 (Pluronic F-127) modified with antimicrobial peptide AMP, and PF127 modified with arginine-glycine-aspartate peptide RGD demonstrated good antibacterial adhesion, bactericidal, and tissue integration capabilities (Muszanska et al., 2014).

On red phosphorus nanomembranes of titanium implants, researchers created polyvinyl alcohol hydrophilic adhesive hydrogels (Ti-RP/PCP/RSNO) with CS, polydopamine, and NO-releasing donors. The structure could create NO with superoxide when exposed to 808 nm near-infrared light (NIR), which could upregulate the expression of Opn and Ocn genes as well as TNF-α, promoting osteogenic differentiation, and regulating inflammatory polarization while acting as an antibacterial agent (Li et al., 2020). Similarly, a novel multifunctional implant surface consisting of MXene nanosheets, gelatin methacrylate hydrogel, tobramycin, and bioinert sulfonated polyetheretherketone, showed strong antibacterial properties and osteogenic ability under 808 nm NIR illumination (Yin et al., 2020). Chlorogenic acid (CGA) and sodium alginate (SA) were grafted on the surface of sulfonated polyetheretherketone (SPEEK) implants to create the SPEEK@SA(CGA)@BFP hydrogel system. CGA was produced during the hydrogel's disintegration to prevent bacterial growth. In contrast, osteoinductive growth factor (BFP) boosted osteoblast proliferation and differentiation. Hence the coating played a more significant part in antimicrobial bone regeneration (He et al., 2019). In addition, grafting polyethylene glycol-arginine-glycine-aspartic acid polymer brushes on the titanium surface effectively inhibited the growth of *Streptococcus mutans* and *Actinomyces naeslundii* and promoted osteoblast adhesion (Liu et al., 2016).

TiO_2 Nanotube Coating

Anodic oxidation, hydrothermal synthesis, and templating procedures can be used to form TiO_2 nanotubes (TNT) on the surface of implants. TNT with nanoscale sizes increase their specific surface area, thus improving their photoelectrochemical characteristics (Hajjaji et al., 2018). TNT could promote the adhesion and proliferation of osteoblasts through osteogenic signaling pathways to achieve the long-term stability of implant osseointegration. For instance, TNT with nanomorphology provides locations for cell signaling *via* adsorbed proteins, which activate FAK and ERK1/2 pathways, enhancing hBMSCs cell motility, proliferation, and adhesion (Yang and Huang, 2019). In addition, TNT could achieve their dual antibacterial osteogenic function by forming micro-nano structures and combining them with metal ions, proteins, polymers, and medicines.

By disrupting bacterial cell walls and cell membranes, TNT can reduce bacterial adhesion and colonization, as well as kill bacteria by generating a pair of negatively charged free electrons and positively charged electron holes with strong redox properties through UV excitation. TNT react with water and oxygen to produce reactive oxygen species such as hydroxyl radicals, superoxide anions, and hydrogen peroxide (Liou and Chang, 2012). Drug molecules with antibacterial and osteogenic properties were loaded into TNT using various techniques, including physical adsorption, electrophoretic deposition, and magnetron sputtering. Changing the surface morphology of TNT can prolong the elution time of the drug and extend the duration of action of functional drug molecules against infection and contribute to bone regeneration (Wang K. et al., 2021). Jiao et al. prepared implant coatings containing BMP2 and GelMA/PMAA-Cl on TNT. They exhibited excellent antibacterial properties against the adhesion and growth of *S.*

aureus and *E. coli* and played a positive role in osteoblasts' adhesion, proliferation, and differentiation (Jiao et al., 2020).

In terms of enzyme response, Sutrisno et al. deposited bone morphogenetic protein 2 (BMP2) on the surface of titanium dioxide nanotubes to create a hyaluronidase-sensitive CS (Chi)/ sodium hyaluronate-laurate (SL) coating (Sutrisno et al., 2018). Among them, hyaluronidase triggered the release of lauric acid from the SL coating and accelerated the release of BMP2 from the system. As a result, this coating not only inhibited *S. aureus* and *E. coli* from proliferation, but also boosted the expression of osteogenic markers such as collagen type I, osteocalcin, osteopontin, and alkaline phosphatase. In terms of pH response, a pH-responsive composite coating on TNT was developed that contains BMP2/alginate dialdehyde/gentamicin/ CS (Tao et al., 2019). The release of gentamicin and BMP2 from the coating could be triggered by an acidic environment, which boasted antibacterial efficacy against *S. aureus* and promoted osteoblast development, alkaline phosphatase activity, mineralization ability, and the expression of osteogenic-related genes. In terms of photothermal response, Moon et al. created a nanoparticle coating on TNT that contained Au and platinum for the photothermal response (Moon et al., 2020). Under 470 nm visible light irradiation, the coating had strong antibacterial action against *S. aureus* and improved osteogenesis of human mesenchymal stem cells under 600 nm visible light irradiation.

Metal Ion/Nanoparticle Coating

When a metal atom loses electrons, metal ions form as positively charged cations. Metal nanoparticles are small metal particles that range in size from 1 to 100 nm (Baranwal et al., 2018). Metal ions, in general, have a positive charge and are dissolved in water. Metal ions can use coulomb forces to firmly adsorb to bacterial cell membranes and react with bacteria for antibacterial purposes. Moreover, metal ions can be indirectly antibacterial *via* regulating macrophages and being direct contact bactericidal. Huang et al. created a copper-containing micro/nanomorphic bioceramic surface (Cu-Hier-Ti surface) that improved macrophages' ability to take up and destroy bacteria, despite not being bactericidal. Cu^{2+} was carried to macrophage phagosomes by the copper transport signal protein ATP7A (Huang et al., 2019). It conducted a Fenton reaction with bacteria for sterilization and generated reactive oxygen species (ROS) in mitochondria to damage bacterial mitochondria. By modifying macrophages and increasing the expression of M1-type macrophage surface markers CD11c, growth factor BMP-6, OCN, and Runx-2, the Cu^{2+} surface promoted osseointegration. A dual delivery system (AH-Sr-AgNPs) on the titanium surface was created by alkali heat treatment (AH) for releasing Ag^{+} and Sr^{2+}, which activated pro-osteoclast differentiation by regulating macrophage polarization and effectively resisted *S. aureus*-induced infections (Li et al., 2019).

Nanoparticles, on the other hand, are suspended in water. By interacting with bacterial cell membranes, cell walls, essential proteins, and enzymes, nanoparticles can operate as antibacterial agents, and their antibacterial efficacy is dependent on particle size (Friedman et al., 2013). Larger nanoparticles (>10 nm) release fewer ions, and their antibacterial capabilities are mostly manifested in direct contact with bacteria, whereas smaller nanoparticles (>10 nm) release more ions and their antimicrobial qualities are primarily manifested in direct contact with bacteria (Chernousova and Epple, 2013). As a result, modifying nanoparticles' physicochemical attributes, such as size and shape, can increase their biological properties. Yang et al. developed a PLGA-encapsulated superparamagnetic Ag-Fe_3O_4 nanoparticle surface coating on implants with good antibacterial activity when exposed to a magnetic field to prevent *Streptococcus pyogenes* adherent colonization and promoted osteoblast proliferation and differentiation (Yang et al., 2018). Polyetheretherketone implants could be coated with copper CuO microspheres, silver nanoparticles, polydopamine, and filamentous protein. The coating released high doses of metal ions at pH 5.0, which killed 99.99% of planktonic bacteria, and low concentrations of metal ions in a physiological environment promoted ALP production, collagen secretion, calcium deposition, and NO production, thus promoting bone regeneration and osseointegration with being antibacterial contemporaneously (Yan et al., 2020).

EFFECT OF ANTIMICROBIAL-OSTEOGENIC MODIFICATIONS OF IMPLANT SURFACE ON SOFT TISSUE INTEGRATION

The peri-implant soft tissue, being the biological barrier that protects the implant from bacterial invasion and maintains the long-term stability of the underlying bone tissue, is similar to natural gingival tissue and consists primarily of connecting epithelium and connective tissue (Chu et al., 2019). Whereas the absence of Sharpey fibers around the implant, combined with parallel collagen fibers encircling the implant surface, makes it easier for the epithelial layer to move towards the implant's root side, disrupting the marginal closure (Ivanovski and Lee, 2018). As a result, implant surface modification should enhance epithelial and connective tissue to adhere to the implant surface.

The implant's rigid properties and two-dimensional surface make it difficult for soft tissues to integrate optimally with the implant. Developing a "buffer zone" between the titanium implant and the soft tissue can attract cell migration and infiltration, restore the cellular microenvironment, and improve tissue integration (Leng et al., 2021). A hybrid hydrogel coating with ZnO nanoflowers and methacrylated gelatin and methacrylated hyaluronic acid was created on the titanium surface (Leng et al., 2021). This coating acted as a buffer for inward cell development and soft tissue integration, promoting fibroblast growth and CTGF and COL-I expression while inhibiting *S. aureus*-induced infections. Similarly, Mathur et al. created a bionanofiber coating doped with silver nanoparticles and electrospun gelatin(Mathur et al., 2021). They found that this coating had an excellent antibacterial activity against *S. aureus* and *E. coli* and promoted fibroblast adhesion, growth, and differentiation.

Recently, Matter et al. developed a triple-functional implant surface, which possessed antimicrobial, osteogenic, and soft tissue integration properties (Matter et al., 2021). Bioactive glass, cerium

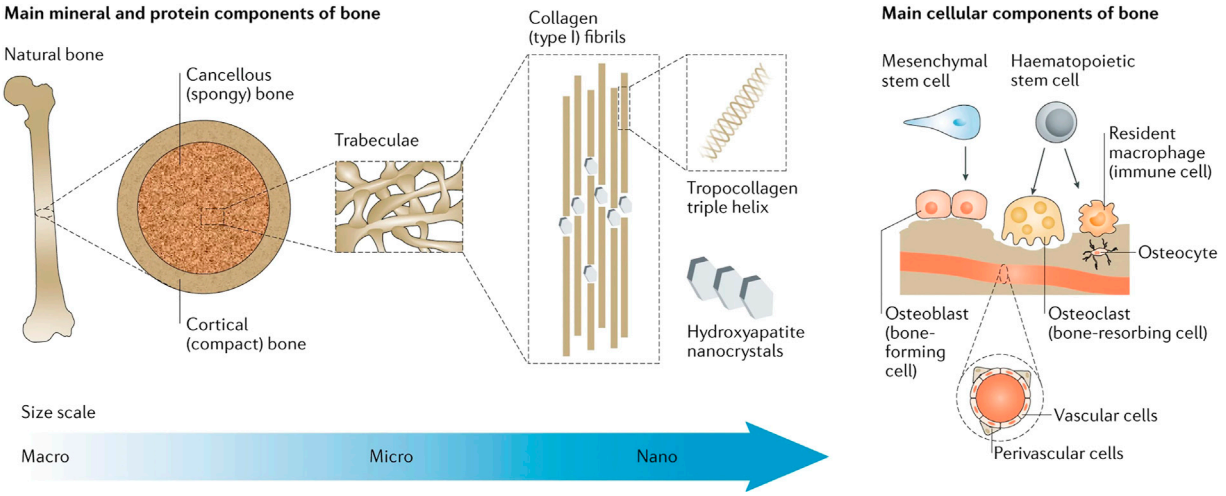

FIGURE 1 | Bone physiology for biomimicry of candidate biomaterials for bone-tissue engineering. Reproduced with permission from Koons et al. (2020).

dioxide nanoparticles, and 2% of zinc doping were used to create the intriguing nanocoating. The coating not only enhanced the integration of bone and soft tissues by stimulating the growth and adhesion of osteoblasts and fibroblasts, but also prevented the growth of methicillin-resistant *S. aureus*.

EFFECT OF ANTIMICROBIAL-OSTEOGENIC MODIFICATIONS OF IMPLANT SURFACE ON BONE REGENERATION

While resisting bacterial infection, the antimicrobial-osteogenic modification on the implant surface should promote the adhesion, proliferation, osteogenic differentiation of bone marrow mesenchymal stem cells, and subsequently increase their mineralization capacity, therefore upregulating the expression of osteogenic markers as type I collagen, osteocalcin, osteopontin, and ALP.

However, previous studies have also shown that some antimicrobial modifications on the implant surface can inhibit osteogenesis. For example, zinc ions could disrupt cellular energy metabolic processes by generating ROS to kill bacteria. Nevertheless, once larger doses of zinc ions were incorporated into Ca-Si-based bioactive glass ceramics, the excess zinc ions affected the deposition of calcium ions and affected the formation and growth of hydroxyapatite (Wu et al., 2008). A similar study showed that zinc ions promoted the death of osteoblasts and facilitated the process of bone resorption during the bacteriocidal process (Hu et al., 2012). ZnO nanorods, which had the antimicrobial effect, also reduced the cell viability of macrophages and decreased the adhesion and proliferation of macrophages (Zaveri et al., 2010). Therefore, the balance of antimicrobial and osteogenic effects of zinc ions is crucial for the effective antimicrobial-osteogenic modifications of implant surfaces. Lactoferrin is known for its ability to bind iron, which will lead to the discovery of its antibacterial activity. However, it has been found that lactoferrin could decrease the proliferative activity of osteoblasts and the bone formation capacity due to the conformational changes of lactoferrin (Wang et al., 2013). Hence, given the differences in their activities of antibiosis and osteogenesis, the molecules for implant surface modification should be considered comprehensively to achieve antimicrobial-osteogenic dual function.

Nowadays, lactoferrin has been successfully loaded on the implant surface, which effectively inhibited the adhesion and proliferation of *Streptococcus sanguis* and *S. aureus* and promoted osteogenic differentiation (Chen et al., 2021). Ding et al. loaded poly-L-glutamic acid and polyallylamine hydrochloride, silver nanoparticles, mesoporous silica nanoparticles, and polydopamine on a titanium surface to address the previously mentioned problem(Ding et al., 2020). The coating inhibited the growth of *Streptococcus. aureus* and increased the thickness of bone trabeculae and the volume and area of new bone. Yuan et al. also created a functional molybdenum disulfide (MoS_2)/polydopamine -arginine-glycine-aspartate coating on the surface of titanium implants that not only resisted bacterial infection of *Streptococcus. aureus* and *Escherichia. coli* when illuminated with NIR but also increased the expression of osteogenesis-related genes (Yuan et al., 2019). Thereupon, the inhibitory effect of active antimicrobial molecules on osteogenesis should not be ignored in the research phase of antimicrobial-osteogenic modifications on implant surfaces.

EFFECT OF ANTIMICROBIAL-OSTEOGENIC MODIFICATIONS OF IMPLANT SURFACE ON IMMUNOLOGICAL ASPECTS

After implant implantation, macrophages play a crucial part in the immune cascade response (Koons et al., 2020) (**Figure 1**). Pattern recognition receptors (PRRs) on the cell surface of the body, such as

macrophages, recognize bacteria and their metabolites as pathogen-associated molecular patterns (PAMPs) in the early stages of bacterial infection. TNF-α, IL-1, IL-1β, IL-6, and NO are produced by macrophages that have been activated and polarized to the M1 type, a pro-inflammatory phenotype that produces a great variety of pro-inflammatory mediators. Pro-inflammatory factors have vasodilatory and chemotactic actions, which might attract more leukocytes to the site and speed up PAMP clearance (Liu et al., 2014). The first inflammatory response after biomaterial implantation aids tissue repair and regeneration; however, the overabundance of M1-type macrophages can lead to chronic inflammation, stymie wound healing, and damaged tissue repair (Batool et al., 2021). M2 macrophages, which have immunosuppressive and anti-inflammatory properties, are essential in this situation.

Researchers tried to alter the physical properties of the implant surface to a more osteointegration-friendly M2-macrophage type that facilitate angiogenesis and bone regeneration around implants, namely immunomodulating the implant surface and modulating the macrophage phenotype (Kim, 2020). Nanoscale surface treatment of implant surfaces can influence macrophage morphology and phenotypic characteristics, while functionalized bioactive molecular materials can increase anti-inflammatory factors and decrease the release of pro-inflammatory factors by adjusting their surface hydrophilicity, surface charge, and surface coating (Batool et al., 2021).

In recent years, polyarginine coatings became prevailing for their excellent properties. In addition to its superb surface antimicrobial properties, polyarginine has been associated with the phenotypic transformation of macrophages and the synthesis of factors related to vascular endothelial cells. Researchers have developed multifunctional implant coatings containing gelatin, aldehyde-modified hyaluronic acid, and polyarginine, which effectively resisted infections caused by *S. aureus* and promote anti-inflammatory polarization and angiogenesis (Knopf-Marques et al., 2019). Other scholars designed implant coatings based on polyarginine, hyaluronic acid, and natural host defense peptide (catestatin), which were found to have long-term stable antimicrobial activity, and reduce the pro-inflammatory potential of macrophages, decrease the release of chronic inflammation-related factors, and facilitate tissue remodeling and healing (Ozcelik et al., 2015). In addition, polyarginine with a degree of polymerization of 30 reduced lipopolysaccharide-stimulated macrophage inflammatory response, accelerated fibroblast migration in macrophage/fibroblast co-culture systems and had a positive effect on wound healing (Gribova et al., 2022).

TNT have been found to reduce macrophage inflammatory responses by inhibiting MAPK and NF-κB pathways and reducing the expression levels of mitogen-activated protein kinase signaling molecules p38, ERK1/2, and JNK phosphorylation, which promotes macrophage polarization to M2 type to promote tissue repair (Neacsu et al., 2015).

Metal ions, such as Ag^{+} and Sr^{2+}, can modify macrophage polarization toward the M2 phenotype and enhance pro-osteoblast development while reducing *S. aureus* survival in the dual delivery system (AH-Sr-AgNPs) on titanium surfaces (Li et al., 2019). Silver nanoparticles have also been found to efficiently suppress inflammation by modifying TLR-mediated signaling and decreasing TLR ligand-mediated IL-6 production. It can also be used to reduce reactive oxygen species levels and restrict T-lymphocyte proliferation, thus reducing IL-2 release and controlling the immune system's inflammatory response (Ninan et al., 2020).

Different from the above research, Huang et al. polarized macrophages to the M1 phenotype purposely by creating a Cu-containing micro/nanomorphic bioceramic surface, which activated Cu translocation signaling in macrophages through the regulation of integrin (α5, αM, β1, β2) and TLR (TLR-3, TLR-4, Myd88, and Ticam-1/2) signaling to exert some inflammatory effects. The surface inhibited *Streptococcus. aureus* growth and proliferation, and intriguingly increased the proliferation and differentiation of human osteoblasts SaOS-2 (Huang et al., 2019). Comprehensively, polarizing to M2 phenotype of macrophages is not the unique protocol for promoting osteointegration. Appropriate activation of M1 phenotype of macrophage might be instrumental in solving inflammation more rapidly.

PERSPECTIVE AND CHALLENGES

The osseointegrated interface is the hallmark of successful dental implants and the basis for the physiological function of the implant. Since plaque biofilm is closely related to peri-implantitis, inhibiting microbial adhesion and biofilm formation on the implant surface and promoting the formation of stable osseointegration are the main strategies to prevent and treat peri-implantitis. Currently, methods to improve the antimicrobial properties of implants include creating antimicrobial implant surface morphology, forming an antimicrobial coating. However, most of these methods have disadvantages, such as limited application and unsatisfactory results. Owing to the complex environment inside the oral cavity, antimicrobial implant surface modification should be optimized to a multifunctional modification to promote soft and bone tissue bonding while effectively inhibiting bacteria. The targeting, responsiveness, and stability of the antimicrobial-osteogenic coating, and long-term stability of the surface-tissue interface are also issues that need to be investigated in the future. Improving the binding of the active ingredients and whether the active ingredients can be released on demand with long-term efficacy need to be thoroughly explored.

AUTHOR CONTRIBUTIONS

ZW and BL have summarized and wrote the article. QC, XL, ZY, BL, ZL, and WM commented and revised the submitted version.

FUNDING

This work was supported by the Department of Finance of Jilin Province, China (Grant numbers JCSZ2019378-3 and JCSZ2020304-15) and Department of Science and Technology of Jilin Province (20200404108YY).

REFERENCES

Aita, H., Att, W., Ueno, T., Yamada, M., Hori, N., Iwasa, F., et al. (2009a). Ultraviolet Light-Mediated Photofunctionalization of Titanium to Promote Human Mesenchymal Stem Cell Migration, Attachment, Proliferation and Differentiation. *Acta Biomater.* 5, 3247–3257. doi:10.1016/j.actbio.2009.04.022

Aita, H., Hori, N., Takeuchi, M., Suzuki, T., Yamada, M., Anpo, M., et al. (2009b). The Effect of Ultraviolet Functionalization of Titanium on Integration with Bone. *Biomaterials* 30, 1015–1025. doi:10.1016/j.biomaterials.2008.11.004

Baranwal, A., Srivastava, A., Kumar, P., Bajpai, V. K., Maurya, P. K., and Chandra, P. (2018). Prospects of Nanostructure Materials and Their Composites as Antimicrobial Agents. *Front. Microbiol.* 9, 422. doi:10.3389/fmicb.2018.00422

Batool, F., Özçelik, H., Stutz, C., Gegout, P. Y., Benkirane-Jessel, N., Petit, C., et al. (2021). Modulation of Immune-Inflammatory Responses through Surface Modifications of Biomaterials to Promote Bone Healing and Regeneration. *J. Tissue Eng.* 12, 20417314211041428. doi:10.1177/20417314211041428

Chen, S., He, Y., Zhong, L., Xie, W., Xue, Y., and Wang, J. (2021). Lactoferrin/Calcium Phosphate-Modified Porous Ti by Biomimetic Mineralization: Effective Infection Prevention and Excellent Osteoinduction. *Mater. (Basel)* 14, 992. doi:10.3390/ma14040992

Chernousova, S., and Epple, M. (2013). Silver as Antibacterial Agent: Ion, Nanoparticle, and Metal. *Angew. Chem. Int. Ed.* 52, 1636–1653. doi:10.1002/anie.201205923

Chu, S. J., Kan, J. Y., Lee, E. A., Lin, G. H., Jahangiri, L., Nevins, M., et al. (2019). Restorative Emergence Profile for Single-Tooth Implants in Healthy Periodontal Patients: Clinical Guidelines and Decision-Making Strategies. *Int. J. Periodontics Restor. Dent.* 40, 19–29. doi:10.11607/prd.3697

Cloutier, M., Mantovani, D., and Rosei, F. (2015). Antibacterial Coatings: Challenges, Perspectives, and Opportunities. *Trends Biotechnol.* 33, 637–652. doi:10.1016/j.tibtech.2015.09.002

Coelho, P. G., Jimbo, R., Tovar, N., and Bonfante, E. A. (2015). Osseointegration: Hierarchical Designing Encompassing the Macrometer, Micrometer, and Nanometer Length Scales. *Dent. Mater.* 31, 37–52. doi:10.1016/j.dental.2014.10.007

De Avila, E. D., Lima, B. P., Sekiya, T., Torii, Y., Ogawa, T., Shi, W., et al. (2015). Effect of UV-Photofunctionalization on Oral Bacterial Attachment and Biofilm Formation to Titanium Implant Material. *Biomaterials* 67, 84–92. doi:10.1016/j.biomaterials.2015.07.030

Ding, F., Nie, Z., Deng, H., Xiao, L., Du, Y., and Shi, X. (2013). Antibacterial Hydrogel Coating by Electrophoretic Co-deposition of Chitosan/alkynyl Chitosan. *Carbohydr. Polym.* 98, 1547–1552. doi:10.1016/j.carbpol.2013.07.042

Ding, Y., Hao, Y., Yuan, Z., Tao, B., Chen, M., Lin, C., et al. (2020). A Dual-Functional Implant with an Enzyme-Responsive Effect for Bacterial Infection Therapy and Tissue Regeneration. *Biomater. Sci.* 8, 1840–1854. doi:10.1039/c9bm01924c

European Association for Osseointegration (2019). Key Points for Clinical Practice from the EAO 2018 Consensus Conference. *Zhonghua Kou Qiang Yi Xue Za Zhi* 54, 297–302. doi:10.3760/cma.j.issn.1002-0098.2019.05.002

Friedman, A. J., Phan, J., Schairer, D. O., Champer, J., Qin, M., Pirouz, A., et al. (2013). Antimicrobial and Anti-inflammatory Activity of Chitosan-Alginate Nanoparticles: a Targeted Therapy for Cutaneous Pathogens. *J. Investigative Dermatology* 133, 1231–1239. doi:10.1038/jid.2012.399

Gribova, V., Petit, L., Kocgozlu, L., Seguin, C., Fournel, S., Kichler, A., et al. (2022). Polyarginine as a Simultaneous Antimicrobial, Immunomodulatory, and miRNA Delivery Agent within Polyanionic Hydrogel. *Macromol. Biosci.* 22, e2200043. doi:10.1002/mabi.202200043

Guglielmotti, M. B., Olmedo, D. G., and Cabrini, R. L. (2019). Research on Implants and Osseointegration. *Periodontol. 2000* 79, 178–189. doi:10.1111/prd.12254

Guizzardi, S., Galli, C., Martini, D., Belletti, S., Tinti, A., Raspanti, M., et al. (2004). Different Titanium Surface Treatment Influences Human Mandibular Osteoblast Response. *J. Periodontology* 75, 273–282. doi:10.1902/jop.2004.75.2.273

Hajjaji, A., Elabidi, M., Trabelsi, K., Assadi, A. A., Bessais, B., and Rtimi, S. (2018). Bacterial Adhesion and Inactivation on Ag Decorated TiO2-Nanotubes under Visible Light: Effect of the Nanotubes Geometry on the Photocatalytic Activity. *Colloids Surfaces B Biointerfaces* 170, 92–98. doi:10.1016/j.colsurfb.2018.06.005

Han, M., Dong, Z., Li, J., Luo, J., Yin, D., Sun, L., et al. (2021). Mussel-inspired Self-Assembly Engineered Implant Coatings for Synergistic Anti-infection and Osteogenesis Acceleration. *J. Mat. Chem. B* 9, 8501–8511. doi:10.1039/d1tb01607e

He, X., Deng, Y., Yu, Y., Lyu, H., and Liao, L. (2019). Drug-loaded/grafted Peptide-Modified Porous PEEK to Promote Bone Tissue Repair and Eliminate Bacteria. *Colloids Surfaces B Biointerfaces* 181, 767–777. doi:10.1016/j.colsurfb.2019.06.038

Hu, H., Zhang, W., Qiao, Y., Jiang, X., Liu, X., and Ding, C. (2012). Antibacterial Activity and Increased Bone Marrow Stem Cell Functions of Zn-Incorporated TiO2 Coatings on Titanium. *Acta Biomater.* 8, 904–915. doi:10.1016/j.actbio.2011.09.031

Huang, Q., Ouyang, Z., Tan, Y., Wu, H., and Liu, Y. (2019). Activating Macrophages for Enhanced Osteogenic and Bactericidal Performance by Cu Ion Release from Micro/nano-Topographical Coating on a Titanium Substrate. *Acta Biomater.* 100, 415–426. doi:10.1016/j.actbio.2019.09.030

Ivanovski, S., and Lee, R. (2018). Comparison of Peri-Implant and Periodontal Marginal Soft Tissues in Health and Disease. *Periodontol. 2000* 76, 116–130. doi:10.1111/prd.12150

Jäger, M., Jennissen, H. P., Dittrich, F., Fischer, A., and Köhling, H. L. (2017). Antimicrobial and Osseointegration Properties of Nanostructured Titanium Orthopaedic Implants. *Mater. (Basel)* 10, 1302. doi:10.3390/ma10111302

Jaggessar, A., Shahali, H., Mathew, A., and Yarlagadda, P. K. D. V. (2017). Bio-mimicking Nano and Micro-structured Surface Fabrication for Antibacterial Properties in Medical Implants. *J. Nanobiotechnol* 15, 64. doi:10.1186/s12951-017-0306-1

Jiao, Y., Liu, Q., and Chen, J. H. (2020). Construction of N-Halamine Biocompatible Multilayers onto BMP2 Loaded Titanium Nanotubes for Bacterial Infection Inhibition and Osteogenic Effect Improvement. *Mater. Lett.* 267, 127526. doi:10.1016/j.matlet.2020.127526

Kim, M. Y., Choi, H., Lee, J. H., Kim, J. H., Jung, H. S., Kim, J. H., et al. (2016). UV Photofunctionalization Effect on Bone Graft in Critical One-Wall Defect Around Implant: A Pilot Study in Beagle Dogs. *Biomed. Res. Int.* 2016, 4385279. doi:10.1155/2016/4385279

Kim, S.-G. (2020). Immunomodulation for Maxillofacial Reconstructive Surgery. *Maxillofac. Plast. Reconstr. Surg.* 42, 5. doi:10.1186/s40902-020-00249-4

Knopf-Marques, H., Barthes, J., Lachaal, S., Mutschler, A., Muller, C., Dufour, F., et al. (2019). Multifunctional Polymeric Implant Coatings Based on Gelatin, Hyaluronic Acid Derivative and Chain Length-Controlled Poly(arginine). *Mater. Sci. Eng. C* 104, 109898. doi:10.1016/j.msec.2019.109898

Koons, G. L., Diba, M., and Mikos, A. G. (2020). Materials Design for Bone-Tissue Engineering. *Nat. Rev. Mater* 5, 584–603. doi:10.1038/s41578-020-0204-2

Kumari, S., Tiyyagura, H. R., Pottathara, Y. B., Sadasivuni, K. K., Ponnamma, D., Douglas, T. E. L., et al. (2021). Surface Functionalization of Chitosan as a Coating Material for Orthopaedic Applications: A Comprehensive Review. *Carbohydr. Polym.* 255, 117487. doi:10.1016/j.carbpol.2020.117487

Kunrath, M., Dos Santos, R., De Oliveira, S., Hubler, R., Sesterheim, P., and Teixeira, E. (2020). Osteoblastic Cell Behavior and Early Bacterial Adhesion on Macro-, Micro-, and Nanostructured Titanium Surfaces for Biomedical Implant Applications. *Int. J. Oral Maxillofac. Implants* 35, 773–781. doi:10.11607/jomi.8069

Leng, J., He, Y., Yuan, Z., Tao, B., Li, K., Lin, C., et al. (2021). Enzymatically-degradable Hydrogel Coatings on Titanium for Bacterial Infection Inhibition and Enhanced Soft Tissue Compatibility *via* a Self-Adaptive Strategy. *Bioact. Mater.* 6, 4670–4685. doi:10.1016/j.bioactmat.2021.05.001

Li, D., Li, Y., Shrestha, A., Wang, S., Wu, Q., Li, L., et al. (2019). Effects of Programmed Local Delivery from a Micro/Nano-Hierarchical Surface on Titanium Implant on Infection Clearance and Osteogenic Induction in an Infected Bone Defect. *Adv. Healthc. Mater* 8, e1900002. doi:10.1002/adhm.201900002

Li, Y., Liu, X., Li, B., Zheng, Y., Han, Y., Chen, D.-f., et al. (2020). Near-Infrared Light Triggered Phototherapy and Immunotherapy for Elimination of Methicillin-Resistant Staphylococcus aureus Biofilm Infection on Bone Implant. *ACS Nano* 14, 8157–8170. doi:10.1021/acsnano.0c01486

Liou, J.-W., and Chang, H.-H. (2012). Bactericidal Effects and Mechanisms of Visible Light-Responsive Titanium Dioxide Photocatalysts on Pathogenic

Bacteria. *Arch. Immunol. Ther. Exp.* 60, 267–275. doi:10.1007/s00005-012-0178-x

Liu, D., Gong, Y. J., Xiao, Q., and Li, Z. A. (2016). Effect of Modification of Titanium Surfaces to Graft Poly(ethylene Glycol)methacrylate-Arginine-Glycine-Aspartic Polymer Brushes on Bacterial Adhesion and Osteoblast Cell Attachment. *Zhonghua Kou Qiang Yi Xue Za Zhi* 51, 491–495. doi:10.3760/cma.j.issn.1002-0098.2016.08.011

Liu, H.-W., Wei, D.-X., Deng, J.-Z., Zhu, J.-J., Xu, K., Hu, W.-H., et al. (2018). Combined Antibacterial and Osteogenic *In Situ* Effects of a Bifunctional Titanium Alloy with Nanoscale Hydroxyapatite Coating. *Artif. Cells, Nanomedicine, Biotechnol.* 46, S460–S470. doi:10.1080/21691401.2018.1499662

Liu, Y.-C., Zou, X.-B., Chai, Y.-F., and Yao, Y.-M. (2014). Macrophage Polarization in Inflammatory Diseases. *Int. J. Biol. Sci.* 10, 520–529. doi:10.7150/ijbs.8879

Liu, Z., Liu, X., and Ramakrishna, S. (2021). Surface Engineering of Biomaterials in Orthopedic and Dental Implants: Strategies to Improve Osteointegration, Bacteriostatic and Bactericidal Activities. *Biotechnol. J.* 16, e2000116. doi:10.1002/biot.202000116

Lovati, A. B., Bottagisio, M., Maraldi, S., Violatto, M. B., Bortolin, M., De Vecchi, E., et al. (2018). Vitamin E Phosphate Coating Stimulates Bone Deposition in Implant-Related Infections in a Rat Model. *Clin. Orthop. Relat. Res.* 476, 1324–1338. doi:10.1097/01.blo.0000534692.41467.02

Lu, H., Liu, Y., Guo, J., Wu, H., Wang, J., and Wu, G. (2016). Biomaterials with Antibacterial and Osteoinductive Properties to Repair Infected Bone Defects. *Int. J. Mol. Sci.* 17, 334. doi:10.3390/ijms17030334

Lyu, W. L., Deng, W., Liu, D. Y., Yun, X. Y., and Li, C. Y. (2019). Effects of Two Nanotopographies of Ultraviolet-Treated Titanium Implant Surface on Macrophage Behaviour and Inflammatory Cytokines Secretion. *Zhonghua Kou Qiang Yi Xue Za Zhi* 54, 183–187. doi:10.3760/cma.j.issn.1002-0098.2019.03.007

Mathur, A., Kharbanda, O. P., Koul, V., Dinda, A. K., Anwar, M. F., and Singh, S. (2021). Fabrication and Evaluation of Antimicrobial Biomimetic Nanofiber Coating for Improved Dental Implant Bioseal: An *In Vitro* Study. *J. Periodontol.* 93, 1–11. doi:10.1002/JPER.21-0255

Matter, M. T., Maliqi, L., Keevend, K., Guimond, S., Ng, J., Armagan, E., et al. (2021). One-Step Synthesis of Versatile Antimicrobial Nano-Architected Implant Coatings for Hard and Soft Tissue Healing. *ACS Appl. Mat. Interfaces* 13, 33300–33310. doi:10.1021/acsami.1c10121

Matthes, R., Duske, K., Kebede, T. G., Pink, C., Schlüter, R., Von Woedtke, T., et al. (2017). Osteoblast Growth, after Cleaning of Biofilm-Covered Titanium Discs with Air-Polishing and Cold Plasma. *J. Clin. Periodontol.* 44, 672–680. doi:10.1111/jcpe.12720

Mendonça, G., Mendonça, D. B. S., Aragão, F. J. L., and Cooper, L. F. (2008). Advancing Dental Implant Surface Technology - from Micron- to Nanotopography. *Biomaterials* 29, 3822–3835. doi:10.1016/j.biomaterials.2008.05.012

Moon, K. S., Choi, E. J., Bae, J. M., Park, Y. B., and Oh, S. (2020). Visible Light-Enhanced Antibacterial and Osteogenic Functionality of Au and Pt Nanoparticles Deposited on TiO2 Nanotubes. *Mater. (Basel)* 13, 3721. doi:10.3390/ma13173721

Muszanska, A. K., Rochford, E. T. J., Gruszka, A., Bastian, A. A., Busscher, H. J., Norde, W., et al. (2014). Antiadhesive Polymer Brush Coating Functionalized with Antimicrobial and RGD Peptides to Reduce Biofilm Formation and Enhance Tissue Integration. *Biomacromolecules* 15, 2019–2026. doi:10.1021/bm500168s

Neacsu, P., Mazare, A., Schmuki, P., and Cimpean, A. (2015). Attenuation of the Macrophage Inflammatory Activity by TiO_2 Nanotubes *via* Inhibition of MAPK and NF-Kb Pathways. *Int. J. Nanomedicine* 10, 6455–6467. doi:10.2147/IJN.S92019

Nejadnik, M. R., Van Der Mei, H. C., Norde, W., and Busscher, H. J. (2008). Bacterial Adhesion and Growth on a Polymer Brush-Coating. *Biomaterials* 29, 4117–4121. doi:10.1016/j.biomaterials.2008.07.014

Ninan, N., Goswami, N., and Vasilev, K. (2020). The Impact of Engineered Silver Nanomaterials on the Immune System. *Nanomater. (Basel)* 10, 967. doi:10.3390/nano10050967

Ogawa, T. (2014). Ultraviolet Photofunctionalization of Titanium Implants. *Int. J. Oral Maxillofac. Implants* 29, e95–e102. doi:10.11607/jomi.te47

Ota, T., Chiba, M., and Hayashi, H. (2016). Vibrational Stimulation Induces Osteoblast Differentiation and the Upregulation of Osteogenic Gene Expression *In Vitro*. *Cytotechnology* 68, 2287–2299. doi:10.1007/s10616-016-0023-x

Özçelik, H., Vrana, N. E., Gudima, A., Riabov, V., Gratchev, A., Haikel, Y., et al. (2015). Harnessing the Multifunctionality in Nature: a Bioactive Agent Release System with Self-Antimicrobial and Immunomodulatory Properties. *Adv. Healthc. Mat.* 4, 2026–2036. doi:10.1002/adhm.201500546

Rupp, F., Liang, L., Geis-Gerstorfer, J., Scheideler, L., and Hüttig, F. (2018). Surface Characteristics of Dental Implants: A Review. *Dent. Mater.* 34, 40–57. doi:10.1016/j.dental.2017.09.007

Schünemann, F. H., Galárraga-Vinueza, M. E., Magini, R., Fredel, M., Silva, F., Souza, J. C. M., et al. (2019). Zirconia Surface Modifications for Implant Dentistry. *Mater. Sci. Eng. C* 98, 1294–1305. doi:10.1016/j.msec.2019.01.062

Schwarz, F., Rothamel, D., Sculean, A., Georg, T., Scherbaum, W., and Becker, J. (2003). Effects of an Er : YAG Laser and the Vector Ultrasonic System on the Biocompatibility of Titanium Implants in Cultures of Human Osteoblast-like Cells. *Clin. Oral Implants Res.* 14, 784–792. doi:10.1046/j.0905-7161.2003.00954.x

Shahali, H., Hasan, J., Mathews, A., Wang, H., Yan, C., Tesfamichael, T., et al. (2019). Multi-biofunctional Properties of Three Species of Cicada Wings and Biomimetic Fabrication of Nanopatterned Titanium Pillars. *J. Mat. Chem. B* 7, 1300–1310. doi:10.1039/c8tb03295e

Souza, J. C. M., Sordi, M. B., Kanazawa, M., Ravindran, S., Henriques, B., Silva, F. S., et al. (2019). Nano-scale Modification of Titanium Implant Surfaces to Enhance Osseointegration. *Acta Biomater.* 94, 112–131. doi:10.1016/j.actbio.2019.05.045

Sutrisno, L., Hu, Y., Shen, X., Li, M., Luo, Z., Dai, L., et al. (2018). Fabrication of Hyaluronidase-Responsive Biocompatible Multilayers on BMP2 Loaded Titanium Nanotube for the Bacterial Infection Prevention. *Mater. Sci. Eng. C* 89, 95–105. doi:10.1016/j.msec.2018.03.024

Swartjes, J. J. T. M., Sharma, P. K., Kooten, T. G., Mei, H. C., Mahmoudi, M., Busscher, H. J., et al. (2015). Current Developments in Antimicrobial Surface Coatings for Biomedical Applications. *Curr. Med. Chem.* 22, 2116–2129. doi:10.2174/0929867321666140916121355

Tao, B., Deng, Y., Song, L., Ma, W., Qian, Y., Lin, C., et al. (2019). BMP2-loaded Titania Nanotubes Coating with pH-Responsive Multilayers for Bacterial Infections Inhibition and Osteogenic Activity Improvement. *Colloids Surfaces B Biointerfaces* 177, 242–252. doi:10.1016/j.colsurfb.2019.02.014

Tsukimura, N., Yamada, M., Iwasa, F., Minamikawa, H., Att, W., Ueno, T., et al. (2011). Synergistic Effects of UV Photofunctionalization and Micro-nano Hybrid Topography on the Biological Properties of Titanium. *Biomaterials* 32, 4358–4368. doi:10.1016/j.biomaterials.2011.03.001

Wang, G., Zhu, Y., Zan, X., and Li, M. (2021). Endowing Orthopedic Implants' Antibacterial, Antioxidation, and Osteogenesis Properties through a Composite Coating of Nano-Hydroxyapatite, Tannic Acid, and Lysozyme. *Front. Bioeng. Biotechnol.* 9, 718255. doi:10.3389/fbioe.2021.718255

Wang, K., Jin, H., Song, Q., Huo, J., Zhang, J., and Li, P. (2021). Titanium Dioxide Nanotubes as Drug Carriers for Infection Control and Osteogenesis of Bone Implants. *Drug Deliv. Transl. Res.* 11, 1456–1474. doi:10.1007/s13346-021-00980-z

Wang, S., Deng, Y., Yang, L., Shi, X., Yang, W., and Chen, Z.-G. (2018). Enhanced Antibacterial Property and Osteo-Differentiation Activity on Plasma Treated Porous Polyetheretherketone with Hierarchical Micro/nano-Topography. *J. Biomaterials Sci. Polym. Ed.* 29, 520–542. doi:10.1080/09205063.2018.1425181

Wang, X. Y., Guo, H. Y., Zhang, W., Wen, P. C., Zhang, H., Guo, Z. R., et al. (2013). Effect of Iron Saturation Level of Lactoferrin on Osteogenic Activity *In Vitro* and *In Vivo*. *J. Dairy Sci.* 96, 33–39. doi:10.3168/jds.2012-5692

Wang, Z., Mei, L., Liu, X., and Zhou, Q. (2021). Hierarchically Hybrid Biocoatings on Ti Implants for Enhanced Antibacterial Activity and Osteogenesis. *Colloids Surfaces B Biointerfaces* 204, 111802. doi:10.1016/j.colsurfb.2021.111802

Wu, C., Ramaswamy, Y., Chang, J., Woods, J., Chen, Y., and Zreiqat, H. (2008). The Effect of Zn Contents on Phase Composition, Chemical Stability and Cellular Bioactivity in Zn-Ca-Si System Ceramics. *J. Biomed. Mat. Res.* 87B, 346–353. doi:10.1002/jbm.b.31109

Yan, J., Xia, D., Zhou, W., Li, Y., Xiong, P., Li, Q., et al. (2020). pH-Responsive Silk Fibroin-Based CuO/Ag Micro/nano Coating Endows Polyetheretherketone with Synergistic Antibacterial Ability, Osteogenesis, and Angiogenesis. *Acta Biomater.* 115, 220–234. doi:10.1016/j.actbio.2020.07.062

Yang, W.-E., and Huang, H.-H. (2019). Multiform TiO2 Nano-Network Enhances Biological Response to Titanium Surface for Dental Implant Applications. *Appl. Surf. Sci.* 471, 1041–1052. doi:10.1016/j.apsusc.2018.11.244

Yang, Y., Ren, S., Zhang, X., Yu, Y., Liu, C., Yang, J., et al. (2018). Safety and Efficacy of PLGA(Ag-Fe3O4)-coated Dental Implants in Inhibiting Bacteria Adherence and Osteogenic Inducement under a Magnetic Field. *Int. J. Nanomedicine* 13, 3751–3762. doi:10.2147/ijn.s159860

Yin, J., Han, Q., Zhang, J., Liu, Y., Gan, X., Xie, K., et al. (2020). MXene-Based Hydrogels Endow Polyetheretherketone with Effective Osteogenicity and Combined Treatment of Osteosarcoma and Bacterial Infection. *ACS Appl. Mat. Interfaces* 12, 45891–45903. doi:10.1021/acsami.0c14752

Yuan, Z., Tao, B., He, Y., Liu, J., Lin, C., Shen, X., et al. (2019). Biocompatible MoS2/PDA-RGD Coating on Titanium Implant with Antibacterial Property *via* Intrinsic ROS-independent Oxidative Stress and NIR Irradiation. *Biomaterials* 217, 119290. doi:10.1016/j.biomaterials.2019.119290

Zaveri, T. D., Dolgova, N. V., Chu, B. H., Lee, J., Wong, J., Lele, T. P., et al. (2010). Contributions of Surface Topography and Cytotoxicity to the Macrophage Response to Zinc Oxide Nanorods. *Biomaterials* 31, 2999–3007. doi:10.1016/j.biomaterials.2009.12.055

Zhang, Y., Gulati, K., Li, Z., Di, P., and Liu, Y. (2021). Dental Implant Nano-Engineering: Advances, Limitations and Future Directions. *Nanomater. (Basel)* 11, 2489. doi:10.3390/nano11102489

Zhu, Y., Gu, Y., Qiao, S., Zhou, L., Shi, J., and Lai, H. (2017). Bacterial and Mammalian Cells Adhesion to Tantalum-Decorated Micro-/nano-structured Titanium. *J. Biomed. Mat. Res.* 105, 871–878. doi:10.1002/jbm.a.35953

Conflict of Interest: The authors declare that the research was conducted in the absence of any commercial or financial relationships that could be construed as a potential conflict of interest.

Publisher's Note: All claims expressed in this article are solely those of the authors and do not necessarily represent those of their affiliated organizations, or those of the publisher, the editors and the reviewers. Any product that may be evaluated in this article, or claim that may be made by its manufacturer, is not guaranteed or endorsed by the publisher.

frontiers | Frontiers in Bioengineering and Biotechnology

ORIGINAL RESEARCH
published: 30 May 2022
doi: 10.3389/fbioe.2022.892385

Improving the Stability of a Hemipelvic Prosthesis Based on Bone Mineral Density Screw Channel and Prosthesis Optimization Design

*Rongqi Zhou†, Haowen Xue†, Jincheng Wang†, Xiaonan Wang, Yanbing Wang, Aobo Zhang, Jiaxin Zhang, Qing Han and Xin Zhao**

Department of Orthopedics, The Second Hospital of Jilin University, Changchun, China

In pelvic reconstruction surgery, the hemipelvic prosthesis can cause significant changes in stress distribution due to its high stiffness, and its solid structure is not suitable for osseointegration. The purpose of this study was to identify a novel bone mineral density screw channel and design the structure of the prosthesis so as to improve the distribution of stress, promote bone growth, and enhance the biomechanical properties of the prosthesis. The mechanical characteristics of bone mineral density screw and traditional screw were compared by finite element analysis method, and redesigned by topology optimization. The direction of the newly proposed screw channel was the posterolateral entrance of the auricular surface, ending at the contralateral sacral cape. Compared to the original group, the maximum stress of the optimized prosthesis was decreased by 24.39%, the maximum stress of the sacrum in the optimized group was decreased by 27.23%, and the average strain energy density of the sacrum in the optimized group was increased by 8.43%. On the surface of screw and connecting plate, the area with micromotion more than 28 μm is reduced by 12.17%. On the screw surface, the area with micromotion more than 28 μm is reduced by 22.9%. The newly determined screw channel and optimized prosthesis design can effectively improve the biomechanical properties of a prosthesis and the microenvironment of osseointegration. This method can provide a reference for the fixation of prostheses in clinical pelvic reconstruction.

Keywords: bone mineral density, topological optimization, porous structure, hemipelvic prosthesis, screw channel

OPEN ACCESS

Edited by:
Roman Surmenev, Tomsk Polytechnic University, Russia

Reviewed by:
Tao Ji, Peking University People's Hospital, China
Abdelwahed Barkaoui, International University of Rabat, Morocco

****Correspondence:***
Xin Zhao
zhaoxin429@hotmail.com

†These authors have contributed equally to this work and share first authorship

Specialty section:
This article was submitted to Biomaterials, a section of the journal Frontiers in Bioengineering and Biotechnology

Received: *09 March 2022*
Accepted: *16 May 2022*
Published: *30 May 2022*

Citation:
Zhou R, Xue H, Wang J, Wang X, Wang Y, Zhang A, Zhang J, Han Q and Zhao X (2022) Improving the Stability of a Hemipelvic Prosthesis Based on Bone Mineral Density Screw Channel and Prosthesis Optimization Design. Front. Bioeng. Biotechnol. 10:892385. doi: 10.3389/fbioe.2022.892385

1 INTRODUCTION

Primary pelvic sarcoma seriously impacts the survival and quality of life of patients. Limb-salvage surgery through prosthesis placement or biological reconstruction is more popular than traditional hemipelectomy (Muller et al., 2002). With the progress to date in artificial prostheses and surgical technology, many limb-salvage methods have been developed, such as the implantation of a modular hemipelvic endoprosthesis (Ji et al., 2010), a customized endoprosthesis (Iqbal et al., 2017), or a massive allograft (Matejovsky et al., 2006). Most of these approaches have achieved good results in follow-up (Zhou et al., 2011; Zhou et al., 2013). However, when patients experience recurrence or prosthesis instability, orthopedics doctors face significant challenges in resolving the issue (Ji et al., 2013).

During sacral pelvic reconstruction and repair, a screw–rod system (Zang et al., 2014) and cancellous bone screw (Zhao X. et al., 2018) are two common hemipelvic prosthesis–fixation methods that may be used. However, these fixation methods are often accompanied by some complications, such as neurovascular injury (Zhao Y. et al., 2018; Alkhateeb et al., 2020), screw loosening (Lu et al., 2000), and fracture (Shao et al., 2015). Previous studies have shown that patients with osteoporosis are more prone to low-energy traumatic fractures (den Teuling et al., 2017) and pedicle screw–loosening (Weiser et al., 2017). Related studies have measured and analyzed sacral bone mineral density (BMD) (Salazar et al., 2015; Thiesen et al., 2020). However, few studies to date have characterized the effect of BMD on the strength of sacral screw fixation. At present, there is no study reporting the results of finite element analysis (FEA) of sacral screw fixation and BMD. Therefore, we used FEA to verify the relationship between the difference of BMD and the strength of sacral screw fixation.

The huge mismatch in mechanical properties between the sacrum and prosthesis materials can easily lead to a stress-shielding effect (Al-Tamimi et al., 2017), and significant bone resorption may occur around the prosthesis as a result of this effect (Iolascon et al., 2010). To reduce the amount of stress shielding, structural design methods are needed to render the stress distribution between the prosthesis and bone more uniform (Liu et al., 2021). Topology optimization (TO) is one such method of structural design. It provides the best shape of the structure from the specified area under certain design considerations, such as load and boundary conditions (Park et al., 2019). Through the TO approach, the stress between the prosthesis and bone can be better distributed. In addition, based on the TO design, adding a porous structure on the surface of the screw and prosthesis can reduce the elasticity modulus of the prosthesis, providing a suitable microenvironment for bone growth and maintaining the stability of the prosthesis (Zhang et al., 2020). Therefore, this study combines TO technology with a porous structure. A porous structure can effectively reduce stiffness, so it has been widely used in orthopedics (Hu et al., 2019; Chen et al., 2020).

In this study, we aimed to measure the sacral BMD and determine the position of the screw according to the BMD distribution, then conduct FEA to verify its mechanical stability. Combined with a TO design, a porous structure was added on the surface to obtain good stability, promote bone growth, and reduce complications.

2 MATERIALS AND METHODS

2.1 BMD Measurement

Two researchers collected computed tomography (CT) data from 40 patients, including 20 men and 20 women, with an average age of 67.23 ± 4.26 years (range, 33–79 years). The CT data were imported into the medical image–processing software OsiriX Lite (Pixmeo SARL, Bernex, Switzerland), which was used to measure the BMD in the sagittal plane of the patient's sacrum. Seven layers of sacral sagittal plane were scanned for BMD measurement, including the BMD of the sagittal sections of the bilateral auricular surface, bilateral sacral ala midline, bilateral sacral canal edge, and sacral midline. A sectional diagram of the seven layers of the sacral sagittal plane and the measurement method were shown in **Figure 1**. The cancellous bone region of the S1 level was divided into four regions of interest (ROIs), and the average BMD of each region was measured using an ROI tool.

2.2 Three-Dimensional (3D) Modeling

The geometry of the sacral model was based on CT data of the pelvis of a female volunteer. Pelvic CT data were acquired using the iCT 256 scanner with an X-ray tube (Philips, Amsterdam, Netherlands) with the following parameters: current, 232 mA; voltage, 120 kV; pixel size, 0.52 mm; section thickness, 0.9 mm; and spacing between sections, 0.45 mm. The CT data were imported into the Mimics version 21.0 software program (Materialise, Leuven, Belgium), and the sacrum was reconstructed into a 3D model. The 3D model of the sacrum was then imported into Magics version 24.0 (Materialise), and its left auricular surface was intercepted. On this basis, three S1 screw channels (long screw, short screw, and BMD screw) were designed, and fixed with a long screw at the S2 level. BMD screw placement is a way to implant screws near a high BMD area. A hemipelvic prosthesis with acetabulum was designed and reconstructed using Magics version 24.0. The hemipelvic prosthesis was mainly composed of three parts: a connecting plate in contact with the auricular surface, an acetabular cup, and the connecting device present between the connecting plate and the acetabular cup. The screws were tightly connected with the prosthesis through the connecting plate and fixed on the auricular surface. These screws were simplified to cylinders for later application of FEA. The design of the three parts of the prosthesis and screws is shown in **Figure 2**. This study was approved by the ethics committee of the Second Hospital of Jilin University, and we obtained the informed consent of all participants.

2.3 FEA Model

We imported the 3D model of the prosthesis into the HyperMesh 2020 software program (Altair engineering, Troy, Michigan, United States). The triangle-based surface mesh in the prosthesis model is set to 1 mm using self-animation mesh technology. After generating the two-dimensional mesh, it is transformed into a 4-node linear tetrahedral element (C3D4). Using Mimics, a 3D sacral model with inhomogeneous material properties was defined according to the gray value of the CT scan. The material properties of inhomogeneous sacrum are shown in **Figure 3**. According to previous literature (Rho et al., 1995), the material properties of the sacrum were determined according to the following equations:

$$\rho\left(g/m^3\right) = 47 + 1.122 \times GV\,(HU)$$
$$E\,(Pa) = 0.63 \times \rho^{1.35} g/m^3$$

where ρ is the bone density, GV is the gray value of the bone in CT data, and E is the elastic modulus. The element size of the sacral model was set to 1 mm. In the analysis, the material was assumed

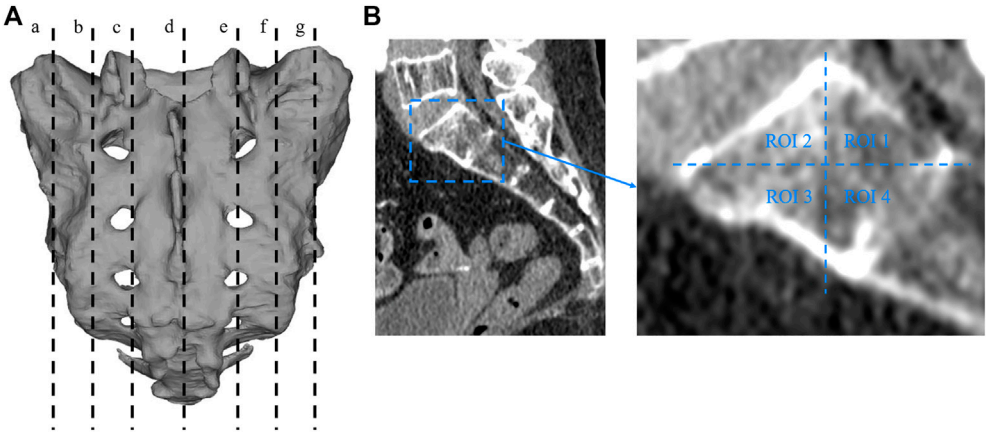

FIGURE 1 | Sectional diagram of seven layers of sacral sagittal plane and the measurement method of BMD. **(A)** a: The junction of the left auricular surface and the dorsal side. b: Middle of the left sacral wing. c: Left margin of the sacral canal. d: Median sacral line. e: Right margin of the sacral canal. f: Middle of the right sacral wing. g: The right auricular surface is at the junction with the dorsal side. **(B)** The sagittal plane is divided into four regions, and the bone mineral density of each region is measured with a region-of-interest tool in the OsiriX Lite software.

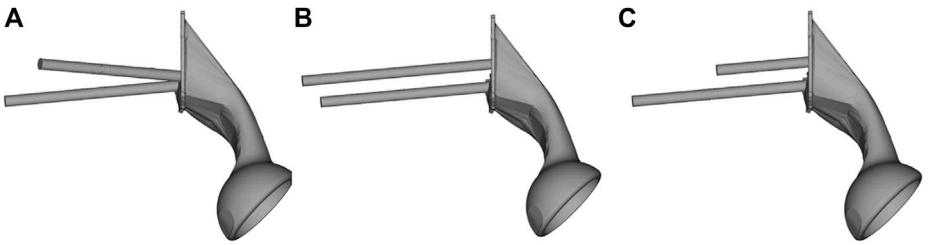

FIGURE 2 | The S1 and S2 screws are tightly connected to the hemipelvic prosthesis with acetabulum through a connecting plate. The screw is replaced by a cylinder. **(A)** Bone mineral density screw. **(B)** Long screw, and **(C)** short screw.

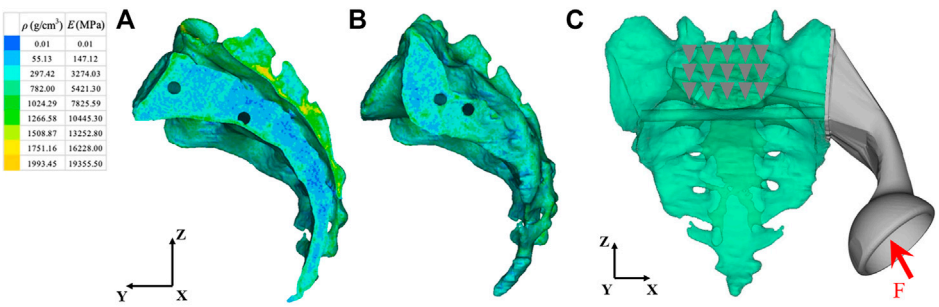

FIGURE 3 | Material properties of inhomogeneous sacrum and model load and constraint. **(A)** Internal material properties of the sacrum. **(B)** External material properties of the sacrum. **(C)** A load was applied to the center of the acetabulum. The constraint was set on the upper surface of S1 vertebral body. ρ: Bone mineral density; E: Elastic modulus. The arrow and triangles represent the load and constraint of the FEA respectively.

to be of a linear elastic type. According to previous literature, the Poisson's ratio of bone was set to 0.3 (Dong et al., 2018). The material properties of the finite element model were determined according to our previous research data (Liu et al., 2021). The material characteristics of various implants and sacrum were shown in **Table 1**.

The load conditions of the static analysis carried out in this study were the same as those used by (Bergmann et al., 2001). A load of 1948 N was applied to the center of the acetabulum, and the magnitude and direction of the force were normalized to 100%. In terms of boundary conditions, the area of the upper surface of S1 vertebral body was considered to be

TABLE 1 | The material characteristics of various components.

Component	Material	Elastic modulus (MPa)	Poisson's ratio	Element
BMD screw	Ti6Al4V	110,000	0.3	9,793
Long screw	Ti6Al4V	110,000	0.3	16,544
Short screw	Ti6Al4V	110,000	0.3	6,998
S2 screw	Ti6Al4V	110,000	0.3	12,737
Connecting plate	Ti6Al4V	110,000	0.3	22,049
Hemipelvic prosthesis	Ti6Al4V	110,000	0.3	177,820
Sacrum	Inhomogeneous bone	Inhomogeneous bone	0.3	747,607

TABLE 2 | Friction types between components.

Contact surface A	Contact surface B	Friction type
Sacrum	Porous surface	μ1 = 0.667, μ2 = 0.431
Sacrum	Solid surface	μ1 = 0.647, μ2 = 0.348
Connecting plate	Screw	Stick

Note: μ_1 is the static friction coefficient, μ_2 is the dynamic friction coefficient.

completely limited. The load and boundary conditions of prosthesis and sacrum are shown in **Figure 3**. The simulation process adopted quasi-static loading nonlinear analysis, with 20 steps of iteration until convergence, and the iterative method adopted Newton Raphson method. The stress distribution and relative micromotion were selected as the main parameters to verify the stress shielding effect and bone growth effect. The results were obtained and measured in HyperView (Altair Engineering, Troy, MI, United States). Based on the previous research data (Bartolomeu et al., 2019), the friction type of each contact surface was determined, and the contact surface was regarded as a nonlinear contact surface. The types of friction between components were shown in **Table 2**.

2.4 TO of Screws and Connecting Plate

According to the stress distribution of the prosthesis, the BMD screw and connecting plate were topologically optimized. TO of the connecting plate and screws was performed in HyperMesh 2020. Referring to previous literature (Chen and Shih, 2018), the minimally compliant TO under the volume fraction constraint was adopted. The optimization equation was as follows:

Objective function: to minimize (Uc).

Constraint: $0 < \eta_i < 1$ (i = 1, 2, 3 . . . n)

$$V \le V_0 - V *$$
$$V = \sum_i \eta_i V_i$$
$$E_i = E(\eta_i)$$
$$\{\sigma_i\} = [E_i]\{\varepsilon_i\}$$

where U_c is the compliance, η_i represents the internal pseudodensity assigned to each finite element (i) in the optimization equation, V is the computed volume, V_0 is the original volume, V* represents the amount of volume to be removed, V_i is the volume of element i, E_i is the elasticity tensor for each element, E represents the elasticity tensor, σ_i is the stress vector of element i, and ε_i represents the strain vector of element. η, as the density index, ranged from 0 to 1. An η value close to 0 indicates the material to be removed, and an η value close to 1 indicates the material to be retained. The program was set to reduce the volume by up to 50% and iterate 30 times at most.

Next, we input the results of TO into Magics version 21.0. The parts to be removed were obtained by performing Boolean operations between the intact model and the optimized parts obtained by TO. In this study, the newly designed prosthesis retained the same shape as the original prosthesis. The removed parts and optimized parts were designed to have a high-strength body-centered cubic structure. The removable part was designed with an optimal porosity of 70% and an aperture of 200 μm to allow for early and extensive bone ingrowth (Arabnejad et al., 2016; Bartolomeu et al., 2019). The porosity of the optimized part of the screw surface and the connecting plate was 30% and the pore diameter was 200 μm to maintain stiffness and promote proper bone growth (Chen et al., 2017; Bartolomeu et al., 2019). Then, the biomechanical changes between the original prosthesis and the optimized prosthesis were compared through FEA.

The FEA results were processed using HyperView 2020. Von Mises stress values of the sacrum and prosthesis were recorded. The prosthesis consists of screws, a connecting plate, and the hemipelvic prosthesis. The strain energy density (SED) can be used as an index of shielding stress (Ahmed et al., 2020). Inserting a relatively rigid prosthesis into the bone will lead to a reduction in the distribution of non-physiological load and bone strain around the prosthesis. The insertion of the prosthesis reduces the physiological load borne by bone, so the stress is shielded. In addition, when stress shielding occurs, the strain of the bone around the prosthesis will be reduced. Therefore, a high SED indicates low stress shielding (Zhang et al., 2020).

2.5 Data Analysis

Using the SPSS software (IBM Corporation, Armonk, NY, United States), the BMD data were statistically analyzed by one-way ANOVA. Paired *t*-test was used to statistically analyze the data of topology optimized prosthesis. Statistical significance was set as $p < 0.05$.

TABLE 3 | Results of one-way analysis of variance of sacral bone mineral density.

ANOVA		SS	v	MS	F	PR
A	Group	69,351.674	3	23,117.225	14.812	0.000
	Residual	243,464.596	156	1,560.670	—	—
	Total	312,816.270	159	—	—	—
B	Group	116,910.076	3	38,970.025	27.723	0.000
	Residual	219,285.470	156	1,405.676	—	—
	Total	336,195.546	159	—	—	—
C	Group	178,988.181	3	59,662.727	8.127	0.000
	Residual	1,145,263.065	156	7,341.430	—	—
	Total	1,324,251.246	159	—	—	—
D	Group	303,818.741	3	101,272.914	34.849	0.000
	Residual	453,344.150	156	2,906.052	—	—
	Total	757,162.891	159	—	—	—
E	Group	171,339.808	3	57,113.269	11.810	0.000
	Residual	754,385.772	156	4,835.806	—	—
	Total	925,725.580	159	—	—	—
F	Group	158,005.185	3	52,668.395	48.005	0.000
	Residual	171,155.495	156	1,097.151	—	—
	Total	329,160.680	159	—	—	—
G	Group	71,624.126	3	23,874.709	9.597	0.000
	Residual	388,070.197	156	2,487.629	—	—
	Total	459,694.323	159	—	—	—

(A) *the junction of the left auricular surface and the dorsal side;* ***(B)*** *middle of the left sacral wing;* ***(C)*** *left margin of the sacral canal;* ***(D)*** *median sacral line;* ***(E)*** *right margin of the sacral canal;* ***(F)*** *middle of the right sacral wing;* ***(G)*** *the right auricular surface is at the junction with the dorsal side.* Abbreviations: *ANOVA, analysis of variance; F, F value, MS, mean square; PR,* p *value; SS, sum of squares; v, degrees of freedom.*

3 RESULTS

3.1 BMD Measurement Results

In the measurement, it was found that the BMD distribution on both sides of the sacrum was symmetrical. The mean and standard deviation values of BMD were determined in Hounsfield units (Thiesen et al., 2020). The measured sacral BMD data are shown through one-way analysis of variance in **Table 3** and BMD of the ROI in seven sagittal planes (mean ± standard deviation, Hu) in **Table 4**. In the junction between the left auricular surface and the dorsal side, the BMD in the fourth quadrant was the highest, and the average value was 182.33 ± 39.31 HU ($p < 0.01$). In the middle of the left sacral ala, the first quadrant had the highest BMD, with an average value of 103.90 ± 39.04 HU ($p < 0.01$). In the left margin of the sacral canal, the BMD in the third quadrant was the highest, and the average value was 264.51 ± 88.75 HU ($p < 0.01$). In the middle sacral line, the BMD in the second quadrant was the highest, with an average value of 240.81 ± 65.30 HU ($p < 0.01$). In the right margin of sacral canal, the BMD in the third quadrant was the highest, and the average value was 247.19 ± 67.47 HU ($p < 0.01$). In the middle of the right sacral ala, the first quadrant had the highest BMD, with an average value of 107.02 ± 39.09 HU ($p < 0.01$). Finally, at the junction of the right auricular surface and the dorsal side, the BMD in the fourth quadrant was the highest, with an average value of 187.21 ± 52.91 HU ($p < 0.01$).

3.2 Von Mises Stress of the Original Prosthesis

The stress distribution of the prosthesis varies according to the three different fixation methods. As shown in **Figure 4**, on the BMD screw, the stress is mainly distributed at the connection between the connecting plate and S1 screw, and no obvious stress concentration was observed. The maximum stress is 350.33 MPa, which is located at the base of the S1 screw. On the long screw, the stress is mainly distributed in the first half of the S1 screw, and an obvious stress concentration could be observed at the connection position between the S1 screw and connecting plate, with the maximum stress being 442.34 MPa. On the short screw, the stress distribution is similar to that on the long screw, and the stress concentration is located at the connection between the S1 screw and connecting plate, with the maximum stress being 446.92 MPa.

3.3 TO Results and von Mises Stress of the Sacrum and Prosthesis

The TO program was iterated six times. The algorithm mainly removed the middle two portions of the connecting plate; about 84% of the connecting plate was retained. As shown in **Figure 5**, the connecting plate and screws with porous structure were newly added to the surface. The porosity of the removed parts was designed to be 70%, and that of the optimized connecting plate and screws surface was designed to be 30%.

As shown in **Figure 6**, the von Mises stress values of the original group and the optimized group. The maximum stress of

TABLE 4 | BMD of the region of interest in seven sagittal planes (mean ± SD, Hu).

Group (*N* = 40)	Mean ± SD			
	ROI 1	ROI 2	ROI 3	ROI 4
A	135.11 ± 41.98	133.88 ± 41.85	167.09 ± 34.40	182.33 ± 39.31
B	103.90 ± 39.04	97.49 ± 44.18	51.34 ± 31.89	42.96 ± 33.62
C	203.03 ± 79.37	241.83 ± 114.22	264.51 ± 88.75	178.25 ± 46.31
D	140.25 ± 45.63	240.81 ± 65.30	212.83 ± 54.59	143.71 ± 47.94
E	187.44 ± 68.42	239.41 ± 88.44	247.19 ± 67.47	170.86 ± 47.83
F	107.02 ± 39.09	100.91 ± 31.64	45.74 ± 31.43	37.36 ± 29.53
G	142.55 ± 42.51	134.73 ± 44.84	170.63 ± 57.73	187.21 ± 52.91

A, the junction of the left auricular surface and the dorsal side; B, middle of the left sacral wing; C, left margin of the sacral canal; D, median sacral line; E, right margin of the sacral canal; F, middle of the right sacral wing; G, the right auricular surface is at the junction with the dorsal side. Abbreviations: *Average: average value; N, number of samples; ROI, region of interest; SD: standard deviation.*

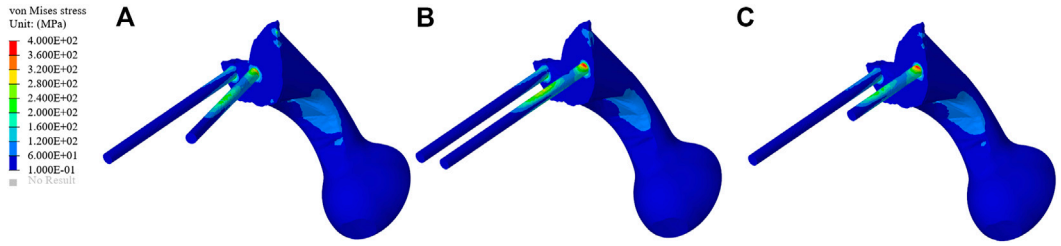

FIGURE 4 | Stress distribution of the three different fixation methods. **(A–C)** The stress distribution of the bone mineral density screw, long screw, and short screw.

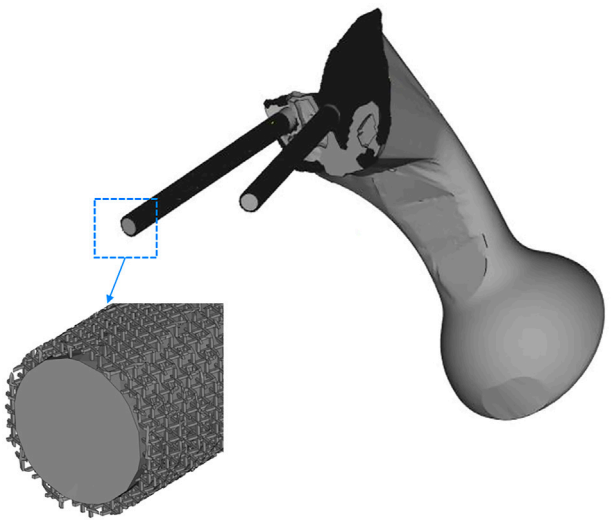

FIGURE 5 | The middle two areas of the connecting plate are optimized and removed, and a porous structure with a porosity of 30% was added to the screw surface and the high-density area of the connecting plate.

the original prosthesis was 350.33 MPa; after TO, however, the maximum stress of the prosthesis was reduced to 264.87 MPa, demonstrating a decrease of 24.39%. In addition, the high-stress area of the optimized prosthesis was significantly reduced. Moreover, the maximum stress of the sacrum in the original group was 183.36 MPa, while that in the optimized group was 133.43 MPa, showing a decrease of 27.23%. **Figure 7A** shows the average stress on S1 screw, S2 screw and connecting plate. The stress of each screw and connecting plate in the optimized group was significantly lower than that in the original group ($p < 0.05$).

3.4 SED of the Sacrum

The SEDs of the sacrum in the original group and the optimization group are shown in **Figure 8**. The average SED of sacrum in the original group was 9.96 kPa, and that in the optimization group was 10.80 kPa, showing an increase of 8.43%.

3.5 Micromotion Results of Prosthesis

3.5.1 Micromotion Results of Original Prosthesis

The micromotion distribution of prosthesis varies with three different fixation methods. As shown in **Figure 9**, A, B, and C represent the micromotion distribution of BMD screw, D, E, and F represent the micromotion distribution of long screw, and G, H, and I represent the micromotion distribution of short screw. The colored parts of B, E, and H represent the area with micromotion less than 28 μm, and the colored parts of C, F, and I represent the area with micromotion less than 40 μm. In BMD screw, the area where the micromotion on the screw surface is more than 28 μm is 368.85 mm^2, and there is no area where the micromotion is more than 40 μm. In long screw, the area of the screw surface with micromotion more than 28 μm is 441.26 mm^2, and the area of the screw surface with micromotion more than 40 μm is 66.59 mm^2. In short screw, the area of the screw surface with a micromotion more than 28 μm is 180.93 mm^2, and the area of the screw surface with a micromotion more than 40 μm is 17.54 mm^2. The maximum micromotion of the three screws is at the top of the connecting plate. The maximum micromotion of BMD screw is 229 μm, the maximum micromotion of long screw is 191 μm, and the maximum micromotion of short screw is 173 μm.

3.5.2 Micromotion Results of TO Prosthesis

As shown in **Figure 10**, the micromotion distribution of the original group and the optimization group. A represents the original prosthesis and B represents the topology optimized prosthesis. On the surface of the screw and connecting plate, compared with the original group, the area with micromotion more than 28 μm in the optimization group was reduced from 684.45 mm^2 to 601.13 mm^2, a decrease of 12.17%. On the screw surface, area with micromotion more than 28 μm in the optimization group was reduced from 368.85 to 284.38 mm^2, a decrease of 22.9%. However, the maximum micromotion increased from 229 to 252 μm. **Figure 7B** shows the average micromotion on S1 screw, S2 screw and connecting plate. The surface micronmotion of each screw was significantly less than that of the original group ($p < 0.05$), and the micromotion on the connecting plate was increased compared with that of the original group.

4 DISCUSSION

As one of the most commonly used options for pelvic ring reconstruction, a hemipelvic prosthesis is usually a solid structure with high stiffness, which leads to the non-physiological distribution of stress, and is not suitable for bone integration (Young et al., 2021). The most serious

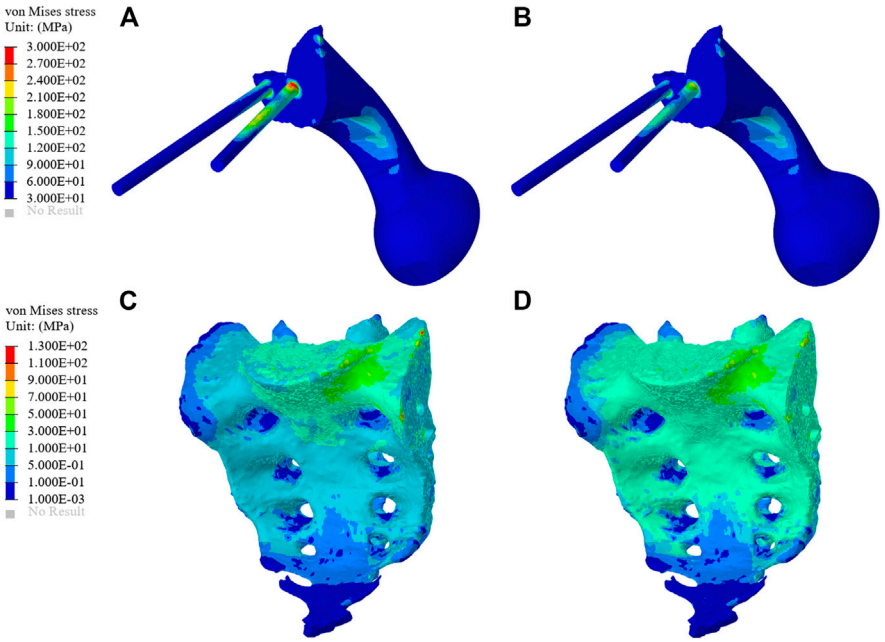

FIGURE 6 | Stress comparison of the prosthesis and sacrum between the original group and the optimization group. **(A)** The stress distribution of prosthesis in the original group. **(B)** The stress distribution of prosthesis in the optimization group. **(C)** The stress distribution of the sacrum in the original group. **(D)** The stress distribution of the sacrum in the optimization group.

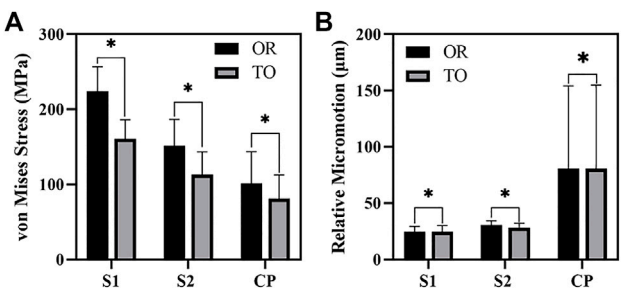

FIGURE 7 | The results of von Mises Stress and relative micromotion on S1, S2 and CP. **(A)** The results of average stress. **(B)** The results of average micromotion. S1, S2 represented the S1, S2 screw, and CP represented the connecting plate. OR and TO represented original group and topological optimization group, respectively. * represented $p < 0.05$.

problem caused by this change is stress shielding. Over time, stress shielding leads to bone resorption, facilitating aseptic loosening and even possible fractures around the prosthesis (Kurcz et al., 2018). In addition, the full solid structure without osseointegration does not support long-term stability (Jing et al., 2016). In this study, a new screw channel was determined according to the distribution of sacral BMD, and the screw and connecting plate were subsequently improved based on TO technology and a porous structure so as to enhance biomechanical properties and the stability of the prosthesis. Then, its stability was verified by biomechanics evaluation through FEA.

In order to reduce the stress-shielding effect caused by the mismatch between vertebral cancellous BMD and screw stiffness, this study divided the sacral sagittal plane into several regions and measured the average BMD of each so as to obtain a screw channel with high BMD distribution. The measurement results of sacral BMD clearly showed the distribution pattern of sacral BMD. The BMD in the sacral vertebral body was higher than that in other areas, and the anterior and upper sides of vertebral body was the area with the most highly concentrated BMD. The BMD near the auricular surface was also high, and the posterolateral area was an area with concentrated BMD. Meanwhile, in the sacral wing, the BMD was low. Overall, there were significant differences in BMD distribution at the S1 level, consistent with the results reported by Darius et al. (Thiesen et al., 2020).Lu et al. (2000) previously showed that BMD is a good indicator of the strength of preoperative sacral screw fixation in previous *in vitro* mechanical experiments. Their study showed that the BMD screw can significantly improve the mechanical distribution on the screw, reduce the peak stress on the screw, and decrease the incidence of postoperative complications, consistent with our expected results. Compared to the other two known fixation methods, the area of high-stress concentration at the connection between the screw and the connecting plate can also be eliminated. The position of the BMD screw is similar to the mechanical conduction path of the pelvis (Snijders et al., 1993), so it can render the amount of stress distribution more reasonable. BMD screw effectively reduces the risk of screw loosening or even breaking. The direction of the newly proposed screw channel is the posterolateral entrance of the auricular surface, ending at the contralateral sacral cape. The above results show that this new

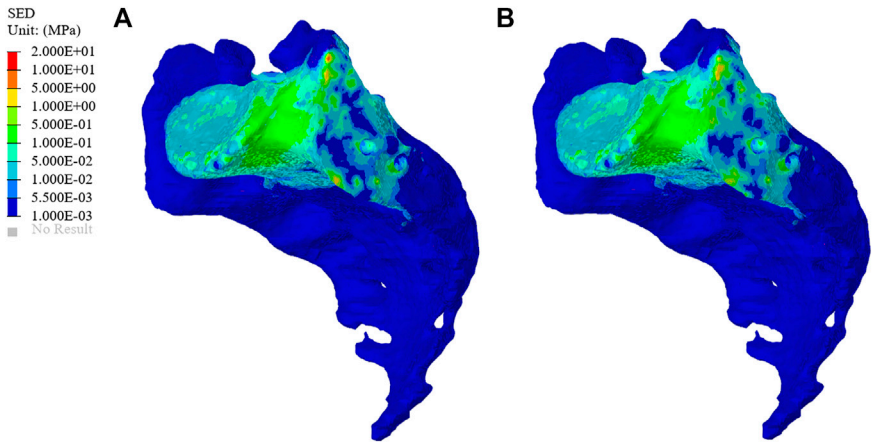

FIGURE 8 | Distribution of sacral strain energy density (SED) in the original group and optimized group. **(A)** The SED distribution of the sacrum in the original group. **(B)** The SED distribution of the sacrum in the optimization group.

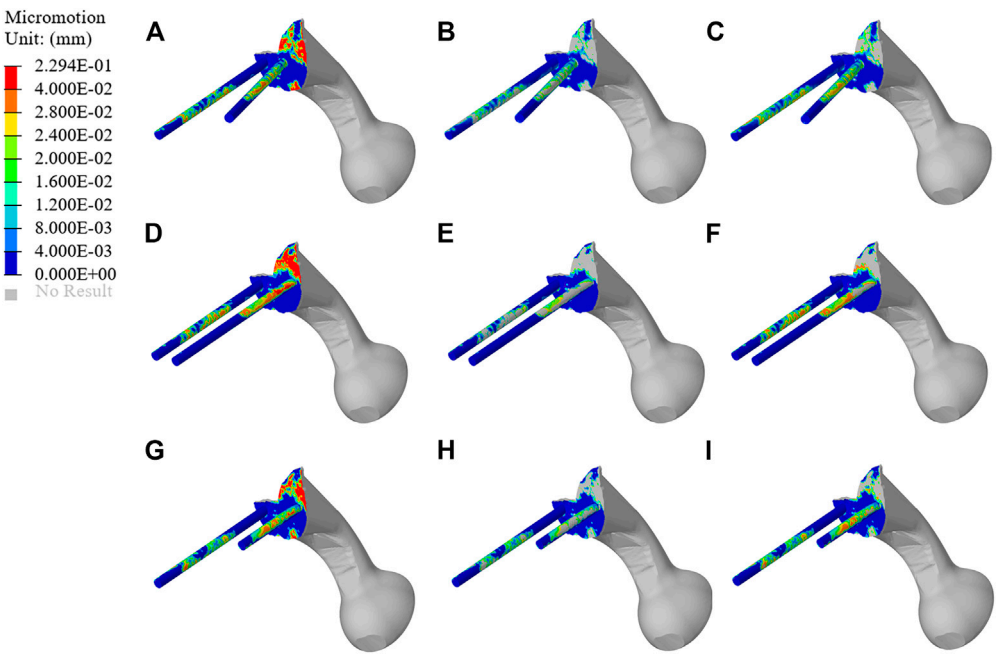

FIGURE 9 | Micromotion results of original prosthesis. **(A–C)** represent the micromotion distribution of BMD screws, **(D–F)** represent the micromotion distribution of long screws, and **(G–I)** represent the micromotion distribution of short screws. The colored parts of **(B,E,H)** represent the area with micromotion less than 28 μm, and the colored parts of **(C,F,I)** represent the area with micromotion less than 40 μm.

BMD screw channel is safer than traditional transverse screw fixation and has a lower incidence of complications (**Table 3** and **4**).

In this study, an inhomogeneous sacral model was reconstructed to simulate the real sacrum. The material properties of the sacrum were determined according to the gray values of CT images. The inhomogeneous sacral model used in this study can improve the accuracy of FEA. Ahmet et al. previously explored the correlation between bone inhomogeneity and reported that inhomogeneous bones can lead to significant differences in stress values compared to rigid bones (Ün and Çalık, 2016). We designed three screw-fixation methods—BMD screw, long screw, and short screw—and by comparing the results of FEA and sacral BMD distribution, we found that the BMD screw had a more reasonable stress distribution. Then, we carried out TO and porous structure surface design. During FEA, von Mises stress can effectively reflect the biomechanical characteristics and record the stress distribution on the screws (Maslov et al., 2021). As shown in **Figure 6**, the maximum stress of the optimized prosthesis was

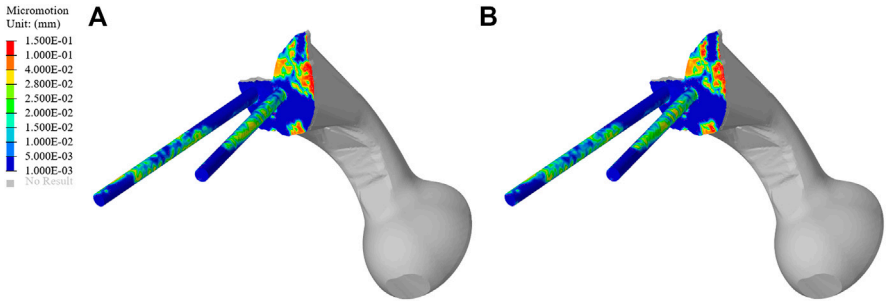

FIGURE 10 | Micromotion results of TO prosthesis. **(A)** Original prosthesis, **(B)** TO prosthesis.

reduced in this study by 24.39%. The maximum stress of the screw (264.87 MPa) was also lower than the yield strength (789–1,013 MPa) of Ti6Al4V material (Dong et al., 2018), which indicated that the strength of the screws can withstand a static load. In addition, long-term survival of the screw also requires its maximum stress to be far lower than the fatigue strength limit of the material (310–610 MPa) (Long and Rack, 1998). The maximum sacral stress in the optimization group was 133.43 MPa, which was 27.23% lower than that in the original group, without exceeding the yield strength (150 MPa) (Li et al., 2007). At the same time, it was observed that the sacral stress distribution was more uniform and could accept stress stimulation, providing good conditions for bone growth. The results of TO show that TO and a porous structure design can decrease the amount of bone resorption caused by stress shielding so as to reduce the possibility of postoperative prosthesis instability.

Prosthesis micromotion is an important assessment related to prosthesis stability and postoperative pain. Previous studies indicated that 28 μm was considered to be the micromotion boundary value most conducive to bone growth, and the interface micromotion of about 40 μm could lead to partial inward growth, while 100–150 μm was considered to prevent inward bone growth, more than 150 μm would completely inhibit the inward growth of bone (Pilliar et al., 1986; Zhao X. et al., 2018; Zhang et al., 2020). As shown in **Figure 9**, both BMD screw and long screw can obtain better micromotion results, and have better distal fixation than short screw. However, previous studies have pointed out that the fixation method of long screw may lead to iatrogenic nerve injury and vascular injury (Zhao Y. et al., 2018; Alkhateeb et al., 2020). Therefore, we believe that BMD screw can obtain a larger safe area, meet the requirements of bone growth and obtain satisfactory bone integration. At the same time, As shown in **Figure 10**, after the topology optimization of the prosthesis, the area of the surface of the screw and connecting plate that is not suitable for bone growth is decreased. This indicated that the BMD screw and prosthesis after topology optimization can achieve satisfactory long-term bone integration effect and reduce patient pain on the basis of meeting the initial stability.

SED is another index for evaluating stress shielding. The difference between the optimized group and the original group can be used to evaluate bone resorption. As shown in **Figure 8**, the average SED of sacrum in the original group and the optimization group were 9.96 and 10.80 kPa, respectively. The above results show that the combination of TO design and a porous structure plays an important role in realizing the osseointegration of a prosthesis. The surface of a porous structure can reduce the elastic modulus of the prosthesis, and with an increase in porosity, the pore volume of bone growth also increases so as to improve the performance of bone integration (Kelly et al., 2021). Shah et al. (2016) also confirmed that metal implants with an interconnected pore structure have the potential to promote bone growth, and they may also reduce the stiffness mismatch between implant and bone so as to eliminate the stress-shielding effect.

In this new study of prosthesis fixation, we preliminarily verified the initial stability of screw and prosthesis by finite element analysis, and obtained satisfactory results. However, there are some limitations in this study. First, we did not consider the effect of postoperative stress-dependent BMD change on prosthesis fixation. This study exists in our next plan. We will study this phenomenon through animal experiments and postoperative follow-up of patients. Second, we only considered the mechanical interaction between bone tissue and a prosthesis and did not introduce the supporting effect of muscle and ligament on bone or the prosthesis, although the FEA results support the effectiveness in reducing stress shielding. Such operation simplified the finite element model and may cause some deviation in the results. In the future research, we will use a more accurate and more physiological model. Finally, this study only includes a single hemipelvic pelvic model, which may have an impact on the applicability of the prosthesis. Future research will further improve upon the content of this study.

5 CONCLUSION

In this study, we proposed an improved scheme to reduce the probability of stress shielding after pelvic reconstruction, determine a new screw channel, and optimize the structure and porous surface design of the prosthesis. We also used FEA to verify the biomechanical properties of the prosthesis. The maximum stress of the optimized prosthesis was 24.39% lower than that of the original prosthesis, the maximum stress of the

sacrum in the optimization group decreased by 27.23%, and the average SED of the sacrum in the optimization group rose by 8.43%. On the surface of screw and connecting plate, the area with micromotion more than 28 μm was reduced by 12.17%. On the screw surface, the area with micromotion more than 28 μm was reduced by 22.9%. The newly determined screw channel and optimized prosthesis design can effectively improve the biomechanical properties of the relationship between a prosthesis and bone. Some limitations of this study, such as the impact of postoperative stress-dependent BMD change on the stability of prosthesis and the failure to use complete pelvis, muscle and ligament structures, may affect the accuracy of the experiment. These limitations have been included in our next experimental plan. This series of studies will provide reference for the stable fixation of prosthesis in clinical pelvic reconstruction.

DATA AVAILABILITY STATEMENT

The original contributions presented in the study are included in the article/Supplementary Material, further inquiries can be directed to the corresponding author.

ETHICS STATEMENT

The studies involving human participants were reviewed and approved by This study was approved by the ethics committee of the Second Hospital of Jilin University, and we obtained the informed consent of all participants. Written informed consent for participation was not required for this study in accordance with the national legislation and the institutional requirements. Written informed consent was obtained from the individual(s) for the publication of any potentially identifiable images or data included in this article.

AUTHOR CONTRIBUTIONS

RZ: Writing-original draft, Software preparation. JW: Investigation, Funding acquisition. HX: Supervision, Data collation. XW: Investigation. YW: Validation. AZ: Supervision. JZ: Software. QH: Reviewing, Editing. XZ: Investigation, Methodology.

FUNDING

This work was supported and funded by the following grants: National Natural Science Foundation of China (Grant Nos 82072456 and 81802174); National Key R&D Program of China (Grant No. 2018YFB1105100); Wu Jieping Medical Foundation (3R119C073429); Bethune plan of Jilin University (Grant No. 419161900014); Department of Science and Technology of Jilin Province, P.R.C. (Grant Nos 20200404202YY and 20200201453JC); Department of Finance in Jilin province (Grant Nos 2019SCZT034, 2019SCZT037, 2019SCZT046, 2020SCZT086, and 2020SCZT037); undergraduate teaching reform research project of Jilin University (Grant No. 4Z2000610852); key training plan for outstanding young teachers of Jilin University (Grant No. 419080520253); Jilin Province Development and Reform Commission, P.R.C. (Grant No. 2018C010) and Natural Science Foundation of Jilin Province (Grant No. 20200201345JC); Beijing Chunlizhengda Medical Instruments Co.,Ltd. (Grant No. 2019YX231).

ACKNOWLEDGMENTS

The authors would like to acknowledge JW, HX, XW, YW, AZ, JZ, QH, and XZ for their contributions of providing professional advices to this study.

REFERENCES

Ahmed, K., Greene, R. J., Aston, W., Briggs, T., Pendegrass, C., Moazen, M., et al. (2020). Experimental Validation of an ITAP Numerical Model and the Effect of Implant Stem Stiffness on Bone Strain Energy. *Ann. Biomed. Eng.* 48 (4), 1382–1395. doi:10.1007/s10439-020-02456-6

Al-Tamimi, A. A., Peach, C., Fernandes, P. R., Cseke, A., and Bartolo, P. J. D. S. (2017). Topology Optimization to Reduce the Stress Shielding Effect for Orthopedic Applications. *Procedia CIRP* 65, 202–206. doi:10.1016/j.procir.2017.04.032

Alkhateeb, J. M., Chelli, S. S., and Aljawder, A. A. (2020). Percutaneous Removal of Sacroiliac Screw Following Iatrogenic Neurologic Injury in Posterior Pelvic Ring Injury: A Case Report. *Int. J. Surg. Case Rep.* 66, 416–420. doi:10.1016/j.ijscr.2020.01.004

Arabnejad, S., Burnett Johnston, R., Pura, J. A., Singh, B., Tanzer, M., and Pasini, D. (2016). High-Strength Porous Biomaterials for Bone Replacement: A Strategy to Assess the Interplay between Cell Morphology, Mechanical Properties, Bone Ingrowth and Manufacturing Constraints. *Acta Biomater.* 30, 345–356. doi:10.1016/j.actbio.2015.10.048

Bartolomeu, F., Costa, M. M., Gomes, J. R., Alves, N., Abreu, C. S., Silva, F. S., et al. (2019). Implant Surface Design for Improved Implant Stability - A Study on Ti6Al4V Dense and Cellular Structures Produced by Selective Laser Melting. *Tribol. Int.* 129, 272–282. doi:10.1016/j.triboint.2018.08.012

Bergmann, G., Deuretzbacher, G., Heller, M., Graichen, F., Rohlmann, A., Strauss, J., et al. (2001). Hip Contact Forces and Gait Patterns from Routine Activities. *J. Biomechanics* 34 (7), 859–871. doi:10.1016/s0021-9290(01)00040-9

Chen, C.-S., and Shih, S.-L. (2018). Biomechanical Analysis of a New Lumbar Interspinous Device with Optimized Topology. *Med. Biol. Eng. Comput.* 56 (8), 1333–1341. doi:10.1007/s11517-017-1767-y

Chen, H., Han, Q., Wang, C., Liu, Y., Chen, B., and Wang, J. (2020). Porous Scaffold Design for Additive Manufacturing in Orthopedics: A Review. *Front. Bioeng. Biotechnol.* 8, 609. doi:10.3389/fbioe.2020.00609

Chen, Y., Frith, J. E., Dehghan-Manshadi, A., Attar, H., Kent, D., Soro, N. D. M., et al. (2017). Mechanical Properties and Biocompatibility of Porous Titanium Scaffolds for Bone Tissue Engineering. *J. Mech. Behav. Biomed. Mater.* 75, 169–174. doi:10.1016/j.jmbbm.2017.07.015

den Teuling, J. W. A. M., Pauwels, B. S., Janssen, L., Wyers, C. E., Janzing, H. M. J., van den Bergh, J. P. W., et al. (2017). The Influence of Bone Mineral Density and Cortical Index on the Complexity of Fractures of the Proximal Humerus. *Bone Jt. Res.* 6 (10), 584–589. doi:10.1302/2046-3758.610.bjr-2017-0080

Dong, E., Wang, L., Iqbal, T., Li, D., Liu, Y., He, J., et al. (2018). Finite Element Analysis of the Pelvis after Customized Prosthesis Reconstruction. *J. Bionic Eng.* 15 (3), 443–451. doi:10.1007/s42235-018-0035-7

Hu, J., Wang, J. H., Wang, R., Yu, X. B., Liu, Y., and Baur, D. A. (2019). Analysis of Biomechanical Behavior of 3D Printed Mandibular Graft with Porous Scaffold Structure Designed by Topological Optimization. *3D Print Med.* 5 (1), 5. doi:10.1186/s41205-019-0042-2

Iolascon, G., Di Pietro, G., Capaldo, A., Gioia, C., Gatto, S., and Gimigliano, F. (2010). Periprosthetic Bone Density as Outcome of Therapeutic Response. *Clin. Cases Min. Bone Metab.* 7 (1), 27–31.

Iqbal, T., Shi, L., Wang, L., Liu, Y., Li, D., Qin, M., et al. (2017). Development of Finite Element Model for Customized Prostheses Design for Patient with Pelvic Bone Tumor. *Proc. Inst. Mech. Eng. H.* 231 (6), 525–533. doi:10.1177/0954411917692009

Ji, T., Guo, W., Tang, X.-D., and Yang, Y. (2010). Reconstruction of Type II+III Pelvic Resection with a Modular Hemipelvic Endoprosthesis: A Finite Element Analysis Study. *Orthop. Surg.* 2 (4), 272–277. doi:10.1111/j.1757-7861.2010.00099.x

Ji, T., Guo, W., Yang, R. L., Tang, X. D., and Wang, Y. F. (2013). Modular Hemipelvic Endoprosthesis Reconstruction-Experience in 100 Patients with Mid-term Follow-Up Results. *Eur. J. Surg. Oncol. (EJSO)* 39 (1), 53–60. doi:10.1016/j.ejso.2012.10.002

Jing, D., Zhai, M., Tong, S., Xu, F., Cai, J., Shen, G., et al. (2016). Pulsed Electromagnetic Fields Promote Osteogenesis and Osseointegration of Porous Titanium Implants in Bone Defect Repair through a Wnt/β-Catenin Signaling-Associated Mechanism. *Sci. Rep.* 6, 32045. doi:10.1038/srep32045

Kelly, C. N., Wang, T., Crowley, J., Wills, D., Pelletier, M. H., Westrick, E. R., et al. (2021). High-Strength, Porous Additively Manufactured Implants with Optimized Mechanical Osseointegration. *Biomaterials* 279, 121206. doi:10.1016/j.biomaterials.2021.121206

Kurcz, B., Lyons, J., Sayeed, Z., Anoushiravani, A. A., and Iorio, R. (2018). Osteolysis as it Pertains to Total Hip Arthroplasty. *Orthop. Clin. N. Am.* 49 (4), 419–435. doi:10.1016/j.ocl.2018.06.001

Li, Z., Kim, J.-E., Davidson, J. S., Etheridge, B. S., Alonso, J. E., and Eberhardt, A. W. (2007). Biomechanical Response of the Pubic Symphysis in Lateral Pelvic Impacts: A Finite Element Study. *J. Biomechanics* 40 (12), 2758–2766. doi:10.1016/j.jbiomech.2007.01.023

Liu, Y., Chen, B., Wang, C., Chen, H., Zhang, A., Yin, W., et al. (2021). Design of Porous Metal Block Augmentation to Treat Tibial Bone Defects in Total Knee Arthroplasty Based on Topology Optimization. *Front. Bioeng. Biotechnol.* 9, 765438. doi:10.3389/fbioe.2021.765438

Long, M., and Rack, H. J. (1998). Titanium Alloys in Total Joint Replacement-A Materials Science Perspective. *Biomaterials* 19 (18), 1621–1639. doi:10.1016/s0142-9612(97)00146-4

Lu, W. W., Zhu, Q., Holmes, A. D., Luk, K. D. K., Zhong, S., and Leong, C. Y. (2000). Loosening of Sacral Screw Fixation Underin Vitro Fatigue Loading. *J. Orthop. Res.* 18 (5), 808–814. doi:10.1002/jor.1100180519

Maslov, L., Borovkov, A., Maslova, I., Soloviev, D., Zhmaylo, M., and Tarasenko, F. (2021). Finite Element Analysis of Customized Acetabular Implant and Bone after Pelvic Tumour Resection throughout the Gait Cycle. *Mater. (Basel)* 14 (22), 7066. doi:10.3390/ma14227066

Matejovsky, Z., Jr., Matejovsky, Z., and Kofranek, I. (2006). Massive Allografts in Tumour Surgery. *Int. Orthop. (SICOT)* 30 (6), 478–483. doi:10.1007/s00264-006-0223-7

Muller, P. E., Durr, H. R., Wegener, B., Pellengahr, C., Refior, H. J., and Jansson, V. (2002). Internal Hemipelvectomy and Reconstruction with a Megaprosthesis. *Int. Orthop.* 26 (2), 76–79. doi:10.1007/s00264-001-0322-4

Park, J., Lee, D., and Sutradhar, A. (2019). Topology Optimization of Fixed Complete Denture Framework. *Int. J. Numer. Method Biomed. Eng.* 35 (6), e3193. doi:10.1002/cnm.3193

Pilliar, R. M., Lee, J. M., and Maniatopoulos, C. (1986). Observations on the Effect of Movement on Bone Ingrowth into Porous-Surfaced Implants. *Clin. Orthop. Relat. Res.* 208, 108–113. doi:10.1097/00003086-198607000-00023

Rho, J. Y., Hobatho, M. C., and Ashman, R. B. (1995). Relations of Mechanical Properties to Density and CT Numbers in Human Bone. *Med. Eng. Phys.* 17 (5), 347–355. doi:10.1016/1350-4533(95)97314-f

Salazar, D., Lannon, S., Pasternak, O., Schiff, A., Lomasney, L., Mitchell, E., et al. (2015). Investigation of Bone Quality of the First and Second Sacral Segments Amongst Trauma Patients: Concerns about Iliosacral Screw Fixation. *J. Orthopaed Traumatol.* 16 (4), 301–308. doi:10.1007/s10195-015-0354-y

Shah, F. A., Snis, A., Matic, A., Thomsen, P., and Palmquist, A. (2016). 3D Printed Ti6Al4V Implant Surface Promotes Bone Maturation and Retains a Higher Density of Less Aged Osteocytes at the Bone-Implant Interface. *Acta Biomater.* 30, 357–367. doi:10.1016/j.actbio.2015.11.013

Shao, Q. D., Yan, X., Sun, J. Y., and Xu, T. M. (2015). Internal Hemipelvectomy with Reconstruction for Primary Pelvic Neoplasm: A Systematic Review. *ANZ J. Surg.* 85 (7-8), 553–560. doi:10.1111/ans.12895

Snijders, C. J., Vleeming, A., and Stoeckart, R. (1993). Transfer of Lumbosacral Load to Iliac Bones and Legs. *Clin. Biomech.* 8 (6), 285–294. doi:10.1016/0268-0033(93)90002-y

Thiesen, D. M., Ntalos, D., Berger-Groch, J., Petersik, A., Hofstätter, B., Frosch, K.-H., et al. (2020). The Three-Dimensional Bone Mass Distribution of the Posterior Pelvic Ring and its Key Role in Transsacral Screw Placement. *Sci. Rep.* 10 (1), 5690. doi:10.1038/s41598-020-61954-8

Ün, K., and Çalık, A. (2016). Relevance of Inhomogeneous-Anisotropic Models of Human Cortical Bone: A Tibia Study Using the Finite Element Method. *Biotechnol. Biotechnol. Equip.* 30 (3), 538–547. doi:10.1080/13102818.2016.1154803

Weiser, L., Huber, G., Sellenschloh, K., Viezens, L., Püschel, K., Morlock, M. M., et al. (2017). Insufficient Stability of Pedicle Screws in Osteoporotic Vertebrae: Biomechanical Correlation of Bone Mineral Density and Pedicle Screw Fixation Strength. *Eur. Spine J.* 26 (11), 2891–2897. doi:10.1007/s00586-017-5091-x

Young, P. S., Macarico, D. T., Silverwood, R. K., Farhan-Alanie, O. M., Mohammed, A., Periasamy, K., et al. (2021). Anatomical Pelvic Loading of a Monoblock Polyethylene Acetabular Component. *Bone Jt. J.* 103-B (5), 872–880. doi:10.1302/0301-620x.103b5.bjj-2020-1321.r2

Zang, J., Guo, W., Yang, Y., and Xie, L. (2014). Reconstruction of the Hemipelvis with a Modular Prosthesis after Resection of a Primary Malignant Peri-Acetabular Tumour Involving the Sacroiliac Joint. *Bone Jt. J.* 96-B (3), 399–405. doi:10.1302/0301-620x.96b3.32387

Zhang, A., Chen, H., Liu, Y., Wu, N., Chen, B., Zhao, X., et al. (2020). Customized Reconstructive Prosthesis Design Based on Topological Optimization to Treat Severe Proximal Tibia Defect. *Bio-Des. Manuf.* 4 (1), 87–99. doi:10.1007/s42242-020-00102-7

Zhao, X., Xiao, J., Sun, Y., Zhu, Z., Xu, M., Wang, X., et al. (2018a). Novel 3D Printed Modular Hemipelvic Prosthesis for Successful Hemipelvic Arthroplasty: A Case Study. *J. Bionic Eng.* 15 (6), 1067–1074. doi:10.1007/s42235-018-0094-9

Zhao, Y., You, L., Lian, W., Zou, D., Dong, S., Sun, T., et al. (2018b). Anatomical Relation between S1 Sacroiliac Screws' Entrance Points and Superior Gluteal Artery. *J. Orthop. Surg. Res.* 13 (1), 15. doi:10.1186/s13018-018-0713-5

Zhou, Y., Duan, H., Liu, Y., Min, L., Kong, Q., and Tu, C. (2011). Outcome after Pelvic Sarcoma Resection and Reconstruction with a Modular Hemipelvic Prostheses. *Int. Orthop. (SICOT)* 35 (12), 1839–1846. doi:10.1007/s00264-011-1222-x

Zhou, Y., Min, L., Liu, Y., Shi, R., Zhang, W., Zhang, H., et al. (2013). Finite Element Analysis of the Pelvis after Modular Hemipelvic Endoprosthesis Reconstruction. *Int. Orthop.* 37 (4), 653–658. doi:10.1007/s00264-012-1756-6

Conflict of Interest: The authors declare that the research was conducted in the absence of any commercial or financial relationships that could be construed as a potential conflict of interest.

frontiers | Frontiers in Bioengineering and Biotechnology

ORIGINAL RESEARCH
published: 03 June 2022
doi: 10.3389/fbioe.2022.921545

Mechanical Distribution and New Bone Regeneration After Implanting 3D Printed Prostheses for Repairing Metaphyseal Bone Defects: A Finite Element Analysis and Prospective Clinical Study

Bingchuan Liu[1,2†], Xingcai Li[1,2†], Weipeng Qiu[1], Zhongjun Liu[1,2], Fang Zhou[1,2], Yufeng Zheng[3], Peng Wen[4] and Yun Tian[1,2]**

[1]Department of Orthopaedics, Peking University Third Hospital, Beijing, China, [2]Engineering Research Center of Bone and Joint Precision Medicine, Ministry of Education, Peking University Third Hospital, Beijing, China, [3]School of Materials Science and Engineering, Peking University, Beijing, China, [4]Department of Mechanical Engineering, Tsinghua University, Beijing, China

Critical metaphyseal bone defects caused by nonunion and osteomyelitis are intractable to repair in clinical practice owing to the rigorous demanding of structure and performance. Compared with traditional treatment methods, 3D printing of customized porous titanium alloy prostheses offer feasible and safe opportunities in repairing such bone defects. Yet, so far, no standard guidelines for optimal 3D printed prostheses design and fixation mode have been proposed to further promote prosthesis stability as well as ensure the continuous growth of new bone. In this study, we used a finite element analysis (FEA) to explore the biomechanical distribution and observed new bone regeneration in clinical practice after implanting 3D printed prostheses for repairing metaphyseal bone defects. The results reflected that different fixation modes could result in diverse prosthesis mechanical conductions. If an intramedullary (IM) nail was applied, the stress mainly conducted equally along the nail instead of bone and prosthesis structure. While the stress would transfer more to the lateral bone and prosthesis's body when the printed wing and screws are selected to accomplish fixation. All these fixation modes could guarantee the initial and long-term stability of the implanted prosthesis, but new bone regenerated with varying degrees under special biomechanical environments. The fixation mode of IM nail was more conducive to new bone regeneration and remodeling, which conformed to the Wolff's law. Nevertheless, when the prosthesis was fixed by screws alone, no dense new callus could be observed. This fixation mode was optional for defects extremely close to the articular surface. In conclusion, our innovative study could provide valuable references for the fixation mode selection of 3D printed prosthesis to repair metaphyseal bone defect.

Keywords: 3D printing technology, finite element analysis, metaphyseal bone defect, new bone regeneration, clinical study

OPEN ACCESS

Edited by:
He Liu,
Jilin University, China

Reviewed by:
Hua Chen,
Fourth Medical Center of PLA General Hospital, China
Junlin Yang,
Xinhua Hospital Affiliated to Shanghai Jiao Tong University School of Medicine, China

****Correspondence:***
Peng Wen
wenpeng@tsinghua.edu.cn
Yun Tian
tiany@bjmu.edu.cn

[†]These authors have contributed equally to this work

Specialty section:
This article was submitted to Biomaterials, a section of the journal Frontiers in Bioengineering and Biotechnology

Received: *16 April 2022*
Accepted: *17 May 2022*
Published: *03 June 2022*

Citation:
Liu B, Li X, Qiu W, Liu Z, Zhou F, Zheng Y, Wen P and Tian Y (2022) Mechanical Distribution and New Bone Regeneration After Implanting 3D Printed Prostheses for Repairing Metaphyseal Bone Defects: A Finite Element Analysis and Prospective Clinical Study. Front. Bioeng. Biotechnol. 10:921545. doi: 10.3389/fbioe.2022.921545

1 INTRODUCTION

The treatment of critical bone defects in extremities, especially those located at the metaphysis, remains a challenging issue for orthopedic surgeons. These defects are characterized by obvious morphological abnormality, as well as distinctive changes in microstructure and biomechanical distribution, considering there is the transition zone from cylindroid to irregular bone (Blokhuis, 2017). Metaphyseal bone defects of extremities can be caused by severe trauma, osteomyelitis, tumor and revision surgery (Mancuso et al., 2017; Lu et al., 2019; Benulic et al., 2020). Traditional therapeutic methods such as bone grafting, distraction osteogenesis, and induced-membrane technique cannot accomplish simultaneous reconstruction of both complete anatomical structure and stable biomechanical conduction to support early weight-bearing (Migliorini et al., 2021).

Applying 3D printed titanium alloy prostheses to repair critical metaphyseal bone defects is a feasible treatment option, whose major advantages include: 1) the shape and structure of a prosthesis can be customized based on the irregular defect outline; 2) the appropriate mechanical strength of titanium alloy can rebuild the local biomechanical stability and help patients perform weight-bearing and functional exercise; 3) it can stimulate the bone growth in contact with the prosthesis (Ji et al., 2020; Migliorini et al., 2021; Xu et al., 2021). Tetsworth et al. (2017) and Nwankwo et al. (2019) successfully applied 3D printed framed-structured scaffolds to reconstruct distal femoral and tibial metaphyseal defects caused by comminuted fractures. In addition, in our previous study, we reported the effective repair of distal femoral metaphyseal defects caused by osteomyelitis and nonunion using 3D printed porous prosthesis; the follow-up results showed stable prosthesis location and continuous bone growth (Hou et al., 2020). However, there is still a lack of systematic effect reports about the clinical application of 3D printed prostheses to reconstruct metaphyseal bone defects.

Durable prosthesis stability, new bone regeneration, and implant-bone interface fusion are desirable conditions after the 3D printed prosthesis implantation for bone defect repair. According to Wolff's law, bone could do adaptive response to appropriate mechanical loading changes (Brand, 2010), that is to say, different internal fixation modes and biomechanical environments surrounding the prosthesis have a significant impact on the rate and direction of new bone growth. The mechanical mode of local fixation can be divided into the mode of interlocking intramedullary (IM) nail, the mode of the single prosthesis with screws, and the combination of the two (Tetsworth et al., 2017; Nwankwo et al., 2019). Too strong fixation can produce stress shielding and reduce the micromotion at the implant-bone interface, which in turn harms new bone regeneration, while too weak fixation leads to initial stability of prosthesis, which is not conducive to limb weight-bearing and may lead to implant failure. As for applying 3D prostheses to repair metaphyseal bone defects, no one so far has raised a unified reference standard about the optimal prosthesis design and fixation mode. Hence, there is still no definite conclusion on how to achieve the initial and long-term prosthesis stability as well as ensure the continuous growth of new bone.

Finite element analysis (FEA) has become an increasingly powerful approach for predicting the biomechanical behavior of the bone-implant interface and identifying areas of greater stress concentration (Campbell and Glüer, 2017). Once refined and validated with experimental data, FEA provides comprehensive and accurate datasets illustrating the physical response at all locations in a model. We carried out a FEA and prospective clinical study focusing on repairing metaphyseal defects in the present study. Following two research aspects were summarized and investigated in detail: 1) clarifying the stress distribution characteristics under different prosthesis fixation modes *via* 3D finite element models, and 2) investigating the rules of new bone regeneration related to different prosthesis fixation modes *via* the clinical study. We hypothesized that different fixation patterns could influence the local mechanical distribution and bone regeneration.

2 MATERIALS AND METHODS

2.1 Design of a Customized Prosthesis

The design process of a 3D printed prosthesis is displayed in **Figure 1**. First, the computed tomography (CT) scan data of bilateral limbs were acquired and reconstructed using Mimics 19.0 software (Materialise, Belgium). Second, the healthy bone was mirrored to the disease-affected side, and the defect regions overlapped one another (automatically and manually). Third, the bone defect model obtained from Mimics was imported into Geomagic Studio 12 software (Geomagic, United States) for modification, after which personal prostheses with various shapes were designed according to specific defects and doctor's requests. Fourth, the prosthesis insertion and fixation procedures were simulated *via* medical interaction platform; size, matching degree, and screw position was further evaluated. Any design that could not meet the surgical requirements was redesigned or modified and locally optimized.

2.2 Finite Element Analysis

FEA was used to accurately calculate the biomechanical distribution and concentration characteristics of bone and prosthesis (Yan et al., 2020; Yao et al., 2021). The metaphyseal bone defect of the distal femur was used as an example to conduct FEA models, and the results were applicable to all the long bones of extremities.

2.2.1 Modeling of the Femur, Prosthesis, and Intramedullary Nail

For a better simulation of the real structure of the natural skeleton, cortical and cancellous bone were separately constructed based on the CT Hounsfield unit, and the thickness of cortical bone ranged from 1.4 to 8.8 mm. The elasticity modulus and Poisson's ratio of cortical bone were set as 16,600 MPa and 0.3, and the elasticity modulus and Poisson's ratio of cancellous bone were 8,000 MPa and 0.3. The 3D printed prosthesis was defined as porous titanium alloy structure with the

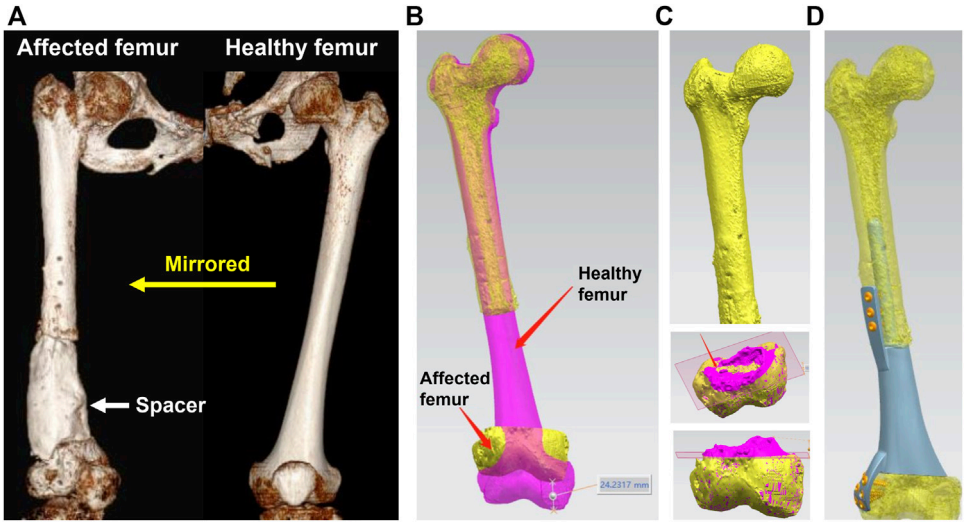

FIGURE 1 | Design process of a 3D printed prosthesis. **(A)** 3D CT reconstruction of bilateral femurs, the bone defect was occupied by a cement spacer, the healthy femur was mirrored to the disease-affected side; **(B)** Overlapping femurs could reveal the size and shape of metaphyseal bone defect; **(C)** The overlapping 3D models could help to determine the osteotomy scope; **(D)** Simulation of the prosthesis insertion and internal fixation.

elasticity of 3,000 MPa. The IM nail was defined as a cylinder, whose length and diameter were 400 and 11 mm respectively. Due to the IM nail was a solid titanium alloy model, its elasticity modulus and Poisson's ratio were set as 110,000 MPa and 0.3. Surface smoothing and tanglesome point removal were performed using UG 12.0 software (Siemens PLM Software, United States), after which an STP file was acquired. After that, the STP file was imported into HyperMesh 14.0 software (Altair, United States) for geometric cleaning.

2.2.2 Mesh Division

Since the bone-prosthesis interface experiences large deformations under load, it was necessary to mesh them into small elements. The mesh types included tetrahedral and shell elements, with the size of 2 mm. The tetrahedron simulated cancellous bone, and the shell unit simulated cortical bone.

2.2.3 Bone-Prosthesis Contact Setting and Stress Loading

Interaction between the bone and prosthesis is complex and requires the definition of contact conditions. All contacts between fracture fragments and implants were modelled as frictional contacts, except the interfaces between threaded parts of the locking screw heads and plate holes, which were modelled as bonded contacts. The friction coefficients for the frictional contacts were set at 0.6 for bone-prosthesis interfaces. In applying stress, the proximal femur was secured, and a 700 N pressure was applied along the force line at the articular surface of the distal femur. The maximum von Mises and distribution were used to evaluate mechanical performance.

2.3 Clinical Study

This clinical study was approved by the Medical Science Research Ethics Committee of Peking University Third Hospital (No. M2018174), and informed consent was obtained from patients and family members. Besides, we have finished the clinical trials registry in the United States National Library of Medicine.

We prospectively enrolled patients with metaphyseal bone defects of extremities. The corresponding prosthesis type and internal fixation mode were selected according to different scopes and shapes of defects. The inclusion criteria included: 1) metaphyseal defects caused by osteomyelitis and nonunion; 2) the length of the bone defect was more than 6 cm; 3) patients aging from 18 to 70 years old. The exclusion criteria included: 1) tumor-related bone defects; 2) patients with articular surface defect; 3) systemic diseases contraindicating the use of artificial prosthesis; 4) patients unable to undergo the entire treatment process and follow-up. Patients' clinical information were collected in detail, including age, gender, defect cause, defect location, defect length, fixation mode of the prosthesis, the evaluation scores of patients' extremity function and life state.

The whole surgical process consisted of three main steps. First, the affected soft and bone tissues were debrided and cut thoroughly, and the bone defect was occupied by a polymethyl methacrylate (PMMA) spacer. Second, when the infection was completely contained, the critical metaphyseal defect was repaired using a 3D printed porous Ti6Al4V prosthesis. Finally, the interlocking IM nail or screws were used to enhance fixation according to specific situations.

Postoperatively, patients were encouraged to carry out early weight-bearing and functional exercises. The whole rehabilitation process was guided by professional specialists, including joint movement, anti-resistance and compression training, balance exercise and so on. Once the pain degree became significantly reduced after activity, and no loosening or breakage of implants were confirmed by postoperative X-ray, patients would be allowed to restore full limb weight-bearing gradually.

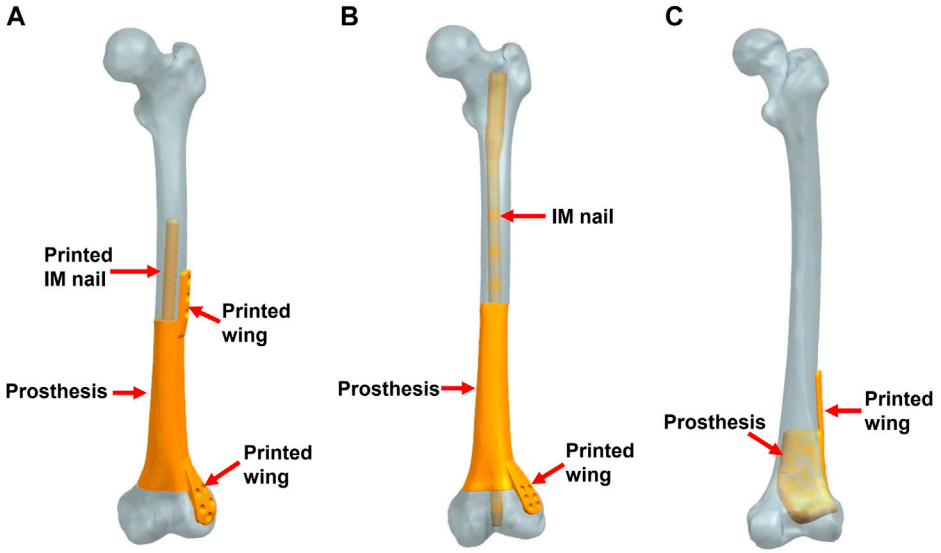

FIGURE 2 | Three fixation modes of different prostheses (IM: intramedullary). **(A)** Mode I, the integral prosthesis with printed IM nail and wings; **(B)** Mode II, the integral prosthesis with one printed wing; **(C)** Mode III, the integral prosthesis with one printed wing.

During the postoperative follow-up, routine X-rays and CT were utilized to assess implant stability and bone growth. Also, all complications were recorded. Patients' upper and lower extremity functions were quantificationally evaluated by the Disability of Arm Shoulder and Hand (DASH) and Lower Extremity Functional Scale (LEFS), respectively. The state of patients' daily life was evaluated *via* the SF-36 questionnaire.

2.4 Statistical Analysis

SPSS 22.0 software was used for statistical analysis. The Chi-square test was used to compare the excellent and good rate of extremity function scores among different groups. A F-test was used to compare the difference in SF-36 scores. $p < 0.05$ was considered to be statistically significant.

3 RESULTS

3.1 Different Fixation Modes of Prostheses

A total of three modes of prosthesis fixation were accomplished. As shown in **Figure 2**, Mode I indicated the integral prosthesis with printed IM nails and wings (**Figure 2A**), which can be fixed by screws alone. Mode II indicated the integral prosthesis with one printed wing (**Figure 2B**), which can be fixed by interlocking IM nails and screws. There were two main differences between Mode I and Mode II: 1) the integratedly printed IM nail in Mode I could offer stabler prosthesis fixation strength compared with the additionally inserted IM nail in Mode II; 2) the proximal end of the prosthesis had integrally printed lateral wing, which would lead to less local relative micromotion at the bone-prosthesis interface after being fixed by screws. The different biomechanical environments around the proximal prosthesis might influence new bone regeneration. Mode III indicated the integral prosthesis with one printed wing (**Figure 2C**), which can be fixed by screws. The first two fixation modes of prostheses are suitable for most metaphyseal defects, and the third fixation mode of the prosthesis is only suitable for the partial metaphyseal defects, in which the bony structure on one side is intact and continuous.

3.2 Von Mises Stress Distribution Displayed by Finite Element Analysis

In FEA results, a qualitative and quantitative analysis was performed based on progressive visual color scales ranging from blue to red, which corresponded to the weakest and the strongest stress intensity, respectively.

In **Figure 3**, for Mode I, the stress was evenly conducted along the inner and outer sides of both femur and prosthesis, with the maximum stress located at the proximal prosthesis end as directed by red arrows. The stress distributed on the printed IM nail was relatively weak. The proximal printed wing shared stronger stress than the distal wing.

In **Figure 4**, for Mode II, the stress was mainly conducted along the femurs and IM nails. The maximum stress was concentrated at the middle of the IM nail and the proximal end of the prosthesis as directed by red arrows. The printed wing shared less stress.

In **Figure 5**, for Mode III, the stress was mostly conducted along with the femur structure uniformly. The stress distributed on the overall prosthesis was relatively weak. The maximum stress of the prosthesis is concentrated on the proximal end as directed by red arrows.

The maximum von Mises stress intensity of the proximal femur, distal femur, and implants (IM nail and prosthesis) are presented in **Figure 6**. The maximum von Mises values of proximal and distal femur were observed in Mode I (76.1 and

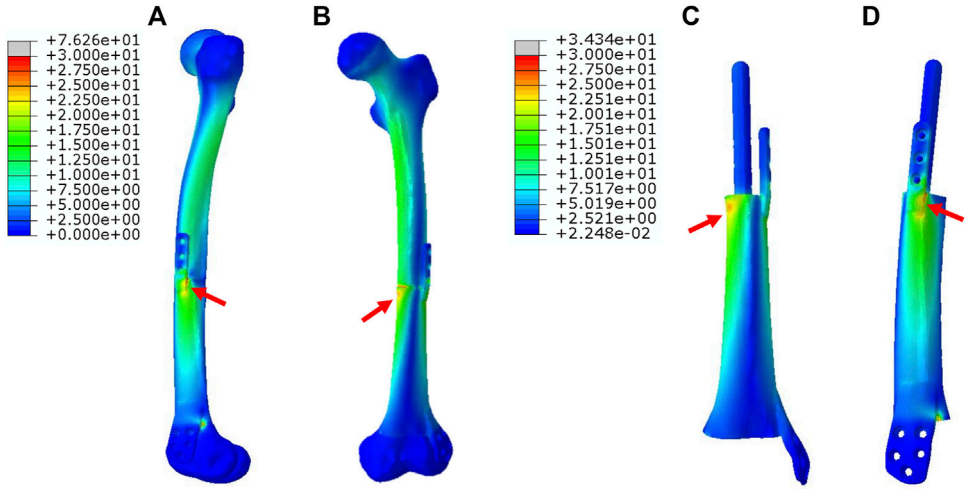

FIGURE 3 | Von Mises stress distribution in Mode I fixation pattern, the red arrows direct the maximum stress concentration.

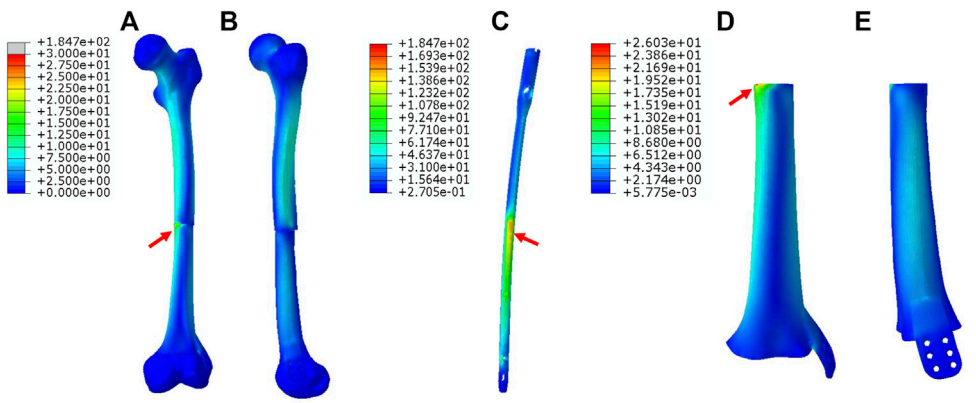

FIGURE 4 | Von Mises stress distribution in Mode II fixation pattern, the red arrows direct the maximum stress concentration.

38.8 MPa), and their minimum values in Mode III and Mode II, respectively (17.2 and 16.4 MPa). The interlocking IM nails were applied in Mode II, which decreased the maximum stress of the femur. However, the von Mises stress on the IM nail was significantly larger than the prosthesis, which was 184.7 MPa.

3.3 Prosthesis's Stability and Bone Regeneration Under Different Fixation Modes.

We treated 16 patients, eight males and eight females, with critical metaphyseal bone defects of extremities by implanting 3D printed porous prostheses. Their average age was 54.4 years old. The enrolled patients were divided into three groups according to different prosthesis fixation modes: group 1: five patients underwent Mode I; group 2: six patients underwent Mode II; group 3: five patients underwent Mode III. Their clinical information were presented in **Table 1**. As shown in **Figure 7**, postoperative serial X-rays showed that the prostheses, nails, and screws were stable in three groups, and no obvious loosening, subsidence, or breakage occurred. Yet, the new bone regeneration was not the same in all groups. For Mode II, continuous bone regeneration could be observed. As directed by yellow arrows, new bone mainly grew from the proximal end of the bone defect and crept on the surface of the prosthesis, whereas, for both Mode I and III, the new bone did not grow densely. As directed by red and pink arrows, the low-density gaps between the bone and prosthesis were gradually blurred but did not disappear. There was no obvious new bone growing around the prosthesis.

3.4 Evaluation of Patients' Extremity Function and Life State

At the last follow-up, the excellent and good rate of extremity function scores (LEFS or DASH) did not show significant difference between Mode I and Mode II groups (p = 0.819). While the rate of Mode III group was significantly higher than other two groups (p = 0.038 and 0.022, respectively). With regard

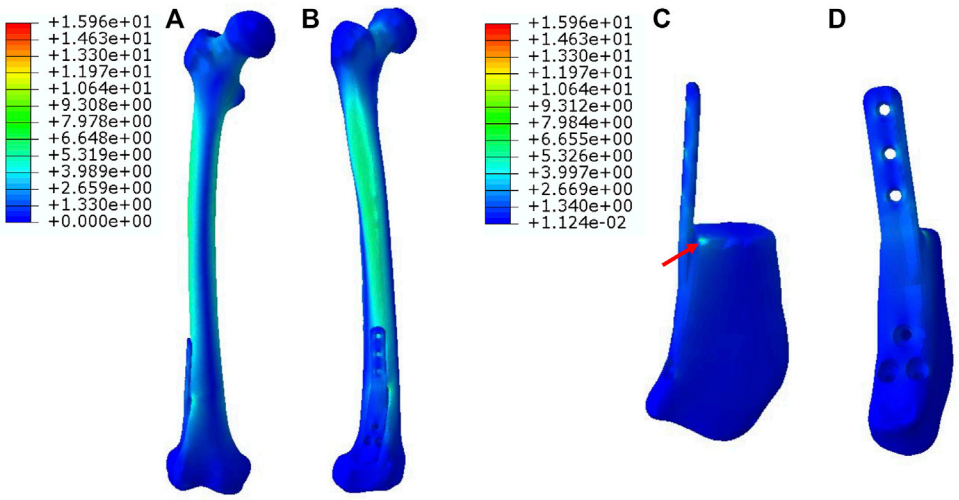

FIGURE 5 | Von Mises stress distribution in Mode III fixation pattern, the red arrow directs the maximum stress concentration.

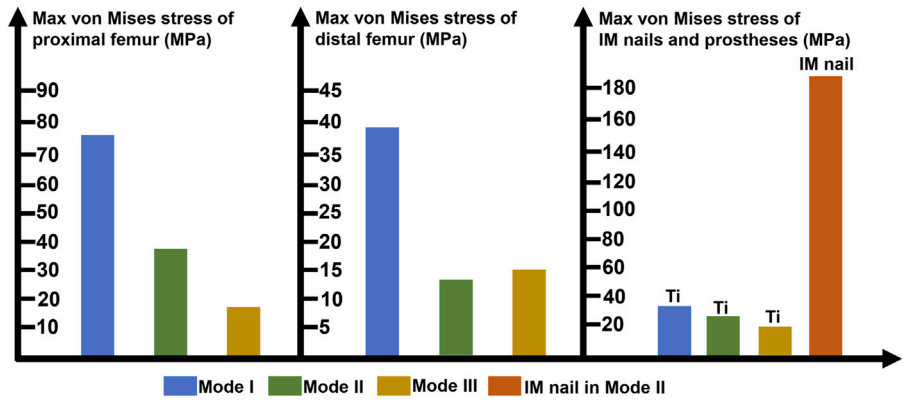

FIGURE 6 | Diagram of the maximum von Mises stress of proximal femur, distal femur, prostheses and intramedullary (IM) nail (Ti: 3D printed Ti6Al4V prosthesis).

to the comparison of SF-36 scores at the time of the last follow-up, no significant difference was found among the three groups (p = 0.076).

4 DISCUSSION

Due to special characteristics such as customized morphology and appropriate mechanical strength (Tshephe et al., 2022), 3D printed titanium alloy prostheses have been widely applied to repair bone defects in extremities. In this study, we investigated the biomechanical distributions of different prosthesis fixation modes combined with finite element 3D simulated models and observed the treatment effects of 3D printed Ti6Al4V prostheses in critical metaphyseal bone defects. The reported results could represent a valuable reference for orthopedic surgeons to make clinical decision-making.

Different prosthesis fixation leads to different local biomechanical environments. As shown in **Figure 2**, the three fixation modes of prostheses for repairing metaphyseal bone defects proposed in this study were classified into two categories based on whether the interlocking IM nail was applied. On the one hand, when the prosthesis was fixed by IM nails and screws, the stress under such conditions could be transmitted along with the IM nail, whose main curvature is close to the normal force line and the interlocking screws have a good anti-rotation and shear resistance function. Besides, studies have demonstrated that when applying a vertical load to simulate the early postoperative internal fixation load-bearing, the stress is mainly concentrated in the middle of the IM nail (Chen et al., 2018; Wang et al., 2020). Wu et al. (2022) applied the 3D printed polyether ether ketone prosthesis to repair the femoral shaft defect and observed middle-concentrated stress of the IM nail. As shown by the FEA results in the present study, when the interlocking IM nail was applied to stabilize prostheses for metaphyseal bone defects, the stress was mainly distributed along

TABLE 1 | The clinical information of the enrolled patients.

	Age/Gender	Characteristics of bone defects			Fixation mode	F/U (mths)	Scores at the last follow-up	
		Cause	Location	Length (cm)			LEFS/DASH	SF-36
1	64/F	osteomyelitis	distal femur	17.2	II	40	51	57.6
2	61/M	aseptic nonunion	distal femur	14.1	II	38	57	48.1
3	69/F	aseptic nonunion	distal femur	9.5	II	30	46	56.5
4	67/F	osteomyelitis	distal femur	13.3	II	26	51	51.1
5	41/M	osteomyelitis	distal femur	14.2	I	18	47	63.6
6	26/M	osteomyelitis	distal femur	17.8	III	16	61	69.6
7	36/M	aseptic nonunion	distal femur	17.3	II	13	56	46.0
8	42/F	aseptic nonunion	distal femur	14.4	II	26	48	55.7
9	67/F	osteomyelitis	distal femur	10.5	III	14	56	55.1
10	46/F	osteomyelitis	distal femur	14.2	I	10	44	53.4
11	65/M	osteomyelitis	distal tibia	9.7	I	23	55	64.5
12	68/M	osteomyelitis	proximal tibia	14.2	I	23	56	53.2
13	69/M	osteomyelitis	proximal tibia	6.7	III	14	55	57.2
14	54/M	osteomyelitis	distal tibia	6.8	III	10	58	54.2
15	53/F	aseptic nonunion	distal humerus	9.5	I	25	26	64.5
16	43/F	osteomyelitis	proximal humerus	7.1	III	14	19	66.2

F, female; M: male; Pre-Op, Preoperative operative; F/U, Follow-up; LEFS, lower extremity functional scale; DASH, disability of arm shoulder and hand.

the IM nail (the maximum stress concentration occurred at the middle of the nail) (**Figure 4**), which is consistent with previous studies. In addition, the screw fixation between the lateral wing and distal bone mass could increase the local stability between the prosthesis and the bone, promoting the micromotion at the local bone-prosthesis interface. On the other hand, for metaphyseal bone defects located close to the articular surface and possessing irregular shapes, there is little residual bone near the articular surface, and the interlocking fixation is difficult to perform. Hence, the prosthesis was printed with integrally lateral wings and/or nails and was only fixed by screws. Under these circumstances (**Figure 3**), the stress shared by the printed nail was relatively weak and was mainly conducted along the bone structure and prosthesis body. At the same time, the function of the printed lateral wing was similar to a plate, which could provide eccentric fixation force and result in lateral stress concentration. As for the fixation pattern in Mode III (**Figure 5**), the partially intact bone structure became the main pathway of stress conduction; the stress shared by the prosthesis body and printed wing were both relatively weak.

Sustained prosthesis stability, which can be divided into primary and secondary stability, is the main guarantee for patients to safely carry out limb weight-bearing. The primary stability refers to the period after surgical insertion, before the healing progress. After implanting the prosthesis inside a defective cavity, the nail and screws can provide necessary mechanical fixation, and the frictional properties at the bone-implant interface can sustain the shear load and ensure proper implant stability. In addition, the nail and screws can also provide necessary mechanical fixation. Insufficient primary stability tends to lead to excessive interfacial micromotion following surgery, which may imply a higher occurrence of migration and implant failure. Besides, the low fixation strength brings no additional benefit to the healing process and can actually promote the growth of fibrous tissue instead of bone. From another aspect, the primary stability and fixation strength should not be too high since excessive stress levels may lead to bone necrosis (Campbell and Glüer, 2017). Therefore, a combination of IM nail and lateral screws was chosen for clinical application to fix the metaphyseal prostheses in this study, avoiding the too strong or too weak fixation state and meeting the mechanical environment requirements for primary stability and new bone regeneration. The secondary stability occurs in the stage of bone regeneration and remodeling. During bone healing, newly formed bone is produced to fill the gap between host bone tissue and prosthesis surface. Several weeks or months after the implantation surgery, newly formed bone tissue is progressively replaced by mature bone tissue, thus promoting mechanical interlocking. As shown in **Figures 7D–F**, the new bone gradually surrounded the prosthesis from the proximal end. Bone-prosthesis interface is suggested to be the weakest domain in the bone-implant complex (Gao et al., 2019). Osseointegration, which was first defined by Brånemark et al. (1977), helps integrate and stabilize the prosthesis with the surrounding bone and has an important role in strengthening the bone-prosthesis interface. As shown in **Figure 7**, the three fixation modes that were applied in the present study all achieved good early and medium-term prosthesis stability.

After the prosthesis is implanted into the bone defect, the regeneration process of new bone is mainly achieved with "secondary bone repair" (Roberts et al., 2018). During this process, the growth and remodeling of new bone follow Wolff's law, illustrated by the increased bone resorption associated with immobilization or microgravity and increased bone formation in response to mechanical load. In this study, different fixation modes led to different subsequent stress distributions and affected the regeneration of new bone. As shown in **Figures 7A–C** and **Figures 7G–I**, the fixation of the prosthesis with screws alone resulted in concentrated

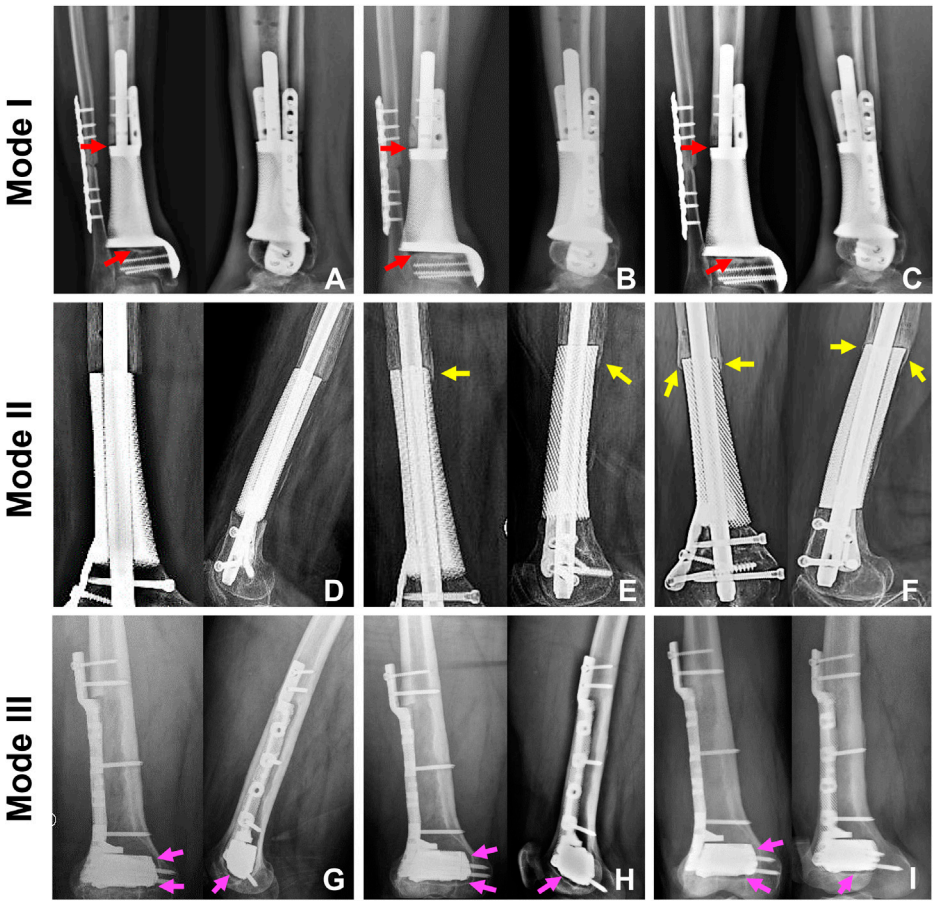

FIGURE 7 | The state of prosthesis's stability and new bone regeneration in three groups. For Mode I, the typical patient was a 65-year-old male who suffered distal tibial metaphyseal defect due to osteomyelitis. Along with his postoperative X-rays at 1 **(A)**, 7 **(B)**, and 22 **(C)** months, we could observe the stable location of both prosthesis and screws. The low-density gap at bone-prosthesis interface gradually blurred but not disappeared as directed by the red arrows. For Mode II, the typical patient was a 67-year-old female who suffered distal femoral metaphyseal defect due to osteomyelitis. Along with her postoperative X-rays at 1 **(D)**, 9 **(E)** and 25 **(F)** months, we could observe the stable location of prosthesis, nail and screws. Besides, new bone continuously regenerated around the prosthesis as directed by the yellow arrows. For Mode III, the typical patient was a 26-year-old male who suffered distal femoral partial metaphyseal defect due to osteomyelitis. Along with his postoperative X-rays at 1 **(G)**, 5 **(H)** and 14 **(I)** months, we could observe the stable location of both prosthesis and screws. The low-density gap at bone-prosthesis interface existed persistently as directed by the pink arrows.

biomechanical conduction between bone and prosthesis interface, which induced the new bone to grow gradually at the bone-prosthesis gap instead of growing on the surface of prostheses. At the same time, the application of IM nail was more conducive to the surrounding new bone regeneration (**Figures 7D–F**). Under this circumstance, stress is equably distributed along with the IM nail and bone-prosthesis interface, resulting in new bone growth from the end of the bone defect, continuously surrounding the prosthesis. Generally, an adaptation of bone structure to the mechanical environment consists of several mechanisms. The trabecular bone exhibits a phenomenon in which the apparent bone density and orientation characteristics change according to the stress magnitudes as well as the principal directions. The structure change couples the bone resorption by osteoclastic cells and bone formation by osteoblastic cells. The various cells contributing to the remodeling detect mechanical stimuli and transduce them to biochemical signals (Gao et al., 2019). This complex process can be changed according to the local mechanical environments. In this way, bone remodeling based on mechanical stimulus at the cellular level leads to structural and functional adaptive changes corresponding to the load direction and magnitude, aiming to achieve a uniform mechanical stimulus state.

The limb function of all patients could meet the weight-bearing requirements of daily life at the last follow-up, meaning all patients benefited from the advantages of customized titanium alloy prostheses and stable internal fixation options. Patients in Mode III group had a significantly higher rate of excellent or good limb function scores, which was associated with the initially smaller extent of bone loss in these patients. Besides, at the last follow-up, there was no significant difference in the SF-36 scores among the three groups, proving that applying 3D printed prostheses could achieve similarly

good clinical curative effects in patients with metaphyseal bone defects of extremities.

The main limitation of this study was the number of included patients, which was relatively small. In our future work, we plan to include more cases and conduct a wider multicenter clinical study in view of applying 3D printed prostheses to repair metaphyseal bone defects, which will be more conducive to the systematic investigation on clinical efficacy and new bone growth.

5 CONCLUSION

The treatment of metaphyseal bone defects is a great challenge in clinical practice. Applying 3D printed prostheses to repair metaphyseal bone defects of extremities can result in good recovery of limb function, thus allowing patients to normally engage in their daily activities. Yet, different fixation patterns can lead to different biomechanical distributions. The use of IM nails for prosthesis fixation is more conducive to equal conduction of stress and new bone regeneration. Besides, the fixation mode in which the prosthesis was only fixed by screws was also optional for defects extremely close to the articular surface.

DATA AVAILABILITY STATEMENT

The original contributions presented in the study are included in the article/supplementary material, further inquiries can be directed to the corresponding authors.

ETHICS STATEMENT

The studies involving human participants were reviewed and approved by Medical Science Research Ethics Committee of Peking University Third Hospital. The patients/participants provided their written informed consent to participate in this study.

AUTHOR CONTRIBUTIONS

BL, XL, and WQ followed the patients, collected the data and wrote the article. ZL, FZ, and YZ designed and supervised the study. PW designed the study and completed the fabrication of prostheses. YT supervised the study, finished the surgeries and revisions of the manuscript.

FUNDING

This study was supported by the Beijing Municipal Science & Technology Commission (No. Z181100001718195), National Key R&D Program of China (No. 2018YFE0104200) and National Natural Science Foundation of China (No. 82172065).

ACKNOWLEDGMENTS

The authors are grateful to Xiaoyan Niu for her help in clinical data collection.

REFERENCES

Benulic, C., Canton, G., Gril, I., MurenaKristan, L. A., and Kristan, A. (2020). Management of Acute Bone Loss Following High Grade Open Tibia Fractures. *Acta Biomed.* 91, e2020012. doi:10.23750/abm.v91i14-S.10890

Blokhuis, T. J. (2017). Management of Traumatic Bone Defects: Metaphyseal versus Diaphyseal Defects. *Injury* 48, S91–S93. doi:10.1016/j.injury.2017.04.021

Brand, R. A. (2010). Biographical Sketch: Julius Wolff, 1836-1902. *Clin. Orthop. Relat. Res.* 468, 1047–1049. doi:10.1007/s11999-010-1258-z

Brånemark, P. I., Hansson, B. O., Adell, R., Breine, U., Lindström, J., Hallén, O., et al. (1977). Osseointegrated Implants in the Treatment of the Edentulous Jaw. Experience from a 10-year Period. *Scand. J. Plast. Reconstr. Surg. Suppl.* 16, 1–132.

Campbell, G. M., and Glüer, C.-C. (2017). Skeletal Assessment with Finite Element Analysis: Relevance, Pitfalls and Interpretation. *Curr. Opin. Rheumatol.* 29, 402–409. doi:10.1097/BOR.0000000000000405

Chen, F., Zhao, Z., Gao, C., Liu, J., Su, X., Zhao, J., et al. (2018). Clustering of Morphological Features for Identifying Femur Cavity Subtypes with Difficulties of Intramedullary Nail Implantation. *IEEE J. Biomed. Health Inf.* 22, 1209–1217. doi:10.1109/JBHI.2017.2761980

Gao, X., Fraulob, M., and Haïat, G. (2019). Biomechanical Behaviours of the Bone-Implant Interface: A Review. *J. R. Soc. Interface.* 16, 20190259. doi:10.1098/rsif.2019.0259

Hou, G., Liu, B., Tian, Y., Liu, Z., Zhou, F., Ji, H., et al. (2020). An Innovative Strategy to Treat Large Metaphyseal Segmental Femoral Bone Defect Using Customized Design and 3D Printed Micro-porous Prosthesis: A Prospective Clinical Study. *J. Mater Sci. Mater Med.* 31, 66. doi:10.1007/s10856-020-06406-5

Ji, T., Yang, Y., Tang, X., Liang, H., Yan, T., Yang, R., et al. (2020). 3D-Printed Modular Hemipelvic Endoprosthetic Reconstruction Following Periacetabular Tumor Resection: Early Results of 80 Consecutive Cases. *J. Bone Jt. Surg. Am.* 102, 1530–1541. doi:10.2106/JBJS.19.01437

Lu, Y., Chen, G., Long, Z., Li, M., Ji, C., Wang, F., et al. (2019). Novel 3D-Printed Prosthetic Composite for Reconstruction of Massive Bone Defects in Lower Extremities after Malignant Tumor Resection. *J. Bone Oncol.* 16, 100220. doi:10.1016/j.jbo.2019.100220

Mancuso, F., Beltrame, A., Colombo, E., Miani, E., and Bassini, F. (2017). Management of Metaphyseal Bone Loss in Revision Knee Arthroplasty. *Acta Biomed.* 88, 98–111. doi:10.23750/abm.v88i2-S.6520

Migliorini, F., La, Padula, G., Torsiello, E., Spiezia, F., Oliva, F., and Maffulli, N. (2021). Strategies for Large Bone Defect Reconstruction after Trauma, Infections or Tumour Excision: A Comprehensive Review of the Literature. *Eur. J. Med. Res.* 26, 118. doi:10.1186/s40001-021-00593-9

Nwankwo, E. C., Chen, F., Nettles, D. L., and Adams, S. B. (2019). Five-Year Follow-Up of Distal Tibia Bone and Foot and Ankle Trauma Treated with a 3D-Printed Titanium Cage. *Case Rep. Orthop.* 2019, 1–6. doi:10.1155/2019/7571013

Roberts, J. L., Paglia, D. N., and Drissi, H. (2018). Transcriptional Mechanisms of Secondary Fracture Healing. *Curr. Osteoporos. Rep.* 16, 146–154. doi:10.1007/s11914-018-0429-9

Tetsworth, K., Block, S., and Glatt, V. (2017). Putting 3D Modelling and 3D Printing into Practice: Virtual Surgery and Preoperative Planning to Reconstruct Complex Post-Traumatic Skeletal Deformities and Defects. *SICOT-J* 3, 16. doi:10.1051/sicotj/2016043

Tshephe, T. S., Akinwamide, S. O., Olevsky, E., and Olubambi, P. A. (2022). Additive Manufacturing of Titanium-Based Alloys- A Review of Methods, Properties, Challenges, and Prospects. *Heliyon* 8, e09041. doi:10.1016/j.heliyon.2022.e09041

Wang, J., Ma, J.-X., Lu, B., Bai, H.-H., Wang, Y., and Ma, X.-L. (2020). Comparative Finite Element Analysis of Three Implants Fixing Stable and Unstable Subtrochanteric Femoral Fractures: Proximal Femoral Nail Antirotation (PFNA), Proximal Femoral Locking Plate (PFLP), and Reverse Less Invasive Stabilization System (LISS). *Orthop. Traumatology Surg. Res.* 106, 95–101. doi:10.1016/j.otsr.2019.04.027

Wu, C., Zeng, B., Deng, J., Shen, D., Wang, X., Tan, L., et al. (2022). Custom Design and Biomechanical Clinical Trials of 3D -printed Polyether Ether Ketone Femoral Shaft Prosthesis. *J. Biomed. Mater Res.* doi:10.1002/jbm.b.35055

Xu, L., Qin, H., Cheng, Z., Jiang, W.-B., Tan, J., Luo, X., et al. (2021). 3D-Printed Personalised Prostheses for Bone Defect Repair and Reconstruction Following Resection of Metacarpal Giant Cell Tumours. *Ann. Transl. Med.* 9, 1421. doi:10.21037/atm-21-3400

Yan, L., Lim, J. L., Lee, J. W., Tia, C. S. H., O'Neill, G. K., and Chong, D. Y. R. (2020). Finite Element Analysis of Bone and Implant Stresses for Customized 3D-Printed Orthopaedic Implants in Fracture Fixation. *Med. Biol. Eng. Comput.* 58, 921–931. doi:10.1007/s11517-019-02104-9

Yao, Y., Mo, Z., Wu, G., Guo, J., Li, J., Wang, L., et al. (2021). A Personalized 3D-Printed Plate for Tibiotalocalcaneal Arthrodesis: Design, Fabrication, Biomechanical Evaluation and Postoperative Assessment. *Comput. Biol. Med.* 133, 104368. doi:10.1016/j.compbiomed.2021.104368

Conflict of Interest: The authors declare that the research was conducted in the absence of any commercial or financial relationships that could be construed as a potential conflict of interest.

frontiers | Frontiers in Materials

ORIGINAL RESEARCH
published: 03 June 2022
doi: 10.3389/fmats.2022.828838

Combined Application of Er:YAG and Nd:YAG Lasers Enhances Osseointegration at Dental Bone-Implant Interface

*Tianyuan Zhao and Meihua Li**

Department of Stomatology, The Second Hospital of Jilin University, Changchun, China

The combination of a bone and an implant surface is a dynamic biological process. By improving the osseointegration efficiency of the bone tissue around the implant surface, the implant can obtain long-term stability. In this study, we have investigated the potential applications of dual-wavelength lasers (Er:YAG laser and Nd:YAG laser) in implantations and observed their possible efficacy in promoting tissue repair around the implant. The animal experimental model of a rabbit femoral defect implant was used to simulate the process of tissue reconstruction around the implant in humans. The results indicated that by micro-CT observation, it was obvious that the bone mineral density (BMD) values of the dual-wavelength laser group were significantly higher than those of other groups. Furthermore, VG staining clearly showed that there was no obvious physiological gap detected between the implant and the surrounding bone tissues in the dual-wavelength laser group. HE staining further revealed that no significant influx of inflammatory cells was observed around the implants. Immunohistochemical staining of OCN and VEGF showed that the positive area percentages of the dual-wavelength laser group were significantly higher than other groups at the same time point. Therefore, the application of a dual-wavelength laser in implantations can exhibit a positive effect on promoting the reconstruction of bone tissues.

Keywords: osseointegration, bone-implant interface, dental implant, micro CT, Er:YAG laser, Nd:YAG laser

OPEN ACCESS

Edited by:
Jianxun Ding,
Changchun Institute of Applied Chemistry (CAS), China

Reviewed by:
Livia Visai,
University of Pavia, Italy
Shanchang Li,
Affiliated Stomatological Hospital of Suzhou University, China
Guoliang Zhang,
Jiamusi University, China

****Correspondence:***
Meihua Li
meihua@jlu.edu.cn

Specialty section:
This article was submitted to Biomaterials, a section of the journal Frontiers in Materials

Received: *04 December 2021*
Accepted: *19 April 2022*
Published: *03 June 2022*

Citation:
Zhao T and Li M (2022) Combined Application of Er:YAG and Nd:YAG Lasers Enhances Osseointegration at Dental Bone-Implant Interface. Front. Mater. 9:828838. doi: 10.3389/fmats.2022.828838

1 INTRODUCTION

In dental implant surgery, optimal bone integration of an implant and the surrounding tissues constitutes the foundation and focus of implant-supported denture restoration (Albrektsson and Wennerberg, 2019). At present, the surface of implants for clinical application has been generally roughened to increase its biocompatibility with the bone tissues. For instance, studies by Alsaadi et al. (2006) have revealed that titanium implants with rough surfaces have a significantly higher survival rate than titanium implants with traditional machined surfaces. Moreover, an Er:YAG laser that has been approved by the FDA has exhibited good biological effects as a dental hard tissue laser. Therefore, an Er: YAG laser might have good developmental prospects for the treatment of implants and bone tissue surfaces (Schwarz et al., 2006).

Many previous studies have shown that the surface of bone tissue irradiated by an Er:YAG laser can potentially accelerate the osteoblasts to produce new bones and enhance the retention rate of fibrin and blood clots (Safioti et al., 2017). Moreover, titanium implants treated with an Er:YAG laser

can effectively improve the surface wettability and thereby substantially improve the adhesion of tissue cells for early bone repair (Nejem Wakim et al., 2018). In addition, the research conducted by Kazemzadeh-Narbat et al. (2010) has indicated that the potential application of antibacterial coatings and organic molecules on the implant surface could significantly reduce the generation of dental plaque biofilm. However, the implant stability could not be achieved on the implant surface by physical adsorption, and moreover, the biological safety still remains to be verified. However, the use of Er:YAG laser irradiation on the implant and the surrounding bone tissues *via* the photothermal effect has been found to be relatively safe and can demonstrate efficient bactericidal effects (Romanos et al., 2019). The Er:YAG laser also displayed significant bactericidal activity against Gram-negative anaerobes (Kreisler et al., 2002). The Er:YAG laser is currently being used clinically for the treatment of peri-implantitis to efficiently remove the dental plaques on the implant surface without affecting the implant surface structure (Ali et al., 2020). For example, Crippa et al. (2020) have reported the use of the Er:YAG laser to treat patients with immediate dental implant infection and obtained a success rate of 94.6%.

The Nd:YAG laser primarily acts on tissues such as dyes and hemoglobin (Mordon et al., 2003) and can be used for rapid coagulation and the treatment of soft tissue inflammation during implant surgery to reduce the time of implant surgery (Evrard et al., 1996). At the same time, the Nd:YAG laser can display the function of rapidly generating photothermal and photochemical effects after being absorbed by the biological tissues and, thus, can rapidly eliminate deeply embedded bacteria (Mellado-Valero et al., 2013). In addition, the Nd:YAG laser low-intensity laser treatment (LLLT) can also significantly promote the proliferation and maturation of human osteoblasts (Li et al., 2017) and accelerate the formation and metabolism of new bones at an early period (Karoussis et al., 2017). However, during clinical applications, the irradiation time and dose of the Nd:YAG laser should be strictly controlled to avoid extensive damage being caused to the surrounding soft and hard tissues (Van Nimwegen et al., 2008). Therefore, in this study, we have used a combination of the Er:YAG laser and the Nd:YAG laser in animal implant surgery to analyze the potential improvement of the early inflammatory response of the tissues around the implant and the possible effects on bone tissue repair after the combination of two-wavelength lasers, which will provide a theoretical basis for the application of the Er:YAG laser and Nd:YAG laser together in oral implant surgery.

2 EXPERIMENTAL SECTION

2.1 Materials and Apparatus

The Fotona LightWalker AT dual-wavelength laser system, H14-N hand tool, and R21-C2 hand tool were supplied by FT medical (Beijing, China). The Surgic XT Plus, Straumann planting implement, and Straumann sandblasted with large grits and acid-etched (SLA) bone level implant (φ3.3 mm NC, SLA 8 mm) were obtained from Straumann (Beijing, China). Coolabar (Beijing, China) supplied paraformaldehyde and phosphate-buffered saline (PBS). OCN and VEGF used for immunohistochemistry were purchased from Abcam (Cambridge, United Kingdom). Van Gieson's (VG) solution and the hematoxylin-eosin/HE staining kit were purchased from Solarbio (Beijing, China). Saline was supplied by DZ medicine (Tianjin, China).

2.2 Preparation of Two-Wavelength Laser Application Parameters

In this experiment, a Fotona dual-wavelength laser treatment system was used to assist the implantation surgery as shown in **Schemes 1**. First, the instrument was turned on, and the Hc14-N hand tool, R21-C2 hand tool, and tapered fiber tip were connected, respectively. The first therapeutic parameters of the Er:YAG laser (2,940 nm) were set as SSP, 120 mJ, and 15 Hz for cortical bone drilling. The treatment of cortical bone with the Er:YAG laser results in a significant reduction in the risk of cortical bone fracture and improved the initial stability of the implant (Matys et al., 2018). The second therapeutic parameter of the Er:YAG laser (2,940 nm) was set as SP, 80 mJ, and 15 Hz for laser washing at the bone interface. The washing effect of the Er:YAG laser on the implant socket can effectively improve the osseointegration efficiency around the implant (Kesler et al., 2006). The first treatment parameter of the Nd:YAG laser (1064 nm) was set as VLP, 20 Hz, and 4 W for coagulation in implant surgery. The second therapeutic parameter of the Nd:YAG laser (1,064 nm) was set as MSP, 15 Hz, and 1.5 W to improve postoperative bone integration. The Nd:YAG laser can effectively promote the efficiency of new bone formation.(Kim et al., 2015).

2.3 Preparation of SLA Dental Implants

An SLA titanium implant (φ3.3 mm NC, SLA 8 mm) was selected as the animal experimental implant to verify the effect of the dual-wavelength laser on osseointegration around the implant. The surface treatment of SLA titanium implants is mainly completed by mechanical roughening, sandblasting, and chemical etching. The SLA pure titanium implants after surface roughening have good compatibility with the bone tissue in the early stage (Kim et al., 2008). The titanium implants of Straumann SLA selected in this experiment were tested according to the standard of SEM images before application.

2.4 Experiments on Improving Osseointegration by Laser

2.4.1 Establishment of Bone Defect Animal Models

All animal experimental programs were approved by the Animal Care and Use Ethics Committee of Jilin University. In this study, 36 adult Japanese white rabbits (average weight 2 kg, Beijing HFK Biotechnology Co., Ltd., Beijing, China) with large ears were maintained in the feeding room of the Animal Experimental Center of the School of Basic Medical Science, Jilin University (all the animals were fed under the same conditions of light and temperature). In the operation, Straumann planting implements and Surgic XT Plus were used to prepare the implantation fossa in

the lower part of the femoral head of rabbits step by step to simulate the preparation process of bone tissue during dental implantation.

2.4.2 Dual-Wavelength Laser-Assisted Implantation of Dental Implants

Thirty-six adult rabbits (average weight 2 kg) were randomly divided into four groups: Er:YAG, Nd:YAG, combination, and control. After skin preparation and towel laying disinfection under anesthesia, a 3-cm linear longitudinal skin incision was made on the lateral side of the femur, and the muscle tissue and periosteum were carefully separated. In the Er:YAG laser group, the implantation sites of the bone tissues were fixed using the Er:YAG laser (SSP, 120 mJ, and 15 Hz) in a non-contact manner. The holes (3.3 mm diameter and 8.0 mm depth) were prepared gradually in a step-by-step manner to 8 mm by using the Straumann planting implement, with 0.9% sodium chloride isotonic solution. Thereafter, the liquid for cooling irrigation was applied to prevent the bone tissue temperature from overheating. Thereafter, during each reaming drill switching, the Er:YAG laser (QSP, 80 mJ, and 15 Hz) was used for laser swing washing of the implant socket two consecutive times. In the Nd:YAG laser group, the holes (3.3 mm diameter and 8.0 mm depth) were prepared gradually step by step to 8 mm, cooled, and then rinsed with 0.9% sodium chloride isotonic solution. The intraoperative assistant used the Nd:YAG laser (VLP, 20 Hz, and 4 W) for further coagulation to ensure a clear operation field. After the operation was conducted, the sutured implant region was irradiated with the Nd:YAG laser (MSP, 15 Hz, and 1.5 W) low-intensity laser therapy (LLLT) for 120 s for three consecutive days, which could significantly reduce wound pain and accelerate wound healing. In the combination laser group, the Er:YAG laser and the Nd:YAG laser were simultaneously used in the laser application manner described previously. In the control group, the holes (3.3 mm diameter and 8.0 mm depth) were prepared gradually step by step to 8 mm, cooled, and then rinsed with 0.9% sodium chloride isotonic solution.

Thereafter, one Straumann implant (φ3.3 mm NC and SLA 8 mm) was implanted into the same position at the lower end of the femoral head of the rabbits, and the tissues were properly aligned and layer-sutured using a 3–0 nylon suture at the operation site. All the procedures were performed by the same physician without selective bias. After the surgery on animals, gentamicin was administered at (0.1 ml/kg) with antibiotic medication for 3 days.

2.4.3 Micro-CT Analysis

The specimens were scanned by micro-CT (90 kV, 114 mA, and 18 μm image pixel size) to evaluate the effect of bone regeneration and osseointegration. A cylinder (4.0 mm diameter and 8 mm height) was selected as the region of interest (ROI). The 3D reconstruction was performed by multimodal 3D visualization software (NRecon 1.7.1.0 software, Kontich, Belgium). The quantitative analysis of the ROI was conducted by micro-CT auxiliary software (VGStudio Volume Graphics GmbH, Germany), including bone mineral density (BMD, g/cm3), trabecular thickness (Tb. Th, mm), trabecular separation (Tb. Sp, mm), and trabecular number (Tb. N, 1/mm).

2.4.4 Histological Evaluation

The samples were immobilized in 4% paraformaldehyde solution for 2 weeks before decalcification for 1 month. The samples were then dehydrated in a series of fractionated ethanol solutions. After vitrification with xylene, the samples were embedded in paraffin wax and cut into slices with 30 μm thickness for VG staining. The inward bone growth was observed *via* an inverted microscope (DSX 500; Olympus Corporation, Tokyo, Japan), and ImageJ was used to analyze the surface area of the newly formed bone tissue. In addition, proximal femurs were immersed in 10% ethylenediaminetetraacetic acid to demineralize for 1 month, after which the specimens were embedded in paraffin and sectioned into 5 μm slices by the microtome. Then, the prepared sections were stained with H&E to investigate the effects of the dual-wavelength laser on bone integration around the implant.

2.4.5 Immunohistochemistry

The specimens were fixed in 4% paraformaldehyde for 2 weeks before decalcification for 1 month. After the removal of the implants, the remaining bone tissues were sectioned for an immunohistochemical analysis. In short, the sections were made after a 3% H_2O_2 treatment. Then, they were sealed with serum, incubated with primary antibodies and then secondary antibodies, stained, counterstained, and dehydrated. Finally, an optical microscope was used for observation at a magnification of ×100.

2.5 Statistical Analysis

Data are presented as mean ± standard deviation. Each group of data was obtained from three independent experiments. Differences between multiple experimental groups were statistically analyzed *via* one-way analysis of variance (ANOVA) and Tukey's multiple comparison test. GraphPad Prism v. 8.2 was used for all statistical analyses. $p < 0.05$ indicated significant difference.

3 RESULTS AND DISCUSSION

3.1 Microstructural Analysis of Bone Ingrowth

The early process of osseointegration around the implant is related to the activity of endogenous BMSCs. Therefore, dual-wavelength laser-assisted implant surgery is an effective treatment to improve the efficiency of osseointegration around the implant (Yin et al., 2017). Statistical analyses of micro-CT are depicted in **Figures 1A–E**. The Tb. N values of the Er:YAG, Nd:YAG, combination, and control groups in 14 days were 2.26 ± 0.05, 1.96 ± 0.04, 2.56 ± 0.05, and 1.28 ± 0.03 /mm, respectively. It is consistent with the three-dimensional reconstructed image. The bone mineral density (BMD), trabecular separation (Tb. Sp), trabecular number (Tb. N), and trabecular thickness (Tb. Th) of the bone tissues around the implant were calculated for each experimental group. As shown in **Figure 1B**, the BMD of the laser group was significantly greater than that of the control group when compared at the same time ($p < 0.001$), and the bone mineral density of the combined laser group was the largest. However, as shown in **Figure 1C**, the trabecular separation was the smallest in the laser combined treatment group, thereby indicating that the laser combined treatment exhibited the most significant osteogenic effect on bone tissue ($p < 0.001$). The trabecular separation of the Er:YAG laser group was less than that of the constituent bones of the control group, and the trabecular

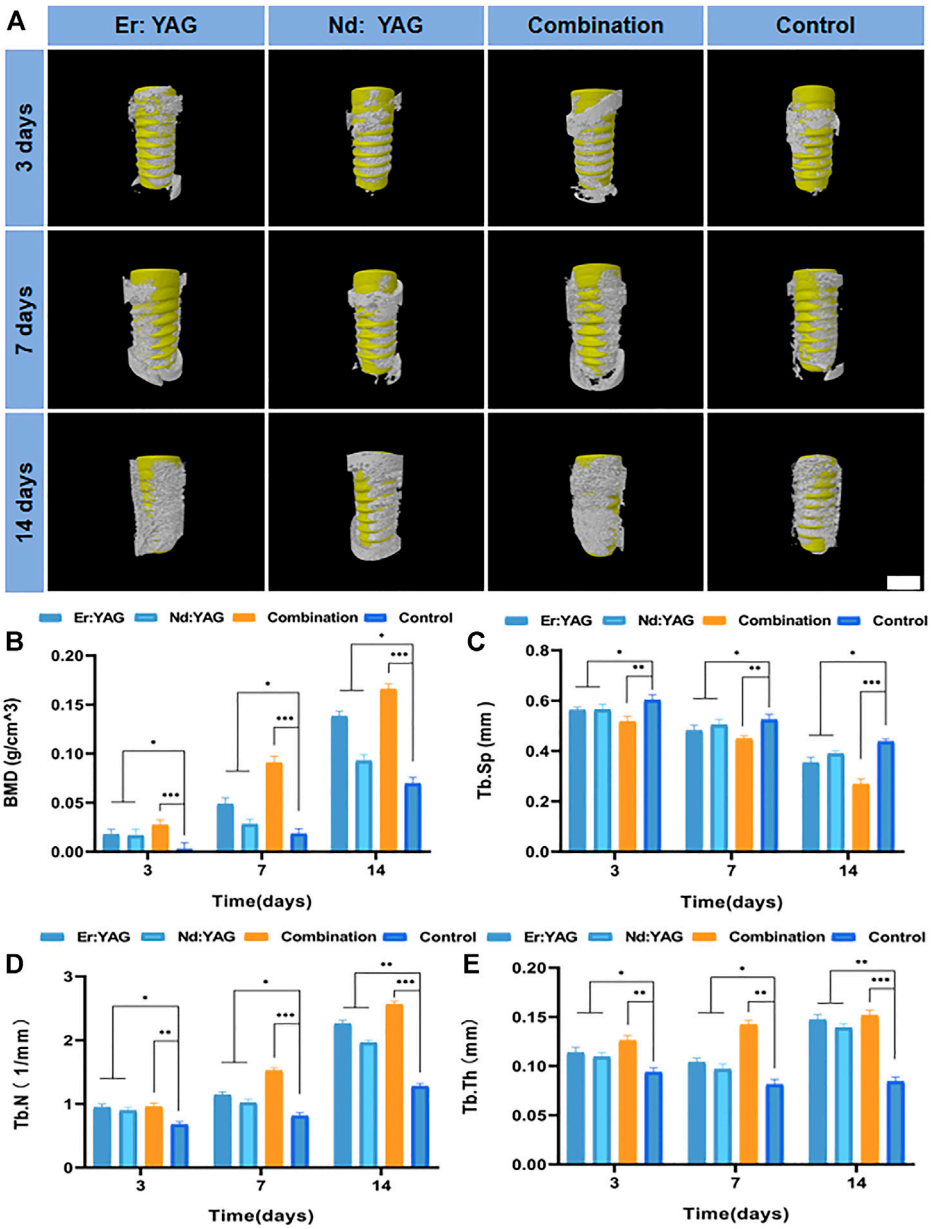

FIGURE 1 | Micro-CT analysis of bone integration. **(A)** Representative 3D reconstructed micro-CT images around the implant (scale bar = 4 mm) and the **(B)** BMD, **(C)** Tb. Sp, **(D)** Tb. N, and **(E)** Tb. Th of each group after 3, 7, and 14 days of implantation ($n = 3$, *indicates significant differences between the groups, $^{*}p < 0.05$; $^{**}p < 0.01$; $^{***}p < 0.001$).

separation in the Nd:YAG laser group was markedly less than that in the control group at 14 days ($p < 0.05$). Overall, based on the data analysis of micro-CT, it could be seen that the combined application of laser resulted in an effective peri-implant bone formation, and the effect was statistically significant ($p < 0.001$).

3.2 Osseointegration at SLA Implant Interfaces With Surrounding Bone

The histological results based on HE staining were applied to evaluate the bone integration effect of the peri-implant bone tissue (**Figures 2A–C**). As shown in **Figure 2A**, on comparison between the laser group and the control group in 3 days, it could be clearly observed that thermal injury of the bone tissues around implants in the laser group was not significant. The number of inflammatory cells in the bone tissues of the experimental group after Er laser washing treatment was significantly lesser than that of the control group. It was observed that the inflammatory infiltration in the peripheral bone tissues of the Nd laser group was slightly better than that of the control group. However, in the combined laser group, bone integration of the bone tissues around the implant was significant, and there was no necrotic bone tissue area observed on day 3 (**Figure 2A**). Moreover, the laser groups

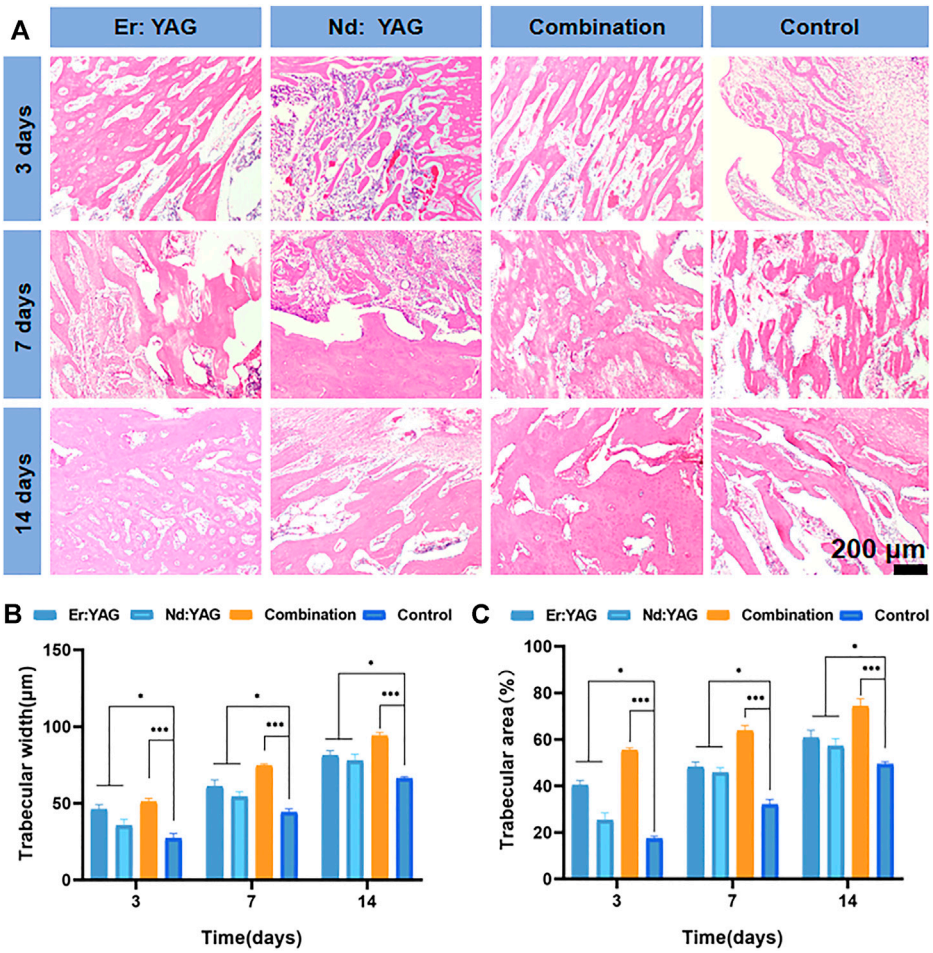

FIGURE 2 | Histological analysis of bone integration. Representative images of **(A)** HE staining of the defect site after 3, 7, and 14 days of implantation (pink in HE staining shows collagen fibers of the new bone at the interface between the implant and bone), trabecular width of the regenerated bone **(B),** and the area of the regenerated bone, following **(C)** HE staining (n = 3, *indicates significant differences between the groups, $^{*}p < 0.05$; $^{**}p < 0.01$; $^{***}p < 0.001$).

clearly showed that the osteoblasts were surrounded by the bone matrix, and inflammatory infiltration was markedly less than that in the control group in 7 days. These findings suggested that the laser played a positive role during early bone tissue integration (**Figure 2A**). The trabeculae in the laser combined group were clearly visible in 14 days, and they were found to be significantly thicker and denser than those in the other experimental groups and the control group. The thickness and density of the trabecular meshwork in the Er laser group were observed to be superior to those in the Nd laser group (**Figure 2A**). As shown in **Figures 2A and B**, the histological analysis further showed that the osteogenic effect of the laser combined group was substantially superior to that of the control group at all time-points ($p < 0.001$), and it also depicted a novel trend of higher bone formation. In addition, the bone-forming effect of the Er laser was relatively better than that of the Nd laser group.

At 14 days, histological data based on van Gieson staining were used to evaluate implant-bone combinations in different experimental groups (**Figures 3A,B**). As shown in **Figure 3A**, on comparing the hard tissue sections of the implants obtained at 14 days, it could be clearly noted that there was no obvious physiological gap between the implant and the surrounding bones in the combination laser group, and the bone repair rate was the highest (**Figure 3B**). In addition, the bone-forming effect of the Er laser was relatively better than that of the Nd laser group. Overall, it could be seen that the combined application of lasers resulted in an effective peri-implant bone formation, and the effect was statistically significant ($p < 0.001$).

3.3 Effect of Laser on Osteogenic Differentiation

As shown in **Figure 4A**, the quantitative analysis of immunohistochemical sections of osteocalcin (OCN) clearly showed that the percentage of osteocalcin-positive areas in each group increased significantly with an increase in the number of days. Moreover, the percentage of osteocalcin-positive areas in the laser combined group was significantly higher than that in the other experimental groups and the control group at the same time point, as shown in **Figure 4C**.

Osteocalcin (OCN), also known as bone R-hydroxyglutamic acid protein, is synthesized primarily by osteoblasts and can

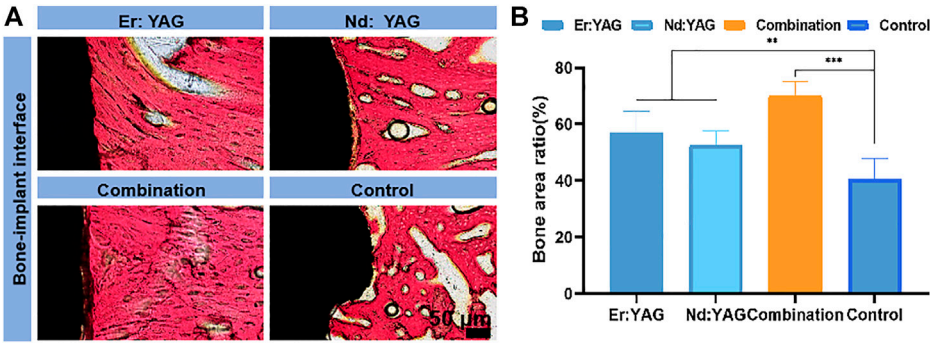

FIGURE 3 | Histological analysis of bone integration. Representative images of **(A)** van Gieson staining of bone tissue around the implant after 14 days of implantation (black represents the titanium alloy interface, and red in van Gieson staining shows collagen fibers of the new bone at the interface between the implant and bone) and proportion of the area of the regenerated bone, following **(B)** van Gieson staining. (n = 3, *indicates significant differences between groups, $^{*}p < 0.05$; $^{**}p < 0.01$; $^{***}p < 0.001$).

substantially promote early peri-implant bone integration (Mastrangelo et al., 2020). The immunohistochemical results in this study also revealed that the positive expressions of OCN in the Er:YAG, Nd:YAG, and the combination laser groups at 14 days were significantly increased and strikingly higher than those found in the control group (**Figure 4A**). Therefore, an increased positive expression of this important osteogenic marker protein in the peri-implant tissues provided strong evidence for the promotion of new bone formation upon the application of dual-wavelength laser light during implant surgery. This finding also indicated that the combined application of the Er:YAG laser and Nd:YAG laser could markedly promote early bone integration and tissue repair around the implants.

Bone integration and tissue repair in dental implant surgery remain the key factors that can facilitate a successful surgery. For instance, Pourzarandian et al. (2004) have reported that after treatment with the Er:YAG laser, the surface of the bone tissue could effectively promote the adhesion of osteoblasts but did not affect the migration and proliferation of bone tissue cells. The surface of the bone tissue treated with Er:YAG laser swing washing has been found to be associated with several irregularities (Pantawane et al., 2019) such that the bone surface could be more easily adhered to fibrin (Cekici et al., 2013) and thereby effectively promote blood clot stabilization and tissue formation (Niimi et al., 2020). In this experimental study, the bone mineral density (BMD) of the new bone around the implant was analyzed by micro-CT and measurement software. It was clearly observed that the applications of the Er:YAG and Nd:YAG laser groups and these two laser groups in combination were significantly better than those of the control group. Moreover, in the hard tissue sections stained with VG, it could be clearly seen that the space between the implant and the new bone in the Er:YAG, Nd:YAG, and the combination laser groups for 14 days was found to be significantly smaller than that in the control group. Bone binding is a dynamic physiological process (Chang and Giannobile, 2012) and minute movements during the early stages of implantation can negatively affect bone remodeling and generate cicatrix tissue (Sennerby and Meredith, 2008). It has been established that the larger the contact area between the implant and bone during the early stages, the more significant the impact of bone integration will be. In addition, a number of studies have found that the treatment of cortical bone with the Er:YAG laser and subsequent implantation of the implant can also effectively reduce the risk of bone fractures and adjacent tooth injury around the implant (Matys et al., 2018). It has been observed that the bone tissue treated with the Er:YAG laser can provide better initial stability for the immediate weight-bearing ability of the implant. We also noted that the experimental group using the Er:YAG laser to fix the implantation sites of the bone tissues was significantly superior to the control group based on the effect of bone integration through observations of the tissues under the microscope. A number of previous studies have shown that the Nd:YAG laser postoperative adjuvant treatment of bone defects has a significant role in promoting bone regeneration (Ninomiya et al., 2003). It has also been found that the promotion of bone repair by the Nd laser was primarily due to the biological stimulation of LLLT (Vescovi et al., 2013). For example, Kim et al. (2010) found that the wavelength of the Nd:YAG laser (1064 nm) allowed the laser to effectively penetrate the skin and the different muscle layers and promoted the expressions of BMP-2 and IGF-1 cytokines around bone tissue. Moreover, postoperative irradiation of the wound with the Nd:YAG laser was found to play an important role in mediating bone regeneration (Bouvet-Gerbettaz et al., 2009). Furthermore, HE staining sections of the bone tissues around the implants in this study also indicated that the number and quantity of bone trabeculae around the implants in the laser group were superior to those observed in the control group.

In addition, in this study, the Er:YAG laser was primarily used to fix the implant position, and the 0.9% sodium chloride isotonic solution was used to cool and wash the implants during the dimple washing process, which could significantly avoid thermal damage caused by the laser. A number of studies have shown that excessive bone temperature during implantations can adversely affect the rate of bone tissue incorporation (Trisi et al., 2015). However, the Nd:YAG laser was used in this study to irradiate and induce new bone

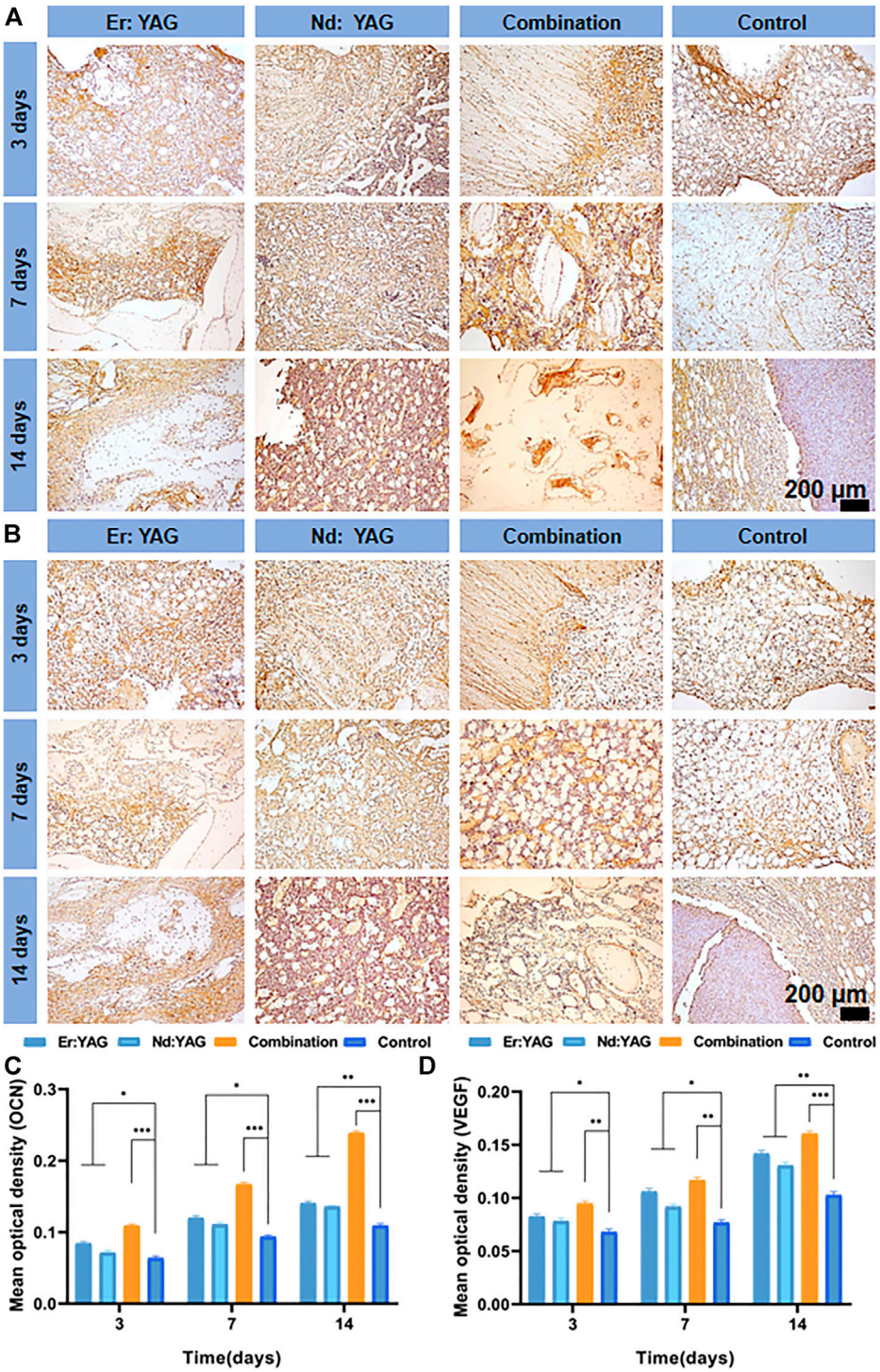

FIGURE 4 | Immunohistochemical analysis of the bone around the implant. Representative images of the expressions of **(A)** OCN, **(B)** VEGF, and **(C)** mean optical density of positive areas in the bone around the implants at 3, 7, and 14 days after implantation. ($n = 3$, *indicates significant differences between the groups, $^{*}p < 0.05$; $^{**}p < 0.01$; $^{***}p < 0.001$).

formation in the implantation area using LLLT low-intensity laser irradiation at an intensity of 1.5 W. Moreover, a previous study by Kim et al. (2015) found that the heat generated by the Nd:YAG laser at the low power (1.25–2 W) was rather limited, and it could not damage the healthy tissues but exhibited the most significant effects in promoting the repair of the soft and hard tissues around the implants.

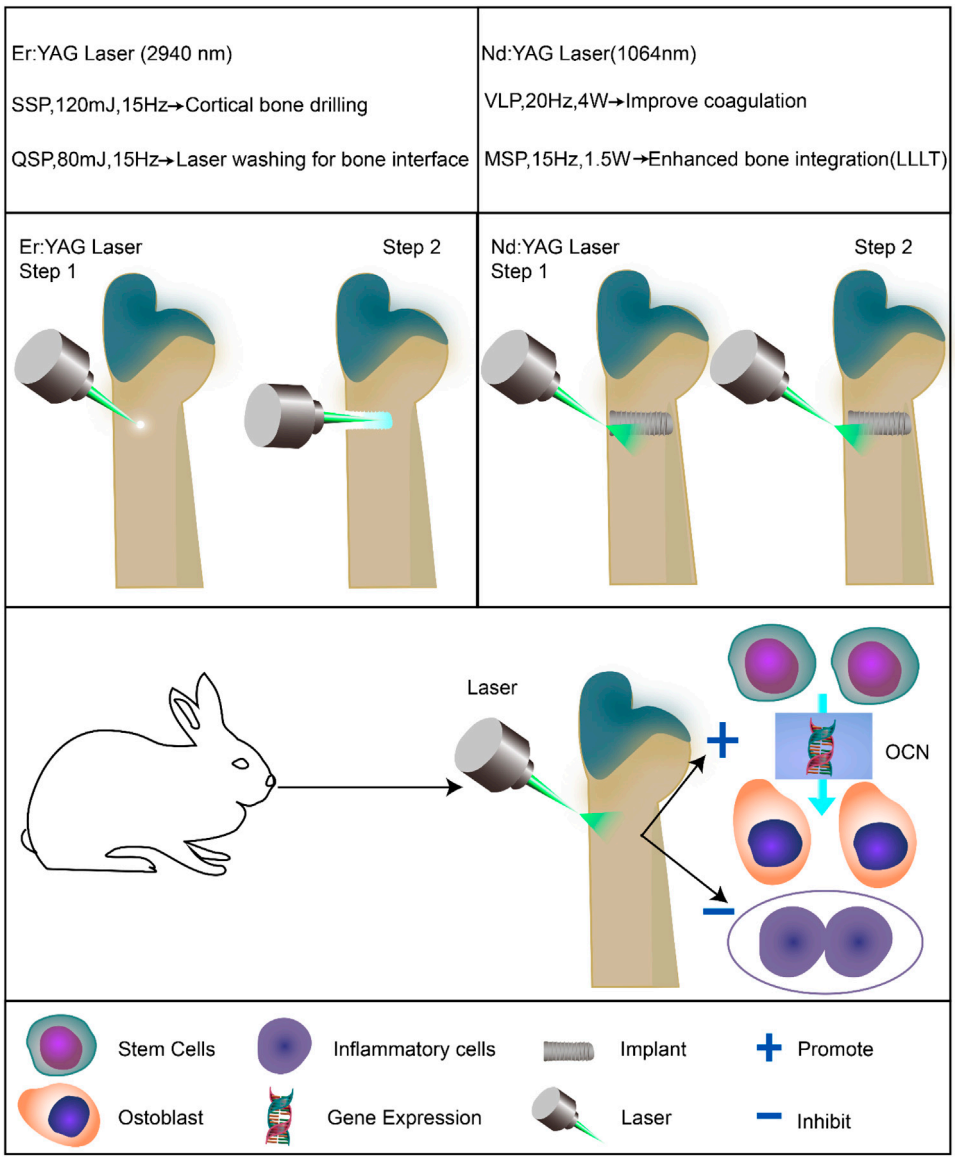

SCHEME 1 | Application of dual-wavelength laser-assisted implantation surgery and its effect on promoting osteoblast differentiation, which results in enhanced peri-implant bone integration.

3.4 Effect of Laser on Vascular Regeneration Around the Bone-Implant Interface

The rate of bone tissue repair around the implants might also be limited by the rate of neo-vascularization in the body (Santos and Reis, 2010). For instance, the vascular endothelial growth factor (VEGF) *in vivo* has a significant angiogenic effect, which can promote the accelerated recovery of the soft and hard tissues around the implant (Zavan et al., 2017).

As shown in **Figure 4B**, the percentage of VEGF-positive areas in each group gradually increased and was found to reach the peak at 14 days. It was observed that the percentage of positive areas in the Er laser group at the same time point was slightly larger than that in the Nd laser group. The percentage of VEGF-positive areas in the laser combined group was significantly better than in the other experimental groups and the control group, as shown in **Figure 4D** ($p < 0.001$).

4 CONCLUSION

In summary, the results of the present study clearly demonstrated the positive effects of early osseointegration of the dental implants upon the application of Er:YAG and Nd:YAG lasers. It was observed that a simultaneous combined application of the Er:YAG and Nd:YAG lasers can achieve the best results for both bone repair and tissue

reconstruction of the implants. These findings of the study thus provide a new clinical method for effectively promoting early bone integration of the implants. However, further clinical trials are needed to also evaluate the potential effects of dual-wavelength laser-assisted implant placement for bone repair.

DATA AVAILABILITY STATEMENT

The original contributions presented in the study are included in the article/**Supplementary Material**, further inquiries can be directed to the corresponding author.

ETHICS STATEMENT

The animal study was reviewed and approved by the Animal Care and Use Ethics Committee of Jilin University.

AUTHOR CONTRIBUTIONS

TZ and ML designed and carried out the experiments and analyzed experimental results. TZ wrote the manuscript. TZ and ML critically reviewed this manuscript and approved the final draft.

FUNDING

This study was supported by the Program of the Jilin Provincial Finance Department (2019SCZT039) and the Scientific Development Program of Jilin Province (20200403115SF).

SUPPLEMENTARY MATERIAL

The Supplementary Material for this article can be found online at: https://www.frontiersin.org/articles/10.3389/fmats.2022.828838/full#supplementary-material

REFERENCES

Albrektsson, T., and Wennerberg, A. (2019). On Osseointegration in Relation to Implant Surfaces. *Clin. Implant Dent. Relat. Res.* 21, 4–7. doi:10.1111/cid.12742

Ali, S., Salameh, A., Alammory, M., and Hamadah, O. (2020). Comparative Effect of Laser Treatment on Streptococcus Mutans Biofilm Adhered to Dental Implant Surface. *Rese. Jour. Pharm. Technol.* 13 (7), 3311–3316. doi:10.5958/0974-360x.2020.00587.9

Alsaadi, G., Quirynen, M., and van Steenberghe, D. (2006). The Importance of Implant Surface Characteristics in the Replacement of Failed Implants. *Int. J. Oral Maxillofac. Implants* 21 (2), 270–274.

Bouvet-Gerbettaz, S., Merigo, E., Rocca, J. P., Carle, G. F., and Rochet, N. (2009). Effects of Low-Level Laser Therapy on Proliferation and Differentiation of Murine Bone Marrow Cells into Osteoblasts and Osteoclasts. *Lasers Surg. Med.* 41 (4), 291–297. doi:10.1002/lsm.20759

Cekici, A., Maden, I., Yildiz, S., San, T., and Isik, G. (2013). Evaluation of Blood Cell Attachment on Er:Yag Laser Applied Root Surface Using Scanning Electron Microscopy. *Int. J. Med. Sci.* 10 (5), 560–566. doi:10.7150/ijms.5233

Chang, P. C., and Giannobile, W. V. (2012). Functional Assessment of Dental Implant Osseointegration. *Int. J. Periodontics Restor. Dent.* 32 (5), e147–53.

Crippa, R., Aiuto, R., Guardincerri, M., Peñarrocha Diago, M., and Angiero, F. (2020). Effect of Laser Radiation on Infected Sites for the Immediate Placement of Dental Implants. *Photobiomodulation, Photomed. laser Surg.* 38 (3), 186–192. doi:10.1089/photob.2019.4636

Evrard, V. A. C., Deprest, J. A., Van Ballaer, P., Lerut, T. E., Vandenberghe, K., and Brosens, I. A. (1996). Underwater Nd:YAG Laser Coagulation of Blood Vessels in a Rat Model. *Fetal Diagn Ther.* 11 (6), 422–426. doi:10.1159/000264359

Karoussis, I. K., Kyriakidou, K., Psarros, C., Lang, N. P., and Vrotsos, I. A. (2017). Nd:YAG Laser Radiation (1.064 Nm) Accelerates Differentiation of Osteoblasts to Osteocytes on Smooth and Rough Titanium Surfacesin Vitro. *Clin. Oral Impl. Res.* 28 (7), 785–790. doi:10.1111/clr.12882

Kazemzadeh-Narbat, M., Kindrachuk, J., Duan, K., Jenssen, H., Hancock, R. E. W., and Wang, R. (2010). Antimicrobial Peptides on Calcium Phosphate-Coated Titanium for the Prevention of Implant-Associated Infections. *Biomaterials* 31 (36), 9519–9526. doi:10.1016/j.biomaterials.2010.08.035

Kesler, G., Romanos, G., and Koren, R. (2006). Use of Er:YAG Laser to Improve Osseointegration of Titanium Alloy Implants-Aa Comparison of Bone Healing. *Int. J. Oral Maxillofac. Implants* 21 (3), 375–379. doi:10.1016/J.PROSDENT.2006.09.005

Kim, H., Choi, S.-H., Ryu, J.-J., Koh, S.-Y., Park, J.-H., and Lee, I.-S. (2008). The Biocompatibility of SLA-Treated Titanium Implants. *Biomed. Mat.* 3 (2), 025011. doi:10.1088/1748-6041/3/2/025011

Kim, I. S., Cho, T. H., Kim, K., Weber, F. E., and Hwang, S. J. (2010). High Power-Pulsed Nd:YAG Laser as a New Stimulus to Induce BMP-2 Expression in MC3T3-E1 Osteoblasts. *Lasers Surg. Med.* 42 (6), 510–518. doi:10.1002/lsm.20870

Kim, K., Kim, I. S., Cho, T. H., Seo, Y.-K., and Hwang, S. J. (2015). High-intensity Nd:YAG Laser Accelerates Bone Regeneration in Calvarial Defect Models. *J. Tissue Eng. Regen. Med.* 9 (8), 943–951. doi:10.1002/term.1845

Kreisler, M., Kohnen, W., Marinello, C., Götz, H., Duschner, H., Jansen, B., et al. (2002). Bactericidal Effect of the Er:YAG Laser on Dental Implant Surfaces: An *In Vitro* Study. *J. periodontology* 73 (11), 1292–1298. doi:10.1902/jop.2002.73.11.1292

Li, Q., Chen, Y., Dong, S., Liu, S., Zhang, X., Si, X., et al. (2017). Laser Irradiation Promotes the Proliferation of Mouse Pre-osteoblast Cell Line MC3T3-E1 through Hedgehog Signaling Pathway. *Lasers Med. Sci.* 32 (7), 1489–1496. doi:10.1007/s10103-017-2269-8

Mastrangelo, F., Quaresima, R., Canullo, L., Scarano, A., Muzio, L. L., and Piattelli, A. (2020). Effects of Novel Laser Dental Implant Microtopography on Human Osteoblast Proliferation and Bone Deposition. *Int. J. Oral Maxillofac. Implants* 35 (2), 320–329. doi:10.11607/jomi.7606

Matys, J., Flieger, R., Tenore, G., Grzech-Leśniak, K., Romeo, U., and Dominiak, M. (2018). Er:YAG Laser, Piezosurgery, and Surgical Drill for Bone Decortication during Orthodontic Mini-Implant Insertion: Primary Stability Analysis-An Animal Study. *Lasers Med. Sci.* 33 (3), 489–495. doi:10.1007/s10103-017-2381-9

Mellado-Valero, A., Buitrago-Vera, P., Sola-Ruiz, M., and Ferrer-Garcia, J. (2013). Decontamination of Dental Implant Surface in Peri-Implantitis Treatment: a Literature Review. *Med. Oral* 18 (6), e869–e876. doi:10.4317/medoral.19420

Mordon, S., Brisot, D., and Fournier, N. (2003). Using a ?non Uniform Pulse Sequence? Can Improve Selective Coagulation with a Nd:YAG Laser (1.06 ?m) Thanks to Met-Hemoglobin Absorption: A Clinical Study on Blue Leg Veins. *Lasers Surg. Med.* 32 (2), 160–170. doi:10.1002/lsm.10135

Nejem Wakim, R., Namour, M., Nguyen, H., Peremans, A., Zeinoun, T., Vanheusden, A., et al. (2018). Decontamination of Dental Implant Surfaces by the Er:YAG Laser Beam: A Comparative *In Vitro* Study of Various Protocols. *Dent. J.* 6 (4), 66. doi:10.3390/dj6040066

Niimi, H., Ohsugi, Y., Katagiri, S., Watanabe, K., Hatasa, M., Shimohira, T., et al. (2020). Effects of Low-Level Er:YAG Laser Irradiation on Proliferation and Calcification of Primary Osteoblast-like Cells Isolated from Rat Calvaria. *Front. Cell. Dev. Biol.* 8, 459. doi:10.3389/fcell.2020.00459

Ninomiya, T., Miyamoto, Y., Ito, T., Yamashita, A., Wakita, M., and Nishisaka, T. (2003). High-intensity Pulsed Laser Irradiation Accelerates Bone Formation in Metaphyseal Trabecular Bone in Rat Femur. *J. bone mineral metabolism* 21 (2), 67–73. doi:10.1007/s007740300011

Pantawane, M. V., Chipper, R. T., Robertson, W. B., Khan, R. J., Fick, D. P., and Dahotre, N. B. (2019). Evolution of Surface Morphology of Er: YAG Laser-Machined Human Bone. *Lasers Med. Sci.* 35, 1–9. doi:10.1007/s10103-019-02927-w

Pourzarandian, A., Watanabe, H., Aoki, A., Ichinose, S., Sasaki, K. M., Nitta, H., et al. (2004). Histological and TEM Examination of Early Stages of Bone Healing after Er:YAG Laser Irradiation. *Photomed. Laser Surg.* 22 (4), 342–350. doi:10.1089/pho.2004.22.342

Romanos, G. E., Motwani, S. V., Montanaro, N. J., Javed, F., and Delgado-Ruiz, R. (2019). Photothermal Effects of Defocused Initiated versus Noninitiated Diode Implant Irradiation. *Photobiomodulation, Photomed. laser Surg.* 37 (6), 356–361. doi:10.1089/photob.2018.4545

Safioti, L. M., Kotsakis, G. A., Pozhitkov, A. E., Chung, W. O., and Daubert, D. M. (2017). Increased Levels of Dissolved Titanium Are Associated with Peri-Implantitis - A Cross-Sectional Study. *J. periodontology* 88 (5), 436–442. doi:10.1902/jop.2016.160524

Santos, M. I., and Reis, R. L. (2010). Vascularization in Bone Tissue Engineering: Physiology, Current Strategies, Major Hurdles and Future Challenges. *Macromol. Biosci.* 10 (1), 12–27. doi:10.1002/mabi.200900107

Schwarz, F., Bieling, K., Nuesry, E., Sculean, A., and Becker, J. (2006). Clinical and Histological Healing Pattern of Peri-Implantitis Lesions Following Non-surgical Treatment with an Er:YAG Laser. *Lasers Surg. Med.* 38 (7), 663–671. doi:10.1002/lsm.20347

Sennerby, L., and Meredith, N. (2008). Implant Stability Measurements Using Resonance Frequency Analysis: Biological and Biomechanical Aspects and Clinical Implications. *Periodontol. 2000* 47 (1), 51–66. doi:10.1111/j.1600-0757.2008.00267.x

Trisi, P., Berardini, M., Falco, A., and Vulpiani, M. P. (2015). Effect of Temperature on the Dental Implant Osseointegration Development in Low-Density Bone. *Implant Dent.* 24 (1), 96–100. doi:10.1097/id.0000000000000204

Van Nimwegen, S. A., L'eplattenier, H. F., Rem, A. I., Van Der Lugt, J. J., and Kirpensteijn, J. (2008). Nd:YAG Surgical Laser Effects in Canine Prostate Tissue: Temperature and Damage Distribution. *Phys. Med. Biol.* 54 (1), 29–44. doi:10.1088/0031-9155/54/1/003

Vescovi, P., Meleti, M., Merigo, E., Manfredi, M., Fornaini, C., Guidotti, R., et al. (2013). Case Series of 589 Tooth Extractions in Patients under Bisphosphonates Therapy. Proposal of a Clinical Protocol Supported by Nd:YAG Low-Level Laser Therapy. *Med. Oral* 18 (4), e680–e685. doi:10.4317/medoral.18812

Yin, K., Zhu, R., Wang, S., and Zhao, R. C. (2017). Low-level Laser Effect on Proliferation, Migration, and Antiapoptosis of Mesenchymal Stem Cells. *Stem cells Dev.* 26 (10), 762–775. doi:10.1089/scd.2016.0332

Zavan, B., Ferroni, L., Gardin, C., Sivolella, S., Piattelli, A., and Mijiritsky, E. (2017). Release of VEGF from Dental Implant Improves Osteogenetic Process: Preliminary *In Vitro* Tests. *Materials* 10 (9), 1052. doi:10.3390/ma10091052

Conflict of Interest: The authors declare that the research was conducted in the absence of any commercial or financial relationships that could be construed as a potential conflict of interest.

Publisher's Note: All claims expressed in this article are solely those of the authors and do not necessarily represent those of their affiliated organizations, or those of the publisher, the editors, and the reviewers. Any product that may be evaluated in this article, or claim that may be made by its manufacturer, is not guaranteed or endorsed by the publisher.

frontiers | Frontiers in Bioengineering and Biotechnology

REVIEW
published: 15 June 2022
doi: 10.3389/fbioe.2022.920378

Bone Engineering Scaffolds With Exosomes: A Promising Strategy for Bone Defects Repair

Mingming Zhang[1,2†], Yi Li[1,2†], Taojin Feng[1,2], Ran Li[1,2], Zhongqi Wang[1,2], Licheng Zhang[1,2], Pengbin Yin[1,2*] and Peifu Tang[1,2]*

[1]Department of Orthopedics, Chinese PLA General Hospital, Beijing, China, [2]National Clinical Research Center for Orthopedics, Sports Medicine and Rehabilitation, Beijing, China

The treatment of bone defects is still an intractable clinical problem, despite the fact that numerous treatments are currently available. In recent decades, bone engineering scaffolds have become a promising tool to fill in the defect sites and remedy the deficiencies of bone grafts. By virtue of bone formation, vascular growth, and inflammation modulation, the combination of bone engineering scaffolds with cell-based and cell-free therapy is widely used in bone defect repair. As a key element of cell-free therapy, exosomes with bioactive molecules overcome the deficiencies of cell-based therapy and promote bone tissue regeneration via the potential of osteogenesis, angiogenesis, and inflammation modulation. Hence, this review aimed at overviewing the bone defect microenvironment and healing mechanism, summarizing current advances in bone engineering scaffolds and exosomes in bone defects to probe for future applications.

Keywords: bone tissue engineering, scaffold, bone defect, bone regeneration, cell-free therapy, exosome

OPEN ACCESS

Edited by:
Jianxun Ding,
Changchun Institute of Applied Chemistry (CAS), China

Reviewed by:
Xiaoxiao Cai,
Sichuan University, China
Lei Sui,
Tianjin Medical University, China

***Correspondence:**
Licheng Zhang
zhanglcheng218@126.com
Pengbin Yin
yinpengbin@gmail.com

[†]These authors have contributed equally to this work

Specialty section:
This article was submitted to Biomaterials, a section of the journal Frontiers in Bioengineering and Biotechnology

Received: *14 April 2022*
Accepted: *06 May 2022*
Published: *15 June 2022*

Citation:
Zhang M, Li Y, Feng T, Li R, Wang Z, Zhang L, Yin P and Tang P (2022) Bone Engineering Scaffolds With Exosomes: A Promising Strategy for Bone Defects Repair. Front. Bioeng. Biotechnol. 10:920378. doi: 10.3389/fbioe.2022.920378

INTRODUCTION

Bone is one of the important organs of the musculoskeletal system, which has load-bearing abilities and can perform locomotion as well as protect the internal organs. When suffering from high-energy trauma, nonunion, osteomyelitis, and tumor resection, loss of bone tissues will result in bone defects (Ma et al., 2021). Bone tissues are constantly remodeled and have better self-repair and regeneration ability, which allows the damaged bone tissues to fully recover to pre-injury integrity and mechanical properties (Majidinia et al., 2018). On the contrary, when the defects exceed the regeneration ability due to insufficient blood supply, local infection, drug side effects, malnutrition, etc., it will be difficult for large-sized bone defects to return to normal and seriously affect the patients' motor function and life quality, which necessitates extra clinical treatments (Nauth et al., 2018).

For bone defects, the aim of rehabilitation is to recover the mechanical and functional integrity of the structure, so bone grafts and bone graft substitutes become suitable choices, which are widely explored for a better therapeutic effect (Li S. et al., 2021). The current available grafts include autologous bone grafts, allogeneic bone grafts, heterogenous bone grafts, and synthetic grafts, as well as cell-based therapy and cell-free therapy such as stem cells, bioactive factors, and extracellular vesicles (Baldwin et al., 2019; Wang and Yeung, 2017). Whether autologous bones or allogeneic and heterogenous bones, all have limitations for the treatment of bone defects, which make it difficult to meet the clinical demands (Schmidt, 2021). Consequently, it is urgent to develop alternative synthetic graft substitutes such as bone engineering scaffolds. An ideal bone engineering scaffold should meet the following criteria: excellent biocompatibility, biodegradability, osteoconduction, osteoinduction, and osteogenesis (Turnbull et al., 2018). To date, inorganic components, natural polymers, synthetic

polymers, and metals, such as hydroxyapatite, collagen, poly(lactic acid), black phosphorus, and magnesium alloys, have been utilized in bone tissue engineering scaffolds (Amiryaghoubi et al., 2020; Bharadwaz and Jayasuriya, 2020; Zhang B. et al., 2021).

To fill in the bone defect sites and achieve desired therapeutic outcomes, bone engineering scaffolds are often integrated with stem cells, bioactive molecules, and extracellular vesicles (Brennan et al., 2020). Though bone engineering scaffolds provide stem cells with a platform for cell adhesion, migration, proliferation, and differentiation, the stem cells are also not ideal supplementary materials due to low survival rate, immunological rejection, tumorigenesis, and microthrombosis (Brennan et al., 2020). The extracellular vesicles, such as exosomes, have been proven to present parental cells and deliver bioactive molecules (e.g., nucleic acids, proteins, lipids, and metabolites), thus having the ability of osteogenesis, angiogenesis, and inflammation modulation, which promise to be desirable components combining with bone engineering scaffolds to repair bone defects (Huber et al., 2022; Li et al., 2020; Liu et al., 2018). The applications of exosomes and bone engineering scaffolds are still to be further researched, and there remain some problems to be solved. Therefore, this review will first focus on the bone defect microenvironment and bone healing mechanism. Based on this, we will discuss current treatments of bone defects and especially highlight bone engineering scaffolds and cell-free therapy. Then we will summarize the applications of exosomes and bone engineering scaffolds in bone defects. The potential problems and improvements to optimize exosome-integrated bone engineering scaffolds are also discussed.

BONE DEFECT MICROENVIRONMENT AND BONE HEALING MECHANISM

The bone tissue structures are composed of cortical bone and cancellous bone (Buck and Dumanian, 2012). The cortical bone, consisting of osteons, acts as a supporter due to high mechanical strength. The cancellous bone, a porous structure, is composed of trabecular bones and bone marrows, which is the harbor of hematopoiesis and bone metabolism (Buck and Dumanian, 2012). In general, bone tissues are constantly in the state of dynamic absorption and remodeling, making it possible for bone tissues to adapt to growth, development, and dynamic mechanic load (Oftadeh et al., 2015). However, the normal function of the bone depends on its structural and compositional integrity, and bone regeneration depends on an ideal microenvironment. For a critical-sized defect, a bone engineering scaffold will provide the damaged bones with mechanical support and a microenvironment favorable for regeneration (Roseti et al., 2017). Therefore, an in-depth understanding of the bone defect microenvironment will provide clues for developing a better bone engineering scaffold system and promoting bone regeneration.

Bone Defect Microenvironment

The bone defect microenvironment refers to the dynamic composition and cross-interactions of various cells and molecules in the bone defect sites (**Figure 1**). The microenvironment is extremely complex. On one hand, it spans the various stages of bone healing in terms of time, including the inflammation stage, bone formation stage, and remodeling stage (Oryan et al., 2015). On the other hand, its composition includes a wide variety of cells, such as mesenchymal stem cells (MSCs), hematopoietic stem cells, immune cells, endothelial cells, osteoblasts and osteoclasts, and various bioactive factors, such as receptor activator of nuclear factor-kappa B ligand (RANKL), platelet-derived growth factor (PDGF), bone morphogenetic proteins (BMPs), and interferon-gamma (IFN-γ), which engage in osteogenesis, angiogenesis, and inflammation modulation (Safari et al., 2021; Zhou et al., 2021). Detailed summaries and discussions have been reviewed by Zhu et al. (2021). In the meanwhile, a recent single-cell sequencing study revealed that skeletal muscle-derived mesenchymal progenitors also engage in bone repair, which will explain why adjacent tissues also matter (Julien et al., 2021). In addition, Zhang H. et al. (2021) suggest that B cells are key regulators of bone healing in the bone marrow microenvironment due to the opposite pattern between B cells and bone formation and resorption activities. Considering the fact that outcomes of bone defect healing are uncertain under the influence of different risk factors, such as age, nutritional status, and contamination degree (Nicholson et al., 2021), we suspected that differences in the bone defect microenvironment may contribute to it. Therefore, further research studies on the bone defect microenvironment will help to explain the bone healing mechanism and pathogenesis of nonunion and delayed union, providing novel ideas and more personalized strategies for clinical practice.

Bone Healing Mechanism

The defects sites initiate a cellular cascade to repair injury and promote regeneration shortly after the occurrence of bone defects. These cells participate in several continuous events, including hematoma formation, inflammatory reaction, fibrous callus formation, intramembranous ossification, endochondral ossification, and bone remodeling, which accompany an orderly cascade of anabolism and catabolism (Li et al., 2019). Specifically, blood clots in the damaged areas and immune cells migrate to remove the necrotic components. Next, recruited fibroblasts, osteoprogenitor cells, and MSCs proliferate and differentiate to form a fibrous tissue, followed by intramembranous and endochondral ossification. In the final stage, the new bone tissues are constantly absorbed and remodeled under mechanical forces, forming an orderly bone structure and returning to normal function (Kalfas, 2001; Zhu et al., 2021). Intramembranous ossification means that MSCs migrate and proliferate to form condensation, differentiate into osteoblasts, and secrete collagen, followed by vascular ingrowth and cortical bone and cancellous bone formation (Percival and Richtsmeier, 2013). Endochondral ossification means that MSCs differentiate into chondrocytes and secrete collagen matrix, followed by vascular ingrowth and cartilage degradation, finally forming the primary ossification center and secondary ossification center, and forming mature bone structure (Mackie et al.,

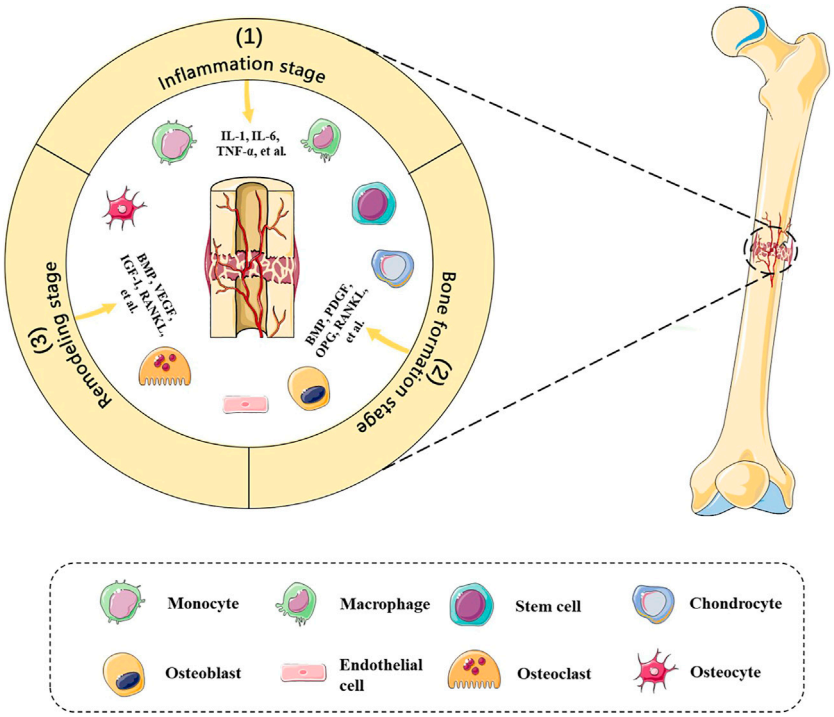

FIGURE 1 | Bone defect microenvironment. Dynamic composition and cross-interactions of various cells and molecules are involved in the bone defect microenvironment. The bone healing stages include 1) inflammation stage, 2) bone formation stage, and 3) remodeling stage, which entails immune cells, chondrocytes, stem cells, osteoblasts, etc., and RANKL, PDGF, BMPs, TNF-α, etc., in a spatiotemporal manner.

2011). In addition, many other cytokines are also involved in the process of bone healing (Zhu et al., 2021). Although bone tissues have the remarkable ability of healing, bone defects still do not return to normal when the defect ranges exceed the critical-sized bone defect, which means loss of a length exceeding 2–2.5 times the diameter of the damaged bone (Wiese and Pape, 2010). This will overwhelm the ability of bone regeneration because of mechanical instability and biological disadvantage, indicated by poor vasculature, bone nonunion, and pseudarthrosis, which requires clinical treatments to support mechanical stability and a suitable microenvironment so as to achieve functional reconstruction (Elliott et al., 2016). Consequently, the in-depth understanding of bone biology, bone defect microenvironment, and bone healing mechanisms will provide references for the design and application of bone engineering scaffolds with bioactive factors.

CURRENT TREATMENTS OF BONE DEFECTS

The interventions of large segmental bone defects usually require repair and reconstruction techniques (Nauth et al., 2018). However, the treatments of bone defects remain a striking challenge to date because of the shortage of autologous bone tissues and the lack of ideal graft materials (Wang and Yeung, 2017). With the development of materials science and engineering technology, the combination of advanced manufacturing technology with ideal materials, bone-implant interface modification, and the supplement of bioactive factors provides a broad space for the treatment of bone defects (Tovar et al., 2018; Turnbull et al., 2018).

Bone Graft Reconstruction

Bone grafts include autologous bone grafts, allogeneic bone grafts, and heterogenous bone grafts, all of which have different characteristics (Shang et al., 2021). Autologous bone grafts have fresh cortical and cancellous bone tissues containing viable osteoblasts, osteocytes, MSCs, and growth factors, thus possessing good osteoconductive, osteoinductive, and osteogenic properties. Owing to the maintenance of osteogenic potential and basis, autologous bone grafts are considered as the gold standard in the treatment of bone defects (Baldwin et al., 2019). However, some shortcomings restrict its application, for example, limited availability, donor site infection, hematoma, and pain (Schmidt, 2021). Allogeneic bone grafts refer to bone tissues from other individuals, which are immunogenic and have the risk of the spread of potential pathogens (Wang and Yeung, 2017). Therefore, processed and modified allogeneic bones overcome their own shortcomings and become the most available grafts, considered the best alternative to autografts. Demineralized bone matrix (DBM) is a highly processed allogeneic graft, which is often used to fill in bone defects (Hao et al., 2022). Similarly, heterogenous bone grafts face the same concerns, such as

TABLE 1 | Brief comparison of bone engineering scaffold materials.

Material type	Example	Advantage	Disadvantage	References
Inorganic components	Hydroxyapatite, CaP cements, and ceramics	High compressive strength and low ductility	Brittleness	Gao et al. (2014)
Natural polymers	Collagen and chitosan	Good biocompatibility, osteoconductivity, and low immunogenicity	Degradation rate difficult to control and low mechanical stability	Ebhodaghe, (2021)
Synthetic polymers	Poly(lactic-co-glycolic acid) and poly(lactic acid)	Controlled degradation rate, the possibility to design or tune bone mechanical properties, plasticity, and the potential to deliver soluble molecules	Lower ability to interact with cells	Amiryaghoubi et al. (2020)
Metals	Magnesium alloys and titanium alloys	High strength and modulus, good biocompatibility	Degradation and hydrogen generation	Zhang et al. (2021c)
Ideal scaffold	Biocompatible, non-toxic, bioresorbable, biodegradable, non-immunogenic, bioactive, biomimetic, customized shape, high porosity, and mechanical properties			Roseti et al. (2017)

immunogenicity and disease transference (Amiryaghoubi et al., 2020). In general, due to the aforementioned drawbacks, bone grafts may not be the optimal ones, so it is necessary to design and manufacture promising bone engineering grafts with excellent osteoconduction, osteoinduction, and osteogenesis.

Bone Graft Substitute Reconstruction

The development of bone graft substitutes aimed at simulating natural bone tissues to produce bone scaffolds with excellent capacity for osteoconduction, osteoinduction, osteogenesis, and angiogenesis (Tan et al., 2021). At present, a variety of alternative materials have been utilized for scaffold engineering, including inorganic components (e.g., hydroxyapatite, CaP cement, and ceramics), natural polymers (e.g., collagen, chitosan, alginate, and hyaluronic acid), synthetic polymers (e.g., poly(lactic-co-glycolic acid), poly(lactic acid), and poly(caprolactone)), and metals (e.g., magnesium and magnesium alloys, Zn and Zn alloys, and titanium and titanium alloys) (**Table 1**) (Amiryaghoubi et al., 2020). The summaries of types and manufacturing technologies have been reviewed recently (Bharadwaz and Jayasuriya, 2020; Wang and Yeung, 2017). In addition, new engineering techniques are used to solve practical application problems, for example, a microfluidic 3D printing strategy fabricates photothermal responsive channeled scaffolds, which facilitate vascular ingrowth and bone regeneration (Wang et al., 2021). In general, advances in materials science and engineering technology gradually make it possible for more bone engineering scaffolds to be used in clinical practice.

Masquelet's Induced Membrane Technique

Masquelet's induced membrane technique is a two-stage surgical procedure to treat segmental bone defects, which was first reported in the mid-1980s (Alford et al., 2021). This procedure combines surgical techniques, bone healing mechanisms, and bone grafts, significantly promoting bone defect repair (Nauth et al., 2018). This procedure is divided into two stages. The first stage is to remove damaged tissue, implant a bone cement spacer, and install a fixation device, followed by waiting for formation of the surrounding foreign-body membrane. The secondary stage is to remove the spacer and fill the cavity with bone grafts or bone graft substitutes, followed by several months of healing (Alford et al., 2021). Though this procedure is promising, there are some problems to be solved, for example, time consumption, the lack of standard surgical details, and the shortage of evidence to supplement bioactive factors and optimize individual outcomes (Morelli et al., 2016).

Cell-Based Therapy and Cell-Free Therapy

Cell-based and cell-free scaffolds often combine bone engineering scaffolds with cells, cytokines, nucleic acids, or extracellular vesicles, which enhance the osteoinductive and osteogenic capacity of the scaffolds (Li et al., 2019). With multilineage differentiation potential and intrinsic properties, MSCs are the most promising stem cells being applied in bone regeneration medicine to promote wound healing, osteogenesis, and inflammation modulation (Chew et al., 2019). The advancing applications of MSCs in bone regeneration have been reviewed by Shang et al. (2021). Though relevant basic and clinical translational research studies are being carried out vigorously, cell-based therapy has some limitations, such as low viability, immune rejection reaction, tumorigenesis, and microthrombosis (Watanabe et al., 2021). Alternative options are based on the secretion and paracrine signaling of MSCs, that is, cell-free therapy; for example, growth factors, cytokines, nucleic acids, and extracellular vesicles (Zhang et al., 2022; Swanson et al., 2020). The types, time, and dosage of growth factors and cytokines supplementing scaffolds are important parameters, which depend on the stages of bone healing because the biomolecules' interaction is pretty intricate in a spatiotemporal manner (Safari et al., 2021). More efforts have been made to achieve controlled release of cytokines, which deserves further exploration. Moreover, as an important gene regulator at the post-transcriptional level, nucleic acids are supplemented to regulate gene expression and promote osteogenesis, which usually requires a carrier to transport them into the cells (Li Z. et al., 2021). In addition, extracellular vesicles possess the inherent capacity to carry biomolecules, thus mediating molecule delivery to promote regeneration (Ramis, 2020). Extracellular vesicles, including exosomes, apoptotic bodies, and microvesicles, particularly exosomes, have been reported to recapitulate the advantageous properties of stem cells and enhance the

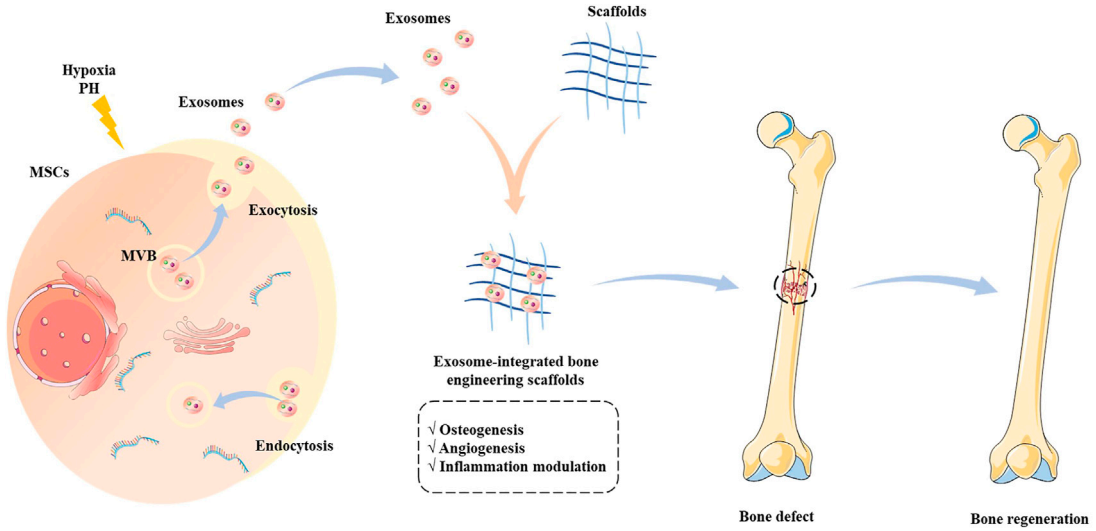

FIGURE 2 | Schematic illustration of the source of exosomes and the application of exosome-integrated bone engineering scaffolds. The exosomes originate from multivesicular bodies, which engage in intercellular communications and deliver biomolecules to regulate the biological functions. The exosome-integrated bone engineering scaffolds possess the capacity for osteogenesis, angiogenesis, and inflammation modulation, which promote bone regeneration and repair bone defects.

effects of bone engineering scaffolds (Pishavar et al., 2021; Qin et al., 2016). The advancing applications of exosomes and scaffolds will be elaborated in the next section.

APPLICATIONS OF BONE ENGINEERING SCAFFOLDS WITH EXOSOMES IN BONE DEFECTS

The exosome-integrated bone engineering scaffolds synergize mechanical support and the ability of osteoconductivity, osteoinduction, and osteogenesis, which have been widely explored in bone defect animal models and achieve good therapeutic effects (**Figure 2**) (Wei et al., 2019). In recent years, the osteogenic property of bone engineering scaffolds has been continuously explored, and the investigation of angiogenesis has also been widely conducted (Turnbull et al., 2018).

Exosome Overview

Exosomes, originating from multivesicular bodies, are widely found in biofluids and cell mediums, which range from 30 to 150 nm in diameter (Liu A. et al., 2021). They carry nucleic acids, proteins, lipids, and metabolites, playing key roles in intercellular communication (Lu et al., 2019). It has been reported that exosomes have diagnostic and therapeutic potential in various diseases, including bone defects (Al-Sowayan et al., 2020; Furuta et al., 2016). Compared with cell-based therapy, the sources of exosomes applied in bone defects are more widespread, which is not limited to stem cells. In addition, exosome-based therapy has several benefits, such as no immunogenicity, similar functional properties to stem cells, and no risks of tumorigenesis and engineering modification (Fan et al., 2020).

Exosomes in Osteogenesis, Angiogenesis, and Inflammation Modulation in Bone Defect Microenvironment

Nucleic acids, proteins, lipids, and metabolites in exosomes engage in intercellular communication and impact the recipient cells to regulate biological functions (Escude et al., 2021). Relevant research studies show that exosomes are engulfed by surrounding target cells, such as osteoprogenitors, osteoblasts, endothelial cells, and immune cells, in the bone defect microenvironment, thereby widely participating in osteogenesis, angiogenesis, and inflammation modulation.

Exosomes and Osteogenesis

In bone regeneration, the exosomes with osteogenic potential are able to promote MSCs to increase the expression of osteogenic factors and osteogenesis-related proteins, such as RUNX2, COL1A1, OPN, and ALP (Narayanan et al., 2016). Bioactive molecules in exosomes are key mediators of osteogenesis, and several reports show that microRNA (miRNA) is an important post-transcript regulator to modulate the expression of osteogenic-related genes(Liu W.-z. et al., 2021; Yin et al., 2021). For example, the RNA-sequencing of osteogenic exosomes from human MSCs suggests that exosomes include upregulated osteogenic miRNAs (Hsa-miR-146a-5p, Hsa-miR-503-5p, Hsa-miR-483-3p, and Hsa-miR-129-5p) or downregulated anti-osteogenic miRNAs (Hsa-miR-32-5p, Hsa-miR-133a-3p, and Hsa-miR-204-5p), which activate the PI3K/Akt and MAPK signaling pathways (Zhai et al., 2020). In addition, MSC-released exosomal miR-1260a (Wu et al., 2021); miR-335 (Cao et al., 2021); miR-140 and miR-375 (Chen et al., 2019); miR-26a, miR-199a, miR-21, and miR-23a-3p (Hu et al., 2020); let-7a-5p, let-7c-5p, miR-328a-5p, and miR-31a-5p (Liu A. et al., 2021); and miR-150-5p (Jing et al., 2022) have been

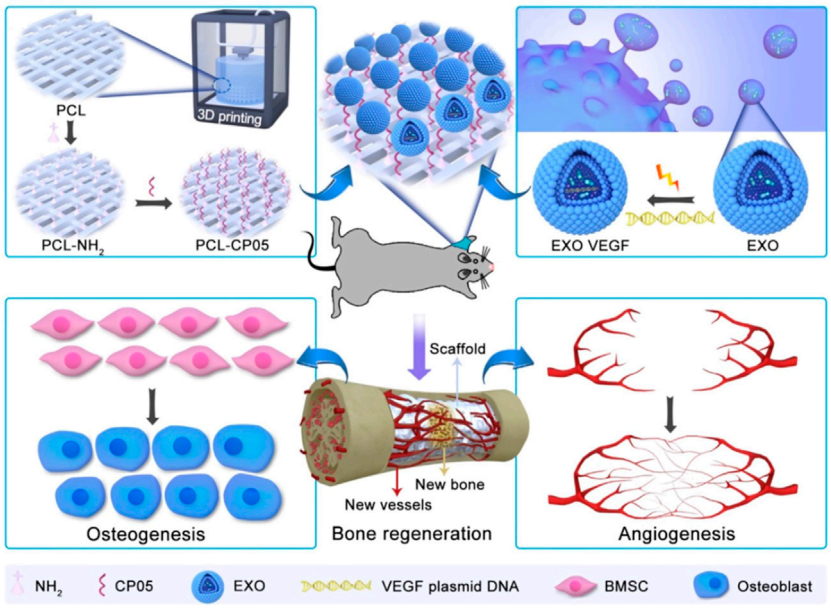

FIGURE 3 | The combination of engineering exosomes endowed with VEGF plasmid with 3D-printed scaffolds promotes bone regeneration via enhancing osteogenesis and angiogenesis (Zha et al., 2021).

reported to promote osteogenesis. The exosomes promoting osteogenesis involve many pathways, such as BMP/Smad, Wnt/β-catenin, PTEN/PI3K/Akt, and Hippo signaling pathways (Cao et al., 2021; Cui et al., 2016; Hu et al., 2020; Zhang et al., 2016). There are other cell-derived exosomes promoting or inhibiting osteogenesis. For example, Li et al. (2016) showed that osteoclast-derived exosomal miR-214-3p inhibits osteogenesis and reduces bone formation. Weilner et al. (2016) reported that osteoblast-derived exosomal galectin-3 levels are positively correlated with osteoinductive potential. Qi et al. (2016) reported that human-induced pluripotent stem cell–derived MSC-released exosomes significantly promote osteogenesis and angiogenesis. Li et al. (2018) showed that human adipose stem cell–derived exosomes promote the proliferation and differentiation of MSCs. Swanson et al. (2020) found that human dental pulp stem cell–derived exosomes facilitate MSC differentiation and mineralization. Wu et al. (2020) reported that Schwann cell–derived exosomes can promote the proliferation and differentiation of MSCs. Cao et al. (2021) found that mature dendritic cell–derived exosomes enhance osteogenic differentiation of MSCs. Moreover, some studies have focused on regulating exosomes to increase their osteogenic activity, such as aptamer-functionalized exosomes, static magnetic field–treated exosomes, exosomes endowed with plasmids, genetic engineered exosomes, hypoxic environment-treated exosomes, hydrogel-assisted 3D cultured exosomes, and exosomes with fusion peptide (Li et al., 2022; Luo et al., 2019; Ma et al., 2022; Shen et al., 2022; Wu et al., 2021; Yu et al., 2022; Zha et al., 2021). In general, the treatment of exosomes increases the osteogenic ability in the bone defect microenvironment, which is beneficial for bone defect repair.

Exosomes and Angiogenesis

Adequate blood supply is an important basis for successful bone regeneration. The effects of angiogenesis mediated by exosomes have been reported, indicated by the increased expression of angiogenesis factors, tube formation, endothelial cell proliferation, and migration (Zhang J. et al., 2021). For example, Wu et al. (2022) suggested that MSC-derived exosomal miR-21 target SPRY2, promotes angiogenesis. Another report shows that miR-21 promotes angiogenesis by the miR-21/NOTCH1/DLL4 signaling axis (Zhang Y. et al., 2021). Wu et al. (2021) found that MSC-derived exosomal miR-1260a enhanced angiogenesis via the inhibition of COL4A2. Sahoo et al. (2011) showed that MSC-derived exosomes increased endothelial cell viability. Jing et al. (2022) reported that stem cells from apical papilla-derived exosomes promote angiogenesis by miR-126-5p, indicated by increased expression of VEGF and ANG-1. In addition, hypoxic condition–treated cell-derived exosomes increase the tube formation (Liu et al., 2020). Zha et al. (2021) also reported that progenitor cell–derived exosomes endowed with VEGF plasmids release the VEGF gene to promote angiogenesis (**Figure 3**).

Exosomes and Inflammation Modulation

Inflammatory cells and immune cells are important components of the bone defect microenvironment, and a moderate inflammatory response is imperative for bone defect repair (Lin et al., 2022). It has been reported that exosomes play a role in inflammation modulation. For example, MSC-derived exosomes can promote macrophage polarization toward the M2 phenotype and inhibit the inflammatory response, indicated by the reduced gene and

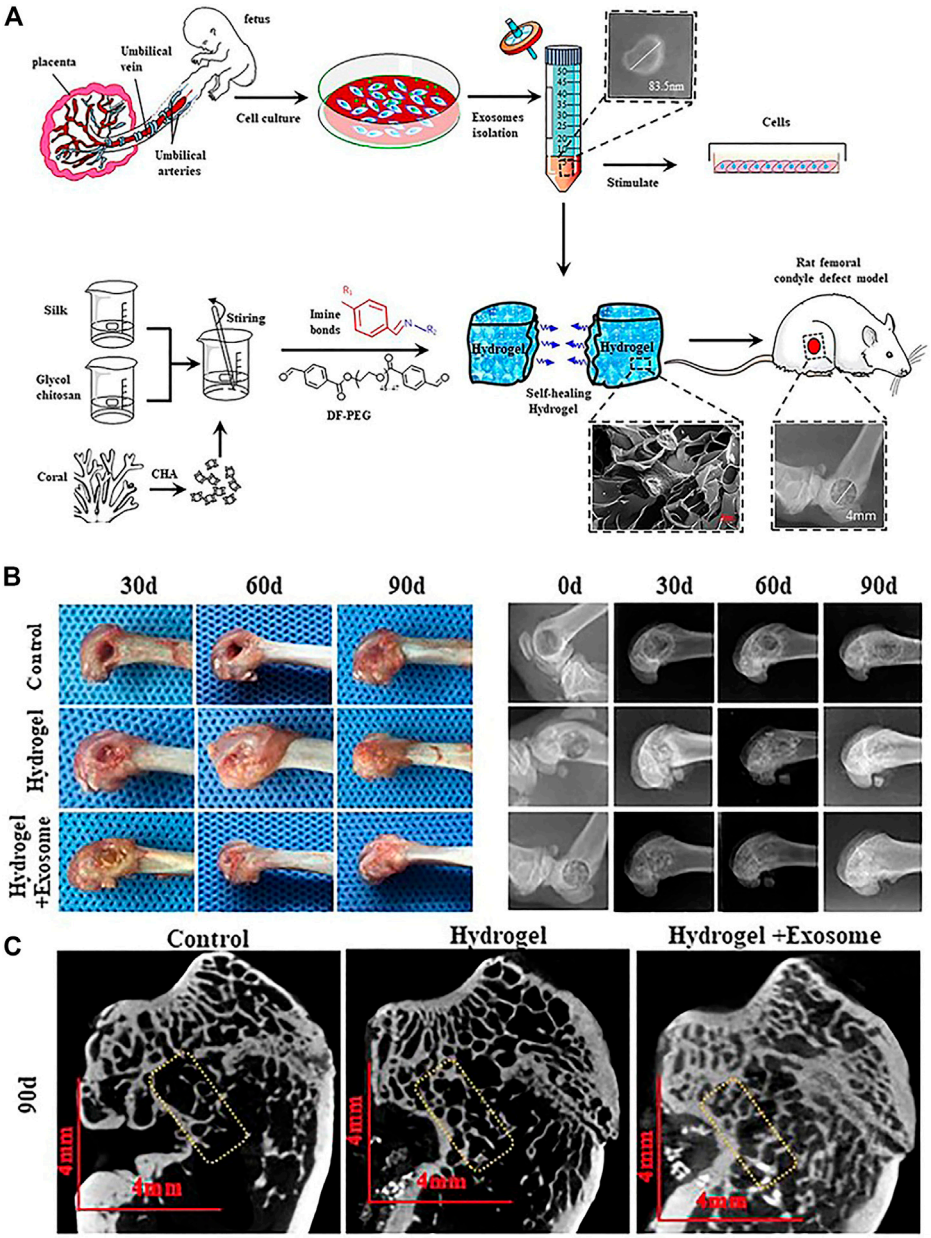

FIGURE 4 | Self-healing hydrogel containing exosomes (Wang L. et al., 2020). **(A)** Schematic illustration of the isolation and characterization of exosomes and preparation of self-healing hydrogel for applying in rat femoral condyle defect. **(B)** Gross observation and X-ray evaluation of the effects of self-healing hydrogel containing exosomes. **(C)** Micro-CT evaluation of the effects of self-healing hydrogel containing exosomes.

protein expression of inflammatory cytokines, such as IL-6 and TNF-α (Guan et al., 2022; Jiang et al., 2021; Lu et al., 2021; Wang X. et al., 2020). Research shows that MSC-derived exosomes promote macrophage M2 polarization via the NF-κB pathway (Fan et al., 2021). In addition, Lin et al. (2022) showed that HUVEC-derived exosomes overexpressing PD-L1 bind to PD-1 on the T-cell surface, which suppresses the activation of T cells and promotes MSCs toward osteogenic differentiation because of the inhibition of overactive inflammation. Consequently, exosomes are important regulators of immune response and bone regeneration in the bone defect microenvironment.

To sum up, the role exosomes play in bone defect repair is multifaceted, including osteogenesis, angiogenesis, and inflammation regulation, which supplement each other. Specifically, the effects of exosomes in the bone defect microenvironment are due to 1) promotion of osteogenic differentiation of the target cells, 2) promotion of angiogenesis for providing an optimal bone regeneration niche, and 3) inflammation modulation for maintaining a moderate immune

TABLE 2 | Summary of the applications of exosome-integrated bone engineering scaffolds in bone defects.

Source of Exosomes	Isolation method	Scaffold	*In vivo* model	Effect of exosome-integrated bone engineering scaffolds	References
Human umbilical cord MSCs	Ultracentrifugation	Coralline hydroxyapatite (CHA)/silk fibroin (SF)/glycol chitosan (GCS)/difunctionalized polyethylene glycol (DF-PEG) self-healing hydrogel	Femoral condyle defect	Pro-bone regeneration and pro-angiogenic activities *in vitro* and *in vivo*	Wang et al. (2020a)
Human umbilical cord MSCs	Ultracentrifugation	Injectable hydroxyapatite-embedded *in situ* cross-linked hyaluronic acid-alginate (HA-ALG) hydrogel	Calvarial defect	Pro-bone regeneration activities *in vitro* and *in vivo*	Yang et al. (2020)
Bone marrow stem cells	Ultracentrifugation	Tannic acid–modified sulfonated polyetheretherketone	Femoral condyle defect	Inflammation modulation and pro-bone regeneration activities *in vitro* and *in vivo*	Fan et al. (2021)
Human adipose-derived stem cells	Ultracentrifugation	Polydopamine-coating PLGA (PLGA/pDA) scaffolds	Calvarial defect	Pro-bone regeneration activities *in vitro* and *in vivo*	Li et al. (2018)
MSCs derived from human-induced pluripotent stem cells	Ultracentrifugation	Tricalcium phosphate scaffolds	Calvarial defect	Pro-bone regeneration and pro-angiogenic activities *in vitro* and *in vivo*	Qi et al. (2016)
MSCs and preosteoblasts	ExoEasy kit	Calcium sulfate-nano-hydroxyapatite nanocement bone filler	Tibia defect	Pro-bone regeneration activities *in vitro* and *in vivo*	Teotia et al. (2021)
MSCs	Ultracentrifugation	Mesoporous bioactive glass	Calvarial defect	Pro-bone regeneration activities *in vitro* and *in vivo*	Liu et al. (2021a)
Schwann cells	Ultracentrifugation	Porous Ti6Al4V scaffolds	Femoral condyle defect	Pro-bone regeneration activities *in vitro* and *in vivo*	Wu et al. (2020)
Human dental pulp stem cells	Ultracentrifugation	Poly(lactic-co-glycolic acid) and poly(ethylene glycol) triblock copolymer microspheres	Calvarial defect	Pro-bone regeneration activities *in vitro* and *in vivo*	Swanson et al. (2020)
MSCs	ExoQuick-TC kit	3D-printed titanium alloy scaffolds	Radial bone defect	Pro-bone regeneration activities *in vitro* and *in vivo*	Zhai et al. (2020)
Chondrogenic progenitor cell line, ATDC5	Ultracentrifugation	3D-printed polycaprolactone scaffolds	Radial bone defect	Pro-bone regeneration and pro-angiogenic activities *in vitro* and *in vivo*	Zha et al. (2021)
Human adipose mesenchymal stem cells	Ultracentrifugation	Hydrogel	Calvarial defect	Pro-bone regeneration activities *in vitro* and *in vivo*	Chen et al. (2019)
Bone marrow stem cells	Ultracentrifugation	Injectable thermo-sensitive hydrogels	Calvarial defect	Pro-bone regeneration activities *in vitro* and *in vivo*	Ma et al. (2022)
Umbilical MSCs	Ultracentrifugation	Hyaluronic acid hydrogel	Calvarial defect	Pro-bone regeneration and pro-angiogenic activities *in vitro* and *in vivo*	Zhang et al. (2021d)
Mature dendritic cells	Ultracentrifugation	Carboxymethyl cellulose-based hydrogel	Femoral bone defect	Pro-bone regeneration activities *in vitro* and *in vivo*	Cao et al. (2021)
MSCs derived from human-induced pluripotent stem cells	Ultracentrifugation	Tricalcium phosphate scaffolds	Calvarial defect	Pro-bone regeneration activities *in vitro* and *in vivo*	Zhang et al. (2016)

response. Thus, the exosome is a kind of promising cell-free therapeutic material to repair bone defects.

Exosome-Integrated Bone Engineering Scaffolds *In Vivo* Bone Defects

The treatment of exosome-integrated bone engineering scaffolds provides not only mechanical support for bone defects but a suitable microenvironment for bone regeneration. The research studies on bone engineering scaffolds for bone defects primarily focus on the components, characteristics, interface modification, and the release of bioactive factors (Gandolfi et al., 2020; Nikhil and Kumar, 2022; Zhang et al., 2018). Although most of the scaffolds have been proven to possess the definite potential of osteogenesis, the supplement of exosomes can enhance their performance (**Figure 4**) (Tan et al., 2020; Wang et al., 2020a). Exosome-integrated bone engineering scaffolds can promote osteogenesis, angiogenesis, and inflammation modulation, which have been applied in various bone defect models, such as critical-sized mouse calvarial defects, mandibular bone defects, femoral condyle defects, and tibia defects in mice, rats, and sheep (Jia et al., 2021; Luo et al., 2019). The details of applications of exosome-integrated bone engineering scaffolds have been summarized in **Table 2**. In addition, exosome-integrated bone engineering scaffolds promote the recruitment and migration of resident MSCs, the activation of local potential, and the homing ability to the injured sites and newly formed bone tissue sites (Re et al., 2021). For example, Schwann cell–derived exosomes with porous titanium alloy can improve the effects of scaffolds in bone repair (Wu et al., 2020). Ma et al. (2022) reported that hydrogels combined with

exosomes and fusion peptides can enhance the therapeutic effect and the retention of exosomes. Yang et al. (2020) revealed that MSC-derived exosomes with injectable hydroxyapatite-embedded *in situ* cross-linked hyaluronic acid-alginate hydrogel can significantly enhance bone regeneration and retain the exosomes at the defect sites. Although bone engineering scaffolds with exosomes show great potential, there are still some questions to be answered. First, the contents and their functions in exosomes have not yet been illustrated completely, and the effectors of exosomes of different parent sources for bone defect repair are different. Second, the scaffold materials with better osteoconductivity, osteoinduction, osteogenesis, and mechanical support need to be improved. Lastly, the strategies of engineering exosomes, interface modifications, and controlled release in a spatiotemporal manner need to be designed and optimized. To sum up, the progress in materials and engineering technology drives the bone graft substitutes to solve the clinical problems, pointing out the direction of future research studies.

CONCLUSION

The treatment of bone defects is an intractable clinical problem and has attracted great attention around the world. In this review, the current treatments of bone defects and applications of bone engineering scaffolds with exosomes in bone defects are summarized. In addition, the bone defect microenvironment and bone healing mechanism are discussed. In bone defect repair, the supplement of exosomes enhances the effects of bone engineering scaffolds, in which miRNA is one of the important regulators. With the recognition of exosome contents, future patterns of specific miRNA or bioactive molecules with carriers will promote bone regeneration more precisely. Thus, a big step forward would be taken toward the successful treatment of bone defects, delayed union, and non-union.

AUTHOR CONTRIBUTIONS

LZ, PY, and PT made major contributions to the conception of the work. MZ and YL drafted the manuscript. TF, RL, and ZW participated in the discussion, revised the manuscript, and drew the figures.

FUNDING

This work was supported by the National Natural Science Foundation of China (Nos. 81972115 and 82002330) and Young Elite Scientist Sponsorship Program by the China Association for Science and Technology (No. 2020-JCJQ-QT-033).

ACKNOWLEDGMENTS

The original elements used in the figures are from Servier Medical Art (http://smart.servier.com/).

REFERENCES

Al-Sowayan, B., Alammari, F., and Alshareeda, A. (2020). Preparing the Bone Tissue Regeneration Ground by Exosomes: From Diagnosis to Therapy. *Molecules* 25 (18), 4205. doi:10.3390/molecules25184205

Alford, A. I., Nicolaou, D., Hake, M., and McBride-Gagyi, S. (2021). Masquelet's Induced Membrane Technique: Review of Current Concepts and Future Directions. *J. Orthop. Res.* 39 (4), 707–718. doi:10.1002/jor.24978

Amiryaghoubi, N., Fathi, M., Pesyan, N. N., Samiei, M., Barar, J., and Omidi, Y. (2020). Bioactive Polymeric Scaffolds for Osteogenic Repair and Bone Regenerative Medicine. *Med. Res. Rev.* 40 (5), 1833–1870. doi:10.1002/med.21672

Baldwin, P., Li, D. J., Auston, D. A., Mir, H. S., Yoon, R. S., and Koval, K. J. (2019). Autograft, Allograft, and Bone Graft Substitutes: Clinical Evidence and Indications for Use in the Setting of Orthopaedic Trauma Surgery. *J. Orthop. Trauma.* 33 (4), 203–213. doi:10.1097/BOT.0000000000001420

Bharadwaz, A., and Jayasuriya, A. C. (2020). Recent Trends in the Application of Widely Used Natural and Synthetic Polymer Nanocomposites in Bone Tissue Regeneration. *Mater. Sci. Eng. C* 110, 110698. doi:10.1016/j.msec.2020.110698

Brennan, M. Á., Layrolle, P., and Mooney, D. J. (2020). Biomaterials Functionalized with MSC Secreted Extracellular Vesicles and Soluble Factors for Tissue Regeneration. *Adv. Funct. Mat.* 30 (37), 1909125. doi:10.1002/adfm.201909125

Buck, D. W., and Dumanian, G. A. (2012). Bone Biology and Physiology. *Plastic Reconstr. Surg.* 129 (6), 1314–1320. doi:10.1097/PRS.0b013e31824eca94

Cao, Z., Wu, Y., Yu, L., Zou, L., Yang, L., Lin, S., et al. (2021). Exosomal miR-335 Derived from Mature Dendritic Cells Enhanced Mesenchymal Stem Cell-Mediated Bone Regeneration of Bone Defects in Athymic Rats. *Mol. Med.* 27 (1). doi:10.1186/s10020-021-00268-5

Chen, S., Tang, Y., Liu, Y., Zhang, P., Lv, L., Zhang, X., et al. (2019). Exosomes Derived from miR-375-overexpressing Human Adipose Mesenchymal Stem Cells Promote Bone Regeneration. *Cell Prolif.* 52 (5). doi:10.1111/cpr.12669

Chew, J. R. J., Chuah, S. J., Teo, K. Y. W., Zhang, S., Lai, R. C., Fu, J. H., et al. (2019). Mesenchymal Stem Cell Exosomes Enhance Periodontal Ligament Cell Functions and Promote Periodontal Regeneration. *Acta Biomater.* 89, 252–264. doi:10.1016/j.actbio.2019.03.021

Cui, Y., Luan, J., Li, H., Zhou, X., and Han, J. (2016). Exosomes Derived from Mineralizing Osteoblasts Promote ST2 Cell Osteogenic Differentiation by Alteration of microRNA Expression. *FEBS Lett.* 590 (1), 185–192. doi:10.1002/1873-3468.12024

Ebhodaghe, S. O. (2021). Natural Polymeric Scaffolds for Tissue Engineering Applications. *J. Biomaterials Sci. Polym. Ed.* 32 (16), 2144–2194. doi:10.1080/09205063.2021.1958185

Elliott, D. S., Newman, K. J. H., Forward, D. P., Hahn, D. M., Ollivere, B., Kojima, K., et al. (2016). A Unified Theory of Bone Healing and Nonunion. *Bone & Jt. J.* 98-B (7), 884–891. doi:10.1302/0301-620X.98B7.36061

Escudé Martinez de Castilla, P., Tong, L., Huang, C., Sofias, A. M., Pastorin, G., Chen, X., et al. (2021). Extracellular Vesicles as a Drug Delivery System: A Systematic Review of Preclinical Studies. *Adv. Drug Deliv. Rev.* 175, 113801. doi:10.1016/j.addr.2021.05.011

Fan, J., Lee, C.-S., Kim, S., Chen, C., Aghaloo, T., and Lee, M. (2020). Generation of Small RNA-Modulated Exosome Mimetics for Bone Regeneration. *ACS Nano* 14 (9), 11973–11984. doi:10.1021/acsnano.0c05122

Fan, L., Guan, P., Xiao, C., Wen, H., Wang, Q., Liu, C., et al. (2021). Exosome-functionalized Polyetheretherketone-Based Implant with Immunomodulatory Property for Enhancing Osseointegration. *Bioact. Mater.* 6 (9), 2754–2766. doi:10.1016/j.bioactmat.2021.02.005

Furuta, T., Miyaki, S., Ishitobi, H., Ogura, T., Kato, Y., Kamei, N., et al. (2016). Mesenchymal Stem Cell-Derived Exosomes Promote Fracture Healing in a

Mouse Model. *Stem Cells Transl. Med.* 5 (12), 1620–1630. doi:10.5966/sctm.2015-0285

Gandolfi, M. G., Gardin, C., Zamparini, F., Ferroni, L., Esposti, M. D., Parchi, G., et al. (2020). Mineral-doped Poly(L-Lactide) Acid Scaffolds Enriched with Exosomes Improve Osteogenic Commitment of Human Adipose-Derived Mesenchymal Stem Cells. *Nanomaterials* 10 (3), 432. doi:10.3390/nano10030432

Gao, C., Deng, Y., Feng, P., Mao, Z., Li, P., Yang, B., et al. (2014). Current Progress in Bioactive Ceramic Scaffolds for Bone Repair and Regeneration. *Ijms* 15 (3), 4714–4732. doi:10.3390/ijms15034714

Guan, P., Liu, C., Xie, D., Mao, S., Ji, Y., Lin, Y., et al. (2022). Exosome-loaded Extracellular Matrix-Mimic Hydrogel with Anti-inflammatory Property Facilitates/promotes Growth Plate Injury Repair. *Bioact. Mater.* 10, 145–158. doi:10.1016/j.bioactmat.2021.09.010

Hao, J., Bai, B., Ci, Z., Tang, J., Hu, G., Dai, C., et al. (2022). Large-sized Bone Defect Repair by Combining a Decalcified Bone Matrix Framework and Bone Regeneration Units Based on Photo-Crosslinkable Osteogenic Microgels. *Bioact. Mater.* 14, 97–109. doi:10.1016/j.bioactmat.2021.12.013

Hu, H., Dong, L., Bu, Z., Shen, Y., Luo, J., Zhang, H., et al. (2020). miR-23a-3p-abundant Small Extracellular Vesicles Released from Gelma/nanoclay Hydrogel for Cartilage Regeneration. *J. Extracell. Vesicles* 9 (1), 1778883. doi:10.1080/20013078.2020.1778883

Huber, J., Griffin, M. F., Longaker, M. T., and Quarto, N. (2022). Exosomes: A Tool for Bone Tissue Engineering. *Tissue Eng. Part B Rev.* 28 (1), 101–113. doi:10.1089/ten.teb.2020.0246

Jia, B., Yang, H., Zhang, Z., Qu, X., Jia, X., Wu, Q., et al. (2021). Biodegradable Zn-Sr Alloy for Bone Regeneration in Rat Femoral Condyle Defect Model: *In Vitro* and *In Vivo* Studies. *Bioact. Mater.* 6 (6), 1588–1604. doi:10.1016/j.bioactmat.2020.11.007

Jiang, S., Tian, G., Yang, Z., Gao, X., Wang, F., Li, J., et al. (2021). Enhancement of Acellular Cartilage Matrix Scaffold by Wharton's Jelly Mesenchymal Stem Cell-Derived Exosomes to Promote Osteochondral Regeneration. *Bioact. Mater.* 6 (9), 2711–2728. doi:10.1016/j.bioactmat.2021.01.031

Jing, X., Wang, S., Tang, H., Li, D., Zhou, F., Xin, L., et al. (2022). Dynamically Bioresponsive DNA Hydrogel Incorporated with Dual-Functional Stem Cells from Apical Papilla-Derived Exosomes Promotes Diabetic Bone Regeneration. *ACS Appl. Mat. Interfaces* 14, 16082–16099. doi:10.1021/acsami.2c02278

Julien, A., Kanagalingam, A., Martínez-Sarrà, E., Megret, J., Luka, M., Ménager, M., et al. (2021). Direct Contribution of Skeletal Muscle Mesenchymal Progenitors to Bone Repair. *Nat. Commun.* 12 (1). doi:10.1038/s41467-021-22842-5

Kalfas, I. H. (2001). Principles of Bone Healing. *Foc* 10 (4), 1–4. doi:10.3171/foc.2001.10.4.2

Li, D., Liu, J., Guo, B., Liang, C., Dang, L., Lu, C., et al. (2016). Osteoclast-derived Exosomal miR-214-3p Inhibits Osteoblastic Bone Formation. *Nat. Commun.* 7 (1). doi:10.1038/ncomms10872

Li, F., Wu, J., Li, D., Hao, L., Li, Y., Yi, D., et al. (2022). Engineering Stem Cells to Produce Exosomes with Enhanced Bone Regeneration Effects: An Alternative Strategy for Gene Therapy. *J. Nanobiotechnol.* 20 (1). doi:10.1186/s12951-022-01347-3

Li, L., Lu, H., Zhao, Y., Luo, J., Yang, L., Liu, W., et al. (2019). Functionalized Cell-free Scaffolds for Bone Defect Repair Inspired by Self-Healing of Bone Fractures: A Review and New Perspectives. *Mater. Sci. Eng. C* 98, 1241–1251. doi:10.1016/j.msec.2019.01.075

Li, S., Liu, Y., Tian, T., Zhang, T., Lin, S., Zhou, M., et al. (2021a). Bioswitchable Delivery of microRNA by Framework Nucleic Acids: Application to Bone Regeneration. *Small* 17 (47), 2104359. doi:10.1002/smll.202104359

Li, W., Liu, Y., Zhang, P., Tang, Y., Zhou, M., Jiang, W., et al. (2018). Tissue-Engineered Bone Immobilized with Human Adipose Stem Cells-Derived Exosomes Promotes Bone Regeneration. *ACS Appl. Mat. Interfaces* 10 (6), 5240–5254. doi:10.1021/acsami.7b17620

Li, Y., Chen, M., Zhao, Y., Li, M., Qin, Y., Cheng, S., et al. (2020). Advance in Drug Delivery for Ageing Skeletal Muscle. *Front. Pharmacol.* 11. doi:10.3389/fphar.2020.01016

Li, Z., Zhang, X., Ouyang, J., Chu, D., Han, F., Shi, L., et al. (2021b). Ca2+-supplying Black Phosphorus-Based Scaffolds Fabricated with Microfluidic Technology for Osteogenesis. *Bioact. Mater.* 6 (11), 4053–4064. doi:10.1016/j.bioactmat.2021.04.014

Lin, Z., Xiong, Y., Meng, W., Hu, Y., Chen, L., Chen, L., et al. (2022). Exosomal PD-L1 Induces Osteogenic Differentiation and Promotes Fracture Healing by Acting as an Immunosuppressant. *Bioact. Mater.* 13, 300–311. doi:10.1016/j.bioactmat.2021.10.042

Liu, A., Lin, D., Zhao, H., Chen, L., Cai, B., Lin, K., et al. (2021a). Optimized BMSC-Derived Osteoinductive Exosomes Immobilized in Hierarchical Scaffold via Lyophilization for Bone Repair through Bmpr2/Acvr2b Competitive Receptor-Activated Smad Pathway. *Biomaterials* 272, 120718. doi:10.1016/j.biomaterials.2021.120718

Liu, M., Sun, Y., and Zhang, Q. (2018). Emerging Role of Extracellular Vesicles in Bone Remodeling. *J. Dent. Res.* 97 (8), 859–868. doi:10.1177/0022034518764411

Liu, W.-z., Ma, Z.-j., Li, J.-r., and Kang, X.-w. (2021b). Mesenchymal Stem Cell-Derived Exosomes: Therapeutic Opportunities and Challenges for Spinal Cord Injury. *Stem Cell Res. Ther.* 12 (1), 102. doi:10.1186/s13287-021-02153-8

Liu, W., Li, L., Rong, Y., Qian, D., Chen, J., Zhou, Z., et al. (2020). Hypoxic Mesenchymal Stem Cell-Derived Exosomes Promote Bone Fracture Healing by the Transfer of miR-126. *Acta Biomater.* 103, 196–212. doi:10.1016/j.actbio.2019.12.020

Lu, H., Zhang, Y., Xiong, S., Zhou, Y., Xiao, L., Ma, Y., et al. (2021). Modulatory Role of Silver Nanoparticles and Mesenchymal Stem Cell-Derived Exosome-Modified Barrier Membrane on Macrophages and Osteogenesis. *Front. Chem.* 9. doi:10.3389/fchem.2021.699802

Lu, J., Wang, Q.-Y., and Sheng, J.-G. (2019). Exosomes in the Repair of Bone Defects: Next-Generation Therapeutic Tools for the Treatment of Nonunion. *BioMed Res. Int.* 2019, 1–11. doi:10.1155/2019/1983131

Luo, Z.-W., Li, F.-X. -Z., Liu, Y.-W., Rao, S.-S., Yin, H., Huang, J., et al. (2019). Aptamer-functionalized Exosomes from Bone Marrow Stromal Cells Target Bone to Promote Bone Regeneration. *Nanoscale* 11 (43), 20884–20892. doi:10.1039/C9NR02791B

Ma, L., Wang, X., Zhou, Y., Ji, X., Cheng, S., Bian, D., et al. (2021). Biomimetic Ti-6Al-4V Alloy/gelatin Methacrylate Hybrid Scaffold with Enhanced Osteogenic and Angiogenic Capabilities for Large Bone Defect Restoration. *Bioact. Mater.* 6 (10), 3437–3448. doi:10.1016/j.bioactmat.2021.03.010

Ma, S., Wu, J., Hu, H., Mu, Y., Zhang, L., Zhao, Y., et al. (2022). Novel Fusion Peptides Deliver Exosomes to Modify Injectable Thermo-Sensitive Hydrogels for Bone Regeneration. *Mater. Today Bio* 13, 100195. doi:10.1016/j.mtbio.2021.100195

Mackie, E. J., Tatarczuch, L., and Mirams, M. (2011). The Skeleton: A Multi-Functional Complex Organ. The Growth Plate Chondrocyte and Endochondral Ossification. *J. Endocrinol.* 211 (2), 109–121. doi:10.1530/JOE-11-0048

Majidinia, M., Sadeghpour, A., and Yousefi, B. (2018). The Roles of Signaling Pathways in Bone Repair and Regeneration. *J. Cell. Physiol.* 233 (4), 2937–2948. doi:10.1002/jcp.26042

Morelli, I., Drago, L., George, D. A., Gallazzi, E., Scarponi, S., and Romanò, C. L. (2016). Masquelet Technique: Myth or Reality? A Systematic Review and Meta-Analysis. *Injury* 47, S68–S76. doi:10.1016/S0020-1383(16)30842-7

Narayanan, R., Huang, C.-C., and Ravindran, S. (2016). Hijacking the Cellular Mail: Exosome Mediated Differentiation of Mesenchymal Stem Cells. *Stem Cells Int.* 2016, 1–11. doi:10.1155/2016/3808674

Nauth, A., Schemitsch, E., Norris, B., Nollin, Z., and Watson, J. T. (2018). Critical-Size Bone Defects: Is There a Consensus for Diagnosis and Treatment? *J. Orthop. Trauma.* 32 (3), S7–S11. doi:10.1097/BOT.0000000000001115

Nicholson, J., Makaram, N., Simpson, A., and Keating, J. (2021). Fracture Nonunion in Long Bones: A Literature Review of Risk Factors and Surgical Management. *Injury* 52, S3–S11. doi:10.1016/j.injury.2020.11.029

Nikhil, A., and Kumar, A. (2022). Evaluating Potential of Tissue-engineered Cryogels and Chondrocyte Derived Exosomes in Articular Cartilage Repair. *Biotech Bioeng.* 119 (2), 605–625. doi:10.1002/bit.27982

Oftadeh, R., Perez-Viloria, M., Villa-Camacho, J. C., Vaziri, A., and Nazarian, A. (2015). Biomechanics and Mechanobiology of Trabecular Bone: A Review. *J. Biomech. Eng.* 137 (1). doi:10.1115/1.4029176

Oryan, A., Monazzah, S., and Bigham-Sadegh, A. (2015). Bone Injury and Fracture Healing Biology. *Biomed. Environ. Sci.* 28 (1), 57–71. doi:10.3967/bes2015.006

Percival, C. J., and Richtsmeier, J. T. (2013). Angiogenesis and Intramembranous Osteogenesis. *Dev. Dyn.* 242 (8), 909–922. doi:10.1002/dvdy.23992

Pishavar, E., Luo, H., Naserifar, M., Hashemi, M., Toosi, S., Atala, A., et al. (2021). Advanced Hydrogels as Exosome Delivery Systems for Osteogenic

Differentiation of MSCs: Application in Bone Regeneration. *Ijms* 22 (12), 6203. doi:10.3390/ijms22126203

Qi, X., Zhang, J., Yuan, H., Xu, Z., Li, Q., Niu, X., et al. (2016). Exosomes Secreted by Human-Induced Pluripotent Stem Cell-Derived Mesenchymal Stem Cells Repair Critical-Sized Bone Defects through Enhanced Angiogenesis and Osteogenesis in Osteoporotic Rats. *Int. J. Biol. Sci.* 12 (7), 836–849. doi:10.7150/ijbs.14809

Qin, Y., Sun, R., Wu, C., Wang, L., and Zhang, C. (2016). Exosome: A Novel Approach to Stimulate Bone Regeneration through Regulation of Osteogenesis and Angiogenesis. *Ijms* 17 (5), 712. doi:10.3390/ijms17050712

Ramis, J. M. (2020). Extracellular Vesicles in Cell Biology and Medicine. *Sci. Rep.* 10 (1). doi:10.1038/s41598-020-65826-z

Re, F., Gabusi, E., Manferdini, C., Russo, D., and Lisignoli, G. (2021). Bone Regeneration Improves with Mesenchymal Stem Cell Derived Extracellular Vesicles (EVs) Combined with Scaffolds: A Systematic Review. *Biology* 10 (7), 579. doi:10.3390/biology10070579

Roseti, L., Parisi, V., Petretta, M., Cavallo, C., Desando, G., Bartolotti, I., et al. (2017). Scaffolds for Bone Tissue Engineering: State of the Art and New Perspectives. *Mater. Sci. Eng. C* 78, 1246–1262. doi:10.1016/j.msec.2017.05.017

Safari, B., Davaran, S., and Aghanejad, A. (2021). Osteogenic Potential of the Growth Factors and Bioactive Molecules in Bone Regeneration. *Int. J. Biol. Macromol.* 175, 544–557. doi:10.1016/j.ijbiomac.2021.02.052

Sahoo, S., Klychko, E., Thorne, T., Misener, S., Schultz, K. M., Millay, M., et al. (2011). Exosomes from Human CD34 + Stem Cells Mediate Their Proangiogenic Paracrine Activity. *Circ. Res.* 109 (7), 724–728. doi:10.1161/CIRCRESAHA.111.253286

Schmidt, A. H. (2021). Autologous Bone Graft: Is it Still the Gold Standard? *Injury* 52, S18–S22. doi:10.1016/j.injury.2021.01.043

Shang, F., Yu, Y., Liu, S., Ming, L., Zhang, Y., Zhou, Z., et al. (2021). Advancing Application of Mesenchymal Stem Cell-Based Bone Tissue Regeneration. *Bioact. Mater.* 6 (3), 666–683. doi:10.1016/j.bioactmat.2020.08.014

Shen, K., Duan, A., Cheng, J., Yuan, T., Zhou, J., Song, H., et al. (2022). Exosomes Derived from Hypoxia Preconditioned Mesenchymal Stem Cells Laden in a Silk Hydrogel Promote Cartilage Regeneration via the miR-205-5p/PTEN/AKT Pathway. *Acta Biomater.* 143, 173–188. doi:10.1016/j.actbio.2022.02.026

Swanson, W. B., Zhang, Z., Xiu, K., Gong, T., Eberle, M., Wang, Z., et al. (2020). Scaffolds with Controlled Release of Pro-mineralization Exosomes to Promote Craniofacial Bone Healing without Cell Transplantation. *Acta Biomater.* 118, 215–232. doi:10.1016/j.actbio.2020.09.052

Tan, B., Tang, Q., Zhong, Y., Wei, Y., He, L., Wu, Y., et al. (2021). Biomaterial-based Strategies for Maxillofacial Tumour Therapy and Bone Defect Regeneration. *Int. J. Oral Sci.* 13 (1), 9. doi:10.1038/s41368-021-00113-9

Tan, S. H. S., Wong, J. R. Y., Sim, S. J. Y., Tjio, C. K. E., Wong, K. L., Chew, J. R. J., et al. (2020). Mesenchymal Stem Cell Exosomes in Bone Regenerative Strategies-A Systematic Review of Preclinical Studies. *Mater. Today Bio* 7, 100067. doi:10.1016/j.mtbio.2020.100067

Teotia, A. K., Qayoom, I., Singh, P., Mishra, A., Jaiman, D., Seppälä, J., et al. (2021). Exosome-Functionalized Ceramic Bone Substitute Promotes Critical-Sized Bone Defect Repair in Rats. *ACS Appl. Bio Mat.* 4 (4), 3716–3726. doi:10.1021/acsabm.1c00311

Tovar, N., Witek, L., Atria, P., Sobieraj, M., Bowers, M., Lopez, C. D., et al. (2018). Form and Functional Repair of Long Bone Using 3D-printed Bioactive Scaffolds. *J. Tissue Eng. Regen. Med.* 12 (9), 1986–1999. doi:10.1002/term.2733

Turnbull, G., Clarke, J., Picard, F., Riches, P., Jia, L., Han, F., et al. (2018). 3D Bioactive Composite Scaffolds for Bone Tissue Engineering. *Bioact. Mater.* 3 (3), 278–314. doi:10.1016/j.bioactmat.2017.10.001

Wang, L., Wang, J., Zhou, X., Sun, J., Zhu, B., Duan, C., et al. (2020a). A New Self-Healing Hydrogel Containing hucMSC-Derived Exosomes Promotes Bone Regeneration. *Front. Bioeng. Biotechnol.* 8. doi:10.3389/fbioe.2020.564731

Wang, W., and Yeung, K. W. K. (2017). Bone Grafts and Biomaterials Substitutes for Bone Defect Repair: A Review. *Bioact. Mater.* 2 (4), 224–247. doi:10.1016/j.bioactmat.2017.05.007

Wang, X., Ao, J., Lu, H., Zhao, Q., Ma, Y., Zhang, J., et al. (2020b). Osteoimmune Modulation and Guided Osteogenesis Promoted by Barrier Membranes Incorporated with S-Nitrosoglutathione (GSNO) and Mesenchymal Stem Cell-Derived Exosomes. *Ijn* 15, 3483–3496. doi:10.2147/IJN.S248741<

Wang, X., Yu, Y., Yang, C., Shao, C., Shi, K., Shang, L., et al. (2021). Microfluidic 3D Printing Responsive Scaffolds with Biomimetic Enrichment Channels for Bone Regeneration. *Adv. Funct. Mater.* 31 (40), 2105190. doi:10.1002/adfm.202105190

Watanabe, Y., Tsuchiya, A., and Terai, S. (2021). The Development of Mesenchymal Stem Cell Therapy in the Present, and the Perspective of Cell-free Therapy in the Future. *Clin. Mol. Hepatol.* 27 (1), 70–80. doi:10.3350/cmh.2020.0194

Wei, F., Li, M., Crawford, R., Zhou, Y., and Xiao, Y. (2019). Exosome-integrated Titanium Oxide Nanotubes for Targeted Bone Regeneration. *Acta Biomater.* 86, 480–492. doi:10.1016/j.actbio.2019.01.006

Weilner, S., Keider, V., Winter, M., Harreither, E., Salzer, B., Weiss, F., et al. (2016). Vesicular Galectin-3 Levels Decrease with Donor Age and Contribute to the Reduced Osteo-Inductive Potential of Human Plasma Derived Extracellular Vesicles. *Aging* 8 (1), 16–30. doi:10.18632/aging.100865

Wiese, A., and Pape, H. C. (2010). Bone Defects Caused by High-Energy Injuries, Bone Loss, Infected Nonunions, and Nonunions. *Orthop. Clin. N. Am.* 41 (1), 1–4. doi:10.1016/j.ocl.2009.07.003

Wu, D., Chang, X., Tian, J., Kang, L., Wu, Y., Liu, J., et al. (2021). Bone Mesenchymal Stem Cells Stimulation by Magnetic Nanoparticles and a Static Magnetic Field: Release of Exosomal miR-1260a Improves Osteogenesis and Angiogenesis. *J. Nanobiotechnol.* 19 (1). doi:10.1186/s12951-021-00958-6

Wu, D., Qin, H., Wang, Z., Yu, M., Liu, Z., Peng, H., et al. (2022). Bone Mesenchymal Stem Cell-Derived sEV-Encapsulated Thermosensitive Hydrogels Accelerate Osteogenesis and Angiogenesis by Release of Exosomal miR-21. *Front. Bioeng. Biotechnol.* 9. doi:10.3389/fbioe.2021.829136

Wu, Z., Pu, P., Su, Z., Zhang, X., Nie, L., and Chang, Y. (2020). Schwann Cell-Derived Exosomes Promote Bone Regeneration and Repair by Enhancing the Biological Activity of Porous Ti6Al4V Scaffolds. *Biochem. Biophysical Res. Commun.* 531 (4), 559–565. doi:10.1016/j.bbrc.2020.07.094

Yang, S., Zhu, B., Yin, P., Zhao, L., Wang, Y., Fu, Z., et al. (2020). Integration of Human Umbilical Cord Mesenchymal Stem Cells-Derived Exosomes with Hydroxyapatite-Embedded Hyaluronic Acid-Alginate Hydrogel for Bone Regeneration. *ACS Biomater. Sci. Eng.* 6 (3), 1590–1602. doi:10.1021/acsbiomaterials.9b01363

Yin, B., Ma, Q., Song, C., Zhao, L., Yu, F., Wang, C., et al. (2021). Exosome-Derived Noncoding RNAs as a Promising Treatment of Bone Regeneration. *Stem Cells Int.* 2021, 1–8. doi:10.1155/2021/6696894

Yu, W., Li, S., Guan, X., Zhang, N., Xie, X., Zhang, K., et al. (2022). Higher Yield and Enhanced Therapeutic Effects of Exosomes Derived from MSCs in Hydrogel-Assisted 3D Culture System for Bone Regeneration. *Mater. Sci. Eng. C*, 112646. doi:10.1016/j.msec.2022.112646

Zha, Y., Li, Y., Lin, T., Chen, J., Zhang, S., and Wang, J. (2021). Progenitor Cell-Derived Exosomes Endowed with VEGF Plasmids Enhance Osteogenic Induction and Vascular Remodeling in Large Segmental Bone Defects. *Theranostics* 11 (1), 397–409. doi:10.7150/thno.50741

Zhai, M., Zhu, Y., Yang, M., and Mao, C. (2020). Human Mesenchymal Stem Cell Derived Exosomes Enhance Cell-Free Bone Regeneration by Altering Their miRNAs Profiles. *Adv. Sci.* 7 (19), 2001334. doi:10.1002/advs.202001334

Zhang, B., Huang, J., Liu, J., Lin, F., Ding, Z., and Xu, J. (2021a). Injectable Composite Hydrogel Promotes Osteogenesis and Angiogenesis in Spinal Fusion by Optimizing the Bone Marrow Mesenchymal Stem Cell Microenvironment and Exosomes Secretion. *Mater. Sci. Eng. C* 123, 111782. doi:10.1016/j.msec.2020.111782

Zhang, H., Wang, R., Wang, G., Zhang, B., Wang, C., Li, D., et al. (2021b). Single-Cell RNA Sequencing Reveals B Cells Are Important Regulators in Fracture Healing. *Front. Endocrinol.* 12. doi:10.3389/fendo.2021.666140

Zhang, J., Jiang, Y., Shang, Z., Zhao, B., Jiao, M., Liu, W., et al. (2021c). Biodegradable Metals for Bone Defect Repair: A Systematic Review and Meta-Analysis Based on Animal Studies. *Bioact. Mater.* 6 (11), 4027–4052. doi:10.1016/j.bioactmat.2021.03.035

Zhang, J., Liu, X., Li, H., Chen, C., Hu, B., Niu, X., et al. (2016). Exosomes/tricalcium Phosphate Combination Scaffolds Can Enhance Bone Regeneration by Activating the PI3K/Akt Signaling Pathway. *Stem Cell Res. Ther.* 7 (1). doi:10.1186/s13287-016-0391-3

Zhang, T., Tian, T., and Lin, Y. (2022). Functionalizing Framework Nucleic-Acid-Based Nanostructures for Biomedical Application. *Adv. Mater.*, 2107820. doi:10.1002/adma.202107820

Zhang, Y., Chen, Y., Kou, H., Yang, P., Wang, Y., and Lu, T. (2018). Enhanced Bone Healing in Porous Ti Implanted Rabbit Combining Bioactive Modification and Mechanical Stimulation. *J. Mech. Behav. Biomed. Mater.* 86, 336–344. doi:10.1016/j.jmbbm.2018.06.042

Zhang, Y., Xie, Y., Hao, Z., Zhou, P., Wang, P., Fang, S., et al. (2021d). Umbilical Mesenchymal Stem Cell-Derived Exosome-Encapsulated Hydrogels Accelerate Bone Repair by Enhancing Angiogenesis. *ACS Appl. Mat. Interfaces* 13 (16), 18472–18487. doi:10.1021/acsami.0c22671

Zhou, P., Xia, D., Ni, Z., Ou, T., Wang, Y., Zhang, H., et al. (2021). Calcium Silicate Bioactive Ceramics Induce Osteogenesis through Oncostatin M. *Bioact. Mater.* 6 (3), 810–822. doi:10.1016/j.bioactmat.2020.09.018

Zhu, G., Zhang, T., Chen, M., Yao, K., Huang, X., Zhang, B., et al. (2021). Bone Physiological Microenvironment and Healing Mechanism: Basis for Future Bone-Tissue Engineering Scaffolds. *Bioact. Mater.* 6 (11), 4110–4140. doi:10.1016/j.bioactmat.2021.03.043

Conflict of Interest: The authors declare that the research was conducted in the absence of any commercial or financial relationships that could be construed as a potential conflict of interest.

Publisher's Note: All claims expressed in this article are solely those of the authors and do not necessarily represent those of their affiliated organizations, or those of the publisher, the editors, and the reviewers. Any product that may be evaluated in this article, or claim that may be made by its manufacturer, is not guaranteed or endorsed by the publisher.

frontiers | Frontiers in Bioengineering and Biotechnology

REVIEW
published: 16 June 2022
doi: 10.3389/fbioe.2022.907356

Progress of Platelet Derivatives for Cartilage Tissue Engineering

Siyu Wu[1], *Wenlai Guo*[1], *Rui Li*[1], *Xi Zhang*[2]* *and Wenrui Qu*[1]*

[1]*Department of Hand Surgery, The Second Hospital of Jilin University, Changchun, China,* [2]*Department of Burn Surgery, The First Hospital of Jilin University, Changchun, China*

Articular cartilage has limited self-regeneration ability for lacking of blood vessels, nerves, and lymph that makes it a great challenge to repair defects of the tissue and restore motor functions of the injured or aging population. Platelet derivatives, such as platelet-rich plasma, have been proved effective, safe, and economical in musculoskeletal diseases for their autologous origin and rich in growth factors. The combination of platelet derivatives with biomaterials provides both mechanical support and localized sustained release of bioactive molecules in cartilage tissue engineering and low-cost efficient approaches of potential treatment. In this review, we first provide an overview of platelet derivatives and their application in clinical and experimental therapies, and then we further discuss the techniques of the addition of platelet derivatives and their influences on scaffold properties. Advances in cartilage tissue engineering with platelet derivatives as signal factors and structural components are also introduced before prospects and concerns in this research field. In short, platelet derivatives have broad application prospects as an economical and effective enhancement for tissue engineering–based articular cartilage repair.

Keywords: platelet-rich plasma, platelet-derived growth factor, cartilage tissue engineering, articular cartilage, scaffolds

OPEN ACCESS

Edited by:
Chao Zhao,
University of Alabama, United States

Reviewed by:
Jia Xian Law,
Universiti Kebangsaan Malaysia, Malaysia
Wen Shi,
University of Nebraska Medical Center, United States

***Correspondence:**
Xi Zhang
bethunezx@jlu.edu.cn
Wenrui Qu
quwenrui@jlu.edu.cn

Specialty section:
This article was submitted to Biomaterials, a section of the journal Frontiers in Bioengineering and Biotechnology

Received: *29 March 2022*
Accepted: *05 May 2022*
Published: *16 June 2022*

Citation:
Wu S, Guo W, Li R, Zhang X and Qu W (2022) Progress of Platelet Derivatives for Cartilage Tissue Engineering. Front. Bioeng. Biotechnol. 10:907356. doi: 10.3389/fbioe.2022.907356

1 INTRODUCTION

Articular cartilage is a highly specialized connective tissue whose function is to provide a smooth, lubricated surface for articulation. As simple tissue without blood vessels, nerves, or lymphatics, it is nourished with oxygen and nutrients diffused from the synovium and the subchondral bone. The total volume of cells in human articular cartilage is only 1.65% on average (Hunziker et al., 2002; Tang et al., 2018), and the rest is made up of the extracellular matrix (ECM), a highly hydrated network of collagens (mostly type II collagen) and proteoglycans (Sophia Fox et al., 2009).

Injury to articular cartilage occurs *via* trauma, abnormal wear of an instable joint, excessive load such as sports injuries or obesity, or simply during the aging process. The aforementioned are the main causes of osteoarthritis (OA) and the rapid increase in the incidence of OA, primarily driven by

Abbreviations: ACI, autologous chondrocytes implantation; AdMSC, adipose-derived mesenchymal stem cell; Alg, alginate; BMP, bone morphogenetic protein; BMSC, bone marrow mesenchymal stem cell; β-TCP, beta-tricalcium phosphate; CPC, chondrogenic progenitor cell; CS, chondroitin sulfate; CTE, cartilage tissue engineering; ECM, extracellular matrix; GAG, glycosaminoglycan; Gel MA, methacrylated gelatin; GF, growth factor; HA, hyaluronic acid; HAP, hydroxyapatite; MSC, mesenchymal stem cell; OA, osteoarthritis; OAT, osteochondral autograft transplantation; PEG, poly(ethylene glycol); PL, platelet lysate; PLGA, poly(lactide-co-glycolide); PRF, platelet-rich fibrin; PRP, platelet-rich plasma; SF, silk fibroin; TGF-β, transforming growth factor beta; VEGF, vascular endothelial growth factor; 3D, three-dimensional.

the aging global population, leads to an annually increasing burden on health services and societies worldwide (Quicke et al., 2022).

Due to the less vascularity and restricted number of chondrocytes with weakened proliferative ability and migration, cartilage has a limited capacity for self-repair, especially in large defects (Pearle et al., 2005). Therefore, surgical treatment is necessary, either to accelerate the regeneration or directly fill the defect. Various techniques, including microfracture, autologous chondrocytes implantation (ACI), osteochondral autograft transplantation (OAT), and osteochondral allograft transplantation, have been applied for hyaline cartilage repair. However, the long-term clinical results are not promising. In addition to a higher incidence of complications at the donor site, poor integration between neo-tissue or graft with the native leads to cartilage degeneration and formation of fibrous cartilage that compromises the therapeutic efficacy (Lane et al., 2004; Marcacci et al., 2007; Qi et al., 2009). Cartilage hypertrophy and osteochondrosis have been common adverse reactions of ACI (Niemeyer et al., 2020).

With the growing interest in non-operative treatments and biological adjuncts to surgical treatments to promote cartilage healing and curb degeneration, platelet-rich plasma (PRP), an autologous blood product containing growth factors (GFs), and cytokines have gained significant interest owing to the safety of its autologous origin and relative ease of production. Numerous studies support that PRP has beneficial effects on cartilage pathology and alleviation of pain (Lopez-Vidriero et al., 2010; Fice et al., 2019). It is also been verified to improve the integration of autologous osteochondral grafts at the cartilage interface and decrease graft degeneration, with a raised histological score and few adverse events observed (Smyth et al., 2013).

To overcome the limitations of surgical treatments, such as injury or insufficient supply of the donor site and the potential risk of viral transmission in allograft transplantation, cartilage tissue engineering (CTE) has gained a lot of attention and achievements over years (Zhang B. et al., 2020). Tissue engineering typically involves three main elements: scaffolds, cells, and signaling factors (Langer and Vacanti, 1993). To some extent, the import of biomaterials is a great upgrade of ACI that improves the environment of cell adhesion and anabolism or osteochondral transplantation with less donor site damage. Constructs based on various kinds of biomaterial scaffolds seeded with or without cells have been investigated to improve cartilage repair, for not only maintenance and improvement of the afflicted region but most importantly full regeneration of function (Anderson et al., 2017). Scaffolds are supposed to provide a three-dimensional (3D) normal tissue–mimicking microenvironment for proliferation and differentiation of seeded cells. Ideally, the scaffold used for CTE should be fabricated with biocompatible and biodegradable materials, provide enough mechanical stability during the regeneration process, and support articulate contact. Polymers and decellularized ECM are the most popular materials for CTE scaffolds. Hydrogels composed of highly hydrated polymeric networks possess properties to mimic natural cartilage ECM, such as high water content, biocompatibility, and controllable mechanical strength, and have attracted extra attention for applications in CTE (Yang et al., 2017). Similar to bone tissue engineering, which aims at the diaphysis of long-bones, inorganic materials are also used in the construction of the subchondral bone part of a biphasic or multiphasic scaffold (Bal et al., 2010; Jang et al., 2014; Kosik-Koziol et al., 2020). Another application is to process inorganic materials to nanoscale and incorporate with polymers to create nanocomposite hydrogels for improved bioactivity and mechanical strength (Gaharwar et al., 2014; Qi et al., 2014).

Suitable cells for hyaline cartilage construction include autologous chondrocytes and mesenchymal stem cells (MSCs) obtained from different tissues such as bone marrow, adipose tissue, umbilical cord, synovial membrane or synovial fluid, and chondrogenic progenitor cells (CPCs) (Lee et al., 2013; Wang et al., 2019; Zhang et al., 2020b; Huynh et al., 2021). Although the cellular composition of articular cartilage is rather simple, intercellular communication is still a modulator of cell behavior. A mixture of populations of cells could exceed a single component; as evidence showed, cocultured MSCs and differentiated chondrocytes interact with each other that enhance the functional properties of CTE components and reduce MSC hypertrophy (Bian et al., 2011).

The signal factors used in CTE are supposed to mediate growth, proliferation, and differentiation of seeded cells by specific pathway activation and stimulate synthesis and secretion of relevant proteins and glycoproteins for ECM generation and maintenance. Transforming growth factor-β (TGF-β), bone morphogenetic proteins (BMPs), insulin GFs, and fibroblast GFs are among the most popular GFs in cartilage formation (Wei and Dai, 2021). However, recombinant GFs are too expensive for expanded use in clinics, and animal-derived GFs may result in disease transmission or inflammation. Autologous platelet derivatives can be used as a potent and reliable resource of GF cocktail for tissue engineering, as shown in **Scheme 1**, with low immunogenicity, easy accessibility, and low-cost.

In this review, the characteristics of platelet derivatives and biomaterials, their interaction, and the technology of their combination are discussed. Challenges associated with the use of platelet derivatives in cartilage defects and recommendations for future directions are considered in the final section.

2 PLATELET DERIVATIVES IN CARTILAGE REPAIR

Platelets are cytoplasmic fragments of multinucleated megakaryocytes with a life span of 7–10 days, and they play an important role in hemostasis and other aspects. Secretory granules, including α-granules, dense granules, and lysosomes, are critical for normal platelet functions (Frojmovic and Milton, 1982). Among those, α-granules are the most abundant and contain bioactive molecules, including not only GFs and chemokines but also adhesive proteins such as fibrinogen, factors, and enzymes that regulate coagulation and anticoagulation and other basic proteins (Blair and

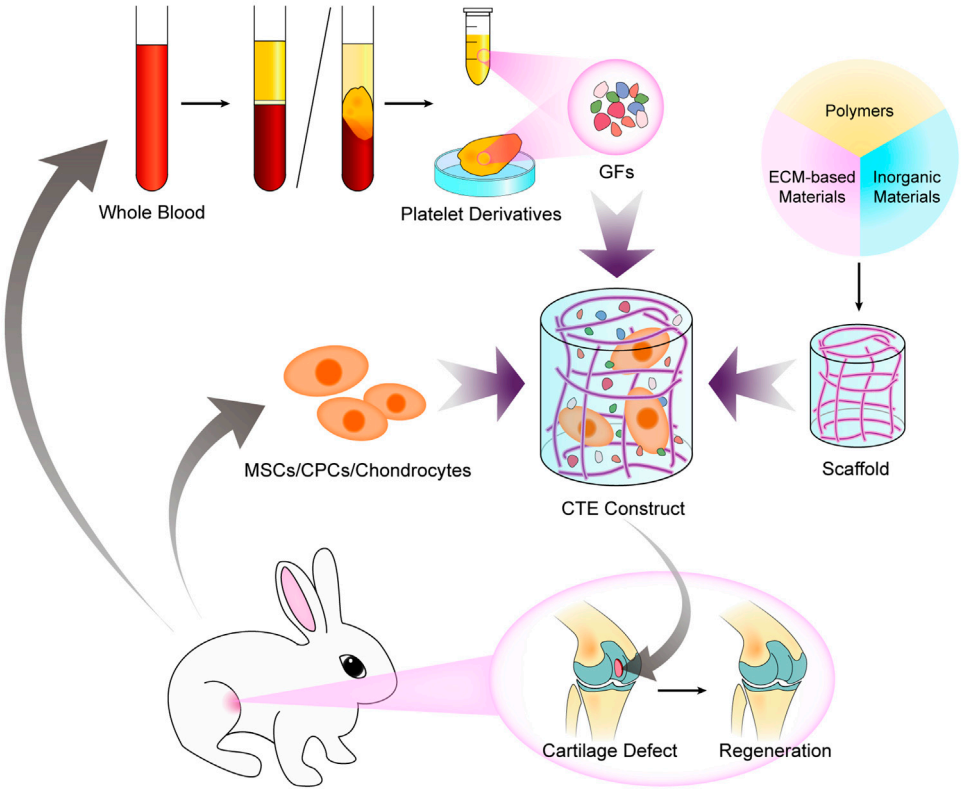

SCHEME 1 | Fabrication of a CTE construct with autologous platelet derivatives, seed cells, and a scaffold for improved regeneration of articular cartilage defects.

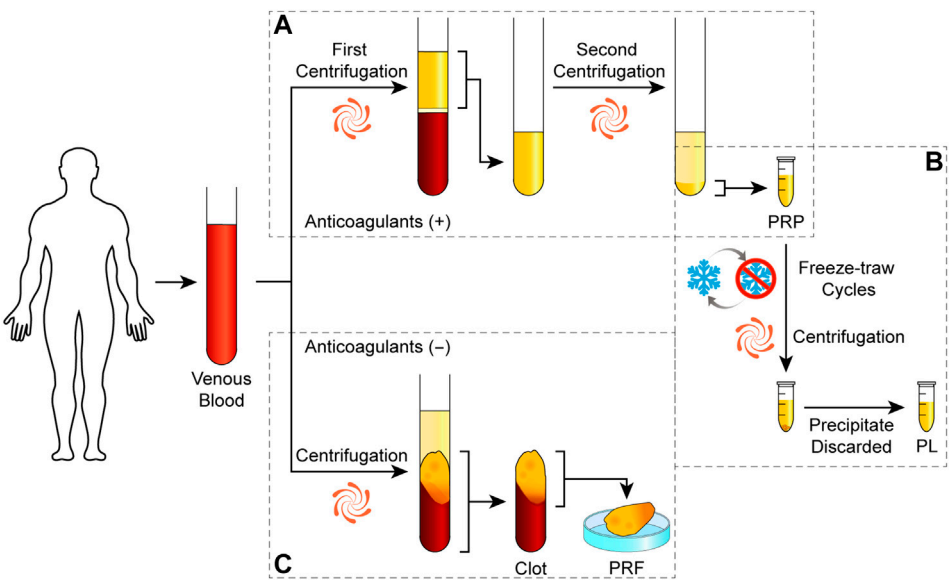

SCHEME 2 | Preparation protocols of platelet derivatives. Schematic drawing of the classical preparation protocols of PRP **(A)**, PL **(B)**, and PRF **(C)**.

Flaumenhaft, 2009; Foster et al., 2009). GFs, including platelet-derived GF-AB and BB, TGF-β1, vascular endothelial growth factor (VEGF), basic fibroblast GF, epidermal GF, and hepatocyte GF, are stored in α-granules and released after activation (Boswell et al., 2012). The delayed upregulation of insulin GF-1 after PRP use indicates that it regulates local production of these factors (Lyras et al., 2011). PRP and platelet-rich fibrin (PRF) are the most widely used platelet derivatives in clinics, and there are other experimental forms.

2.1 Forms of Platelet Derivatives

2.1.1 Platelet-Rich Plasma

PRP refers to a sample of plasma with platelet concentrations above baseline values. One million/ml of platelet count is required based on the working definition, which is approximately five times that of whole blood, based on studies of cell proliferation and tissue healing (Marx, 2001; Dhurat and Sukesh, 2014). It is of a liquid form that is available for injection and coagulation and induced at the same time to prolong the retention.

As illustrated in **Scheme 2A**, it can be produced with a double-spin procedure that first reduces the number of erythrocytes and second concentrates platelets, or a single-spin procedure for both purposes. Whole venous blood with anticoagulant undergoes the separating centrifugation. After the first spin, three layers of components are separated: erythrocytes at the bottom, leukocyte-containing buffy coat in the middle, and platelet-containing plasma on the top. Erythrocytes are discarded, while whether to retain the buffy coat leads to different concentration of leukocytes and influences the bio-function of PRP. *In vitro* studies suggest that leukocyte-rich PRP had higher levels of GFs and interleukin-1 receptor antagonist than leukocyte-poor PRP (Cavallo et al., 2014; Ziegler et al., 2019), but their clinical efficacy depends on specific indications (Le et al., 2018; Kim et al., 2021).

2.1.2 Platelet-Rich Fibrin

PRF is the second-generation platelet concentrate derived from PRP. It can be assumed as a piece of hydrogel with a skeleton of fibrin fibers containing platelets and leukocytes. As illustrated in **Scheme 2B**, the technique requires a blood sample without anticoagulant immediately centrifuged in a glass tube, resulting in a PRF clot in the middle of acellular plasma and a red corpuscle base. It can be transformed into a membrane shape by dry gauze or a compressor for clinical application or cell culture scaffold (Gassling et al., 2010; Kobayashi et al., 2012).

The natural process of production and the absence of anticoagulants or gel agents evaded potential side effects (Dohan et al., 2007). However, the colloidal form could restrict its mixing and combination with materials. Injectable PRF can be prepared with the concept of low-speed centrifugation in a non-coating plastic tube and allows about 80 s for operation before spontaneously clotting (Thanasrisuebwong et al., 2019).

2.1.3 Other Forms of Platelet Derivatives

Bioactive molecules in platelets are also concentrated in other forms for more convenient use. Platelet lysate (PL) is prepared by PRP with two or three freeze–thaw cycles in order to break the platelet membranes and release the bioactive molecules, and the remnants are removed by centrifugation as illustrated in **Scheme 2C** or by filters (Zaky et al., 2008; Moroz et al., 2013). Platelet-rich concentrate refers to concentrated platelet pellets resuspended in sterile phosphate-buffered saline (Samuel et al., 2019). Plasma with anticoagulant is removed such as washing red cells, which may reduce potential adverse immune reactions when using allogenic resources (Akbarzadeh et al., 2021). Aggregates can be removed by centrifugation after the induced degranulation, which leaves only soluble components for application (Gruber et al., 2002; Verrier et al., 2010). It indicates the possibility to use apheresis platelet concentrates for less erythrocyte waste or blood bank–pooled platelets that might be discarded through blood donation services.

Platelet-derived extracellular vesicles including exosomes and microvesicles are regarded as important effectors of platelet derivatives for encapsulation of bioactive content and enrichment of micro RNAs (Torreggiani et al., 2014; Johnson et al., 2021). Their isolation from activated PRP or PL requires more complicated methods such as differential centrifugation, ultracentrifugation, tangential-flow filtration, and size-exclusion chromatography and also leads to waste of free molecules released from platelets (Aatonen et al., 2014; Torreggiani et al., 2014; Gomes et al., 2022). Despite the need of production optimization, extracellular vesicles showed a potential way to extract or eliminate specific subsets of platelet-derived bioactive molecules through different stimulus or by the characteristic of extracellular vesicles (Aatonen et al., 2014; Ferreira et al., 2020). Therefore, extracellular vesicles, as an important carrier of cellular paracrine, have a phospholipid bilayer membrane structure, contain a large number of bioactive molecules, and participate in the development and repair of important organs; the application of platelet-derived extracellular vesicles in CTE has great potential. For the aforementioned reasons, its therapeutic effect needs to be further verified.

Regarding the acting mechanism of platelet derivatives, the most current researches on their promotion of cartilage regeneration stayed at the level of therapeutic effect, and the mechanisms behind are rarely studied because of their complex composition. We believe that the in-depth mechanism research will effectively promote the progress of platelet derivatives in CTE.

2.2 Activation of Platelet Derivatives

Activation of platelet concentrates leads to not only the release or derivation of stored GFs and cytokines but also rapid translation of preexisting mRNA (Senzel et al., 2009). Typically, exogenous thrombin and/or calcium should be added to PRP for platelet activation and coagulation for the initial burst release of GFs, followed by further sustained synthesis and secretion for the remaining several days of their life span (Freymiller, 2004). The contact with a silica surface activates platelets in PRF and the coagulation cascades, while trapping GFs and cytokines in the fibrin network for prolonged life span and slow release (Dohan et al., 2006; Ehrenfest et al., 2012). Bioactive molecules can also be released by simply breaking the membrane of platelets

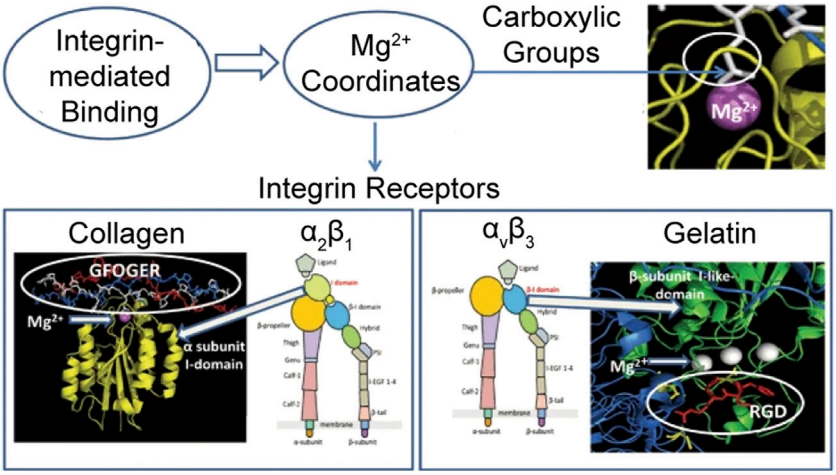

FIGURE 1 | Graphical representation of integrin-mediated adhesion on collagen and gelatin. Reproduced with permission from Davidenko et al. (2016).

during the production of PL or by mechanical force through a 0.45-μm syringe filter (Huynh et al., 2021).

Alternatively, local tissue can mediate endogenous release that results in a slower release of GFs and other chemical mediators (Mehta and Watson, 2008). The integrin signaling pathway of platelet activation is firstly recapitulated by Qureshi et al. from a protein–protein interaction network, as shown in **Figure 1** (Qureshi et al., 2009). Platelets can be activated *via* connection to integrin receptors on collagen or gelatin that initiate the degranulation and the release of GFs without additions or mechanical forces (Davidenko et al., 2016). Other approaches, such as thrombin receptor agonist peptide, showed less clot retraction and delayed release of GFs (Landesberg et al., 2005). Irmak et al. realized photo-activation of PRP by polychromatic light in the near-infrared region (PAC) and a constant release of GFs for several weeks (Irmak and Gumusderelioglu, 2020).

There are many available commercial platelet-rich concentrations producing systems with various platelet, white blood cell (WBC), and GF content (Castillo et al., 2011; Kushida et al., 2014), and the convenience of production and extensive use in clinics showed mutual promotion to the maturity and spread of the procedure.

2.3 Biological Function of Platelet Derivatives

Platelet derivatives have been applied in fields including wound healing, dental and oral surgery, and sports medicine (Crovetti et al., 2004; Lopez-Vidriero et al., 2010; Albanese et al., 2013). There are numerous clinical objectives, including promotion of tissue regeneration, prevention, or treatment of infectious diseases and pain relief (Bibbo and Hatfield, 2010; Drago et al., 2013; Drago et al., 2014; Chen et al., 2018).

PRP has been reported to significantly downgrade the expression of inflammation-induced cytokines and chemokines in chondrocytes, thus preserving proliferation and chondrogenic phenotypes reduced by pro-inflammatory cytokines with or without the enhancement by hyaluronic acid (HA) (Chen et al., 2014). Although a concentration of IL-1β is detected in some platelet derivatives, which is considered a defect of regeneration (Sundman et al., 2011), its rich in chemokine release upregulation of MSCs could reduce OA pathology through attraction and phagocytosis enhance of polymorphonuclear cells (Van Dalen et al., 2019).

In cartilage repair, platelet derivatives increase chondrocyte viability, proliferation, and migration (Chien et al., 2012; Fice et al., 2019). Chondrocytes cocultured with platelets showed significantly increased production of BMP-7, which upregulates proliferation by autocrine or paracrine and accelerates the appearance of hyaline-like tissue (Hidaka et al., 2003; Zhou et al., 2016). They enhance phenotype maintaining sulfated glycosaminoglycans (GAGs) secretion for ECM accumulation resulting in the presence of better mechanical properties (Akeda et al., 2006; Petrera et al., 2013; De Angelis et al., 2020). As shown in **Figures 2A,B**, implants soaked in PRP showed better integration to native tissue with both mechanical and histological evidence (Sermer et al., 2018; Wu C.-Y. et al., 2020). Furthermore, PRP induces redifferentiation of dedifferentiated chondrocytes (Jeyakumar et al., 2017).

Platelet derivatives showed similar promotive influences to MSCs too, as shown in **Figure 2C** (Mishra et al., 2009; Van Pham et al., 2013). Zaky et al. suggest conspecific PL being an effective and more beneficial substitute of fetal bovine serum to support the *in vitro* expansion of human bone marrow mesenchymal stem cells (BMSCs) for tissue-engineering applications based on findings that BMSCs cultured in media with PL and deprived of serum showed a high proliferation potential and formed organized ECM with embedded chondrocytes in lacunae (Zaky et al., 2008). Platelet-derived microparticles, fragments shed from the plasma membrane of activated platelets, were found in contact with synovial membrane–derived MSCs and promote their homing and adhesion to cartilage defects (Liang et al., 2020). In addition, platelet can elicit

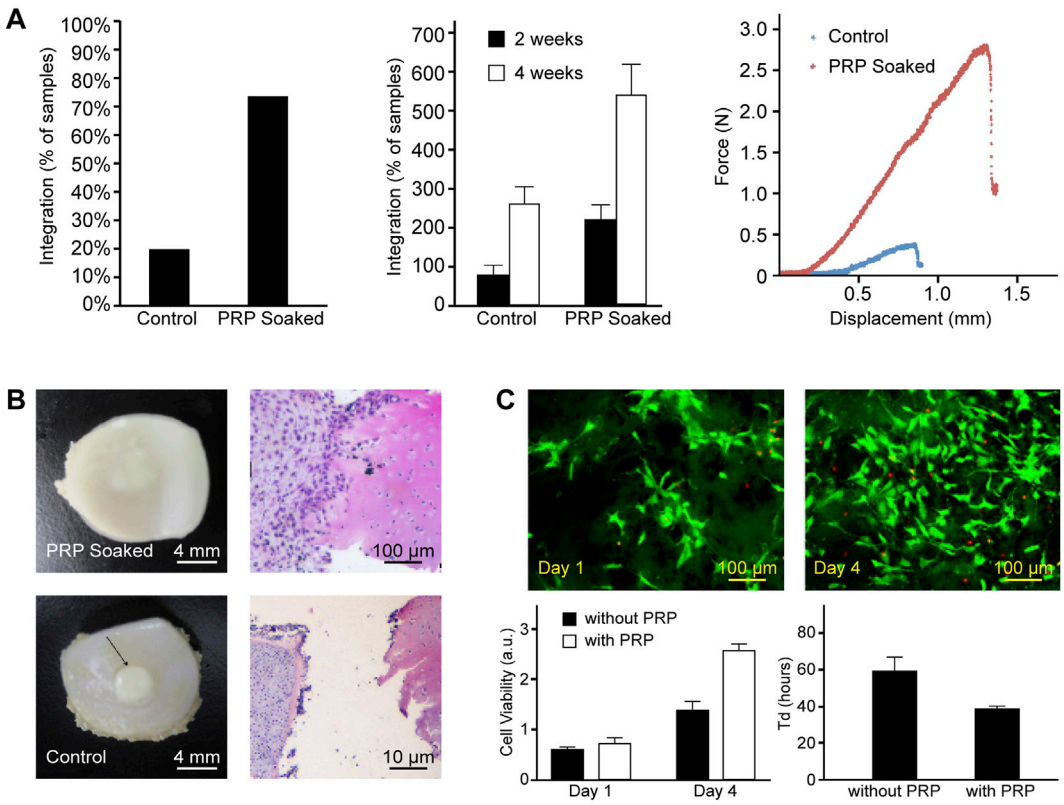

FIGURE 2 | Encapsulation of PRP enhances integration of implants with native tissue and MSC proliferation on scaffolds. **(A)** PRP-soaked bioengineered implants showed a higher percentage and greater strength of integration. **(B)** Gross and histological appearance of PRP-soaked and untreated implant–explant constructs. Reproduced with permission from Sermer et al. (2018). **(C)** Fluorescence images by LIVE/DEAD staining. Statistical results showed enhanced cell viability and a shortened doubling time of MSCs in the parylene-based scaffold when compared to the sample group without PRP. Reproduced with permission from Wu et al. (2020a).

chemotaxis and chemokinesis of MSCs, thus inducing recruitment of endogenous joint-resident MSCs and serve the regeneration purpose (Holmes et al., 2018; Zhang S. et al., 2020). Therefore, platelet derivative–loaded scaffold without seeded cells can still induce the repair of cartilage defects (Sun et al., 2010; Liu et al., 2015), and in some circumstance, additional MSCs are redundant (Zhang et al., 2015).

Previous prevailing views suggested that GFs are the main mediators of platelet derivatives' regenerative effects, and they are adopted as important characterization parameters second only to cell count (Fernandez-Medina et al., 2019; Oneto et al., 2020). With further insight into exosomes and their role in intercellular communication, it is also revealed that the packaged non-coding RNAs also contribute to their treatment of OA (Maehara et al., 2021; Puhm et al., 2021).

The mechanisms of GFs and micro RNAs in cartilage regeneration have been studied individually and thoroughly reviewed in the literature (Qian et al., 2017; Barbon et al., 2019; Chen et al., 2020). However, as biologics are complex mixtures, the biological action of platelet derivatives is due to the synergistic action of the components, and the crosstalk, synergism, or mutual antagonism between signaling pathways is unevaluable. Therefore, the underlying mechanism remains partially covered. In addition, their composition and efficacy are influenced by many factors, such as the extraction protocols, storage conditions, physical status, and gender of the donor (Evanson et al., 2014; Do Amaral et al., 2016; Yin et al., 2017; Fernandez-Medina et al., 2019; Kim et al., 2020; Delgado et al., 2021).

Standardization of platelet derivatives is urgently needed, although their biological origin ensures variability to some extent. Additional information is required to maximize reproducibility of results, not only characterizations of the final product, including detailed cell counts and quantities of representative GFs, but also protocols as detailed as a needle size used for drawing blood, temperature, and time from preparation to use (Fadadu et al., 2019). A standardized preparation protocol for robust production and an optimized dosage needs to be determined. However, it should be noted that the detailed characterization should be done in clinic only for research purposes rather than on every patient, as it violates the original intention of reducing the cost, and that may explain the insufficiency of product data for previous retrospective studies (Landi et al., 2011).

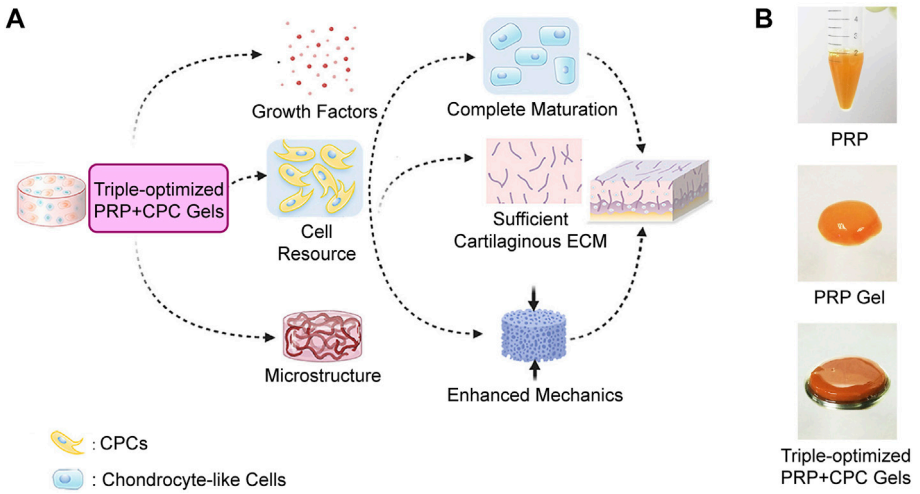

FIGURE 3 | Cellular, biochemical, and biomechanical triple-optimized PRP + CPC constructs enhance cartilage regeneration. **(A)** Schematic of the optimization strategy and potency of cartilage regeneration. **(B)** Gross appearance of PRP, PRP gel and triple-optimized PRP + CPC construct. Reproduced with permission from Wang et al. (2021).

3 ADDITION OF PLATELET DERIVATIVES IN CTE

The addition of platelet derivatives mainly serves two purposes. The first and most important is the rich biomolecules, such as GFs, it contains. The second is the fibrinogen and gelling ability after activation as all or part of the scaffold structure.

Platelet derivatives act as a bioactive cell scaffold to fill defects and enhance cartilage regeneration. The fibrin matrix not only forms a 3D system for cell culture but also reserves biomolecules with binding domains and releases them gradually during degradation (Xie et al., 2012; Martino et al., 2013). The mechanical stiffness of the fibrin clots depends upon the concentration of agonist (thrombin, calcium, fibrinogen, etc.), fibrin network, and crosslinking densities. For better mechanical properties, 10% $CaCl_2$-40 U/ml bovine thrombin in 1:9 v/v was recommended by Wang et al. and used as the scaffold for CPCs culture and cartilage defect repair *in vivo* (**Figure 3**) (Wang et al., 2021). Though the matrix of fibrin showed limited preservation of GFs, the release was significantly slowed down after 2 days (Liu et al., 2017). In fact, thrombin-activated platelets degranulate and release nearly 100% of the GFs within an hour (Marx, 2001). Moreover, its rapid degradation *in vivo* or with enzyme presents and low mechanical stiffness compared to articular cartilage expand the limitations of the scaffolds made of platelet derivatives alone (Lucarelli et al., 2010; Isobe et al., 2017; Huynh et al., 2021), while the integration with biomaterials will possess the scaffold of more controllable mechanical properties, proper degradation rate, and long-term release of bioactive molecules such as GFs (Sell et al., 2011; Bolandi et al., 2021).

3.1 CTE Scaffold With Platelet Derivatives

In this part of the review, the designs of platelet derivative–based CTE constructs are discussed by fabrication and composition. The designs of CTE constructs with addition of platelet derivatives in the scaffolds are summarized in **Table 1**.

3.1.1 Design of CTE Constructs From Application Point of View

When compared to the surgical options in clinic, the CTE constructs can be cultivated into artificial hyaline cartilage *in vitro*, trimmed, and transplanted into the defect as an improved OAT with sufficient graft but no donor site damage. With the help of developed bioreactors, automatic nutrition, standardized oxygen concentration, dynamic mechanical stimulation, and other improvements are applied for high-quality artificial cartilage (Guo et al., 2016; Fu et al., 2021). In addition, the condition of neo-cartilage formation is available for histological examination and non-invasive monitoring such as an ultrasonic signal analysis (Melchor et al., 2018). Otherwise, the cell-laden scaffolds can be implanted right after the fabrication as scaffold-assisted ACI with better cell adhesion and anabolism and form neo-cartilage internal. The procedure is simplified and fewer devices are required.

Both open surgery and arthroscopic surgery are available for the implantation of CTE construct. The arthroscopic procedure fits the cosmetical pursuit of the patients. On the contrary, the open procedure provides sufficient exposure and direct access to intra-articular lesions and thus has advantages over arthroscopy when the defect is large or in restricted areas (Kizaki et al., 2021).

From the perspective of form, the CTE construct can be either solid or liquid before implantation, which is described as injectability.

3.1.1.1 Uninjectable Constructs

Strategies for uninjectable CTE constructs include those use solid scaffolds or injectable formula but are cultivated *in vitro* for graft. Various mature and innovative techniques are used for solid scaffold fabrication, such as solvent casting/particulate leaching,

TABLE 1 | Designs of CTE constructs with platelet derivatives in the scaffolds.

Category	Material	Design	Platelet derivatives	Activation method	Loading method technique	GFs reservation	Cell *in vitro*	Cell *in vivo*	References
ECM-based materials	Decellularized human placental	Solid scaffold	PRP	Integrin pathway	Immersion	Adsorption GF–binding domains	BMSCs	BMSCs	Ozdemir et al. (2020)
	Decellularized porcine cartilage	Microparticle + PRP Gel	PRP	Ca^{2+} and thrombin	Mixing and clotting	Adsorption GF–binding domains	Chondrocytes	Chondrocytes	Chen et al. (2021)
Natural polymers	Collagen	Bilayer solid scaffold	PRP	Integrin pathway	Dripping	Adsorption	N/A	None	Qi et al. (2009)
	Fibrin	Hydrogel	PRF exudates	Coagulation	Mixing	Physical encapsulation GF–binding domains	Chondrocytes	N/A	Chien et al. (2012)
	SF	Solid scaffold	PRP	None	Mixing	Physical encapsulation	Chondrocytes	N/A	Li et al. (2020)
	Agarose	Hydrogel	PRP	None	Mixing	Physical encapsulation	Chondrocytes	N/A	Yin et al. (2014)
	Algae	Injectable hydrogel	PRP	Ca^{2+}	Mixing	Adsorption Physical encapsulation	BMSCs	N/A	Gao et al. (2019)
	Gel MA	Triphasic 3D-printed hydrogel	PRP	Polychromatic light	Mixing	Adsorption Physical encapsulation	AdMSCs	N/A	Irmak and Gumusderelioglu (2021)
	Gel MA	3D-printed hydrogel	PRP	Integrin pathway	Mixing	Adsorption Physical encapsulation	BMSCs	None	Jiang et al. (2021)
	Gel MA	3D-printed hydrogel	PRP	Ca^{2+}	Coating	Attaching Adsorption	BMSCs	BMSCs	Luo et al. (2020)
	Gelatin–PEG–tyramine	Injectable hydrogel	PRP	Integrin pathway	Mixing	Adsorption Physical encapsulation	Chondrocytes	Chondrocytes	Lee et al. (2012a), Lee et al. (2012b)
	HA–tyramine	Injectable hydrogel	PL	Lysis	Mixing	Adsorption Physical encapsulation GF–binding domains	BMSCs	N/A	Jooybar et al. (2019)
	HA-o-nitrobenzyl alcohol	Injectable hydrogel	PRP	Integrin pathway	Mixing	Adsorption Physical encapsulation GF–binding domains	BMSCs	None	Liu et al. (2017)
	Chitosan/CS	Injectable nanoparticle hydrogel	PL	Lysis	Mixing	Adsorption GF–binding domains	AdMSCs	N/A	Santo et al. (2015)
	HA/CS/chitosan	Hydrogel	PRP	Integrin pathway	Mixing	Adsorption Physical encapsulation	AdMSCs	N/A	Khalilijafarabad et al. (2021)
	Fibrin/heparin/linker peptide	Hydrogel	PRP	Thrombin	Mixing	Physical encapsulation GF–binding domains	BMSCs	N/A	Ahmed et al. (2011)
Synthetic polymers	PLGA	Solid scaffold	PRP	Ca^{2+} and thrombin	Immersion-clotting	Adsorption	BMSCs	BMSCs	Tang et al. (2021b)
	PLGA	Bilayer solid scaffold	PRP	Ca^{2+}	Immersion	Adsorption	BMSCs	BMSCs	Zhang et al. (2015)
	PPX	Solid scaffold	PRP	None	Mixing	Physical encapsulation	AdMSCs	N/A	Wu et al. (2020a)
	PCLT–citrate	Solid scaffold	PRP clot exudates	Ca^{2+}	Immersion	Adsorption	Chondrocyte	N/A	Rothan et al. (2017)
	Dextran–tyramine	Injectable hydrogel	PL	Lysis	Mixing	Adsorption Physical encapsulation	BMSCs/ chondrocytes	N/A	Teixeira et al. (2012b)
	PCL/gelatin	Solid scaffold	PRP	Ca^{2+}	Mixing	Adsorption Physical encapsulation	BMSCs	None	Liu et al. (2015)
	Alg sulfate, PVA/Alg	Microparticle + Injectable hydrogel	PRP	Ca^{2+}	Mixing	Adsorption Physical encapsulation	AdMSCs	N/A	Bolandi et al. (2021)
	EPL/Heparin, PLEL	Nanoparticle + Injectable hydrogel	PL	Lysis	Mixing	Adsorption Physical encapsulation GF–binding domains	Chondrocytes	None	Tang et al. (2021)

(Continued on following page)

TABLE 1 | (*Continued*) Designs of CTE constructs with platelet derivatives in the scaffolds.

Category	Material	Design	Platelet derivatives	Activation method	Loading method technique	GFs reservation	Cell *in vitro*	Cell *in vivo*	References
Inorganic materials	PCL/chitosan/PEG-biotin, collagen/fibrin	Microparticle + Hydrogel	Platelet-rich concentrate	Ca^{2+} and thrombin	Mixing	Physical encapsulation GF–binding domains	Chondrocytes	None	Filova et al. (2020)
	Calcium polyphosphate	Solid scaffold	PRP	None	Immersion	Adsorption	Chondrocytes	N/A	Sermer et al. (2018)
	β-TCP/gelatin	Biphasic Solid scaffold	PRP	Integrin pathway	Dripping	Adsorption	BMSCs	BMSCs	Seo et al. (2013); Seo et al. (2015)
	HAP/fibrin	Biphasic Solid scaffold	PRP	Ca^{2+} and thrombin	Immersion-clotting	Adsorption GF–binding domains	BMSCs	BMSCs	Jang et al. (2014)
	Nano-HAP/chitosan/SF	Solid scaffold	PRP	None	Dripping	Adsorption	BMSCs	BMSCs	Ruan et al. (2018)

Abbreviations: N/A, not applicable; PCL, poly(ε-caprolactone); PVA, poly(vinyl alcohol); EPL, ε-poly(L-lysine); PLEL, poly(d,L-lactide)-poly(ethylene glycol)-poly(d,L-lactide); PPX, poly(p-xylylene); PCLT, poly(caprolactone triol).

melt molding, gas foaming, phase separation, freeze drying, electrospinning, and additive manufacturing (Mabrouk et al., 2020). In addition to the highly control over the scaffold structure and evaluation of neo-tissue, uninjectable strategies easily realize the manufactory of multiphasic scaffolds to satisfy different mechanical and biological requirements in both cartilage and subchordal bone layer for cell specialization (Yousefi et al., 2015). The addition of platelet derivatives will be discussed in a later section of this article.

In situ assembly of CTE constructs with several commercialized materials is another option for convenient clinical use. The platelet derivatives are used as both GF-resources and structural components that hold everything together. HA-derivative felt, PRP or PRF, and cartilage fragments are orderly assembled as cell resource in the defect site with the bridge reinforced by additional fibrin glue (Marmotti et al., 2012; Marmotti et al., 2013). In the original hypothesis, cartilage harvesting should be performed right before implantation in the same operation, thus eliminating the effort and cost of cultivation (Marmotti et al., 2012). Though the sufficiency of chondrocyte is suspicious, the result supports the strategy which is closer to the clinic.

3.1.1.2 Injectable Constructs

The advantage of injectable CTE constructs is obvious: In addition to the cooperation with micro-invasive surgery, the initial fluidity allows conformal filling of irregular defects. The constructs are typically processed into small particles or *in situ* crosslinking hydrogels. As cartilage kibbling is a necessary procedure to minimize the time of chemical exposure during decellularization, ECM-based materials are sometimes present as particles available for injection (Sutherland et al., 2015). The addition of platelet derivatives synergizes the particle strategy as the coagulation entraps the particles in fibrin network and fixes them to the defect. The fixation and biophysical modification could also be realized by embedding in hydrogels (Williams et al., 2015; Raj et al., 2020). Chen et al. made a 3D semisolid gel of a mixture of decellularized porcine cartilage, chondrocyte suspension, and freshly activated PRP for *in vitro* and *in vivo* evaluation (Chen et al., 2021). The composite mimics the natural niche for chondrocytes and accelerated the regeneration of full-thickness osteochondral defects in mini-pigs. A similar system without cell transplantation was used through intra-articular administration in a rat OA model and proved efficient in cartilage repair (Wu et al., 2021).

As for injectable hydrogels, both physical and chemical crosslinking reactions are applicable. The former is generally induced in milder conditions with fewer toxicity problems, and the latter provides more stable networks and better mechanical properties (Wu J. et al., 2020). Ion-induced cross-linking is the most compatible physical cross-linking method for platelet derivatives as the most frequently used ionic agent, $CaCl_2$, also induces assembly of fibrinogen to form an interpenetrating polymeric network with the material that modulates properties of the hydrogel (Faramarzi et al., 2018). Thermosensitive

hydrogels that are present in the sol state at room temperature and gels at body temperature is used for PL-conducting nanoparticles delivery (Tang Q. et al., 2021).

Photo-crosslinking is a widely used chemical crosslinking strategy for *in situ* gelation. As illustrated in **Figure 4**, the procedure of surgery includes debridement of the lesion, application of liquid materials, and ultraviolet irradiation. Liu et al. developed an *o*-nitrobenzyl alcohol–modified HA hydrogel system, based on the photoinduced imine crosslinking reaction (Liu et al., 2017). Under light irradiation, aldehyde groups are generated that subsequently react with amino groups distributed on fibrinogen in the components of PRP and tissue surface, which forms hydrogels *in situ* and synchronously realizes covalent hydrogel-tissue adhesiveness and integration. In addition, the GFs were almost linearly released with no trend of decline shown in the release of GFs even after 14 days. Enzymatic crosslinking is another commonly used option for injectable application strategy of functionalized polymers that circumvents ultraviolet-induced free radicals (Klotz et al., 2016). Gelation of polymers with tyramine moieties can be catalyzed within minutes by horseradish peroxidase at very low concentrations of H_2O_2, and the injectable hydrogel system is used for local delivery of platelet derivatives and seed cells for chondrogenesis *in vitro* and *in vivo* (Lee et al., 2012a; b; Jooybar et al., 2019). Horseradish peroxidase also enables covalent crosslinking between tyramine groups on polymers and tyrosine-containing cartilaginous ECM proteins. Teixeira et al. fabricated a dextran–tyramine injectable hydrogel with a sustained release of PL. During *in situ* gelation, covalent bonding of the hydroxyphenyl residues in the material to tyrosine residues in cartilage matrix proteins enhances the adhesion and retention of the hydrogel, thus improving the integration of the newly regenerated tissue with native cartilage (Teixeira et al., 2012a; Teixeira et al., 2012b).

3.1.2 Techniques of Addition and the Influences on Scaffold Proprieties

On a micro level of most strategies, GFs are directly attached to biomaterial surface by noncovalent methods, including adsorption, physical encapsulation, or ECM components with GF-binding domains such as heparin, chondroitin sulfate, and hyaluronic acid (Seims et al., 2021). Hydrogen bonding, electrostatic interaction, and pore filling effect hold the bioactive molecules to the surface of material (Wang et al., 2020). Compared to covalent methods, fewer agents or linkers are involved and disruption of GF conformation is minimized. In addition, the molecular complexity of platelet derivatives greatly increases the difficulty of covalent techniques. On the other hand, fibrin/fibrinogen, component of platelet derivatives, shows high affinity for various kinds of GFs, and the promiscuously bound through heparin-binding domain will prolong the retention of GFs (Martino et al., 2013). Thus, compared to single GF-conducting, the combination of platelet derivatives and biomaterial is much simpler as both direct reservation of GFs and the tangle with fibrin can serve the purpose of a sustained release.

On a macro level, the combination of platelet derivatives and biomaterials is much simpler based on their solid or liquid form and technology roadmap. As the porous structure of scaffolds is necessary for cell ingrowth and nutrition transport, plenty of solid scaffolds possess the ability to absorb and contain liquids such as a sponge and hydrogels can take in soluble molecules during swelling (Hollister, 2005). Most of the platelet derivatives are presented in liquid form, thus the easiest way to load them onto molded scaffolds is by soaking (Rothan et al., 2017; Sermer et al., 2018). Additional small pores were discovered on the scaffold surface after PRP treatment and may improve cell adhesion (Gentile et al., 2010; Wei et al., 2019).

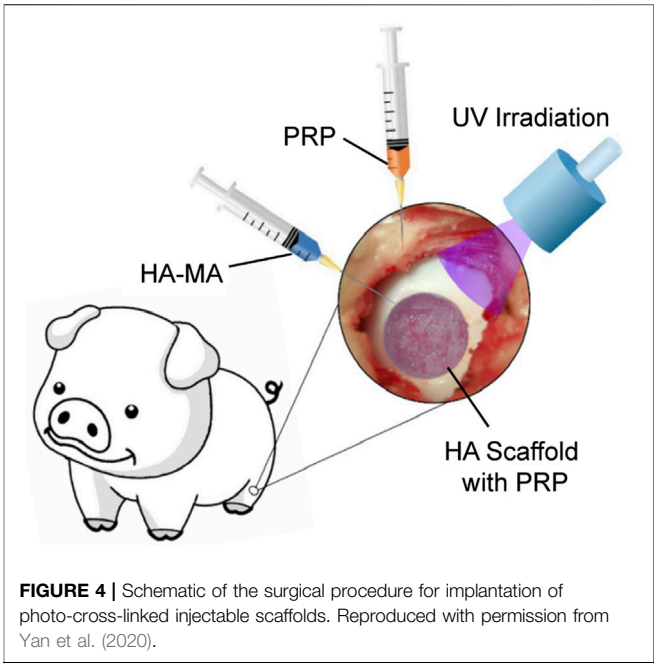

FIGURE 4 | Schematic of the surgical procedure for implantation of photo-cross-linked injectable scaffolds. Reproduced with permission from Yan et al. (2020).

The clotting ability of activated platelet derivatives expands their application so that they can be applied to the surface of CTE constructures as a coating (Luo et al., 2020), or gel with a 3D printed frame emerging-in as shown in **Figure 5A** (Tang Y. et al., 2021). In such cases, the platelet derivatives are attached to molded biomaterials, therefore the influences on mechanical and degradation properties are minor. Otherwise, the platelet derivatives are mixed with biomaterials before molding and participate in the structure of CTE as illustrated in **Figure 5B**. Mild molding conditions are required for activity reservation of platelets or molecules.

Freeze-dried PL is a powdered mixture of GFs and was first incorporated into an electrospun tissue engineering scaffold by (Sell et al., 2011). The addition of the product resulted in uneven fiber diameters and pore areas and decreased mechanical properties. The release of GFs varied from material to material, while all prolonged to more than 35 days. In some strategies with particle materials involved as previously mentioned, platelet derivatives are not only used as bioactive agent sources for biological promotion but also as a material to establish links between the particles and provide at least part of the mechanical support (Santo et al., 2015; Filova et al., 2020; Wu et al., 2021).

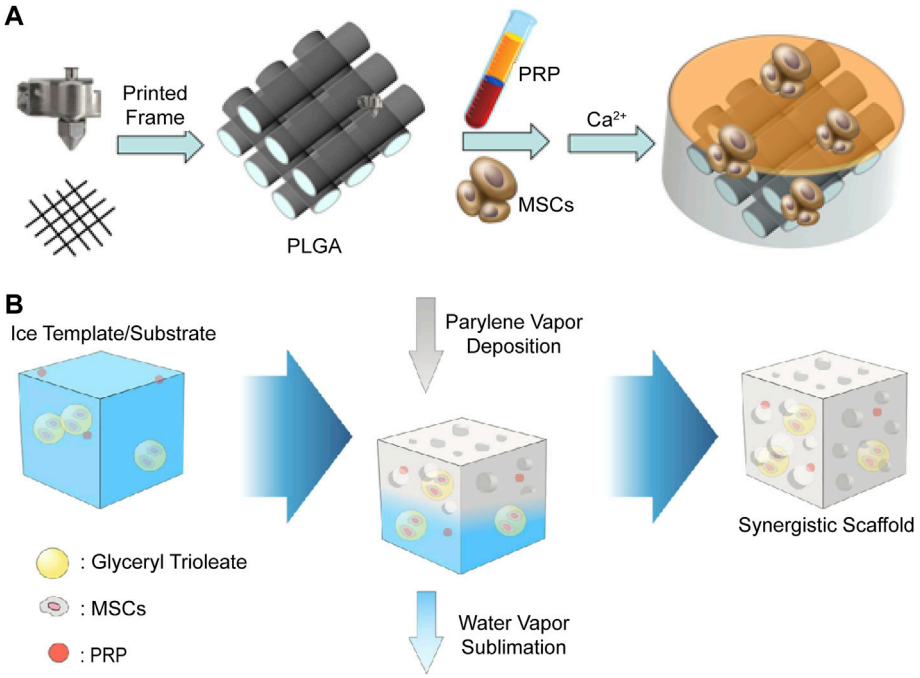

FIGURE 5 | Schematic illustration of two methods to add platelet derivatives into the scaffolds. **(A)** 3D printed PLGA frames are immersed in MSC-suspended PRP solution, and then the gelation of PRP is induced by addition of $CaCl_2$ solution with thrombin to complete the CTE construct. Reproduced with permission from Tang Y. et al. (2021). **(B)** Biomaterials, MSCs, and PRP are all mixed together before fabrication process to construct the synergistic scaffold. Reproduced with permission from Wu et al. (2020a).

When taken into the formula of a hydrogel, the fibrinogen/fibrin could participate in the cross-linked network. Therefore, the physical properties and biological performance of the scaffolds are influenced by the addition of platelet derivatives, roughly according to their form, the blending ratio, characteristic of the biomaterials, and the crosslinking methods. For example, when added into alginate (Alg) hydrogel, with the increase in PRP concentration, the compressive strength and elastic modulus increase, while the degradation is accelerated. In addition, the addition of PRP decreases the gelation rate and forms a more homogeneous structure (Faramarzi et al., 2018; Gao et al., 2019). Similar improvements in mechanical properties and degradation rate are observed in hybrid hydrogels composed of silk fibroin (SF) and PRP, while little variation of gelation time happens, which is mainly correlated with the ratio of poly (ethylene glycol) (PEG) agent and silk concentration (Zheng et al., 2018; Li et al., 2020). 20% (v/v) PRP-mixed 15% (w/v) methacrylated gelatin (Gel MA) hydrogel showed a slight increase in internal pore size and porosity, higher swelling ratio, and lower compressive modulus compared to those without PRP (Jiang et al., 2021). When PRP composed 50% of the hydrogel with a lower Gel MA concentration and was activated before photo-crosslinking, a significant increase in storage modulus, complex modulus, and weight loss were observed (Irmak and Gumusderelioglu, 2021). It is hard to find a pattern as the quality of platelet derivatives, blending ratio, and cross-linking degree vary from formula to formula and factors interact with each other. For example, with some functional groups of polymer chains occupied by electrostatic and hydrogen bonds, the addition of PRP reduces the extent of chemical crosslinking (Khalilijafarabad et al., 2021). In addition, components in platelet derivatives such as catalase could decompose the H_2O_2, thus inhibiting enzymatic crosslinking, and the addition of excess reagent can restore the storage modulus value (Jooybar et al., 2019). In conclusion, the optimum concentration of platelet derivatives is determined not only by their own bioactivity but also by the properties of the whole construct.

3.1.3 Materials of Platelet Derivative Conducting CTE Scaffolds

3.1.3.1 ECM-Based Materials

ECM is the natural template for synthesized scaffolds, which not only provides structural stability of tissue but also acts as a reservoir of signaling molecules that regulate behaviors and characteristics of the cells within (**Figure 6**) (Yue, 2014). ECM-based materials are harvested from native cartilage tissue or cultured chondrocytes or MSCs *in vitro*, decellularized with chemicals or devitalized by physical methods to minimize their immunogenicity (Sutherland et al., 2015). With advanced decellularization and devitalization techniques for better mechanical property preservation and recellularization, ECM-based materials appear to be promising for hyaline CTE applications (Huang et al., 2017). In addition, the avascularity and dense nature of articular cartilage may help reduce immune response. So far, xenogeneic decellularized cartilaginous biomaterials have shown good biocompatibility and little excessive rejection (Von Bomhard et al., 2019; Das et al., 2021). Ozdemir et al. loaded allogenic PRP and human

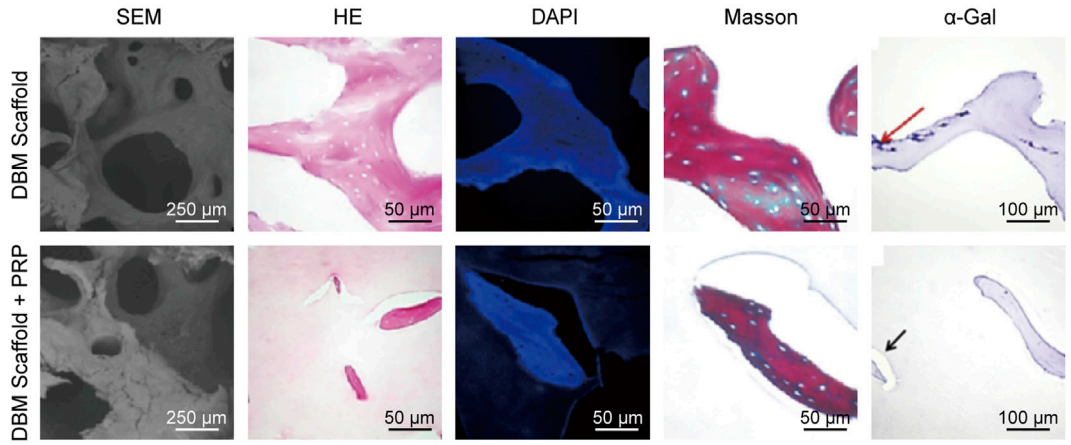

FIGURE 6 | Characterization of decellularized bone matrix scaffolds with PRP. Reproduced with permission from Leng et al. (2020).

BMSCs onto decellularized human placenta scaffolds for treatment of rat osteochondral defects. Though only non-significant improvement by PRP and BMSCs is observed in histological evaluation, evidence of strong chondrocyte proliferation and matrix production and MSCs' living and differentiation still supports the use of xenogeneic decellularized ECM for cartilage regeneration (Ozdemir et al., 2020).

3.1.3.2 Polymers

Compared to ECM-based materials, polymers are from broader and more abundant sources, with more controllable composition and properties. Natural polymers that exist in the natural ECM of cartilage are popularly used as biomaterials in CTE, including HA, chondroitin sulfate, collagen and its derivative, gelatin (Jiang et al., 2021; Khalilijafarabad et al., 2021). Other natural polymers such as SF, chitosan, agarose, and Alg are also of wide use in tissue engineering. In addition to reliable biocompatibility and biodegradability, biological cues inherent in many natural polymers that promote desirable cell responses also support their use in CTE. Rapid degradation and weak mechanical properties that most natural polymers mutually possess can be remedied with chemical modification or in cooperation with other materials.

Gelatin is a widely used biodegradable and biocompatible protein-based material derived from sources rich in type I collagen at a low cost by thermal denaturation and partial hydrolysis (Young et al., 2005). It is suitable for controlled release of bioactive molecules due to polyelectrolyte complexation and degradation itself (Yamamoto et al., 2001). To overcome its instability at body temperature, crosslinking methods are required to form a covalent network. Massive active groups such as –OH, –COOH, $–NH_2$, and –SH on the side chains of gelatin are available for functionalization (Sun et al., 2018), and a few are suitable for simultaneous crosslinking and cell encapsulation (Klotz et al., 2016). Of all the methods, photoinitiation provides the best temporal and spatial manipulation over the crosslinking process (Nguyen and West, 2002). Gel MA is the most welcome photo-crosslinking form, with most of the functional amino acid motifs undisturbed and compatible with 3D printing (Yue et al., 2015). Luo et al. 3D printed uniform porous scaffolds with BMSC-laden Gel MA at low concentration of 5% (w/v) for better cell migration and molecule exchange. After 3-week culture, the constructs are evenly applied with freshly activated PRP gel for GFs delivery and implanted intramuscularly in nude mice for another 4 weeks, resulting in hyaline-like tissue with islands of mature chondrocytes dispersed (Luo et al., 2020). As bioprinting is performed in a mild condition where cells can survive, platelet derivatives are able to be components of the bio-ink. Irmak and Gumusderelioglu diluted Gel MA into gradient concentrations with different ratios of PRP, added adipose-derived mesenchymal stem cells (AdMSCs) and gradually 3D printed, photo-activated and cross-linked a tri-layered scaffold to mimic the natural cartilage–interface–bone structure. Constructs are cultured with a mixture of equivalent osteogenic medium and chondrogenic medium in an incubator. AdMSCs were evenly distributed in the osteochondral constructs, differentiated into chondrogenic, hypertrophic, and osteogenic phenotypes based on their location in different phases of the scaffold and formed corresponding tissues *in vitro* (Irmak and Gumusderelioglu, 2021).

HA, chondroitin sulfate (CS) and keratan sulfate are the main GAGs in adult articular cartilage (Kuiper and Sharma, 2015). In particular, various dosage forms of HA and CS are of wide clinical use in OA (Bishnoi et al., 2016; Gupta et al., 2019). Reviews assessing the therapeutic mechanisms of HA indicate that it generally expresses antioxidative, anti-inflammatory, and analgesic effects, and by direct interaction with chondrocytes through particular receptors, it mediates chondroprotective, anti-apoptosis, and cartilage repair effects (Gupta et al., 2019). Similarly, the anti-inflammatory and structure-modifying activities also support the application of CS as a symptomatic slow-acting drug (Bishnoi et al., 2016). As biomaterials, both HA and CS exhibit long-term safety and high biocompatibility for CTE applications. A chemical cross-linked HA/CS/

carboxymethyl Chitosan hydrogel was used as a PRP conveyer and induced the process of differentiation of stem cells into cartilage *in vitro*. Through interaction between the aldehyde group of the hydrogel and the amino groups of PRP, it was loaded onto the hydrogel for prolonged release along with the degradation of crosslinking network (Khalilijafarabad et al., 2021). Both HA and CS are negatively charged polymeric molecules available for polyelectrolyte complexation that form particles or aggregates for drug delivery systems (Meka et al., 2017). Santo et al. fabricated CS/Chitosan nanoparticles and PL is loaded through adsorption with an expected burst release of GFs. Through a centrifugation step, the nanoparticles are assembled together, obtaining a hydrogel-like construct that entraps the stem cells in the network. The presence of PL stabilized the construct and held the cells, especially before the deposit of new ECM (Santo et al., 2015).

SF is a protein-based polymer derived from silk produced by insects such as silkworms and spiders. It is immunologically inert and possesses low inflammatory potential, purified by complete removal of potential inflammation-inducing proteins and debris (Kundu et al., 2014). The degradation rate depends on the methods of isolation and reconstruction process of the material, the different formats it's fabricated into, and the abundance of enzymes in the implantation site (Debari et al., 2021). Bio-ink composed of SF and PRP is 3D-printed to scaffolds and cross linked with PEG. With a cumulative GF release increase compared to thrombin-activated PRP gel, the GFs were almost linearly released for 14 days (**Figure 7**) (Li et al., 2020).

Compared to some proteins, polysaccharides do not suffer from some of the disadvantages, such as immunogenicity and potential risk of animal-originated pathogen transmission. Chitosan is a natural polysaccharide derived from chitin, a structural element in the exoskeleton of crustacean, which is easily extracted from the protective shells of crabs and shrimp (Hamed et al., 2016). It is distinctive due to the cationic nature capable of polyelectrolyte complexes forming and its broad use in drug delivery and ECM mim icking (Bhattarai et al., 2010; Zhang Z. et al., 2021).

Agarose is the unmodified neutral backbone of agar, extracted from cell walls of algae, that can self-assemble into a thermal-reversible gel (Michel et al., 2006). Its mechanical behaviors are easily modified by concentration to mimic articular cartilage upon static or dynamic loading (Salati et al., 2020). Lacking integrin binding sites, agarose shows less promotion of cell adhesion compared to collagen, but exceeds in cellular metabolism and biosynthesis of chondrocytes (Guaccio et al., 2008). Yin et al. fabricated PRP–agarose gels encapsulated with chondrocytes via physical blend and accelerated cell proliferation in the early stage of *in vitro* cultivation (Yin et al., 2014). Agarose exhibits neutral surface charge at different pH that results in weak electrostatic forces for GFs adsorption and reservation, thus chemical modification and copolymerization with other polymers are recommended for sustained release (Yazdi et al., 2020).

Alginic acid is another abundant marine bio-polymer, extracted from brown seaweed. Its linear structure is composed of alternating blocks of 1–4 linked α-L-guluronic and β-D-mannuronic acid residues, and the stacking of guluronic-blocks with divalent cations such as Ca^{2+} presence causes gelation and cross-linking under mild conditions (George and Abraham, 2006). As previously mentioned, calcium ion also triggers platelet degranulation and coagulation cascades, and therefore the gelation agent matches and forms a more homogeneous structure (Gao et al., 2019). Similar to agarose, pure Alg is short of cell adhesion signaling moieties and the blending of adhesive proteins, such as fibrinogen in platelet derivatives, mends the drawback and provides extra promotion for rich in GFs.

Synthetic polymers are attractive candidates for CTE for typically more flexible and controllable mechanical and chemical properties than those of natural materials, readily available, and relatively low cost of industrial scale production. Poly (α-hydroxy) acids are the most widely used synthetic degradable polymers such as polycaprolactone, poly (glycolic acid), poly (lactic acid), and their copolymers (Place et al., 2009). Bioresorbable devices made from aliphatic polyesters are now used worldwide in surgery and controlled drug delivery (Albertsson and Varma, 2003). Platelet derivatives can be loaded onto such commercialized scaffolds by methods as simple as immersing (Kreuz et al., 2013). Their simplicity compared to protein-based polymers leaves them with low immunogenicity but also limited bioactivity. Chemical modification is an important method of functionalization, but the addition of platelet derivatives is an easier way. Tang et al. 3D printed the frame with poly (lactide-co-glycolide) (PLGA) and laden BMSCs and PRP onto the scaffold in one step though induced gelation. The scaffold had been completely absorbed 8 weeks after the implantation (Tang Y. et al., 2021). Zhang et al. manufactured bilayer PLGA scaffolds with different pore sizes by compression molding and particulate leaching. BMSCs are seeded onto the scaffold and incubated for attachment, and PRP is loaded prior to implantation surgery. The addition of platelet derivatives resulted in better cartilage repair, and BMSCs enhanced osteogenesis of subchondral bone, while the PLGA scaffolds have not been completely degraded 6 months after the implantation (Zhang et al., 2015). Elasticity shock absorbent material is a direction for mechanical modification of synthetic polymers that physically mimics the natural ECM of chondrocytes, and addition of platelet derivatives serves as a biological improvement. Rothan et al. structured polycaprolactone triol–citrate with the solvent-casting/particulate leaching method, soaked in soluble platelet releasates and freeze-dried to produce an elastomeric porous scaffold (Rothan et al., 2017).

3.1.3.3 Inorganic Materials

Inorganic materials, including metallic materials, bioactive glasses, and bio-ceramics, are widely used in bone tissue engineering, for their load-bearing ability (Collins et al., 2021). As one of two nourishing pathways, subchondral bone plays an important role in cartilage regeneration and influences the quality of regenerated tissue (Nishitani et al., 2009; Zhang S.-Y. et al., 2021). In addition, a stronger structure for the subchondral bone layer could reduce the shear forces and benefit the integration of the cartilage layer under dynamic conditions. Thus, the introduction of bone-mimicking materials for subchondral

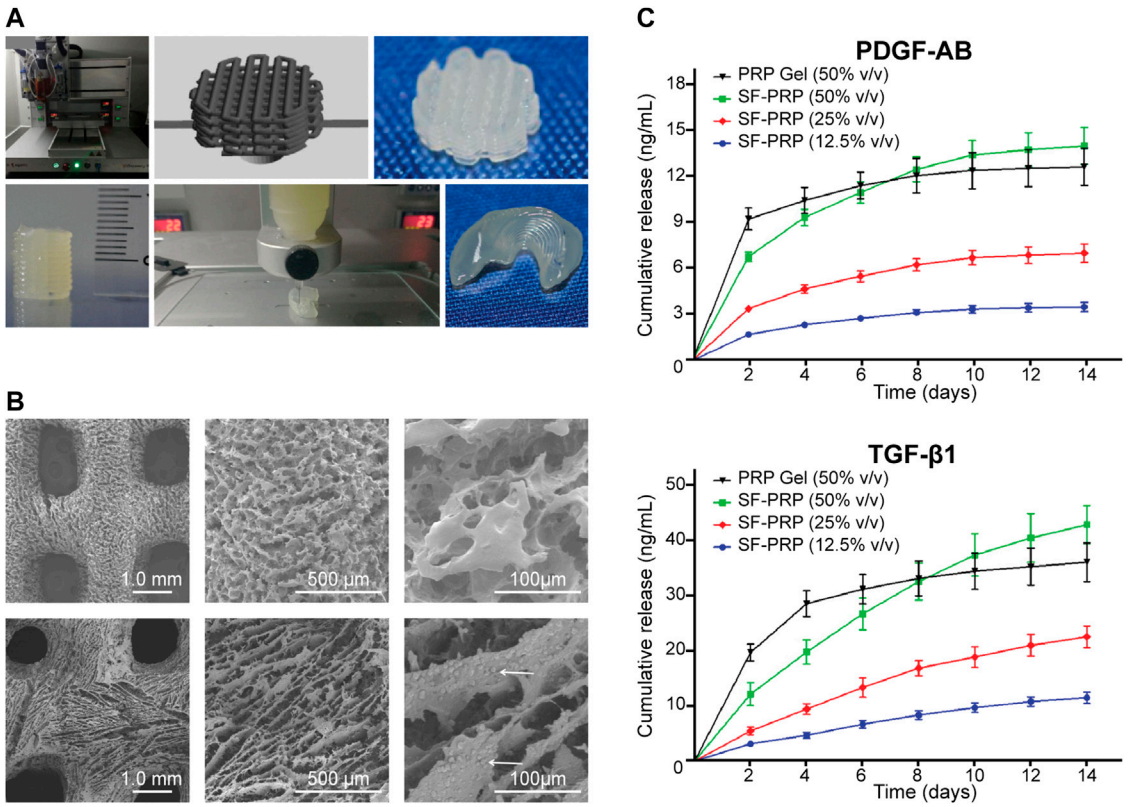

FIGURE 7 | 3D bio-printed scaffolds of SF-PRP bio-inks with high resolution, shape fidelity, and controlled release of GFs. **(A)** Three-dimensional printing process of objects with various shapes and dimensions. **(B)** Microstructure of 3D printed scaffolds (white arrows indicate platelets attached in the scaffold). **(C)** Sustained release of GFs from SF-PRP hydrogels. Reproduced with permission from Li et al. (2020).

bone reconstruction in a biphasic or multiphasic scaffold has drawn a lot of attention.

Of all the inorganic materials for bone reconstruction, calcium phosphate ceramics hold the most similarity to the mineral components of bone. By chemical compositions and crystal phases, they are classified into different types, among which hydroxyapatite (HAP), beta-tricalcium phosphate (β-TCP), and their mixture known as biphasic calcium phosphate. In addition structure-based osteoconductivity, they also serve as a source of calcium ions for ossification through surface dissolution (Tang et al., 2018). They have been studied extensively and put into clinical use in bone substitution, reconstruction, and drug delivery (Ragaey and Van Sickels, 2017; Maenhoudt et al., 2018; Zhao et al., 2020). The porous structure of the materials also provides good absorption of liquid state platelet derivatives. Calcium polyphosphate substrates seeded with chondrocytes were used as bio-engineered cartilage in an *in vitro* model for study of integration (Theodoropoulos et al., 2011). Soaking in PRP before press-fit implantation increased expression of matrix degrading/remodeling genes at the interface and strengthened the integration to the host (Sermer et al., 2018). Jang et al. immersed cylinders of HAP into platelet-rich fibrin glue with MSCs and left a 2 mm depth of hydrogel as the cartilage layer. The platelet derivatives serve as cell-seeding media, the scaffold of the cartilage layer, and bioactive-molecule resources for both layers (Jang et al., 2014).

Combination of inorganic materials and polymers unites their advantages in osteochondral regeneration. With the addition of nano-HAP, the compressive strength was increased by more than two-fold compared to the CS/SF scaffold, with minor influence on degradation rate and facilitated cell adhesion and proliferation (Qi et al., 2014). PRP and lentivirus-transduced BMSCs with stable expression of BMP-2 was further loaded on the CS/SF/nano-HAP scaffold and provided promising results *in vivo*. In particular, the BMP-2 expression is significantly increased with the treatment of PRP, which indicates platelet derivatives as stimulators of transferred genes (Ruan et al., 2018). As most of the GFs in platelet derivatives are basic, acidic gelatin showed increased sorption through the formation of poly-ion complexes (Yamamoto et al., 2001). Seo et al. used an acidic gelatin β-TCP sponge as a carrier of PRP for cartilage and a basic sponge with BMP-2 for bone regeneration, and implanted MSC-loaded constructs sequentially into the osteochondral defect (Seo et al., 2013).

3.2 Other Usage of Platelet Derivatives in CTE

There are approaches to extended use of platelet derivatives other than scaffold ingredients for bioactive upgrade and structural

unity. For example, Brehm et al. use autologous PRP gel as an adhesive between the graft and the subchondral bone yet get little improvement in retention of the implant because of its poor mechanical strength and adhesion force (Brehm et al., 2006).

Successful attempts generally take advantage of bioactive molecules they content. As previously mentioned, platelet derivatives can be used as a culture medium supplement for CTE constructs before implantation for better cell proliferation, differentiation, and ECM accumulation (Petrera et al., 2013). As the metabolic activation of cells will not fade away so quickly and the reservation of active components by the scaffold, the improvement of cartilage formation could last after the implantation and improve the integrity of regenerated tissue to the surrounding tissue (Van Pham et al., 2013; Beigi et al., 2018).

Derived from PRP treatment of knee OA, intra-articular platelet derivatives can be used as treatment adjuvants for improvement after transplantation. Once per 2 weeks intra-articular injection of PRP enhanced BMSC-laden collagen scaffold implantation, resulted in a higher level of chondrogenic differentiation markers and historical score (Fang et al., 2019). Dominguez Perez et al. treated full-thickness articular cartilage defects of sheep with implantation of an autologous-based matrix of hyaline cartilage chips combined with plasma clot and intraarticular injection of PRP, resulting in hyaline cartilage regeneration and integration with surrounding margin at 6 months, with a similar structure and collagen expression pattern compared to the healthy adjacent cartilage (Dominguez Perez et al., 2019).

4 CONCLUSION AND PERSPECTIVES

Biological is a complex mixture of numerous bioactive molecules ideally functional in tissue regeneration. Although most of the main components of platelet derivatives have been independently studied in cartilage repair, the content of individual bioactive molecule varies depending on the protocol of extraction, format of the product, process of activation, and even health condition of the donor. Elucidation of the molecular complexity of these products and determining the dosing for specific tissue regeneration remain great challenges. The combination with biomaterials sustains the release of bioactive molecules and has made it even more complicated that both temporal and spatial distribution should be considered to meet the needs of developing CTE tissue and cells. Removal of defect components in platelet derivatives such as VEGF in cartilage diseases might be realized by "filter-like" advanced biomaterials or through an optimized extraction process (Zhu et al., 2013; Hamilton et al., 2016). Recent studies have emphasized mechanical stimulation and mechanical properties of the scaffold (Zhang and Yao, 2021), because the stem cell lineages are largely specified by matrix elasticity, in spite of the addition of soluble induction factors (Engler et al., 2006). According to these theories, the addition of platelet derivatives initiates the proliferation and differentiation of the stem cells, while the proper scaffold manufactured and the microenvironment the cell makes for itself will ultimately determine its destiny. Unlike most of the soluble factors, the addition of platelet derivatives sometimes influences the mechanical properties and degradation of the CTE construct. In those situations, they should be considered as a hybrid material rather than an additive AND a material. In addition, most of the studies evaluate the osteochondral regeneration by histological, histochemical, and biomechanical analysis. Although articular injection of PRP may not be as effective as previously thought in knee OA (Bennell et al., 2021), the improvement of motor function and alleviation of pain is still the ultimate purpose of the preclinical treatment of CTE and needs to be evaluated in follow-up studies.

In conclusion, the combination of platelet derivatives and biomaterials takes full advantage of the safe and low-cost resource of bioactive molecules that have been proved to accelerate cartilage regeneration and integration of neo-tissue and the origin parts. As variability is a common defect in biologicals, detailed information about platelet derivatives is required to maximize reproducibility of results. Further research of platelet derivatives in combination with biomaterials should aim to realize spatiotemporal delivery to meet the regeneration of articular cartilage, restore the function of the joint, and ultimately improve patients' quality of life.

AUTHOR CONTRIBUTIONS

SW wrote the manuscript. XZ, WG, and WQ designed this work of review and revised the manuscript. RL and SW revised the manuscript. All authors contributed to manuscript revision, read, and approved the submitted version.

FUNDING

This work was funded by the National Natural Science Foundation of China, Grant/Award Number: 81901365, and Department of Finance of Jilin Province, Grant/Award Number: 2019SRCJ005, 2019SCZT007.

REFERENCES

Aatonen, M. T., Öhman, T., Nyman, T. A., Laitinen, S., Grönholm, M., and Siljander, P. R.-M. (2014). Isolation and Characterization of Platelet-Derived Extracellular Vesicles. *J. Extracell. Vesicles* 3, 24692. doi:10.3402/jev.v3.24692

Ahmed, T. A. E., Giulivi, A., Griffith, M., and Hincke, M. (2011). Fibrin Glues in Combination with Mesenchymal Stem Cells to Develop a Tissue-Engineered Cartilage Substitute. *Tissue Eng. Part A* 17, 323–335. doi:10.1089/ten.tea.2009.0773

Akbarzadeh, S., Mckenzie, M. B., Rahman, M. M., and Cleland, H. (2021). Allogeneic Platelet-Rich Plasma: Is it Safe and Effective for Wound Repair? *Eur. Surg. Res.* 62, 1–9. doi:10.1159/000514223

Akeda, K., An, H. S., Okuma, M., Attawia, M., Miyamoto, K., Thonar, E. J.-M. A., et al. (2006). Platelet-rich Plasma Stimulates Porcine Articular Chondrocyte Proliferation and Matrix Biosynthesis. *Osteoarthr. Cartil.* 14, 1272–1280. doi:10.1016/j.joca.2006.05.008

Albanese, A., Licata, M. E., Polizzi, B., and Campisi, G. (2013). Platelet-rich Plasma (PRP) in Dental and Oral Surgery: from the Wound Healing to Bone Regeneration. *Immun. Ageing* 10, 23. doi:10.1186/1742-4933-10-23

Albertsson, A.-C., and Varma, I. K. (2003). Recent Developments in Ring Opening Polymerization of Lactones for Biomedical Applications. *Biomacromolecules* 4, 1466–1486. doi:10.1021/bm034247a

Anderson, D. E., Williams, R. J., Deberardino, T. M., Taylor, D. C., Ma, C. B., Kane, M. S., et al. (2017). Magnetic Resonance Imaging Characterization and Clinical Outcomes after NeoCart Surgical Therapy as a Primary Reparative Treatment for Knee Cartilage Injuries. *Am. J. Sports Med.* 45, 875–883. doi:10.1177/0363546516677255

Bal, B. S., Rahaman, M. N., Jayabalan, P., Kuroki, K., Cockrell, M. K., Yao, J. Q., et al. (2010). In Vivooutcomes of Tissue-Engineered Osteochondral Grafts. *J. Biomed. Mat. Res.* 9999B, NA. doi:10.1002/jbm.b.31571

Barbon, S., Stocco, E., Macchi, V., Contran, M., Grandi, F., Borean, A., et al. (2019). Platelet-Rich Fibrin Scaffolds for Cartilage and Tendon Regenerative Medicine: From Bench to Bedside. *Ijms* 20, 1701. doi:10.3390/ijms20071701

Beigi, M.-H., Atefi, A., Ghanaei, H.-R., Labbaf, S., Ejeian, F., and Nasr-Esfahani, M.-H. (2018). Activated Platelet-Rich Plasma Improves Cartilage Regeneration Using Adipose Stem Cells Encapsulated in a 3D Alginate Scaffold. *J. Tissue Eng. Regen. Med.* 12, 1327–1338. doi:10.1002/term.2663

Bennell, K. L., Paterson, K. L., Metcalf, B. R., Duong, V., Eyles, J., Kasza, J., et al. (2021). Effect of Intra-articular Platelet-Rich Plasma vs Placebo Injection on Pain and Medial Tibial Cartilage Volume in Patients with Knee Osteoarthritis. *JAMA* 326, 2021–2030. doi:10.1001/jama.2021.19415

Bhattarai, N., Gunn, J., and Zhang, M. (2010). Chitosan-based Hydrogels for Controlled, Localized Drug Delivery. *Adv. Drug Deliv. Rev.* 62, 83–99. doi:10.1016/j.addr.2009.07.019

Bian, L., Zhai, D. Y., Mauck, R. L., and Burdick, J. A. (2011). Coculture of Human Mesenchymal Stem Cells and Articular Chondrocytes Reduces Hypertrophy and Enhances Functional Properties of Engineered Cartilage. *Tissue Eng. Part A* 17, 1137–1145. doi:10.1089/ten.TEA.2010.0531

Bibbo, C., and Hatfield, P. S. (2010). Platelet-Rich Plasma Concentrate to Augment Bone Fusion. *Foot Ankle Clin.* 15, 641–649. doi:10.1016/j.fcl.2010.09.002

Bishnoi, M., Jain, A., Hurkat, P., and Jain, S. K. (2016). Chondroitin Sulphate: a Focus on Osteoarthritis. *Glycoconj J.* 33, 693–705. doi:10.1007/s10719-016-9665-3

Blair, P., and Flaumenhaft, R. (2009). Platelet α-granules: Basic Biology and Clinical Correlates. *Blood Rev.* 23, 177–189. doi:10.1016/j.blre.2009.04.001

Bolandi, B., Imani, R., Bonakdar, S., and Fakhrzadeh, H. (2021). Chondrogenic Stimulation in Mesenchymal Stem Cells Using Scaffold-based Sustained Release of Platelet-rich Plasma. *J. Appl. Polym. Sci.* 138, 50075. doi:10.1002/app.50075

Boswell, S. G., Cole, B. J., Sundman, E. A., Karas, V., and Fortier, L. A. (2012). Platelet-Rich Plasma: A Milieu of Bioactive Factors. *Arthrosc. J. Arthrosc. Relat. Surg.* 28, 429–439. doi:10.1016/j.arthro.2011.10.018

Brehm, W., Aklin, B., Yamashita, T., Rieser, F., Trüb, T., Jakob, R. P., et al. (2006). Repair of Superficial Osteochondral Defects with an Autologous Scaffold-free Cartilage Construct in a Caprine Model: Implantation Method and Short-Term Results. *Osteoarthr. Cartil.* 14, 1214–1226. doi:10.1016/j.joca.2006.05.002

Castillo, T. N., Pouliot, M. A., Kim, H. J., and Dragoo, J. L. (2011). Comparison of Growth Factor and Platelet Concentration from Commercial Platelet-Rich Plasma Separation Systems. *Am. J. Sports Med.* 39, 266–271. doi:10.1177/0363546510387517

Cavallo, C., Filardo, G., Mariani, E., Kon, E., Marcacci, M., Pereira Ruiz, M. T., et al. (2014). Comparison of Platelet-Rich Plasma Formulations for Cartilage Healing. *J. Bone Jt. Surg. Am.* 96, 423–429. doi:10.2106/jbjs.M.00726

Chen, L., Liu, J., Guan, M., Zhou, T., Duan, X., and Xiang, Z. (2020). Growth Factor and its Polymer Scaffold-Based Delivery System for Cartilage Tissue Engineering. *Ijn* Vol. 15, 6097–6111. doi:10.2147/ijn.S249829

Chen, W.-H., Lo, W.-C., Hsu, W.-C., Wei, H.-J., Liu, H.-Y., Lee, C.-H., et al. (2014). Synergistic Anabolic Actions of Hyaluronic Acid and Platelet-Rich Plasma on Cartilage Regeneration in Osteoarthritis Therapy. *Biomaterials* 35, 9599–9607. doi:10.1016/j.biomaterials.2014.07.058

Chen, X., Jones, I. A., Park, C., and Vangsness, C. T., Jr. (2018). The Efficacy of Platelet-Rich Plasma on Tendon and Ligament Healing: A Systematic Review and Meta-Analysis with Bias Assessment. *Am. J. Sports Med.* 46, 2020–2032. doi:10.1177/0363546517743746

Chen, Y. T., Lee, H. S., Hsieh, D. J., Periasamy, S., Yeh, Y. C., Lai, Y. P., et al. (2021). 3D Composite Engineered Using Supercritical CO 2 Decellularized Porcine Cartilage Scaffold, Chondrocytes, and PRP: Role in Articular Cartilage Regeneration. *J. Tissue Eng. Regen. Med.* 15, 163–175. doi:10.1002/term.3162

Chien, C.-S., Ho, H.-O., Liang, Y.-C., Ko, P.-H., Sheu, M.-T., and Chen, C.-H. (2012). Incorporation of Exudates of Human Platelet-Rich Fibrin Gel in Biodegradable Fibrin Scaffolds for Tissue Engineering of Cartilage. *J. Biomed. Mat. Res.* 100B, 948–955. doi:10.1002/jbm.b.32657

Collins, M. N., Ren, G., Young, K., Pina, S., Reis, R. L., and Oliveira, J. M. (2021). Scaffold Fabrication Technologies and Structure/Function Properties in Bone Tissue Engineering. *Adv. Funct. Mat.* 31, 2010609. doi:10.1002/adfm.202010609

Crovetti, G., Martinelli, G., Issi, M., Barone, M., Guizzardi, M., Campanati, B., et al. (2004). Platelet Gel for Healing Cutaneous Chronic Wounds. *Transfus. Apher. Sci.* 30, 145–151. doi:10.1016/j.transci.2004.01.004

Das, P., Mishra, R., Devi, B., Rajesh, K., Basak, P., Roy, M., et al. (2021). Decellularized Xenogenic Cartilage Extracellular Matrix (ECM) Scaffolds for the Reconstruction of Osteochondral Defects in Rabbits. *J. Mat. Chem. B* 9, 4873–4894. doi:10.1039/d1tb00314c

Davidenko, N., Schuster, C. F., Bax, D. V., Farndale, R. W., Hamaia, S., Best, S. M., et al. (2016). Evaluation of Cell Binding to Collagen and Gelatin: a Study of the Effect of 2D and 3D Architecture and Surface Chemistry. *J. Mat. Sci. Mat. Med.* 27, 148. doi:10.1007/s10856-016-5763-9

De Angelis, E., Grolli, S., Saleri, R., Conti, V., Andrani, M., Berardi, M., et al. (2020). Platelet Lysate Reduces the Chondrocyte Dedifferentiation during *In Vitro* Expansion: Implications for Cartilage Tissue Engineering. *Res. Veterinary Sci.* 133, 98–105. doi:10.1016/j.rvsc.2020.08.017

Debari, M. K., King, C. I., Iii, Altgold, T. A., and Abbott, R. D. (2021). Silk Fibroin as a Green Material. *ACS Biomater. Sci. Eng.* 7, 3530–3544. doi:10.1021/acsbiomaterials.1c00493

Delgado, D., Bilbao, A. M., Beitia, M., Garate, A., Sánchez, P., González-Burguera, I., et al. (2021). Effects of Platelet-Rich Plasma on Cellular Populations of the Central Nervous System: The Influence of Donor Age. *Ijms* 22, 1725. doi:10.3390/ijms22041725

Dhurat, R., and Sukesh, M. (2014). Principles and Methods of Preparation of Platelet-Rich Plasma: A Review and Author′s Perspective. *J. Cutan. Aesthet. Surg.* 7, 189–197. doi:10.4103/0974-2077.150734

Do Amaral, R. J. F. C., Da Silva, N. P., Haddad, N. F., Lopes, L. S., Ferreira, F. D., Filho, R. B., et al. (20162016). Platelet-Rich Plasma Obtained with Different Anticoagulants and Their Effect on Platelet Numbers and Mesenchymal Stromal Cells Behavior *In Vitro*. *Stem Cells Int.* 2016, 1–11. doi:10.1155/2016/7414036

Dohan, D. M., Choukroun, J., Diss, A., Dohan, S. L., Dohan, A. J. J., Mouhyi, J., et al. (2006). Platelet-rich Fibrin (PRF): a Second-Generation Platelet Concentrate. Part II: Platelet-Related Biologic Features. *Oral Surg. Oral Med. Oral Pathology, Oral Radiology, Endodontology* 101, e45–e50. doi:10.1016/j.tripleo.2005.07.009

Dohan, D. M., Del Corso, M., and Charrier, J.-B. (2007). Cytotoxicity Analyses of Choukroun's Platelet-Rich Fibrin (PRF) on a Wide Range of Human Cells: The Answer to a Commercial Controversy. *Oral Surg. Oral Med. Oral Pathology, Oral Radiology, Endodontology* 103, 587–593. doi:10.1016/j.tripleo.2007.03.016

Domínguez Pérez, J. M., Fernández-Sarmiento, J. A., Aguilar García, D., Granados Machuca, M. d. M., Morgaz Rodríguez, J., Navarrete Calvo, R., et al. (2019). Cartilage Regeneration Using a Novel Autologous Growth Factors-Based Matrix for Full-Thickness Defects in Sheep. *Knee Surg. Sports Traumatol. Arthrosc.* 27, 950–961. doi:10.1007/s00167-018-5107-z

Drago, L., Bortolin, M., Vassena, C., Romanò, C. L., Taschieri, S., and Fabbro, M. D. (2014). Plasma Components and Platelet Activation Are Essential for the Antimicrobial Properties of Autologous Platelet-Rich Plasma: An *In Vitro* Study. *PLoS One* 9, e107813. doi:10.1371/journal.pone.0107813

Drago, L., Bortolin, M., Vassena, C., Taschieri, S., and Del Fabbro, M. (2013). Antimicrobial Activity of Pure Platelet-Rich Plasma against Microorganisms Isolated from Oral Cavity. *BMC Microbiol.* 13, 47. doi:10.1186/1471-2180-13-47

Engler, A. J., Sen, S., Sweeney, H. L., and Discher, D. E. (2006). Matrix Elasticity Directs Stem Cell Lineage Specification. *Cell.* 126, 677–689. doi:10.1016/j.cell.2006.06.044

Evanson, J. R., Guyton, M. K., Oliver, D. L., Hire, J. M., Topolski, R. L., Zumbrun, S. D., et al. (2014). Gender and Age Differences in Growth Factor Concentrations from Platelet-Rich Plasma in Adults. *Mil. Med.* 179, 799–805. doi:10.7205/milmed-d-13-00336

Fadadu, P. P., Mazzola, A. J., Hunter, C. W., and Davis, T. T. (2019). Review of Concentration Yields in Commercially Available Platelet-Rich Plasma (PRP) Systems: a Call for PRP Standardization. *Reg. Anesth. Pain Med.* 44, 652–659. doi:10.1136/rapm-2018-100356

Fang, D., Jin, P., Huang, Q., Yang, Y., Zhao, J., and Zheng, L. (2019). Platelet-rich Plasma Promotes the Regeneration of Cartilage Engineered by Mesenchymal Stem Cells and Collagen Hydrogel via the TGF-β/SMAD Signaling Pathway. *J. Cell. Physiol.* 234, 15627–15637. doi:10.1002/jcp.28211

Faramarzi, N., Yazdi, I. K., Nabavinia, M., Gemma, A., Fanelli, A., Caizzone, A., et al. (2018). Patient-Specific Bioinks for 3D Bioprinting of Tissue Engineering Scaffolds. *Adv. Healthc. Mat.* 7, 1701347. doi:10.1002/adhm.201701347

Fernández-Medina, T., Vaquette, C., and Ivanovski, S. (2019). Systematic Comparison of the Effect of Four Clinical-Grade Platelet Rich Hemoderivatives on Osteoblast Behaviour. *Ijms* 20, 6243. doi:10.3390/ijms20246243

Ferreira, P. M., Bozbas, E., Tannetta, S. D., Alroqaiba, N., Zhou, R., Crawley, J. T. B., et al. (2020). Mode of Induction of Platelet-Derived Extracellular Vesicles Is a Critical Determinant of Their Phenotype and Function. *Sci. Rep.* 10, 18061. doi:10.1038/s41598-020-73005-3

Fice, M. P., Miller, J. C., Christian, R., Hannon, C. P., Smyth, N., Murawski, C. D., et al. (2019). The Role of Platelet-Rich Plasma in Cartilage Pathology: An Updated Systematic Review of the Basic Science Evidence. *Arthrosc. J. Arthrosc. Relat. Surg.* 35, 961–976. doi:10.1016/j.arthro.2018.10.125

Filová, E., Tonar, Z., Lukášová, V., Buzgo, M., Litvinec, A., Rampichová, M., et al. (2020). Hydrogel Containing Anti-CD44-labeled Microparticles, Guide Bone Tissue Formation in Osteochondral Defects in Rabbits. *Nanomaterials* 10, 1504. doi:10.3390/nano10081504

Foster, T. E., Puskas, B. L., Mandelbaum, B. R., Gerhardt, M. B., and Rodeo, S. A. (2009). Platelet-Rich Plasma. *Am. J. Sports Med.* 37, 2259–2272. doi:10.1177/0363546509349921

Freymiller, E. G. (2004). Platelet-rich Plasma: Evidence to Support its Use. *J. Oral Maxillofac. Surg.* 62, 1046. doi:10.1016/j.joms.2004.05.205

Frojmovic, M. M., and Milton, J. G. (1982). Human Platelet Size, Shape, and Related Functions in Health and Disease. *Physiol. Rev.* 62, 185–261. doi:10.1152/physrev.1982.62.1.185

Fu, L., Li, P., Li, H., Gao, C., Yang, Z., Zhao, T., et al. (2021). The Application of Bioreactors for Cartilage Tissue Engineering: Advances, Limitations, and Future Perspectives. *Stem Cells Int.* 2021, 1–13. doi:10.1155/2021/6621806

Gaharwar, A. K., Peppas, N. A., and Khademhosseini, A. (2014). Nanocomposite Hydrogels for Biomedical Applications. *Biotechnol. Bioeng.* 111, 441–453. doi:10.1002/bit.25160

Gao, X., Gao, L., Groth, T., Liu, T., He, D., Wang, M., et al. (2019). Fabrication and Properties of an Injectable Sodium Alginate/PRP Composite Hydrogel as a Potential Cell Carrier for Cartilage Repair. *J. Biomed. Mat. Res.* 107, 2076–2087. doi:10.1002/jbm.a.36720

Gassling, V., Douglas, T., Warnke, P. H., Açil, Y., Wiltfang, J., and Becker, S. T. (2010). Platelet-rich Fibrin Membranes as Scaffolds for Periosteal Tissue Engineering. *Clin. Oral Implants Res.* 21, 543–549. doi:10.1111/j.1600-0501.2009.01900.x

Gentile, F., Tirinato, L., Battista, E., Causa, F., Liberale, C., Di Fabrizio, E. M., et al. (2010). Cells Preferentially Grow on Rough Substrates. *Biomaterials* 31, 7205–7212. doi:10.1016/j.biomaterials.2010.06.016

George, M., and Abraham, T. E. (2006). Polyionic Hydrocolloids for the Intestinal Delivery of Protein Drugs: Alginate and Chitosan - a Review. *J. Control. Release* 114, 1–14. doi:10.1016/j.jconrel.2006.04.017

Gomes, F. G., Andrade, A. C., Wolf, M., Hochmann, S., Krisch, L., Maeding, N., et al. (2022). Synergy of Human Platelet-Derived Extracellular Vesicles with Secretome Proteins Promotes Regenerative Functions. *Biomedicines* 10, 238. doi:10.3390/biomedicines10020238

Gruber, R., Karreth, F., Fischer, M. B., and Watzek, G. (2002). Platelet-released Supernatants Stimulate Formation of Osteoclast-like Cells through a prostaglandin/RANKL-dependent Mechanism. *Bone* 30, 726–732. doi:10.1016/s8756-3282(02)00697-x

Guaccio, A., Borselli, C., Oliviero, O., and Netti, P. A. (2008). Oxygen Consumption of Chondrocytes in Agarose and Collagen Gels: A Comparative Analysis. *Biomaterials* 29, 1484–1493. doi:10.1016/j.biomaterials.2007.12.020

Guo, T., Yu, L., Lim, C. G., Goodley, A. S., Xiao, X., Placone, J. K., et al. (2016). Effect of Dynamic Culture and Periodic Compression on Human Mesenchymal Stem Cell Proliferation and Chondrogenesis. *Ann. Biomed. Eng.* 44, 2103–2113. doi:10.1007/s10439-015-1510-5

Gupta, R. C., Lall, R., Srivastava, A., and Sinha, A. (2019). Hyaluronic Acid: Molecular Mechanisms and Therapeutic Trajectory. *Front. Vet. Sci.* 6. doi:10.3389/fvets.2019.00192

Hamed, I., Özogul, F., and Regenstein, J. M. (2016). Industrial Applications of Crustacean By-Products (Chitin, Chitosan, and Chitooligosaccharides): A Review. *Trends Food Sci. Technol.* 48, 40–50. doi:10.1016/j.tifs.2015.11.007

Hamilton, J. L., Nagao, M., Levine, B. R., Chen, D., Olsen, B. R., and Im, H.-J. (2016). Targeting VEGF and its Receptors for the Treatment of Osteoarthritis and Associated Pain. *J. Bone Min. Res.* 31, 911–924. doi:10.1002/jbmr.2828

Hidaka, C., Goodrich, L. R., Chen, C.-T., Warren, R. F., Crystal, R. G., and Nixon, A. J. (2003). Acceleration of Cartilage Repair by Genetically Modified Chondrocytes over Expressing Bone Morphogenetic Protein-7. *J. Orthop. Res.* 21, 573–583. doi:10.1016/s0736-0266(02)00264-4

Hollister, S. J. (2005). Porous Scaffold Design for Tissue Engineering. *Nat. Mater* 4, 518–524. doi:10.1038/nmat1421

Holmes, H. L., Wilson, B., Goerger, J. P., Silverberg, J. L., Cohen, I., Zipfel, W. R., et al. (2018). Facilitated Recruitment of Mesenchymal Stromal Cells by Bone Marrow Concentrate and Platelet Rich Plasma. *PLoS One* 13, e0194567. doi:10.1371/journal.pone.0194567

Huang, Z., Godkin, O., and Schulze-Tanzil, G. (2017). The Challenge in Using Mesenchymal Stromal Cells for Recellularization of Decellularized Cartilage. *Stem Cell. Rev Rep* 13, 50–67. doi:10.1007/s12015-016-9699-8

Hunziker, E. B., Quinn, T. M., and Häuselmann, H.-J. (2002). Quantitative Structural Organization of Normal Adult Human Articular Cartilage. *Osteoarthr. Cartil.* 10, 564–572. doi:10.1053/joca.2002.0814

Huynh, P. D., Vu, N. B., To, X. H.-V., and Le, T. M. (2021). Culture and Differentiation of Human Umbilical Cord-Derived Mesenchymal Stem Cells on Growth Factor-Rich Fibrin Scaffolds to Produce Engineered Cartilages. *Adv. Exp. Med. Biol.* [Epub ahead of print]. doi:10.1007/5584_2021_670

Irmak, G., and Gümüşderelioğlu, M. (2021). Patients- and Tissue-specific Bio-Inks with Photoactivated PRP and Methacrylated Gelatin for the Fabrication of Osteochondral Constructs. *Mater. Sci. Eng. C* 125, 112092. doi:10.1016/j.msec.2021.112092

Irmak, G., and Gümüşderelioğlu, M. (2020). Photo-activated Platelet-Rich Plasma (PRP)-based Patient-specific Bio-Ink for Cartilage Tissue Engineering. *Biomed. Mat.* 15, 065010. doi:10.1088/1748-605X/ab9e46

Isobe, K., Watanebe, T., Kawabata, H., Kitamura, Y., Okudera, T., Okudera, H., et al. (2017). Mechanical and Degradation Properties of Advanced Platelet-Rich Fibrin (A-PRF), Concentrated Growth Factors (CGF), and Platelet-Poor Plasma-Derived Fibrin (PPTF). *Int. J. Implant Dent.* 3, 17. doi:10.1186/s40729-017-0081-7

Jang, K.-M., Lee, J.-H., Park, C. M., Song, H.-R., and Wang, J. H. (2014). Xenotransplantation of Human Mesenchymal Stem Cells for Repair of Osteochondral Defects in Rabbits Using Osteochondral Biphasic Composite Constructs. *Knee Surg. Sports Traumatol. Arthrosc.* 22, 1434–1444. doi:10.1007/s00167-013-2426-y

Jeyakumar, V., Niculescu-Morzsa, E., Bauer, C., Lacza, Z., and Nehrer, S. (2017). Platelet-rich Plasma Supports Proliferation and Redifferentiation of Chondrocytes during *In Vitro* Expansion. *Front. Bioeng. Biotechnol.* 5. doi:10.3389/fbioe.2017.00075

Jiang, G., Li, S., Yu, K., He, B., Hong, J., Xu, T., et al. (2021). A 3D-Printed PRP-GelMA Hydrogel Promotes Osteochondral Regeneration through M2 Macrophage Polarization in a Rabbit Model. *Acta Biomater.* 128, 150–162. doi:10.1016/j.actbio.2021.04.010

Johnson, J., Wu, Y.-W., Blyth, C., Lichtfuss, G., Goubran, H., and Burnouf, T. (2021). Prospective Therapeutic Applications of Platelet Extracellular Vesicles. *Trends Biotechnol.* 39, 598–612. doi:10.1016/j.tibtech.2020.10.004

Jooybar, E., Abdekhodaie, M. J., Alvi, M., Mousavi, A., Karperien, M., and Dijkstra, P. J. (2019). An Injectable Platelet Lysate-Hyaluronic Acid Hydrogel Supports Cellular Activities and Induces Chondrogenesis of Encapsulated Mesenchymal Stem Cells. *Acta Biomater.* 83, 233–244. doi:10.1016/j.actbio.2018.10.031

Khalilijafarabad, N., Behnamghader, A., Khorasani, M. T., and Mozafari, M. (2021). Platelet-rich Plasma-hyaluronic Acid/chondrotin Sulfate/carboxymethyl Chitosan Hydrogel for Cartilage Regeneration. *Biotech App Biochem.* 69, 534–547. doi:10.1002/bab.2130

Khodadadi Yazdi, M., Taghizadeh, A., Taghizadeh, M., Stadler, F. J., Farokhi, M., Mottaghitalab, F., et al. (2020). Agarose-based Biomaterials for Advanced Drug Delivery. *J. Control. Release* 326, 523–543. doi:10.1016/j.jconrel.2020.07.028

Kim, J.-H., Park, Y.-B., Ha, C.-W., Roh, Y. J., and Park, J.-G. (2021). Adverse Reactions and Clinical Outcomes for Leukocyte-Poor versus Leukocyte-Rich Platelet-Rich Plasma in Knee Osteoarthritis: A Systematic Review and Meta-Analysis. *Orthop. J. Sports Med.* 9, 232596712110119. doi:10.1177/23259671211011948

Kim, J. I., Bae, H. C., Park, H. J., Lee, M. C., and Han, H. S. (2020). Effect of Storage Conditions and Activation on Growth Factor Concentration in Platelet-Rich Plasma. *J. Orthop. Res.* 38, 777–784. doi:10.1002/jor.24520

Kizaki, K., El-Khechen, H. A., Yamashita, F., Duong, A., Simunovic, N., Musahl, V., et al. (2021). Arthroscopic versus Open Osteochondral Autograft Transplantation (Mosaicplasty) for Cartilage Damage of the Knee: A Systematic Review. *J. Knee Surg.* 34, 094–107. doi:10.1055/s-0039-1692999

Klotz, B. J., Gawlitta, D., Rosenberg, A. J. W. P., Malda, J., and Melchels, F. P. W. (2016). Gelatin-Methacryloyl Hydrogels: Towards Biofabrication-Based Tissue Repair. *Trends Biotechnol.* 34, 394–407. doi:10.1016/j.tibtech.2016.01.002

Kobayashi, M., Kawase, T., Horimizu, M., Okuda, K., Wolff, L. F., and Yoshie, H. (2012). A Proposed Protocol for the Standardized Preparation of PRF Membranes for Clinical Use. *Biologicals* 40, 323–329. doi:10.1016/j.biologicals.2012.07.004

Kosik-Kozioł, A., Heljak, M., and Święszkowski, W. (2020). Mechanical Properties of Hybrid Triphasic Scaffolds for Osteochondral Tissue Engineering. *Mater. Lett.* 261, 126893. doi:10.1016/j.matlet.2019.126893

Kreuz, P. C., Gentili, C., Samans, B., Martinelli, D., Krüger, J. P., Mittelmeier, W., et al. (2013). Scaffold-assisted Cartilage Tissue Engineering Using Infant Chondrocytes from Human Hip Cartilage. *Osteoarthr. Cartil.* 21, 1997–2005. doi:10.1016/j.joca.2013.09.007

Kuiper, N. J., and Sharma, A. (2015). A Detailed Quantitative Outcome Measure of Glycosaminoglycans in Human Articular Cartilage for Cell Therapy and Tissue Engineering Strategies. *Osteoarthr. Cartil.* 23, 2233–2241. doi:10.1016/j.joca.2015.07.011

Kundu, B., Kurland, N. E., Bano, S., Patra, C., Engel, F. B., Yadavalli, V. K., et al. (2014). Silk Proteins for Biomedical Applications: Bioengineering Perspectives. *Prog. Polym. Sci.* 39, 251–267. doi:10.1016/j.progpolymsci.2013.09.002

Kushida, S., Kakudo, N., Morimoto, N., Hara, T., Ogawa, T., Mitsui, T., et al. (2014). Platelet and Growth Factor Concentrations in Activated Platelet-Rich Plasma: a Comparison of Seven Commercial Separation Systems. *J. Artif. Organs* 17, 186–192. doi:10.1007/s10047-014-0761-5

Landesberg, R., Burke, A., Pinsky, D., Katz, R., Vo, J., Eisig, S. B., et al. (2005). Activation of Platelet-Rich Plasma Using Thrombin Receptor Agonist Peptide. *J. Oral Maxillofac. Surg.* 63, 529–535. doi:10.1016/j.joms.2004.12.007

Landi, A., Tarantino, R., Marotta, N., Ruggeri, A. G., Domenicucci, M., Giudice, L., et al. (2011). The Use of Platelet Gel in Postero-Lateral Fusion: Preliminary Results in a Series of 14 Cases. *Eur. Spine J.* 20, 61–67. doi:10.1007/s00586-011-1760-3

Lane, J. G., Massie, J. B., Ball, S. T., Amiel, M. E., Chen, A. C., Bae, W. C., et al. (2004). Follow-Up of Osteochondral Plug Transfers in a Goat Model. *Am. J. Sports Med.* 32, 1440–1450. doi:10.1177/0363546504263945

Langer, R., and Vacanti, J. P. (1993). Tissue Engineering. *Science* 260, 920–926. doi:10.1126/science.8493529

Le, A. D. K., Enweze, L., Debaun, M. R., and Dragoo, J. L. (2018). Current Clinical Recommendations for Use of Platelet-Rich Plasma. *Curr. Rev. Musculoskelet. Med.* 11, 624–634. doi:10.1007/s12178-018-9527-7

Lee, H.-R., Park, K. M., Joung, Y. K., Park, K. D., and Do, S. H. (2012a). Platelet-rich Plasma Loaded Hydrogel Scaffold Enhances Chondrogenic Differentiation and Maturation with Up-Regulation of CB1 and CB2. *J. Control. Release* 159, 332–337. doi:10.1016/j.jconrel.2012.02.008

Lee, H.-R., Park, K. M., Joung, Y. K., Park, K. D., and Do, S. H. (2012b). Platelet-rich Plasma Loadedin Situ-Formed Hydrogel Enhances Hyaline Cartilage Regeneration by CB1 Upregulation. *J. Biomed. Mat. Res.* 100A, 3099–3107. doi:10.1002/jbm.a.34254

Lee, J.-C., Min, H. J., Park, H. J., Lee, S., Seong, S. C., and Lee, M. C. (2013). Synovial Membrane-Derived Mesenchymal Stem Cells Supported by Platelet-Rich Plasma Can Repair Osteochondral Defects in a Rabbit Model. *Arthrosc. J. Arthrosc. Relat. Surg.* 29, 1034–1046. doi:10.1016/j.arthro.2013.02.026

Leng, Y., Ren, G., Cui, Y., Peng, C., Wang, J., Wu, D., et al. (2020). Platelet-rich Plasma-Enhanced Osseointegration of Decellularized Bone Matrix in Critical-Size Radial Defects in Rabbits. *Ann. Transl. Med.* 8, 198. doi:10.21037/atm.2020.01.53

Li, Z., Zhang, X., Yuan, T., Zhang, Y., Luo, C., Zhang, J., et al. (2020). Addition of Platelet-Rich Plasma to Silk Fibroin Hydrogel Bioprinting for Cartilage Regeneration. *Tissue Eng. Part A* 26, 886–895. doi:10.1089/ten.tea.2019.0304

Liang, C., Huang, J., Luo, P., Wang, Z., He, J., Wu, S., et al. (2020). Platelet-Derived Microparticles Mediate the Intra-articular Homing of Mesenchymal Stem Cells in Early-Stage Cartilage Lesions. *Stem Cells Dev.* 29, 414–424. doi:10.1089/scd.2019.0137

Liu, J., Nie, H., Xu, Z., Guo, F., Guo, S., Yin, J., et al. (2015). Construction of PRP-Containing Nanofibrous Scaffolds for Controlled Release and Their Application to Cartilage Regeneration. *J. Mat. Chem. B* 3, 581–591. doi:10.1039/c4tb00515e

Liu, X., Yang, Y., Niu, X., Lin, Q., Zhao, B., Wang, Y., et al. (2017). An *In Situ* Photocrosslinkable Platelet Rich Plasma - Complexed Hydrogel Glue with Growth Factor Controlled Release Ability to Promote Cartilage Defect Repair. *Acta Biomater.* 62, 179–187. doi:10.1016/j.actbio.2017.05.023

Lopez-Vidriero, E., Goulding, K. A., Simon, D. A., Sanchez, M., and Johnson, D. H. (2010). The Use of Platelet-Rich Plasma in Arthroscopy and Sports Medicine: Optimizing the Healing Environment. *Arthrosc. J. Arthrosc. Relat. Surg.* 26, 269–278. doi:10.1016/j.arthro.2009.11.015

Lucarelli, E., Beretta, R., Beretta, R., Dozza, B., Tazzari, P., O'Connell, S., et al. (2010). A Recently Developed Bifacial Platelet-Rich Fibrin Matrix. *eCM* 20, 13–23. doi:10.22203/ecm.v020a02

Luo, C., Xie, R., Zhang, J., Liu, Y., Li, Z., Zhang, Y., et al. (2020). Low-Temperature Three-Dimensional Printing of Tissue Cartilage Engineered with Gelatin Methacrylamide. *Tissue Eng. Part C. Methods* 26, 306–316. doi:10.1089/ten.tec.2020.0053

Lyras, D. N., Kazakos, K., Georgiadis, G., Mazis, G., Middleton, R., Richards, S., et al. (2011). Does a Single Application of PRP Alter the Expression of IGF-I in the Early Phase of Tendon Healing? *J. Foot Ankle Surg.* 50, 276–282. doi:10.1053/j.jfas.2011.02.010

Mabrouk, M., Beherei, H. H., and Das, D. B. (2020). Recent Progress in the Fabrication Techniques of 3D Scaffolds for Tissue Engineering. *Mater. Sci. Eng. C* 110, 110716. doi:10.1016/j.msec.2020.110716

Maehara, M., Toyoda, E., Takahashi, T., Watanabe, M., and Sato, M. (2021). Potential of Exosomes for Diagnosis and Treatment of Joint Disease: Towards a Point-of-Care Therapy for Osteoarthritis of the Knee. *Ijms* 22, 2666. doi:10.3390/ijms22052666

Maenhoudt, W., Hallaert, G., Kalala, J.-P., Baert, E., Dewaele, F., Bauters, W., et al. (2018). Hydroxyapatite Cranioplasty: a Retrospective Evaluation of Osteointegration in 17 Cases. *Acta Neurochir.* 160, 2117–2124. doi:10.1007/s00701-018-3694-6

Marcacci, M., Kon, E., Delcogliano, M., Filardo, G., Busacca, M., and Zaffagnini, S. (2007). Arthroscopic Autologous Osteochondral Grafting for Cartilage Defects of the Knee. *Am. J. Sports Med.* 35, 2014–2021. doi:10.1177/0363546507305455

Marmotti, A., Bruzzone, M., Bonasia, D. E., Castoldi, F., Rossi, R., Piras, L., et al. (2012). One-step Osteochondral Repair with Cartilage Fragments in a Composite Scaffold. *Knee Surg. Sports Traumatol. Arthrosc.* 20, 2590–2601. doi:10.1007/s00167-012-1920-y

Marmotti, A., Bruzzone, M., Bruzzone, M., Bonasia, D., Castoldi, F., Von Degerfeld, M., et al. (2013). Autologous Cartilage Fragments in a Composite Scaffold for One Stage Osteochondral Repair in a Goat Model. *eCM* 26, 15–32. doi:10.22203/eCM.v026a02

Martino, M. M., Briquez, P. S., Ranga, A., Lutolf, M. P., and Hubbell, J. A. (2013). Heparin-binding Domain of Fibrin(ogen) Binds Growth Factors and Promotes Tissue Repair when Incorporated within a Synthetic Matrix. *Proc. Natl. Acad. Sci. U.S.A.* 110, 4563–4568. doi:10.1073/pnas.1221602110

Marx, R. E. (2001). Platelet-rich Plasma (PRP): what Is PRP and what Is Not PRP? *Implant Dent.* 10, 225–228. doi:10.1097/00008505-200110000-00002

M. Dohan Ehrenfest, D., Bielecki, T., Jimbo, R., Barbe, G., Del Corso, M., Inchingolo, F., et al. (2012). Do the Fibrin Architecture and Leukocyte Content Influence the Growth Factor Release of Platelet Concentrates? an Evidence-Based Answer Comparing a Pure Platelet-Rich Plasma (P-PRP) Gel and a Leukocyte- and Platelet-Rich Fibrin (L-PRF). *Cpb* 13, 1145–1152. doi:10.2174/138920112800624382

Mehta, S., and Watson, J. T. (2008). Platelet Rich Concentrate: Basic Science and Current Clinical Applications. *J. Orthop. Trauma* 22, 432–438. doi:10.1097/BOT.0b013e31817e793f

Meka, V. S., Sing, M. K. G., Pichika, M. R., Nali, S. R., Kolapalli, V. R. M., and Kesharwani, P. (2017). A Comprehensive Review on Polyelectrolyte Complexes. *Drug Discov. Today* 22, 1697–1706. doi:10.1016/j.drudis.2017.06.008

Melchor, J., López-Ruiz, E., Soto, J., Jiménez, G., Antich, C., Perán, M., et al. (2018). In-bioreactor Ultrasonic Monitoring of 3D Culture Human Engineered Cartilage. *Sensors Actuators B Chem.* 266, 841–852. doi:10.1016/j.snb.2018.03.152

Michel, G., Nyval-Collen, P., Barbeyron, T., Czjzek, M., and Helbert, W. (2006). Bioconversion of Red Seaweed Galactans: a Focus on Bacterial Agarases and Carrageenases. *Appl. Microbiol. Biotechnol.* 71, 23–33. doi:10.1007/s00253-006-0377-7

Mishra, A., Tummala, P., King, A., Lee, B., Kraus, M., Tse, V., et al. (2009). Buffered Platelet-Rich Plasma Enhances Mesenchymal Stem Cell Proliferation and Chondrogenic Differentiation. *Tissue Eng. Part C. Methods* 15, 431–435. doi:10.1089/ten.tec.2008.0534

Moroz, A., Bittencourt, R. A. C., Almeida, R. P., Felisbino, S. L., and Deffune, E. (2013). Platelet Lysate 3D Scaffold Supports Mesenchymal Stem Cell Chondrogenesis: An Improved Approach in Cartilage Tissue Engineering. *Platelets* 24, 219–225. doi:10.3109/09537104.2012.686255

Nguyen, K. T., and West, J. L. (2002). Photopolymerizable Hydrogels for Tissue Engineering Applications. *Biomaterials* 23, 4307–4314. doi:10.1016/s0142-9612(02)00175-8

Niemeyer, P., Laute, V., Zinser, W., John, T., Becher, C., Diehl, P., et al. (2020). Safety and Efficacy of Matrix-Associated Autologous Chondrocyte Implantation with Spheroid Technology Is Independent of Spheroid Dose after 4 Years. *Knee Surg. Sports Traumatol. Arthrosc.* 28, 1130–1143. doi:10.1007/s00167-019-05786-8

Nishitani, K., Shirai, T., Kobayashi, M., Kuroki, H., Azuma, Y., Nakagawa, Y., et al. (2009). Positive Effect of Alendronate on Subchondral Bone Healing and Subsequent Cartilage Repair in a Rabbit Osteochondral Defect Model. *Am. J. Sports Med.* 37, 139–147. doi:10.1177/0363546509350984

Oneto, P., Zubiry, P. R., Schattner, M., and Etulain, J. (2020). Anticoagulants Interfere with the Angiogenic and Regenerative Responses Mediated by Platelets. *Front. Bioeng. Biotechnol.* 8. doi:10.3389/fbioe.2020.00223

Özdemir, E., Emet, A., Hashemihesar, R., Yürüker, A. C. S., Kılıç, E., Uçkan Çetinkaya, D., et al. (2020). Articular Cartilage Regeneration Utilizing Decellularized Human Placental Scaffold, Mesenchymal Stem Cells and Platelet Rich Plasma. *Tissue Eng. Regen. Med.* 17, 901–908. doi:10.1007/s13770-020-00298-w

Pearle, A. D., Warren, R. F., and Rodeo, S. A. (2005). Basic Science of Articular Cartilage and Osteoarthritis. *Clin. Sports Med.* 24, 1–12. doi:10.1016/j.csm.2004.08.007

Petrera, M., De Croos, J. N. A., Iu, J., Hurtig, M., Kandel, R. A., and Theodoropoulos, J. S. (2013). Supplementation with Platelet-Rich Plasma Improves the *In Vitro* Formation of Tissue-Engineered Cartilage with Enhanced Mechanical Properties. *Arthrosc. J. Arthrosc. Relat. Surg.* 29, 1685–1692. doi:10.1016/j.arthro.2013.07.259

Place, E. S., George, J. H., Williams, C. K., and Stevens, M. M. (2009). Synthetic Polymer Scaffolds for Tissue Engineering. *Chem. Soc. Rev.* 38, 1139–1151. doi:10.1039/b811392k

Puhm, F., Boilard, E., and Machlus, K. R. (2021). Platelet Extracellular Vesicles. *Atvb* 41, 87–96. doi:10.1161/atvbaha.120.314644

Qi, X.-N., Mou, Z.-L., Zhang, J., and Zhang, Z.-Q. (2014). Preparation of Chitosan/silk Fibroin/hydroxyapatite Porous Scaffold and its Characteristics in Comparison to Bi-component Scaffolds. *J. Biomed. Mat. Res.* 102, 366–372. doi:10.1002/jbm.a.34710

Qi, Y. Y., Chen, X., Jiang, Y. Z., Cai, H. X., Wang, L. L., Song, X. H., et al. (2009). Local Delivery of Autologous Platelet in Collagen Matrix Simulated *In Situ* Articular Cartilage Repair. *Cell. Transpl.* 18, 1161–1169. doi:10.3727/096368909x12483162197169

Qian, Y., Han, Q., Chen, W., Song, J., Zhao, X., Ouyang, Y., et al. (2017). Platelet-Rich Plasma Derived Growth Factors Contribute to Stem Cell Differentiation in Musculoskeletal Regeneration. *Front. Chem.* 5. doi:10.3389/fchem.2017.00089

Quicke, J. G., Conaghan, P. G., Corp, N., and Peat, G. (2022). Osteoarthritis Year in Review 2021: Epidemiology & Therapy. *Osteoarthr. Cartil.* 30, 196–206. doi:10.1016/j.joca.2021.10.003

Qureshi, A. H., Chaoji, V., Maiguel, D., Faridi, M. H., Barth, C. J., Salem, S. M., et al. (2009). Proteomic and Phospho-Proteomic Profile of Human Platelets in Basal, Resting State: Insights into Integrin Signaling. *PLoS One* 4, e7627. doi:10.1371/journal.pone.0007627

Ragaey, M., and Van Sickels, J. E. (2017). Prevalence of Infection with the Use of β-tricalcium Phosphate as a Bone Graft Substitute during Le Fort I Osteotomy. *Int. J. Oral Maxillofac. Surg.* 46, 62–66. doi:10.1016/j.ijom.2016.10.001

Raj, R., Sobhan, P. K., Pratheesh, K. V., and Anilkumar, T. V. (2020). A Cholecystic Extracellular Matrix-based Hybrid Hydrogel for Skeletal Muscle Tissue Engineering. *J. Biomed. Mater Res.* 108, 1922–1933. doi:10.1002/jbm.a.36955

Rothan, H. A., Mahmod, S. A., Djordjevic, I., Golpich, M., Yusof, R., and Snigh, S. (2017). Polycaprolactone Triol-Citrate Scaffolds Enriched with Human Platelet Releasates Promote Chondrogenic Phenotype and Cartilage Extracellular Matrix Formation. *Tissue Eng. Regen. Med.* 14, 93–101. doi:10.1007/s13770-017-0023-8

Ruan, S., Deng, J., Yan, L., and Huang, W. (2018). Evaluation of the Effects of the Combination of BMP-2-modified BMSCs and PRP on C-artilage D-efects. *Exp. Ther. Med.* 16, 4569–4577. doi:10.3892/etm.2018.6776

Salati, M. A., Khazai, J., Tahmuri, A. M., Samadi, A., Taghizadeh, A., Taghizadeh, M., et al. (2020). Agarose-Based Biomaterials: Opportunities and Challenges in Cartilage Tissue Engineering. *Polymers* 12, 1150. doi:10.3390/polym12051150

Samuel, S., Ahmad, R. E., Ramasamy, T. S., Karunanithi, P., Naveen, S. V., and Kamarul, T. (2019). Platelet-rich Concentrate in Serum-free Medium Enhances Cartilage-specific Extracellular Matrix Synthesis and Reduces Chondrocyte Hypertrophy of Human Mesenchymal Stromal Cells Encapsulated in Alginate. *Platelets* 30, 66–74. doi:10.1080/09537104.2017.1371287

Santo, V. E., Popa, E. G., Mano, J. F., Gomes, M. E., and Reis, R. L. (2015). Natural Assembly of Platelet Lysate-Loaded Nanocarriers into Enriched 3D Hydrogels for Cartilage Regeneration. *Acta Biomater.* 19, 56–65. doi:10.1016/j.actbio.2015.03.015

Seims, K. B., Hunt, N. K., and Chow, L. W. (2021). Strategies to Control or Mimic Growth Factor Activity for Bone, Cartilage, and Osteochondral Tissue Engineering. *Bioconjugate Chem.* 32, 861–878. doi:10.1021/acs.bioconjchem.1c00090

Sell, S. A., Wolfe, P. S., Ericksen, J. J., Simpson, D. G., and Bowlin, G. L. (2011). Incorporating Platelet-Rich Plasma into Electrospun Scaffolds for Tissue Engineering Applications. *Tissue Eng. Part A* 17, 2723–2737. doi:10.1089/ten.tea.2010.0663

Senzel, L., Gnatenko, D. V., and Bahou, W. F. (2009). The Platelet Proteome. *Curr. Opin. Hematol.* 16, 329–333. doi:10.1097/MOH.0b013e32832e9dc6

Seo, J.-P., Kambayashi, Y., Itho, M., Haneda, S., Yamada, K., Furuoka, H., et al. (2015). Effects of a Synovial Flap and Gelatin/β-Tricalcium Phosphate Sponges Loaded with Mesenchymal Stem Cells, Bone Morphogenetic Protein-2, and Platelet Rich Plasma on Equine Osteochondral Defects. *Res. Veterinary Sci.* 101, 140–143. doi:10.1016/j.rvsc.2015.06.014

Seo, J.-P., Tanabe, T., Tsuzuki, N., Haneda, S., Yamada, K., Furuoka, H., et al. (2013). Effects of Bilayer Gelatin/β-Tricalcium Phosphate Sponges Loaded with Mesenchymal Stem Cells, Chondrocytes, Bone Morphogenetic Protein-2, and Platelet Rich Plasma on Osteochondral Defects of the Talus in Horses. *Res. Veterinary Sci.* 95, 1210–1216. doi:10.1016/j.rvsc.2013.08.016

Sermer, C., Kandel, R., Anderson, J., Hurtig, M., and Theodoropoulos, J. (2018). Platelet-rich Plasma Enhances the Integration of Bioengineered Cartilage with

Native Tissue in an *In Vitro* Model. *J. Tissue Eng. Regen. Med.* 12, 427–436. doi:10.1002/term.2468

Smyth, N. A., Haleem, A. M., Murawski, C. D., Do, H. T., Deland, J. T., and Kennedy, J. G. (2013). The Effect of Platelet-Rich Plasma on Autologous Osteochondral Transplantation. *J. Bone & Jt. Surg.* 95, 2185–2193. doi:10.2106/jbjs.L.01497

Sophia Fox, A. J., Bedi, A., and Rodeo, S. A. (2009). The Basic Science of Articular Cartilage: Structure, Composition, and Function. *Sports Health* 1, 461–468. doi:10.1177/1941738109350438

Sun, M., Sun, X., Wang, Z., Guo, S., Yu, G., and Yang, H. (2018). Synthesis and Properties of Gelatin Methacryloyl (GelMA) Hydrogels and Their Recent Applications in Load-Bearing Tissue. *Polymers* 10, 1290. doi:10.3390/polym10111290

Sun, Y., Feng, Y., Zhang, C. Q., Chen, S. B., and Cheng, X. G. (2010). The Regenerative Effect of Platelet-Rich Plasma on Healing in Large Osteochondral Defects. *Int. Orthop. (SICOT)* 34, 589–597. doi:10.1007/s00264-009-0793-2

Sundman, E. A., Cole, B. J., and Fortier, L. A. (2011). Growth Factor and Catabolic Cytokine Concentrations Are Influenced by the Cellular Composition of Platelet-Rich Plasma. *Am. J. Sports Med.* 39, 2135–2140. doi:10.1177/0363546511417792

Sutherland, A. J., Converse, G. L., Hopkins, R. A., and Detamore, M. S. (2015). The Bioactivity of Cartilage Extracellular Matrix in Articular Cartilage Regeneration. *Adv. Healthc. Mat.* 4, 29–39. doi:10.1002/adhm.201400165

Tang, Q., Lim, T., Shen, L.-Y., Zheng, G., Wei, X.-J., Zhang, C.-Q., et al. (2021). Well-dispersed Platelet Lysate Entrapped Nanoparticles Incorporate with Injectable PDLLA-PEG-PDLLA Triblock for Preferable Cartilage Engineering Application. *Biomaterials* 268, 120605. doi:10.1016/j.biomaterials.2020.120605

Tang, Y., Wang, H., Sun, Y., Jiang, Y., Fang, S., Kan, Z., et al. (2021). Using Platelet-Rich Plasma Hydrogel to Deliver Mesenchymal Stem Cells into Three-Dimensional PLGA Scaffold for Cartilage Tissue Engineering. *ACS Appl. Bio Mat.* 4, 8607–8614. doi:10.1021/acsabm.1c01160

Tang, Z., Li, X., Tan, Y., Fan, H., and Zhang, X. (2018). The Material and Biological Characteristics of Osteoinductive Calcium Phosphate Ceramics. *Regen. Biomater.* 5, 43–59. doi:10.1093/rb/rbx024

Teixeira, L. S. M., Bijl, S., Pully, V. V., Otto, C., Jin, R., Feijen, J., et al. (2012a). Self-attaching and Cell-Attracting Iin-Ssitu Forming Dextran-Tyramine Conjugates Hydrogels for Arthroscopic Cartilage Repair. *Biomaterials* 33, 3164–3174. doi:10.1016/j.biomaterials.2012.01.001

Teixeira, L. S. M., Leijten, J. C. H., Wennink, J. W. H., Chatterjea, A. G., Feijen, J., Van Blitterswijk, C. A., et al. (2012b). The Effect of Platelet Lysate Supplementation of a Dextran-Based Hydrogel on Cartilage Formation. *Biomaterials* 33, 3651–3661. doi:10.1016/j.biomaterials.2012.01.051

Thanasrisuebwong, P., Surarit, R., Bencharit, S., and Ruangsawasdi, N. (2019). Influence of Fractionation Methods on Physical and Biological Properties of Injectable Platelet-Rich Fibrin: An Exploratory Study. *Ijms* 20, 1657. doi:10.3390/ijms20071657

Theodoropoulos, J. S., Amritha De Croos, J. N., Park, S. S., Pilliar, R., and Kandel, R. A. (2011). Integration of Tissue-Engineered Cartilage with Host Cartilage: An *In Vitro* Model. *Clin. Orthop. Relat. Res.* 469, 2785–2795. doi:10.1007/s11999-011-1856-4

Torreggiani, E., Perut, F., Perut, F., Roncuzzi, L., Zini, N., Baglìo, S., et al. (2014). Exosomes: Novel Effectors of Human Platelet Lysate Activity. *eCM* 28, 137–151. doi:10.22203/eCM.v028a11

Van Dalen, S. C. M., Blom, A. B., Walgreen, B., Slöetjes, A. W., Helsen, M. M. A., Geven, E. J. W., et al. (2019). IL-1β-Mediated Activation of Adipose-Derived Mesenchymal Stromal Cells Results in PMN Reallocation and Enhanced Phagocytosis: A Possible Mechanism for the Reduction of Osteoarthritis Pathology. *Front. Immunol.* 10. doi:10.3389/fimmu.2019.01075

Van Pham, P., Bui, K. H.-T., Ngo, D. Q., Vu, N. B., Truong, N. H., Phan, N. L.-C., et al. (2013). Activated Platelet-Rich Plasma Improves Adipose-Derived Stem Cell Transplantation Efficiency in Injured Articular Cartilage. *Stem Cell. Res. Ther.* 4, 91. doi:10.1186/scrt277

Verrier, S., Meury, T. R., Meury, T., Kupcsik, L., Heini, P., Stoll, T., et al. (2010). Platelet-released Supernatant Induces Osteoblastic Differentiation of Human Mesenchymal Stem Cells: Potential Role of BMP-2. *eCM* 20, 403–414. doi:10.22203/ecm.v020a33

Von Bomhard, A., Elsaesser, A., Riepl, R., Pippich, K., Faust, J., Schwarz, S., et al. (2019). Cartilage Regeneration Using Decellularized Cartilage Matrix: Long-Term Comparison of Subcutaneous and Intranasal Placement in a Rabbit Model. *J. Cranio-Maxillofacial Surg.* 47, 682–694. doi:10.1016/j.jcms.2019.01.010

Wang, K., Li, J., Li, Z., Wang, B., Qin, Y., Zhang, N., et al. (2019). Chondrogenic Progenitor Cells Exhibit Superiority over Mesenchymal Stem Cells and Chondrocytes in Platelet-Rich Plasma Scaffold-Based Cartilage Regeneration. *Am. J. Sports Med.* 47, 2200–2215. doi:10.1177/0363546519854219

Wang, K., Li, J., Wang, Y., Wang, Y., Qin, Y., Yang, F., et al. (2021). Orchestrated Cellular, Biochemical, and Biomechanical Optimizations Endow Platelet-Rich Plasma-Based Engineered Cartilage with Structural and Biomechanical Recovery. *Bioact. Mater.* 6, 3824–3838. doi:10.1016/j.bioactmat.2021.03.037

Wang, L., Shi, C., Wang, L., Pan, L., Zhang, X., and Zou, J.-J. (2020). Rational Design, Synthesis, Adsorption Principles and Applications of Metal Oxide Adsorbents: a Review. *Nanoscale* 12, 4790–4815. doi:10.1039/c9nr09274a

Wei, L., Wu, S., Kuss, M., Jiang, X., Sun, R., Reid, P., et al. (2019). 3D Printing of Silk Fibroin-Based Hybrid Scaffold Treated with Platelet Rich Plasma for Bone Tissue Engineering. *Bioact. Mater.* 4, 256–260. doi:10.1016/j.bioactmat.2019.09.001

Wei, W., and Dai, H. (2021). Articular Cartilage and Osteochondral Tissue Engineering Techniques: Recent Advances and Challenges. *Bioact. Mater.* 6, 4830–4855. doi:10.1016/j.bioactmat.2021.05.011

Williams, C., Budina, E., Stoppel, W. L., Sullivan, K. E., Emani, S., Emani, S. M., et al. (2015). Cardiac Extracellular Matrix-Fibrin Hybrid Scaffolds with Tunable Properties for Cardiovascular Tissue Engineering. *Acta Biomater.* 14, 84–95. doi:10.1016/j.actbio.2014.11.035

Wu, C.-Y., Guo, C.-L., Yang, Y.-C., Huang, C.-W., Zeng, J.-Y., Guan, Z.-Y., et al. (2020). Parylene-Based Porous Scaffold with Functionalized Encapsulation of Platelet-Rich Plasma and Living Stem Cells for Tissue Engineering Applications. *ACS Appl. Bio Mat.* 3, 7193–7201. doi:10.1021/acsabm.0c00995

Wu, C. C., Tarng, Y. W., Hsu, D. Z., Srinivasan, P., Yeh, Y. C., Lai, Y. P., et al. (2021). Supercritical Carbon Dioxide Decellularized Porcine Cartilage Graft with PRP Attenuated OA Progression and Regenerated Articular Cartilage in ACLT-induced OA Rats. *J. Tissue Eng. Regen. Med.* 15, 1118–1130. doi:10.1002/term.3252

Wu, J., Chen, Q., Deng, C., Xu, B., Zhang, Z., Yang, Y., et al. (2020). Exquisite Design of Injectable Hydrogels in Cartilage Repair. *Theranostics* 10, 9843–9864. doi:10.7150/thno.46450

Xie, X., Wang, Y., Zhao, C., Guo, S., Liu, S., Jia, W., et al. (2012). Comparative Evaluation of MSCs from Bone Marrow and Adipose Tissue Seeded in PRP-Derived Scaffold for Cartilage Regeneration. *Biomaterials* 33, 7008–7018. doi:10.1016/j.biomaterials.2012.06.058

Yamamoto, M., Ikada, Y., and Tabata, Y. (2001). Controlled Release of Growth Factors Based on Biodegradation of Gelatin Hydrogel. *J. Biomaterials Sci. Polym. Ed.* 12, 77–88. doi:10.1163/156856201744461

Yan, W., Xu, X., Xu, Q., Sun, Z., Jiang, Q., and Shi, D. (2020). Platelet-rich Plasma Combined with Injectable Hyaluronic Acid Hydrogel for Porcine Cartilage Regeneration: a 6-month Follow-Up. *Regen. Biomater.* 7, 77–90. doi:10.1093/rb/rbz039

Yang, J., Zhang, Y. S., Yue, K., and Khademhosseini, A. (2017). Cell-laden Hydrogels for Osteochondral and Cartilage Tissue Engineering. *Acta Biomater.* 57, 1–25. doi:10.1016/j.actbio.2017.01.036

Yin, W., Xu, H., Sheng, J., Zhu, Z., Jin, D., Hsu, P., et al. (2017). Optimization of Pure Platelet-Rich Plasma Preparation: A Comparative Study of Pure Platelet-Rich Plasma Obtained Using Different Centrifugal Conditions in a Single-Donor Model. *Exp. Ther. Med.* 14, 2060–2070. doi:10.3892/etm.2017.4726

Yin, Z., Yang, X., Jiang, Y., Xing, L., Xu, Y., Lu, Y., et al. (2014). Platelet-rich Plasma Combined with Agarose as a Bioactive Scaffold to Enhance Cartilage Repair: An *In Vitro* Study. *J. Biomater. Appl.* 28, 1039–1050. doi:10.1177/0885328213492573

Young, S., Wong, M., Tabata, Y., and Mikos, A. G. (2005). Gelatin as a Delivery Vehicle for the Controlled Release of Bioactive Molecules. *J. Control. Release* 109, 256–274. doi:10.1016/j.jconrel.2005.09.023

Yousefi, A.-M., Hoque, M. E., Prasad, R. G. S. V., and Uth, N. (2015). Current Strategies in Multiphasic Scaffold Design for Osteochondral Tissue Engineering: A Review. *J. Biomed. Mat. Res.* 103, 2460–2481. doi:10.1002/jbm.a.35356

Yue, B. (2014). Biology of the Extracellular Matrix. *J. Glaucoma* 23, S20–S23. doi:10.1097/ijg.0000000000000108

Yue, K., Trujillo-De Santiago, G., Alvarez, M. M., Tamayol, A., Annabi, N., and Khademhosseini, A. (2015). Synthesis, Properties, and Biomedical Applications of Gelatin Methacryloyl (GelMA) Hydrogels. *Biomaterials* 73, 254–271. doi:10.1016/j.biomaterials.2015.08.045

Zaky, S. H., Ottonello, A., Strada, P., Cancedda, R., and Mastrogiacomo, M. (2008). Platelet Lysate Favoursin Vitroexpansion of Human Bone Marrow Stromal Cells for Bone and Cartilage Engineering. *J. Tissue Eng. Regen. Med.* 2, 472–481. doi:10.1002/term.119

Zhang, B., Huang, J., and Narayan, R. J. (2020). Gradient Scaffolds for Osteochondral Tissue Engineering and Regeneration. *J. Mat. Chem. B* 8, 8149–8170. doi:10.1039/d0tb00688b

Zhang, J., Liu, Y., Chen, Y., Yuan, L., Liu, H., Wang, J., et al. (2020). Adipose-Derived Stem Cells: Current Applications and Future Directions in the Regeneration of Multiple Tissues. *Stem Cells Int.* 2020, 1–26. doi:10.1155/2020/8810813

Zhang, S.-Y., Xu, H.-H., Xiao, M.-M., Zhang, J.-J., Mao, Q., He, B.-J., et al. (2021). Subchondral Bone as a Novel Target for Regenerative Therapy of Osteochondritis Dissecans: A Case Report. *Wjcc* 9, 3623–3630. doi:10.12998/wjcc.v9.i15.3623

Zhang, S., Hu, B., Liu, W., Wang, P., Lv, X., Chen, S., et al. (2020c). Articular Cartilage Regeneration: The Role of Endogenous Mesenchymal Stem/progenitor Cell Recruitment and Migration. *Seminars Arthritis Rheumatism* 50, 198–208. doi:10.1016/j.semarthrit.2019.11.001

Zhang, S., and Yao, Y. (2021). The Role of Mechanical Regulation in Cartilage Tissue Engineering. *CscrStem Cell. Res. Ther.* 16, 939–948. doi:10.2174/1574888x16666210303151538

Zhang, Y. T., Pan, Z., Xia, L. H., Liu, X. N., Guo, X. L., He, Y., et al. (2015). Bilayered Poly(lactide-Co-Glycolide) Scaffold with Platelet-Rich Plasma and Mesenchymal Stem Cells Improves Restoration of Osteochondral Defects. *J. Biomater. Tissue Eng.* 5, 757–765. doi:10.1166/jbt.2015.1388

Zhang, Z., Zhang, L., Li, C., Xie, X., Li, G., Hu, Z., et al. (2021). Research Progress of Chitosan-Based Biomimetic Materials. *Mar. Drugs* 19, 372. doi:10.3390/md19070372

Zhao, Z., Wang, G., Zhang, Y., Luo, W., Liu, S., Liu, Y., et al. (2020). The Effect of Calcium Sulfate/calcium Phosphate Composite for the Treatment of Chronic Osteomyelitis Compared with Calcium Sulfate. *Ann. Palliat. Med.* 9, 1821–1833. doi:10.21037/apm.2020.03.23

Zheng, Z., Wu, J., Liu, M., Wang, H., Li, C., Rodriguez, M. J., et al. (2018). 3D Bioprinting of Self-Standing Silk-Based Bioink. *Adv. Healthc. Mater.* 7, 1701026. doi:10.1002/adhm.201701026

Zhou, Q., Xu, C., Cheng, X., Liu, Y., Yue, M., Hu, M., et al. (2016). Platelets Promote Cartilage Repair and Chondrocyte Proliferation via ADP in a Rodent Model of Osteoarthritis. *Platelets* 27, 212–222. doi:10.3109/09537104.2015.1075493

Zhu, Y., Yuan, M., Meng, H. Y., Wang, A. Y., Guo, Q. Y., Wang, Y., et al. (2013). Basic Science and Clinical Application of Platelet-Rich Plasma for Cartilage Defects and Osteoarthritis: a Review. *Osteoarthr. Cartil.* 21, 1627–1637. doi:10.1016/j.joca.2013.07.017

Ziegler, C. G., Van Sloun, R., Gonzalez, S., Whitney, K. E., Dephillipo, N. N., Kennedy, M. I., et al. (2019). Characterization of Growth Factors, Cytokines, and Chemokines in Bone Marrow Concentrate and Platelet-Rich Plasma: A Prospective Analysis. *Am. J. Sports Med.* 47, 2174–2187. doi:10.1177/0363546519832003

Conflict of Interest: The authors declare that the research was conducted in the absence of any commercial or financial relationships that could be construed as a potential conflict of interest.

Publisher's Note: All claims expressed in this article are solely those of the authors and do not necessarily represent those of their affiliated organizations, or those of the publisher, the editors, and the reviewers. Any product that may be evaluated in this article, or claim that may be made by its manufacturer, is not guaranteed or endorsed by the publisher.

frontiers | Frontiers in Bioengineering and Biotechnology

ORIGINAL RESEARCH
published: 24 June 2022
doi: 10.3389/fbioe.2022.938337

Novel Design of the Compound Sleeve and Stem Prosthesis for Treatment of Proximal Femur Bone Defects Based on Topology Optimization

Haowen Xue[1†], *Haotian Bai*[1†], *Rongqi Zhou*[1†], *Jincheng Wang*[1†], *Bin Zhou*[2], *Xiaonan Wang*[1], *Wenbin Luo*[1] *and Xin Zhao*[1*]

[1]*Department of Orthopedics, the Second Hospital of Jilin University, Changchun, China,* [2]*The Second Clinical Medical College, Jilin University, Changchun, China*

OPEN ACCESS

Edited by:
Jianxun Ding,
Changchun Institute of Applied Chemistry (CAS), China

Reviewed by:
Shi Qingyu,
Harbin Medical University Cancer Hospital, China
Guanning Shang,
China Medical University, China
Yongcheng Hu,
Tianjin Hospital, China

***Correspondence:**
Xin Zhao
zhaoxin429@hotmail.com

[†]*These authors have contributed equally to this work and share first authorship*

Specialty section:
This article was submitted to Biomaterials, a section of the journal Frontiers in Bioengineering and Biotechnology

Received: *07 May 2022*
Accepted: *01 June 2022*
Published: *24 June 2022*

Citation:
Xue H, Bai H, Zhou R, Wang J, Zhou B, Wang X, Luo W and Zhao X (2022) Novel Design of the Compound Sleeve and Stem Prosthesis for Treatment of Proximal Femur Bone Defects Based on Topology Optimization. Front. Bioeng. Biotechnol. 10:938337. doi: 10.3389/fbioe.2022.938337

The loosening of traditional prosthetics is among the leading causes of surgical failure of proximal femoral bone defects. A novel compound sleeve and stem prosthesis was designed using an optimization methodology that combined an octet-truss porous structure with density-based topology optimization to improve stability, promote bone ingrowth, and enhance biomechanical properties. Biomechanical changes were assessed using finite element analysis. The distribution of stress, the strain energy density, and the relative micromotion in the optimized group were considered. The optimized sleeve prosthesis achieved a 31.5% weight reduction. The maximum stresses in the optimized group were observed to decrease by 30.33 and 4.74% at the back sleeve and neck part of stem prosthesis, with a 29.52% increase in the femur, respectively. The average stress in most selected regions in the optimized group was significantly greater than that in the original group ($p < 0.05$). The maximum relative micromotion decreased by 15.18% (from 63.9 to 54.2 μm) in the optimized group. The novel designed compound sleeve and stem prosthesis could effectively improve the biomechanical performance of next-generation prosthetics and provide a microenvironment for bone ingrowth. The presented method could serve as a model for clinical practice and a platform for future orthopedic surgery applications.

Keywords: finite element analysis, topology optimization, porous structure, bone defect, prosthesis design, proximal femur

INTRODUCTION

Proximal femoral bone defects often occur in patients with bone tumors, comminuted intertrochanteric fractures, and a history of revision hip arthroplasty (Gocer et al., 2016; De Martino et al., 2019; Toepfer et al., 2021). Due to substantial bone loss and altered anatomical features, the treatments are often challenging to implement. Several types of prostheses have been used in recent surgeries, including extension biotype stems and tumor prostheses for tight press-fit fixation through the distal femoral isthmus (Hasegawa et al., 2021). Porous structural femoral stems have been developed as biotype stems to achieve biological fixation by bone ingrowth, as proved in clinical and experimental practice (Wallace et al., 2020). However, long-term follow-up has revealed that current-generation prostheses with isthmus fixation appear to fail, and their loosening is often

characterized by bone loss and compromises revision and anchorage of further implants (Perry et al., 2016). Furthermore, preserving bone stock is especially crucial in patients with bone defects. As a result, it is necessary to create a novel prosthesis to improve the stability of prostheses and avoid bone resorption.

In current total hip arthroplasty (THA), significant peri-implant bone resorption and aseptic loosening can occur as a result of several factors, including stress shielding and wear failure (Wang, et al., 2018; Bartolomeu et al., 2019a). The primary reason for bone resorption and prosthesis loosening secondary to stress shielding is that the orthopedic implants that are stiffer than bone limit the transfer of a load to bones (Moyen et al., 1978; Zhang et al., 2020; Liu et al., 2021). According to Wolff's law, homeostatic mechanisms shift toward a catabolic state if the load on a bone is reduced (Frost, 1994). In order to ameliorate the mismatch of stiffness between the implant and the adjacent host bone, most relevant research work has focused on developing new porous metal materials, surface treatments, and prosthesis geometry designs (Wang et al., 2018; Bai et al., 2019). However, conventional THA stems are prone to causing stress shielding with proximal unloading and more distal load transfer (Yan et al., 2020; Hamilton, 2021). Short-stem prostheses have received increased attention in recent years owing to their bone-protective properties, which provide favorable conditions for revision and biomechanical advantages to reduce stress shielding (Bieger et al., 2013; Boese et al., 2016). However, using a short-stem prosthesis to treat proximal femoral bone defects is still under debate. Hence, a sleeve prosthesis was designed based on the principle of short-stem proximal fixation.

Topology optimization (TO) is a structural design approach that provides the optimal material distribution to reduce higher strength-to-weight ratios by eliminating material from the point of lowest stress while retaining high-stress regions (Zhang et al., 2020). Meanwhile, graded porous structures may be added to the optimized region of implants to provide a bone growth microenvironment and control surface modifications on the premise of providing biomechanical properties (Rahimizadeh et al., 2018; Bartolomeu et al., 2019a; Bai et al., 2019). Furthermore, several studies have concluded that less stiff materials and rougher surfaces generate better initial micromotions, which can be used to predict the process of osseointegration with adequate long-term stability (Pilliar et al., 1986; Alkhatib et al., 2019). To our knowledge, no relevant study has yet designed a proximal femoral sleeve prosthesis based on the TO technique. In addition, to further assess design rationality, finite element analysis (FEA) can be used to demonstrate differences in biomechanical conditions during the pre-clinical evaluation.

Therefore, this study proposed a novel TO prosthesis design for addressing bone defects in the proximal femur. According to a rational analysis of prosthesis and bone biomechanical properties, the new product could optimize the design of a sleeve prosthesis, secure the strength, and provide a biomechanical environment for bone ingrowth and long-term stability.

MATERIALS AND METHODS

Geometry and Meshing

Computationally designed novel implants were constructed using SolidWorks version 2021 (Dassault Systèmes, Vélizy-Villacoublay, France). The implant included an intramedullary needle–type stem prosthesis (length, 225 mm; diameter, 10 mm) and a proximal femoral sleeve (inner height, 65 mm; outer height, 100 mm; inner diameter, 10 mm; outer diameter, 15 mm) (**Figure 1**). A series of CT images from the imaging database of the Second Hospital of Jilin University were included in the present study. After excluding femur deformity, osteoporosis and any other factors that may change the normal femur anatomies such as fracture, infection, and tumor, a healthy 66-year-old male volunteer (weight, 75 kg) was selected. The femur 3-dimensional model from this volunteer was created via computed tomography (CT) imaging using the iCT 256 C T scanner (Philips, Eindhoven, Netherlands) with a slice thickness of 0.602 mm at 156 mA and 120 kVp. The medical image processing software program Mimics (version 19.0; Materialise, Leuven, Belgium) was applied to reconstruct the 3-dimensional model using the CT data and then convert this model into STL format. Magics version 21.0 (Materialise, Leuven, Belgium) was used to create an Evans type III intertrochanteric fracture bone defect to mimic a proximal femur bone defect (Evans, 1949). The femur was first resected at a 60-degree inclination horizontally from the lesser trochanter. Then, another horizontal resection was performed to generate the bone defect through the midpoint of the greater trochanter. For simplification purposes, the effects of the ligaments were neglected in the models. This study was approved by the ethics committee of the Second Hospital of Jilin University, and informed consent was obtained from all volunteers.

HyperMesh version 2020 (Altair Engineering, Troy, MI, United States) was used to generate triangular meshes and convert them into 4-node linear tetrahedron elements (C3D4). A sensitivity analysis of mesh quality was carried out until a change of <5% in the maximum principal stress was obtained by mesh refinement. Finally, an average mesh size of 1 mm was set onto the designed components.

Material Properties

The femur was defined as inhomogeneous with assigned material properties in Mimics for bone density (ρ) (Kg/m^3), elastic modulus (E) (MPa), and Poisson's ratio (ν) according to the gray values of the CT scan (**Figure 1A** and **Table 1**). According to the previous literature, Poisson's ratio was set to 0.30, and the bone density and elastic modulus of the femur were determined based on the following formulae (Rho et al., 1995):

$$\rho\left(Kg/m^3\right) = 131 + 1.067 \times GV\,(HU) \quad (1)$$

$$E(MPa) = 0.004 \times \rho^{2.01}\left(Kg/m^3\right) \quad (2)$$

The intramedullary needle–type stem prosthesis and proximal femoral sleeve were linear, homogeneous, and isotropic (Ti_6Al_4V, E = 110 GPa, ν = 0.34) (Bartolomeu et al., 2019b). The elastic modulus of the graded porous structures was obtained from a mathematical relationship between the design open-cell (x) (μm) and wall size (y) (μm), as follows (Bartolomeu et al., 2019b):

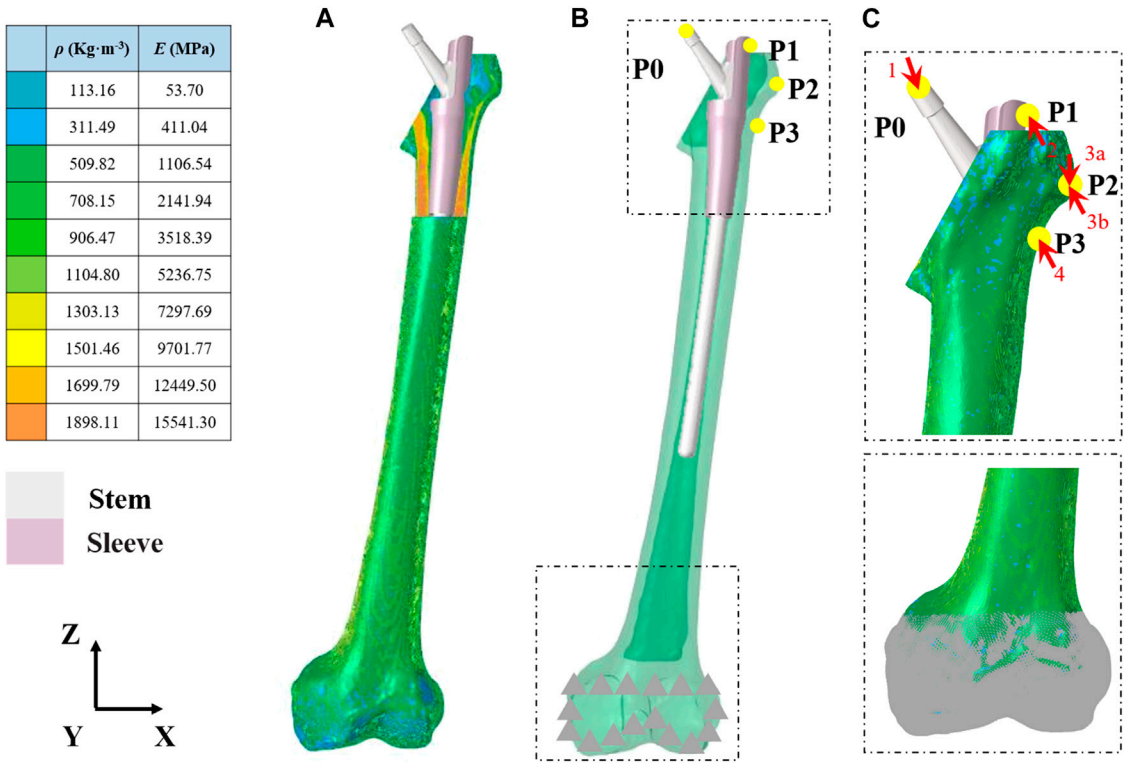

FIGURE 1 | Finite element model of the femur and prosthesis **(A)** Material properties of the inhomogeneous femur **(B)** The entire assembled model of the femur and prosthesis **(C)** Load and boundary conditions. Arrowheads and triangles indicate the loads and constraint, respectively. P0–P4 indicate the point of muscle attachment.

TABLE 1 | Material properties of components.

Component	Material	Elastic Modulus (MPa)	Poisson's Ratio
Bone	Non-homogeneous	Non-homogeneous	0.30
Stem prosthesis	Ti_6Al_4V	110,000	0.34
Sleeve prosthesis	Ti_6Al_4V	110,000	0.34
200-μm porous part	Ti_6Al_4V	35,849.6	0.34
400-μm porous part	Ti_6Al_4V	28,766.8	0.34

$$E(MPa) = 39.7205 - 0.1217x + 0.4415y + 9.4232 \times 10^{-5}x^2 - 5.1581 \times 10^{-4}xy - 8.6838 \times 10^{-5}y^2 \quad (3)$$

An octet-truss lattice architecture with a porosity of 70% was selected to design the graded porous structures (x_1 = 200 μm, y_1 = 50 μm, E_1 = 35849.6 MPa; x_2 = 400 μm, y_2 = 100 μm, E_2 = 28766.8 MPa) under the constraints of bone growth and electron beam melting (Bartolomeu et al., 2019a). Related material properties are presented in **Figure 1A** and **Table 1**.

Load and Boundary Conditions

The loading conditions of this study adopted the results from Heller et al. (2005), who took the effects of joint and muscle strength into account under a normal walking gait. Corresponding loads were applied to the proximal femur and the prosthesis and presented in Figures 1B,C and **Table 2**. The friction response between Ti_6Al_4V and its porous surface against bone was applied in the research by Bartolomeu et al., 2019a. Sticky contact was set for the interface sleeve and intramedullary needle–type stem prosthesis. The contact surfaces were considered to exhibit non-linear contact conditions, and the friction coefficient is shown in **Table 3**. The nodes at the contact surface between different components were set in the common spatial location to create closed gaps. The nodes on the superior surface of the distal femur were fully constrained for all degrees of freedom (DOFs).

TO

An optimal design was determined from the TO process by modifying the material's distribution. The central regions providing strength elements from the analysis would be

TABLE 2 | The joint and muscle forces under walking conditions.

Force	Acts at Point	X	y	z
Hip contact (1)	P0	370.6	225.2	−1,572.3
Abductor (2)	P1	−397.0	−29.5	593.4
Tensor fascia latae, proximal part (3a)	P2	−49.4	−79.6	90.6
Tensor fascia latae, distal part (3 b)		3.4	4.8	−130.3
Vastus lateralis (4)	P3	6.1	−126.9	−637.3

Note: *Loading conditions refer to* ***Figure 1C****.*

TABLE 3 | Friction types between components.

Contact Surface A	Contact Surface B	Friction Type
Sleeve	Stem	Stick
Sleeve	Bone	$\mu_1 = 0.713$, $\mu_2 = 0.326$
200-μm porous part	Bone	$\mu_1 = 0.667$, $\mu_2 = 0.431$
400-μm porous part	Bone	$\mu_1 = 0.660$, $\mu_2 = 0.459$

Note: *μ_1 is defined as the static friction coefficient and μ_2 is defined as the kinetic friction coefficient.*

preserved, and the optimized regions would be modified as porous structures to increase friction. The optimum purpose was that the sleeve prosthesis would be effectively designed to strengthen stability, reduce relative micromotion, and provide the biomechanical environment for bone ingrowth. Moreover, the newly designed prosthesis would maintain the original shape. Hence, the minimum compliance of the TO subject to a volume fraction constraint was utilized under the loads and boundary conditions mentioned above.

The Optimization Equation Is as Follows

Objective Function: Minimize (Uc)

Constraint: 0 < ηi < 1 (i = 1, 2, 3 . . . n)

$$V \le V_0 - V^*,$$

$$V = \sum_i \eta_i V_i,$$

$$E_i = E(\eta_i),$$

and

$$\{\sigma_i\} = [E_i]\{\varepsilon_i\},$$

where Uc is the compliance, ηi represents the internal pseudo-densities assigned to each finite element (i) in the optimization equation, V is the computed volume, V0 is the original volume, V* represents the amount of volume to be removed, Vi is the volume of element i, Ei is the elasticity tensor for each element, E represents the elasticity tensor, σi is the stress vector of element i, and εi represents the strain vector of the element. η, as the density index, ranges from 0 to 1; an η value close to 0 indicates the material to be removed, and an η value close to 1 indicates the material to be retained. The program is set to reduce the volume by ≤ 20% and to iterate up to 30 times. The convergence tolerance was 0.0001. In the TO postprocessing software Hyperview (Altair Engineering, Troy, MI, United States), the optimized region was divided into 2 parts according to the volume fraction chosen for 40–60% and 60–100%, respectively. To prevent porous structure collapse in the area of contact with the intramedullary needle–type stem prosthesis and to assure sufficient strength, the top and bottom contact parts of the sleeve prosthesis were preserved. Then, the optimized parts were imported into the Magics software program to design the internal architecture and assemble optimized parts with the preserved part. The optimized parts were designed as a 70% porosity octet-truss lattice structure, which was a good choice, being combined with stable mechanical properties that promote bone formation (Arabnejad et al., 2016; Feng et al., 2021). Depending on the different choices of volume fraction, a pore size of 200 μm or 400 μm was filled to the region of 40–60% or 60–100% to provide different amounts of roughness, promoting proper bone ingrowth (El Elmi et al., 2020). Then, the optimized parts and the preserved parts were fixed together (**Figure 2**).

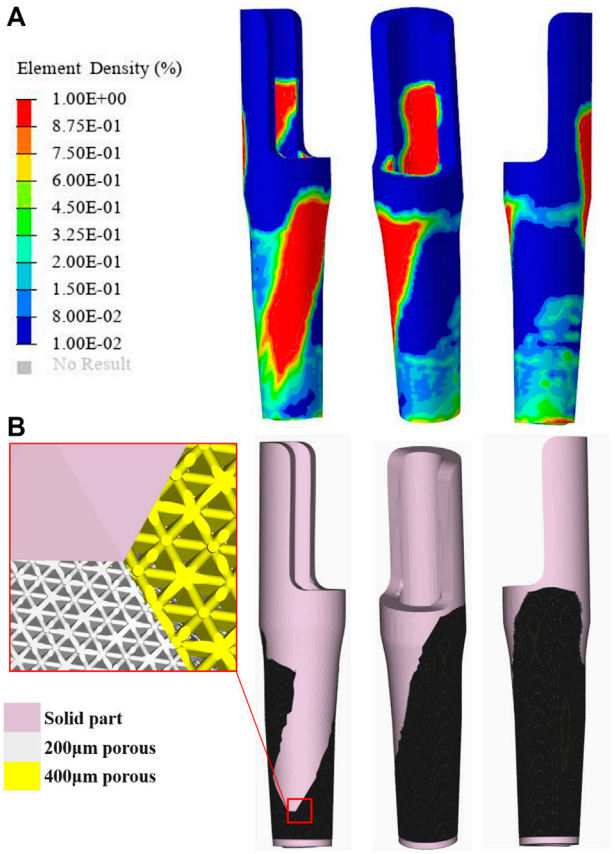

FIGURE 2 | Topological optimization process and the porous structure sleeve prosthesis **(A)** The result of element density distribution **(B)** Optimized prosthesis and its porous structure.

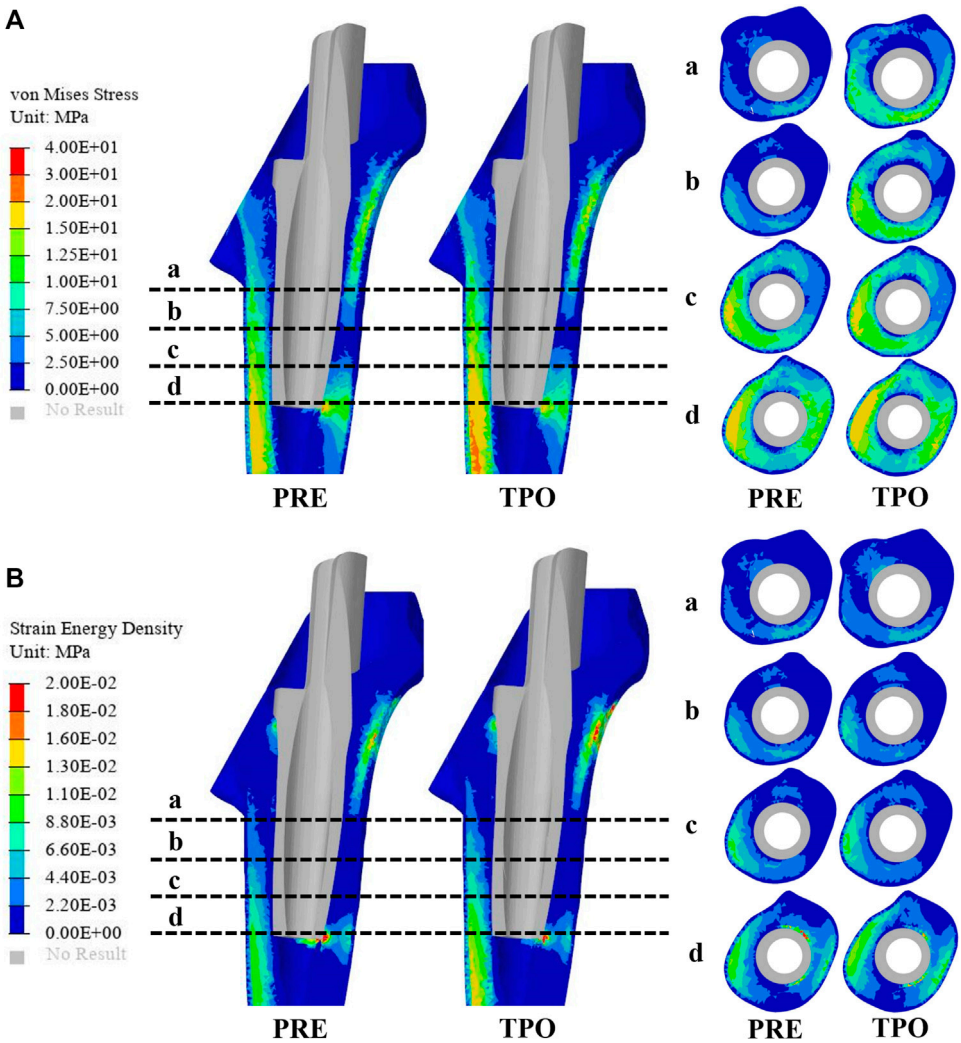

FIGURE 3 | Comparison of the stress and strain energy density distribution on the femur between the original group (PRE) and optimized group (TPO) **(A)** Distribution of von Mises stress **(B)** Distribution of strain energy density. The a, b, c, and d indicate cross-section layers of femur.

FEM

In this study, quasi-static loading non-linear analysis was employed in the simulation procedure with 30 steps iterated until convergence, and the iterative method was performed using the Newton–Raphson approach. To evaluate the adjusted biomechanical effect between the original and optimization groups, the strain energy density (SED), maximum stress, stress distribution, and relative micromotion were selected using the Optistuct software program (Altair Engineering, Troy, MI, United States). As a result, the differences in SED and the stress distribution between the original and optimized prostheses indicated an improved situation of bone resorption and stress shielding. According to the method of Zhang et al. and Wang et al., the average von Mises stresses were acquired at the medial and lateral femurs in 4 layers, which were located every 2 cm from the inferior border of the lesser trochanter to the bottom of the sleeve prosthesis to explore stress shielding (**Figure 3**) (Wang et al., 2018; Zhang et al., 2020). At each iteration, failure analyses were performed using the maximum principal stress to guarantee the implant's necessary strength level under daily walking gait conditions. In addition, the distribution of relative micromotion, which was defined as an index to discriminate bone ingrowth requirements, was obtained from the relative distance of the opened gaps between the nodes at the contact surface. Statistical analyses were performed using the SPSS version 26.0 software program (IBM Corporation, Armonk, NY, United States). The significance level was $p < 0.05$.

RESULTS

TO Results

The density distribution of the sleeve prosthesis was mainly distributed on the top medial side (20%) and bottom lateral side (20–40%), as shown in **Figure 2**. The top and bottom protective devices were redesigned based on the initial optimization. As a result, the volume of the optimized prosthesis when redesigned was reduced from 14786.56 to 10,129.13 mm^3, achieving a 31.5% weight reduction.

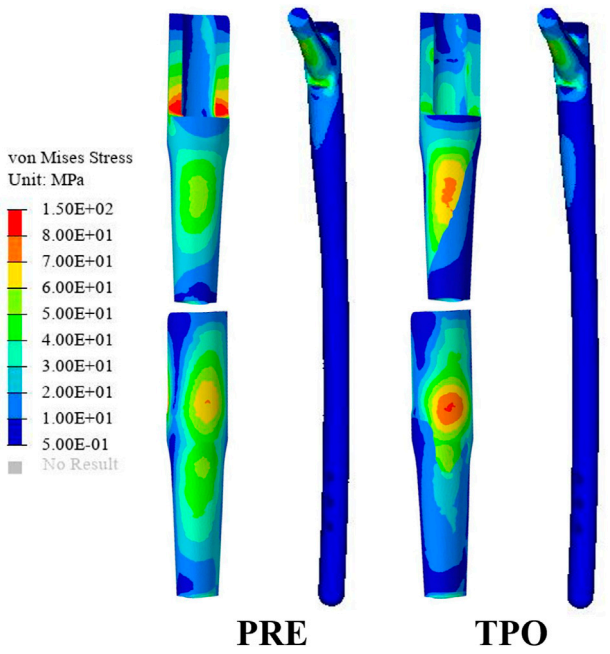

FIGURE 4 | Comparison of the stress distribution on the prosthesis between the original group (PRE) and the optimized group (TPO).

Stress

As shown in **Figure 3A**, the stress distribution in the proximal femur was observed to increase in most regions after optimization. Compared to the original group the average von Mises stress of all selected femoral layers was significantly increased on all medial sides (a–d) and the bottom lateral side (d) ($p < 0.05$) in the optimized group. The stress distribution in the prosthesis showed that optimized regions had a smaller concentration area than that in the original group (**Figure 4**). In addition, the maximum stress had reductions of 30.33% (81.31 MPa) and 4.74% (225.2 MPa) in back part of sleeve and neck part of stem prosthesis and a 29.52% (44.88 MPa) increase in femur compared to the original groups (116.7, 236.4, and 34.65 MPa) (**Figure 5**).

SED

The results of SED in the proximal femur of the original and optimized groups are shown in **Figure 3B**. The distribution of SED in the proximal femur showed that most regions of the optimized group were increased. The maximum SED in the original and optimized groups experienced an increase of 50.97% (from 0.086 to 0.175 MPa).

Relative Micromotion

The distribution of relative micromotion between the sleeve prosthesis's external surface and the femur's internal surface is presented in **Figure 6**. The regions with relative micromotion >28 μm in the optimized group showed a 24.5% increase (from 76.79 to 101.61 mm^2) compared to the original group. In addition, the maximum relative micromotion decreased by 15.18% (from 63.9 to 54.2 μm) in the optimized group.

DISCUSSION

Successful bone defect surgery necessitates the implantation of both axially and rotationally stable components in the presence of physiological forces. While the choice of prosthesis has been controversial in previous studies, the use of extensively porous-coated stems in THA has, for many years, been the standard by which to address these defects (Wallace et al., 2020). Biomechanical challenges in such cases may include poor proximal bone stock, compound bone loss from a loose primary implant moving against the surrounding bone, and additional bone loss in initially installed prostheses (Wiik et al., 2021). The most severe problem caused by this alteration is stress shielding and wear failure, which would cause bone resorption and aseptic loosening around the prosthesis with long-term fixation (Wallace et al., 2020). A novel prosthesis design philosophy involving a porous metal material, surface treatments, and prosthesis geometry design was applied in this study. Although short-stem prostheses positively affect standard THA, remaining cortical bone in femur bone defect may make it challenging to provide sufficient prosthetic support and avoid additional bone collapse (Gotfried, 2007). In this study, in order to preserve the distal femoral bone reserve in the femoral cavity, obtain primary stability by biological fixation, and reduce stress shielding and referring to the successful application of porous short-stem prostheses in THA, a novel sleeve prosthesis was designed. Meanwhile, the point of the abductor's muscle could be damaged during bone defect creation, leading to abductor weakness (Fuchs et al., 2021). A sleeve prosthesis could be applied to reconstruct abductor muscle attachment. Furthermore, to prevent the novel prosthesis from sinking, an intramedullary needle–type stem prosthesis that can be distally fixed with screws was added to the design. Then, a porous implant was optimized to improve its biomechanical performance based on the TO technique.

Porous structures are now widely used in orthopedic and dental bone implants. As a biomaterial, they provide pore interconnectivity and pore architecture for bone ingrowth for secondary long-term biologic fixation (Arabnejad et al., 2016). Bone ingrowth into an implanted structure is a highly complex phenomenon exhibiting biomechanical properties, including structural properties, strength, surface roughness, and biological conditions (Bartolomeu et al., 2019a). In addition, porous structures could regulate stress shielding to reduce bone resorption accordingly to match the stiffness of the local host bone. Some studies reported that the octet-truss structure is a good choice because of appropriate strength and bone ingrowth at high porosity (70% designed) (Feng et al., 2021; Korshunova et al., 2021). In addition, implants with different amounts of roughness have been proven to affect the ability of osseointegration via multiple factors, including enhancing the differentiation of osteoblasts, reducing the activity of osteoclasts, and promoting bone attachment to the implant surface and its mineralization. Bartolomeu et al., 2019a stated that 200 and 400 μm could be considered optimal pore sizes with suitable strength and roughness values to enhance bone ingrowth. Therefore, 200- and 400-μm octet-truss structures were chosen to be combined with the TO design. Then, an inhomogeneous femur model with muscle and joint force was simulated to realize an actual femur walking status in this study. The strength of optimized implants and their effects on host tissue were determined via FEA.

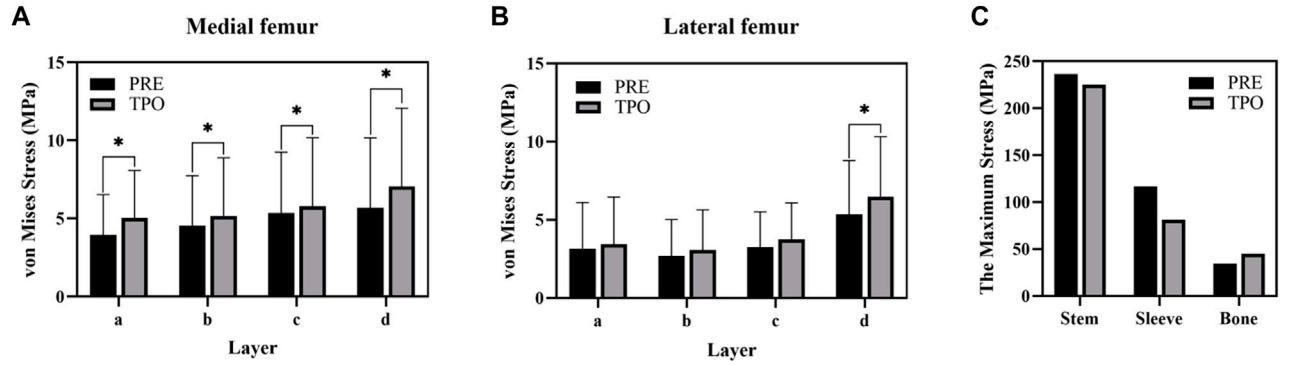

FIGURE 5 | Comparison of the stress result **(A)** The average stress in the medial femur **(B)** The average stress **(C)** The maximum stress in components. The * indicates $p < 0.05$.

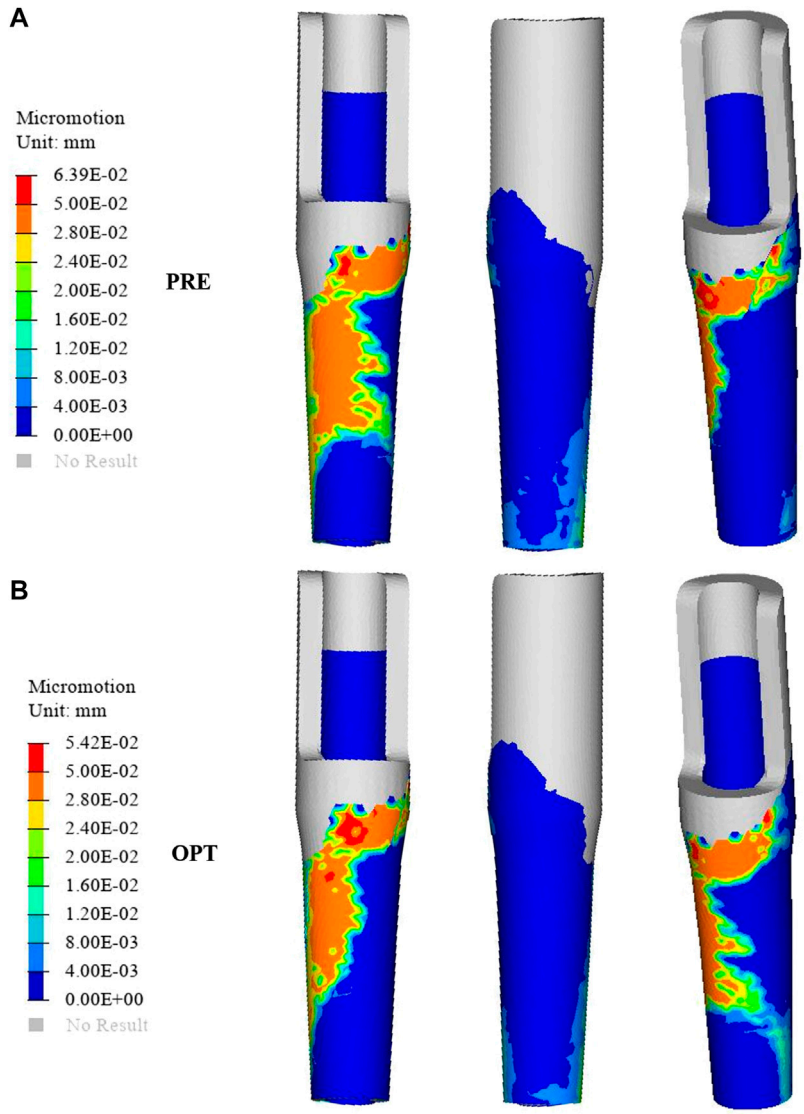

FIGURE 6 | Comparison of the relative micromotion distribution between the original group **(A)** and the optimized group **(B)**.

The stresses on the femur are used to indicate the stress shielding resulting from the various sleeve prosthesis insertions, as shown in **Figure 3A**. Compared to the bone applying original prosthesis, stress distribution was observed to increase in the femur model of the optimized group. The fully dense original prothesis exhibited a lower maximum principal stress (34.65 MPa) than the optimized group (44.88 MPa). This indicates that the load could be better transferred to the bone when altering the material properties from those of the porosity structure. This conclusion was also proved in our previous research (Liu et al., 2021; Zhao et al., 2021). Furthermore, the lesser trochanteric region is considered one of the most critical zones close to the calcar region of the femur and provides prosthetic stability (Wang et al., 2018). Because bone resorption occurs in this region, the implant design should involve some attention paid to minimizing stress shielding. The cross-section and integral view results show that this region experiences a greater stress increase, which is considered to yield a higher stress transfer to the bone to reduce stress shielding (**Figure 3A**, **Figure 4**). Mechanical stress is an essential factor in bone tissue remodeling, but an excessive load is one of the main inducers of fatigue damage (Maslov et al., 2021). According to the results in **Figure 5**, the maximum principal stress in the original group (bone, 34.65 MPa; prosthesis, 236.4 MPa) and optimized group (bone, 44.88 MPa; prosthesis, 225.2 MPa) were less than their corresponding fatigue strengths (cortical bone, 80–150 MPa; Ti_6Al_4V prosthesis, 310–610 MPa). This could indicate that the porous prosthesis's strength is enough to sustain the loading requirement under walking conditions. The SED is another index used for evaluating stress shielding (Moussa et al., 2020). A higher SED result implies a lower stiffness, which could reduce the stiffness mismatch with bone (Wang et al., 2018). In our study, the maximum SED had a 50.97% increase in the femur of the optimized group (0.175 MPa) compared to the original group (0.086 MPa). Meanwhile, after optimization, the SED distribution increased noticeably in all femur layers, indicating decreased bone resorption and stress shielding (**Figure 3B**). Hence, the novel designed compound prosthesis would suit for some patients with bone defects and osteoporosis, because the poor femur proximal bone stock, stress shielding would be improved from the optimization design to deduce the risk of fracture.

Relative micromotion at the bone–implant interface is a vital consideration that may affect the biomechanical environment of bone ingrowth. Previous research has shown that micromotion >150 μm results in fibrous tissue formation, while adequate osseous contact and fixation can reduce micromotion and prevents fibrous ingrowth; meanwhile, micromotion of 30–150 μm results in bone and fibrous tissue formation, and micromotion of 28 μm results predominantly in bone formation (Pilliar et al., 1986). The success of long-term stability is dependent on the initial fixation of the implant, which is dependent on interface micromotion (Zhao et al., 2021). In this work, we designed a graded porous prosthesis to provide space for bone ingrowth and decreased the elastic modulus while increasing the friction coefficient to reduce relative micromotion. Here, the amount of micromotion was computed from the relative nodal sliding distance of mesh elements between the bone and the implant surfaces. As shown in **Figure 6**, the distribution of relative micromotion >28 μm decreased by 24.5% with the optimized prosthesis (76.79 mm^2) compared to the original one (101.61 mm^2). The affected region was mainly in the medial area of the prosthesis. Meanwhile, the maximum relative micromotion decreased by 15.18% (from 63.9 to 54.2 μm). The increase in micromotion can also be associated with postoperative pain; thus, this result indicated that the optimized prosthesis was capable of efficiently preventing micromotion, promoting bone ingrowth, and alleviating patients' pain.

There are a few limitations to this study. First, characteristics specific to individual patients (bone density, dynamic biomechanical properties, and surrounding soft tissue) were not addressed. In addition, biomechanical changes relative to the original prosthesis were only analyzed by FEA. Biomechanical experiments and clinical applications should be considered to increase the integrity of future studies.

CONCLUSION

In the study, a novel femoral sleeve prosthesis and intramedullary needle–type stem prosthesis were designed to treat proximal femur bone defects. Meanwhile, TO and a porous structure were applied to improve the prosthesis' biomechanical performance to promote bone ingrowth and reduce stress shielding. Compared to the original prosthesis, the TO prosthesis exhibited reductions in weight (by 31.5%) and the maximum relative micromotion (by 15.18%) and an increased distribution of relative micromotion to promote bone formation (by 24.5%). In addition, the TO prosthesis could provide better stress distributions and reduce stress shielding. As a result, the novel designed compound prosthesis could serve as a model for clinical practice and a platform for future orthopedic surgery applications.

DATA AVAILABILITY STATEMENT

The original contributions presented in the study are included in the article/Supplementary Material, further inquiries can be directed to the corresponding author.

ETHICS STATEMENT

The studies involving human participants were reviewed and approved by The ethics committee of the Second Hospital of Jilin University. The patients/participants provided their written informed consent to participate in this study.

AUTHOR CONTRIBUTIONS

HX: software and writing—original draft preparation; HB: contributed to the writing—review and editing; RZ: software; JW: supervision, and funding acquisition; BZ: Data collection; XW: visualization and investigation; WL: methodology; XZ: conceptualization and funding acquisition.

FUNDING

This work was supported and funded by the following grants: National Key R&D Program of China (Grant Number

2018YFB1105100); Wu Jieping Medical Foundation (Grant Number 320.6750.18522); Bethune plan of Jilin University (Grant Number 419161900014); Department of Science and Technology of Jilin Province, P.R.C. (Grant Numbers 20200404202YY, YDZJ202201ZYTS086); Department of Finance in Jilin province (Grant Numbers 2019SCZT034 and 2020SCZT086); Jilin Province Development and Reform Commission, P.R.C. (Grant Numbers 2018C010 and 2022C044-2); and Beijing Chunlizhengda Medical Instruments Co.,Ltd (Grant Number 2019YX231).

REFERENCES

Alkhatib, S. E., Tarlochan, F., Mehboob, H., Singh, R., Kadirgama, K., and Harun, W. S. B. W. (2019). Finite Element Study of Functionally Graded Porous Femoral Stems Incorporating Body-Centered Cubic Structure. *Artif. Organs* 43, E152–E164. doi:10.1111/aor.13444

Arabnejad, S., Burnett Johnston, R., Pura, J. A., SinghTanzer, B. M., Tanzer, M., and Pasini, D. (2016). High-strength Porous Biomaterials for Bone Replacement: A Strategy to Assess the Interplay between Cell Morphology, Mechanical Properties, Bone Ingrowth and Manufacturing Constraints. *Acta Biomater.* 30, 345–356. doi:10.1016/j.actbio.2015.10.048

Bai, L., Gong, C., Chen, X., Sun, Y., Zhang, J., Cai, L., et al. (2019). Additive Manufacturing of Customized Metallic Orthopedic Implants: Materials, Structures, and Surface Modifications. *Metals* 9, 1004. doi:10.3390/met9091004

Bartolomeu, F., Costa, M. M., Gomes, J. R., Alves, N., Abreu, C. S., Silva, F. S., et al. (2019a). Implant Surface Design for Improved Implant Stability - A Study on Ti6Al4V Dense and Cellular Structures Produced by Selective Laser Melting. *Tribol. Int.* 129, 272–282. doi:10.1016/j.triboint.2018.08.012

Bartolomeu, F., Fonseca, J., Peixinho, N., Alves, N., Gasik, M., Silva, F. S., et al. (2019b). Predicting the Output Dimensions, Porosity and Elastic Modulus of Additive Manufactured Biomaterial Structures Targeting Orthopedic Implants. *J. Mech. Behav. Biomed. Mater.* 99, 104–117. doi:10.1016/j.jmbbm.2019.07.023

Bieger, R., Ignatius, A., Reichel, H., and Dürselen, L. (2013). Biomechanics of a Short Stem: *In Vitro* Primary Stability and Stress Shielding of a Conservative Cementless Hip Stem. *J. Orthop. Res.* 31, 1180–1186. doi:10.1002/jor.22349

Boese, C. K., Bredow, J., Ettinger, M., Eysel, P., Thorey, F., Lechler, P., et al. (2016). The Influence of Hip Rotation on Femoral Offset Following Short Stem Total Hip Arthroplasty. *J. Arthroplasty* 31, 312–316. doi:10.1016/j.arth.2015.07.027

De Martino, I., D'Apolito, R., Nocon, A. A., Sculco, T. P., Sculco, P. K., and Bostrom, M. P. (2019). Proximal Femoral Replacement in Non-oncologic Patients Undergoing Revision Total Hip Arthroplasty. *Int. Orthop. (SICOT)* 43, 2227–2233. doi:10.1007/s00264-018-4220-4

El Elmi, A., Melancon, D., Asgari, M., Liu, L., and Pasini, D. (2020). Experimental and Numerical Investigation of Selective Laser Melting-Induced Defects in Ti-6Al-4V Octet Truss Lattice Material: the Role of Material Microstructure and Morphological Variations. *J. Mat. Res.* 35, 1900–1912. doi:10.1557/jmr.2020.75

Evans, E. M. (1949). The Treatment of Trochanteric Fractures of the Femur. *J. Bone Jt. Surg. Br. volume* 31-B, 190–203. doi:10.1302/0301-620x.31b2.190

Feng, J., Liu, B., Lin, Z., and Fu, J. (2021). Isotropic Octet-Truss Lattice Structure Design and Anisotropy Control Strategies for Implant Application. *Mater. Des.* 203, 109595. doi:10.1016/j.matdes.2021.109595

Frost, H. M. (1994). Wolff's Law and Bone's Structural Adaptations to Mechanical Usage: an Overview for Clinicians. *Angle. Orthod.* 64, 175–188. doi:10.1043/0003-3219(1994)064<0175:WLABSA>2.0.CO;2

Fuchs, M., Hein, M.-A., Faschingbauer, M., Sgroi, M., Bieger, R., Reichel, H., et al. (2021). Abductor Muscle Force after Straight-Stem Compared to Short-Stem Total Hip Arthroplasty through a Modified Direct Lateral Approach: Functional Assessment of 70 Consecutive Patients of a Randomized Controlled Clinical Trial. *Jcm* 10, 1235. doi:10.3390/jcm10061235

Gocer, H., Coskun, S., and Karaismailoglu, N. (2016). Comparison of Treatment of Unstable Intertrochanteric Fracture with Different Arthroplasty Methods. *Niger. Med. J.* 57, 81–85. doi:10.4103/0300-1652.182081

Gotfried, Y. (2007). Integrity of the Lateral Femoral Wall in Intertrochanteric Hip Fractures. *J. Bone & Jt. Surg.* 89, 2552–2553. doi:10.2106/00004623-200711000-00037

Hamilton, W. G. (2021). CORR Insights: No Clinically Important Differences in Thigh Pain or Bone Loss between Short Stems and Conventional-Length Stems in THA: A Randomized Clinical Trial. *Clin. Orthop. Relat. Res.* 479, 778–780. doi:10.1097/corr.0000000000001567

Hasegawa, M., Tone, S., Naito, Y., Wakabayashi, H., and Sudo, A. (2021). Minimum Ten-Year Results in Revision Total Hip Arthroplasty Using Titanium Fully Porous Long Stem. *Int. Orthop. (SICOT)* 45, 1727–1733. doi:10.1007/s00264-021-05030-4

Heller, M. O., Bergmann, O., G., Bergmann, G., Kassi, J.-P., Claes, L., Haas, N. P., et al. (2005). Determination of Muscle Loading at the Hip Joint for Use in Pre-clinical Testing. *J. Biomechanics* 38, 1155–1163. doi:10.1016/j.jbiomech.2004.05.022

Korshunova, N., Alaimo, G., Hosseini, S. B., Carraturo, M., Reali, A., Niiranen, J., et al. (2021). Bending Behavior of Octet-Truss Lattice Structures: Modelling Options, Numerical Characterization and Experimental Validation. *Mater. Des.* 205, 109693. doi:10.1016/j.matdes.2021.109693

Liu, Y., Chen, B., Wang, C., Chen, H., Zhang, A., Yin, W., et al. (2021). Design of Porous Metal Block Augmentation to Treat Tibial Bone Defects in Total Knee Arthroplasty Based on Topology Optimization. *Front. Bioeng. Biotechnol.* 9, 765438. doi:10.3389/fbioe.2021.765438

Maslov, L., Borovkov, A., Maslova, I., Soloviev, D., Zhmaylo, M., and Tarasenko, F. (2021). Finite Element Analysis of Customized Acetabular Implant and Bone after Pelvic Tumour Resection throughout the Gait Cycle. *Materials* 14, 7066. doi:10.3390/ma14227066

Moussa, A., Rahman, S., Xu, M., Tanzer, M., and Pasini, D. (2020). Topology Optimization of 3D-Printed Structurally Porous Cage for Acetabular Reinforcement in Total Hip Arthroplasty. *J. Mech. Behav. Biomed. Mater.* 105, 103705. doi:10.1016/j.jmbbm.2020.103705

Moyen, B. J., Lahey, P. J., Jr., Weinberg, E. H., and Harris, W. H. (1978). Effects on Intact Femora of Dogs of the Application and Removal of Metal Plates. A Metabolic and Structural Study Comparing Stiffer and More Flexible Plates. *J. Bone & Jt. Surg.* 60, 940–947. doi:10.2106/00004623-197860070-00012

Perry, D., Metcalfe, D., and Costa, M. (2016). Inequalities in Access to Total Hip Arthroplasty for Hip Fracture: a Population-Based Study. *Lancet* 387, S81. doi:10.1016/s0140-6736(16)00468-2

Pilliar, R. M., Lee, J. M., and Maniatopoulos, C. (1986). Observations on the Effect of Movement on Bone Ingrowth into Porous-Surfaced Implants. *Clin. Orthop. Relat. Res.* 208, 108–113. doi:10.1097/00003086-198607000-00023

Rahimizadeh, A., Nourmohammadi, Z., Arabnejad, S., Tanzer, M., and Pasini, D. (2018). Porous Architected Biomaterial for a Tibial-Knee Implant with Minimum Bone Resorption and Bone-Implant Interface Micromotion. *J. Mech. Behav. Biomed. Mater.* 78, 465–479. doi:10.1016/j.jmbbm.2017.11.041

Rho, J. Y., Hobatho, M. C., and Ashman, R. B. (1995). Relations of Mechanical Properties to Density and CT Numbers in Human Bone. *Med. Eng. Phys.* 17, 347–355. doi:10.1016/1350-4533(95)97314-f

Toepfer, A., Strasser, V., LadurnerCalek, A. A. K., Calek, A.-K., Potocnik, P., and von Eisenhart-Rothe, R. (2021). Different Outcomes after Proximal Femoral Replacement in Oncologic and Failed Revision Arthroplasty Patients - a Retrospective Cohort Study. *Bmc. Musculoskelet. Disord.* 22, 813. doi:10.1186/s12891-021-04673-z

Wallace, C. N., Chang, J. S., Kayani, B., Moriarty, P. D., Tahmassebi, J. E., and Haddad, F. S. (2020). Long-term Results of Revision Total Hip Arthroplasty Using a Modern Extensively Porous-Coated Femoral Stem. *J. Arthroplasty* 35, 3697–3702. doi:10.1016/j.arth.2020.06.052

Wang, Y., Arabnejad, S., Tanzer, M., and Pasini, D. (2018). Hip Implant Design with Three-Dimensional Porous Architecture of Optimized Graded Density. *J. Mech. Des.* 140, 103705. doi:10.1115/1.4041208

Wiik, A. V., Aqil, A., Al-Obaidi, B., Brevadt, M., and Cobb, J. P. (2021). The Impact of Reducing the Femoral Stem Length in Total Hip Arthroplasty during Gait. *Arch. Orthop. Trauma. Surg.* 141, 1993–2000. doi:10.1007/s00402-021-03852-w

Yan, S. G., Chevalier, Y., Liu, F., Hua, X., Schreiner, A., Jansson, V., et al. (2020). Metaphyseal Anchoring Short Stem Hip Arthroplasty Provides a More

Physiological Load Transfer: a Comparative Finite Element Analysis Study. *J. Orthop. Surg. Res.* 15, 498. doi:10.1186/s13018-020-02027-4

Zhang, A., Chen, H., Liu, Y., Wu, N., Chen, B., Zhao, X., et al. (2020). Customized Reconstructive Prosthesis Design Based on Topological Optimization to Treat Severe Proximal Tibia Defect. *Bio-Des. Manuf.* 4, 87–99. doi:10.1007/s42242-020-00102-7

Zhao, X., Xue, H., Sun, Y., Zhang, A., Liu, Y., Chen, H., et al. (2021). Application of Novel Design Bone Grafting for Treatment of Segmental Acetabular Rim Defects during Revision Total Hip Arthroplasty. *J. Bionic. Eng.* 18, 1369–1377. doi:10.1007/s42235-021-00097-6

Conflict of Interest: The authors declare that the research was conducted in the absence of any commercial or financial relationships that could be construed as a potential conflict of interest.

Publisher's Note: All claims expressed in this article are solely those of the authors and do not necessarily represent those of their affiliated organizations, or those of the publisher, the editors and the reviewers. Any product that may be evaluated in this article, or claim that may be made by its manufacturer, is not guaranteed or endorsed by the publisher.

frontiers | Frontiers in Bioengineering and Biotechnology

TYPE Original Research
PUBLISHED 03 August 2022
DOI 10.3389/fbioe.2022.928041

OPEN ACCESS

EDITED BY
He Liu,
Jilin University, China

REVIEWED BY
Chao Yang,
Zhejiang Ocean University, China
Zhipeng Gu,
Sichuan University, China
Ke Wang,
Xi'an Jiaotong University, China

*CORRESPONDENCE
Weidong Leng,
Lengweidong68@163.com
Jie Luo,
Luojie_th67@163.com

SPECIALTY SECTION
This article was submitted to Biomaterials, a section of the journal Frontiers in Bioengineering and Biotechnology

RECEIVED 25 April 2022
ACCEPTED 28 June 2022
PUBLISHED 03 August 2022

CITATION
Yu H, Xia L, Leng X, Chen Y, Zhang L, Ni X, Luo J and Leng W (2022), Improved repair of rabbit calvarial defects with hydroxyapatite/chitosan/polycaprolactone composite scaffold-engrafted EPCs and BMSCs. *Front. Bioeng. Biotechnol.* 10:928041. doi: 10.3389/fbioe.2022.928041

Improved repair of rabbit calvarial defects with hydroxyapatite/chitosan/polycaprolactone composite scaffold-engrafted EPCs and BMSCs

Hedong Yu[1,2], Lingyun Xia[1,2], Xieyuan Leng[3], Yongji Chen[1,2], Li Zhang[1,2], Xiaobing Ni[1,2], Jie Luo[4]* and Weidong Leng[1,2]*

[1]Department of Stomatology, Taihe Hospital, Hubei University of Medicine, Shiyan, China, [2]Institute of Dental Research, School of Dentistry, Hubei University of Medicine, Shiyan, China, [3]The First Clinical College, Anhui Medical University, Hefei, China, [4]Department of Neurosurgery, Taihe Hospital, Hubei University of Medicine, Shiyan, China

Endothelial progenitor cells (EPCs) expressing vascular endothelial growth factor (VEGF) and platelet-derived growth factor (PDGF) and bone marrow mesenchymal stem cells (BMSCs) expressing endogenous bone morphogenetic protein-2 (BMP-2) play the important role in new bone formation. This study investigated the effects of a porous hydroxyapatite (HA)/chitosan (CS)/polycaprolactone (PCL) composite scaffold-engrafted EPCs and BMSCs on the expression of BMP-2, VEGF, and PDGF in the calvarial defect rabbit model *in vivo*. It showed that a three-dimensional composite scaffold was successfully constructed by physical interaction with a pore size of 250 μm. The HA/CS/PCL scaffold degraded slowly within 10 weeks and showed non-cytotoxicity. By X-ray, micro-CT examination, and H&E staining, compared with the HA/CS/PCL group, HA/CS/PCL + EPCs, HA/CS/PCL + BMSCs, and HA/CS/PCL + EPCs + BMSCs groups performed a more obvious repair effect, and the dual factor group presented particularly significant improvement on the percentages of bone volume at week 4 and week 8, with evident bone growth. Osteogenesis marker (BMP-2) and vascularization marker (VEGF and PDGF) expression in the dual factor group were much better than those of the HA/CS/PCL control group and single factor groups. Collectively, the HA/CS/PCL composite scaffold-engrafting EPCs and BMSCs is effective to repair calvarial defects by regulating endogenous expression of BMP-2, VEGF, and PDGF. Thus, this study provides important implications for the potential clinical application of biomaterial composite scaffold-engrafted engineering cells.

KEYWORDS

HA/CS/PCL composite scaffold, endothelial progenitor cells, bone marrow mesenchymal stem cells, calvarial defect, BMP-2, VEGF, PDGF

Introduction

High incidence diseases such as tumor, trauma, and infection contribute to different degrees of bone defect that cannot be healed by the natural recovery (Baroli, 2009). Biomaterials for bone tissue regeneration and repair are the frontier and hot issue of regenerative medicine research, and scaffold biomaterials are one of the key elements for bone tissue engineering. High biocompatibility, osteogenic ability, and biodegradation are of particular significance for the discovery of scaffold biomaterials. Therefore, there is still a great development for tissue-engineered bone in clinical application (Dumont et al., 2016; Kai et al., 2016).

Hydroxyapatite (HA) is similar to the inorganic components of calvaria in composition and structure, but it is fragile and easy to crack (Oliveira et al., 2017). Chitosan (CS) is a linear natural polysaccharide macromolecule, which has excellent biocompatibility, biodegradability, hydrophilicity, cell affinity, and adhesion (Tian et al., 2022). Polycaprolactone (PCL) is a linear polymer with high mechanical strength and easy processing, and its degradation products are easy to metabolize and eliminate (Lee et al., 2016). HA, CS, and PCL have been applied in bone repair for years. Natural bone tissue is mainly formed by the interaction of nanohydroxyapatite inorganic minerals and collagen organic matter in an orderly arrangement. In order to highly simulate the three-dimensional nanostructure of natural bone, our research group proposed the construction technology of three-component and porous bone composite scaffold containing PCL, CS, and HA and resolved the morphology control of the scaffold by 3D printing (Yu et al., 2020). The biomaterial showed good mechanical properties, bone conductivity, and induction, of which superior mechanical and biological properties displayed a good application prospect for bone defect repair (Gao et al., 2015). However, the biological characteristics of the HA/CS/PCL composite scaffold still need to be evaluated, biocompatibility, effectiveness in loading seed cells, and *in vitro* and *in vivo* osteogenic activity are needed to be tested.

As the seed cells for tissue engineering bone, bone marrow mesenchymal stem cells (BMSCs) are difficult to survive *in vivo*, so that the vascularization could be restricted, which is of decisive significance for bone regeneration and fusion (Stegen et al., 2015). Meanwhile, the endothelial progenitor cells (EPCs) extracted from the peripheral blood and BMSCs are co-cultured together to build a microenvironment in line with the physiological conditions of the human body, which could build the microvasculature by EPCs to supply the blood for the osteogenesis of tissue engineering bone, and promote the survival and osteogenesis of BMSCs (Goerke et al., 2015).

In this study, our research group intended to construct HA/CS/PCL scaffolds inoculating EPCs and BMSCs. In addition, the biocompatibility and bone repair effect of this composite were evaluated, and the effects of this composite on osteogenesis and vascularization using bone morphogenetic protein-2 (BMP-2), vascular endothelial growth factor (VEGF), and platelet-derived growth factor (PDGF) expression were measured as well.

Materials and methods

Reagents

The chitosan and hydroxyapatite were purchased from Solarbio (Beijing, China), polycaprolactone and simulated body fluid (SBF) from Sigma-Aldrich (Merck KGaA, Darmstadt, Germany), reagents used for cell culture all from Thermo Fisher Scientific (Loughborough, United Kingdom), and CCK-8 reagent from Beyotime (Shanghai, China).

Microscopic examination

The HA/CS/PCL scaffold was observed using the Hitachi S-4300 cold field emission scanning electron microscope (Hitachi, Tokyo, Japan), and its morphology was analyzed with gold coating.

X-ray diffraction study

X-ray diffraction (XRD) of the HA/CS/PCL scaffold was detected using D8 ADVANCE (BRUKER, Germany). JCPDS files 09-0432 were used to confirm the various peaks developed in HA.

Immersion test

The *in vitro* immersion test was conducted to observe and evaluate the degradation behavior of scaffolds in SBF (M_{SBF}: $M_{scaffold}$ = 100:1), where the scaffolds were dried, weighed, immersed, and incubated with shaking at 100 rpm at 37°C. Every week one scaffold was randomly taken out to weigh the quality to analyze the degradation performance, and the degradation rate was calculated according to the equation, degradation rate = $(M_0 - M)/M_0 \times 100\%$, where M_0 and M are the initial mass and mass at specific time point, respectively.

Cytocompatibility tests

Immersed in DMEM containing 10% FBS (V_{medium}: $M_{scaffold}$ = 10 ml:1 g), the scaffold was incubated at 37°C for 120 h in a CO_2 incubator, and then the medium was sterilized with a 0.22-μm micron bacteria-retentive filter to obtain the extracts. Moreover, for the cell viability test, the L929 cells were seeded in 96-well plates, with 2,000 cells/well. After overnight incubation, the medium was replaced with the HA/CS/PCL

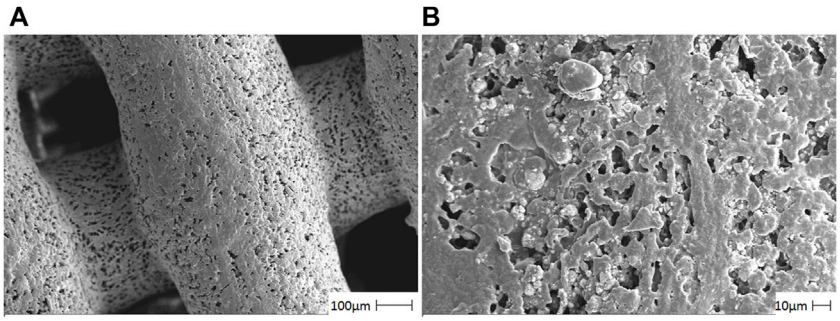

FIGURE 1
Photomicrographs of the HA/CS/PCL composite scaffold material by using a scanning electron microscope. The representative figures were observed on 100 μm **(A)** and 10 μm **(B)**, respectively.

scaffold extracts (10, 30, 50, and 100%) for 2, 4, and 7 days cell culture. The test of cell viability was performed by CCK-8 kit, according to the manufacturer's instructions.

Animals

Twenty four subjects of this study, New Zealand rabbits, were purchased from Nanchang Longping Rabbit Industry Co., Ltd. with license No. scxk (GAN) 2014-0005. The ethics committee of Hubei University of Medicine approved the animal protocols.

Isolation, culture, and immunophenotyping of BMSCs

After the removal of the femur and tibia, the bone marrow was extruded from the central canal of the bone, and the whole marrow cells were cultured with α-MEM supplemented with 10% fetal bovine serum and antibiotics. By removing the non-adherent cells after 24 h with the medium replacement, BMSCs were obtained and serially subcultured in the ratio of 1:3. BMSCs were used within four passages.

As the adherent cells reach 80%–90% confluence (generally about 10 days), BMSCs were stained with FITC-conjugated CD29 and PE-conjugated CD45 antibodies for 30 min at 4°C and washed with PBS. With at least 10,000 cells per sample analyzed, the expression of cell surface antigens CD29 and CD45 was detected by using a flow cytometer.

Isolation, culture, and immunophenotyping of EPCs

The isolation of EPCs from the bone marrow was made by the lymphocyte separation solution as described previously (Ding et al., 2019). The isolated cells, incubated in a CO_2 incubator at 37°C, were collected and stained with APC-conjugated CD133 antibody, PE-conjugated CD309 antibody, or PE-conjugated CD34 antibody. After staining for 30 min at 4°C in dark and washing with PBS, the utilization of the flow cytometer helped to detect the CD133, CD309, or CD34 expression of EPCs.

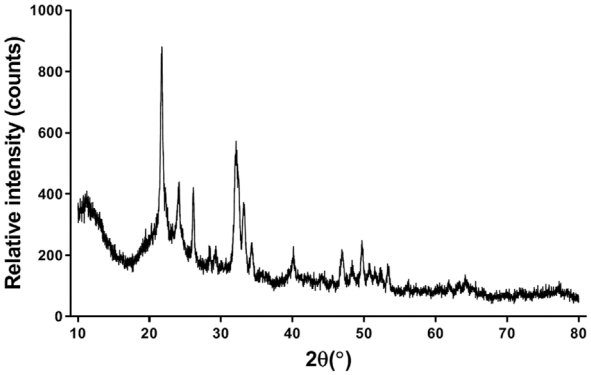

FIGURE 2
XRD spectra of the HA/CS/PCL composite scaffold.

Calvarial defect model

First, rabbits were anesthetized and fixed in the prone position, and they were trephine drilled into the anterior fontanelle with 1-cm diameter. Calvarial defects under copious saline irrigation with care to maintain the dura mater intact. Then, the composite scaffold with presence and absence of engrafted cells was placed in each defect, and the incision was sutured layer-by-layer and wrapped by the sterile dressing. After surgery, all animals were postoperatively cared by monitoring infection and diarrhea with subcutaneous injections of

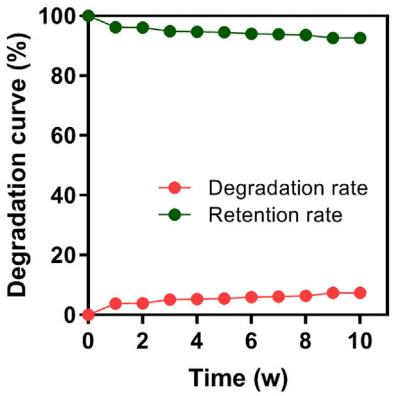

FIGURE 3
Degradation rate of the HA/CS/PCL composite scaffold in 1–10 weeks of immersion in simulated body fluid (SBF).

0.1 mg kg^{-1} buprenorphine for 3 days and drinking water including trimethoprim–sulfamethoxazole. After 8 weeks, the specimens were harvested for the subsequent examination.

The rabbits were randomly divided into four groups (n = 6), namely, as the HA/CS/PCL scaffold group, HA/CS/PCL scaffold + EPCs group, HA/CS/PCL scaffold + BMSCs group, and HA/CS/PCL scaffold + EPCs + BMSCs group. Each piece of scaffold was soaked in cell suspension of the third-generation of BMSCs or EPCs with 0.5 × 10^6/ml for 4 h in the CO_2 incubator and before implantation, the scaffolds engrafted cells were washed by PBS. At the post-surgery of the 2nd, 4th, and 8th week, two rabbits (n = 2) from each group were randomly chosen for analysis.

X-ray examination

As time progressed to weeks 2, 4, and 6 post-surgery, X-ray examination was performed by an X-ray machine (OEC9800, Shanghai Xianwei Optoelectronic Technology Co., Ltd.) to observe the repair of calvarial defects.

Micro-CT

At the post-surgery of the 2nd, 4th, and 8th week, approximating images of calvaria with new bone deposition were reconstructed by three-dimensional micro-computerized tomography (micro-CT), whose scanning parameters are 80kV, 500 μA, and resolution of 27 μM, and the reestablishment of three-dimensional (3D) images and volumetric analysis were performed by the Inveon Research Workplace 2.2. Bone volume (BV) and tissue volume (TV) were used to quantify the calvaria with new bone, and their percentages of bone volume (BV/TV) of each graft site were measured.

Hematoxylin and eosin (H&E) staining

After micro-CT imaging, the calvaria were decalcified for 5 weeks. The specimens of the calvarial defect region were dehydrated and embedded in paraffin and sectioned coronally with 5-μm thickness. The sections were stained with hematoxylin and eosin to visualize tissue structure.

Western blot

The extraction of total protein from the bone tissues in the defect areas of the calvaria was performed by using the triplePrep kit (GE Healthcare Life Sciences), and its concentration was determined with a BCA assay kit. 25 μg protein per sample was separated *via* 10% SDS-PAGE and transferred to the PVDF membrane as described (Luo et al., 2021). After blocking in 5% skim milk at room temperature for 2 h, PVDF membranes were treated with the following primary antibodies overnight at

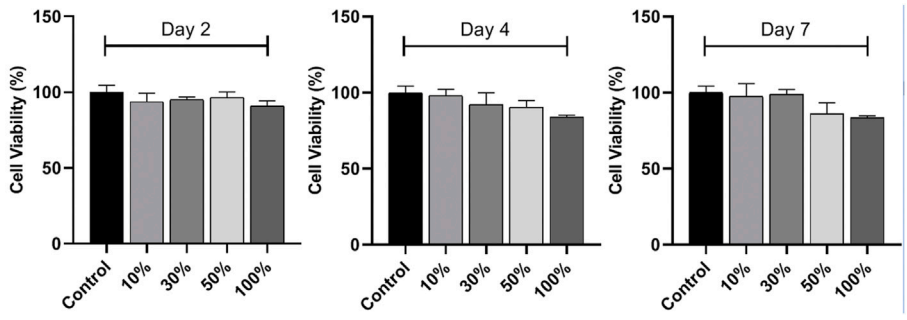

FIGURE 4
In vitro cytocompatibility of the HA/CS/PCL scaffold. CCK-8 assay of L929 cell proliferation on the HA/CS/PCL scaffold after 2, 4, and 7 days incubation. The data represent the mean ± SD.

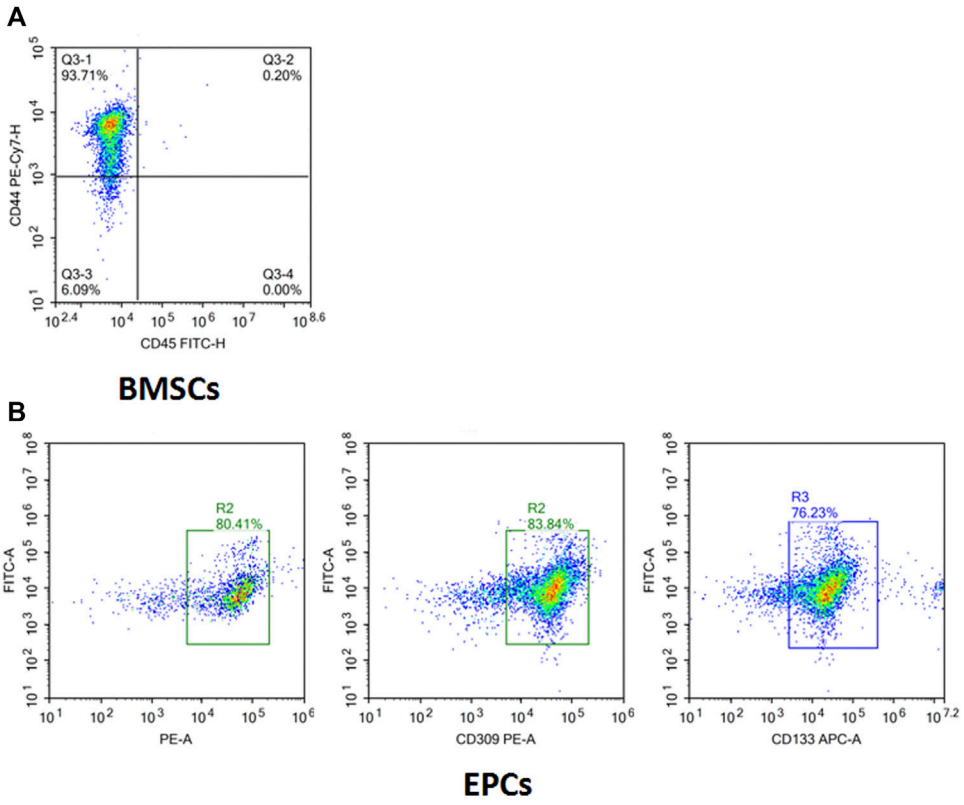

FIGURE 5
Surface markers of isolated and cultured BMSCs and EPCs. **(A)** Isolated cells were CD44$^+$ (93.71%) and CD45$^+$ (0.2%) determined by flow cytometry analysis. **(B)** Isolated cells were CD34$^+$ (80.41%), CD309$^+$ (83.84%), and CD133$^+$ (76.23%) determined by flow cytometry analysis.

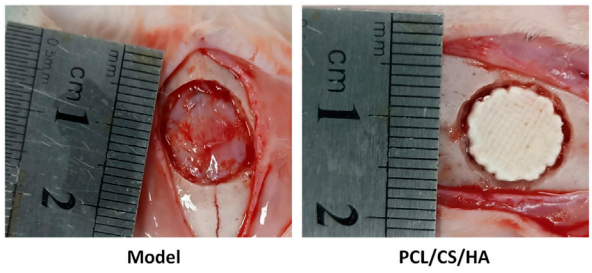

FIGURE 6
Representative images of the calvarial defect model (left) and HA/CS/PCL composite scaffold implantation (right).

4°C, rabbit polyclonal anti-BMP-2 (1:1000, bs-1012R, Bioss), rabbit polyclonal anti-VEGF (1:1000, bs-1313R, Bioss), and rabbit polyclonal anti-PDGF (1:1000, bs-0196R, Bioss), followed by incubation with HRP-labeled IgG at 37°C for 2 h. The western blots were stained with an ECL reagent (Santa Cruz Biotech, CA, United States) and visualized by the ChemiDoc Touch Imaging System—Bio-Rad Laboratories (Bio-Rad Lab, Hercules, CA, United States).

Statistical analysis

All the data were presented as mean and standard deviation and analyzed by SPSS 19.0. Overall significant differences among groups were determined by one-way ANOVA. When overall analysis demonstrated the presence of significant differences among all of the different groups studied, the differences between specific groups were tested using a *post-hoc* analysis, Tukey's test. $p < 0.05$ was set as the threshold to indicate significant difference between groups.

Results

SEM ultrastructure analysis

In Figure 1, the HA/CS/PCL scaffold showed the neatly arranged fibers composed of CS and PCL in grid shape with

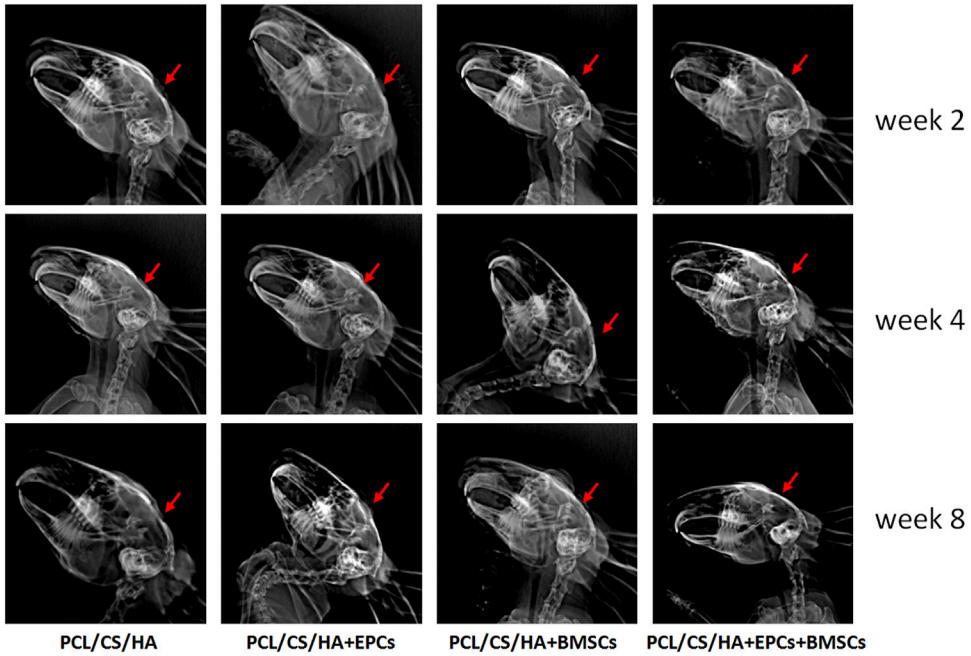

FIGURE 7
Evaluation of calvarial repair by X-ray images after 2, 4, and 8 weeks of implantation. The red arrow indicates the defect area receiving scaffold implantation.

an average pore size of about 250 μm. HA distributed evenly on the fiber surface in granular form, which proved that the ternary composite presented uniform and loose macroporous structure.

XRD analysis

For the HA/CS/PCL composite scaffold, peaks corresponding to HA crystalline phases appeared (Figure 2). The peaks of HA match well with JCPDS No. 09-0432. It indicated that the scaffold was combined with HA, CS, and PCL by physical interaction, which did not affect the biological function of HA.

In vitro degradation behavior

After 10 consecutive weeks, the degradation rate of the HA/CS/PCL composite scaffold in SBF was 7.39%, indicating that the HA/CS/PCL scaffold possessed certain mechanical stability and degraded slowly over time (Figure 3). This property meets the degradation and mechanical performance requirements of the biomaterial scaffold.

In vitro cytocompatibility of HA/CS/PCL scaffold

L929 is the earliest and most widely used cell line in the cytotoxicity test because of its stable passage, rapid propagation, and low culture conditions *in vitro*. The cell viabilities were above 80% after 2, 4, and 7 days cell culture in the scaffold extracts compared with that of the blank control, indicating non-cytotoxicity and acceptable cytocompatibility of the scaffolds, according to the criteria for the evaluation of cell toxicity test recommended in GB/T16886.5-1997-ISO10993-5:1992 (Figure 4).

Identification of BMSCs and EPCs

The flow cytometry results (Figure 5A) showed the cell surface antigen profile of BMSCs, which was identified that 93.71% of the cells expressed CD44, but was homogeneously negative for CD45 (0.2%). It confirmed the identification of isolated BMSCs. In addition to BMSCs, the isolated cells were positive for EPCs markers CD34 (80.41%), CD133 (83.84%), and CD309 (76.23%) (Figure 5B), which manifested that EPCs were successfully separated from rabbit bone marrow by the Ficoll density gradient method.

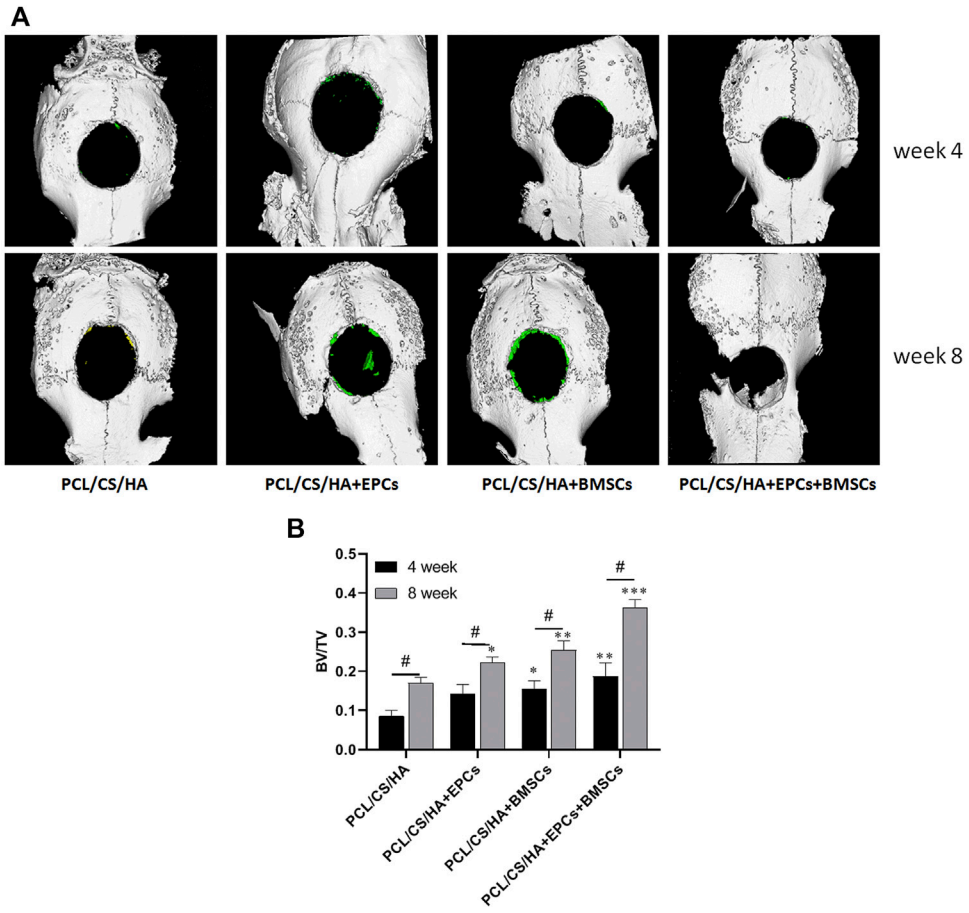

FIGURE 8
Three-dimensional micro-CT images of calvarial defect areas. The representative images **(A)** of micro-CT reconstruction and the quantitative data of BV/TV **(B)** from micro-CT evaluations of the four groups. *$p < 0.05$, **$p < 0.01$, ***$p < 0.001$ vs. HA/CS/PCL group (the same time point), #$p < 0.05$.

Calvarial defect model and scaffold implantation

As shown in Figure 6, after the composite scaffold was implanted into the calvaria, none of the rabbits died throughout the experiment, and all rabbits were under healthy conditions without infection or ulceration in the wound.

EPCs and BMSCs improved the *in vivo* performance of HA/CS/PCL

As shown in Figure 7, HA/CS/PCL + EPCs, HA/CS/PCL + BMSCs, and HA/CS/PCL + EPCs + BMSCs, presenting obvious repair on the injured calvaria of rabbits, were more remarkable compared with HA/CS/PCL at the 8th week after scaffold implantation.

EPCs and BMSCs accelerates HA/CS/PCL-based new bone formation

As shown in Figure 8A, compared with the HA/CS/PCL, BV/TV of HA/CS/PCL + EPCs, HA/CS/PCL + BMSCs, and HA/CS/PCL + EPCs + BMSCs groups increased significantly after 4 weeks and 8 weeks ($p < 0.05$), and the HA/CS/PCL + EPCs + BMSCs group presented the best calvarial repair effect at both the 4th and 8th week (Figure 8B).

EPCs and BMSCs improves the histological repair results of calvarial defects

As shown in Figure 9, by the 2nd week, all the groups failed to form bone after implantation. By the 4th week, connective tissue (CT) was found around the HA/CS/PCL composite scaffold,

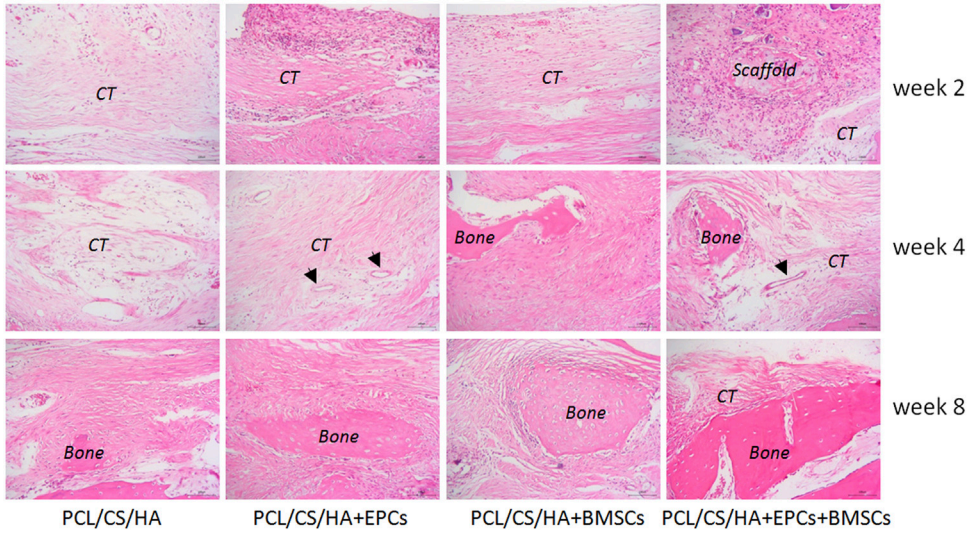

FIGURE 9
Histological structure of defected calvaria with composite scaffold repair at the post-surgery of the 2nd, 4th, and 8th week. New bone (bone), connective tissue (CT), and arrows indicate blood vessel.

while there was significantly more CT in the HA/CS/PCL + EPCs + BMSCs group than those of the other three groups. New blood vessels could be found even in the HA/CS/PCL + EPCs and HA/CS/PCL + EPCs + BMSCs groups. By 8 weeks, new bone was observed in all the groups. Moreover, implantation of the composite scaffold of HA/CS/PCL, at calvarial defect site, performed moderate bone regeneration, but failed to completely repair the defects, while implantation of HA/CS/PCL + BMSCs and HA/CS/PCL + EPCs composite scaffolds, there were more new bone in the calvarial defect area, however, the HA/CS/PCL + EPCs + BMSCs composite scaffold resulted in the most significant repair of the defects.

EPCs and BMSCs enhances the expression of BMP-2, VEGF, and PDGF

As shown in Figure 10, compared with the HA/CS/PCL group, BMP-2 expression in the HA/CS/PCL + BMSCs and HA/CS/PCL + EPCs + BMSCs groups was significantly higher at the 2nd and 4th week ($p < 0.05$). The HA/CS/PCL + EPCs, HA/CS/PCL + BMSCs, and HA/CS/PCL + EPCs + BMSCs groups all showed remarkably higher levels of BMP-2 at the 8th week compared with the HA/CS/PCL group ($p < 0.05$).

VEGF levels in the HA/CS/PCL + BMSCs and HA/CS/PCL + EPCs + BMSCs groups were greatly higher than that in the HA/CS/PCL group at the 2nd week ($p < 0.05$). At the 4th week, VEGF expression in the HA/CS/PCL + EPCs + BMSCs group exceeded that in the HA/CS/PCL group ($p < 0.05$). At the 8th week, VEGF expression in the HA/CS/PCL + BMSCs and HA/CS/PCL + EPCs + BMSCs groups were significantly higher than that in the HA/CS/PCL group ($p < 0.05$), which indicated potential neovascularization ability of HA/CS/PCL scaffolds engrafted BMSCs or EPCs.

The expression of PDGF in the HA/CS/PCL + EPCs, HA/CS/PCL + BMSCs, and HA/CS/PCL + EPCs + BMSCs groups increased remarkably at the 2nd, 4th, and 8th week compared with the HA/CS/PCL group ($p < 0.05$).

Discussion

In this study, the composite scaffolds engrafted EPCs and BMSCs were developed, of which function in the calvarial repair was confirmed. Moreover, this study, providing the new experimental evidence for the treatment of calvarial repair, presented that the HA/CS/PCL scaffold possessed a mild repair effect, while the inoculation with EPCs and BMSCs obviously promoted the calvarial repair.

It has been found in our previous study that BMSCs possess the ability of directional migration by microphotography, which lays the foundation for the construction of tissue-engineered bone in this present study (Yang et al., 2014). Niemeyer et al. (2010) reported that human mesenchymal stem cells were transplanted into the critical-size bone defect of rabbit to examine the regeneration potential. Zong et al. (2010) evaluated the osteogenic effect of BMSCs and osteoblast-like cells combined with poly lactic-co-glycolic acid (PLGA) on

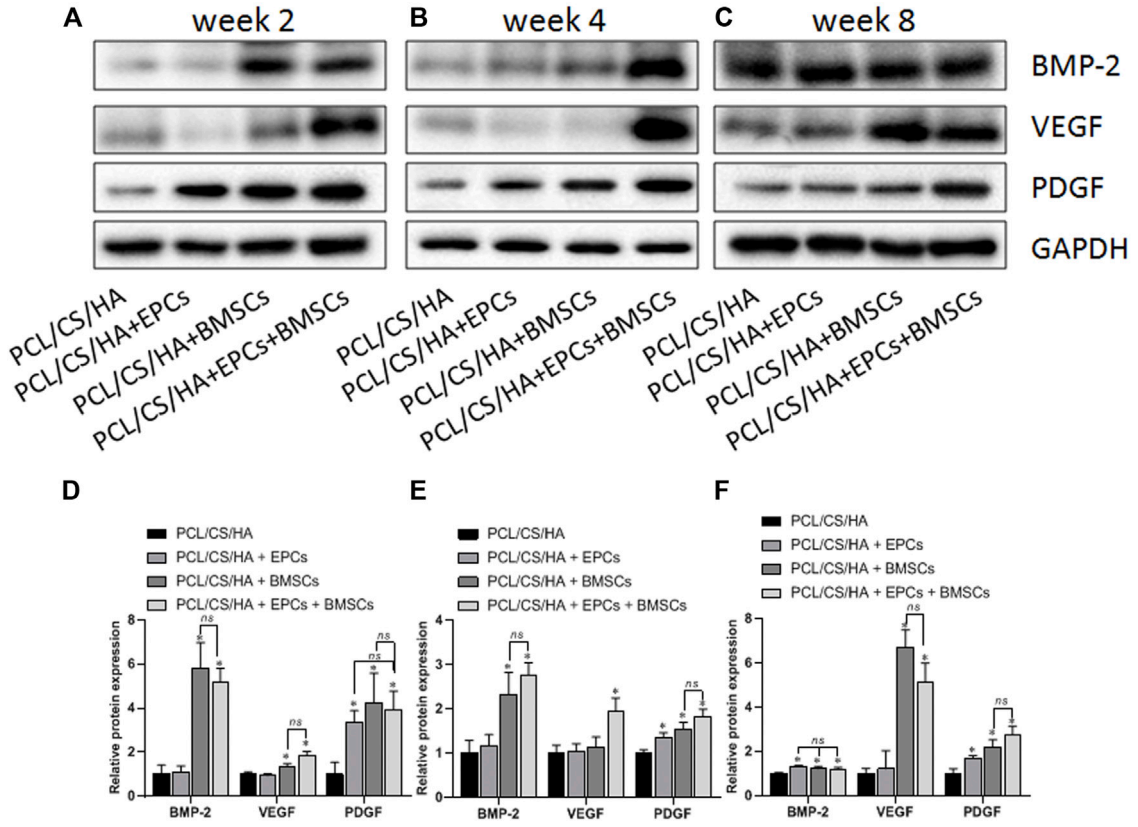

FIGURE 10
Expression levels of BMP-2, VEGF, and PDGF in the repaired calvaria with composite scaffold by western blot analysis. The representative bands and the quantified gray scale normalized to GAPDH for BMP-2, VEGF, and PDGF expression at the 2nd week **(A,D)**, 4th week **(B,E)**, and 8th week **(C,F)**. *$p < 0.05$ vs. HA/CS/PCL group, ns $p > 0.05$.

the calvarial defect of rats and revealed that BMSCs were superior to osteoblasts in bone reconstruction. In this study, BMSCs and EPCs were isolated and identified on the basis of the surface markers and were used as seed cells, and then the reconstruction effects were evaluated on the calvarial defect of rabbits by BMSCs, EPCs, or combined BMSCs and EPCs in HA/CS/PCL scaffolds.

Scaffold material plays a crucial role in bone tissue engineering not only in supporting and maintaining the shape of original bone tissue but also as a biomaterial template providing attachment for engrafted cells to live, grow, and differentiate, and guiding the regeneration of damaged tissue and controlling the regenerated structure (Szpalski et al., 2012). In this study, the HA/CS/PCL porous ternary composite scaffold was prepared by three-dimensional printing and molding technology. As the scaffold was effectively solved by the three-dimensional and controllable internal and external structures, the obtained multi-scale structure and shape of scaffolds could be used to simulate the ideal bone repair material. Some studies have shown that scaffold using calcium-deficient hydroxyapatite and BMP-2–loaded sulfate chitosan could repair rat calvarial defect and promote new bone formation *in vivo* (Zhao et al., 2012). Chen et al. (2013) used macroporous calcium phosphate seeded with human umbilical cord mesenchymal stem cells to repair 8-mm rat cranial defects, which promoted new bone regeneration. In this study, X-ray, micro-CT, and pathological results manifested that HA/CS/PCL + EPCs, HA/CS/PCL + BMSCs, and HA/CS/PCL + EPCs + BMSCs groups had remarkable repair effect on bone defects. Particularly, at the 8th week, HA/CS/PCL + EPCs + BMSCs scaffold implantation performed more significantly. These results suggest that BMSCs may be combined with EPCs as seed cells, which possess neovascularization ability, to exert both the directional migration ability of BMSCs and the vascularization ability of EPCs to facilitate new bone formation.

The differentiation of BMSCs into osteoblast-like cells, osteogenesis induction by BMP-2 is of importance for improving the osteoinduction and osteoconduction properties

of bone scaffold materials (Yamaguchi et al., 1996; Partridge et al., 2002; Li et al., 2006). The new bone formation by scaffold materials promotes vascularization, depending on the participation of growth factors, such as VEGF, PDGF (Nguyen et al., 2012), and transforming growth factor β (TGF-β) (Thurston, 2002). BMP is the main signaling pathway in osteogenic differentiation to boost the formation of new bone (Liu et al., 2017). As the strongest member in bone induction in the BMP family (Sun et al., 2017), BMP-2 can promote bone formation by direct application or local application in carriers (Demiray et al., 2017; Khorsand et al., 2017; Kuttappan et al., 2018) and enhance the expression of Runx2, a key transcription factor in bone differentiation, thus to activate the osteogenic process (Li et al., 2017). VEGF is recognized as the most powerful and specific angiogenic factor (Ju et al., 2018), which regulates bone formation by stimulating the differentiation and proliferation of osteoblasts, accelerating the formation and remodeling of bone (Huang et al., 2016). Both BMP-2 and VEGF play the important roles in bone regeneration as osteogenic factors and angiogenic factors, respectively (Kempen et al., 2009). It is reported that the expression of BMP-2 and VEGF enhance each other in the fracture healing (Zhang et al., 2011). VEGF could upregulate the expression of BMP-2 in osteoblasts and accelerate bone healing (Samee et al., 2008). In the initial steps of bone regeneration, PDGF promotes mitosis and angiogenesis, increases the synthesis of collagen and strengthens the local stress (Yang et al., 2017). Nash et al. (1994) injected collagen-containing rhPDGF into rabbits that underwent unilateral tibial osteotomy and found that rhPDGF increased the callus density, callus volume, and osteogenic differentiation. This present study showed that the expression of BMP-2, VEGF, and PDGF in the HA/CS/PCL + EPCs + BMSCs group increased at the 2nd, 4th, and 8th weeks, and there was a clear improvement in new bone formation and pathological change compared with the other three groups, which suggest that the better effect of HA/CS/PCL + EPCs + BMSCs on repairing bone defects may be related to the significantly increased expression of BMP-2, VEGF, and PDGF and their additive effect on bone regeneration.

In conclusion, this study proves that HA/CS/PCL + EPCs + BMSCs possess a better bone repair effect in the rabbit calvarial injury model, likely through increasing the expression of BMP-2, VEGF, and PDGF and, simultaneously, provides the experimental evidence for the future clinical application of the cell–matrix composite scaffold.

Data availability statement

The original contributions presented in the study are included in the article/Supplementary Material; further inquiries can be directed to the corresponding authors.

Ethics statement

The animal study was reviewed and approved by the ethics committee of Hubei University of Medicine.

Author contributions

HY and WL conceived and designed the experiments. HY, LX, XL, YC, LZ, XN, and JL performed the experiments and analyzed the data. HY, JL, and WL wrote the manuscript. All authors read and approved the manuscript and agree to be accountable for all aspects of the research in ensuring that the accuracy or integrity of any part of the work are appropriately investigated and resolved.

Funding

This study was supported by the National Natural Science Foundation of China (No. 81671831).

Conflict of interest

The authors declare that the research was conducted in the absence of any commercial or financial relationships that could be construed as a potential conflict of interest.

Publisher's note

All claims expressed in this article are solely those of the authors and do not necessarily represent those of their affiliated organizations, or those of the publisher, the editors, and the reviewers. Any product that may be evaluated in this article, or claim that may be made by its manufacturer, is not guaranteed or endorsed by the publisher.

References

Baroli, B. (2009). From natural bone grafts to tissue engineering therapeutics: Brainstorming on pharmaceutical formulative requirements and challenges. *J. Pharm. Sci.* 98 (4), 1317–1375. doi:10.1002/jps.21528

Chen, W., Liu, J., Manuchehrabadi, N., Weir, M. D., Zhu, Z., Xu, H. H., et al. (2013). Umbilical cord and bone marrow mesenchymal stem cell seeding on macroporous calcium phosphate for bone regeneration in rat cranial defects. *Biomaterials* 34 (38), 9917–9925. doi:10.1016/j.biomaterials.2013.09.002

Demiray, S. B., Yilmaz, O., Goker, E., Tavmergen, E., Calimlioglu, N., Sezerman, U., et al. (2017). Expression of the bone morphogenetic protein-2 (BMP2) in the

human cumulus cells as a biomarker of oocytes and embryo quality. *J. Hum. Reprod. Sci.* 10 (3), 194. doi:10.4103/jhrs.JHRS_21_17

Ding, P., Zhang, W., Tan, Q., Yao, C., and Lin, S. (2019). Impairment of circulating endothelial progenitor cells (EPCs) in patients with glucocorticoid-induced avascular necrosis of the femoral head and changes of EPCs after glucocorticoid treatment *in vitro*. *J. Orthop. Surg. Res.* 14 (1), 226. doi:10.1186/s13018-019-1279-6

Dumont, V. C., Mansur, H. S., Mansur, A. A., Carvalho, S. M., Capanema, N. S., Barrioni, B. R., et al. (2016). Glycol chitosan/nanohydroxyapatite biocomposites for potential bone tissue engineering and regenerative medicine. *Int. J. Biol. Macromol.* 93 (Pt B), 1465–1478. doi:10.1016/j.ijbiomac.2016.04.030

Gao, G., Lu, S., Dong, B., Zhang, Z., Zheng, Y., Ding, S., et al. (2015). One-pot synthesis of carbon coated Fe3O4 nanosheets with superior lithium storage capability. *J. Mat. Chem. A Mat.* 3 (8), 4716–4721. doi:10.1039/C4TA05725B

Goerke, S. M., Obermeyer, J., Plaha, J., Stark, G. B., and Finkenzeller, G. (2015). Endothelial progenitor cells from peripheral blood support bone regeneration by provoking an angiogenic response. *Microvasc. Res.* 98, 40–47. doi:10.1016/j.mvr.2014.12.001

Huang, Y., Wu, G., Dou, Y., and Cao, S. (2016). Mechanism of Shensu IV intervention on podocyte injury in rats with puromycin nephropathy. *Shanxi Zhongyi* 37, 1559–1562. doi:10.1042/BSR20203362

Ju, X., Xue, D., Wang, T., Ge, B., Zhang, Y., Li, Z., et al. (2018). Catalpol promotes the survival and VEGF secretion of bone marrow-derived stem cells and their role in myocardial repair after myocardial infarction in rats. *Cardiovasc. Toxicol.* 18 (5), 471–481. doi:10.1007/s12012-018-9460-4

Kai, D., Prabhakaran, M. P., Chan, B. Q., Liow, S. S., Ramakrishna, S., Xu, F., et al. (2016). Elastic poly(ε-caprolactone)-polydimethylsiloxane copolymer fibers with shape memory effect for bone tissue engineering. *Biomed. Mat.* 11 (1), 015007. doi:10.1088/1748-6041/11/1/015007

Kempen, D. H., Lu, L., Heijink, A., Hefferan, T. E., Creemers, L. B., Maran, A., et al. (2009). Effect of local sequential VEGF and BMP-2 delivery on ectopic and orthotopic bone regeneration. *Biomaterials* 30 (14), 2816–2825. doi:10.1016/j.biomaterials.2009.01.031

Khorsand, B., Elangovan, S., Hong, L., Dewerth, A., Kormann, M. S., Salem, A. K., et al. (2017). A comparative study of the bone regenerative effect of chemically modified RNA encoding BMP-2 or BMP-9. *AAPS J.* 19 (2), 438–446. doi:10.1208/s12248-016-0034-8

Kuttappan, S., Anitha, A., Minsha, M. G., Menon, P. M., Sivanarayanan, T. B., Vijayachandran, L. S., et al. (2018). BMP2 expressing genetically engineered mesenchymal stem cells on composite fibrous scaffolds for enhanced bone regeneration in segmental defects. *Mater. Sci. Eng. C* 85, 239–248. doi:10.1016/j.msec.2018.01.001

Lee, S. J., Lee, D., Yoon, T. R., Kim, H. K., Jo, H. H., Park, J. S., et al. (2016). Surface modification of 3D-printed porous scaffolds via mussel-inspired polydopamine and effective immobilization of rhBMP-2 to promote osteogenic differentiation for bone tissue engineering. *Acta biomater.* 40, 182–191. doi:10.1016/j.actbio.2016.02.006

Li, C., Vepari, C., Jin, H. J., Kim, H. J., and Kaplan, D. L. (2006). Electrospun silk-BMP-2 scaffolds for bone tissue engineering. *Biomaterials* 27 (16), 3115–3124. doi:10.1016/j.biomaterials.2006.01.022

Li, Z., Wang, W., Xu, H., Ning, Y., Fang, W., Liao, W., et al. (2017). Effects of altered CXCL12/CXCR4 axis on BMP2/Smad/Runx2/Osterix axis and osteogenic gene expressions during osteogenic differentiation of MSCs. *Am. J. Transl. Res.* 9 (4), 1680–1693.

Liu, J., Liang, C., Guo, B., Wu, X., Li, D., Zhang, Z., et al. (2017). Increased PLEKHO1 within osteoblasts suppresses Smad-dependent BMP signaling to inhibit bone formation during aging. *Aging Cell.* 16 (2), 360–376. doi:10.1111/acel.12566

Luo, T., Fu, X., Liu, Y., Ji, Y., and Shang, Z. (2021). Sulforaphane inhibits osteoclastogenesis via suppression of the autophagic pathway. *Mol. (Basel, Switz.* 26 (2), 347. doi:10.3390/molecules26020347

Nash, T. J., Howlett, C. R., Martin, C., Steele, J., Johnson, K. A., Hicklin, D. J., et al. (1994). Effect of platelet-derived growth factor on tibial osteotomies in rabbits. *Bone* 15 (2), 203–208. doi:10.1016/8756-3282(94)90709-9

Nguyen, L. H., Annabi, N., Nikkhah, M., Bae, H., Binan, L., Park, S., et al. (2012). Vascularized bone tissue engineering: Approaches for potential improvement. *Tissue Eng. Part B Rev.* 18 (5), 363–382. doi:10.1089/ten.TEB.2012.0012

Niemeyer, P., Szalay, K., Luginbühl, R., Südkamp, N. P., and Kasten, P. (2010). Transplantation of human mesenchymal stem cells in a non-autogenous setting for bone regeneration in a rabbit critical-size defect model. *Acta biomater.* 6 (3), 900–908. doi:10.1016/j.actbio.2009.09.007

Oliveira, H. L., Da Rosa, W., Cuevas-Suárez, C. E., Carreño, N., da Silva, A. F., Guim, T. N., et al. (2017). Histological evaluation of bone repair with hydroxyapatite: A systematic review. *Calcif. Tissue Int.* 101 (4), 341–354. doi:10.1007/s00223-017-0294-z

Partridge, K., Yang, X., Clarke, N. M., Okubo, Y., Bessho, K., Sebald, W., et al. (2002). Adenoviral BMP-2 gene transfer in mesenchymal stem cells: *In vitro* and *in vivo* bone formation on biodegradable polymer scaffolds. *Biochem. biophysical Res. Commun.* 292 (1), 144–152. doi:10.1006/bbrc.2002.6623

Samee, M., Kasugai, S., Kondo, H., Ohya, K., Shimokawa, H., Kuroda, S., et al. (2008). Bone morphogenetic protein-2 (BMP-2) and vascular endothelial growth factor (VEGF) transfection to human periosteal cells enhances osteoblast differentiation and bone formation. *J. Pharmacol. Sci.* 108 (1), 18–31. doi:10.1254/jphs.08036fp

Stegen, S., van Gastel, N., and Carmeliet, G. (2015). Bringing new life to damaged bone: The importance of angiogenesis in bone repair and regeneration. *Bone* 70, 19–27. doi:10.1016/j.bone.2014.09.017

Sun, J., Zhang, Y., Li, B., Gu, Y., and Chen, L. (2017). Controlled release of BMP-2 from a collagen-mimetic peptide-modified silk fibroin-nanohydroxyapatite scaffold for bone regeneration. *J. Mat. Chem. B* 5 (44), 8770–8779. doi:10.1039/c7tb02043k

Szpalski, C., Wetterau, M., Barr, J., and Warren, S. M. (2012). Bone tissue engineering: Current strategies and techniques—Part I: Scaffolds. *Tissue Eng. Part B Rev.* 18 (4), 246–257. doi:10.1089/ten.TEB.2011.0427

Thurston, G. (2002). Complementary actions of VEGF and angiopoietin-1 on blood vessel growth and leakage. *J. Anat.* 200 (6), 575–580. doi:10.1046/j.1469-7580.2002.00061.x

Tian, Y., Wu, D., Wu, D., Cui, Y., Ren, G., Wang, Y., et al. (2022). Chitosan-based biomaterial scaffolds for the repair of infected bone defects. *Front. Bioeng. Biotechnol.* 10, 899760. doi:10.3389/fbioe.2022.899760

Yamaguchi, A., Ishizuya, T., Kintou, N., Wada, Y., Katagiri, T., Wozney, J. M., et al. (1996). Effects of BMP-2, BMP-4, and BMP-6 on osteoblastic differentiation of bone marrow-derived stromal cell lines, ST2 and MC3T3-G2/PA6. *Biochem. biophysical Res. Commun.* 220 (2), 366–371. doi:10.1006/bbrc.1996.0411

Yang, X., Dong, M., Wen, H., Liu, X., Zhang, M., Ma, L., et al. (2017). MiR-26a contributes to the PDGF-BB-induced phenotypic switch of vascular smooth muscle cells by suppressing Smad1. *Oncotarget* 8 (44), 75844–75853. doi:10.18632/oncotarget.17998

Yang, Z. S., Tang, X. J., Guo, X. R., Zou, D. D., Sun, X. Y., Feng, J. B., et al. (2014). Cancer cell-oriented migration of mesenchymal stem cells engineered with an anticancer gene (PTEN): An imaging demonstration. *Onco. Targets. Ther.* 7, 441–446. doi:10.2147/OTT.S59227

Yu, H. D., Zhang, L., Xia, L. Y., Mao, M., Ni, X. B., Leng, W. D., et al. (2020). Construction and characterization of nano-hydroxyapatite/chitosan/polycaprolactone composite scaffolds by 3D printing. *Chin. J. Tissue Eng. Res.* 24 (10), 1496–1501. doi:10.3969/j.issn.2095-4344.2238

Zhang, W., Wang, X., Wang, S., Zhao, J., Xu, L., Zhu, C., et al. (2011). The use of injectable sonication-induced silk hydrogel for VEGF(165) and BMP-2 delivery for elevation of the maxillary sinus floor. *Biomaterials* 32 (35), 9415–9424. doi:10.1016/j.biomaterials.2011.08.047

Zhao, J., Shen, G., Liu, C., Wang, S., Zhang, W., Zhang, X., et al. (2012). Enhanced healing of rat calvarial defects with sulfated chitosan-coated calcium-deficient hydroxyapatite/bone morphogenetic protein 2 scaffolds. *Tissue Eng. Part A* 18 (1-2), 185–197. doi:10.1089/ten.TEA.2011.0297

Zong, C., Xue, D., Yuan, W., Wang, W., Shen, D., Tong, X., et al. (2010). Reconstruction of rat calvarial defects with human mesenchymal stem cells and osteoblast-like cells in poly-lactic-co-glycolic acid scaffolds. *Eur. Cell. Mat.* 20, 109–120. doi:10.22203/ecm.v020a10

frontiers | Frontiers in Bioengineering and Biotechnology

TYPE Review
PUBLISHED 06 September 2022
DOI 10.3389/fbioe.2022.994655

OPEN ACCESS

EDITED BY
Chao Zhao,
University of Alabama, United States

REVIEWED BY
Xianglong Hu,
University of Science and Technology of China, China
Chunyang Sun,
Tianjin Medical University General Hospital, China
Yuce Li,
Sungkyunkwan University, South Korea
Xianwen Wang,
Anhui Medical University, China
Yingqi Hua,
Shanghai General Hospital, China

*CORRESPONDENCE
Peng Zhang,
peng.zhang@ciac.ac.cn
Zhiyu Zhang,
zyzhang@cmu.edu.cn

†These authors have contributed equally to this work

SPECIALTY SECTION
This article was submitted to Biomaterials, a section of the journal Frontiers in Bioengineering and Biotechnology

RECEIVED 15 July 2022
ACCEPTED 17 August 2022
PUBLISHED 06 September 2022

CITATION
Cheng Z, Li Y, Zhao D, Zhao W, Wu M, Zhang W, Cui Y, Zhang P and Zhang Z (2022), Nanocarriers for intracellular co-delivery of proteins and small-molecule drugs for cancer therapy. *Front. Bioeng. Biotechnol.* 10:994655. doi: 10.3389/fbioe.2022.994655

Nanocarriers for intracellular co-delivery of proteins and small-molecule drugs for cancer therapy

Zhihong Cheng[1,2†], Yongshuang Li[3†], Duoyi Zhao[1], Wei Zhao[1], Meng Wu[1], Weilin Zhang[1], Yan Cui[1], Peng Zhang[2*] and Zhiyu Zhang[1*]

[1]Department of Orthopedics, The Fourth Affiliated Hospital of China Medical University, Shenyang, China, [2]Key Laboratory of Polymer Ecomaterials, Changchun Institute of Applied Chemistry, Chinese Academy of Sciences, Changchun, China, [3]Department of General Surgery, The Fourth Affiliated Hospital of China Medical University, Shenyang, China

In the past few decades, the combination of proteins and small-molecule drugs has made tremendous progress in cancer treatment, but it is still not satisfactory. Because there are great differences in molecular weight, water solubility, stability, pharmacokinetics, biodistribution, and the ways of release and action between macromolecular proteins and small-molecule drugs. To improve the efficacy and safety of tumor treatment, people are committed to developing protein and drug co-delivery systems. Currently, intracellular co-delivery systems have been developed that integrate proteins and small-molecule drugs into one nanocarrier *via* various loading strategies. These systems significantly improve the blood stability, half-life, and biodistribution of proteins and small-molecule drugs, thus increasing their concentration in tumors. Furthermore, proteins and small-molecule drugs within these systems can be specifically targeted to tumor cells, and are released to perform functions after entering tumor cells simultaneously, resulting in improved effectiveness and safety of tumor treatment. This review summarizes the latest progress in protein and small-molecule drug intracellular co-delivery systems, with emphasis on the composition of nanocarriers, as well as on the loading methods of proteins and small-molecule drugs that play a role in cells into the systems, which have not been summarized by others so far.

KEYWORDS

nanocarriers, proteins, small-molecule drugs, intracellular co-delivery, cancer therapy

1 Introduction

Cancer is the leading cause of death worldwide, and the treatment of cancer remains one of the most challenging problems (DeSantis et al., 2014; Ward et al., 2014; Zheng et al., 2021a). Over the past few decades, the clinical treatment of cancer mainly depends on the surgery, radiotherapy, and chemotherapy (Hu J et al., 2016). In recent years, the new

tumor treatment strategies have also made great progress in the clinic (Sanchez-Garcia et al., 2016; Chudy et al., 2018; Li et al., 2022). Protein-based therapies play an important role in biomedicine because of their pharmacological action and highly selective biological activity (Mitragotri et al., 2014; Su et al., 2018; Liu et al., 2019). However, proteins have unfavorable physical and chemical properties, such as fragile tertiary structure, large molecular size, and poor membrane permeability, which make the efficiency of intracellular protein delivery very low (Qin et al., 2019). And so far, protein delivery system is mainly focused on extracellular targets, but there are many potential applications that require protein delivery into the cytoplasm (Leader et al., 2008; Cheng et al., 2018; Scaletti et al., 2018; Shao et al., 2018). Protein-based therapies for clinical application are currently limited to those that function outside cells, such as cytokines and monoclonal antibodies. Protein biologics with intracellular anticancer activity have not been widely studied for clinical application due to poor cell membrane permeability.

Due to the complexity of cancer mechanism, the use of a single anticancer agent for tumor treatment may be insufficient, so the combined use of a variety of therapeutic agents to enhance the anti-tumor effect has been investigated (Hu Q et al., 2016; Chen et al., 2017; Yang and Ding 2022). The combined therapy with a variety of free anticancer agents has stronger anticancer effect than a single anticancer agent, but it also has some limitations, such as short blood circulation time, poor tumor selectivity, insufficient tumor accumulation, severe side effects and so on (Thao et al., 2015; You et al., 2018). With the development of nanocarriers, a variety of anticancer agents are loaded into a single carrier to improve and unify the pharmacokinetics, enhance tumor selectivity and drug accumulation at the tumor sites, minimize side effects and optimize the therapeutic effects (Lee et al., 2011; Wu et al., 2015; Lin et al., 2017; Wei L et al., 2021; Yang et al., 2021). Multiple co-delivery systems loaded with antineoplastic drug combinations have been developed to treat tumors, such as two chemotherapeutics, chemotherapeutic and gene, chemotherapeutic and protein, etc. (Yin et al., 2018; Zhou et al., 2018; Gao et al., 2019; Wan et al., 2021) Among them, it is relatively difficult to load small-molecule drugs and macromolecular proteins together in the nanocarriers (Fumoto and Nishida 2020). Because small-molecule drugs and proteins have unique physical and chemical properties, such as size, hydrophilic/hydrophobic properties, charge properties, specificity, stability and cell membrane permeability (Peng et al., 2019). The development of monotherapy based on multiple drug delivery techniques of small-molecule drugs or proteins is undoubtedly a very active research field of cancer therapy, but several or more drugs in combination therapy can cause the death of tumor cells by targeting different apoptotic pathways at the same time, resulting in a synergistic anticancer effect. It can also reduce the dosage of drugs and reduce side effects, which shows greater potential as an alternative to monotherapy (Lehár et al., 2009; Hu et al., 2010; Hu and Zhang 2012).

Many biological drugs work by binding to intracellular targets, so intracellular delivery is required (He et al., 2020). Therefore, to achieve the intracellular co-delivery of proteins and small-molecule drugs, we should first consider the inherent properties of proteins and small-molecule drugs, which have distinct physical and chemical properties, hindering their integration into a single nanocarrier (Kim et al., 2015). Unlike extracellular proteins, the intracellular proteins are usually encapsulated in the endosome, so they are degraded in lysosomes, resulting in very low therapeutic efficacy (Kaczmarczyk et al., 2011; Fu et al., 2014). Most traditional nanocarriers are internalized by endocytosis, and then through endocytosis escape to achieve intracellular delivery of biopharmaceuticals (He, Xing, Wang, Wu, Wu, Guo and Mitragotri 2020). Moreover, another challenge is the system stability of the co-delivery system, as the early release of cargoes in the blood may lead to adverse reactions and reduced tumor accumulation through enhanced permeability and retention of (EPR) effects (Mura et al., 2013). Nanoparticles need to stay in systemic circulation for a long time and are stable for plasma dilution, regulation, and clearance of the reticuloendothelial system (Liu et al., 2014; Zhang R et al., 2018). These challenges must be taken into account in the rational design of a co-delivery system.

This review introduces the latest development of various delivery carrier systems for intracellular co-delivery of small-molecule drugs and proteins, such as nanocapsules, liposome-based nanocarriers, polymeric nanocarriers, silica-based nanocarriers, metal–organic frameworks, and other nanocarriers, and focuses on how various proteins and small molecules are concurrently loaded into the delivery systems, as summarized in Figure 1. A recent overview of strategies for intracellular co-delivery of proteins and small-molecule drugs can provide clues about how to load multiple agents with different physicochemical properties into one single nanocarrier, and help to develop new intracellular co-delivery systems to achieve improved tumor treatment effects and reduced side effects.

2 Nanocarriers for intracellular co-delivery of proteins and small-molecule drugs

Due to the different biological distribution behaviors of macromolecules and small molecules, nanocarriers are the preferred drug delivery method to realize the synchronous biological distribution of proteins and drugs *in vivo* (Chiper et al., 2018; Peng et al., 2019). Therefore, in recent years, there have been some delivery systems for co-delivery of small-

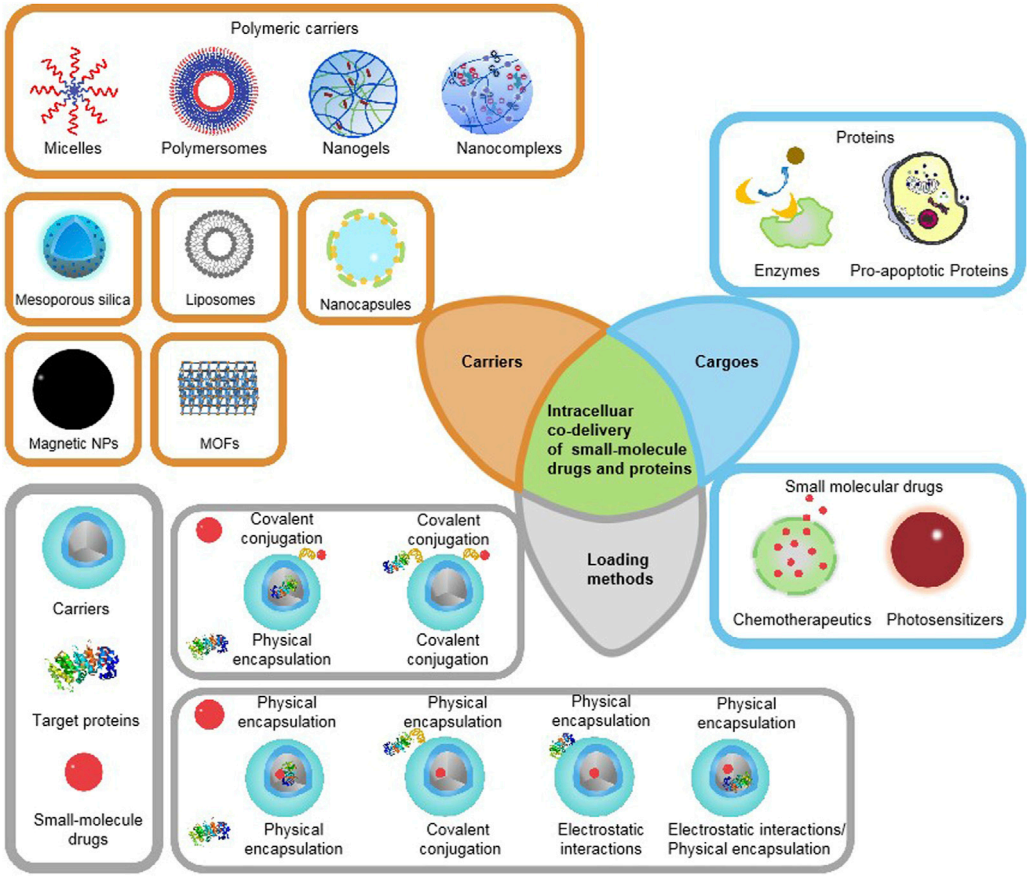

FIGURE 1
Schematic illustration of existing therapeutic proteins, small-molecule drugs, major categories of co-delivery systems, and commonly used loading/encapsulation strategies, as discussed in this Review.

molecule drugs and proteins to tumor cells, by applying different ligands to locate the required subcellular compartments, such as cytoplasm, nuclei, and mitochondria. This enables targeted intracellular co-delivery of small-molecule drugs and proteins, allowing the simultaneous release of two or more drugs in a controlled manner (Biju 2014; Zhong et al., 2015; Wei Q et al., 2021). Representative carrier types and combination strategies are presented in Table 1. The covalent bonds applied for the loading of proteins or small-molecule drugs into intracellular co-delivery systems are summarized in Table 2.

2.1 Nanocapsules

In recent years, polymeric nanocapsules have aroused great interest in the field of drug sustained-release due to the advantages of core-shell structure. Compared with polymeric nanospheres, the solid/oil core of nanocapsules can effectively improve the drug loading efficiency and reduce the polymeric matrix content of nanoparticles (Raffin Pohlmann et al., 2002; Wang et al., 2021). The encapsulated payload can be isolated from the tissue environment through the polymeric shell, avoiding degradation or sudden release caused by pH, temperature, enzymes, and other factors (Trindade et al., 2018). By loading the drug into the polymeric nanocapsules, the drug can be protected from the destruction or degradation of the biological environment. At the same time, it can also reduce the side effects of drugs on healthy tissues (Deng et al., 2020a). The core of polymeric nanocapsules can be made from not only a hydrophobic core but also from a hydrophilic core to deliver hydrophilic molecules, such as hydrophilic anticancer drugs gemcitabine hydrochloride (Cosco et al., 2015) and doxorubicin (Vrignaud et al., 2013), water-soluble protein albumin (Li et al., 2005).

However, in order to realize the co-delivery of proteins and drugs, nanocapsules need to be further modified. For example, M. Rotello and his colleagues developed nanoparticle-stabilized capsules (NPSCs) that could be used to deliver proteins directly into the cytoplasm, and later they used the nanocapsules to deliver small-molecule drugs and proteins together (Tang et al.,

TABLE 1 Summary of recently reported intracellular co-delivery nano-systems of proteins and drugs for tumor treatment.

Large categories of nanocarriers	Detailed categories of nanocarriers	Therapeutic proteins/Loading mode	Small-molecule drugs/Loading mode	Ref.
Nanocapsules	Nanocapsules	CASP3/Electrostatic interactions	PTX/Physical encapsulation	Kim et al. (2015)
	Chitosan nanocapsules	CASP3/Electrostatic interactions	PTX/Physical encapsulation	Wu et al. (2017)
	Dual-cargo nanocapsules	RNase A/Electrostatic interactions	Dox/Covalent conjugation	Liew et al. (2021)
Liposome-based nanocarriers	Lipid-calcium carbonate nanoparticles	Superoxide dismutase/Electrostatic interactions or hydrophobic interaction	PTX/Physical encapsulation	Peng et al. (2019)
	Liposomes	CAT/Physical encapsulation	Cisplatin/Covalent conjugation	Zhang et al. (2017)
	Dual loaded liposomal carriers	Ran-RCC1 inhibitory peptide/Physical encapsulation	Dox/Physical encapsulation	Haggag et al. (2020)
Polymeric nanocarriers	Triblock copolymer	RNase A/Covalent conjugation	Dox/Hydrophobic interaction	Zhang et al. (2020)
	Copolymer	CRISPR-Cas9 ribonucleoprotein/Covalent conjugation	Ce6/Hydrophobic interaction	Deng et al. (2020a)
	Polymeric Nanogels	β-galactosidase/Electrostatic interactions	DiI/Hydrophobic interaction	González-Toro et al. (2012)
	Polymersomes	Exogenous proteins/Electrostatic interactions and/or hydrophobic interaction	Dox/Hydrophobic interaction	Liu et al. (2010)
	Polymeric Nanocomplex	RNase A/Covalent conjugation	Oxaliplatin/Covalent conjugation	Lim et al. (2019)
	Multi-functional nanocarrier	RNase A/Covalent conjugation	Hematoporphyrin/Covalent conjugation	He et al. (2018)
Silica-based nanocarriers	Mesoporous silica nanoparticles	Cyt c/Covalent conjugation	Dox/Physical encapsulation	Pei et al. (2018)
	Silica nanoparticles	HAase/Physical encapsulation	Dox/Covalent conjugation	Chen et al. (2018)
	Large-pore mesoporous silica	RNase A/Physical encapsulation	DSP/Covalent conjugation	Teng et al. (2021)
	Multistage responsive nanoparticles	CAT/Physical encapsulation	Ce6/Covalent conjugation	Yang et al. (2018)
	Mesoporous silica nanoparticles	CRISPR-Cas9/Covalent conjugation	Axitinib/Physical encapsulation	Liu et al. (2020)
Metal–Organic Framework	Co-delivery nanoplatforms	Cyt c/Physical encapsulation	Ce6/Physical encapsulation	Ding et al. (2020)
Other nanocarriers	Magnetic nanoparticles	Trypsin/Covalent conjugation	QCy7/Covalent conjugation	Xu et al. (2019)
	Nano-Self-Assembly	TCS/Electrostatic interactions	ABZ/Physical encapsulation	Tang et al. (2017)
	Protein–polymer conjugates	Bovine serum albumin/Covalent conjugation	immune-modulators/ Hydrophobic interaction	Vanparijs et al. (2015)
	Upconversion nanocrystal-dendrimer composite	CAT/Electrostatic interactions	Ce6/Hydrophobic interaction	Liang et al. (2020)
	catalase-encapsulated hyaluronic-acid-based nanoparticles	CAT/Covalent conjugation	Ce6/Supramolecular encapsulation	Phua et al. (2019)
	DNA nanoassemblies	CAT/Physical encapsulation	Porphyrin photosensitizer/ Intercalation	Pan et al. (2020)

2013; Kim et al., 2015). The paclitaxel (PTX) was first dissolved in linoleic acid to prepare the nanocapsules, which were then made into emulsions using a commercial amalgamator. Arginine ligand functionalized gold nanoparticles (Arg-AuNPs) were assembled on the surface by electrostatic attraction. The negatively charged apoptosis-inducing protein caspase-3 (CASP3) was loaded into the NPSC shells through the electrostatic interaction with Arg-AuNPs, and the mitotic spindle assembly inhibitor, PTX, was loaded into the nanocapsules through physical encapsulation (Figure 2). Finally, CASP3 and PTX were delivered into the cells and played a synergistic effect. Apoptosis study and *in vitro* cell viability measurement showed that NPSC co-delivery of PTX and CASP3 compared with NPSC loaded with PTX or CASP3 alone led to a higher percentage of HeLa cell apoptosis, indicating a higher killing rate. The final results of the Chou-Talalay analysis showed that PTX and CASP3 had an overall synergistic effect on tumor cells (Kim et al., 2015). Although the nanoparticles stabilized capsules have the advantages of negative surface charge, moderate particle size, and improved protein stability, there are still some shortcomings, such as an additional non-fouling shell may be required for prolonged blood circulation, and the metabolism of gold nanoparticles *in vivo* requires further study (He et al., 2016).

In addition, in the field of nanoscience, chitosan nano-polymers have become potential carriers because of their

TABLE 2 Summary of covalent bonds applied for the loading of proteins or small-molecule drugs into intracellular co-delivery systems.

	Cargoes	Types of covalent conjugations	Release modes	Ref.
Proteins	RNase A	RNBC and then through phenylboronic acid–catechol interactions	ROS-triggered release	Zhang et al. (2020)
	CRISPR-Cas9 RNP	His-tagged Cas9 RNP	Near infrared-triggered release and reductant-triggered release	Deng et al. (2020b)
		Disulfide bonds	GSH-triggered release	Liu et al. (2020)
	Cyt c	Boronic ester bonds	ROS-triggered release	Pei et al. (2018)
	Trypsin	Trypsin conjugated with phenylboronic acid	H_2O_2-triggered release	Xu et al. (2019)
	CAT	β-cyclodextrin was first functionalized onto HA, followed by conjugation with CAT	—	Phua et al. (2019)
Small-molecule drugs	Cisplatin (IV) pro-drug	Pt (IV)-liposomes	Redox-triggered release	Zhang et al. (2017)
	Oxaliplatin (IV) pro-drug	PEI-oxliPt (IV)	Redox-triggered release	Lim et al. (2019)
	Hematoporphyrin	HA-HP	—	He et al. (2018)
	Dox	HA-DOX	Hyaluronidase-triggered release	Chen et al. (2018)
		BB-DOX	GSH/ROS-triggered release	Liew et al. (2021)
	Ce6	Covalently conjugated to APTES	—	Teng et al. (2021)
	Cisplatin pro-drug	Covalently conjugated to APTES	—	Yang et al. (2018)
	QCy7	QCy7 conjugated with phenylboronic acid	H_2O_2-triggered release	Xu et al. (2019)

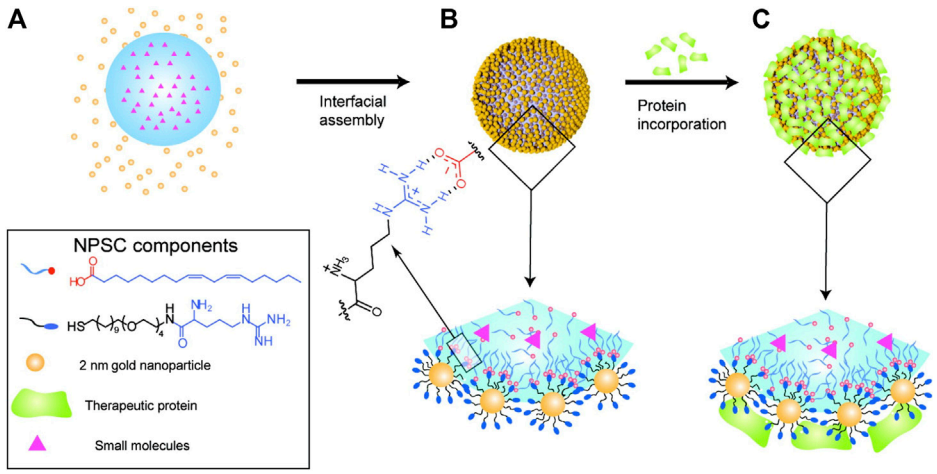

FIGURE 2
NPSC fabrication. **(A)** Template droplets (with or without PTX) were generated using an amalgamator. **(B)** Droplets were transferred to Arg-AuNP solution to generate NPSCs. **(C)** Incorporation of CASP3 or transferrin (control) onto the NPSC surface. Reproduced with permission from Ref. (Kim et al., 2015).

biodegradability and biocompatibility. The easy modification of chitosan nano-polymers and the versatility of drug delivery have attracted researchers to combine chemotherapeutics, proteins, and genetic drugs to target tumor cell-specific therapeutics (Shanmuganathan et al., 2019). Chitosan forms polycations by protonation of amino groups under the condition of low pH, which has high affinity and strong targeting to negatively charged cell membranes (Dutta et al., 2003; Fu et al., 2016). The

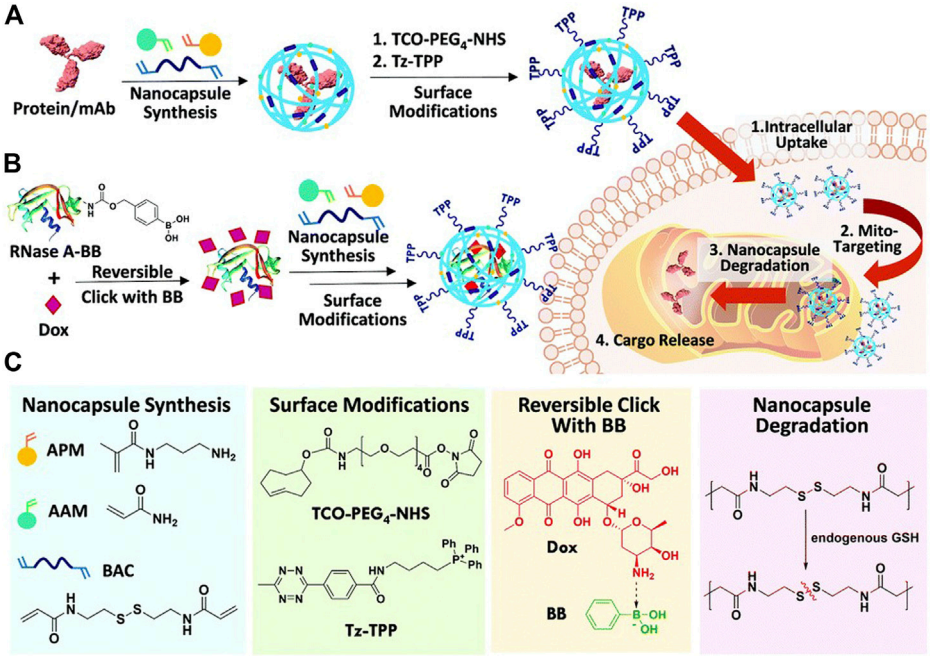

FIGURE 3
(A) Scheme summarizing the preparation of TPP–modified protein nanocapsules, intracellular uptake, TPP-directed mitochondrial accumulation, mitochondria GSH-triggered cargo release, and finally target binding/engagement. **(B)** Scheme showing co-encapsulation of phenyl boronic acid (BB)-modified RNase A/Doxorubicin (Dox) in a dual-cargo nanocapsule. **(C)** Chemical structures of reagents used. Reproduced with permission from Ref. (Liew et al., 2021).

hydrophobic drug paclitaxel can be loaded into LA droplets, and the positively charged recombinant human caspase-3 stabilizes the optimized Arg-CS nanocapsules (Arg-CNCS) on its negative surface (Wu et al., 2017). *In vitro* anti-tumor experiments showed that the co-administration system for co-delivery of paclitaxel and recombinant human caspase-3 showed lower IC_{50} values and higher apoptosis rates compared with the control group. Macromolecular proteins can be loaded by electrostatic interaction with polymeric nanoparticles with opposite charges, and small-molecule drugs can be combined through covalent modification to realize the co-delivery of proteins and small-molecule drugs.

The application of dual-cargo nanocapsules in mitochondrial targeting therapy with a protein and small-molecular drug (ribonuclease A/doxorubicin) was reported for the first time (Liew et al., 2021). Ribonuclease A (RNase A) was first modified with phenyl boronic acid (BB) and then clicked with doxorubicin (Dox) to form RNase A-BB-Dox conjugate, which was then crosslinked with monomers acrylamide (AAM), N-(3-aminopropyl) methacrylamide (APM) and N, N′-bis(acryloyl) cystamine (BAC) to form protein nanocapsules. Then the surface was modified with *trans*-cyclooctene (TCO)-PEG_4-NHS due to the positive charge introduced by the APM monomer, and finally functionalized with tetrazine triphenylphosphosphonium (Tz-TPP) *via* a Tz-TCO click (Figure 3). TPP is a kind of lipophilic cation, which can target the highly negative charge site of the mitochondrial membrane, thus possessing mitochondrial targeting capability.

2.2 Liposomal nanocarriers

The liposome is a spherical structure formed by one or more concentric lipid bilayers around the discrete water space. Compared with other drug delivery systems, liposomes exhibit several different characteristics, including biocompatibility, non-immunogenicity, self-assembly ability, loading hydrophilic and hydrophobic reagents and improving their solubility, carrying large drug payloads, and protecting encapsulation agents from external media, reducing the toxicity of encapsulation agents and the ability to expose sensitive tissues to toxic drugs and to have site-specific targeting and improve permeability to tissues (Zununi Vahed et al., 2017). Due to their special structure, liposomes can transfer several bioactive compounds and macromolecules (such as DNA, peptides, proteins, and imaging agents) in lipid bilayers (hydrophobic molecules) and lumens (hydrophilic molecules) (Naseri et al., 2015). When different drugs are co-loaded into a liposome formulation, the pharmacokinetics and biological

distribution of drugs can be improved by spatiotemporal co-administration, so that they have a specific activity in the tumor site (Mo et al., 2014).

The charge and hydrophobic interaction between lipids and proteins can load proteins into lipid nanoparticles (Wang et al., 2014). Koyo Nishida and his colleagues hypothesized that a certain proportion of the mixture of cationic lipids and neutral lipids would interact with lipophilic drugs and proteins at the same time, followed by the formation of nanoparticle skeletons (Peng et al., 2019). A complex nanoparticle consisting of lipids, calcium carbonate, and RGD peptide ligands was made by Nishida and his team to achieve intracellular co-delivery of superoxide dismutase (SOD) and PTX. They used a "one-step" ethanol injection method to prepare polyethylene glycol nanoparticles encapsulating proteins and drugs and found that when the weight ratio of EPC (Egg phosphatidylcholine)/DOTAP (1,2-dioleoyl-3-trimethylammonium-propane) was 10:1, the performance and entrapment efficiency of the nanoparticles were the best. Finally, the spherical nanoparticles with a diameter of about 130 nm were obtained by scanning electron microscope and dynamic light scattering. The formation of nanoparticles is mainly based on the electrostatic and hydrophobic interaction between proteins and lipids. The cytotoxicity of free conjugates and nanoparticles in colon26 tumor cells showed that the combination of SOD and PTX had stronger cytotoxicity than SOD and PTX alone. The results of the biodistribution study in mice with transplanted colon cancer showed that the drug delivery *via* nanoparticles was superior to free drugs in inhibiting tumor growth. The addition of SOD dismutase further increased the level of hydrogen peroxide in PTX-treated tumor cells and enhanced the cytotoxicity *in vitro*. The synchronous biological distribution of the SOD/PTX combination and the targeting of RGD modified nanoparticles to tumor areas are considered as the reasons for significant anti-tumor effects and low toxicity.

In a recent work by Liu and their team, it was found that cisplatin (IV) pre-drug coupled phospholipids can easily form Pt (IV) liposomes together with other commercial lipids (Feng et al., 2016). In order to enhance radiotherapy and chemotherapy for tumors, the antioxidant enzyme catalase (CAT) was encapsulated in cisplatin (IV)-prodrug coupled phospholipid liposomes to form CAT@Pt (IV)-liposomes (Zhang et al., 2017). Water-soluble CAT was encapsulated inside the liposomes formed with cisplatin (IV) pro-drug conjugated 1,2-distearoyl-sn-glycero-3-phosphoethanolamine (Pt (IV)-DSPE),1,2-dipalmitoyl-sn-glycero-3-phosphocholine (DPPC), cholesterol, and polyethylene glycol (PEG) conjugated DSPE. CAT in CAT@Pt (IV)-liposome has preserved and well-protected enzyme activity. After intravenous injection, the CAT@Pt (IV)-liposome can effectively accumulate in the tumor. The experiment of combined radiotherapy and chemotherapy showed that the combination of CAT@Pt (IV) and liposome had the best inhibitory effect on tumor growth.

It is feasible to co-transport peptides and drugs into cells through lipid carriers. Using the thin-film rehydration technique, a liposome nanocarrier was prepared to transfer Ran-RCC1 inhibitory peptide (Ran-IP) and Dox into breast cancer cells. By changing the pH value of the dispersion medium, combined with a number of peptides and the loading amount of Dox, the best double-loaded liposomes were selected in the preparation of polypeptide liposomes. The optimal loading rate of peptides was 85%, the particle size was about 80 nm, and the release of peptides and Dox could be maintained for 3 days. The results of *in vivo* experiments confirmed that the anticancer activity of double-loaded liposomes was enhanced, and the tumor growth inhibition rate was significantly increased after treatment with a gradient dose of double-loaded liposomes. *In vitro* cell activity studies showed that compared with free peptides and free Dox, peptides liposomes had a better cytotoxic effect. The final toxicity test showed that the combined drug delivery system was safer for liver and kidney tissue than free Dox (Haggag et al., 2020).

2.3 Polymeric nanocarriers

Among many nanomaterials, polymeric nanoparticles have the characteristics of adjustable chemical structure, simple synthesis, controllable relative molecular weight, low cost, environmental friendliness, easy coupling of functional groups (after functionalization), biocompatibility and biodegradability, it has important application value in the field of drug sustained release (Li et al., 2018; Jiang et al., 2022). The hydrophobic interaction between drug and polymer is the main driving force of drug entrapment. However, the hydrophobic interaction is non-specific and occurs between free drug molecules as well. Therefore, unwanted drug aggregation will occur in the process of self-assembly, which reduces the drug loading efficiency and heterogeneity of the preparation (Lv et al., 2018). It is reported that polymers, especially cationic polymers, have high cell uptake and intimal escape ability (Yang et al., 2015; Hu J et al., 2016). Therefore, the strategy of intracellular co-delivery of proteins and drugs based on polymer design is very promising.

2.3.1 Polymeric micelles

Polymeric micelles are generally assembled by amphiphilic copolymers, in order to generate a nano-sized core/shell (Wang et al., 2011). The hydrophobic core of the micelles promotes the dissolution and encapsulation of small-molecule hydrophobic drugs. Hydrophilic molecules are usually carried by micelles through physical interaction or covalent conjugation (He et al., 2016). Hydrophilic Dox and hydrophobic paclitaxel (TAX) are co-delivered with amphiphilic methoxy PEG-PLGA copolymeric nanoparticles (Wang et al., 2011). However, these two drugs are both small-molecule drugs. If the hydrophobic small-molecule drugs are replaced with hydrophobic macromolecular proteins, there may be more challenges to be

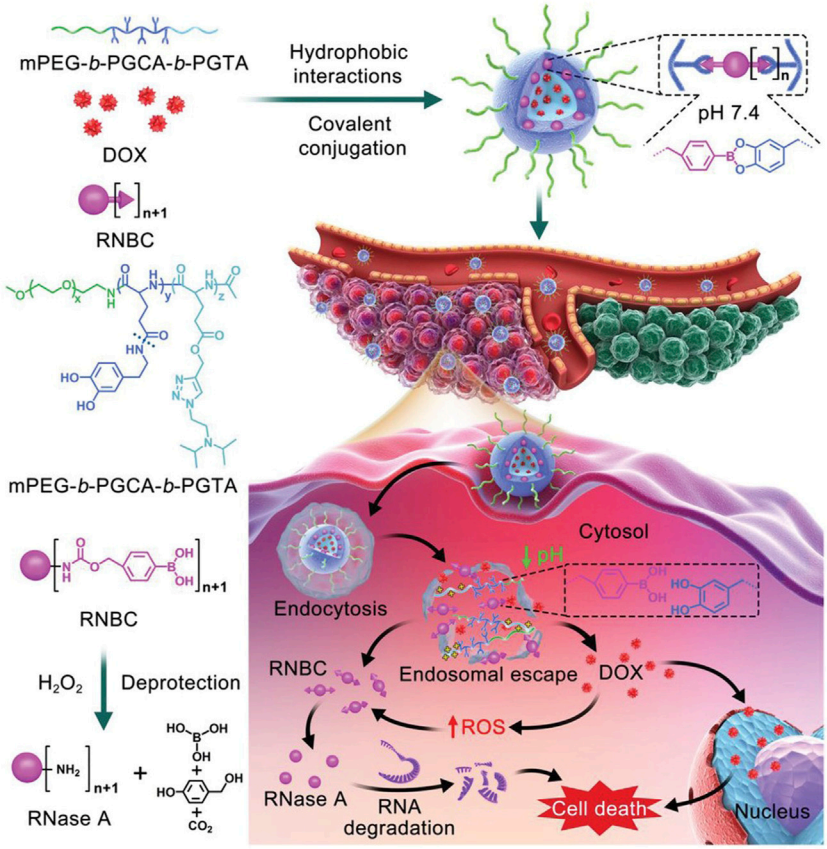

FIGURE 4
Schematic illustration of intracellular co-delivery of RNase A and Dox using a multistage cooperative drug delivery nanoplatform formed by mPEG-*b*-PGCA-*b*-PGTA for combination cancer therapy. Reproduced with permission from Ref. (Zhang et al., 2020).

faced. Polymeric micelles are widely used in the delivery of hydrophobic drugs, but their drug loading, colloid uniformity, preparation stability, and drug release performance are not ideal (Lv et al., 2018).

In a recent study by Chen and others, a multistage cooperative nanoplatform was prepared by a well-designed triblock copolymer, mPEG-*b*-PGCA-*b*-PGTA, for the intracellular co-delivery of phenylboronic-acid-modified proteins and hydrophobic drugs (Figure 4) (Zhang et al., 2020). The mPEG-*b*-PGCA-*b*-PGTA contains a mPEG block, which could provide a hydrophilic domain and a shield from immune recognition, a middle PGCA block, which could be used for pH-reversible covalent conjugation of phenylboronic-acid-modified proteins to form dynamic lock-in micelles because of its catechol groups, and the terminal PGTA block that was used for pH-responsive release of hydrophobic drugs and endolysosomal buffering to mediate escape of proteins into cytosol. Specifically, hydrophobic Dox was loaded into the cores of micelles by hydrophobic interactions, and RNase A formed RNBC (RNase A modified with nitrophenyl tetramethyl-dioxaborolanyl benzyl carbamate groups), which was attached by reversible covalent conjugation.[43] Based on circular dichroism, the structure of RNase A before and after covalent modification was consistent with that of natural RNase A, meanwhile, agarose gel retardation analysis and enzymatic reaction rate analysis proved that the activity of RNase A was not affected. In the synergistic anticancer experiment of tumor-bearing mice *in vivo* and TUNEL assay, NP-DOX-RNBC RNase A modified with nitrophenyl tetramethyl-dioxaborolanyl benzyl carbamate groups showed a stronger inhibitory effect on tumor growth than Dox and other groups, although NP-DOX-RNBC and Dox had similar cytotoxicity to B16F10 cells *in vitro*. The stability of the structure was verified *in vitro* and *in vivo*, indicating that this nanoplatform can effectively deliver proteins and small-molecule drugs into the cells.

A nanocarrier for co-delivery of photosensitizer chlorine e6 (Ce6) and CRISPR-Cas9 ribonucleoprotein (RNP) has also been reported to achieve the synergism of drug action. Nitrilotriacetic acid–disulfanediyldipropionate–polyethyleneglycol–*b*-polycaprolactone (NTA-SS-PEG-PCL)

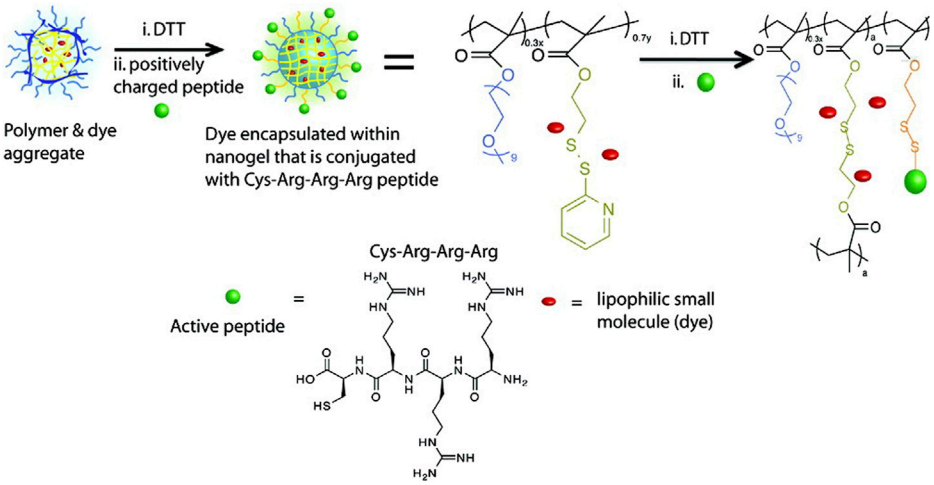

FIGURE 5
Structures of the nanogel's polymer precursor and tri-arginine peptide. Reproduced with permission from Ref. (González-Toro et al., 2012).

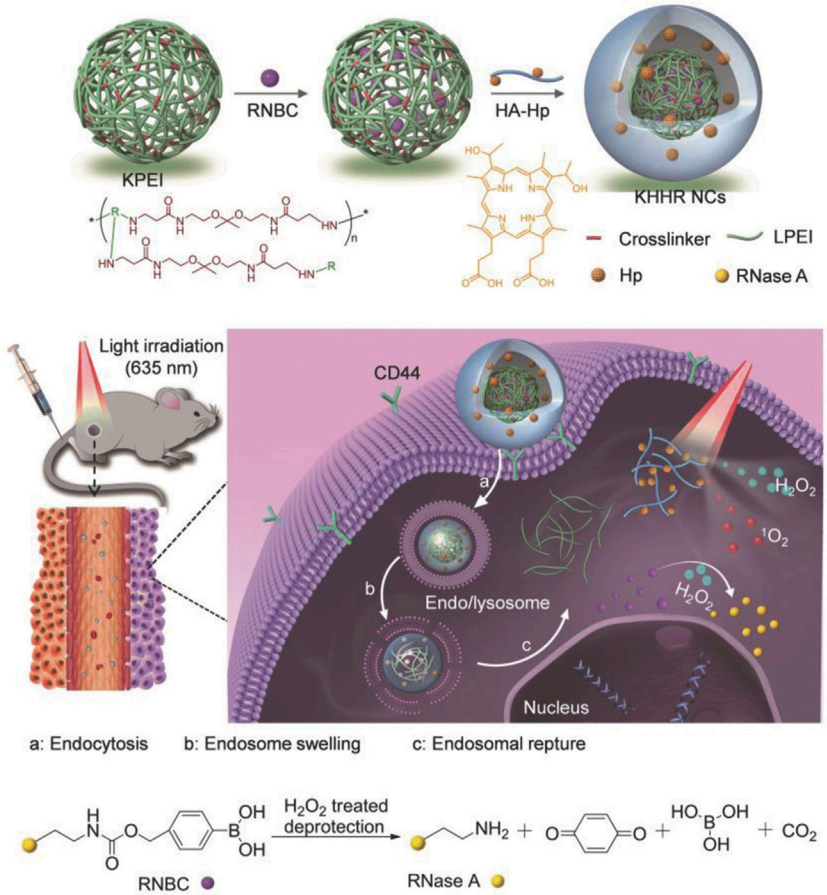

FIGURE 6
Schematic illustration of light-controlled protein delivery assisted by the "all-functions-in-one" nanocomplexes (NCs) toward synergistic cancer therapy. Reproduced with permission from Ref. (He et al., 2018).

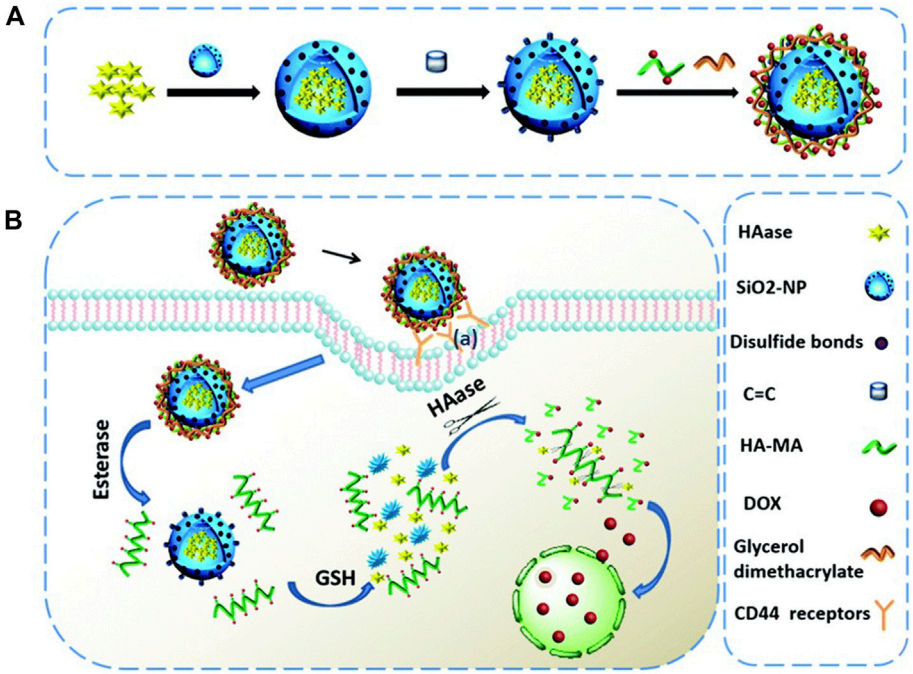

FIGURE 7
Schematic representation of **(A)** the fabrication of the HAase@SiO_2@prodrug nanoplatform and **(B)** the tumor targeted cargo delivery, dual responsive cargo release and intracellular generation of cytotoxic antitumor drugs based on this nanoplatform. Reproduced with permission from Ref. (Chen et al., 2018).

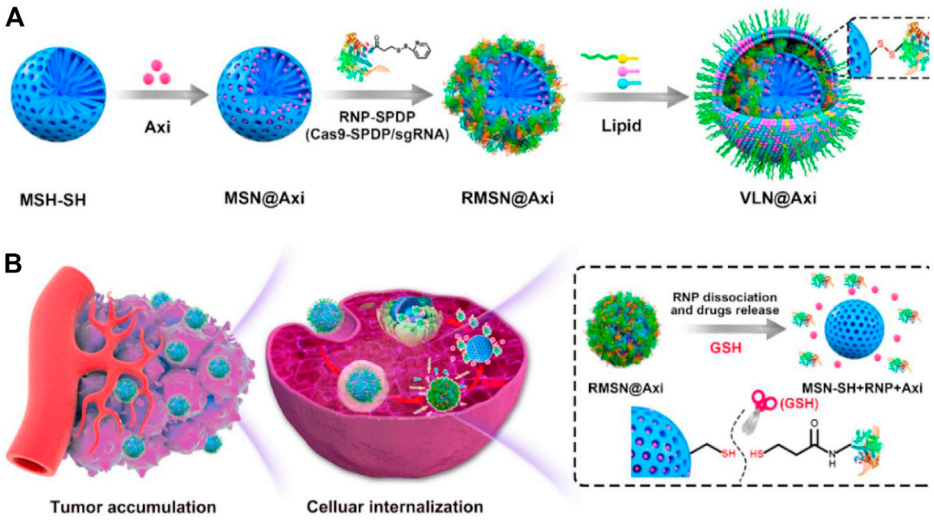

FIGURE 8
Schematic illustration for the synthesis of VLN@Axi **(A)** and delivery process **(B)** after intravenous injection. Reproduced with permission from Ref (Liu et al., 2020).

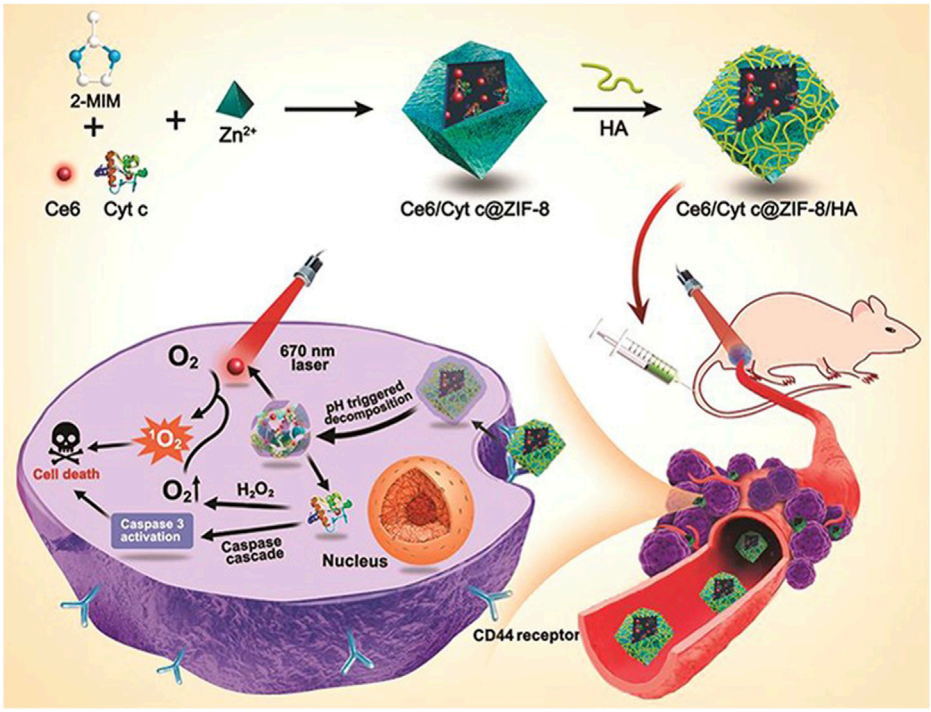

FIGURE 9
Illustration for the Synthesis of Ce6/Cyt c@ZIF-8/HA NPs and Their Applications in *Cancer* Cells Targeted Photodynamic and Protein Synergy Therapy. Reproduced with permission from Ref. (Ding et al., 2020).

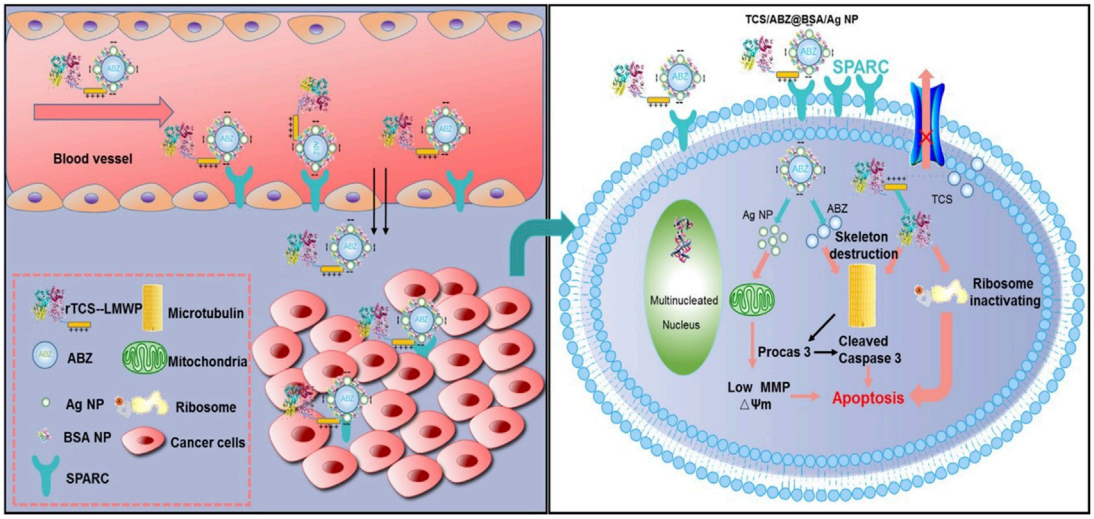

FIGURE 10
Schematic illustration of tumor delivery and synergistic effect *via* co-delivery of TCS and ABZ by silver nanoparticles. Reproduced with permission from Ref. (Tang et al., 2017).

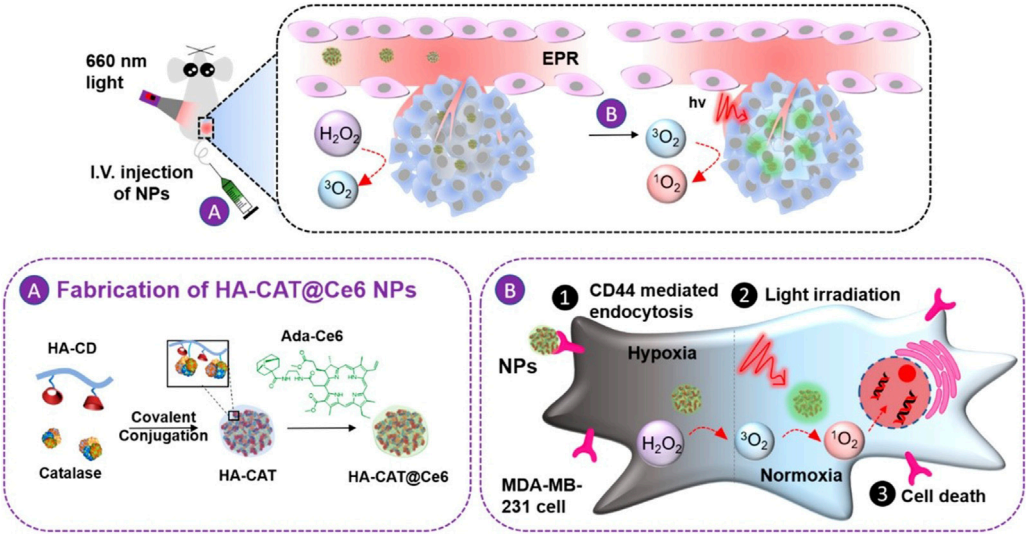

FIGURE 11
Schematic illustration of the preparation of HA-CAT@aCe6 NPs and the processes after intravenous injection into tumor-bearing mice. Reproduced with permission from Ref. (Phua et al., 2019).

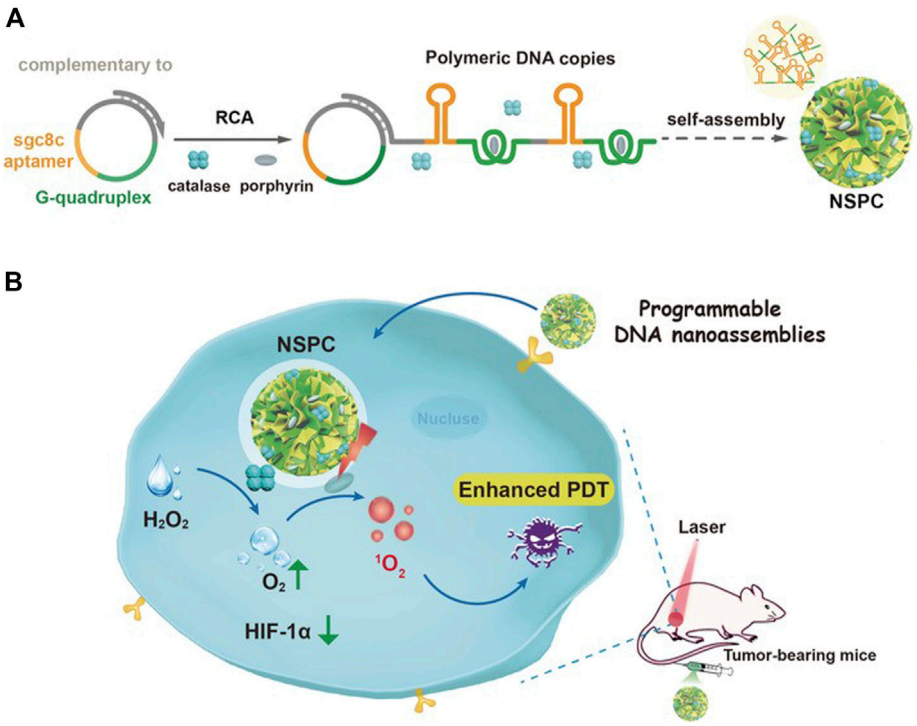

FIGURE 12
Illustration of designed DNA nanoassemblies for safe and effective PDT. **(A)** Design and synthesis of DNA nanosponges. **(B)** Proposed strategy for enhanced PDT with programmable nanoassemblies. Reproduced with permission from Ref. (Pan et al., 2020).

assembles into micellar nanoparticles (NTANPs), and hydrophobic photosensitizer Ce6 was encapsulated by its micellar core PCL block, HIS-tagged Cas9 RNP can be combined with the NTA-terminated PEG block on the micellar surface, then anionic micelles were coated with cationic iRGD modified copolymer. According to the experimental results *in vivo*, it is confirmed that there is a synergistic effect between Ce6 photodynamic therapy and Nrf2 gene editing (Deng et al., 2020b). This nanocarrier overcomes the problem of the uncontrolled release of Cas9 RNP from endocytosis nanoparticles, which provides a potential strategy for the co-delivery of gene-editing proteins and small-molecule drugs (Wang et al., 2017).

2.3.2 Polymeric nanogels

Nanogels have been proved to have the advantages of small size, easy intracellular penetration, high stability in blood circulation, and good biocompatibility in various medical applications (Eckmann et al., 2014). Nanogels can encapsulate various bioactive compounds, such as hydrophilic and lipophilic drugs, DNA sequences, siRNA, peptides, and proteins. Depending on the structure of the nanogels and the interactions between drugs, drugs can be released by breaking the chemical bond or degrading the nanogels matrix (Hajebi et al., 2019).

A general strategy for nanocarriers combined with water-soluble proteins and lipophilic small molecules has been proposed by S. Thayumanavan and his colleagues, which is a self-assembled polymeric nanogel. β-galactosidase (β-gal, pI: 4.8) was used as the model protein, and 1,1′-dioctadecyl-3,3,3′,3′-tetramethyl-indocarbocyanine perchlorate (DiI) dye was used as the model small molecule (Figure 5). By using dithiothreitol (DTT) to initiate a thiol-disulfide exchange reaction between pyridyldisulfide (PDS) units, the self-assembly structure and lipophilic guest molecules were combined. Given that the surface of the nanogel contains charge-neutral functional groups, tri-arginine, which can provide a positive charge and show the characteristics of a cell-penetrating peptide, was used as a functional group to react with residual PDS to make it positively charged. Finally, it is bound to negatively charged protein by electrostatic interactions. Related studies have shown that nanogel can be effectively functionalized with cell-penetrating peptides, and the complex shows effective cellular uptake, in which lipophilic small molecules and proteins are internalized by cells at the same time. However, because proteins are bound to their surfaces by electrostatic interaction, the charge density on the surface of the nanogel will affect the binding efficiency of complementary charged proteins (González-Toro et al., 2012).

2.3.3 Polymersomes

Polymersomes, also known as polymer vesicles, were made by self-assembly of amphiphilic block copolymers, predominantly with soft rubber hydrophobic segments (Chidanguro et al., 2018). The polymersomes have a core-shell structure, which wraps the hydrophilic molecules in the aqueous compartment and the hydrophobic molecules in the double layers of the vesicles (Mohammadi et al., 2017). Polymersomes can be designed with adjustable shape, fluidity, entanglement, permeability, stability, and responsiveness, and polymers can be customized according to appropriate physical properties or biocompatibility (Rideau et al., 2018). Polymersomes are increasingly being studied as carriers of imaging probes and therapeutic drugs because they can load large and small molecules that we are interested in (Leong et al., 2018).

A biodegradable chimeric polymersome was proposed by Zhong and his collaborators, based on asymmetric poly (ethylene glycol)-*b*-poly (ε-caprolactone)-*b*-poly (2-(diethylamino) ethyl methacrylate) (PEG-PCL-PDEA) triblock copolymers, which could load and transport protein and doxorubicin to the cytoplasm and/or cell nucleus at the same time (Liu et al., 2010). The PEG block was located on the surface of the polymersomes, providing good biocompatibility and stability for circulation, and the cationic PDEA blocks would be preferentially located inside the polymer, which was beneficial to the effective encapsulation and stability of proteins, and the hydrophobic PCL block was used to load DOX. During the formation of the polymer with pH 5.3, there was an effective electrostatic and/or hydrogen bond interaction between the exogenous proteins and the PDEA blocks, which may be the reason for the high protein loading of the chimeric polymer. The encapsulation of the protein did not significantly change the size distribution and zeta potential of the polymersomes, and the activity of the protein was preserved. *In vitro* studies suggested that the polymersomes could concurrently deliver proteins and Dox into the cytosol and cell nuclei.

2.3.4 Polymeric nanocomplexes

Zhao and coworkers have developed a cationic polymeric nanocomplex to deliver cytotoxic proteins and drugs for use in combination cancer therapy. RNase A was used as the model protein. Firstly, the modification of phenylboronic acid to lysine residues blocked the activity of RNase A, forming phenylboronic-coupled compound RNBC. Then, in order to restore the biological function of the protein, glucose oxidase (GOD) was co-transferred to the nanocarrier to continuously produce hydrogen peroxide and restore the activity of RNase A. The final nanocomposite (PEI-oxliPt (IV)@RNBC/GOD) was formed by electrostatic interaction between cross-linked polyethyleneimine (PEI)-oxliPt (IV), RNBC and GOD (Lim et al., 2019). After accumulation in cancer cells, the nanocomplex can be restored to activated RNase A and cytotoxic platinum (II) drugs. RNase A inhibits cellular protein synthesis and active oxaliplatin inhibits DNA replication, leading to synergistic treatment of cancer (Hu et al., 2018).

Photodynamic therapy (PDT) has gradually become a new type of tumor therapy because of its low invasiveness, high cure rate, and little damage to the body, which has attracted great attention in preclinical research and clinical practice (Lucky et al., 2015; Zhang Y et al., 2018; Miao et al., 2019; Zhong et al., 2021; Zhang et al., 2022). In recent years, more and more tumor therapy systems combined with protein therapy and photodynamic therapy have emerged and achieved promising results. A multi-functional nanocarrier doped with photosensitizer (PS) was developed, and combined with the reversible protein engineering of reactive oxygen species (ROS) response, the targeted intracellular co-delivery of photosensitizer and protein was realized. In order to prepare the nanoparticles, the protein drug RNase A is immobilized on its lysine residue by H_2O_2 cleavable phenylboronic acid to form an inactivated prodrug RNBC (Figure 6). Cationic, acid degradable, ketal-crosslinked polyethyleneimine (KPEI) that form nanocomposite (NCS) with RNBC through electrostatic interactions, can improve the stability of protein and promote its internalization. The coupling of hyaluronic acid (HA) with hematoporphyrin (HP), namely PS (HA-HP), is further coated on the surface of NCS to enhance their serum stability by shielding positive charges, so that they can circulate in the blood for a long time, and promote tumor accumulation by the permeability and retention (EPR) effect. *In vitro* and *in vivo* results showed that the synergistic combination of PS-mediated photodynamic therapy and protein-mediated therapy achieved a strong anticancer effect compared with the control group (He et al., 2018).

2.4 Silica nanocarriers

Biomineralization-based nanoparticle drug delivery system has attracted wide attention in tumor therapy because of its simple preparation, good biocompatibility, degradability, easy modification, versatility, good targeting, and so on. As the main material for the biological application of silica, mesoporous silica nanoparticles have obvious advantages over other inorganic nanoparticles, such as adjustable porous structure, large specific surface area, easy surface functionalization and so on (Wan et al., 2013; Díez et al., 2016; Wang W et al., 2020). These unique properties enable mesoporous silica nanoparticles to load not only small-molecule drugs (Chang et al., 2010), but also proteins (Liu and Xu 2019), and siRNAs (Hom et al., 2010).In addition, the hydrophilicity of the surface makes it easier for silicon nanomaterials to be internalized by cells, and special porous forms can provide a protective environment for unstable molecules (Castillo et al., 2020).

A yolk shell nano-platform for co-delivery of tumor-specific cytochrome c (Cyt c) prodrug and doxorubicin was developed by Cai and his colleagues. The yolk-shell mesoporous silica nanoparticles (YMSNs) were used to load the water-soluble anticancer drug Dox, cytochrome c was immobilized on the surface of YMSNs by ROS cleavable borate ester bond. The results of the ABTS assay showed that the biological activity of Cyt c did not change through the binding and release process. The synergistic cytotoxic effects toward HepG2 cells through the co-delivery of Cyt c and Dox were proved by the cytotoxicity tests and apoptosis assay. The release of Cyt c can initiate the apoptosis pathway of mitochondria and Dox molecules can inhibit the nuclear DNA fragmentation induced by topoisomerase, which is considered to be involved in the killing process of tumor cells (Pei et al., 2018).

The strategy of loading Dox into nanocarriers through chemical modification has always been an effective method, including conjugated modification, coupling with antibodies and so on (Shi et al., 2009; Zhu et al., 2011). For example, a multi-responsive nano-platform, containing hyaluronidase as the core, biodegradable silicon dioxide with disulfide bond as shell, and polyester-hyaluronic acid-adriamycin (PE-HA_{1000k}-DOX) prodrug as crown, was synthesized. After CD44 mediated endocytosis, esterase and glutathione in tumor cells degraded polyester and silicon dioxide, respectively, releasing HA-DOX and hyaluronidase. Hyaluronidase catalyzed the decomposition of HA-DOX to produce highly toxic Dox to induce apoptosis of tumor cells (Figure 7). In this case, Dox is loaded into the prodrug by amidation, while hyaluronidase is loaded into the blurred core by physical encapsulation (Chen et al., 2018). This study suggests that co-delivery of enzymes and prodrugs based on the tumor response nano-platform may be a promising strategy for accurate tumor therapy.

In addition, nucleic acid targeted drug therapy is an efficient tumor therapy strategy, which has attracted wide attention (Okholm and Kjems 2016; Crooke et al., 2018). Recently, a nano-delivery system for dual targeting tumor therapy with intracellular RNA and nuclear DNA was developed by Ma and his colleagues, to achieve intracellular co-delivery of cis-platinum pro-drugs (DSP) and cytotoxic protein RNase A. They used large-pore mesoporous silica-coated β-$NaYF_4$:20%Yb, 2% Er@β-$NaGdF_4$(UCS) nanoparticles as carriers, which were prepared according to their previous work (Ding et al., 2018). First, UCS nanoparticles were modified with 3-Aminopropyltriethoxysilane. Then DSP was covalently conjugated with it to form UCSPt, and RNase A with macromolecular structure was loaded by physical adsorption to form the final product UCSPtR. The results of *in vitro* and *in vivo* studies showed that the prepared nanoplatform successfully delivered cytotoxic protein RNase A and DSP into tumor cells, and induced intracellular RNA degradation mediated and nuclear DNA targeted killing of tumor cells, showing a good therapeutic effect on the tumor (Teng et al., 2021).

Compared with normal cells, tumor cells accumulate a large amount of hydrogen peroxide (Lin et al., 2018). Therefore, carriers that co-deliver CAT and photosensitizers into cells to

enhance their anti-tumor effect have been developed. For example, a multi-stage responsive intelligent nanoparticle system is designed to improve the efficacy of photodynamic therapy through intracellular delivery of CAT and photosensitizers (Yang et al., 2018). The water-soluble CAT were directly encapsulated in hollow silica nanoparticles by a simple reaction, and the photosensitizer Ce6, which was covalently conjugated to (3-aminopropyl) triethoxysilane, was doped into the silica lattice structure. Then the nanoparticles were modified with mitochondrial targeting molecule (3-carboxypropyl) triphenylphosphine bromide (CTPP), and further modified with acidic pH-responsive charge convertible polymers synthesized according to their previous work (Wang et al., 2013) by electrostatic interaction. The designed nanoparticles can not only encapsulate CAT and transport it into the tumor but also decompose tumor endogenous H_2O_2 to generate oxygen, overcome tumor hypoxia and greatly improve the therapeutic effect of PDT on solid tumors.

Interestingly, a virus-like nanoparticle (VLN), has been reported as a multi-functional nanoplatform, which can deliver CRISPR/Cas9 system and small-molecule drugs for effective malignant tumor therapy (Liu et al., 2020). The model drug, tyrosine kinase inhibitor Axitinib (AXI), was first loaded into the pores of surface vulcanized mesoporous silica nanoparticles (denoted as MSN-SH), and then RNP was connected to MSN-SH (denoted as RMSN) by a disulfide bond to lock the pores. Finally, liposomes containing PEG_{2000}-DSPE were introduced to encapsulate RMSN to form VLN, to prolong the circulation and prevent RNP from being degraded by enzymes in the physiological environment (Figure 8). Results indicates that the VLN has great potential as a general platform for the development of advanced combined therapy for malignant tumors.

2.5 Metal-organic frameworks

The metal-organic frame (MOF) is a kind of hybrid porous material developed in recent years, which is composed of metal ions or clusters bridged by organic connectors (Wu and Yang 2017). MOF not only has various functions, high drug loading, and good biocompatibility but also has excellent adaptability of frame structure design and almost unparalleled surface adjustment, which makes it an ideal drug carrier (Huskić et al., 2016; Lian et al., 2017).

Recently, a nano-platform based on MOF has been developed to achieve tumor cell targeted co-delivery of photosensitizers and therapeutic proteins to abtain collaborative photodynamic and protein therapy effects (Ding et al., 2020). Through a mild one-pot biomimetic mineralization process, the photosensitizer Ce6 and Cyt c were co-encapsulated in ZIF-8 nanoparticles to form a structure (Ce6/Cytc@ZIF-8) (Figure 9). Zn^{2+} ions interact with abundant carboxyl or amide bonds in proteins, and Ce6 is captured *in situ* in the pores of ZIF-8, which promotes the co-encapsulation of Cyt c and Ce6 into ZIF-8. Due to the small pore size of ZIF-8, the embedded protein and photosensitizer can not only reduce the leakage in the process of transportation but also protect the protein from being degraded by enzymes and ensure its activity. Using the coordination and electrostatic interaction between the carboxyl group and Zn^{2+} ions, the tumor-targeting ligand hyaluronic acid (HA) was coated on Ce6/Cytc@ZIF-8, and the nanoplatform (Ce6/Cyt c@ZIF-8/HA) was obtained. The experimental results *in vivo* and *in vitro* show that Ce6/Cytc@ZIF-8/HA nanoparticles have a good synergistic anticancer effect and low systemic toxicity, indicating that the MOF-based nano-platform is a promising strategy for intracellular co-delivery of proteins and drugs.

2.6 Other nanocarriers

With the development of nanotechnology, more and more kinds of drug delivery carriers are reported (Farokhzad and Langer 2009). In addition to the nanocarriers described above, some other nanocarriers that can realize the intracellular co-delivery of proteins and small-molecule drugs are also developed.

For example, a pH/H_2O_2 dual-responsive near-infrared fluorescence (NIRF) turn-on protein delivery system has been developed, which combines the NIRF turn-on probe and protein into a single magnetic nanoparticle (MNP)-based nanocarrier. QCy7 and trypsin were used as model agents for the study. Active fluorophore QCy7 can be coupled with phenylboronic acid (PBA) to form QCy7-PBA and can be released in the presence of hydrogen peroxide. Trypsin was chemically modified with PBA to form Try-PBA. Using polydopamine (PDA) coated MNP (MNP@PDA) as a scaffold, MNP@PDA@PEG/SHA was obtained by mixing with SHA (salicyl hydroxamates)-NH_2 and PEG-SH, respectively. QCy7-PBA and Try-PBA are covalently linked to MNP@PDA@PEG/SHA through complexation between SHA and PBA, thus MNP@PDA@PEG/SHA-Q/T is successfully prepared. Under the intracellular condition of low pH and high level of H_2O_2, the system can realize the controlled release of active protein and mediate the restoration of QCy7 fluorescence to monitor the intracellular protein delivery (Xu et al., 2019).

As a natural polymer, albumin is highly attractive because of its non-toxicity, non-immunogenicity, biodegradability, and biocompatibility (Tan and Ho 2018). Albumin also has received special attention as a drug carrier because of its affinity to albumin receptors on tumor cells, such as SPARC and gp60 (Desale et al., 2018). A self-assembled bovine serum albumin (BSA)-based nano-system has been developed for the combined delivery of trichosanthin (TCS) and albendazole (ABZ) to overcome multidrug resistance and metastasis (Figure 10). TCS is a type I ribosome-inactivating protein, which has high anti-tumor activity through the mechanism of

ribosome inactivation and apoptosis, while ABZ is a β-tubulin inhibitor, which shows strong anti-tumor activity. Firstly, ABZ is physically encapsulated in albumin-coated silver nanoparticles (called ABZ@BSA/Ag NP), and then a recombinant cell-penetrating TCS (referred to as RTL) was loaded by charge interactions between negatively charged ABZ@BSA/Ag NP and cationic RTL to form the nano-system RTL/ABZ@BSA/Ag NP. *In vitro* experiments suggested that this co-delivery system inhibited the proliferation of drug-resistant A549/T and HCT8/ADR cells. Furthermore, *in vivo* studies indicated that RTL/ABZ@BSA/Ag NP effectively inhibited the tumor metastasis to the lung (Tang et al., 2017).

Interestingly, Geest and coworkers synthesized transiently responsive BSA-polymer conjugates through a "grafting-from" reversible addition–fragmentation chain transfer (RAFT) polymerization of a dioxolane-containing acrylamide with a BSA-based chain transfer agent (CTA) (Vanparijs et al., 2015). The as-prepared BSA-polymer conjugates could self-assemble into nanoparticles at physiological pH and temperature. Hydrophobic small molecule immune-modulators could be loaded into the hydrophobic cores of the nanoparticles. Under acidic conditions, the hydrolysis of hydrophobic dioxolane groups into hydrophilic diol units resulted in the disassembly of nanoparticles and the release of small drugs. Therefore, this platform holds great application potential as intracellular co-delivery system of proteins and hydrophobic drugs.

In addition, an organic/inorganic nanocomposite system targeting mitochondria was developed to simultaneously load and deliver Ce6 and hydrophilic CAT for improved PDT activated by NIR laser. For the preparation of this system, oleic acid (OA) capped upconversion nanoparticles (UCNPs) were first prepared. Then using the double bond of oleic acid ligands, the active azide group was directly introduced by the thiol-ene click reaction, thus the hydrophobic pocket was retained on the periphery of the nanoparticles, and the hydrophobic photosensitizer Ce6 was loaded into the hydrophobic pocket composed of oleic acid molecules. Dendrimers can be further grafted onto UCNPs by azide-acetylene click reaction, thus constructing hydrophobic and hydrophilic "pockets" in a single nanoparticle at the same time. CAT was encapsulated in hydrophilic dendrimers with tertiary amine groups due to electrostatic interaction. The surface of dendrimer contains a large number of hydroxyl functional groups, which realizes the further surface modification of nanoparticles by mitochondrial targeting molecule (3-carboxypropyl) triphenylphosphonium bromide (CTPP). This co-delivery system significantly improved PDT efficacy by CAT catalysis-mediated alleviation of tumor hypoxia and CTPP-mediated mitochondria targeting upon irradiation using 980 nm laser (Liang et al., 2020).

Zhao et al. developed another strategy for intracellular co-delivery of CAT and Ce6. Firstly, CAT was covalently coupled to hyaluronic acid that was functionalized with β-cyclodextrin to form HA-CAT NPs. Then Ce6 was modified with adamantane to obtain adamantine-modified Ce6 (aCe6). The aCe6 could be encapsulated into HA-CAT by supramolecular ways between β-cyclodextrin and adamantane to obtain HA-CAT@aCe6 (Figure 11). *In vitro* and *in vivo* experiments showed that HA-CAT@aCe6 showed great potential in overcoming hypoxia of photodynamic therapy (Phua et al., 2019). The advantage of this supramolecular loading mode is that it is controllable and predictable, and it can adjust the loading ratio between photosensitizer and CAT because it enables different components to be stored separately (Webber and Langer 2017).

Moreover, Liu and coworkers prepared a programming DNA nanoassembly to simultaneously deliver CAT and porphyrin (Pan et al., 2020). DNA nanoassemblies with multiple functions were constructed by rolling circle amplification (RCA) with a circular DNA template complementary to sgc8c aptamer and G-quadruple. Sgc8c aptamer targets cancer cells overexpressing tyrosine-protein kinase 7 (PTK-7), and G-quadruplex can intercalate with photosensitizer porphyrin. In the process of RCA reaction, photosensitizer and CAT were added at the same time to prepare dual-drug-loaded DNA nanosponges NSPC (Figure 12). The assembled DNA nanoparticles can effectively load photosensitizers and CAT, and accurately target tumor cells. Upon being internalized by cancer cells, NSPC catalyzed endogenous hydrogen peroxide into oxygen, relieving the hypoxic tumor microenvironment, resulting in enhanced photodynamic therapy.

3 Conclusion and prospects

In this review, we summarize the recent intracellular co-delivery systems of proteins and small-molecule drugs and their applications in tumor therapy. Obviously, the combination of proteins and small-molecule drugs, such as therapeutic proteins/chemotherapeutics, therapeutic proteins/photosensitizers, and CAT/photosensitizers, results in enhanced synergistic anti-tumor effects in preclinical trials. However, the clinical applications of these systems remain elusive due to the existence of several challenges.

First, the heterogeneity of the materials and the complexity of various nanocarriers result in the difficulty in reproducible and large-scale preparation of optimal intracellular co-delivery systems of proteins and drugs for clinical translation (Zheng et al., 2021b). Therefore, new synthesis methodologies need to be developed to synthesize novel materials with high homogeneity and precise characterization. Meanwhile, simplification should be kept in mind during the design of new intracellular co-delivery systems in order to promote their market arrival by easing upscaling and reducing costs. In addition, due consideration needs to be given to the availability and cost of the desired

proteins and drugs in the co-delivery systems during the clinical conversion process. It can not only achieve the treatment of a variety of diseases, but also achieve the integration of diagnosis and treatment.

Second, proteins and small-molecule drugs loaded on nanocarriers can be accurately delivered to the tumor site. Although it can be targeted by the specificity of the tumor site or tumor cells, it can also be driven by some external conditions, such as magnetic field, ultrasound, or light and heat, so that the nanocarriers can release drugs at the tumor site (Yang et al., 2018; Wang et al., 2019; Wang Xet al., 2020; Dai et al., 2021; Zheng et al., 2021c). However, it is difficult to guarantee the effective rate and activity release of small molecular drugs and proteins to the tumor site. Recently, it has been reported that nanocarriers are modified by cell membranes or exosomes, these functionalized and biologically recognized nanocarriers greatly improve the membrane permeability and bioavailability, which also provides an idea for the design of co-delivery carriers for proteins and small-molecule drugs (Fu et al., 2020; Zhu et al., 2022).

Third, proteins and small-molecule drugs need to be loaded and released in a controlled manner, which requires in-depth exploration of the physical and chemical properties of proteins and small drugs, and making full use of the different structural properties of both agents, including their specific functional groups, hydrophilicity/hydrophobicity, charge density and so on. The rational applications of chemical or physical methods are able to endow the nanocarriers a controlled drug release profile, such as reversible covalent modification, electrostatic interactions, hydrophobic interactions, hydrogen bond, and van der Waals force.

Fourth, the proteins and small-molecule drugs co-loaded in the intracellular co-delivery system need to be thoroughly biologically evaluated to ensure that they enter the cell to be active and to avoid potential adverse reactions, which requires a full understanding of the molecular and cellular mechanisms involved. The protein needs a complete structure to exert its activity, and the covalently modified protein is more stable in the process of delivery, but it is difficult to restore its activity in the cell. The strategy of restoring the activity of modified proteins through stimuli-responsive cleavage of covalent bonds in cells is a promising way. Meanwhile, the endosomal entrapment of protein therapeutics will induce the enzymatic degradation of proteins, which requires the development of more potent endosomal escape strategies.

With the development of chemistry, material technology and nanomedicine, the emerging of new design concepts, and the deeper insights into molecular and cellular mechanisms involved in intracellular drug delivery, we believe that new intracellular co-delivery systems that can address the above challenges will be developed to further improve the combined anticancer effects of various combinations of proteins and small molecular drugs and promote their clinical translation in the cancer treatment.

Author contributions

ZC: Formal analysis, Resources, Writing—Original Draft, Visualization, Writing—Review and Editing. YL: Formal analysis, Resources, Writing—Original Draft, Visualization, Writing—Review and Editing. DZ: Writing—Review and Editing. WZ: Writing—Review and Editing, Supervision. MW: Writing—Review and Editing. WZ: Writing—Review and Editing. YC: Writing—Review and Editing, Supervision. PZ: Conceptualization, Review and Editing, Supervision, Funding acquisition. ZZ: Conceptualization, Review and Editing, Supervision, Funding acquisition.

Acknowledgments

The authors acknowledge the financial support by the National Natural Science Foundation of China (52173145 and 51803209), the Jilin Provincial Science and Technology Development Program (20210101063JC), and the Youth Innovation Promotion Association of CAS (2022226).

Conflict of interest

The authors declare that the research was conducted in the absence of any commercial or financial relationships that could be construed as a potential conflict of interest.

Publisher's note

All claims expressed in this article are solely those of the authors and do not necessarily represent those of their affiliated organizations, or those of the publisher, the editors and the reviewers. Any product that may be evaluated in this article, or claim that may be made by its manufacturer, is not guaranteed or endorsed by the publisher.

References

Biju, V. J. C. S. R. (2014). Chemical modifications and bioconjugate reactions of nanomaterials for sensing, imaging, drug delivery and therapy. *Chem. Soc. Rev.* 43, 744–764. doi:10.1039/c3cs60273g

Castillo, R. R., Lozano, D., and Vallet-Regi, M. (2020). Mesoporous silica nanoparticles as carriers for therapeutic biomolecules. *Pharmaceutics*. 12. 432. doi:10.3390/pharmaceutics12050432

Chang, B., Guo, J., Liu, C., Qian, J., and Yang, W. (2010). Surface functionalization of magnetic mesoporous silica nanoparticles for controlled drug release. *J. Mat. Chem.* 20, 9941–9947. doi:10.1039/c0jm01237h

Chen, H., Wang, Y., Yao, Y., Qiao, S., Wang, H., and Tan, N. (2017). Sequential delivery of cyclopeptide RA-V and doxorubicin for combination therapy on resistant tumor and *in situ* monitoring of cytochrome c release. *Theranostics* 7, 3781–3793. doi:10.7150/thno.20892

Chen, L., Liu, Z., Jin, R., Yang, X., Bai, Y., Liu, S., et al. (2018). Stepwise co-delivery of an enzyme and prodrug based on a multi-responsive nanoplatform for accurate tumor therapy. *J. Mat. Chem. B* 6, 6262–6268. doi:10.1039/c8tb01182f

Cheng, L., Yang, L., Meng, F. H., and Zhong, Z. Y. (2018). Protein nanotherapeutics as an emerging modality for cancer therapy. *Advanced Healthcare Materials*. 7. e1800685. doi:10.1002/adhm.201800685

Chidanguro, T., Ghimire, E., Liu, C. H., and Simon, Y. C. (2018). Polymersomes: Breaking the glass ceiling? *Small*. 14:e1802734. doi:10.1002/smll.201802734

Chiper, M., Niederreither, K., and Zuber, G. (2018). Transduction methods for cytosolic delivery of proteins and bioconjugates into living cells. *Adv. Healthc. Mat.* 7, 1701040. doi:10.1002/adhm.201701040

Chudy, M., Tokarska, K., Jastrzębska, E., Bułka, M., Drozdek, S., Lamch, Ł., et al. (2018). Lab-on-a-chip systems for photodynamic therapy investigations. *Biosens. Bioelectron. X.* 101. 37–51. doi:10.1016/j.bios.2017.10.013

Cosco, D., Paolino, D., De Angelis, F., Cilurzo, F., Celia, C., Di Marzio, L., et al. (2015). Aqueous-core PEG-coated PLA nanocapsules for an efficient entrapment of water soluble anticancer drugs and a smart therapeutic response. *Eur. J. Pharm. Biopharm.* 89, 30–39. doi:10.1016/j.ejpb.2014.11.012

Crooke, S. T., Witztum, J. L., Bennett, C. F., and Baker, B. F. (2018). RNA-targeted therapeutics. *Cell metab.* 27. 714–739. doi:10.1016/j.cmet.2018.03.004

Dai, Y., Bai, X., Jia, L., Sun, H., Feng, Y., Wang, L., et al. (2021). Precise control of customized macrophage cell robot for targeted therapy of solid tumors with minimal invasion. *Small.* 17. 2103986. doi:10.1002/smll.202103986

Deng, S., Gigliobianco, M. R., Censi, R., and Di Martino, P. (2020a). Polymeric nanocapsules as nanotechnological alternative for drug delivery system: Current status, challenges and opportunities. *Nanomaterials* 10, 847. doi:10.3390/nano10050847

Deng, S., Li, X., Liu, S., Chen, J., Li, M., Chew, S. Y., et al. (2020b). Codelivery of CRISPR-Cas9 and chlorin e6 for spatially controlled tumor-specific gene editing with synergistic drug effects. *Sci. Adv.* 6, eabb4005. doi:10.1126/sciadv.abb4005

Desale, J. P., Swami, R., Kushwah, V., Katiyar, S. S., and Jain, S. (2018). Chemosensitizer and docetaxel-loaded albumin nanoparticle: Overcoming drug resistance and improving therapeutic efficacy. *Nanomedicine* 13, 2759–2776. doi:10.2217/nnm-2018-0206

DeSantis, C. E., Lin, C. C., Mariotto, A. B., Siegel, R. L., Stein, K. D., Kramer, J. L., et al. (2014)., 64. CA, 252–271. doi:10.3322/caac.21235Cancer treatment and survivorship statistics, 2014*CA. A Cancer J. Clin.*

Díez, P., Sánchez, A., Torre, C., Gamella, M., Martínez-Ruíz, P., Aznar, E., et al. (2016). Neoglycoenzyme-gated mesoporous silica nanoparticles: Toward the design of nanodevices for pulsatile programmed sequential delivery. *ACS Appl. Mat. Interfaces* 8, 7657–7665. doi:10.1021/acsami.5b12645

Ding, B., Shao, S., Yu, C., Teng, B., Wang, M., Cheng, Z., et al. (2018). Large-pore mesoporous-silica-coated upconversion nanoparticles as multifunctional immunoadjuvants with ultrahigh photosensitizer and antigen loading efficiency for improved cancer photodynamic immunotherapy. *Adv. Mat.* 30, 1802479. doi:10.1002/adma.201802479

Ding, L., Lin, X., Lin, Z., Wu, Y., Liu, X., Liu, J., et al. (2020). Cancer cell-targeted photosensitizer and therapeutic protein Co-delivery nanoplatform based on a metal–organic framework for enhanced synergistic photodynamic and protein therapy. *ACS Appl. Mater Interfaces*. 12(33):36906-36916. doi:10.1021/acsami.0c09657

Dutta, P., Dutta, J., and Tripathi, V. (2003). Chitin and chitosan: Chemistry, properties and applications. *J. Sci. Indus Res.* 11/30, 63.

Eckmann, D. M., Composto, R. J., Tsourkas, A., and Muzykantov, V. R. (2014). Nanogel carrier design for targeted drug delivery. *J. Mat. Chem. B* 2, 8085–8097. doi:10.1039/c4tb01141d

Farokhzad, O. C., and Langer, R. (2009). Impact of nanotechnology on drug delivery. *ACS Nano* 27 (3), 16–20. doi:10.1021/nn900002m

Feng, L., Gao, M., Tao, D., Chen, Q., Wang, H., Dong, Z., et al. (2016). Cisplatin-prodrug-constructed liposomes as a versatile theranostic nanoplatform for bimodal imaging guided combination cancer therapy. *Adv. Funct. Mat.* 26, 2207–2217. doi:10.1002/adfm.201504899

Fu, A., Tang, R., Hardie, J., Farkas, M. E., and Rotello, V. M. (2014). Promises and pitfalls of intracellular delivery of proteins. *Bioconjug. Chem.* 25, 1602–1608. doi:10.1021/bc500320j

Fu, S., Xia, J., and Wu, J. (2016). Functional chitosan nanoparticles in cancer treatment. *J. Biomed. Nanotechnol.* 12, 1585–1603. doi:10.1166/jbn.2016.2228

Fu, S., Wang, Y., Xia, X., and Zheng, J. C. (2020). Exosome engineering: Current progress in cargo loading and targeted delivery. *NanoImpact* 20, 100261. doi:10.1016/j.impact.2020.100261

Fumoto, S., and Nishida, K. (2020). Co-Delivery systems of multiple drugs using nanotechnology for future cancer therapy. *Chem. Pharm. Bull.* 68, 603–612. doi:10.1248/cpb.c20-00008

Gao, Y-E., Bai, S., Ma, X., Zhang, X., Hou, M., Shi, X., et al. (2019). Codelivery of doxorubicin and camptothecin by dual-responsive unimolecular micelle-based β-cyclodextrin for enhanced chemotherapy. *Colloids Surfaces B Biointerfaces* 183, 110428. doi:10.1016/j.colsurfb.2019.110428

González-Toro, D. C., Ryu, J-H., Chacko, R. T., Zhuang, J., and Thayumanavan, S. (2012). Concurrent binding and delivery of proteins and lipophilic small molecules using polymeric nanogels. *J. Am. Chem. Soc.* 134, 6964–6967. doi:10.1021/ja3019143

Haggag, Y., Abu Ras, B., El-Tanani, Y., Tambuwala, M. M., McCarron, P., Isreb, M., et al. (2020). Co-delivery of a RanGTP inhibitory peptide and doxorubicin using dual-loaded liposomal carriers to combat chemotherapeutic resistance in breast cancer cells. *Expert Opin. Drug Deliv.* 17, 1655–1669. doi:10.1080/17425247.2020.1813714

Hajebi, S., Rabiee, N., Bagherzadeh, M., Ahmadi, S., Rabiee, M., Roghani-Mamaqani, H., et al. (2019). Stimulus-responsive polymeric nanogels as smart drug delivery systems. *Acta Biomater.* 92. 1–18. doi:10.1016/j.actbio.2019.05.018

He, C., Tang, Z., Tian, H., and Chen, X. (2016). Co-delivery of chemotherapeutics and proteins for synergistic therapy. *Adv. Drug Deliv. Rev.* 98, 64–76. doi:10.1016/j.addr.2015.10.021

He, H., Chen, Y., Li, Y., Song, Z., Zhong, Y., Zhu, R., et al. (2018). Effective and selective anti-cancer protein delivery via all-functions-in-one nanocarriers coupled with visible light-responsive, reversible protein engineering. *Adv. Funct. Mat.* 28, 1706710. doi:10.1002/adfm.201706710

He, W., Xing, X. Y., Wang, X. L., Wu, D., Wu, W., Guo, J. L., et al. (2020). Nanocarrier-mediated cytosolic delivery of biopharmaceuticals. *Advanced functional materials*. 1. 30. doi:10.1002/adfm.201910566

Hom, C., Lu, J., Liong, M., Luo, H., Li, Z., Zink, J. I., et al. (2010). Mesoporous silica nanoparticles facilitate delivery of siRNA to shutdown signaling pathways in mammalian cells. *Small (Weinheim der Bergstrasse, Ger.* 6, 1185–1190. doi:10.1002/smll.200901966

Hu, C-M. J., and Zhang, L. (2012). Nanoparticle-based combination therapy toward overcoming drug resistance in cancer. *Biochem. Pharmacol.* 83, 1104–1111. doi:10.1016/j.bcp.2012.01.008

Hu, C-M. J., Aryal, S., and Zhang, L. (2010). Nanoparticle-assisted combination therapies for effective cancer treatment. *Ther. Deliv.* 1, 323–334. doi:10.4155/tde.10.13

Hu, S., Chen, X., Lei, C., Tang, R., Kang, W., Deng, H., et al. (2018). Charge designable and tunable GFP as a target pH-responsive carrier for intracellular functional protein delivery and tracing. *Chem. Commun.* 54, 7806–7809. doi:10.1039/c8cc03285h

Hu, J., Hu, K., and Cheng, Y. (2016). Tailoring the dendrimer core for efficient gene delivery. *Acta Biomater.* 35, 1–11. doi:10.1016/j.actbio.2016.02.031

Hu, Q., Sun, W., Wang, C., and Gu, Z. (2016). Recent advances of cocktail chemotherapy by combination drug delivery systems. *Adv. Drug Deliv. Rev.* 98, 19–34. doi:10.1016/j.addr.2015.10.022

Huskić, I., Pekov, I. V., Krivovichev, S. V., and Friščić, T. (2016). Minerals with metal-organic framework structures. *Sci. Adv.* 2, e1600621. doi:10.1126/sciadv.1600621

Jiang, Z., Liu, Y., Shi, R., Feng, X., Xu, W., Zhuang, X., et al. (2022). Versatile polymer-initiating biomineralization for tumor blockade therapy. *Adv. Mat.* 34, e2110094. doi:10.1002/adma.202110094

Kaczmarczyk, S. J., Sitaraman, K., Young, H. A., Hughes, S. H., and Chatterjee, D. K. (2011). Protein delivery using engineered virus-like particles. *Proc. Natl. Acad. Sci. U. S. A.* 108, 16998–17003. doi:10.1073/pnas.1101874108

Kim, C. S., Mout, R., Zhao, Y., Yeh, Y-C., Tang, R., Jeong, Y., et al. (2015). Co-delivery of protein and small molecule therapeutics using nanoparticle-stabilized nanocapsules. *Bioconjug. Chem.* 26, 950–954. doi:10.1021/acs.bioconjchem.5b00146

Leader, B., Baca, Q. J., and Golan, D. E. (2008). Protein therapeutics: A summary and pharmacological classification. *Nat. Rev. Drug Discov.* 7, 21–39. doi:10.1038/nrd2399

Lee, A. L. Z., Dhillon, S. H. K., Wang, Y., Pervaiz, S., Fan, W., and Yang, Y. Y. (2011). Synergistic anti-cancer effects via co-delivery of TNF-related

apoptosis-inducing ligand (TRAIL/Apo2L) and doxorubicin using micellar nanoparticles. *Mol. Biosyst.* 7, 1512. doi:10.1039/c0mb00266f

Lehár, J., Krueger, A. S., Avery, W., Heilbut, A. M., Johansen, L. M., Price, E. R., et al. (2009). Synergistic drug combinations tend to improve therapeutically relevant selectivity. *Nat. Biotechnol.* 27, 659–666. doi:10.1038/nbt.1549

Leong, J., Teo, J. Y., Aakalu, V. K., Yang, Y. Y., and Kong, H. (2018). Engineering polymersomes for diagnostics and therapy. *Adv. Healthc. Mat.* 7, e1701276. doi:10.1002/adhm.201701276

Li, S., He, Y., Li, C., and Liu, X. (2005). *In vitro* release of protein from poly (butylcyanoacrylate) nanocapsules with an aqueous core. *Colloid Polym. Sci.* 283, 480–485. doi:10.1007/s00396-004-1173-5

Li, Y., Thambi, T., and Lee, D. S. (2018). Co-delivery of drugs and genes using polymeric nanoparticles for synergistic cancer therapeutic effects. *Advanced Healthcare Materials*. 7. 1. doi:10.1002/adhm.201700886

Li, Z., Xu, W., Yang, J., Wang, J., Wang, J., Zhu, G., et al. (2022). A tumor microenvironments-adapted polypeptide hydrogel/nanogel composite boosts antitumor molecularly targeted inhibition and immunoactivation. *Adv. Mat.* 34, e2200449. doi:10.1002/adma.202200449

Lian, X., Fang, Y., Joseph, E., Wang, Q., Li, J., Banerjee, S., et al. (2017). Enzyme-MOF (metal-organic framework) composites. *Chem. Soc. Rev.* 6 (46), 3386–3401. doi:10.1039/c7cs00058h

Liang, S., Sun, C., Yang, P., Ma, P., Huang, S., Cheng, Z., et al. (2020). Core-shell structured upconversion nanocrystal-dendrimer composite as a carrier for mitochondria targeting and catalase enhanced anti-cancer photodynamic therapy. *Biomaterials*. 240. 119850. doi:10.1016/j.biomaterials.2020.119850

Liew, S. S., Zhou, J., Li, L., and Yao, S. Q. (2021). Co-delivery of proteins and small molecule drugs for mitochondria-targeted combination therapy. *Chem. Commun.* 57, 3215–3218. doi:10.1039/d0cc08020a

Lim, W. Q., Phua, S. Z. F., and Zhao, Y. L. (2019). Redox-responsive polymeric nanocomplex for delivery of cytotoxic protein and chemotherapeutics. *ACS Appl. Mat. Interfaces* 11, 31638–31648. doi:10.1021/acsami.9b09605

Lin, Y-W., Raj, E. N., Liao, W-S., Lin, J., Liu, K-K., Chen, T-H., et al. (2017). Co-delivery of paclitaxel and cetuximab by nanodiamond enhances mitotic catastrophe and tumor inhibition. *Sci. Rep.* 7, 9814. doi:10.1038/s41598-017-09983-8

Lin, H., Chen, Y., and Shi, J. (2018). Nanoparticle-triggered: *In situ* catalytic chemical reactions for tumour-specific therapy. *Chem. Soc. Rev.* 47, 1938–1958. doi:10.1039/c7cs00471k

Liu, H-J., and Xu, P. (2019). Smart mesoporous silica nanoparticles for protein delivery. *Nanomaterials* 9, 511. doi:10.3390/nano9040511

Liu, G., Ma, S., Li, S., Cheng, R., Meng, F., Liu, H., et al. (2010). The highly efficient delivery of exogenous proteins into cells mediated by biodegradable chimaeric polymersomes. *Biomaterials* 31, 7575–7585. doi:10.1016/j.biomaterials.2010.06.021

Liu, T., Choi, H., Zhou, R., and Chen, I. W. (2014). Quantitative evaluation of the reticuloendothelial system function with dynamic MRI. *PLOS ONE* 9, e103576. doi:10.1371/journal.pone.0103576

Liu, X., Wu, F., Ji, Y., and Yin, L. C. (2019). Recent advances in anti-cancer protein/peptide delivery. *Bioconjug. Chem.* 30, 305–324. doi:10.1021/acs.bioconjchem.8b00750

Liu, Q., Wang, C., Zheng, Y., Zhao, Y., Wang, Y., Hao, J., et al. (2020). Virus-like nanoparticle as a co-delivery system to enhance efficacy of CRISPR/Cas9-based cancer immunotherapy. *Biomaterials* 258, 120275. doi:10.1016/j.biomaterials.2020.120275

Lucky, S. S., Soo, K. C., and Zhang, Y. (2015). Nanoparticles in photodynamic therapy. *Chem. Rev.* 115, 1990–2042. doi:10.1021/cr5004198

Lv, S., Wu, Y., Cai, K., He, H., Li, Y., Lan, M., et al. (2018). High drug loading and sub-quantitative loading efficiency of polymeric micelles driven by donor–receptor coordination interactions. *J. Am. Chem. Soc.* 140, 1235–1238. doi:10.1021/jacs.7b12776

Miao, Z., Chen, S., Xu, C-Y., Ma, Y., Qian, H., Xu, Y., et al. (2019). PEGylated rhenium nanoclusters: A degradable metal photothermal nanoagent for cancer therapy. *Chem. Sci.* 10, 5435–5443. doi:10.1039/c9sc00729f

Mitragotri, S., Burke, P. A., and Langer, R. (2014). Overcoming the challenges in administering biopharmaceuticals: Formulation and delivery strategies. *Nat. Rev. Drug Discov.* 13, 655–672. doi:10.1038/nrd4363

Mo, R., Jiang, T., and Gu, Z. (2014). Recent progress in multidrug delivery to cancer cells by liposomes. *Nanomedicine* 9, 1117–1120. doi:10.2217/nnm.14.62

Mohammadi, M., Ramezani, M., Abnous, K., and Alibolandi, M. (2017). Biocompatible polymersomes-based cancer theranostics: Towards multifunctional nanomedicine. *Int. J. Pharm. X.* 15 (519), 287–303. doi:10.1016/j.ijpharm.2017.01.037

Mura, S., Nicolas, J., and Couvreur, P. J. N. (2013). Stimuli-responsive nanocarriers for drug delivery. *Nat. Mat.* 12, 991–1003. doi:10.1038/nmat3776

Naseri, N., Valizadeh, H., and Zakeri-Milani, P. (2015). Solid lipid nanoparticles and nanostructured lipid carriers: Structure, preparation and application. *Adv. Pharm. Bull.%J Adv. Pharm. Bull.* 5, 305–313. doi:10.15171/apb.2015.043

Okholm, A. H., and Kjems, J. (2016). DNA nanovehicles and the biological barriers. *Adv. Drug Deliv. Rev.* 15 (106), 183–191. doi:10.1016/j.addr.2016.05.024

Pan, M., Jiang, Q., Sun, J., Xu, Z., Zhou, Y., Zhang, L., et al. (2020). Programming DNA nanoassembly for enhanced photodynamic therapy. *Angew. Chem. Int. Ed. Engl.* 59, 1913–1921. doi:10.1002/ange.201912574

Pei, Y., Li, M., Hou, Y., Hu, Y., Chu, G., Dai, L., et al. (2018). An autonomous tumor-targeted nanoprodrug for reactive oxygen species-activatable dual-cytochrome c/doxorubicin antitumor therapy. *Nanoscale* 10, 11418–11429. doi:10.1039/c8nr02358a

Peng, J. Q., Fumoto, S., Suga, T., Miyamoto, H., Kuroda, N., Kawakami, S., et al. (2019). Targeted co-delivery of protein and drug to a tumor *in vivo* by sophisticated RGD-modified lipid-calcium carbonate nanoparticles. *J. Control. Release* 302, 42–53. doi:10.1016/j.jconrel.2019.03.021

Phua, S. Z. F., Yang, G., Lim, W. Q., Verma, A., Chen, H., Thanabalu, T., et al. (2019). Catalase-integrated hyaluronic acid as nanocarriers for enhanced photodynamic therapy in solid tumor. *ACS Nano* 13, 4742–4751. doi:10.1021/acsnano.9b01087

Qin, X. F., Yu, C. M., Wei, J., Li, L., Zhang, C. W., Wu, Q., et al. (2019). Rational design of nanocarriers for intracellular protein delivery. *Adv. Mat.* 1. 1902791. doi:10.1002/adma.201902791

Raffin Pohlmann, A., Weiss, V., Mertins, O., Pesce da Silveira, N., and Guterres, S. (2002). Spray-dried indomethacin-loaded polyester nanocapsules and nanospheres: Development, stability evaluation and nanostructure models. *Eur. J. Pharm. Sci.* 16, 305–312. doi:10.1016/s0928-0987(02)00127-6

Rideau, E., Dimova, R., Schwille, P., Wurm, F. R., and Landfester, K. (2018). Liposomes and polymersomes: A comparative review towards cell mimicking. *Chem. Soc. Rev.* 47, 8572–8610. doi:10.1039/c8cs00162f

Sanchez-Garcia, L., Martín, L., Mangues, R., Ferrer-Miralles, N., Vázquez, E., and Villaverde, A. (2016). Recombinant pharmaceuticals from microbial cells: A 2015 update. *Microb. Cell Fact.* 15, 33. doi:10.1186/s12934-016-0437-3

Scaletti, F., Hardie, J., Lee, Y-W., Luther, D. C., Ray, M., and Rotello, V. M. (2018). Protein delivery into cells using inorganic nanoparticle–protein supramolecular assemblies. *Chem. Soc. Rev.* 47, 3421–3432. doi:10.1039/c8cs00008e

Shanmuganathan, R., Edison, T., LewisOscar, F., Kumar, P., Shanmugam, S., and Pugazhendhi, A. (2019). Chitosan nanopolymers: An overview of drug delivery against cancer. *Int. J. Biol. Macromol.* 130, 727–736. doi:10.1016/j.ijbiomac.2019.02.060

Shao, D., Li, M., Wang, Z., Zheng, X., Lao, Y-H., Chang, Z., et al. (2018). Protein delivery: Bioinspired diselenide-bridged mesoporous silica nanoparticles for dual-responsive protein delivery (adv. Mater. 29/2018). *Adv. Mat.* 30, 1870209. doi:10.1002/adma.201870209

Shi, M., Ho, K., Keating, A., and Shoichet, M. S. (2009). Doxorubicin-conjugated immuno-nanoparticles for intracellular anticancer drug delivery. *Adv. Funct. Mat.* 19, 1689–1696. doi:10.1002/adfm.200801271

Su, S., Wang, Y. Y., Du, F. S., Lu, H., and Li, Z. C. (2018). Dynamic covalent bond-assisted programmed and traceless protein release: High loading nanogel for systemic and cytosolic delivery. *Advanced Functional Materials*. 28. 1. doi:10.1002/adfm.201805287

Tan, Y. L., and Ho, H. K. (2018). Navigating albumin-based nanoparticles through various drug delivery routes. *Drug Discov. today* 23, 1108–1114. doi:10.1016/j.drudis.2018.01.051

Tang, R., Kim, C. S., Solfiell, D. J., Rana, S., Mout, R., Velázquez-Delgado, E. M., et al. (2013). Direct delivery of functional proteins and enzymes to the cytosol using nanoparticle-stabilized nanocapsules. *ACS Nano* 7, 6667–6673. doi:10.1021/nn402753y

Tang, Y., Liang, J., Wu, A., Chen, Y., Zhao, P., Lin, T., et al. (2017). Co-delivery of trichosanthin and albendazole by nano-self-assembly for overcoming tumor multidrug-resistance and metastasis. *ACS Appl. Mat. Interfaces* 9, 26648–26664. doi:10.1021/acsami.7b05292

Teng, B., Ding, B., Shao, S., Wang, Z., Tong, W., Wang, S.., et al. (2021). Intracellular RNA and nuclear DNA-dual-targeted tumor therapy via upconversion nanoplatforms with UCL/MR dual-mode bioimaging. *Chem. Eng. J.* 405, 126606. doi:10.1016/j.cej.2020.126606

Thao, L. Q., Byeon, H. J., Lee, C., Lee, S., Lee, E. S., Choi, Y. W., et al. (2015). Doxorubicin-bound albumin nanoparticles containing a TRAIL protein for targeted treatment of colon cancer. *Pharm. Res.* 33, 615–626. doi:10.1007/s11095-015-1814-z

Trindade, I. C., Pound-Lana, G., Pereira, D. G. S., de Oliveira, L. A. M., Andrade, M. S., Vilela, J. M. C., et al. (2018). Mechanisms of interaction of biodegradable polyester nanocapsules with non-phagocytic cells. *Eur. J. Pharm. Sci.* 124, 89–104. doi:10.1016/j.ejps.2018.08.024

Vanparijs, N., De Coen, R., Laplace, D., Louage, B., Maji, S., Lybaert, L., et al. (2015). Transiently responsive protein-polymer conjugates via a 'grafting-from' RAFT approach for intracellular co-delivery of proteins and immune-modulators. *Chem. Commun.* 51, 13972–13975. doi:10.1039/c5cc04809e

Vrignaud, S., Anton, N., Passirani, C., Benoit, J-P., and Saulnier, P. (2013). Aqueous core nanocapsules: A new solution for encapsulating doxorubicin hydrochloride. *Drug Dev. industrial Pharm.* 39, 1706–1711. doi:10.3109/03639045.2012.730526

Wan, X., Liu, T., Hu, J., and Liu, S. (2013). Photo-degradable, protein–polyelectrolyte complex-coated, mesoporous silica nanoparticles for controlled Co-release of protein and model drugs. *Macromol. Rapid Commun.* 34, 341–347. doi:10.1002/marc.201200673

Wan, T., Pan, Q., Liu, C., Guo, J., Li, B., Yan, X., et al. (2021). A duplex CRISPR-cas9 ribonucleoprotein nanomedicine for colorectal cancer gene therapy. *Nano Lett.* 21, 9761–9771. doi:10.1021/acs.nanolett.1c03708

Wang, H., Zhao, Y., Wu, Y., Hu, Y-l., Nan, K., Nie, G., et al. (2011). Enhanced anti-tumor efficacy by co-delivery of doxorubicin and paclitaxel with amphiphilic methoxy PEG-PLGA copolymer nanoparticles. *Biomaterials* 32, 8281–8290. doi:10.1016/j.biomaterials.2011.07.032

Wang, C., Cheng, L., Liu, Y., Wang, X., Ma, X., Deng, Z., et al. (2013). Imaging-guided pH-sensitive photodynamic therapy using charge reversible upconversion nanoparticles under near-infrared light. *Adv. Funct. Mat.* 23, 3077–3086. doi:10.1002/adfm.201202992

Wang, M., Alberti, K., Sun, S., Arellano, C. L., and Xu, Q. (2014). Combinatorially designed lipid-like nanoparticles for intracellular delivery of cytotoxic protein for cancer therapy. *Angew. Chem. Int. Ed. Engl.* 53, 2937–2942. doi:10.1002/ange.201311245

Wang, H. X., Li, M., Lee, C. M., Chakraborty, S., Kim, H. W., Bao, G., et al. (2017). CRISPR/Cas9-Based genome editing for disease modeling and therapy: Challenges and opportunities for nonviral delivery. *Chem. Rev.* 9 (117), 9874–9906. doi:10.1021/acs.chemrev.6b00799

Wang, X., Zhong, X., Lei, H., Geng, Y., Zhao, Q., Gong, F., et al. (2019). Hollow Cu2Se nanozymes for tumor photothermal-catalytic therapy. *Chem. Mat.* 31, 6174–6186. doi:10.1021/acs.chemmater.9b01958

Wang, Z., Zhan, M., Li, W., Chu, C., Xing, D., Lu, S., et al. (2021). Photoacoustic cavitation-ignited reactive oxygen species to amplify peroxynitrite burst by photosensitization-free polymeric nanocapsules. *Angew. Chem. Int. Ed.* 60, 4720–4731. doi:10.1002/anie.202013301

Wang, W. C., Liu, X. F., Zheng, X. J., Jin, H. J., and Li, X. M. (2020). Biomineralization: An opportunity and challenge of nanoparticle drug delivery systems for cancer theraphy. *Advanced healthcare materials*. 9. 1. doi:10.1002/adhm.202001117

Wang, X., Zhong, X., Bai, L., Xu, J., Gong, F., Dong, Z., et al. (2020). Ultrafine titanium monoxide (TiO_{1+x}) nanorods for enhanced sonodynamic therapy. *J. Am. Chem. Soc.* 142, 6527–6537. doi:10.1021/jacs.9b10228

Ward, E., DeSantis, C., Robbins, A., Kohler, B., and Jemal, A. (2014)., 64. CA, 83–103. doi:10.3322/caac.21219Childhood and adolescent cancer statistics, 2014*CA. A Cancer J. Clin.*

Webber, M. J., and Langer, R. (2017). Drug delivery by supramolecular design. *Chem. Soc. Rev.* 46, 6600–6620. doi:10.1039/c7cs00391a

Wei, L., Chen, J., and Ding, J. (2021). Sequentially stimuli-responsive anticancer nanomedicines. *Nanomedicine* 16, 261–264. doi:10.2217/nnm-2021-0019

Wei, Q., Su, Y., Xin, H., Zhang, L., Ding, J., and Chen, X. (2021). Immunologically effective biomaterials. *ACS Appl. Mat. Interfaces* 13, 56719–56724. doi:10.1021/acsami.1c14781

Wu, M. X., and Yang, Y. W. (2017). Metal-organic framework (MOF)-Based drug/cargo delivery and cancer therapy. *Adv. Mat.* 29, 1606134. doi:10.1002/adma.201606134

Wu, X., He, C., Wu, Y., Chen, X., and Cheng, J. (2015). Nanogel-incorporated physical and chemical hybrid gels for highly effective chemo-protein combination therapy. *Adv. Funct. Mat.* 25, 6744–6755. doi:10.1002/adfm.201502742

Wu, D-Y., Ma, Y., Hou, X-S., Zhang, W-J., Wang, P., Chen, H., et al. (2017). Co-delivery of antineoplastic and protein drugs by chitosan nanocapsules for a collaborative tumor treatment. *Carbohydr. Polym.* 157, 1470–1478. doi:10.1016/j.carbpol.2016.11.027

Xu, H., Wang, Y., Pei, Z., Ji, W., and Pei, Y. J. C. C. (2019). NIRF turn-on nanoparticles based on the tumor microenvironment for monitoring intracellular protein delivery. *Chem. Commun.* 55, 14930–14933. doi:10.1039/c9cc07768e

Yang, J-z., and Ding, J-x. (2022). Antitumor nanomaterials. *Chin. J. Appl. Chem.* 39, 855–856.

Yang, J., Zhang, Q., Chang, H., and Cheng, Y. (2015). Surface-Engineered dendrimers in gene delivery. *Chem. Rev.* 115, 5274–5300. doi:10.1021/cr500542t

Yang, G., Xu, L., Xu, J., Zhang, R., Song, G., Chao, Y., et al. (2018). Smart nanoreactors for pH-responsive tumor homing, mitochondria-targeting, and enhanced photodynamic-immunotherapy of cancer. *Nano Lett.* 18, 2475–2484. doi:10.1021/acs.nanolett.8b00040

Yang, J-z., Zou, H-y., Ding, J-x., and Chen, X-s. (2021). Controlled synthesis and biomedical applications of cystine-based polypeptide nanomaterials. *Acta Polym. sin.* 52, 960–977.

Yin, Y., Hu, Q., Xu, C., Qiao, Q., Qin, X., Song, Q., et al. (2018). Co-Delivery of doxorubicin and interferon-γ by thermosensitive nanoparticles for cancer immunochemotherapy. *Mol. Pharm.* 15, 4161–4172. doi:10.1021/acs.molpharmaceut.8b00564

You, C. Q., Wu, H. S., Gao, Z. G., Sun, K., Chen, F. H., Tao, W. A., et al. (2018). Subcellular co-delivery of two different site-oriented payloads based on multistage targeted polymeric nanoparticles for enhanced cancer therapy. *J. Mat. Chem. B* 6, 6752–6766. doi:10.1039/c8tb02230e

Zhang, R., Song, X., Liang, C., Yi, X., Song, G., Chao, Y., et al. (2017). Catalase-loaded cisplatin-prodrug-constructed liposomes to overcome tumor hypoxia for enhanced chemo-radiotherapy of cancer. *Biomaterials* 138, 13–21. doi:10.1016/j.biomaterials.2017.05.025

Zhang, P., Zhang, Y., Ding, X., Shen, W., Li, M., Wagner, E., et al. (2020). A multistage cooperative nanoplatform enables intracellular Co-delivery of proteins and chemotherapeutics for cancer therapy. *Adv. Mat.* 32, 2000013. doi:10.1002/adma.202000013

Zhang, W., Lyu, X., Zhang, L., Wang, W., Shen, Q., Lu, S., et al. (2022). Rationally driven drug nonradiative decay via a label-free polyprodrug strategy to renew tumor cascade photothermal-chemotherapy. *Macromol. Rapid Commun.* 43, 2100918. doi:10.1002/marc.202100918

Zhang, R., Feng, L., Dong, Z., Wang, L., Liang, C., Chen, J.., et al. (2018). Glucose & oxygen exhausting liposomes for combined cancer starvation and hypoxia-activated therapy. *Biomaterials* 162, 123–131. doi:10.1016/j.biomaterials.2018.02.004

Zhang, Y., Cai, K., Li, C., Guo, Q., Chen, Q., He, X.., et al. (2018). Macrophage-membrane-coated nanoparticles for tumor-targeted chemotherapy. *Nano Lett.* 18, 1908–1915. doi:10.1021/acs.nanolett.7b05263

Zheng, C., Li, M., and Ding, J. (2021a). Challenges and opportunities of nanomedicines in clinical translation. *BIO Integr.* 2, 57–60. doi:10.15212/bioi-2021-0016

Zheng, P., Ding, B., Jiang, Z., Xu, W., Li, G., Ding, J., et al. (2021b). Ultrasound-augmented mitochondrial calcium ion overload by calcium nanomodulator to induce immunogenic cell death. *Nano Lett.* 21, 2088–2093. doi:10.1021/acs.nanolett.0c04778

Zheng, P., Ding, B., Shi, R., Jiang, Z., Xu, W., Li, G., et al. (2021c). A multichannel Ca(2+) nanomodulator for multilevel mitochondrial destruction-mediated cancer therapy. *Adv. Mat.* 33, e2007426. doi:10.1002/adma.202007426

Zhong, J., Li, L., Zhu, X., Guan, S., Yang, Q., Zhou, Z., et al. (2015). A smart polymeric platform for multistage nucleus-targeted anticancer drug delivery. *Biomaterials* 65, 43–55. doi:10.1016/j.biomaterials.2015.06.042

Zhong, X., Wang, X., Li, J., Hu, J., Cheng, L., and Yang, X. (2021). ROS-based dynamic therapy synergy with modulating tumor cell-microenvironment mediated by inorganic nanomedicine. *Coord. Chem. Rev.* 437, 213828. doi:10.1016/j.ccr.2021.213828

Zhou, X., Xu, L., Xu, J., Wu, J., Kirk, T. B., Ma, D., et al. (2018). Construction of a high-efficiency drug and gene Co-delivery system for cancer therapy from a pH-sensitive supramolecular inclusion between oligoethylenimine-graft-β-cyclodextrin and hyperbranched polyglycerol derivative. *ACS Appl. Mat. Interfaces* 10, 35812–35829. doi:10.1021/acsami.8b14517

Zhu, S., Qian, L., Hong, M., Zhang, L., Pei, Y., and Jiang, Y. (2011). RGD-modified PEG-PAMAM-DOX conjugate: *In vitro* and *in vivo* targeting to both tumor neovascular endothelial cells and tumor cells. *Adv. Mat.* 23, H84–H89. doi:10.1002/adma.201003944

Zhu, D., Ling, R., Chen, H., Lyu, M., Qian, H., Wu, K., et al. (2022). Biomimetic copper single-atom nanozyme system for self-enhanced nanocatalytic tumor therapy. *Nano Res.* 15, 7320–7328. doi:10.1007/s12274-022-4359-6

Zununi Vahed, S., Salehi, R., Davaran, S., and Sharifi, S. (2017). Liposome-based drug co-delivery systems in cancer cells. *Mater. Sci. Eng. C* 71, 1327–1341. doi:10.1016/j.msec.2016.11.073

frontiers | Frontiers in Bioengineering and Biotechnology

TYPE Review
PUBLISHED 13 September 2022
DOI 10.3389/fbioe.2022.985881

OPEN ACCESS

EDITED BY
He Liu,
Jilin University, China

REVIEWED BY
Lunguo Xia,
Shanghai Jiao Tong University, China
Cristian Covarrubias,
University of Chile, Chile
Jinshan Guo,
Southern Medical University, China

*CORRESPONDENCE
Zhihua Li,
lizhihua@ncu.edu.cn
Junchao Wei,
weijunchao@ncu.edu.cn

SPECIALTY SECTION
This article was submitted to Biomaterials, a section of the journal Frontiers in Bioengineering and Biotechnology

RECEIVED 04 July 2022
ACCEPTED 22 August 2022
PUBLISHED 13 September 2022

CITATION
Xu J, Shi H, Luo J, Yao H, Wang P, Li Z and Wei J (2022), Advanced materials for enamel remineralization. *Front. Bioeng. Biotechnol.* 10:985881. doi: 10.3389/fbioe.2022.985881

Advanced materials for enamel remineralization

Jiarong Xu[1], Hui Shi[1,2], Jun Luo[1,2], Haiyan Yao[1,3], Pei Wang[1,2,3], Zhihua Li[1,2,3]* and Junchao Wei[1,2,3]*

[1]School of Stomatology, Nanchang University, Nanchang, Jiangxi, China, [2]Jiangxi Province Clinical Research Center for Oral Diseases, Nanchang, China, [3]Jiangxi Province Key Laboratory of Oral Biomedicine, Nanchang, Jiangxi, China

Dental caries, a chronic and irreversible disease caused by caries-causing bacteria, has been listed as one of the three major human diseases to be prevented and treated. Therefore, it is critical to effectively stop the development of enamel caries. Remineralization treatment can control the progression of caries by inhibiting and reversing enamel demineralization at an early stage. In this process, functional materials guide the deposition of minerals on the damaged enamel, and the structure and hardness of the enamel are then restored. These remineralization materials have great potential for clinical application. In this review, advanced materials for enamel remineralization were briefly summarized, furthermore, an outlook on the perspective of remineralization materials were addressed.

KEYWORDS

advanced materials, enamel caries, demineralization, remineralization, hydroxyapatite

1 Introduction

The enamel, consisting of 96–97 wt% inorganic hydroxyapatite (HA, $Ca_{10}(PO_4)_6(OH)_2$), 3wt% water and 1wt% organic material, is the hardest tissue in the human body (Bowen et al., 2018; Harper et al., 2021). However, enamel is susceptible to acid, causing enamel demineralization and even developing cavities (Pitts et al., 2017). Currently, hundreds of millions of people in the world is under the enamel damage (Peres et al., 2019). It is difficult to repair enamel on its own due to the lack of sufficient calcium and phosphate ions in saliva (Lawn et al., 2010; Lacruz et al., 2017). Therefore, artificial materials such as resin, metal or bioglass are commonly used for clinical repair of cavities (Dorri et al., 2017). In terms of composition, mechanical properties, and appearance, these composites differ significantly from enamel. By comparison, enamel remineralization can be an effective clinical method for restoring the natural properties and structure of enamel while avoiding the problems associated with filling materials. Remineralization requires replacing minerals lost during the early stages of demineralization to restore enamel hardness or structure.

Remineralized materials are essential to enamel repair. Functional materials can promote and arrange the deposition of calcium and phosphate ions or alter the solubility of the HA. They can be divided into inorganic materials, organic materials, and polymeric materials (Figure 1). These functional materials are designed to rebuild remineralized

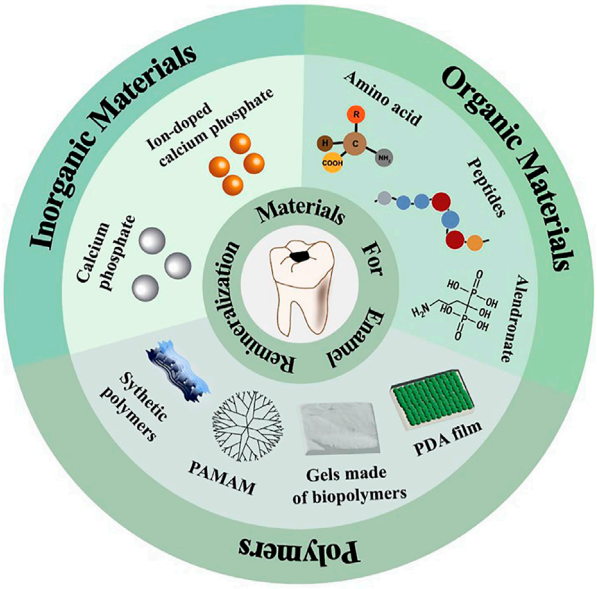

FIGURE 1
Schematic diagram of advanced materials promoting remineralization and repairing enamel.

tissue on damaged enamel surfaces, thereby preventing disease progression while also improving aesthetics and mechanical strength. Therefore, materials for enamel remineralization have a bright future in clinic. Although several reviews of remineralized materials have been published (Cochrane et al., 2010; Ding et al., 2017; Pandya and Diekwisch, 2019), enamel remineralized materials have been innovated and developed. As a result, it is critical to review the relevant research progress in time for the construction and upgrading of the enamel remineralization system. In this review, the characteristics and working mechanism of remineralized materials are briefly summarized. The specific functions of various functional materials will be clarified by category, with reference opinions provided for future material design and synthesis.

2 Functional inorganic materials

Functional inorganic materials can induce the formation of apatite layers or release ions, which can promote the remineralization of enamel. When the remineralized layer forms, calcium phosphates (CaPs) provide exogenous ions to compensate minerals lost by enamel, while fluoride and magnesium ions can exchange with calcium ions in HA, changing the solubility and mechanical properties of ion-doped HA. Therefore, the ability of inorganic materials to release ions and the change in enamel properties caused by their participation in HA are the primary focal point of researches.

2.1 Calcium phosphates

CaPs can provide ions to reconstruct damaged enamel. Remineralization solutions containing calcium and phosphorus ions are usually used in remineralization experiments, which must be replaced or replenished on a regular basis. Some stable CaPs materials can provide ions required for an extended time. Amorphous calcium phosphate (ACP), tricalcium phosphate (TCP), and nano-hydroxyapatite (nHA) are common CaPs materials used for remineralization. The type and size of the CaPs crystals can influence the ion supply capacity and the depth of ion entry into the lesion. Therefore, the mineralization effects of these materials are different.

ACP, the precursor phase of biogenic HA of bone and tooth, is the basic mineralization unit in the biological mineralization process (Gelli et al., 2019). Aqueous ACP solutions contain abundant Ca^{2+} and PO_4^{3-} ions, which form highly hydrated clusters. The structure and composition of the crystalline phase change after further aggregation of clusters until the thermodynamically stable crystalline HA (alkaline conditions) or carbon brushes (acidic conditions) formed (He et al., 2020). Usually, such reaction time is fast in the absence of external interference. Only ACP solutions failed to restore enamel (Shao et al., 2019). Therefore, enamel remineralization requires ensuring the stability of ACP in solution and prolonging its phase transition time. Acidic groups, such as carboxyl and phosphoric groups, can bind calcium ions in solution, preventing Ca^{2+} and PO_4^{3-} from aggregating. Organic compounds with carboxyl or phosphate groups are the most common ACP stabilizers. It is a good method to use amino acids such as aspartate (Asp), glutamate (Glu), citrate (Delgado-López et al., 2014; Iafisco et al., 2015), and the phosphate stabilizer triethylamine (Shao et al., 2019) to maintain the size of ACP particles, ensuring ion supply in the subsequent mineralization process. In addition, the casein phosphopeptide (CPP) that containing four to seven phosphate groups can attach to ACP nanoclusters, forming CPP-ACP. CPP-ACP complexes have been used as common additives for caries prevention. Furthermore, CPP-ACP in combination with fluoride show advantages in remineralization of existing lesions (Bijle et al., 2018; Tao et al., 2018). However, CPP-containing products should be used with caution in individuals with lactose intolerance issues.

TCP can be divided into α-TCP and β-TCP according to the crystal form. β-TCP is often used in dental materials because of its great biodegradability and biocompatibility. When exposed to acid, β-TCP degrades to release ions for enamel restoration. After surface functionalization by carboxylic acid and surfactants,

functionalized TCP (fTCP) can prevent fluoride from binding with calcium ions on the enamel surface prematurely to build a low-dose fluoride release system (Karlinsey and Pfarrer, 2012; Shen et al., 2018; Viana et al., 2020). After combining with fumaric acid, fTCP can show significantly higher calcium bioavailability than β-TCP and better remineralization of subsurface enamel damage (Karlinsey et al., 2010).

nHA is a bioactive and biocompatible material with a small particle size of 10–20 nm in diameter and 60–80 nm in length (Huang et al., 2011). The nanometer size enables nHA to penetrate deeper lesion layers through large lesion pores and repair enamel damage (Juntavee et al., 2018; Bossu et al., 2019; Memarpour et al., 2019). However, high-concentrating nHA tend to self-aggregate into large-sized nHA, which can affect the amount and depth of nHA entering the lesion (Huang et al., 2009). As a carrier, the gel effectively extends the contact time between the active ingredient and the enamel, allowing nHA to fill the small holes and depressions. Both silica-based glycerol hydrogel (Khonina et al., 2020) and carbomer-based gel (Sari et al., 2021) containing nHA can repair damaged enamel.

2.2 Fluorinated compounds

Fluorinated compounds have been commonly utilized since the previous century to reverse or prevent enamel defects from spreading. Consequently, the global incidence rate of dental caries has decreased dramatically (Jokstad, 2016; Clark et al., 2020). Fluoride reduces demineralization by altering enamel solubility (Lynch et al., 2004). Fluoride and calcium ions are more strongly bound than hydroxyl groups. Therefore fluoride can replace hydroxyl to form fluorapatite (FAP), which has high acid resistance and poor solubility (Clark et al., 2020). Fluorides, on the other hand, can promote remineralization by encouraging Ca^{2+} in saliva to attach to the tooth surface. In addition, fluoride can reduce the adhesion and growth of germs by blocking the activities of numerous enzymes.

Fluoride is primarily ingested through drinking water (75%). Fluoridation of home water is a typical measure to prevent dental caries in many countries, and it can successfully reduce the incidence of dental caries. Fluoride can also be found in a variety of oral care treatments and dental materials, including sodium fluoride (NaF), stannous fluoride, silver diamine fluoride, acidulated phosphate fluoride, ammonium fluoride, and others (Barrera-Ortega et al., 2020). Fluoride sustained-release ability could be altered by combining fluoride ions with different cations and complexing it with different organic molecules. In toothpaste and rinses, polyvalent fluorides with tin and titanium as cations exhibit excellent corrosion resistance (Zanatta et al., 2020). This is due to the fact that they can not only produce CaF_2 on the enamel surface, but can also generate metallic precipitates on the enamel surface, which contributes to the reduction of calcium ion loss when subjected to external erosion.

However, fluorides have caused certain issues when they are used. Fluoride tends to develop a disordered layered structure of remineralization layer, which is considerably different from natural enamel. The mechanical characteristics of the remineralized layer can be weakened by these disordered formations. Organic compounds like amelogenin can help minimize the occurrence of disordered structures in the reaction system (Yu et al., 2019) (Figure 2). Moreover, excessive fluoride use can result in hazardous effects like dental fluorosis and skeletal fluorosis (Philip, 2019). It also has the possibility to make cariogenic bacteria resistant, diminishing the effectiveness of follow-up prophylaxis (Liao et al., 2017). Fluorinated hydroxyapatite is rapidly formed in the superficial enamel layer of very concentrated F^- solutions, preventing Ca^{2+} and PO_4^{3-} from penetrating deeper into the lesion. As a result, subsurface enamel lesions can fail to mineralize adequately. Therefore, fluoride slow-release systems made of copolymer acrylic reservoirs and glass ionomer cement can be great alternatives for promoting enamel mineralization by extending the trailing effect (Chong et al., 2018).

Fluoride compounds, as traditional enamel remineralization materials, have a relatively well-studied mineralization mechanism, which facilitates the development of novel fluoride-mediated remineralization systems. However, the functions of fluoride compounds are still need to be improved, and thus, blends or composites of fluoride compounds, which can combine multifunction together to achieve satisfactory clinical results, are greatly needed in the future.

2.3 Magnesium related materials

Magnesium presents in the hard tissues of the body. In enamel, the content of Mg^{2+} is ranging from 0.2 to 0.5 wt%. Mg^{2+} is present near the grain boundaries as an intergranular phase of Mg substituted amorphous calcium phosphate (Mg-ACP) (La Fontaine et al., 2016). Such amorphous phases have been proved to make a significant impact on the mechanical characteristics and wear resistance of enamel (Gordon et al., 2015). Mg^{2+} slows crystal growth by competing with calcium ions at the growth point during mineralization, affecting the production of apatite (Ren et al., 2010; Abdallah et al., 2016). As a result, Mg^{2+} can act as a competitive inhibitor to guide narrower crystal columns, which promotes a highly ordered arrangement and increases mineralized tissue hardness. As the concentration of Mg^{2+} on the enamel surface increases, the nano-hardness of the enamel rises dramatically (Kis et al., 2021). Layer by layer mineralization process is used to create multilayer arrays of enamel-like FAP/polymer nanocomposites controlled by Mg^{2+} (FPN-M) at room temperature (Li Y. et al., 2021) (Figure 3). In the presence of Mg^{2+}, the single nanorods are refined in size and a highly compact array is formed, eventually, $(FPN\text{-}M)_n$ exhibits

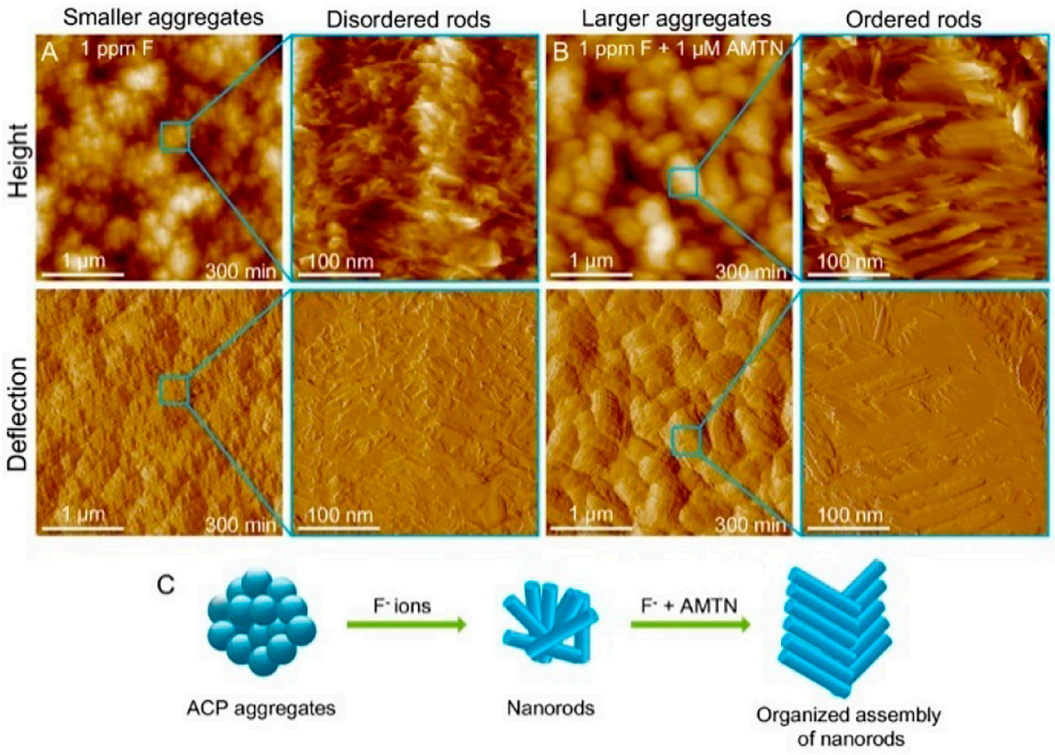

FIGURE 2
AFM height and deflection images of NPF solution in the presence of **(A)** 1 ppm F and **(B)** 1 ppm F and 1 μM AMTN for 300 min. **(C)** Schematic representation of nanorod tissue assembly in the presence of F ions and AMTN. Reprinted with permission from [(Yu et al., 2019)]. Copyright © 2019 American Chemical Society.

excellent mechanical strength and transparency. The present researches have demonstrated Mg^{2+} have great importance during the process of enamel remineralization, therefore, more and more attention should be paid to Magnesium related materials. Besides, further understanding of the relationship between Mg^{2+} and biomineralization can help develop strategies to improve the mechanical properties of mineralized tissues and improve the functions of repaired tooth enamel.

3 Functionalized organic materials

Inorganic matter production and growth require a relatively constant environment, which organic materials can offer. Organic molecules are rich in acidic functional groups such as carboxyl, phosphate, and sulfonic acid. These functional groups can induce inorganic compound nucleation, inhibit overgrowth, or interact with hydroxyapatite on the surface of the enamel to increase adsorption capacity. Understanding the specific role of these organic compounds can help to clarify the mechanism of enamel mineralization and provide ideas for future remineralized material design.

3.1 Amino acids

Amino acid molecules contain different amounts of amino and carboxyl groups. Depending on the isoelectric point, amino acids can be classified as acidic, neutral, and basic amino acids. Among them, acidic amino acids are negatively charged in weakly acidic solutions, which can influence the nucleation, crystallization, growth, and crystal transformation of HA. Glu and Asp can operate as soft templates, connecting two calcium ions diagonally to generate ordered HA crystals that parallel to the enamel column while stabilizing calcium ions in the solution. The crystals on the enamel surface can grow more ordered with the amino acid concentration rises. Asp and Glu is used to deposit the $CaCO_3$ layer as a sacrificial template on the enamel's surface (Wu et al., 2015). The acidic amino acids then absorbed phosphate and carbonate ions, depositing HA into the $CaCO_3$ layer to form the rod crystal. Glycine (Gly), a highly hydrophilic amino acid, can also be used as a biological additive to create enamel-like structures (Tao et al., 2007). According to the molecular dynamics experiment, Gly exhibits the same adsorption abilities and coverage in all directions of the crystal surface, which maintains HA's *c*-axis propensity (Pan

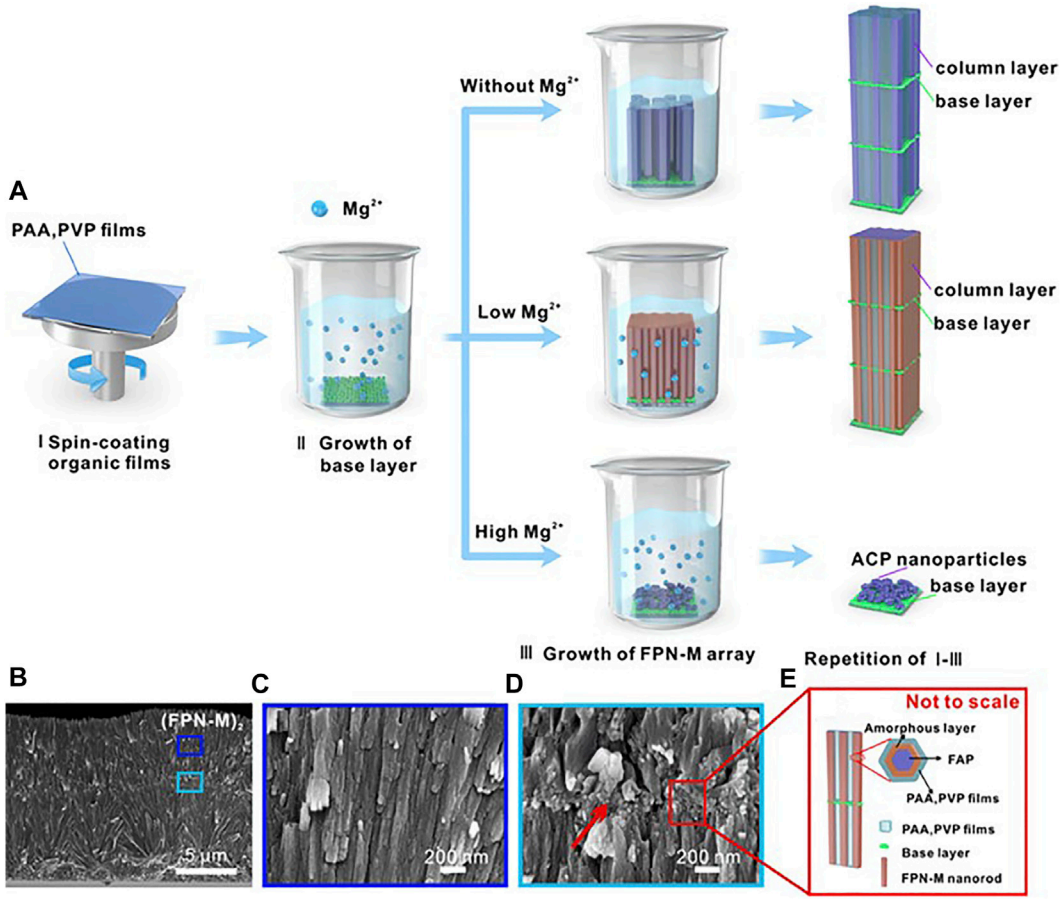

FIGURE 3
(A) The schematic diagram of the synthetic multilayer FAP/polymer nanocomposite controlled by Mg^{2+}. **(B)—(C)** Cross-sectional SEM images of $(FPN\text{-}M)_2$ with corresponding details. **(D)** Granular interlaminar base layer (indicated by red arrows). **(E)** Interlayer structure and amorphous-reinforced architecture schematic diagram. Reprinted with permission from [(Li Y. et al., 2021)]. Copyright© 2021 American Chemical Society.

et al., 2007). In the carboxymethyl chitosan-stabilized ACP remineralization system, a rod-shaped crystal layer is successfully produced in artificial caries when Gly is introduced to the system, whereas the system without Gly fail (Wang et al., 2017). Arginine (Arg), a basic amino acid, positively affects pH homeostasis, bacterial ecology, and pathogenicity. Arg is metabolized in oral biofilms to produce ammonia mainly through the internal arginine deiminase system (ADS) of bacteria (*Streptococcus sanguis* and *Streptococcus*). Ammonia produced under this pathway has a significant pH-raising effect, while inhibiting tooth demineralization by neutralizing acids in the peripheral environment (Bijle et al., 2021b). It also facilitates the formation of arginine-friendly microorganisms while disrupting the internal homeostasis of caries-causing bacteria (Nascimento et al., 2019). The combination of Arg and fluoride can create a pH-responsive fluoride pool that inhibit acid production and has potential synergistic effects in maintaining a healthy oral microbial balance (Agnello et al., 2017; Bijle et al., 2021a). The pool can also significantly improve the fluoride uptake and surface hardness of damaged enamel compared to fluoride alone (Zheng et al., 2015; Bijle et al., 2020).

3.2 Enamel matrix proteins and proteases

Enamel matrix proteins (EMPs) and proteases control the formation of enamel (Jia et al., 2020; Shin et al., 2020). EMPs govern the parallelism between the glazing columns and organize them in a dense and slender hexagonal prism structure at the micro-level by regulating the creation and structure of HA crystals (Bartlett, 2013; Uskokovic, 2015; Bai et al., 2020). These highly co-oriented glaze columns give enamel its remarkable shear strength and make it resistant to everyday abrasion (Yeom et al., 2017). Over 90% of the EMPs consists of amelogenin. Amelogenin can be enzymatically processed into different peptides. These peptides undergo a change in spatial

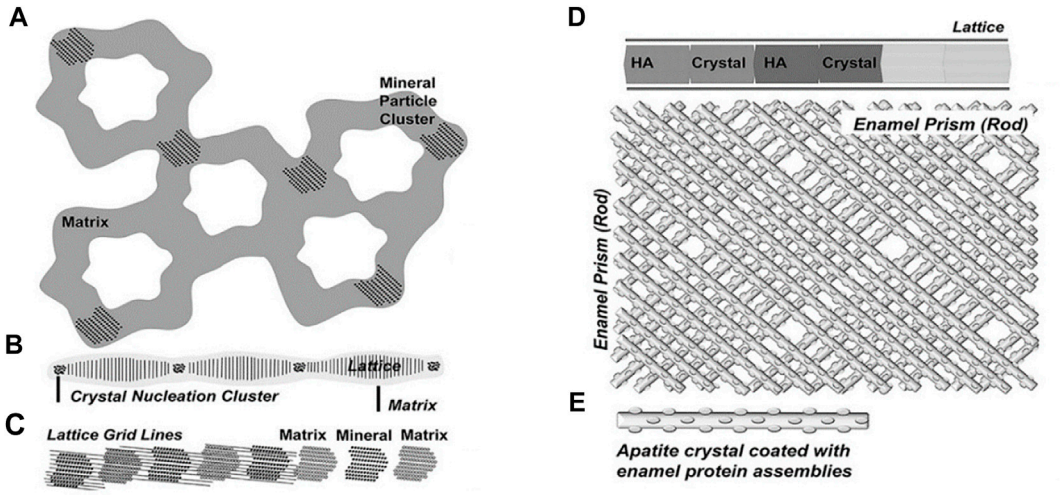

FIGURE 4
Five successive stages of enamel crystal precipitation and extension. **(A)** Stage of calcium phosphate particles precipitating and adhering to the organized enamel protein matrix, **(B)** Formation of initial crystal needle through single nucleation sites, **(C)** Extension of enamel crystals by lattice-guided alignment of individual apatite crystals, **(D)** Stage of crystal further extension and growing, **(E)** Enamel prisms (rods) are formed by the cross arrangement of single enamel crystals. Reprinted with permission from [(Jokisaari et al., 2019)]. Copyright © 2019 American Chemical Society.

conformation, manifested by α-helix unraveling and β-sheet and β-turns formation, at which point amyloid-like aggregation occur in the proteins (Carneiro et al., 2016; Bai et al., 2020). Then, they self-assemble into oligomers and nanospheres (Fang et al., 2011; Engelberth et al., 2018; Bai et al., 2020). These oligomeric nanospheres further form nanochains that concentrate Ca^{2+} and PO_4^{3-} in the peripheral matrix, generating mineralized precursors during enamel development, which then serve as templates to guide the crystal phase transition, eventually generating HA (Gil-Bona and Bidlack, 2020) (Figure 4). The enamel columns then elongate in one direction to form a hexagonal prismatic structure (Jokisaari et al., 2019).

Enzymes are critical requirements for enamel biomineralization. Enzymes activate the biological function of amelogenin and degrade organic matter in the matrix until a sufficiently hard tissue formed (Prajapati et al., 2016). Matrix metalloproteinase 20 (MMP-20) cleaves amelogenin, and the product peptide controls the lengthening and growth of crystal nucleus and induces HA mineralization (Fukae et al., 1998; Nagano et al., 2009; Gil-Bona and Bidlack, 2020). Addition of MMP-20 to full-length porcine amelogenin can promote neatly aligned bundles of enamel-like HA, whereas in the absence of MMP-20, only ACP particles seen (Kwak et al., 2016). Another important enzyme is Kallikrein-related peptidase 4 (KLK4). During enamel maturation, KLK4 degrades the organic matrix in the mineral (Smith et al., 2017; Sari et al., 2021). The width and thickness of the microcrystals can increase when proteins are removed from mature enamel. If the enzyme is deficient, the enamel will undergo hypoplasia (Simmer et al., 2009; Smith et al., 2017).

In-depth studies of the enzymatic cleavage products revealed three major functional domains of the amelogenin (Mukherjee et al., 2019; Dissanayake et al., 2020). N-terminal: a hydrophobic tyrosine-rich N-terminal region, known as tyrosine-rich amelogenin peptide (TRAP), is critical in the directed assembly of amelogenin (Buchko et al., 2018). The central region: the central hydrophobic proline-rich region is mainly composed of X-Y-proline (X and Y are usually glutamine) repeat motifs, which is rich in β-sheets and β-turns. The C-terminal: a highly hydrophilic domain contains a large number of acidic amino acid residues. These residues could combine with Ca^{2+} to provide nucleation sites and bind to the (100) face of octacalcium phosphate (OCP), the intermediate sub-stable phase in early enamel, thereby govern the direction in which the enamel column extends (Wu et al., 2017) (Figure 5). Leucine-rich amelogenin peptide (LRAP), which contains two self-assembled domains of full-length amelogenin, is the most common alternative splicing product of amelogenin (Xia et al., 2016; Green et al., 2019). It is discovered that depending on the phosphorylated version of the peptide on serine 16, LRAP can perform distinct activities. Phosphorylated LRAP (+P) inhibits calcium phosphate crystallization and stabilizes ACP, whereas LRAP (–P) directs the production of aligned enamel crystals (Yamazaki et al., 2017; Le Norcy et al., 2018). *In vitro*, LARP and PP_i are used to remineralize the eroded enamel, and acicular HA crystals are successfully regenerated on the surface (Kwak

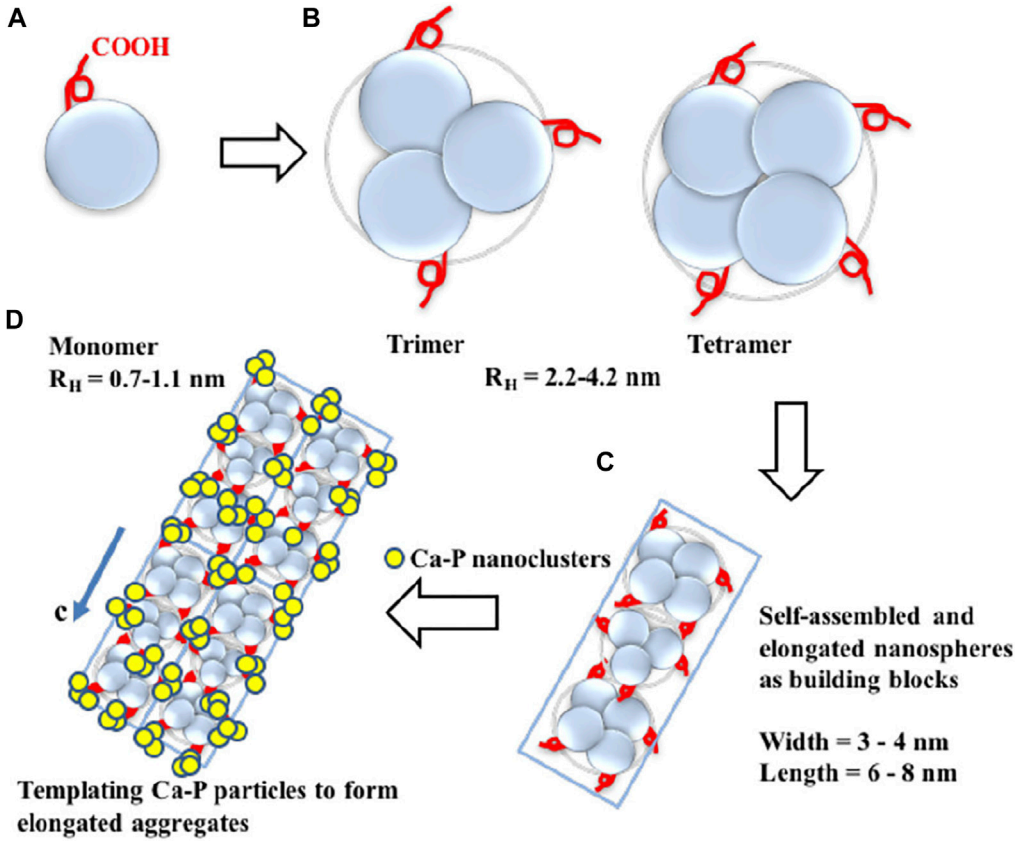

FIGURE 5
Diagram of amelogenin C-terminal peptides self-assembly to guide the extension of OCP crystallization. **(A)** The monomeric structure of amelogenin's C-terminal peptide. The red curve represents the -COOH terminus. **(B)** Hydrophobic interactions lead to the formation of oligomeric amelogenin's C-terminal peptides. **(C)** Nanorod structures as building blocks are formed by the association of oligomers. **(D)** Elongated organic-inorganic complex aggregates formed by the building blocks nanorods and CaP nanoclusters. Reprinted with permission from [(Wu et al., 2017)]. Copyright © 2017 American Chemical Society.

et al., 2017). Inspired by these structural domains, amelogenin analogs are designed and synthesized to induce *in vitro* bionic remineralization. After grafting different fragments, these synthetic functional peptides can be easier to obtain and show certain functional enhancements, such as adsorption ability.

Non-amelogenins work in early enamel formation, including enamelin and tuftelin. Enamelin acts as a transport and nucleation protein that affects amelogenin to regulate early enamel development (Bartlett et al., 2006; Lacruz et al., 2017; Yan et al., 2017). Tuftelin is an acidic protein produced by ameloblasts during the early stages of enamel formation. It is concentrated near the dentin-enamel intersection, in which enamel mineralization begins. The tuftelin-derived peptide (TDP) is created based on the structure of tuftelin. The group repaired by TDP demonstrate comparable enamel hardness and lesion depth healing results after pH cycling to NaF groups (Ding et al., 2020).

3.3 Functional peptides

Functional peptides inspired by bioproteins can in some ways replicate the unique functions of these bioproteins, as well as easier access. Assembly of these peptides with different functions can produce multifunctional peptides, such as peptides with high enamel binding and remineralization capacity or peptides with antibacterial and remineralization activities (Table 1).

3.3.1 Amelogenin analogs

Amelogenin analogs are created by mimicking the functional domain of amelogenin. These synthetic peptides outperform full-length amelogenin in synthesis, purification, and retention (Gungormus et al., 2012; Dogan et al., 2018). The focus of recreating enamel structure and function *in vitro* is inducing columns growth and elongation directly, which is predominantly regulated by the C-tail. Therefore, peptides with C-terminal can stimulate remineralization *in vitro*. Amelogenin inspired

TABLE 1 Synthetic peptides for biomineralization.

Peptide	Sequence	Remineralization effect	References
Chimeric peptide	SVSVGMKPSPRP-GGGGS-LEAWPATDKTKREEVD	Hardness 0.70 ± 0.21 GPa, elastic modulus 66.7 ± 2.4 GPa	Xiao et al. (2017)
TDP	DRNLGDSLHRQEI	%SMH_R of TDP increased; a significantly thicker and brighter remineralization layer with shallower lesions obtained	Ding et al. (2020)
P32	MPLPSYEVLTPLKWPSTDKTKREEVD	1.8-fold increase in elastic modulus and a 1.9-fold increase in hardness compared to demineralized enamel	Mukherjee et al. (2018)
QP5	QPYQPVQPHQPMQPQTKREEVD	%SMH_R: 50.06, similar to NaF (58.48)	Wang Y. et al. (2020)
ADP5	SYENSHSQAINVDRT (AA sequence)	Vicker's microhardness: 141 + 8 HV10; hardness: 2.23 + 0.23 GPa; elastic modulus: 58.6 + 4.7 GPa	Dogan et al. (2018)
Peptide-7	Asp-Asp-Asp-Glu-Glu-Lys-Cys	Ra and Rz: 19.0 ± 4.3 nm and 223.6 ± 23.6 nm; the hardness 497.79 ± 19.63; % SMH_R: 84.13; adhesion force 63.80 ± 4.58 N	Liu et al. (2018)
Sp-H5	phosphoserine-DSHAKRHHGYKRKFHEKHHSHRGY	2.5-μm-thick crystal layer is regenerated on the enamel surface	Zhou et al. (2020)
P-113-DPS	AKRHHGYKRKFH-SpSp	The thickness of the regenerated crystal layer in 24 h: 8.5 μm	Zhou et al. (2021)
LCPS-CP	^{37}SYSGYS^{42}	Elastic modulus of 65.43 ± 15.57 GPa and surface hardness of 1.831 ± 0.5852 GPa for the LCPS-CP group	Chang et al. (2022)
8DSS	$(Asp\text{-}Ser\text{-}Ser)_8$	lesions became shallower after pH cycling; shows remineralization results similar to 1 g/L NaF *in vitro* test	Yang et al. (2014)

Abbreviations: %SMH_R, surface microhardness recovery ratio; ADP5, amelogenin derived peptide 5; LCPS-CP: LCPS-CP, low-complexity protein segments containing phosphonate group.

peptides of 26 and 32 amino acid residues (P26 and P32) with hydrophilic inner N- and C-terminal are produced to mimic the "nanosphere" structure in the enamel matrix (Mukherjee et al., 2018). A firm mineralized layer is successfully produced on the enamel surface after 7 days of *in-situ* culturing with polypeptide solution. *C*-axis oriented nanorods are generated on the enamel surface by repeating the peptide application process. P32 can restore the hardness of etched enamel better because the crystals created by P26 are smaller than those produced by P32. A chimeric peptide is created by grafting the C-terminal onto HA6-1, which can be selectively attached to the enamel surface (Xiao et al., 2017). The C-terminals of the chimeric peptide increases the peptide adsorption and facilitates the formation of a mechanically strong remineralized layer. QP5 is consisting of five highly conserved Gln-Pro-X repeat sequence in the center region and a hydrophilic C-tail (Lv et al., 2015; Chu et al., 2018; Ren et al., 2018; Li et al., 2020). When compared to amino acids, QP5 has a better remineralization impact, which effectively restored enamel surface hardness and reduced surface roughness value (Li et al., 2020; Wang Y. et al., 2020). Moreover, QP5 can enhance remineralization in a complicated oral environment, as demonstrated by the rat caries model (Han et al., 2017). Shortened amelogenin derived peptide 5 (shADP5) is employed as an active ingredient to generate a mineralized layer in solution. The enamel surface is healed after 1 h of mineralization, and the average hardness and elastic modulus are higher than control samples, with the hardness of 2.23 ± 0.23 GPa vs. 2.10 ± 0.26 GPa and elastic modulus of 58.6 ± 4.7 GPa vs. 55.1 ± 4.3 GPa (Dogan et al., 2018). A phase transfer lysozyme (PTL) membrane can be used to simulate the N-terminal of amelogenin (Wang D. et al., 2020). After the occurrence of amyloid aggregation, the internal structure of lysozyme is changed: the α-helixes unravel and the β-sheets is formed through hydrophobic interactions, which is similar to the spatial phase shift of amelogenin self-assembling. At the liquid/solid interface, those β-sheet-rich proteins are quickly organized into nanoparticles, forming a nanofilm that could be adsorbed on the enamel surface and serve as a scaffold for subsequent remineralization. The hydrophilic C-tail is then grafted onto PTL to produce PTL/C-AMG, which can guide HA growing in a direction. A 2.0–2.8 μm thick remineralization layer is produced after applying 1 mg/ml PTL/C-AMG to demineralized tooth slices for 7 days. These remineralized layers have similar properties to natural enamel with a "fish-scale" structure.

3.3.2 Statherin derived peptide

Statherin, a tyrosine-rich peptide with 43 amino acid residues, is a salivary protein that is found in the oral acquired membrane. Because of a unique combination of high negative charged domains on the N-terminal and enamel surface, statherin can securely cling to the enamel surface (Raj et al., 1992; Gururaja and Levine, 1996). To replicate the property of high HA binding, several peptides derived from statherin are created (Shuturminska et al., 2017; Luo et al., 2019; Carvalho et al., 2020). Separating the N-terminal of statherin can yield the peptide SN15 (Dodds et al., 2005; Shimotoyodome et al., 2006; Luo et al., 2019). Grafting SN15 onto PAMAM can improve its absorption on enamel surface (Gao et al., 2020). The statherin stimulated peptide and tannic acid are used to

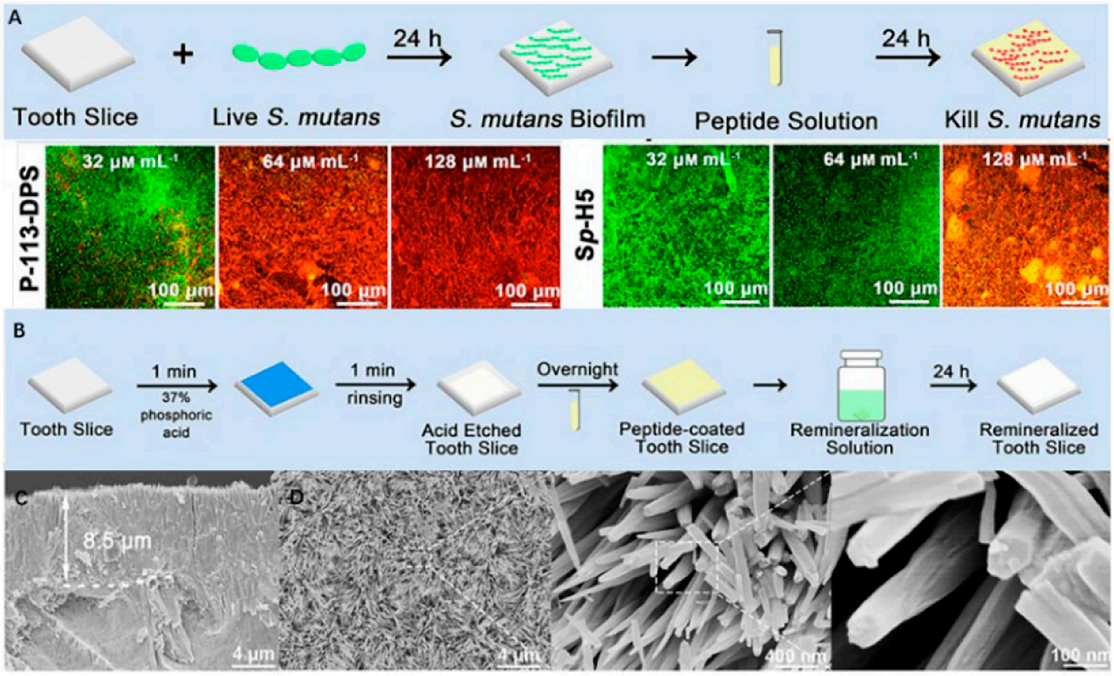

FIGURE 6
(A) Schematic diagram of anti-*S. mutans* biofilm on the enamel surface and fluorescence images (×20) of *S. mutans* biofilm in various concentrations of P-113-DPS and Sp-H5 solutions. **(B)** Remineralization experiment schematic. **(C)** 8.5 μm needle-like remineralized layers formed by P-113- remineralized layers and **(D)** its FE-SEM micrographs (×5000, ×50,000, and ×200,000). Reprinted with permission from [(Zhou et al., 2021)]. Copyright © 2021 American Chemical Society.

make SAP-TA (Yang et al., 2017). Polyphenol groups in TA can grab Ca^{2+} and trigger HA crystal renewal. Iron ions work in tandem with SAP-TA to generate a thick layer that boosts adsorption capacity. Therefore, SAP-TA/Fe (III) can improve the adhesion and mechanical properties of the remineralization interface (surface microhardness recovery >80%, binding force 64.85 N). Peptide-7 is designed and synthesized with a significant number of carboxyl groups on its side chain to help in firmly interacting with HA and directional elongation of HA crystals (Liu et al., 2018). Under the guidance of Peptide 7, a dense mineralized crystal layer with tight adhesion was formed.

3.3.3 Antibacterial peptide inspired bioactive peptides

Bioactive peptides have antibacterial and remineralization properties, which can be obtained by grafting units capable of promoting remineralization onto the active sequences of antimicrobial peptides. This bioactive peptide can protect enamel against demineralization while also promoting self-healing regeneration in a remineralized environment. P-113 is the smallest antibacterial unit of histatin 5, which is a type of natural antimicrobial peptide (Zhou et al., 2020). A study coupled dopamine (DA), SpSp (DPS) domains, and binding peptide binding peptide SKHKGGKHKGGKHKG on P-113 to find the most cost-effective peptide (Zhou et al., 2021). The experiment has discovered that P-113-DPS show similar antibacterial effect to Sp-H5 and can kill the majority of *Streptococcus mutans (S. mutans)* at low concentrations. After a 24-hour remineralization experiment, an 8.5 μm thick needle-like remineralization layer is formed on the enamel surface in the P -113-DPS group, twice as thick as the control group (4 μm) (Figure 6). The low-complexity protein segments (LCPSs) ^{37}SYSGYS^{42} in the fused in sarcoma protein is capable of forming nucleation structures that form reversible amyloid fibrils (Hughes et al., 2018). LCPSs are highly hydrophilic and structurally flexible. Due to weak multivalent interactions, proteins are entangled and subsequently form web-like structures. LCPSs containing a phosphate or phosphonate group is named LCPS-OP and LCPS-CP. These acidified polypeptides can bind calcium ions and acts as soft templates to induce HA formation. At the same time, the hydrophilic negatively charged peptide coating can reduce the bacterial adhesion of caries-causing bacteria by virtue of the negative electric mutual repulsion (Chang et al., 2022). Given that this bioactive peptide may more effectively repair damaged enamel while inhibiting further erosion of dental cariogenic bacteria, it may be an ideal material for the prevention of dental caries. In addition, some antimicrobial materials have been added to the

TABLE 2 Antibacterial remineralization dual materials.

Materials	Antibacterial mechanism	Bacterial used	Antibacterial adhesion results	Antibacterial test results	References
PASP-PEG	The PEG film on the enamel surface is resistant to bacterial adhesion	*S. sanguis*/*S. mutans*	Almost no bacterial attachment is detected on the surface	NA	Hou et al. (2020)
ZHA@ ALN-PAA	The released Zn^{2+} are antibacterial	*S. mutans UA159*	NA	IR: 75.05%	Xu et al. (2020)
Sp-H5	The cationic amino acid residues in H5 bind to cell wall, enhance membrane permeability and interact with intracellular DNA of *S. mutans* to induce cell death	*S. mutans*	Viability counts at 16× MIC [6.11E+05 (CFU/ml)]	MIC: 2 μmol/ml MBC: 4 μmol/ml	Zhou et al. (2020)
P-113-DPS	P-113-DPS crosslink with bacterial membrane phospholipids, increasing membrane permeability and forming perforation, preferentially occupy the binding site to inhibit the adhesion of *S. mutans*	*S. mutans*	Viable counts of *S. mutans* in P-113-DPS-coated [2.03E+05 (CFU ml^{-1})]	MIC:8 μM ml^{-1} MBC:16 μM ml^{-1}	Zhou et al. (2021)
LCPS-CP	Hydrophilic LCPSs eliminate adsorbed biomolecules by forming an anti-sewage ensemble; negatively charged phosphate coatings cause electrostatic repulsion between the bacterial film and the enamel, ultimately reducing adhesion	*S. mutans*	relative biomass value of the no peptide and LCPS-OH are more than eightfold greater of LCPS-OP and LCPS-CP	NA	Chang et al. (2022)
CMC/ACP	CMC neutralizes the negative charge on the surface of bacteria through a large number of positive charges to reduce the early adhesion of bacteria	*S. mutans*/*S. Gordonii*	adherence of *S. mutans* inhibited by 89.7%; *S. gordonii* by 86.1%	Biofilm formation decreased by 45.3% (*S. mutans*) and 44.0% (*S. Gordonii*)	He et al. (2019)
CS-QP5	CS captures free hydrogen ions, slows pH fall, damages the bacterial cell wall, and causes bacterial death	*S. mutans*	inhibited adhesion up to 95.43%	MIC/MBC: 5 mg/ml^{-1}	Ren et al. (2019)
PAMAM-NH_2	PAMAM-NH_2 destroy the bacterial wall by contacting bacteria for sterilization, improve the smoothness of remineralized layer and reduce bacterial adhesion	*S. mutans UA159*	Bacterial adhesion forces 3.64 ± 1.52 nN (control group: 5.52 ± 1.6 nN)	Colony-forming unit counting 5.78 ± 0.27 (control group: 6.13 ± 0.2)	Jia et al. (2020)

Abbreviations: NA, not available; PASP-PEG, poly (aspartic acid)-polyethylene glycol; ZHA@ALN-PAA, zinc-substituted hydroxyapatite/alendronate-grafted polyacrylic acid; IR, inhibition ratio; MIC, minimal inhibitory concentration; LCPS-CP, low-complexity protein segments containing phosphonate group; MBC, minimal bactericidal concentration.

remineralization system to promote enamel remineralization. The first type of materials can cover the enamel surface with an antifouling layer, and the second type can be used to destroy the bacterial biomass through the positive charges. Table 2 summarizes these materials that combine antimicrobial and remineralization functions and Figure 7 shows their modes.

3.3.4 Dentin phosphoprotein derived peptide

Dentin phosphoprotein, made up of a significant amount of aspartate serine repeat sequences that have a strong affinity for HA, can act as a nucleation template in the process of dentin mineralization (He and George, 2004). Therefore, inspired by dentin phosphoprotein, the peptide 8DSS containing eight DSS repetitions is synthesized. 8DSS can capture Ca^{2+} and act as a diffusion barrier that prevent CaP from dissolving. In the repair of both surface cavities and deep lesions, 8DSS demonstrated equal remineralization ability to NaF (Yang et al., 2014; Liang et al., 2015; Zheng et al., 2019). In addition, 8DSS is able to resist hydrolase assault and sustain its action in the mouth due to the short peptide chain length, which is conductive to clinical application.

3.3.5 Self-assembly peptide 11-4 (P_{11}-4)

Self-assembly peptide P_{11}-4 is a well-studied small molecule peptide. When activated by external stimuli, P_{11}-4 can self-assemble through intermolecular hydrogen bonds between peptide backbones and form three-dimensional scaffolds in lesions (Alkilzy et al., 2018a). At this time, the negative group formed by 4 Glu-residues on P_{11}-4 can attract calcium ions and induce mineralization. According to μCT imaging, the mineralization of the samples treated by P_{11}-4 increase by 68% in 14 days (Kind et al., 2017). It is worth noting that P_{11}-4 guided remineralization occurs in the subsurface of lesions, which can compensate for the shortcomings of fluoride. As a result, the combination of P_{11}-4 and fluoride varnish can produce good results in clinical applications. In an experiment on children over 5 years old with obvious active early caries, P_{11}-4 + fluoride varnish are superior to fluoride in terms of vision and safety (Alkilzy et al., 2018b). In some other

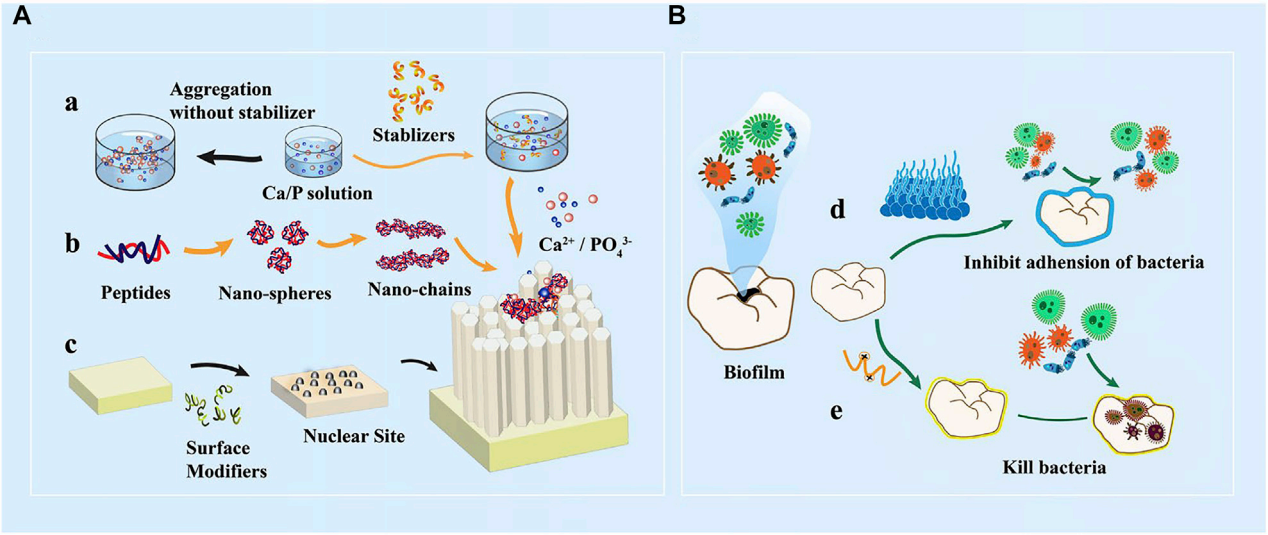

FIGURE 7
(A) *In vitro* peptide-induced bionic remineralization process. a) Organic matter stabilized calcium and phosphorus solution provides sufficient amount of ions b) Self-assembly of peptides into nanospheres, nano-chain structures orderly guide the deposition of calcium and phosphorus ions and extension of ordered orientation c) Organic matter modifies the substrate surface to form nucleation sites. **(B)** Mechanism of action of antibacterial anti-caries materials. d) Enamel surface coating reduces microbial adhesion; e) Positively charged peptides direct killing of caries-causing bacteria.

clinical trials, P_{11}-4 successfully treated white spot lesions caused by enamel demineralization and significantly improved the appearance (Doberdoli et al., 2020; Jablonski-Momeni et al., 2020; Sedlakova Kondelova et al., 2020).

3.4 Alendronate

Alendronate (ALN), a powerful bone resorption inhibitor with a high affinity for HA, is used to treat and prevent osteoporosis (Chen S. et al., 2020). The phosphate of ALN exchanges with the phosphate of HA in enamel, forming coordination chains that tightly bind it to the enamel surface (Palazzo et al., 2007). Therefore, ALN can act as a "glue" in the mineralization system to increase the adsorption of materials. ALN modified poly (amino amine) dendrimers (Wu et al., 2013) and carboxymethyl chitosan (Wang et al., 2017) can significantly increase their absorption on the enamel surface. In addition, after forming a HA layer around the ALN-modified polyacrylic acid (PAA), the outer layer of HA is zinc-modified to synthesize ZHA@ALN (Xu et al., 2020). Once ZHA@ALN dissolved by acid, a substantial number of calcium, phosphorus, and zinc ions can be released for remineralization and sterilizing. The inner layer of ALN-PAA adheres quickly to the enamel surface due to the ALN. Then, PAA serves as an antifouling layer with 75.05% bacteriostatic efficiency.

4 Polymer materials

Polymer materials have complex side groups and spatial structures, which enable them to mimic the enamel matrix and induce mineralization. Some are used to keep ions stable, and some can be made into gel carriers to transport functional peptides while forming a protective layer on the enamel surface. Due to their high biocompatibility and adaptability, polymer materials can be an ideal choice for promoting enamel remineralization.

4.1 Non-collagenous protein analogs

Non-collagenous proteins (NCPs) stabilize crystal precursors during dentin and bone collagen mineralization. NCP analogs, such as polyaspartic acid (pAsp), polyglutamic acid (PGA), and biocompatible polymers polyacrylic acid (PAA), contain a large number of carboxyl groups. These polymers can be used to create induced liquid precursors by stabilizing calcium ions. PGA and pAsp can also bind to calcium ions on the enamel surface, strengthening adhesion and providing nucleation sites (Ustriyana et al., 2020a; Ustriyana et al., 2020b). It has been discovered that the α-helical of pAsp or PGA can promote HA crystal nucleation by templating Ca^{2+} distribution. The HPO and -COO- can work

together to attract Ca^{2+} and form stable Ca^{2+} triangles, which can develop into the nucleation core of ACP (Zeng et al., 2021). PAA can also chelate with Ca^{2+} while maintaining liquid phase stability and transporting ions continuously for subsequent biomineralization (Chen R. et al., 2020; Xu et al., 2020; Li N. et al., 2021). Furthermore, PAA can direct the transformation of ACP to form acicular microcrystals (Wang et al., 2018).

4.2 Poly (amino amine) (PAMAM)

Poly (amino amine) (PAMAM) is a kind of synthetic protein with a dendritic structure. PAMAM can self-assemble into nanospheres, nanochains, and nanoribbons (Yang et al., 2015). Grafting different groups such as $-NH_2$, -COOH and -OH onto PAMAM can improve its ability to bind Ca^{2+}or promote its adsorption on the enamel surface. The mineralization effects decrease in the order of $-NH_2$ > -COOH > -OH (Fan et al., 2020). This is because positive charged PAMAM-NH_2 can be more adsorbed on the negatively charged enamel surface. In addition, the adherence of *S. mutans* is also evaluated. Both PAMAM-COOH and PAMAM-NH_2 are shown to be effective in forming a smooth remineralized layer and minimizing *S. mutans* adherence (Jia et al., 2020). Grafted with SN15, SN15-PAMAM can increase adsorption on the enamel surface and achieve 90% higher mineralization effect than the control group. (Gao et al., 2020).

4.3 Polydopamine

Polydopamine (PDA), the polymer of dopamine that rich in amino and phenolic groups, shows great hydrophilicity. It has been used as a functional agent to increase the wettability and biocompatibility of substrate (Barclay et al., 2017; Ghorbani et al., 2019). After being immersed in PDA solution, a dense film can be formed on the surface of the material in a short time (Kaushik et al., 2020). The film contains a large number of charged groups, to which calcium and phosphorus ions will be attracted and form a stable bond (Ryu et al., 2010; Murari et al., 2020). It is also observed that the HA crystals on the PDA modified enamel surface accumulated more closely, suggesting that PDA might help in inducing uniform crystal nucleation (Zhou et al., 2012). This may be because PDA can increase surface hydrophilicity, decrease the interfacial energy, and accelerate crystallization speed of HA (Qu et al., 2020). Based on the super adhesion of PDA, HA layer can be synthesized on the subsurface of different materials after being modified (Chen et al., 2019; Wong et al., 2022).

4.4 Biopolymers

Biopolymers, including proteins and polysaccharides, have been used for the bionic formation of HA. Most of these polymers are mostly used in mineralized systems in the form of gels. All of these biopolymers show excellent non-immune and biocompatible properties, meanwhile with the advantages of easy storage and clinic application.

Chitosan (CS), a cationic polysaccharide, can rarely produce allergic or inflammatory reactions in humans (Younes and Rinaudo, 2015). Therefore, CS has been used to construct organic templates and scaffolds, which can ensure the bioactivity of peptides for mineralization guidance (Ruan et al., 2016; Ren et al., 2018). Furthermore, CS is also able to prevent bacteria from adhering and reproducing. The adherence of *S. mutans* may be decreased by 94.91% by employing CS alone (Ren et al., 2019). This is because chitosan is positively charged. When CS comes into touch with the negatively charged bacterial wall, the structure of the bacterial wall would be disrupted. Simultaneously, positive charged CS can adhere to the negatively charged enamel surface, preventing acid erosion (He et al., 2019; Boda et al., 2020). In addition, the antibacterial function can be enhanced when CS paired with fluoride (Wassel and Khattab, 2017; Ren et al., 2019). Carboxymethyl chitosan (CMC), formed by CS carboxylation, also has excellent ACP stabilization and can promote the formation of enamel remineralization layers. (Chen et al., 2015; Xiao et al., 2017). The mineralization system using chitosan as a gel carrier is summarized in Table 3.

Agarose is a natural polysaccharide with -OH groups that can form a thermally reversible gel. Agarose aqueous gel is widely used in medical systems such as mineral regeneration and drug delivery (Zarrintaj et al., 2018). The abundant hydroxyl groups in agarose molecules have a strong mutual attraction with Ca^{2+}, allowing agarose to control the formation of nano ACP precursors and act as an ion reservoir to transport mineral precursors to the enamel surface for mineral mesomorphic transformation. The average elastic modulus and nano hardness of enamel increased significantly to 89.46 ± 11.82 and 3.04 ± 0.75 GPA after 6 days of the interaction of agarose gel with 500 ppm F (Cao et al., 2014a). When chitosan is added to the agarose aqueous gel, the groups between the two gels are cross-linked with each other, forming a fiber structure together with calcium ions, which can further simulate the protein matrix for enamel repair. The regeneration layer is 7.5–8.5 μm thick and regained 77.4% of the natural enamel's microhardness (Musat et al., 2021). Agarose can also be combined with amelogenin to form oriented hexagonal prism enamel columns on the enamel surface (Cao et al., 2014b).

Gelatin is a peptide molecular polymer. Gel peptides in gelatin can form salt bonds with phosphate groups on the surface of apatite, causing enamel-like minerals to regenerate. The limited directional diffusion of ions in the gel environment

TABLE 3 Summary of chitosan basing remineralization systems.

Materials	Approach	Remineralization effect	Reference
CS-AMEL	15 min CS-AMEL 2 times per day; 8 h modified remineralization solution, 16 h remineralization solution	The depth of caries decreased from ~100 to ~30 μm	Ruan et al. (2016)
CMC-ALN/ACP + GLY	10 min CMC-ALN/ACP + Gly, remineralization solution per day for 7 d	$\%SMH_R$: 49.4; Modulus recovered by 68.6%	Wang et al. (2017)
MMP-20–CS-AMEL	MMP-20–CS-AMEL hydrogel 15 min; AS with 1 ppm at 37°C, 5 d	Obtained a 2.4-fold increase in hardness and 2.6-fold increase in modulus	Prajapati et al. (2018)
CS-QP5	2.5 mg/ml CS-QP5 for 5 min, 4 times daily; remineralization and demineralization solution alternated for 12 d at 37°C, low-speed magnetic stirring (100 rpm)	$\%SMH_R$: 50.6; Modulus recovered by 68.6%	Ren et al. (2019)
CMC/LYZ-ACP	CMC/LYZ-ACP nanogels 10 min; 0.15 M 30 s; Tris–HCl buffer at pH 8 for 30 min	The hardness is 3.8 ± 0.3 Gpa, Modulus 80.3 ± 5 GP; compared to the nature enamel group hardness of 4.3 ± 0.5 Gpa; modulus 89.5 ± 5.1 Gpa	Song et al. (2021)
CS-A hydrogels	1 M $CaCl_2$ 15 min, CS-A hydrogel 2 h, AS at 37°C, 7 d	A layer of 7.5–8.5 μm thick for 7d; the hardness 2.26 Gpa, and $\%SMH_R$ reached 77.4	Musat et al. (2021)

Abbreviations: $\%SMH_R$, surface microhardness recovery ratio; CS-AMEL, chitosan-amelogenin; CMC-ALN/ACP + Gly, carboxymethyl chitosan-alendronate/amorphous calcium phosphate; MMP-20–CS-AMEL, matrix metalloproteinase-20- chitosan-amelogenin; CMC/LYZ-ACP, carboxymethyl chitosan/lysozyme-amorphous calcium phosphate; CS-A hydrogels, chitosan (CS) and agarose (A) hydrogels.

promotes heterogeneous nucleation, resulting in a crystal with a clear structure (Zhang et al., 2010). Using the bionic double-layer gel system assisted by anodic aluminum oxide, it is possible to successfully prepare HA crystals with good orientation (Chen et al., 2019).

Silk fibroin (SF) governs the synthesis of calcium carbonate in mollusks and the creation of animal shells. SF contains a large number of β-sheets, which are rich in acid aspartic acid and have a high affinity for calcium ions. In the rotary thermal evaporation approach, SF serves as a template to guide heterogeneous nucleation of HA and mineral layers with natural enamel-like shape, organization, and mechanical characteristics swiftly formed (Wang S. et al., 2020).

Abalone water-soluble matrix (AWSM) plays an important role in the formation abalone shells. The proportion of organic matter and inorganic minerals in abalone shells is very similar to enamel (95% calcium carbonate and less than 5% organic matter). Therefore, AWSM can promote the formation of crystals. High AWSM concentration can increase the content of calcium and phosphate in the mineralized layer and promote to form a parallel, dense and highly ordered structure (Wen et al., 2016).

4.5 Other polymers

Carboxy betaine (CB) polymers are amphoteric polymers with functional carboxyl and quaternary ammonium groups. The carboxyl groups can serve as Ca^{2+} and PO_4^{3-} deposition sites, whereas the positive quaternary amino group has bactericidal properties (Xu et al., 2018). Furthermore, CB can resist bacterial adhesion via electrostatically induced hydration. ACP can be stabilized by amphoteric ionic poly (carboxy betaine acrylamide) (PCBAA). PCBAA/ACP nanocomposites contribute to the growth of HAP in the damaged sublayer of enamel by blocking spontaneous ion conversion on the enamel surface while releasing sufficient ions (He et al., 2022). Thus, PCBAA/ACP nanocomposites performed admirably in both remineralization (10.08 μm thick remineralized layer in mice intraoral for 14 days) and antimicrobial experiments (almost no bacterial adherence). ACP and poly (vinylpyrrolidone) nanofibers are mixed, and making electrospun mats. The mats can be hydrated to form a gel in the savila containing fluoride. Then, calcium and phosphorus ions crystallize under the guidance of fluorine ions to form HA (Fletcher et al., 2011).

5 Conclusion and perspective

Enamel caries have been common problem in our daily life, great efforts have been paid to design new materials and realize the remineralization of enamel. However, it is still a great challenge to repair the defect enamel and restore its functions, as for the emerging materials for enamel remineralization, there is still a long way to go to satisfy the clinic applications. Firstly, most of the current materials used for the remineralization still need a long time, from several days to more than 10 days, secondly, the stability and mechanical properties are not satisfying enough, in addition, most of the remineralization systems depends a lot on the solution or concentration of mineralization medium. Therefore, it is critical important to design advanced materials that can be used in enamel remineralization and solve the clinic problems.

In the next decades, materials, both inorganic materials or polymers that can promote the mineralization speed, especially which could tune the alignment of mineralized apatite along the

native mineral structure or composition, should be a charming field, besides, on considering the complicated oral environment, bacterial infections also threaten the treatment of dental health, therefore, materials with multifunction should also be designed and may pave the way of enamel remineralization. In addition, further researches in the remineralization mechanisms are also much important, which may be helpful to direct the design of new materials and their final applications.

Author contributions

Conceptualization, JW and ZL; writing-original draft preparation, JX, HS, and JL; writing—review and editing, JW, HS, HY, PW; supervision, ZL; project administration, ZL and JW; funding acquisition, ZL and JW. All authors are involved in the revision and approved the submitted manuscript.

Funding

This work is supported by the financial support from the National Natural Science Foundation of China (No.52163016&81960205), Jiangxi Key Research and Development Program (20202BBG73012), Jiangxi Provincial program for the academic and technological leaders of main subjects (20213BCJL22051), and the Technological Plan of Health Commission of Jiangxi Province of China (SKJP520204072).

Conflict of interest

The authors declare that the research was conducted in the absence of any commercial or financial relationships that could be construed as a potential conflict of interest.

Publisher's note

All claims expressed in this article are solely those of the authors and do not necessarily represent those of their affiliated organizations, or those of the publisher, the editors and the reviewers. Any product that may be evaluated in this article, or claim that may be made by its manufacturer, is not guaranteed or endorsed by the publisher.

References

Abdallah, M. N., Eimar, H., Bassett, D. C., Schnabel, M., Ciobanu, O., Nelea, V., et al. (2016). Diagenesis-inspired reaction of magnesium ions with surface enamel mineral modifies properties of human teeth. *Acta Biomater.* 37, 174–183. doi:10.1016/j.actbio.2016.04.005

Agnello, M., Cen, L., Tran, N. C., Shi, W., McLean, J. S., and He, X. (2017). Arginine improves pH homeostasis via metabolism and microbiome modulation. *J. Dent. Res.* 96 (8), 924–930. doi:10.1177/0022034517707512

Alkilzy, M., Santamaria, R. M., Schmoeckel, J., and Splieth, C. H. (2018a). Treatment of carious lesions using self-assembling peptides. *Adv. Dent. Res.* 29 (1), 42–47. doi:10.1177/0022034517737025

Alkilzy, M., Tarabaih, A., Santamaria, R. M., and Splieth, C. H. (2018b). Self-assembling peptide P11-4 and fluoride for regenerating enamel. *J. Dent. Res.* 97 (2), 148–154. doi:10.1177/0022034517730531

Bai, Y., Yu, Z., Ackerman, L., Zhang, Y., Bonde, J., Li, W., et al. (2020). Protein nanoribbons template enamel mineralization. *Proc. Natl. Acad. Sci. U. S. A.* 117 (32), 19201–19208. doi:10.1073/pnas.2007838117

Barclay, T. G., Hegab, H. M., Clarke, S. R., and Ginic-Markovic, M. (2017). Versatile surface modification using polydopamine and related polycatecholamines: Chemistry, structure, and applications. *Adv. Mat. Interfaces* 4 (19), 1601192. doi:10.1002/admi.201601192

Barrera-Ortega, C. C., Vázquez-Olmos, A. R., Sato-Berrú, R. Y., and Araiza-Téllez, M. A. (2020). Study of demineralized dental enamel treated with different fluorinated compounds by Raman spectroscopy. *J. Biomed. Phys. Eng.* 10 (5), 635–644. doi:10.31661/jbpe.v0i0.2003-1089

Bartlett, J. D. (2013). Dental enamel development: Proteinases and their enamel matrix substrates. *ISRN Dent.* 2013, 1–24. doi:10.1155/2013/684607

Bartlett, J. D., Ganss, B., Goldberg, M., Moradian-Oldak, J., Paine, M. L., Snead, M. L., et al. (2006). 3. Protein-protein interactions of the developing enamel matrix. *Curr. Top. Dev. Biol.* 74, 57–115. doi:10.1016/S0070-2153(06)74003-0

Bijle, M. N., Abdalla, M. M., Ashraf, U., Ekambaram, M., and Yiu, C. K. Y. (2021a). Enamel remineralization potential of arginine-fluoride varnish in a multi-species bacterial pH-cycling model. *J. Dent.* 104, 103528. doi:10.1016/j.jdent.2020.103528

Bijle, M. N. A., Yiu, C. K. Y., and Ekambaram, M. (2018). Calcium-based caries preventive agents: A meta-evaluation of systematic reviews and meta-analysis. *J. Evid. Based Dent. Pract.* 18 (3), 203–217.e4. doi:10.1016/j.jebdp.2017.09.003

Bijle, M. N., Ekambaram, M., Lo, E. C., and Yiu, C. K. Y. (2020). The enamel remineralization potential of fluoride varnishes containing arginine. *J. Dent. (Shiraz).* 99, 103411. doi:10.1016/j.jdent.2020.103411

Bijle, M. N., Pichika, M. R., Mak, K. K., Parolia, A., Babar, M. G., Yiu, C., et al. (2021b). Concentration-dependent multi-potentiality of L-arginine: Antimicrobial effect, hydroxyapatite stability, and MMPs inhibition. *Molecules* 26 (21), 6605. doi:10.3390/molecules26216605

Boda, S. K., Fischer, N. G., Ye, Z., and Aparicio, C. (2020). Dual oral tissue adhesive nanofiber membranes for pH-responsive delivery of antimicrobial peptides. *Biomacromolecules* 21 (12), 4945–4961. doi:10.1021/acs.biomac.0c01163

Bossu, M., Saccucci, M., Salucci, A., Di Giorgio, G., Bruni, E., Uccelletti, D., et al. (2019). Enamel remineralization and repair results of biomimetic hydroxyapatite toothpaste on deciduous teeth: An effective option to fluoride toothpaste. *J. Nanobiotechnology* 17 (1), 17. doi:10.1186/s12951-019-0454-6

Bowen, W. H., Burne, R. A., Wu, H., and Koo, H. (2018). Oral biofilms: Pathogens, matrix, and polymicrobial interactions in microenvironments. *Trends Microbiol.* 26 (3), 229–242. doi:10.1016/j.tim.2017.09.008

Buchko, G. W., Jayasinha Arachchige, R., Tao, J., Tarasevich, B. J., and Shaw, W. J. (2018). Identification of major matrix metalloproteinase-20 proteolytic processing products of murine amelogenin and tyrosine-rich amelogenin peptide using a nuclear magnetic resonance spectroscopy based method. *Arch. Oral Biol.* 93, 187–194. doi:10.1016/j.archoralbio.2018.06.001

Cao, Y., Mei, M. L., Li, Q. L., Lo, E. C., and Chu, C. H. (2014a). Agarose hydrogel biomimetic mineralization model for the regeneration of enamel prismlike tissue. *ACS Appl. Mat. Interfaces* 6 (1), 410–420. doi:10.1021/am4044823

Cao, Y., Mei, M. L., Li, Q. L., Lo, E. C., and Chu, C. H. (2014b). Enamel prism-like tissue regeneration using enamel matrix derivative. *J. Dent. (Shiraz).* 42 (12), 1535–1542. doi:10.1016/j.jdent.2014.08.014

Carneiro, K. M., Zhai, H., Zhu, L., Horst, J. A., Sitlin, M., Nguyen, M., et al. (2016). Amyloid-like ribbons of amelogenins in enamel mineralization. *Sci. Rep.* 6, 23105. doi:10.1038/srep23105

Carvalho, T. S., Araujo, T. T., Ventura, T. M. O., Dionizio, A., Camara, J. V. F., Moraes, S. M., et al. (2020). Acquired pellicle protein-based engineering protects against erosive demineralization. *J. Dent. (Shiraz).* 102, 103478. doi:10.1016/j.jdent.2020.103478

Chang, R., Liu, Y. J., Zhang, Y. L., Zhang, S. Y., Han, B. B., Chen, F., et al. (2022). Phosphorylated and phosphonated low-complexity protein segments for biomimetic mineralization and repair of tooth enamel. *Adv. Sci.* 9 (6), 2103829. doi:10.1002/advs.202103829

Chen, R., Jin, R., Li, X., Fang, X., Yuan, D., Chen, Z., et al. (2020). Biomimetic remineralization of artificial caries dentin lesion using Ca/P-PILP. *Dent. Mat.* 36, 1397–1406. doi:10.1016/j.dental.2020.08.017

Chen, S., Guo, R., Xie, C., Liang, Q., and Xiao, X. (2020). Biomimetic mineralization of nanocrystalline hydroxyapatites on aminated modified polylactic acid microspheres to develop a novel drug delivery system for alendronate. *Mater. Sci. Eng. C* 110, 110655. doi:10.1016/j.msec.2020.110655

Chen, Z., Cao, S., Wang, H., Li, Y., Kishen, A., Deng, X., et al. (2015). Biomimetic remineralization of demineralized dentine using scaffold of CMC/ACP nanocomplexes in an *in vitro* tooth model of deep caries. *PLoS One* 10 (1), e0116553. doi:10.1371/journal.pone.0116553

Chen, Z., Miao, Z., Zhang, P., Xiao, H., Liu, H., Ding, C., et al. (2019). Bioinspired enamel-like oriented minerals on general surfaces: Towards improved mechanical properties. *J. Mat. Chem. B* 7 (34), 5237–5244. doi:10.1039/c9tb00676a

Chong, L. Y., Clarkson, J. E., Dobbyn-Ross, L., and Bhakta, S. (2018). Slow-release fluoride devices for the control of dental decay. *Cochrane Database Syst. Rev.* 3, CD005101. doi:10.1002/14651858.CD005101.pub4

Chu, Q., Gao, Y., Gao, X., Dong, Z., Song, W., Xu, Z., et al. (2018). Ablation of Runx2 in ameloblasts suppresses enamel maturation in tooth development. *Sci. Rep.* 8 (1), 9594. doi:10.1038/s41598-018-27873-5

Clark, M. B., Keels, M. A., Slayton, R. L., Section On Oral, H., Fisher-Owens, S. A., Huff, Q. A., et al. (2020). Fluoride use in caries prevention in the primary care setting. *Pediatrics* 146 (6), e2020034637. doi:10.1542/peds.2020-034637

Cochrane, N. J., Cai, F., Huq, N. L., Burrow, M. F., and Reynolds, E. C. (2010). New approaches to enhanced remineralization of tooth enamel. *J. Dent. Res.* 89 (11), 1187–1197. doi:10.1177/0022034510376046

Delgado-López, J. M., Frison, R., Cervellino, A., Gómez-Morales, J., Guagliardi, A., and Masciocchi, N. (2014). Crystal size, morphology, and growth mechanism in bio-inspired apatite nanocrystals. *Adv. Funct. Mat.* 24 (8), 1090–1099. doi:10.1002/adfm.201302075

Ding, C., Chen, Z., and Li, J. (2017). From molecules to macrostructures: Recent development of bioinspired hard tissue repair. *Biomater. Sci.* 5 (8), 1435–1449. doi:10.1039/c7bm00247e

Ding, L., Han, S., Peng, X., Wang, K., Zheng, S., Li, H., et al. (2020). Tuftelin-derived peptide facilitates remineralization of initial enamel caries *in vitro*. *J. Biomed. Mat. Res.* 108 (8), 3261–3269. doi:10.1002/jbm.b.34663

Dissanayake, S. S. M., Ekambaram, M., Li, K. C., Harris, P. W. R., and Brimble, M. A. (2020). Identification of Key functional motifs of native amelogenin protein for dental enamel remineralisation. *Molecules* 25 (18), 4214. doi:10.3390/molecules25184214

Doberdoli, D., Bommer, C., Begzati, A., Haliti, F., Heinzel-Gutenbrunner, M., and Juric, H. (2020). Randomized clinical trial investigating self-assembling peptide P11-4 for treatment of early occlusal caries. *Sci. Rep.* 10 (1), 4195. doi:10.1038/s41598-020-60815-8

Dodds, M. W., Johnson, D. A., and Yeh, C. K. (2005). Health benefits of saliva: A review. *J. Dent. (Shiraz).* 33 (3), 223–233. doi:10.1016/j.jdent.2004.10.009

Dogan, S., Fong, H., Yucesoy, D. T., Cousin, T., Gresswell, C., Dag, S., et al. (2018). Biomimetic tooth repair: Amelogenin-derived peptide enables *in vitro* remineralization of human enamel. *ACS Biomater. Sci. Eng.* 4 (5), 1788–1796. doi:10.1021/acsbiomaterials.7b00959

Dorri, M., Martinez-Zapata, M. J., Walsh, T., Marinho, V. C., Sheiham Deceased, A., and Zaror, C. (2017). Atraumatic restorative treatment versus conventional restorative treatment for managing dental caries. *Cochrane Database Syst. Rev.* 12, CD008072. doi:10.1002/14651858.CD008072.pub2

Engelberth, S. A., Bacino, M. S., Sandhu, S., Li, W., Bonde, J., and Habelitz, S. (2018). Progression of self-assembly of amelogenin protein supramolecular structures in simulated enamel fluid. *Biomacromolecules* 19 (10), 3917–3924. doi:10.1021/acs.biomac.8b00808

Fan, M., Zhang, M., Xu, H. H. K., Tao, S., Yu, Z., Yang, J., et al. (2020). Remineralization effectiveness of the PAMAM dendrimer with different terminal groups on artificial initial enamel caries *in vitro*. *Dent. Mat.* 36 (2), 210–220. doi:10.1016/j.dental.2019.11.015

Fang, P. A., Conway, J. F., Margolis, H. C., Simmer, J. P., and Beniash, E. (2011). Hierarchical self-assembly of amelogenin and the regulation of biomineralization at the nanoscale. *Proc. Natl. Acad. Sci. U. S. A.* 108 (34), 14097–14102. doi:10.1073/pnas.1106228108

Fletcher, J., Walsh, D., Fowler, C. E., and Mann, S. (2011). Electrospun mats of PVP/ACP nanofibres for remineralization of enamel tooth surfaces. *CrystEngComm* 13 (11), 3692. doi:10.1039/c0ce00806k

Fukae, M., Tanabe, T., Uchida, T., Lee, S. K., Ryu, O. H., Murakami, C., et al. (1998). Enamelysin (matrix metalloproteinase-20): Localization in the developing tooth and effects of pH and calcium on amelogenin hydrolysis. *J. Dent. Res.* 77 (8), 1580–1588. doi:10.1177/00220345980770080501

Gao, Y., Liang, K., Weir, M. D., Gao, J., Imazato, S., Tay, F. R., et al. (2020). Enamel remineralization via poly(amido amine) and adhesive resin containing calcium phosphate nanoparticles. *J. Dent.* 92, 103262. doi:10.1016/j.jdent.2019.103262

Gelli, R., Ridi, F., and Baglioni, P. (2019). The importance of being amorphous: Calcium and magnesium phosphates in the human body. *Adv. Colloid Interface Sci.* 269, 219–235. doi:10.1016/j.cis.2019.04.011

Ghorbani, F., Zamanian, A., Behnamghader, A., and Joupari, M. D. (2019). A facile method to synthesize mussel-inspired polydopamine nanospheres as an active template for *in situ* formation of biomimetic hydroxyapatite. *Mater. Sci. Eng. C* 94, 729–739. doi:10.1016/j.msec.2018.10.010

Gil-Bona, A., and Bidlack, F. B. (2020). Tooth enamel and its dynamic protein matrix. *Int. J. Mol. Sci.* 21 (12), 4458. doi:10.3390/ijms21124458

Gordon, L. M., Cohen, M. J., MacRenaris, K. W., Pasteris, J. D., Seda, T., and Joester, D. (2015). Amorphous intergranular phases control the properties of rodent tooth enamel. *Science* 347 (6223), 746–750. doi:10.1126/science.1258950

Green, D. R., Schulte, F., Lee, K. H., Pugach, M. K., Hardt, M., and Bidlack, F. B. (2019). Mapping the tooth enamel proteome and amelogenin phosphorylation onto mineralizing porcine tooth crowns. *Front. Physiol.* 10, 925. doi:10.3389/fphys.2019.00925

Gungormus, M., Oren, E. E., Horst, J. A., Fong, H., Hnilova, M., Somerman, M. J., et al. (2012). Cementomimetics-constructing a cementum-like biomineralized microlayer via amelogenin-derived peptides. *Int. J. Oral Sci.* 4 (2), 69–77. doi:10.1038/ijos.2012.40

Gururaja, T. L., and Levine, M. J. (1996). Solid-phase synthesis and characterization of human salivary statherin: A tyrosine-rich phosphoprotein inhibitor of calcium phosphate precipitation. *Pept. Res.* 9 (6), 283–289.

Han, S., Fan, Y., Zhou, Z., Tu, H., Li, D., Lv, X., et al. (2017). Promotion of enamel caries remineralization by an amelogenin-derived peptide in a rat model. *Arch. Oral Biol.* 73, 66–71. doi:10.1016/j.archoralbio.2016.09.009

Harper, R. A., Shelton, R. M., James, J. D., Salvati, E., Besnard, C., Korsunsky, A. M., et al. (2021). Acid-induced demineralisation of human enamel as a function of time and pH observed using X-ray and polarised light imaging. *Acta Biomater.* 120, 240–248. doi:10.1016/j.actbio.2020.04.045

He, G., and George, A. (2004). Dentin matrix protein 1 immobilized on type I collagen fibrils facilitates apatite deposition *in vitro*. *J. Biol. Chem.* 279 (12), 11649–11656. doi:10.1074/jbc.M309296200

He, J., Bao, Y., Li, J., Qiu, Z., Liu, Y., and Zhang, X. (2019). Nanocomplexes of carboxymethyl chitosan/amorphous calcium phosphate reduce oral bacteria adherence and biofilm formation on human enamel surface. *J. Dent. (Shiraz).* 80, 15–22. doi:10.1016/j.jdent.2018.11.003

He, J., Yang, J., Li, M., Li, Y., Pang, Y., Deng, J., et al. (2022). Polyzwitterion manipulates remineralization and antibiofilm functions against dental demineralization. *ACS Nano* 16 (2), 3119–3134. doi:10.1021/acsnano.1c10812

He, K., Sawczyk, M., Liu, C., Yuan, Y., Song, B., Deivanayagam, R., et al. (2020). Revealing nanoscale mineralization pathways of hydroxyapatite using *in situ* liquid cell transmission electron microscopy. *Sci. Adv.* 6 (47), eaaz7524. doi:10.1126/sciadv.aaz7524

Hou, A., Luo, J., Zhang, M., Li, J., Chu, W., Liang, K., et al. (2020). Two-in-one strategy: A remineralizing and anti-adhesive coating against demineralized enamel. *Int. J. Oral Sci.* 12 (1), 27. doi:10.1038/s41368-020-00097-y

Huang, S. B., Gao, S. S., and Yu, H. Y. (2009). Effect of nano-hydroxyapatite concentration on remineralization of initial enamel lesion *in vitro*. *Biomed. Mat.* 4 (3), 034104. doi:10.1088/1748-6041/4/3/034104

Huang, S., Gao, S., Cheng, L., and Yu, H. (2011). Remineralization potential of nano-hydroxyapatite on initial enamel lesions: An *in vitro* study. *Caries Res.* 45 (5), 460–468. doi:10.1159/000331207

Hughes, M. P., Sawaya, M. R., Boyer, D. R., Goldschmidt, L., Rodriguez, J. A., Cascio, D., et al. (2018). Atomic structures of low-complexity protein segments reveal kinked beta sheets that assemble networks. *Science* 359 (6376), 698–701. doi:10.1126/science.aan6398

Iafisco, M., Ramírez-Rodríguez, G. B., Sakhno, Y., Tampieri, A., Martra, G., Gómez-Morales, J., et al. (2015). The growth mechanism of apatite nanocrystals

assisted by citrate: Relevance to bone biomineralization. *CrystEngComm* 17 (3), 507–511. doi:10.1039/c4ce01415d

Jablonski-Momeni, A., Nothelfer, R., Morawietz, M., Kiesow, A., and Korbmacher-Steiner, H. (2020). Impact of self-assembling peptides in remineralisation of artificial early enamel lesions adjacent to orthodontic brackets. *Sci. Rep.* 10 (1), 15132. doi:10.1038/s41598-020-72185-2

Jia, L., Tao, S., Yang, J., Liang, K., Yu, Z., Gao, Y., et al. (2020). Adhesion of Streptococcus mutans on remineralized enamel surface induced by poly(amido amine) dendrimers. *Colloids Surfaces B Biointerfaces* 197, 111409. doi:10.1016/j.colsurfb.2020.111409

Jokisaari, J. R., Wang, C., Qiao, Q., Hu, X., Reed, D. A., Bleher, R., et al. (2019). Particle-attachment-mediated and matrix/lattice-guided enamel apatite crystal growth. *ACS Nano* 13 (3), 3151–3161. doi:10.1021/acsnano.8b08668

Jokstad, A. (2016). Secondary caries and microleakage. *Dent. Mat.* 32 (1), 11–25. doi:10.1016/j.dental.2015.09.006

Juntavee, N., Juntavee, A., and Plongniras, P. (2018). Remineralization potential of nano-hydroxyapatite on enamel and cementum surrounding margin of computer-aided design and computer-aided manufacturing ceramic restoration. *Int. J. Nanomedicine* 13, 2755–2765. doi:10.2147/IJN.S165080

Karlinsey, R. L., Mackey, A. C., Walker, E. R., and Frederick, K. E. (2010). Preparation, characterization and *in vitro* efficacy of an acid-modified beta-TCP material for dental hard-tissue remineralization. *Acta Biomater.* 6 (3), 969–978. doi:10.1016/j.actbio.2009.08.034

Karlinsey, R. L., and Pfarrer, A. M. (2012). Fluoride plus functionalized beta-TCP: A promising combination for robust remineralization. *Adv. Dent. Res.* 24 (2), 48–52. doi:10.1177/0022034512449463

Kaushik, N., Nhat Nguyen, L., Kim, J. H., Choi, E. H., and Kumar Kaushik, N. (2020). Strategies for using polydopamine to induce biomineralization of hydroxyapatite on implant materials for bone tissue engineering. *Int. J. Mol. Sci.* 21 (18), 6544. doi:10.3390/ijms21186544

Khonina, T. G., Chupakhin, O. N., Shur, V. Y., Turygin, A. P., Sadovsky, V. V., Mandra, Y. V., et al. (2020). Silicon-hydroxyapatiteglycerohydrogel as a promising biomaterial for dental applications. *Colloids Surfaces B Biointerfaces* 189, 110851. doi:10.1016/j.colsurfb.2020.110851

Kind, L., Stevanovic, S., Wuttig, S., Wimberger, S., Hofer, J., Muller, B., et al. (2017). Biomimetic remineralization of carious lesions by self-assembling peptide. *J. Dent. Res.* 96 (7), 790–797. doi:10.1177/0022034517698419

Kis, V. K., Sulyok, A., Hegedus, M., Kovacs, I., Rozsa, N., and Kovacs, Z. (2021). Magnesium incorporation into primary dental enamel and its effect on mechanical properties. *Acta Biomater.* 120, 104–115. doi:10.1016/j.actbio.2020.08.035

Kwak, S. Y., Litman, A., Margolis, H. C., Yamakoshi, Y., and Simmer, J. P. (2017). Biomimetic enamel regeneration mediated by leucine-rich amelogenin peptide. *J. Dent. Res.* 96 (5), 524–530. doi:10.1177/0022034516688659

Kwak, S. Y., Yamakoshi, Y., Simmer, J. P., and Margolis, H. C. (2016). MMP20 proteolysis of native amelogenin regulates mineralization *in vitro*. *J. Dent. Res.* 95 (13), 1511–1517. doi:10.1177/0022034516662814

La Fontaine, A., Zavgorodniy, A., Liu, H., Zheng, R., Swain, M., and Cairney, J. (2016). Atomic-scale compositional mapping reveals Mg-rich amorphous calcium phosphate in human dental enamel. *Sci. Adv.* 2 (9), e1601145. doi:10.1126/sciadv.1601145

Lacruz, R. S., Habelitz, S., Wright, J. T., and Paine, M. L. (2017). Dental enamel formation and implications for oral health and disease. *Physiol. Rev.* 97 (3), 939–993. doi:10.1152/physrev.00030.2016

Lawn, B. R., Lee, J. J. W., and Chai, H. (2010). Teeth: Among nature's most durable biocomposites. *Annu. Rev. Mat. Res.* 40 (1), 55–75. doi:10.1146/annurev-matsci-070909-104537

Le Norcy, E., Lesieur, J., Sadoine, J., Rochefort, G. Y., Chaussain, C., and Poliard, A. (2018). Phosphorylated and non-phosphorylated leucine rich amelogenin peptide differentially affect ameloblast mineralization. *Front. Physiol.* 9, 55. doi:10.3389/fphys.2018.00055

Li, N., Cui, W., Cong, P., Tang, J., Guan, Y., Huang, C., et al. (2021). Biomimetic inorganic-organic hybrid nanoparticles from magnesium-substituted amorphous calcium phosphate clusters and polyacrylic acid molecules. *Bioact. Mat.* 6 (8), 2303–2314. doi:10.1016/j.bioactmat.2021.01.005

Li, Y., Ping, H., Wei, J., Zou, Z., Zhang, P., Xie, J., et al. (2021). Bioprocess-inspired room-temperature synthesis of enamel-like fluorapatite/polymer nanocomposites controlled by magnesium ions. *ACS Appl. Mat. Interfaces* 13 (21), 25260–25269. doi:10.1021/acsami.1c04575

Li, Z., Ren, Q., Cui, J., Hu, D., Tian, T., He, T., et al. (2020). Comparing the efficacy of hydroxyapatite nucleation regulated by amino acids, poly-amino acids and an amelogenin-derived peptide. *CrystEngComm* 22 (22), 3814–3823. doi:10.1039/c9ce01925a

Liang, K., Xiao, S., Shi, W., Li, J., Yang, X., Gao, Y., et al. (2015). 8DSS-promoted remineralization of demineralized dentin *in vitro*. *J. Mat. Chem. B* 3 (33), 6763–6772. doi:10.1039/c5tb00764j

Liao, Y., Brandt, B. W., Li, J., Crielaard, W., Van Loveren, C., and Deng, D. M. (2017). Fluoride resistance in Streptococcus mutans: A mini review. *J. Oral Microbiol.* 9 (1), 1344509. doi:10.1080/20002297.2017.1344509

Liu, Y., Ding, C., He, L., Yang, X., Gou, Y., Xu, X., et al. (2018). Bioinspired heptapeptides as functionalized mineralization inducers with enhanced hydroxyapatite affinity. *J. Mat. Chem. B* 6 (13), 1984–1994. doi:10.1039/c7tb03067c

Luo, M., Gao, Y., Yang, S., Quan, X., Sun, D., Liang, K., et al. (2019). Computer simulations of the adsorption of an N-terminal peptide of statherin, SN15, and its mutants on hydroxyapatite surfaces. *Phys. Chem. Chem. Phys.* 21 (18), 9342–9351. doi:10.1039/c9cp01638d

Lv, X., Yang, Y., Han, S., Li, D., Tu, H., Li, W., et al. (2015). Potential of an amelogenin based peptide in promoting reminerlization of initial enamel caries. *Arch. Oral Biol.* 60 (10), 1482–1487. doi:10.1016/j.archoralbio.2015.07.010

Lynch, R. J., Navada, R., and Walia, R. (2004). Low-levels of fluoride in plaque and saliva and their effects on the demineralisation and remineralisation of enamel; role of fluoride toothpastes. *Int. Dent. J.* 54 (5), 304–309. doi:10.1111/j.1875-595x.2004.tb00003.x

Memarpour, M., Shafiei, F., Rafiee, A., Soltani, M., and Dashti, M. H. (2019). Effect of hydroxyapatite nanoparticles on enamel remineralization and estimation of fissure sealant bond strength to remineralized tooth surfaces: An *in vitro* study. *BMC Oral Health* 19 (1), 92. doi:10.1186/s12903-019-0785-6

Mukherjee, K., Ruan, Q., and Moradian-Oldak, J. (2019). Peptide-mediated biomimetic regrowth of human enamel *in situ*. *Methods Mol. Biol.* 1922, 129–138. doi:10.1007/978-1-4939-9012-2_13

Mukherjee, K., Ruan, Q., Nutt, S., Tao, J., De Yoreo, J. J., and Moradian-Oldak, J. (2018). Peptide-based bioinspired approach to regrowing multilayered aprismatic enamel. *ACS Omega* 3 (3), 2546–2557. doi:10.1021/acsomega.7b02004

Murari, G., Bock, N., Zhou, H., Yang, L., Liew, T., Fox, K., et al. (2020). Effects of polydopamine coatings on nucleation modes of surface mineralization from simulated body fluid. *Sci. Rep.* 10 (1), 14982. doi:10.1038/s41598-020-71900-3

Musat, V., Anghel, E. M., Zaharia, A., Atkinson, I., Mocioiu, O. C., Busila, M., et al. (2021). A chitosan-agarose polysaccharide-based hydrogel for biomimetic remineralization of dental enamel. *Biomolecules* 11 (8), 1137. doi:10.3390/biom11081137

Nagano, T., Kakegawa, A., Yamakoshi, Y., Tsuchiya, S., Hu, J. C. C., Gomi, K., et al. (2009). Mmp-20 and Klk4 cleavage site preferences for amelogenin sequences. *J. Dent. Res.* 88 (9), 823–828. doi:10.1177/0022034509342694

Nascimento, M. M., Alvarez, A. J., Huang, X., Browngardt, C., Jenkins, R., Sinhoreti, M. C., et al. (2019). Metabolic profile of supragingival plaque exposed to arginine and fluoride. *J. Dent. Res.* 98 (11), 1245–1252. doi:10.1177/0022034519869906

Palazzo, B., Iafisco, M., Laforgia, M., Margiotta, N., Natile, G., Bianchi, C. L., et al. (2007). Biomimetic hydroxyapatite-drug nanocrystals as potential bone substitutes with antitumor drug delivery properties. *Adv. Funct. Mat.* 17 (13), 2180–2188. doi:10.1002/adfm.200600361

Pan, H., Tao, J., Xu, X., and Tang, R. (2007). Adsorption processes of Gly and Glu amino acids on hydroxyapatite surfaces at the atomic level. *Langmuir* 23 (17), 8972–8981. doi:10.1021/la700567r

Pandya, M., and Diekwisch, T. G. H. (2019). Enamel biomimetics-fiction or future of dentistry. *Int. J. Oral Sci.* 11 (1), 8. doi:10.1038/s41368-018-0038-6

Peres, M. A., Macpherson, L. M. D., Weyant, R. J., Daly, B., Venturelli, R., Mathur, M. R., et al. (2019). Oral diseases: A global public health challenge. *Lancet* 394 (10194), 249–260. doi:10.1016/S0140-6736(19)31146-8

Philip, N. (2019). State of the art enamel remineralization systems: The next frontier in caries management. *Caries Res.* 53 (3), 284–295. doi:10.1159/000493031

Pitts, N. B., Zero, D. T., Marsh, P. D., Ekstrand, K., Weintraub, J. A., Ramos-Gomez, F., et al. (2017). Dental caries. *Nat. Rev. Dis. Prim.* 3, 17030. doi:10.1038/nrdp.2017.30

Prajapati, S., Ruan, Q., Mukherjee, K., Nutt, S., and Moradian-Oldak, J. (2018). The presence of MMP-20 reinforces biomimetic enamel regrowth. *J. Dent. Res.* 97 (1), 84–90. doi:10.1177/0022034517728504

Prajapati, S., Tao, J., Ruan, Q., De Yoreo, J. J., and Moradian-Oldak, J. (2016). Matrix metalloproteinase-20 mediates dental enamel biomineralization by preventing protein occlusion inside apatite crystals. *Biomaterials* 75, 260–270. doi:10.1016/j.biomaterials.2015.10.031

Qu, Y., Gu, T., Du, Q., Shao, C., Wang, J., Jin, B., et al. (2020). Polydopamine promotes dentin remineralization via interfacial control. *ACS Biomater. Sci. Eng.* 6 (6), 3327–3334. doi:10.1021/acsbiomaterials.0c00035

Raj, P. A., Johnsson, M., Levine, M. J., and Nancollas, G. H. (1992). Salivary statherin. Dependence on sequence, charge, hydrogen bonding potency, and helical conformation for adsorption to hydroxyapatite and inhibition of mineralization. *J. Biol. Chem.* 267 (9), 5968–5976. doi:10.1016/s0021-9258(18)42650-6

Ren, F., Leng, Y., Xin, R., and Ge, X. (2010). Synthesis, characterization and *ab initio* simulation of magnesium-substituted hydroxyapatite. *Acta Biomater.* 6 (7), 2787–2796. doi:10.1016/j.actbio.2009.12.044

Ren, Q., Ding, L., Li, Z., Wang, X., Wang, K., Han, S., et al. (2019). Chitosan hydrogel containing amelogenin-derived peptide: Inhibition of cariogenic bacteria and promotion of remineralization of initial caries lesions. *Arch. Oral Biol.* 100, 42–48. doi:10.1016/j.archoralbio.2019.02.004

Ren, Q., Li, Z., Ding, L., Wang, X., Niu, Y., Qin, X., et al. (2018). Anti-biofilm and remineralization effects of chitosan hydrogel containing amelogenin-derived peptide on initial caries lesions. *Regen. Biomater.* 5 (2), 69–76. doi:10.1093/rb/rby005

Ruan, Q., Liberman, D., Bapat, R., Chandrababu, K. B., Phark, J. H., and Moradian-Oldak, J. (2016). Efficacy of amelogenin-chitosan hydrogel in biomimetic repair of human enamel in pH-cycling systems. *J. Biomed. Eng. Inf.* 2 (1), 119–128. doi:10.5430/jbei.v2n1p119

Ryu, J., Ku, S. H., Lee, H., and Park, C. B. (2010). Mussel-inspired polydopamine coating as a universal route to hydroxyapatite crystallization. *Adv. Funct. Mat.* 20 (13), 2132–2139. doi:10.1002/adfm.200902347

Sari, M., Ramadhanti, D. M., Amalina, R., ChotimahAna, I. D., and Yusuf, Y. (2021). Development of a hydroxyapatite nanoparticle-based gel for enamel remineralization -A physicochemical properties and cell viability assay analysis. *Dent. Mat. J.* 41, 68–77. doi:10.4012/dmj.2021-102

Sedlakova Kondelova, P., Mannaa, A., Bommer, C., Abdelaziz, M., Daeniker, L., di Bella, E., et al. (2020). Efficacy of P11-4 for the treatment of initial buccal caries: A randomized clinical trial. *Sci. Rep.* 10 (1), 20211. doi:10.1038/s41598-020-77057-3

Shao, C., Jin, B., Mu, Z., Lu, H., Zhao, Y., Wu, Z., et al. (2019). Repair of tooth enamel by a biomimetic mineralization frontier ensuring epitaxial growth. *Sci. Adv.* 5 (8), eaaw9569. doi:10.1126/sciadv.aaw9569

Shen, P., Walker, G. D., Yuan, Y., Reynolds, C., Stanton, D. P., Fernando, J. R., et al. (2018). Importance of bioavailable calcium in fluoride dentifrices for enamel remineralization. *J. Dent. (Shiraz).* 78, 59–64. doi:10.1016/j.jdent.2018.08.005

Shimotoyodome, A., Kobayashi, H., Tokimitsu, I., Matsukubo, T., and Takaesu, Y. (2006). Statherin and histatin 1 reduce parotid saliva-promoted Streptococcus mutans strain MT8148 adhesion to hydroxyapatite surfaces. *Caries Res.* 40 (5), 403–411. doi:10.1159/000094286

Shin, N. Y., Yamazaki, H., Beniash, E., Yang, X., Margolis, S. S., Pugach, M. K., et al. (2020). Amelogenin phosphorylation regulates tooth enamel formation by stabilizing a transient amorphous mineral precursor. *J. Biol. Chem.* 295 (7), 1943–1959. doi:10.1074/jbc.RA119.010506

Shuturminska, K., Tarakina, N. V., Azevedo, H. S., Bushby, A. J., Mata, A., Anderson, P., et al. (2017). Elastin-like protein, with statherin derived peptide, controls fluorapatite formation and morphology. *Front. Physiol.* 8, 368. doi:10.3389/fphys.2017.00368

Simmer, J. P., Hu, Y., Lertlam, R., Yamakoshi, Y., and Hu, J. C. (2009). Hypomaturation enamel defects in Klk4 knockout/LacZ knockin mice. *J. Biol. Chem.* 284 (28), 19110–19121. doi:10.1074/jbc.M109.013623

Smith, C. E. L., Poulter, J. A., Antanaviciute, A., Kirkham, J., Brookes, S. J., Inglehearn, C. F., et al. (2017). Amelogenesis imperfecta; genes, proteins, and pathways. *Front. Physiol.* 8, 435. doi:10.3389/fphys.2017.00435

Song, J., Li, T., Gao, J., Li, C., Jiang, S., and Zhang, X. (2021). Building an aprismatic enamel-like layer on a demineralized enamel surface by using carboxymethyl chitosan and lysozyme-encapsulated amorphous calcium phosphate nanogels. *J. Dent. (Shiraz).* 107, 103599. doi:10.1016/j.jdent.2021.103599

Tao, J., Pan, H., Zeng, Y., Xu, X., and Tang, R. (2007). Roles of amorphous calcium phosphate and biological additives in the assembly of hydroxyapatite nanoparticles. *J. Phys. Chem. B* 111 (47), 13410–13418. doi:10.1021/jp0732918

Tao, S., Zhu, Y., Yuan, H., Tao, S., Cheng, Y., Li, J., et al. (2018). Efficacy of fluorides and CPP-ACP vs fluorides monotherapy on early caries lesions: A systematic review and meta-analysis. *PLoS One* 13 (4), e0196660. doi:10.1371/journal.pone.0196660

Uskokovic, V. (2015). When 1+1>2: Nanostructured composites for hard tissue engineering applications. *Mater. Sci. Eng. C* 57, 434–451. doi:10.1016/j.msec.2015.07.050

Ustriyana, P., Harmon, E., Chen, K., Michel, F. M., and Sahai, N. (2020a). Oligo(l-glutamic acids) in calcium phosphate precipitation: Chain length effect. *J. Phys. Chem. B* 124 (29), 6278–6287. doi:10.1021/acs.jpcb.0c01689

Ustriyana, P., Michel, F. M., Wilson, M. C., Harmon, E., Chen, J., Liu, T., et al. (2020b). Oligo(l-glutamic acids) in calcium phosphate precipitation: Mechanism of delayed phase transformation. *J. Phys. Chem. B* 124 (29), 6288–6298. doi:10.1021/acs.jpcb.0c01690

Viana, Í. E. L., Lopes, R. M., Silva, F. R. O., Lima, N. B., Aranha, A. C. C., Feitosa, S., et al. (2020). Novel fluoride and stannous -functionalized β-tricalcium phosphate nanoparticles for the management of dental erosion. *J. Dent.* 92, 103263. doi:10.1016/j.jdent.2019.103263

Wang, D., Deng, J., Deng, X., Fang, C., Zhang, X., and Yang, P. (2020). Controlling enamel remineralization by amyloid-like amelogenin mimics. *Adv. Mat.* 32 (31), e2002080. doi:10.1002/adma.202002080

Wang, H., Xiao, Z., Yang, J., Lu, D., Kishen, A., Li, Y., et al. (2017). Oriented and ordered biomimetic remineralization of the surface of demineralized dental enamel using HAP@ACP nanoparticles guided by Glycine. *Sci. Rep.* 7, 40701. doi:10.1038/srep40701

Wang, S., Zhang, L., Chen, W., Jin, H., Zhang, Y., Wu, L., et al. (2020). Rapid regeneration of enamel-like-oriented inorganic crystals by using rotary evaporation. *Mater. Sci. Eng. C* 115, 111141. doi:10.1016/j.msec.2020.111141

Wang, Y., Hu, D., Cui, J., Zeng, Y., Gan, X., Chen, Z., et al. (2020). Unraveling the mechanism for an amelogenin-derived peptide regulated hydroxyapatite mineralization via specific functional domain identification. *J. Mat. Chem. B* 8, 10373–10383. doi:10.1039/d0tb00949k

Wang, Z., Ouyang, Y., Wu, Z., Zhang, L., Shao, C., Fan, J., et al. (2018). A novel fluorescent adhesive-assisted biomimetic mineralization. *Nanoscale* 10 (40), 18980–18987. doi:10.1039/c8nr02078g

Wassel, M. O., and Khattab, M. A. (2017). Antibacterial activity against Streptococcus mutans and inhibition of bacterial induced enamel demineralization of propolis, miswak, and chitosan nanoparticles based dental varnishes. *J. Adv. Res.* 8 (4), 387–392. doi:10.1016/j.jare.2017.05.006

Wen, Z., Chen, J., Wang, H., Zhong, S., Hu, Y., Wang, Z., et al. (2016). Abalone water-soluble matrix for self-healing biomineralization of tooth defects. *Mater. Sci. Eng. C* 67, 182–187. doi:10.1016/j.msec.2016.05.015

Wong, H. M., Zhang, Y. Y., and Li, Q. L. (2022). An enamel-inspired bioactive material with multiscale structure and antibacterial adhesion property. *Bioact. Mat.* 7, 491–503. doi:10.1016/j.bioactmat.2021.05.035

Wu, D., Yang, J., Li, J., Chen, L., Tang, B., Chen, X., et al. (2013). Hydroxyapatite-anchored dendrimer for *in situ* remineralization of human tooth enamel. *Biomaterials* 34 (21), 5036–5047. doi:10.1016/j.biomaterials.2013.03.053

Wu, S., Yu, M., Li, M., Wang, L., Putnis, C. V., and Putnis, A. (2017). *In situ* atomic force microscopy imaging of octacalcium phosphate crystallization and its modulation by amelogenin's C-terminus. *Cryst. Growth & Des.* 17 (4), 2194–2202. doi:10.1021/acs.cgd.7b00129

Wu, X., Zhao, X., Li, Y., Yang, T., Yan, X., and Wang, K. (2015). *In situ* synthesis carbonated hydroxyapatite layers on enamel slices with acidic amino acids by a novel two-step method. *Mater. Sci. Eng. C* 54, 150–157. doi:10.1016/j.msec.2015.05.006

Xia, Y., Ren, A., and Pugach, M. K. (2016). Truncated amelogenin and LRAP transgenes improve Amelx null mouse enamel. *Matrix Biol.* 52-54, 198–206. doi:10.1016/j.matbio.2015.11.005

Xiao, Z., Que, K., Wang, H., An, R., Chen, Z., Qiu, Z., et al. (2017). Rapid biomimetic remineralization of the demineralized enamel surface using nano-particles of amorphous calcium phosphate guided by chimaeric peptides. *Dent. Mat.* 33 (11), 1217–1228. doi:10.1016/j.dental.2017.07.015

Xu, M., Ji, F., Qin, Z., Dong, D., Tian, X., Niu, R., et al. (2018). Biomimetic mineralization of a hydroxyapatite crystal in the presence of a zwitterionic polymer. *CrystEngComm* 20 (17), 2374–2383. doi:10.1039/c8ce00119g

Xu, X., Wang, N., Wu, M., Wang, J., Wang, D., Chen, Z., et al. (2020). Programmed antibacterial and mineralization therapy for dental caries based on zinc-substituted hydroxyapatite/alendronate-grafted polyacrylic acid hybrid material. *Colloids Surfaces B Biointerfaces* 194, 111206. doi:10.1016/j.colsurfb.2020.111206

Yamazaki, H., Beniash, E., Yamakoshi, Y., Simmer, J. P., and Margolis, H. C. (2017). Protein phosphorylation and mineral binding affect the secondary structure of the leucine-rich amelogenin peptide. *Front. Physiol.* 8, 450. doi:10.3389/fphys.2017.00450

Yan, W. J., Ma, P., Tian, Y., Wang, J. Y., Qin, C. L., Feng, J. Q., et al. (2017). The importance of a potential phosphorylation site in enamelin on enamel formation. *Int. J. Oral Sci.* 9 (11), e4. doi:10.1038/ijos.2017.41

Yang, X., Shang, H., Ding, C., and Li, J. (2015). Recent developments and applications of bioinspired dendritic polymers. *Polym. Chem.* 6 (5), 668–680. doi:10.1039/c4py01537a

Yang, X., Yang, B., He, L., Li, R., Liao, Y., Zhang, S., et al. (2017). Bioinspired peptide-decorated tannic acid for *in situ* remineralization of tooth enamel: *In vitro* and *in vivo* evaluation. *ACS Biomater. Sci. Eng.* 3 (12), 3553–3562. doi:10.1021/acsbiomaterials.7b00623

Yang, Y., Lv, X. P., Shi, W., Li, J. Y., Li, D. X., Zhou, X. D., et al. (2014). 8DSS-promoted remineralization of initial enamel caries *in vitro*. *J. Dent. Res.* 93 (5), 520–524. doi:10.1177/0022034514522815

Yeom, B., Sain, T., Lacevic, N., Bukharina, D., Cha, S. H., Waas, A. M., et al. (2017). Abiotic tooth enamel. *Nature* 543 (7643), 95–98. doi:10.1038/nature21410

Younes, I., and Rinaudo, M. (2015). Chitin and chitosan preparation from marine sources. Structure, properties and applications. *Mar. Drugs* 13 (3), 1133–1174. doi:10.3390/md13031133

Yu, M., Wang, L., Zhang, W., and Ganss, B. (2019). Organized assembly of fluorapatite nanorods controlled by amelotin: Implications for enamel regeneration. *ACS Appl. Nano Mat.* 2 (12), 7566–7576. doi:10.1021/acsanm.9b01661

Zanatta, R. F., Caneppele, T. M. F., Scaramucci, T., El Dib, R., Maia, L. C., Ferreira, D., et al. (2020). Protective effect of fluorides on erosion and erosion/abrasion in enamel: A systematic review and meta-analysis of randomized *in situ* trials. *Arch. Oral Biol.* 120, 104945. doi:10.1016/j.archoralbio.2020.104945

Zarrintaj, P., Manouchehri, S., Ahmadi, Z., Saeb, M. R., Urbanska, A. M., Kaplan, D. L., et al. (2018). Agarose-based biomaterials for tissue engineering. *Carbohydr. Polym.* 187, 66–84. doi:10.1016/j.carbpol.2018.01.060

Zeng, J., Yang, S., Yu, H., Xu, Z., Quan, X., and Zhou, J. (2021). Simulation insight into the synergic role of citrate and polyaspartic peptide in biomineralization. *Langmuir* 37 (11), 3410–3419. doi:10.1021/acs.langmuir.0c03626

Zhang, J., Jiang, D., Zhang, J., Lin, Q., and Huang, Z. (2010). Synthesis of dental enamel-like hydroxyapaptite through solution mediated solid-state conversion. *Langmuir* 26 (5), 2989–2994. doi:10.1021/la9043649

Zheng, W., Ding, L., Wang, Y., Han, S., Zheng, S., Guo, Q., et al. (2019). The effects of 8DSS peptide on remineralization in a rat model of enamel caries evaluated by two nondestructive techniques. *J. Appl. Biomater. Funct. Mat.* 17 (1), 228080001982779. doi:10.1177/2280800019827798

Zheng, X., Cheng, X., Wang, L., Qiu, W., Wang, S., Zhou, Y., et al. (2015). Combinatorial effects of arginine and fluoride on oral bacteria. *J. Dent. Res.* 94 (2), 344–353. doi:10.1177/0022034514561259

Zhou, L., Li, Q. L., and Wong, H. M. (2021). A novel strategy for caries management: Constructing an antibiofouling and mineralizing dual-bioactive tooth surface. *ACS Appl. Mat. Interfaces* 13 (26), 31140–31152. doi:10.1021/acsami.1c06989

Zhou, L., Wong, H. M., Zhang, Y. Y., and Li, Q. L. (2020). Constructing an antibiofouling and mineralizing bioactive tooth surface to protect against decay and promote self-healing. *ACS Appl. Mat. Interfaces* 12 (2), 3021–3031. doi:10.1021/acsami.9b19745

Zhou, Y. Z., Cao, Y., Liu, W., Chu, C. H., and Li, Q. L. (2012). Polydopamine-induced tooth remineralization. *ACS Appl. Mat. Interfaces* 4 (12), 6901–6910. doi:10.1021/am302041b

frontiers | Frontiers in Bioengineering and Biotechnology

TYPE Review
PUBLISHED 30 September 2022
DOI 10.3389/fbioe.2022.1003484

OPEN ACCESS

EDITED BY
Jianxun Ding,
Changchun Institute of Applied Chemistry (CAS), China

REVIEWED BY
Xing Wang,
Institute of Chemistry (CAS), China
Qiang Yang,
Tianjin Hospital, China

*CORRESPONDENCE
Yanbo Zhang,
zhangyb2012@jlu.edu.cn
Tong Liu,
liutong1986@jlu.edu.cn
Jianlin Zuo,
zuojl@jlu.edu.cn

†These authors have contributed equally to this work and share first authorship

SPECIALTY SECTION
This article was submitted to Biomaterials, a section of the journal Frontiers in Bioengineering and Biotechnology

RECEIVED 26 July 2022
ACCEPTED 16 September 2022
PUBLISHED 30 September 2022

CITATION
Peng Y, Lu M, Zhou Z, Wang C, Liu E, Zhang Y, Liu T and Zuo J (2022), Natural biopolymer scaffold for meniscus tissue engineering.
Front. Bioeng. Biotechnol. 10:1003484.
doi: 10.3389/fbioe.2022.1003484

Natural biopolymer scaffold for meniscus tissue engineering

Yachen Peng[1†], Meng Lu[2†], Zhongsheng Zhou[3], Chenyu Wang[1], Enbo Liu[1], Yanbo Zhang[1*], Tong Liu[1*] and Jianlin Zuo[1*]

[1]Department of Orthopedics, China-Japan Union Hospital of Jilin University, Changchun, China, [2]Department of Nursing, The First Bethune Hospital of Jilin University, Changchun, China, [3]Scientific Research Center, China-Japan Union Hospital of Jilin University, Changchun, China

Meniscal injuries caused by trauma, degeneration, osteoarthritis, or other diseases always result in severe joint pain and motor dysfunction. Due to the unique anatomy of the human meniscus, the damaged meniscus lacks the ability to repair itself. Moreover, current clinical treatments for meniscal injuries, including meniscal suturing or resection, have significant limitations and drawbacks. With developments in tissue engineering, biopolymer scaffolds have shown promise in meniscal injury repair. They act as templates for tissue repair and regeneration, interacting with surrounding cells and providing structural support for newly formed meniscal tissue. Biomaterials offer tremendous advantages in terms of biocompatibility, bioactivity, and modifiable mechanical and degradation kinetics. In this study, the preparation and composition of meniscal biopolymer scaffolds, as well as their properties, are summarized. The current status of research and future research prospects for meniscal biopolymer scaffolds are reviewed in terms of collagen, silk, hyaluronic acid, chitosan, and extracellular matrix (ECM) materials. Overall, such a comprehensive summary provides constructive suggestions for the development of meniscal biopolymer scaffolds in tissue engineering.

KEYWORDS

sport medicine, tissue engineering, meniscus, natural biopolymer, clinic transition

1 Introduction

Meniscal tear is one of the commonplace injuries of the knee joint, which is often caused by trauma, degeneration, and osteoarthritis (Beaufils et al., 2017; Culvenor et al., 2019; Kopf et al., 2020). Partial or total meniscectomy and meniscus suture repair are commonly used to treat meniscus injuries and knee pain, but in terms of long-term prognosis, therapeutic effects are often limited (van de Graaf et al., 2018; Abram et al., 2020), and there are certain complications of treatment, such as cartilage injuries

Abbreviations: 3D, three dimension; AC, articular chondrocyte; ADCS, adipose- derived stem cell; BMSC, bone mesenchymal stem cells; Col, collagen; CS, chitosan; DCB, demineralized cancellous bone; ECM, extracellular matrix; GAG, glycosaminoglycan; IPFP, infrapatellar fat pad; MDM, meniscus-derived matrix; PCL, polycaprolactone; PRP, platelet riched plasma; PVA, polyvinyl alcohol; TGF-β, transforming growth factor-β; TMSC, tonsil-derived mesenchymal stem cells.

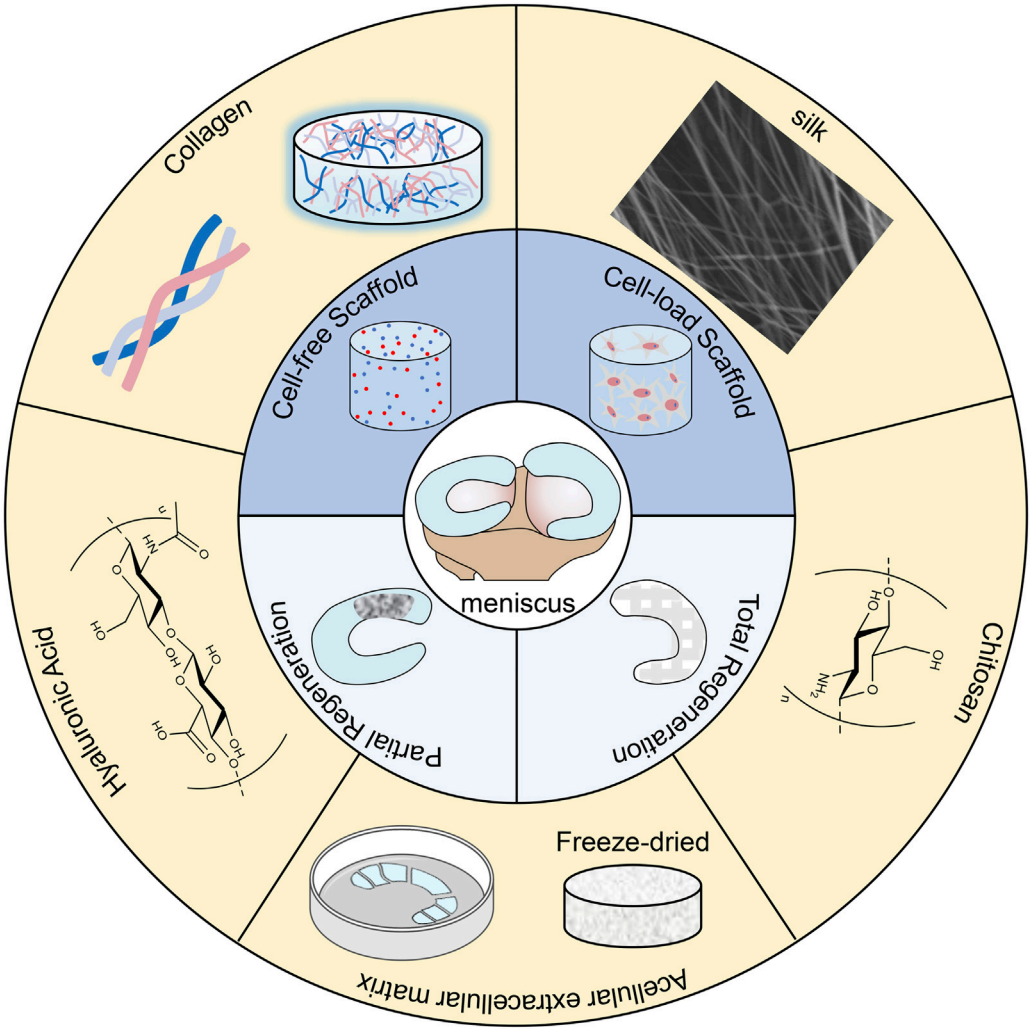

FIGURE 1
Schematic illustration of natural materials for meniscus tissue engineering.

(Venjakob et al., 2019). Therefore, finding a safe and effective alternative therapy to repair meniscal tears is critical for orthopedists.

The repair capacity of the meniscus is related to the degree of vascular infiltration and structure. Compared to lateral edge of the meniscus, the medial edge lacks vascularity and therefore meniscus is less capable of self-repair. The complex anisotropic structure of meniscus increases the difficulty of self-repair. To adapt to compression, stretch, and torsion stresses of the knee from all directions at rest or during sports, the collagen arrangement of meniscus shows a gradient change. The continuous development of tissue engineering has made it possible to repair the meniscus perfectly. Tissue engineering can mimic the original natural tissue and stimulate the body's regenerative potential to promote the growth of tissue into the scaffold and complete the gradual replacement to form functional tissue.

Recent researches have found that biopolymer scaffolds have favorable development foreground in the repair of a variety of tissue injuries (Sandri et al., 2019; Stoppel et al., 2015). They act as patterns for tissue repair and regeneration, interacting with surrounding cells and providing structural support for newly formed tissue (Hsu et al., 2016). Polymers of natural origin, such as collagen, silk, hyaluronic acid, chitosan, and extracellular matrix, are used for tissue engineering due to their good biocompatibility and bioactivity as well as their adjustable mechanical and degradation properties (Figure 1) (Stoppel et al., 2015; Wubneh et al., 2018; Zhang et al., 2019). And biopolymer scaffolds are receiving soaring attention from researchers in the treatment of meniscal injuries (Lin et al., 2017). For example, a collagen meniscus implant (CMI) made from type I collagen from the bovine achilles tendon has been used in clinical treatment (Stone et al., 1997). CMI provides good and consistent clinical effects, especially in terms of knee function and pain, with a low incidence of

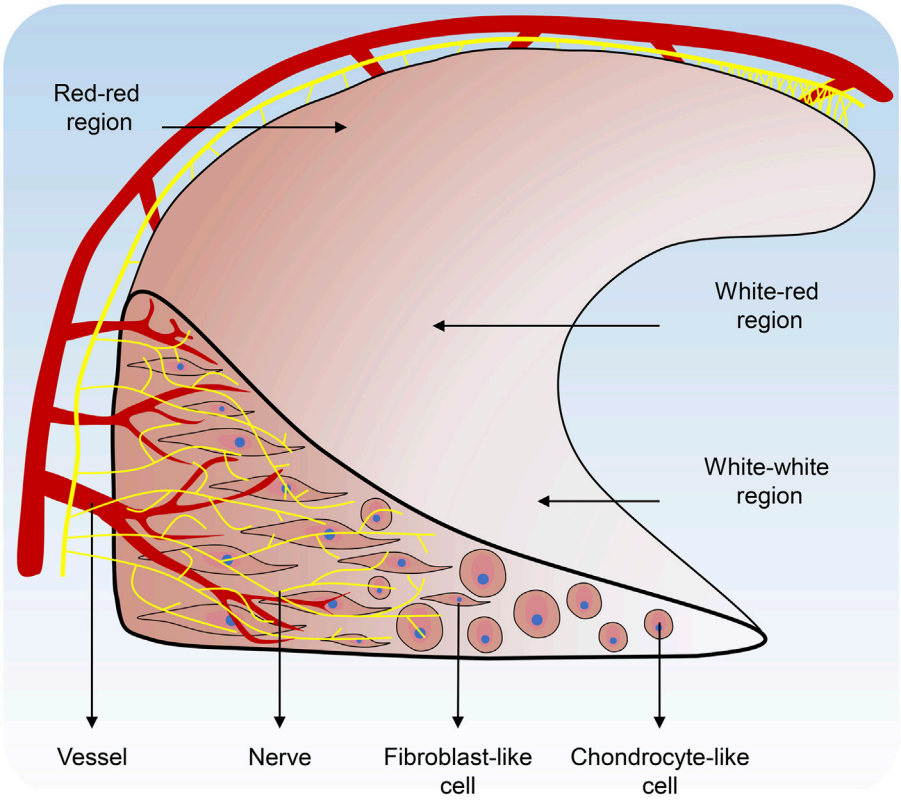

FIGURE 2
Regional variations in vascularization, nerve distribution, and cell populations of the Meniscus.

complications and reoperation (Grassi et al., 2014). However, meniscal scaffolds still have many problems to be solved (Veronesi et al., 2021), such as the lack of gradient bionic and insufficient mechanical properties. Although natural material scaffolds have many advantages in repairing meniscus, they can still be optimized in terms of gradient bionic structure, anti-inflammatory, and repair synergy to improve the repair efficiency (Hao et al., 2021). There is a wide variety of biopolymer scaffolds and most of them are still in the experimental stage, and we still lack a systematic understanding of their investigation. In this review, we refer to the research literature of recent years to systematically elucidate biopolymer meniscal scaffolds from various aspects.

2 Basic properties of the meniscus

2.1 Vascular, neural, and basic anatomy of the meniscus

The meniscus is unique in that it manifests as discrete cartilage-like tissue during embryonic life and subsequently depends on its location to be shaped by different external environmental stimuli. Ultimately, the vascular formation and innervation would be affected to develop into different tissue stratum. Signal transduction, vascular formation, innervation, stem cell origin, and location in the body all produce subtle tissue development differences. These distinctions guide the subpopulations of cells that will ultimately make up the tissue (Figure 2).

The capillary plexus surrounding the meniscus, which originates from the joint capsule and synovial tissue, provides 10–25% of the blood supply to the meniscus and is confined to the peripheral third of the meniscus (Day et al., 1985). The meniscus anterior and posterior horn attachments are covered by vascular synovial tissue, which provides an adequate blood supply to the meniscus (Arnoczky & Warren, 1982). The meniscus can be divided into three regions: the outer red-red region (vascular/nerve region), the inner white-white region (non-vascular/non-nerve region), and the transitional red-white region.

The nerves and mechanoreceptors of the meniscus are mainly located in the anterior and posterior horns of the meniscus and the lateral two-thirds of the body. The medial third of the meniscus is thin and lacks nerves (Gray, 1999). This particular nerve arrangement in the meniscus excites the internal mechanical drive system for proper joint alignment and

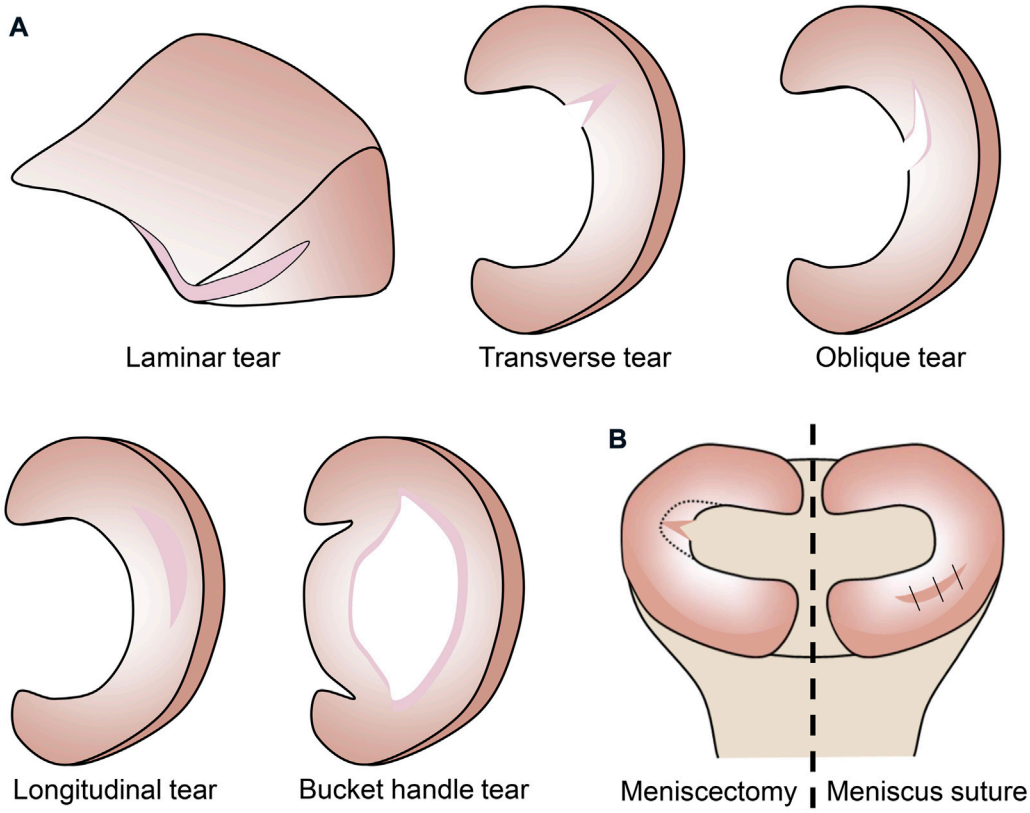

FIGURE 3
(A) Classification of meniscus injuries. **(B)** Treatment of meniscus injuries.

biomechanical function when the meniscus is subjected to forces, resulting in a degree of pressure and tension on the meniscal surface (Zimny et al., 1988).

There is a significant difference in size between the lateral and medial meniscus in humans. The medial meniscus is C-shaped and covers 51%–74% of the area of the medial tibia plateau. The medial meniscus is slightly thinner in volume (Fox et al., 2015). It is more widely open to the medial intercondylar notch and has a relatively flat tibiofemoral articular surface (Renström & Johnson, 1990). The lateral meniscus is rounded and smaller but more flexible than the medial meniscus. It is located in the lateral intercondylar fossa of the tibial plateau and covers 75%–93% of the lateral tibial plateau (Kummer, 1987; Masouros et al., 2008).

2.2 Matrix microenvironment and biochemistry of the meniscus

The meniscus comprises cells and an extracellular matrix of collagen, proteoglycan, matrix glycoproteins, and elastin. The outer third of the Meniscus is dominated by fibroblasts and the inner third is by chondrocytes. The middle third of the meniscus has fibro chondrocytes (Markes et al., 2020). Collagen is the main fibrous component of the meniscus, mainly resists the tensile stress experienced by the meniscus, and its content varies greatly in the different regions of the meniscus. In the red-red region, type I collagen accounts for 80% of the dry weight (Cheung, 1987). The collagen fibers in the main body of the meniscus are arranged in circular patterns, allowing pressure loads to be distributed, while the surface and middle of the meniscus are radially distributed to resist longitudinal tears caused by external forces (Beaupré et al., 1986). Radial fibers are also present in the deeper regions of the meniscus, where they hold the circumferential fibers in place and maintain structural integrity (Shen et al., 2022). In the white-white region, collagen is composed of only Col II (60%) and Col I (40%) (Fox et al., 2012; Bansal et al., 2020).

Therefore, the meniscus is an anisotropic structure, which results in a low capacity for self-repair and the site of injury can influence the choice of treatment options for the orthopedic surgeon. According to the mechanism of injury, meniscal injuries can be classified as laminar, transverse, longitudinal, bucket handle, and oblique tears (Figure 3A). Only injuries that are

TABLE 1 Natural materials used for meniscus tissue engineering.

Materials	Processing technology	Repair area	Comparator	Loaded impact factors	Loaded cells	Results	References
Collagen	Electrospinning	*In vitro* culture	Scaffold with hydrogel or without hydrogel, with different cells	TGF-β1, TGF-β3	Meniscus cell, BMSC, synovial cell, cell from the IPFP	Collagen scaffolds with hydrogels loaded with IPFP cells yielded the highest cell densities with greater deposition of Col I and the highest mechanical properties compared to other cells.	Baek et al. (2018)
	Electrospinning	*Ex vivo* repair model	Collagen scaffold with meniscus cells	-	Meniscus cell	Cell-seeded collagen scaffolds resulted in better integration of new tissue with native tissue.	Baek et al. (2016)
	Freeze-drying	Partial meniscus repair	Intra-articular injections of vehicle or gefitinib	gefitinib	-	Intra-articular injection of gefitinib and implantation of a collagen scaffold enhanced meniscal regeneration.	Pan et al. (2017)
	Chemical crosslinking	*In vitro* culture	Scaffold with different PRP or whole blood	PRP	Meniscus cell	PRP has a higher effect on meniscus cell growth and gene expression than whole blood	Howard et al. (2014)
	Photocrosslinking	Partial meniscus repair	Cells expanded with conditioned medium or growth medium	TGF-β3	TMSC	Chondrogenic induced cells in the scaffold have more cell proliferation, GAG and collagen deposition for the best meniscal repair	(Heo et al., 2016; Koh et al., 2017)
Silk	Salt porogen leaching, freeze-drying	*In vitro* culture	Different layers of meniscal scaffold	-	Fibroblasts at the periphery and chondrocytes at the scaffold center	Chondrocytes in the inner region enhanced Col I and Col II production, and fibroblasts in the outer region enhanced Col I production.	Mandal et al. (2011a)
	3D printing	Subcutaneous implantation	-	-	Fibrochondrocytes	The scaffold supported to maintain cell phenotype.	Bandyopadhyay & Mandal, (2019)
	Processing into porous matrix	Partial meniscus repair	Meniscectomy	-	-	The scaffold provided a degree of articular cartilage protection, improved tibiofemoral contact pressures.	(Gruchenberg et al., 2014; S. Stein et al., 2019a; S. E. C. Stein et al., 2019b)
	Electrospinning	Partial meniscus repair	Meniscectomy	Sr^{2+}	-	The SP-Sr group regenerated the meniscus, which provided better protection to the articular cartilage and slowed down the progression of arthritis.	(Y. Li Y et al., 2020)
Hyaluronic acid	3D printing	Partial meniscus repair	Meniscectomy	-	-	Fibrochondrocyte tissue growed inward and integrated firmly with the surroundings.	Ghodbane et al. (2019b)
	Photocrosslinking	*In vitro* culture	Agarose, gelatin, and PCL	-	Fibrochondrocyte	Cells in MeHA were round, and the ratio of deposited Col II to Col I was close to the value of the inner area region of the native meniscus.	Bahcecioglu et al. (2019b)
	Electrospinning	Subcutaneous implantation	-	-	Fibrochondrocyte	The stiffness of the fibers influenced cell behavior, and cellularity and collagen	Song et al. (2020)

(Continued on following page)

TABLE 1 (*Continued*) Natural materials used for meniscus tissue engineering.

Materials	Processing technology	Repair area	Comparator	Loaded impact factors	Loaded cells	Results	References
						deposition were greater in the stiffer scaffold.	
Chitosan	Gel casting	*In vitro* culture	Different ratios of chitosan and gelatin scaffolds	-	-	All groups of scaffolds had good meniscal cytocompatibility and the scaffolds conforming to the mechanical strength of the different layers of the meniscus were prepared by different ratios of chitosan and gelatin.	Sarem et al. (2013)
	Crosslinking and dialyzing	Total meniscus repair	PVA/CS scaffold with different seed cells	-	ADSC and AC	Extracellular matrix-rich meniscus tissue was regenerated in all experiment groups, but the meniscus in the AC group had the best protection of the femur and tibia.	Moradi et al. (2017)
Extracellular matrix	Freeze-drying	*Ex vivo* repair model	Different amounts of porcine MDM	-	-	Endogenous meniscal cells and MSCs migrated to the scaffolds, 8% MDM scaffold promoted repair of partial meniscal defects.	Ruprecht et al. (2019)
	Freeze-drying	*Ex vivo* repair model	Meniscus suture	PRP	Fibrochondrocyte	The scaffold promoted cell proliferation and infiltration, generated an amorphous extracellular matrix.	Monibi et al. (2016)
	Freeze-drying	Subcutaneous implantation	Sham-operated	-	-	No sign of inflammation showed on the surrounding of tissues.	Chen et al. (2015)
	Freeze-drying	Total meniscus repair	DCB scaffold, ECM/DCB scaffold	-	-	The ECM/DCB scaffold promoted fibrochondrocyte proliferation and secretion of collagen and GAG, and also promoted meniscal regeneration and prevented cartilage degeneration.	Yuan et al. (2016)
	Thermoresponsive gel	*In vitro* culture	-	-	Chondrocyte, fibroblast	Cell infiltration and proliferation	Wu et al. (2015)
	Thermoresponsive gel	Partial meniscus repair	Collagen scaffold	-	BMSC	ECM scaffolds induced fibrochondrogenesis of BMSCs and enhanced overall healing and cartilage protection of the meniscus	Zhong et al. (2020)

limited to the vascular red-red and red-white zones are considered to have repair potential with meniscal suturing. Injuries involving the avascular white-white zone have low repair capacity, and orthopedic surgeons often opt for meniscectomy (Figure 3B) to address the patient's pain. However, when the cartilage loses the protection of the meniscus, degenerative changes may occur and eventually the inevitable development of osteoarthritis.

3 Natural materials used for meniscus tissue engineering

Tissue engineering is the implantation of a scaffold loaded with cytokines or cells into tissue damage, and the gradual transformation of the scaffold into biological tissues, to achieve the purpose of repairing the damage. Scaffolds are the carriers of cytokines and cells. Therefore, as the key to tissue

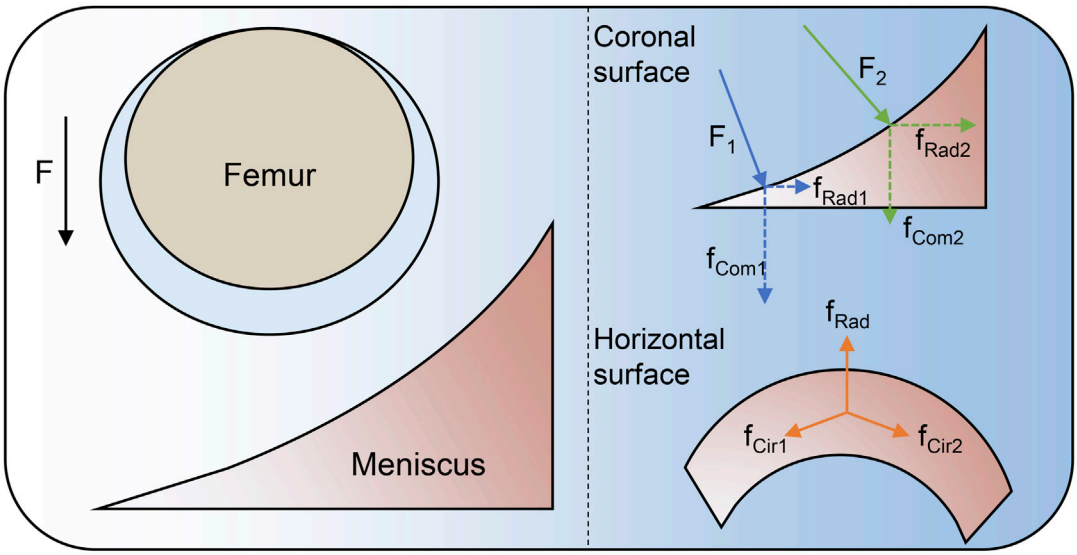

FIGURE 4
Force analysis of meniscus.

engineering, the selection of scaffold materials is very important. Compared with synthetic materials, natural materials have many significant advantages (Table 1), such as good biocompatibility and biodegradability, a structure similar to tissues, and the most important biological inducing activity. For the repair of the meniscus, good biocompatibility and degradability can make the material or the degradation products of the material not produce an inflammatory response, and the scaffold can be degraded as the tissue grows in. The structure similar to the tissue allows the normal tissue around the injury to better integrate with the repair tissue. The most important bio-inducing activity can maintain the consistency of the regenerated tissue with the original tissue, to restore the function perfectly.

However, homogeneous scaffolds are unable to meet the individualized repair of meniscus, so it is important to design scaffolds that properly guide meniscal repair according to the characteristics of each meniscal department. The fibrous arrangement of the natural meniscus should be simulated so that the meniscal scaffold can resist circumferential and radial stresses in the horizontal direction and compressive stresses in the vertical direction (Figure 4) (Berni et al., 2021). Bahcecioglu et al. 3D printed meniscal scaffolds that mimic the natural collagen arrangement, containing circumferential fibers in the periphery and crossed fibers in the interior. This scaffold exhibited increased compressive and tensile modulus and promoted region-specific protein expression (Bahcecioglu et al., 2019a). In the meantime, well-aligned fibers facilitate the directional migration of cells (Prendergast et al., 2021). In addition, if it involves the repair of the outer two-thirds of meniscus, the scaffold should have a gradient of pores. The gradient reduction of the scaffold pore size from lateral to medial facilitates vascular infiltration, thus allowing the vascular distribution of the repaired tissue to be consistent with that of the natural meniscus (Bahcecioglu et al., 2019a; Guo et al., 2021). We summarize the cases of various natural scaffolds in meniscal injury repair, describe the advantages and disadvantages of structure design of natural material scaffolds, predict the future development direction, and provide ideas for clinical translation of meniscal tissue engineering.

3.1 Collagen

Collagen is the most abundant ECM protein, with biodegradability, low immunogenicity, and adequate sources. Collagen self-assembles into cross-striated fibers that provide support for cell growth and are responsible for the mechanical elasticity of connective tissue (Sorushanova et al., 2019). Col I is the major collagen not only in the red-red region of the meniscus (Kwon et al., 2019), but also in mature tendons and ligaments, giving them weight-bearing mechanical properties (Varma et al., 2016). Based on the wide distribution of Col I in living organisms, its easy access to materials, and superior biological properties, it has great potential for meniscal scaffold development.

Meniscal cells derived from different regions, human bone marrow-derived mesenchymal stem cells (BMSCs), synovial cells, and cells from the infrapatellar fat pad were seeded onto aligned electrospun Col I scaffolds and optionally encapsulated in a hydrogel (Baek et al., 2018). Treatment of the scaffolds with

transforming growth factor-β1 (TGF-β1) and TGF-β3 increased Col I deposition in all cell types and increased expression of *COL1A1*, cartilage oligomeric matrix protein (*COMP*), Tenascin C (*TNC*), and Scleraxis (*SCX*) genes (Baek et al., 2018). Meniscal cells seeded on collagen scaffolds produced higher levels of Col I than cells seeded on polylactic acid (PLA) (Baek et al., 2016), suggesting a potential advantage of biopolymer scaffolds in promoting collagen deposition. However, the initial mechanical properties of the collagen scaffold may not be as good as the natural meniscus based on the processing technic and the collagenic own characteristic (Meyer, 2019)

The ability of the injured meniscus to repair itself is limited to vascularized areas and is more susceptible to permanent post-traumatic and retrogression in internal non-vascular areas. Human meniscus cells were seeded and cultured on a Col I scaffold for 4 weeks. A collagen scaffold was implanted into a longitudinal tear injury model established in the avascular region of the bovine meniscus and incubated *in vitro* for 3 weeks. Cell-seeded collagen scaffolds showed better integration of natural tissue compared to cell-free collagen scaffolds or the control group (Baek et al., 2016). Histological analysis of *in vivo* animal experiments showed active integration of meniscus-like cartilage into a tissue-engineered biological scaffold in animal models. Active cellular resorption of collagen scaffold decreased over time. Besides, four cases showed mild nonspecific chronic inflammation, and another showed inflammatory engulfment of the scaffold with giant cells at 3 weeks. More importantly, no clinical or histological infections were found in all animal models at any time (Hansen et al., 2013).

Evidence suggests that treatment of meniscal injuries by implantation of a resorbable collagen scaffold may provide more satisfactory clinical outcomes than partial meniscectomy alone (Warth & Rodkey, 2015). The clinical prognosis after CMI implantation is good and relatively stable, particularly relating to restoring knee functions and relieving pain, and the incidence of postoperative complications and reoperations is low (Grassi et al., 2014). When used in combination with concomitant surgeries, such as anterior cruciate ligament reconstruction and high tibial osteotomy, short-term postoperative clinical outcomes improved in invalids who received CMI, with no significant difference between Actifit polyurethane meniscal scaffold and CMI (Houck et al., 2018). Follow-up results at least 10 years after surgery have shown that the implant size usually decreases, but the long-term outcome of the procedure is safe with a low rate of implant failure. Further progression of degenerative knee disease was not observed in most patients (Monllau et al., 2011). Postoperative magnetic resonance imaging (MRI) follow-up results showed an ongoing remodeling with reduced signal intensity and diminished size in CMI. However, since meniscus extrusion remained at the same level, bone marrow edema decreased from 1 year to longer follow-up and appeared to end remodeling at about 5 years after CMI (Schenk et al., 2020). Depending on the histology, new tissue growth to CMI may also be due to the process of synovial overgrowth, but other regenerative mechanisms may also be possible.

Collagen scaffolds provide strong mechanical strength and effectively promote meniscus regeneration (Pan et al., 2017). However, isolated collagen meniscal scaffolds still have certain limitations of their inherent limitation. For example, the operation and suturing of collagen implants are challenging (Kwon et al., 2019). Because the scaffold has a highly porous surface, which is essential for the differentiation and proliferation of fibrocartilage cells, sutures tend to cut through the implant, making good fixation difficult to achieve. Therefore, most postoperative complications of CMI are due to the suture material rather than the meniscal scaffold (Gwinner et al., 2017). This led us to think about the need to make collagen meniscus scaffolds work better by using a more refined tissue engineering strategy. Since the activation level of epidermal growth factor receptor (EGFR) is in an abnormally high state after meniscal injury, the combination of cell-free collagen scaffold and gefitinib enhances meniscal regeneration (Figures 5A,B A and B) (Pan et al., 2017). Photo-crosslinking using riboflavin and ultraviolet exposure increases the mechanical properties of collagen scaffolds and delays enzyme-triggered degradation of scaffolds (Figures 5C,D) (Heo et al., 2016; Koh et al., 2017). In general, the greatest advantage of collagen is its good biocompatibility, providing a good growth environment for the seed cells, but its lack of processability is also a significant disadvantage, so it needs to be modified or mixed with other materials.

3.2 Silk

Silks are natural fibrin polymers (Huang et al., 2018), which embody superior material characteristics and biological functions achieved through a fine hierarchical structure. Through gentle and efficient processing, and careful and rational material design, they can be used to make high-performance, multifunctional, and well-biocompatible materials (López Barreiro et al., 2019). Although a complete study and analysis of the wide variety of silks remain difficult, regardless of the origin, silks are mainly composed of proteins and a few amounts of polysaccharides and lipids (Bhattacharjee et al., 2017). SF is a linear, water-insoluble protein, and could be combined with other biomaterials to form composites (Huang et al., 2018), while sericin is a globular, water-soluble glycoprotein (Chen et al., 2019). The advantages of silk include good biodegradability, biocompatibility, low immunogenicity (Wang et al., 2019), and the competence to remodel *in vivo* and serve on a pattern for natural tissue growth, resulting in vascularization and inward tissue growth.

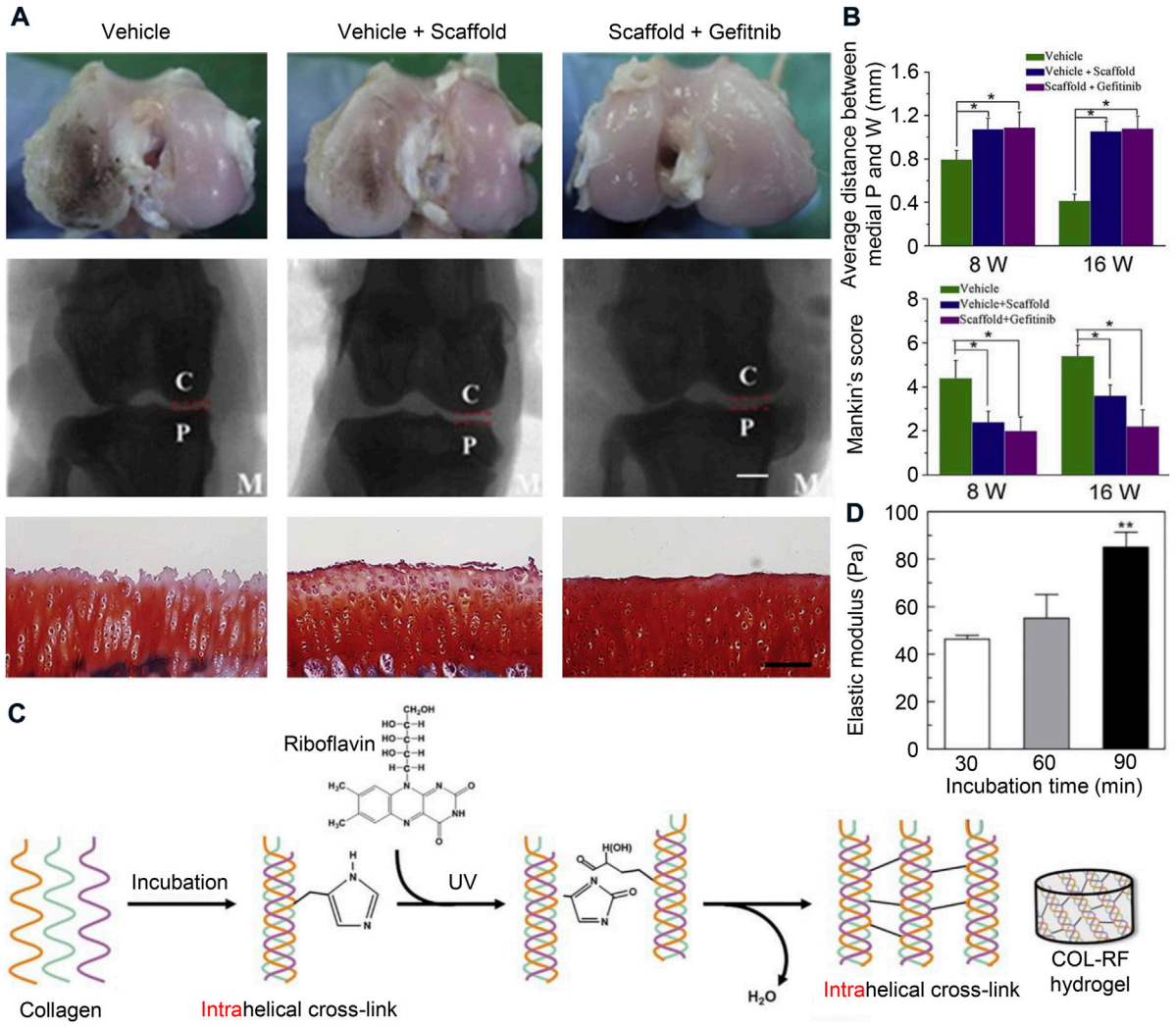

FIGURE 5
Collagen materials used for meniscus tissue engineering. **(A)** Gross morphology, radiological analysis, and histological staining of the femoral cartilage surface after implantation of collagen scaffold. Bar = 200 μm. C, condyles of femur; P, tibial plateau; M, medial of the knee joint. **(B)** Average distance between medial knee joint, and histological evaluation according to Mankin's scoring system. Reprinted with permission (Pan et al., 2017). Copyright (2017), Elsevier. **(C)** Synthetic routes of riboflavin-induced photocrosslinked collagen (COL-RF) hydrogel. **(D)** The relationship between elastic modulus and incubation time. Reprinted with permission (Koh et al., 2017). Copyright (2017), Elsevier.

Silk scaffolds have been widely used for meniscal tissue engineering studies. To generate meniscus-like tissues by *in vitro* experiments, a three-dimensional (3D) silk meniscal scaffold system was designed to mimic the natural meniscal structure by inoculating the scaffold with chondrocytes, human fibroblasts, or adipose-derived stem cells in a spatial separation pattern similar to that of natural tissues (Mandal et al., 2011a; Yang et al., 2017; Ying et al., 2018). The degree of silk scaffold remodeling, tissue inward growth, or other specific cellular behavior can be regulated by increasing growth factors or other signaling factors (Thurber et al., 2015). In a chondrogenic culture in the presence of TGF-β3, cell-seeded constructs increased in cellularity and ECM content. Histology and immunohistochemistry confirmed that having lofty levels of sulfated GAG and type I and II collagen maintained the chondrocyte phenotype (Mandal et al., 2011a). Elevated levels of *COL1A1*, *aggrecan*, and *SOX9* gene expression further confirmed the differentiated and mature cell phenotype (Mandal et al., 2011b). The compressive elastic modulus of the silk scaffold increased significantly with incubation time (Yang et al., 2017). These *in vitro* experiments suggest that porous silk structures can serve as an effective micro-patterned template for endogenous cell

migration, proliferation, and differentiation during the fresh meniscus-like tissue forming process.

In vivo studies have confirmed that transplantation of different forms of silk products into muscles, skins, bones, or brains showed good biocompatibility (Uebersax et al., 2013; Fernández-García et al., 2016; Ju et al., 2016), causing only low inflammatory responses, such as low infiltration of inflammatory cells, and that these responses were usually transient, this normal response decreases within several weeks after implantation. Depending on the properties of the material and the implantation site, which involves macrophage recruitment and activation, a mild foreign body reaction can result in the formation of multinucleated giant cells (Thurber et al., 2015). All mice were in good condition with no adverse reaction after 4 weeks of subcutaneous transplantation of three types of SF scaffolds, either decellularized, implanted with human meniscus cells, or implanted with human adipose-derived stem cells, into 5-week-old male nude mice (Cengiz et al., 2019). *Bandyopadhyay A et al.* implanted cell-free scaffolds into the subcutaneous abdominal pocket of SD rats. Enhanced degradation and absorption of structures were observed 14 days after implantation of scaffolds compared to day 7, and they had excellent immunocompatibility (Bandyopadhyay & Mandal, 2019). H&E stained images and Masson's trichrome stained images show that all scaffolds have a high degree of excellent tissue infiltration, angiogenesis, and collagenous ECM formation. And cross-sections show a homogeneous appearance throughout the sample (Cengiz et al., 2019). A partial meniscectomy was operated on the medial meniscus of sheep and an SF scaffold was implanted into the defect. The joint caused no inflammatory reaction 6 months after surgery, and there was no significant difference in cartilage degeneration between the experimental and sham-operated groups. The compression properties of the scaffold were close to those of natural meniscal tissue (Gruchenberg et al., 2014). Nevertheless, the compressive stiffness of the scaffold is greatly increased after implantation, which may interfere with the permanent binding of sents to the meniscal tissue and reduce the chondroprotection of the underlying cartilage (S. E. C. Stein S. et al., 2019; Warnecke et al., 2018). The current study demonstrates the SF scaffold has the attribute of significantly improving tibiofemoral contact pressures, with up to 81% of tibiofemoral contact pressures being transmitted through the meniscus, within the knee after partial meniscectomy (S. Stein S. E. C. et al., 2019). However, the failure of the SF scaffold to fully recapitulate the contact area and pressure of the intact meniscus, especially at high flexion angles, suggests that the biomechanical properties of the scaffold may need further improvements to fully restore tibiofemoral contact mechanics (S. Stein et al., 2019a). It has been demonstrated in friction tests that SF hydrogels have a friction response similar to that of cartilage, dominated by this interstitial fluid support (Parkes et al., 2015). To elucidate the tribological properties of the fibroin meniscal scaffold, the friction of the implant against cartilage and glass was tested. The coefficient of friction between the silk scaffold and cartilage is 0.056, which is greater than the natural meniscus, but less than the threshold required for meniscus replacement (Warnecke et al., 2017).

Silk fibroin scaffolds still have some shortcomings. The mechanical properties of pure SF scaffolds after freeze-drying are usually unsatisfactory. Fortunately, the biodegradability and mechanical characteristics of SF can be modulated by other suitable polymers (Bandyopadhyay & Mandal, 2019; Y. Li Y et al., 2020; Z. Li Z et al., 2020). For instance, the internally coated collagen enhanced the biocompatibility of the silk sponge, but the outer layer of the collagen would increase the friction properties (Yan et al., 2019). SF and strontium were incorporated with Ɛ-Polycaprolactone by wet-electrospinning method to manufacture the meniscus scaffold, which enhances the secretion of collagen and aggrecan (Figure 6) (Y. Li Y et al., 2020). The combination of silk and cellulose significantly improved the toughness of the hydrogel and promoted the biological activity of fibroblasts (Dorishetty et al., 2020). Compared to collagen, silk proteins are better processed, but silk proteins form β-sheets autonomously, which affect the mechanical properties of the scaffold.

3.3 Hyaluronic acid

Hyaluronic acid (HA) is a GAG consisting of the repeating disaccharide portion of d-glucuronic acid and N-acetyl-d-glucosamine and is found in large amounts in the skin and musculoskeletal tissues. Hyaluronic acid has been widely used in tissue regeneration and medicine due to its superior physiological function and biocompatibility. It also has a well-controlled degradation rate and mechanical properties. HA alone has a relatively fast degradation rate and weak mechanical strength, and the most common modification method is the reaction of methacrylic anhydride with HA to form methacrylated hyaluronic acid (MeHA), which has photocrosslinking properties (Kenne et al., 2013). The photocrosslinked HA has a slower degradation rate and higher mechanical stage and is related to the degree of methyl substitution (D'Amora et al., 2018). *Zhang et al.* obtained a series of photocurable hydrogels with different degrees of crosslinking by adding different concentrations of the water-based tetrathiol crosslinker (PE(NAC)4) to MeHA, which had different gelling time, mechanical strengths, and degradation rates (Zhang et al., 2020). In addition, HA has functional groups that can be chemically modified, carboxyl and hydroxyl. The carboxyl of glucuronic acid is a good target for 1-ethyl-3- [3-(dimethylamino)-propyl]-carbodiimide (EDC) mediated amide and ester formation of HA (Knopf-Marques et al., 2016). *Kim et al.* covalently bound tyramine (TA) to hyaluronan by EDC and mixed it with gelatin to obtain hydrogels mediated by tyrosinase (TYR) cross-linking. Compared to gelatine alone, mixtures of

10.3389/fbioe.2022.1003484

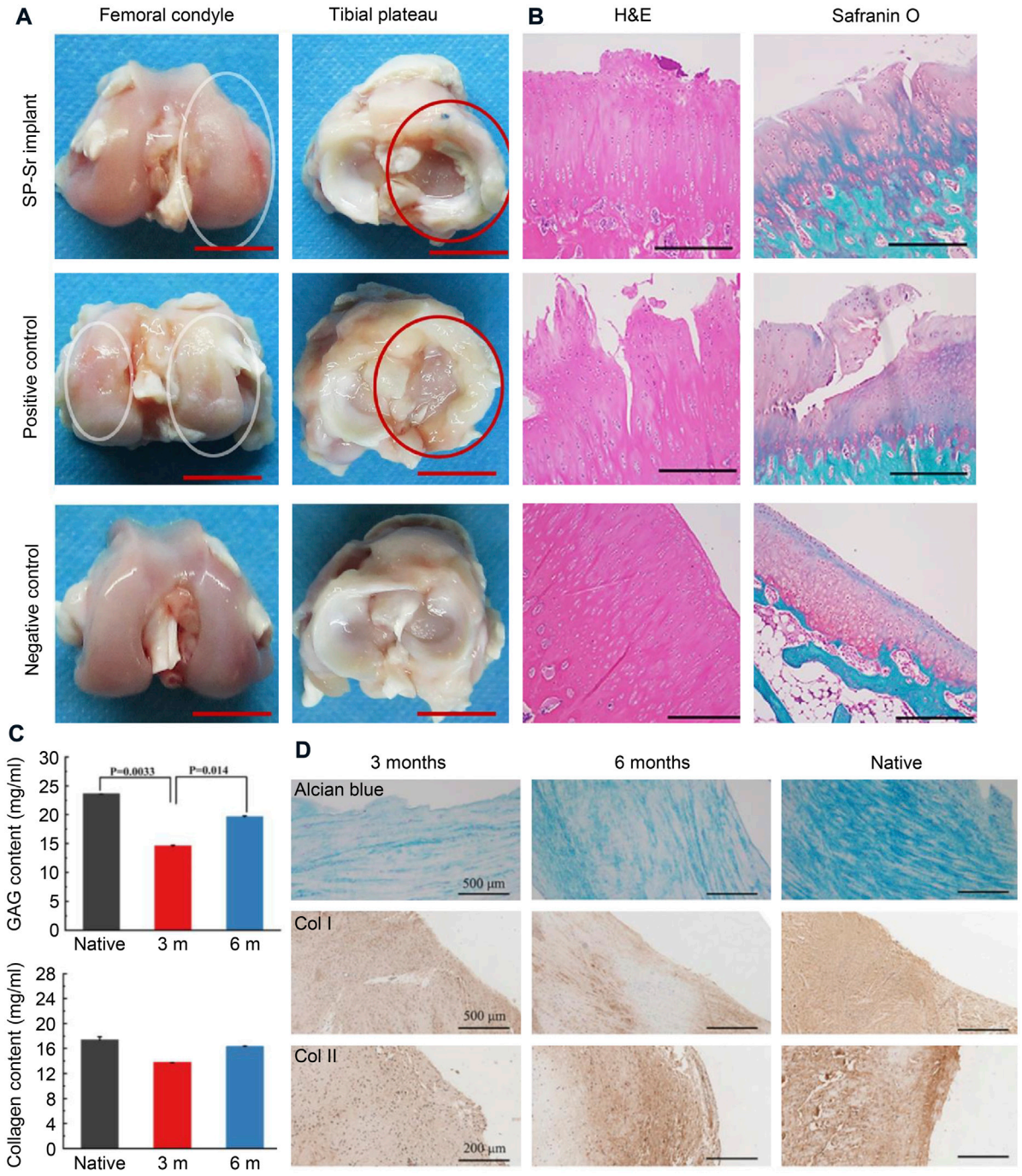

FIGURE 6
Silk materials used for meniscus tissue engineering. **(A)** Macroscopic observations of regenerated menisci and the corresponding femoral condyles. The red ellipses referred to the meniscus and the white ellipses referred to worn cartilage. Bars = 1 cm. **(B)** H&E and Safranin O-Fast Green staining of articular cartilage surfaces in the femur cartilage. Bars = 500 μm. **(C)** The total GAG and collagen content were estimated in native meniscus and neomeniscus. **(D)** The alcian blue and immunohistochemical staining in native meniscus and neomeniscus. Reprinted with permission (Y. Li Y et al., 2020). Copyright (2017), Elsevier.

HA and gelatine in the presence of TYR have faster gel transformation time and higher mechanical properties, and the mechanical peculiarities and degradation kinetics were regulated by TA substitution and TYR concentration (Kim et al., 2018).

HA and its modifications have been widely used to repair with good results. Intra-articular injection of high molecular weight HA has a positive therapeutic effect on osteoarthritis or acute cartilage injury, and it regulates the expression of a variety of mi-RNAs that are associated with cartilage degeneration, apoptosis, and inflammation (Genemaras et al., 2018). However, viscosupplementation therapy prevents macroscopic damage to the meniscus but does not recover its collagen fibrous tissue and viscoelasticity (Levillain et al., 2017). However, cell proliferation and migration were observed when HA was added to the culture medium to stimulate meniscal cells. Not only that, but when the injured meniscal tissue was cultured in cultures containing HA, the accumulation of collagen II around the tear was also observed, but collagen I accumulation around the meniscal injury site was not induced (Tanaka et al., 2017). Thus, the use of HA as raw material and the application of tissue engineering methods to repair damaged meniscus have become a recent research hotspot. *Ghodbane et al.* injected collagen HA sponge as an extracellular matrix into the meniscal scaffold, which matched the circumferential tensile and axial compressive properties of the natural meniscus and had appropriate porosity (Ghodbane et al., 2019a). At 24 weeks after implantation, inward cell growth was observed, producing dense tissue liked fibrocartilage with significant collagen and GAG deposition. On the downside, some of the scaffolds were displaced postoperatively, resulting in low meniscal repair and loss of meniscal protective effect on articular cartilage (Ghodbane et al., 2019b). *Bahcecioglu et al.* inoculated porcine fibrocartilage cells with agarose, methacrylated gelatin (GelMA), and MeHA, hybrid hydrogels, and 3D printed PCL scaffolds, and then evaluated the potential for *ex vivo* meniscal regeneration under dynamic compression. The results showed that hydrogels had a higher potential for meniscal regeneration compared to PCL, with agarose and MeHA favoring the regeneration of the inner meniscal region and gelatin favoring the regeneration of the outer meniscal region. (Bahcecioglu et al., 2019b). *Song et al.* synthesized soft and stiff MeHA scaffolds by electrostatic spinning, in which stiffness was varied by the degree of MeHA cross bonding. The adhesion and migration of meniscal fibrochondrocytes (MFC) to the fibermesh were also investigated, in which the softer MeHA fibermesh was susceptible to deformation and densification by cell traction, whereas the stiffer MeHA fibrous network supported more MFC invasion when placed near the meniscal tissue (Song et al., 2020). In conclusion, the use of HA scaffolds for tissue repair is a promising approach, and enough investigation has been done on this material, yet its use in meniscal repair is often used as an adjunct to synthesis (Halili et al., 2014; Heo et al., 2016). Most notably because of its good biocompatibility but weak mechanical strength, although the suitability of HA has been enhanced by various modifications, the potential damage of these modifiers to the tissue has yet to be investigated.

3.4 Chitosan

Chitosan (CS) is a biopolymer made by deacetylation of chitin with a structure similar to GAG. CS has a wide range of applications in biomedical fields due to its splendid biodegradability, bioactivity, and biocompatibility. CS can provide active sites for cell adhesion, cell-cell, and cell-matrix interactions, which in turn plays an important role in regulating cell proliferation and function. The cationic property of CS allows for the immobilization of negatively charged enzymes, proteins, GAGs, polysaccharides, or other negatively charged molecules under mildly acidic conditions (Sultankulov et al., 2019). CS can also form interconnected porous structures after lyophilization and allows for large numbers of cells to be inoculated at once, improving cell migration and proliferation. The *in vivo* degradation of CS also shows synergistic effects on the long-term performance of tissue engineering cells by affecting many cellular processes such as cell growth, tissue regeneration, and host response (Ahmed et al., 2018). The molecular chain of CS contains reactive amino and hydroxyl making it susceptible to chemical modifications. Combining the major ECM molecules, collagen and chondroitin-6-sulfate, onto a hyaluronic acid/chitosan multilayer can be used as a bionic surface for meniscus repair to reverse meniscus cell dedifferentiation (Tan et al., 2010).

Nevertheless, the properties of isolated CS scaffold materials have some limitations in the preparation of meniscal scaffolds, and the modification of CS is currently a hot spot for research in the field of biomaterials. *Sarem M et al.* prepared chitosan/gelatin composite scaffolds exhibiting highly inter-connected pore architecture with swelling and degradation behavior using genipin as a biocompatible cross-linking agent. Gelatin improves the biocompatibility of CS, and gelatin/chitosan scaffolds have excellent compatibility with meniscus-derived cells (Sarem et al., 2013). In addition, the chitosan/calcium polyphosphate composite scaffold enhances the necessary mechanical properties of the meniscal scaffold. The degradation rate of the scaffold can be controlled by varying the amount of calcium polyphosphate to avoid premature degradation and ensure that the scaffold is filled with new tissue. *Moradi et al.* produced a polyvinyl alcohol/chitosan scaffold that compared the meniscal repair effects of adipose-derived stem cells and articular chondrocytes. The scaffold inoculated with chondrocytes promoted meniscal regeneration well and improved the mechanical properties of the regenerated meniscal tissue (Moradi et al., 2017).

Overall, CS has good properties and is a significant element of scaffold material research and one of the future research directions in the field of biomaterials. Researchers are continuously exploring the potential of CS as a biomaterial, aiming to eliminate the limitations of existing materials. New CS derivatives and composites could certainly make it an ideal scaffold material.

3.5 Extracellular matrix

ECM is acellular component of tissues that provides scaffolding for cells and regulates normal tissue morphogenesis, differentiation, matrix renewal, and dynamic homeostasis (Swinehart & Badylak, 2016). Bioactive molecules that maintain tissue homeostasis and promote regeneration are present in ECM and can act through a range of cell-cell and cell-matrix interactions (Watt & Huck, 2013; Monibi & Cook, 2017). The tissue-derived stroma has a guiding function in the differentiation of stem cells (Rothrauff et al., 2017; Yuan et al., 2017). A specific comparison of the effects of meniscus-derived ECMs (mECMs) on hBMSCs in different regions showed that internal mECMs promoted fibrocartilage differentiation of hBMSCs, whereas external mECMs enhanced more fibroblast phenotypes (Shimomura et al., 2017). The meniscus of rats, sheep, pigs, and humans can be decellularized using numerous techniques, including physical, (freeze-thawing and sonication), chemicals (detergents, EDTA, and hypotonic buffers), biological (enzymatic digestion), and their combinations (Chen et al., 2017; Monibi & Cook, 2017). *In vitro* experiments are remarkable for testing the performance of ECM meniscal scaffolds. Porcine meniscus-derived matrixes (MDM) were prepared and tested for their effectiveness in promoting meniscal repair by migrating endogenous meniscus cells from the surrounding meniscus or exogenously seeded hBMSCs. Both endogenous meniscus cells and hBMSCs permeated into the MDM scaffold. In the absence of exogenous cells, 8% of the MDM scaffold promoted the overall repair of meniscal defects *in vitro* (Ruprecht et al., 2019). *In vitro* experiments to assess cytotoxicity and cytocompatibility of ECM meniscal scaffold, synovial cells, and meniscal chondrocytes were seeded onto decellularized meniscal scaffolds, after 8 days of incubation under basic conditions, the scaffold was not cytotoxic to either cell. In an *in vitro* model of meniscal repair, ECM-derived scaffolds were inoculated into excised menisci and cultivated for 42 days, and histological evaluation showed normal tissue architecture and cellularity of meniscus (Monibi et al., 2016). In addition, the scaffolds were implanted subcutaneously into rats for 7, 14, and 28 days. No inflammatory cells were detected to infiltrate the implant. The structure of the scaffold was stable for more than 14 days. Absorption and turnover of the scaffolds were observed on day 28. The tissue around the implant showed no signs of inflammation and was comparable to the sham operation control group (Chen et al., 2015).

The intermediate region of the bovine meniscus is an excellent material for the preparation of ECM scaffolds. The collagenous fibrils of the meniscal fibrocartilage in the middle zone become more highly oriented perpendicular to the direction of compression (Sizeland et al., 2020). The decellularized porcine medial meniscus maintains the tensile biomechanical properties of the native meniscus but has lower elastic moduli in tension and compression compared to the native meniscus. These changes in biomechanical properties may be due to the reduction of GAG content during decellularization (Abdelgaied et al., 2015). GAG plays a significant role in water regulation within the meniscus. Although some compositional changes in the ECM are to be expected during processing, it is clear that numerous essential structural components remained functional while maintaining biomechanical properties (Stabile et al., 2010). Demineralized cancellous bone (DCB) is an extensively used bioactive scaffold for tissue engineering with a natural 3D porous structure and pretty biocompatibility (Wang et al., 2016). Acellular meniscus extracellular matrix (AMECM) and DCB were used to construct different types of triaxial porous meniscal scaffolds, and the AMECM and DCB played a good synergistic repair effect on the meniscus (Figure 7) (Yuan et al., 2016).

Injectable hydrogels can be derived from tissue-specific ECM, thus providing a bionic environment for cell delivery and allowing seamless regeneration of tissue defects (Yuan et al., 2017). An injectable ECM hydrogel material was developed in the porcine meniscus. This meniscus-derived ECM hydrogel displays a fibrous morphology with adjustable compressive force and initial modulus. The hydrogel promoted the growth of bovine chondrocytes and mouse 3T3 fibroblasts, showing good biocompatibility. Furthermore, the subcutaneous implantation dedicated that the hydrogels were favorable for cell infiltration. (Wu et al., 2015). Decellularized ECM retains essential proteoglycans and collagen and encapsulates BMSCs in ECM or hydrogels. When applied to an orthotopic model of meniscal injury in SD rats, ECM outperformed collagen I scaffold in reducing bone redundancy formation and preventing narrowing of joint space and osteoarthritis development, as demonstrated in histological and micro-CT analyses(Zhong et al., 2020). Although the mECM had higher concentrations of TGF-β and bFGF (Rothrauff et al., 2017), mECM hydrogels did not significantly support fibrochondrogenesis of hMSCs in the absence of TGF-β3, with a decrease in cell numbers and OHP content of hydrogels, and the lack of sulfated GAG production (Yuan et al., 2017).

However, the traditional AMECM preparation process ignores the regionality of the meniscus and processes the entire meniscus into a homogeneous scaffold. It is important to maintain the regional specificity of meniscus. Yun et al. decellularized the inner cartilage region, transition region, and outer fibrous region of the porcine meniscus,

10.3389/fbioe.2022.1003484

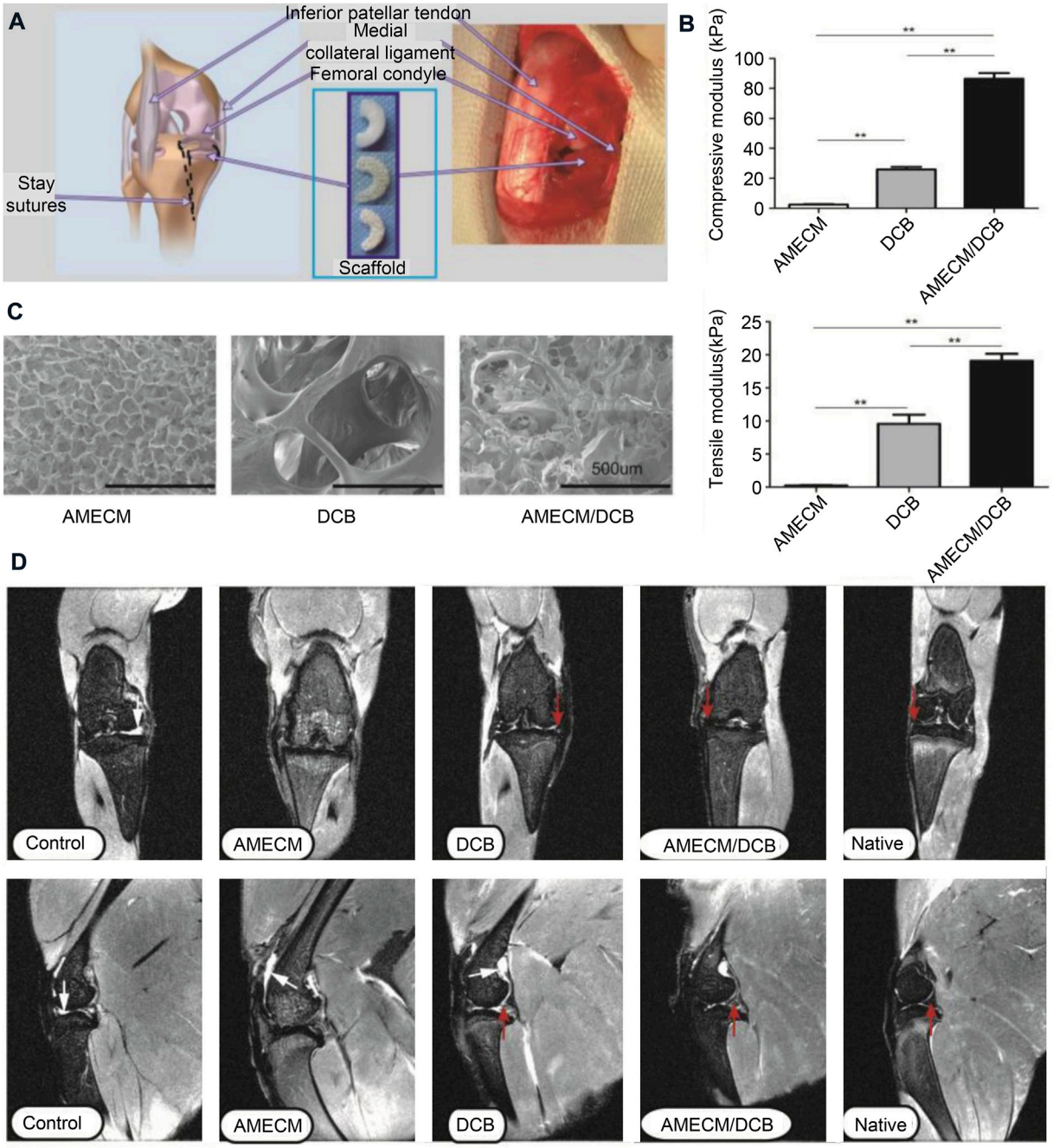

FIGURE 7
Extracellular matrix used for meniscus tissue engineering. **(A)** Surgical strategies for repairing meniscus with extracellular matrix scaffolds. **(B)** Comparative mechanical modulus of the different scaffolds. **(C)** Scanning electron micrographs of the different scaffolds. **(D)** Magnetic resonance imaging (MRI) of rabbit knees 6 months after surgery. The red arrow indicates the regenerated menisci. Reprinted with permission (Yuan et al., 2016). Copyright (2016), Elsevier.

respectively, to prepare a meniscal scaffold with a composition gradient. After this scaffold was implanted *in vivo*, the expression of region-specific proteins was induced, with a large amount of GAG secreted on the inner side and fibrin mainly on the outer side (Yun et al., 2021). Therefore, ACECM is also an ideal material for meniscal tissue engineering, not only for its biocompatibility and ability to promote stem cell differentiation, but also for its ability to be

processed into structurally controlled scaffolds through various techniques.

4 Future directions and conclusion

There is no perfect method for meniscus injury in clinical practice. Meniscectomy removes the damaged part of the meniscus, which to some extent solves the patient's pain and joint interlocking symptoms, but it may cause direct contact with articular cartilage, leading to more serious cartilage wear, and eventually osteoarthritis. Meniscus suture surgery requires very high postoperative rehabilitation for patients. Patients who have undergone this procedure need to strictly control the angle of joint flexion and extension, and the timing of lower limb weight-bearing. For patients with large meniscus injuries, if they have stable, correctly aligned joints and are in the early or earlier stages of arthritis, it is best to use meniscus replacement. Although it can significantly improve the prognosis of patients, the source of the allogeneic meniscus is very scarce, and artificial meniscus may become the key to meniscus injury repair. A large number of artificial meniscuses have been developed, among which natural material meniscus prosthesis accounts for a large proportion due to its good biocompatibility and biological activity. Various natural materials have their advantages and disadvantages, decellularized ECM is taken from the natural meniscus, and by partitioning decellularization, a scaffold with a highly similar structure to the natural meniscus can be prepared, but the clinical translation must face ethical review; collagen and hyaluronic acid are also components of the organism and are biocompatible, but they need to be modified or mixed with other polymers to improve processability; well-processed silk proteins and chitosan are also ideal materials for meniscal scaffolds, but they are not mammalian in origin and may cause inflammatory reactions in the organism.

Although many kinds of natural materials have been developed to repair the meniscus and achieved some gratifying results. But it is undeniable that there is still a long way to go before the clinical transformation of natural materials meniscus tissue engineering. Natural materials have advantages over synthetic materials in terms of access, biocompatibility, degradation, etc. As the therapeutic power of seed cells is gradually explored, more accurate and efficient loading of seed cells will play a more important role in tissue engineering, and natural materials are ideal carriers for seed cells. With advances in 3D printing technology, such as the development of stereo lithography appearance printing and bio-ink printing, the processing performance of natural materials has also improved considerably. Although it still does not reach the level of controllability of synthetic materials, the mixture of natural and synthetic materials is also an effective way to combine the advantages of both, such as synthetic materials as a skeleton and natural materials as a filler. Therefore, natural materials are ideal for meniscal tissue engineering, but how to improve natural materials for better repair and higher efficiency is still an important trend for natural materials in the future.

Then, the complex regionalized structure of the meniscus is also one of the difficulties of repair. The white-white area of the meniscus has no blood vessels, so its inherent repairability is very poor. This also leads to a defect in this area that cannot be repaired well even in the presence of the meniscus scaffold. This requires future research to focus on the repair of the white-white area. Perhaps finding clues for the specific differentiation of stem cells into the chondrocyte-like cell of the white-white area is the key to the white-white area repair, including mechanical stimulation, differentiation factors, and special arrangements of materials, etc. The red-white area is the junction of the red-red area and the white-white area. The cell phenotype and collagen arrangement gradually change in this area, so it has the function of two areas in meantime. In the face of meniscus damage that spans the red-white zone, reconstructing the gradient of cells and collagen in this area is conducive to the integration of tissues and surroundings, better transmitting the stress on the meniscus, and transforming radial force into circumferential force, to avoid stress concentration. The red-red area is the area rich in blood vessels. The main point of repair in this area is to expand the porosity of the scaffold as much as possible under the premise of ensuring the mechanical strength, to facilitate the penetration and metabolism of nutrients.

As for the entire replacement of the meniscus, it is still a difficult problem. As mentioned above, the three areas of the meniscus have different repair points. Therefore, it is necessary to meet the repair requirements of the three areas on a scaffold. It is best to include some gradient signals that simulate the natural meniscus. Future research directions should design pore size gradients to influence the infiltration of meniscal vessels and precisely replicate the vessels distribution; mechanical strength gradients should also follow the force analysis of the natural meniscus to simulate the mechanical properties of each region, resulting in a collagen arrangement consistent with the natural structure; or load gradient inducing factors to promote regional differentiation of stem cells to form functionally compatible tissues.

In addition, inflammatory and oxidative reactions from meniscal injuries and implantation cannot be ignored, and attention to the immune microenvironment of injured area is an important future direction. Natural materials have good biocompatibility and degradation products can participate in the normal metabolism process, so they won't cause excessive inflammation or oxidative reactions. In addition, although inflammatory and oxidative responses do not persist throughout the meniscal repair process, modulating the immune microenvironment and terminating the inflammatory response at the right time can improve the

efficiency of meniscal repair. A good transition between anti-inflammation and repair can be achieved by releasing anti-inflammatory and inducing agents in a consistent sequence, and the difference in material degradation rates can also be used to construct an integrated anti-inflammatory-repair meniscal scaffold.

In conclusion, the research on the tissue engineering of the meniscus needs to be further in-depth, mainly including the following aspects: 1) Continuing to optimise the materials used in the preparation of meniscal scaffolds; 2) A bionic integrated meniscus prosthesis based on the differences in the various regions of the meniscus; 3) In-depth study of the mechanism of differentiation of stem cells into different cell phenotypes of the meniscus (mechanical stimulation, differentiation factors); 4) Observe the long-term repair effect of the meniscus scaffold implantation.

Author contributions

YP and ML have contributed equally to this work and share the first authorship. YZ, TL and JZ contributed to conception and design. YP, ML, ZZ and CW wrote the manuscript. YP designed the figures and the table. LE performed literature search, and provided valuable comments. All authors contributed to the article and approved the final manuscript.

Funding

This work was supported by the Science and Technology Department Program of Jilin Province (Grant Nos. YDZJ202201ZYTS520, 20190304124YY, and 20190304121YY) and the Department of Finance of Jilin Province (No. 2020SCZ53).

Conflict of interest

The authors declare that the research was conducted in the absence of any commercial or financial relationships that could be construed as a potential conflict of interest.

Publisher's note

References

Abdelgaied, A., Stanley, M., Galfe, M., Berry, H., Ingham, E., and Fisher, J. (2015). Comparison of the biomechanical tensile and compressive properties of decellularised and natural porcine meniscus. *J. Biomech.* 48 (8), 1389–1396. doi:10.1016/j.jbiomech.2015.02.044

Abram, S. G. F., Hopewell, S., Monk, A. P., Bayliss, L. E., Beard, D. J., and Price, A. J. (2020). Arthroscopic partial meniscectomy for meniscal tears of the knee: A systematic review and meta-analysis. *Br. J. Sports Med.* 54 (11), 652–663. doi:10.1136/bjsports-2018-100223

Ahmed, S., AnnuAli, A., and Sheikh, J. (2018). A review on chitosan centred scaffolds and their applications in tissue engineering. *Int. J. Biol. Macromol.* 116, 849–862. doi:10.1016/j.ijbiomac.2018.04.176

Arnoczky, S. P., and Warren, R. F. (1982). Microvasculature of the human meniscus. *Am. J. Sports Med.* 10 (2), 90–95. doi:10.1177/036354658201000205

Baek, J., Sovani, S., Choi, W., Jin, S., Grogan, S. P., and D'Lima, D. D. (2018). Meniscal tissue engineering using aligned collagen fibrous scaffolds: Comparison of different human cell sources. *Tissue Eng. Part A* 24 (1-2), 81–93. doi:10.1089/ten.TEA.2016.0205

Baek, J., Sovani, S., Glembotski, N. E., Du, J., Jin, S., Grogan, S. P., et al. (2016). Repair of avascular meniscus tears with electrospun collagen scaffolds seeded with human cells. *Tissue Eng. Part A* 22 (5-6), 436–448. doi:10.1089/ten.TEA.2015.0284

Bahcecioglu, G., Bilgen, B., Hasirci, N., and Hasirci, V. (2019a). Anatomical meniscus construct with zone specific biochemical composition and structural organization. *Biomaterials* 218, 119361. doi:10.1016/j.biomaterials.2019.119361

Bahcecioglu, G., Hasirci, N., Bilgen, B., and Hasirci, V. (2019b). Hydrogels of agarose, and methacrylated gelatin and hyaluronic acid are more supportive for *in vitro* meniscus regeneration than three dimensional printed polycaprolactone scaffolds. *Int. J. Biol. Macromol.* 122, 1152–1162. doi:10.1016/j.ijbiomac.2018.09.065

Bandyopadhyay, A., and Mandal, B. B. (2019). A three-dimensional printed silk-based biomimetic tri-layered meniscus for potential patient-specific implantation. *Biofabrication* 12 (1), 015003. doi:10.1088/1758-5090/ab40fa

Bansal, S., Peloquin, J. M., Keah, N. M., O'Reilly, O. C., Elliott, D. M., Mauck, R. L., et al. (2020). Structure, function, and defect tolerance with maturation of the radial tie fiber network in the knee meniscus. *J. Orthop. Res.* 38 (12), 2709–2720. doi:10.1002/jor.24697

Beaufils, P., Becker, R., Kopf, S., Englund, M., Verdonk, R., Ollivier, M., et al. (2017). Surgical management of degenerative meniscus lesions: The 2016 ESSKA meniscus consensus. *Knee Surg. Sports Traumatol. Arthrosc.* 25 (2), 335–346. doi:10.1007/s00167-016-4407-4

Beaupré, A., Choukroun, R., Guidouin, R., Garneau, R., Gérardin, H., and Cardou, A. (1986). Correlation between microstructure and biomechanics. *Clin. Orthop. Relat. Res.* 208, 72–75. doi:10.1097/00003086-198607000-00016

Berni, M., Marchiori, G., Cassiolas, G., Grassi, A., Zaffagnini, S., Fini, M., et al. (2021). Anisotropy and inhomogeneity of permeability and fibrous network response in the pars intermedia of the human lateral meniscus. *Acta Biomater.* 135, 393–402. doi:10.1016/j.actbio.2021.08.020

Bhattacharjee, P., Kundu, B., Naskar, D., Kim, H.-W., Maiti, T. K., Bhattacharya, D., et al. (2017). Silk scaffolds in bone tissue engineering: An overview. *Acta Biomater.* 63, 1–17. doi:10.1016/j.actbio.2017.09.027

Cengiz, I. F., Pereira, H., Espregueira-Mendes, J., Kwon, I. K., Reis, R. L., and Oliveira, J. M. (2019). Suturable regenerated silk fibroin scaffold reinforced with 3D-printed polycaprolactone mesh: Biomechanical performance and subcutaneous implantation. *J. Mat. Sci. Mat. Med.* 30 (6), 63. doi:10.1007/s10856-019-6265-3

Chen, R., Zhu, C., Hu, M., Zhou, L., Yang, H., Zheng, H., et al. (2019). Comparative analysis of proteins from *Bombyx mori* and *Antheraea pernyi* cocoons for the purpose of silk identification. *J. Proteomics* 209, 103510. doi:10.1016/j.jprot.2019.103510

Chen, Y. C., Chen, R. N., Jhan, H. J., Liu, D. Z., Ho, H. O., Mao, Y., et al. (2015). Development and characterization of acellular extracellular matrix scaffolds from porcine menisci for use in cartilage tissue engineering. *Tissue Eng. Part C. Methods* 21 (9), 971–986. doi:10.1089/ten.TEC.2015.0036

Chen, Y., Chen, J., Zhang, Z., Lou, K., Zhang, Q., Wang, S., et al. (2017). Current advances in the development of natural meniscus scaffolds: Innovative approaches to decellularization and recellularization. *Cell. Tissue Res.* 370 (1), 41–52. doi:10.1007/s00441-017-2605-0

Cheung, H. S. (1987). Distribution of type I, II, III and V in the pepsin solubilized collagens in bovine menisci. *Connect. Tissue Res.* 16 (4), 343–356. doi:10.3109/03008208709005619

Culvenor, A. G., Oiestad, B. E., Hart, H. F., Stefanik, J. J., Guermazi, A., and Crossley, K. M. (2019). Prevalence of knee osteoarthritis features on magnetic resonance imaging in asymptomatic uninjured adults: A systematic review and meta-analysis. *Br. J. Sports Med.* 53 (20), 1268–1278. doi:10.1136/bjsports-2018-099257

D'Amora, U., Ronca, A., Raucci, M. G., Lin, H., Soriente, A., Fan, Y., et al. (2018). Bioactive composites based on double network approach with tailored mechanical, physico-chemical, and biological features. *J. Biomed. Mat. Res. A* 106 (12), 3079–3089. doi:10.1002/jbm.a.36498

Day, B., Mackenzie, W. G., Shim, S. S., and Leung, G. (1985). The vascular and nerve supply of the human meniscus. *Arthrosc. J. Arthrosc. Relat. Surg.* 1 (1), 58–62. doi:10.1016/s0749-8063(85)80080-3

Dorishetty, P., Balu, R., Athukoralalage, S. S., Greaves, T. L., Mata, J., de Campo, L., et al. (2020). Tunable biomimetic hydrogels from silk fibroin and nanocellulose. *ACS Sustain. Chem. Eng.* 8 (6), 2375–2389. doi:10.1021/acssuschemeng.9b05317

Fernández-García, L., Marí-Buyé, N., Barios, J. A., Madurga, R., Elices, M., Pérez-Rigueiro, J., et al. (2016). Safety and tolerability of silk fibroin hydrogels implanted into the mouse brain. *Acta Biomater.* 45, 262–275. doi:10.1016/j.actbio.2016.09.003

Fox, A. J., Bedi, A., and Rodeo, S. A. (2012). The basic science of human knee menisci: Structure, composition, and function. *Sports Health.* 4 (4), 340–351. doi:10.1177/1941738111429419

Fox, A. J., Wanivenhaus, F., Burge, A. J., Warren, R. F., and Rodeo, S. A. (2015). The human meniscus: A review of anatomy, function, injury, and advances in treatment. *Clin. Anat.* 28 (2), 269–287. doi:10.1002/ca.22456

Genemaras, A. A., Ennis, H., Bradshaw, B., Kaplan, L., and Huang, C. C. (2018). Effects of anti-inflammatory agents on expression of early responsive inflammatory and catabolic genes in *ex vivo* porcine model of acute knee cartilage injury. *Cartilage* 9 (3), 293–303. doi:10.1177/1947603516684589

Ghodbane, S. A., Brzezinski, A., Patel, J. M., Plaff, W. H., Marzano, K. N., Gatt, C. J., et al. (2019a). Partial meniscus replacement with a collagen-hyaluronan infused three-dimensional printed polymeric scaffold. *Tissue Eng. Part A* 25 (5-6), 379–389. doi:10.1089/ten.TEA.2018.0160

Ghodbane, S. A., Patel, J. M., Brzezinski, A., Lu, T. M., Gatt, C. J., and Dunn, M. G. (2019b). Biomechanical characterization of a novel collagen-hyaluronan infused 3D-printed polymeric device for partial meniscus replacement. *J. Biomed. Mat. Res.* 107 (8), 2457–2465. doi:10.1002/jbm.b.34336

Grassi, A., Zaffagnini, S., Marcheggiani Muccioli, G. M., Benzi, A., and Marcacci, M. (2014). Clinical outcomes and complications of a collagen meniscus implant: A systematic review. *Int. Orthop.* 38 (9), 1945–1953. doi:10.1007/s00264-014-2408-9

Gray, J. C. (1999). Neural and vascular anatomy of the menisci of the human knee. *J. Orthop. Sports Phys. Ther.* 29 (1), 23–30. doi:10.2519/jospt.1999.29.1.23

Gruchenberg, K., Ignatius, A., Friemert, B., von Lübken, F., Skaer, N., Gellynck, K., et al. (2014). *In vivo* performance of a novel silk fibroin scaffold for partial meniscal replacement in a sheep model. *Knee Surg. Sports Traumatol. Arthrosc.* 23 (8), 2218–2229. doi:10.1007/s00167-014-3009-2

Guo, W., Chen, M., Wang, Z., Tian, Y., Zheng, J., Gao, S., et al. (2021). 3D-printed cell-free PCL-MECM scaffold with biomimetic micro-structure and micro-environment to enhance *in situ* meniscus regeneration. *Bioact. Mat.* 6 (10), 3620–3633. doi:10.1016/j.bioactmat.2021.02.019

Gwinner, C., von Roth, P., Schmidt, S., Ode, J. E., Wulsten, D., and Hoburg, A. (2017). Biomechanical performance of a collagen meniscus implant with regard to suture material and irrigation fluid. *Knee* 24 (4), 726–732. doi:10.1016/j.knee.2017.04.003

Halili, A. N., Hasirci, N., and Hasirci, V. (2014). A multilayer tissue engineered meniscus substitute. *J. Mat. Sci. Mat. Med.* 25 (4), 1195–1209. doi:10.1007/s10856-014-5145-0

Hansen, R., Bryk, E., and Vigorita, V. (2013). Collagen scaffold meniscus implant integration in a canine model: A histological analysis. *J. Orthop. Res.* 31 (12), 1914–1919. doi:10.1002/jor.22456

Hao, L., Tianyuan, Z., Zhen, Y., Fuyang, C., Jiang, W., Zineng, Y., et al. (2021). Biofabrication of cell-free dual drug-releasing biomimetic scaffolds for meniscal regeneration. *Biofabrication* 14 (1), 015001. doi:10.1088/1758-5090/ac2cd7

Heo, J., Koh, R. H., Shim, W., Kim, H. D., Yim, H. G., and Hwang, N. S. (2016). Riboflavin-induced photo-crosslinking of collagen hydrogel and its application in meniscus tissue engineering. *Drug Deliv. Transl. Res.* 6 (2), 148–158. doi:10.1007/s13346-015-0224-4

Houck, D. A., Kraeutler, M. J., Belk, J. W., McCarty, E. C., and Bravman, J. T. (2018). Similar clinical outcomes following collagen or polyurethane meniscal scaffold implantation: A systematic review. *Knee Surg. Sports Traumatol. Arthrosc.* 26 (8), 2259–2269. doi:10.1007/s00167-018-4838-1

Howard, D., Shepherd, J. H., Kew, S. J., Hernandez, P., Ghose, S., Wardale, J. A., et al. (2014). Release of growth factors from a reinforced collagen GAG matrix supplemented with platelet rich plasma: Influence on cultured human meniscal cells. *J. Orthop. Res.* 32 (2), 273–278. doi:10.1002/jor.22495

Hsu, S. H., Hung, K. C., and Chen, C. W. (2016). Biodegradable polymer scaffolds. *J. Mat. Chem. B* 4 (47), 7493–7505. doi:10.1039/c6tb02176j

Huang, W., Ling, S., Li, C., Omenetto, F. G., and Kaplan, D. L. (2018). Silkworm silk-based materials and devices generated using bio-nanotechnology. *Chem. Soc. Rev.* 47 (17), 6486–6504. doi:10.1039/c8cs00187a

Ju, H. W., Lee, O. J., Lee, J. M., Moon, B. M., Park, H. J., Park, Y. R., et al. (2016). Wound healing effect of electrospun silk fibroin nanomatrix in burn-model. *Int. J. Biol. Macromol.* 85, 29–39. doi:10.1016/j.ijbiomac.2015.12.055

Kenne, L., Gohil, S., Nilsson, E. M., Karlsson, A., Ericsson, D., Helander Kenne, A., et al. (2013). Modification and cross-linking parameters in hyaluronic acid hydrogels--definitions and analytical methods. *Carbohydr. Polym.* 91 (1), 410–418. doi:10.1016/j.carbpol.2012.08.066

Kim, S. H., An, Y. H., Kim, H. D., Kim, K., Lee, S. H., Yim, H. G., et al. (2018). Enzyme-mediated tissue adhesive hydrogels for meniscus repair. *Int. J. Biol. Macromol.* 110, 479–487. doi:10.1016/j.ijbiomac.2017.12.053

Knopf-Marques, H., Pravda, M., Wolfova, L., Velebny, V., Schaaf, P., Vrana, N. E., et al. (2016). Hyaluronic acid and its derivatives in coating and delivery systems: Applications in tissue engineering, regenerative medicine and immunomodulation. *Adv. Healthc. Mat.* 5 (22), 2841–2855. doi:10.1002/adhm.201600316

Koh, R. H., Jin, Y., Kang, B.-J., and Hwang, N. S. (2017). Chondrogenically primed tonsil-derived mesenchymal stem cells encapsulated in riboflavin-induced photocrosslinking collagen-hyaluronic acid hydrogel for meniscus tissue repairs. *Acta Biomater.* 53, 318–328. doi:10.1016/j.actbio.2017.01.081

Kopf, S., Beaufils, P., Hirschmann, M. T., Rotigliano, N., Ollivier, M., Pereira, H., et al. (2020). Management of traumatic meniscus tears: The 2019 ESSKA meniscus consensus. *Knee Surg. Sports Traumatol. Arthrosc.* 28 (4), 1177–1194. doi:10.1007/s00167-020-05847-3

Kummer, B. (1987). Anatomy and biomechanics of the meniscus of the knee joint. *Langenbecks Arch. Chir.* 372, 241–246. Biomechanik des Kniegelenksmeniscus.). doi:10.1007/bf01297822

Kwon, H., Brown, W. E., Lee, C. A., Wang, D., Paschos, N., Hu, J. C., et al. (2019). Surgical and tissue engineering strategies for articular cartilage and meniscus repair. *Nat. Rev. Rheumatol.* 15 (9), 550–570. doi:10.1038/s41584-019-0255-1

Levillain, A., Magoariec, H., Boulocher, C., Decambron, A., Viateau, V., and Hoc, T. (2017). Effects of a viscosupplementation therapy on rabbit menisci in an anterior cruciate ligament transection model of osteoarthritis. *J. Biomech.* 58, 147–154. doi:10.1016/j.jbiomech.2017.04.034

Li, Y., Chen, M., Zhou, W., Gao, S., Luo, X., Peng, L., et al. (2020). Cell-free 3D wet-electrospun PCL/silk fibroin/Sr(2+) scaffold promotes successful total meniscus regeneration in a rabbit model. *Acta Biomater.* 113, 196–209. doi:10.1016/j.actbio.2020.06.017

Li, Z., Wu, N., Cheng, J., Sun, M., Yang, P., Zhao, F., et al. (2020). Biomechanically, structurally and functionally meticulously tailored polycaprolactone/silk fibroin scaffold for meniscus regeneration. *Theranostics* 10 (11), 5090–5106. doi:10.7150/thno.44270

Lin, D. D., Picardo, N. E., Adesida, A., and Khan, W. S. (2017). Clinical studies using biological and synthetic materials for meniscus replacement. *Curr. Stem Cell. Res. Ther.* 12 (4), 348–353. doi:10.2174/1574888x11666160429123110

López Barreiro, D., Yeo, J., Tarakanova, A., Martin-Martinez, F. J., and Buehler, M. J. (2019). Multiscale modeling of silk and silk-based biomaterials-A review. *Macromol. Biosci.* 19 (3), e1800253. doi:10.1002/mabi.201800253

Mandal, B. B., Park, S. H., Gil, E. S., and Kaplan, D. L. (2011a). Multilayered silk scaffolds for meniscus tissue engineering. *Biomaterials* 32 (2), 639–651. doi:10.1016/j.biomaterials.2010.08.115

Mandal, B. B., Park, S. H., Gil, E. S., and Kaplan, D. L. (2011b). Stem cell-based meniscus tissue engineering. *Tissue Eng. Part A* 17 (21-22), 2749–2761. doi:10.1089/ten.TEA.2011.0031

Markes, A. R., Hodax, J. D., and Ma, C. B. (2020). Meniscus form and function. *Clin. Sports Med.* 39 (1), 1–12. doi:10.1016/j.csm.2019.08.007

Masouros, S. D., McDermott, I. D., Amis, A. A., and Bull, A. M. (2008). Biomechanics of the meniscus-meniscal ligament construct of the knee. *Knee Surg. Sports Traumatol. Arthrosc.* 16 (12), 1121–1132. doi:10.1007/s00167-008-0616-9

Meyer, M. (2019). Processing of collagen based biomaterials and the resulting materials properties. *Biomed. Eng. OnLine* 18 (1), 24. doi:10.1186/s12938-019-0647-0

Monibi, F. A., Bozynski, C. C., Kuroki, K., Stoker, A. M., Pfeiffer, F. M., Sherman, S. L., et al. (2016). Development of a micronized meniscus extracellular matrix scaffold for potential augmentation of meniscal repair and regeneration. *Tissue Eng. Part C. Methods* 22 (12), 1059–1070. doi:10.1089/ten.TEC.2016.0276

Monibi, F. A., and Cook, J. L. (2017). Tissue-derived extracellular matrix bioscaffolds: Emerging applications in cartilage and meniscus repair. *Tissue Eng. Part B Rev.* 23 (4), 386–398. doi:10.1089/ten.TEB.2016.0431

Monllau, J. C., Gelber, P. E., Abat, F., Pelfort, X., Abad, R., Hinarejos, P., et al. (2011). Outcome after partial medial meniscus substitution with the collagen meniscal implant at a minimum of 10 years' follow-up. *Arthrosc. J. Arthrosc. Relat. Surg.* 27 (7), 933–943. doi:10.1016/j.arthro.2011.02.018

Moradi, L., Vasei, M., Dehghan, M. M., Majidi, M., Farzad Mohajeri, S., and Bonakdar, S. (2017). Regeneration of meniscus tissue using adipose mesenchymal stem cells-chondrocytes co-culture on a hybrid scaffold: *In vivo* study. *Biomaterials* 126, 18–30. doi:10.1016/j.biomaterials.2017.02.022

Pan, Z., Wu, Y., Zhang, X., Fu, Q., Li, J., Yang, Y., et al. (2017). Delivery of epidermal growth factor receptor inhibitor via a customized collagen scaffold promotes meniscal defect regeneration in a rabbit model. *Acta Biomater.* 62, 210–221. doi:10.1016/j.actbio.2017.07.008

Parkes, M., Myant, C., Dini, D., and Cann, P. (2015). Tribology-optimised silk protein hydrogels for articular cartilage repair. *Tribol. Int.* 89, 9–18. doi:10.1016/j.triboint.2014.11.024

Prendergast, M. E., Davidson, M. D., and Burdick, J. A. (2021). A biofabrication method to align cells within bioprinted photocrosslinkable and cell-degradable hydrogel constructs via embedded fibers. *Biofabrication* 13 (4), 044108. doi:10.1088/1758-5090/ac25cc

Renström, P., and Johnson, R. J. (1990). Anatomy and biomechanics of the menisci. *Clin. Sports Med.* 9 (3), 523–538. doi:10.1016/s0278-5919(20)30704-3

Rothrauff, B. B., Shimomura, K., Gottardi, R., Alexander, P. G., and Tuan, R. S. (2017). Anatomical region-dependent enhancement of 3-dimensional chondrogenic differentiation of human mesenchymal stem cells by soluble meniscus extracellular matrix. *Acta Biomater.* 49, 140–151. doi:10.1016/j.actbio.2016.11.046

Ruprecht, J. C., Waanders, T. D., Rowland, C. R., Nishimuta, J. F., Glass, K. A., Stencel, J., et al. (2019). Meniscus-derived matrix scaffolds promote the integrative repair of meniscal defects. *Sci. Rep.* 9 (1), 8719. doi:10.1038/s41598-019-44855-3

Sandri, G., Rossi, S., Bonferoni, M. C., Miele, D., Faccendini, A., Del Favero, E., et al. (2019). Chitosan/glycosaminoglycan scaffolds for skin reparation. *Carbohydr. Polym.* 220, 219–227. doi:10.1016/j.carbpol.2019.05.069

Sarem, M., Moztarzadeh, F., Mozafari, M., and Shastri, V. P. (2013). Optimization strategies on the structural modeling of gelatin/chitosan scaffolds to mimic human meniscus tissue. *Mater. Sci. Eng. C* 33 (8), 4777–4785. doi:10.1016/j.msec.2013.07.036

Schenk, L., Bethge, L., Hirschmann, A., Berbig, R., Luthi, U., Arnold, M. P., et al. (2020). Ongoing MRI remodeling 3-7 years after collagen meniscus implantation in stable knees. *Knee Surg. Sports Traumatol. Arthrosc.* 28 (4), 1099–1104. doi:10.1007/s00167-019-05714-w

Shen, J., Zhao, Q., Qi, Y., Cofer, G., Johnson, G. A., and Wang, N. (2022). Tractography of porcine meniscus microstructure using high-resolution diffusion magnetic resonance imaging. *Front. Endocrinol.* 13, 876784. doi:10.3389/fendo.2022.876784

Shimomura, K., Rothrauff, B. B., and Tuan, R. S. (2017). Region-specific effect of the decellularized meniscus extracellular matrix on mesenchymal stem cell-based meniscus tissue engineering. *Am. J. Sports Med.* 45 (3), 604–611. doi:10.1177/0363546516674184

Sizeland, K. H., Wells, H. C., Kirby, N. M., Hawley, A., Mudie, S. T., Ryan, T. M., et al. (2020). Bovine meniscus middle zone tissue: Measurement of collagen fibril behavior during compression. *Int. J. Nanomedicine* 15, 5289–5298. doi:10.2147/IJN.S261298

Song, K. H., Heo, S. J., Peredo, A. P., Davidson, M. D., Mauck, R. L., and Burdick, J. A. (2020). Influence of fiber stiffness on meniscal cell migration into dense fibrous networks. *Adv. Healthc. Mat.* 9 (8), e1901228. doi:10.1002/adhm.201901228

Sorushanova, A., Delgado, L. M., Wu, Z., Shologu, N., Kshirsagar, A., Raghunath, R., et al. (2019). The collagen suprafamily: From biosynthesis to advanced biomaterial development. *Adv. Mat.* 31 (1), e1801651. doi:10.1002/adma.201801651

Stabile, K. J., Odom, D., Smith, T. L., Northam, C., Whitlock, P. W., Smith, B. P., et al. (2010). An acellular, allograft-derived meniscus scaffold in an ovine model. *Arthrosc. J. Arthrosc. Relat. Surg.* 26 (7), 936–948. doi:10.1016/j.arthro.2009.11.024

Stein, S. E. C., von Luebken, F., Warnecke, D., Gentilini, C., Skaer, N., Walker, R., et al. (2019b). The challenge of implant integration in partial meniscal replacement: An experimental study on a silk fibroin scaffold in sheep. *Knee Surg. Sports Traumatol. Arthrosc.* 27 (2), 369–380. doi:10.1007/s00167-018-5160-7

Stein, S., Höse, S., Warnecke, D., Gentilini, C., Skaer, N., Walker, R., et al. (2019a). Meniscal replacement with a silk fibroin scaffold reduces contact stresses in the human knee. *J. Orthop. Res.* 37 (12), 2583–2592. doi:10.1002/jor.24437

Stone, K. R., Steadman, J. R., Rodkey, W. G., and Li, S. T. (1997). Regeneration of meniscal cartilage with use of a collagen scaffold. Analysis of preliminary data. *J. Bone Jt. Surg.* 79 (12), 1770–1777. doi:10.2106/00004623-199712000-00002

Stoppel, W. L., Ghezzi, C. E., McNamara, S. L., Black, L. D., 3rd, and Kaplan, D. L. (2015). Clinical applications of naturally derived biopolymer-based scaffolds for regenerative medicine. *Ann. Biomed. Eng.* 43 (3), 657–680. doi:10.1007/s10439-014-1206-2

Sultankulov, B., Berillo, D., Sultankulova, K., Tokay, T., and Saparov, A. (2019). Progress in the development of chitosan-based biomaterials for tissue engineering and regenerative medicine. *Biomolecules* 9 (9), 470. doi:10.3390/biom9090470

Swinehart, I. T., and Badylak, S. F. (2016). Extracellular matrix bioscaffolds in tissue remodeling and morphogenesis. *Dev. Dyn.* 245 (3), 351–360. doi:10.1002/dvdy.24379

Tan, G. K., Dinnes, D. L., Butler, L. N., and Cooper-White, J. J. (2010). Interactions between meniscal cells and a self assembled biomimetic surface composed of hyaluronic acid, chitosan and meniscal extracellular matrix molecules. *Biomaterials* 31 (23), 6104–6118. doi:10.1016/j.biomaterials.2010.04.018

Tanaka, T., Furumatsu, T., Miyazawa, S., Fujii, M., Inoue, H., Kodama, Y., et al. (2017). Hyaluronan stimulates chondrogenic gene expression in human meniscus cells. *Connect. Tissue Res.* 58 (6), 520–530. doi:10.1080/03008207.2016.1264944

Thurber, A. E., Omenetto, F. G., and Kaplan, D. L. (2015). *In vivo* bioresponses to silk proteins. *Biomaterials* 71, 145–157. doi:10.1016/j.biomaterials.2015.08.039

Uebersax, L., Apfel, T., Nuss, K. M., Vogt, R., Kim, H. Y., Meinel, L., et al. (2013). Biocompatibility and osteoconduction of macroporous silk fibroin implants in cortical defects in sheep. *Eur. J. Pharm. Biopharm.* 85 (1), 107–118. doi:10.1016/j.ejpb.2013.05.008

van de Graaf, V. A., Noorduyn, J. C. A., Willigenburg, N. W., Butter, I. K., de Gast, A., Mol, B. W., et al. (2018). Effect of early surgery vs physical therapy on knee function among patients with nonobstructive meniscal tears: The ESCAPE randomized clinical trial. *JAMA* 320 (13), 1328–1337. doi:10.1001/jama.2018.13308

Varma, S., Orgel, J. P., and Schieber, J. D. (2016). Nanomechanics of type I collagen. *Biophys. J.* 111 (1), 50–56. doi:10.1016/j.bpj.2016.05.038

Venjakob, A. J., Föhr, P., Henke, F., Tischer, T., Sandmann, G. H., Blanke, F., et al. (2019). Influence of sutures on cartilage integrity: Do meniscus sutures harm cartilage? An experimental animal study. *Arthrosc. J. Arthrosc. Relat. Surg.* 35 (5), 1509–1516. doi:10.1016/j.arthro.2018.11.040

Veronesi, F., Di Matteo, B., Vitale, N. D., Filardo, G., Visani, A., Kon, E., et al. (2021). Biosynthetic scaffolds for partial meniscal loss: A systematic review from animal models to clinical practice. *Bioact. Mat.* 6 (11), 3782–3800. doi:10.1016/j.bioactmat.2021.03.033

Wang, S. J., Jiang, D., Zhang, Z. Z., Huang, A. B., Qi, Y. S., Wang, H. J., et al. (2016). Chondrogenic potential of peripheral blood derived mesenchymal stem cells seeded on demineralized cancellous bone scaffolds. *Sci. Rep.* 6, 36400. doi:10.1038/srep36400

Wang, Y., Wang, F., Xu, S., Wang, R., Chen, W., Hou, K., et al. (2019). Genetically engineered bi-functional silk material with improved cell proliferation and anti-inflammatory activity for medical application. *Acta Biomater.* 86, 148–157. doi:10.1016/j.actbio.2018.12.036

Warnecke, D., Schild, N. B., Klose, S., Joos, H., Brenner, R. E., Kessler, O., et al. (2017). Friction properties of a new silk fibroin scaffold for meniscal replacement. *Tribol. Int.* 109, 586–592. doi:10.1016/j.triboint.2017.01.038

Warnecke, D., Stein, S., Haffner-Luntzer, M., de Roy, L., Skaer, N., Walker, R., et al. (2018). Biomechanical, structural and biological characterisation of a new silk fibroin scaffold for meniscal repair. *J. Mech. Behav. Biomed. Mat.* 86, 314–324. doi:10.1016/j.jmbbm.2018.06.041

Warth, R. J., and Rodkey, W. G. (2015). Resorbable collagen scaffolds for the treatment of meniscus defects: A systematic review. *Arthrosc. J. Arthrosc. Relat. Surg.* 31 (5), 927–941. doi:10.1016/j.arthro.2014.11.019

Watt, F. M., and Huck, W. T. (2013). Role of the extracellular matrix in regulating stem cell fate. *Nat. Rev. Mol. Cell. Biol.* 14 (8), 467–473. doi:10.1038/nrm3620

Wu, J., Ding, Q., Dutta, A., Wang, Y., Huang, Y. H., Weng, H., et al. (2015). An injectable extracellular matrix derived hydrogel for meniscus repair and regeneration. *Acta Biomater.* 16, 49–59. doi:10.1016/j.actbio.2015.01.027

Wubneh, A., Tsekoura, E. K., Ayranci, C., and Uludağ, H. (2018). Current state of fabrication technologies and materials for bone tissue engineering. *Acta Biomater.* 80, 1–30. doi:10.1016/j.actbio.2018.09.031

Yan, R., Chen, Y., Gu, Y., Tang, C., Huang, J., Hu, Y., et al. (2019). A collagen-coated sponge silk scaffold for functional meniscus regeneration. *J. Tissue Eng. Regen. Med.* 13 (2), 156–173. doi:10.1002/term.2777

Yang, Q., Teng, B. H., Wang, L. N., Li, K., Xu, C., Ma, X. L., et al. (2017). Silk fibroin/cartilage extracellular matrix scaffolds with sequential delivery of TGF-β3 for chondrogenic differentiation of adipose-derived stem cells. *Int. J. Nanomedicine* 12, 6721–6733. doi:10.2147/IJN.S141888

Ying, X. Z., Qian, J. J., Peng, L., Zheng, Q., Zhu, B., and Jin, Y. H. (2018). Model research on repairing meniscus injury in rabbits using bone marrow mesenchymal stem cells and silk fibroin meniscus porous scaffold. *Eur. Rev. Med. Pharmacol. Sci.* 22 (12), 3689–3693. doi:10.26355/eurrev_201806_15247

Yuan, X., Wei, Y., Villasante, A., Ng, J. J. D., Arkonac, D. E., Chao, P.-h. G., et al. (2017). Stem cell delivery in tissue-specific hydrogel enabled meniscal repair in an orthotopic rat model. *Biomaterials* 132, 59–71. doi:10.1016/j.biomaterials.2017.04.004

Yuan, Z., Liu, S., Hao, C., Guo, W., Gao, S., Wang, M., et al. (2016). AMECM/DCB scaffold prompts successful total meniscus reconstruction in a rabbit total meniscectomy model. *Biomaterials* 111, 13–26. doi:10.1016/j.biomaterials.2016.09.017

Yun, H. W., Song, B. R., Shin, D. I., Yin, X. Y., Truong, M. D., Noh, S., et al. (2021). Fabrication of decellularized meniscus extracellular matrix according to inner cartilaginous, middle transitional, and outer fibrous zones result in zone-specific protein expression useful for precise replication of meniscus zones. *Mater. Sci. Eng. C* 128, 112312. doi:10.1016/j.msec.2021.112312

Zhang, Q., Wei, X., Ji, Y., Yin, L., Dong, Z., Chen, F., et al. (2020). Adjustable and ultrafast light-cured hyaluronic acid hydrogel: Promoting biocompatibility and cell growth. *J. Mat. Chem. B* 8 (25), 5441–5450. doi:10.1039/c9tb02796c

Zhang, Y., Liu, X., Zeng, L., Zhang, J., Zuo, J., Zou, J., et al. (2019). Polymer fiber scaffolds for bone and cartilage tissue engineering. *Adv. Funct. Mat.* 29 (36), 1903279. doi:10.1002/adfm.201903279

Zhong, G., Yao, J., Huang, X., Luo, Y., Wang, M., Han, J., et al. (2020). Injectable ECM hydrogel for delivery of BMSCs enabled full-thickness meniscus repair in an orthotopic rat model. *Bioact. Mat.* 5 (4), 871–879. doi:10.1016/j.bioactmat.2020.06.008

Zimny, M. L., Albright, D. J., and Dabezies, E. (1988). Mechanoreceptors in the human medial meniscus. *Cells Tissues Organs* 133 (1), 35–40. doi:10.1159/000146611

frontiers | Frontiers in Bioengineering and Biotechnology

TYPE Original Research
PUBLISHED 05 October 2022
DOI 10.3389/fbioe.2022.994925

OPEN ACCESS

EDITED BY
He Liu,
Jilin University, China

REVIEWED BY
Jinshan Guo,
Southern Medical University, China
Bo Lu,
Wuhan University of Technology, China
Chengcheng Yin,
China Medical University, China
Fu Yin Hsu,
National Taiwan Ocean University, Taiwan

*CORRESPONDENCE
Zhihua Li,
lizhihua@ncu.edu.cn
Junchao Wei,
weijunchao@ncu.edu.cn

SPECIALTY SECTION
This article was submitted to Biomaterials, a section of the journal Frontiers in Bioengineering and Biotechnology

RECEIVED 15 July 2022
ACCEPTED 13 September 2022
PUBLISHED 05 October 2022

CITATION
Yao H, Luo J, Deng Y, Li Z and Wei J (2022), Alginate-modified mesoporous bioactive glass and its drug delivery, bioactivity, and osteogenic properties. *Front. Bioeng. Biotechnol.* 10:994925. doi: 10.3389/fbioe.2022.994925

Alginate-modified mesoporous bioactive glass and its drug delivery, bioactivity, and osteogenic properties

Haiyan Yao[1,2,3], Jun Luo[1,3,4], Yunyun Deng[1,3], Zhihua Li[1,3,4]* and Junchao Wei[1,2,3,4]*

[1]School of Stomatology, Nanchang University, Nanchang, China, [2]College of Chemistry, Nanchang University, Nanchang, China, [3]Jiangxi Province Key Laboratory of Oral Biomedicine, Nanchang, China, [4]Jiangxi Province Clinical Research Center for Oral Disease, Nanchang, China

Mesoporous bioactive glass (MBG) is widely used in bone tissue repairing and drug loading. However, burst release of drug and poor compatibility with other materials limited its application. It is an effective way to modify MBG with a polymer brush to improve the properties. Herein, an alginate-modified MBG was prepared, and then, the effects of ALG on the properties of MBG were investigated. The results demonstrate that ALG could improve the drug loading efficiency, prolong drug release times, and make orderly deposition of apatite on the surface of MBG. Furthermore, MBG@ALG significantly promoted the osteogenic differentiation of MC3T3-E1 cells, demonstrating that surface modification of MBG by ALG can improve its properties, which will further broaden the application of MBG in tissue engineering.

KEYWORDS

mesoporous bioactive glass, surface modification, alginate, drug loading, bone regeneration

1 Introduction

Bioactive glass (BG) is widely used in bone tissue engineering scaffold (Vallet-Regi and Salinas, 2021) and polymer composites for bone regeneration (Zhao et al., 2021) due to its excellent biocompatibility and osteogenic properties. Mesoporous bioactive glass (MBG) not only possesses the advantages of BG but also showed superior *in vitro* bone-forming bioactivities (Rahaman et al., 2011; Schumacher et al., 2021), high porosity, and specific surface area. Therefore, MBG has been widely used as a drug delivery system (Lopez-Noriega et al., 2010) for the treatment of bone tissue diseases; for example, various functional molecules, such as small molecule drugs (alendronate) (Ravanbakhsh et al., 2019) and growth factors (BMP-2, VEGF) have been loaded into MBG (Kim et al., 2016; Schumacher et al., 2017). However, the poor binding ability with other materials (Kargozar et al., 2019), burst release of drugs, and easy formation of protein crowns in biological media (Pontremoli et al., 2020; Sharifi et al., 2022) have limited the application of MBG. Therefore, it is of much importance to tailor the properties of MBG to improve its applications.

The surface of nanomaterials play critical roles in many physical and chemical processes, while the surface ligands or molecules binding to the surface are essential components of nanomaterials and affect its interactions with other materials or biological systems (Kango et al., 2013; Boles et al., 2016), and thus many works have been carried out to tune the surface of nanomaterials with organic ligands and polymer brushes (Boles et al., 2016; Heinz et al., 2017). As for MBG, the surface molecules or polymer brushes may work as gatekeepers and tune its drug delivery ability, for example, various molecules, such as 3-aminopropyltrimethoxysilane (Wang et al., 2018) and poly-L-glutamic acid (Das et al., 2021) have been used to enhance its drug loading efficiency and prolong the drug release time. In addition, the surface polymer brushes may have great effect on the bioactivity of MBG (Kargozar et al., 2019), which will greatly affect the biomineralization of the apatite and the binding ability of MBG to tissues. For example, poly (amidoamine) (PAMAM) dendrimer-coated mesoporous bioactive glass nanoparticles (MBG) (PAMAM@MBG) were prepared and used for treatment of dentine hypersensitivity (Bae et al., 2019), while the results demonstrated that the PAMAM@MBG had excellent mineralization ability and showed a better occluding effect for dentinal tubules than that of MBG. In addition, the surface modification of nanomaterials improves the phase compatibility between nanomaterials and polymer matrix, and thus improves the mechanical properties of polymer composites (Kango et al., 2013). For instance, polydopamine has been coated on the surface of MBG, which greatly improves the mechanical properties of MBG/PLLA scaffolds (Xu et al., 2018). Generally, it has been an effective method to graft polymers or organic molecules on the surface of MBG to improve its charming properties. However, it is still a great challenge to modify the surface of MBG with mild conditions and improve multiple performances of MBG simultaneously.

Alginate (ALG) is an anionic polymer with good biocompatibility and low toxicity, and has been widely applied in biomedical applications (Lee and Moone, 2012). ALG can be tethered on the surface of nanomaterials to improve the colloidal stability of various nanobuilding blocks. For example, ALG-modified SiO_2 (Yan et al., 2019), carbon nanotubes (Yao et al., 2021), and upconversion nanoparticles (Cao et al., 2020) show good colloidal stability and biocompatibility. Furthermore, the ALG molecules can also reduce protein adsorption to nanomaterials and inhibit the formation of protein crowns. Mooney's group prepared cysteine-functionalized ALG--derived polymers as stabilizers to coat the surface of gold nanoparticles (GNPs), which increase the stability of the GNPs and reduce the adsorption of proteins on GNPs (Kodiyan et al., 2012). In addition, ALG has immunomodulatory effect, which can accelerate the wound healing by promoting the anti-inflammatory polarization of macrophages (Bygd and Bratlie, 2016; Kerschenmeyer et al., 2017). In addition, the ALG polymers contain multiple reactive groups, such as hydroxyl and carboxyl groups, which could be an ideal candidate for the further functionalization of materials with special functions, for example, cell targeting ligands and therapeutic drugs (Ahmad Raus et al., 2021). Therefore, it is definite that ALG as a polymer brush can greatly alter the biological properties of nanomaterials. Herein, if ALG was combined with MBG, the advantages of both the materials may have synergistic effect and realize the improvements of the multifunction of MBG.

In this work, ALG was grafted on MBG (MBG@ALG) *via* a simple method (Figure 1), and all the reactions were conducted at mild temperature and no toxic solvents were used. In addition, the method is universal and can be used to modify the surface of other kinds of nanomaterials and improve their properties. In addition, the effect of ALG on drug loading efficiency, bioactivity, biocompatibility, and osteogenic properties of MBG were investigated. The results demonstrated that ALG brush can enhance drug loading efficiency, prolong drug release time, promote the orderly deposition of apatite, and improve osteogenic performance of MBG, having a positive effect to improve the performance of MBG and broaden its application in bone tissue engineering.

2 Materials and methods

2.1 Materials

Hexadecyl trimethyl ammonium bromide (CTAB, 98%), tetraethyl orthosilicate (TEOS), triethyl phosphate (TEP), calcium nitrate tetrahydrate ($Ca(NO_3)_2.4H_2O$), ammonium hydroxide ($NH_3.H_2O$), and ethanol were purchased from Sinopharm Chemical Reagent Co., Ltd. (Shanghai, China.). Sodium alginate (ALG, the viscosity of ALG (1%, Brookfield LV, 20°C) is 350–550 cP), 3-aminopropyltrimethoxysilane (APTES), ethyl-3-(3-dimethylaminopropyl) carbodiimide hydrochloride (EDC), N-hydroxysuccinimide (NHS, 98%), and sodium alginate (98%) were purchased from Aladdin Scientific Co., Ltd. (Shanghai, China). Acridine orange/ethidium bromide was purchased from BestBio Co., Ltd. (Shanghai, China). The MTT kit and Alkaline Phosphatase Color Development Kit were purchased from Beyotime Co., Ltd. (Shanghai, China). Alizarin Red S (ARS) staining was purchased from Solarbio Co., Ltd. (Beijing, China).

2.2 Methods

2.2.1 Preparation of MBG@ALG

First, MBG was synthesized by a reported method (Ravanbakhsh et al., 2019). Briefly, 0.7 g of CTAB was dissolved in 33 ml of water under stirring, and then 10 ml of

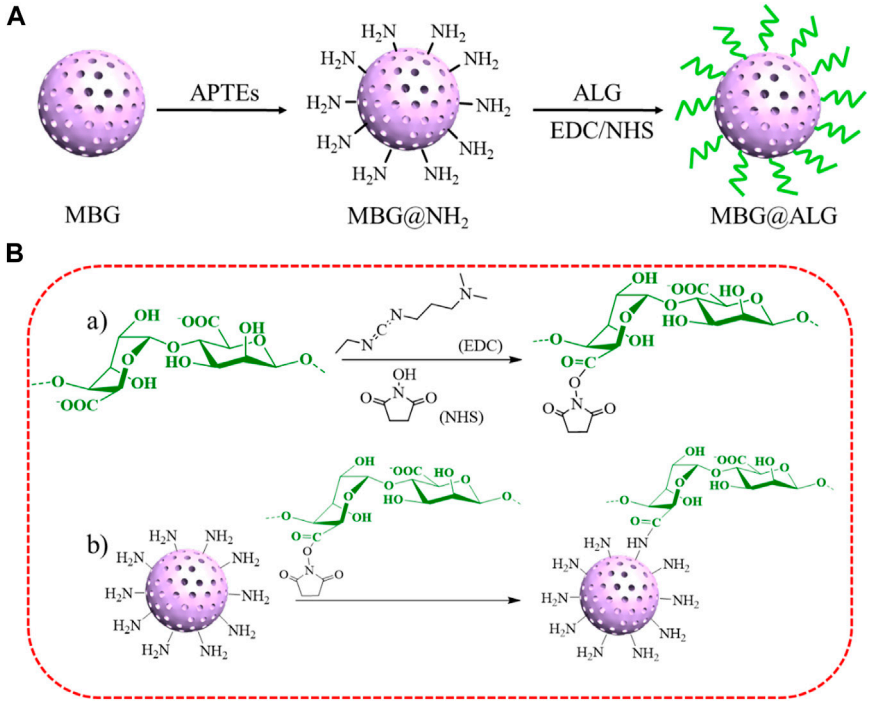

FIGURE 1
Schematic illustration of the construction of MBG@ALG **(A)** and reaction scheme **(B)**.

ethyl acetate was added. 30 min later, 7 ml of aqueous ammonia (3 mol. L^{-1}) was added. 15 min later, 3.6 ml of TEOS, 0.36 ml of TEP, and 2.277 g of $Ca(NO_3)_2.4H_2O$ were sequentially added to the abovementioned mixture at every 30 min interval. The solution was vigorously stirred for another 4 h, the precipitate was collected by centrifugation, and then washed three times with ethanol and water in turn. The raw product was dried at 60°C for 24 h and then calcined at 650°C for 6 h to obtain MBG.

Second, 0.3 g of MBG and 0.6 ml of APTES were added in 100 ml of ethanol, and then the mixed solution was refluxed at 80°C for 24 h. The precipitate was collected by centrifugation, washed three times with ultrapure water, and freeze-dried to obtain $MBG@NH_2$.

Third, 0.25 g of ALG was dissolved in 50 ml of water and stirred for 24 h, then 0.2399 g of EDC and 0.1439 g of NHS were added in the solution and stirred for 2 h. 0.25 g of $MBG@NH_2$ was added in the abovementioned solution and stirred for 24 h and then centrifuged and washed with deionized water and lyophilized.

2.2.2 Characterization

The weight loss of different samples was measured by using a thermal gravimetric analyzer (TGA, Perkin Elmer, TGA 4000, United States). The crystalline structure was measured on X-ray diffraction (XRD, SmartLab 9 KW, Japan). The morphology of different samples was observed using a transmission electron microscope (TEM, JEOL, JEM-2100, Japan) and scanning electron microscope (SEM, Thermo Fisher Scientific, Apero C HiVac, United States).

2.2.3 Drug loading and release

Simvastatin (SIM) was used as a model drug. Briefly, 10 mg of MBG and MBG@ALG was dispersed in 10 ml of ethanol, and 5 mg of SIM was added and stirred for 24 h, respectively. Then, the supernatant was centrifuged and the absorbance value at 238 nm of the supernatant was measured. The mass of SIM in the supernatant was calculated using the measured SIM standard curve. The loading efficiency (%) and drug content (%) were calculated using the following formula:

$$\text{Loading efficiency (\%)} = (\text{weight of drug in MBG}/\text{initial weight of drug}) \times 100\%,$$

$$\text{Drug content (\%)} = (\text{weight of drug in MBG}/\text{weight of MBG}) \times 100\%.$$

in vitro drug release of SIM from MBG and MBG@ALG was performed by the dialysis bag diffusion method. 2 mg of MBG and MBG@ALG loaded with SIM was suspended in 2 ml of phosphate-buffered saline (PBS, pH7.4) and introduced into the dialysis bag. The dialysis bag was kept at 30 ml of PBS containing 20% ethanol and transferred to constant temperature shaker. At each time point (1, 3, 12, 24, 24, 48, and 96 h), 2 ml of the release medium was taken out and replaced with equal amounts of fresh medium. The amount of released SIM was evaluated by ultraviolet-visible (UV) analysis at a wavelength of 238 nm.

2.2.4 Bioactivity test in simulated body fluids

An SBF (simulated body fluid) solution was first prepared according a reported method (Kokubo and Takadama, 2006), and then 20 mg of MBG and MBG@ALG powder were soaked in 20 ml of SBF at 37°C for 7 days in a shaking incubator. The SBF was refreshed every 24 h. Then, SEM was conducted to evaluate apatite formation.

2.2.5 Biocompatibility test

The samples were irradiated under UV for 2 h, and then added into a culture medium. The concentration was diluted with a culture medium to 500, 250, 125, 50, and 25 μg/ml 100 μl of the culture medium containing MC3T3-E1 cells at a density of 8×10^4 cells/mL were seeded into a 96-well plate and incubated for 24 h for cell attachment. Subsequently, the culture media was replaced with 100 μl of materials at concentrations of 500, 250, 125, 50, and 25 μg/ml. After the cells were coincubated with nanoparticles for 24 h, the medium was sucked out and PBS was added for washing several times, then the MTT reagent (10 μl) mixed with 100 μl of fresh medium was added to each well. After 4 h of incubation, the medium was removed and 150 μl of DMSO was added to fully dissolve the formazan, and then the OD value at 490 nm was measured.

AO/EB (Acridine Orange/Ethidium Brmide) staining was used to further detect the apoptosis of MC3T3-E1 cells. 100 μl of culture media containing MC3T3-E1 cells at a density of 8×10^4 cells/mL were seeded into a 96 plate and incubated at 37°C under atmosphere of 5% CO_2 for 24 h. Subsequently, the culture media was replaced with 100 μl of fresh medium containing samples at various concentrations of 500, 250, 125 μg/ml. After 24 h co-incubation, fresh medium was used to wash each well several times, and then AO/EB reagent was added to each well for 30 s. Finally, the survival of cells was observed by fluorescence microscopy.

2.2.6 Osteogenesis differentiation

100 μl of culture media containing MC3T3-E1 cells at a density of 1×10^4 cells/mL were seeded into a 96-well plate and incubated at 37°C under atmosphere of 5% CO_2 for 24 h. Subsequently, the culture media was replaced with 100 μl of medium containing samples at concentrations of 250 μg/ml. After 7 and 14 days, PBS was used to wash the plate several times, and the cells were fixed with 4% paraformaldehyde for 30 min. Then, the cells were stained with Alkaline Phosphatase (ALP) Color Development Kit and Alizarin Red S (ARS) Staining.

3 Results and discussion

3.1 Characterization of different samples

MBG was spherical, mono-dispersed, and porous particles (Figures 2A,B), the diameter of MBG was 222 ± 19 nm (Figure 2C). When ALG was grafted on the surface of MBG, a polymer coating could be clearly observed on the surface of MBG (Figures 2D,E), and the mean diameter of the MBG@ALG was 232 ± 22 nm (Figure 2F), which demonstrated that ALG was successfully grafted onto the MBG surface.

In the FT-IR spectrum of MBG, the peaks at 1,080 cm^{-1}, 806 cm^{-1}, and 1,633 cm^{-1} (Figure 3A) were ascribed to Si–O–Si, O–Si–O, and Si–OH bands, respectively (Yan et al., 2017). For the spectrum of MBG@ALG, a new peak located at 944 cm^{-1} was corresponded to the C–O stretching, which was derived from ALG (Ding et al., 2021), demonstrating that ALG was successfully anchored onto MBG. The XRD patterns displays a wide-angle diffraction peak centered at $2\theta = 20.4^{\circ}$, which was attributed to the amorphous nature of pristine MBG. After ALG was grafted, the wide-angle diffraction peak did not change, which is in consistence with the pattern of MBG (Figure 3B), demonstrating that the original crystalline structure of MBG remains unaltered after ALG surface modification. The TGA results showed that the weight loss of MBG@ALG was 24.7%, which consist of 5.2% weight loss of absorbed solvent before 150°C and 19.5% weight loss of the ALG between 150 and 800°C (Figure 3C). The 13.4% weight loss of MBG was due to the absorption of the solvent. The results show that the ALG coating was successfully prepared on the MBG surface.

The N_2 adsorption isotherms and pore size distribution of MBG, MBG@NH_2, and MBG@ALG demonstrated the characteristic of mesoporous (Figure 4). The surface area, pore volume, and pore diameter of MBG were 196 m^2/g, 0.55 cm^3/g, and 11.3 nm (Table 1), respectively. After being treated with APTES, the surface area, pore volume, and pore diameter showed some changes, and the corresponding results of MBG@NH_2 were found to be 171 m^2/g, 0.458 cm^3/g, and 10.7nm, respectively. When ALG polymer chains were grated with MBG@NH_2, evident changes of the surface area, pore volume, and pore diameter of MBG@ALG were found, and the results were 162 m^2/g, 0.427 cm^3/g, and 10.5 nm (Table 1), respectively, much smaller than that of MBG, further demonstrating that ALG was successfully grafted on the surface and have an evident affection on its physical properties.

3.2 Drug loading and release assays

The surface can significantly alter the drug loading efficiency and the drugs release time, and various surface molecules are found to be very useful for improving drug delivery (Cui et al., 2020). SIM was selected as a model drug, the loading efficiency of MBG was 24.5% (Xiao et al., 2019a; Xiao et al., 2019b). After ALG polymer chains were grated on the MBG, the loading efficiency was found to be improved, and the result was 31.2% (Figure 5A). The drug content of MBG and MBG@ALG was 12.2% and 15.6%, respectively (Figure 5B). The results demonstrated that ALG polymer chains can significantly improve the drug loading efficiency of MBG.

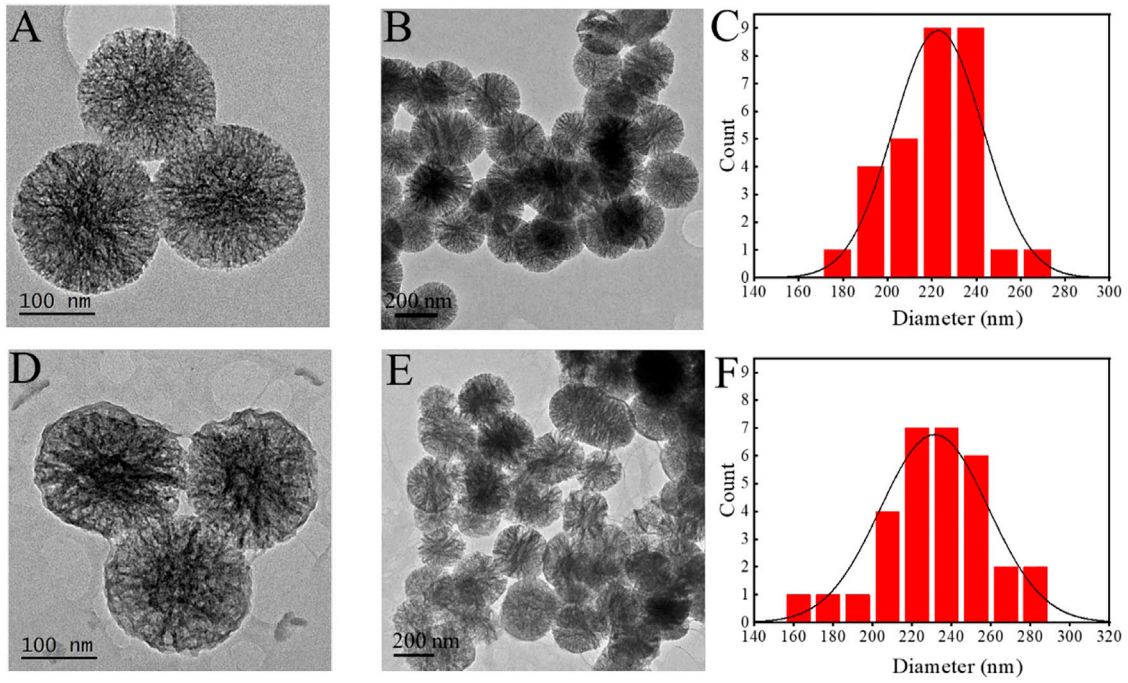

FIGURE 2
TEM images of MBG **(A,B)** and MBG@ALG **(D,E)**. Particle size analysis of MBG **(C)** and MBG@ALG **(F)**.

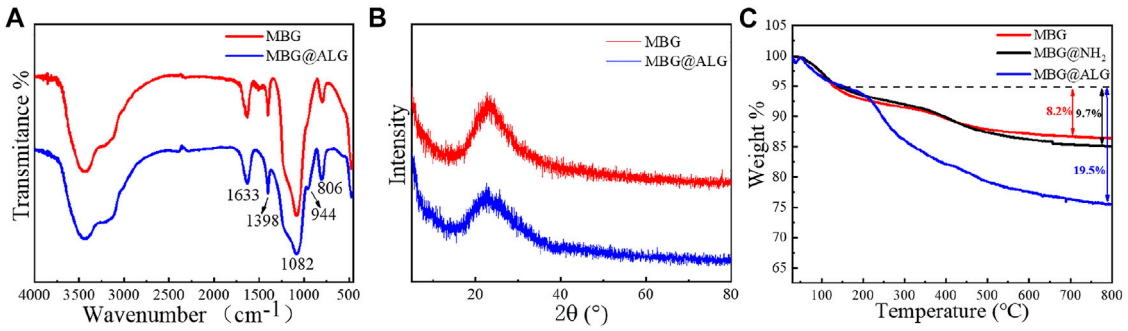

FIGURE 3
(A) FTIR spectra of MBG and MBG@ALG, **(B)** XRD patterns of MBG and MBG@ALG, and **(C)** TGA curve of MBG, MBG@NH_2, and MBG@ALG.

The drug release curves of MBG and MBG@ALG can be divided into three stages (Figure 5C). In the first stage, a burst release could be observed in the curves of MBG and MBG@ALG, which can be ascribed to the adsorbed SIM on the surface of MBG and MBG@ALG, rapidly diffusing into the solution. In the second stage, the release velocity of the SIM was significantly lower than that of the first stage, while this period of drug release is resulted from the SIM molecules which have entered the mesoporous channel, and therefore it takes a long time for the drug molecules to diffuse into the solution. However, when compared with the drug release curves in the second stage, it can be found that the release rate of SIM from MBG is faster than that of MBG@ALG. This is because the ALG polymer chains on the surface of MBG@ALG can hinder the diffusion of the SIM. In the third stage (after 48 h), the drug release rate decays to nearly zero, which means that, in this stage the drug diffusion and drug adsorption is dynamically balanced.

Furthermore, as shown in Figure 5C, in the second stage, there was an evident linear region both in the curves of MBG and MBG@ALG (shown in the rectangle), the drug release rate is

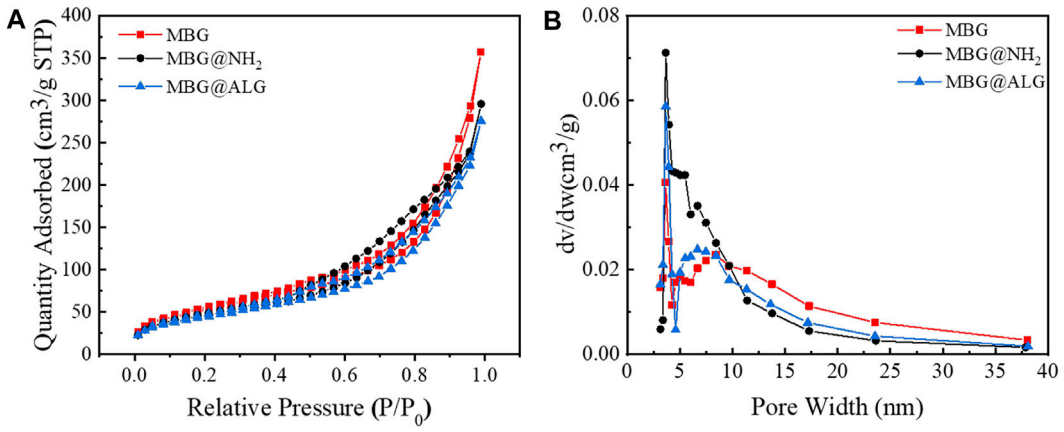

FIGURE 4
N_2 adsorption–desorption isotherms **(A)** and pore-size distribution **(B)** of MBG, MBG@NH_2, and MBG@ALG.

TABLE 1 Summary of the including specific surface area, pore volume, and pore size as determined from N_2 adsorption–desorption isotherms.

Sample	Specific surface area (m^2/g)	Pore volume (cm^3/g)	Pore size (nm)
MBG	196	0.552	11.3
MBG@NH2	171	0.458	10.7
MBG@ALG	162	0.427	10.5

linear with time, which is consistent with the zero-order kinetics (Marcos Luciano, 2015). In addition, on considering the porous structure of MBG and MBG@ALG, we try to use the Higuchi model to describe the release of SIM, the relationship between drug release amount and the square root of time was calculated and shown in Figure 5D, showing linear relationships and equations, implying that the release profiles can be explained *via* the Higuchi model, and this result is also consistent with the published work about MBG (Xiao et al., 2019a; Zhu and Stefan, 2019). All these results may demonstrate that ALG modification can improve the drug loading efficiency of MBG and prolong the drug release time without affecting its release mechanism.

3.3 *In vitro* bioactivity

The surface ligands have great influence on mineral deposition, such as defining the mineral-deposition site and affecting the morphology of apatite (Meldrum F, 2008; Gordon and Joester, 2011). The SEM images showed both MBG and MBG@ALG are spherical nanoparticles with a particle size of about 200 nm (Figures 6A,B). After treated in SBF, many irregular apatite plates are formed around MBG (Figure 6C), which may be that the released Ca^{2+} increases the concentration of Ca^{2+} around MBG, inducing nucleation and the growth of apatite. Generally, due to the biodegradation ability of MBG, when the MBG samples were immersed into the SBF solution, the mineralization behaviors also happens and this may be a dissolve-regrowth scheme. After the ALG polymer chains were grafted on MBG, compared with MBG that treated with SBF for 7 days, a regular and tightly arranged plate structure can be observed on the surface of the MBG@ALG (Figure 6D). Since SBF were used as a mineralization medium, the ALG can chelate Ca^{2+} from the solution and induce nucleation as crystal seed, therefore, orderly growth of apatite on the surface of MBG@ALG formed, in addition, the amount of plate apatite of MBG@ALG (Figure 6D) is much more than that of MBG (Figure 6C), demonstrating that grafting of ALG can control the morphology and accelerate the mineralization of apatite, which may broaden the application of MBG in bone tissue engineering.

3.4 Biocompatibility test of MBG and MBG@ALG

MBG and MBG@ALG show excellent biocompatibility, even when the concentration of the materials reached to 500 μg/ml.

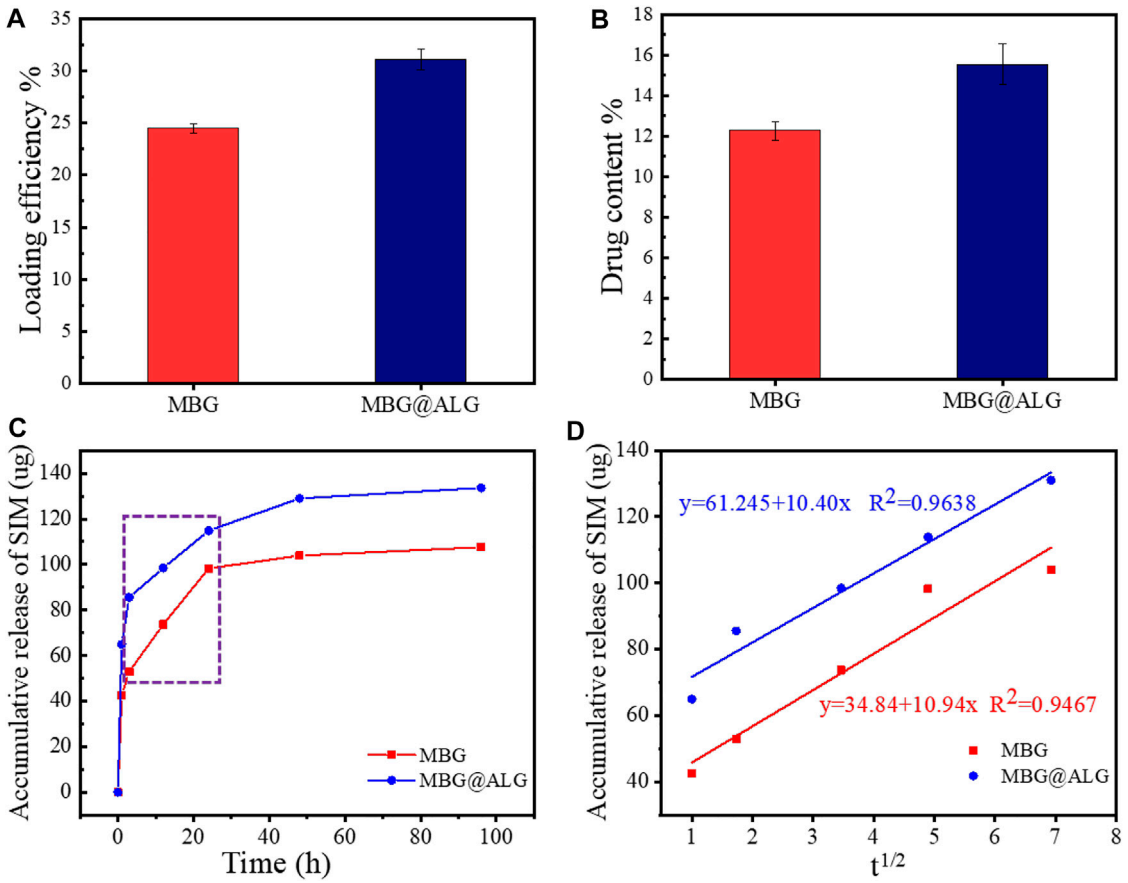

FIGURE 5
(A) Loading efficiency of MBG and MBG@ALG, **(B)** drug content of MBG and MBG@ALG, **(C)** release curves of MBG and MBG@ALG, and **(D)** the linear relationship between drug release and the square root of release time at the Higuchi model release phase.

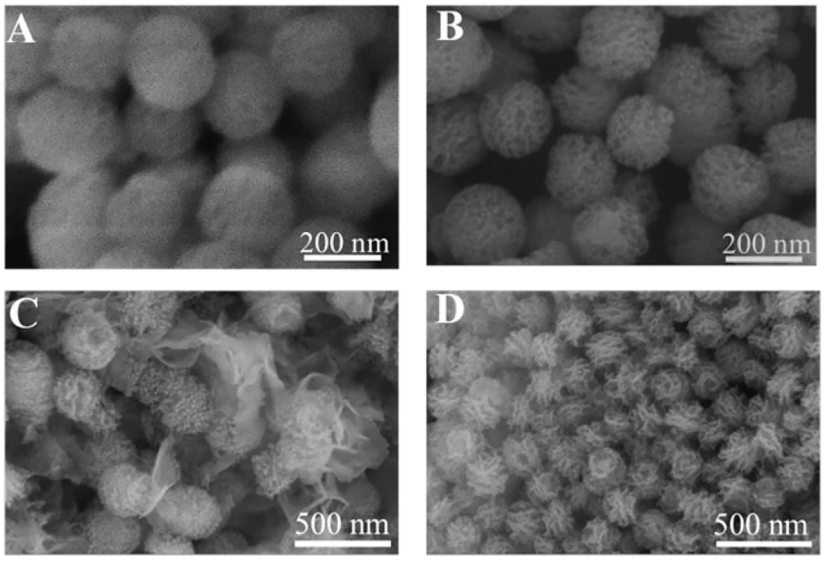

FIGURE 6
SEM image of MBG **(A)** and MBG@ALG **(B)**. SEM image of MBG **(C)** and MBG@ALG **(D)** after treated with SBF for 7 days.

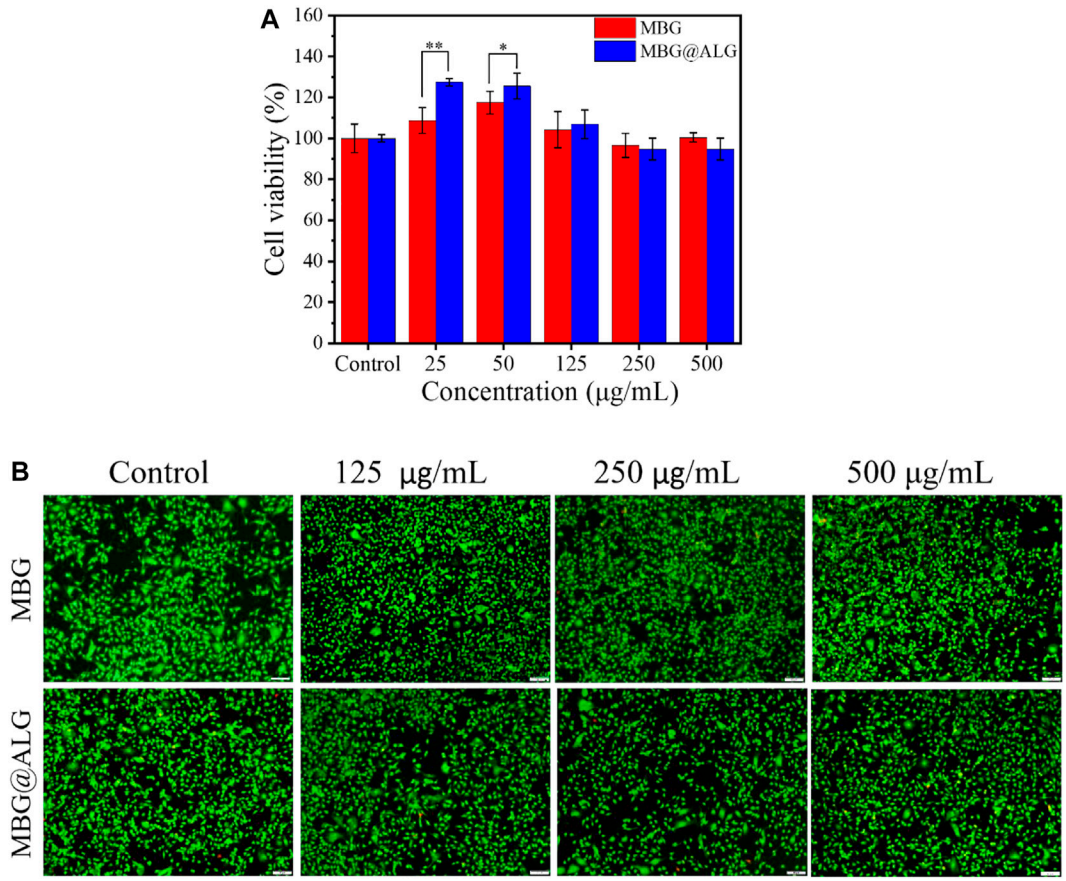

FIGURE 7
(A) Cell viability of MC3T3-E1 cells after being cocultured with MBG and MBG@ALG. **(B)** AO/EB staining fluorescence images of MC3T3-E1 cells after being cocultured with MBG and MBG@ALG. (Bar = 100 μm n = 5, *$p < 0.05$, **$p < 0.01$)

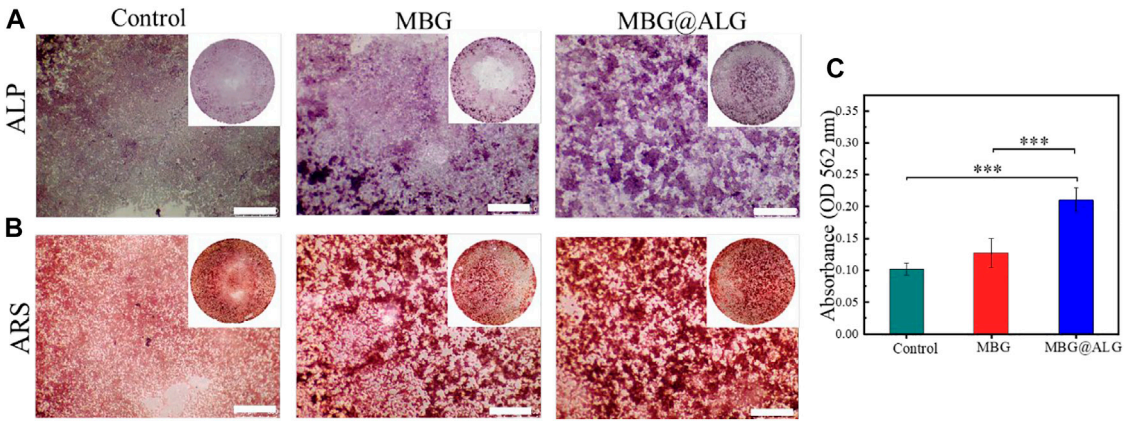

FIGURE 8
(A) ALP staining after MC3T3-E1 cell was cocultured with MBG and MBG@ALG for 7 days. **(B)** ARS staining after MC3T3-E1 cell was cocultured with MBG and MBG@ALG for 14 days. **(C)** ARS staining quantification after 14 days. (Bar = 500 μm, ***$p < 0.001$)

When the concentration was 25 μg/ml, the cell viability of MBG and MBG@ALG was 108% and 127%, respectively. At the concentration of 50 μg/ml, the cell viability of MBG and MBG@ALG was 117% and 125% (Figure 7A), respectively. These indicate that MBG and MBG@ALG can significantly promote cell proliferation at low concentrations, and the cell viability of MBG@ALG is significantly higher than that of MBG at the same concentration. When the concentration of MBG was 100 , 250 , and 500 μg/ml, the cell viability was 104%, 96%, and 100%, respectively. When the concentration of MBG@ALG was 100 , 250 , and 500 μg/ml, the cell viability was 107%, 94%, and 95%, respectively (Figure 7A). MBG and MBG@ALG showed good compatibility at these concentrations, and the effects of MBG and MBG@ALG on cell viability at these concentrations were not significantly different.

AO/EB staining further verified the excellent biocompatibility of MBG@ALG (Figure 7B). The cells survived well after being cocultured with the material (green fluorescence), with only a few apoptotic cells (red fluorescence). These results of MBG@ALG was biocompatible and can promote cell proliferation at low concentrations.

3.5 Osteogenesis differentiation of MC3T3-E1 cells

MBG has good osteoconductivity and osteoinductive properties, which can promote the osteogenic differentiation of cells. ALP, an early marker of osteogenic differentiation and mineralized nodules-a late marker of osteogenic differentiation, were detected by ALP staining and ARS staining, respectively. After the cells were cocultured with the MBG and MBG@ALG for 7 days, respectively, the purple color in the MBG@ALG group was significantly stronger than that in the MBG group (Figure 8A), indicating that the cells in the MBG@ALG group expressed more ALP. This result demonstrated that MBG@ALG has a great effect on promoting the early osteogenic differentiation of MC3T3-E1 cells. After 14 days of coculture, the ARS staining images and quantification date showed that the number and density of mineralized nodules in the MBG@ALG group were higher than those in the MBG group (Figures 8B,C), indicating that MBG@ALG had an excellent effect on promoting extracellular matrix mineralization. These results demonstrate that the surface modification of ALG promotes both early osteogenic differentiation and late osteoblast maturation, which will further broaden the application of MBG.

4 Conclusion

In this work, an ALG-modified MBG was successfully prepared (MBG@ALG), while the ALG chains on the surface of MBG could improve the drug loading efficiency and restrain the drug release speed. Furthermore, MBG@ALG showed excellent biocompatibility and could promote the osteogenic differentiation of cells, demonstrating that the surface functionalization of MBG with ALG has a significant impact on its properties, which may promote the further application of MBG in drug delivery and bone tissue engineering.

Data availability statement

The raw data supporting the conclusion of this article will be made available by the authors, without undue reservation.

Author contributions

HY: investigation, methodology, and writing original draft. JL: conceptualization. YD: methodology. ZL: project administration. JW: conceptualization, project administration, and writing—review and editing.

Funding

This work was supported by the financial support from the National Natural Science Foundation of China (Nos. 52163016 and 81960205), Jiangxi Provincial program for the academic and technological leaders of main subjects (20213BCJL22051), and Jiangxi Key Research and Development Program (20202BBG73012).

Conflict of interest

The authors declare that the research was conducted in the absence of any commercial or financial relationships that could be construed as a potential conflict of interest.

Publisher's note

References

Ahmad Raus, R., Wan Nawawi, W. M. F., and Nasaruddin, R. R. (2021). Alginate and alginate composites for biomedical applications. *Asian J. Pharm. Sci.* 16, 280–306. doi:10.1016/j.ajps.2020.10.001

Bae, J., Son, W. S., Yoo, K. H., Yoon, S. Y., Bae, M. K., Lee, D. J., et al. (2019). Effects of poly(amidoamine) dendrimer-coated mesoporous bioactive glass nanoparticles on dentin remineralization. *Nanomaterials* 9, 591. doi:10.3390/nano9040591

Boles, M. A., Ling, D., Hyeon, T., and Talapin, D. V. (2016). Erratum: The surface science of nanocrystals. *Nat. Mat.* 15, 364. doi:10.1038/nmat4578

Bygd, H. C., and Bratlie, K. M. (2016). The effect of chemically modified alginates on macrophage phenotype and biomolecule transport. *J. Biomed. Mat. Res. A* 104, 1707–1719. doi:10.1002/jbm.a.35700

Cao, C., Hong, C., Li, Y., Li, G., and Jiang, G. (2020). A long-term and stable surface modification method for lanthanide doped upconversion nanoparticles by oxidized alginate. *Z. Anorg. Allg. Chem.* 646, 1607–1610. doi:10.1002/zaac.202000262

Cui, L., Zhang, J., Zou, J., Yang, X., Guo, H., Tian, H., et al. (2020). Electroactive composite scaffold with locally expressed osteoinductive factor for synergistic bone repair upon electrical stimulation. *Biomaterials* 230, 119617. doi:10.1016/j.biomaterials.2019.119617

Das, M. P., Pandey, G., Neppolian, B., and Das, J. (2021). Design of poly-l-glutamic acid embedded mesoporous bioactive glass nanospheres for pH-stimulated chemotherapeutic drug delivery and antibacterial susceptibility. *Colloids Surfaces B Biointerfaces* 202, 111700. doi:10.1016/j.colsurfb.2021.111700

Ding, X., Shi, J., Wei, J., Li, Y., Wu, X., Zhang, Y., et al. (2021). A biopolymer hydrogel electrostatically reinforced by amino-functionalized bioactive glass for accelerated bone regeneration. *Sci. Adv.* 7, eabj7857. doi:10.1126/sciadv.abj7857

Gordon, L. M., and Joester, D. (2011). Nanoscale chemical tomography of buried organic-inorganic interfaces in the chiton tooth. *Nature* 469, 194–197. doi:10.1038/nature09686

Heinz, H., Pramanik, C., Heinz, O., Ding, Y., Mishra, R. K., Marchon, D., et al. (2017). Nanoparticle decoration with surfactants: Molecular interactions, assembly, and applications. *Surf. Sci. Rep.* 72, 1–58. doi:10.1016/j.surfrep.2017.02.001

Kango, S., Kalia, S., Celli, A., Njuguna, J., Habibi, Y., and Kumar, R. (2013). Surface modification of inorganic nanoparticles for development of organic–inorganic nanocomposites—a review. *Prog. Polym. Sci.* 38, 1232–1261. doi:10.1016/j.progpolymsci.2013.02.003

Kargozar, S., Kermani, F., Mollazadeh Beidokhti, S., Hamzehlou, S., Verné, E., Ferraris, S., et al. (2019). Functionalization and surface modifications of bioactive glasses (BGs): Tailoring of the biological response working on the outermost surface layer. *Materials* 12, 3696. doi:10.3390/ma12223696

Kerschenmeyer, A., Arlov., Ø., Malheiro, V., Steinwachsd, M., Rottmar, M., Maniura-Weber, K., et al. (2017). Anti-oxidant and immune-modulatory properties of sulfated alginate derivatives on human chondrocytes and macrophages. *Biomater. Sci.* 00, 1756–1765. doi:10.1039/c7bm00341b

Kim, T. H., Singh, R. K., Kang, M. S., Kim, J. H., and Kim, H. W. (2016). Gene delivery nanocarriers of bioactive glass with unique potential to load BMP2 plasmid DNA and to internalize into mesenchymal stem cells for osteogenesis and bone regeneration. *Nanoscale* 8, 8300–8311. doi:10.1039/c5nr07933k

Kodiyan, A., Silva, E. A., Kim, J., Aizenberg, M., and Mooney D, J. (2012). Surface modification with alginate-derived polymers for stable, protein-repellent, long-circulating gold nanoparticles. *Acs Nano* 6, 4796–4805. doi:10.1021/nn205073n

Kokubo, T., and Takadama, H. (2006). How useful is SBF in predicting *in vivo* bone bioactivity? *Biomaterials* 27, 2907–2915. doi:10.1016/j.biomaterials.2006.01.017

Lee, K. Y., and Moone, y. D. J. (2012). Alginate: Properties and biomedical applications. *Prog. Polym. Sci.* 37, 106–126. doi:10.1016/j.progpolymsci.2011.06.003

Lopez-Noriega, A., Arcos, D., and Vallet-Regi, M. (2010). Functionalizing mesoporous bioglasses for long-term anti-osteoporotic drug delivery. *Chem. Eur. J.* 16, 10879–10886. doi:10.1002/chem.201000137

Marcos Luciano, B. (2015). *Strategies to modify the drug release from pharmaceutical systems*. Sawston, United Kingdom: Woodhead Publishing, 63–86.

Meldrum F, C. (2008). Controlling mineral morphologies and structures in biological and synthetic systems. *Chem. Rev.* 108, 4332–4432. doi:10.1021/cr8002856

Pontremoli, C., Izquierdo-Barba, I., Montalbano, G., Vallet-Regi, M., Vitale-Brovarone, C., and Fiorilli, S. (2020). Strontium-releasing mesoporous bioactive glasses with anti-adhesive zwitterionic surface as advanced biomaterials for bone tissue regeneration. *J. colloid interface Sci.* 563, 92–103. doi:10.1016/j.jcis.2019.12.047

Rahaman, M. N., Day, D. E., Bal, B. S., Fu, Q., Jung, S. B., Bonewald, L. F., et al. (2011). Bioactive glass in tissue engineering. *Acta biomater.* 7, 2355–2373. doi:10.1016/j.actbio.2011.03.016

Ravanbakhsh, M., Labbaf, S., Karimzadeh, F., Pinna, A., Houreh, A. B., and Nasr-Esfahani, M. H. (2019). Mesoporous bioactive glasses for the combined application of osteosarcoma treatment and bone regeneration. *Mater. Sci. Eng. C* 104, 109994. doi:10.1016/j.msec.2019.109994

Schumacher, M., Habibovic, P., and van Rijt, S. (2021). Mesoporous bioactive glass composition effects on degradation and bioactivity. *Bioact. Mater.* 6, 1921–1931. doi:10.1016/j.bioactmat.2020.12.007

Schumacher, M., Reither, L., Thomas, J., Kampschulte, M., Gbureck, U., Lode, A., et al. (2017). Calcium phosphate bone cement/mesoporous bioactive glass composites for controlled growth factor delivery. *Biomater. Sci.* 5, 578–588. doi:10.1039/c6bm00903d

Sharifi, E., Bigham, A., Yousefiasl, S., Trovato, M., Ghomi, M., Esmaeili, Y., et al. (2022). Mesoporous bioactive glasses in cancer diagnosis and therapy: Stimuli-responsive, toxicity, immunogenicity, and clinical translation. *Adv. Sci.* 9, e2102678. doi:10.1002/advs.202102678

Vallet-Regi, M., and Salinas, A. J. (2021). Mesoporous bioactive glasses for regenerative medicine. *Mater. today Bio* 11, 100121. doi:10.1016/j.mtbio.2021.100121

Wang, X., Zeng, D., Weng, W., Huang, Q., Zhang, X., Wen, J., et al. (2018). Alendronate delivery on amino modified mesoporous bioactive glass scaffolds to enhance bone regeneration in osteoporosis rats. *Artif. cells, nanomedicine, Biotechnol.* 46, 171–181. doi:10.1080/21691401.2018.1453825

Xiao, J., Wan, Y., Yang, Z., Huang, Y., Zhu, Y., Yao, F., et al. (2019). Bioactive glass nanotube scaffold with well-ordered mesoporous structure for improved bioactivity and controlled drug delivery. *J. Mater. Sci. Technol.* 35, 1959–1965. doi:10.1016/j.jmst.2019.04.027

Xiao, J., Wan, Y., Yang, Z., Huang, Y., Zhu, Y., Yao, F., et al. (2019). Simvastatin-loaded nanotubular mesoporous bioactive glass scaffolds for bone tissue engineering. *Microporous Mesoporous Mater.* 288, 109570. doi:10.1016/j.micromeso.2019.109570

Xu, Y., Wu, P., Feng, P., Guo, W., Yang, W., and Shuai, C. (2018). Interfacial reinforcement in a poly-l-lactic acid/mesoporous bioactive glass scaffold via polydopamine. *Colloids Surfaces B Biointerfaces* 170, 45–53. doi:10.1016/j.colsurfb.2018.05.065

Yan, H., Chen, X., Bao, C., Wu, S., He, S., and Lin, Q. (2019). Alginate derivative-functionalized silica nanoparticles: Surface modification and characterization. *Polym. Bull. Berl.* 77, 73–84. doi:10.1007/s00289-019-02736-9

Yan, S., Sun, Y., Chen, A., Liu, L., Zhang, K., Li, G., et al. (2017). Templated fabrication of pH-responsive poly(l-glutamic acid) based nanogels via surface-grafting and macromolecular crosslinking. *RSC Adv.* 7, 14888–14901. doi:10.1039/c7ra00631d

Yao, H., Zhu, M., Wang, P., Liu, Y., and Wei, J. (2021). Combination of mussel inspired method and "thiol-michael" click reaction for biocompatible alginate-modified carbon nanotubes. *Nanomaterials* 11, 2191. doi:10.3390/nano11092191

Zhao, D., Zhu, T., Li, J., Cui, L., Zhang, Z., Zhuang, X., et al. (2021). Poly(lactic-co-glycolic acid)-based composite bone-substitute materials. *Bioact. Mater.* 6, 346–360. doi:10.1016/j.bioactmat.2020.08.016

Zhu, Y., and Stefan, K. (2019). Comparison of the *in vitro* bioactivity and drug release property of mesoporous bioactive glasses (MBGs) and bioactive glasses (BGs) scaffolds. *Microporous Mesoporous Mater.* 118, 176–182. doi:10.1016/j.micromeso.2008.08.046

frontiers | Frontiers in Bioengineering and Biotechnology

TYPE Systematic Review
PUBLISHED 05 October 2022
DOI 10.3389/fbioe.2022.921092

OPEN ACCESS

EDITED BY
He Liu,
Jilin University, China

REVIEWED BY
Jinshan Guo,
Southern Medical University, China
Menekse Ermis Sen,
Terasaki Institute for Biomedical Innovation, United States

*CORRESPONDENCE
Xianzuo Zhang,
zhangxianzuo@foxmail.com

†These authors contribute equally to this manuscript and share the first authorship

SPECIALTY SECTION
This article was submitted to Biomaterials, a section of the journal Frontiers in Bioengineering and Biotechnology

RECEIVED 15 April 2022
ACCEPTED 25 August 2022
PUBLISHED 05 October 2022

CITATION
Zhang X, Li Q, Wang Z, Zhou W, Zhang L, Liu Y, Xu Z, Li Z, Zhu C and Zhang X (2022), Bone regeneration materials and their application over 20 years: A bibliometric study and systematic review.
Front. Bioeng. Biotechnol. 10:921092.
doi: 10.3389/fbioe.2022.921092

Bone regeneration materials and their application over 20 years: A bibliometric study and systematic review

Xudong Zhang[1†], Qianming Li[2†], Zhengxi Wang[3†], Wei Zhou[2,4], Linlin Zhang[2], Yingsheng Liu[2], Ze Xu[2], Zheng Li[2], Chen Zhu[1,2] and Xianzuo Zhang[2*]

[1]Department of Orthopedics, The Affiliated Provincial Hospital of Anhui Medical University, Anhui Medical University, Hefei, China, [2]The First Affiliated Hospital of USTC, Division of Life Sciences and Medicine, University of Science and Technology of China, Hefei, China, [3]Department of Orthopedics, Anhui Provincial Hospital, Wannan Medical College, Hefei, China, [4]Department of Orthopedics, Union Hospital, Tongji Medical College, Huazhong University of Science and Technology, Wuhan, China

Bone regeneration materials (BRMs) bring us new sights into the clinical management bone defects. With advances in BRMs technologies, new strategies are emerging to promote bone regeneration. The aim of this study was to comprehensively assess the existing research and recent progress on BRMs, thus providing useful insights into contemporary research, as well as to explore potential future directions within the scope of bone regeneration therapy. A comprehensive literature review using formal data mining procedures was performed to explore the global trends of selected areas of research for the past 20 years. The study applied bibliometric methods and knowledge visualization techniques to identify and investigate publications based on the publication year (between 2002 and 2021), document type, language, country, institution, author, journal, keywords, and citation number. The most productive countries were China, United States, and Italy. The most prolific journal in the BRM field was *Acta Biomaterialia*, closely followed by *Biomaterials*. Moreover, recent investigations have been focused on extracellular matrices (ECMs) (370 publications), hydrogel materials (286 publications), and drug delivery systems (220 publications). Research hotspots related to BRMs and extracellular matrices from 2002 to 2011 were growth factor, bone morphogenetic protein (BMP)-2, and mesenchymal stem cell (MSC), whereas after 2012 were composite scaffolds. Between 2002 and 2011, studies related to BRMs and hydrogels were focused on BMP-2, *in vivo*, and *in vitro* investigations, whereas it turned to the exploration of MSCs, mechanical properties, and osteogenic differentiation after 2012. Research hotspots related to BRM and drug delivery were fibroblast growth factor, mesoporous materials, and controlled release during 2002–2011, and electrospinning, antibacterial activity, and *in vitro* bioactivity after 2012. Overall, composite scaffolds, 3D printing technology, and antibacterial activity were found to have an important intersection within BRM investigations, representing relevant research fields for the future. Taken together, this extensive analysis highlights the existing literature and findings

that advance scientific insights into bone tissue engineering and its subsequent applications.

KEYWORDS

bibliometric analysis, bone regeneration material, drug delivery, extracellular matrix, hydrogel

1 Introduction

The osseous tissue, which is a living structure that serves multiple important functions in the body, has a strong ability to repair and regenerate after injury. However, its natural healing process is slow and lengthy. Moreover, the new tissue fails to achieve the original strength and structure in a short time period, resulting in physical and social disability of the patients (Gong et al., 2015). Trauma, infection, and failed surgery may all lead to the destruction of the bone structure and consequent function loss. Therefore, bone grafting or osteogenic biomaterials are usually required to accelerate the bone healing process while maintaining the quantity and quality of the bone mass.

Bone transplantation is a commonly used method for osteogenesis in clinical practice. Autologous, allogeneic, and new artificial bone materials are some commonly used bone implant materials. Autologous bone has good osteogenic, osteoinductive, and osteoconductive properties, so it is the most successful material for repairing bone defects. Fibula, ilium, and ribs are all good bone grafting sites. However, autologous bone has limitations, such as prolonged operation time, insufficient bone supply, and infection. Allogeneic bone transplantation is a commonly used method of allogeneic bone transplantation in clinical practice. This transplantation can be divided into deep-frozen bone, freeze-dried bone, fresh allogeneic bone, and demineralized bone matrix (Pina et al., 2015; Iaquinta et al., 2019; Lee et al., 2019; Kačarević et al., 2020; Daneshmandi et al., 2021). However, allogeneic bone also has defects, such as immune rejection and increased transmission of infectious diseases. Most of the new artificial bone materials are composite materials. Synthetic materials include metal, bioceramic, and polymer chemical materials, among others. These materials have been widely used in bone regeneration. In recent years, applying nano-artificial bone materials has opened a new era of bone regeneration. The representative materials mainly include nano-hydroxyapatite (nHAP), alumina nano-compounds, nHAP/poly-L-lactic acid (PLLA), and other composite materials.

Tissue engineering is a promising approach in bone regenerative medicine. Bone tissue engineering implants precursor cells into biocompatible scaffolds combined with growth factors to form bone (Lanza, 2016; Birlea et al., 2017; Trohatou and Roubelakis, 2017; Borrelli et al., 2020). The scaffold provides structural support for the bone defect and can stimulate the body's regeneration potential, promoting cell proliferation, migration, and differentiation in bone regeneration. Scaffolds have been widely used in combination with growth factors, autologous bones, and cells for tissue regeneration. In addition to scaffolds, BMPs, platelet-derived growth factor, and vascular endothelial growth factor can all act on stem cells and osteoblasts to induce bone regeneration at the defect site. MSCs are widely used in bone tissue engineering and have the ability of self-renewal, abundant proliferation, and multi-lineage differentiation. MSCs are easy to isolate, culture, and expand and can maintain multi-directional differentiation potential for a long time. Thus, their use in bone tissue engineering is increasing (Pina et al., 2015; Yu et al., 2015; Hasan et al., 2018; Lee et al., 2019).

Scientific publications are central to discipline development and academic exchange, as well as for the creation of clinical practice guidelines. Evaluative bibliometrics is a field of quantitative science that uses different methods to assess research performance. For example, citation data is used to quantify the impact of an article over time, as shown by the number of times the article is cited. Thus, bibliometric analysis can be used to identify influential articles that shape medical practice and promote new research ideas. Previous bibliometric studies have pointed out the most highly cited papers in the field of bone regeneration in recent years (Huang et al., 2020), and qualitatively or quantitatively described commonly used polymer materials (Hussin et al., 2021) and artificial extracellular matrices (Simmons et al., 2020) in the field of bone tissue regeneration. Although these studies have identified several classic references in the field of bone tissue regeneration, they focused mainly in the field of materials research, whereas a comprehensive perspective on the related medical concepts is still lacking. To close this knowledge gap, a bibliometric analysis was conducted to identify all relevant scientific papers published on the Institute for Scientific Information (ISI) network, and assess the research trends on bone regeneration materials and their applications over the past 20 years.

2 Materials and methods

The ISI Web of Science Core Collection (WOS), which includes the Science Citation Index Expanded and other citation indexes, was used to retrieve scholarly articles and literature related to bone regeneration materials (BRMs) that were published between 2002 and 2021. For this review, the keyword 'mHealth' was used, and the analyses and conclusions

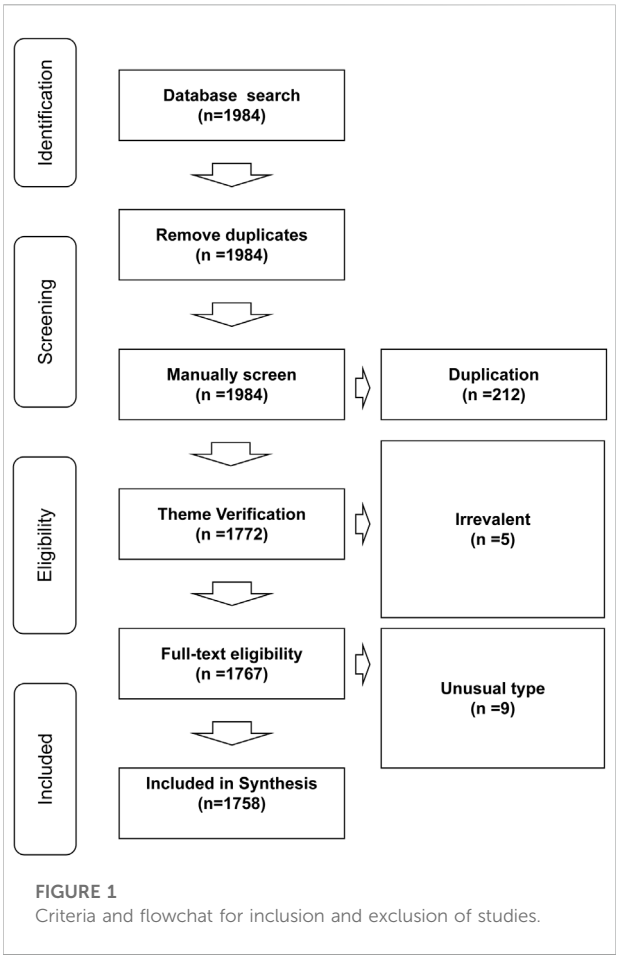

FIGURE 1
Criteria and flowchat for inclusion and exclusion of studies.

followed the recommendations of Preferred Reporting Items for Systematic Reviews and Meta-Analyses.

2.1 Systemic search strategy

A structured search on the WOS database was conducted using the following research strategy. First, 'biomaterials' and 'bone regeneration' terms were searched in the title, keywords, and abstract fields. From the obtained 1,758 literature citations, keywords were extracted, and statistical analysis was performed. The retrieved documents were exported in Bibtex format and documented using Endnote 20 desktop version (Clarivate, Philadelphia, PA, United States) (Gotschall, 2021). All documents were selected by two independent reviewers (ZXD and ZXZ).

2.2 Eligibility Criteria

To be included in the study, the bibliographic documents had to agree to the following inclusion criteria: 1) be original/review articles, proceedings papers, book chapters, or other common types of publications retrieved by WOS; 2) had been published between 2002 and 2021 (including publications in various languages such as English, Chinese, French, Latin, Korean, among others); 3) report basic experiments, animal experiments, or clinical trial data on BRMs. Duplicated files, documents that did not covered BRMs, and publication files of uncommon categories (such as meeting abstract, early access, editorial materials) were excluded from the study. The inclusion/exclusion criteria applied in the present systematic review are shown in Figure 1.

2.3 Bibliometric Data Analysis

Citation metrics were assessed using Rstudio v4.1.3 software (2017-06-30; http://www.rstudio.com/) equipped with the *bibliometrix* package http://www.bibliometrix.org). Bibliometric networks and bibliographic coupling, including author, author keyword, citation, co-citation, collaboration, country, co-word analysis, keyword plus networks, and keyword co-occurrences, were visualized using *bibliometrix*. The H-index, G-index, and M-index calculated were limited to the corresponding subsets in the study field. The method of document processing and measurement is shown in Supplementary Figure S1. In addition to bibliometric data analysis, an in-depth reading of publications in many authoritative journals (including articles, reviews, proceedings, papers, etc.) was conducted. We summarized the research done in the field of bone regeneration based on three keywords, such as "ECM," "hydrogel," and "drug delivery" in the past 20 years, focusing on the most popular materials used, their osteogenic mechanisms, and their engineering applications in bone tissue. We also analyzed the application of scaffolds in osteogenesis based on the three searched topics or subsets. In addition, we also briefly discussed 3D printing and citrate research in bone tissue engineering.

3 Results

A total of 1,758 articles met the inclusion criteria that yielded various keywords (Figure 2) in the fields of ECMs (n = 298) and hydrogel (n = 269). It was also found that the number of articles published in the journals increased between 2002 and 2021, indicating a growing interest in and expansion of the bone regeneration research field. After manually filtering out the keywords that were irrelevant or meaningless to the subject of analysis, 'ECM,' 'hydrogels,' and 'drug delivery' were found to be high-frequency words. Therefore, the selected documents were further assessed according to these three subset keywords. In addition, due to changes in the research subject during the past 20 years, which was highlighted by visual analysis, the selected

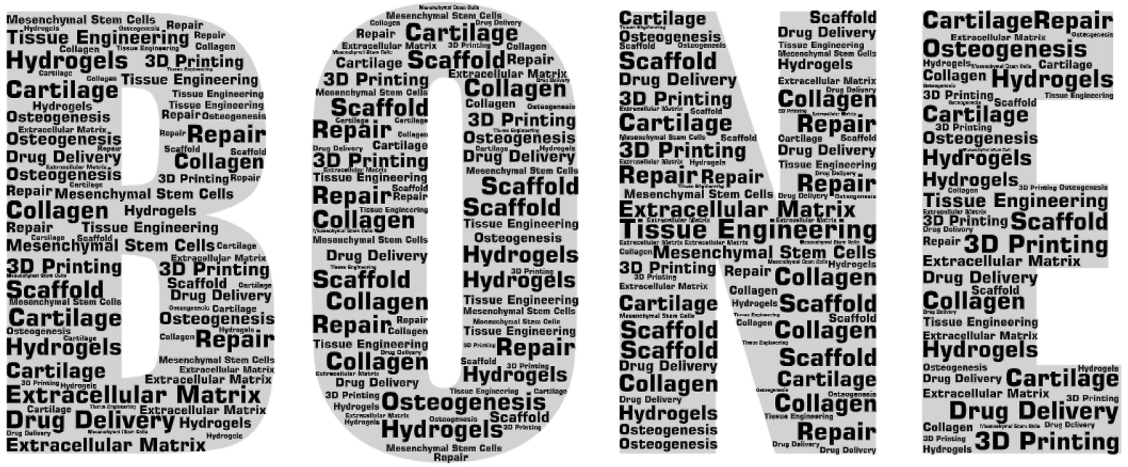

FIGURE 2
Wordcloud of the collection of literature keywords included in the study.

documents were divided in two groups (2002–2011 and 2012–2021) according to their publication date using the PUBYEAR keyword as filter.

3.1 Publication journals and article types

The 10 professional journals with the most published papers in each subset are listed in Figure 3. The most prolific journal was *Acta Biomaterialia*, closely followed by *Biomaterials*. Overall, 96 articles were published in *Acta Biomaterialia*, 69 articles were published in *Biomaterials*, and 45 articles were published in the *International Journal of Molecular Science*.

Concerning publication type (Table 1), articles accounted for more than 50% of all publications. Analysis of these documents according the three most common keywords showed that 185 articles were related to the ECM, whereas 160 and 91 covered hydrogels and drug delivery systems.

3.2 Most active authors and visualized analysis (authors, countries,keywords)

As in shown in Table 2, Rui L. Reis from I3Bs Research Institute on Biomaterials, Biodegradables and Biomimetics of UMinho (Braga, Portugal) published the most articles between 2002 and 2021, including more than 20 high-quality papers in the field of BRMs, and achieved the highest H-indexes in the hydrogels and drug delivery fields. The scholar who had most papers published in the 'ECM' subset was Cato T. Laurencin from the University of Connecticut (Storrs, CT, United States), who was found to work closely Kevin W. H. Lo, Hao-Min Lan, Karen M. Ashe, and Tao Jiang in the field of three-dimensional (3D) bioprinting technology.

Xiaoling Zhang from the College of Polymer Science and Engineering, Sichuan University (Chengdu, China) and Ying Zhang from the School of Chemical Engineering and Technology, Hebei University of Technology (Tianjin, China) were found to be leaders in the research of hydogels, being close collaborators in areas of nanocomposite adhesive hydrogels. Co-author visualization was used to illustrate the collaboration pattern of the authors (Figure 4A).

Concerning publishing countries, United States, China, Italy, South Korea, and Switzerland were found to have the highest total number of published articles. During 2002–2011, China published fewer papers, with 32, 34, and 38 papers published in the fields of ECM, hydrogels, and drug delivery, respectively. However, from 2012 to 2021, which marked a breakthrough in the research of BRMs in China, the number of reports published by Chinese teams in the above fields rose to 857, 699, and 665, respectively, surpassing those of teams from the United States and becoming the country with the most research publications in these fields. Noteworthily, although Switzerland-based teams did not publish the most articles, the average number of citations per report was the highest in 2002–2011 and 2012–2021. A network representing the collaboration between countries in the field of ECM, hydrogels, and drug delivery is shown in Figure 4B. China–United States, United Kingdom–United States, and United States–Korea collaborations ranked first concerning investigations on the ECM. The country distribution of published papers is shown in Table 3.

As mentioned above, the keywords of the published documents were extracted and counted. ECM, hydrogels, and drug delivery were found to be high-frequency words; thus, were used as subset variable names. In addition, other keywords were

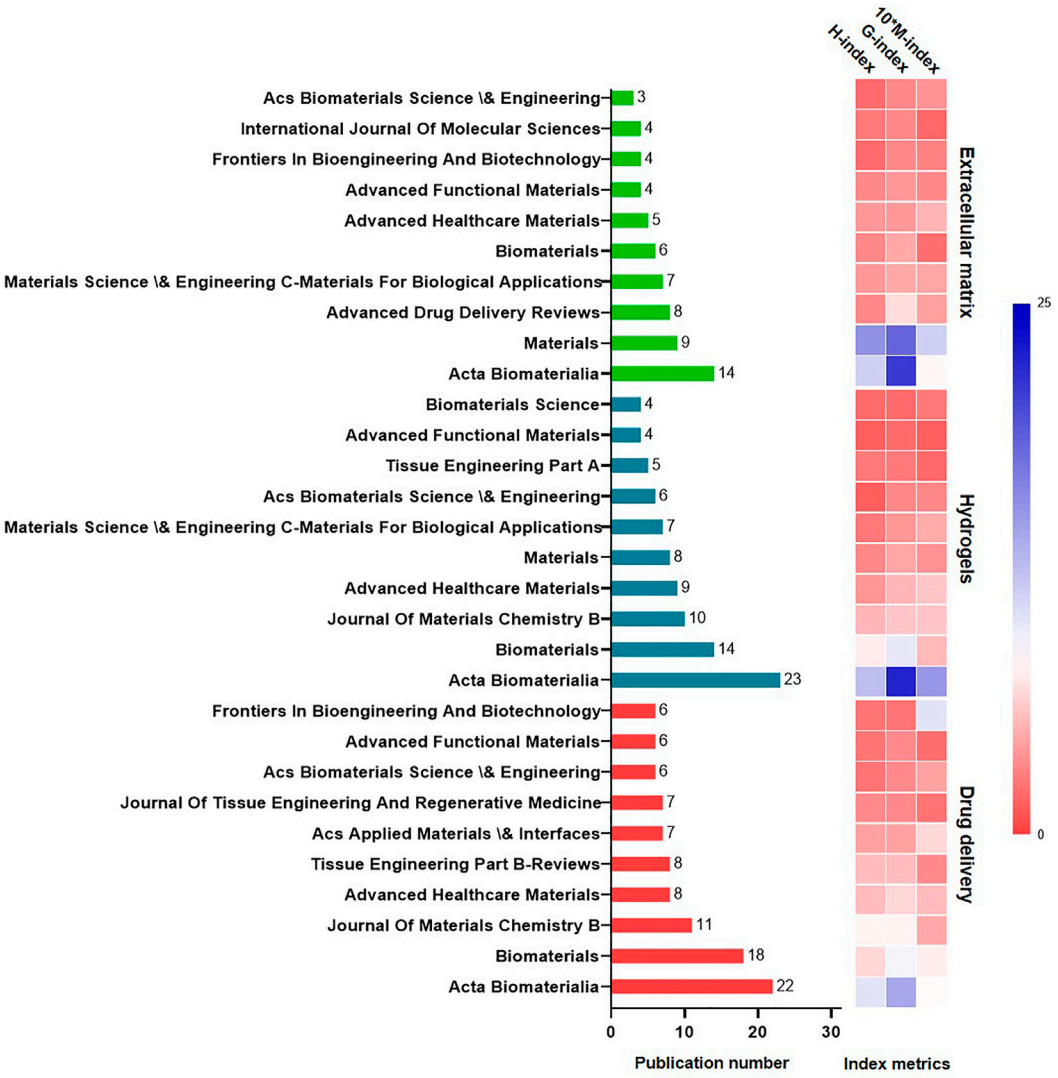

FIGURE 3
Publication number and index metrics for top 10 prolific journals.

TABLE 1 Publication types of selected research.

	Extracellular matrix (n = 370)	Hydrogels (n = 286)	Drug delivery (n = 220)
Article	185 (50%)	160 (55.94%)	91 (41.36%)
Review	164 (44.32%)	109 (38.11%)	115 (52.27%)
Proceedings paper	4 (1.08%)	4 (0.00%)	1 (0.45%)
Book chapter	8 (2.16%)	6 (0.61%)	5 (2.27%)
Other	9 (2.43%)	7 (0.61%)	8 (3.63%)

TABLE 2 Most active authors, their publications and H-index.

	Extracellular matrix			Hydrogels			Drug-delivery	
	Pulications	H-Index		Pulications	H-Index		Pulications	H-Index
Laurencin Ct	8	7	Reis RL	7	6	Reis RL	7	5
Li X	6	5	Alsberg E	5	5	Vallet-Regi M	5	5
Reis Rl	6	5	Zhang X	5	4	Arcos D	4	4
Zhang Y	6	5	Jeon O	4	4	Chen FM	4	4
Kaplan Dl	5	5	Liu X	4	4	Kaplan DL	4	4
Wang Z	5	5	Wang H	4	4	Orive G	4	4
Zhang X	5	3	Wang X	4	4	Tabata Y	4	4
Chen Fm	4	4	Zhang Y	4	4	Wang Z	4	4
Chen X	4	2	Ameer GA	3	3	Webster TJ	4	4
Ghezzi Ce	4	4	Censi R	3	3	Baino F	3	3

also commonly indicated in papers published in BRM-related fields, such as MSCs, osteogenesis, among others. Co-occurrence relationship between the most commonly used keywords were also assessed (Figure 4C), which showed the existence of five clusters characterized by the most commonly used keywords in the 'ECM' subset. The representative papers of each cluster were Badylak et al. (2009), Lutolf and Hubbell (2005), Discher (2009), Engler et al. (2006), and Murphy and Atala (2014). Moreover, the content described in these reports covered the relationship between several clusters centered on keywords such as "tissue engineering," "MSCs," "scaffold," "osteogenesis," and "3D printing." For example, Badylak et al. (2009) showed that bioscaffolds composed of ECM can promote the remodeling of various tissues.

3.3 Time distribution measures for publications and thematic evolution

Between 2002 and 2021, the number of publications related to BRMs increased exponentially (Figure 5A). Specifically, under the 'ECM' subset, a total of 370 articles were published from 2002 to 2021, but only single-digit articles were published each year before 2009. The turning point occurred in 2010, with the publication of the article "Chondrogenic mRNA expression in prechondrogenic cells after blue laser irradiation" (18 citations to date) by Kushibiki et al. (2010), which opened a new research era on the ECM. In 2020, the number of studies using "ECM" as keyword reached its peak, with a total of 52 articles published. Hydrogels have been a hot topic in the field of biological tissue engineering research, with the number of articles related to hydrogels increasing yearly between 2011 and 2020. The first literature on bone regeneration materials with 'hydrogel' as keyword was published in 2006 (108 citations to date). As a long-term research hotspot in material chemistry, drug delivery can empower relatively inert bone regeneration materials, as well as improve the speed and promote the direction of tissue regeneration. Research on drug delivery targeting bone regeneration was firstly published before 2002, and has generally maintained an upward trend over the past 20 years. The publication trends related to the above subject terms are shown in Figure 5A.

We also performed a co-word analysis of the co-occurrence of keywords, aiming at representing the conceptual structure of a framework. The conceptual structure map was created using the Multiple Correspondence Analysis method, which allows to determine the association between two or more qualitative variables. The map revealed two clusters, of which one (in red) had the most meaningful keywords, which means that the researchers were highly focused on the BRMs field (Figure 5B).

From 2002 to 2011, investigations on BRMs covered varied subjects and topics, among which "delivery", "*in vitro*," "controlled release," and "ECM" were of particular interest. During the same period, some scholars focused on topics such as "endothelial cells" and "calcium-phosphate ceramics." From 2012 to 2021, authors who originally studied "controlled release," "ECM," "endothelial cells," and "calcium phosphate ceramics" had turned their attention to "*in vitro*" and "therapy" focused investigations (Figure 5C).

4 Discussion

Bibliometric analysis is a meaningful evaluation method that can be used to reflect research status and trends. Based on publications publicly available in the WOS database, this study provides the first comprehensive analysis of BRMs. The analysis also serves as a way to rank journals, institutions, and universities worldwide. The field of research related to biomaterials for bone regeneration is constantly evolving, which is reflected by the increased number of publications

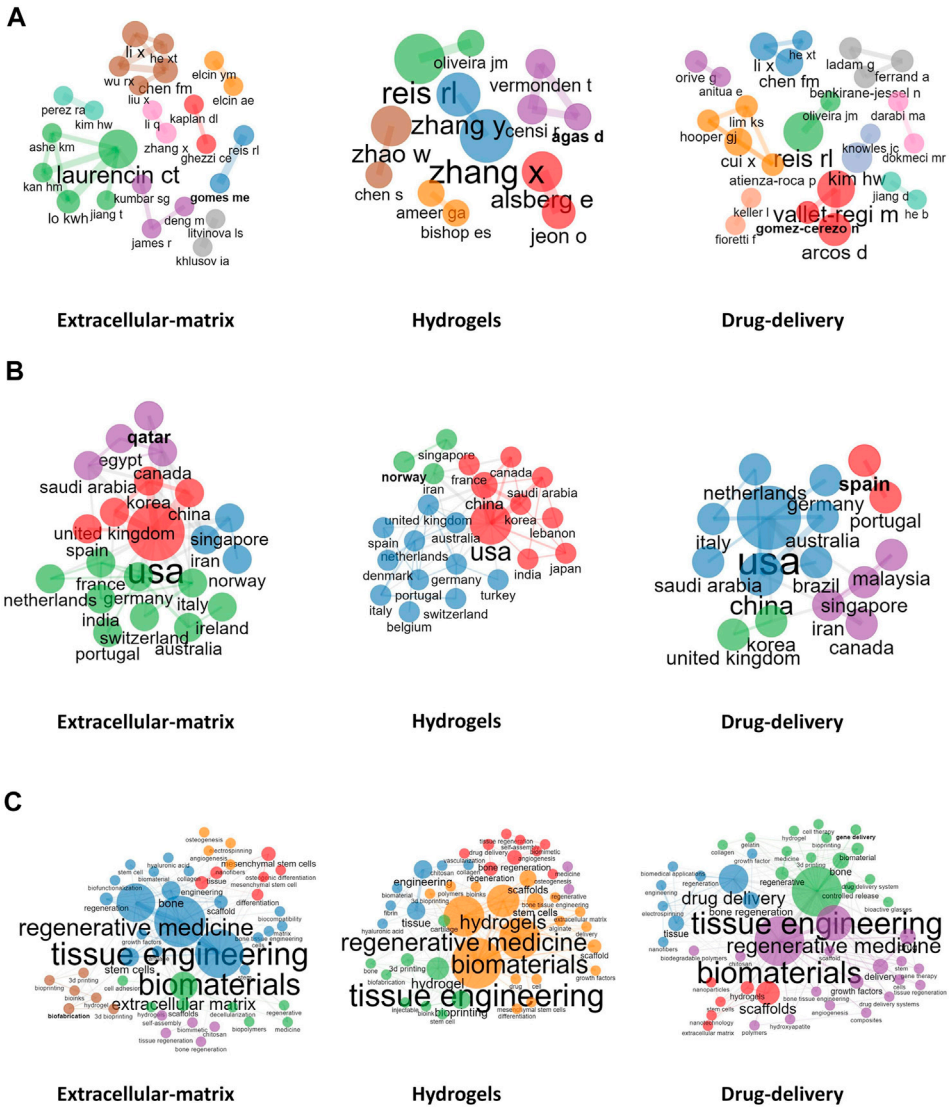

FIGURE 4
Visualized analysis. **(A)**: Collaboration between authors; **(B)**: Collaboration between countries; **(C)**: Collaboration between Author keywords.

and the expansion of the research fields covered throughout the years. Trends over the past decade reflect the growing number of terms associated with clinical topics, such as ECM, hydrogels, drug delivery, bone marrow-derived MSCs, BMP-2, *in vitro*, and others.

4.1 Research on extracellular matrices and applications of scaffolds in osteogenesis

Subset 1 mainly focused on ECM research in the field of BRMs. Relatively few studies are available regarding this topic from 2002 to 2011. During the last 10 years, researchers have been interested in 1) bone ECM composition and integrins and 2) the relationship between ECM mimetic peptides and osteogenesis. After 2012, ECM research focused more on scaffolds, such as acellular extracellular matrix scaffolds and 3D electrospun nanofiber scaffolds.

4.1.1 Bone extracellular matrices composition and integrins

Different ECM molecules can differentially regulate cell differentiation by interacting with specific cell receptors (Aplin et al., 2002). The ECM in the bone consists primarily of an organic phase and a mineral phase, which includes non-collagenous components, type I collagen, and other minor

TABLE 3 Statistics of publication country related to bone regenerative materials between 2002-2021.

	Extracellular-matrix			Hydrogels			Drug-delivery	
	Publications	Total citations	Average article citations	Publications	Total citations	Average article citations	Publications	Total citations	Average article citations
2002–2011									
United States	139	6,195	177	123	4,545	162.3	69	2,960	174.1
CHINA	32	772	128.7	34	628	69.8	38	1,011	84.2
ITALY	56	551	42.4	14	46	15.3	8	221	73.7
SOUTH KOREA	41	430	61.4	20	178	44.5	24	414	82.8
SWITZERLAND	32	1,620	202.5	21	1,534	255.7	11	446	148.7
PORTUGAL	9	112	112	14	572	190.7	21	330	55
GERMANY	18	176	44	1	0	0	4	247	247
United Kingdom	5	143	71.5	12	1,072	268	4	0	0
FRANCE	8	184	61.3	15	221	73.7	6	72	72
CANADA	10	114	38	1	0	0	20	226	45.2
2012–2021									
United States	615	5,086	44.61	671	5,236	45.93	435	4,029	53.72
CHINA	857	4,305	26.57	699	4,450	31.79	665	5,148	37.85
ITALY	160	1848	54.35	104	530	25.24	72	453	26.65
SOUTH KOREA	197	1,411	36.18	179	893	24.14	164	1,208	35.53
SWITZERLAND	36	435	62.14	27	393	98.25	4	116	78.96
PORTUGAL	97	606	28.86	149	882	35.28	72	578	41.29
GERMANY	154	848	33.92	144	523	18.68	101	972	44.18
United Kingdom	65	685	71.5	121	819	30.33	39	257	28.56
FRANCE	60	579	46.5	48	487	33.91	64	214	21.40
CANADA	55	149	12.42	40	416	16.23	43	221	15.47

collagens. Non-collagenous proteins include proteoglycans, such as hyaluronic acid, decorin, and versican, as well as osteonectin, osteopontin, osteocalcin, fibronectin, and vitronectin (Shekaran and Garcia, 2011). The mineral phase of consists of the calcium phosphate compound hydroxyapatite. Integrins are a ensemble of receptors that promote cell binding to extracellular matrix proteins (Hynes, 2002). Studies have found that the α2β1 integrin is highly expressed in osteoblast-like cells and is also the main adhesion receptor used by these cells to adhere to collagen. The α2β1 integrin is related to the osteogenic pathway (Gronthos et al., 1997). Furthermore, the α2β1-mediated adhesion of mouse MC3T3-E1 pre-osteoblasts to type I collagen was found to activate Runx2/Cbfa1, a transcription factor that promots osteoblast differentiation (Takeuchi et al., 1997; Xiao et al., 1998; Xiao, 2000; Tamura et al., 2001). Several other integrin isoforms, such as α5β1 and αvβ3, have also been shown to regulate osteogenesis (Moursi et al., 1997; Xiao et al., 1998; Keselowsky, 2005; Martino et al., 2009; Hu et al., 2010).

4.1.2 Relationship between extracellular matrices mimetic peptide and osteogenesis

Full-length native ECM polymers include collagen, fibrin, hyaluronic acid, acellular matrix, and bone sialoproteins (Caiazza, 2000; Perka, 2000; Karp et al., 2004; Rammelt et al., 2006; Ben-Ari, 2009). In recent years, gels, cross-linked membranes, and demineralized bone particles have been widely used for osteogenesis (Suckow et al., 1999; Kim et al., 2007; Kurkalli et al., 2010). ECM-derived peptides can circumvent the limitations of full-length native ECM polymers that are difficult to modify and control. FHRRIKA as an ECM-derived peptidehas the ability to promote osteoblast differentiation. It is a heparin-binding sequence found on many ECM proteins (Rapuano et al., 2004; Dettin, 2006;

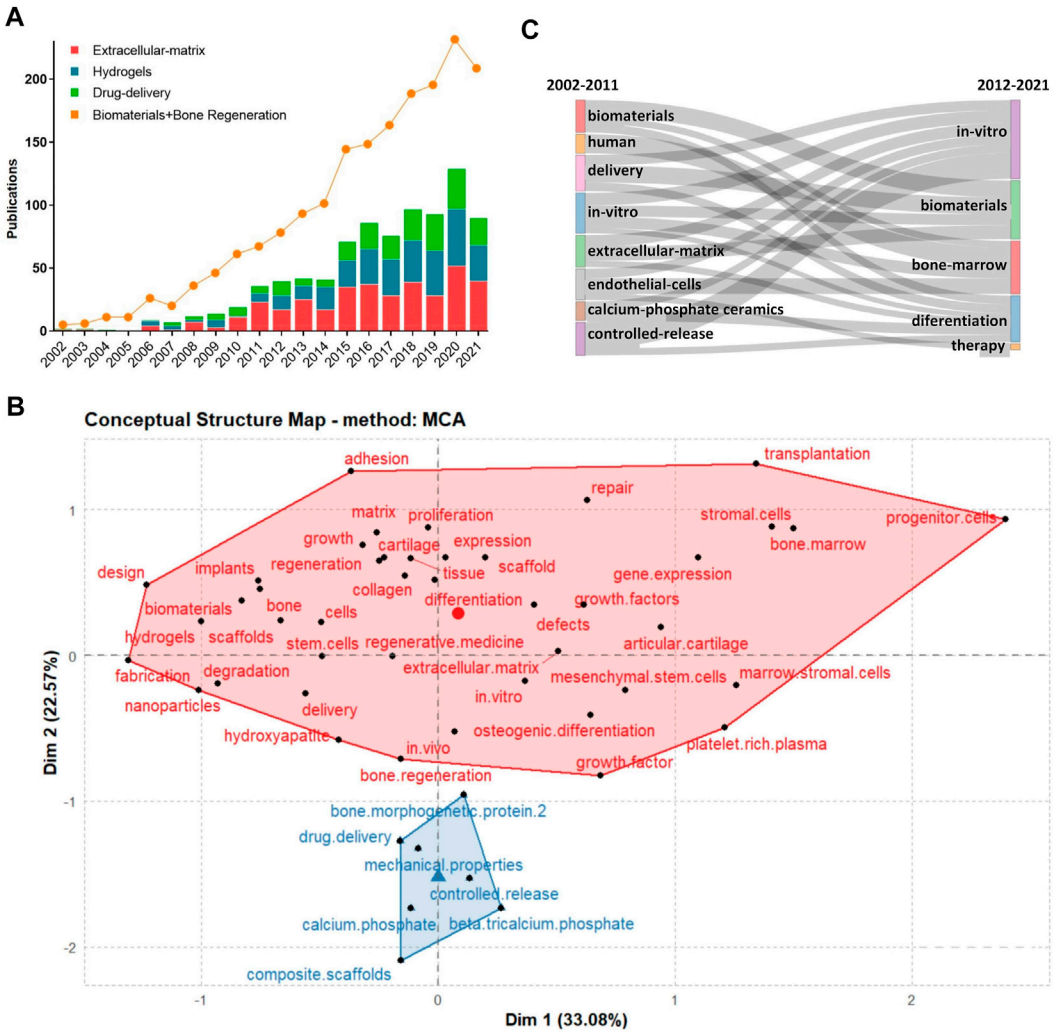

FIGURE 5
(A): Study and publication trends between 2002–2021; **(B)**:Concept structure map of author keywords; **(C)**:Thematic evolution of studies during 2002–2021.

Dettin et al., 2009). Martino et al. also found that the engagement of FNIII9-10 and α5β1 may enhance osteogenesis.

4.1.3 Decellularized extracellular matrix scaffolds

The dECM scaffold is a three-dimensional framework mainly composed of ECM, mainly containing fibronectin, collagen, laminin, elastin, matrix cell proteins, etc (Chen and Liu, 2016; Liu et al., 2017a). Bernhard et al. also demonstrated that tissue-engineered bone grafts using dECM scaffolds can regenerate bone through endochondral ossification (Hesse et al., 2010; Scotti et al., 2010) (Figure 6A). They prepared decellularized bone scaffolds and used them for the treatment of rat femoral defects. The scaffolds were infused with adipose stem cells and cultured in a chondrogenic medium for 2 weeks, followed by a hypertrophy medium for 3 weeks to form hypertrophic cartilage. The cell-seeded structure showed excellent bone regeneration characteristics after implantation (Bernhard et al., 2017) (Figure 6B).

4.1.4 Three-dimensional electrospun nanofibrous scaffolds

Electrospun nanofibers have a similar morphology to the ECM and possess properties for regulating cellular behavior and function; thus, they are frequently used in tissue engineering. 3D electrospun nanofibrous scaffolds can provide osteoblast with biomimetic fibrous structures and 3D microenvironments; therefore, they are good materials for tissue regeneration engineering. (Figure 6C) 3D ENF-S is classified into the following, according to different fabrication methods: 1)

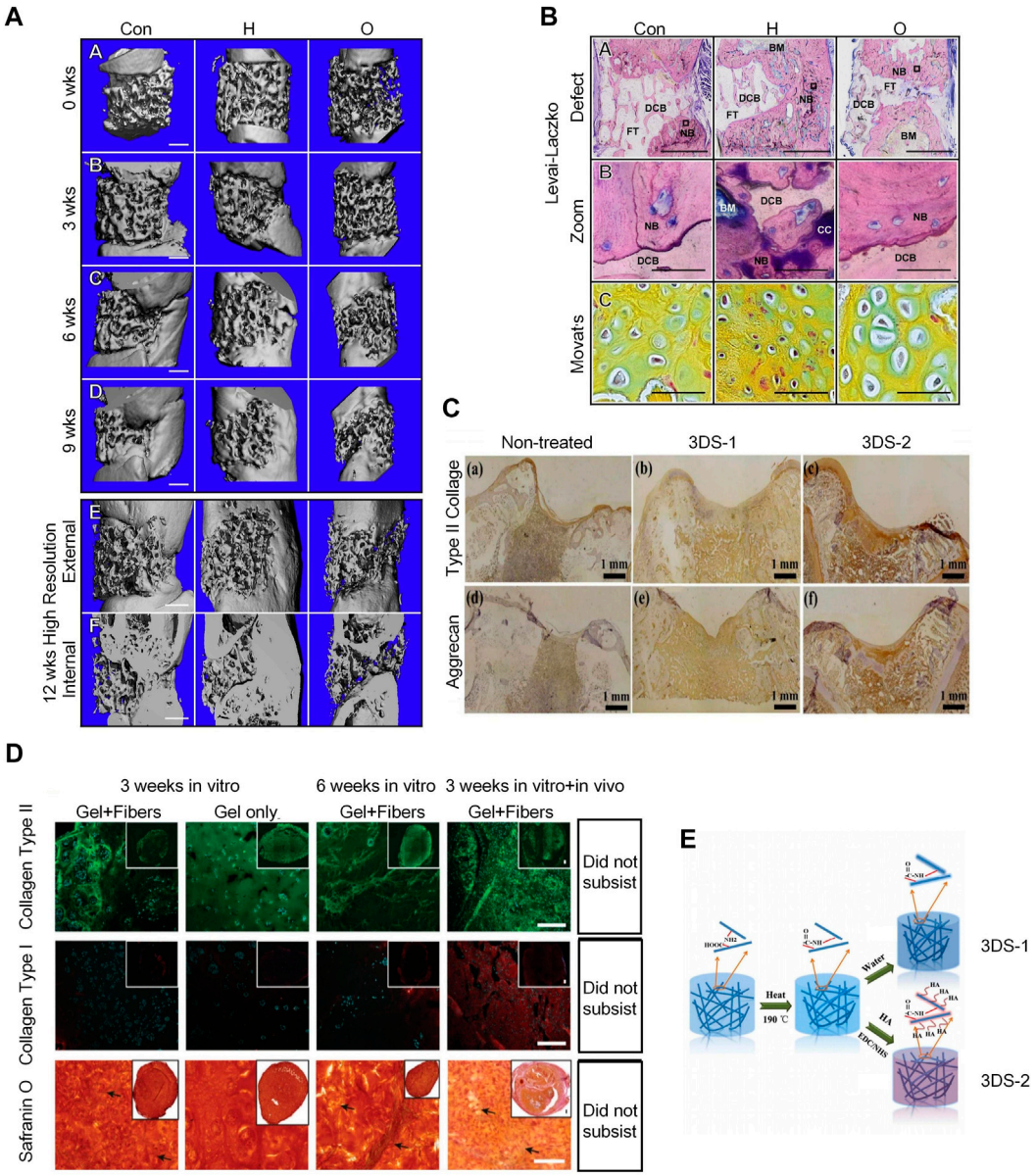

FIGURE 6
Application of dECMs and 3D Electrospun Nanofibrous Scaffolds in osteogenesis. **(A)** 3D μCT reconstruction of rat femurs with decellularized scaffolds, hypertrophic chondrocyte and osteoblast grafts at 0, 3, 6, and 9 weeks post-implantation to bridge severely sized femoral defects. The inner and outer areas are shown at 12 weeks. Defect regeneration and bone formation were seen 12 weeks after implantation. (Bernhard et al., 2017)(Reprinted with permission) **(B)**. Histology of hard bone using Levai-Laczko staining. The magnified view allows detection of calcified cartilage. At the site of new bone formation, there is cartilage primordium characteristic of endochondral ossification (green staining in Movat pentachrome sections) (Bernhard et al., 2017) (Reprinted with permission) **(C)**. Immunohistochemical staining results of type II collagen and aggrecan of untreated 3DS-1 and 3DS-2 scaffolds 12 weeks after implantation *in vivo*. (Chen et al., 2016) (Reprinted with permission)**(D)**. The hydrogel/nanofiber composite structures exhibited better chondrogenic ECM deposition and higher stability than pure hydrogel scaffolds in in vitro cell culture and *in vivo* implantation. (Chen et al., 2016) (Reprinted with permission) **(E)**. Schematic illustration of fabrication and cross-linking of electrospun nanofibrous porous 3D scaffolds (3DS-1) and hyaluronic acid scaffolds (3DS-2) cross-linking. (Chen et al., 2016) (Reprinted with permission).

electrospun nanofibers created via direct electrospinning through post-processing techniques and tuning fiber collection techniques (Subramanian et al., 2011); 2) electrospun nanofibers/hydrogel composite 3D scaffolds fabricated by embedding the assembled electrospun nanofibers in a hydrogel precursor solution (Xu et al., 2010), and 3)

electrospun nanofibers/porous matrix composite 3D scaffolds fabricated via 3D printing. 3D printing is a common method to fabricate porous scaffolds with complex structures, wherein the structural size and scale of electrospun nanofiber pores gradually increase from nanoscale to macroscale, similar to the topographical features of ECM (Lee et al., 2017). 3D ENF-S with a porous structure can also be easily formed by freeze-drying, which offers good stability and mechanical properties. In recent years, electrospun nanofibers have been widely used in cartilage tissue engineering. Chen et al. prepared gelatin/PLA nanofiber-based 3D porous scaffolds via freeze-drying and heating, then used 1-ethyl-3-(3-dimethylaminopropyl) carbodiimide (EDC)/N-hydroxyl succinimide (NHS) to cross-link the scaffold with hyaluronic acid (Figure 6D), which can ultimately further promote cartilage regeneration (Chen et al., 2016). A team also developed a double-layer collagen/PLLA nanofiber composite scaffold for bone tissue regeneration (Figure 6E). MSCs cultured as described above had a stronger osteogenic differentiation ability (Zhang et al., 2013).

4.2 Application of hydrogels in osteogenesis

Documents related to subset 2 were mainly associated with the use of hydrogels in the field of BRM. There were a few studies on hydrogels in the field of bone regeneration from 2002 to 2011. Most scholars have devoted themselves to studying the synthesis of hydrogels which can promote the differentiation of MSCs. Since 2012, research on hydrogels in the field of bone regeneration has been in full bloom. In recent years, researchers have been interested in hydrogels with photothermal effects, conductive hydrogels, and biomimetic self-assembled peptide hydrogels.

4.2.1 Hydrogel-induced differentiation of mesenchymal stem cell

Native hydrogels can be used for regeneration and bone tissue repair; these can thus provide clues for inducing the differentiation of MSCs. However, some hydrogels have limitations in fine-tuning mechanical properties, leading to the consistent formation of gels with similar properties. Mauck et al.(2006) compared the growing of bone tissue that differentiated from MSCs in gels with that of native tissue. The results revealed that differentiated MSCs generate much less cartilage matrix than native cartilage tissue. Synthetic hydrogels provide materials with more easily controlled and reproducible properties. Polyethylene glycol (PEG) or poly (vinyl alcohol) (PVA), being the most widely used synthetic hydrogels for encapsulating MSCs, can be easily fine-tuned by changing the crosslink density as well as the expansion and compressive moduli of the system (Burdick, 2002). These have been shown to successfully generate an osteoid matrix with encapsulated osteoblasts. However, MSC encapsulation in these types of hydrogels may render cells unable to survive (Bryant et al., 2003; Nuttelman et al., 2005).

4.2.2 Development of hydrogels for 3D culture of mesenchymal stem cell

From 2002 to 2011, good progress was made in developing hydrogel environments for the 3D culture of MSCs, which greatly helped in inducing MSC differentiation and matrix deposition. In addition, MSCs responded better to environments with a combination of TGFβ-1 and IGF-1 or BMP-6 than to those with either factor alone in directing cartilage matrix deposition (Indrawattana et al., 2004). BMP-2 and TGFβ-1 have synergistic effects on the chondrogenic differentiation of MSCs (Toh et al., 2005). It has also been shown that early delivery of FGF-2 prolongs the pre-osteoblast differentiation of MSCs in culture, while a much later delivery of BMP-2 promotes bone development (Maegawa et al., 2007).

4.2.3 Hydrogels with photothermal effects

Two main types of hydrogels with photothermal effects, such as inorganic and organic material hybrid hydrogels, are available. Inorganic materials include carbon nanotubes (Deng et al., 2019), gold nanoparticles (Mauck et al., 2006; Matai et al., 2020; Liao et al., 2021), reduced graphene oxide (rGO) (Li et al., 2018; Lima-Sousa et al., 2020), platinum nanoparticles, BP, Au Pds, and TiO2 (15), while organic materials include dopamine (DA) and indocyanine green (ICG). DA has excellent photothermal conversion and adhesion ability, and ICG has excellent photothermal conversion efficiency. While studying the mechanism of osteogenesis, Sanchez's team fabricated a fibrin/GNPs hydrogel and successfully embedded C3H-BMP-2 high cells into the hydrogel (Figure 7A). Under the simultaneous action of near-infrared irradiation and rapamycin-induced heat treatment, C3H-BMP-2 high cells are stimulated to synthetic BMP-2 for promoting osteogenesis (Figures 7B,C). BMP-2 promotes the differentiation of MSCs into osteoblasts and promotes the role of MSCs in bone defect areas (Pensak et al., 2015; Sanchez-Casanova et al., 2020).

4.2.4Biomimetic self-assembling peptide hydrogels

In the past decade, research has increasingly focused on self-assembling peptide hydrogels used in osteogenesis; Self-assembling peptides of various structures can be fabricated into scaffolds to culture cells and promote bone regeneration. (Sargeant et al., 2012). Quan's team developed a 3D bioactive scaffold from self-assembling oligopeptides of D9 KIPKASSVPTELSAIS RGDS (DSR) and D9 KIPKASS(p)V PTELSAIS RGDS (DSpR) and included bone morphogenetic protein-2 biomimetic peptide (BMPMP) as a potent osteoinductive cytokine (Figure 7D), polyaspartic acid (D9) as an organic template, calcium chelator, and RGDs as cell adhesion

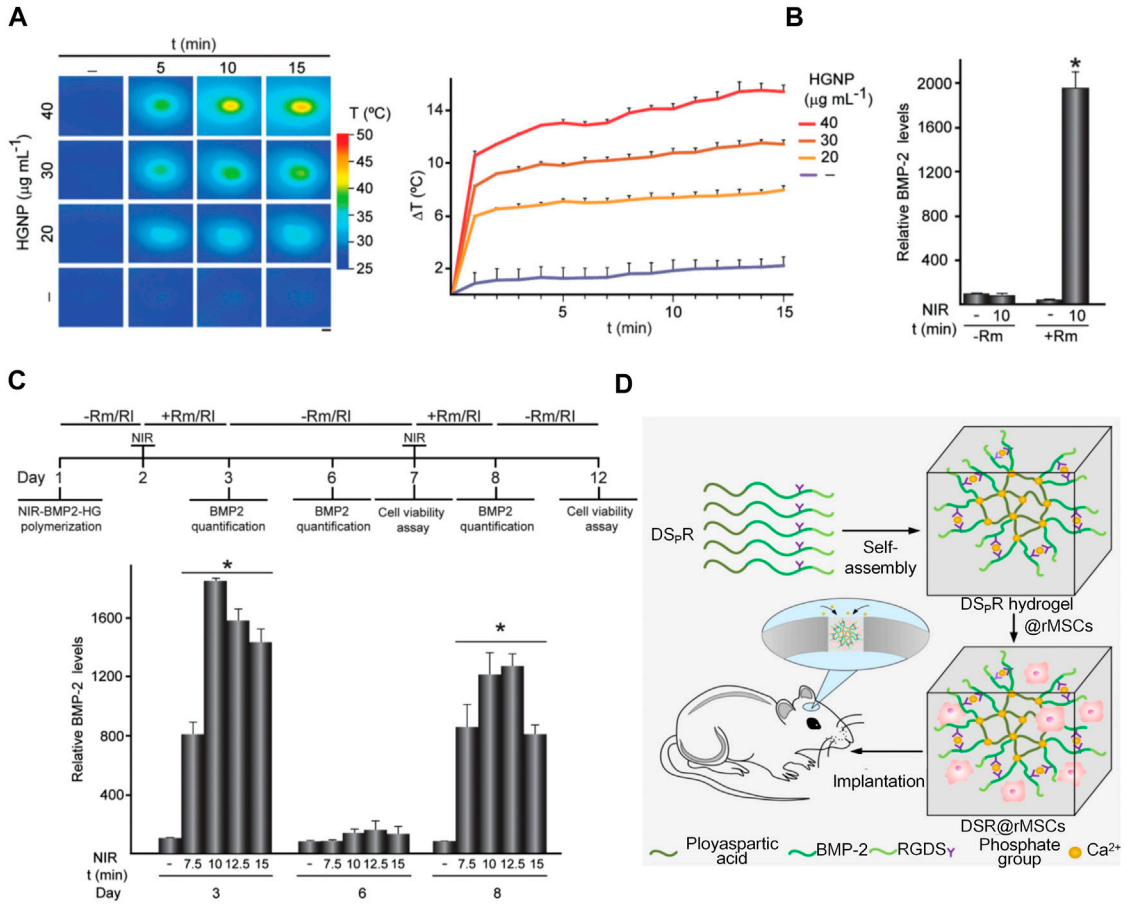

FIGURE 7
Application of hydrogels with photothermal effects and synthesis of biomietic self-assembling peptide hydrogels. **(A)**NIR-BMP-2-HG, polymerized with the indicated concentrations of HGNP, incubated for 1 day, and then irradiated with NIR laser for the indicated time. Infrared thermal image (left). The figure shows the mean +SD value of the maximum temperature rise detected during NIR irradiation (right), *n* = 3. Scale bar = 1 mm. (Pensak et al., 2015; Sanchez-Casanova et al., 2020)(Reprinted with permission) **(B)**BMP-2 concentration in media conditioned with 30 μg ml-1 HGNP-polymerized NIR-BMP-2-HG. (Pensak et al., 2015; Sanchez-Casanova et al., 2020)(Reprinted with permission) **(C)**NIR-BMP-2-HG, aggregated with 30 μg ml-1 HGNP, irradiated by NIR in the presence of 10 nM rapamycin (Rm) or 100 nM rapalog AP21967 (Rl). Timeline protocol for NIR-BMP-2-HG preparation, NIR irradiation of hydrogels (NIR), in the absence (-Rm/Rl) or presence (+Rm/Rl) of rapamycin or rapalog and analytically determined cultivated under circumstances. On days 3, 6, and 8, the medium was collected and replaced with fresh medium lacking dimers. Histograms show BMP-2 concentrations on days 3, 6, and 8 in NIR-BMP-2-HG-conditioned media that were NIR-irradiated in the presence of Rm for the indicated times (Pensak et al., 2015; Sanchez-Casanova et al., 2020)(Reprinted with permission). **(D)**Illustration of a 3D bioactive gel scaffold of self-assembled DSpR oligopeptides for repairing rat calvarial defects. (Quan et al., 2019)(Reprinted with permission).

factors that synergistically promote bone regeneration. RGDs and BMPMP promoted the expression of osteogenic genes and accelerated differentiation of MSCs into osteoblasts (Quan et al., 2019).

4.2.5 Conductive hydrogels

Conductive materials in hydrogels have been shown to increase osteoconductivity and mechanical strength. Gold nanoparticles (GNPs) can promote the osteogenic differentiation of MSCs, which are the most valuable substance for bone regeneration. Heo al. used GNPs to synthesize biodegradable hydrogels to promote osteogenesis (Heo et al., 2014). In animal experiments, conductive GNP hydrogels significantly increased osteoblastic activity, proliferation, and bone formation. Conductive fibers were incorporated into hydrogels using graphene nanoparticles and polyaniline to increase their elastic modulus, roughness, and electrical conductivity (Khorshidi and Karkhaneh, 2018). Ezazi designed a bone hydrogel and its main composition are hydroxyapatite, gelatin, and mesoporous silica. Incorporating PPy macromolecules into this hydrogel can provide electrical conductivity; PPy-containing supports exhibit superior mechanical properties than non-conductive supports (Ezazi et al., 2018).

4.3 Osteogenic mechanisms associated with drug delivery

Subset 3 covered research on drug delivery in the field of BRMs. From 2002 to 2011, researchers focused on applying three-dimensional scaffolds to drug delivery in bone tissue engineering. After 2012, the research hotspots were mainly the following: 1) Bone tissue engineering and growth factor delivery; 2) Nanobiomaterials used as delivery systems to promote osteogenesis *in vivo*; 3) the potential of *in vivo* exosomal delivery in articular cartilage regeneration, and 4)Autologous platelet-rich fibrin as a drug for bone regeneration.

4.3.1 Application of three-dimensional scaffolds in drug delivery

From 2002 to 2011, widely developed three-dimensional bioactive scaffolds were studied as potential delivery systems for therapeutic drugs that promote bone repair. The main scaffold materials include ceramics, polymers, and composites. As a synthetic bioactive ceramic, CaP (HA, α-tricalcium phosphate (TCP)) has structural and chemical properties similar to the inorganic components of bone and thus has been widely studied as a scaffold material (Karageorgiou and Kaplan, 2005). The rapid development of mesoporous inorganic materials has accelerated the development of composite materials with drug delivery and osteogenic capabilities. Natural polymers, including collagen and polysaccharides (e.g., alginate, hyaluronic acid, and chitosan), have excellent biocompatibility and promote osteogenesis (Mi et al., 2002; Shanmugasundaram et al., 2006; Aoyagi et al., 2007). Composite scaffolds have combined properties of biodegradable polymers and bioactive materials for osteogenesis, which are essentially composite materials with improved mechanical properties. Rezwan K. showed that bioactive inorganic particles such as HA, bioglass, or tricalcium phosphate form strong bonds throughout the growing carbonate HA layer, thereby inducing an efficient interaction between the scaffold and the surrounding bone tissue (Rezwan et al., 2006).

4.3.2 Bone tissue engineering and growth factor delivery

Osteoinductive growth factors such as transforming growth factors (TGF-β) have long been shown to promote bone healing and regulate osteogenesis. Behavioral potentials include recruitment, migration, adhesion, proliferation, and differentiation (Termaat et al., 2005; Bessa et al., 2008; Khojasteh et al., 2013). BMP-2, BMP-6, and BMP-9 can trigger MSC differentiation to stimulate local bone regeneration in osteoblasts (Tong et al., 2019). The delivery of GF relies on polymer scaffolds or composite scaffolds; Linh et al. bound the natural collagen polymers and BMP-2 to the surface of porous HAp scaffolds and found that the composite scaffolds showed higher compressive strength (50.7 MPa) than the HAp scaffolds (45.8 MPa) (Linh et al., 2020). The delivery system produced using this scaffold can effectively induce osteogenic differentiation of adipose-derived stem cells (Walsh et al., 2019).

4.3.3 Nanobiomaterials for bone tissue engineering

Nano-hydroxyapatite (nHA) is widely used as a drug delivery vehicle because of its chemical and structural similarities to bone minerals (Teotia et al., 2017). Several studies have shown that the osteogenic properties of nHA can be improved when combined with other bioactive molecules or drugs. Curtin et al. found that defects implanted with nHA scaffolds containing only BMP-2 or both BMP-2 and bFGF showed higher rates of new bone formation than defects implanted with nHA scaffolds alone (Curtin et al., 2015; Zaffarin, 2021). Raina's and Teotia's teams researched the co-delivery of BMP-2 and zoledronic acid by using nano cement whose principal component is nHA; their results revealed that the nanomaterials combined with BMP-2 accelerated osteogenesis (Tran et al., 2014; Teotia et al., 2017).

4.3.4 Potential of *in vivo* exosomal delivery to promote bone regeneration

Exosomes can be derived from various cellsl. However, Most studies choose to extract exosomes from MSCs because MSCs play a significant role in the field of bone tissue repair and osteogenesis (Maas et al., 2017; Cai et al., 2020) (Figure 8). Direct injection is the most widely used delivery method, while the use of scaffolds for exosomal delivery is relatively less studied. Liu et al. (2017b) found that combining exosomes with biomaterials (such as hydrogels) can produce a synergistic effect. Furthermore, they found that compared with *in situ* hydrogel gel implantation and iPSC-MSC-derived exosome injection, iPSC-MSC-derived exosomes implanted into *in situ* hydrogels are more effective in promoting cartilage regeneration (Figure 8).

4.3.5 Autologous platelet-rich Fibrin for osteogenesis

Platelet-rich fibrin (PRF), which can be extracted from a person's blood, is an easily produced autologous material that promotes wound healing and tissue regeneration. Platelet concentrates also contain growth factors and host immune cells that promote osteogenesis and repair. I-PRF, a recently introduced platelet concentrate, is a liquid injectable PRF that can be added to drugs and drug delivery systems before coagulation (Kour, 2018). A-PRF, on the other hand, is a PRF prepared in the form of a clot; in the A-PRF prepared by Choukroun's team, more neutrophils are included in the white blood cell count, ensuring their ability to promote the anti-inflammatory state of macrophages, as well as tissue regeneration and angiogenesis (Cabaro et al., 2018; Caruana et al., 2019). PRF can be used as a carrier and can also be combined with other materials to play a role. In one study, freshly

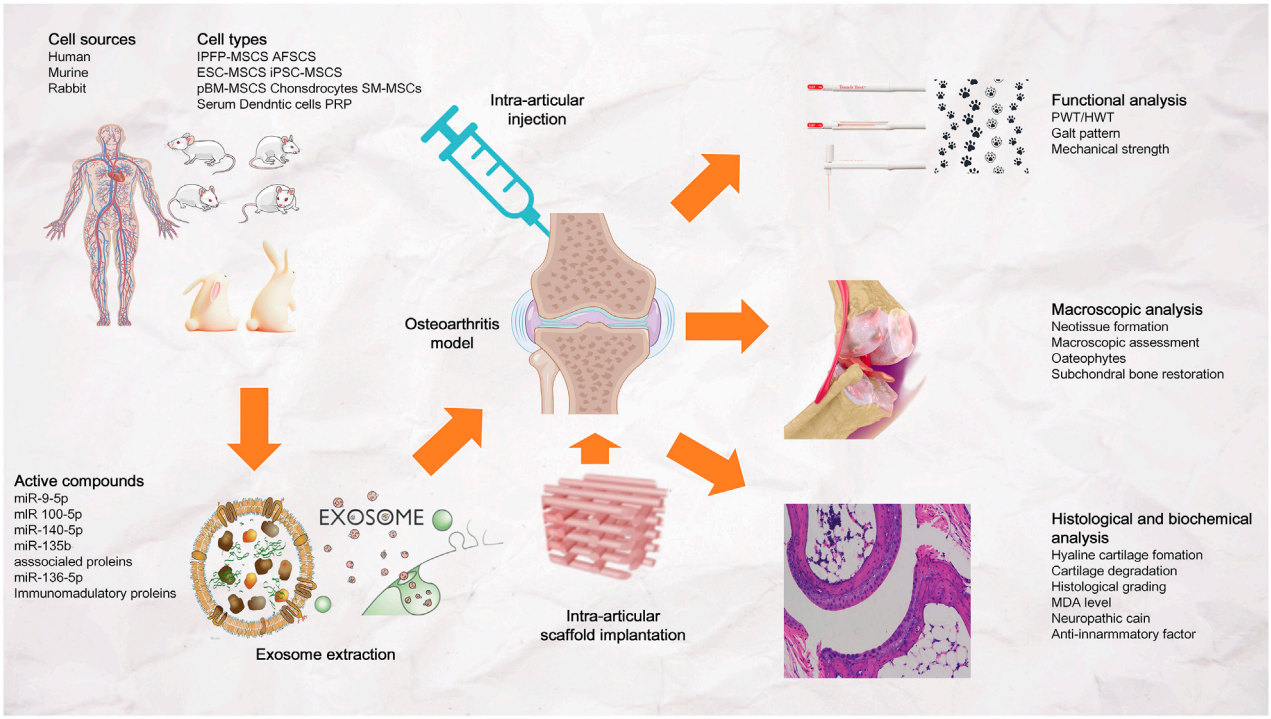

FIGURE 8
Exosomal bioactive compounds play an important role in cartilage and subchondral bone repair and regeneration. The exosomes were derived from human, murine or rabbit amniotic fluid stem cells (AFSCs), embryonic stem cell-derived mesenchymal stem/stromal cells (ESC-MSCs), induced pluripotent stem cell-derived MSCs (iPSC-MSCs), bone marrow-derived MSCs (BM-MSCs), polydactyly BM-MSCs, synovial membrane-derived MSCs (SM-MSCs), infrapatellar fat pad-derived MSCs (IPFP-MSCs), umbilical cord-derived MSCs (UC-MSCs), chondrocytes, dendritic cells, platelet rich plasma (PRP) and serum. Exosomes were administered to osteoarthritis joints by intra-articular injection or stent implantation.

pelleted lyophilized platelet-rich fibrin (GL-PRF) was incorporated into polyvinyl alcohol (PVA) hydrogels for sustained release of up to 9 days from GL-PRF/PVA scaffolds. This finding is important because the controlled release of growth factors promotes bone tissue healing and osteogenesis (Xu et al., 2018).

4.4 Three-dimensional printing technology

Three-dimensional printing is an essential component of additive manufacturing (AM). Compared with conventional techniques, 3D printing can provide better therapeutic effects and more optimized material properties in clinical applications (Raisian et al., 2017; Simoneti et al., 2022). Several commonly used 3D printing technologies are as listed: 1) Fused deposition modeling (FDM), in which the wire-like hot-melt material is delivered to the hot-melt printing nozzle through a wire feeding mechanism, and the material is heated to a molten state in the nozzle. Under the control of a computer, the nozzle follows the shape contour of the part and the trajectory such that it is deposited in the desired location and then solidifies. (101-102) It can not only improve the biocompatibility and osteoconductivity of scaffolds but can also print personalized scaffolds with different porosities and pore sizes to adapt to the growth and differentiation of stem cells (Gremare et al., 2018; Tian et al., 2020); 2) Stereolithography (SLA), which uses photocurable resins to prepare printed structures. In the SLA equipment, the bottom of the structure is formed by polymerization on the top surface of a moving platform, and the thin layers are aggregated into a two-dimensional pattern drawn by a guided laser beam. Subsequently, the fabrication platform lowers the pattern on top of the upper layer of the polymer to form the desired structure (Su et al., 2021). Studies have shown that the surface modification of SLA implants with Sr nanostructures has a favorable effect on osteoblast function, thereby enhancing osseointegration outcomes (Choi and Park, 2018). 3) PolyJets are similar to FDM and SLA; they work by printing parts one layer at a time using an extruder nose, depositing tiny droplets of a selected photopolymer material on a bed, which is then cured with UV light. Researchers added a polydopamine (PDA)/hydroxyapatite (HA) coating to printed MED610 subjects and found that the PDA/HA coating improved

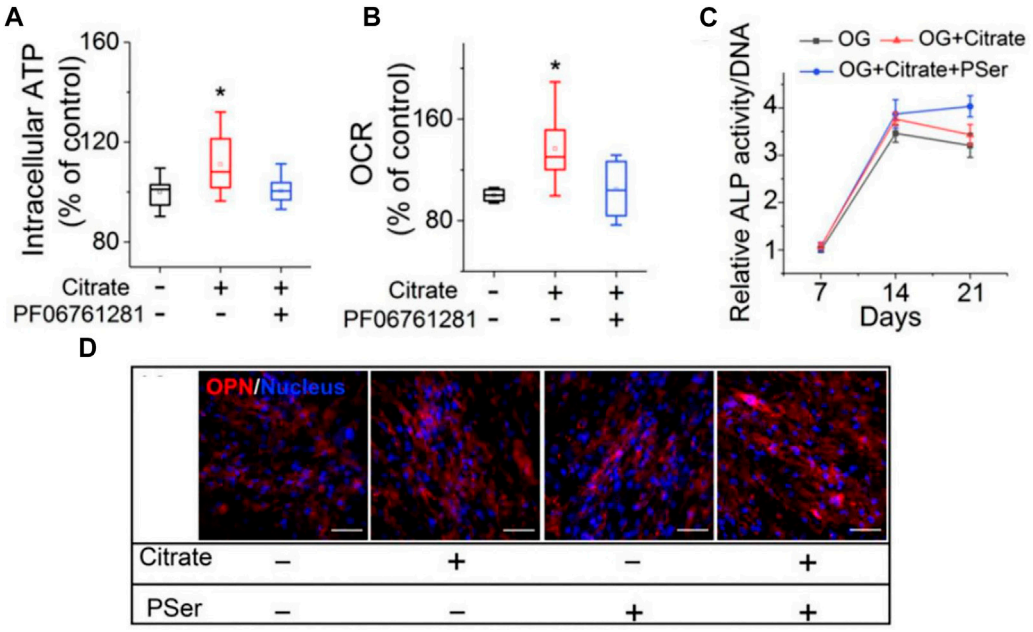

FIGURE 9
Citrate promotes osteogenesis by regulating metabolism. **(A)**Intracellular ATP assay. **(B)**OCR study. **(C)**ALP production of differentiated hMSCs after 7, 14 and 21 days of differentiation in OG medium supplemented with citrate or citrate and PSer. $n = 4$ biological replicates per group; all data are presented as mean ± SD; $^*p < 0.05$. **(D)**Immunofluorescence staining of OPN (red) with DAPI nuclear counterstain (blue) expression after 21 days of differentiation in OG medium supplemented with citrate, PSer, or both. Plus (+) and minus (–) signs indicate the presence and absence, respectively, of citrate and other specific chemicals in GM/OG medium. (Huard et al., 2015; Ma et al., 2018)(Reprinted with permission).

scaffold stiffness, biocompatibility, and osteogenic differentiation potential (Chen et al., 2019; Su et al., 2021).

4.5 Citrate for the development of biomimetic composites

In addition to the materials outlined above, citrate is also frequentlyapplied in the development of biomimetic composites for osteogenesis. CBPBHA composites are synthesized based on cross-linked urethane doped polyester (CUPE), polyoctane citrate (POC), and hydroxyapatite (HA). The main synthesis steps are as follows: 1) POC and CUPE premixes were combined to synthesis a homogeneous citrate-based polymer blend (CBPB); 2) various CBPBs were mixed with HA and incubated in Teflon preheated to 50°C to aid solvent evaporation; 3) then, the composites were post-polymerized for 5 days to synthesize cross-linked CBPBHA-X composites (Tran et al., 2014). Richard T et al. implanted CBPBHA-100 and CBPBHA-90 cylindrical composites into the lateral femoral condyle of rabbit knees. Six weeks after implantation, micro-CT images clearly showed the complete fusion of the implant with the surrounding new bone tissue (Tran et al., 2014). Studies have also shown that citrate-based materials can fuel bone regeneration by regulating metabolism to fuel human stem cells. Ma et al. (2018) investigated the expression of the citrate plasma membrane transporter SLC13a5 before and after the osteogenesis of hMSCs. SLC13a5 was found to be the most expressed in undifferentiated and early differentiated hMSCs, and gradually decreased after 4 days of differentiation. Importantly, the addition of the SLC13a5 inhibitor PF06761281 abolished the citrate-induced increase in alkaline phosphatase (ALP) production. Thus, citrate can enhance the bone phenotype through SLC13a5 (Huard et al., 2015).

Citrate can also increase intracellular ATP through metabolic regulation. In a study by Chuying Ma, hMSCs exhibited elevated intracellular ATP levels (Figure 9A) after 24 h of citrate treatment and increased the oxygen consumption rate (OCR) (Figure 9B) (Ma et al., 2018). At the same time, Chuying Ma also found an interesting phenomenon in the experiment: dual treatment with citrate and PSer (a rich functional part of the non-collagen protein (NCP) of the natural bone) had the most obvious bone-promoting effect in the late stage of osteogenesis, and the maintenance is high. Furthermore, in the dual treatment group, the ALP and OPN levels increased until day 21, whereas the ALP levels decreased in the citrate-only treatment and control groups (Park et al., 2011; Ying et al., 2014; Ma et al., 2018) (Figures 9C,D). The research and application of citrate in bone tissue engineering have become a hot topic in recent years. This article focuses only on the tip of the iceberg; the application of such materials in bone tissue engineering is expected to soar in the future.

4.6 Limitations

The present study has several limitations. The bibliometric analysis was only based on documents available in WOS. Despite the wide coverage of the WOS database (which is highly similar to that of the Scopus database), we cannot exclude the potential impact on the integrated analysis of the lack of documents from other sources such as the Scopus database. Second, the research topic of bone regenerative biomaterials contains multiple medical disciplines. As only few search terms were used to identify the relevant studies, and only some types of documents were included in the analysis, some potentially valuable documents may have been dismissed.

Data availability statement

The raw data supporting the conclusions of this article will be made available by the authors, without undue reservation.

Author contributions

Conceptualization: XZ; Methodology: XZ; Formal analysis and investigation: XuZ, QL, ZW; Writing—original draft preparation: XuZ; Writing—review and editing: ZW, QL, WZ, LZ, YL, ZX; Resources: XZ, ZL; Supervision: CZ.

Funding

This work was supported by the National Natural Science Foundation of China (Grant No. 81871788 and No. 82202672), the Key Research and Development Program of Anhui Province (No. 202004j07020013 and 2022e07020017), the Natural Science Foundation of Anhui Province (Grant No. 2108085QH319), the Fundamental Research Funds for the Central Universities (Grant No. WK9110000173 and WK9110000161).

Conflict of interest

The authors declare that the research was conducted in the absence of any commercial or financial relationships that could be construed as a potential conflict of interest.

Publisher's note

All claims expressed in this article are solely those of the authors and do not necessarily represent those of their affiliated organizations, or those of the publisher, the editors and the reviewers. Any product that may be evaluated in this article, or claim that may be made by its manufacturer, is not guaranteed or endorsed by the publisher.

Supplementary material

The Supplementary Material for this article can be found online at: https://www.frontiersin.org/articles/10.3389/fbioe.2022.921092/full#supplementary-material

SUPPLEMENTARY FIGURE.S1
Flowchart for document processing and measurement.

References

Aoyagi, S., Onishi, H., and Machida, Y. (2007). Novel chitosan wound dressing loaded with minocycline for the treatment of severe burn wounds. *Int. J. Pharm. X.* 330 (1-2), 138–145. doi:10.1016/j.ijpharm.2006.09.016

Aplin, A. E., Hogan, B. P., Tomeu, J., and Juliano, R. L. (2002). Cell adhesion differentially regulates the nucleocytoplasmic distribution of active MAP kinases. *J. Cell Sci.* 115, 2781–2790. doi:10.1242/jcs.115.13.2781

Ben-Ari, A. (2009). Isolation and implantation of bone marrow-derived mesenchymal stem cells with fibrin micro beads to repair a critical-size bone defect in mice. *Tissue Eng. Part A* 15 (9), 2537–2546. doi:10.1089/ten.tea.2008.0567

Bernhard, J., Ferguson, J., Rieder, B., Heimel, P., Nau, T., Tangl, S., et al. (2017). Tissue-engineered hypertrophic chondrocyte grafts enhanced long bone repair. *Biomaterials* 139, 202–212. doi:10.1016/j.biomaterials.2017.05.045

Bessa, P. C., Casal, M., and Reis, R. L. (2008). Bone morphogenetic proteins in tissue engineering: The road from laboratory to clinic, part II (BMP delivery). *J. Tissue Eng. Regen. Med.* 2 (2-3), 81–96. doi:10.1002/term.74

Birlea, S. A., Costin, G. E., Roop, D. R., and Norris, D. A. (2017). Trends in regenerative medicine: Repigmentation in vitiligo through melanocyte stem cell mobilization. *Med. Res. Rev.* 37 (4), 907–935. doi:10.1002/med.21426

Borrelli, M. R., Hu, M. S., Longaker, M. T., and Lorenz, H. P. (2020). Tissue engineering and regenerative medicine in craniofacial reconstruction and facial aesthetics. *J. Craniofac. Surg.* 31 (1), 15–27. doi:10.1097/scs.0000000000005840

Bryant, S. J., Durand, K. L., and Anseth, K. S. (2003). Manipulations in hydrogel chemistry control photoencapsulated chondrocyte behavior and their extracellular matrix production. *J. Biomed. Mat. Res. A* 67A, 1430–1436. doi:10.1002/jbm.a.20003

Burdick, J. A. (2002). Photoencapsulation of osteoblasts in injectable RGD-modified PEG hydrogels for bone tissue engineering. *Biomaterials* 23 (22), 4315–4323. doi:10.1016/s0142-9612(02)00176-x

Cabaro, S., D'Esposito, V., Gasparro, R., Borriello, F., Granata, F., Mosca, G., et al. (2018). White cell and platelet content affects the release of bioactive factors in different blood-derived scaffolds. *Platelets* 29 (5), 463–467. doi:10.1080/09537104.2017.1319046

Cai, J., Wu, J., Wang, J., Li, Y., Hu, X., Luo, S., et al. (2020). Extracellular vesicles derived from different sources of mesenchymal stem cells: Therapeutic effects and translational potential. *Cell Biosci.* 10, 69. doi:10.1186/s13578-020-00427-x

Caiazza, S. (2000). Evaluation of guided bone regeneration in rabbit femur using collagen membranes. *Implant. Dent.* 9 (3), 219–225. doi:10.1097/00008505-200009030-00007

Caruana, A., Savina, D., Macedo, J. P., and Soares, S. C. (2019). From platelet-rich plasma to advanced platelet-rich fibrin: Biological achievements and clinical advances in modern surgery. *Eur. J. Dent.* 13 (2), 280–286. doi:10.1055/s-0039-1696585

Chen, F. M., and Liu, X. (2016). Advancing biomaterials of human origin for tissue engineering. *Prog. Polym. Sci.* 53, 86–168. doi:10.1016/j.progpolymsci.2015.02.004

Chen, W., Chen, S., Morsi, Y., El-Hamshary, H., El-Newhy, M., Fan, C., et al. (2016). Superabsorbent 3D scaffold based on electrospun nanofibers for cartilage

tissue engineering. *ACS Appl. Mat. Interfaces* 8 (37), 24415–24425. doi:10.1021/acsami.6b06825

Chen, Y.-W., Fang, H. Y., Shie, M. Y., and Shen, Y. F. (2019). The mussel-inspired assisted apatite mineralized on PolyJet material for artificial bone scaffold. *Int. J. Bioprint.* 5, 197. doi:10.18063/ijb.v5i2.197

Choi, S. M., and Park, J. W. (2018). Multifunctional effects of a modification of SLA titanium implant surface with strontium-containing nanostructures on immunoinflammatory and osteogenic cell function. *J. Biomed. Mat. Res. A* 106 (12), 3009–3020. doi:10.1002/jbm.a.36490

Curtin, C. M., Tierney, E. G., McSorley, K., Cryan, S. A., Duffy, G. P., and O'Brien, F. J. (2015). Combinatorial gene therapy accelerates bone regeneration: Non-viral dual delivery of VEGF and BMP2 in a collagen-nanohydroxyapatite scaffold. *Adv. Healthc. Mat.* 4 (2), 223–227. doi:10.1002/adhm.201400397

Daneshmandi, L., Barajaa, M., Tahmasbi Rad, A., Sydlik, S. A., and Laurencin, C. T. (2021). Graphene-based biomaterials for bone regenerative engineering: A comprehensive review of the field and considerations regarding biocompatibility and biodegradation. *Adv. Healthc. Mat.* 10 (1), e2001414. doi:10.1002/adhm.202001414

Deng, Z., Hu, T., Lei, Q., He, J., Ma, P. X., and Guo, B. (2019). Stimuli-Responsive conductive nanocomposite hydrogels with high stretchability, self-healing, adhesiveness, and 3D printability for human motion sensing. *ACS Appl. Mat. Interfaces* 11 (7), 6796–6808. doi:10.1021/acsami.8b20178

Dettin, M., Bagno, A., Gambaretto, R., Iucci, G., Conconi, M. T., Tuccitto, N., et al. (2009). Covalent surface modification of titanium oxide with different adhesive peptides: Surface characterization and osteoblast-like cell adhesion. *J. Biomed. Mat. Res. A* 90 (1), 35–45. doi:10.1002/jbm.a.32064

Dettin, M. (2006). Evaluation of silicon dioxide-based coating enriched with bioactive peptides mapped on human vitronectin and fibronectin: *In vitro* and *in vivo* assays. *Tissue Eng.* 12 (12), 3509–3523. doi:10.1089/ten.2006.12.3509

Ezazi, N. Z., Shahbazi, M. A., Shatalin, Y. V., Nadal, E., Makila, E., Salonen, J., et al. (2018). Conductive vancomycin-loaded mesoporous silica polypyrrole-based scaffolds for bone regeneration. *Int. J. Pharm. X.* 536, 241–250. doi:10.1016/j.ijpharm.2017.11.065

Gong, T., Xie, J., Liao, J., Zhang, T., Lin, S., and Lin, Y. (2015). Nanomaterials and bone regeneration. *Bone Res.* 3, 15029. doi:10.1038/boneres.2015.29

Gotschall, T. (2021). EndNote 20 desktop version. *J. Med. Libr. Assoc.* 109 (3), 520–522. doi:10.5195/jmla.2021.1260

Gremare, A., Guduric, V., Bareille, R., Heroguez, V., Latour, S., L'heureux, N., et al. (2018). Characterization of printed PLA scaffolds for bone tissue engineering. *J. Biomed. Mat. Res. A* 106 (4), 887–894. doi:10.1002/jbm.a.36289

Gronthos, S., Stewart, K., Graves, S. E., Hay, S., and Simmons, P. J. (1997). Integrin expression and function on human osteoblast-like cells. *J. Bone Min. Res.* 12, 1189–1197. doi:10.1359/jbmr.1997.12.8.1189

Hasan, A., Byambaa, B., Morshed, M., Cheikh, M. I., Shakoor, R. A., Mustafy, T., et al. (2018). Advances in osteobiologic materials for bone substitutes. *J. Tissue Eng. Regen. Med.* 12 (6), 1448–1468. doi:10.1002/term.2677

Heo, D. N., Ko, W. K., Bae, M. S., Lee, J. B., Lee, D. W., Byun, W., et al. (2014). Enhanced bone regeneration with a gold nanoparticle-hydrogel complex. *J. Mat. Chem. B* 2, 1584–1593. doi:10.1039/c3tb21246g

Hesse, E., Kluge, G., Atfi, A., Correa, D., Haasper, C., Berding, G., et al. (2010). Repair of a segmental long bone defect in human by implantation of a novel multiple disc graft. *Bone* 46 (5), 1457–1463. doi:10.1016/j.bone.2010.02.011

Hu, D., Lu, C., Sapozhnikova, A., Barnett, M., Sparrey, C., Miclau, T., et al. (2010). Absence of beta3 integrin accelerates early skeletal repair. *J. Orthop. Res.* 28 (1), 32–37. doi:10.1002/jor.20955

Huang, X., Liu, X., Shang, Y., Qiao, F., and Chen, G. (2020). Current trends in research on bone regeneration: A bibliometric analysis. *Biomed. Res. Int.* 2020, 1–12. doi:10.1155/2020/8787394

Huard, K., Brown, J., Jones, J. C., Cabral, S., Futatsugi, K., Gorgoglione, M., et al. (2015). Discovery and characterization of novel inhibitors of the sodium-coupled citrate transporter (NaCT or SLC13A5). *Sci. Rep.* 5, 17391. doi:10.1038/srep17391

Hussin, M. S. F., Mohd Serah, A., Azlan, K. A., Abdullah, H. Z., Idris, M. I., Ghazali, I., et al. (2021). A bibliometric analysis of the global trend of using alginate, gelatine, and hydroxyapatite for bone tissue regeneration applications. *Polym. (Basel)* 13 (4), 647. doi:10.3390/polym13040647

Hynes, R. O. (2002). Integrins: Bidirectional, allosteric signaling machines. *Cell* 110 (6), 673–687. doi:10.1016/s0092-8674(02)00971-6

Iaquinta, M. R., Mazzoni, E., Manfrini, M., D'Agostino, A., Trevisiol, L., Nocini, R., et al. (2019). Innovative biomaterials for bone regrowth. *Int. J. Mol. Sci.* 20 (3), 618. doi:10.3390/ijms20030618

Indrawattana, N., Chen, G., Tadokoro, M., Shann, L. H., Ohgushi, H., Tateishi, T., et al. (2004). Growth factor combination for chondrogenic induction from human mesenchymal stem cell. *Biochem. Biophys. Res. Commun.* 320 (3), 914–919. doi:10.1016/j.bbrc.2004.06.029

Kačarević, Ž. P., Rider, P., Alkildani, S., Retnasingh, S., Pejakic, M., Schnettler, R., et al. (2020). An introduction to bone tissue engineering. *Int. J. Artif. Organs* 43, 69–86. doi:10.1177/0391398819876286

Karageorgiou, V., and Kaplan, D. (2005). Porosity of 3D biomaterial scaffolds and osteogenesis. *Biomaterials* 26 (27), 5474–5491. doi:10.1016/j.biomaterials.2005.02.002

Karp, J. M., Sarraf, F., Shoichet, M. S., and Davies, J. E. (2004). Fibrin-filled scaffolds for bone-tissue engineering: An *in vivo* study. *J. Biomed. Mat. Res.* 71 (1), 162–171. doi:10.1002/jbm.a.30147

Keselowsky, B. G. (2005). Integrin binding specificity regulates biomaterial surface chemistry effects on cell differentiation. *Proc. Natl. Acad. Sci. U. S. A.* (Suppl. 2), S325–S330. doi:10.4103/ccd.ccd_367_18

Khojasteh, A., Behnia, H., Naghdi, N., Esmaeelinejad, M., Alikhassy, Z., and Stevens, M. (2013). Effects of different growth factors and carriers on bone regeneration: A systematic review. *Oral Surg. Oral Med. Oral Pathol. Oral Radiol.* 116 (6), e405–23. doi:10.1016/j.oooo.2012.01.044

Khorshidi, S., and Karkhaneh, A. (2018). Hydrogel/fiber conductive scaffold for bone tissue engineering. *J. Biomed. Mat. Res. A* 106, 718–724. doi:10.1002/jbm.a.36282

Kim, S. J., Jang, J. D., and Lee, S. K. (2007). Treatment of long tubular bone defect of rabbit using autologous cultured osteoblasts mixed with fibrin. *Cytotechnology* 54 (2), 115–120. doi:10.1007/s10616-007-9084-1

Kour, P. (2018). Comparative evaluation of antimicrobial efficacy of platelet-rich plasma, platelet-rich fibrin, and injectable platelet-rich fibrin on the standard strains of porphyromonas gingivalis and aggregatibacter actinomycetemcomitans. *Contemp. Clin. Dent.* 11 (8), 745–746. doi:10.2217/rme-2016-0500

Kurkalli, B. G. S., Gurevitch, O., Sosnik, A., Cohn, D., and Slavin, S. (2010). Repair of bone defect using bone marrow cells and demineralized bone matrix supplemented with polymeric materials. *Curr. Stem Cell Res. Ther.* 5, 49–56. doi:10.2174/157488810790442831

Lanza, R. (2016). Regenerative medicine: The last 10 years. *Regen Med.* 21 (11), 1145–1153. doi:10.1016/s0142-9612(99)00280-x

Lee, J., Byun, H., Madhurakkat Perikamana, S. K., Lee, S., and Shin, H. (2019). Current advances in immunomodulatory biomaterials for bone regeneration. *Adv. Healthc. Mat.* 8 (4), e1801106. doi:10.1002/adhm.201801106

Lee, S. J., Nowicki, M., Harris, B., and Zhang, L. G. (2017). Fabrication of a highly aligned neural scaffold via a table top Stereolithography 3D printing and electrospinning. *Tissue Eng. Part A* 23 (11-12), 491–502. doi:10.1089/ten.tea.2016.0353

Li, D., Nie, W., Chen, L., McCoul, D., Liu, D., Zhang, X., et al. (2018). Self-assembled hydroxyapatite-graphene scaffold for photothermal cancer therapy and bone regeneration. *J. Biomed. Nanotechnol.* 14, 2003–2017. doi:10.1166/jbn.2018.2646

Liao, J., Shi, K., Jia, Y., Wu, Y., and Qian, Z. (2021). Gold nanorods and nanohydroxyapatite hybrid hydrogel for preventing bone tumor recurrence via postoperative photothermal therapy and bone regeneration promotion. *Bioact. Mat.* 6, 2221–2230. doi:10.1016/j.bioactmat.2021.01.006

Lima-Sousa, R., de Melo-Diogo, D., Alves, C. G., Cabral, C. S., Miguel, S. P., Mendonca, A. G., et al. (2020). Injectable *in situ* forming thermo-responsive graphene based hydrogels for cancer chemo-photothermal therapy and NIR light-enhanced antibacterial applications. *Mater. Sci. Eng. C* 117, 111294. doi:10.1016/j.msec.2020.111294

Linh, N. T. B., Abueva, C. D. G., Jang, D., and Lee, B. (2020). Collagen and bone morphogenetic protein-2 functionalized hydroxyapatite scaffolds induce osteogenic differentiation in human adipose-derived stem cells. *J. Biomed. Mat. Res.* 108 (4), 1363–1371. doi:10.1002/jbm.b.34485

Liu, M., Zeng, X., Ma, C., Yi, H., Ali, Z., Mou, X., et al. (2017). Injectable hydrogels for cartilage and bone tissue engineering. *Bone Res.* 5, 17014. doi:10.1038/boneres.2017.14

Liu, X., Yang, Y., Li, Y., Niu, X., Zhao, B., Wang, Y., et al. (2017). Integration of stem cell-derived exosomes with *in situ* hydrogel glue as a promising tissue patch for articular cartilage regeneration. *Nanoscale* 9 (13), 4430–4438. doi:10.1039/c7nr00352h

Ma, C., Tian, X., Kim, J. P., Xie, D., Ao, X., Shan, D., et al. (2018). Citrate-based materials fuel human stem cells by metabonegenic regulation. *Proc. Natl. Acad. Sci. U. S. A.* 115 (50), E11741–E11750. doi:10.1073/pnas.1813000115

Maas, S. L. N., Breakefield, X. O., and Weaver, A. M. (2017). Extracellular vesicles: Unique intercellular delivery vehicles. *Trends Cell Biol.* 27 (3), 172–188. doi:10.1016/j.tcb.2016.11.003

Maegawa, N., Kawamura, K., Hirose, M., Yajima, H., Takakura, Y., and Ohgushi, H. (2007). Enhancement of osteoblastic differentiation of mesenchymal stromal cells cultured by selective combination of bone morphogenetic protein-2 (BMP-2) and fibroblast growth factor-2 (FGF-2). *J. Tissue Eng. Regen. Med.* 1 (4), 306–313. doi:10.1002/term.41

Martino, M. M., Mochizuki, M., Rothenfluh, D. A., Rempel, S. A., Hubbell, J. A., and Barker, T. H. (2009). Controlling integrin specificity and stem cell differentiation in 2D and 3D environments through regulation of fibronectin domain stability. *Biomaterials* 30 (6), 1089–1097. doi:10.1016/j.biomaterials.2008.10.047

Matai, I., Kaur, G., Soni, S., Sachdev, A., and Mishra, S. (2020). Near-infrared stimulated hydrogel patch for photothermal therapeutics and thermoresponsive drug delivery. *J. Photochem. Photobiol. B* 210, 111960. doi:10.1016/j.jphotobiol.2020.111960

Mauck, R. L., Yuan, X., and Tuan, R. S. (2006). Chondrogenic differentiation and functional maturation of bovine mesenchymal stem cells in long-term agarose culture. *Osteoarthr. Cartil.* 14 (2), 179–189. doi:10.1016/j.joca.2005.09.002

Mi, F. L., Wu, Y. B., Shyu, S. S., Schoung, J. Y., Huang, Y. B., Tsai, Y. H., et al. (2002). Control of wound infections using a bilayer chitosan wound dressing with sustainable antibiotic delivery. *J. Biomed. Mat. Res.* 59 (3), 438–449. doi:10.1002/jbm.1260

Moursi, A. M., Globus, R. K., and Damsky, C. H. (1997). Interactions between integrin receptors and fibronectin are required for calvarial osteoblast differentiation *in vitro*. *J. Cell Sci.* 110 (18), 2187–2196. doi:10.1242/jcs.110.18.2187

Nuttelman, C. R., Tripodi, M. C., and Anseth, K. S. (2005). Synthetic hydrogel niches that promote hMSC viability. *Matrix Biol.* 24 (3), 208–218. doi:10.1016/j.matbio.2005.03.004

Park, J. W., Kim, Y. J., Jang, J. H., and An, C. H. (2011). MC3T3-E1 cell differentiation and *in vivo* bone formation induced by phosphoserine. *Biotechnol. Lett.* 33 (7), 1473–1480. doi:10.1007/s10529-011-0565-0

Pensak, M., Hong, S., Dukas, A., Tinsley, B., Drissi, H., Tang, A., et al. (2015). The role of transduced bone marrow cells overexpressing BMP-2 in healing critical-sized defects in a mouse femur. *Gene Ther.* 22 (6), 467–475. doi:10.1038/gt.2015.14

Perka, C. (2000). *Segmental bone repair by tissue-engineered periosteal cell transplants with bioresorbable fleece and fibrin scaffolds in rabbits*. Biomaterials. 21 (11), 1145–1153. doi:10.1016/s0142-9612(99)00280-x

Pina, S., Oliveira, J. M., and Reis, R. L. (2015). Natural-based nanocomposites for bone tissue engineering and regenerative medicine: A review. *Adv. Mat.* 27 (7), 1143–1169. doi:10.1002/adma.201403354

Quan, C., Zhang, Z., Liang, P., Zheng, J., Wang, J., Hou, Y., et al. (2019). Bioactive gel self-assembled from phosphorylate biomimetic peptide: A potential scaffold for enhanced osteogenesis. *Int. J. Biol. Macromol.* 121, 1054–1060. doi:10.1016/j.ijbiomac.2018.10.148

Raisian, S., Fallahi, H. R., Khiabani, K. S., Heidarizadeh, M., and Azdoo, S. (2017). Customized titanium mesh based on the 3D printed model vs. Manual intraoperative bending of titanium mesh for reconstructing of orbital bone fracture: A randomized clinical trial. *Rev. Recent Clin. Trials* 12 (3), 154–158. doi:10.2174/1574887112666170821165206

Rammelt, S., Illert, T., Bierbaum, S., Scharnweber, D., Zwipp, H., and Schneiders, W. (2006). Coating of titanium implants with collagen, RGD peptide and chondroitin sulfate. *Biomaterials* 27 (32), 5561–5571. doi:10.1016/j.biomaterials.2006.06.034

Rapuano, B. E., Wu, C., and MacDonald, D. E. (2004). Osteoblast-like cell adhesion to bone sialoprotein peptides. *J. Orthop. Res.* 22, 353–361. doi:10.1016/s0736-0266(03)00180-3

Rezwan, K., Chen, Q., Blaker, J., and Boccaccini, A. R. (2006). Biodegradable and bioactive porous polymer/inorganic composite scaffolds for bone tissue engineering. *Biomaterials* 27 (18), 3413–3431. doi:10.1016/j.biomaterials.2006.01.039

Sanchez-Casanova, S., Martin-Saavedra, F. M., Escudero-Duch, C., Falguera Uceda, M. I., Prieto, M., Arruebo, M., et al. (2020). Local delivery of bone morphogenetic protein-2 from near infrared-responsive hydrogels for bone tissue regeneration. *Biomaterials* 241, 119909. doi:10.1016/j.biomaterials.2020.119909

Sargeant, T. D., Aparicio, C., Goldberger, J. E., Cui, H., and Stupp, S. I. (2012). Mineralization of peptide amphiphile nanofibers and its effect on the differentiation of human mesenchymal stem cells. *Acta Biomater.* 8 (7), 2456–2465. doi:10.1016/j.actbio.2012.03.026

Scotti, C., Tonnarelli, B., Papadimitropoulos, A., Scherberich, A., Schaeren, S., Schauerte, A., et al. (2010). Recapitulation of endochondral bone formation using human adult mesenchymal stem cells as a paradigm for developmental engineering. *Proc. Natl. Acad. Sci. U. S. A.* 107 (16), 7251–7256. doi:10.1073/pnas.1000302107

Shanmugasundaram, N., Sundaraseelan, J., Uma, S., Selvaraj, D., and Babu, M. (2006). Design and delivery of silver sulfadiazine from alginate microspheres-impregnated collagen scaffold. *J. Biomed. Mat. Res.* 77 (2), 378–388. doi:10.1002/jbm.b.30405

Shekaran, A., and Garcia, A. J. (2011). Extracellular matrix-mimetic adhesive biomaterials for bone repair. *J. Biomed. Mat. Res. A* 96 (1), 261–272. doi:10.1002/jbm.a.32979

Simmons, P., McElroy, T., and Allen, A. R. (2020). A bibliometric review of artificial extracellular matrices based on tissue engineering technology literature: 1990 through 2019. *Mater. (Basel)* 13 (13), 2891. doi:10.3390/ma13132891

Simoneti, D. M., Pereira-Cenci, T., and Dos Santos, M. B. F. (2022). Comparison of material properties and biofilm formation in interim single crowns obtained by 3D printing and conventional methods. *J. Prosthet. Dent.* 127 (1), 168–172. doi:10.1016/j.prosdent.2020.06.026

Su, X., Wang, T., and Guo, S. (2021). Applications of 3D printed bone tissue engineering scaffolds in the stem cell field. *Regen. Ther.* 16, 63–72. doi:10.1016/j.reth.2021.01.007

Subramanian, A., Krishnan, U. M., and Sethuraman, S. (2011). Fabrication of uniaxially aligned 3D electrospun scaffolds for neural regeneration. *Biomed. Mat.* 6 (2), 025004. doi:10.1088/1748-6041/6/2/025004

Suckow, M. A., Voytik-Harbin, S. L., Terril, L. A., and Badylak, S. F. (1999). Enhanced bone regeneration using porcine small intestinal submucosa. *J. Invest. Surg.* 12, 277–287. doi:10.1080/089419399272395

Takeuchi, Y., SuzawaM.Kikuchi, T., Nishida, E., FujiTa, T., and MaTsumoTo, T. (1997). Differentiation and transforming growth factor-beta receptor down-regulation by collagen-alpha2beta1 integrin interaction is mediated by focal adhesion kinase and its downstream signals in murine osteoblastic cells. *J. Biol. Chem.* 272, 29309–29316. doi:10.1074/jbc.272.46.29309

Tamura, Y., Takeuchi, Y., Suzawa, M., Fukumoto, S., Kato, M., Miyazono, K., et al. (2001). Focal adhesion kinase activity is required for bone morphogenetic protein--Smad1 signaling and osteoblastic differentiation in murine MC3T3-E1 cells. *J. Bone Min. Res.* 16, 1772–1779. doi:10.1359/jbmr.2001.16.10.1772

Teotia, A. K., Raina, D. B., Singh, C., Sinha, N., Isaksson, H., Tagil, M., et al. (2017). Nano-hydroxyapatite bone substitute functionalized with bone active molecules for enhanced cranial bone regeneration. *ACS Appl. Mat. Interfaces* 9 (8), 6816–6828. doi:10.1021/acsami.6b14782

Termaat, M. F., Den Boer, F. C., Bakker, F. C., Patka, P., and Haarman, H. J. T. M. (2005). Bone morphogenetic proteins. Development and clinical efficacy in the treatment of fractures and bone defects. *J. Bone Jt. Surg. Am.* 87, 1367–1378. doi:10.2106/JBJS.D.02585

Tian, L., Zhang, Z., Tian, B., Zhang, X., and Wang, N. (2020). Study on antibacterial properties and cytocompatibility of EPL coated 3D printed PCL/HA composite scaffolds. *RSC Adv.* 10, 4805–4816. doi:10.1039/c9ra10275b

Toh, W. S., Liu, H., Heng, B. C., Rufaihah, A. J., Ye, C. P., and Cao, T. (2005). Combined effects of TGFβ1 and BMP2 in serum-free chondrogenic differentiation of mesenchymal stem cells induced hyaline-like cartilage formation. *Growth factors.* 23 (4), 313–321. doi:10.1080/08977190500252763

Tong, Z., Guo, J., Glen, R. C., Morrell, N. W., and Li, W. (2019). A bone morphogenetic protein (BMP)-derived peptide based on the type I receptor-binding site modifies cell-type dependent BMP signalling. *Sci. Rep.* 9 (1), 13446. doi:10.1038/s41598-019-49758-x

Tran, R. T., Wang, L., Zhang, C., Huang, M., Tang, W., Zhang, C., et al. (2014). Synthesis and characterization of biomimetic citrate-based biodegradable composites. *J. Biomed. Mat. Res. A* 102 (8), 2521–2532. doi:10.1002/jbm.a.34928

Trohatou, O., and Roubelakis, M. G. (2017). Mesenchymal stem/stromal cells in regenerative medicine: Past, present, and future. *Cell. Reprogr.* 19 (4), 217–224. doi:10.1089/cell.2016.0062

Walsh, D. P., Raftery, R. M., Chen, G., Heise, A., O'Brien, F. J., and Cryan, S. (2019). Rapid healing of a critical-sized bone defect using a collagen-hydroxyapatite scaffold to facilitate low dose, combinatorial growth factor delivery. *J. Tissue Eng. Regen. Med.* 13 (10), 1843–1853. doi:10.1002/term.2934

Xiao, G. (2000). *MAPK Pathw. activate phosphorylate osteoblast-specific Transcr. factor, Cbfa1J Biol Chem* 75 (6), 4453–4459. doi:10.1074/jbc.275.6.4453

Xiao, G., Wang, D., Benson, M. D., Karsenty, G., and Franceschi, R. T. (1998). Role of the alpha2-integrin in osteoblast-specific gene expression and activation of the Osf2 transcription factor. *J. Biol. Chem.* 273, 32988–32994. doi:10.1074/jbc.273.49.32988

Xu, F., Zou, D., Dai, T., Xu, H., An, R., Liu, Y., et al. (2018). Effects of incorporation of granule-lyophilised platelet-rich fibrin into polyvinyl alcohol

hydrogel on wound healing. *Sci. Rep.* 8 (1), 14042. doi:10.1038/s41598-018-32208-5

Xu, W., Ma, J., and Jabbari, E. (2010). Material properties and osteogenic differentiation of marrow stromal cells on fiber-reinforced laminated hydrogel nanocomposites. *Acta Biomater.* 6 (6), 1992–2002. doi:10.1016/j.actbio.2009.12.003

Ying, X., Chen, X., Cheng, S., Guo, X., Chen, H., and Xu, H. z. (2014). Phosphoserine promotes osteogenic differentiation of human adipose stromal cells through bone morphogenetic protein signalling. *Cell Biol. Int.* 38 (3), 309–317. doi:10.1002/cbin.10203

Yu, X., Tang, X., Gohil, S. V., and Laurencin, C. T. (2015). Biomaterials for bone regenerative engineering. *Adv. Healthc. Mat.* 4 (9), 1268–1285. doi:10.1002/adhm.201400760

Zaffarin, A. S. M. (2021). *Nano-hydroxyapatite as a delivery system for promoting bone regeneration* in vivo*: A systematic review*. Nanomaterials (Basel).

Zhang, S., Chen, L., Jiang, Y., Cai, Y., Xu, G., Tong, T., et al. (2013). Bi-layer collagen/microporous electrospun nanofiber scaffold improves the osteochondral regeneration. *Acta Biomater.* 9 (7), 7236–7247. doi:10.1016/j.actbio.2013.04.003

Frontiers in
Bioengineering and Biotechnology

Accelerates the development of therapies, devices, and technologies to improve our lives

A multidisciplinary journal that accelerates the development of biological therapies, devices, processes and technologies to improve our lives by bridging the gap between discoveries and their application.

Discover the latest Research Topics

See more →

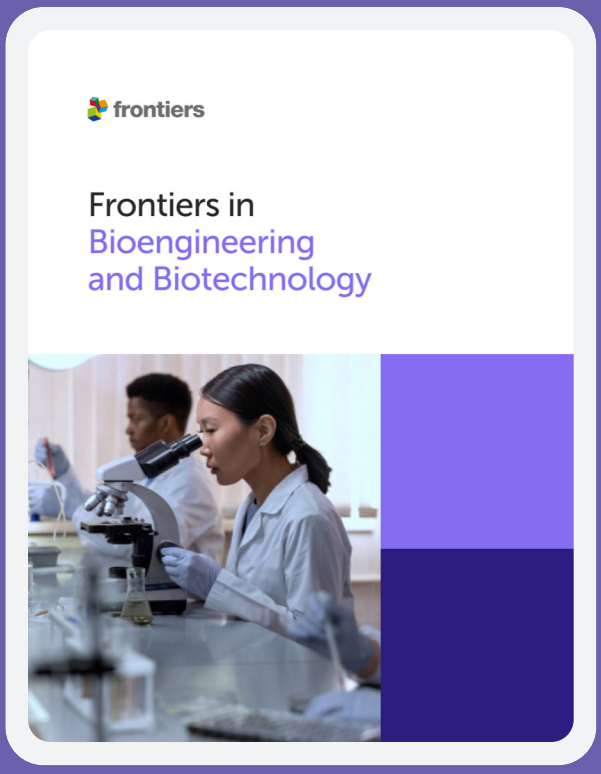

Frontiers

Avenue du Tribunal-Fédéral 34
1005 Lausanne, Switzerland
frontiersin.org

Contact us

+41 (0)21 510 17 00
frontiersin.org/about/contact